

Treball final de grau

Estudi: Grau en Tecnologies Industrials

Títol:

A RESEARCH ON CONCRETE FRACTURE MECHANICS.
TESTING AND ANALYZING THE FRACTURE ENERGY OF CONCRETE.

Document: Memòria i Annexos de l'Estudi

Alumne: Santiago Rodríguez Lorente

Tutor: Cristina Barris Peña

Departament: Enginyeria Mecànica i de la Construcció Industrial

Àrea: Enginyeria de la Construcció i de Mecànica dels Medis Continus i Teoria d'Estructures

Convocatòria (mes/any): Juny/2016

A RESEARCH ON CONCRETE FRACTURE MECHANICS

TESTING AND ANALYZING THE FRACTURE ENERGY OF CONCRETE

Written by

SANTIAGO RODRÍGUEZ LORENTE

Tutored by

CRISTINA BARRIS PEÑA

ESCOLA POLITÈCNICA SUPERIOR – UNIVERSITAT DE GIRONA

GIRONA, YEAR 2016

LIST OF CONTENTS

<u>LIST OF CONTENTS</u>	<u>I</u>
<u>LIST OF FIGURES</u>	<u>IX</u>
<u>LIST OF TABLES</u>	<u>XXIII</u>
<u>ACKNOWLEDGEMENTS</u>	<u>XXVII</u>
<u>ABSTRACT</u>	<u>XXVIII</u>
<u>RESUMEN</u>	<u>XXIX</u>
<u>ABBREVIATIONS AND NOTATIONS</u>	<u>XXX</u>
<u>1 INTRODUCTION</u>	<u>1</u>
1.1 BACKGROUND	1
1.2 PURPOSE OF THIS PROJECT	5
1.3 SCOPE	6
1.4 STRUCTURE	8
<u>2 FUNDAMENTALS OF FRACTURE MECHANICS IN QUASIBRITTLE MATERIALS</u>	<u>9</u>
2.1 FRACTURE MODEL APPLICABLE TO CONCRETE FRACTURE. THE COHESIVE CRACK MODEL	9
2.2 THE SOFTENING PHENOMENON IN THE FRACTURE PROCESS ZONE AND THE FRACTURE ENERGY	14
2.3 LOCAL FRACTURE ENERGY MODEL	20
<u>3 THE TEST AND PROCEDURES FOR OBTAINING THE FRACTURE ENERGY OF CONCRETE</u>	<u>23</u>
3.1 EXPERIMENTAL PROCEDURES AND THE THREE-POINT BEND TEST	23
3.2 DETERMINATION OF THE FRACTURE ENERGY OF CONCRETE. REASONS FOR THE CORRECTION	25
3.2.1 FIRST REASON: SELF-WEIGHT ACTION	26
3.2.2 SECOND REASON: SOLID BEHAVIOR	28

3.2.3	THIRD REASON: SUPPORTS AND THE TESTING MACHINE	29
3.2.4	FOURTH REASON: INCOMPLETE TEST	29
3.3	THE REAL FRACTURE ENERGY OF CONCRETE THROUGH THE TAIL CORRECTION OF THE LOAD VS. DISPLACEMENT GRAPH	30
3.3.1	A BILINEAR APPROXIMATION FOR THE SOFTENING CURVE OF CONCRETE THROUGH THE LOAD VS. DISPLACEMENT TAIL CORRECTION	34
3.4	THE REAL FRACTURE ENERGY OF CONCRETE THROUGH THE LOCAL FRACTURE ENERGY THEORY	36
4	<u>MATERIALS, SPECIMENS AND TESTS: THE CAMPAIGNS' JOURNAL</u>	37
4.1	TEST CAMPAIGN, MATERIALS, DIMENSIONS, PROPERTIES AND GENERAL CAMPAIGN DATA	37
4.1.1	23X2015: 1 ST TEST CAMPAIGN	38
4.1.2	14XII2015: 2 ND TEST CAMPAIGN	40
4.1.3	29I2016: 3 RD TEST CAMPAIGN	42
4.1.4	10III2016: 4 TH TEST CAMPAIGN	44
4.1.5	17III2016: 5 TH TEST CAMPAIGN	46
4.1.6	01IV2016: 6 TH TEST CAMPAIGN	48
4.1.7	07IV2016: 7 TH TEST CAMPAIGN	50
4.1.8	14IV2016: 8 TH TEST CAMPAIGN	52
4.1.9	21IV2016: 9 TH TEST CAMPAIGN	54
4.2	TESTS PROCEDURES, METHODOLOGY AND GENERAL TEST INFORMATION	56
4.2.1	THREE POINT BEND TEST APPARATUS	56
4.2.2	THREE POINT BEND TEST CONFIGURATION	63
4.3	SUMMARY OF THE TESTED CAMPAIGNS	66
5	<u>COMPUTING THE FRACTURE ENERGY OF CONCRETE</u>	67
5.1	FIRST APPROACHES AND COMPARISONS. THE APPROPRIATENESS OF THE METHODOLOGY	67
5.1.1	ABOUT THE TEST STABILITY	67
5.1.2	ABOUT THE RESULTS AND THE ACQUIRED DISPLACEMENT AND LOAD VALUES	72
5.1.3	ABOUT THE CORRECTION METHOD	78
5.2	DETERMINATION OF THE SIZE-INDEPENDENT FRACTURE ENERGY OF CONCRETE. RESULTS	79
5.2.1	INFLUENCE OF THE SAND PROPORTION	81
5.2.2	INFLUENCE OF THE AGGREGATE PROPORTION	82
5.2.3	INFLUENCE OF THE AGGREGATE SIZE	83
5.2.4	INFLUENCE OF THE CEMENT PROPORTION	84
5.2.5	INFLUENCE OF THE WATER TO CEMENT RATIO	85

5.2.6	INFLUENCE OF THE COMPRESSIVE STRENGTH	86
5.2.7	INFLUENCE OF THE TENSILE STRENGTH	87
5.3	BUILDING THE SOFTENING CURVE OF CONCRETE WITH A BILINEAR APPROXIMATION. RESULTS	88
6	SUMMARY OF THE ECONOMIC VALUATION AND THE SCHEDULE	91
6.1	ECONOMIC SUMMARY	91
6.2	SCHEDULE SUMMARY	91
7	CONCLUSIONS AND FUTURE RESEARCH	92
7.1	CONCLUSIONS OF THE RESEARCH	92
7.2	FUTURE WORK	94
8	REFERENCES	95
	APPENDICES	99
A	DETERMINATION OF OTHER MECHANICAL PROPERTIES	99
A.1	DETERMINATION OF THE ELASTIC MODULUS BY A THREE POINT BEND TEST	99
A.2	ELASTIC MODULI OF THE TESTED CAMPAIGNS	100
A.2.1	23X2015 CAMPAIGN	100
A.2.2	14XII2015 CAMPAIGN	103
A.2.3	29I2016 CAMPAIGN	108
A.2.4	10III2016 CAMPAIGN	114
A.2.5	17III2016 CAMPAIGN	117
A.2.6	01IV2016 CAMPAIGN	120
A.2.7	07IV2016 CAMPAIGN	123
A.2.8	14IV2016 CAMPAIGN	126
A.2.9	21IV2016 CAMPAIGN	129
A.3	DETERMINATION OF THE TENSILE STRENGTH OF CONCRETE BY A BRAZILIAN TEST	132
A.3.1	BRAZILIAN TEST APPARATUS	133
A.3.2	BRAZILIAN TEST CONFIGURATION	135
A.4	TENSILE STRENGTH OF THE TESTED CAMPAIGNS	137
A.4.1	23X2015 CAMPAIGN	137
A.4.2	14XII2015 CAMPAIGN	138
A.4.3	29I2016 CAMPAIGN	141

A.4.4	10III2016 CAMPAIGN	144
A.4.5	17III2016 CAMPAIGN	146
A.4.6	01IV2016 CAMPAIGN	148
A.4.7	07IV2016 CAMPAIGN	150
A.4.8	14IV2016 CAMPAIGN	152
A.4.9	21IV2016 CAMPAIGN	154
A.5	DETERMINATION OF THE COMPRESSIVE STRENGTH OF CONCRETE BY MEANS OF A COMPRESSION TEST	156
A.5.1	DIRECT COMPRESSION TEST APPARATUS	157
A.5.2	DIRECT COMPRESSION TEST CONFIGURATION	158
A.6	COMPRESSIVE STRENGTH OF THE TESTED CAMPAIGNS	159
A.6.1	23X2015 CAMPAIGN	159
A.6.2	14XII2015 CAMPAIGN	161
A.6.3	29I2016 CAMPAIGN	162
A.6.4	10III2016 CAMPAIGN	164
A.6.5	17III2016 CAMPAIGN	165
A.6.6	01IV2016 CAMPAIGN	166
A.6.7	07IV2016 CAMPAIGN	167
A.6.8	14IV2016 CAMPAIGN	168
A.6.9	21IV2016 CAMPAIGN	169
B	THREE POINT BENDING TESTS MISCELLANEA	170
B.1	FORMER TEST ATTEMPTS: 17VI2015 AND 13X2015 TESTS	170
B.2	MEASUREMENT STUDIES	173
B.2.1	STUDY OF THE DISPLACEMENT RECORDING	173
B.2.2	STUDY OF THE CRACK MOUTH OPENING DISPLACEMENT RECORDING	178
C	USED CODES	182
C.1	MATLAB SCRIPTS	182
C.1.1	BASIS FOR THE TAIL CORRECTION IN THE LOAD VS. DISPLACEMENT GRAPH DATA PROCESSING CODE	182
C.1.2	BASIS FOR THE STRENGTH TEST DATA PROCESSING CODE	187
C.1.3	BASIS FOR THE BILINEAR APPROXIMATION BUILDING CODE	188
C.1.4	BASIS FOR THE COMPARISON OF ALL TESTS FROM ONE SINGLE CAMPAIGN	189
C.1.5	BASIS FOR THE LOCAL FRACTURE ENERGY METHOD DATA PROCESSING CODE	192
C.1.6	BASIS FOR THE FINAL CORRECTION OF THE FRACTURE ENERGY THROUGH THE LOCAL FRACTURE MODEL	196
C.1.7	FINAL PROCESSING CODE	197

C.2	MATLAB FUNCTIONS	204
C.2.1	MAIN PARAMETERS FOR THE BILINEAR APPROXIMATION OF THE SOFTENING CURVE	204
C.2.2	FRACTURE ENERGY AND MAIN PARAMETERS THROUGH THE TAIL OF THE LOAD VS. DISPLACEMENT CURVE CORRECTION	205
C.2.3	DETERMINATION OF THE ELASTIC MODULI	206
C.2.4	SIZE-DEPENDENT FRACTURE ENERGY	207
C.2.5	FRACTURE ENERGY AND MAIN PARAMETERS THROUGH THE LOCAL FRACTURE ENERGY MODEL	208
C.2.6	FINDING NON-ZERO VALUES: WITHOUT LIMIT IN THE DATA RANGE	209
C.2.7	FINDING NON-ZERO VALUES: WITH LIMIT IN THE DATA RANGE	209
C.2.8	FINDING NON-ZERO VALUES: WITHIN A DATA RANGE	210
C.2.9	FINDING ZERO VALUES: WITH LIMIT IN THE DATA RANGE	211
C.2.10	FINDING THE MAXIMUM AND MINIMUM, THEIR LOCATIONS, THE MEAN VALUE AND THE STANDARD DEVIATION OF A DATA SET OR VECTOR: WITHOUT LIMIT IN THE DATA RANGE	211
C.2.11	FINDING THE MAXIMUM AND MINIMUM, THEIR LOCATIONS, THE MEAN VALUE AND THE STANDARD DEVIATION OF A DATA VECTOR: WITH LIMIT IN THE DATA RANGE	212
C.2.12	OBTAINING THE UPPER AND LOWER CURVE OF A COUPLED DATA SPECTRUM WITH AN ABSCISSA DATA RANGE AND DIVISION	212
D	MANUAL PROCESSING PROCEDURE FOR THE CAMPAIGNS ANALYSIS	213
D.1	17VI2015 TEST TRIAL	213
D.2	13X2015 TEST TRIAL	214
D.3	23X2015 CAMPAIGN	215
D.4	14XII2015 CAMPAIGN	216
D.5	29I2016 CAMPAIGN	217
D.6	10III2016 CAMPAIGN	218
D.7	17III2016 CAMPAIGN	219
D.8	01IV2016 CAMPAIGN	220
D.9	07IV2016 CAMPAIGN	221
D.10	14IV2016 CAMPAIGN	222
D.11	21IV2016 CAMPAIGN	223
E	TESTS' GRAPHS	224
E.1	17VI2015 TEST TRIAL	224
E.1.1	17VI2015 DATA	224
E.2	13X2015 TEST TRIAL	226

E.2.1	13X2015 DATA	226
E.3	23X2015 CAMPAIGN	228
E.3.1	23X2015 DATA	228
E.3.2	23X2015 CORRECTED LOAD VS. CMOD	235
E.3.3	23X2015 CORRECTED LOAD VS. VERTICAL DISPLACEMENT	237
E.3.4	23X2015 CORRECTED LOAD VS. X	239
E.3.5	23X2015 SOFTENING CURVE BILINEAR APPROXIMATION	241
E.3.6	23X2015 SPECIMENS' COMPARISON	242
E.4	14XII2015 CAMPAIGN	244
E.4.1	14XII2015 DATA	244
E.4.2	14XII2015 CORRECTED LOAD VS. CMOD	257
E.4.3	14XII2015 CORRECTED LOAD VS. VERTICAL DISPLACEMENT	261
E.4.4	14XII2015 CORRECTED LOAD VS. X	265
E.4.5	14XII2015 SOFTENING CURVE BILINEAR APPROXIMATION	269
E.4.6	14XII2015 SPECIMENS' COMPARISON	270
E.5	29I2016 CAMPAIGN	272
E.5.1	29I2016 DATA	272
E.5.2	29I2016 CORRECTED LOAD VS. CMOD	285
E.5.3	29I2016 CORRECTED LOAD VS. VERTICAL DISPLACEMENT	289
E.5.4	29I2016 CORRECTED LOAD VS. X	293
E.5.5	29I2016 SOFTENING CURVE BILINEAR APPROXIMATION	295
E.5.6	29I2016 SPECIMENS' COMPARISON	296
E.6	10III2016 CAMPAIGN	299
E.6.1	10III2016 DATA	299
E.6.2	10III2016 CORRECTED LOAD VS. CMOD	306
E.6.3	10III2016 CORRECTED LOAD VS. VERTICAL DISPLACEMENT	308
E.6.4	10III2016 CORRECTED LOAD VS. X	310
E.6.5	10III2016 SOFTENING CURVE BILINEAR APPROXIMATION	312
E.6.6	10III2016 SPECIMENS' COMPARISON	313
E.7	17III2016 CAMPAIGN	315
E.7.1	17III2016 DATA	315
E.7.2	17III2016 CORRECTED LOAD VS. CMOD	322
E.7.3	17III2016 CORRECTED LOAD VS. VERTICAL DISPLACEMENT	324
E.7.4	17III2016 CORRECTED LOAD VS. X	326
E.7.5	17III2016 SOFTENING CURVE BILINEAR APPROXIMATION	328

E.7.6	17III2016 SPECIMENS' COMPARISON	329
E.8	01IV2016 CAMPAIGN	331
E.8.1	01IV2016 DATA	331
E.8.2	01IV2016 CORRECTED LOAD VS. CMOD	338
E.8.3	01IV2016 CORRECTED LOAD VS. VERTICAL DISPLACEMENT	340
E.8.4	01IV2016 CORRECTED LOAD VS. X	342
E.8.5	01IV2016 SOFTENING CURVE BILINEAR APPROXIMATION	344
E.8.6	01IV2016 SPECIMENS' COMPARISON	345
E.9	07IV2016 CAMPAIGN	347
E.9.1	07IV2016 DATA	347
E.9.2	07IV2016 CORRECTED LOAD VS. CMOD	354
E.9.3	07IV2016 CORRECTED LOAD VS. VERTICAL DISPLACEMENT	356
E.9.4	07IV2016 CORRECTED LOAD VS. X	358
E.9.5	07IV2016 SOFTENING CURVE BILINEAR APPROXIMATION	360
E.9.6	07IV2016 SPECIMENS' COMPARISON	361
E.10	14IV2016 CAMPAIGN	363
E.10.1	14IV2016 DATA	363
E.10.2	14IV2016 CORRECTED LOAD VS. CMOD	370
E.10.3	14IV2016 CORRECTED LOAD VS. VERTICAL DISPLACEMENT	372
E.10.4	14IV2016 CORRECTED LOAD VS. X	374
E.10.5	14IV2016 SOFTENING CURVE BILINEAR APPROXIMATION	376
E.10.6	14IV2016 SPECIMENS' COMPARISON	377
E.11	21IV2016 CAMPAIGN	379
E.11.1	21IV2016 DATA	379
E.11.2	21IV2016 CORRECTED LOAD VS. CMOD	386
E.11.3	21IV2016 CORRECTED LOAD VS. VERTICAL DISPLACEMENT	388
E.11.4	21IV2016 CORRECTED LOAD VS. X	390
E.11.5	21IV2016 SOFTENING CURVE BILINEAR APPROXIMATION	392
E.11.6	21IV2016 SPECIMENS' COMPARISON	393
F	TESTS' INDIVIDUAL RESULTS	395
F.1	23X2015 CAMPAIGN	395
F.2	14XII2015 CAMPAIGN	397
F.3	29I2016 CAMPAIGN	398
F.4	10III2016 CAMPAIGN	400

F.5	17III2016 CAMPAIGN	401
F.6	01IV2016 CAMPAIGN	402
F.7	07IV2016 CAMPAIGN	403
F.8	14IV2016 CAMPAIGN	404
F.9	21IV2016 CAMPAIGN	405
G	MATHEMATICAL DEVELOPMENTS	406
G.1	EXPRESSION FOR THE SOFTENING CURVE BILINEAR APPROXIMATION	406
G.2	APPLICATION OF THE LOCAL FRACTURE ENERGY EQUATIONS	408
G.2.1	CASE A	408
G.2.2	CASE B	409
G.2.3	CASE C	409
G.2.4	CASE D	410
H	ECONOMIC VALUATION	411
H.1	SIMPLE ELEMENTS COSTS	411
H.1.1	UNIT COSTS FOR MATERIALS	411
H.1.2	UNIT COSTS FOR MANPOWER	413
H.1.3	UNIT COSTS FOR MACHINERY AND TESTS	413
H.2	SIMPLE ELEMENTS MEASUREMENT	414
H.2.1	MATERIALS MEASUREMENT	414
H.2.2	MANPOWER MEASUREMENT	419
H.2.3	MACHINERY AND TESTS MEASUREMENT	420
H.3	PROJECT COSTS	422
H.3.1	DIRECT COSTS CLASSIFIED BY NATURE	422
H.3.2	TOTAL COSTS SUMMARY	423
H.3.3	CAMPAIGN COST SUMMARY CLASSIFIED BY NATURE	423
I	SCHEDULE	424
J	GALLERY	426

LIST OF FIGURES

Figure 1: Size effect phenomenon in the nominal stress and applicable failure criteria. From ²	2
Figure 2: Relative sizes of the FPZ (F), the non-linear zone (N) and the linear behavior zone (L) in different type of materials. From ¹⁰	4
Figure 3: Stress distribution near the crack tip in both fracture models	9
Figure 4: Full stress vs. strain curve in a cohesive crack model	10
Figure 5: A three point bending test with the zones visible at Figure 4	10
Figure 6: Adaptation of the displacements along both sides of the cross-section containing the FPZ as a fictitious crack with its cohesive stresses, weaker as displacement increases	11
Figure 7: Real and fictitious crack tip and crack development front	12
Figure 8: Fictitious crack creation and development	12
Figure 9: A stress vs. strain curve in the tensile region applicable to concrete	13
Figure 10: A stress vs. crack opening softening curve applicable to concrete	13
Figure 11: Load vs. displacement curve on a three point bending situation	14
Figure 12: Stress distribution at an earlier point of zone I of Figure 11	15
Figure 13: Stress distribution at an advanced point of zone I of Figure 11.	16
Figure 14: Stress distribution at a point of zone II of Figure 11	16
Figure 15: Stress distribution at the point where the fictitious crack shows the critical crack width at the zone III of Figure 11	16
Figure 16: Stress distribution at a point of zone IV of Figure 11 where stresses moved themselves	17
Figure 17: Coordinate reduction to dimensionless axis of the softening curve	19
Figure 18: Size decrease of the fracture process zone during its approaching to the free edge. From ²⁰	21
Figure 19: Local fracture energy distribution g_f in red and the mean value of the energy distribution G_f along the cross-section in blue	22
Figure 20: Common problems with a direct tensile test on concrete	23
Figure 21: Main dimensions of the beam type specimens for a three point bend test	24
Figure 22: Example of a discrete data record	25
Figure 23: Trapezoidal integration	26
Figure 24: Self-weight action on the central section	27
Figure 25: Self-weight action correction at the central section by a doubled-length specimen	27
Figure 26: Non-measured fracture work. Final test load is slightly higher than zero, what provokes a non-registered area	30
Figure 27: Half specimen represented by one rigid body used for obtaining the tail correction ¹⁵	31

Figure 28: CMOD clip gage EPSILON 3541-005M-120M-ST	57
Figure 29: Notch at the clip gage	57
Figure 30: Steel knives, where the COD clip gage is attached, placed on a notched concrete specimen	57
Figure 31: Universal testing machine SERVOSIS MUE-60	58
Figure 32: Comparison between the loads registered by the machine and by a load cell (#1)	59
Figure 33: Comparison between the loads registered by the machine and by a load cell (#2)	59
Figure 34: Load cell UTILCELL 630 with a nominal load of 2500kg	60
Figure 35: VISHAY Micro-measurements scanner model 5100B	61
Figure 36: Anti-torsion support	61
Figure 37: Machine MUE-60 prepared for a three point bending test	62
Figure 38: Beam-type notched specimen ready for a three point bending test of fracture mechanics	62
Figure 39: StrainSmart 5000 project main window	63
Figure 40: UTILCELL 630 2.5T calibration	64
Figure 41: CMOD clip gage EPSILON 3541-005M-120M-ST calibration	64
Figure 42: Full experimental Load vs. Displacement curve of the longest test carried out (B23X2015III)	68
Figure 43: Full experimental Load vs. CMOD curve of the longest test carried out (B23X2015III)	68
Figure 44: Full experimental Load vs. Displacement curve of the B14XII2015III test	69
Figure 45: Full experimental Load vs. CMOD curve of the B14XII2015III test	70
Figure 46: Full experimental Load vs. Displacement curve of the B14XII2015I test	70
Figure 47: Full experimental Load vs. CMOD curve of the B14XII2015I test	71
Figure 48: Experimental corrected Load vs. Displacement curve of the B17III2016II test	71
Figure 49: Phases of the test at the load recording	73
Figure 50: B23X2015III test: load and displacement at the positioning stage. Displacement is filtered	74
Figure 51: B23X2015II test: load and displacement at the positioning stage. Displacement is not filtered	74
Figure 52: B23X2015III test: load and displacement at the loading stage. Displacement is filtered	75
Figure 53: B23X2015III test: load and displacement at the initial unloading stage. Displacement is filtered	75
Figure 54: B23X2015III test: load and displacement at the crack opening stage. Displacement is filtered	76
Figure 55: B23X2015III test: load and displacement at the final stage. Displacement is filtered	76
Figure 56: Corrected load vs. Displacement for the entire project (peak displacement zero)	80
Figure 57: Corrected load vs. CMOD for the entire project	80
Figure 58: Fracture energy vs. Sand 0-2 proportion	81
Figure 59: Fracture energy vs. Aggregate 5-10 proportion	82
Figure 60: Fracture energy vs. Maximum aggregate size	83
Figure 61: Fracture energy vs. Cement II/B-L 32.5N proportion	84
Figure 62: Fracture energy vs. Water to cement ratio	85
Figure 63: Fracture energy vs. Compressive strength	86
Figure 64: Fracture energy vs. Tensile strength	87
Figure 65: Softening curve bilinear approximation of all campaigns	88

Figure 66: Softening curve bilinear approximation of all campaigns in the reduced form	90
Figure 67: CMOD vs. Uncorrected Load from the 15% of the peak load up to 55% of B23X2015I	100
Figure 68: CMOD vs. Uncorrected Load from the 15% of the peak load up to 55% of B23X2015II	101
Figure 69: CMOD vs. Uncorrected Load from the 15% of the peak load up to 55% of B23X2015III	101
Figure 70: CMOD vs. Uncorrected Load from the 15% of the peak load up to 55% of B23X2015IV	102
Figure 71: CMOD vs. Uncorrected Load from the 15% of the peak load up to 55% of all B23X2015	102
Figure 72: CMOD vs. Uncorrected Load from the 15% of the peak load up to 55% of B14XII2015I	103
Figure 73: CMOD vs. Uncorrected Load from the 15% of the peak load up to 55% of B14XII2015II	104
Figure 74: CMOD vs. Uncorrected Load from the 15% of the peak load up to 55% of B14XII2015III	104
Figure 75: CMOD vs. Uncorrected Load from the 15% of the peak load up to 55% of B14XII2015IV	105
Figure 76: CMOD vs. Uncorrected Load from the 15% of the peak load up to 55% of B14XII2015V	105
Figure 77: CMOD vs. Uncorrected Load from the 15% of the peak load up to 55% of B14XII2015VI	106
Figure 78: CMOD vs. Uncorrected Load from the 15% of the peak load up to 55% of B14XII2015VII	106
Figure 79: CMOD vs. Uncorrected Load from the 15% of the peak load up to 55% of B14XII2015VIII	107
Figure 80: CMOD vs. Uncorrected Load from the 15% of the peak load up to 55% of all B14XII2015	107
Figure 81: CMOD vs. Uncorrected Load from the 15% of the peak load up to 55% of B29I2016I	109
Figure 82: CMOD vs. Uncorrected Load from the 15% of the peak load up to 55% of B29I2016II	109
Figure 83: CMOD vs. Uncorrected Load from the 15% of the peak load up to 55% of B29I2016III	110
Figure 84: CMOD vs. Uncorrected Load from the 15% of the peak load up to 55% of B29I2016IV	110
Figure 85: CMOD vs. Uncorrected Load from the 15% of the peak load up to 55% of B29I2016V	111
Figure 86: CMOD vs. Uncorrected Load from the 15% of the peak load up to 55% of B29I2016VI	111
Figure 87: CMOD vs. Uncorrected Load from the 15% of the peak load up to 55% of B29I2016VII	112
Figure 88: CMOD vs. Uncorrected Load from the 15% of the peak load up to 55% of B29I2016VIII	112
Figure 89: CMOD vs. Uncorrected Load from the 15% of the peak load up to 55% of 29I2016 A-series	113
Figure 90: CMOD vs. Uncorrected Load from the 15% of the peak load up to 55% of all 29I2016	113
Figure 91: CMOD vs. Uncorrected Load from the 15% of the peak load up to 55% of B10III2016I	114
Figure 92: CMOD vs. Uncorrected Load from the 15% of the peak load up to 55% of B10III2016II	115
Figure 93: CMOD vs. Uncorrected Load from the 15% of the peak load up to 55% of B10III2016III	115
Figure 94: CMOD vs. Uncorrected Load from the 15% of the peak load up to 55% of B10III2016IV	116
Figure 95: CMOD vs. Uncorrected Load from the 15% of the peak load up to 55% of all B10III2016	116
Figure 96: CMOD vs. Uncorrected Load from the 15% of the peak load up to 55% of B17III2016I	117
Figure 97: CMOD vs. Uncorrected Load from the 15% of the peak load up to 55% of B17III2016II	118
Figure 98: CMOD vs. Uncorrected Load from the 15% of the peak load up to 55% of B17III2016III	118
Figure 99: CMOD vs. Uncorrected Load from the 15% of the peak load up to 55% of B17III2016IV	119
Figure 100: CMOD vs. Uncorrected Load from the 15% of the peak load up to 55% of all B17III2016	119
Figure 101: CMOD vs. Uncorrected Load from the 15% of the peak load up to 55% of B01IV2016I	120
Figure 102: CMOD vs. Uncorrected Load from the 15% of the peak load up to 55% of B01IV2016II	121
Figure 103: CMOD vs. Uncorrected Load from the 15% of the peak load up to 55% of B01IV2016III	121

Figure 104: CMOD vs. Uncorrected Load from the 15% of the peak load up to 55% of B01IV2016IV	122
Figure 105: CMOD vs. Uncorrected Load from the 15% of the peak load up to 55% of all B01IV2016	122
Figure 106: CMOD vs. Uncorrected Load from the 15% of the peak load up to 55% of B07IV2016I	123
Figure 107: CMOD vs. Uncorrected Load from the 15% of the peak load up to 55% of B07IV2016II	124
Figure 108: CMOD vs. Uncorrected Load from the 15% of the peak load up to 55% of B07IV2016III	124
Figure 109: CMOD vs. Uncorrected Load from the 15% of the peak load up to 55% of B07IV2016IV	125
Figure 110: CMOD vs. Uncorrected Load from the 15% of the peak load up to 55% of all B07IV2016	125
Figure 111: CMOD vs. Uncorrected Load from the 15% of the peak load up to 55% of B14IV2016I	126
Figure 112: CMOD vs. Uncorrected Load from the 15% of the peak load up to 55% of B14IV2016II	127
Figure 113: CMOD vs. Uncorrected Load from the 15% of the peak load up to 55% of B14IV2016III	127
Figure 114: CMOD vs. Uncorrected Load from the 15% of the peak load up to 55% of B14IV2016IV	128
Figure 115: CMOD vs. Uncorrected Load from the 15% of the peak load up to 55% of all B14IV2016	128
Figure 116: CMOD vs. Uncorrected Load from the 15% of the peak load up to 55% of B21IV2016I	129
Figure 117: CMOD vs. Uncorrected Load from the 15% of the peak load up to 55% of B21IV2016II	130
Figure 118: CMOD vs. Uncorrected Load from the 15% of the peak load up to 55% of B21IV2016III	130
Figure 119: CMOD vs. Uncorrected Load from the 15% of the peak load up to 55% of B21IV2016IV	131
Figure 120: CMOD vs. Uncorrected Load from the 15% of the peak load up to 55% of all B21IV2016	131
Figure 121: Sketch of a Brazilian test for cylindrical (left) and cubic (right) specimens with the bearing strip position (in grey)	132
Figure 122: Compression testing machine SERVOSIS MES-200	133
Figure 123: Machine configuration for a Brazilian test	134
Figure 124: Result of a Brazilian test	134
Figure 125: PCD2K control program windows	135
Figure 126: PCD2K functions generator	136
Figure 127: Load vs. vertical displacement for the Brazilian test of C23X2015II	137
Figure 128: Load vs. vertical displacement for the Brazilian test of C14XII2015II	138
Figure 129: Load vs. vertical displacement for the Brazilian test of C14XII2015III	139
Figure 130: Load vs. vertical displacement for the Brazilian test of C14XII2015IV	139
Figure 131: Load vs. vertical displacement for the Brazilian test of C14XII2015V	140
Figure 132: Load vs. vertical displacement for the Brazilian test of all C14XII2015	140
Figure 133: Load vs. vertical displacement for the Brazilian test of C29I2016I	141
Figure 134: Load vs. vertical displacement for the Brazilian test of C29I2016II	142
Figure 135: Load vs. vertical displacement for the Brazilian test of C29I2016III	142
Figure 136: Load vs. vertical displacement for the Brazilian test of C29I2016IV	143
Figure 137: Load vs. vertical displacement for the Brazilian test of all C29I2016	143
Figure 138: Load vs. vertical displacement for the Brazilian test of C10III2016II	144
Figure 139: Load vs. vertical displacement for the Brazilian test of C10III2016III	145
Figure 140: Load vs. vertical displacement for the Brazilian test of all C10III2016	145

Figure 141: Load vs. vertical displacement for the Brazilian test of C17III2016II	146
Figure 142: Load vs. vertical displacement for the Brazilian test of C17III2016III	147
Figure 143: Load vs. vertical displacement for the Brazilian test of all C17III2016	147
Figure 144: Load vs. vertical displacement for the Brazilian test of C01IV2016II	148
Figure 145: Load vs. vertical displacement for the Brazilian test of C01IV2016III	149
Figure 146: Load vs. vertical displacement for the Brazilian test of all C01IV2016	149
Figure 147: Load vs. vertical displacement for the Brazilian test of C07IV2016II	150
Figure 148: Load vs. vertical displacement for the Brazilian test of C07IV2016III	151
Figure 149: Load vs. vertical displacement for the Brazilian test of all C07IV2016	151
Figure 150: Load vs. vertical displacement for the Brazilian test of C14IV2016II	152
Figure 151: Load vs. vertical displacement for the Brazilian test of C14IV2016III	153
Figure 152: Load vs. vertical displacement for the Brazilian test of all C14IV2016	153
Figure 153: Load vs. vertical displacement for the Brazilian test of C21IV2016II	154
Figure 154: Load vs. vertical displacement for the Brazilian test of C21IV2016III	155
Figure 155: Load vs. vertical displacement for the Brazilian test of all C21IV2016	155
Figure 156: Cylinder-type specimen ready for a direct compression test	157
Figure 157: Load vs. vertical displacement for the direct compression test of C23X2015I	159
Figure 158: Load vs. vertical displacement for the direct compression test of D23X2015I	160
Figure 159: Load vs. vertical displacement for the direct compression test of C14XII2015I	161
Figure 160: Load vs. vertical displacement for the direct compression test of D29I2016I	162
Figure 161: Load vs. vertical displacement for the direct compression test of D29I2016II	163
Figure 162: Load vs. vertical displacement for the direct compression test of all D29I2016	163
Figure 163: Load vs. vertical displacement for the direct compression test of C10III2016I	164
Figure 164: Load vs. vertical displacement for the direct compression test of C17III2016I	165
Figure 165: Load vs. vertical displacement for the direct compression test of C01IV2016I	166
Figure 166: Load vs. vertical displacement for the direct compression test of C07IV2016I	167
Figure 167: Load vs. vertical displacement for the direct compression test of C14IV2016I	168
Figure 168: Load vs. vertical displacement for the direct compression test of C21IV2016I	169
Figure 169: Corrected load vs. CMOD at the B17VI2015I test	170
Figure 170: Corrected load vs. Displacement at the B17VI2015I test	171
Figure 171: Corrected load vs. CMOD at the B13X2015I test	171
Figure 172: Corrected load vs. Displacement at the B13X2015I test	172
Figure 173: LDTs to record the absolute machine head displacement (right) and the relative piston-to-load applicator displacement (left) – Campaign 17III2016	173
Figure 174: Setup of LDTs to record other types of displacement, front view – Campaign 17III2016	174
Figure 175: Types of displacement at the B17III2016II test. The line marks the real beginning of the test	176
Figure 176: Types of displacement at the B17III2016III test. The line marks the real beginning of the test	176
Figure 177: Types of displacement at the B17III2016IV test. The line marks the real beginning of the test	177

Figure 178: Example of a speckle pattern	178
Figure 179: Three point bending test with the DIC setup	179
Figure 180: Horizontal displacement at an early stage of the test	179
Figure 181: Horizontal displacement at an advanced stage of the test	180
Figure 182: Horizontal axis strain field at an advanced stage of the test	180
Figure 183: CMOD gage vs. DIC crack width	181
Figure 184: CMOD values recorded at the B17VI2015I test	224
Figure 185: Displacement values recorded at the B17VI2015I test	225
Figure 186: Load values recorded at the B17VI2015I test	225
Figure 187: CMOD values recorded at the B13X2015I test	226
Figure 188: Displacement values recorded at the B13X2015I test	227
Figure 189: Load values recorded at the B13X2015I test	227
Figure 190: CMOD values recorded at the B23X2015I test	228
Figure 191: Displacement values recorded at the B23X2015I test	229
Figure 192: Load values recorded at the B23X2015I test	229
Figure 193: CMOD values recorded at the B23X2015II test	230
Figure 194: Displacement values recorded at the B23X2015II test	230
Figure 195: Load values recorded at the B23X2015II test	231
Figure 196: CMOD values recorded at the B23X2015III test	231
Figure 197: Displacement values recorded at the B23X2015III test	232
Figure 198: Load values recorded at the B23X2015III test	232
Figure 199: CMOD values recorded at the B23X2015IV test	233
Figure 200: Displacement values recorded at the B23X2015IV test	233
Figure 201: Load values recorded at the B23X2015IV test	234
Figure 202: Corrected load vs. CMOD at the B23X2015I test	235
Figure 203: Corrected load vs. CMOD at the B23X2015II test	235
Figure 204: Corrected load vs. CMOD at the B23X2015III test	236
Figure 205: Corrected load vs. CMOD at the B23X2015IV test	236
Figure 206: Corrected load vs. Displacement at the B23X2015I test	237
Figure 207: Corrected load vs. Displacement at the B23X2015II test	237
Figure 208: Corrected load vs. Displacement at the B23X2015III test	238
Figure 209: Corrected load vs. Displacement at the B23X2015IV test	238
Figure 210: Corrected load vs. X at the B23X2015I test with the final upper curve data	239
Figure 211: Corrected load vs. X at the B23X2015II test with the final upper curve data	239
Figure 212: Corrected load vs. X at the B23X2015III test with the final upper curve data	240
Figure 213: Corrected load vs. X at the B23X2015IV test with the final upper curve data	240
Figure 214: Softening curve bilinear approximation of the 23X2015 campaign	241
Figure 215: Softening curve bilinear approximation of the 23X2015 campaign in the reduced form	241

Figure 216: 23X2015 Corrected load vs. CMOD from the entire campaign	242
Figure 217: 23X2015 Corrected load vs. Displacement from the entire campaign	242
Figure 218: 23X2015 Corrected load vs. Displacement from the entire campaign (peak displacement zero)	243
Figure 219: 23X2015 Corrected load vs. X from the entire campaign	243
Figure 220: CMOD values recorded at the B14XII2015I test	244
Figure 221: Displacement values recorded at the B14XII2015I test	245
Figure 222: Load values recorded at the B14XII2015I test	245
Figure 223: CMOD values recorded at the B14XII2015II test	246
Figure 224: Displacement values recorded at the B14XII2015II test	246
Figure 225: Load values recorded at the B14XII2015II test	247
Figure 226: CMOD values recorded at the B14XII2015III test	247
Figure 227: Displacement values recorded at the B14XII2015III test	248
Figure 228: Load values recorded at the B14XII2015III test	248
Figure 229: CMOD values recorded at the B14XII2015IV test	249
Figure 230: Displacement values recorded at the B14XII2015IV test	249
Figure 231: Load values recorded at the B14XII2015IV test	250
Figure 232: CMOD values recorded at the B14XII2015V test	250
Figure 233: Displacement values recorded at the B14XII2015V test	251
Figure 234: Load values recorded at the B14XII2015V test	251
Figure 235: CMOD values recorded at the B14XII2015VI test	252
Figure 236: Displacement values recorded at the B14XII2015VI test	252
Figure 237: Load values recorded at the B14XII2015VI test	253
Figure 238: CMOD values recorded at the B14XII2015VII test	253
Figure 239: Displacement values recorded at the B14XII2015VII test	254
Figure 240: Load values recorded at the B14XII2015VII test	254
Figure 241: CMOD values recorded at the B14XII2015VIII test	255
Figure 242: Displacement values recorded at the B14XII2015VIII test	255
Figure 243: Load values recorded at the B14XII2015VIII test	256
Figure 244: Corrected load vs. CMOD at the B14XII2015I test	257
Figure 245: Corrected load vs. CMOD at the B14XII2015II test	257
Figure 246: Corrected load vs. CMOD at the B14XII2015III test	258
Figure 247: Corrected load vs. CMOD at the B14XII2015IV test	258
Figure 248: Corrected load vs. CMOD at the B14XII2015V test	259
Figure 249: Corrected load vs. CMOD at the B14XII2015VI test	259
Figure 250: Corrected load vs. CMOD at the B14XII2015VII test	260
Figure 251: Corrected load vs. CMOD at the B14XII2015VIII test	260
Figure 252: Corrected load vs. Displacement at the B14XII2015I test	261
Figure 253: Corrected load vs. Displacement at the B14XII2015II test	261

Figure 254: Corrected load vs. Displacement at the B14XII2015III test	262
Figure 255: Corrected load vs. Displacement at the B14XII2015IV test	262
Figure 256: Corrected load vs. Displacement at the B14XII2015V test	263
Figure 257: Corrected load vs. Displacement at the B14XII2015VI test	263
Figure 258: Corrected load vs. Displacement at the B14XII2015VII test	264
Figure 259: Corrected load vs. Displacement at the B14XII2015VIII test	264
Figure 260: Corrected load vs. X at the B14XII2015I test with the final upper curve data	265
Figure 261: Corrected load vs. X at the B14XII2015II test with the final upper curve data	265
Figure 262: Corrected load vs. X at the B14XII2015III test with the final upper curve data	266
Figure 263: Corrected load vs. X at the B14XII2015IV test with the final upper curve data	266
Figure 264: Corrected load vs. X at the B14XII2015V test with the final upper curve data	267
Figure 265: Corrected load vs. X at the B14XII2015VI test with the final upper curve data	267
Figure 266: Corrected load vs. X at the B14XII2015VII test with the final upper curve data	268
Figure 267: Corrected load vs. X at the B14XII2015VIII test with the final upper curve data	268
Figure 268: Softening curve bilinear approximation of the 14XII2015 campaign	269
Figure 269: Softening curve bilinear approximation of the 14XII2015 campaign in the reduced form	269
Figure 270: 14XII2015 Corrected load vs. CMOD from the entire campaign	270
Figure 271: 14XII2015 Corrected load vs. Displacement from the entire campaign	270
Figure 272: 14XII2015 Corrected load vs. Displacement from the entire campaign (peak displacement zero)	271
Figure 273: 14XII2015 Corrected load vs. X from the entire campaign	271
Figure 274: CMOD values recorded at the B29I2016I test	272
Figure 275: Displacement values recorded at the B29I2016I test	273
Figure 276: Load values recorded at the B29I2016I test	273
Figure 277: CMOD values recorded at the B29I2016II test	274
Figure 278: Displacement values recorded at the B29I2016II test	274
Figure 279: Load values recorded at the B29I2016II test	275
Figure 280: CMOD values recorded at the B29I2016III test	275
Figure 281: Displacement values recorded at the B29I2016III test	276
Figure 282: Load values recorded at the B29I2016III test	276
Figure 283: CMOD values recorded at the B29I2016IV test	277
Figure 284: Displacement values recorded at the B29I2016IV test	277
Figure 285: Load values recorded at the B29I2016IV test	278
Figure 286: CMOD values recorded at the B29I2016V test	278
Figure 287: Displacement values recorded at the B29I2016V test	279
Figure 288: Load values recorded at the B29I2016V test	279
Figure 289: CMOD values recorded at the B29I2016VI test	280
Figure 290: Displacement values recorded at the B29I2016VI test	280
Figure 291: Load values recorded at the B29I2016VI test	281

Figure 292: CMOD values recorded at the B29I2016VII test	281
Figure 293: Displacement values recorded at the B29I2016VII test	282
Figure 294: Load values recorded at the B29I2016VII test	282
Figure 295: CMOD values recorded at the B29I2016VIII test	283
Figure 296: Displacement values recorded at the B29I2016VIII test	283
Figure 297: Load values recorded at the B29I2016VIII test	284
Figure 298: Corrected load vs. CMOD at the B29I2016I test	285
Figure 299: Corrected load vs. CMOD at the B29I2016II test	285
Figure 300: Corrected load vs. CMOD at the B29I2016III test	286
Figure 301: Corrected load vs. CMOD at the B29I2016IV test	286
Figure 302: Corrected load vs. CMOD at the B29I2016V test	287
Figure 303: Corrected load vs. CMOD at the B29I2016VI test	287
Figure 304: Corrected load vs. CMOD at the B29I2016VII test	288
Figure 305: Corrected load vs. CMOD at the B29I2016VIII test	288
Figure 306: Corrected load vs. Displacement at the B29I2016I test	289
Figure 307: Corrected load vs. Displacement at the B29I2016II test	289
Figure 308: Corrected load vs. Displacement at the B29I2016III test	290
Figure 309: Corrected load vs. Displacement at the B29I2016IV test	290
Figure 310: Corrected load vs. Displacement at the B29I2016V test	291
Figure 311: Corrected load vs. Displacement at the B29I2016VI test	291
Figure 312: Corrected load vs. Displacement at the B29I2016VII test	292
Figure 313: Corrected load vs. Displacement at the B29I2016VIII test	292
Figure 314: Corrected load vs. X at the B29I2016I test with the final upper curve data	293
Figure 315: Corrected load vs. X at the B29I2016II test with the final upper curve data	293
Figure 316: Corrected load vs. X at the B29I2016III test with the final upper curve data	294
Figure 317: Corrected load vs. X at the B29I2016IV test with the final upper curve data	294
Figure 318: Softening curve bilinear approximation of the 29I2016 campaign	295
Figure 319: Softening curve bilinear approximation of the 29I2016 campaign in the reduced form	295
Figure 320: 29I2016 Corrected load vs. CMOD from the A-series	296
Figure 321: 29I2016 Corrected load vs. Displacement from the A-series (peak displacement zero)	296
Figure 322: 29I2016 Corrected load vs. X from the A-series	297
Figure 323: 29I2016 Corrected load vs. CMOD from the entire campaign	297
Figure 324: 29I2016 Corrected load vs. Displacement from the entire campaign	298
Figure 325: 29I2016 Corrected load vs. Displacement from the entire campaign (peak displacement zero)	298
Figure 326: CMOD values recorded at the B10III2016I test	299
Figure 327: Displacement values recorded by the controller at the B10III2016I test	300
Figure 328: Load values recorded at the B10III2016I test	300
Figure 329: CMOD values recorded at the B10III2016II test	301

Figure 330: Displacement values recorded by the controller at the B10III2016II test	301
Figure 331: Load values recorded at the B10III2016II test	302
Figure 332: CMOD values recorded at the B10III2016III test	302
Figure 333: Displacement values recorded by the controller at the B10III2016III test	303
Figure 334: Load values recorded at the B10III2016III test	303
Figure 335: CMOD values recorded at the B10III2016IV test	304
Figure 336: Displacement values recorded by the controller at the B10III2016IV test	304
Figure 337: Load values recorded at the B10III2016IV test	305
Figure 338: Corrected load vs. CMOD at the B10III2016I test	306
Figure 339: Corrected load vs. CMOD at the B10III2016II test	306
Figure 340: Corrected load vs. CMOD at the B10III2016III test	307
Figure 341: Corrected load vs. CMOD at the B10III2016IV test	307
Figure 342: Corrected load vs. Displacement at the B10III2016I test recorded by the controller	308
Figure 343: Corrected load vs. Displacement at the B10III2016II test recorded by the controller	308
Figure 344: Corrected load vs. Displacement at the B10III2016III test recorded by the controller	309
Figure 345: Corrected load vs. Displacement at the B10III2016IV test recorded by the controller	309
Figure 346: Corrected load vs. X at the B10III2016I test with the final upper curve data	310
Figure 347: Corrected load vs. X at the B10III2016II test with the final upper curve data	310
Figure 348: Corrected load vs. X at the B10III2016III test with the final upper curve data	311
Figure 349: Corrected load vs. X at the B10III2016IV test with the final upper curve data	311
Figure 350: Softening curve bilinear approximation of the 10III2016 campaign	312
Figure 351: Softening curve bilinear approximation of the 10III2016 campaign in the reduced form	312
Figure 352: 10III2016 Corrected load vs. CMOD from the entire campaign	313
Figure 353: 10III2016 Corrected load vs. Displacement from the entire campaign	313
Figure 354: 10III2016 Corrected load vs. Displacement from the entire campaign (peak displacement zero)	314
Figure 355: 10III2016 Corrected load vs. X from the entire campaign	314
Figure 356: CMOD values recorded at the B17III2016I test	315
Figure 357: Displacement values recorded at the B17III2016I test	316
Figure 358: Load values recorded at the B17III2016I test	316
Figure 359: CMOD values recorded at the B17III2016II test	317
Figure 360: Displacement values recorded at the B17III2016II test	317
Figure 361: Load values recorded at the B17III2016II test	318
Figure 362: CMOD values recorded at the B17III2016III test	318
Figure 363: Displacement values recorded at the B17III2016III test	319
Figure 364: Load values recorded at the B17III2016III test	319
Figure 365: CMOD values recorded at the B17III2016IV test	320
Figure 366: Displacement values recorded at the B17III2016IV test	320
Figure 367: Load values recorded at the B17III2016IV test	321

Figure 368: Corrected load vs. CMOD at the B17III2016I test	322
Figure 369: Corrected load vs. CMOD at the B17III2016II test	322
Figure 370: Corrected load vs. CMOD at the B17III2016III test	323
Figure 371: Corrected load vs. CMOD at the B17III2016IV test	323
Figure 372: Corrected load vs. Displacement at the B17III2016I test	324
Figure 373: Corrected load vs. Displacement at the B17III2016II test	324
Figure 374: Corrected load vs. Displacement at the B17III2016III test	325
Figure 375: Corrected load vs. Displacement at the B17III2016IV test	325
Figure 376: Corrected load vs. X at the B17III2016I test with the final upper curve data	326
Figure 377: Corrected load vs. X at the B17III2016II test with the final upper curve data	326
Figure 378: Corrected load vs. X at the B17III2016III test with the final upper curve data	327
Figure 379: Corrected load vs. X at the B17III2016IV test with the final upper curve data	327
Figure 380: Softening curve bilinear approximation of the 17III2016 campaign	328
Figure 381: Softening curve bilinear approximation of the 17III2016 campaign in the reduced form	328
Figure 382: 17III2016 Corrected load vs. CMOD from the entire campaign	329
Figure 383: 17III2016 Corrected load vs. Displacement from the entire campaign	329
Figure 384: 17III2016 Corrected load vs. Displacement from the entire campaign (peak displacement zero)	330
Figure 385: 17III2016 Corrected load vs. X from the entire campaign	330
Figure 386: CMOD values recorded at the B01IV2016I test	331
Figure 387: Displacement values recorded at the B01IV2016I test	332
Figure 388: Load values recorded at the B01IV2016I test	332
Figure 389: CMOD values recorded at the B01IV2016II test	333
Figure 390: Displacement values recorded at the B01IV2016II test	333
Figure 391: Load values recorded at the B01IV2016II test	334
Figure 392: CMOD values recorded at the B01IV2016III test	334
Figure 393: Displacement values recorded at the B01IV2016III test	335
Figure 394: Load values recorded at the B01IV2016III test	335
Figure 395: CMOD values recorded at the B01IV2016IV test	336
Figure 396: Displacement values recorded at the B01IV2016IV test	336
Figure 397: Load values recorded at the B01IV2016IV test	337
Figure 398: Corrected load vs. CMOD at the B01IV2016I test	338
Figure 399: Corrected load vs. CMOD at the B01IV2016II test	338
Figure 400: Corrected load vs. CMOD at the B01IV2016III test	339
Figure 401: Corrected load vs. CMOD at the B01IV2016IV test	339
Figure 402: Corrected load vs. Displacement at the B01IV2016I test	340
Figure 403: Corrected load vs. Displacement at the B01IV2016II test	340
Figure 404: Corrected load vs. Displacement at the B01IV2016III test	341
Figure 405: Corrected load vs. Displacement at the B01IV2016IV test	341

Figure 406: Corrected load vs. X at the B01IV2016I test with the final upper curve data	342
Figure 407: Corrected load vs. X at the B01IV2016II test with the final upper curve data	342
Figure 408: Corrected load vs. X at the B01IV2016III test with the final upper curve data	343
Figure 409: Corrected load vs. X at the B01IV2016IV test with the final upper curve data	343
Figure 410: Softening curve bilinear approximation of the 01IV2016 campaign	344
Figure 411: Softening curve bilinear approximation of the 01IV2016 campaign in the reduced form	344
Figure 412: 01IV2016 Corrected load vs. CMOD from the entire campaign	345
Figure 413: 01IV2016 Corrected load vs. Displacement from the entire campaign	345
Figure 414: 01IV2016 Corrected load vs. Displacement from the entire campaign (peak displacement zero)	346
Figure 415: 01IV2016 Corrected load vs. X from the entire campaign	346
Figure 416: CMOD values recorded at the B07IV2016I test	347
Figure 417: Displacement values recorded at the B07IV2016I test	348
Figure 418: Load values recorded at the B07IV2016I test	348
Figure 419: CMOD values recorded at the B07IV2016II test	349
Figure 420: Displacement values recorded at the B07IV2016II test	349
Figure 421: Load values recorded at the B07IV2016II test	350
Figure 422: CMOD values recorded at the B07IV2016III test	350
Figure 423: Displacement values recorded at the B07IV2016III test	351
Figure 424: Load values recorded at the B07IV2016III test	351
Figure 425: CMOD values recorded at the B07IV2016IV test	352
Figure 426: Displacement values recorded at the B07IV2016IV test	352
Figure 427: Load values recorded at the B07IV2016IV test	353
Figure 428: Corrected load vs. CMOD at the B07IV2016I test	354
Figure 429: Corrected load vs. CMOD at the B07IV2016II test	354
Figure 430: Corrected load vs. CMOD at the B07IV2016III test	355
Figure 431: Corrected load vs. CMOD at the B07IV2016IV test	355
Figure 432: Corrected load vs. Displacement at the B07IV2016I test	356
Figure 433: Corrected load vs. Displacement at the B07IV2016II test	356
Figure 434: Corrected load vs. Displacement at the B07IV2016III test	357
Figure 435: Corrected load vs. Displacement at the B07IV2016IV test	357
Figure 436: Corrected load vs. X at the B07IV2016I test with the final upper curve data	358
Figure 437: Corrected load vs. X at the B07IV2016II test with the final upper curve data	358
Figure 438: Corrected load vs. X at the B07IV2016III test with the final upper curve data	359
Figure 439: Corrected load vs. X at the B07IV2016IV test with the final upper curve data	359
Figure 440: Softening curve bilinear approximation of the 07IV2016 campaign	360
Figure 441: Softening curve bilinear approximation of the 07IV2016 campaign in the reduced form	360
Figure 442: 07IV2016 Corrected load vs. CMOD from the entire campaign	361
Figure 443: 17III2016 Corrected load vs. Displacement from the entire campaign	361

Figure 444: 07IV2016 Corrected load vs. Displacement from the entire campaign (peak displacement zero) _	362
Figure 445: 07IV2016 Corrected load vs. X from the entire campaign _____	362
Figure 446: CMOD values recorded at the B14IV2016I test _____	363
Figure 447: Displacement values recorded at the B14IV2016I test _____	364
Figure 448: Load values recorded at the B14IV2016I test _____	364
Figure 449: CMOD values recorded at the B14IV2016II test _____	365
Figure 450: Displacement values recorded at the B14IV2016II test _____	365
Figure 451: Load values recorded at the B14IV2016II test _____	366
Figure 452: CMOD values recorded at the B14IV2016III test _____	366
Figure 453: Displacement values recorded at the B14IV2016III test _____	367
Figure 454: Load values recorded at the B14IV2016III test _____	367
Figure 455: CMOD values recorded at the B14IV2016IV test _____	368
Figure 456: Displacement values recorded at the B14IV2016IV test _____	368
Figure 457: Load values recorded at the B14IV2016IV test _____	369
Figure 458: Corrected load vs. CMOD at the B14IV2016I test _____	370
Figure 459: Corrected load vs. CMOD at the B14IV2016II test _____	370
Figure 460: Corrected load vs. CMOD at the B14IV2016III test _____	371
Figure 461: Corrected load vs. CMOD at the B14IV2016IV test _____	371
Figure 462: Corrected load vs. Displacement at the B14IV2016I test _____	372
Figure 463: Corrected load vs. Displacement at the B14IV2016II test _____	372
Figure 464: Corrected load vs. Displacement at the B14IV2016III test _____	373
Figure 465: Corrected load vs. Displacement at the B14IV2016IV test _____	373
Figure 466: Corrected load vs. X at the B14IV2016I test with the final upper curve data _____	374
Figure 467: Corrected load vs. X at the B14IV2016II test with the final upper curve data _____	374
Figure 468: Corrected load vs. X at the B14IV2016III test with the final upper curve data _____	375
Figure 469: Corrected load vs. X at the B14IV2016IV test with the final upper curve data _____	375
Figure 470: Softening curve bilinear approximation of the 14IV2016 campaign _____	376
Figure 471: Softening curve bilinear approximation of the 14IV2016 campaign in the reduced form _____	376
Figure 472: 14IV2016 Corrected load vs. CMOD from the entire campaign _____	377
Figure 473: 14IV2016 Corrected load vs. Displacement from the entire campaign _____	377
Figure 474: 14IV2016 Corrected load vs. Displacement from the entire campaign (peak displacement zero) _	378
Figure 475: 14IV2016 Corrected load vs. X from the entire campaign _____	378
Figure 476: CMOD values recorded at the B21IV2016I test _____	379
Figure 477: Displacement values recorded at the B21IV2016I test _____	380
Figure 478: Load values recorded at the B21IV2016I test _____	380
Figure 479: CMOD values recorded at the B21IV2016II test _____	381
Figure 480: Displacement values recorded at the B21IV2016II test _____	381
Figure 481: Load values recorded at the B21IV2016II test _____	382

Figure 482: CMOD values recorded at the B21IV2016III test	382
Figure 483: Displacement values recorded at the B21IV2016III test	383
Figure 484: Load values recorded at the B21IV2016III test	383
Figure 485: CMOD values recorded at the B21IV2016IV test	384
Figure 486: Displacement values recorded at the B21IV2016IV test	384
Figure 487: Load values recorded at the B21IV2016IV test	385
Figure 488: Corrected load vs. CMOD at the B21IV2016I test	386
Figure 489: Corrected load vs. CMOD at the B21IV2016II test	386
Figure 490: Corrected load vs. CMOD at the B21IV2016III test	387
Figure 491: Corrected load vs. CMOD at the B21IV2016IV test	387
Figure 492: Corrected load vs. Displacement at the B21IV2016I test	388
Figure 493: Corrected load vs. Displacement at the B21IV2016II test	388
Figure 494: Corrected load vs. Displacement at the B21IV2016III test	389
Figure 495: Corrected load vs. Displacement at the B21IV2016IV test	389
Figure 496: Corrected load vs. X at the B21IV2016I test with the final upper curve data	390
Figure 497: Corrected load vs. X at the B21IV2016II test with the final upper curve data	390
Figure 498: Corrected load vs. X at the B21IV2016III test with the final upper curve data	391
Figure 499: Corrected load vs. X at the B21IV2016IV test with the final upper curve data	391
Figure 500: Softening curve bilinear approximation of the 21IV2016 campaign	392
Figure 501: Softening curve bilinear approximation of the 21IV2016 campaign in the reduced form	392
Figure 502: 21IV2016 Corrected load vs. CMOD from the entire campaign	393
Figure 503: 21IV2016 Corrected load vs. Displacement from the entire campaign	393
Figure 504: 21IV2016 Corrected load vs. Displacement from the entire campaign (peak displacement zero)	394
Figure 505: 21IV2016 Corrected load vs. X from the entire campaign	394
Figure 506: Basis for the construction of the bilinear approximation function	406
Figure 507: Summarized schedule on a Gantt diagram	424
Figure 508: Material used – Sand 0/2	426
Figure 509: Material used – Aggregate 5/10	426
Figure 510: Material used – CEM II/B-L 32.5N	427
Figure 511: Machinery used – 100L cement mixer	427
Figure 512: Materials for a single campaign made with a cement mixer	428
Figure 513: Example of underwater preservation	429
Figure 514: Just after casting – Beams and cylinders with their molds and a machine used – Needle vibrator	429
Figure 515: On-live recording program – StrainSmart 5000	430
Figure 516: Visible crack after the peak load	430
Figure 517: Crack at an advanced stage of the test, near the end of it	431
Figure 518: Result of a three-point bending test	431

LIST OF TABLES

Table 1: Campaign 23X2015 mixture composition	38
Table 2: Campaign 23X2015 tests	38
Table 3: Main dimensions of the beam specimens from the campaign 23X2015	38
Table 4: 23X2015 campaign mechanical properties. When available, standard deviation in brackets	38
Table 5: 23X2015 campaign journal summary	39
Table 6: Campaign 14XII2015 mixture composition	40
Table 7: Campaign 14XII2015 tests	40
Table 8: 14XII2015 campaign mechanical properties. When available, standard deviation in brackets. When the data is not valid and, even so, it is shown, an asterisk remarks it	40
Table 9: Main dimensions of the beam specimens from the campaign 14XII2015	41
Table 10: 14XII2015 campaign journal summary	41
Table 11: Campaign 29I2016 mixture composition	42
Table 12: Campaign 29I2016 tests	42
Table 13: Main dimensions of the beam specimens from the campaign 29I2016	43
Table 14: 29I2016 campaign mechanical properties. When available, standard deviation in brackets. When the data is not valid and, even so, it is shown, an asterisk remarks it	43
Table 15: 29I2016 campaign journal summary	43
Table 16: Campaign 10III2016 mixture composition	44
Table 17: Campaign 10III2016 tests	44
Table 18: Main dimensions of the beam specimens from the campaign 10III2016	44
Table 19: 10III2016 campaign mechanical properties. When available, standard deviation in brackets	45
Table 20: 10III2016 campaign journal summary	45
Table 21: Campaign 17III2016 mixture composition	46
Table 22: Campaign 17III2016 tests	46
Table 23: Main dimensions of the beam specimens from the campaign 17III2016	46
Table 24: 17III2016 campaign mechanical properties. When available, standard deviation in brackets	46
Table 25: 17III2016 campaign journal summary	47
Table 26: Campaign 01IV2016 mixture composition	48
Table 27: Campaign 01IV2016 tests	48
Table 28: Main dimensions of the beam specimens from the campaign 01IV2016	48
Table 29: 01IV2016 campaign mechanical properties. When available, standard deviation in brackets	48
Table 30: 01IV2016 campaign journal summary	49

Table 31: Campaign 07IV2016 mixture composition _____	50
Table 32: Campaign 07IV2016 tests _____	50
Table 33: Main dimensions of the beam specimens from the campaign 07IV2016 _____	50
Table 34: 07IV2016 campaign mechanical properties. When available, standard deviation in brackets _____	50
Table 35: 07IV2016 campaign journal summary _____	51
Table 36: Campaign 14IV2016 mixture composition _____	52
Table 37: Campaign 14IV2016 tests _____	52
Table 38: Main dimensions of the beam specimens from the campaign 14IV2016 _____	52
Table 39: 14IV2016 campaign mechanical properties. When available, standard deviation in brackets _____	52
Table 40: 14IV2016 campaign journal summary _____	53
Table 41: Campaign 21IV2016 mixture composition _____	54
Table 42: Campaign 21IV2016 tests _____	54
Table 43: Main dimensions of the beam specimens from the campaign 21IV2016 _____	54
Table 44: 21IV2016 campaign mechanical properties. When available, standard deviation in brackets _____	54
Table 45: 21IV2016 campaign journal summary _____	55
Table 46: Summary of the tested campaigns _____	66
Table 47: Fracture work, tail work and fracture energy of concrete. Standard deviation in brackets _____	79
Table 48: Results of the bilinear approximation of the softening curve _____	88
Table 49: Results of the bilinear approximation of the reduced softening curve _____	89
Table 50: Data for the 23X2015 campaign elastic modulus determination. Sizes in millimeters _____	100
Table 51: Data for the 14XII2015 campaign elastic modulus determination. Sizes in millimeters _____	103
Table 52: Data for the 29I2016 campaign elastic modulus determination. Sizes in millimeters _____	108
Table 53: Data for the 10III2016 campaign elastic modulus determination. Sizes in millimeters _____	114
Table 54: Data for the 17III2016 campaign elastic modulus determination. Sizes in millimeters _____	117
Table 55: Data for the 01IV2016 campaign elastic modulus determination. Sizes in millimeters _____	120
Table 56: Data for the 07IV2016 campaign elastic modulus determination. Sizes in millimeters _____	123
Table 57: Data for the 14IV2016 campaign elastic modulus determination. Sizes in millimeters _____	126
Table 58: Data for the 21IV2016 campaign elastic modulus determination. Sizes in millimeters _____	129
Table 59: Data for the 23X2015 campaign tensile strength determination _____	137
Table 60: Data for the 14XII2015 campaign tensile strength determination _____	138
Table 61: Data for the 29I2016 campaign tensile strength determination _____	141
Table 62: Data for the 10III2016 campaign tensile strength determination _____	144
Table 63: Data for the 17III2016 campaign tensile strength determination _____	146
Table 64: Data for the 01IV2016 campaign tensile strength determination _____	148
Table 65: Data for the 07IV2016 campaign tensile strength determination _____	150
Table 66: Data for the 14IV2016 campaign tensile strength determination _____	152
Table 67: Data for the 21IV2016 campaign tensile strength determination _____	154
Table 68: Compressive strength for cylindrical and cubic specimens for different concrete classes _____	156

Table 69: Data for the 23X2015 campaign compressive strength determination for cylindrical specimens	159
Table 70: Data for the 23X2015 campaign compressive strength determination for cubic specimens	159
Table 71: Data for the 14XII2015 campaign compressive strength determination for cylindrical specimens	161
Table 72: Data for the 29I2016 campaign compressive strength determination for cubic specimens	162
Table 73: Data for the 10III2016 campaign compressive strength determination for cylindrical specimens	164
Table 74: Data for the 17III2016 campaign compressive strength determination for cylindrical specimens	165
Table 75: Data for the 01IV2016 campaign compressive strength determination for cylindrical specimens	166
Table 76: Data for the 07IV2016 campaign compressive strength determination for cylindrical specimens	167
Table 77: Data for the 14IV2016 campaign compressive strength determination for cylindrical specimens	168
Table 78: Data for the 21IV2016 campaign compressive strength determination for cylindrical specimens	169
Table 79: Results of the first speed study – 17III2016 campaign	175
Table 80: Campaign 23X2015 individual results	396
Table 81: Campaign 14XII2015 individual results	397
Table 82: Campaign 29I2016 individual results	398
Table 83: Campaign 29I2016 individual results for the local fracture energy theory	398
Table 84: Campaign 10III2016 individual results	400
Table 85: Campaign 17III2016 individual results	401
Table 86: Campaign 01IV2016 individual results	402
Table 87: Campaign 07IV2016 individual results	403
Table 88: Campaign 14IV2016 individual results	404
Table 89: Campaign 21IV2016 individual results	405
Table 90: Measurement for material 1 – Sand 0/2	414
Table 91: Measurement for material 2 – Aggregate 5/10	415
Table 92: Measurement for material 3 – CEM II/B-L 32.5N	415
Table 93: Measurement for material 4 – Water	416
Table 94: Measurement for material 5 – Concrete HA-25/F/15/IIa	416
Table 95: Measurement for material 6 – Dust 0/2	417
Table 96: Measurement for material 7 - Plasticizer	417
Table 97: Measurement for material 8 – CEM I 52.5R	417
Table 98: Measurement for material 9 – Paper, gray scaled, two faces	417
Table 99: Measurement for material 10 – Paper, color, two faces	418
Table 100: Measurement for material 11 – 22m thickness agglomerate waterproof wood	418
Table 101: Measurement for material 12 – Concrete adhesive	418
Table 102: Measurement for material 13 – Iron	418
Table 103: Measurement for material 14 – 100mm long wood bolt	418
Table 104: Measurement for manpower 1 – Concrete building trowel	419
Table 105: Measurement for manpower 2 – Engineer	419
Table 106: Measurement for machine 1 – 100L cement mixer	420

<i>Table 107: Measurement for machine 2 – Needle vibrator</i>	420
<i>Table 108: Measurement for machine 3 – Saw</i>	420
<i>Table 109: Measurement for test 1 – Bending test</i>	421
<i>Table 110: Measurement for test 2 – Brazilian test</i>	421
<i>Table 111: Measurement for test 3 – Direct compression</i>	421
<i>Table 112: Material direct costs by element</i>	422
<i>Table 113: Manpower direct costs by element</i>	422
<i>Table 114: Machinery and tests direct costs by element</i>	422
<i>Table 115: Total costs summary</i>	423
<i>Table 116: Campaign costs by nature</i>	423
<i>Table 117: Mean costs by nature</i>	423
<i>Table 118: Detailed schedule</i>	424

ACKNOWLEDGEMENTS

At this point, I would like to take some time for making a recognition and for saying a few words of thanks for the contributions, the help, the advices and the support of some people which made the work contained and linked to this project possible, easier, more attractive and interesting during the near 13 months I have work for this.

First of all, I am grateful to Cristina Barris for her guidance in the world of concrete mechanics and experimentation. Surely, I would not have done this project in concrete fracture mechanics if she had not given me a research line that caught my attention quite easily, alongside the possibility to have the resources I could require for it and to comment all questions I needed to do.

This gratitude is also extended to the entire research group of structural and materials research at the University, AMADE, with the chance to have the systems and technologies available for them also available for this project and for the comments and remarks from some of the staff about the research which helped to enrich it.

I cannot forget the essential help of Pere Bellvehí, always at the laboratories of the University. Everything that I have done there needs his recognition. With him I learnt all I currently know about the casting of concrete, the proper fabrication of concrete specimens and the use of the testing systems at the University. And I also give him thanks for helping me to move and prepare the specimens for being tested and for fining quickly all I searched in the laboratories.

This project is done thanks to them and other people who encouraged me and who tried ever to cheer me up. These are my friends and my family, especially the women of my family, so I dedicate this work to my mother, my sister, my grandmother, my family, my friends, my mates and anyone that has helped me somehow these four years in the University.

The author, Santi Rodríguez.

ABSTRACT

This research is focused in finding the fracture energy of concrete G_F at common environmental conditions for different concrete mixtures, trying to see how G_F changes while the composition or the properties of concrete change.

For achieving this goal, first, the fracture mechanisms that rule concrete fracture are reviewed, alongside the recommended testing procedures, forming together the first part of this document.

After that, several different series of concrete are casted with significant changes in their compositions, using as parameters the four basic components of concrete, which are sand, aggregate, cement and water. These series are tested and G_F is determined for them.

Finally, the registered G_F is compared for all series, trying to find a connection between the composition and the properties of concrete with G_F . The results shows that a strong bound can exist between G_F and the strength limits, making G_F higher while increasing those strength limits, and also a direct connection can exist with the composition in cement, sand and the water to cement ratio, the first one with higher G_F with higher proportions and for the last two, an inverse relation.

Nevertheless, the results are not absolutely conclusive and more tests are required for giving more information about these relations and for clarifying the connection with other parameters.

RESUMEN

Este trabajo de investigación se centra en encontrar la energía de fractura del hormigón G_F en condiciones ambientales comunes para diferentes mezclas de hormigón, intentando así ver cómo cambia el valor de G_F mientras se varía la composición o las propiedades del hormigón.

Para conseguir este objetivo, primero se estudian los mecanismos que gobiernan la fractura del hormigón, juntamente con los ensayos recomendados para este objetivo, formando ambos la primera parte de este documento.

Después, se hacen varias series de diferentes hormigones con cambios significativos en sus composiciones, usando como parámetros los cuatro componentes básicos del hormigón, sean: arena, árido, cemento y agua. Estas series se ensayan y se determina el valor de G_F para todas ellas.

Finalmente, los valores registrados de G_F son comparados entre todas las series, intentando encontrar conexión alguna entre la composición o las propiedades mecánicas del hormigón y la propiedad G_F . Los resultados muestran que hay una fuerte relación entre el valor de G_F y las resistencias límite, tanto de compresión como de tracción, obteniendo valores mayores de G_F cuán mayor son los valores de la resistencia, y también muestran que puede existir una relación directa entre la composición en cemento, en arena y el ratio agua-cemento, siendo para el primero mayores valores de G_F para proporciones más altas y para los dos últimos, una relación inversa.

No obstante, los resultados no son absolutamente concluyentes y se requieren más ensayos para proporcionar más información sobre estas relaciones y para clarificar la conexión que pueda existir con los otros parámetros.

ABBREVIATIONS AND NOTATIONS A (auxiliary) – First auxiliary constant A (dimension) – Section area A (parameter) – Far tail constant a – Notch depth ABS – Absolute a_i (mathematical function) – Element of i -order at a function $Agg.$ – Aggregate a_1 – Transition zone length B (auxiliary) – Second auxiliary constant B (beam) – Beam width b – Bearing strips width C (auxiliary) – Third auxiliary constant C_i – Initial compliance $CMOD$ – Crack Mouth Opening Displacement COD – Crack Opening Displacement D (auxiliary) – Fourth auxiliary constant D (beam) – Beam depth D (cube) – Edge length D (cylinder) – Diameter DIC – Digital Image Correlation E – Elastic modulus f_c (general property) – Compressive strength f_c (property from tests) – Compressive strength from cylinder-type specimens testing $f_{c,cube}$ – Compressive strength from cubic-type specimens testing f_p – Net plastic flexural strength FPZ – Fracture Process Zone f_t – Axial tensile strength g – Gravity field force g_f – Local fracture energy G_F – Real size-independent specific fracture energy G_f – Size-dependent fracture energy h – Steel knives depth i – Element of a series ID – Identifier

K – Non-used constant at the far tail parabolic fitting

L – Length

l_1 – Brittleness length

LDT – Linear Displacement Transducer

$LEFM$ – Linear Elastic Fracture Mechanics

M – Bending moment

m (mathematical function) – Slope of a first order function

m (physical property) – Mass

N – Notch width

n (mathematical function) – Image at the X-axis origin from a first order function

n (number set) – Length of a series

OX – X-axis

OY – Y-axis

P – Load (general)

P' – Uncorrected load and the directly registered load

P_1 – Corrected load

P_{1u} (or P_{1U}) – Corrected peak load

$P_{ef,max}$ (or P_{ef}) – Effective peak load

P_{eq} – Equivalent load

P_f – Final test load

P_R' (or P_R) – Last record used for the uncorrected load

P_u (or P_U) – Ultimate load

P_u' (or P_U') – Uncorrected peak load

REL – Relative

S – Span length

u – Horizontal displacement

V – Shear force

v – Vertical displacement

V_1 – Function for the elastic modulus determination

w – Crack width

\hat{w} – Reduced crack width

W/C (or w/c) – Water to cement ratio

w_1 – Initial intercept of the softening curve

w_c – Critical crack width

\hat{w}_c – Reduced critical crack width

w_{ch} – Characteristic crack width

W_f – Fracture work

w_G – Gravity center at the crack width axis of the area enclosed down the softening curve respect crack width zero

w_k – Crack width at the kink point of the softening curve bilinear approximation

w_M – The *CMOD* usable record

w_{MA} – First *CMOD* record usable

w_{MR} – Last *CMOD* record usable

W_{tail} – Non-measured fracture work of the $P - \delta$ curve tail and below

X – Artificial independent variable for the far tail parabolic fitting

x – X-axis variable. Independent variable

y – Y-axis variable. Dependent variable

y_c – Critical crack width location at the Y-axis

α – Notch to depth ratio

α_o' – Notch plus knives depth to specimen depth plus knives depth ratio

δ – Displacement

δ_A – First displacement record usable

δ_f – Final test displacement

δ_R – Last displacement record usable

δ_u – Total displacement

ε – Strain

θ – Rotation

σ – Normal stress

$\hat{\sigma}$ – Reduced normal stress

σ_I – Maximum principal stress

σ_k – Stress at the kink point of the softening curve bilinear approximation

Note: About the figures, tables and equation sequence

Figures are numbered from 1 to the total number of figures in this project and they are listed at the “List of figures”. Tables are numbered the same way with a “List of tables”.

Equations have not got any “List of equations”, so, in order to find them faster, they are numbered as “Equation A.X.Y”, where:

- *A is the chapter number or the appendix letter where the equation is written*
- *X is the subchapter number*
- *Y is a number from 1 to the total number of equations at chapter or appendix A.X*

Doing so, if one wants to find Equation 2.3.1, one should look to Chapter 2, Subchapter 3 and find the first equation in it. Equation G.2.5 is the fifth equation at Appendix G.2 and so on.

A RESEARCH ON CONCRETE FRACTURE MECHANICS

TESTING AND ANALYZING THE FRACTURE ENERGY OF CONCRETE

THE MEMORY

1 INTRODUCTION

1.1 BACKGROUND

Whenever somebody talks about the most important materials in civil engineering, it is almost inevitable to associate to the Spanish constructive style materials such as structural steel and concrete in all their diversity. Nevertheless, concrete is the first which comes to our minds, due to the low cost joined to its easy shaping, even though its resistance is lower than steel. These facts have made it widely used. It has a decisive importance in construction, being used in urban construction, bridges, tunnels, etc.

The need of knowing its behavior in conditions of use and the ways of conserving its integrity is, then, clear indeed. Research is needed in order to discover these mechanisms that affect them and, so, engineers will be capable to improve the concrete treatment.

At this point, it appears the main difference between concrete and steel referring to the mechanical behavior. While steel is a ductile material, having the same good response in a tensile stress mode than in a compressive one and showing an internal structure quite uniform at any point, what does not mean it cannot have irregularities, it means just that it is easier to obtain properties in a smaller range; concrete is just the opposite, showing a mainly brittle fracture response, a weakness working at a tensile stress mode, a good response in compression and a probabilistic high irregularity inside it. This means that the inner defects provoked by the water evaporation and a different distribution and type of aggregate can highly affect the properties of concrete, fact that explains the interest of a field research, alongside the model definition, in structural engineering.

The concrete fracture mechanics is one of these fields of study that are of high interest, because the moment of failure and the development of this material failure can help to avoid major damages and personal injuries.

Engineers, looking for simplicity, have used the constitutive models that predict the failure as a result of critical stress surpassing a value of limit strength, when working in uniaxial situations, or more complex models for static failure and fatigue failure for brittle materials. At this point we find model such as the static failure criteria of Mohr-Coulomb and Mohr-Coulomb-modified, mainly for biaxial

stress states, or more complex and modern criteria applicable to triaxial stress states in concrete or rocks with cohesive-frictional forces like the William-Warnke yield criterion ¹.

However, these models are only capable of giving approximate information in terms of a safety factor of when a material fails, depending on how conservative the theory is. This will lead engineers to ensure the safety of a structure with a high safety factor. However, they must be careful. Concrete, as a quasi-brittle material, presents a difference of the final failure criteria depending on the size of the structure, due to its non-linear behavior. If sizes are small, the strength criterion is useful, although large structures do not behave exactly so. That phenomenon is called the *size effect* ^{2,3} (see Figure 1). Moreover, these models can only predict the failure stress state and anything else. When a crack appears and it is able to progress, the strength criterion cannot be applied and it does not give further explanations.

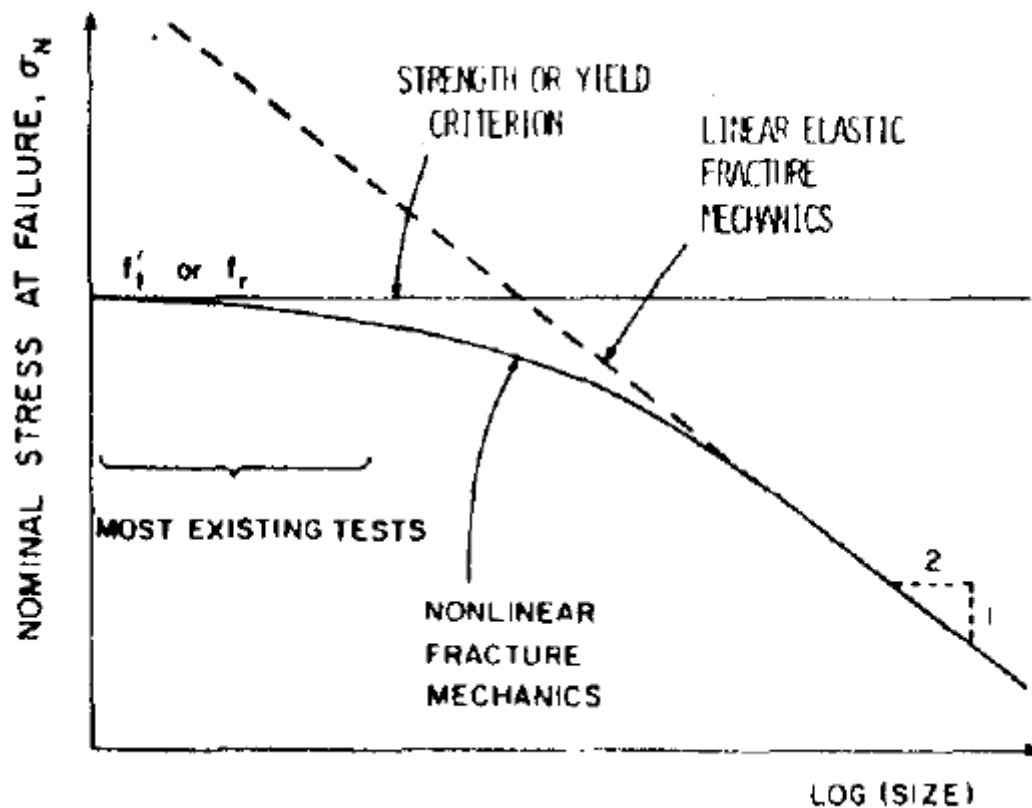


Figure 1: Size effect phenomenon in the nominal stress and applicable failure criteria. From ²

A new model was needed to explain the fracture mechanics, and not only for concrete, in all sort of materials used in every single branch of engineering.

Here, in the early 20s, it makes its entrance the basis of a failure and fracture theory based on energy balances, with a postulate that in an elastic solid the crack propagates thanks to a difference of the strain energy of the non-fractured and the strain energy released in the fractured body ⁴. In other words, the energy amount of a body is formed by the elastic strain energy present in the body plus the energy released in creating new surfaces and the free surface, that means, when a crack propagates the strain energy saved in the volume is released in surface energy and crack opening.

With such a new point of view of the fracture phenomena, some researchers started to study the stress distribution at the tip of some crack on different geometries. Of course, at crack tips exists a stress concentration, not only at the crack tip but at near points, and these stress fields vary according to the fracture mode. Only one parameter is needed to define the stresses and it is the stress intensity factor, which is not the same as the stress concentration factor, and equations using the position of a point to study respect the crack tip provide the stress information of it. For instance, a planar geometry supporting tensile forces in a plane stress or strain state with a crack at its middle has a model which can describe the stress state of all points near the crack tip ⁵.

To sum up, the equations showed a raising stress state as the point approaches to the crack tip. From here, theories such as the *Linear Elastic Fracture Mechanics (LEFM)* were later developed. However, mathematically, they present a stress singularity at the crack tip and they had to be modified. At the end, *LEFM* is capable to explain the fracture mechanics of materials such as steel, which is ductile enough to create plastic strains, but in a zone relatively small near the crack tip, even though a small non-linear zone can exist.

Now, the problem appears on trying to use this theory on concrete fracture. Due to its microscopic structure and its composition, when concrete works in a tensile mode, dislocations and microcracking at a microscopic scale can appear along all tensile stressed zones. This provokes the stress concentration to dissipate and the impossibility to use the stress intensity factor as in the *LEFM*, because it is unrealistic such a strong stress concentration phenomenon near the crack tip ⁶. The final stress intensity factor must be considered zero ⁷ and the *LEFM* has one reason for not being applied on concrete.

Moreover, this does not end here. The zone of fracture development, from now on the *Fracture Process Zone (FPZ)*, has sizes that cannot be unconsidered with respect to the standard concrete specimens dimensions ^{6,8,9}. For a schematic representation, see Figure 2. In this zone the non-linearities and microcracking formation have large importance. It is not a ductile material, but the matrix has a progressive degradation. These reasons are enough for not applying the *LEFM* theory.

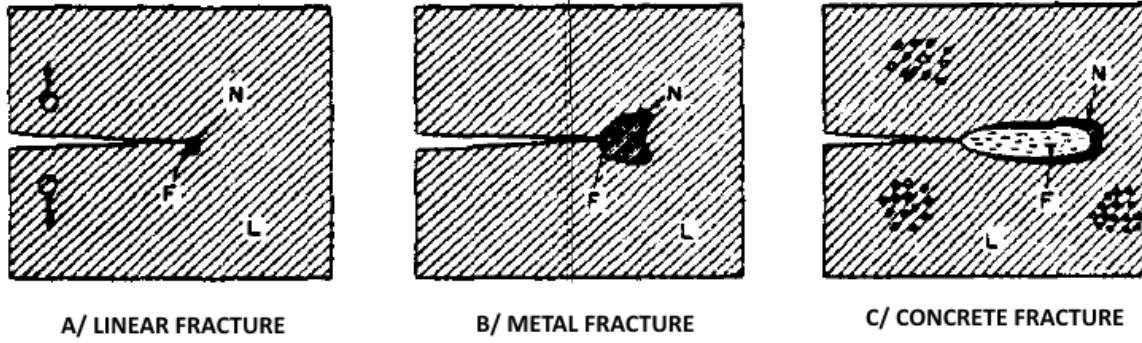


Figure 2: Relative sizes of the FPZ (F), the non-linear zone (N) and the linear behavior zone (L) in different type of materials. From ¹⁰

In the period between the 60s and 80s, it continued the research for a new model that could explain the concrete and mortar fracture. It was found a model that can explain the non-linearities provoked mostly by microcracking through what was called the *cohesive forces* ^{6,8,9,11}, acting in a region comparable as a real crack, but at a non-cracked region, known as the *fictitious crack*.

And here one locates the origin of the currently used theory for concrete fracture mechanics, the *fictitious crack tip*, also known as the *cohesive crack model*. The main concepts of this theory will be later explained and detailed.

All the new fracture theories based on energy balances have one parameter which represents the total amount of energy released in the formation of a unit of surface and it is one of the fundamental parameters at such kind of theories. It is the *specific fracture energy*, or just the *fracture energy*, G_F , which is considered and proved a material size-independent property ¹²⁻¹⁵, even though the *size effect* and its importance in lab-sized concrete specimens did not help on considering this size-independence, for instance, with the G_F recommended test procedures ¹⁶.

Nowadays, it is clear that G_F is a material property for a certain concrete mixture and that it can be used in further analysis, such as the *softening phenomenon* ^{6,12}, which will be also explained later, along the *cohesive crack model*, because it is of interest for this project to provide the theory more detailed. And here relies one of the current researchers' fields of study, which is the characterization of the different concrete types and mixtures fracture mechanics parameters and models, once the basis of a general fracture theory based on common models and material independent properties has been settled.

1.2 PURPOSE OF THIS PROJECT

The main goals that are meant to achieve with this research are:

1. To learn and to show the mechanisms that rule on the concrete fracture
2. To obtain an stable performance at the test for concrete fracture mechanics
3. To characterize the properties of some concrete mixtures associated with concrete fracture mechanics, such as the real size-independent fracture energy of concrete, at common environmental conditions
4. To review some of currently available methods for this last point
5. To develop all the tools that might be required in order to apply properly these methods
6. To compare the fracture parameters between some different concretes, only if the volume of available data allows it
7. To analyze the data for obtaining the results and correct conclusions

These goals define the core of this project, but they bring along other items that have to be considered, being this project an introduction to the concrete research. They are secondary goals, such as:

8. To learn the procedures, machines and other elements for concrete testing
9. To cast and to preserve properly the different specimens to be tested
10. To characterize a concrete mixture with its common mechanical properties and its composition

All these points will be search to be applied, realized or achieved at this project, giving to every one of it the importance it should have according to the central purpose of this research, which is the determination of parameters from concrete fracture mechanics, especially the concrete real fracture energy G_F .

1.3 SCOPE

Once all the goals are defined and their importance is qualified, it is time to plan how to achieve them. The methodology will be the following one.

First, a wide search on the theory of concrete fracture mechanics will be done, finding the theories of application and giving the main points of interest of them in the state of the art of this project, creating the literature review of the project.

Then, the literature review should also give the currently used methodology in order to obtain G_F and other fracture parameters. The mathematical expressions and their development should be found there, along with the testing methods and recommendations.

After all the literature review from the theory field and experimental field, the test procedures must be defined and, as a consequence, we should be able to reproduce them, seeking for their stability with the machines, sensors and elements available in the University.

This part is the most critical. Whenever the tests cannot be stable or properly done, this project will become unfeasible and the goals that need correct results will be automatically impossible to achieve and future actions will discard them temporally, always if this point does not change. If stability is found somehow, even applying the recommendations in a less restrictive way, the project will go on.

Considering now the project feasible, the next point will be a continuous testing and characterization of the mechanical properties and fracture properties from different concrete campaigns, adjusting the testing methodology when this is required.

On one hand, this will be done beginning with low- and normal-strength concrete. If the test stability is an easy point to obtain, this will also open the chance to test high-strength concretes, but only if stability allows it.

On the other hand, some alternative methods will be searched and it will be proposed to use them to verify the results that will be appearing during this project execution. Maybe, this part is not performed if there are not the tools to carry them out properly. However, it is considered that these options have to be explored in order to enhance the results validity.

Finally, results will be extracted. Its use and comparison will allow the creation of the conclusions from this project and the achievement, or not, of its main purpose. The range of the conclusions is bound to the volume of results.

The project will not seek to create new deviations, corrections and procedures from the current theory, because of the lack of knowledge given on this field to future *Industrial Technical Engineers*. They can have the basis for performing a mainly experimental project on fracture mechanics of any type of material, but this issue has not been told with the actual study plans.

For the concrete casting, information is also required so one can know in which direction the properties of concrete will move depending on their composition. This part and all the technical work at the lab section will remain hidden from this project, although concrete structures design is also not an issue dealt on the current industrial technical engineering plans.

The beginning for this project must be set quite early, because testing on concrete means automatically a time lapse of 28 days minimum.

The project decision and first contacts are done at the end of spring or beginning of summer from 2015. Once the first steps and the literature review are done and the feasibility is checked, the planning is a continuous casting and testing within this time lapse of a month between campaign and campaign until the considered deadline of last days of May 2016 or first days of June 2016 arrives. This procedure allows corrections from one campaign to other. This planning is not fixed, but it will be applied, at least, at the first periods.

1.4 STRUCTURE

The structure of this project wants to cover the current theory and methodology through different points of view.

- The initial part contains the lists of contents, figures and tables, the abstract and notation for the entire project and other parts outside the core of this project. The core is formed by every single section called “Chapter”
- The core of the project begins with a prologue with the recent history at concrete fracture mechanics field of research and the definition of this project at this Chapter 1
- The explanatory part of the theories of application is done at Chapter 2
- The test definition and the mathematical development have another chapter for them at Chapter 3
- The most technical definition of the materials used and the test procedures applied have the range of chapter at Chapter 4
- The global results analysis from the fracture mechanics tests is performed at Chapter 5
- A summary of the economic valuation and the schedule is placed at Chapter 6
- Conclusions and further statements begins to close the project core at Chapter 7
- The list of references is the last part of the project’s core at Chapter 8
- An “appendices” section is placed after Chapter 8 to provide:
 - Information about the characterization of the different concrete mixtures and the tests that do not give essential information about fracture properties, such as the strength limits and elastic moduli, at Appendix A
 - A general vision of the first attempts, modifications and other studies in order to perform and to improve stable tests at Appendix B
 - Details of the tools used to obtain the results at Appendix C, based on *MATLAB* codes, which is the main post-processing platform
 - The setup of the codes at Appendix D, then results can be reproduced from the data
 - Individual test and test campaign results from the fracture mechanic tests in graphs at Appendix E and numerical format at Appendix F, in order to reduce the core
 - The mathematical development from expressions given by the literature whose develop is required, because these are not found there, at Appendix G
 - All the information and details of the costs related to this project at Appendix H
 - The detailed schedule used for this project at Appendix I
 - A gallery with images not attached to any specific chapter at Appendix J

2 FUNDAMENTALS OF FRACTURE MECHANICS IN QUASIBRITTLE MATERIALS

2.1 FRACTURE MODEL APPLICABLE TO CONCRETE FRACTURE. THE COHESIVE CRACK MODEL

According to the background of this project, the fracture model applicable to concrete is the *cohesive crack model*, which has two main elements. First, a zone supporting a stress situation that provokes its degradation, which is called the *fracture process zone (FPZ)*. Second, in the *FPZ* it exists an ability of transmitting stresses, but in a weakened mode, and while the fracture process continues on developing, the capacity of transmitting stresses due to the degradation of the tensile-stressed zone will be even weaker. This is called the *softening* of the *cohesive stresses* ¹¹.

The main difference with the *LEFM* theory is the incapability of mortar and concrete to develop a zone of a high stress concentration near the crack tip as a result of microcracking that leads to this softening. See Figure 3 for a representation of both models stress concentrations.

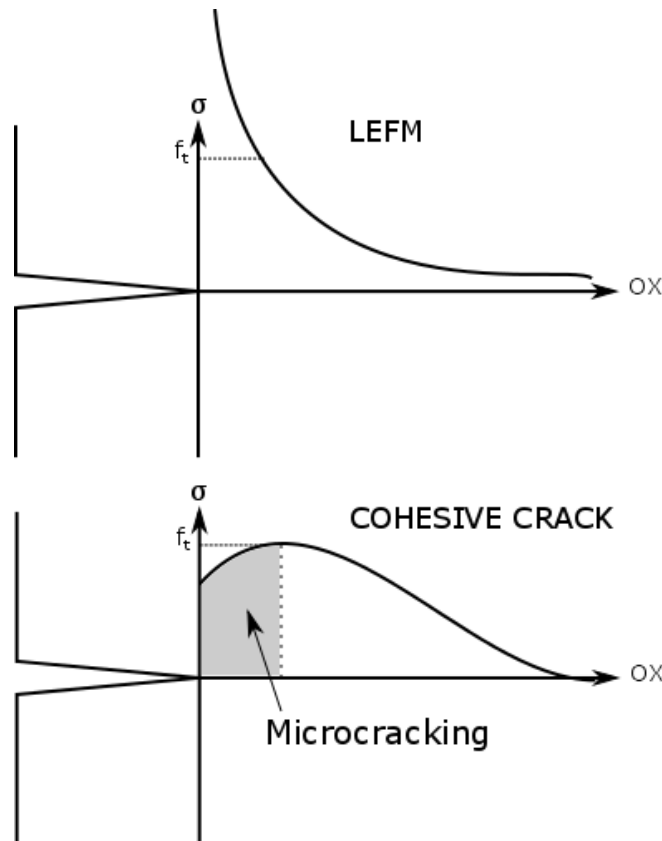


Figure 3: Stress distribution near the crack tip in both fracture models

The cohesive stresses are really important in materials such as concrete, because the *FPZ* sizes are important respect the global sizes. This *FPZ* importance and the presence of non-linearities provoked by microcracking lead one to predict a stress vs. strain curve similar to Figure 4⁶. Make notice that the areas inside the A zone of Figure 4 behave mainly linear elastic, the ones in zone B begin to behave non-linear as a consequence of the microcracking development, although macrocracking does not exist yet. Zone C represents the areas belonging to the *FPZ* where cohesive stress appears and softening has begun. In this part a crack has been created and it is able to develop. It is worth remarking that the initial softening occurs faster than the last. Zones are visible at Figure 5.

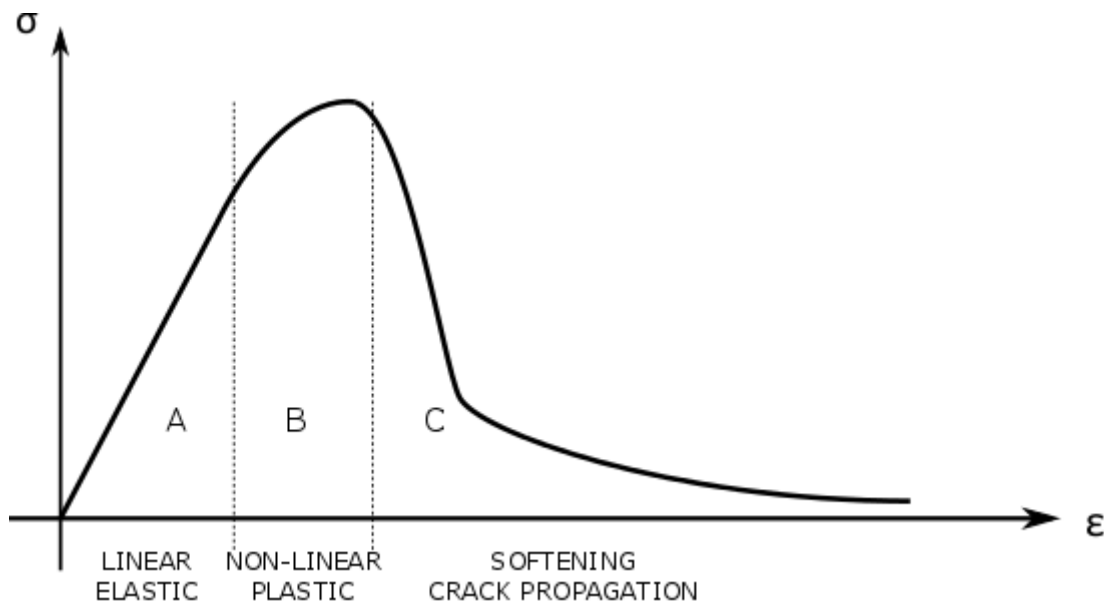


Figure 4: Full stress vs. strain curve in a cohesive crack model

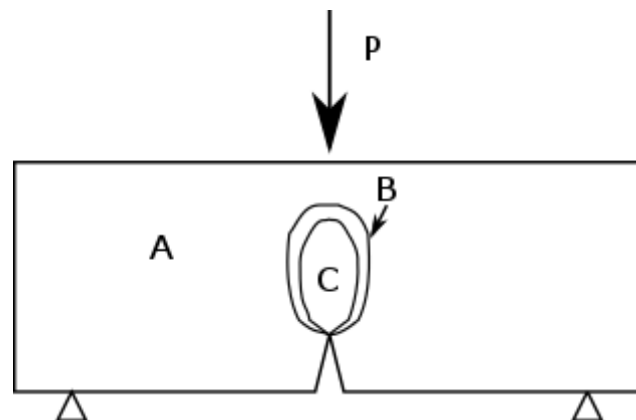


Figure 5: A three point bending test with the zones visible at Figure 4

At the very moment one cross-section fails, that is in the B to C transition at Figure 4, the microcracking formation is concentrated in zones near the *FPZ*, while the rest of the body remains elastically loaded and the cross-section cracked zone is able to progresses.

According to the exposed facts, one can affirm that ⁶:

- *FPZ* starts when a point whose maximum principal stress σ_I equals the tensile strength f_t .
- *FPZ* develops along the perpendicular direction to σ_I .
- *FPZ* is a zone in which the material degrades as a consequence of microcracking. This causes that the stress concentration disappears and the ability of transmitting stresses decreases. All this is called the softening of the material which has its own softening function that is considered a material property ^{6,12}. Same materials soften in a similar way. This is another form of saying that G_F is a material property.
- *FPZ* width equals the maximum crack opening width at any time. Therefore, at the beginning of the softening phenomenon, *FPZ* width is zero ⁶.
- Inside the *FPZ*, the softening function $\sigma(w)$ governs the behavior, where w is the crack opening in the direction of σ_I . Outside, it governs the classic constitutive stress vs. strain curve $\sigma(\epsilon)$.

Nevertheless, the softening occurs before a real visible crack appears, but it is a function of the crack opening. This contradiction is solved with the postulates of the *fictitious crack* ^{6,8,9}. The *FPZ* zone has microcracked regions that create a displacement that can be considered as a crack width. This displacement, caused by the inner cracks, provoke the weaken ability to transfer stresses, so the softening curve is meant to be a function of the crack opening, because the microscopic cracking provokes a measurable displacement between both sides of the cross-section, which is called the fictitious crack, while stresses decrease as long as the displacement is bigger. See Figure 6 for this fictitious crack consideration.



Figure 6: Adaptation of the displacements along both sides of the cross-section containing the *FPZ* as a fictitious crack with its cohesive stresses, weaker as displacement increases

This introduction of a fictitious cracked region gives us an easier way to develop the cohesive crack theory. From now on, on the crack propagation front we will consider three regions (see Figure 7), one with a real visible crack, one where dislocations and microcracking exist and another one as a mainly intact zone (see Figure 7).

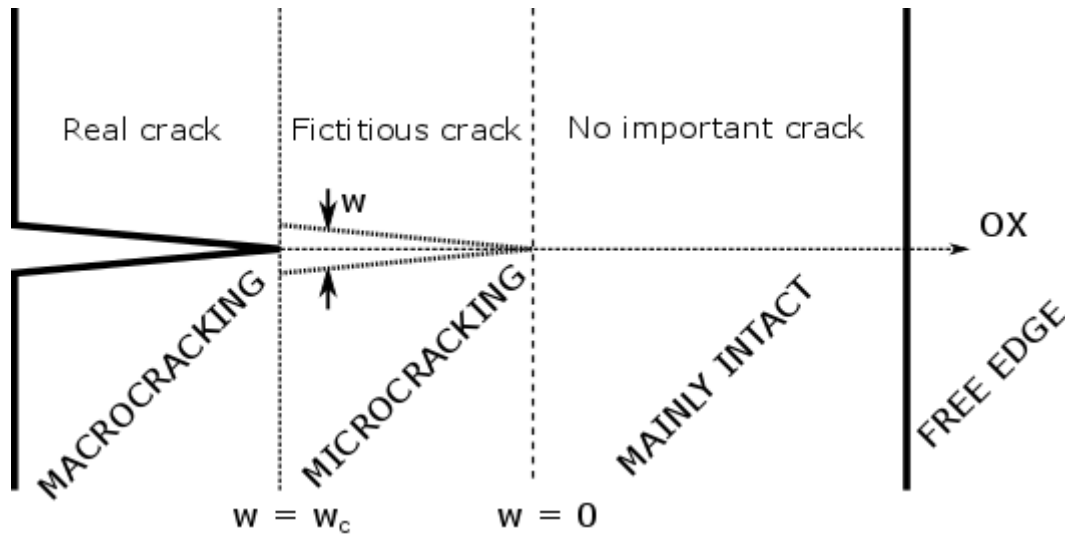


Figure 7: Real and fictitious crack tip and crack development front

The three zones have different behaviors. Consider now the opening parameter w the crack opening of either real or fictitious crack. The fictitious crack develops equally as a real crack, that is, when the fictitious crack progresses (it is the same to say that the *FPZ* progresses), the fictitious crack is considered to make longer and wider (see Figure 8).

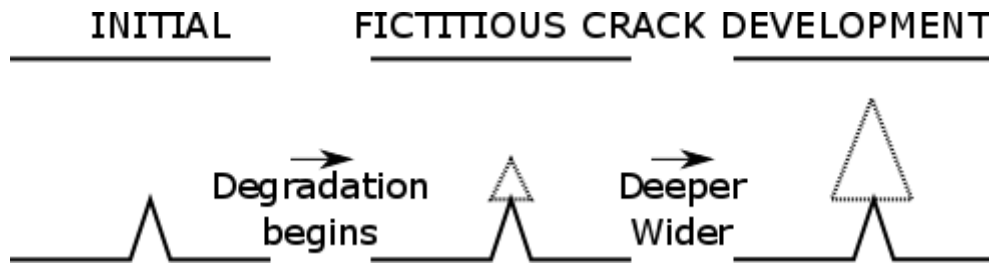


Figure 8: Fictitious crack creation and development

The limit between the 3 zones considered at Figure 7 is defined thanks to w^9 :

- Zones in which does not exist any displacement ($w = 0$), where w does not include now the elastic displacements, are considered mainly intact and the classic $\sigma(\epsilon)$ defines the constitutive equation, both in a linear elastic and non-linear inelastic regions (see Figure 9).
- Zones where a dislocation exists but any visible crack is formed are considered microcracked or fictitiously cracked and the softening function $\sigma(w)$ of the material is applied as the constitutive equation (see Figure 10). The maximum width that allows the stresses to be transferred is called the *critical crack width* w_c .
- Zones where the opening or displacements exceed w_c are considered really cracked and no stress transfers between the two faces of the cross-section exist. That means $\sigma = 0$.

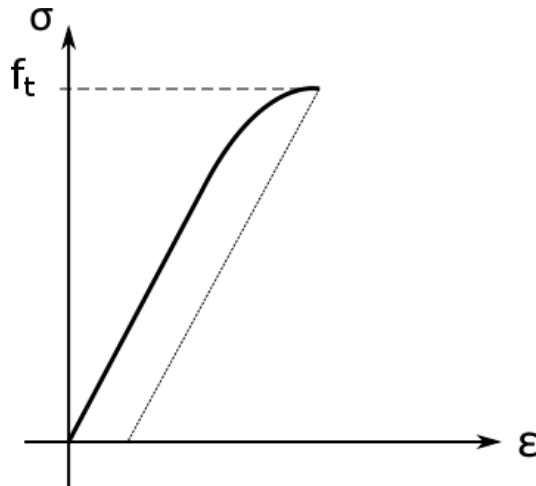


Figure 9: A stress vs. strain curve in the tensile region applicable to concrete

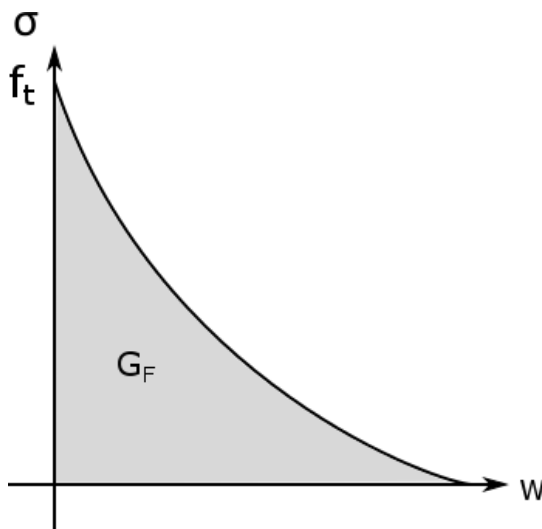


Figure 10: A stress vs. crack opening softening curve applicable to concrete

As a result, one can say that knowing the two curves $\sigma(\epsilon)$ and $\sigma(w)$, the behavior of concrete under fracture is clear ⁹. The problem relies now on obtaining the softening curves and other properties that define the fracture mechanics, such as w_c or the energy released in fracture G_F .

The area enclosed down the softening curve is the fracture energy ¹² (Equation 2.1.1).

$$G_F = \int_0^{+\infty} \sigma(w)dw = \int_0^{w_c} \sigma(w)dw \quad (2.1.1)$$

For this reason, saying that the softening curve is only a material property ^{6,12} is the same to say G_F is also only a material property, then the Equation 2.1.1 development will be unique for a given material.

2.2 THE SOFTENING PHENOMENON IN THE FRACTURE PROCESS ZONE AND THE FRACTURE ENERGY

Let us consider now a concrete notched beam in a three-point bending situation, provoked by a central. According to what has been mentioned before, one would expect a load versus load applicator vertical displacement curve such as the one at Figure 11. Different regions have been pointed out. These regions can be associated with a situation of the stress and crack opening progress.

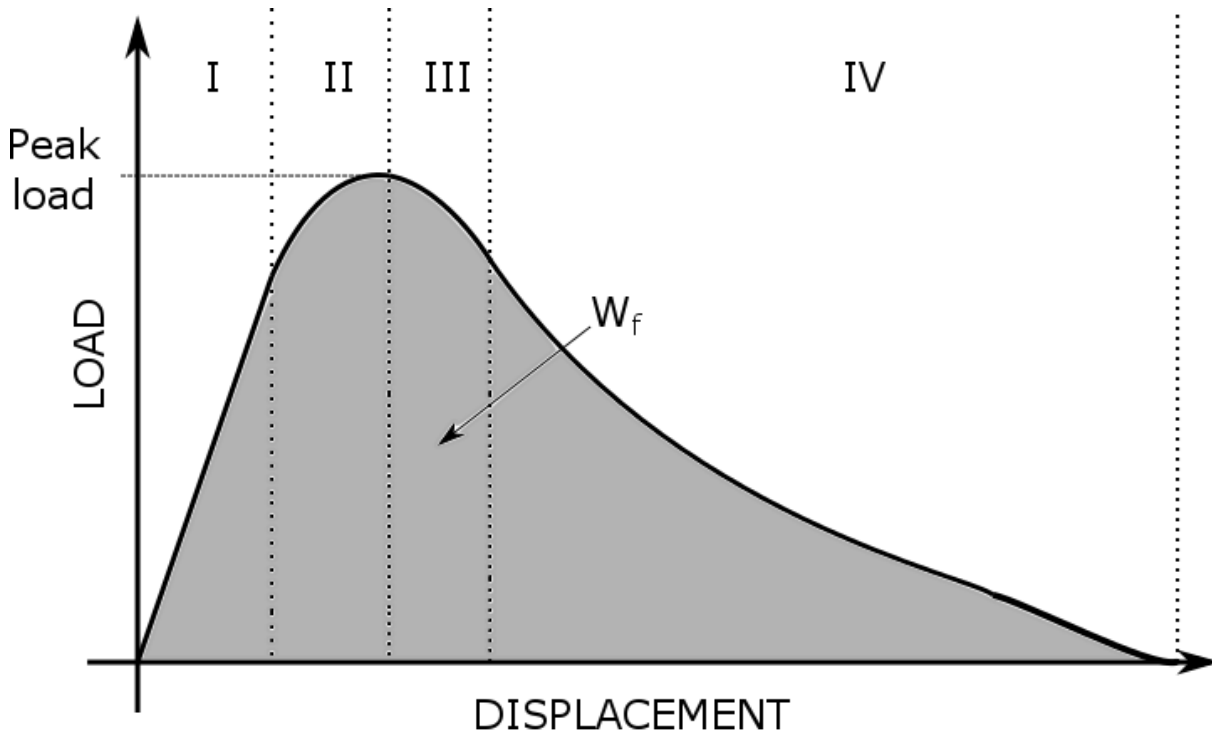


Figure 11: Load vs. displacement curve on a three point bending situation

If we consider that the load P is the only external force, which means that even self-weight does not affect, the total amount of energy introduced to the system is the given by P , where the total energy introduced is represented by Equation 2.2.1, where δ is the load application point displacement.

$$W_P = \int_0^{+\infty} P d\delta = W_f \quad (2.2.1)$$

In an idealized case it would be obvious that the only energy entrance must be balanced somehow, first in form of elastic potential energy and later, as a crack develops and load decreases, the energy is released in fracture. Then, the work introduced by the load can be called the fracture work W_f (Equation 2.2.1).

The zones defined at Figure 11 can be described by the following criteria:

- Zone I: the material behaves mainly linear elastic and the stresses develop as usual (see Figure 12 and Figure 13). Make notice that in a bending situation, for a fast determination of the peak load it is not used the axial tensile strength, but the flexural tensile strength, which is commonly higher¹⁷. Once the axial tensile strength is achieved, and never surpassed, the next situation appears. No stress singularity, as in *LEFM*, is able to appear, which will contradict the nature of the material with its microscopic displacements appearing now.
- Zone II: the material begins to show microcracking and microscopic dislocations. This leads to the presence of major non-linearities inside the body and the stress concentration disappears. The softening of the cohesive stresses and the *FPZ* progression has begun (see Figure 14). At any point, the maximum bending moment is reached and so the maximum load. It is the point where the stress distribution balances with a maximum bending moment. After that, the fictitious crack continues to develop and the next situation appears.
- Zone III: the *FPZ* is longer and wider and the softening continues at the tip of the notch. No real crack has yet appeared but the load is decreasing. Any stress distribution now will lead to lower bending moment and lower load. When the material degradation at the crack tip arrives at a point in which it is unable to transmit stresses, meaning that w_c has been reached, the points at both sides of the cross-section will be considered finally divided and a visible crack will make its appearance (see Figure 15).
- Zone IV: the *FPZ* has its maximum width and while the force continues on introducing energy to the system, the fracture of the cross-section will continue. The stress distribution with the softened stresses just moves along with the crack tip (see Figure 16) with the appropriate values reconfiguration.

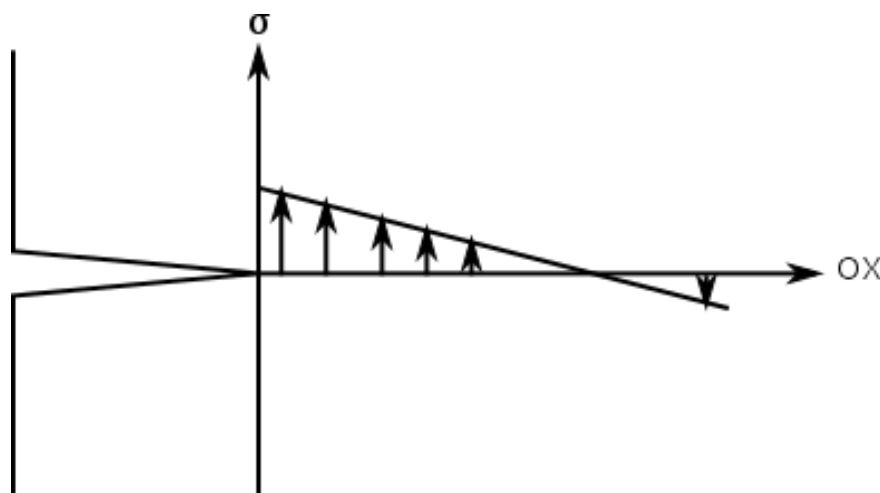


Figure 12: Stress distribution at an earlier point of zone I of Figure 11

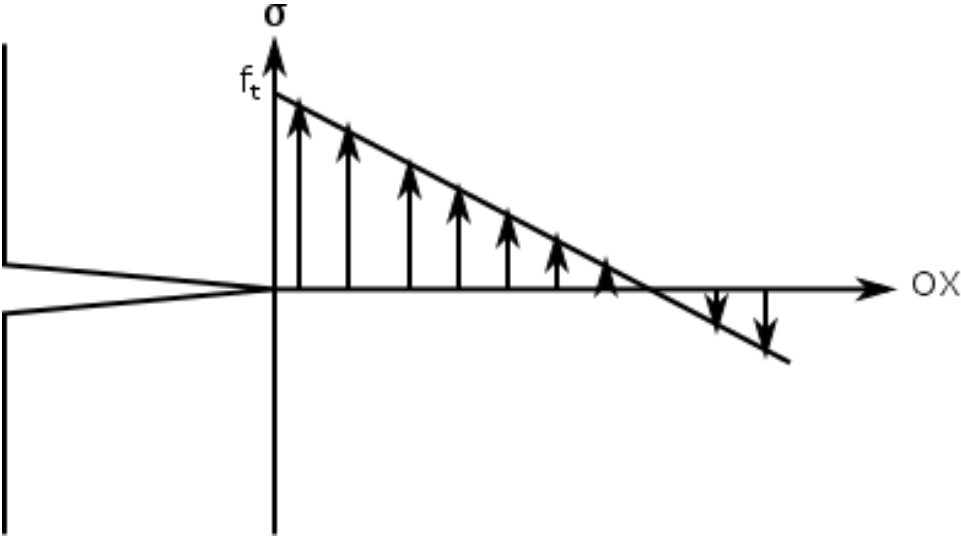


Figure 13: Stress distribution at an advanced point of zone I of Figure 11.

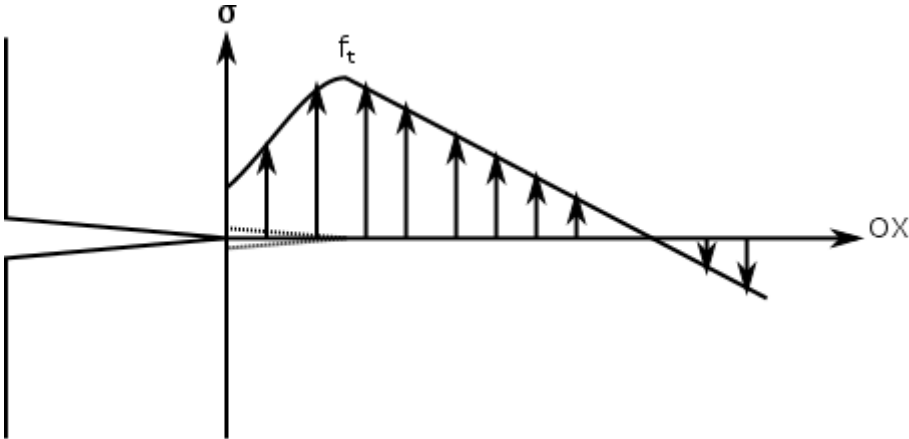


Figure 14: Stress distribution at a point of zone II of Figure 11

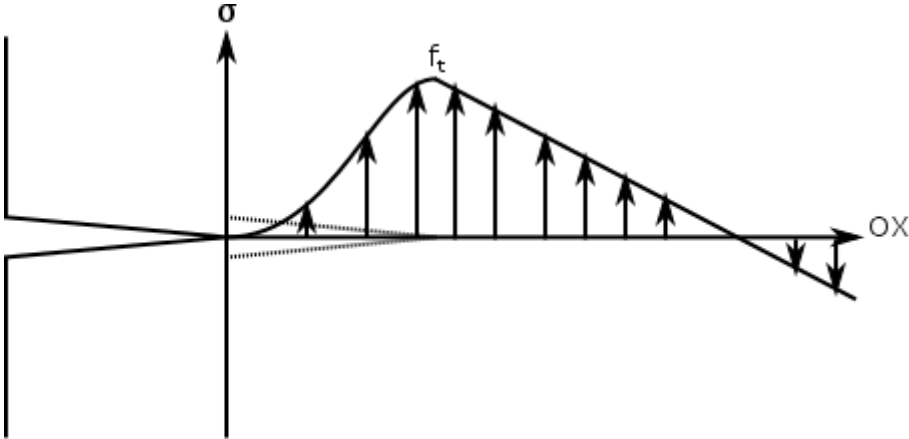


Figure 15: Stress distribution at the point where the fictitious crack shows the critical crack width at the zone III of Figure 11

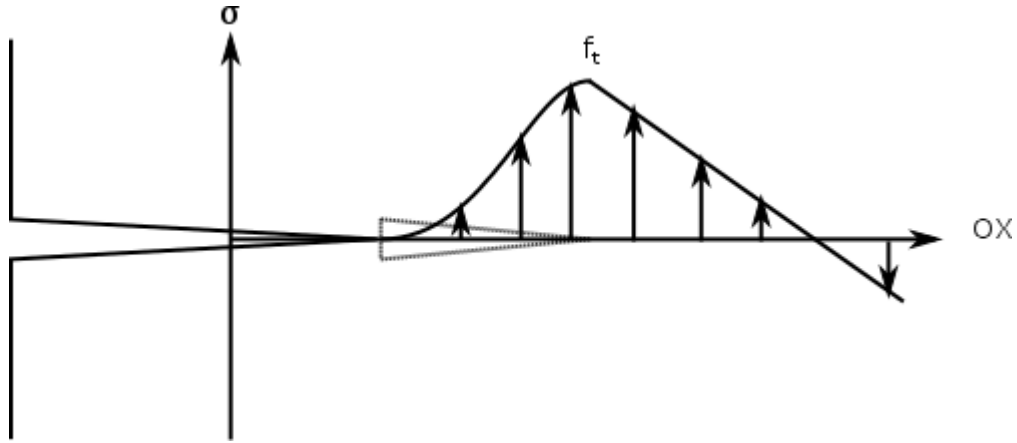


Figure 16: Stress distribution at a point of zone IV of Figure 11 where stresses moved themselves

The softening phenomenon was found thanks to tensile tests of short enough specimens, in which, after the peak load, the strains localized at the more damaged region grew. There, the strains increased even more, due to the microcracking and displacements that will provoke a crack later, while the rest of the specimen was continuously unloading and the strains in that area decreased ¹². That fact can only mean that the axial stress decreases. It is the stress softening before cracking.

Now, we have given to our system a total work through the external force that has been released in the crack formation and development creating two new surfaces of the failed cross-section. That is the fracture work W_f . However, if we refer that energy to the size of the cross-section at which the crack has developed, and make notice that only one crack has progressed, we will obtain a value what can be called the *specific fracture energy* G_F . It can be obtained thanks to Equation 2.2.2, considering a pre-notched section of width B , depth D and notch initial depth a .

$$G_F = \frac{W_f}{B(D-a)} = \frac{1}{B(D-a)} \int_{-\infty}^{+\infty} P d\delta \quad (2.2.2)$$

Nevertheless, the association between the work of the external force W_f and the fracture energy G_F is only theoretical. It means that some conditions must be verified if one makes this association ¹⁸:

- The material must behave always elastically, no matter if linear or non-linear.
- Energy losses at supports and measurement points (that is the point where load is applied) should never exist. Frictional forces at the supports should not exist.
- The whole material must be initially unstressed.
- The test must be carried out fully stable.
- The only force that introduces work must be the external measurable one. Even self-weight should not help on introducing energy.

Whenever one of these conditions is not accomplished, Equation 2.2.2 can be applied, but the result is not the *real energy of fracture* G_F . It will be a *size-dependent fracture energy* G_f (Equation 2.2.3), which must be treated and later corrected.

$$G_f = \frac{W_f}{B(D-a)} = \frac{1}{B(D-a)} \int_{-\infty}^{+\infty} P d\delta \quad (2.2.3)$$

And as the *FPZ* completely develops from a fictitious crack width zero to w_c , Equation 2.1.1 is true. Then, obtaining the G_F will not only give information about the energy required to crack a square meter cross-section, but also is giving information about the softening curve.

For plain concrete, tensile failure is governed by the strength limit and the post-peak stress, that is the initial part of the softening curve, which shows a quick stress reduction, as the peak load exists when the crack width is still low ¹⁹. The two elements are needed, then the axial strength is achievable not only due to loading conditions, but for a short time phenomena as a punctual peak load or an environment change ¹⁸, and that does not mean a general failure.

The initial part of the softening curve is quite interesting because, for any size non-notched elements or a small size notched specimen, it is common to see a sharp decrease of the cohesive stresses ¹², what means a fast degradation of the material at the *FPZ*.

The softening curve has been considered a material property and it is different for any mixture of concrete. It is obvious, because different concretes have different G_F , f_t , E , etc. However, if we consider a coordinate reduction to dimensionless parameters in Equation 2.2.5 for crack openings and in 2.2.6 for cohesive stresses, softening curves can be shown in a reduced form (see Figure 17) and, consequently, they can be compared. In Equation 2.2.5 the characteristic crack width w_{ch} is used (Equation 2.2.4), then the critical crack width w_c cannot be known *a priori*.

$$w_{ch} = \frac{G_F}{f_t} \quad (2.2.4)$$

$$\hat{w} = \frac{w}{w_{ch}} = w \frac{f_t}{G_F} \quad (2.2.5)$$

$$\hat{\sigma} = \frac{\sigma}{f_t} \quad (2.2.6)$$

Where \hat{w} and $\hat{\sigma}$ are the reduced crack width and the reduced normal stress of a certain crack width w and stress σ for a given concrete with a known fracture energy G_F and a tensile strength f_t .

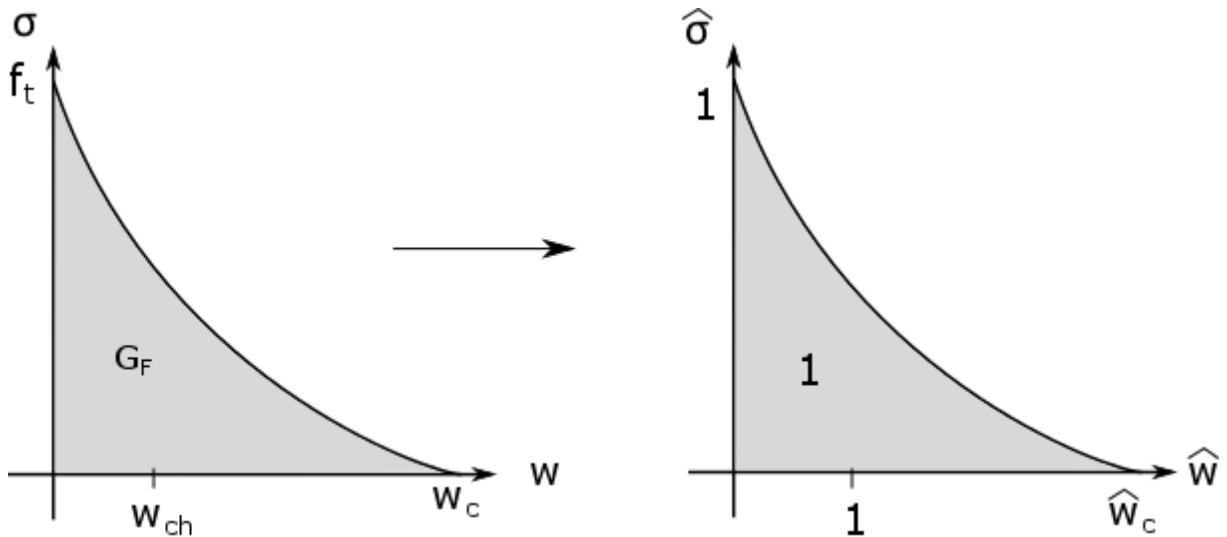


Figure 17: Coordinate reduction to dimensionless axis of the softening curve

Make notice to the fact that now the enclosed area down the dimensionless axis softening curve has change and now it equals the unit (Equation 2.2.7).

$$\int_0^{+\infty} \hat{\sigma}(\hat{w}) d\hat{w} = \int_0^{\hat{w}_c} \hat{\sigma}(\hat{w}) d\hat{w} = 1 \quad (2.2.7)$$

Researchers have concluded that, even that all softening curves for plain concrete are different, applying the dimensionless axis, they are similar in shape ⁶. If this transformation is not done, comparison is impossible.

There are several approximations for the softening curve for concrete: linear, bilinear, trilinear, exponential, an extra-long tail softening approximation, etc ¹². These approximations are used for obtaining other properties, such as w_c , for instance, the extra-long tail approximation has a \hat{w}_c equal to 11.5 ¹²; or the initial slope of the softening curve approximation. These models are helpful in the study of the behavior of the material and the peak load prediction on concrete use.

2.3 LOCAL FRACTURE ENERGY MODEL

Here we review another explanation for the concrete cohesive fracture and the energy required in crack development, or G_f ; the local fracture energy^{20,21}, theory that is also capable of explaining in an approximate form the size-dependence of G_f . This model has been proved and verified that is applicable at concrete fracture with the same three point bend tests²² and is a complement of the fundamentals of concrete and other quasi-brittle materials fracture mechanics.

The fracture energy of the material is explained by the concept of a potential releasable energy distribution along the cross-section, known as the local fracture energy g_f , from the crack tip until the opposite free edge of the specimen.

Theory postulates and models the behavior of concrete macrocracking at the moments that the crack approaches the boundary, giving a sustainable different treatment to g_f distribution at the last zone of the cross-section, the same that is done with the $P - \delta$ tail adjustment¹⁵ (see Chapter 3.3), but in an easier model. The origins of this theory are the problems provoked by the size effect in concrete structures, and, as a result of that, the last part of fracture is differentially considered. The reason is quite simple.

In quasi-brittle materials, like concrete is, the dimension of the fracture process zone (*FPZ*) is not negligible with respect to the element size. This zone moves through the material as the crack develops itself and, at any time, it should arrive until the free edge before the crack tip does so, where there is no more material for *FPZ* to develop. Consequently, *FPZ* size must decrease²⁰. The cohesive fracture theory recognizes a finite size for the *FPZ* where cohesive stresses evolve. These stresses are part from the union capacity between the two parts of the solid. And they do have their importance being just aside the crack tip. Whenever the *FPZ* starts to decrease in length and in width, the area of cohesive stresses will be reduced and thus the union capacity. When the union capacity is reduced, the crack develops easier, that means less energy is required in order to make the same progression, and more decreases the size of the *FPZ*, acting as a chain effect (see Figure 18).

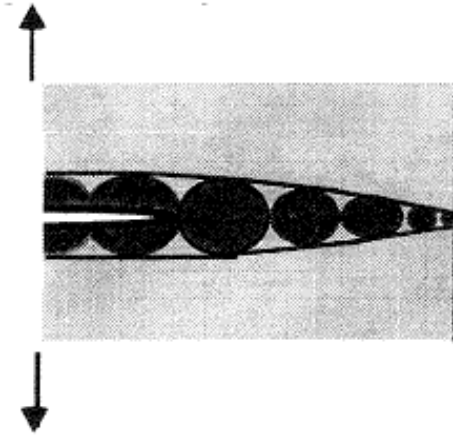


Figure 18: Size decrease of the fracture process zone during its approaching to the free edge. From ²⁰

Consider a notched material zone of depth D and notch depth a in which a crack will be formed and it will move along all fragment $D - a$ in a single axis, call it x -axis. Consider now a finite maximum length for the transition zone a_1 .

According to the situation ahead, as long as the crack progress is confined in a zone where the *FPZ* can assume its maximum length ($x < D - a - a_1$), the material union capacity will remain intact and the energy required to generate and make the crack progresses will be maximum. To sum up, an energy amount similar or near G_F will be necessary.

Instead, when the *FPZ* dimensions begin to be limited, which means the crack tip is near the free edge ($x \geq D - a - a_1$), according to the showed theory, the union mechanisms will weaken gradually, fact which means a less energy amount is required to continue the crack propagation, less than G_F . The g_f will be continually decreasing as the x coordinate approaches the free edge ²⁰.

The local fracture energy model has been studied and approximations of the energy distribution have been proposed, checked and accepted ²¹⁻²³. Firstly, the g_f distribution as a bilinear approximation, following what is exposed in the earlier paragraphs (Equation 2.3.1).

$$g_f(x) = \begin{cases} G_F & \text{if } x < D - a - a_1 \\ G_F \cdot \left(1 - \frac{x - (D - a - a_1)}{a_1}\right) & \text{if } x \geq D - a - a_1 \end{cases} \quad (2.3.1)$$

Then, the mean value of the energy distribution for all the cross-section is what we know as the size-dependent measurable fracture energy G_f (Equation 2.3.2), because Equation 2.3.1 is considering explicitly the size effect by changing the g_f near the boundary of the material.

$$G_f\left(\frac{a}{D}\right) = \frac{1}{D - a} \int_0^{D-a} g_f(x) dx \quad (2.3.2)$$

To make it clear, see Figure 19 for a sketch of the energy distributions, the main sizes, the local fracture energy, its size effect and the mean value.

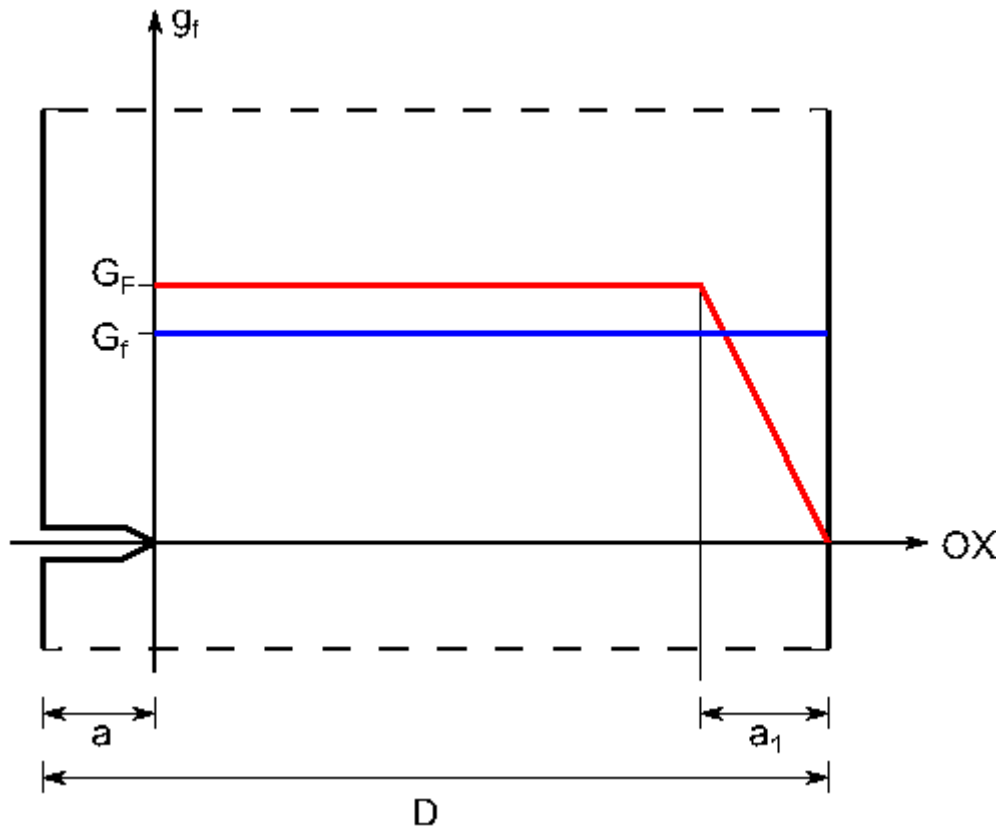


Figure 19: Local fracture energy distribution g_f in red and the mean value of the energy distribution G_f along the cross-section in blue

The purpose of exposing this model is not such as a theory explanation, but in a theory expansion and proposing later an alternative method for the G_F determination to check the methodology in use and to give a wider literature review of this field of research.

3 THE TEST AND PROCEDURES FOR OBTAINING THE FRACTURE ENERGY OF CONCRETE

3.1 EXPERIMENTAL PROCEDURES AND THE THREE-POINT BEND TEST

The principle for obtaining the fracture energy of a material explained with the cohesive crack model is to perform a direct tensile test with a displacement control on a specimen until the material arrives to its axial tensile limit f_t . At that moment, a crack is able to appear and to develop and, while the control relies on the displacement, the force will show a decrease that is related to the softening phenomenon. To consider valid a test for G_F determination, only a single crack shall appear and progress. When this is not accomplished, the recorded energy will be higher than expected, creating a difficulty on the real G_F determination.

The first and easier solution would be, then, to perform a uniaxial tensile test on concrete. The problem lays in the unstable behavior concrete has in the tensile region, for instance, for non-notched specimens, multiple crack can be generated, and if notched specimens are used, it exists the possibility for the crack to be concentrated at a point, provoking a specimen part to rotate, wasting energy, or multiple cracks can appear developing through separate parallel planes, fact that is not desired¹². The test is simply unstable. To illustrate these phenomena, see Figure 20. Another problem is how to place and to hold the concrete specimen for a direct tensile test.

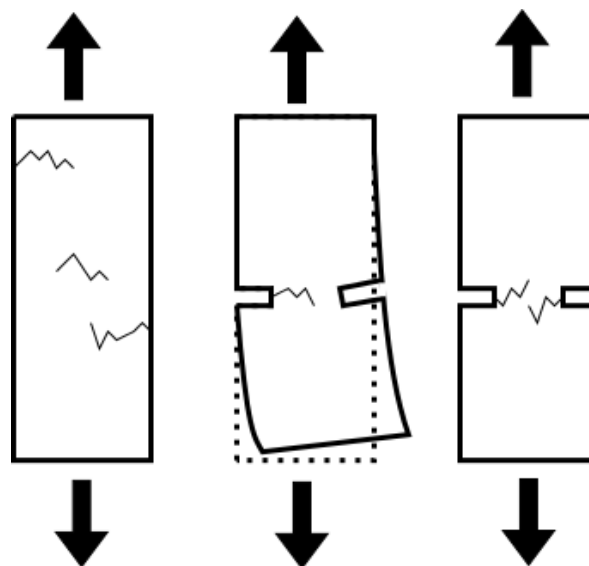


Figure 20: Common problems with a direct tensile test on concrete

So, one needs a new kind of test for the G_F determination that is more stable in the experimental reality and here makes its appearance the three point bending test with its recommended test procedures^{24,25}.

The three point bend test uses a configuration and a specimen such as the one exhibited at Figure 21. The type of supports, the main dimensions, their symbolization and the loading methodology are also represented there.

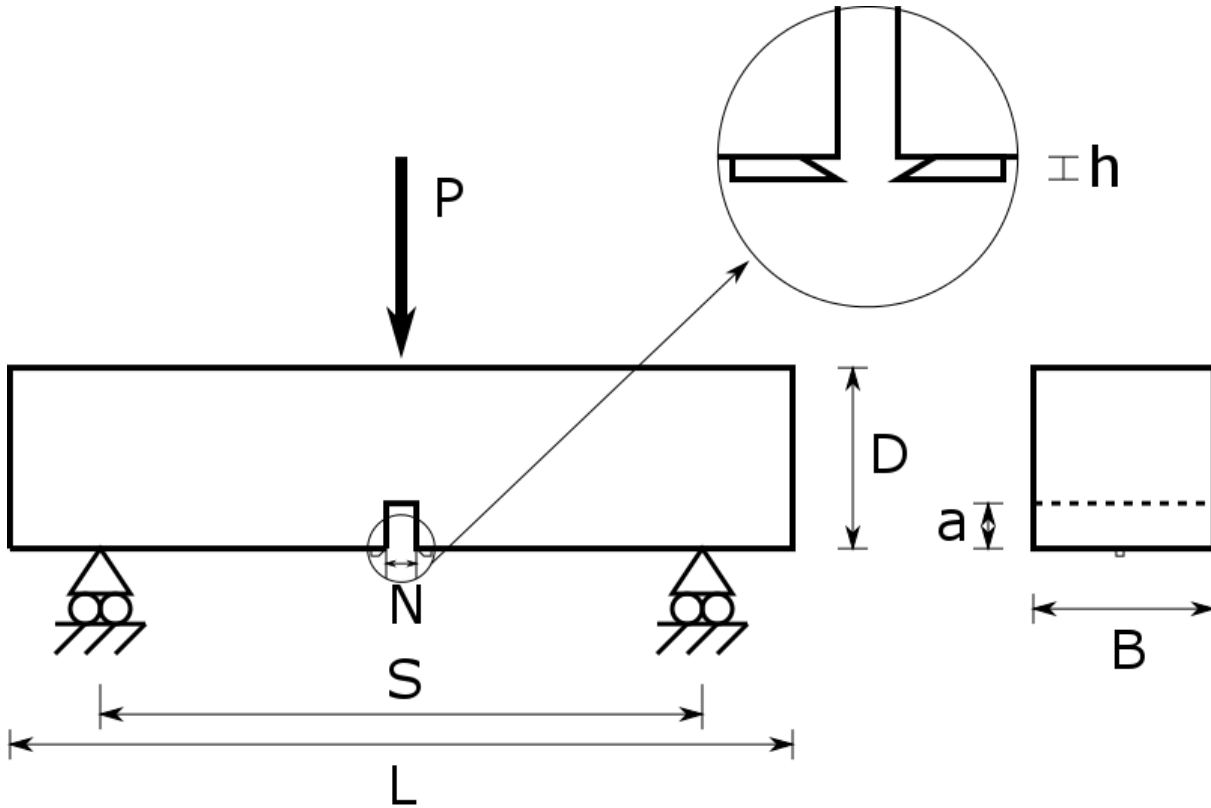


Figure 21: Main dimensions of the beam type specimens for a three point bend test

The basis of this test is to place a prismatic beam specimen on two rolling supports with a load applied at the center by means of a cylindrical or curved load applicator. Using a displacement control of the load applicator or, if a more sophisticated control is used, a crack mouth opening displacement (*CMOD*) control, the entire load vs. displacement curve is obtained, allowing to compute the fracture work. Also the load vs. *CMOD* can be recorded. This will help on the G_F determination and the softening curve bilinear approximation building, because some of the further mentioned correction method uses these values.

When this test is stable, and this means the crack develops in a progressive way and no suddenly, valid values are obtained, but the real fracture energy is not obtained, because a size effect exists^{12–15}. To sum up, G_f is now obtainable (see Chapter 2.1 and 2.2), but not the G_F .

3.2 DETERMINATION OF THE FRACTURE ENERGY OF CONCRETE. REASONS FOR THE CORRECTION

We already know that we will not obtain a real G_F value, but we can obtain a size-dependent fracture energy G_f using the data obtained by a three point bending test. Remember that G_f can be computed with Equation 2.2.3, where the integral defines the fracture work W_f (Equation 2.2.1).

However, the record will not be continuous, so the integral must be made by means of a numerical integration method. The test recordings will be made at high speed acquisition rate (see Chapter 4) in order not to lose the data variation. For this reason, the trapezoidal numerical integration method will be applied and it will be considered a good approximation.

The $P - \delta$ non-continuous record is quite similar to Figure 22, evidently, with a higher data density. The step is variable, but we know it, as the δ register, from the first valid point, let us call it point 1, until the last one, call it n , following every single point i .

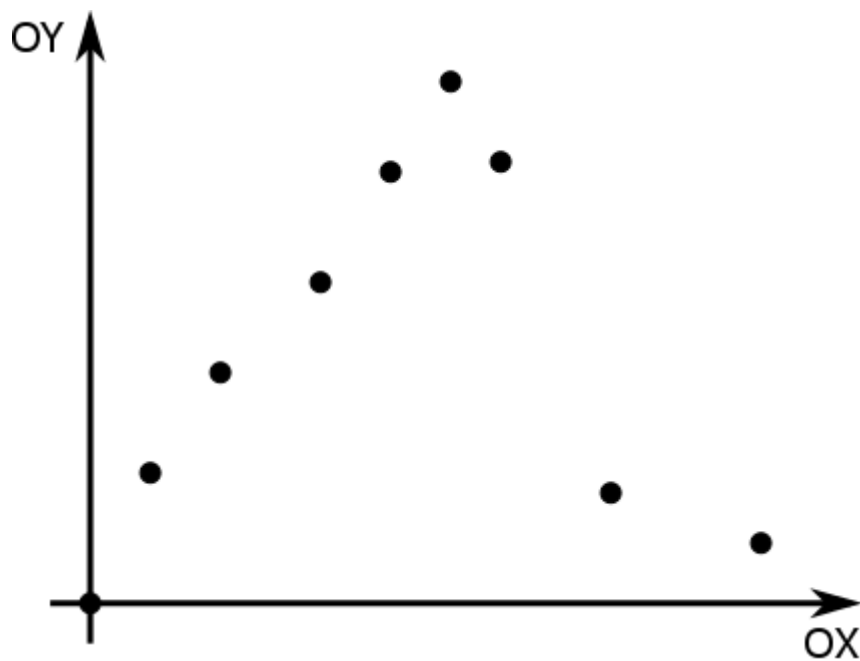


Figure 22: Example of a discrete data record

Consider the reference at Figure 23, where we begin at the second point, because the first one does not have any register before to create an integration area. The integral of Equation 2.2.1, placing displacement at the X-axis and load at the Y-axis, or, generally, a discrete integration on the XY-plane, can be approximated as Equation 3.2.1, when after applying it at Equation 2.2.1, we have W_f computed as Equation 3.2.2.

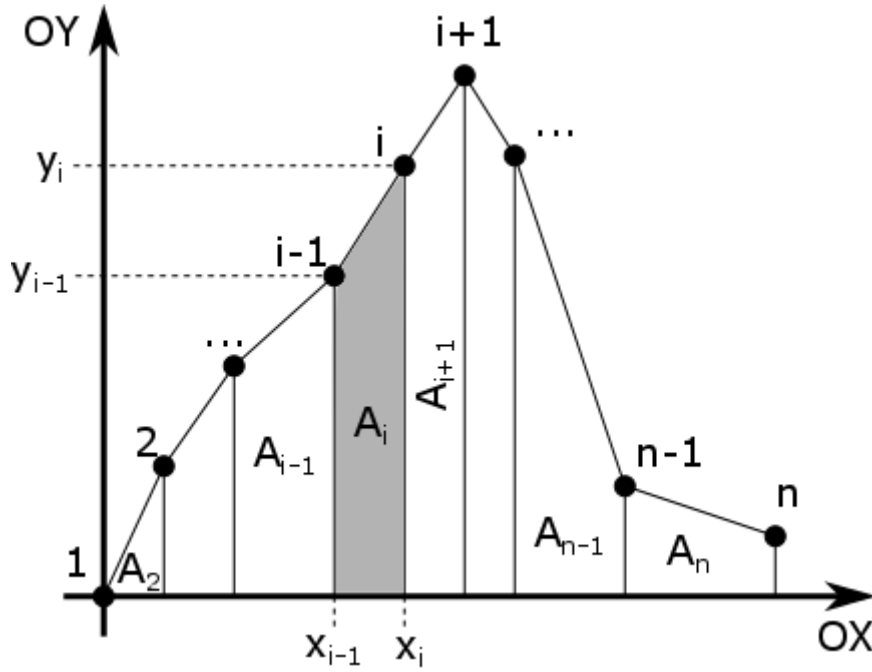


Figure 23: Trapezoidal integration

$$\int_{x_o}^{x_f} y(x) dx \approx \sum_{i=2}^n A_i = \sum_{i=2}^n \frac{y_i + y_{i-1}}{2} \cdot (x_i - x_{i-1}) \quad (3.2.1)$$

$$W_f = \int_0^{+\infty} P d\delta = \int_{\delta_o}^{\delta_f} P d\delta \approx \sum_{i=2}^n \frac{P_i + P_{i-1}}{2} \cdot (\delta_i - \delta_{i-1}) \quad (3.2.2)$$

Now, Equation 2.2.3 can be used, because we can measure the sizes of a specimen central section, the depth D , its width B and the pre-notch depth a , and once the test is finished, recording the load applied P and the load applicator displacement δ , W_f is obtainable and, thus, the size-dependent fracture energy G_f .

Although we can obtain a value similar to G_f , it is not that value and it is because a series of reasons^{13-15,18}, where some of them are detailed next.

3.2.1 FIRST REASON: SELF-WEIGHT ACTION

Considering that self-weight is a gravitational force and that the specimen loading is vertical, we find a situation such as the one shown at Figure 24, where the central section is initially loaded, even though the load is relatively small, creating a stress distribution and, when the test begins, it will help on introducing more energy, because the force applied to the displacement point will be a composition of the machine force and the self-weight. So, self-weight must be corrected.

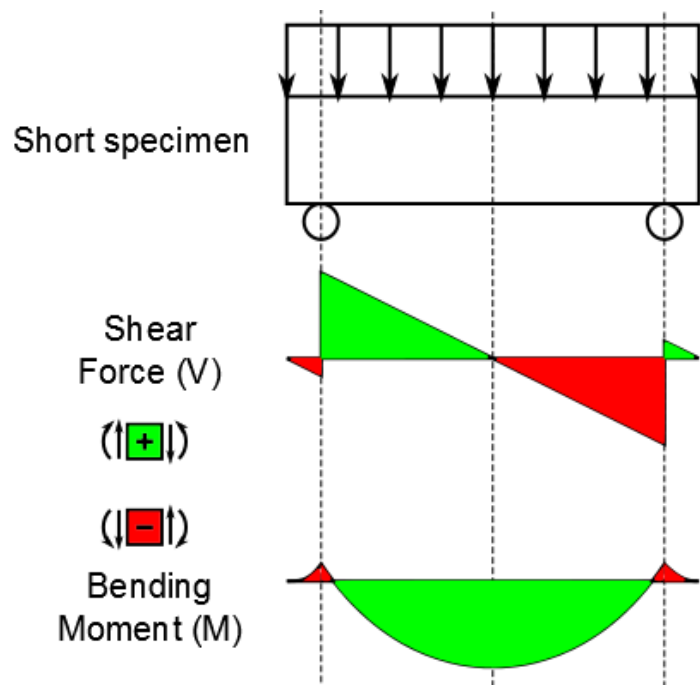


Figure 24: Self-weight action on the central section

This correction wants to compensate the self-weight action in order to obtain a null moment at the central section and, so, it helps to avoid introducing more energy whose source is not the test machine. This correction is also done to prevent an early split of the specimen.

There are several methods, one is to cast a double length specimen (Figure 25) and therefore the central section bending moment is zero.

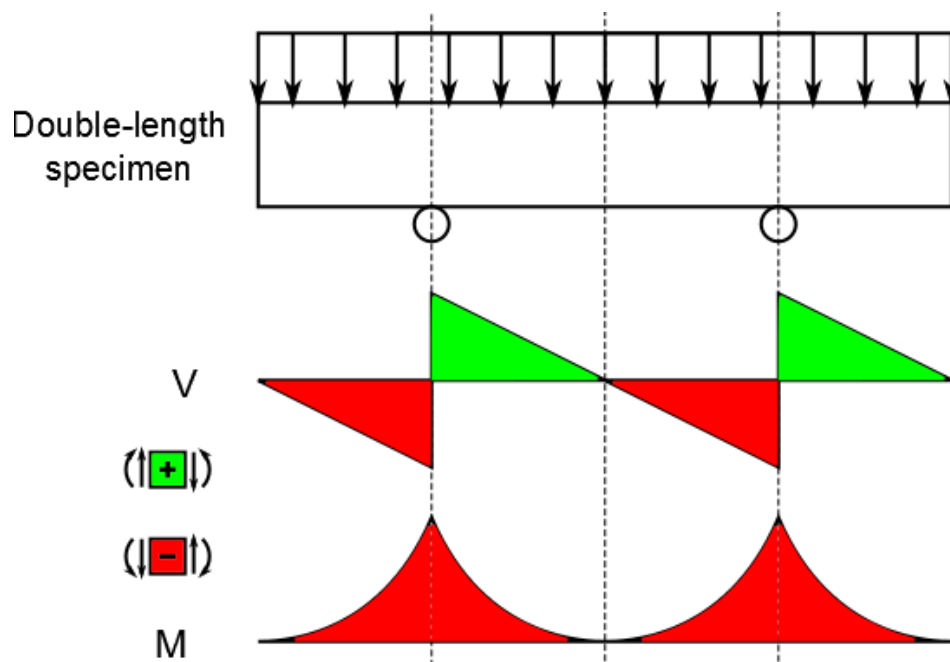


Figure 25: Self-weight action correction at the central section by a doubled-length specimen

Other methods aim the same consequence: the use of springs, a normal length specimen with two weights at each side to create the weight of a double length specimen, etc.

Whenever the self-weight is not corrected, an equivalent load is introduced to the system ²⁵, whose value is given by Equation 3.2.3, in order to correct the registered non-treated values of force and G_f is also corrected ^{13,26} as Equation 3.2.4 shows.

$$P_{eq} = mg \left(1 - \frac{L}{2S} \right) \quad (3.2.3)$$

$$G_f = \frac{1}{B(D-a)} \cdot \left(\int_{-\infty}^{+\infty} P d\delta + mg\delta_u \right) \quad (3.2.4)$$

Where P_{eq} is the self-weight equivalent load, m the mass specimen, g the gravity force field with a standard value of 9.81N/kg, L , S , B , D and a are the specimen sizes (Figure 21) and δ_u is the machine's load head total displacement during the test.

3.2.2 SECOND REASON: SOLID BEHAVIOR

During the entire project we have supposed a perfectly elastic behavior of the entire solid outside the *FPZ* and near regions, but this does not have to be like this. There can be inelastic or non-linear behaviors at certain points of the specimen; near the supports, the loading point or inside the specimen, due to irregularities in it, or cycles of hysteresis ¹⁴.

These regions can dissipate energy that is computed as “introduced energy used for fracture”, because the source of it is essentially the testing machine, giving a higher register of fracture energy than the real one.

To correct this dissipation in an accurate way, special tests must be done, which for some reasons cannot be done for this project. Nevertheless, the influence of this energy dissipation is not so important to make the correction mandatory ¹⁵.

3.2.3 *THIRD REASON: SUPPORTS AND THE TESTING MACHINE*

If an ideal situation occurs, supports should not influence our tests. However, this is not the case.

First, a real support has a little force component on the horizontal axis provoked by friction. There is no instrumentation there, so this axis energy dissipation is not controlled and the part of the energy introduced by the machine flows away from the system and it is not used for fracture.

Second, the stiffness of the supports, the loading apparatus and the machine could not be high enough to avoid that these parts dissipate energy through the support material bulk or through hysteresis of the loading system. These energy dissipations must be the smallest possible to prevent inaccurate readings of the energy introduced to the system.

Both phenomena can be measured and quantified, but this will not be the case in this project, although the highest stiffness possible with the available elements will be searched for the machine and the supports in order to reduce this effect.

3.2.4 *FOURTH REASON: INCOMPLETE TEST*

Incomplete testing is also an important reason for obtaining the real G_F , because the whole energy to break a section of a specimen needs to be measured, although this is usually impossible, because, in order to do so, the test must be carried out until the total division of a specimen, fact that will provoke a really long test, if it is possible. If not, quick crack propagation and an early division of the specimen will provoke the loss of important information.

These two phenomena make almost impossible to acquire a complete load versus displacement curve. A correction method must be set up.

One of the most widely used correction method is explained at Chapter 3.3.

Some other reasons can exist, but these are the most important ones.

At this point we already know how to extract from a three point bending test the size-dependent fracture energy G_f and why this size-dependence. Some of the correction methods to obtain the real G_F are exposed at the following pages, at Chapter 3.3 and 3.4.

The code at Appendix C.2.4 computes G_f with the appropriate corrections.

3.3 THE REAL FRACTURE ENERGY OF CONCRETE THROUGH THE TAIL CORRECTION OF THE LOAD VS. DISPLACEMENT GRAPH

The methodology for correcting the size-dependent fracture energy G_f using the $P - \delta$ curve tail is going to be detail in this chapter. The proposed method^{25,27} has its origins in the fact that while the cohesive zone is approaching to the free edge of the specimen, load tends to zero , but the crack does not reach to open itself completely at this last zone, which makes a certain amount of fracture work that the $P - \delta$ curve is not able to record¹⁵. Pay attention to Figure 26 in order to clearly observe this phenomenon.

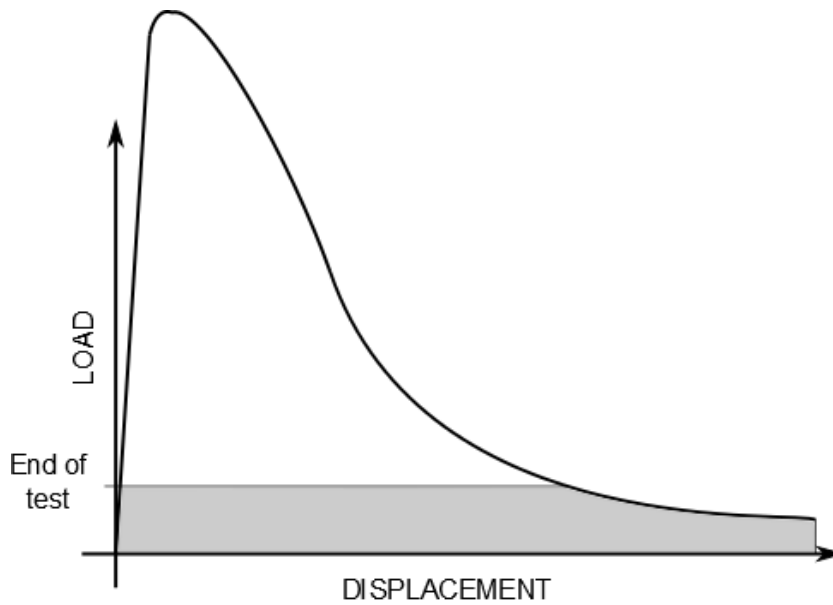


Figure 26: Non-measured fracture work. Final test load is slightly higher than zero, what provokes a non-registered area

The influence of this missing tail has been studied and a mathematical solution has been set, thanks to an idea of a specimen formed by two rigid bodies joined by the surface where the crack propagation is supposed to occur¹⁵. At an advanced stage of the test, both solids are joined only by the surface that represents the cohesive stresses zone with the softening function along it and both bodies present a rotation (see Figure 27). The bending moment of the section created by the external forces must be in equilibrium with the bending moment that provokes the stress distribution on the cross-section surface, because at this advanced point the system is still in equilibrium.

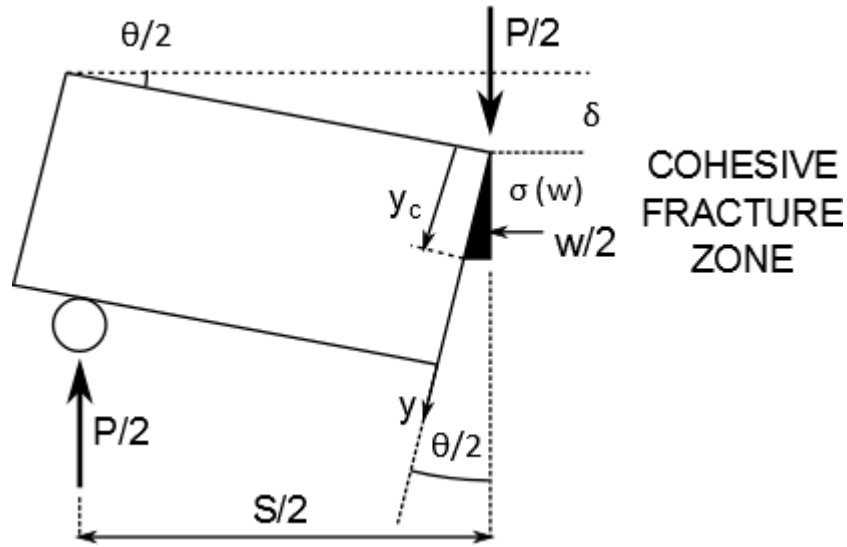


Figure 27: Half specimen represented by one rigid body used for obtaining the tail correction ¹⁵

Starting from this hypothesis, it is required to look for the bending moment of the central section by two different methods. First, as the result of the force equilibrium of the body, taking into account that only the vertical force of the load cell and the support exist and that the distance from the central section and the support has not suffered any significant changes, which means that it is still $S/2$. The bending moment by force equilibrium is represented in Equation 3.3.1.

$$M = \frac{PS}{4} \quad (3.3.1)$$

Second, the bending moment as a result of the central section normal stresses. As the coordinate reference, it is taken the point where the load is applied. There is the cohesive zone; the stress along the face is the one that can be computed with the softening function, from a coordinate y zero, following the face edge until the point where the critical crack width is reached, coordinate y_c . Applying the equilibrium of bending moment, Equation 3.3.2 is obtained.

$$M = \int_0^{y_c} \sigma(w) y \cdot B dy = B \cdot \int_0^{y_c} \sigma(w) y dy \quad (3.3.2)$$

Where the softening curve $\sigma(w)$ is considered to be known.

So, considering a very small rotation of the body, Equation 3.3.2 can be transformed using the relations of Equation 3.3.3 to build Equation 3.3.4, which will give an easier path to solve the integral.

$$\sin\left(\frac{\theta}{2}\right) = \frac{w/2}{y} \rightarrow w = 2y \sin\left(\frac{\theta}{2}\right) \approx 2y \frac{\theta}{2} \rightarrow w \approx \theta y \rightarrow dw = \theta dy \quad (3.3.3)$$

$$M = B \cdot \int_0^{w_c} \sigma(w) \frac{w}{\theta} \frac{dw}{\theta} = \frac{B}{\theta^2} \int_0^{w_c} \sigma(w) w dw \quad (3.3.4)$$

Being the integral shown in Equation 3.3.4 equivalent to the static moment of the area enclosed down the softening curve respect the origin, it can be rewritten, if G_F is the area (Equation 2.1.1) and w_G the horizontal coordinate of the area gravity center respect the axis origin, as Equation 3.3.5.

$$M = \frac{B}{\theta^2} G_F w_G \quad (3.3.5)$$

Making the appropriate changes in the expressions using Equation 3.3.1, 3.3.5 and 3.3.6, represented in Equation 3.3.7, the non-recorded work of fracture is approachable as a tail work W_{tail} (Equation 3.3.8), which is the area down $P - \delta$ curve at loads lower than the last saved value P_f .

$$\tan\left(\frac{\theta}{2}\right) = \frac{\delta}{S/2} \approx \frac{\theta}{2} \rightarrow \theta = \frac{4\delta}{S} \quad (3.3.6)$$

$$M = \frac{PS}{4} = \frac{B}{\theta^2} G_F w_G = \frac{BS^2}{16\delta^2} G_F w_G \rightarrow P = \frac{BS}{4\delta^2} G_F w_G \quad (3.3.7)$$

$$W_{tail} = P_f \delta_f + \int_{\delta_f}^{+\infty} P d\delta = \frac{BS G_F w_G}{2\delta_f} \quad (3.3.8)$$

Equation 3.3.8 is valid while the initial displacement is zero. If not, we will have to introduce a last change in Equation 3.3.8 to include this axis displacement from the initial zero value. The final expression for the work of fracture from the tail of the $P - \delta$ curve is Equation 3.3.9, where A symbolizes the first value of displacement where load is zero and R the last value.

$$W_{tail} = \frac{BS G_F w_G}{2(\delta_R - \delta_A)} \quad (3.3.9)$$

A contradiction is generated at this point. To find the real value of G_F , we need the value of G_F and, besides, another unknown value, w_G . Luckily, a procedure to obtain a new parameter that includes both unknowns has been proposed by fitting the curve in Equation 3.3.10^{25,27}.

$$P_1 = X(A + KX) \quad (3.3.10)$$

Where P_1 is the value of the corrected load, K is a meaningless constant for us, A is known as the far tail constant and it is related with the static moment of the softening curve (see Equation 3.3.11) and X is a new variable, whose expression will be explain later.

$$A = \frac{BSG_F w_G}{4} \quad (3.3.11)$$

The W_{tail} value is obtained by the following procedure:

- a) Delete from the data reading the values whose $CMOD$ record does accomplish the Restriction 3.3.12, where D and $CMOD$ are in the same distance units.

$$CMOD > \frac{4D}{300} \quad (3.3.12)$$

- b) The last $CMOD$ and load value from the new register will be saved as w_{MR} and P_R' .
- c) Generate the corrected load P_1 register using Equation 3.3.13.

$$P_1 = P' - P_R' \quad (3.3.13)$$

Where P' symbolizes the direct load reading, the uncorrected load.

- d) Find the $CMOD$ value whose P_1 value is zero and whose location is at the raising part of the curve. That $CMOD$ record will be saved as w_{MA} .
- e) For every single point located at the falling part of the curve whose P_1 value satisfies the Restriction 3.3.14, where the corrected peak load is represented as P_{1u} , compute the new variable X by means of Equation 3.3.15.

$$P_1 < 0.05P_{1u} \quad (3.3.14)$$

$$X = \left(\frac{4D}{S}\right)^2 \cdot \left(\frac{1}{(w_M - w_{MA})^2} - \frac{1}{(w_{MR} - w_{MA})^2}\right) \quad (3.3.15)$$

Where w_M is the $CMOD$ recorded values associated with P_1 and X has units of inverse square length (m^{-2} , multiple or submultiple).

- f) Fit the $P_1 - X$ values using a second order regression of the curve at Equation 3.3.16.

$$P_1 = X(A + KX) = AX + KX^2 \quad [y = a_0 + a_1x + a_2x^2] \quad (3.3.16)$$

Parameter a_1 is the fair tail constant value, so it will be saved as A , whose unit is force multiplied by a square length (Nm^2 , multiple or submultiple)

For the parabolic fitting it will be forced that a_0 becomes zero.

- g) Finally, compute the non-measured work of fracture W_{tail} through Equation 3.3.17, result of combining equations 3.3.9 and 3.3.11.

$$W_{tail} = \frac{2A}{\delta_R - \delta_A} \quad (3.3.17)$$

By this method, knowing the size-dependent and weight-corrected, if necessary, fracture work W_f , the size-independent fracture energy G_F is finally obtained with Equation 3.3.18.

$$G_F = \frac{W_f + W_{tail}}{B(D - a)} \quad (3.3.18)$$

3.3.1 A BILINEAR APPROXIMATION FOR THE SOFTENING CURVE OF CONCRETE THROUGH THE LOAD VS. DISPLACEMENT TAIL CORRECTION

As an extra procedure for the G_F determination, it is given a method for building a softening curve $\sigma - w$ bilinear approximation suitable to experimental results that allows us to obtain other characteristic values of the fracture mechanics, such as the critical crack width w_c . To obtain this bilinear approximation using the results of the $P - \delta$ tail correction, it is proposed the next procedure^{25,27}.

- a) Determine the brittleness length l_1 with Equation 3.3.19, with units of length (m , multiples or submultiples). It is worth reminding that Equation 3.3.19 is only applicable when the span length S is three times the specimen depth D ($S = 3D$).

$$l_1 = \left(1 - \left(\frac{a}{D}\right)^{1.7}\right) \cdot D \cdot \left(\frac{11.2}{\left(\left(\bar{f}_t/\bar{f}_p\right)^2 - 1\right)^2} + \frac{2.365}{\left(\bar{f}_t/\bar{f}_p\right)^2}\right) \quad (3.3.19)$$

Being \bar{f}_t the mean axial tensile strength of the concrete campaign, which is found in other type of tests (see Appendix A.3 and A.4), and \bar{f}_p the net plastic flexural strength, which can be compute using the same three point bend test and Equation 3.3.20, where, in this case, the effective peak load $P_{ef,max}$ is required (see Equation 3.3.21).

$$\bar{f}_p = \frac{P_{ef,max}S}{2B(D - a)^2} \quad (3.3.20)$$

$$P_{ef,max} = P_{1u} + \frac{A}{(w_{MR} - w_{MA})^2} \quad (3.3.21)$$

Remember that A is the far tail constant and P_{1u} the corrected peak load.

The mean value of l_1 for the same mixture specimens is taken.

- b) Compute the initial intercept w_1 (see Equation 3.3.22).

$$w_1 = \frac{2\bar{f}_t \bar{l}_1}{\bar{E}} \quad (3.3.22)$$

Where E is the mean elastic modulus of the campaign, which is found at the same three point bend test (see Appendix A.1 for the E calculation and A.2 for the campaigns' E).

It is worth reminding that when at an equation appears a symbol with a bar above it refers to the campaign mean value.

- c) Knowing the G_F and f_t value, the characteristic crack width is obtainable with Equation 3.3.23.

$$w_{ch} = \frac{\bar{G}_F}{\bar{f}_t} \quad (3.3.23)$$

- d) Compute the critical crack width, one property of the fracture mechanics, at Equation 3.3.24, with units of length (m , multiples or submultiples).

$$w_c = w_{ch} \cdot \frac{3\bar{w}_G - w_1}{2w_{ch} - w_1} \cdot \left(1 + \sqrt{1 - \frac{2w_1(3\bar{w}_G - 2w_{ch})(2w_{ch} - w_1)}{w_{ch}(3\bar{w}_G - w_1)^2}} \right) \quad (3.3.24)$$

- e) Finally, find the kink point (σ_k, w_k) of the bilinear approximation, the point where the slope suffers its change, at Equation 3.3.25 and 3.3.26. σ_k with units of stress (Pa , multiples or submultiples) and w_k of length.

$$\sigma_k = \bar{f}_t \cdot \frac{2w_{ch} - w_1}{w_c - w_1} \quad (3.3.25)$$

$$w_k = w_1 \cdot \frac{w_c - 2w_{ch}}{w_c - w_1} \quad (3.3.26)$$

- f) The bilinear approximation of the softening curve of a concrete campaign rests as it is seen in Equation 3.3.27, which is not found in the literature review (see Appendix G.1)

$$\sigma(w) = \begin{cases} \bar{f}_t - \frac{\bar{f}_t - \sigma_k}{w_k} \cdot w & \text{for } w \in [0, w_k] \\ \frac{\sigma_k w_c}{w_c - w_k} - \frac{\sigma_k}{w_c - w_k} \cdot w & \text{for } w \in (w_k, w_c] \end{cases} \quad (3.3.27)$$

With a possible coordinate reduction with Equation 2.2.5 and 2.2.6.

Expressions at Chapter 3.3 are employed at the codes at Appendix C.1.1, C.1.3, C.2.1 and C.2.2.

3.4 THE REAL FRACTURE ENERGY OF CONCRETE THROUGH THE LOCAL FRACTURE ENERGY THEORY

Having in hand studies of the local fracture energy model in order to determine the size-independent fracture energy from quasi-brittle materials, particularly for concrete^{20–22,26,28}, the Equation system 3.4.1 is given to find G_F in an easier and simpler method than the $P - \delta$ tail adjustment^{15,25,27}. Nevertheless, this method only tries to control one of the free surface effect, on the depth length, because it has been proved that the width of the specimen can also affect the fracture energy²³.

$$G_f(\alpha) = \begin{cases} G_F \cdot \left(1 - \frac{a_1}{2D(1-\alpha)}\right) & \text{if } 1 - \alpha > \frac{a_1}{D} \quad (\text{if } D - a > a_1) \\ G_F \cdot \frac{(1-\alpha)D}{2a_1} & \text{if } 1 - \alpha \leq \frac{a_1}{D} \quad (\text{if } D - a \leq a_1) \end{cases} \quad (3.4.1)$$

Where G_f is the size-dependent fracture energy, calculated with the corrected load, G_F the size-independent fracture energy, a_1 is the transition zone length and we remember that D , a and α are the specimen depth, the notch depth and the notch to depth ratio correspondingly. Whenever one possesses two valid mean values of G_f and α , the Equation system 3.4.1 can be solved.

The two G_f mean values have to come from two specimen series, one from an α constant value and another from other different α value. This fact means that two series of the same mixture, then G_F is considered a material property^{12–15}, and the same depth and width, to prevent the size-dependence in a same series, have to be tested separately. The notch to depth ratio must be considerably different at both series, for instance, one series will have a notch to depth ratio of 0.5 or higher and other series, 0.1 or lower²⁸. It can also be 0.05 or lower²⁶.

Entering the G_f , D , a and α values in Equation 3.4.1, the system is solved and G_F is obtained, also a_1 . As we know that the system of equations possesses restrictions for using both equations, the conditions from the used expressions must be checked after solving them. If a condition is not fulfilled, another combination of the equations will be used. When the conditions become true, the G_F and a_1 will be considered to be found. The code which applies the method is given at Appendix C.2.5, developed with expressions at Appendix G.2 and basic for Appendix C.1.5 and C.1.6 codes.

The exposed local fracture energy methodology of G_F computation has a significant difference with the tail correction, and it is that the span to depth ratio S/D has to be greater than 4 when the maximum aggregate size does not exceed 10mm and it has to be higher than 7 or 8 whenever the maximum aggregate size becomes bigger than 10mm and does not exceed 20mm. To infringe these span to depth ratios will provoke finding a greater G_F than expected²⁸.

4 MATERIALS, SPECIMENS AND TESTS: THE CAMPAIGNS' JOURNAL

4.1 TEST CAMPAIGN, MATERIALS, DIMENSIONS, PROPERTIES AND GENERAL CAMPAIGN DATA

This chapter has been created separately in order to summarize the different test campaigns that have been carried out. Every campaign data contains:

- a) The mixture mass composition and component types and the proportion of them respect the total solid mass. Water is not included, so the sum of them will exceed the 100%.
- b) The series of specimens cast with a single mixture, which means its shape, its dimensions and the number of elements.
- c) The conditions, the total time amount and the environment where the specimens were placed for their hardening before the tests.
- d) The summary of mechanical properties, which can be found in a detailed way in Appendix A.
- e) The date of casting, the date of testing and other important dates and temporal data.
- f) The kind of test that will be realized on each specimen.
- g) A general overview of the test status. That means if the test was made correctly or if there have existed any kind of remarkable warning.

Before describing the test campaigns, we remark that:

- The entire campaign has as the reference a significant date, usually the date of the specimen removal from the mold, because one can write on its surfaces, following the structure *DMY* (day-month-year), where *D* is a 2 digit number, *M* the month in roman numerals and *Y* a 4 digit number. For example, an unmolding date at the 5th December 2015 is called 05XII2015.
- A single specimen form the campaign is called by the reference *TDMYN* (type-day-month-year-number), an extension of the entire campaign name. *T* is a capital letter that sums up the shape of the specimen, where *T* is replaced for a *B* for beam specimens, a *C* for cylindrical specimens and *D* for cube specimens. After that, *N* uses a roman number to identify the specimen from all those of type *T*. For example, the third beam of the campaign 05XII2015 is called B05XII2015III.

With this structure in mind, we proceed to explain the campaigns tested.

4.1.1 23X2015: 1ST TEST CAMPAIGN

The mixture composition for the 23X2015 campaign is visible at Table 1. The casting was made at Thursday 22nd October 2015 and the removal from the molds at Friday 23rd October 2015. The day 28th after casting is Thursday 19th November 2015. The maximum aggregate size is 10mm.

Table 1: Campaign 23X2015 mixture composition

23X2015	Sand (0-2)	Aggregate (5-10)	Cement II/B-L 32.5N	Water	W/C
Mass	36kg	40kg	9kg	7.8kg	
Mass fraction	42.35%	47.05%	10.60%	9.20%	0.867
Composition	850kg/m ³	950kg/m ³	214kg/m ³	185kg/m ³	

A total of 7 specimens were cast: 4 beam specimens, 2 cylindrical specimens and 1 cubic specimen; where the tests to be done are shown at Table 2, and whose dimensions are: a diameter of 150 millimeters and a length of 300 millimeters for the cylindrical specimens C23X2015I and C23X2015II; a constant edge length of 150 millimeters for the cubic specimen D23X2015I and the dimensions of the beam specimens are visible at Table 3, with references at Figure 21.

Table 2: Campaign 23X2015 tests

SPECIMEN	Test	Date of test
C23X2015I	Direct compression	19/XI/2015 (#5) Day 28 th
C23X2015II	Brazilian test	23/XI/2015 (#7) Day 32 nd
D23X2015I	Direct compression	23/XI/2015 (#6) Day 32 nd
B23X2015I	Three point bend test	19/XI/2015 (#4) Day 28 th
B23X2015II	with the $P - \delta$ tail	19/XI/2015 (#2) Day 28 th
B23X2015III	correction method	19/XI/2015 (#1) Day 28 th
B23X2015IV	and double length	19/XI/2015 (#3) Day 28 th

Table 3: Main dimensions of the beam specimens from the campaign 23X2015

SIZES (mm)	<i>L</i>	<i>D</i>	<i>B</i>	<i>a</i>	<i>N</i>	<i>S</i>	<i>h</i>
B23X2015I	600	100	100	31	2	300	2
B23X2015II	600	100	100	30	2	300	2
B23X2015III	600	100	100	31	2	300	2
B23X2015IV	600	100	100	30	2	300	2

The mechanical properties from this test campaign are visible at Table 4. Details can be seen at Appendix A.2.1, Appendix A.4.1 and Appendix A.6.1.

Table 4: 23X2015 campaign mechanical properties. When available, standard deviation in brackets

PROPERTY	f_t	f_c	$f_{c,cube}$	E
23X2015	0.78MPa	6.7MPa	7.7MPa	16.5GPa (4.0)

The specimens have been preserved at these environments:

- Day 0 to day 1: in molds at indoor conditions of approximate 20°C and humidity 75%
- Day 1 to day 26: submerged in water indoors
- Day 26 to day 28: specimens type B at indoor conditions, specimens type C and D in a controlled chamber at 20°C and 95% of humidity.
- Day 29 to day 32: the remaining specimens of type C and D at indoor conditions to reproduce the conditions that specimens type B have experienced.

Finally, an abstract of the test journal is done at Table 5.

Table 5: 23X2015 campaign journal summary

SPECIMEN	Fracture status	Warnings	General notes
B23X2015I	Satisfactory	None	Nothing remarkable
B23X2015II	Satisfactory	None	Nothing remarkable
B23X2015III	Satisfactory	None	Test brought to an stationary state, longer than an hour
B23X2015IV	Satisfactory	None	Nothing remarkable
C23X2015I	Satisfactory	At specimen: the core is quite wet yet	It breaks earlier than expected. The core is not as compact as the beam specimens' core. The rest will be tested later and preserved outside the chamber
C23X2015II	Satisfactory	None	Nothing remarkable
D23X2015I	Satisfactory	None	The core is now more compact, though quite wet, but men's force has difficulties on breaking the remaining core, not as what happened in C23X2015I

The type of mixture of this campaign was made in order to find in a natural way a low strength concrete, because a low strength will lead to an easier way to make stable tests without fast cracking at the central cross section. This series was meant to be used to check the feasibility of this project, which is the same to say it was searched that the tests were easily stable, as it was observed that former attempts with high strength concrete lead to failure of the tests or fast crack development and the test machine was also changed for another one, stiffer than the previously used.

See Appendix B.1 for further information about former tests attempts.

The campaign has strengths even lower than expected and the core of the biggest specimens, that are the cylindrical type, is not as compact as expected and it looks quite sandy. Even so, results can be obtained and processed with the same methodology and they will have its relevance, because the fracture mechanisms can be applied to concrete, rock and mortar based materials. However, the concrete designation for this mixture is preferable to be avoided for now.

4.1.2 14XII2015: 2ND TEST CAMPAIGN

The mixture composition for the 14XII2015 campaign can be seen at Table 6. The casting was made at Thursday 10th December 2015 and the removal from the molds at Monday 14th December 2015. The day 28th after casting is Thursday 7th January 2016. The maximum aggregate size is 15mm.

Table 6: Campaign 14XII2015 mixture composition

14XII2015	Cement I-52.5R	Admixture	Compressive strength	W/C
Composition	275kg/m ³ ± 15	Neoplast15	25MPa	0.450 ± 0.020
Concrete type	HA-25/F/15/IIa	A plasticizer	Reference: minimum	

Thirteen specimens have been cast: 8 beam type specimens and 5 cylinder type specimens. No cubic specimens were cast for this campaign. The test performed on every single specimen is detailed at Table 7, along with the testing date and order of testing.

The mechanical properties, such as compressive and tensile strength and the elastic modulus, for this campaign are visible at Table 8. Details can be seen at Appendix A.2.2, Appendix A.4.2 and Appendix A.6.2. The dimensions of the specimens from this campaign are:

- A diameter of 150mm and a length of 300mm for the five cylindrical specimens.
- The beam specimen dimensions are shown at Table 9, with reference at Figure 21.

Table 7: Campaign 14XII2015 tests

SPECIMEN	Test	Date of test
C14XII2015I	Direct compression	12/I/2016 (#7) Day 33 rd
C14XII2015II	Brazilian test	12/I/2016 (#8) Day 33 rd
C14XII2015III		12/I/2016 (#9) Day 33 rd
C14XII2015IV		12/I/2016 (#10) Day 33 rd
C14XII2015V		12/I/2016 (#11) Day 33 rd
B14XII2015I	Three point bend test with the $P - \delta$ tail correction method and double length	11/I/2016 (#3) Day 32 nd
B14XII2015II		12/I/2016 (#12) Day 33 rd
B14XII2015III		11/I/2016 (#4) Day 32 nd
B14XII2015IV		11/I/2016 (#5) Day 32 nd
B14XII2015V		12/I/2016 (#13) Day 33 rd
B14XII2015VI		11/I/2016 (#2) Day 32 nd
B14XII2015VII		11/I/2016 (#1) Day 32 nd
B14XII2015VIII		12/I/2016 (#6) Day 33 rd

Table 8: 14XII2015 campaign mechanical properties. When available, standard deviation in brackets. When the data is not valid and, even so, it is shown, an asterisk remarks it

PROPERTY	f_t	f_c	$f_{c,cube}$	E
14XII2015	2.45MPa (0.53)	17.03MPa*	Unavailable	19.76GPa (5.9)

The test journal abstract is shown at Table 10, where the specimens were preserved at the following environments:

- Day 0 to day 3: in molds at indoors conditions of near 17°C and humidity 75%
- Day 4 to day 27: submerged in water indoors
- Day 28 to day 31: inside a chamber at 20°C and humidity 98%
- Day 32: non-tested beam specimens preserved indoors, outside the chamber. Cylindrical specimens inside a chamber at 20°C and humidity 98%

Table 9: Main dimensions of the beam specimens from the campaign 14XII2015

SIZES (mm)	<i>L</i>	<i>D</i>	<i>B</i>	<i>a</i>	<i>N</i>	<i>S</i>	<i>h</i>
B14XII2015I	600	100	100	30	2	300	2
B14XII2015II	600	100	100	29	2	300	2
B14XII2015III	600	100	100	30	2	300	2
B14XII2015IV	600	100	100	30	2	300	2
B14XII2015V	600	100	100	30	2	300	2
B14XII2015VI	600	100	100	30	2	300	2
B14XII2015VII	600	100	100	30	2	300	2
B14XII2015VIII	600	100	100	29	2	300	2

Table 10: 14XII2015 campaign journal summary

SPECIMEN	Fracture status	Warnings	General notes
B14XII2015I	Satisfactory	None	Recording 10 samples per second. There are a good number of data at the initial decreasing part
B14XII2015II	Satisfactory	None	50 samples per second. The same as B14XII2015I
B14XII2015III	Acceptable	At recording	Recording 10 samples per second. It gives few samples at the initial decreasing part. Nevertheless, the fracture data is accepted.
B14XII2015IV	Acceptable	At recording	The same as B14XII2015III
B14XII2015V	Satisfactory	None	Recording 50 samples per second. The result is OK
B14XII2015VI	Acceptable	At recording	The same as B14XII2015III
B14XII2015VII	Acceptable	At recording	The same as B14XII2015III
B14XII2015VIII	Acceptable	At recording and apparatus	50 samples per second. Few acquired data at the initial decreasing part. The CMOD gage moved at a final stage of the test. The test is forced to stop, but near the end. The fracture data is accepted.
C14XII2015I	Failed (F^{29})	At fracture	Fracture is not satisfactory according to the codes
C14XII2015II	Satisfactory	None	Nothing remarkable
C14XII2015III	Satisfactory	At data	There are two peaks, the valid is the first one
C14XII2015IV	Satisfactory	None	Nothing remarkable
C14XII2015V	Satisfactory	None	Nothing remarkable

4.1.3 29I2016: 3RD TEST CAMPAIGN

The casting of this campaign was made at Wednesday 27th January 2016 and the removal from the molds at Friday 29th January 2016. The day 28th after casting is Wednesday 24th February 2016. The mixture composition is shown at Table 11. The maximum aggregate size is 10mm. The casting was made for 2 series, A and B, which by their composition will be considered the same, always if the experimentation does not contradict this. This is because the cement mixer was not big enough.

Table 11: Campaign 29I2016 mixture composition

29I2016		Sand (0-2)	Aggregate (5-10)	CEM II/B-L 32.5N	Water	W/C
A series	Mass	36kg	40.5kg	13.5kg	9.1kg	0.674
	Fraction	40.0%	45.0%	15.0%	10.1%	
	Composition	800kg/m ³	900kg/m ³	300kg/m ³	202kg/m ³	
B series	Mass	36kg	40.5kg	13.5kg	9kg	0.667
	Fraction	40.0%	45.0%	15.0%	10%	
	Composition	800kg/m ³	900kg/m ³	300kg/m ³	200kg/m ³	

A total of 7 specimens per series were cast: 2 cylinders, 1 cube and 4 beams, whose tests are shown at Table 12, where the casting series is remarked. Their dimensions are: for cylinders 300mm long with a 150mm diameter; cubes have a 150mm edge length and beam sizes are at Table 13.

Table 12: Campaign 29I2016 tests

SPECIMEN	Series	Test	Date of test
C29I2016I	A	Brazilian test	25/II/2016 (#10) Day 29 th
C29I2016II	A		25/II/2016 (#11) Day 29 th
C29I2016III	B		25/II/2016 (#13) Day 29 th
C29I2016IV	B		25/II/2016 (#12) Day 29 th
D29I2016I	A	Direct compression	25/II/2016 (#8) Day 29 th
D29I2016II	B		25/II/2016 (#9) Day 29 th
B29I2016I	A	Three point bend test with the $P - \delta$ tail correction method and double length	24/II/2016 (#1) Day 28 th
B29I2016II	A		24/II/2016 (#4) Day 28 th
B29I2016III	A		24/II/2016 (#3) Day 28 th
B29I2016IV	A		24/II/2016 (#2) Day 28 th
B29I2016V	B	Three point bend test with the local fracture energy correction	25/II/2016 (#7) Day 29 th
B29I2016VI	B		24/II/2016 (#5) Day 28 th
B29I2016VII	B		24/II/2016 (#6) Day 28 th
B29I2016VIII	B		25/II/2016 (#14) Day 29 th

The specimens are conserved at the following environments:

- Day 0 to day 1: at indoors conditions of 17°C approx. and a humidity of about 70%
- Day 2 to day 26: underwater indoors

- Day 27 to day 29: indoors at 16°C and a humidity of 65% approx.

The mechanical properties are written at Table 14 (see Appendix A.2.3, Appendix A.4.3 and Appendix A.6.3) and the tests' status at Table 15.

Table 13: Main dimensions of the beam specimens from the campaign 29I2016

SIZES (mm)	<i>L</i>	<i>D</i>	<i>B</i>	<i>a</i>	<i>N</i>	<i>S</i>	<i>h</i>
B29I2016I	600	100	100	30.3	2.1	300	2
B29I2016II	600	100	100	30.1	2.2	300	2
B29I2016III	600	100	100	30.4	2.1	300	2
B29I2016IV	600	100	100	30.3	2.0	300	2
B29I2016V	600	100	100	10.6	2.3	550	2
B29I2016VI	600	100	100	10.6	2.2	550	2
B29I2016VII	600	100	100	42.0	3.2	550	2
B29I2016VIII	600	100	100	42.3	3.3	550	2

Table 14: 29I2016 campaign mechanical properties. When available, standard deviation in brackets. When the data is not valid and, even so, it is shown, an asterisk remarks it

PROPERTY	f_t	f_c	$f_{c,cube}$	E
29I2016	1.42MPa (0.23)	Unavailable	14.29MPa* (2.85)	16.12GPa (3.1)

Table 15: 29I2016 campaign journal summary

SPECIMEN	Fracture status	Warnings	General notes
C29I2016I	Satisfactory	None	Nothing remarkable
C29I2016II	Satisfactory	None	Nothing remarkable
C29I2016III	Satisfactory	None	Nothing remarkable
C29I2016IV	Satisfactory	None	Nothing remarkable
D29I2016I	Failed (1,2,4 ^{29,30})	At fracture	Fracture is not satisfactory according to the codes
D29I2016II	Failed (1,2,4 ^{29,30})	At fracture	Fracture is not satisfactory according to the codes
B29I2016I	Acceptable	At loading	There is a relative maximum and minimum
B29I2016II	Satisfactory	None	Nothing remarkable
B29I2016III	Satisfactory	None	Nothing remarkable
B29I2016IV	Satisfactory	None	Nothing remarkable
B29I2016V	Satisfactory	None	The specimen broke by the action of weight
B29I2016VI	Satisfactory	None	The specimen broke by the action of weight
B29I2016VII	Satisfactory	At zero	The specimen broke by the action of weight. The initial zero is not the absolute zero
B29I2016VIII	Satisfactory	None	The specimen broke by the action of weight

Specimens from V to VIII have got the weight action. The same correction method will be applied to the load recorded by cutting at a *CMOD* value as Equation 3.3.12 says and the load is corrected with Equation 3.3.13. Also, the initial part of the $P - \delta$ curve will be cut until the loading part is reached, because the initial part of little load variation is purely movement without strain energy storage.

4.1.4 10III2016: 4TH TEST CAMPAIGN

The casting was on Monday 7th March 2016 and the date of the removal from the molds is on Thursday 10th March 2016. The day 28th after casting is Monday 4th April 2016. The composition for this campaign is given at Table 16. The maximum aggregate size is 10mm.

Table 16: Campaign 10III2016 mixture composition

10III2016	Sand (0-2)	Aggregate (5-10)	CEM II/B-L 32.5N	Water	W/C	Admixture
Mass	44.1kg	44.1kg	11.25kg	9.66kg		200mL
Fraction	44.34%	44.34%	11.32%	9.71%	0.859	Sikaplast 360
Composition	890kg/m ³	890kg/m ³	225kg/m ³	195kg/m ³		Plasticizer

A total of 7 specimens were cast, three cylinders and 4 beams, the tests performed at every one of them is shown at Table 17.

Table 17: Campaign 10III2016 tests

SPECIMEN	Test	Date of test
C10III2016I	Direct compression	05/IV/2016 (#4) Day 29 th
C10III2016II	Brazilian test	05/IV/2016 (#5) Day 29 th
C10III2016III		05/IV/2016 (#6) Day 29 th
B10III2016I	Three point bend test with the $P - \delta$ tail correction method and double length	05/IV/2016 (#1) Day 29 th
B10III2016II		05/IV/2016 (#2) Day 29 th
B10III2016III		05/IV/2016 (#3) Day 29 th
B10III2016IV		05/IV/2016 (#7) Day 29 th

The sizes of the specimens are the following ones:

- 150mm diameter and 300mm long for the cylinder-type specimens
- Beam specimens sizes are written at Table 18

Table 18: Main dimensions of the beam specimens from the campaign 10III2016

SIZES (mm)	L	D	B	a	N	S	h
B10III2016I	600	100	100	31.97	2.92	300	2
B10III2016II	600	100	100	30.40	2.98	300	2
B10III2016III	600	100	100	30.81	2.10	300	2
B10III2016IV	600	100	100	30.58	2.96	300	2

The resulting mechanical properties for this type of concrete are given at Table 19. Details can be seen at Appendix A.2.4, Appendix A.4.4 and Appendix A.6.4.

Table 19: 10III2016 campaign mechanical properties. When available, standard deviation in brackets

PROPERTY	f_t	f_c	$f_{c,cube}$	E
10III2016	1.09MPa (0.05)	9.27MPa	Unavailable	18.04GPa (5.4)

The specimens were preserved at the following environments:

- Day 0 to day 2: indoors at the wood molds for the beam specimens and metal molds for the cylindrical ones, at 15°C and 45-50% of humidity approx.
- Day 3 to day 27: underwater indoors
- Day 28 and after: indoors, out of water, at 16°C and a humidity of 50% approx.

Table 20: 10III2016 campaign journal summary

SPECIMEN	Fracture status	Warnings	General notes
C10III2016I	Satisfactory	None	Nothing remarkable
C10III2016II	Satisfactory	None	Nothing remarkable
C10III2016III	Satisfactory	None	Nothing remarkable
B10III2016I	Satisfactory	At recording	Due to a mistake, δ is not correctly recorded by the system at 50 samples per second. The safety file from the controller will be taken for $P - \delta$
B10III2016II	Satisfactory	At recording	
B10III2016III	Satisfactory	At recording	
B10III2016IV	Satisfactory	At recording	

This campaign was expected to be slightly stronger than 23X2015 due to a higher content on cement and quite less proportion of water. This fact is accomplished.

Further information about the solution for the lost information about displacement is detailed at Appendix D.6.

4.1.5 17III2016: 5TH TEST CAMPAIGN

This campaign, whose composition is given at Table 21, was cast on Monday 14th March 2016. The day 28th after casting is Monday 11th April 2016. The maximum aggregate size is 10mm.

Table 21: Campaign 17III2016 mixture composition

17III2016	Sand (0-2)	Agg. (5-10)	CEM II/B-L 32.5N	Water	W/C	Admixture
Mass	35.6kg	45.6kg	10.2kg	8.34kg		140mL
Fraction	38.95%	49.90%	11.15%	9.12%	0.818	MasterPozzolith7002
Composition	790kg/m ³	990kg/m ³	225kg/m ³	184kg/m ³		A plasticizer

A total of 7 specimens were cast to perform the tests shown at Table 22: 3 cylinders of 150mm diameter and 300mm long and 4 beams whose dimensions are written at Table 23.

Table 22: Campaign 17III2016 tests

SPECIMEN	Test	Date of test
C17III2016I	Direct compression	12/IV/2016 (#6) Day 29 th
C17III2016II	Brazilian test	12/IV/2016 (#4) Day 29 th
C17III2016III		12/IV/2016 (#5) Day 29 th
B17III2016I	Three point bend test with the $P - \delta$ tail correction method and double length	12/IV/2016 (#1) Day 29 th
B17III2016II		12/IV/2016 (#2) Day 29 th
B17III2016III		12/IV/2016 (#3) Day 29 th
B17III2016IV		12/IV/2016 (#7) Day 29 th

Table 23: Main dimensions of the beam specimens from the campaign 17III2016

SIZES (mm)	<i>L</i>	<i>D</i>	<i>B</i>	<i>a</i>	<i>N</i>	<i>S</i>	<i>h</i>
B17III2016I	600	100	100	29.44	2.86	300	2
B17III2016II	600	100	100	31.62	2.95	300	2
B17III2016III	600	100	100	27.72	3.13	300	2
B17III2016IV	600	100	100	26.25	2.75	300	2

The properties of this concrete mixture are those given at Table 24. Details can be seen at Appendix A.2.5, Appendix A.4.5 and Appendix A.6.5.

Table 24: 17III2016 campaign mechanical properties. When available, standard deviation in brackets

PROPERTY	f_t	f_c	$f_{c,cube}$	E
17III2016	1.69MPa (0.07)	13.87MPa	Unavailable	16.40GPa (4.8)

The specimens were preserved at the following environments:

- Day 0 to day 2: indoors in the molds at 15°C and 40% humidity approx.
- Day 3 to day 27: underwater indoors
- Day 28 and after: out of water, indoors, at 17°C and 50% humidity approx.

Table 25: 17III2016 campaign journal summary

SPECIMEN	Fracture status	Warnings	General notes
C17III2016I	Satisfactory	None	Nothing remarkable
C17III2016II	Satisfactory	None	Nothing remarkable
C17III2016III	Satisfactory	None	Nothing remarkable
B17III2016I	Satisfactory	None	Nothing remarkable
B17III2016II	Satisfactory	At loading	There is a local maximum and minimum at the rising part. The first values are moved at the second rising part in order to give continuity
B17III2016III	Satisfactory	At recording	There is a first rising and unloading part, relatively small compared with a second phenomenon similar. The second is the one considered
B17III2016IV	Satisfactory	At recording	There is a first rising and unloading part, relatively small compared with a second phenomenon similar. The second is the one considered

This campaign is the first done by ourselves that gives mechanical properties of value equal or higher the first concrete class at *Eurocode 2*. Further conclusions have to wait the future campaigns.

This campaign also includes secondary information for a study of the measurement of the displacement used to calculate the introduced energy to the system. Further information about this can be found at Appendix B.2.1.

4.1.6 01IV2016: 6TH TEST CAMPAIGN

The casting of this campaign, whose composition is given at Table 26, was done on Wednesday 30th March 2016. The day 28th after casting is Wednesday 27th April 2016. The maximum aggregate size is 10mm.

Table 26: Campaign 01IV2016 mixture composition

01IV2016	Sand (0-2)	Agg. (5-10)	CEM II/B-L 32.5N	Water	W/C	Admixture
Mass	41.52kg	41.52kg	13.2kg	10.164kg		130mL
Fraction	43.14%	43.14%	13.72%	10.56%	0.770	MasterPozzolith7002
Composition	865kg/m ³	865kg/m ³	275kg/m ³	212kg/m ³		A plasticizer

A total of 7 specimens were cast and the test done at every one of them is shown at Table 27. Three 300mm diameter and 150mm long cylinders and four beams (see Table 28 for their sizes).

Table 27: Campaign 01IV2016 tests

SPECIMEN	Test	Date of test
C01IV2016I	Direct compression	28/IV/2016 (#3) Day 29 th
C01IV2016II	Brazilian test	28/IV/2016 (#1) Day 29 th
C01IV2016III		28/IV/2016 (#2) Day 29 th
B01IV2016I	Three point bend test with the $P - \delta$ tail correction method and double length	28/IV/2016 (#4) Day 29 th
B01IV2016II		28/IV/2016 (#5) Day 29 th
B01IV2016III		28/IV/2016 (#7) Day 29 th
B01IV2016IV		28/IV/2016 (#6) Day 29 th

Table 28: Main dimensions of the beam specimens from the campaign 01IV2016

SIZES (mm)	L	D	B	a	N	S	h
B01IV2016I	600	100	100	30.10	2.11	300	2
B01IV2016II	600	100	100	29.73	2.00	300	2
B01IV2016III	600	100	100	30.03	2.09	300	2
B01IV2016IV	600	100	100	29.81	2.04	300	2

The main mechanical properties are given at Table 29. Details are given at Appendix A.2.6, Appendix A.4.6 and Appendix A.6.6.

Table 29: 01IV2016 campaign mechanical properties. When available, standard deviation in brackets

PROPERTY	f_t	f_c	$f_{c,cube}$	E
01IV2016	1.26MPa (0.02)	12.53MPa	Unavailable	27.13GPa (6.49)

The specimens are preserved at the following environmental conditions:

- Day 0 to day 1: inside the molds indoors at approximately 17°C and 45% humidity
- Day 2 to day 28: underwater indoors
- Day 29 and after: indoors, out of water, at approximately 18°C and 55% humidity

The summary of the tests done at this campaign is given at Table 30.

Table 30: 01IV2016 campaign journal summary

SPECIMEN	Fracture status	Warnings	General notes
C01IV2016I	Satisfactory	None	Nothing remarkable
C01IV2016II	Satisfactory	None	Nothing remarkable
C01IV2016III	Satisfactory	None	Nothing remarkable
B01IV2016I	Correct	At loading	There are relative maxima and minima at the initial elastic loading branch before the peak load
B01IV2016II	Satisfactory	None	Nothing remarkable
B01IV2016III	Satisfactory	None	Nothing remarkable
B01IV2016IV	Correct	At loading	There are relative maxima and minima at the initial elastic loading branch before the peak load

This campaign has a higher strength than the 10III2016 campaign, base for the composition of the 01IV2016 campaign, with the same proportion of sand and aggregate and more cement. The extra strength can also be a consequence of the lower content of water. Further campaigns will give more precise information.

There are not extra contents or information for this campaign.

A phenomenon that only happened at the 17III2016 campaign has reappeared; because the one occurred at a single specimen of the 29I2016 campaign was relatively sudden to have an easy reason for explaining it. There are relative maxima and minima at the elastic loading stage of the three point bend test with a soft progression of the change in slope. If this still happens in the near future, a new object of study must be considered for future research.

4.1.7 07IV2016: 7TH TEST CAMPAIGN

The casting of this campaign was done on Monday 4th April 2016 with the composition given at Table 31. So, the 28th day after casting is Monday 2nd May 2016. The maximum aggregate size is 10mm.

Table 31: Campaign 07IV2016 mixture composition

07IV2016	Sand (0-2)	Agg. (5-10)	CEM II/B-L 32.5N	Water	W/C	Admixture
Mass	36.72kg	46.32kg	13.2kg	10.16kg		130mL
Fraction	38.15%	48.13%	13.72%	10.56%	0.770	MasterPozzolith7002
Composition	765kg/m ³	965kg/m ³	275kg/m ³	212kg/m ³		A plasticizer

A total of 7 specimens were cast: 3 cylinders and 4 beams. The test done on every single one of them is written at Table 32.

Table 32: Campaign 07IV2016 tests

SPECIMEN	Test	Date of test
C07IV2016I	Direct compression	03/V/2016 (#6) Day 29 th
C07IV2016II	Brazilian test	03/V/2016 (#4) Day 29 th
C07IV2016III		03/V/2016 (#5) Day 29 th
B07IV2016I	Three point bend test with the $P - \delta$ tail correction method and double length	03/V/2016 (#1) Day 29 th
B07IV2016II		03/V/2016 (#2) Day 29 th
B07IV2016III		03/V/2016 (#3) Day 29 th
B07IV2016IV		03/V/2016 (#7) Day 29 th

The sizes for the cylinder-type specimens are 300mm long with a diameter of 150mm and for the beam-type specimens, see Table 33.

Table 33: Main dimensions of the beam specimens from the campaign 07IV2016

SIZES (mm)	<i>L</i>	<i>D</i>	<i>B</i>	<i>a</i>	<i>N</i>	<i>S</i>	<i>h</i>
B07IV2016I	600	100	100	29.71	2.30	300	2
B07IV2016II	600	100	100	29.93	2.19	300	2
B07IV2016III	600	100	100	29.81	2.09	300	2
B07IV2016IV	600	100	100	30.03	2.29	300	2

The mechanical properties for this campaign are given at Table 34. Details are given at Appendix A.2.7, Appendix A.4.7 and Appendix A.6.7.

Table 34: 07IV2016 campaign mechanical properties. When available, standard deviation in brackets

PROPERTY	f_t	f_c	$f_{c,cube}$	E
07IV2016	1.44MPa (0.07)	15.37MPa	Unavailable	22.19GPa (5.49)

The specimens were preserved at the following environments:

- Day 0 to day 2: indoors at 16°C and a humidity of 50% approx.
- Day 3 to day 27: underwater indoors
- Day 28 and after: indoors, out of water, at approx. 18°C and 55% humidity

The register of the test status is available at Table 35.

Table 35: 07IV2016 campaign journal summary

SPECIMEN	Fracture status	Warnings	General notes
C07IV2016I	Satisfactory	None	Nothing remarkable
C07IV2016II	Satisfactory	None	Nothing remarkable
C07IV2016III	Satisfactory	None	Nothing remarkable
B07IV2016I	Satisfactory	None	Nothing remarkable
B07IV2016II	Satisfactory	None	Nothing remarkable
B07IV2016III	Correct	At loading	There are relative maxima and minima at the initial elastic loading branch before the peak load. There is a relatively plane zone at the initial stage
B07IV2016IV	Satisfactory	None	Nothing remarkable

This campaign has a higher strength than 01IV2016, which is essentially the same composition changing the sand and aggregate proportion from both equal to a higher content in aggregate. Cement and water have the same proportion. The following two campaigns repeat the same event with a lower content in water. For a conclusion, this phenomenon should be repeated. Nevertheless, what we expect is a higher strength, because the lower water content. This should be confirmed in future tests.

In general, the tests were performed correctly. The only one with an anomaly in the tests is B07IV2016III. The strange event is also less notorious than other tests. It is not clear the reason, but we will have to wait for future tests to really confirm that the phenomena seen in former campaigns reappear the same way, as in 17III2016 and 01IV2016, or not. If it does, it has to be surely taken into account for future studies.

4.1.8 14IV2016: 8TH TEST CAMPAIGN

This campaign was cast on Monday 11th April 2016 with the composition given at Table 36. The maximum aggregate size is 10mm and the 28th day after casting is Monday 9th May 2016.

Table 36: Campaign 14IV2016 mixture composition

14IV2016	Sand (0-2)	Agg. (5-10)	CEM II/B-L 32.5N	Water	W/C	Admixture
Mass	41.52kg	41.52kg	13.2kg	8.58kg		237.5mL
Fraction	43.14%	43.14%	13.72%	8.92%	0.650	MasterPozzolith7002
Composition	865kg/m ³	865kg/m ³	275kg/m ³	179kg/m ³		A plasticizer

A total of 7 specimens were cast. The tests planned to be done on every single one of them is visible at Table 37.

Table 37: Campaign 14IV2016 tests

SPECIMEN	Test	Date of test
C14IV2016I	Direct compression	10/V/2016 (#6) Day 29 th
C14IV2016II	Brazilian test	10/V/2016 (#4) Day 29 th
C14IV2016III		10/V/2016 (#5) Day 29 th
B14IV2016I	Three point bend test with the $P - \delta$ tail correction method and double length	10/V/2016 (#1) Day 29 th
B14IV2016II		10/V/2016 (#3) Day 29 th
B14IV2016III		10/V/2016 (#7) Day 29 th
B14IV2016IV		10/V/2016 (#2) Day 29 th

The cylinders have sizes of 300mm long and a diameter of 150mm and the beam specimens sizes are given at Table 38.

Table 38: Main dimensions of the beam specimens from the campaign 14IV2016

SIZES (mm)	<i>L</i>	<i>D</i>	<i>B</i>	<i>a</i>	<i>N</i>	<i>S</i>	<i>h</i>
B14IV2016I	600	100	100	29.78	1.97	300	2
B14IV2016II	600	100	100	29.95	2.14	300	2
B14IV2016III	600	100	100	29.54	1.98	300	2
B14IV2016IV	600	100	100	29.66	2.00	300	2

The main mechanical properties for the concrete cast for this campaign are given at Table 39. Details are given at Appendix A.2.8, Appendix A.4.8 and Appendix A.6.8.

Table 39: 14IV2016 campaign mechanical properties. When available, standard deviation in brackets

PROPERTY	f_t	f_c	$f_{c,cube}$	E
14IV2016	2.13MPa (0.17)	20.36MPa	Unavailable	21.96GPa (4.01)

The specimens were conserved at the following environmental conditions:

- Day 0 to day 2: inside the molds indoors at 17°C and 50% humidity approx.
- Day 3 to day 9: underwater indoors
- Day 10: indoors, out of water at approximately 18°C and 55% humidity
- Day 11 to day 27: underwater indoors
- Day 28 and after: indoors, out of water, at approximately 19°C and 40% humidity

Table 40: 14IV2016 campaign journal summary

SPECIMEN	Fracture status	Warnings	General notes
C14IV2016I	Satisfactory	None	Nothing remarkable
C14IV2016II	Satisfactory	None	Nothing remarkable
C14IV2016III	Satisfactory	None	Nothing remarkable
B14IV2016I	Satisfactory	None	Nothing remarkable
B14IV2016II	Satisfactory	None	Nothing remarkable
B14IV2016III	Satisfactory	None	Nothing remarkable
B14IV2016IV	Correct	At loading	There are relative maxima and minima at the initial elastic loading branch before the peak load. There is a relatively plane zone at the initial stage

With the same composition as campaign 01IV2016, but changing the water to cement ratio from 0.77 to 0.65, we have changed the strength of the concrete. The improvement of the material properties is easily visible.

About the tests, three of them have a good progress, obtaining a huge amount of points just after the peak load and the other one has registered enough point at this part to correctly draw the curve. Only one test showed again the presence of relative maxima and minima at the elastic loading part of the test. The explanation for that has not been found yet, but, even that it has happened at some tests, there is not a pattern of appearance and the tests are done correctly and this does not happen at sensible stages of the test, only at the elastic loading part at no relatively high loads respect the peak load. Maybe, this can be considered as an isolated phenomenon.

4.1.9 21IV2016: 9TH TEST CAMPAIGN

The casting of this campaign was done at Tuesday 19th April 2016, one day after the planned date at Appendix I. For this campaign, the unmolding date will not coincide with the campaign name for one day. The composition is given at Table 41, where the maximum aggregate size is 10mm.

Table 41: Campaign 21IV2016 mixture composition

21IV2016	Sand (0-2)	Agg. (5-10)	CEM II/B-L 32.5N	Water	W/C	Admixture
Mass	38.56kg	48.64kg	13.86kg	9.01kg		250mL
Fraction	38.15%	48.13%	13.72%	8.23%	0.650	MasterPozzolith7002
Composition	765kg/m ³	965kg/m ³	275kg/m ³	165kg/m ³		A plasticizer

A total of 7 specimens were cast. The tests planned are given at Table 42.

Table 42: Campaign 21IV2016 tests

SPECIMEN	Test	Date of test
C21IV2016I	Direct compression	18/V/2016 (#5) Day 29 th
C21IV2016II	Brazilian test	18/V/2016 (#2) Day 29 th
C21IV2016III		18/V/2016 (#3) Day 29 th
B21IV2016I	Three point bend test with the $P - \delta$ tail correction method and double length	18/V/2016 (#1) Day 29 th
B21IV2016II		18/V/2016 (#7) Day 29 th
B21IV2016III		18/V/2016 (#6) Day 29 th
B21IV2016IV		18/V/2016 (#4) Day 29 th

The campaign has three cylinders of 150mm diameter and 300mm long and 4 beam-type specimens, whose sizes are given at Table 43.

Table 43: Main dimensions of the beam specimens from the campaign 21IV2016

SIZES (mm)	<i>L</i>	<i>D</i>	<i>B</i>	<i>a</i>	<i>N</i>	<i>S</i>	<i>h</i>
B21IV2016I	600	100	100	29.88	2.09	300	2
B21IV2016II	600	100	100	29.98	2.12	300	2
B21IV2016III	600	100	100	29.78	1.98	300	2
B21IV2016IV	600	100	100	29.83	2.09	300	2

The main mechanical properties for this campaign are written at Table 44. Details are given at Appendix A.2.9, Appendix A.4.9 and Appendix A.6.9.

Table 44: 21IV2016 campaign mechanical properties. When available, standard deviation in brackets

PROPERTY	f_t	f_c	$f_{c,cube}$	E
21IV2016	1.31MPa	16.32MPa	Unavailable	23.82GPa (1.65)

The preservation of the specimens of this campaign is done at the following environmental conditions:

- Day 0 to day 2: indoors, inside the molds, at approximately 17°C and 50% humidity
- Day 3 to day 27: underwater indoors
- Day 28 and after: indoors, out of water, at approximately 19°C and 40% humidity

The summary of the tests status for the 21IV2016 campaign is written at Table 45.

Table 45: 21IV2016 campaign journal summary

SPECIMEN	Fracture status	Warnings	General notes
C21IV2016I	Satisfactory	None	Nothing remarkable
C21IV2016II	Failed	At fracture and at peak load	Incomplete splitting. One side shows a vertical division, the other side did not break at the first peak load. The peak is the first maximum
C21IV2016III	Satisfactory	None	Nothing remarkable
B21IV2016I	Satisfactory	At loading	There is a relative maximum and minimum
B21IV2016II	Satisfactory	None	Nothing remarkable
B21IV2016III	Satisfactory	None	Nothing remarkable
B21IV2016IV	Satisfactory	None	Nothing remarkable

This campaign has a lower strength than the 14IV2016 campaign, which is the same composition, but adding less sand than aggregate with the same cement and water proportion. For campaigns 01IV2016 and 07IV2016, this was also done, but the result was that the second one, with more aggregate than sand, has a higher strength than the first one, the same proportion. This does not happen with campaigns 14IV2016 and 21IV2016. As a result of this, no valid conclusions can be extracted for a strength difference with different sand and aggregate proportion.

The tests were done correctly. The only remarkable phenomenon is a sudden load decrease at the loading stage of the B21IV2016I test, but it can be easily related with a break of a little surplus of the specimen near one of the supports.

4.2 TESTS PROCEDURES, METHODOLOGY AND GENERAL TEST INFORMATION

The previous chapter wanted to explain the materials that have been tested, their mixture, their properties, their shape and a general overview of the test status. Now, it is time to explain in detail the test procedure. Every single test performed will be depicted in two parts. The first part will give information about the machinery and apparatus used in the tests and their assembly. The second part refers to the machinery configuration to realize the test properly. If there were differences on the test configuration or apparatus between the tested campaigns, it would be pointed out.

The test whose details will be exposed in this chapter is the three point bending test, because it is the basis to obtain the fracture energy of concrete and other fracture properties, which is the main search of this project. For the tests whose only use is to determine other secondary, but no less important, properties, such as the direct compression or the indirect tensile tests, are exposed at the Appendices section. See Appendix A.5 for the information related to the direct compression test and Appendix A.3 for the details from the Brazilian test procedure. Appendix A.4 and A.6 give the data information of every campaign about the compressive and the tensile strength.

4.2.1 THREE POINT BEND TEST APPARATUS

Performing a three point bend test requires the following elements:

- The measurement of the crack mouth opening displacement *CMOD* is done by means of a clip gage (see Figure 28), from the *Epsilon Technology Corporation*, model 3541-005M-120M-ST. This is the clip gage from the *Epsilon Tech. Corp.* series 3541 of Fracture Mechanics Clip-On Gages, a 5mm gauge length (metric, 005M), a measuring range of +12.0/-2.0mm (120M) and a temperature range from -40°C to 100°C (ST). This data comes from the company catalogue, pages 48-49, available with other specifications and features, at the following link: http://www.epsilontech.com/pdf/Epsilon_extensometer_catalog.pdf.
- The clip gage has 2 steel knives where the extensometer can be placed thanks to two little notches at the end of the two branches (Figure 29 for the clip gage notch and Figure 30 for the steel knives).

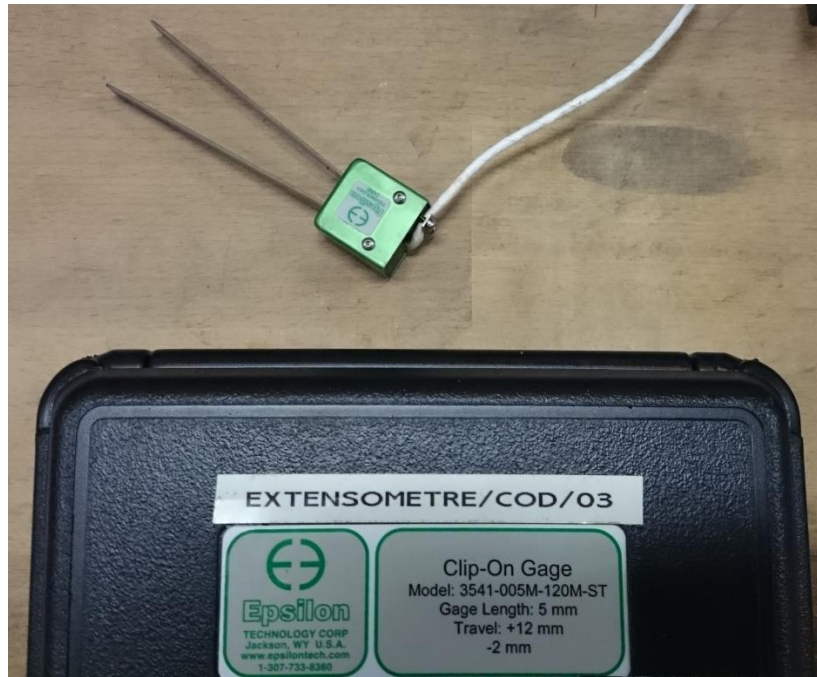


Figure 28: CMOD clip gage EPSILON 3541-005M-120M-ST



Figure 29: Notch at the clip gage

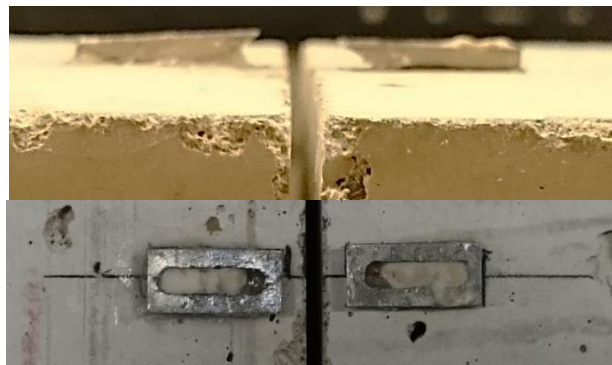


Figure 30: Steel knives, where the COD clip gage is attached, placed on a notched concrete specimen

- A universal testing machine, built by the company *SERVOSIS*, *MUE* series, model 60, from the year 1991, working at 380V connected to a three-phase electric grid (Figure 31). The maximum load the machine is able to apply safely is 60 tones and the maximum displacement of the piston is 280mm, from -140mm until +140mm. The piston is attached to the down support of the machine.

The machine can read load and displacement. An expected displacement of about 1 to 3mm read within a range of 280mm may have certain noise, but the machine is not prepared to control for other lectures than the inner force register or the inner displacement register, so displacement, if no other option is available, will be read from the machine. Moreover, these data are easy to filter after.

An estimated load between 200-500kg within a range of 120000kg (from -60 tones until +60 tones) is, evidently, more possible to have major noise than displacements and this phenomenon happens (see Figure 32 or Figure 33).



Figure 31: Universal testing machine SERVOSIS MUE-60

- A load cell, because the load applied requires more precision. One of the available load cells is from the *UTILCELL* Company, model 630, to use either in tension or compression, of nominal load 2500kg, near 25kN (Figure 34). Catalogue available at the following link: http://www.utilcell.es/pdf/fichas_producto/es_gb/modelo_630_fp_es_en.pdf. At Figure 32 and Figure 33 one can see how it enhances the recording of the load applied.

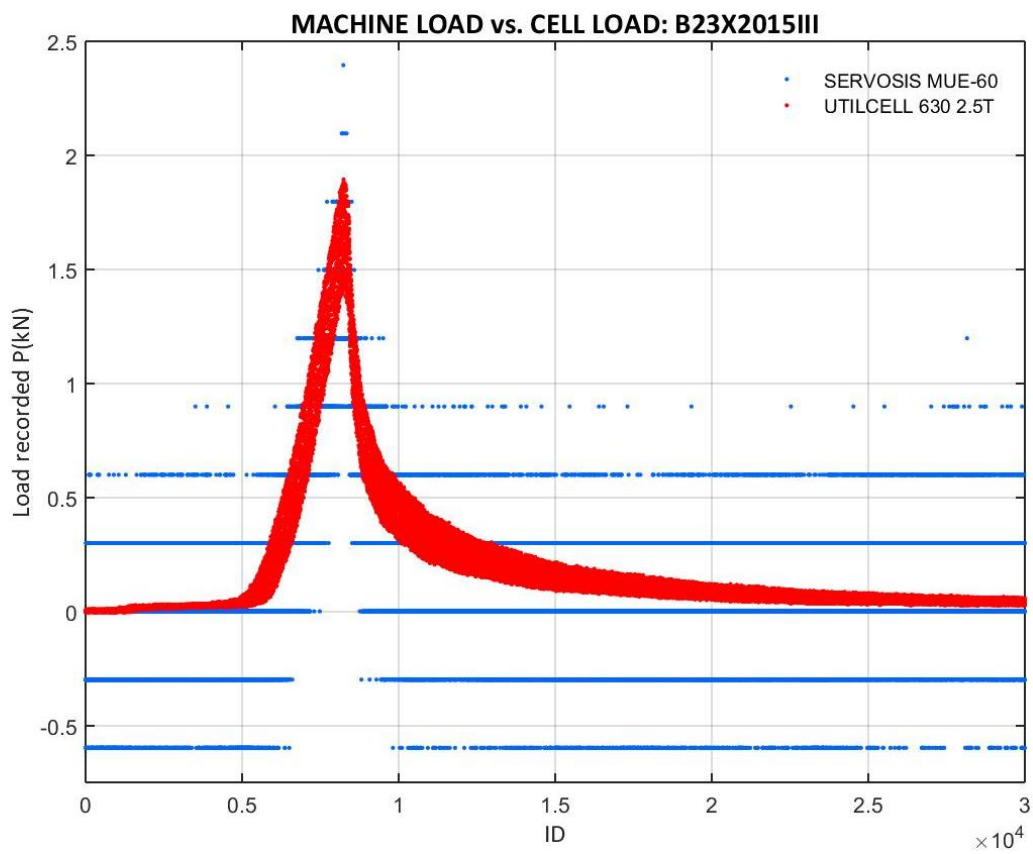


Figure 32: Comparison between the loads registered by the machine and by a load cell (#1)

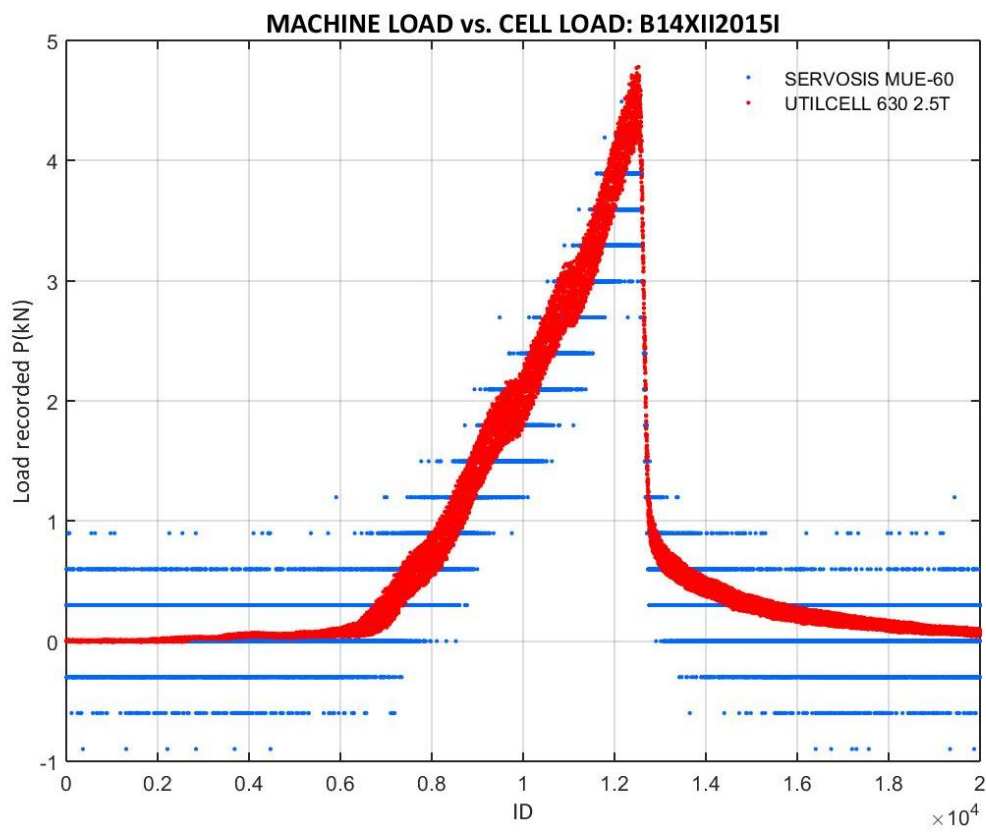


Figure 33: Comparison between the loads registered by the machine and by a load cell (#2)

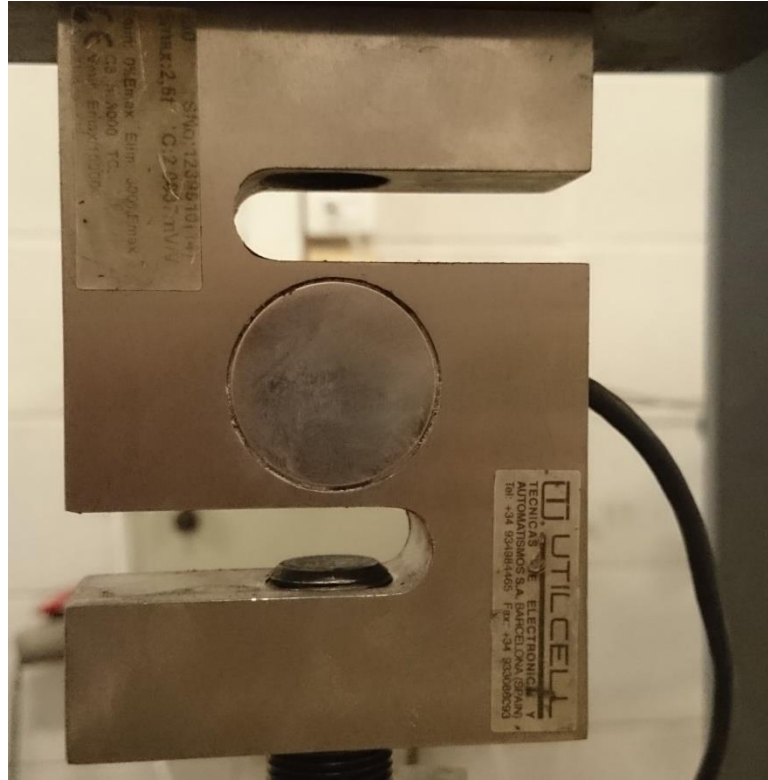


Figure 34: Load cell UTILCELL 630 with a nominal load of 2500kg

- An acquisition system, because, at the very moment we need to record something the testing machine is not able to read, this system is required. The machine tracer records the load from the machine sensor and the displacement from the piston, but nothing else.

The available acquisition system is from *VISHAY PRECISION GROUP*, the digital scanner model *5100B* (Figure 35). The system specifications and other features can be found at pages 37 and 38 of the catalogue at: <http://www.vishaypg.com/docs/50002/50002.pdf>.

At the opposite face there is the PC connector and 4 cards, each one with five 9-pin connectors, which can be for *Strain Gage* sensors or *Strain Gage Based Transducers* and other kind of cards for *High-Level* sensors. The data from the machine is considered a *High-Level* sensor. The load cell and the clip gage are considered *Strain Gage Based Transducers*.

This system is able to read 20 channels at a maximum frequency of 50Hz (50 complete data registers per second maximum).



Figure 35: VISHAY Micro-measurements scanner model 5100B

- Two roller supports must be placed if the test detailed at Chapter 3.1 (Figure 21) in order to give a degree of freedom on the horizontal axis to reduce axial forces and friction (see Chapter 3.2.3). The distance between them is called the *Span length* or *Span* (S). The rollers are placed on a plane slab with two limits to prevent the roller to fall out of the system. The rollers available have a 50mm diameter and 150mm of length. The U-form slabs size is 150x150x25mm. The rollers and their position can be seen at Figure 37 and Figure 38.
- Anti-torsion support to introduce a degree of freedom in torsion, so it cannot influence the results. This is placed under one of the rollers (Figure 37). The support is formed by two 120x120x15mm slabs with a 7mm depth and 18mm width triangular guide and a roller whose diameter is 15mm and it is 120mm long. This makes the separation between slabs of 5mm when they are parallel. The detailed view is given at Figure 36.

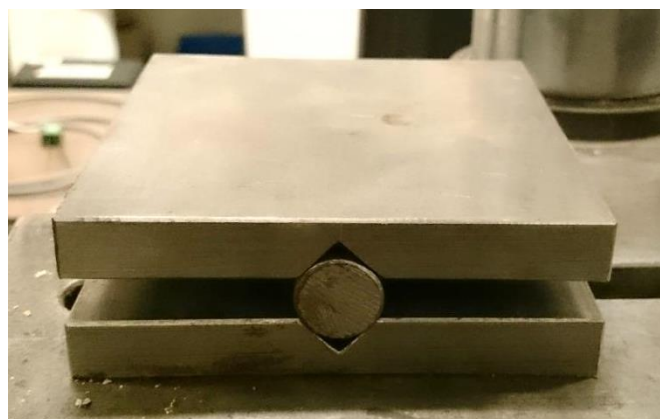


Figure 36: Anti-torsion support

- A load applicator, visible down the load cell at Figure 37, with a semi-cylinder part in contact with the top face of the specimen, so the friction force tends to a low value, fact that helps to the correct development of the test (see Chapter 3.2.3).

The final configuration for the three point bending test is the one showed at Figure 37 and Figure 38 if the beam-type specimen is placed on.



Figure 37: Machine MUE-60 prepared for a three point bending test



Figure 38: Beam-type notched specimen ready for a three point bending test of fracture mechanics

4.2.2 THREE POINT BEND TEST CONFIGURATION

The control program for this machine is *PCD2K*. The control software set up and further details can be found at Appendix A.3.2 and the windows of the program are visible at Figure 125 and Figure 126.

The three point bending tests can be controlled by several parameters:

- The machine's piston displacement, first default control method
- The machine's piston force, second default control method
- The clip gage opening, unavailable at the current system

The ideal would be the clip gage opening control ²⁵. If this is unavailable, the preferred control is the displacement with a constant speed, because force control is not useful.

The control system can acquire data, but the reduction method will make that only 1024 register will be obtained and, for the moment of fracture, this temporal space between the data will provoke the loss of lots of data. This is one of the reasons why introducing an alternative acquisition system will help us. The maximum acquisition rate and the acquisition system have been explained at Chapter 4.2.1. The data recorded is: the machine's load, the piston displacement, the load cell measurement and the clip gage opening. The recording is done with the *StrainSmart 5000* software (window at Figure 39) at the computer which the *VISHAY 5000* is connected to, working with *Windows 2000*.

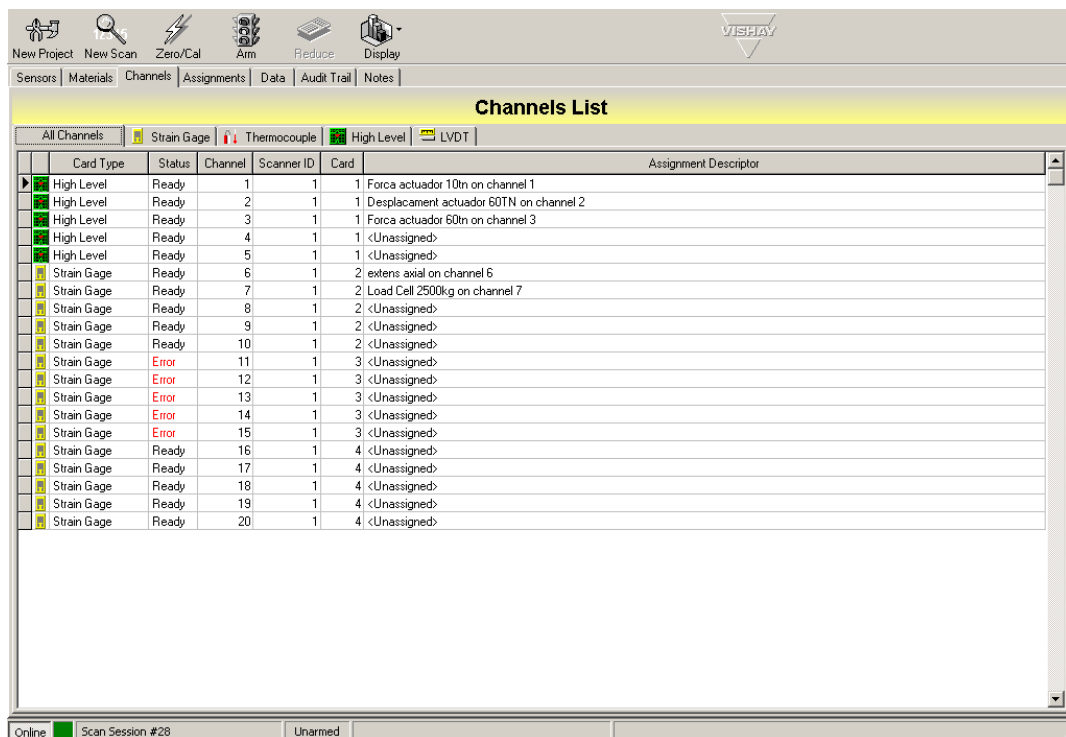


Figure 39: StrainSmart 5000 project main window

The project has the sensors loaded, whose calibrations are the following:

- *SERVOSIS MUE-60* piston displacement: 100mV at 10mm, at a *High-Level* port
- *SERVOSIS MUE-60* load: 100mV every 10000kg, at a *High-Level* port
- *UTILCELL 630 2.5T* linear calibration at Figure 40, at a *Strain Gage* port

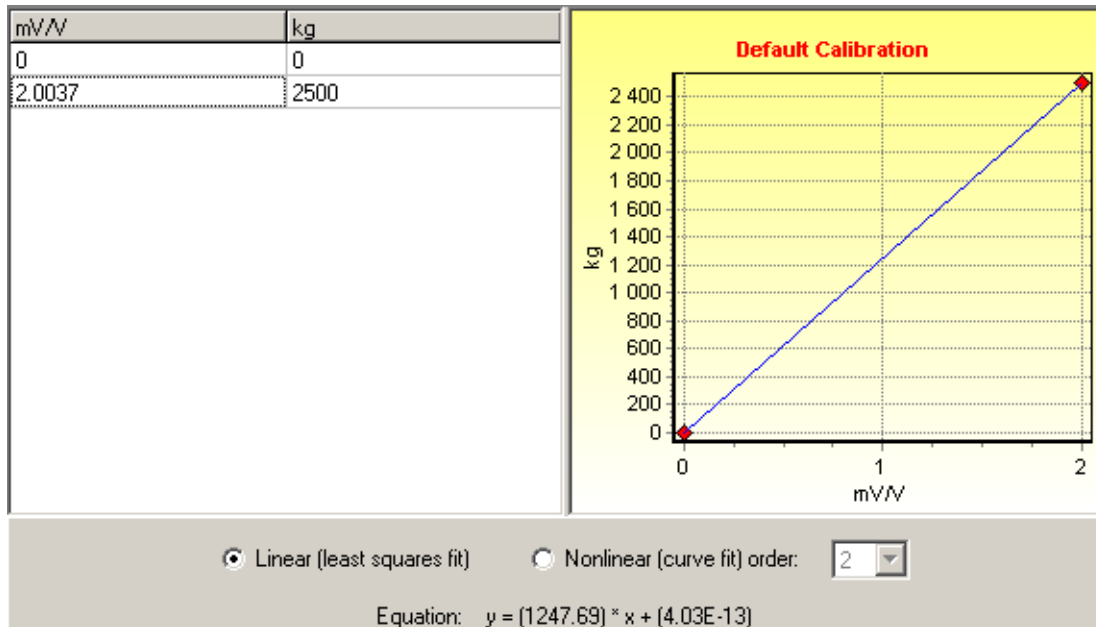


Figure 40: UTILCELL 630 2.5T calibration

- *EPSILON 3541-005M-120M-ST* linear calibration at Figure 41, at a *Strain Gage* port

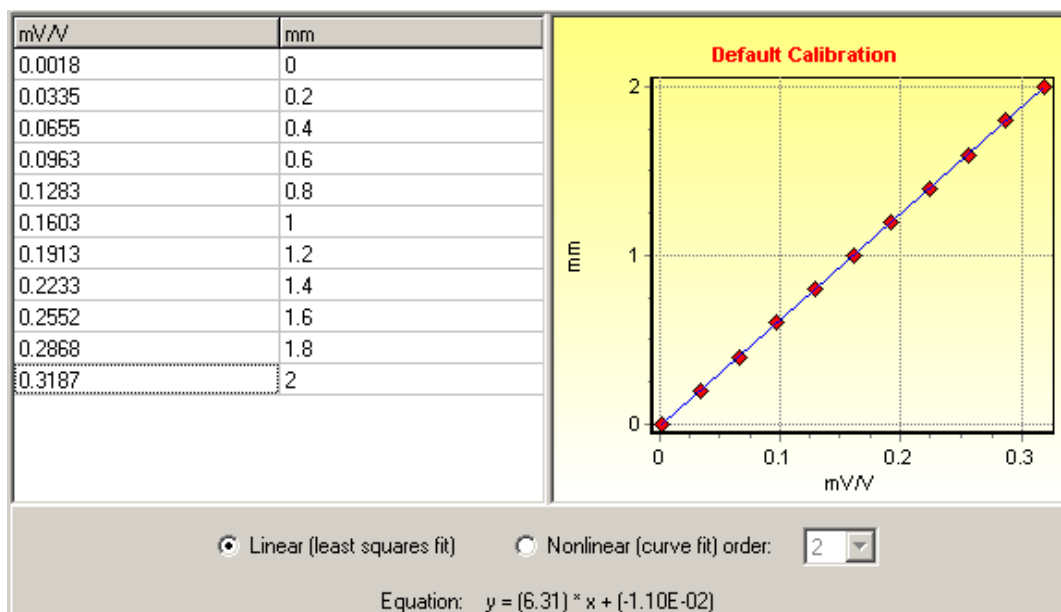


Figure 41: CMOD clip gage EPSILON 3541-005M-120M-ST calibration

A new scan must be done, choosing the proper channels, creating then a zero and, finally, arming the scan session. During the scan creation, the acquisition rate can be chosen:

- If the *Normal* speed is chosen, the maximum recording rate is about 10 registers per second
- If the *Fast* speed is chosen, 50 registers per second can be selected

The three point bending tests are done with the following configurations:

- Every single test from campaign 23X2015 until campaign 21IV2016 is perform at a constant speed of 0.001mm/s; direction, from -140mm to +140mm

Then, the stored data is reduced with its calibrated values with a precision of 3 or 4 decimal positions in a text file. With the proper changes, a platform such as *MATLAB* (or similar) or a calculation sheet is able to work with the recorded numbers.

4.3 SUMMARY OF THE TESTED CAMPAIGNS

As a collection of Chapter 4.1, a summary of the tested campaigns, their composition, properties and other information is given at Table 46.

An alternative designation for the campaigns is also given in form of “*T-S/A/C/W*”, in order to make easier to see the composition of the campaigns at Chapter 5, where:

- *T* is the type of cement and also the maximum aggregate size: *I* is for CEM I 52.5R and a maximum aggregate of 15mm and *II* is for CEM II 32.5N/B-L and a maximum aggregate size of 10mm
- *S* is the sand fraction respect the total dry mass in percentage and as an integer number
- *A* is the aggregate fraction respect the total dry mass in percentage and as an integer number
- *C* is the cement fraction respect the total dry mass in percentage and as an integer number
- *W* is the water to cement ratio represented with the two first decimal numbers of the ratio, considering that always the integer part is zero

Table 46: Summary of the tested campaigns

	CAMPAIGN	2 ND NOTATION	Sand 0-2	Agg. 5-10	Cement	w/c	f_c (MPa)	f_t (MPa)
1 st	23X2015	<i>II-42/47/11/87</i>	42.35%	47.05%	10.60%	0.867	6.43 (0.34)	0.78
2 nd	14XII2015	<i>I-XX/XX/14/45</i>	--.-- %	--.-- %	13.72%	0.450	17.03	2.45 (0.53)
3 rd	29I2016	<i>II-40/45/15/67</i>	40.00%	45.00%	15.00%	0.674	11.43 (2.28)	1.42 (0.23)
4 th	10III2016	<i>II-44/44/11/86</i>	44.34%	44.34%	11.32%	0.859	9.27	1.09 (0.05)
5 th	17III2016	<i>II-39/50/11/82</i>	38.95%	49.90%	11.15%	0.818	13.87	1.69 (0.07)
6 th	01IV2016	<i>II-43/43/14/77</i>	43.14%	43.14%	13.72%	0.770	12.53	1.26 (0.02)
7 th	07IV2016	<i>II-38/48/14/77</i>	38.15%	48.13%	13.72%	0.770	15.37	1.44 (0.07)
8 th	14IV2016	<i>II-43/43/14/65</i>	43.14%	43.14%	13.72%	0.650	20.36	2.13 (0.17)
9 th	21IV2016	<i>II-38/48/14/65</i>	38.15%	48.13%	13.72%	0.650	16.32	1.31

5 COMPUTING THE FRACTURE ENERGY OF CONCRETE

5.1 FIRST APPROACHES AND COMPARISONS. THE APPROPRIATENESS OF THE METHODOLOGY

5.1.1 ABOUT THE TEST STABILITY

One of the first problems to solve at an experimental field is to achieve a correct test performance, in our case this is that the test must be stable, which means that:

- The positioning stage should be done correctly
- The elastic loading must be progressive
- The approach to the peak should be easily visible with a notorious and gradual slope reduction
- Just after the peak the load, the load should be, for some seconds, lower than the peak load, but not so much
- The unloading part, although being a fast phenomenon, does not have to be instantaneous, this means that the system has to be able to catch some points at this stage
- The fast unloading has to be done while displacement continues on advancing or, at least, there should not be a huge step backwards, because it could not be explained only by the existence of noise at the channel. This phenomenon is called *snap-back* and does not have to appear notoriously
- The tail of the curves, the unloading and the progressive opening of the crack have to be gradual
- The specimen should not split completely before the end of the test or, at least, until the last valid register is recorded

Whenever these points are achieved, we can talk about stable three point bend tests for concrete fracture mechanics. The first attempts are explained at Appendix B.1.

The first experimental campaign, 23X2015, confirm the exposed points, which means that the project is feasible with concretes of low strength. The figures of the first test, which was longer than 1 hour and 20 minutes without the total division of the specimen, show the confirmation of this (see Figure 42 and Figure 43).

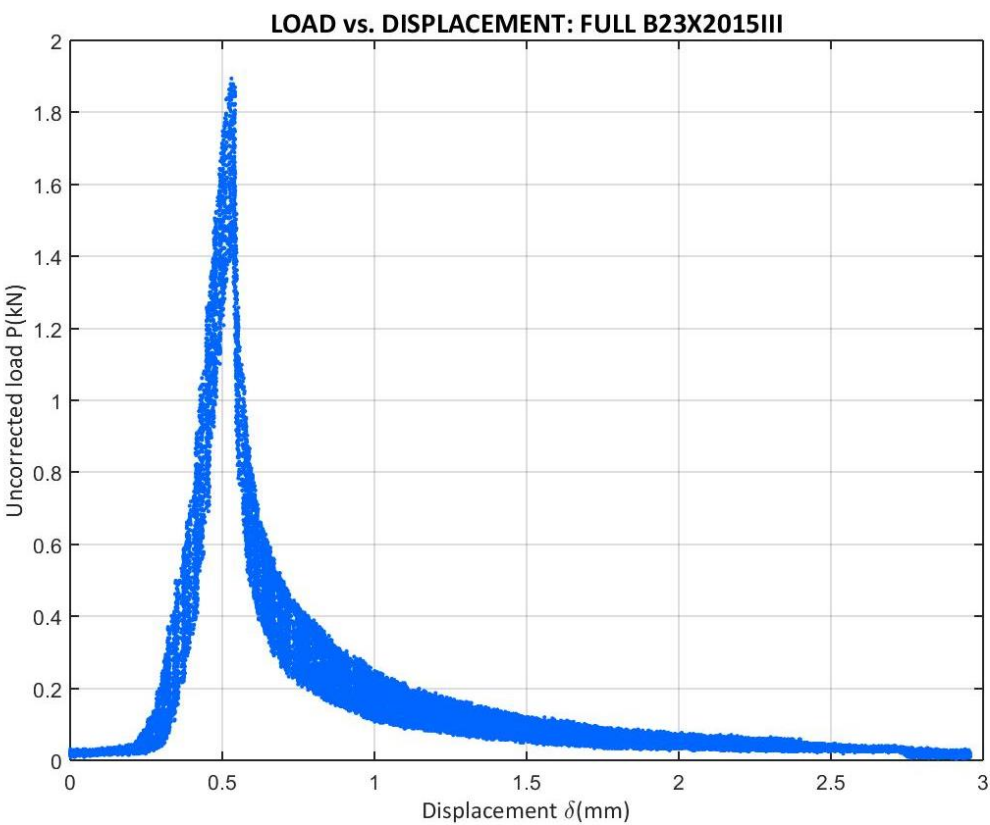


Figure 42: Full experimental Load vs. Displacement curve of the longest test carried out (B23X2015III)

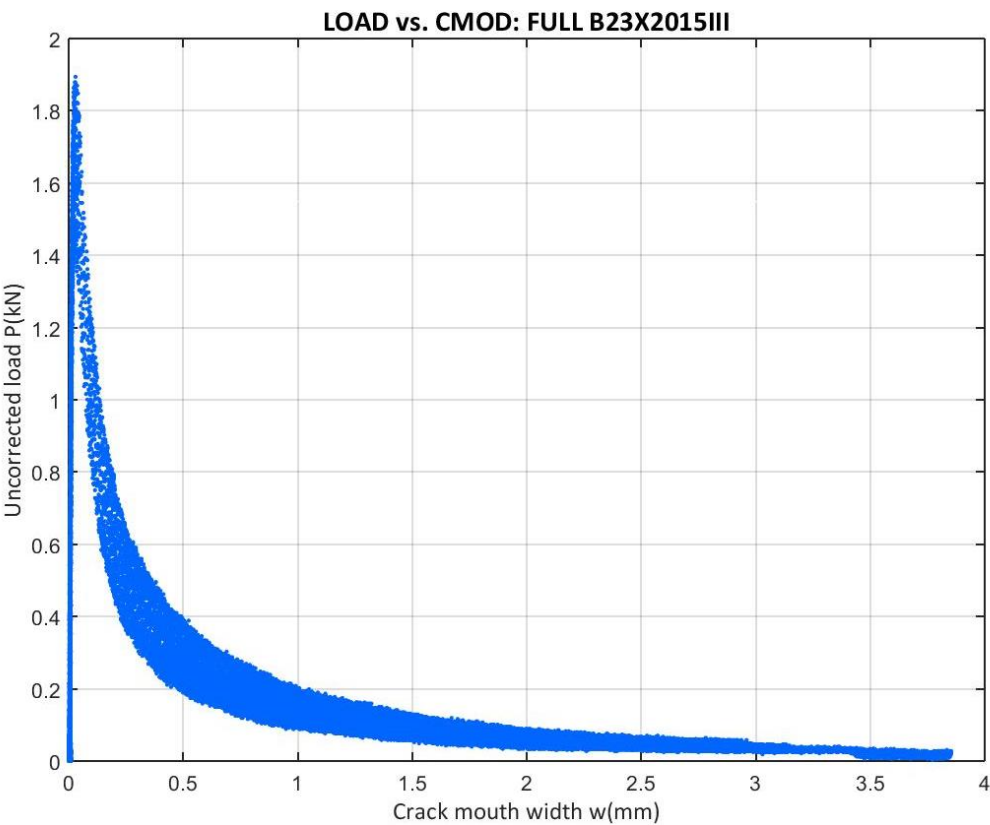


Figure 43: Full experimental Load vs. CMOD curve of the longest test carried out (B23X2015III)

The second campaign was the one with the higher strengths at this project and this meant the possibility that the fracture could have been created suddenly. At the first tests for the 14XII2015 campaign the curves were not completely recorded with an acquisition rate of 10 registers per second (see Figure 44 and Figure 45), but this was solved by changing the acquisition speed from *Normal* to *Fast* and then the curves were registered completely (see Figure 46 and Figure 47).

With this change, the test three point bending test for normal-strength concretes could also be considered stable with the machines and configurations available to us. Nevertheless, we have strict restrictions with the testing machine configuration. These tests can be considered stable, but testing concrete mixtures with even more strength could lead to serious difficulties for the test stability, then this way does not have to be explored yet, without any kind of changes at the testing systems.

For other campaign after 14XII2015, the tests are also stable. The only problem is the presence of relative maxima and minima at the elastic loading stage (see Figure 48). However, this does not mean a huge problem, because, if it is an elastic stage, the same load should represent the same stress, deformation and force distribution at the body. The elastic loading means that points with the same load can be considered equal situations. This is done at the postprocess (see Appendix D and E).

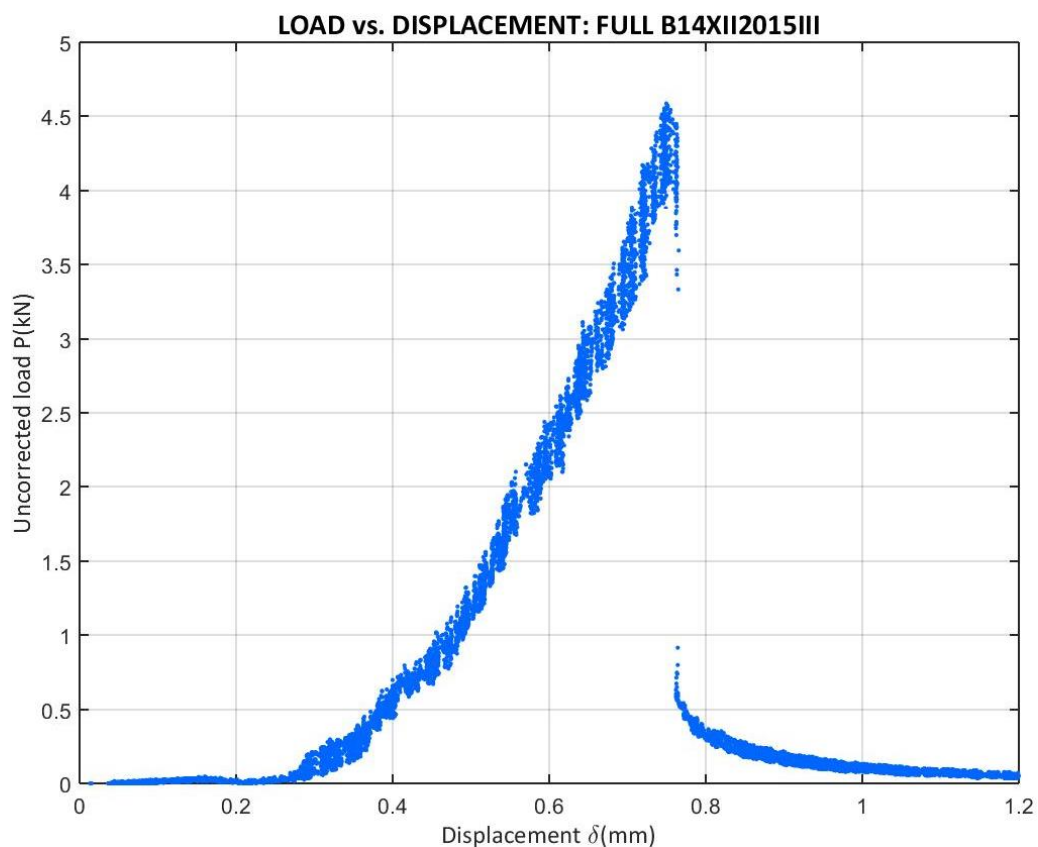


Figure 44: Full experimental Load vs. Displacement curve of the B14XII2015III test

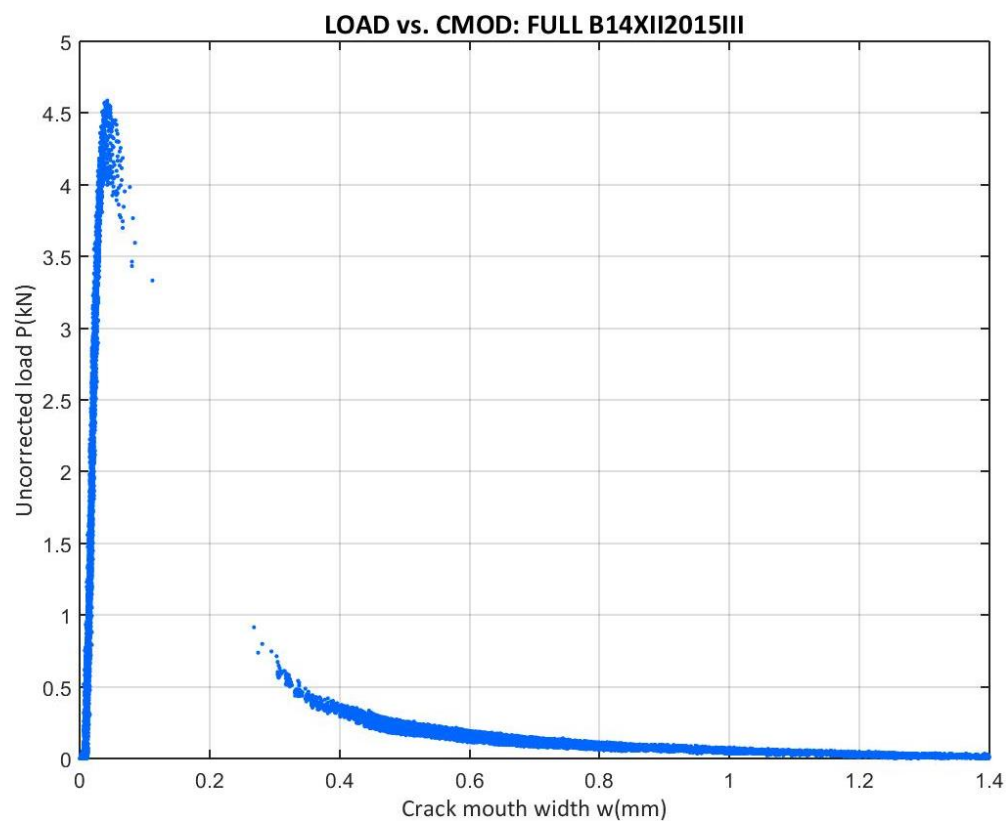


Figure 45: Full experimental Load vs. CMOD curve of the B14XII2015III test

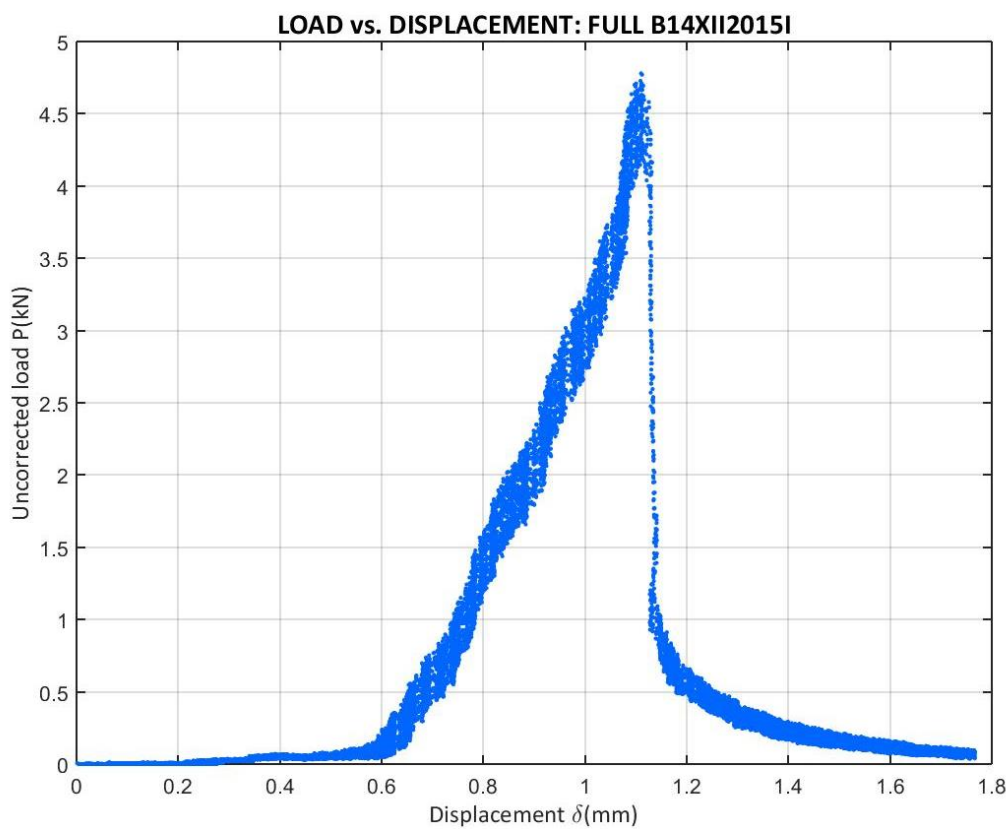


Figure 46: Full experimental Load vs. Displacement curve of the B14XII2015I test

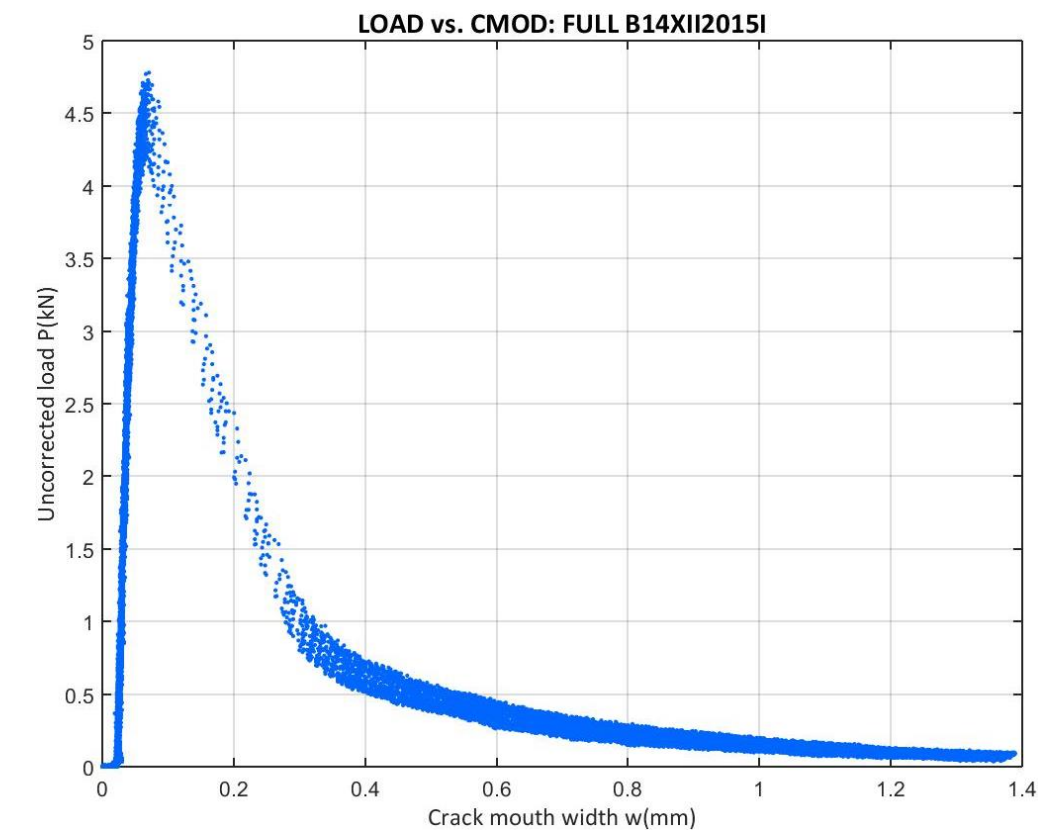


Figure 47: Full experimental Load vs. CMOD curve of the B14XII2015I test

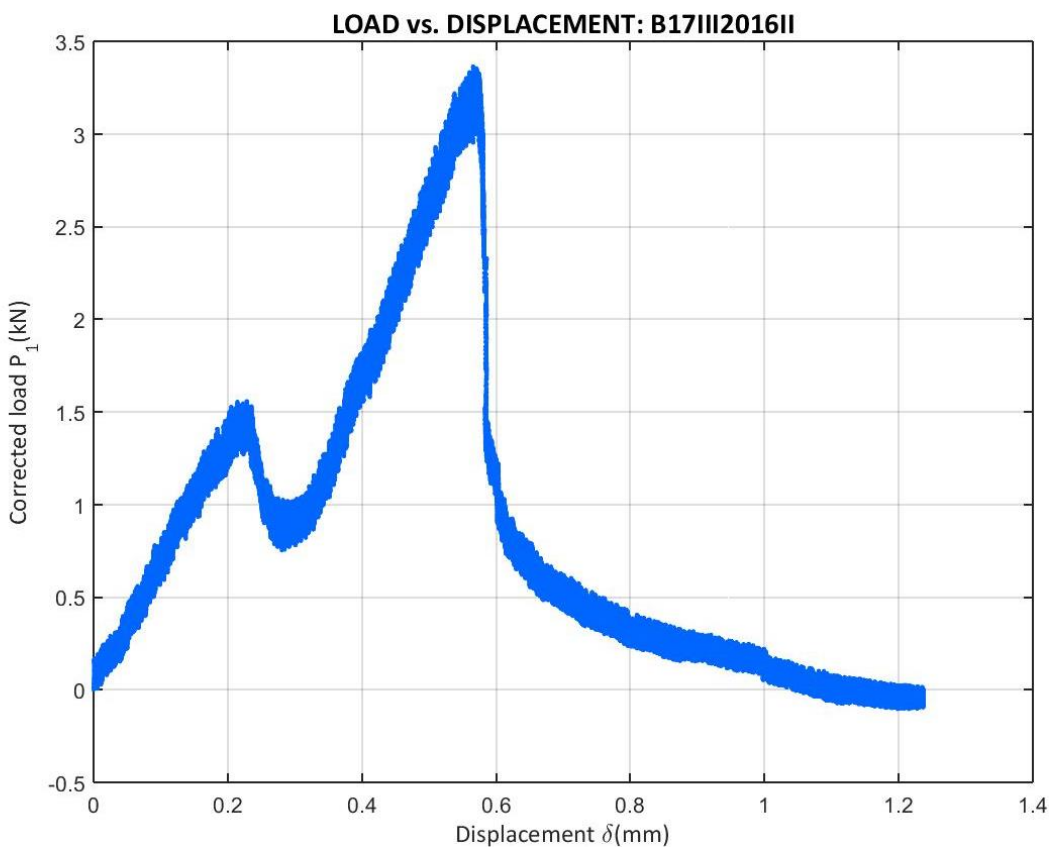


Figure 48: Experimental corrected Load vs. Displacement curve of the B17III2016II test

5.1.2 ABOUT THE RESULTS AND THE ACQUIRED DISPLACEMENT AND LOAD VALUES

Once the test is stable, the next element to analyze is the data registered at the text files reduced with the *StrainSmart 5000*. Three channels are used:

- The load read by the 2.5T load cell
- The displacement of the piston read by the testing machine
- The crack width read by the *COD* gage

All the data acquired for this project can be seen at the Appendices E.X.1, where *X* is any number between 1 and 11, both included. Let us take as a reference the first test: B23X2015III, which registers are visible at Appendix E.3.1 and at Figure 195 for load, Figure 196 for *CMOD* and Figure 197 for displacement. Different stages can be seen:

- The phase of positioning from the beginning until the 5000th register approx.
- The loading and peak arrival phase from the 5000th register until the 8000th register approx.
- The initial unloading until the 10000th register approx.
- The gradual crack opening until the end of the test

These phases exist for every test, although this is only an example.

Now, if one takes a look at the graphs of the registered data for any case, some facts can be seen:

- Displacement records have always and at any phase a high noise, then a filter is needed
- *CMOD* records have always and at any phase minor noise, then, a filter is not necessary
- Load records have different behavior depending on the test phase: the positioning and the end have a little range of load values, but loading and the initial part of the unloading and crack opening have a large range of load values (see Figure 49)

This means that the *CMOD* register can be used the same way as it has been recorded and the piston displacement needs only a filter (*MATLAB* platform has a filter function), but the load values cannot be filtered, because there are phases of low variation in load values, although the registers have high variation at some parts of the test. Then, a solution has to be found.

We can confirm that the *CMOD* register is correct, because it has been checked with the Digital Image Correlation (*DIC*) technique (see Appendix B.2.2) and that the displacement record is the one we need for the G_F calculation, because it has also been checked with some Linear Displacement Transducers (*LDT*) that it is the correct displacement record (see Appendix B.2.1).

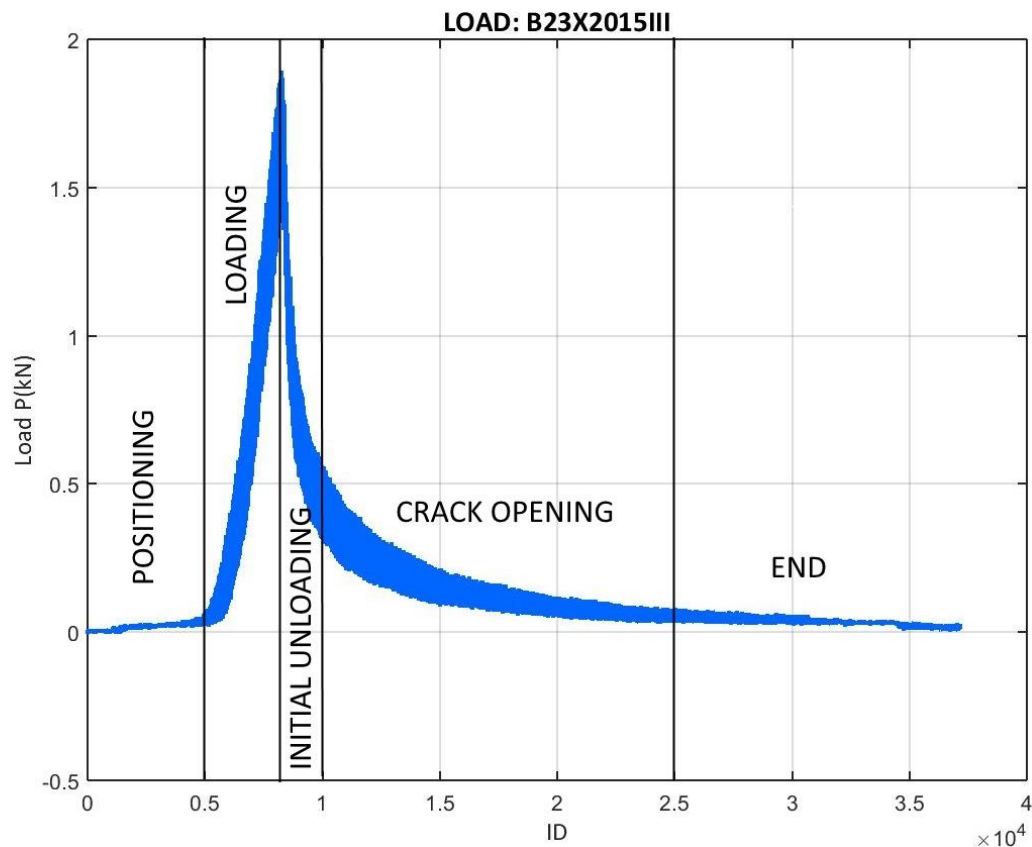


Figure 49: Phases of the test at the load recording

Load is different. Because of that, we make some enlargements at some of the marked stages in order to clarify what is happening.

First, we check the zones of little range at the positioning stage. What we see there is the typical noise of the load cell. If one sees Figure 50 for B23X2015III test (the displacement marked is with the filtered values) and Figure 51 for B23X2015II test (the displacement is not filtered), one can extract that the noise from the load cell, when no important load is applied, has not got a range bigger than 15N and it has a random pattern of appearance.

Now, we will check the other phases: the loading phase at Figure 52, the initial unloading at Figure 53, the crack opening at Figure 54 and the end at Figure 55. Staring these figures, it can be seen that the randomness of the signal is changed for a repetitive pattern similar to a one harmonic signal with ranges of 400N at the loading stage, 300N at the initial unloading and 200-250N at the crack opening phase approximately. The final stage has a range of circa 30N, where it can be seen that the noise has some effect, but at other phases noise is irrelevant against this cyclical load recording.

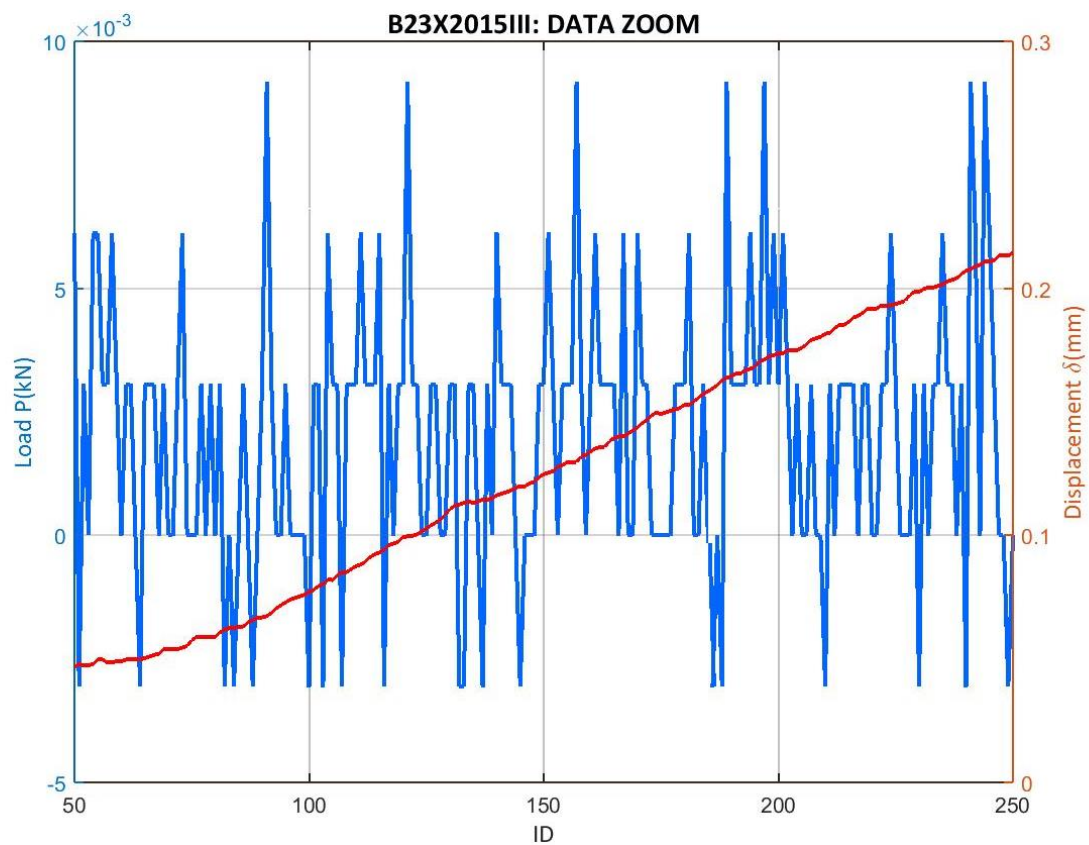


Figure 50: B23X2015III test: load and displacement at the positioning stage. Displacement is filtered

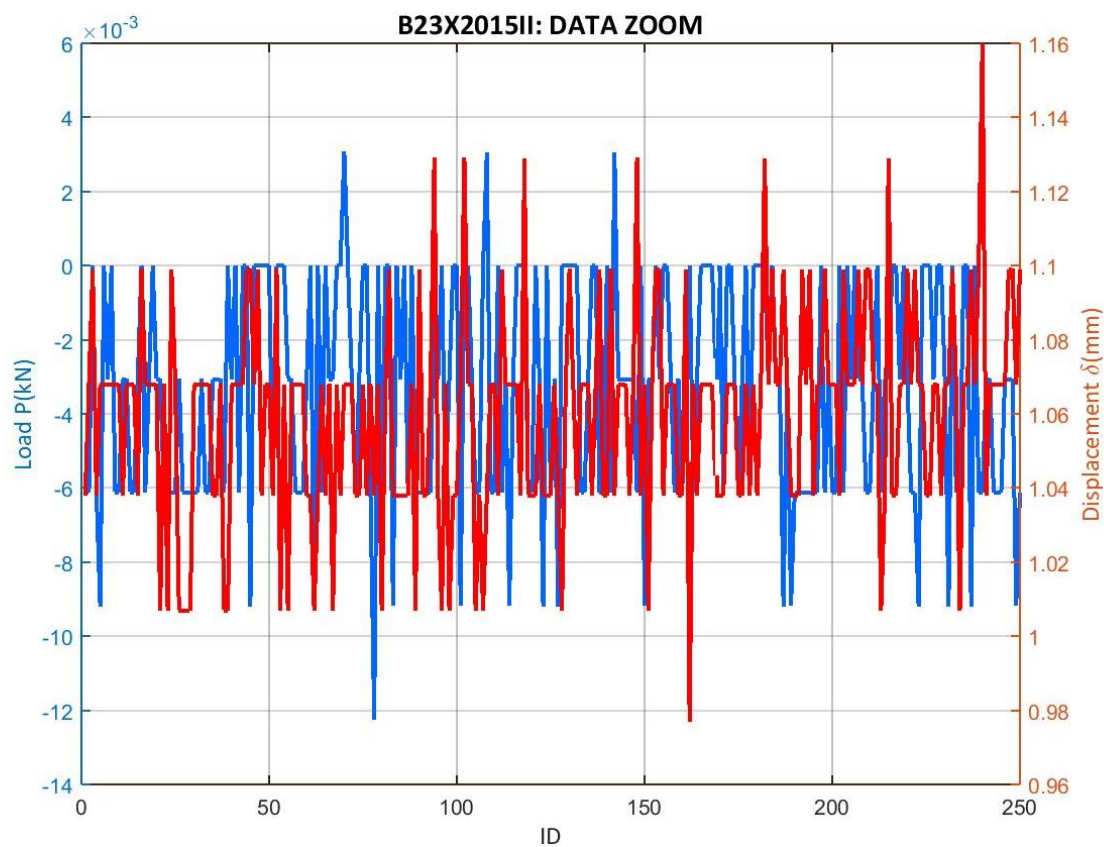


Figure 51: B23X2015II test: load and displacement at the positioning stage. Displacement is not filtered

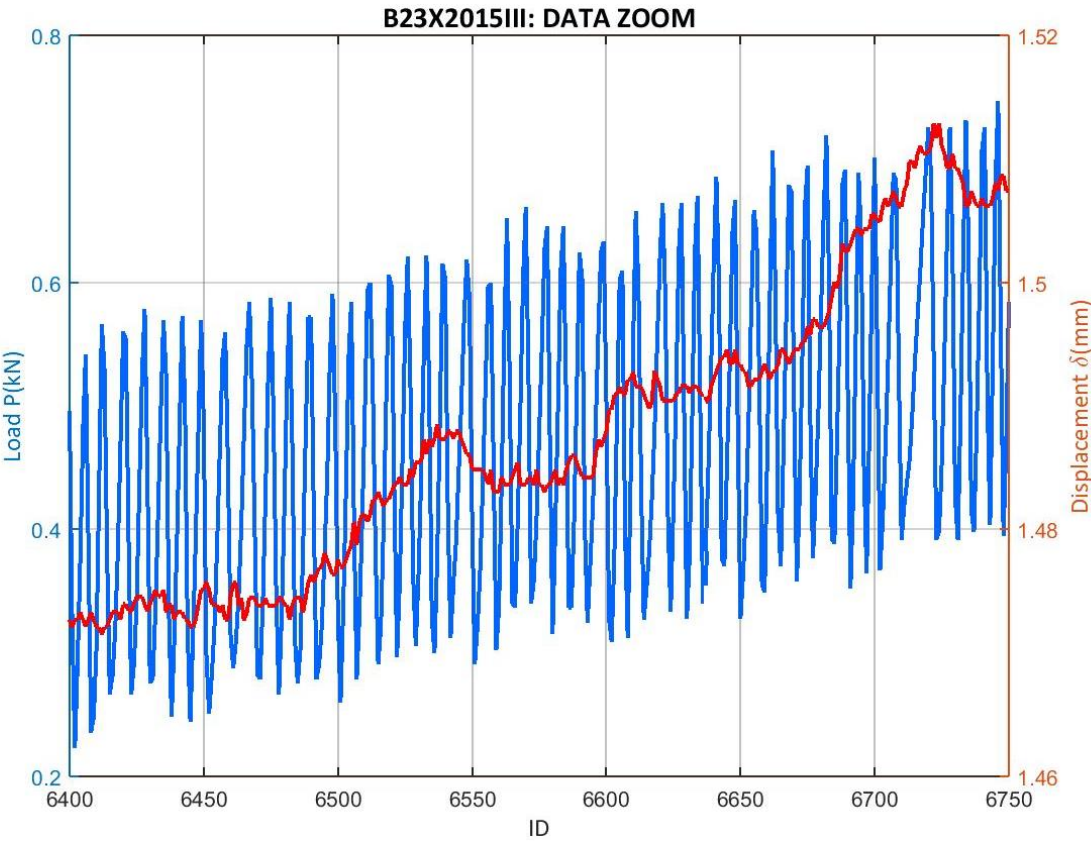


Figure 52: B23X2015III test: load and displacement at the loading stage. Displacement is filtered

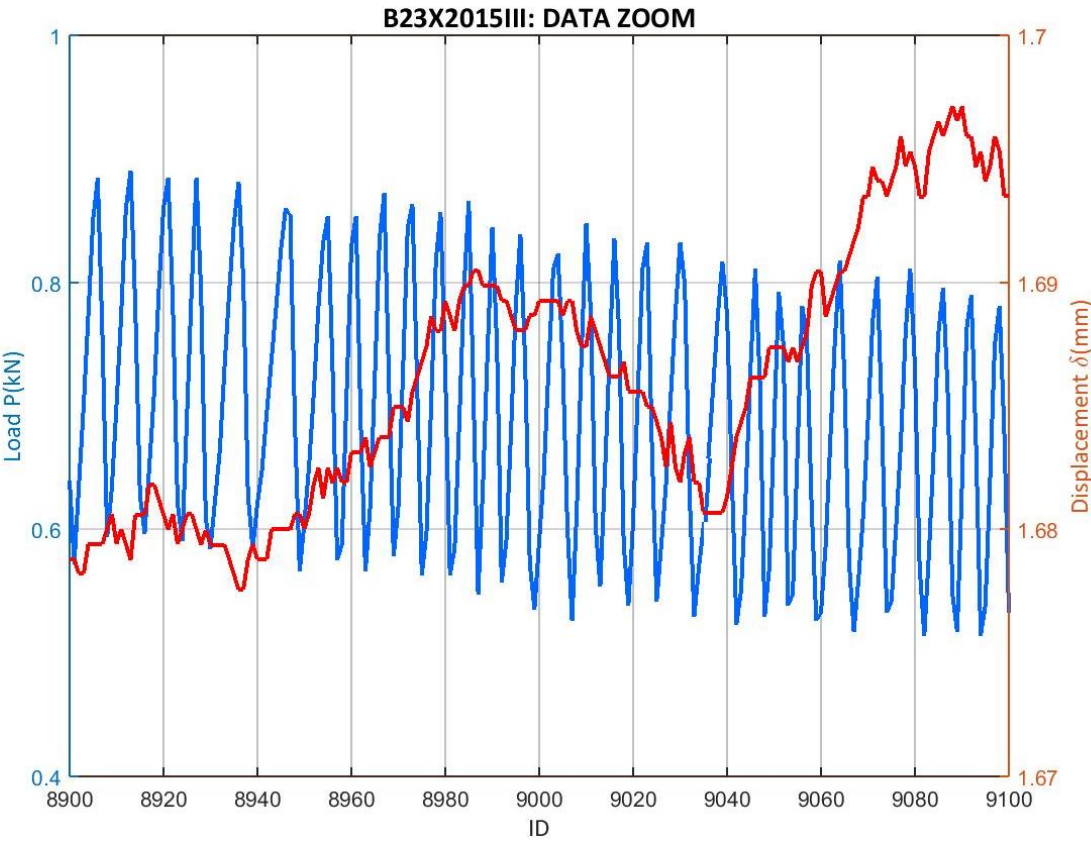


Figure 53: B23X2015III test: load and displacement at the initial unloading stage. Displacement is filtered

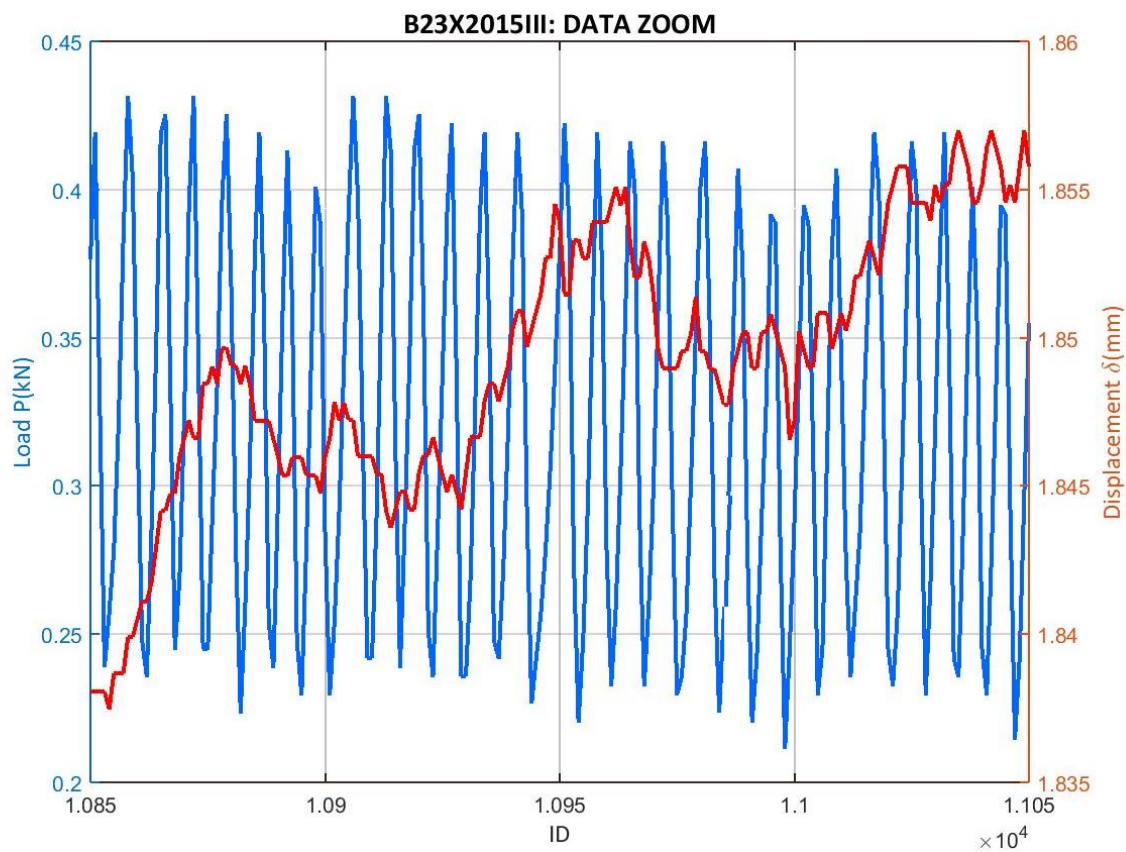


Figure 54: B23X2015III test: load and displacement at the crack opening stage. Displacement is filtered

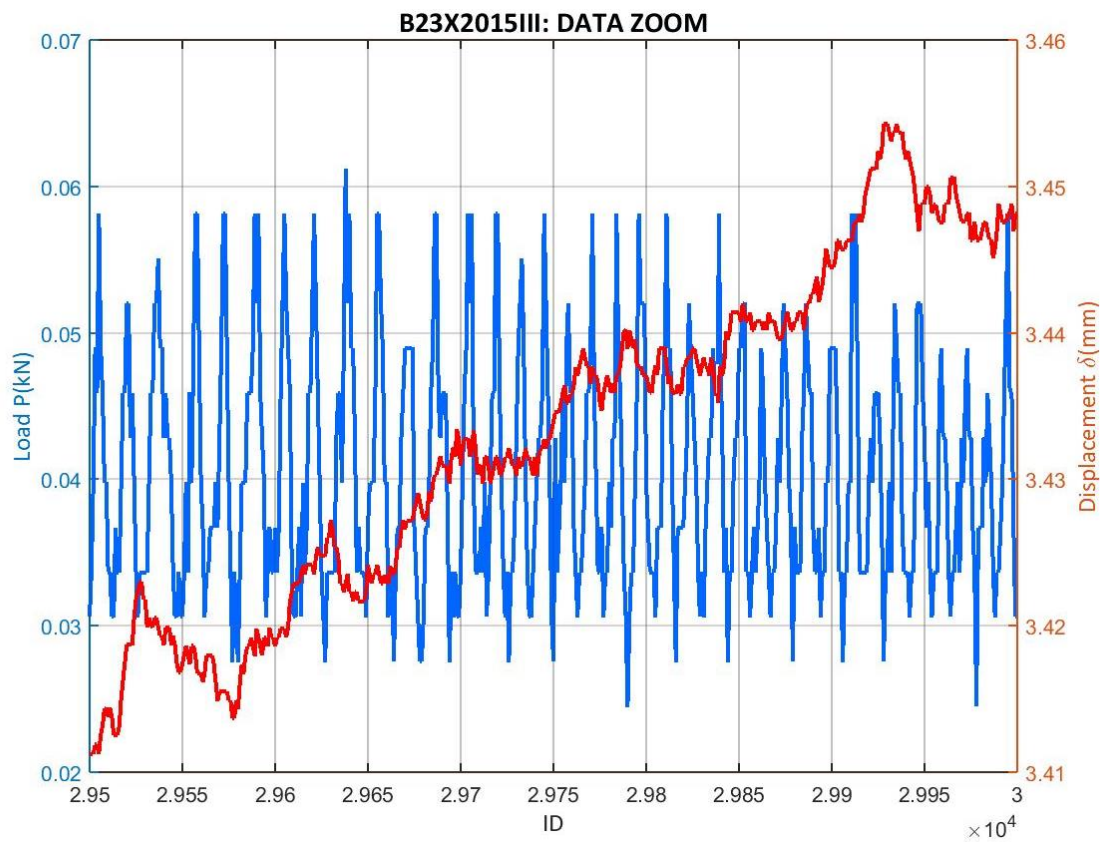


Figure 55: B23X2015III test: load and displacement at the final stage. Displacement is filtered

This difference from a random noise of 15N of amplitude to a harmonic recording of almost 400N of amplitude cannot be a bad operation of the load cell, because it appears at every test, and this increase of the variation of the values and the disappearance of random should have an external explanation, which means that we believe that the load register is true and valid, also because at the control system the load values read on-live are similar with more or less the same variability. This means that the recording is not the problem.

This harmonic behavior 10, 20 or 25 times higher than the noise and without a random behavior can be explained with the hypothesis that a very stiff machine with the most extreme configuration of low speed applied to a not so stiff system (supports and concrete specimen) with noise at the displacement recording create, all together, a situation of little cycles at the test, in order to follow properly the speed introduced. This hypothesis could also explain why the filtered values of displacement show also a behavior of going forward and backwards at some instants.

Then, finally, it has to be considered that the higher values of load at this harmonic recording are achieved and the maximum load is the true peak load for the specimen. This means we have to follow the curves by the upper side and not by the lower bound, the middle or the mean value.

The chosen solution is that once the curves are built, the upper values of a range, set as a step, will be followed (see code at Appendix C.2.12). Doing so, a good new register can be created. This will be done for both planar representations of the $P - \delta$ and $P - w$ curves.

However, this leads to a question that must be treated at future works at this field. The question is if these cyclical loading provokes losses for hysteresis or not and which influence does it have. This fact will not be treated at this project, but it has not to be forgotten.

5.1.3 ABOUT THE CORRECTION METHOD

Finally, once the tests are stable and we know how to process properly the recorded data, the last part of the methodology to check is the correction methods for the G_F calculation. The proposed main correction methodology is based on the tail of the $P - \delta$ curve correction, which is widely used, although there are other corrections, as it is exposed at Chapter 2 and Chapter 3.

For one of the tested campaigns, 29I2016, two different corrections were applied. The correction method and the tests done will be considered valid if the G_F value obtained with the local fracture energy model is inside the range formed by the mean G_F value obtained with the tail correction minus one standard deviation and the same mean value plus one standard deviation. Also if the relative difference of the G_F value from the local fracture energy theory has a difference less than the 10% relative to the G_F mean value obtained with the tail correction.

The results for this campaign and the both methodologies are detailed at Appendix F.3. The most important are:

- Tail correction method, mean G_F (and standard deviation): 145.912J/m² (23.385J/m²)
- Local fracture energy method: 154.359J/m²

Let us see if the selected criteria are achieved: standard deviation criterion at Equation 5.1.1 and Equation 5.1.2 and relative difference criterion at Equation 5.1.3, where G_{Ftail} is the value obtained with the tail correction and G_{Floc} with the local fracture energy theory.

$$Upper\ bound \rightarrow 145.912 + 23.385 = 169.297\ J/m^2 \geq 154.359\ J/m^2 \quad (5.1.1)$$

$$Lower\ bound \rightarrow 145.912 - 23.385 = 122.527\ J/m^2 \leq 154.359\ J/m^2 \quad (5.1.2)$$

$$e = \left| \frac{G_{Ftail} - G_{Floc}}{G_{Ftail}} \right| = \left| \frac{145.912 - 154.359}{145.912} \right| = 5.79\% \leq 10\% \quad (5.1.3)$$

All the criteria selected are accomplished, the value obtained with the alternative methodology is inside the first standard deviation and the relative difference is about 5.79%, less than the 10% and near the 5% of relative difference.

This gives a good point of reference to see that the methodology proposed and applied is correct enough, for the testing ability that we have and the limitations.

5.2 DETERMINATION OF THE SIZE-INDEPENDENT FRACTURE ENERGY OF CONCRETE. RESULTS

The points presented at Chapter 5.1 let us know that we can extract correctly the data for the G_F determination, because the tests are stable (see Chapter 5.1.1), the recorded values are valid (see Chapter 5.1.2) and the methodology is correct (see Chapter 5.1.3). All the curves obtained at this project are shown at Figure 56 for $P - \delta$ curves and at Figure 57 for $P - w$ curves. These two curves are enough for the G_F determination with the $P - \delta$ tail correction method.

Nevertheless, we have to remember that we have the risk that the G_F values obtained at this project can be slightly higher than the same values obtained with the same procedure in other projects or studies, because of the possibility of the influence of hysteresis with our testing system and setup (see Chapter 5.1.2). However, if all tests are done the same way, comparisons and variability tendencies of G_F can be valid, because these events and losses are similar with the same machine and similar stiffness of the specimens.

Considering all these facts, the results of the tests done in order to find the fracture energy of concrete (see the test list at Chapter 4.1 and the setup at Chapter 4.2) are given at Table 47, with the two campaign names, the fracture work, the tail work for the $P - \delta$ tail correction and the mean G_F , alongside with the extreme values for G_F of the specimens for every campaign.

Table 47: Fracture work, tail work and fracture energy of concrete. Standard deviation in brackets

CAMPAIGN		W_f (mJ)	W_{tail} (mJ)	MIN G_F	G_F (J/m ²)	MAX G_F
23X2015	<i>II-42/47/11/87</i>	359.9 (59.9)	208.6 (51.2)	65.2	81.9 (11.6)	89.9
14XII2015	<i>I-XX/XX/14/45</i>	927.6 (232.4)	98.0 (53.4)	89.6	146.1 (35.6)	207.9
29I2016	<i>II-40/45/15/67</i>	807.0 (162.0)	207.0 (54.0)	113.1	145.9 (23.4)	168.5
10III2016	<i>II-44/44/11/86</i>	455.7 (97.7)	188.4 (66.7)	71.3	93.4 (22.3)	123.8
17III2016	<i>II-39/50/11/82</i>	830.2 (117.1)	278.2 (76.1)	133.2	155.9 (17.9)	175.9
01IV2016	<i>II-43/43/14/77</i>	748.8 (33.2)	195.1 (37.6)	129.9	134.7 (8.5)	147.4
07IV2016	<i>II-38/48/14/77</i>	883.7 (92.4)	268.8 (73.6)	150.7	164.3 (10.1)	174.9
14IV2016	<i>II-43/43/14/65</i>	1224.9 (119.9)	280.7 (65.2)	182.9	214.2 (23.2)	237.0
21IV2016	<i>II-38/48/14/65</i>	782.9 (201.3)	239.5 (82.9)	113.2	145.8 (34.7)	188.6

More information about the process after the tests can be seen at Appendix D and the results for all specimens and campaigns at Appendix E for all the figures and Appendix F for all numerical results.

After finding the results for G_F , the next step is to analyze the variability of this variable with the variation of other parameters connected to a concrete type. These parameters can be for composition, such as sand, aggregate, cement or water proportion or type; or mechanical properties, for example, the compressive or tensile strength. All these parameters will be analyzed.

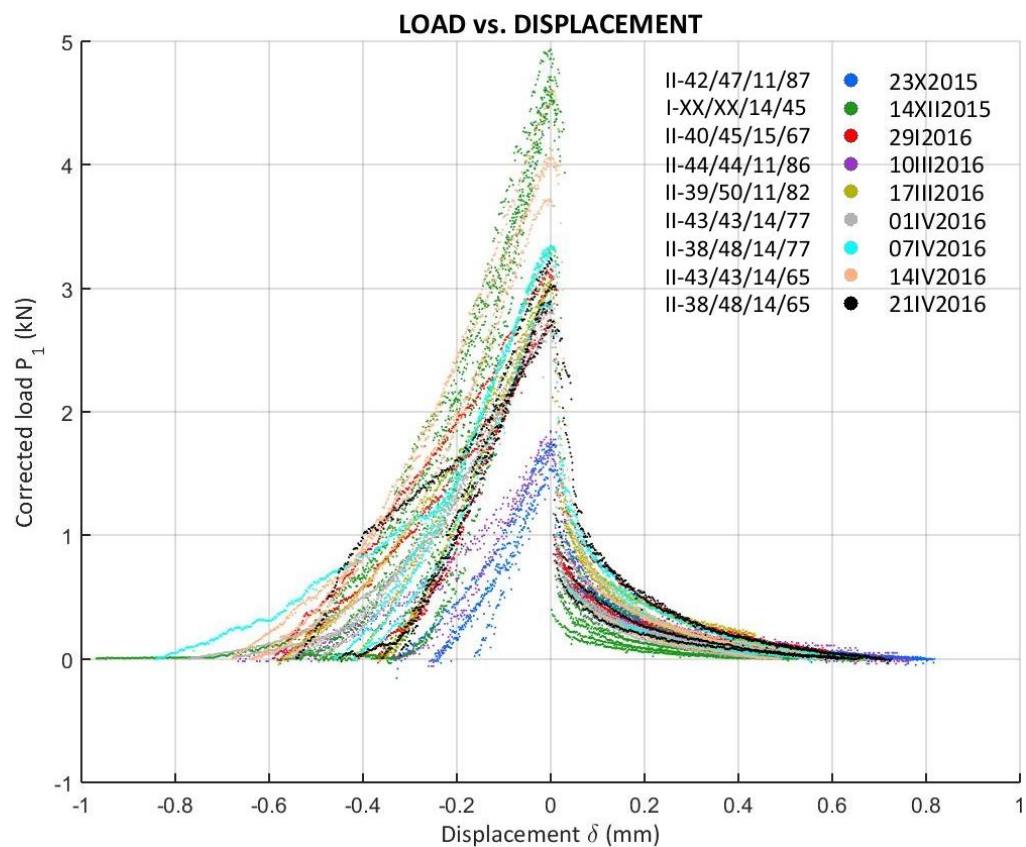


Figure 56: Corrected load vs. Displacement for the entire project (peak displacement zero)

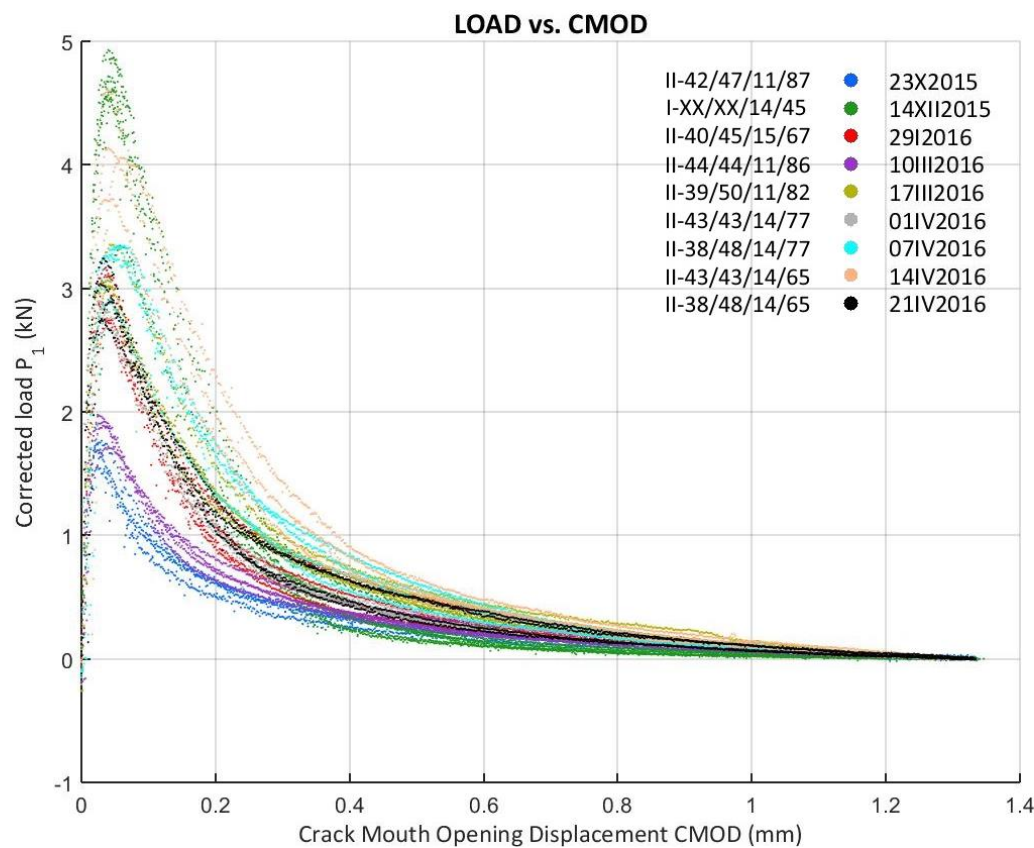


Figure 57: Corrected load vs. CMOD for the entire project

5.2.1 INFLUENCE OF THE SAND PROPORTION

The first parameter of the material composition is the sand proportion. The Figure 58 shows the behavior of G_F with respect to the percentage of sand, size from 0 to 2mm, in the mixture for 8 of the 9 campaigns. Campaign 14XII2015 is not in the list, because the sand proportion is unknown.

This makes that all 8 campaigns are compared with the same type of aggregate, the same maximum aggregate size and the same cement type, but different proportions of the four materials.

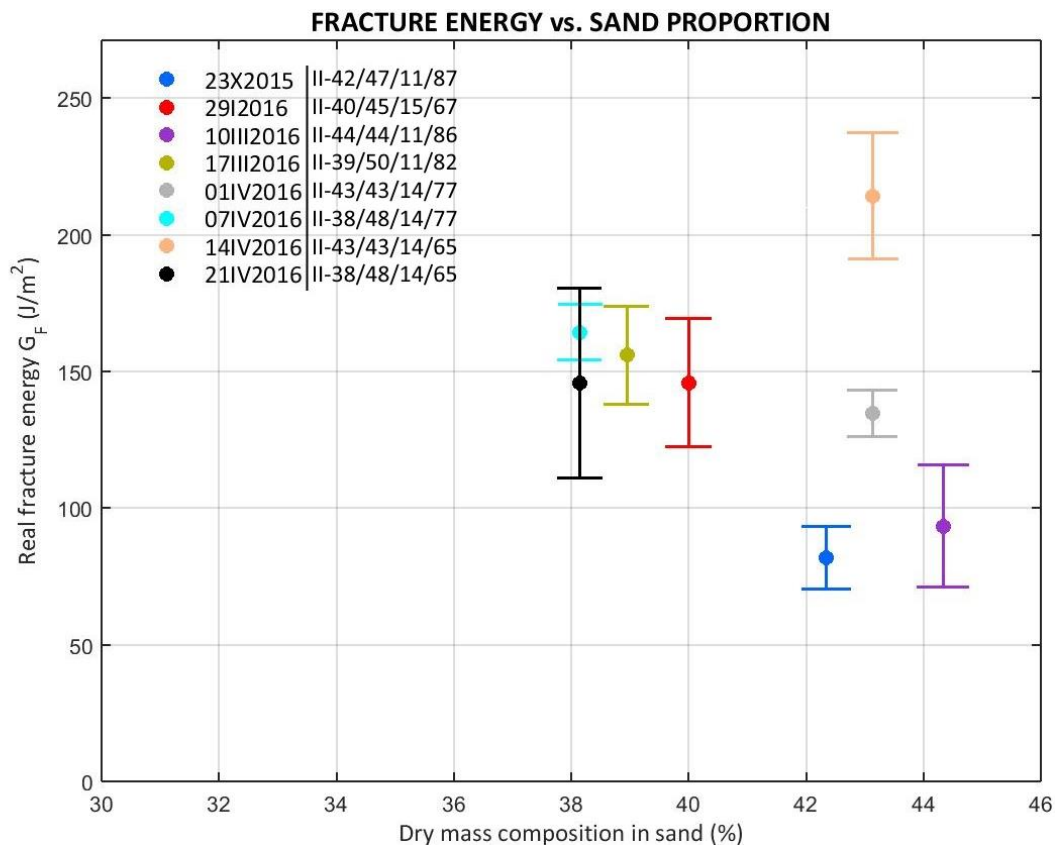


Figure 58: Fracture energy vs. Sand 0-2 proportion

According to Figure 58, it seems that a lower percentage in sand usually provokes higher values of G_F , although this is not fulfilled always.

Let us see some of the last campaigns. Campaigns 10III2016 and 17III2016 have the same cement proportion, but 10III2016 has the same composition in sand and aggregate and 17III2016 has more aggregate than sand and the second of them has a higher value of G_F . This also happens with campaigns 01IV2016 and 07IV2016 and, here, the water to cement ratio is also exactly the same. However, it seems that campaigns 14IV2016 and 21IV2016 contradict this.

5.2.2 INFLUENCE OF THE AGGREGATE PROPORTION

The second parameter of interest is the aggregate proportion. At Figure 59, G_F is shown with respect to the aggregate proportion, size from 5 to 10mm, for 8 of the 9 campaigns, because, for 14XII2016, the aggregate composition is unknown. This makes that the comparison is done with concretes with the same sand, aggregate and cement type and the same maximum aggregate size.

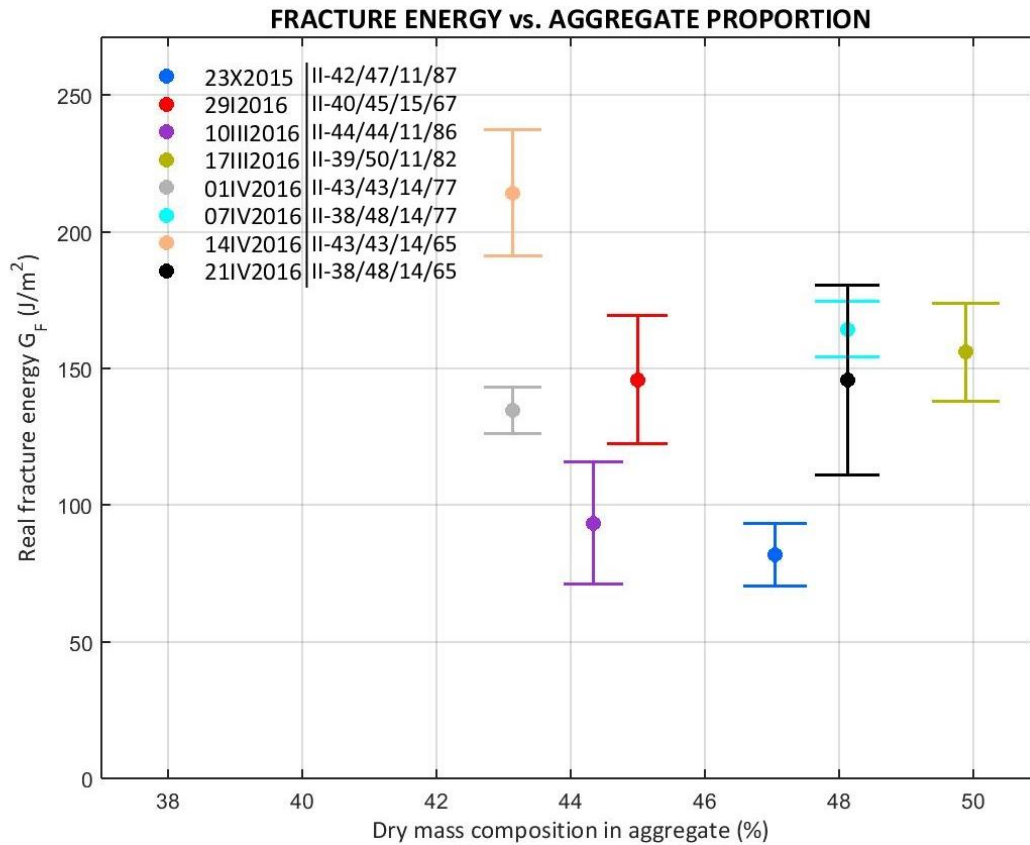


Figure 59: Fracture energy vs. Aggregate 5-10 proportion

The aggregate proportion seems not to have any direct, or easily visible, effect on G_F , according to Figure 59. Nevertheless, we should not forget a comment done at Chapter 5.2.1, which is that with the same cement proportion and water to cement ratio, changing both sand and aggregate proportion from equal to more aggregate than sand, the fracture energy registered was higher with this change for two events (10III2016 and 17III2016; 01IV2016 and 07IV2016) of the three that there are at this project, although a visible direct connection of the aggregate proportion variation and G_F variability is not seen.

5.2.3 INFLUENCE OF THE AGGREGATE SIZE

The third parameter to analyze is the maximum aggregate size. A comparative graph is given at Figure 60 for the 9 campaigns, although only one campaign, 14XII2015, has a different maximum aggregate size.

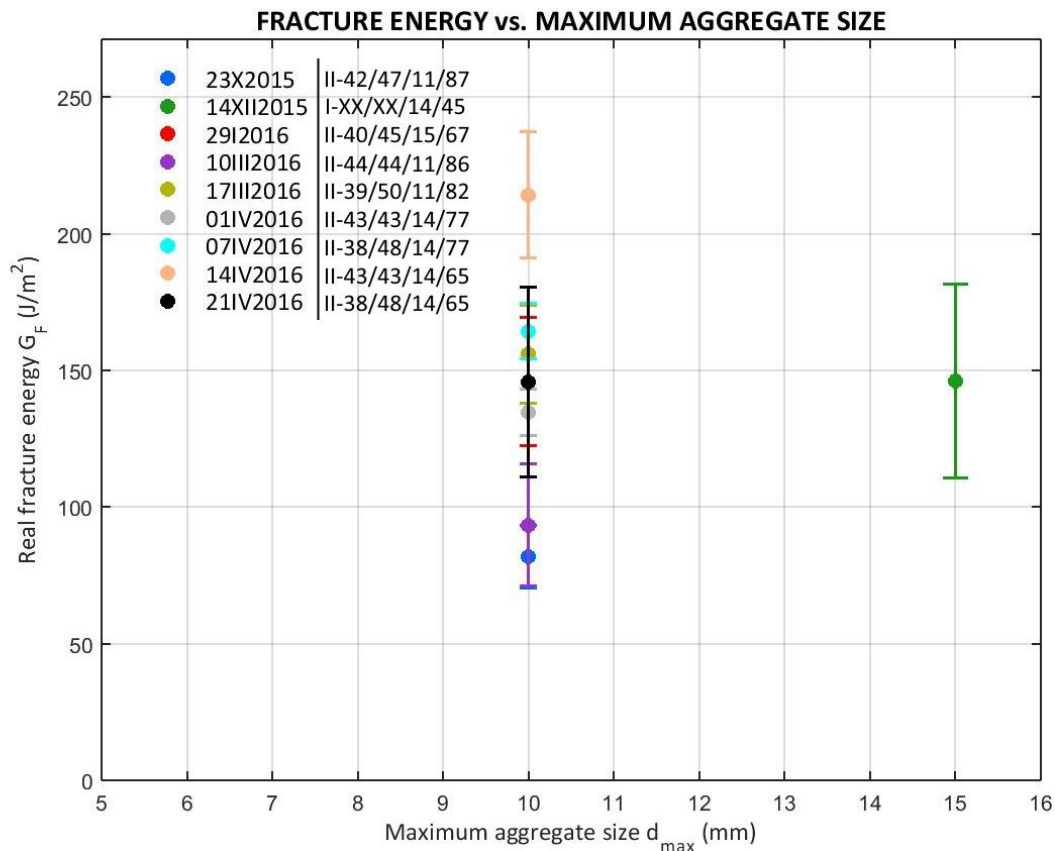


Figure 60: Fracture energy vs. Maximum aggregate size

This figure shows only two facts: first, that this parameter was not one of the most important parameters planned to be studied at this project and, second, that only one experience with different maximum aggregate size and eight different fracture energies with the same maximum aggregate size makes impossible to see any variability pattern.

The results are not conclusive, because of the lack of testing for this parameter. Nothing else can be said by now.

5.2.4 INFLUENCE OF THE CEMENT PROPORTION

The fourth parameter to study is the composition in cement. In order to make a proper comparison, only campaigns with the same type of cement will be compared. This provokes that one campaign cannot be directly compared, which is 14XII2015. At Figure 61, the comparative graph is given.

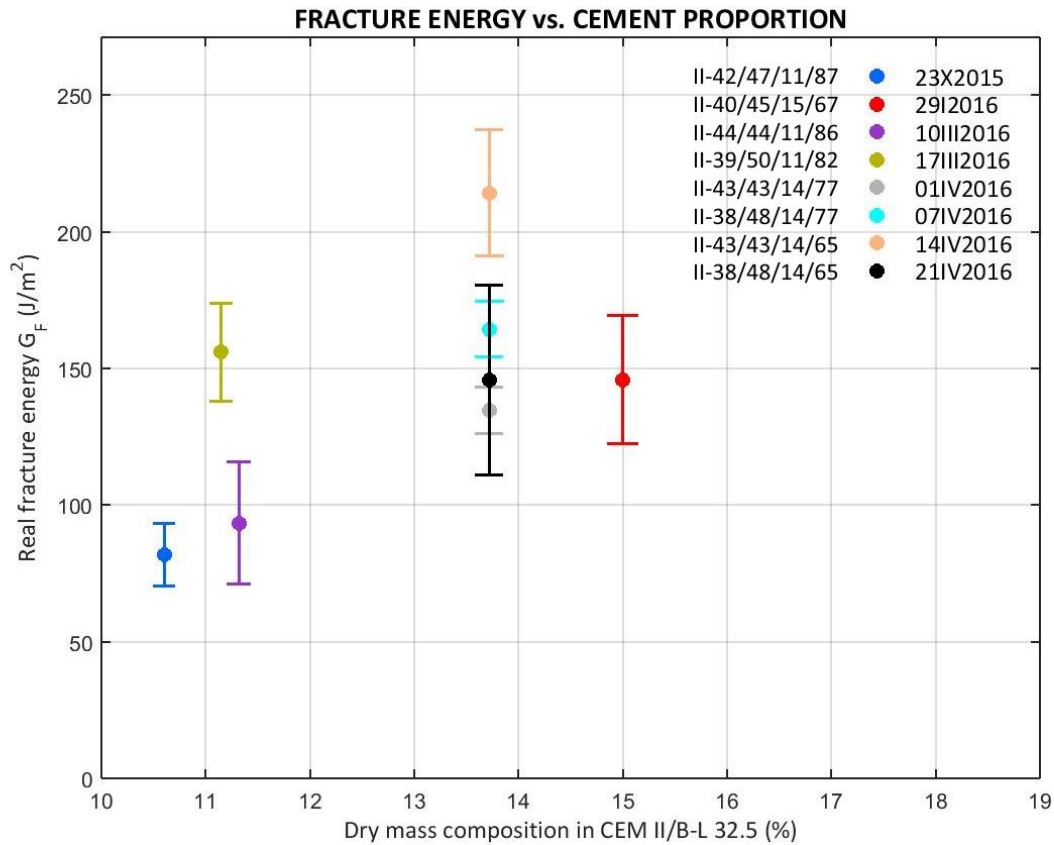


Figure 61: Fracture energy vs. Cement II/B-L 32.5N proportion

Observing the figure, it seems that a higher content in CEM II 32.5N can provoke higher values for the fracture energy, although not always, which means that this is not the only parameter connected to G_F . However, a direct, but not definitive or unique, connection can be seen.

Other types of tendencies are difficult to see, because the campaigns prepared to be compared are the one with the same proportion in sand and aggregate and changing the cement ratio. These are campaign 10III2016 with 01IV2016 and 14IV2016 for one side and 17III2016 with 07IV2016 and 21IV2016 for the other. The difficulty is because of the difference of the water content and, even considering minor influence of that, for one series the lower content in concrete and the same proportion in sand and aggregate leads to lower values of G_F (10III2016 respect 01IV2016 and 14IV2016), but the other shows that a higher content in concrete leads to both higher and lower values of G_F , although the difference between the mean values is less important than the other case.

5.2.5 INFLUENCE OF THE WATER TO CEMENT RATIO

The last parameter for the concrete composition is the water content. This can be measured with the water to cement ratio and, for the 9 campaigns, G_F is given for all ratios at Figure 62.

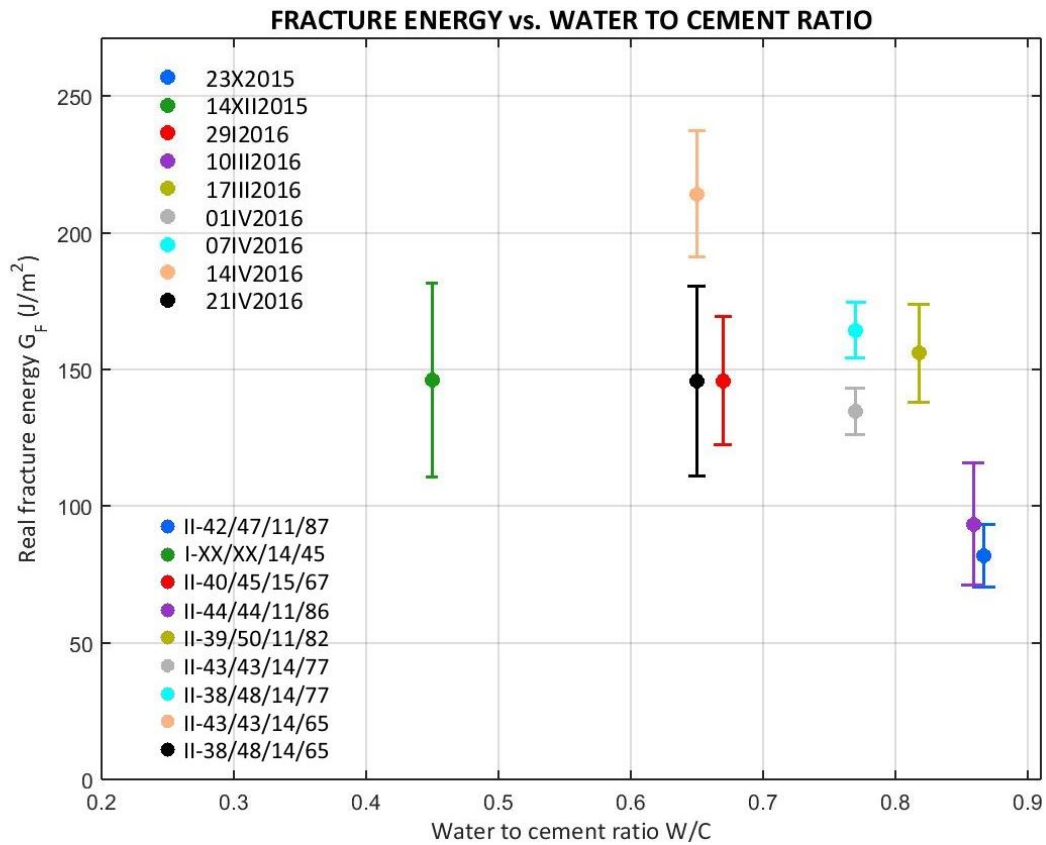


Figure 62: Fracture energy vs. Water to cement ratio

Apparently, according to the figure, lower contents in water respect the cement content help to achieve higher values of G_F , although it is evidently not the only parameter with direct influence, but it seems to have some.

Let us see it with more detail with campaigns 10III2016 (even though it has a lower content in cement), 01IV2016 and 14IV2016. These campaigns have equal proportion in sand and aggregate and from the first to the last one, the water to cement ratio decreases, while G_F increases. It is not sure, however, the part of effect of the lower cement content of 10III2016. Nevertheless, campaigns 07IV2016 and 21IV2016 do not show this clearly, because they contradict the statement that G_F increases when w/c decreases, although the difference is not so important than the other case.

More events should have been studied, but this parameter is difficult to be fixed during casting, because the lack of water at some planned compositions or the lack of fluidity of them.

5.2.6 INFLUENCE OF THE COMPRESSIVE STRENGTH

The first parameter to analyze for the mechanical properties is the compressive strength, a value that is used to classify the concrete classes. The comparative graph is given at Figure 63 for all campaigns.

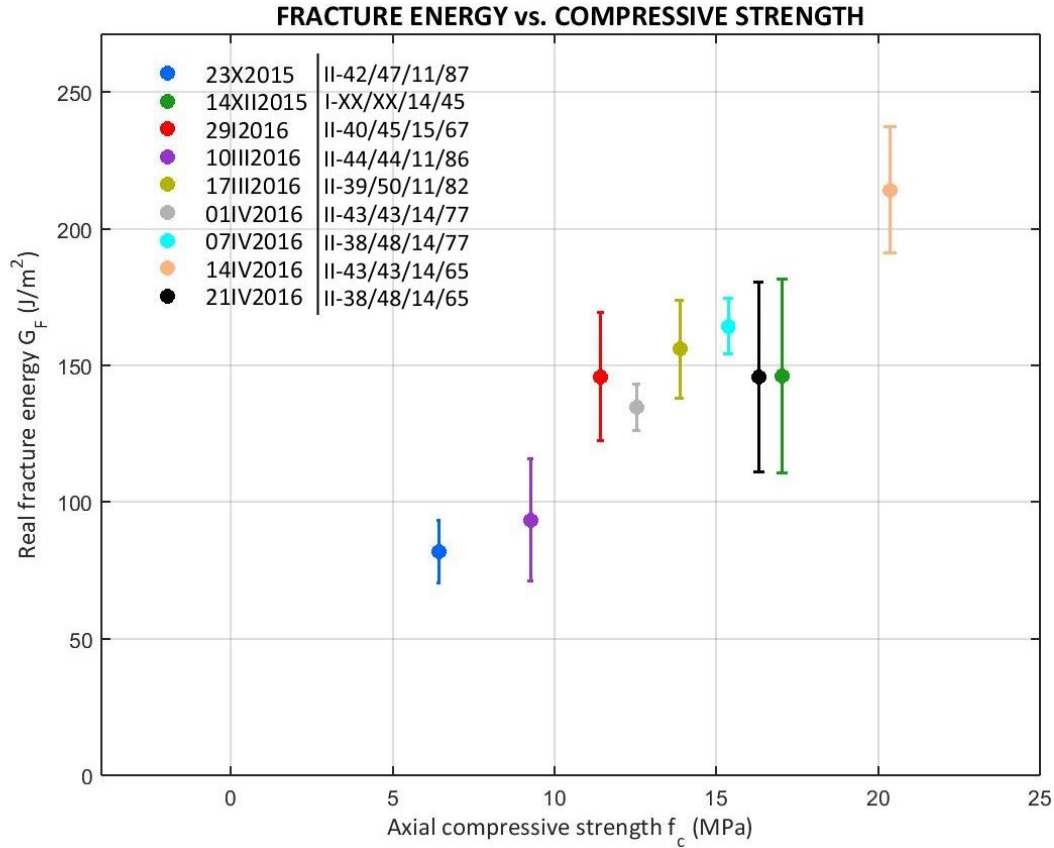


Figure 63: Fracture energy vs. Compressive strength

Here, it is easy to see a pattern: a higher value of f_c seems to lead clearly to higher values of G_F , with a really close connection between the two properties.

The problem now is if there is a model that can be fitted to predict G_F values with our results. Furthermore, there are other problems, which is the fact that we expect our obtained values to be higher than others, due to the possible and considerable effect of hysteresis at our tests, which will provoke our model to be invalid for other testing machines and systems different of the one used.

Nevertheless, we can affirm that for low values of f_c (for example, lower than 12MPa), G_F increases faster with the increase of f_c than with higher values of f_c . At the figure, a zone with relative little variability can be seen after 12MPa, even though a high variation appears with campaign 14IV2016, but it is only one single event, then it is possible that this campaign does not has to show such a high difference of G_F .

5.2.7 INFLUENCE OF THE TENSILE STRENGTH

The second mechanical property to analyze is the tensile strength. A comparative graph for all campaigns is shown at Figure 64.

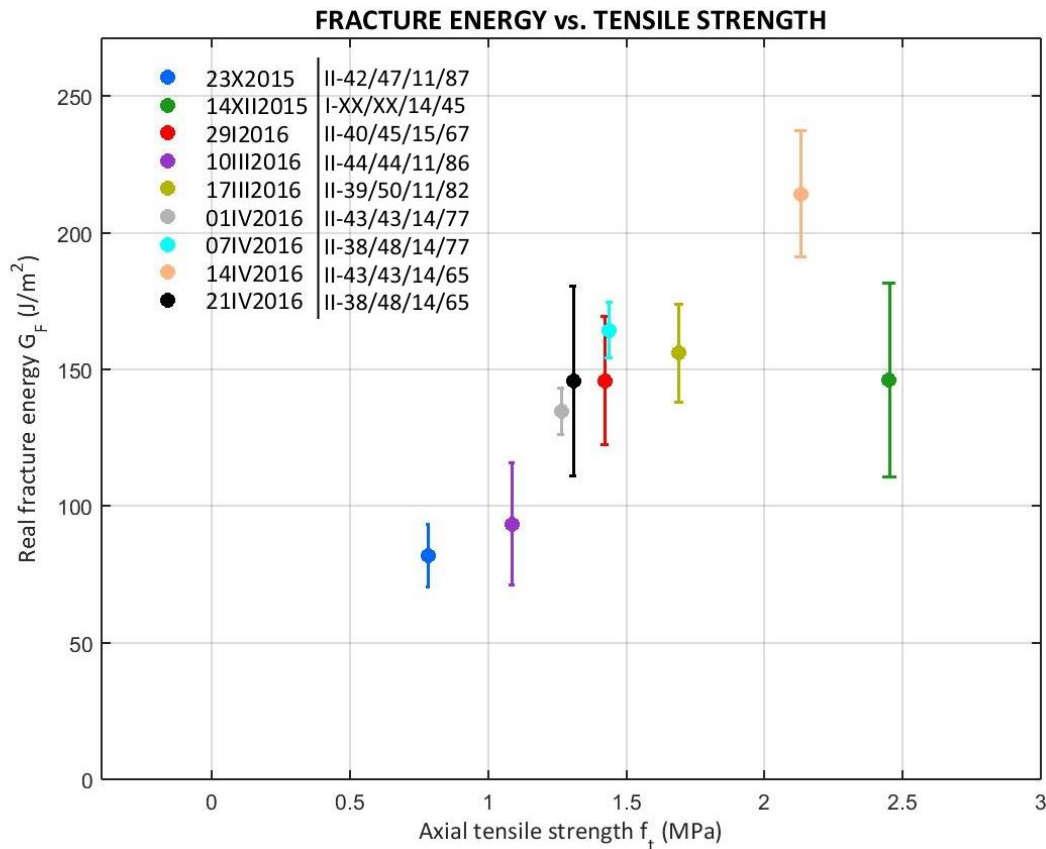


Figure 64: Fracture energy vs. Tensile strength

As with f_c , it seems clearly that f_t has also a close connection with G_F , giving higher values of G_F with a higher tensile strength. The pattern is also similar, high variability with low values and a slightly, but visible, variability while it increases, considering that the value of campaign 14IV2016 might be higher than expected.

A tendency is visible, but the fitting is also not done, because there can be the possibility that our G_F values can give previsions for internal use only. However, if one would have to choose a fitting curve, for f_c or for f_t , with high variability at low values and less variability while increasing the abscissa value, the first options should be root-based functions, style: $a+bx^c$, similar or variations.

A final remark, the campaign 14XII2015 shows a different behavior than the other campaigns. It is the only with a different type of cement. This provokes the question of if it is a mistake, an isolated event or if the type of cement has any type of connection with the variability of G_F with f_t .

5.3 BUILDING THE SOFTENING CURVE OF CONCRETE WITH A BILINEAR APPROXIMATION. RESULTS

The last element whose determination is of interest is the softening curve. At Chapter 3.3.1, a methodology for finding an approximation is detailed. The results of the parameters of the softening curve are given at Table 48 and they help to build the softening curve approximation for all the campaigns. This function is the constitutive equation which rules when fracture appears and it can be used in mechanical analysis. A graph with all softening curve approximations is given at Figure 65.

Table 48: Results of the bilinear approximation of the softening curve

CAMPAIGN	w_G (μm)	w_k (μm)	w_1 (μm)	w_{char} (μm)	w_c (μm)	f_t (MPa)	σ_k (MPa)
23X2015 II-42/47/11/87	177.8	77.5	94.8	104.8	723.5	0.78	0.143
14XII2015 I-XX/XX/14/45	50.9	44.6	78.5	59.6	172.6	2.45	1.060
29I2016 II-40/45/15/67	111.3	97.5	128.1	102.6	450.7	1.42	0.340
10III2016 II-44/44/11/86	158.6	23.3	32.7	86.0	516.6	1.09	0.313
17III2016 II-39/50/11/82	127.3	45.1	65.6	92.2	445.8	1.69	0.528
01IV2016 II-43/43/14/77	112.5	53.0	91.7	106.5	378.9	1.26	0.534
07IV2016 II-38/48/14/77	122.4	102.6	139.2	114.3	479.7	1.44	0.378
14IV2016 II-43/43/14/65	104.9	47.5	84.7	100.6	349.8	2.13	0.936
21IV2016 II-38/48/14/65	118.3	103.4	138.8	111.5	469.0	1.31	0.334

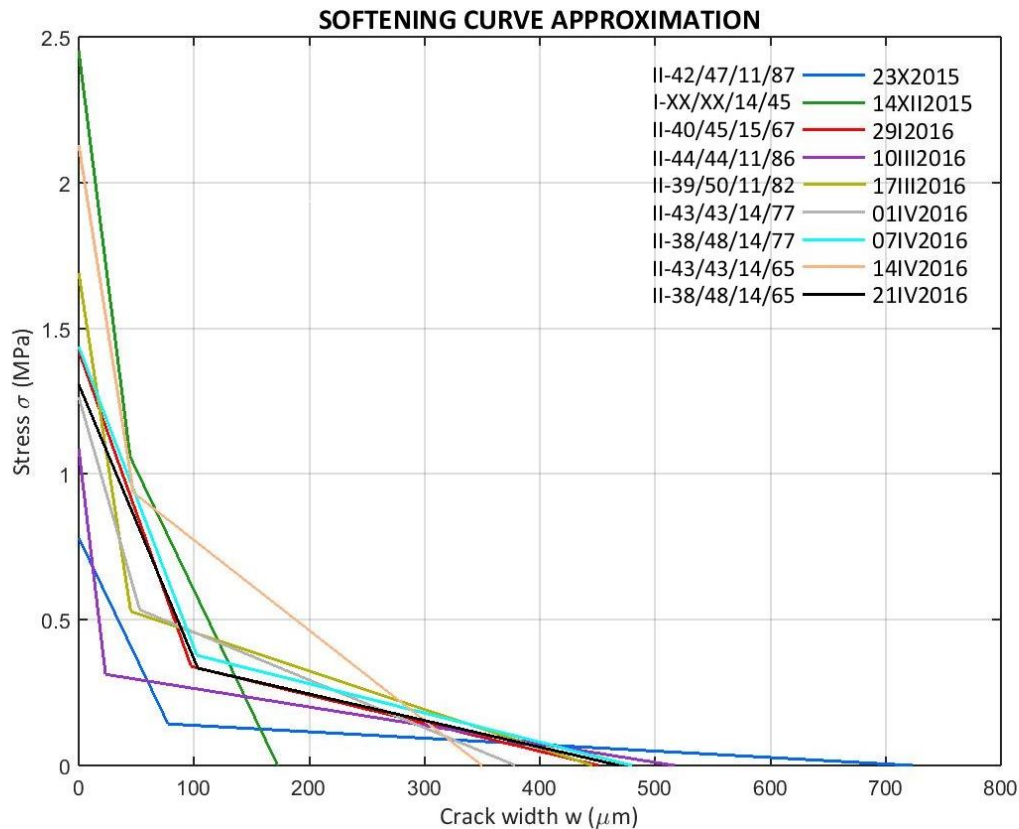


Figure 65: Softening curve bilinear approximation of all campaigns

The first fact which is seen at the figure is that the two campaigns with lower G_F have higher values of the critical crack width w_c . This is for campaigns 23X2015 and 10III2016. However, this can also be connected with f_c or f_t , because these two campaigns have the lowest values of f_c and f_t and the highest values of f_c and f_t for campaigns 14XII2016 and 14IV2016 shows the lowest values of w_c , while campaign 14XII2015 has not one of the highest G_F mean values, although we have to remember that the cement of 14XII2015 is CEM I 52.5R and the rest had CEM II 32.5N.

Then, there could be several parameters that can affect at w_c .

The curves are not shown in their reduced form, so trying to make a comparison is difficult. Nevertheless, there are 3 campaigns, 29I2016, 07IV2016 and 21IV2016, whose bilinear approximations behave similar, with a kink point quite close and similar w_c .

Let us create the reduced form of the softening curve in order they can be compared and a global bilinear approximation will be proposed using the mean values of the reduced kink point and the reduced crack width, considering it can be a good approximation when the area enclosed is near 1.

The reduced values which are used to build the reduced softening curves are written at Table 49 and the comparative graph is attached at Figure 66.

Table 49: Results of the bilinear approximation of the reduced softening curve

CAMPAIGN		\hat{w}_k (μm)	\hat{w}_1 (μm)	\hat{w}_c (μm)	$\hat{\sigma}_k$ (MPa)
23X2015	<i>II-42/47/11/87</i>	0.740	0.905	6.906	0.182
14XII2015	<i>I-XX/XX/14/45</i>	0.748	1.317	2.897	0.432
29I2016	<i>II-40/45/15/67</i>	0.950	1.249	4.393	0.239
10III2016	<i>II-44/44/11/86</i>	0.271	0.380	6.010	0.288
17III2016	<i>II-39/50/11/82</i>	0.489	0.712	4.834	0.313
01IV2016	<i>II-43/43/14/77</i>	0.497	0.861	3.557	0.422
07IV2016	<i>II-38/48/14/77</i>	0.897	1.217	4.195	0.263
14IV2016	<i>II-43/43/14/65</i>	0.472	0.842	3.478	0.439
21IV2016	<i>II-38/48/14/65</i>	0.927	1.244	4.206	0.255
MEAN	AREA	0.666	0.970	4.497	0.315
	1.041	(0.242)	(0.313)	(1.269)	(0.094)

With the mean values of the kink point and the critical width, the global and reduced bilinear approximation has an area of 1.041, a relative deviation of the true value of 1 of a 4.09%. This difference is little enough for us and the approximation is considered valid.

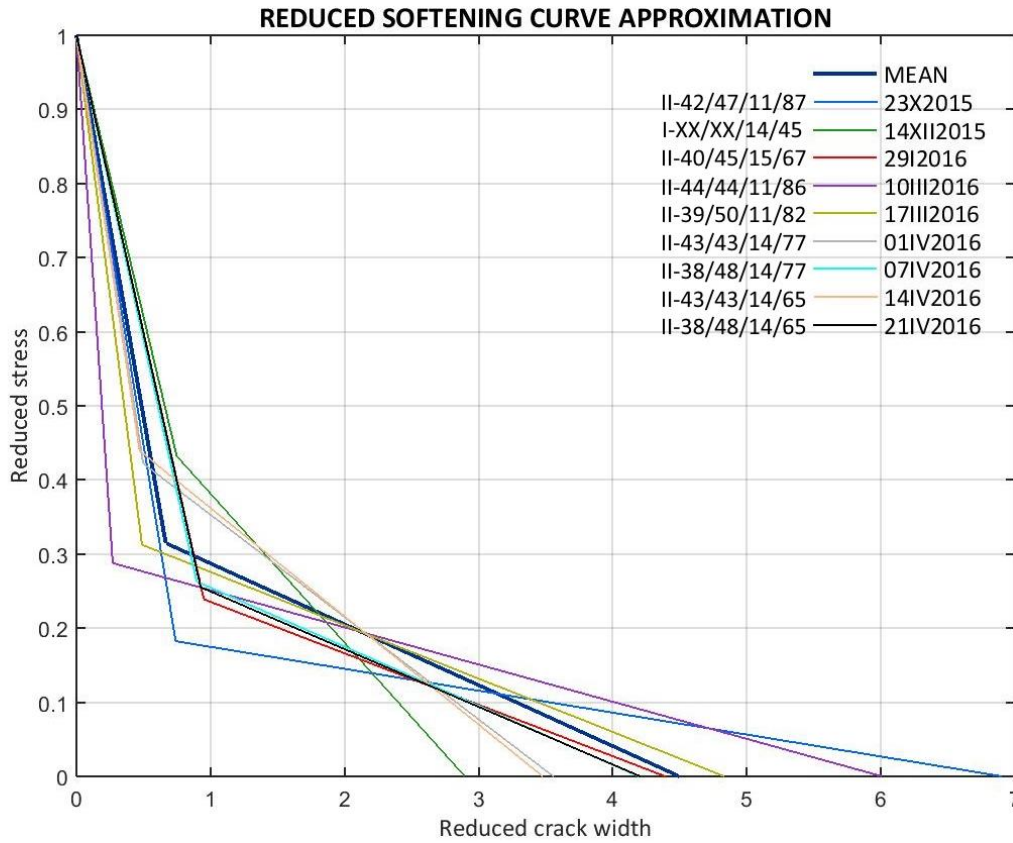


Figure 66: Softening curve bilinear approximation of all campaigns in the reduced form

Applying the reduction method, all softening curves are confined at a region where, compared to Figure 65, the curves seem to have a more similar behavior. The similitude between campaigns 29I2016, 07IV2016 and 21IV2016 is kept with this change, but other similitudes are now found, for example, between campaigns 01IV2016 and 14IV2016.

The two series of campaigns where a similitude has been found have another point in common. Campaigns 29I2016, 07IV2016 and 21IV2016 have a higher content in aggregate than in sand and campaigns 01IV2016 and 14IV2016 have the same content in aggregate and in sand. Maybe, better global bilinear approximations can be found when the composition ratios are similar, even though a general approximation can be also possible, because the one we have found is valid. It means: the area is close to 1; the slopes with the point $(0,1)$ and the mean kink point, which is -1.029 , and the slope with point $(0,1)$ and the mean initial intercept w_1 , which is -1.031 , are practically equal and the global curve moves between all the found bilinear approximations.

This global approximation can be used for future test in order to predict the test curves if we know the tensile strength and an approximation of G_f or it can be used in a reverse analysis for reproducing the three-point bending tests with a software of mechanical analysis after they are done, in order to compare predictive models and real tests.

6 SUMMARY OF THE ECONOMIC VALUATION AND THE SCHEDULE

6.1 ECONOMIC SUMMARY

The total cost of this study, including general costs and profit, is NINE THOUSAND FOUR HUNDRED TWENTY-ONE EUROS AND THIRTY-SIX CENTS (9.421'36€), without taxes.

With a V.A.T. of 21%, the total cost is ELEVEN THOUSAND THREE HUNDRED NINETY-NINE EUROS AND EIGHTY-FIVE CENTS (11.399'85€).

A single campaign for concrete fracture analysis, formed by 3 cylinders and 4 beams and 1 direct compression test, 2 Brazilian tests and 4 three-point bending test has a direct mean cost of TWO HUNDRED EIGHTY-ONE EUROS AND NINETY-FIVE CENTS (281'95€), taxes, profit and other indirect cost not included.

The considered costs and concepts and further details about the economic valuation are available at Appendix H.

6.2 SCHEDULE SUMMARY

The total planned duration of the project, including the stage of searching information, all the testing stage and the document writing, is about 407 natural days.

A single campaign, from the casting until the results extraction, has a length between 30 and 35 natural days.

Further details about the schedule are available at Appendix I.

7 CONCLUSIONS AND FUTURE RESEARCH

7.1 CONCLUSIONS OF THE RESEARCH

Once the project is finished, it is time to review the study from two points of view: the execution of it according to the goals and the procedure proposed at the beginning of it (see Chapter 1.2 and Chapter 1.3) and from the point of results (see Chapter 5).

During the entire document, the mechanisms of concrete fracture are detailed at Chapter 2 and two of the currently available methodologies for the real G_F determination are reviewed at Chapter 3, after taking into consideration the main problems for finding the G_F parameter.

On a basic experimental field with concrete, new knowledge has been acquired about the testing systems available, the proper way of casting and preserving concrete and how to characterize concrete mixtures with their strength limits using the normalized procedures. These points are essential for an experimental project with concrete.

On a specialized experimental field on concrete fracture mechanics, stable tests have been obtained (see Chapter 5.1.1) and a correct methodology for treating the data obtained has been done (see Chapter 5.1.2). With this, parameters related to the fracture of concrete have been obtained, such as G_F (see Chapter 5.2) or w_c (see Chapter 5.3). Moreover, G_F was compared for two different methodologies (see Chapter 5.1.3) and little difference was observed. This means that, at least, for the same methodology, testing machines and calculation procedures developed, the process is correct.

Three individual three-point bending tests and nine campaigns, containing forty-four three-point bending tests, twenty-one Brazilian tests and eleven direct compression tests, have been tested. A total of 79 tests have been carried out for this project (see Chapter 4, Appendix A and Appendix B). Then, this created a volume of data that allows some comparisons (see Chapter 5.2), but some connections between the compared parameters and G_F are difficult to see clearly or shows some contradictory behavior.

As a general statement, the main goal of finding the real G_F is accomplished, but with some remarks.

Although our tests have been proved to be stable and valid and there is not a visible reason to state our values to be invalid, the phenomenon of little cycles seen with the recorded load values might create extra energy recording, provoking our G_F values to be higher than the ones registered by other authors, organizations and labs. Also, we have to remember that our limitations do not let us to proceed according the recommended procedures for G_F determination^{24,25}.

With this reminder, there have been clearly seen some behavior of G_F with other properties at environmental conditions. G_F seems to be higher with higher cement content and higher strength limits, although the type of cement might have an effect on the tensile strength, and with the lower content in sand and water. Other connections were difficult to find due to the lack of experimental testing. Also, a global and valid bilinear approximation has been found. See Chapter 5.2 and 5.3 for more details.

7.2 FUTURE WORK

As future work, there are several improvements and future possible projects.

Let us begin with the improvements that need to be taken into account before beginning other project in concrete fracture mechanics.

First, an improvement of the testing systems, the machine and the setup is required, in order to avoid the extreme testing conditions for the machine available to us, reason of the cyclical reading of the load cell. This phenomenon can be prevented with changes at the current machine or the substitution for other one, but stiff enough. This can make the speed introduced not to be so extreme for the testing system.

A second possible modification can be at the specimen sizes. If we test bigger specimens, it could be a possibility that higher displacement speeds could be lead also to stable tests.

A last change can be done at the control system. The recommended procedures²⁵ proposed a control based on a close loop with the *CMOD* recording, not the displacement recording, which is the only one available for us. This way should be explored if this research field is continued, in order to apply the same procedures than other research labs.

Once these improvements are implemented correctly and with good results, it is time to proceed with new research lines, which can be:

- To continue the current research with a wider experimental work, in order to create a database that makes easier to see the variability of G_F and to propose a predictive model for G_F at environmental condition using as parameters the composition of it or the basic mechanical properties
- To do an experimental work and research with different environmental conditions, in order to propose the same predictive model, but adding environmental parameters
- To improve these predictive model with a study of the influence of the speed of the loading case, adding speed as a parameter or proposing models for high loading speed or impacts
- To study the influence of age introducing new parameters at these models
- Finally, to include a possible effect of fatigue at these predictive models

Evidently, these future research lines require a precise testing system and results, alongside enough time to be done properly.

8 REFERENCES

1. William, K. J. & Warnke, E. P. Constitutive model for the triaxial behavior of concrete. (1975).
2. Bažant, Z. P. Size effect in blunt fracture: concrete, rock, metal. *Journal of Engineering Mechanics* (1984).
3. Bažant, Z. P., Ozbolt, J. & Eligehausen, R. Fracture size effect: review of evidence for concrete structures. *Journal of structural engineering* **120**, 2377–2398 (1994).
4. Griffith, A. A. The phenomena of rupture and flow in solids. *Philosophical Transactions of the Royal Society of London. Series A, Containing Papers of a Mathematical or Physical Character* 163–198 (1921).
5. Irwin, G. R. Analysis of Stresses and Strains Near the End of a Crack Traversing a Plate. *Journal of Applied Mechanics* (1957).
6. Petersson, P.-E. Crack growth and development of fracture zones in plain concrete and similar materials. (Lund University, 1981).
7. Bažant, Z. P. Concrete fracture models: testing and practice. *Engineering fracture mechanics* **69**, 165–205 (2002).
8. Hillerborg, A., Modéer, M. & Petersson, P.-E. Analysis of crack formation and crack growth in concrete by means of fracture mechanics and finite elements. *Cement and concrete research* **6**, 773–781 (1976).
9. Modéer, M. A fracture mechanics approach to failure analyses of concrete materials. (Lund University, 1979).
10. Bažant, Z. P. & Oh, B. H. Crack band theory for fracture of concrete. *Matériaux et construction* **16**, 155–177 (1983).
11. Barenblatt, G. The formation of equilibrium cracks during brittle fracture. General ideas and hypotheses. Axially-symmetric cracks. *Journal of Applied Mathematics and Mechanics* **23**, 622–636 (1959).

12. Bažant, Z. P. & Planas, J. *Fracture and size effect in concrete and other quasibrittle materials*. **16**, (CRC press, 1997).
13. Guinea, G. V, Planas, J. & Elices, M. Measurement of the fracture energy using three-point bend tests: Part 1—Influence of experimental procedures. *Materials and Structures* **25**, 212–218 (1992).
14. Planas, J., Elices, M. & Guinea, G. V. Measurement of the fracture energy using three-point bend tests: Part 2—Influence of bulk energy dissipation. *Materials and Structures* **25**, 305–312 (1992).
15. Elices, M., Guinea, G. V & Planas, J. Measurement of the fracture energy using three-point bend tests: Part 3—Influence of cutting the P- δ tail. *Materials and Structures* **25**, 327–334 (1992).
16. Bažant, Z. P. & Kazemi, M. T. Size dependence of concrete fracture energy determined by RILEM work-of-fracture method. *International Journal of Fracture* **51**, 121–138 (1991).
17. Bamforth, P., Chisholm, D., Gibbs, J. & Harrison, T. Properties of Concrete for use in Eurocode 2. *The Concrete Center Report CCIP-029* (2008).
18. Gustafsson, P.-J. Fracture mechanics studies of non-yielding materials like concrete: modelling of tensile fracture and applied strength analyses. (Lund University, 1985).
19. Elices, M., Guinea, G. V, Gomez, J. & Planas, J. The cohesive zone model: advantages, limitations and challenges. *Engineering fracture mechanics* **69**, 137–163 (2002).
20. Hu, X. Size effects in toughness induced by crack close to free edge. *AEDIFICATIO Publishers, Fracture Mechanics of Concrete Structures*, **3**, 2011–2020 (1998).
21. Duan, K., Hu, X. & Wittmann, F. H. Boundary effect on concrete fracture and non-constant fracture energy distribution. *Engineering Fracture Mechanics* **70**, 2257–2268 (2003).
22. Abdalla, H. M. & Karihaloo, B. L. Determination of size-independent specific fracture energy of concrete from three-point bend and wedge splitting tests. *Magazine of concrete research* **55**, 133–141 (2003).
23. Duan, K., Hu, X.-Z. & Wittmann, F. H. Thickness effect on fracture energy of cementitious materials. *Cement and concrete research* **33**, 499–507 (2003).
24. RILEM 50-FMC. Determination of the Fracture Energy of Mortar and Concrete by Means of Three-Point Bend Tests on Notched Beames. Draft Recommendation. *Materials and*

- Structures* **18**, 285–290 (1985).
25. ACI COMMITTEE 446. ASTM Test procedure: Fracture toughness testing of concrete. 72 (2010).
 26. Cifuentes, H. & Medina, F. Comparación del valor de la energía de fractura real del hormigón obtenido por distintos procedimientos. *Anales de Mecánica de la Fractura* **26** **1**, 51–56 (2009).
 27. Fathy, A. M., Sanz, B., Sancho, J. M. & Planas, J. Determination of the bilinear stress-crack opening curve for normal-and high-strength concrete. *Fatigue & Fracture of Engineering Materials & Structures* **31**, 539–548 (2008).
 28. Karihaloo, B. L., Abdalla, H. M. & Imjai, T. A simple method for determining the true specific fracture energy of concrete. *Magazine of concrete research* **55**, 471–481 (2003).
 29. UNE-EN 12390-3:2009. Ensayos de hormigón endurecido. Parte 3: Determinación de la resistencia a compresión de probetas. (2009).
 30. UNE-EN 12390-3:2009/AC. Ensayos de hormigón endurecido. Parte 3: Determinación de la resistencia a compresión de probetas (Erratum). (2011).
 31. BS EN 1992-1-1:2004. Eurocode 2: Design of concrete structures: Part 1-1: General rules and rules for buildings. *London: British Standards Institution* (2004).
 32. ASTM C496-96. Standard Test Method for Splitting Tensile Strength of Cylindrical Concrete Specimens. *ASTM International, West Conshohocken, PA* (1996).
 33. UNE-EN 12390-6:2010. Ensayos de hormigón endurecido. Parte 6: Resistencia a tracción indirecta de probetas. (2010).
 34. UNE-EN 12390-1:2001. Ensayos de hormigón endurecido. Parte 1: Forma, medidas y otras características de las probetas y moldes. (2001).
 35. UNE-EN 12390-4:2001. Ensayos de hormigón endurecido. Parte 4: Resistencia a compresión. Características de las máquinas de ensayo. (2001).
 36. UNE-EN ISO 7500-1:2006. Materiales metálicos. Verificación de máquinas de ensayos uniaxiales estáticos. Parte 1: Máquinas de ensayo de tracción/compresión. Verificación y calibración del sistema de medida de fuerza. (2006).
 37. ASTM C39/C39M-01. Standard Test Method for Compressive Strength of Cylindrical Concrete Specimens. *ASTM International, West Conshohocken, PA* (1999).

A RESEARCH ON CONCRETE FRACTURE MECHANICS

TESTING AND ANALYZING THE FRACTURE ENERGY OF CONCRETE

THE APPENDICES

APPENDICES**A DETERMINATION OF OTHER MECHANICAL PROPERTIES****A.1 DETERMINATION OF THE ELASTIC MODULUS BY A THREE POINT BEND TEST**

The procedure proposed to determine E is the following one^{25,27}.

- a) On the first load raising part of the test before the peak load, collect the recorded values of P' and $CMOD$ in which P' is between the 15% and the 55% of the measured non-corrected peak load P_u' .
- b) Proceed to realize a linear fitting of the data, placing the $CMOD$ values on the ordinate axis and the P' values on the abscissa axis.
- c) The slope of the linear approximation is recorded as C_i , known as the initial compliance of the specimen. This initial compliance is the slope of a crack width vs. load curve, then the units are distance divided by load (m/N , multiples or submultiples).
- d) Compute the value of $V_1(\alpha_0')$ by means of Equation A.1.1.

$$V_1(\alpha) = 0.8 - 1.7\alpha + 2.4\alpha^2 + \frac{0.66}{(1-\alpha)^2} + \frac{4D}{S}(-0.04 - 0.58\alpha + 1.47\alpha^2 - 2.04\alpha^3) \quad (A.1.1)$$

Where α_0' can be found in Equation A.1.2, in which h means the thickness of the knives where the $CMOD$ gauge is placed, a is the notch depth, D the specimen depth and S the span.

$$\alpha_0' = \frac{a + h}{D + h} \quad (A.1.2)$$

- e) Finally, determine the elastic modulus in Equation A.1.3.

$$E = \frac{6SaV_1(\alpha_0')}{C_iBD^2} \quad (A.1.3)$$

This procedure applies to a single specimen (code at Appendix C.2.3). The only value of interest is E .

A.2 ELASTIC MODULI OF THE TESTED CAMPAIGNS

A.2.1 23X2015 CAMPAIGN

Applying the procedure exposed in Appendix A.1 (main code at Appendix C.1.1 with function at Appendix C.2.3), the results for the elastic moduli for the beam-type specimens from the 23X2015 campaign, on which a three point bend test with a $P - \delta$ tail correction has been performed, are shown at Table 50. At Figure 71 a comparative graph can be seen. When E is similar for some specimens, the slope of the fitting curve should be similar, and this happens with specimens B23X2015I, B23X2015III and B23X2015IV. B23X2015II is evidently higher.

Table 50: Data for the 23X2015 campaign elastic modulus determination. Sizes in millimeters

E 23X2015	Plot	D	S	B	a	h	P_u' (kN)	C_i ($\mu\text{m}/\text{kN}$)	E (GPa)
B23X2015I	Figure 67	100	300	100	31	2	1.759	6.529	14.981
B23X2015II	Figure 68	100	300	100	30	2	1.919	4.119	22.514
B23X2015III	Figure 69	100	300	100	31	2	1.894	6.645	14.719
B23X2015IV	Figure 70	100	300	100	30	2	1.857	6.724	13.790

These results lead to a mean E of 16.5GPa with a standard deviation of 4GPa for the 23X2015 series.

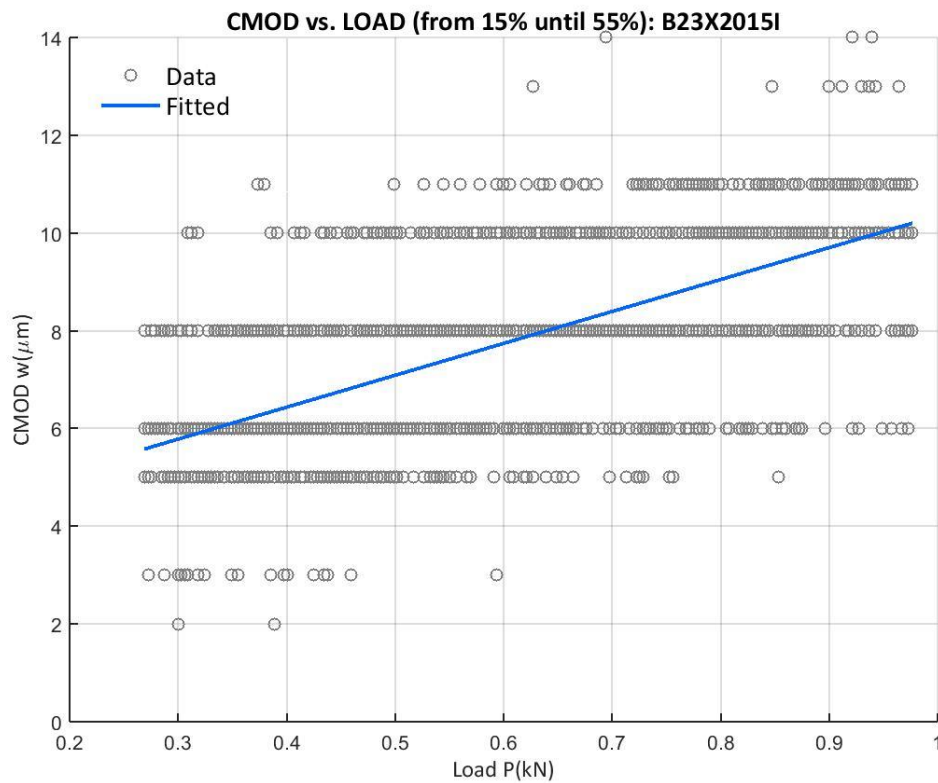


Figure 67: CMOD vs. Uncorrected Load from the 15% of the peak load up to 55% of B23X2015I

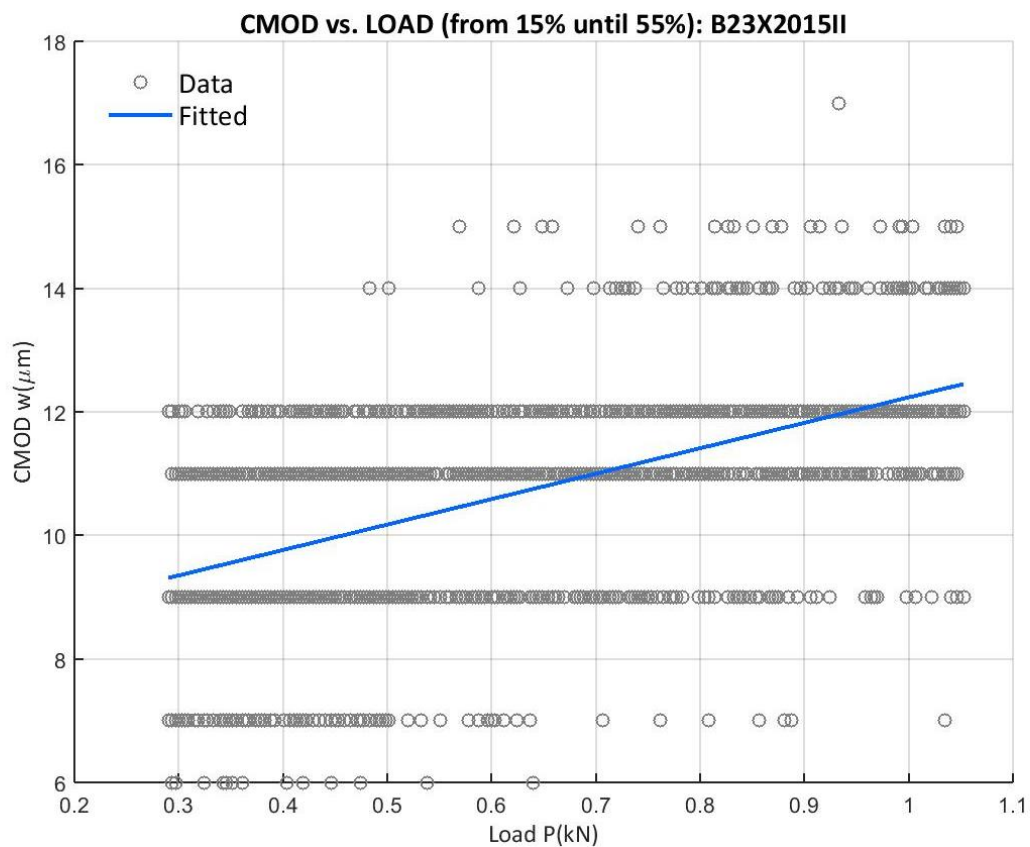


Figure 68: CMOD vs. Uncorrected Load from the 15% of the peak load up to 55% of B23X2015II

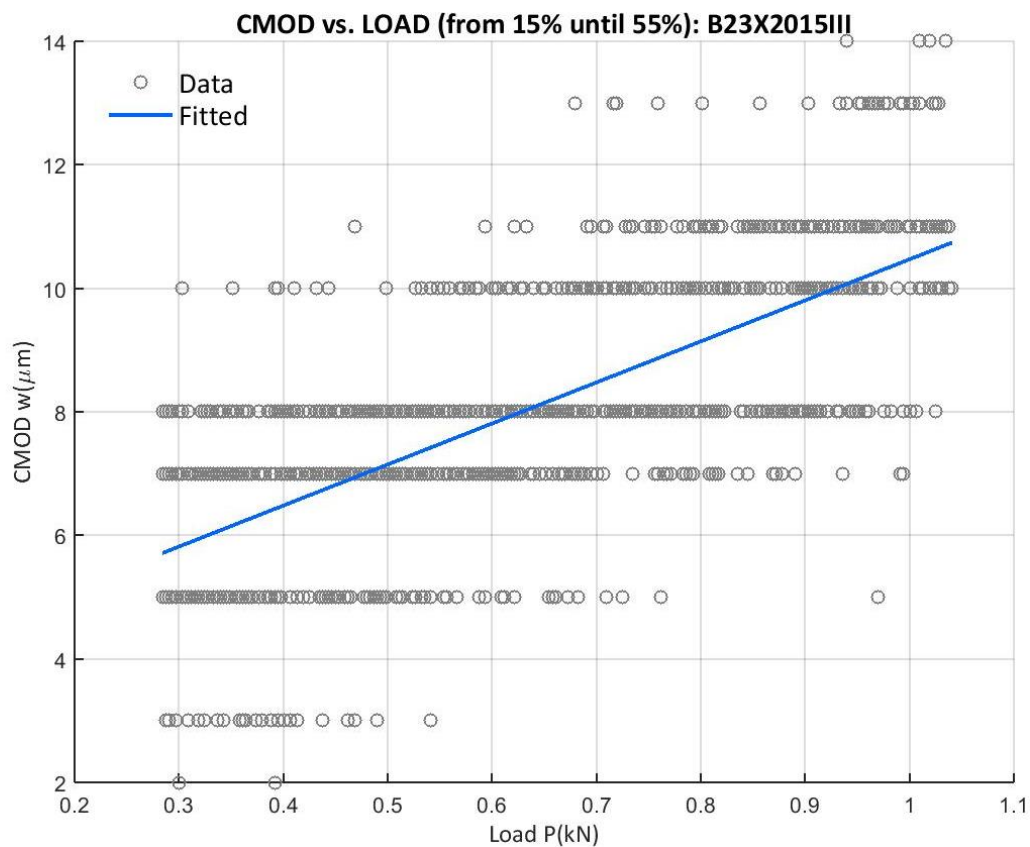


Figure 69: CMOD vs. Uncorrected Load from the 15% of the peak load up to 55% of B23X2015III

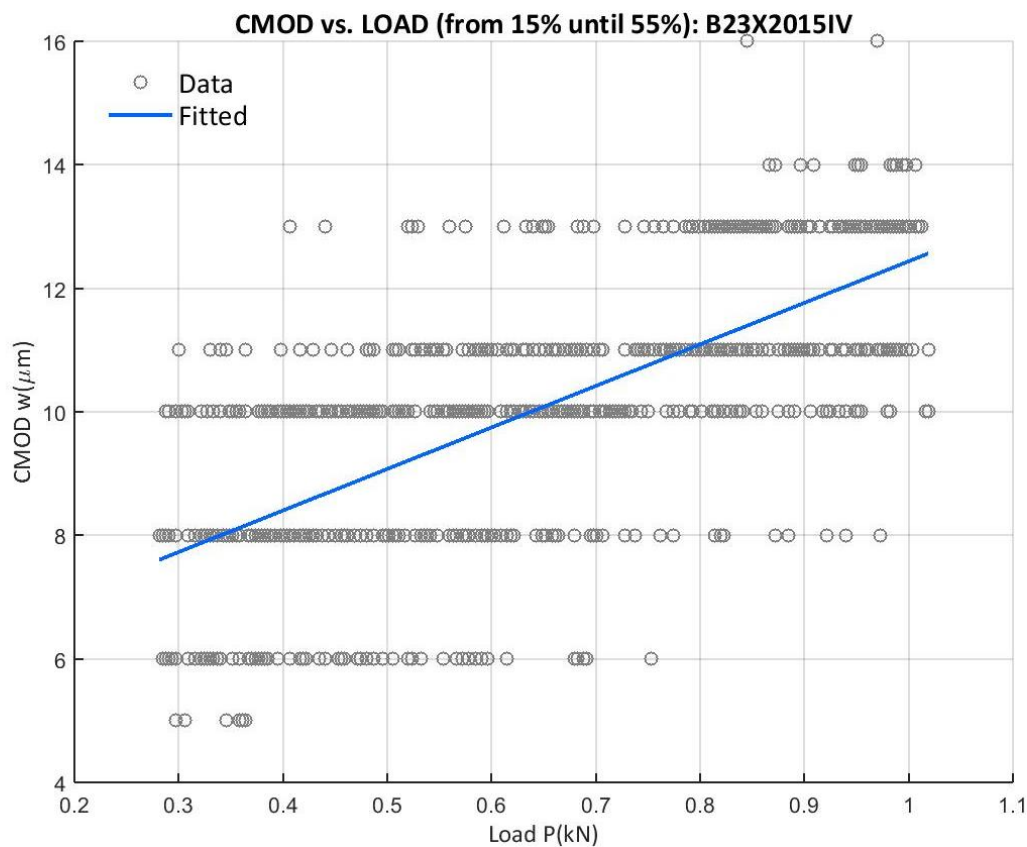


Figure 70: CMOD vs. Uncorrected Load from the 15% of the peak load up to 55% of B23X2015IV

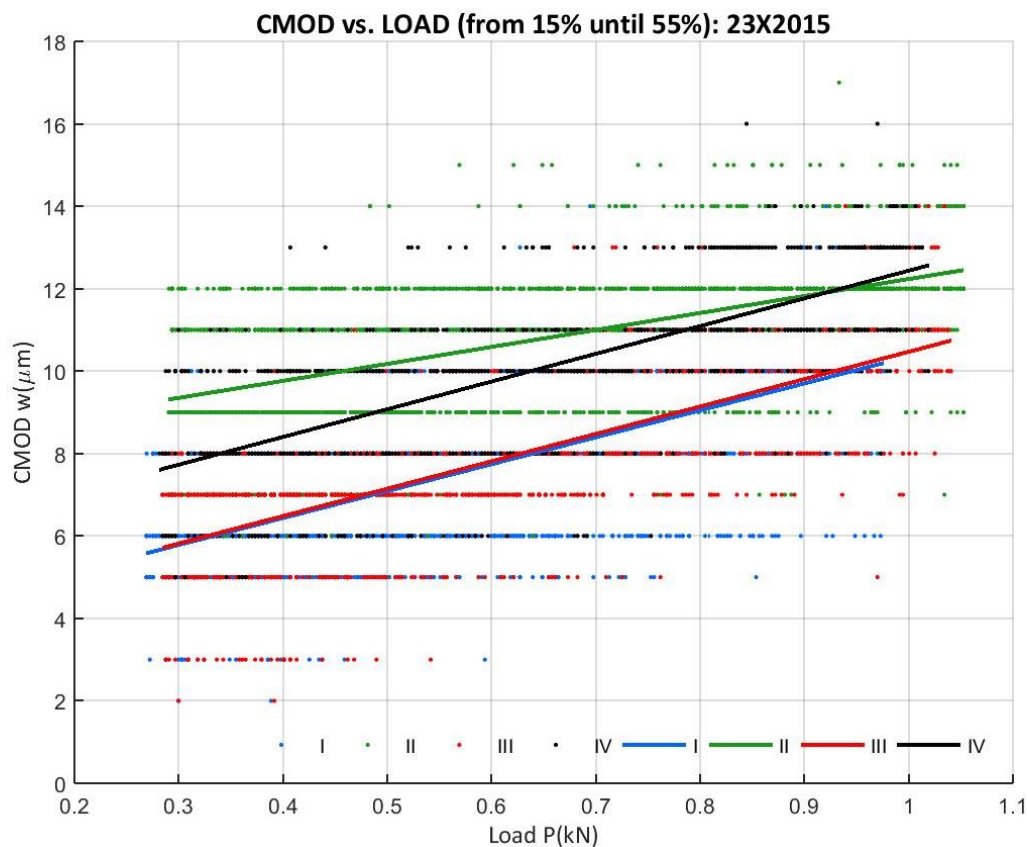


Figure 71: CMOD vs. Uncorrected Load from the 15% of the peak load up to 55% of all B23X2015

A.2.2 14XII2015 CAMPAIGN

The procedure detailed at Appendix A.1 is performed to every single beam-type specimen of the 14XII2015 concrete campaign, whose results are visible at Table 51. As before, the comparative graph is given at Figure 80. It can be seen that almost all specimens have the same, or nearly the same, elastic modulus, except the B14XII2015I specimen, with a slightly lower E than the others, and the B14XII2015II specimen, which has a significantly lower E . Codes at Appendix C.1.1 and C.2.3.

Table 51: Data for the 14XII2015 campaign elastic modulus determination. Sizes in millimeters

E 14XII2015	Plot	D	S	B	a	h	P_u' (kN)	C_i ($\mu\text{m}/\text{kN}$)	E (GPa)
B14XII2015I	Figure 72	100	300	100	30	2	4.780	5.756	16.109
B14XII2015II	Figure 73	100	300	100	29	2	3.360	12.954	6.784
B14XII2015III	Figure 74	100	300	100	30	2	4.587	4.675	19.834
B14XII2015IV	Figure 75	100	300	100	30	2	4.945	3.817	24.292
B14XII2015V	Figure 76	100	300	100	30	2	4.676	4.025	23.041
B14XII2015VI	Figure 77	100	300	100	30	2	4.703	4.050	22.895
B14XII2015VII	Figure 78	100	300	100	30	2	4.569	3.798	24.412
B14XII2015VIII	Figure 79	100	300	100	29	2	4.945	4.245	20.703

The elastic modulus of the 14XII2015 campaign is of 19.76GPa with a standard deviation of 5.9GPa.

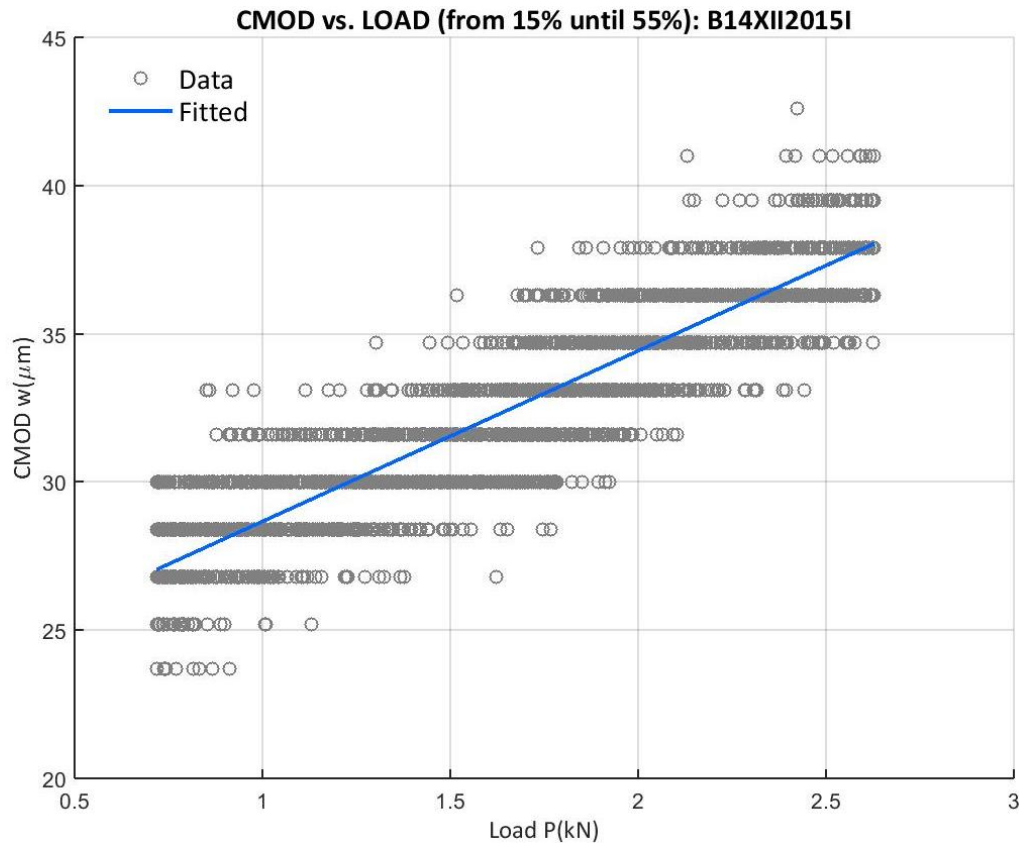


Figure 72: CMOD vs. Uncorrected Load from the 15% of the peak load up to 55% of B14XII2015I

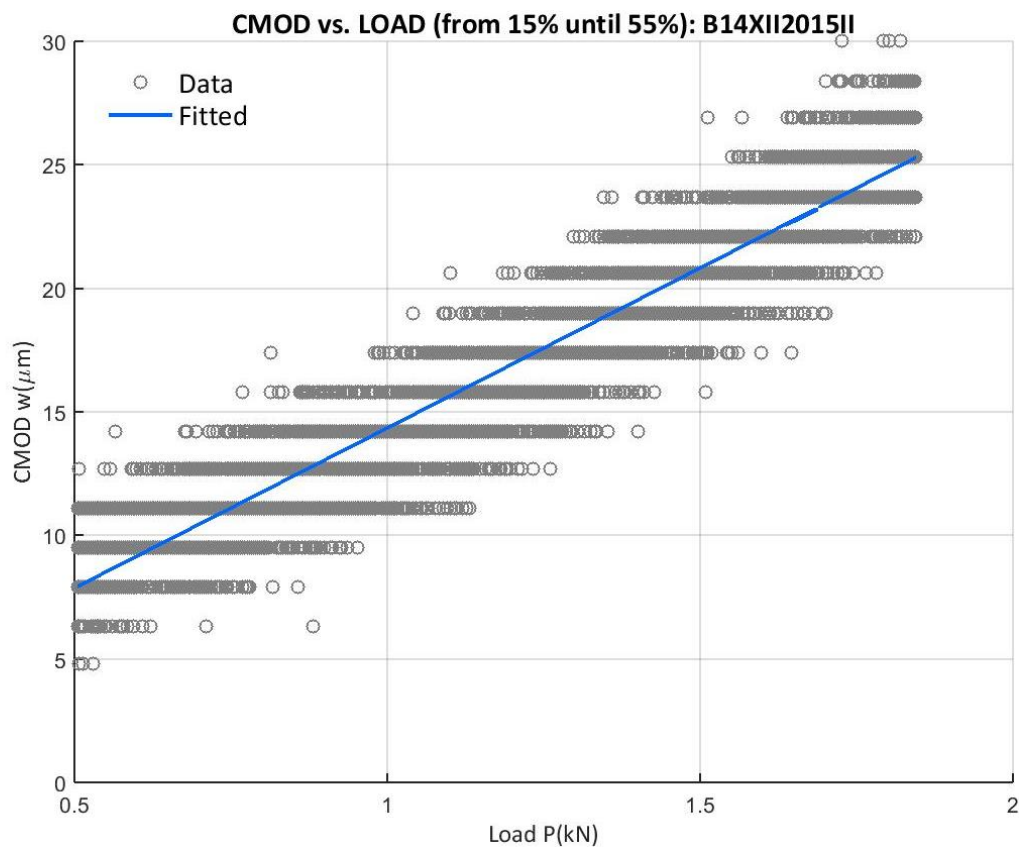


Figure 73: CMOD vs. Uncorrected Load from the 15% of the peak load up to 55% of B14XII2015II

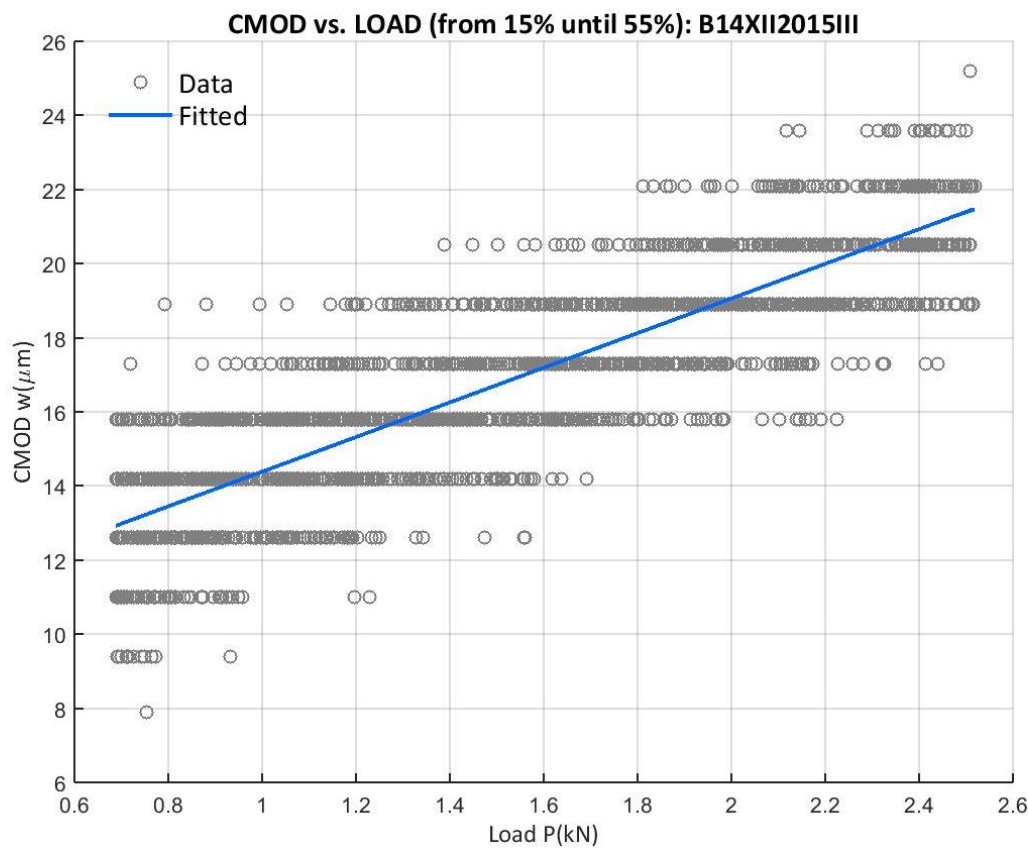


Figure 74: CMOD vs. Uncorrected Load from the 15% of the peak load up to 55% of B14XII2015III

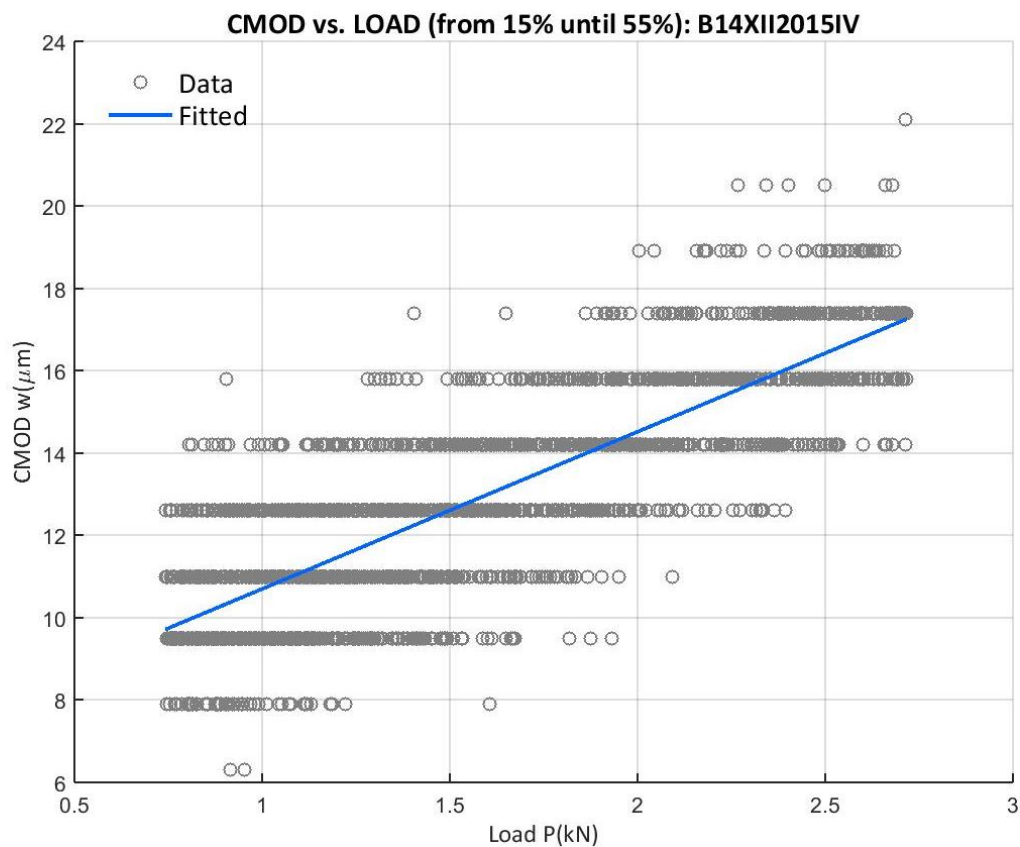


Figure 75: CMOD vs. Uncorrected Load from the 15% of the peak load up to 55% of B14XII2015IV

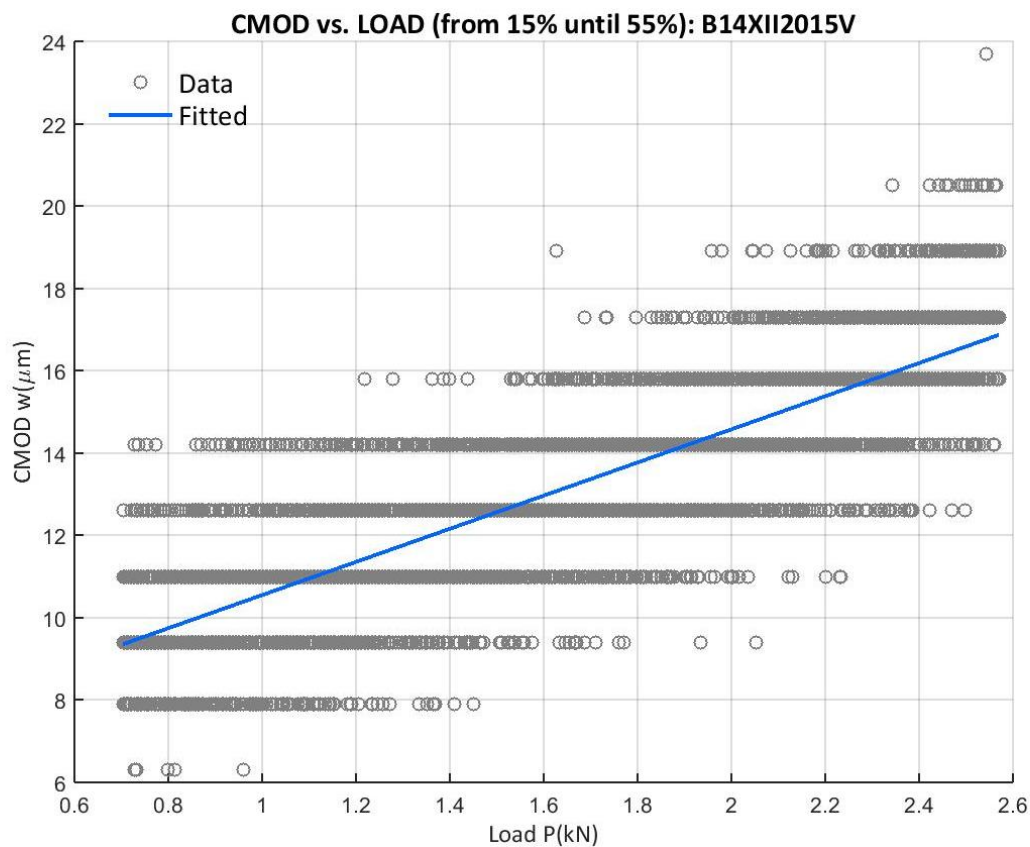


Figure 76: CMOD vs. Uncorrected Load from the 15% of the peak load up to 55% of B14XII2015V

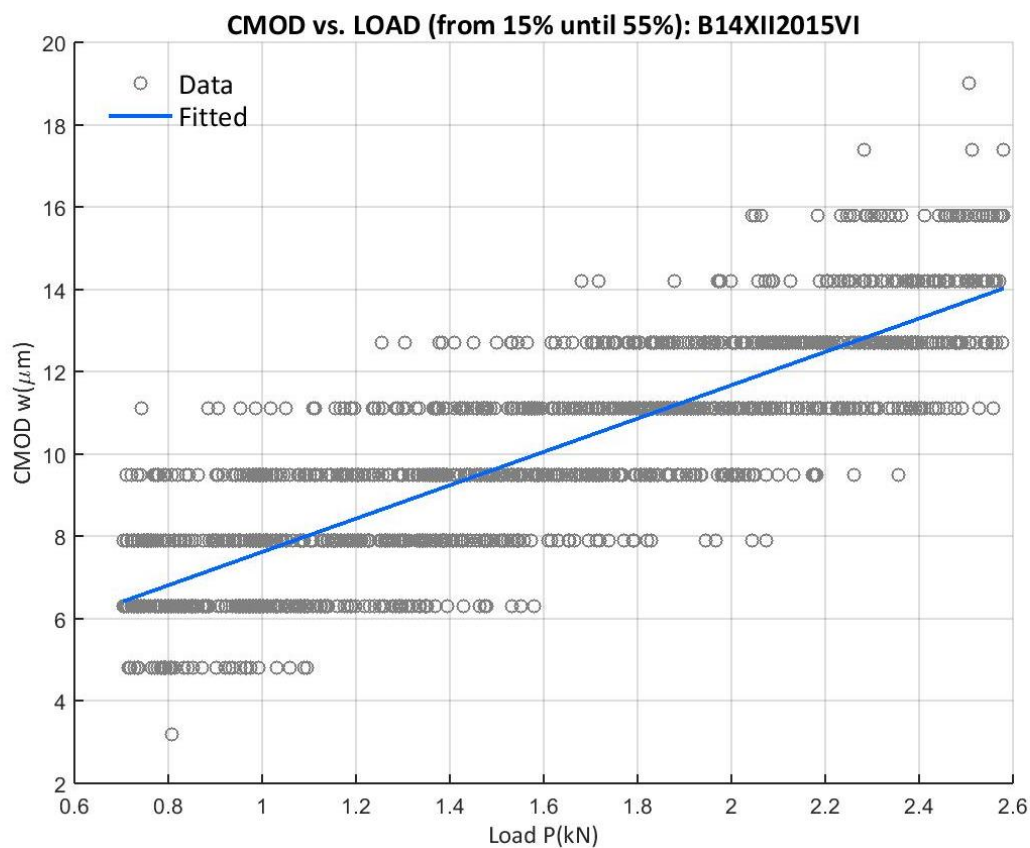


Figure 77: CMOD vs. Uncorrected Load from the 15% of the peak load up to 55% of B14XII2015VI

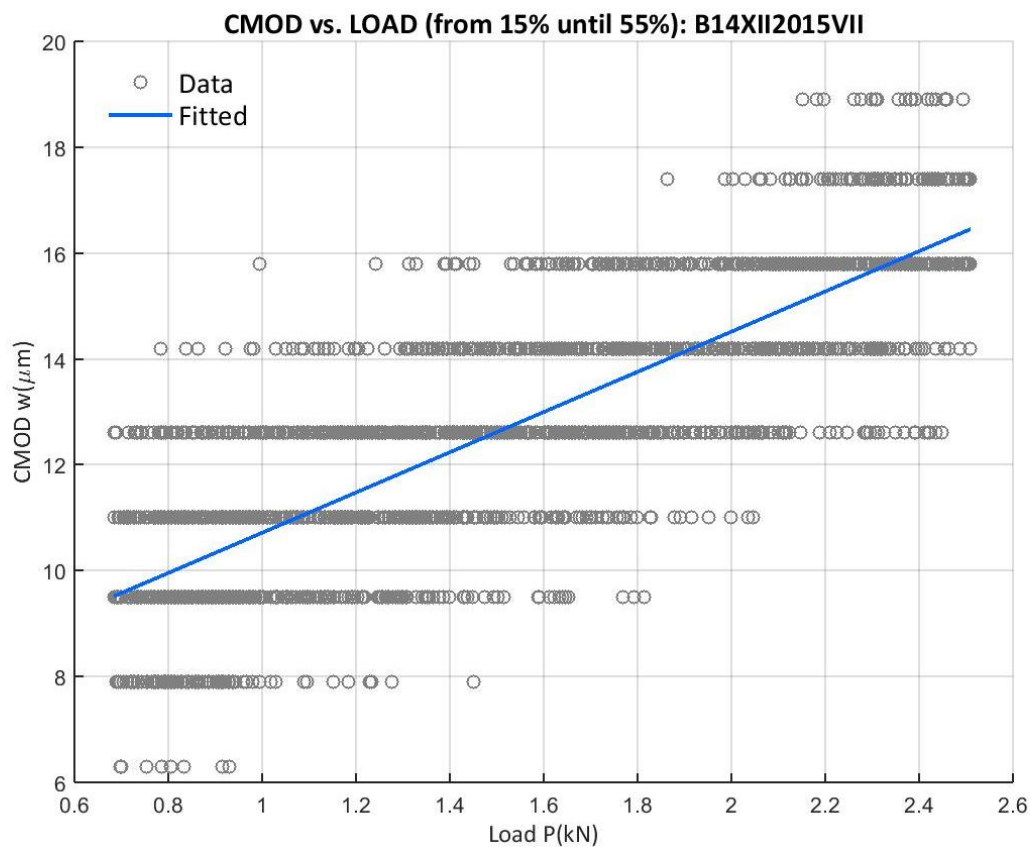


Figure 78: CMOD vs. Uncorrected Load from the 15% of the peak load up to 55% of B14XII2015VII

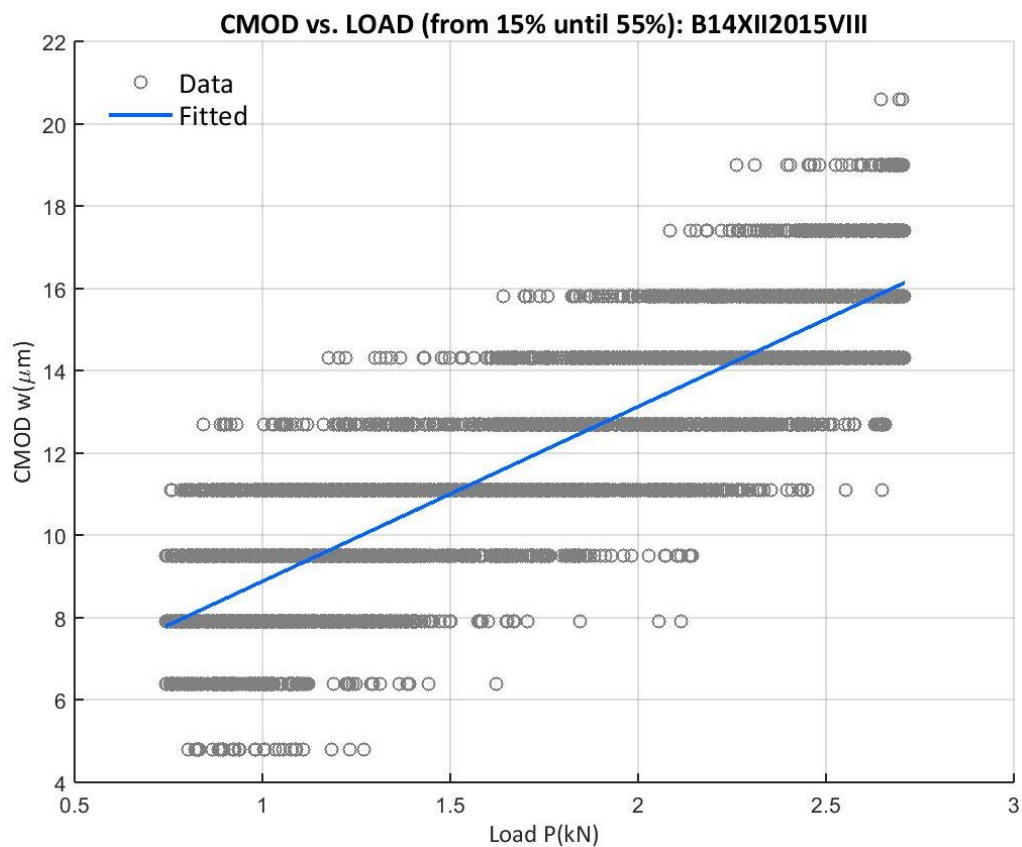


Figure 79: CMOD vs. Uncorrected Load from the 15% of the peak load up to 55% of B14XII2015VIII

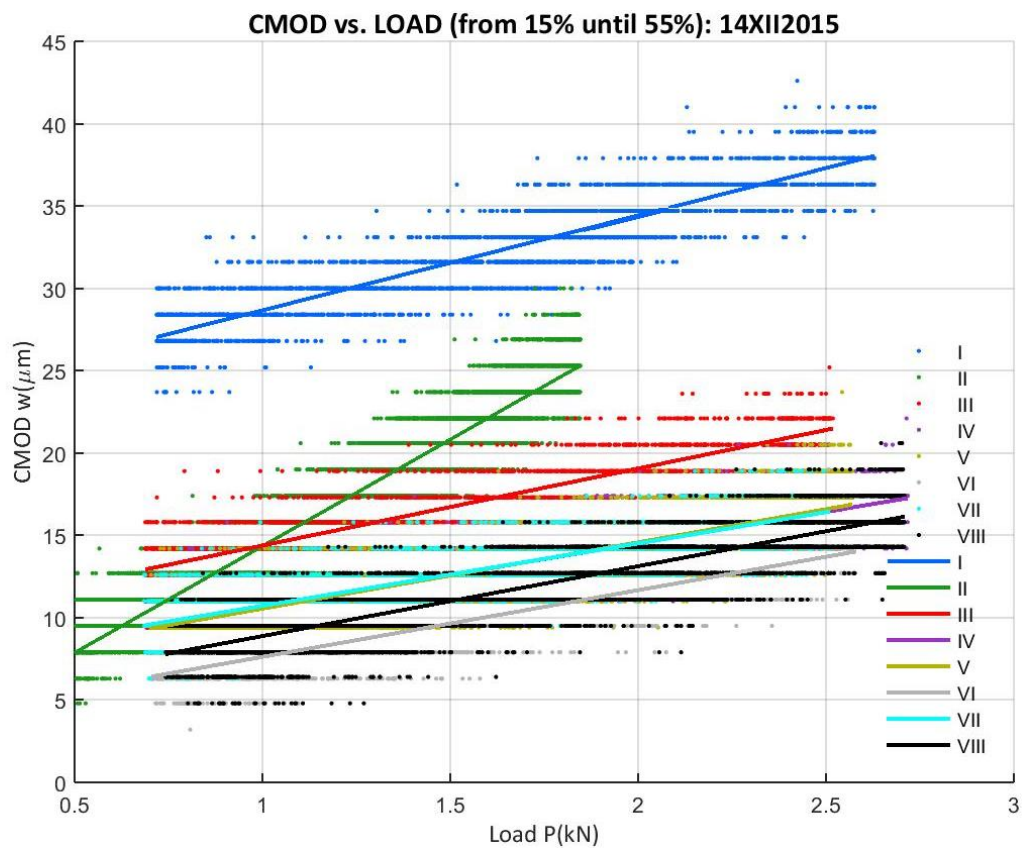


Figure 80: CMOD vs. Uncorrected Load from the 15% of the peak load up to 55% of all B14XII2015

A.2.3 29I2016 CAMPAIGN

For the eight beam-type specimens from the 29I2016, the calculation proposed at Appendix A.1 was applied. The results are given at Table 52. The graphs of the linear fitting are also shown, with a comparative graph for the 4 specimens with the same configuration from the A-series at Figure 89 and the entire campaign at Figure 90.

Table 52: Data for the 29I2016 campaign elastic modulus determination. Sizes in millimeters

<i>E</i> 29I2016	Plot	<i>D</i>	<i>S</i>	<i>B</i>	<i>a</i>	<i>h</i>	<i>P_u'</i> (kN)	<i>C_i</i> (μm/kN)	<i>E</i> (GPa)
B29I2016I	Figure 81	100	300	100	30.3	2	3.271	6.909	13.647
B29I2016II	Figure 82	100	300	100	30.1	2	2.999	4.824	19.357
B29I2016III	Figure 83	100	300	100	30.4	2	3.274	4.854	19.494
B29I2016IV	Figure 84	100	300	100	30.3	2	2.864	7.247	12.996
B29I2016V	Figure 85	100	550	100	10.6	2	2.476	2.761	18.037
B29I2016VI	Figure 86	100	550	100	10.6	2	2.540	0.789	63.065
B29I2016VII	Figure 87	100	550	100	42.0	2	0.814	27.759	12.106
B29I2016VIII	Figure 88	100	550	100	42.3	2	0.973	19.846	17.222

At Figure 90, one can see that changing the span length *S* provokes that the direct graph comparison of *E* cannot be done. It is reasonable, because at Equation A.1.1 and Equation A.1.3, *S* is a parameter which can change if the specimens are identical.

Let us look now to specimens with the same geometrical configuration, this is A-series at Figure 89. A first conclusion can be seen. Specimens I and IV have similar *E*, different of II and III, which between them the difference at *E* is also little. The results at Table 52 support this conclusion.

About the global *E*, a direct statistical treatment without looking at any individual results gives a mean value of 21.991GPa with a standard of 16.848GPa. This means that all values are inside the first standard deviation except specimen VI, which is inside the third standard deviation. Another point which is of interest, apart from the statistical one, is that the usual *E* for concrete is about 15GPa for the minimum of the C12/16 class, with a maximum of 40GPa for the upper bound of the C30/37 class, and 50GP for the upper bound for the C90/105 class ³¹. The highest *E* is with basalt and quartzite aggregate and the lowest with sandstone or limestone aggregate. Our concrete has aggregate more similar to sandstone and limestone with a low resistant class (lower than C35/45).

All these points want to affirm that it would be better to suppress specimen VI result for extremely unrealistic.

Finally, this means that the mean *E* is 16.123GPa with a standard deviation of 3.129GPa.

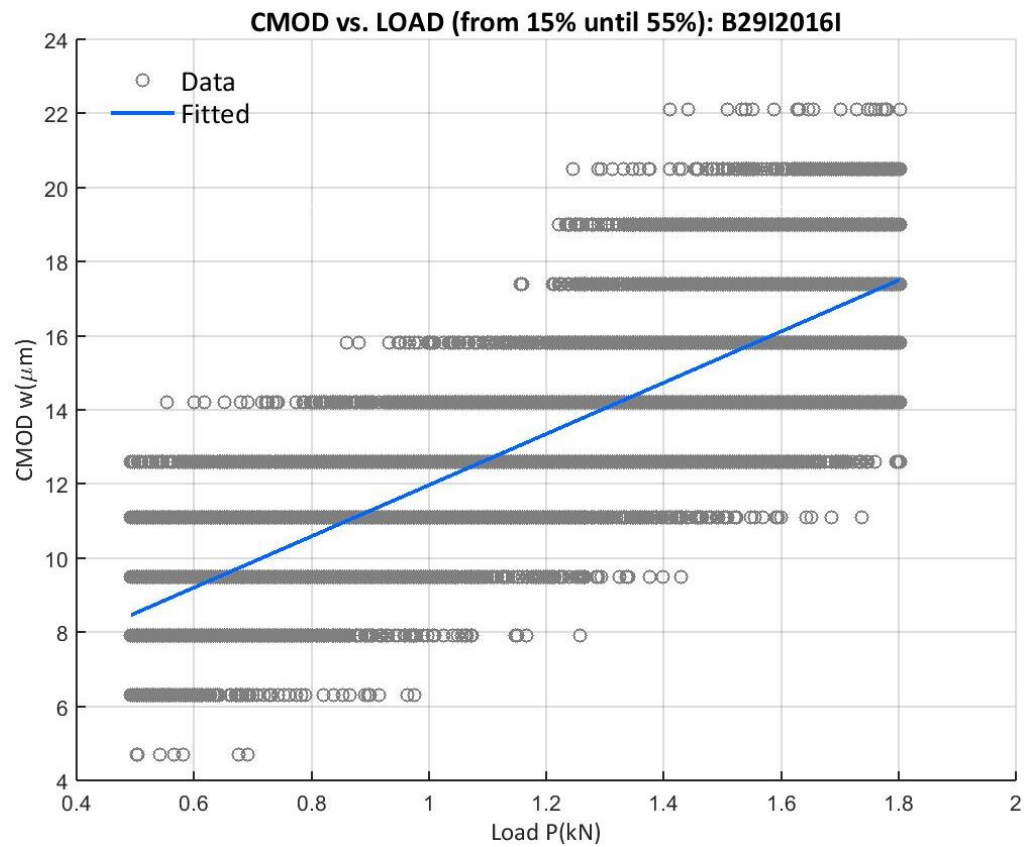


Figure 81: CMOD vs. Uncorrected Load from the 15% of the peak load up to 55% of B29I2016I

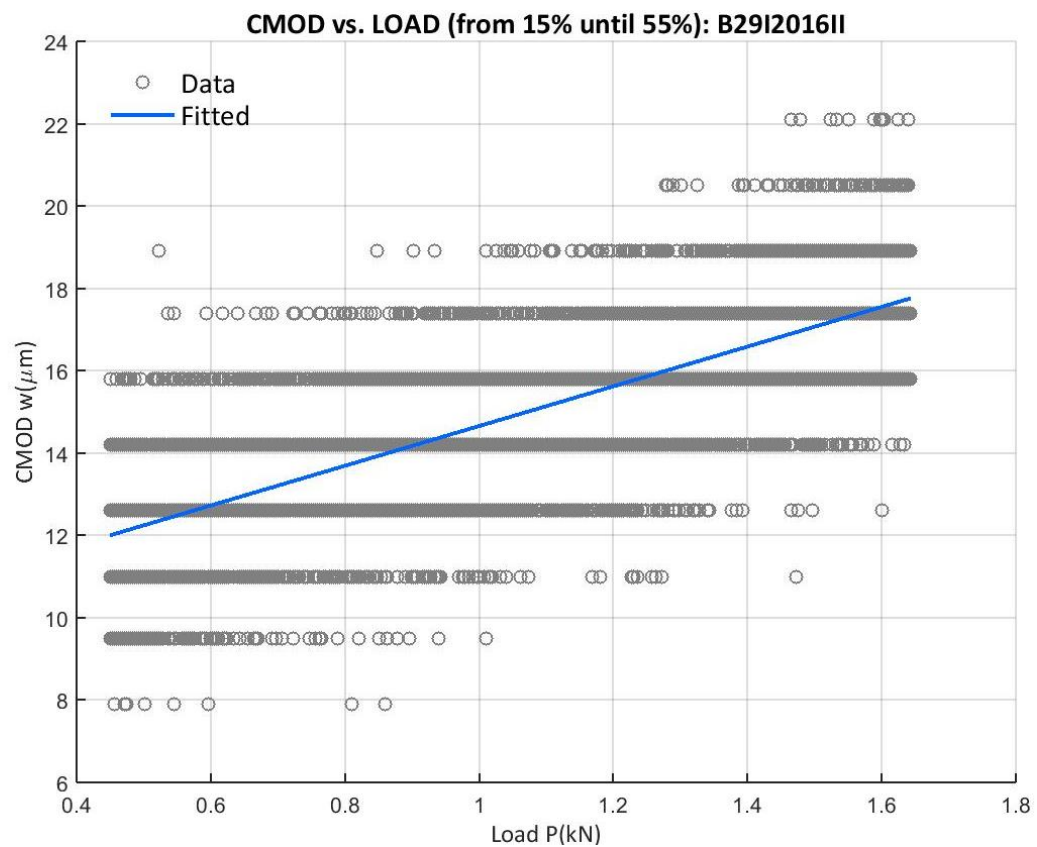


Figure 82: CMOD vs. Uncorrected Load from the 15% of the peak load up to 55% of B29I2016II

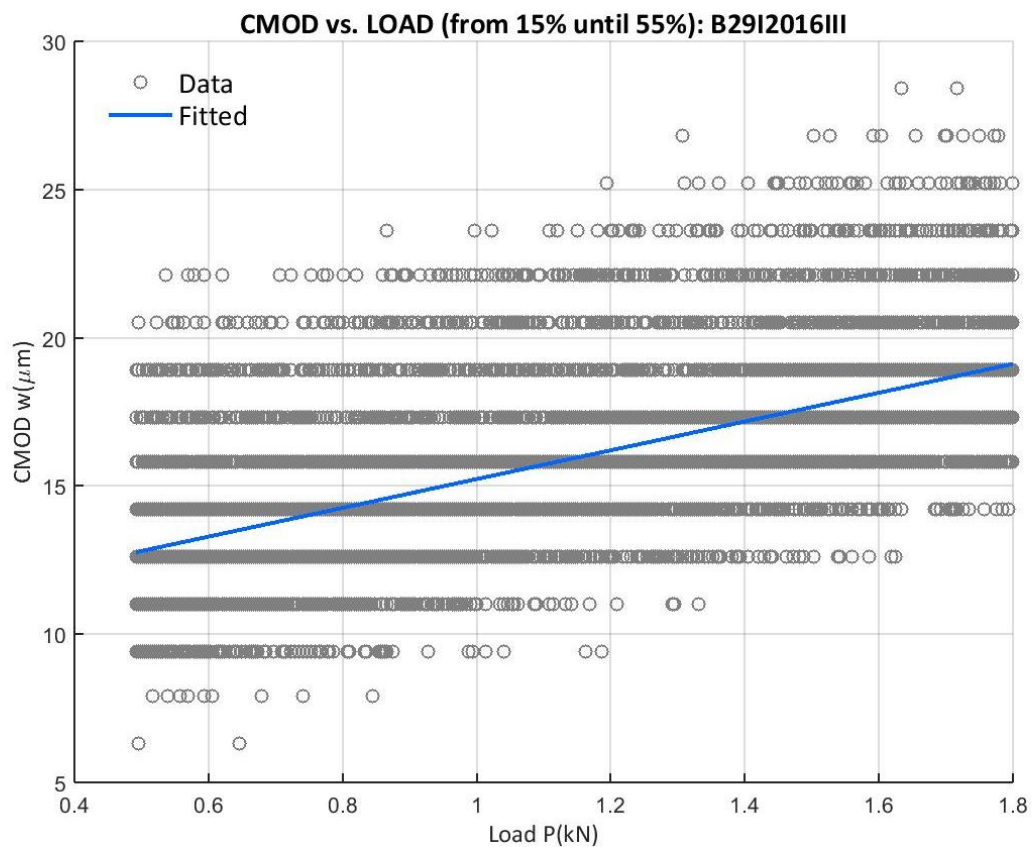


Figure 83: CMOD vs. Uncorrected Load from the 15% of the peak load up to 55% of B29I2016III

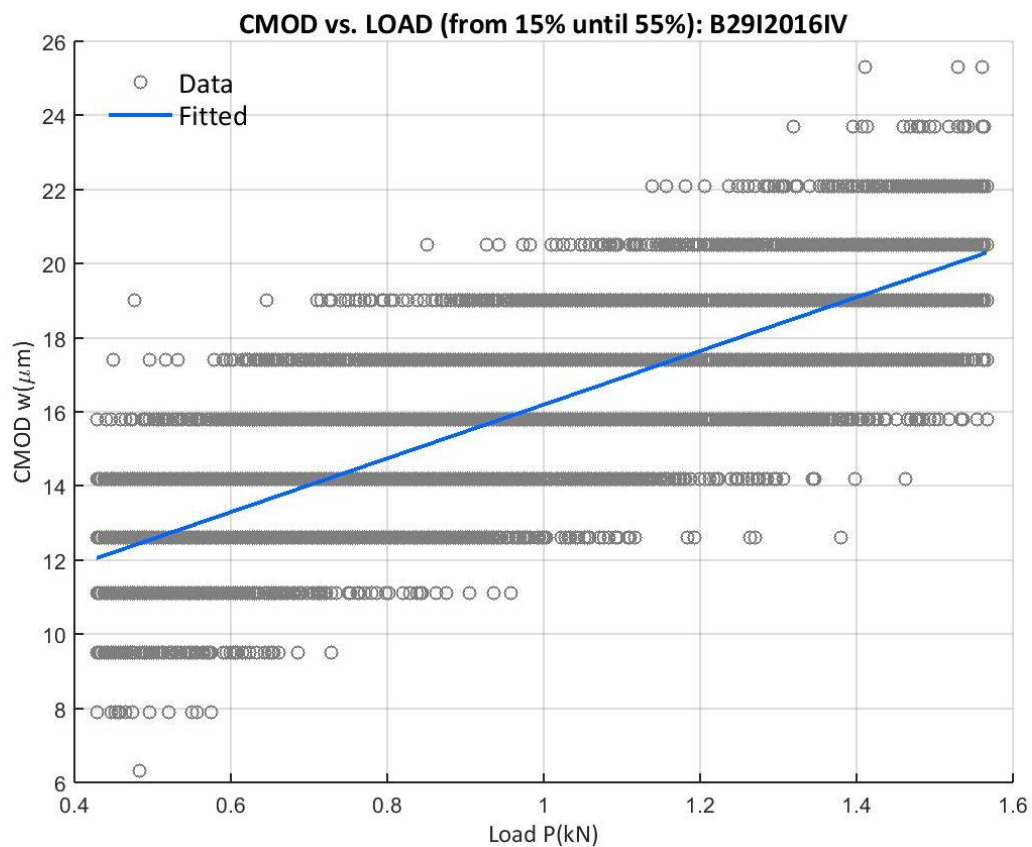


Figure 84: CMOD vs. Uncorrected Load from the 15% of the peak load up to 55% of B29I2016IV

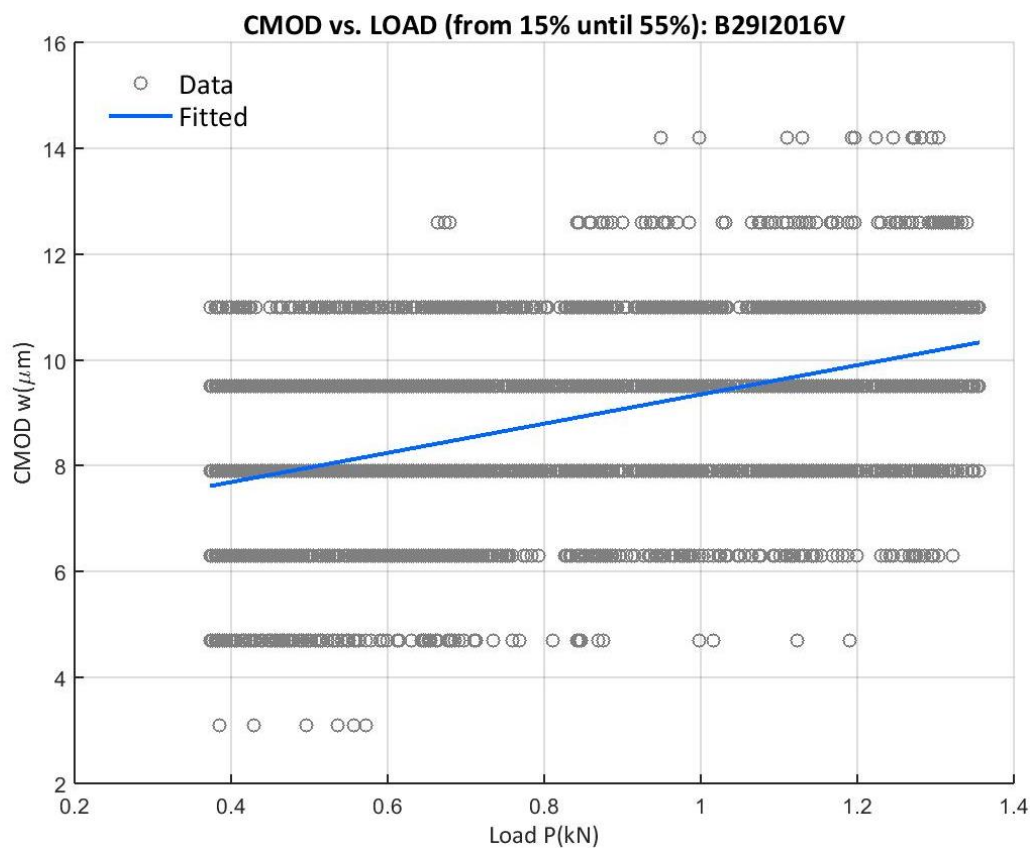


Figure 85: CMOD vs. Uncorrected Load from the 15% of the peak load up to 55% of B29I2016V

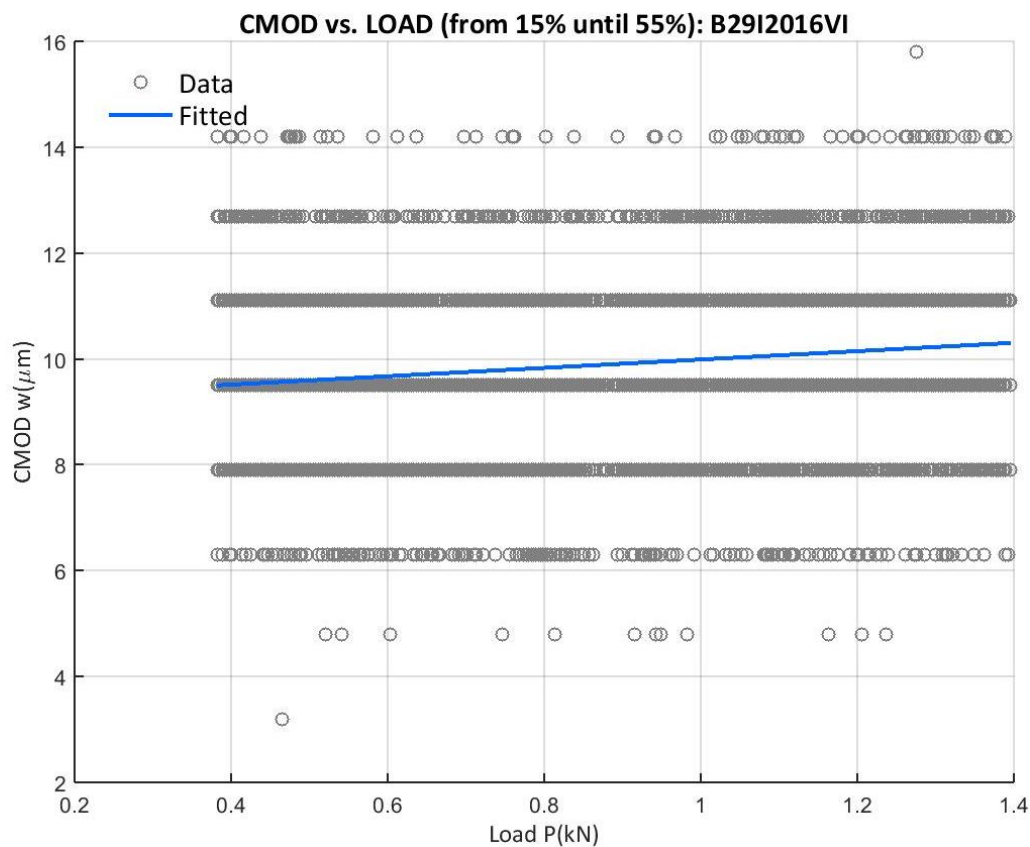


Figure 86: CMOD vs. Uncorrected Load from the 15% of the peak load up to 55% of B29I2016VI

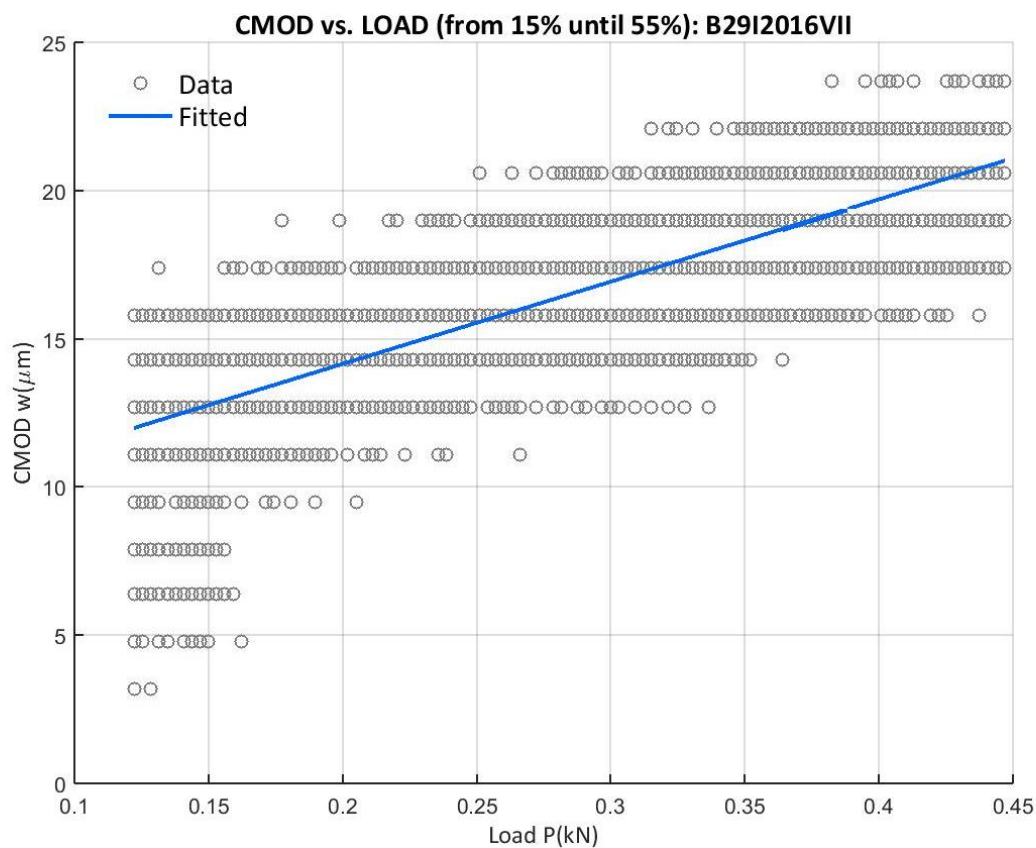


Figure 87: CMOD vs. Uncorrected Load from the 15% of the peak load up to 55% of B29I2016VII

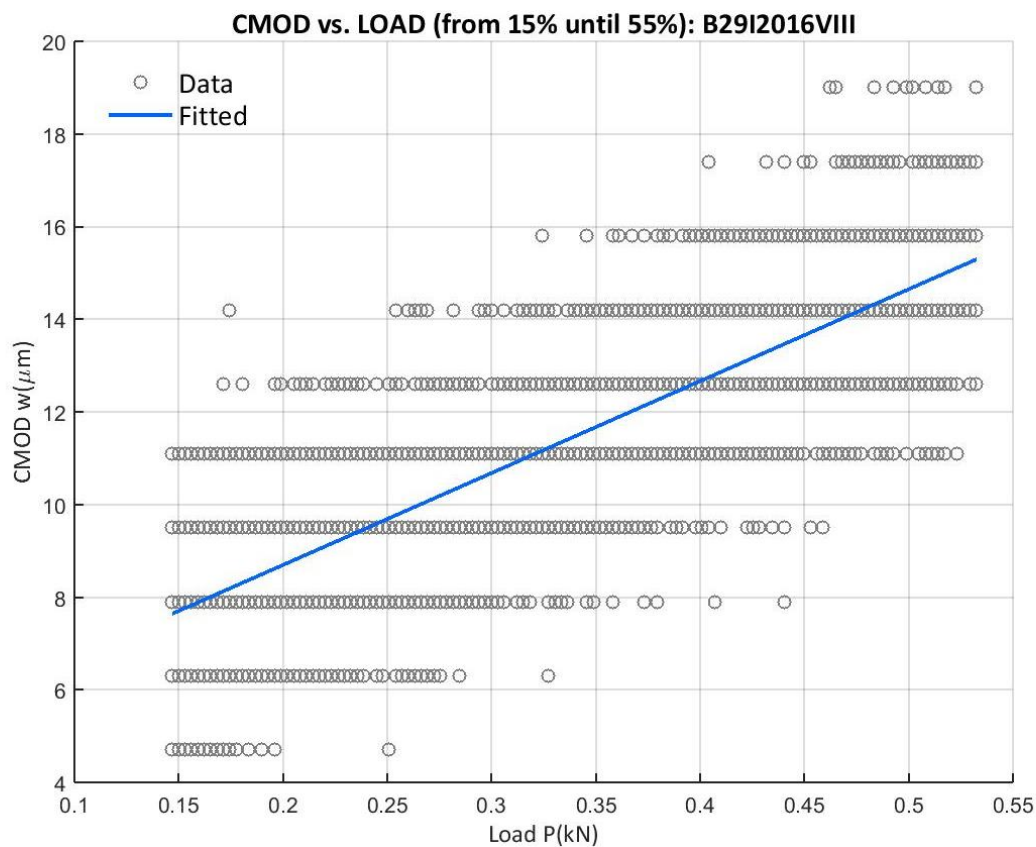


Figure 88: CMOD vs. Uncorrected Load from the 15% of the peak load up to 55% of B29I2016VIII

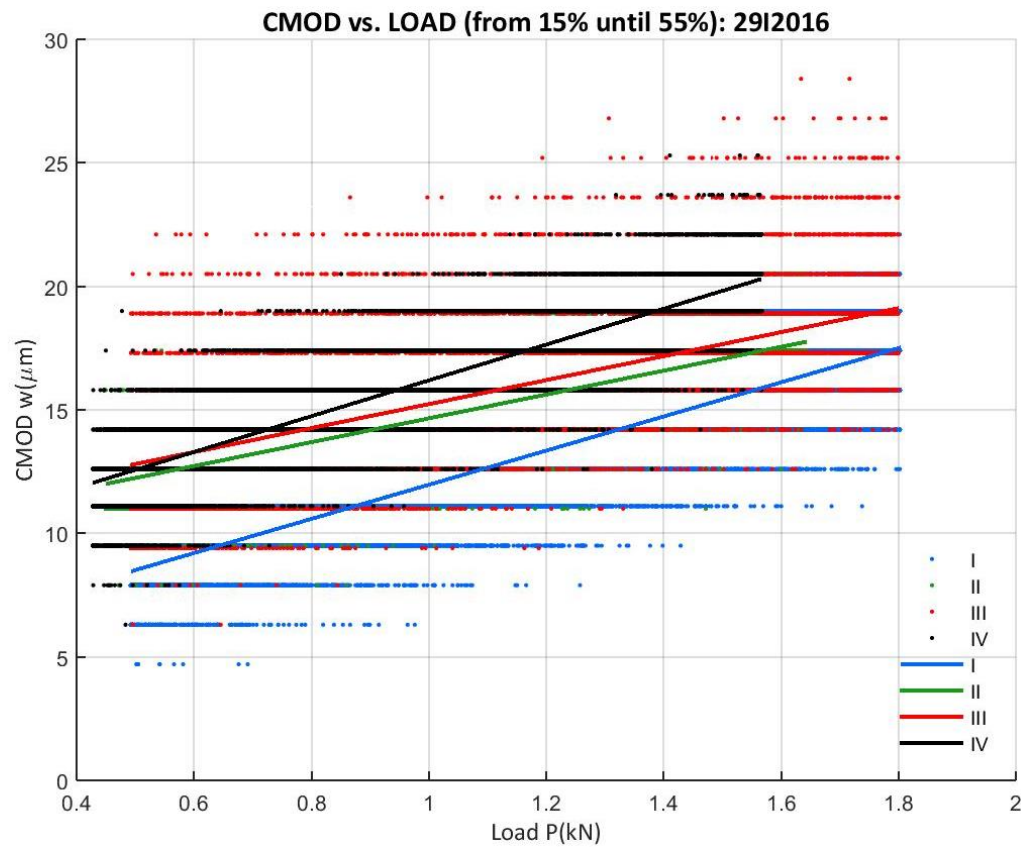


Figure 89: CMOD vs. Uncorrected Load from the 15% of the peak load up to 55% of 29I2016 A-series

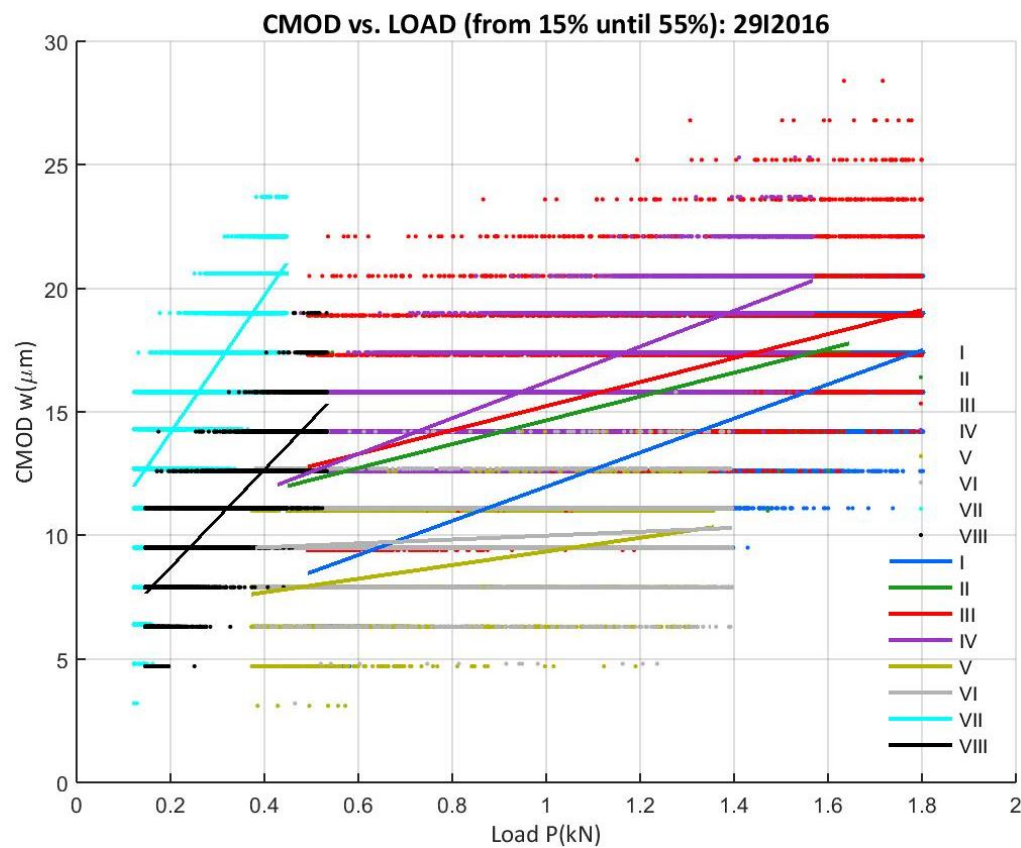


Figure 90: CMOD vs. Uncorrected Load from the 15% of the peak load up to 55% of all 29I2016

A.2.4 10III2016 CAMPAIGN

The calculation process proposed at Appendix A.1 is used for the results of the three point bending test for the 4 specimens of this campaign. The results and information related to this procedure is given at Table 53.

Table 53: Data for the 10III2016 campaign elastic modulus determination. Sizes in millimeters

<i>E</i> 10III2016	Plot	<i>D</i>	<i>S</i>	<i>B</i>	<i>a</i>	<i>h</i>	<i>P_u'</i> (kN)	<i>C_i</i> (μm/kN)	<i>E</i> (GPa)
B10III2016I	Figure 91	100	300	100	31.97	2	1.900	6.496	15.856
B10III2016II	Figure 92	100	300	100	30.40	2	2.059	3.658	25.900
B10III2016III	Figure 93	100	300	100	30.81	2	2.084	5.778	16.757
B10III2016IV	Figure 94	100	300	100	30.58	2	1.992	7.019	13.627

The result is a mean elastic modulus of 18.035GPa for the 10III2016 campaign, with a standard deviation of 5.406GPa.

The individual results for specimens I, III and IV are quite similar and for II is significantly different, as it can be seen at Figure 95.

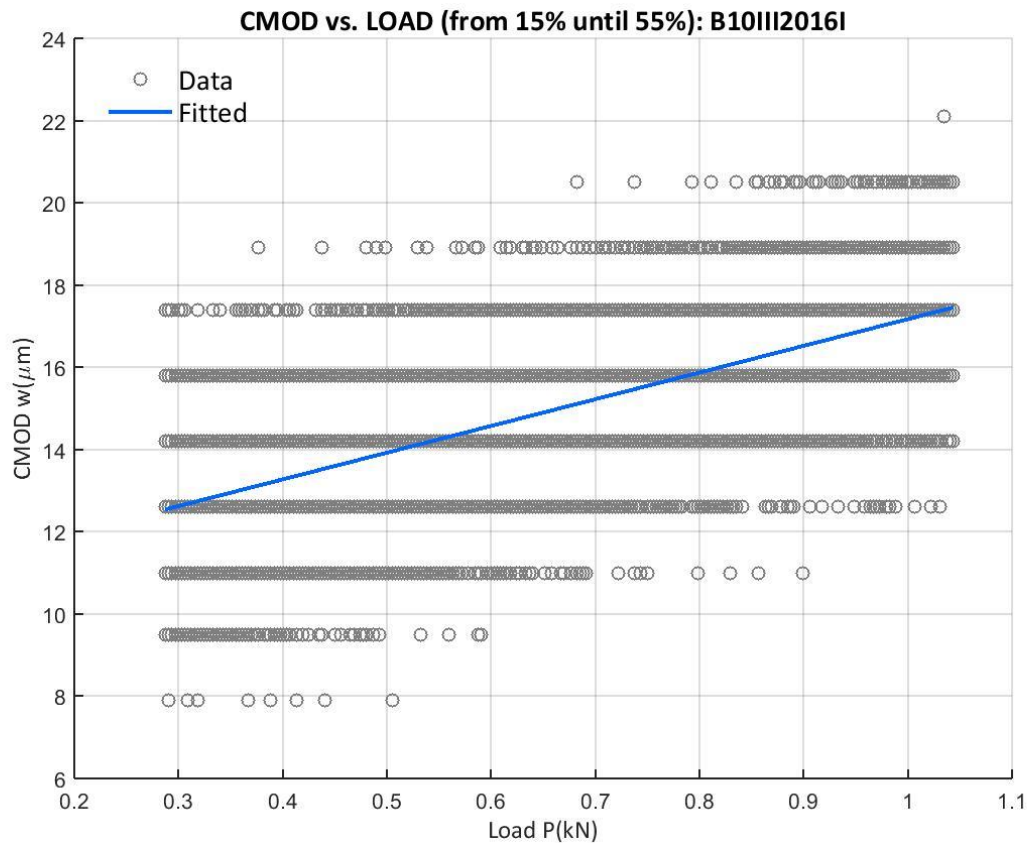


Figure 91: CMOD vs. Uncorrected Load from the 15% of the peak load up to 55% of B10III2016I

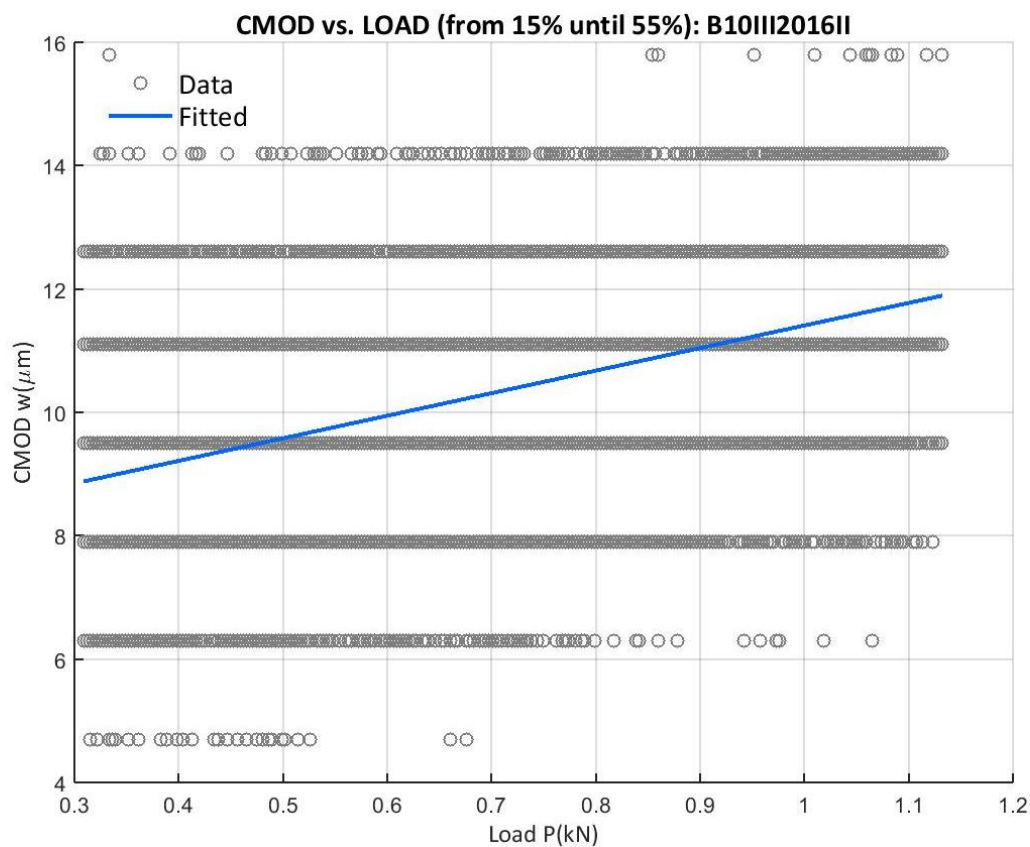


Figure 92: CMOD vs. Uncorrected Load from the 15% of the peak load up to 55% of B10III2016II

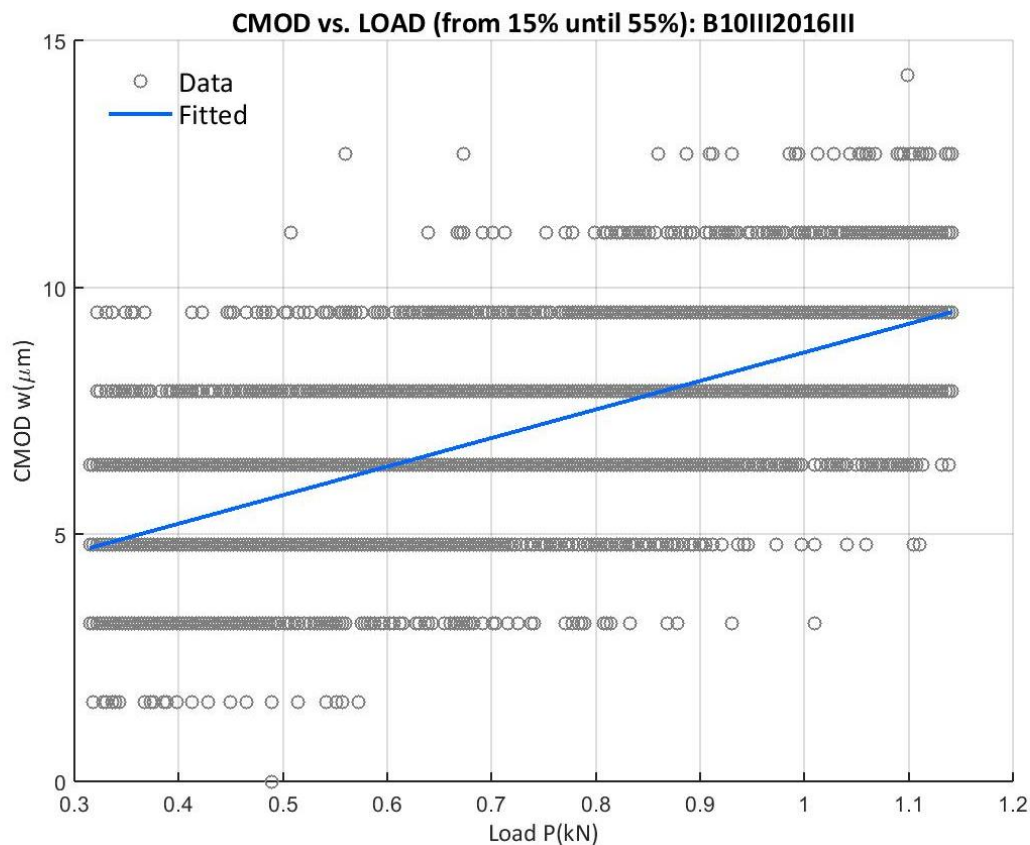


Figure 93: CMOD vs. Uncorrected Load from the 15% of the peak load up to 55% of B10III2016III

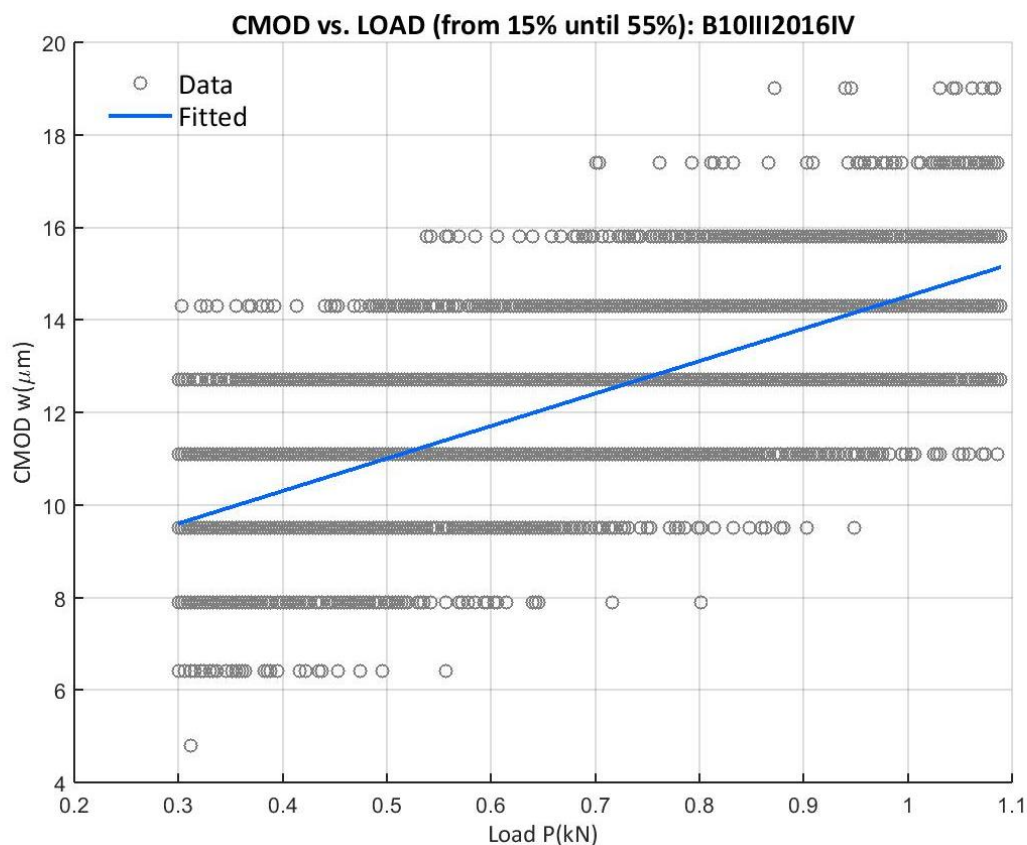


Figure 94: CMOD vs. Uncorrected Load from the 15% of the peak load up to 55% of B10III2016IV

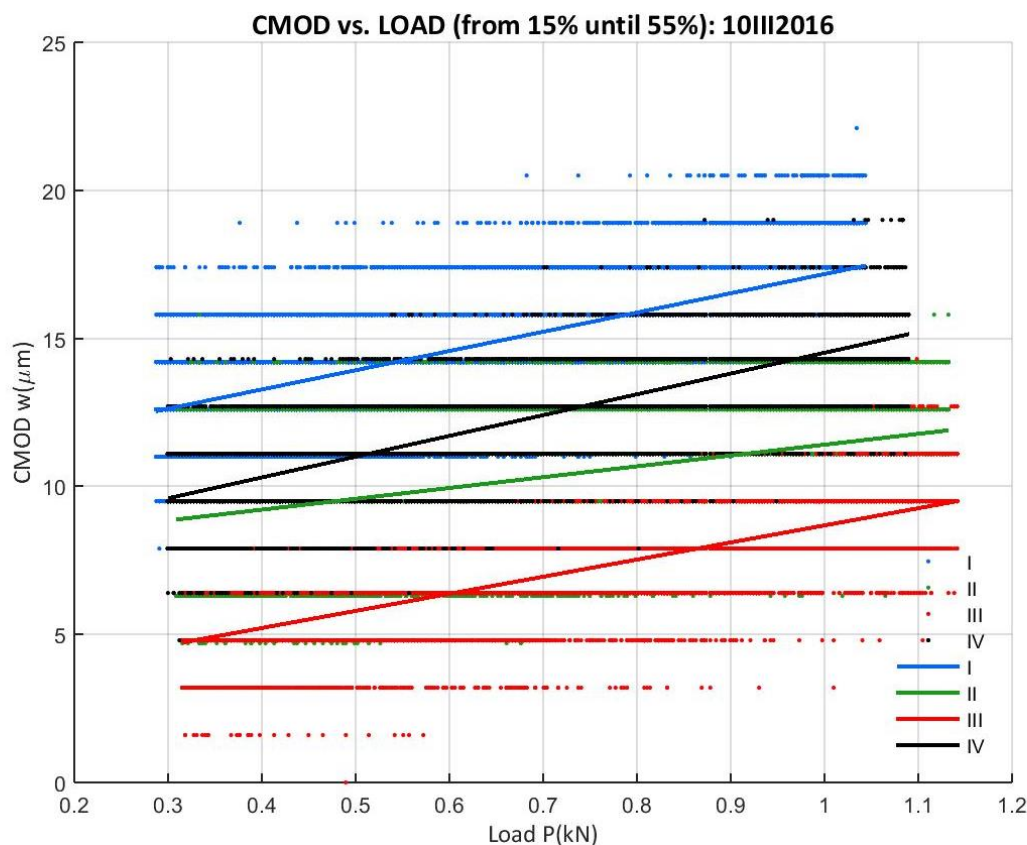


Figure 95: CMOD vs. Uncorrected Load from the 15% of the peak load up to 55% of all B10III2016

A.2.5 17III2016 CAMPAIGN

The methodology explained at Appendix A.1 is applied at the four bending tests for this campaign, giving the results visible at Table 54. The graphs for every single of them are attached along with a comparative one at Figure 100.

Table 54: Data for the 17III2016 campaign elastic modulus determination. Sizes in millimeters

<i>E</i> 17III2016	Plot	<i>D</i>	<i>S</i>	<i>B</i>	<i>a</i>	<i>h</i>	<i>P_u'</i> (kN)	<i>C_i</i> (μm/kN)	<i>E</i> (GPa)
B17III2016I	Figure 96	100	300	100	29.44	2	3.147	7.049	12.765
B17III2016II	Figure 97	100	300	100	31.62	2	3.617	7.354	13.744
B17III2016III	Figure 98	100	300	100	27.72	2	3.330	3.508	23.375
B17III2016IV	Figure 99	100	300	100	26.25	2	3.271	4.808	15.731

With these results one can determine an elastic modulus of 16.404GPa with a standard deviation of 4.808GPa.

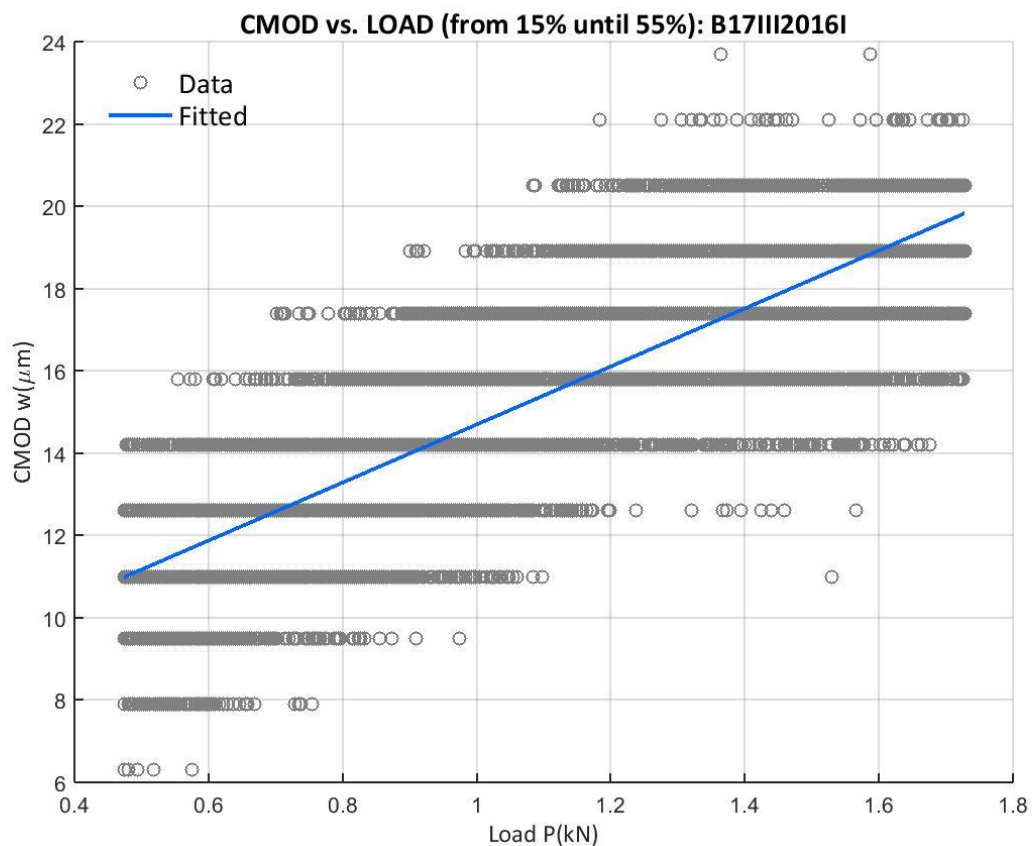


Figure 96: CMOD vs. Uncorrected Load from the 15% of the peak load up to 55% of B17III2016I

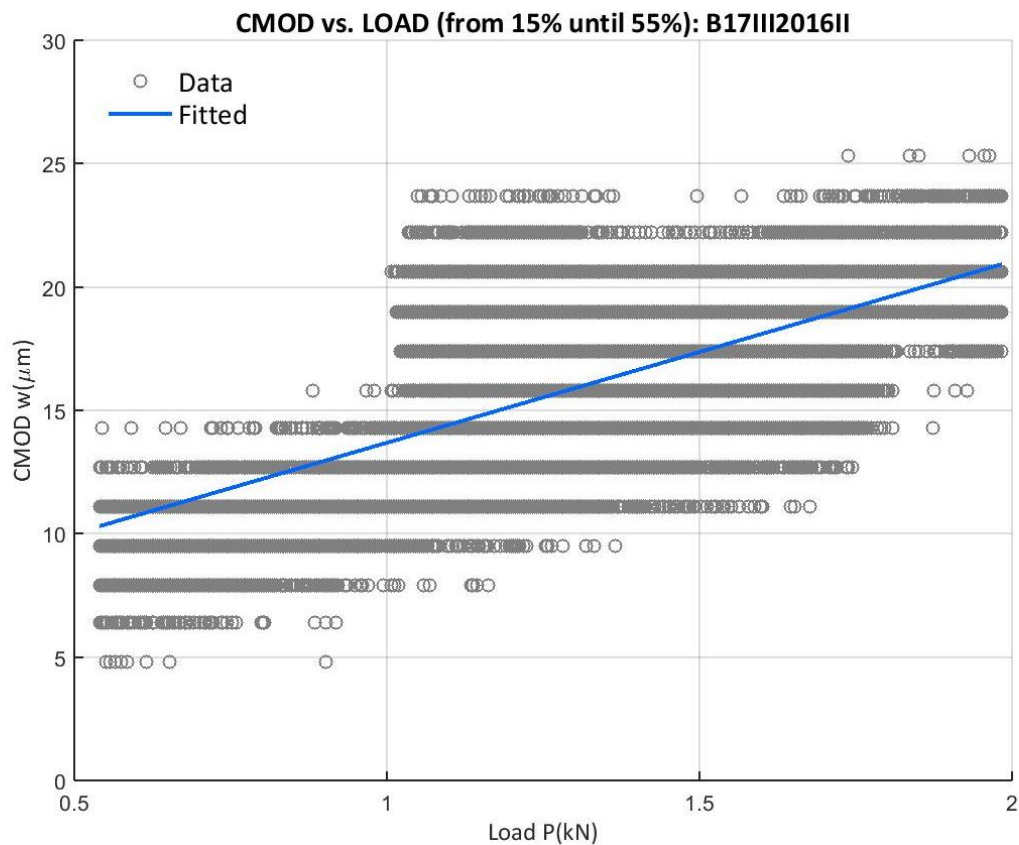


Figure 97: CMOD vs. Uncorrected Load from the 15% of the peak load up to 55% of B17III2016II

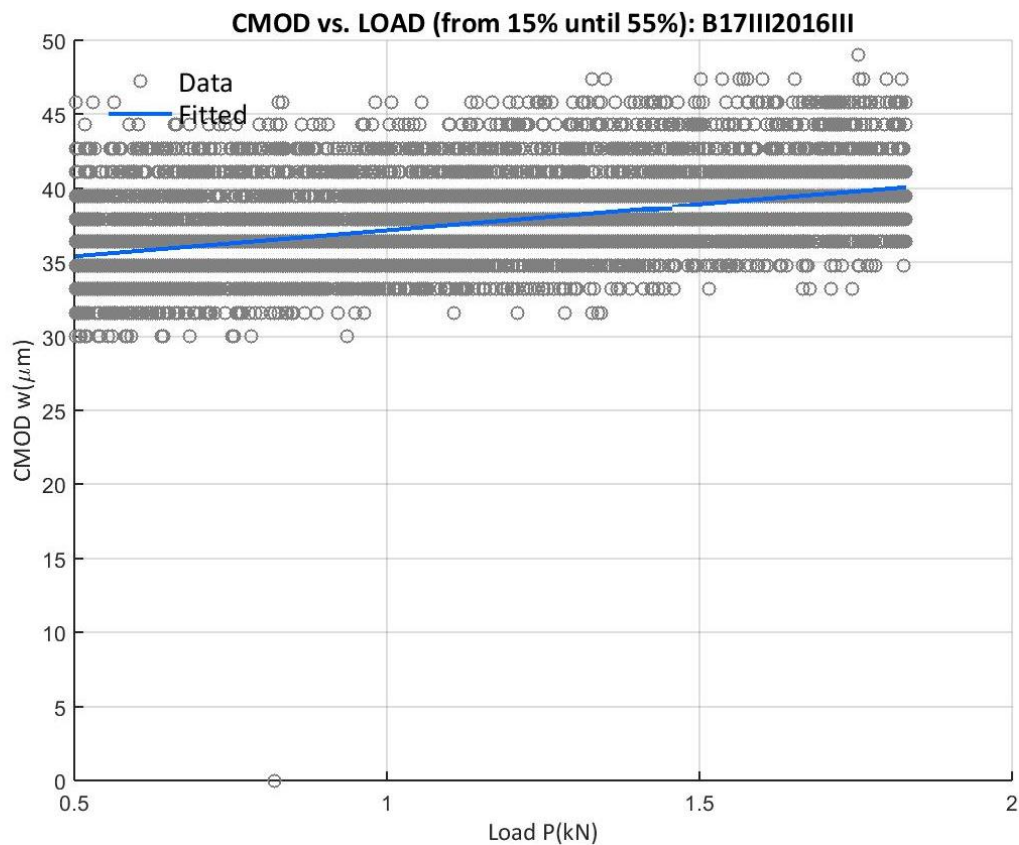


Figure 98: CMOD vs. Uncorrected Load from the 15% of the peak load up to 55% of B17III2016III

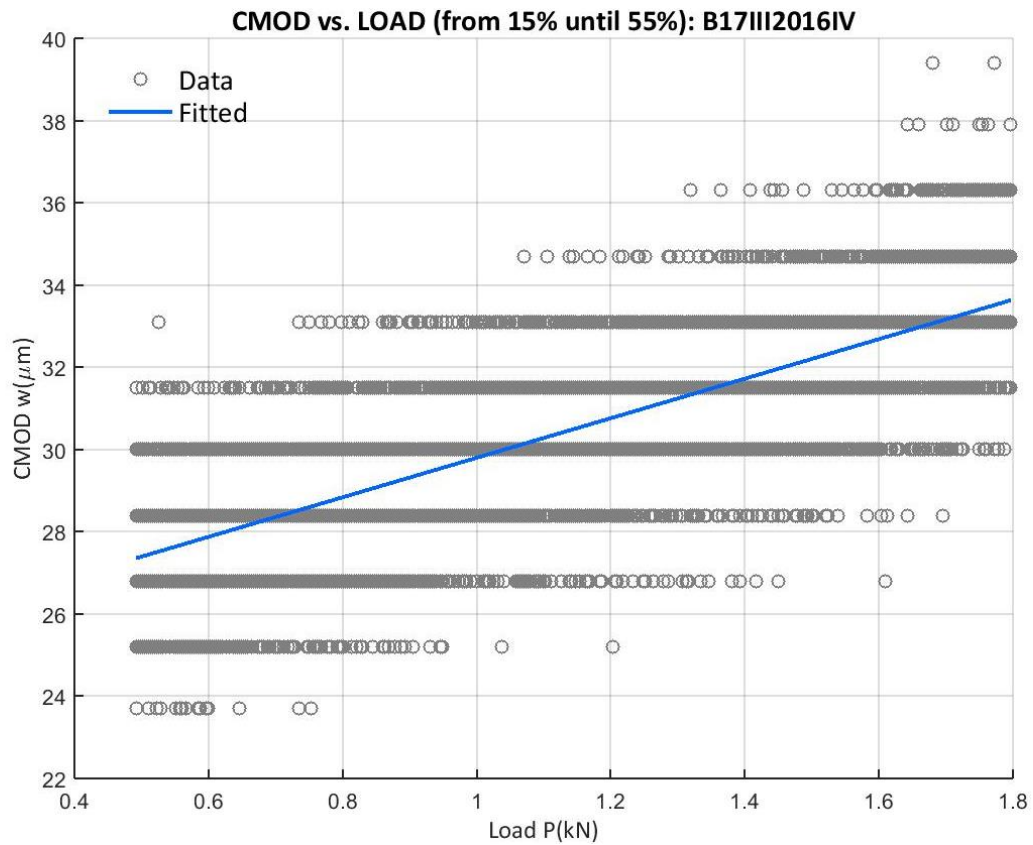


Figure 99: CMOD vs. Uncorrected Load from the 15% of the peak load up to 55% of B17III2016IV

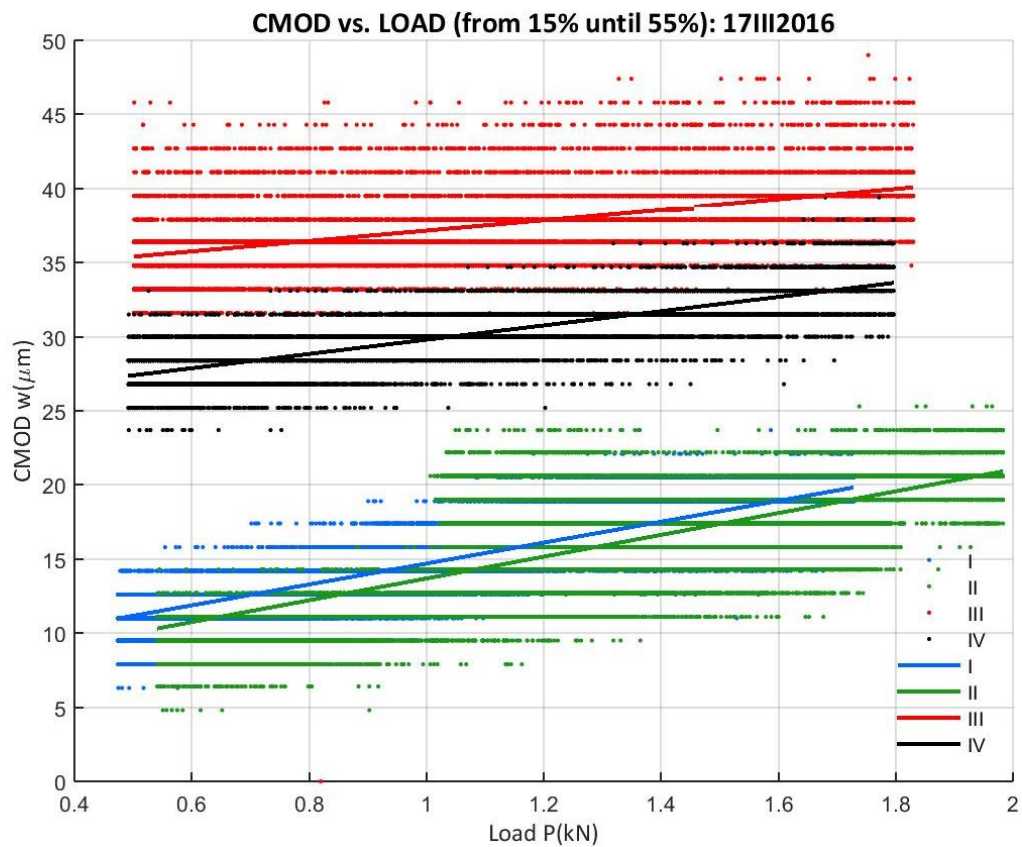


Figure 100: CMOD vs. Uncorrected Load from the 15% of the peak load up to 55% of all B17III2016

A.2.6 01IV2016 CAMPAIGN

The procedure detailed at Appendix A.1 is applied for 4 beam specimens with their performed three point bending tests, giving the results at Table 55. A comparison graph is given at Figure 105.

Table 55: Data for the 01IV2016 campaign elastic modulus determination. Sizes in millimeters

<i>E</i> 01IV2016	Plot	<i>D</i>	<i>S</i>	<i>B</i>	<i>a</i>	<i>h</i>	<i>P_u</i> '(kN)	<i>C_i</i> (μm/kN)	<i>E</i> (GPa)
B01IV2016I	Figure 101	100	300	100	30.10	2	2.800	2.292	40.668
B01IV2016II	Figure 102	100	300	100	29.73	2	2.944	4.054	22.541
B01IV2016III	Figure 103	100	300	100	30.03	2	2.916	2.928	31.712
B01IV2016IV	Figure 104	100	300	100	29.81	2	3.091	-2.255	-40.704

The result for B01IV2016IV is discarded because the elastic modulus has to be positive. The result for B01IV2016I is also discarded, because of a relatively high value for a compressive class near C12/16, where the higher values are near 33-35GPa¹⁷.

With these modifications, the final elastic modulus for this campaign is approx. 27.127GPa with a standard deviation of 6.485GPa.

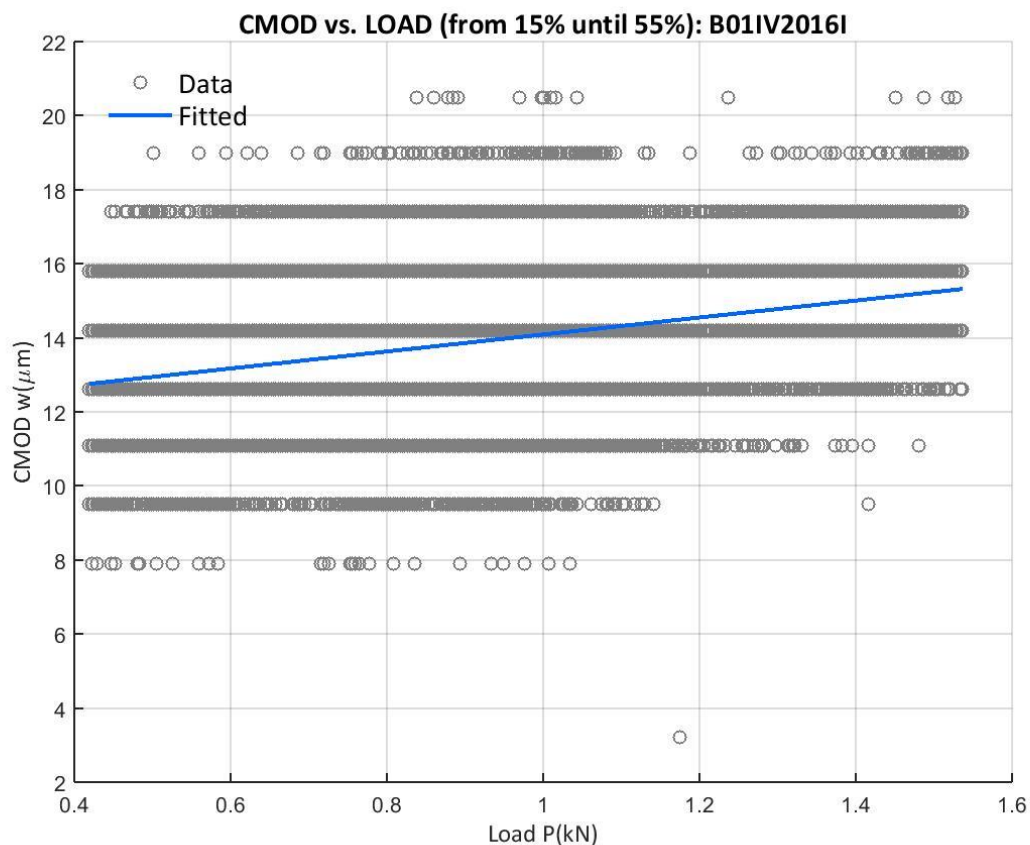


Figure 101: CMOD vs. Uncorrected Load from the 15% of the peak load up to 55% of B01IV2016I

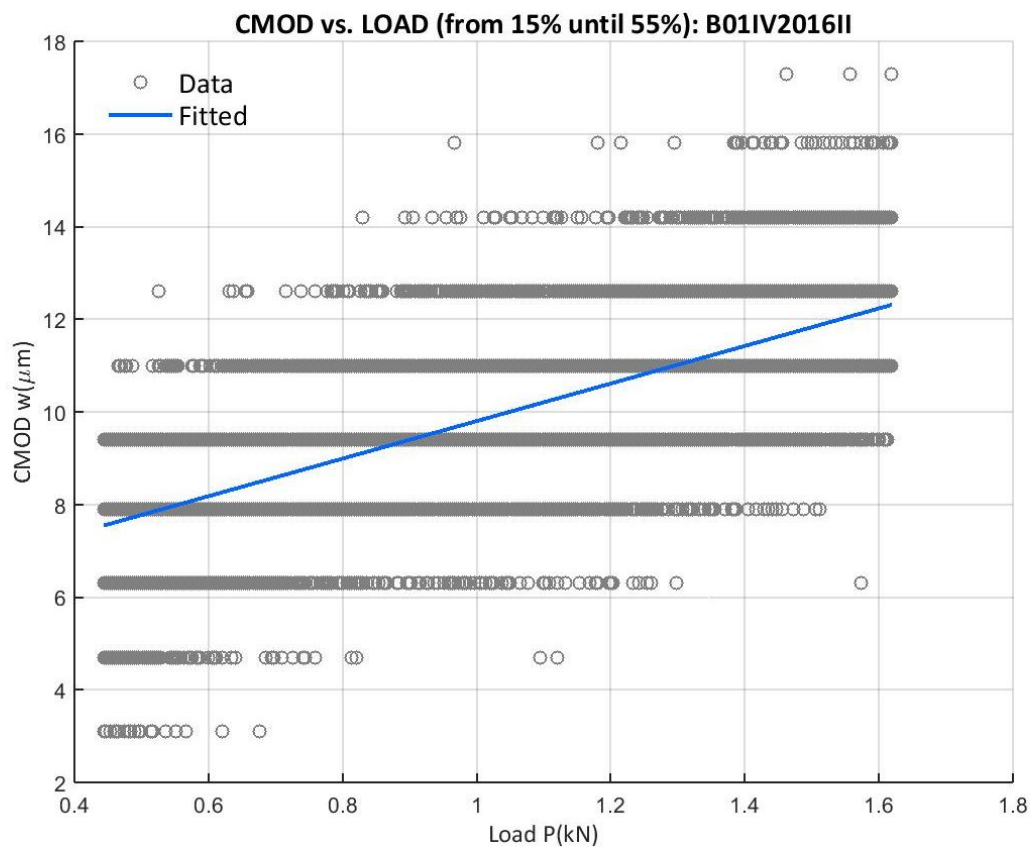


Figure 102: CMOD vs. Uncorrected Load from the 15% of the peak load up to 55% of B01IV2016II

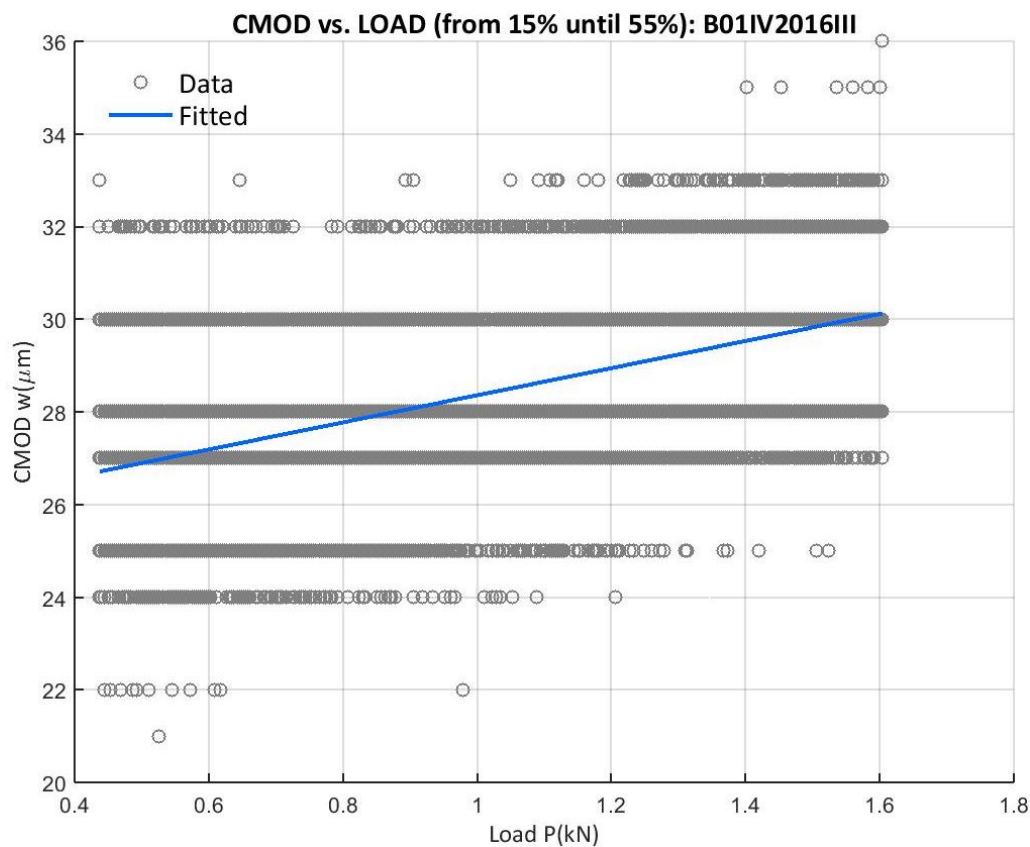


Figure 103: CMOD vs. Uncorrected Load from the 15% of the peak load up to 55% of B01IV2016III

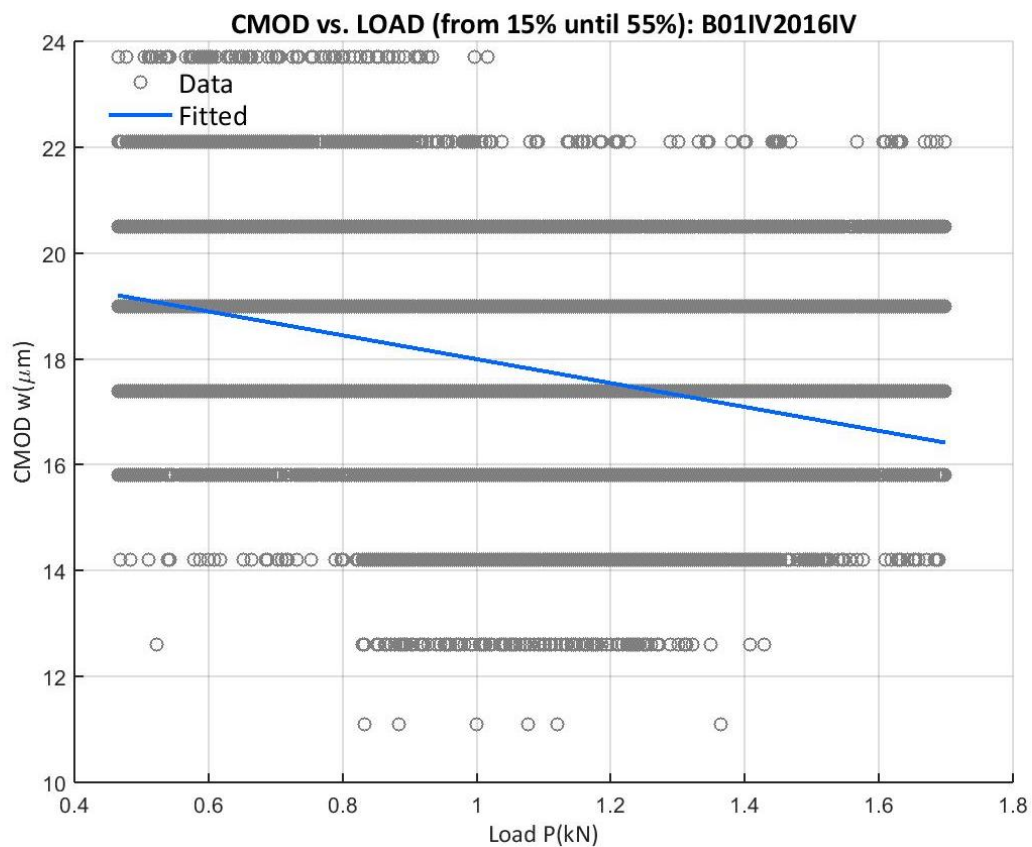


Figure 104: CMOD vs. Uncorrected Load from the 15% of the peak load up to 55% of B01IV2016IV

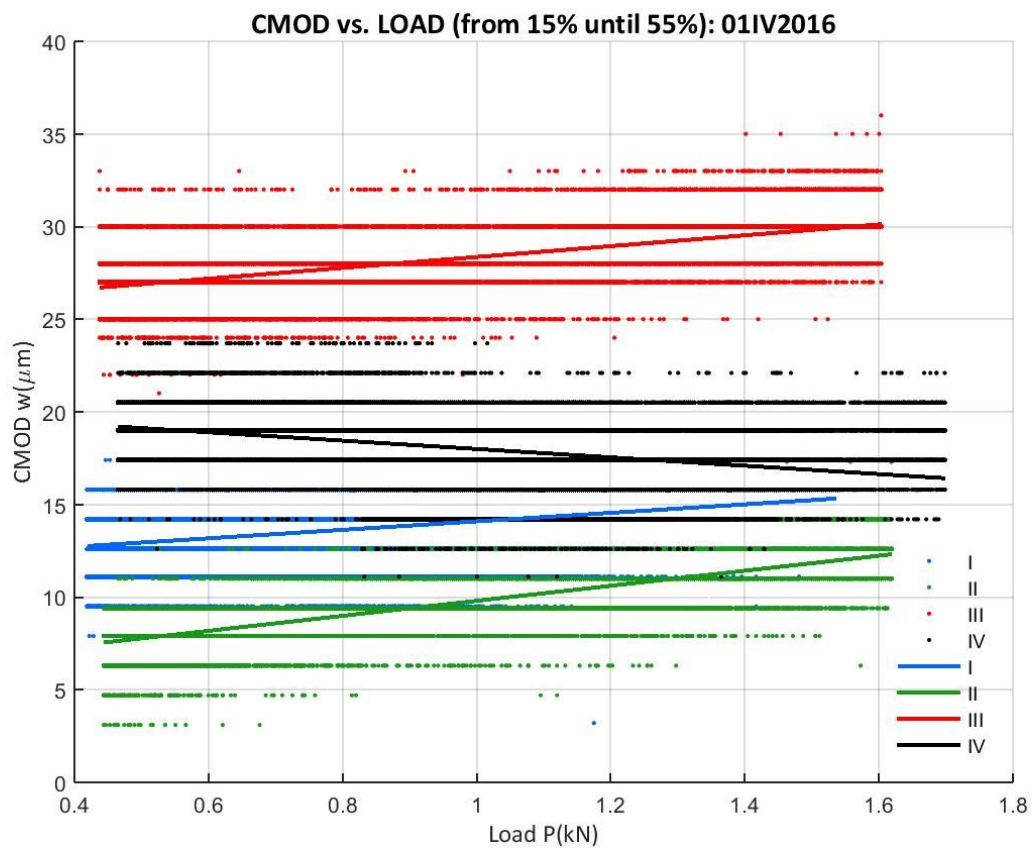


Figure 105: CMOD vs. Uncorrected Load from the 15% of the peak load up to 55% of all B01IV2016

A.2.7 07IV2016 CAMPAIGN

For four three point bending tests from the 07IV2016, the procedure detailed at Appendix A.1 is applied in order to find an approximation for the elastic modulus, giving the results shown at Table 56. A comparison graph is also given at Figure 110.

Table 56: Data for the 07IV2016 campaign elastic modulus determination. Sizes in millimeters

<i>E</i> 07IV2016	Plot	<i>D</i>	<i>S</i>	<i>B</i>	<i>a</i>	<i>h</i>	<i>P_v</i> '(kN)	<i>C_i</i> (μm/kN)	<i>E</i> (GPa)
B07IV2016I	Figure 106	100	300	100	29.71	2	3.436	4.556	20.038
B07IV2016II	Figure 107	100	300	100	29.93	2	3.488	3.393	27.231
B07IV2016III	Figure 108	100	300	100	29.81	2	3.430	3.525	26.036
B07IV2016IV	Figure 109	100	300	100	30.03	2	3.039	6.014	15.445

The mean elastic modulus for this campaign is 22.187GPa with a standard deviation of 5.487GPa.

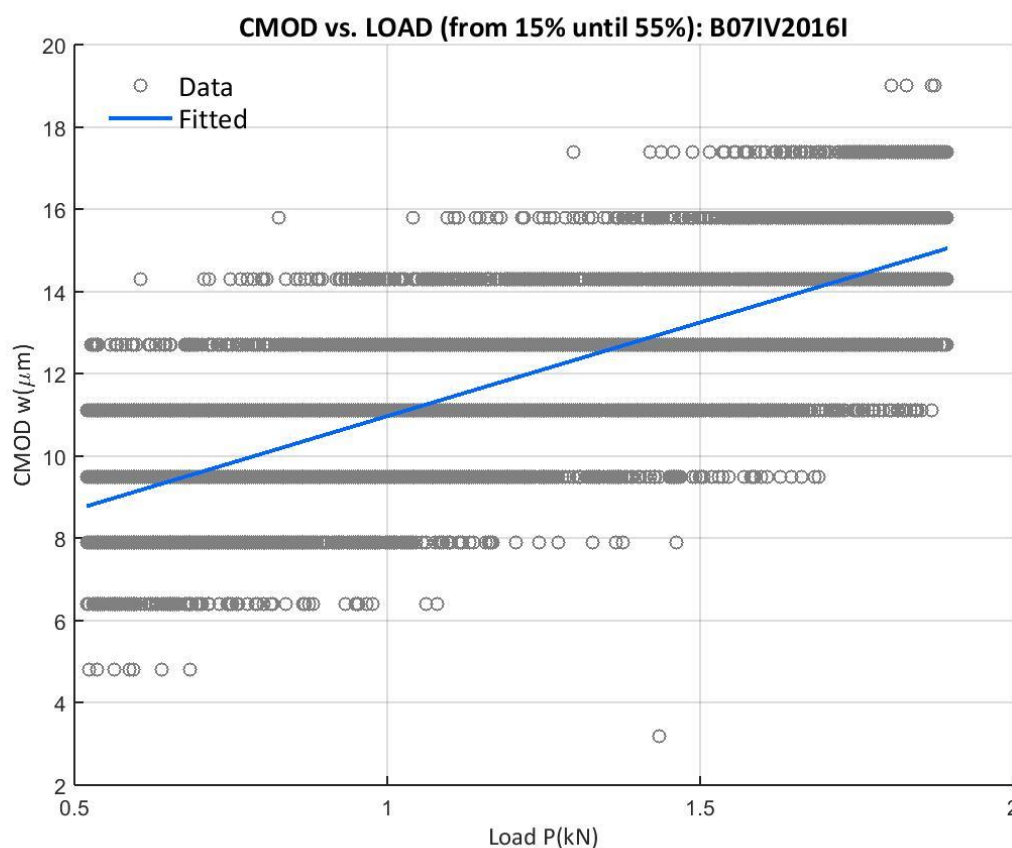


Figure 106: CMOD vs. Uncorrected Load from the 15% of the peak load up to 55% of B07IV2016I

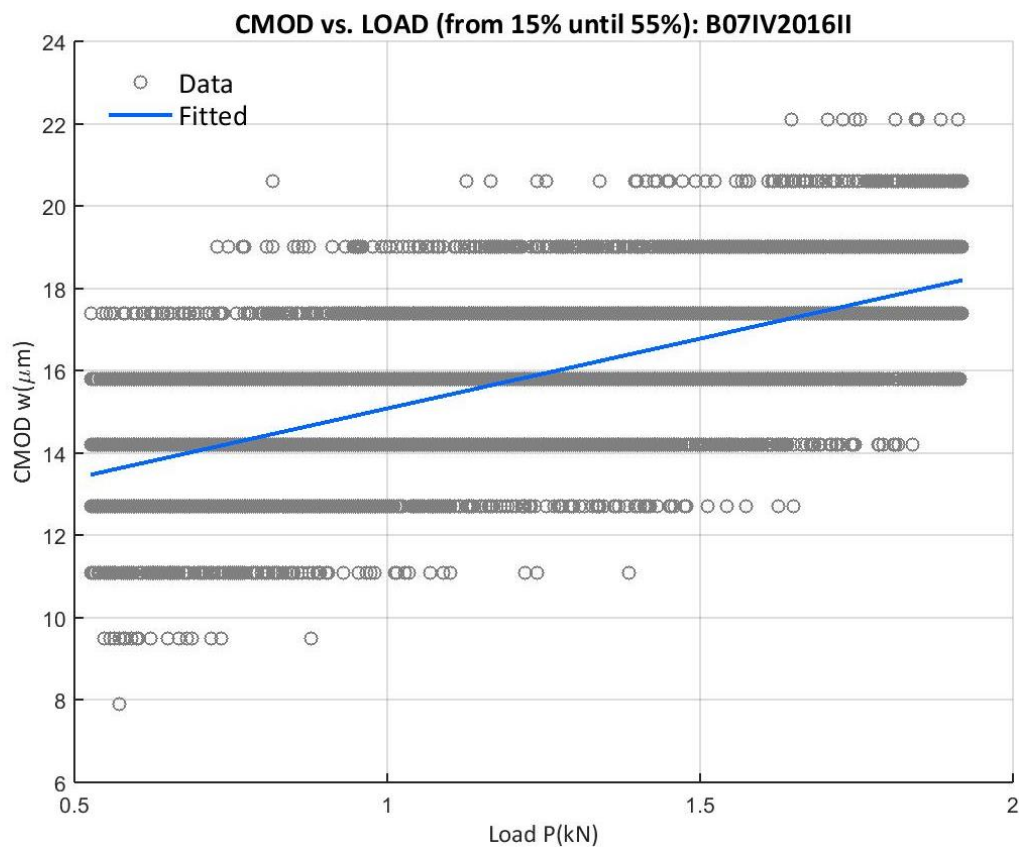


Figure 107: CMOD vs. Uncorrected Load from the 15% of the peak load up to 55% of B07IV2016II

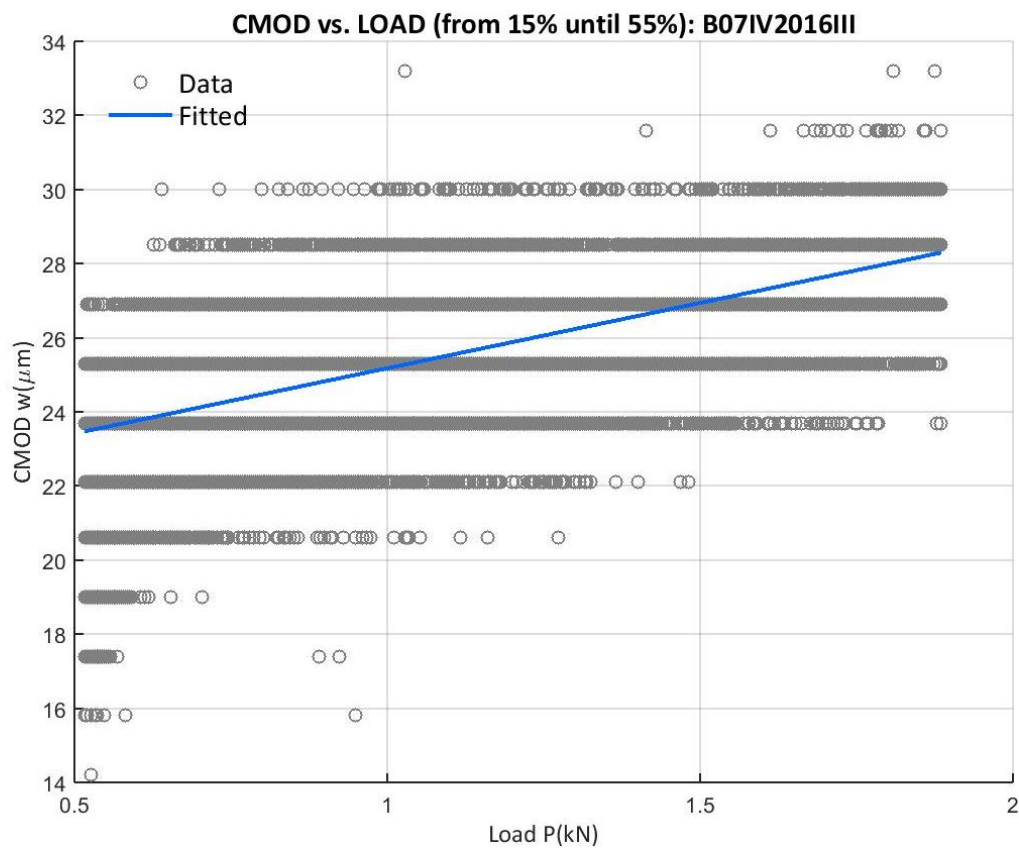


Figure 108: CMOD vs. Uncorrected Load from the 15% of the peak load up to 55% of B07IV2016III

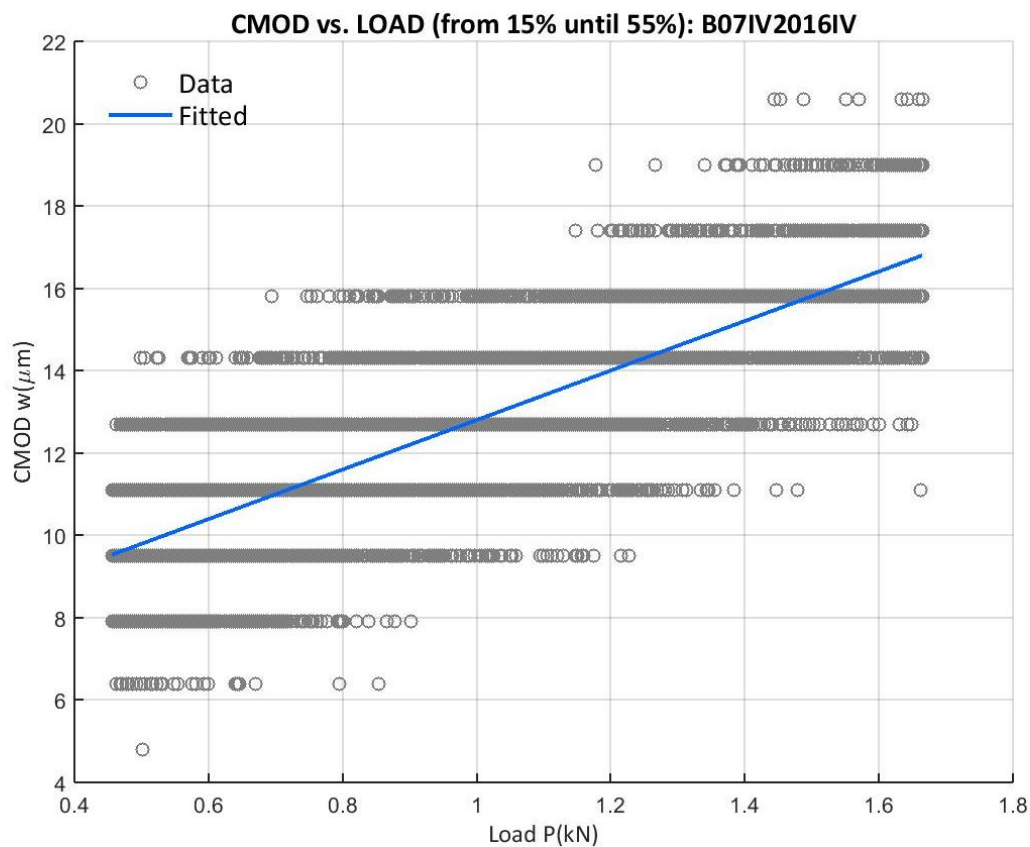


Figure 109: CMOD vs. Uncorrected Load from the 15% of the peak load up to 55% of B07IV2016IV

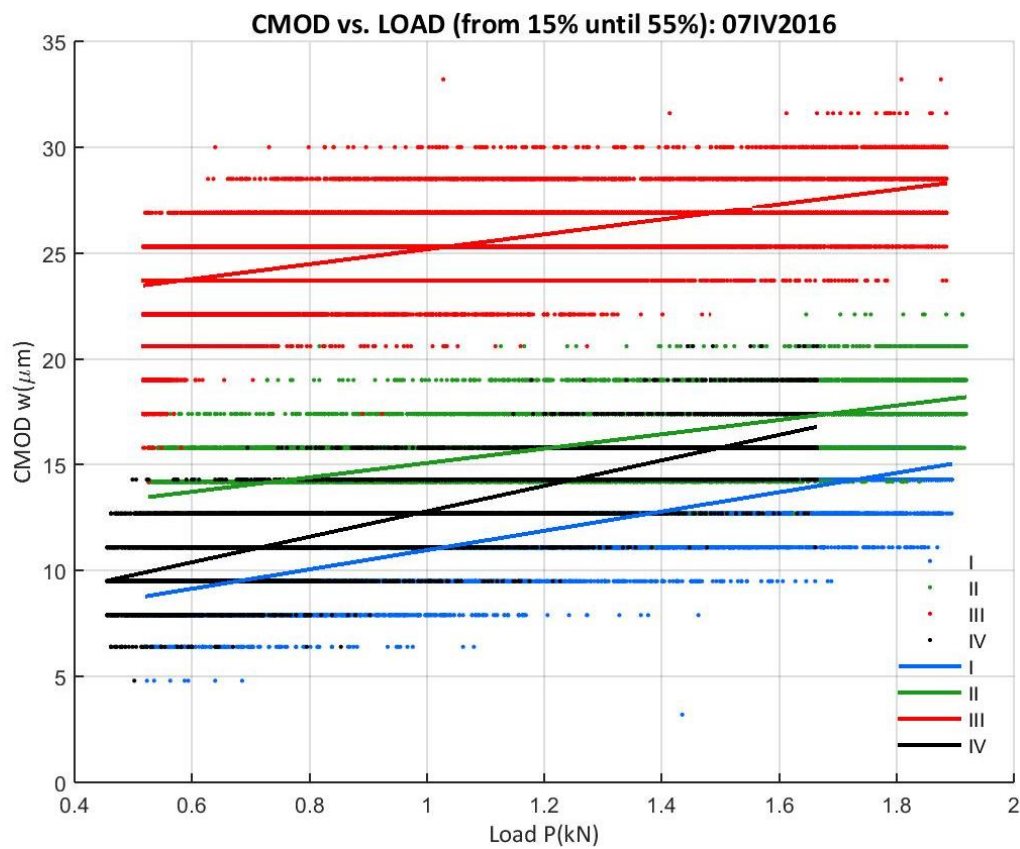


Figure 110: CMOD vs. Uncorrected Load from the 15% of the peak load up to 55% of all B07IV2016

A.2.8 14IV2016 CAMPAIGN

The process detailed at Appendix A.1 is applied four times for the 14IV2016, one per beam and their records from the three-point bend test. The results of this procedure are written at Table 57. A comparison graph is given at Figure 115.

Table 57: Data for the 14IV2016 campaign elastic modulus determination. Sizes in millimeters

<i>E</i> 14IV2016	Plot	<i>D</i>	<i>S</i>	<i>B</i>	<i>a</i>	<i>h</i>	<i>P_u</i> '(kN)	<i>C_i</i> (μm/kN)	<i>E</i> (GPa)
B14IV2016I	Figure 111	100	300	100	29.78	2	3.852	3.451	26.552
B14IV2016II	Figure 112	100	300	100	29.95	2	4.777	4.274	21.640
B14IV2016III	Figure 113	100	300	100	29.54	2	4.305	5.377	16.824
B14IV2016IV	Figure 114	100	300	100	29.66	2	4.247	3.990	22.821

The mean approximation for the elastic modulus from the 14IV2016 campaign is 21.959GPa with a standard deviation of 4.013GPa.

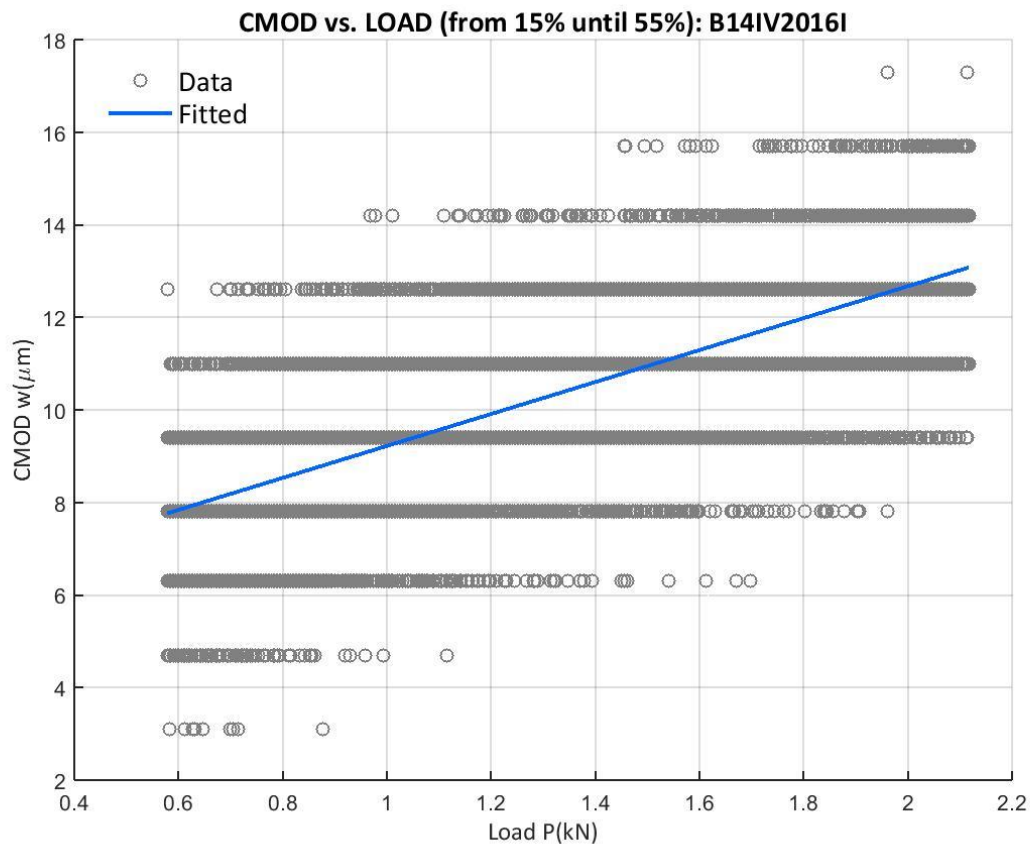


Figure 111: CMOD vs. Uncorrected Load from the 15% of the peak load up to 55% of B14IV2016I

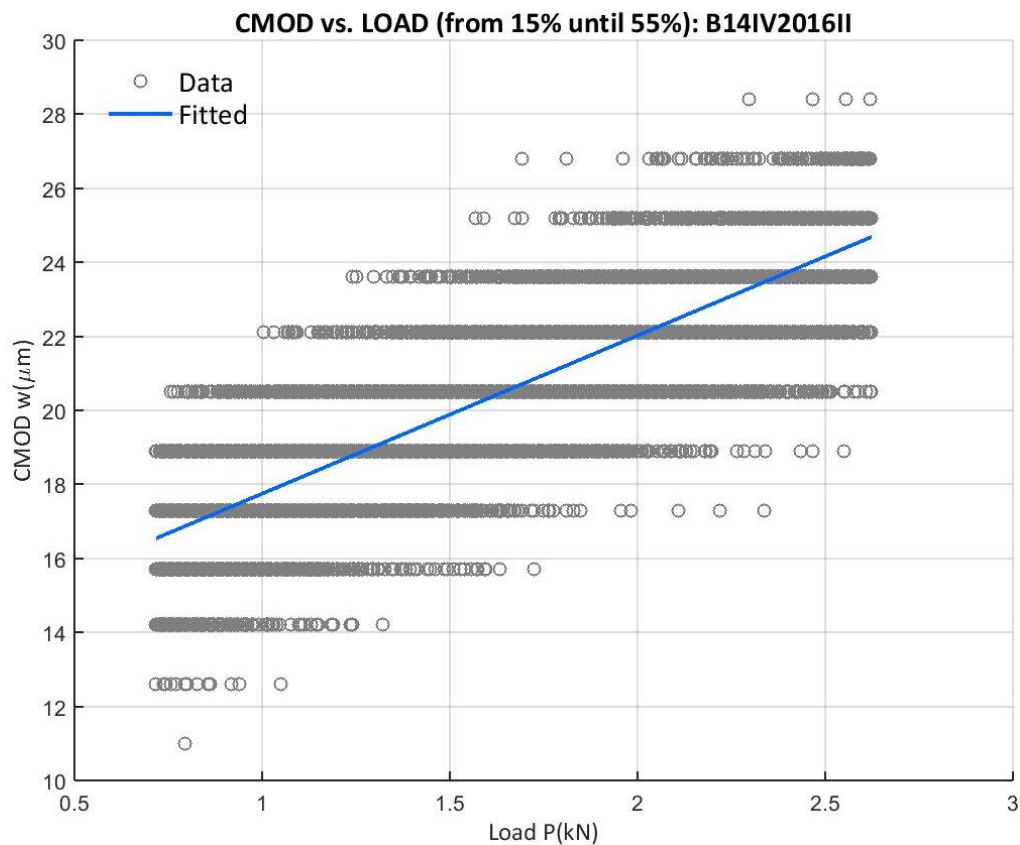


Figure 112: CMOD vs. Uncorrected Load from the 15% of the peak load up to 55% of B14IV2016II

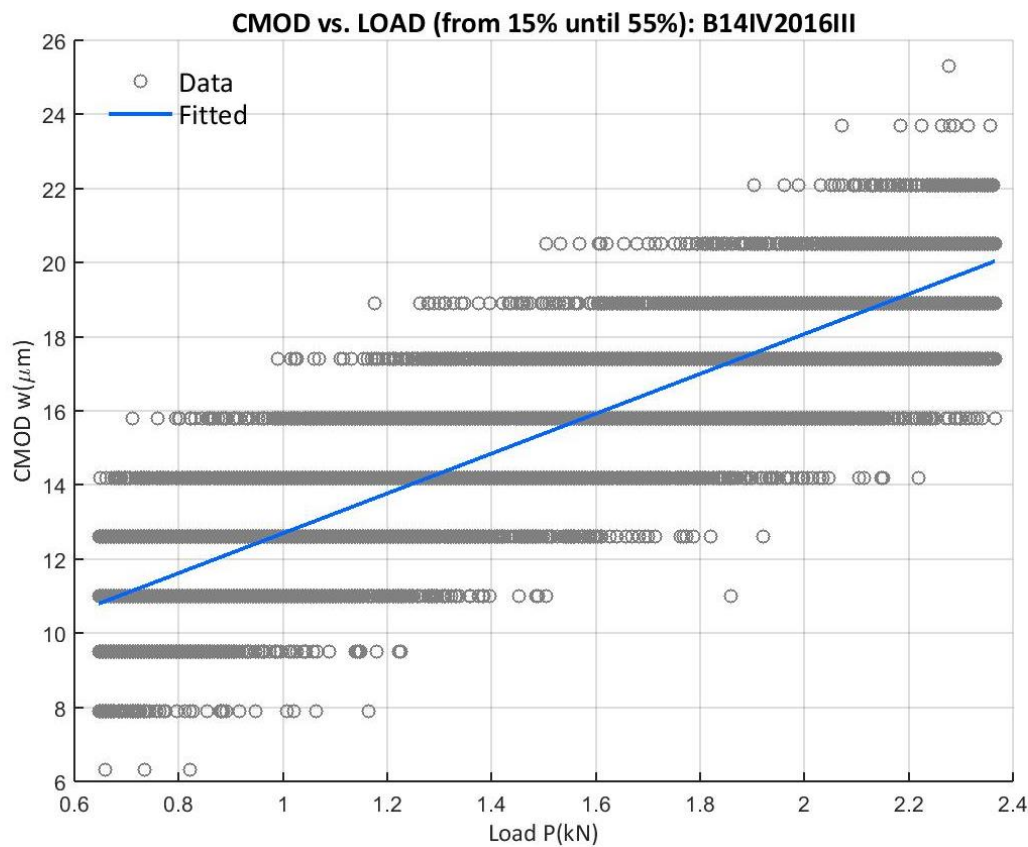


Figure 113: CMOD vs. Uncorrected Load from the 15% of the peak load up to 55% of B14IV2016III

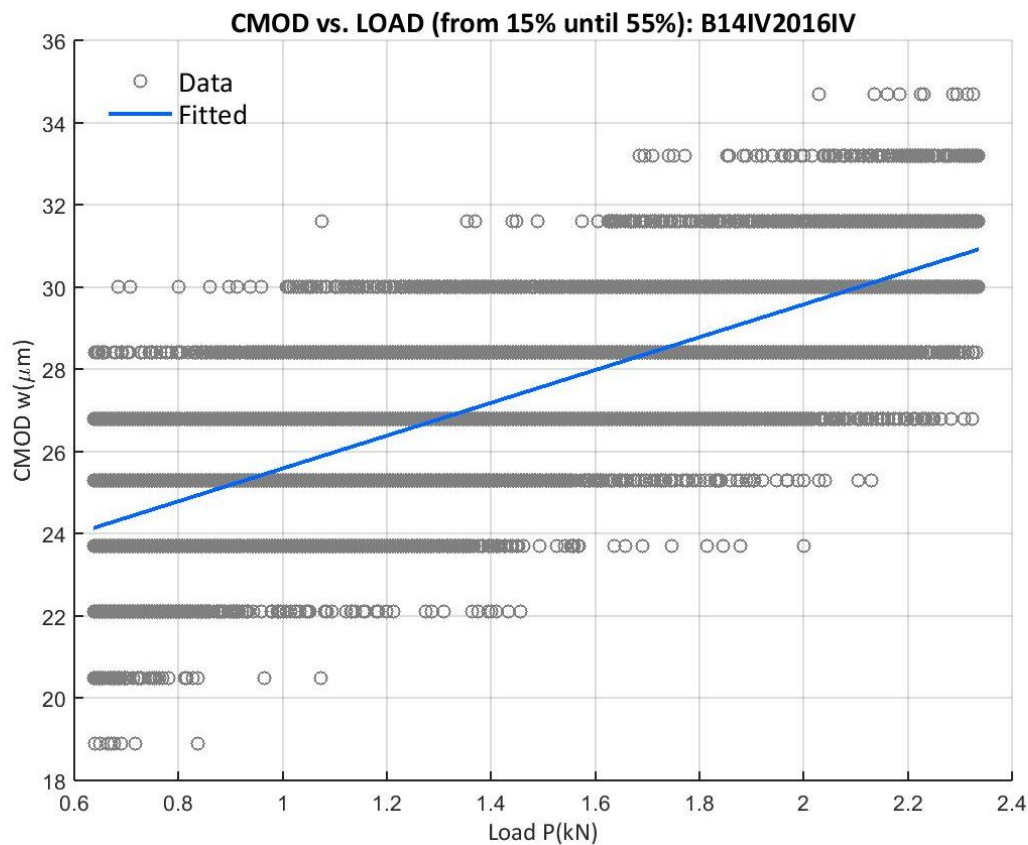


Figure 114: CMOD vs. Uncorrected Load from the 15% of the peak load up to 55% of B14IV2016IV

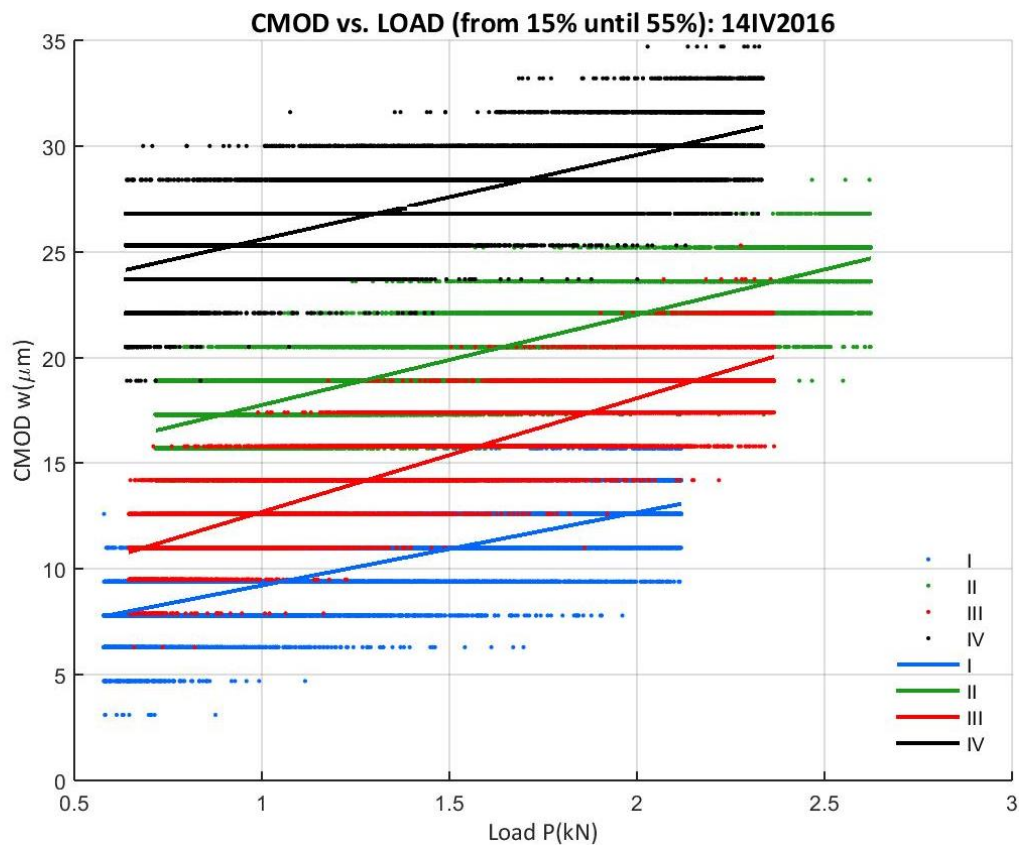


Figure 115: CMOD vs. Uncorrected Load from the 15% of the peak load up to 55% of all B14IV2016

A.2.9 21IV2016 CAMPAIGN

The methodology detailed at Appendix A.1 is applied to four three-point bending tests in order to find an approximation for the elastic modulus. The results for every single test are given at Table 58, with their graphs and a comparative graph at Figure 120.

Table 58: Data for the 21IV2016 campaign elastic modulus determination. Sizes in millimeters

<i>E</i> 21IV2016	Plot	<i>D</i>	<i>S</i>	<i>B</i>	<i>a</i>	<i>h</i>	<i>P_v</i> '(kN)	<i>C_i</i> (μm/kN)	<i>E</i> (GPa)
B21IV2016I	Figure 116	100	300	100	29.88	2	2990.7	3.697	24.922
B21IV2016II	Figure 117	100	300	100	29.98	2	3012.2	3.759	24.643
B21IV2016III	Figure 118	100	300	100	29.78	2	3027.5	3.764	24.344
B21IV2016IV	Figure 119	100	300	100	29.83	2	3382.9	4.302	21.361

The mean elastic modulus for the 21IV2016 campaign is 23.818GPa with a standard deviation of 1.655GPa.

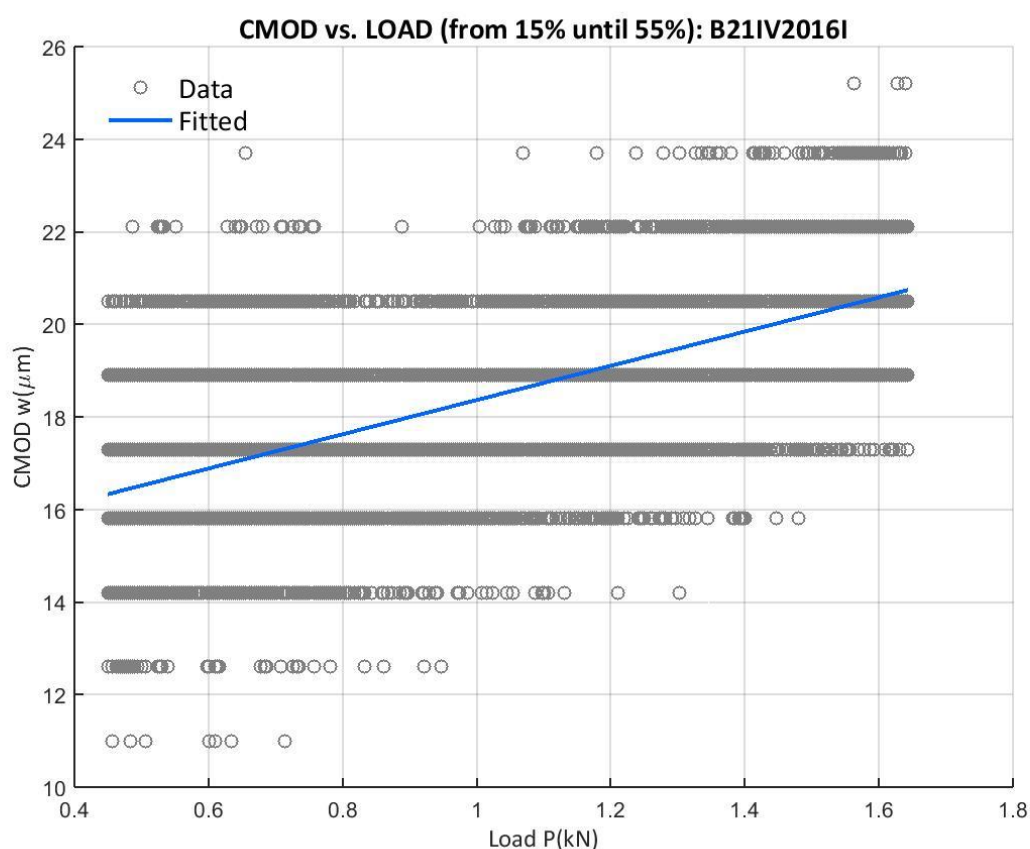


Figure 116: CMOD vs. Uncorrected Load from the 15% of the peak load up to 55% of B21IV2016I

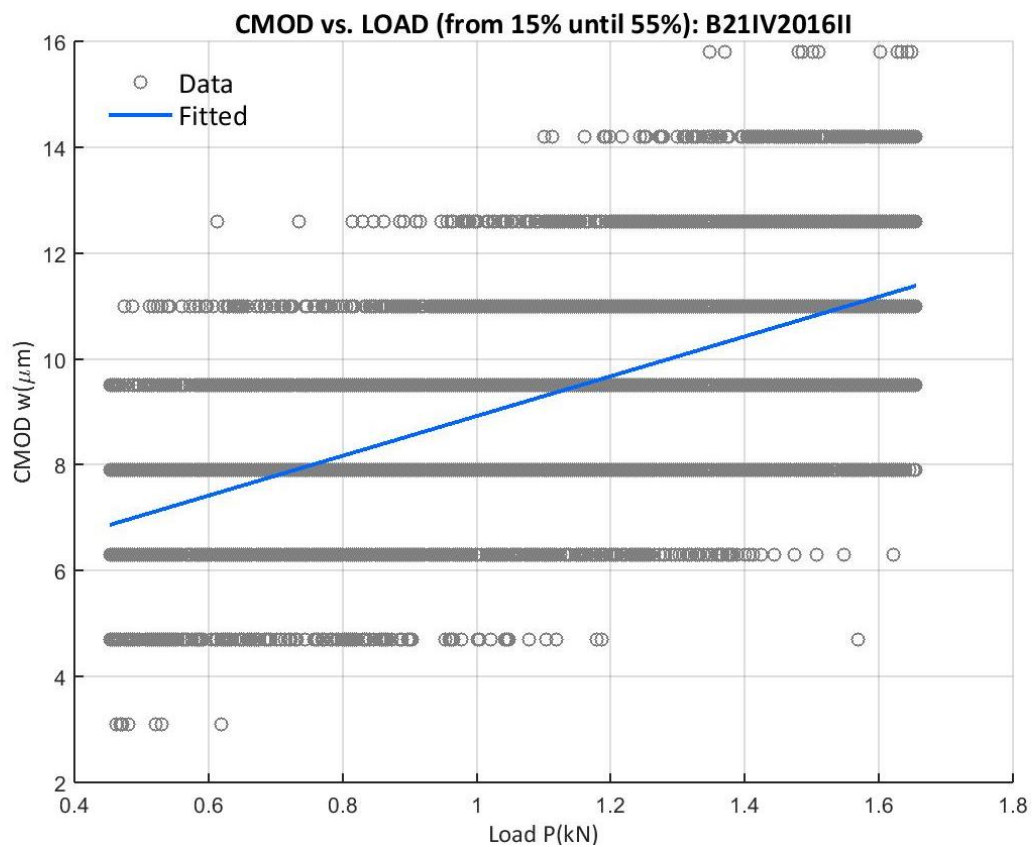


Figure 117: CMOD vs. Uncorrected Load from the 15% of the peak load up to 55% of B21IV2016II

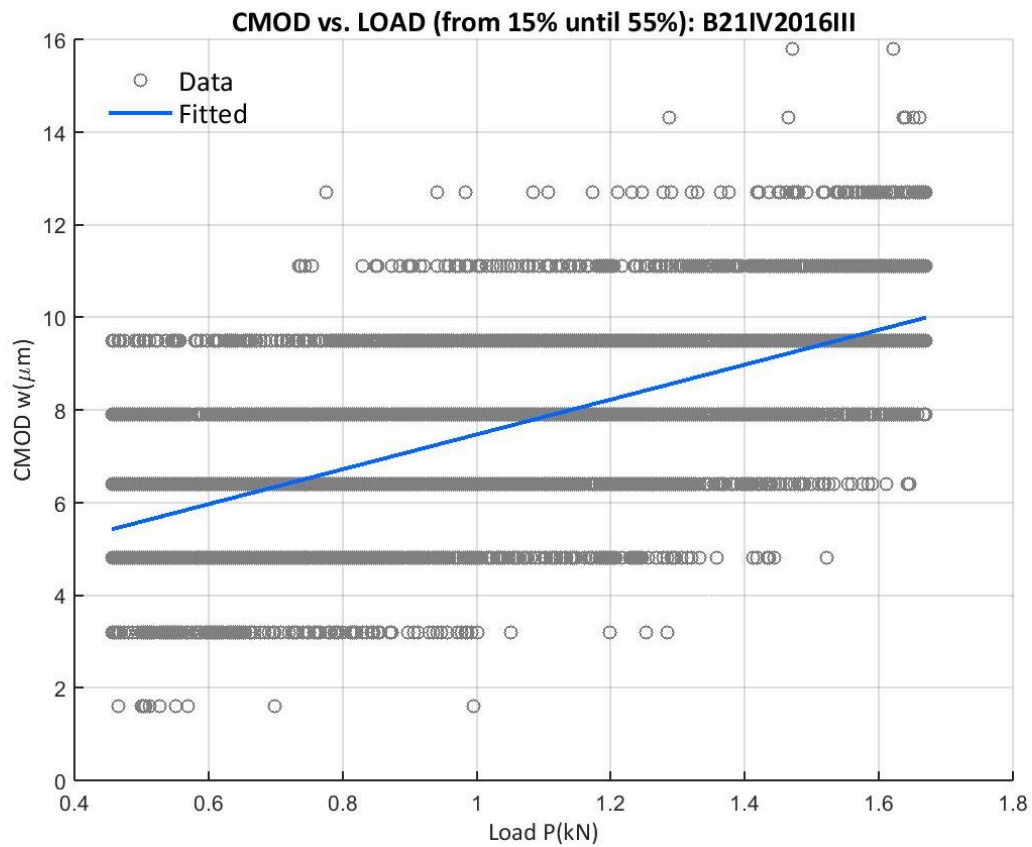


Figure 118: CMOD vs. Uncorrected Load from the 15% of the peak load up to 55% of B21IV2016III

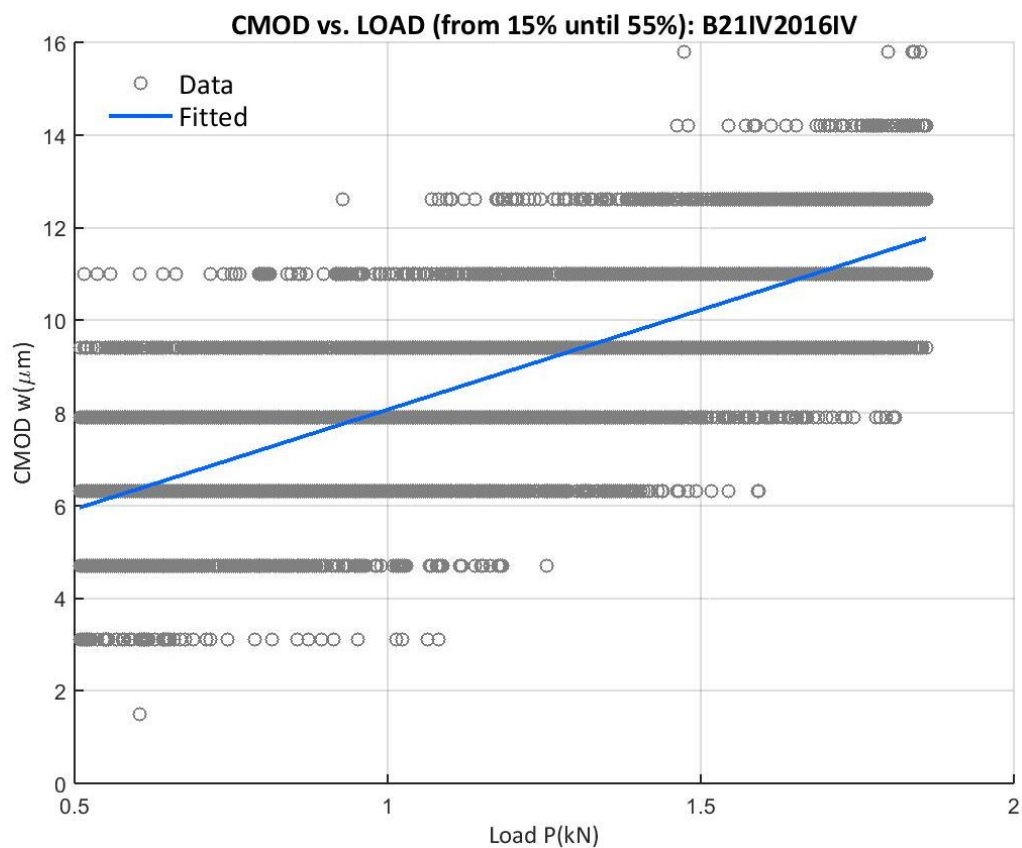


Figure 119: CMOD vs. Uncorrected Load from the 15% of the peak load up to 55% of B21IV2016IV

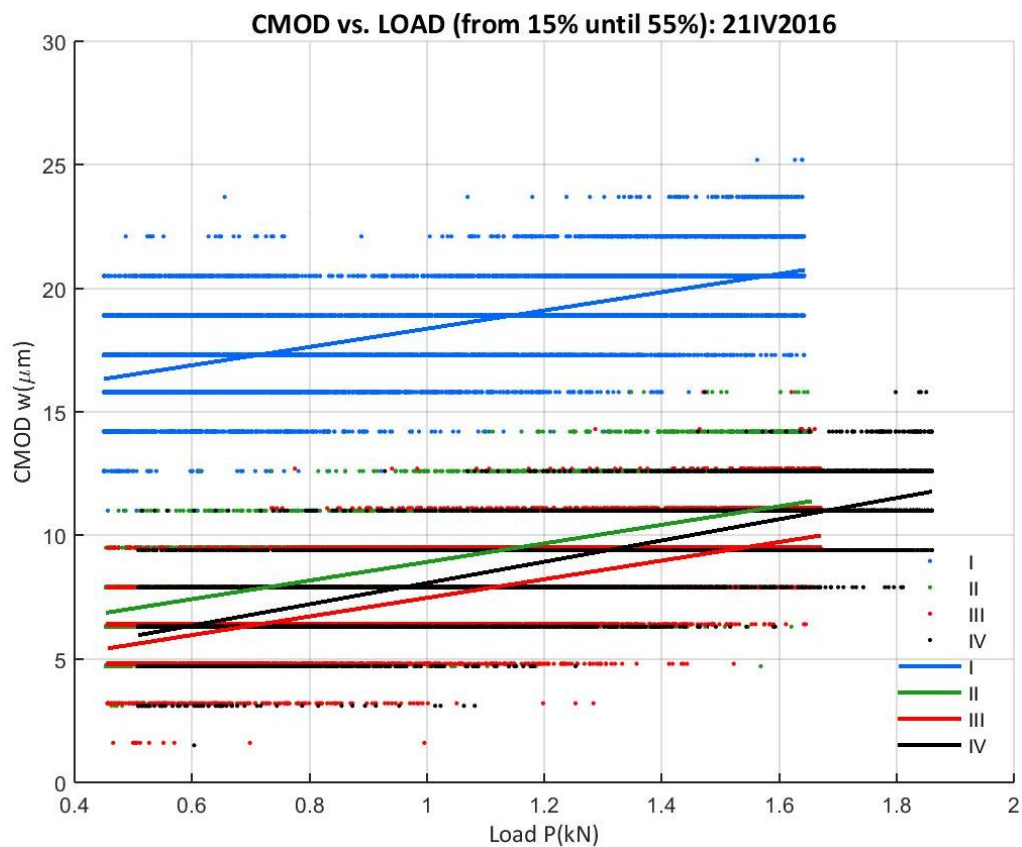


Figure 120: CMOD vs. Uncorrected Load from the 15% of the peak load up to 55% of all B21IV2016

A.3 DETERMINATION OF THE TENSILE STRENGTH OF CONCRETE BY A BRAZILIAN TEST

The procedure used to obtain the tensile strength f_t of concrete is a Brazilian, or indirect tensile strength, test ^{32,33}, in which the specimen shape, dimensions and the loading method is shown at Figure 121, both cylindrical and cubic specimens.

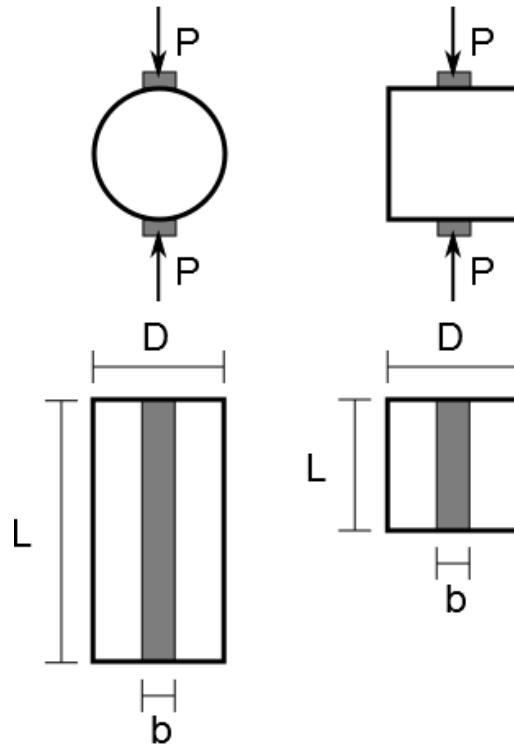


Figure 121: Sketch of a Brazilian test for cylindrical (left) and cubic (right) specimens with the bearing strip position (in grey)

With Equation A.3.1, f_t is found.

$$f_t = \frac{2P_u}{\pi DL} \quad (A.3.1)$$

Where P_u is the maximum load applied and D and L are the specimen sizes, visible at Figure 121.

The dimensions for cylindrical and cubic specimens will be chosen from the nominal dimensions recommended by normalized test procedures ³⁴:

- Cylindrical specimens will have a length double than the diameter, chosen from the nominal dimensions recommendation as 150 millimeters.
- Cubic specimens will have a constant edge length, chosen from the nominal recommendation, of 150 millimeters.

Fracture must develop vertically to be a satisfactory test. A part of the code at C.1.2 applies this.

A.3.1 BRAZILIAN TEST APPARATUS

In order to perform an indirect tensile strength test, we have the following elements:

- A *SERVOSIS* company compression testing machine, *MES* series, model 200, from the year 2007, working at 380V with a three-phase electric network (Figure 122). The series is made for testing on concrete, rocks, cements and construction materials and they are built according the code exposing the specifications for testing on concrete³⁵, condition required by the codes of the concrete tensile strength determination³³ at its Chapter 4, with a precision Class 1 according the code of application on compression testing machines and their calibration³⁶. This data and further information is given at the catalogue from the company, which can be found at the following link: http://www.servosis.com/assets/2_21_serie_mes.pdf.



Figure 122: Compression testing machine SERVOSIS MES-200

- As the position of the specimen makes impossible the contact, stiff slabs will be placed on the support surface, making so that the piston maximum displacement arrives properly to the specimen to test. These slabs can be seen at the bottom part of Figure 123.

- The improvement of the contact of the piston with the specimen is done thanks to a thick enough plate fixed at the piston (Figure 123), with a mechanism to avoid the dispersion of the broken specimen, based on two lateral supports and a spring to join the frontal part. Cylinder-type specimens of 150mm of diameter and 300mm length fit perfectly at this support.



Figure 123: Machine configuration for a Brazilian test

The fracture must develop vertically of a cylinder-type specimen, so it completely splits on two similar semi-cylinders (see Figure 124).



Figure 124: Result of a Brazilian test

A.3.2 BRAZILIAN TEST CONFIGURATION

The molds available only allow creating cylindrical-type specimens of 150mm diameter and 300mm long, which fit correctly to the available elements to perform an indirect tensile strength test. For this reason, these will be the only specimens on which this test will be carried out.

The control is done by the computer of the machine and the software *PCD2K*. The appearance of the software is similar to Figure 125, running at the *Windows XP* platform. There are some modules on the screen at Figure 125:

- *Medida de Canal 2* (Measure at Channel 2): shows the on-live piston position, in millimeters
- *Medida de Canal 1* (Measure at Channel 1): the same but with the piston force, in tones
- *Trazador* (Tracer): shows the test plot force versus displacement (if X-Y plot is on)
- *Generador de funciones* (Function generator): this is the window to create the control orders to perform the tests (Figure 126)
- *Controles* (Control): this is the window to control the piston action manually, with the up and down buttons, or automatically according the introduced function with Test ON (*Ensayo MARCHA*). Also the tracer recording at *Trazador* and the main power of the pump group (*Grupo hidráulico*)

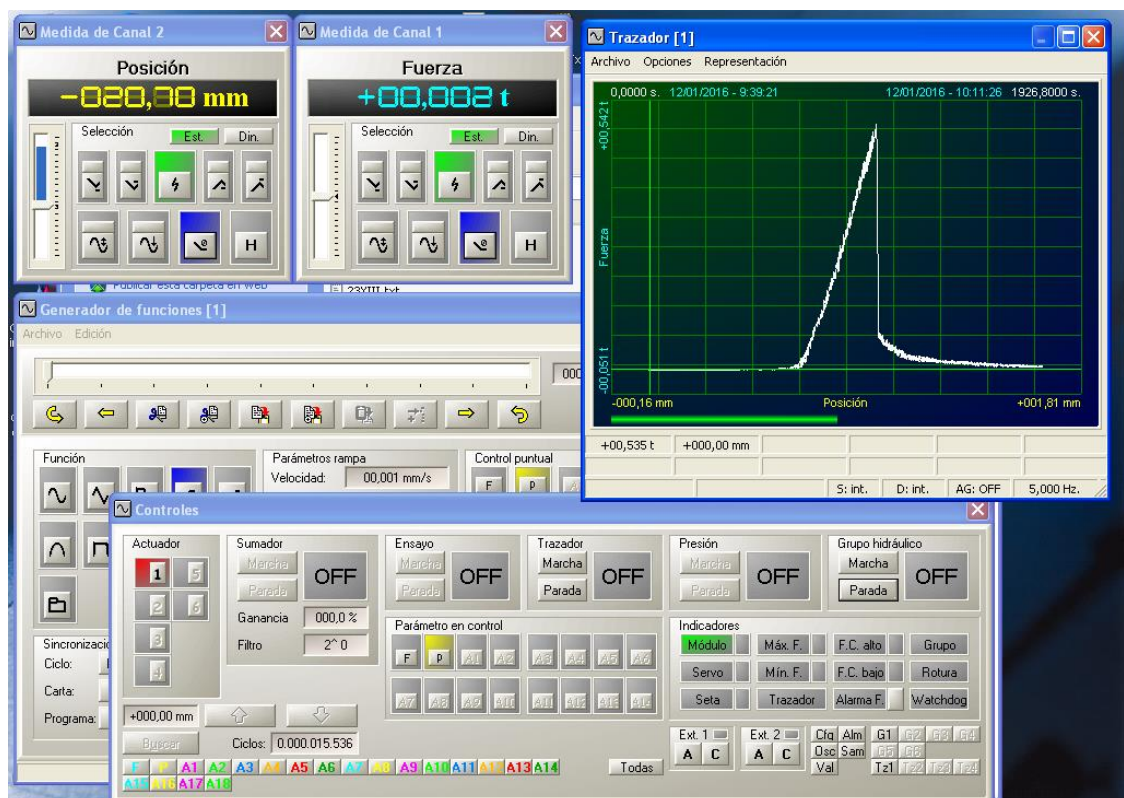


Figure 125: PCD2K control program windows

We want to introduce a force ramp function, so we set the function on *Ramp* at the function generator and the control on force, this is at Figure 126, select the *Control puntual* element on *F* (force), thus the ramp parameters speed (*Velocidad*) and acceleration (*Aceleración*) will change from millimeters to tones.

The calibration is done by the builder of the machine and it is:

- 100mV for the load sensor are 2000kg applied
- 100mV for the displacement sensor is 1mm of movement

When a compression direction of the piston is desired, the direction of the *MES-200* machine (*Destino*) must be set to +100mm, the maximum, placing the Amplitude Control on position.

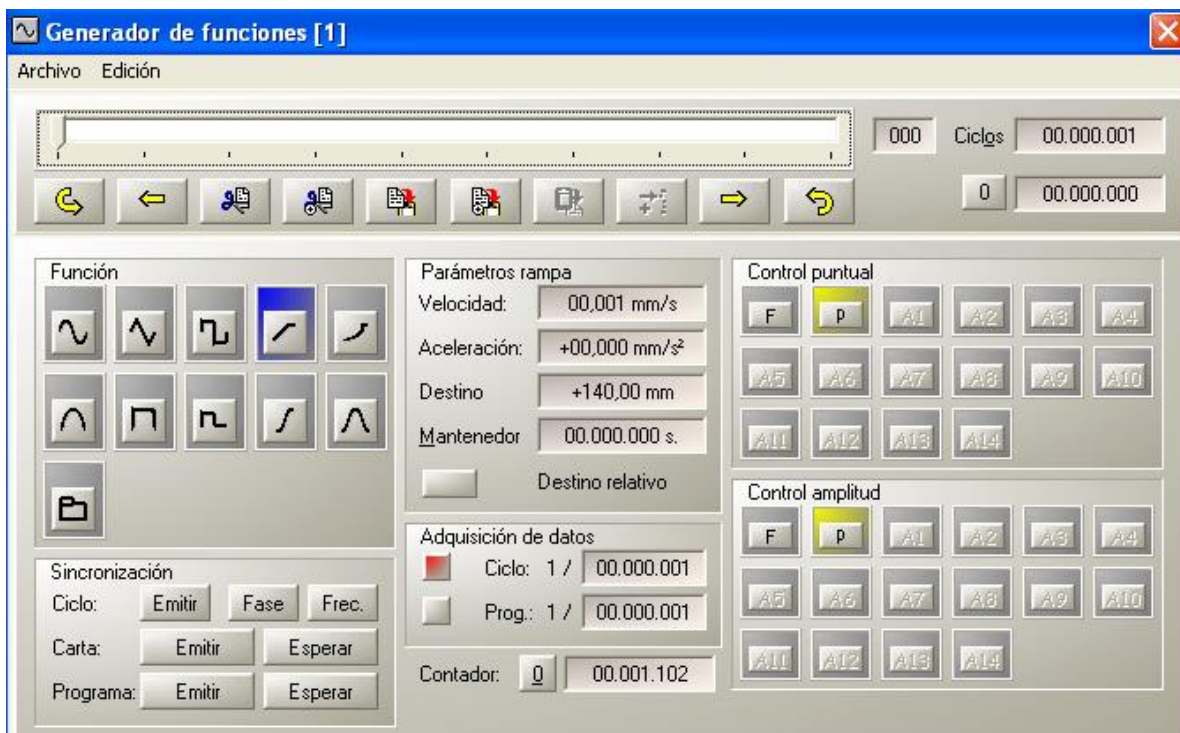


Figure 126: PCD2K functions generator

The function we will introduce to perform the Brazilian tests for 150mm diameter and 300mm long cylinder-type specimens will be 0kg/s^2 acceleration and a speed of 150kg/s (0.02MPa/s approx.).

At the end, the reduction for the acquired data is to export the tracer to an ASCII text file, where the data is exported to a 1024 register text file, which after the appropriate changes the *MATLAB* platform is able to work with it. The tests are fast enough so only 1024 registers do not lose important information.

A.4 TENSILE STRENGTH OF THE TESTED CAMPAIGNS

A.4.1 23X2015 CAMPAIGN

The procedure explained in Appendix A.3 was applied to a specimen for the 23X2015 series tensile strength determination. The results are visible at Table 59.

Table 59: Data for the 23X2015 campaign tensile strength determination

f_t 23X2015	Plot	D (mm)	L (mm)	P_u (kN)	f_t (MPa)
C23X2015II	Figure 127	150	300	55.230	0.78

Only one specimen was tested in this campaign with a Brazilian test, so the mean tensile strength is considered 0.78MPa for the 23X2015 series with an unavailable standard deviation.

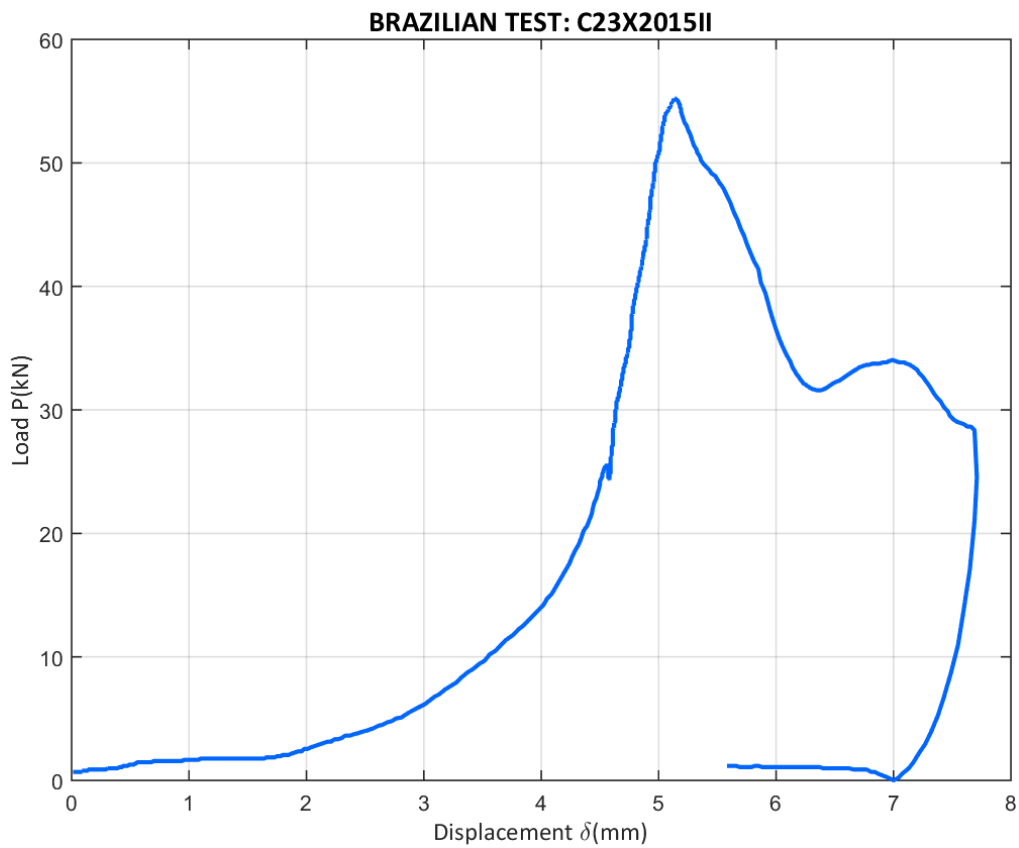


Figure 127: Load vs. vertical displacement for the Brazilian test of C23X2015II

A.4.2 14XII2015 CAMPAIGN

Four cylindrical-type specimens of the 14XII2015 campaign have been tested with the indirect tensile strength test and according the procedure exposed at Appendix A.3, the results of those tests are given at Table 60. A remark is done, at C14XII2015III; the valid peak load is the first record. The comparative graph can be seen at Figure 132.

Table 60: Data for the 14XII2015 campaign tensile strength determination

f_t 14XII2015	Plot	D (mm)	L (mm)	P_u (kN)	f_t (MPa)
C14XII2015II	Figure 128	150	300	155.979	2.207
C14XII2015III	Figure 129	150	300	134.005	1.896
C14XII2015IV	Figure 130	150	300	222.098	3.142
C14XII2015V	Figure 131	150	300	181.092	2.562

The mean tensile strength for the 14XII2015 campaign is 2.45MPa with a standard deviation of 0.53MPa.

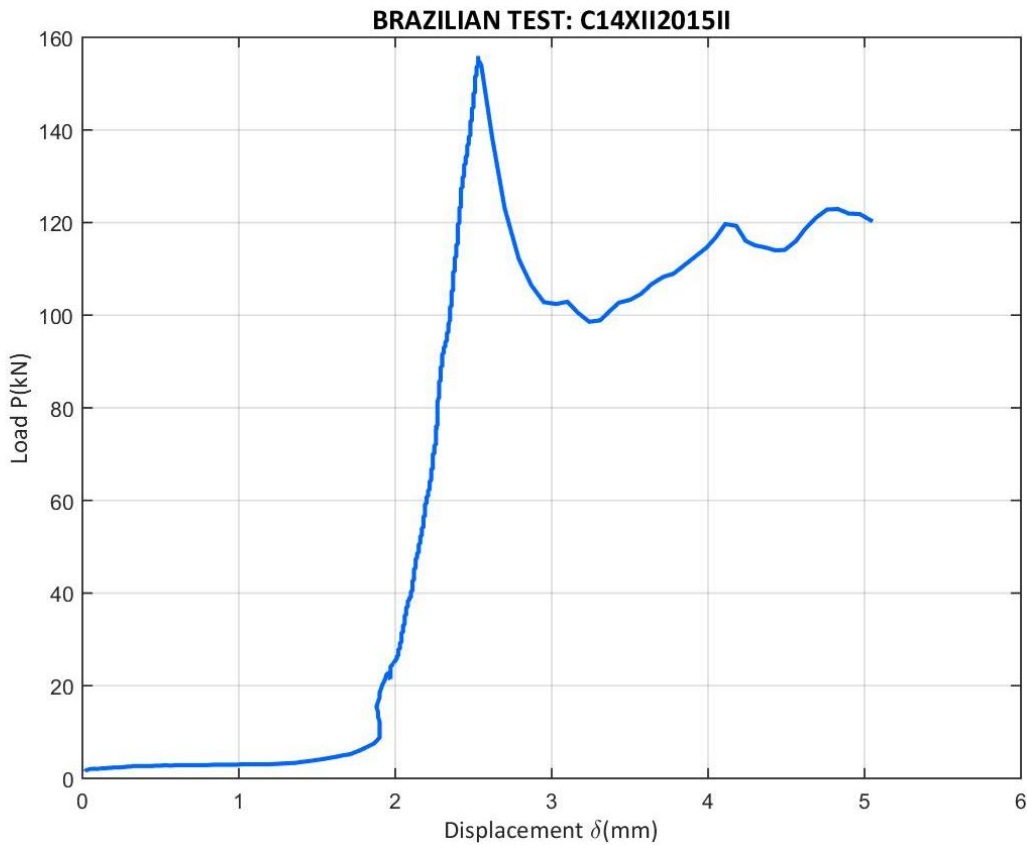


Figure 128: Load vs. vertical displacement for the Brazilian test of C14XII2015II

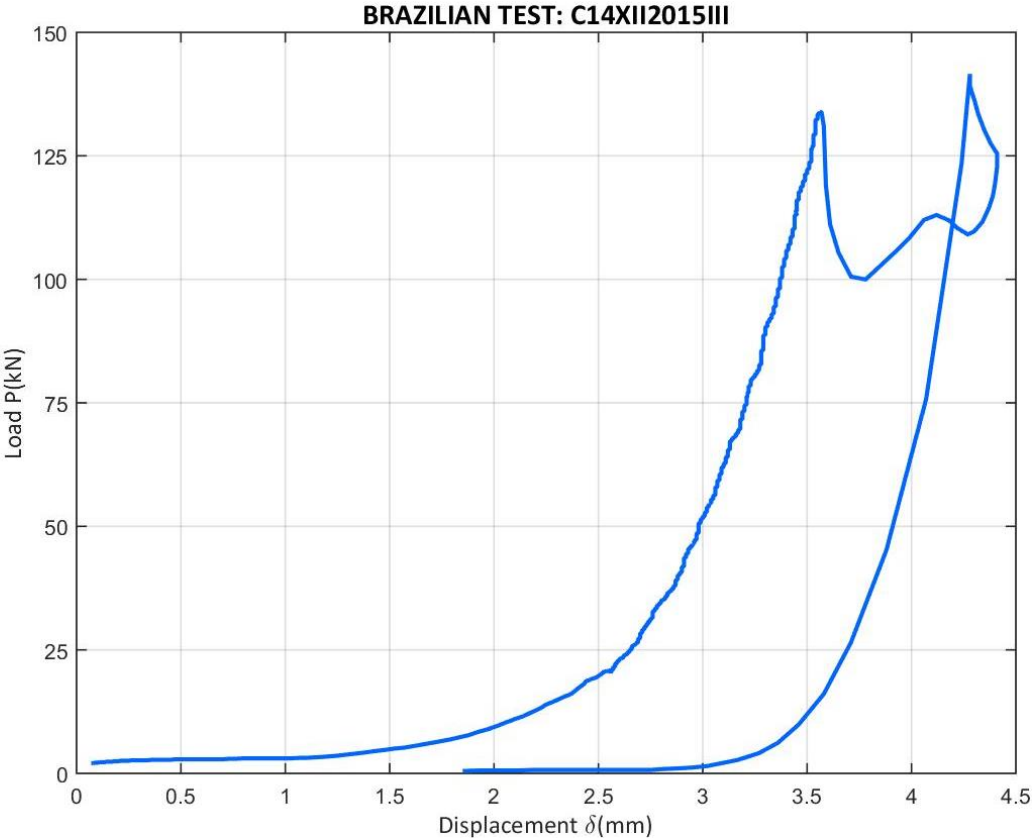


Figure 129: Load vs. vertical displacement for the Brazilian test of C14XII2015III

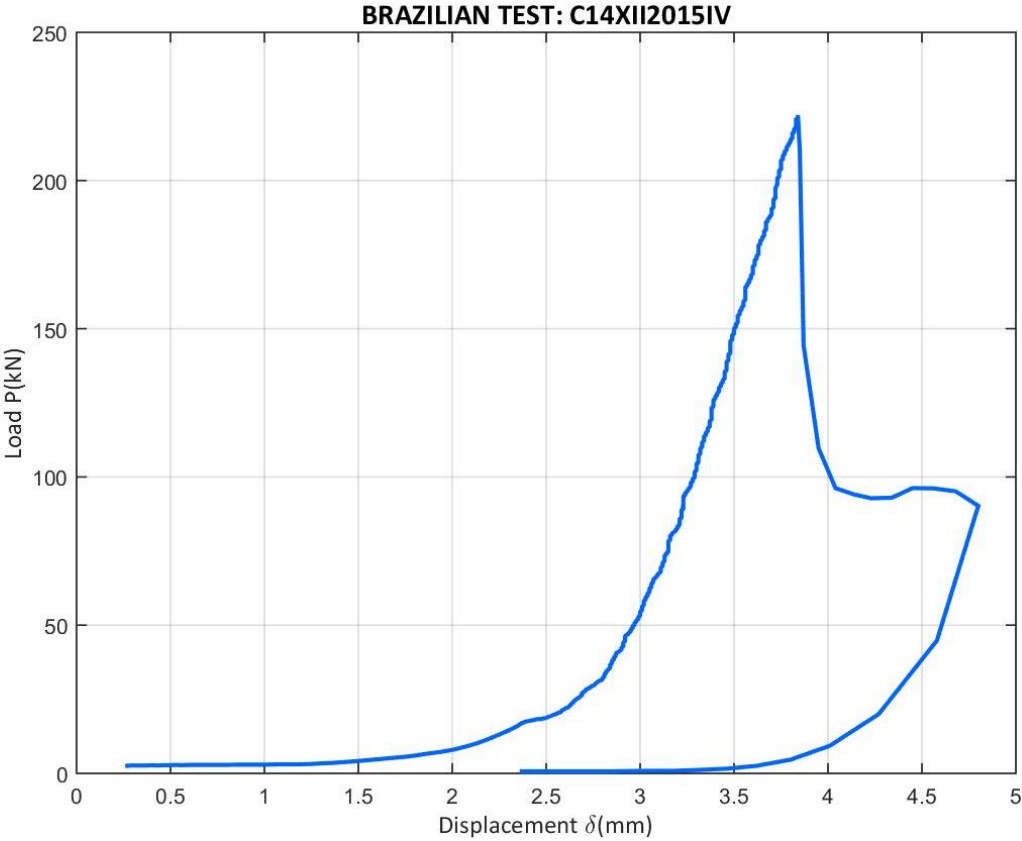


Figure 130: Load vs. vertical displacement for the Brazilian test of C14XII2015IV

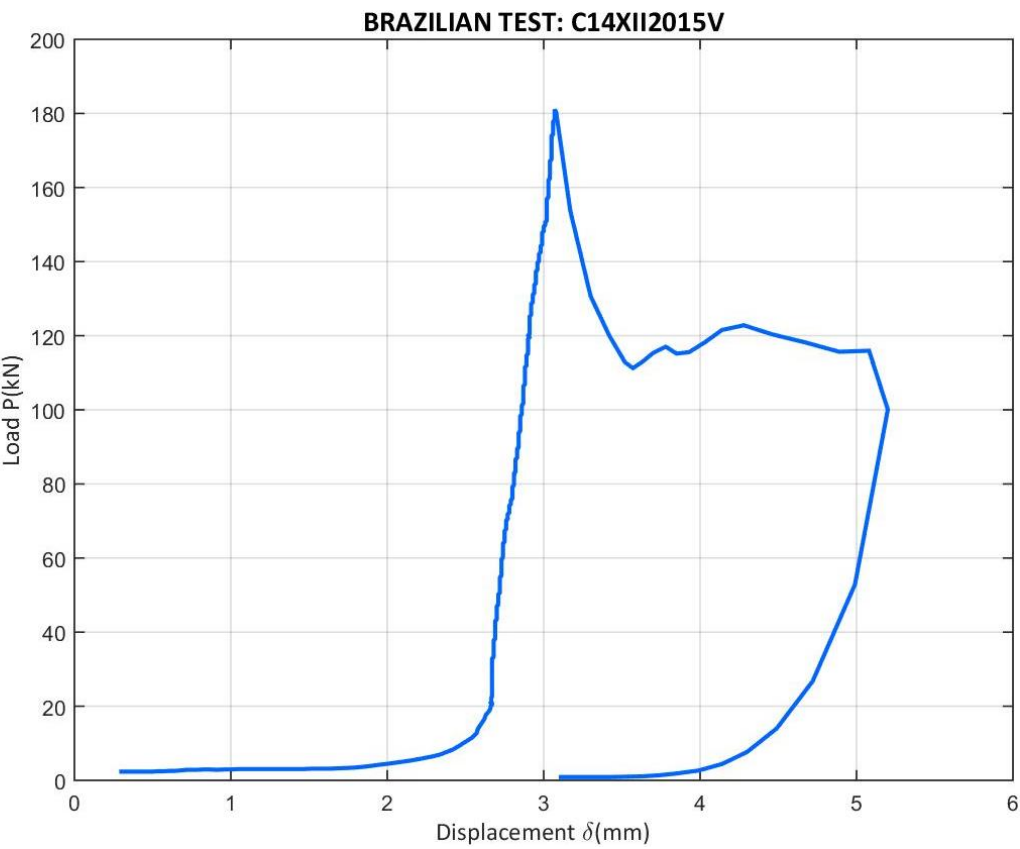


Figure 131: Load vs. vertical displacement for the Brazilian test of C14XII2015V

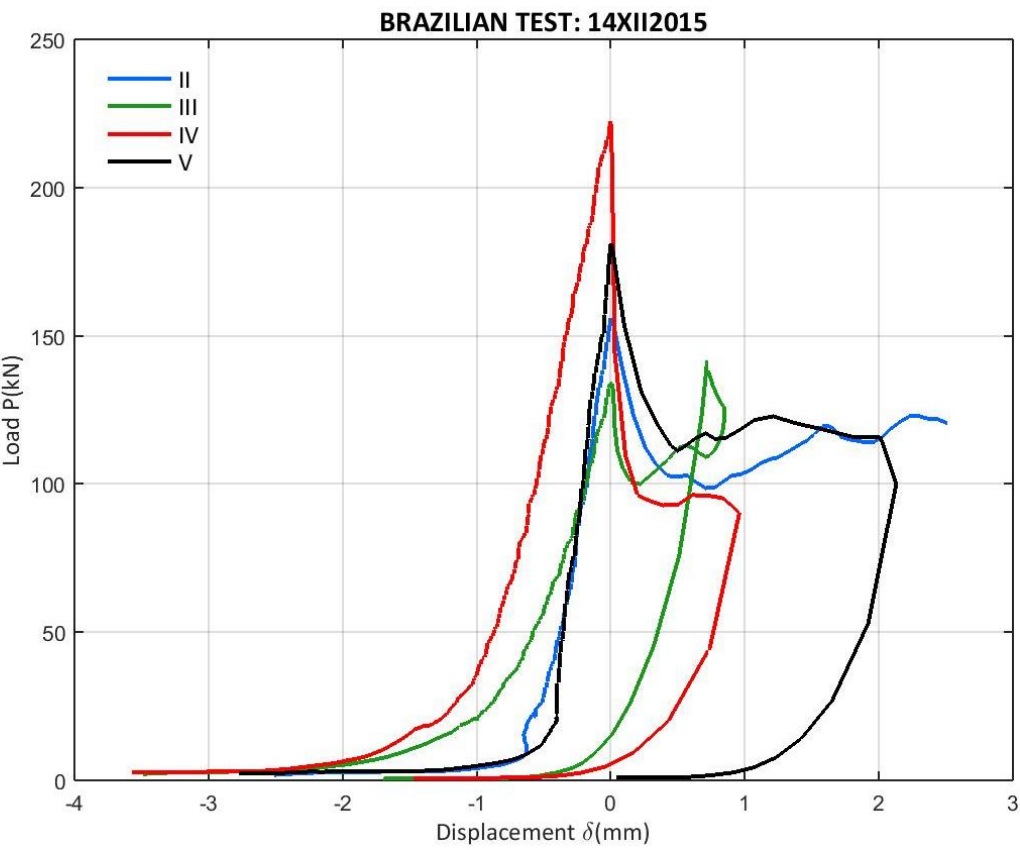


Figure 132: Load vs. vertical displacement for the Brazilian test of all C14XII2015

A.4.3 29I2016 CAMPAIGN

For this campaign, 4 cylinder-type specimens were tested with the procedure detailed at Appendix A.3 in order to find the tensile strength of them. The results are shown, both numeric results at Table 61 and graphic results, with a comparison graph at Figure 137. Specimens I and II belong to the A-series and the other two at the B-series.

Table 61: Data for the 29I2016 campaign tensile strength determination

f_t 29I2016	Plot	$D(\text{mm})$	$L(\text{mm})$	$P_u(\text{kN})$	$f_t(\text{MPa})$
C29I2016I	Figure 133	150	300	89.663	1.269
C29I2016II	Figure 134	150	300	117.033	1.656
C29I2016III	Figure 135	150	300	83.876	1.187
C29I2016IV	Figure 136	150	300	111.540	1.578

A-series has a tensile strength of 1.462MPa with a standard deviation of 0.274MPa and B-series, 1.382MPa with a standard deviation of 0.277MPa. The global mean value is 1.422MPa with a standard deviation of 0.229MPa. The difference between the two series is less than the 5.8% and the mean values are all inside the first standard deviation. The little difference is not enough to consider the two series with different tensile strength, so it will be considered a unique campaign for f_t .

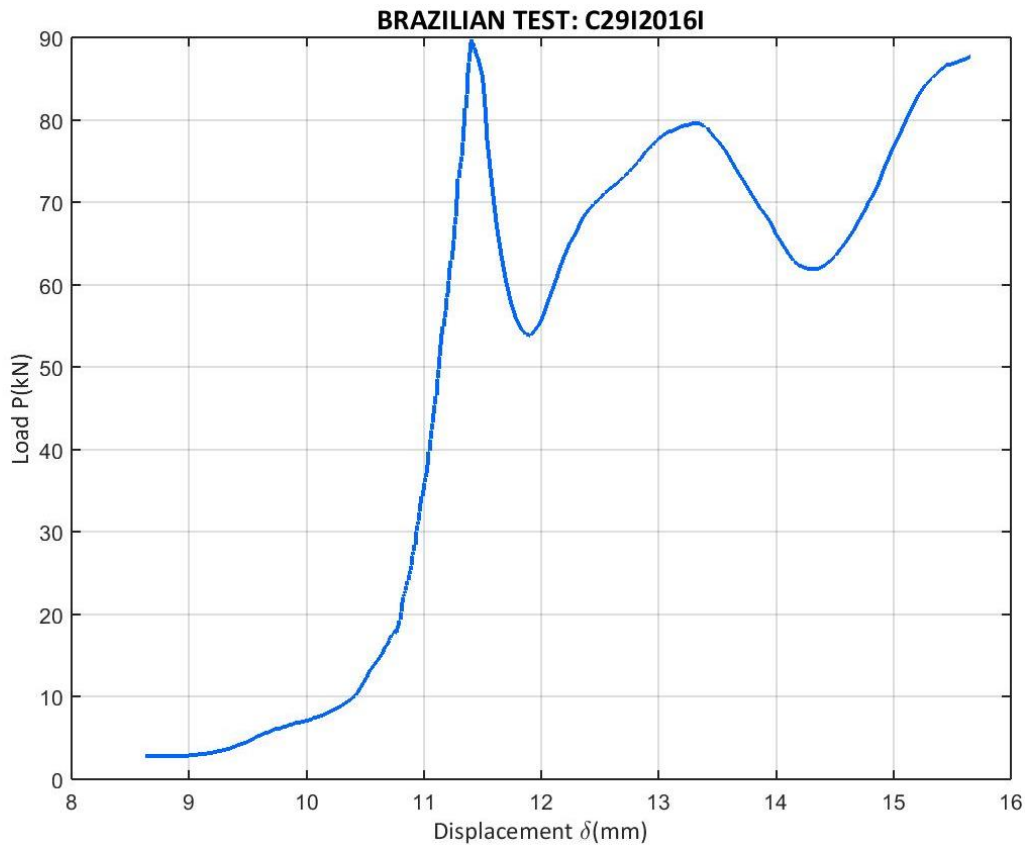


Figure 133: Load vs. vertical displacement for the Brazilian test of C29I2016I

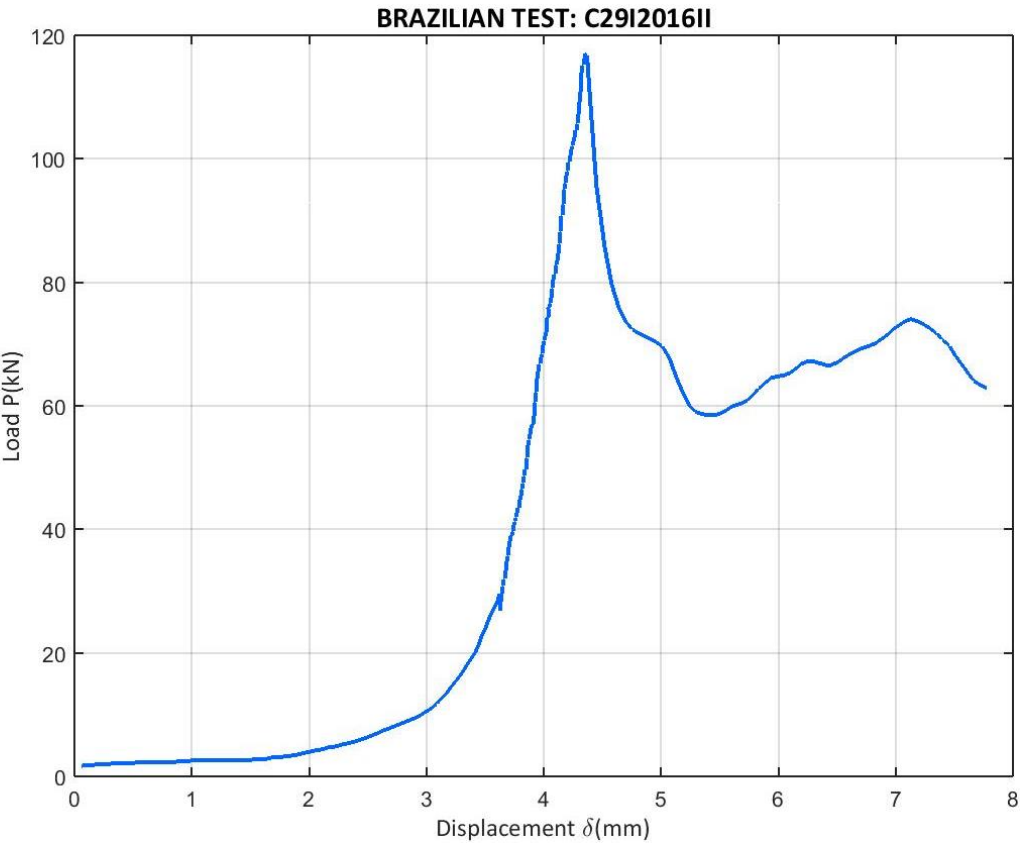


Figure 134: Load vs. vertical displacement for the Brazilian test of C29I2016II

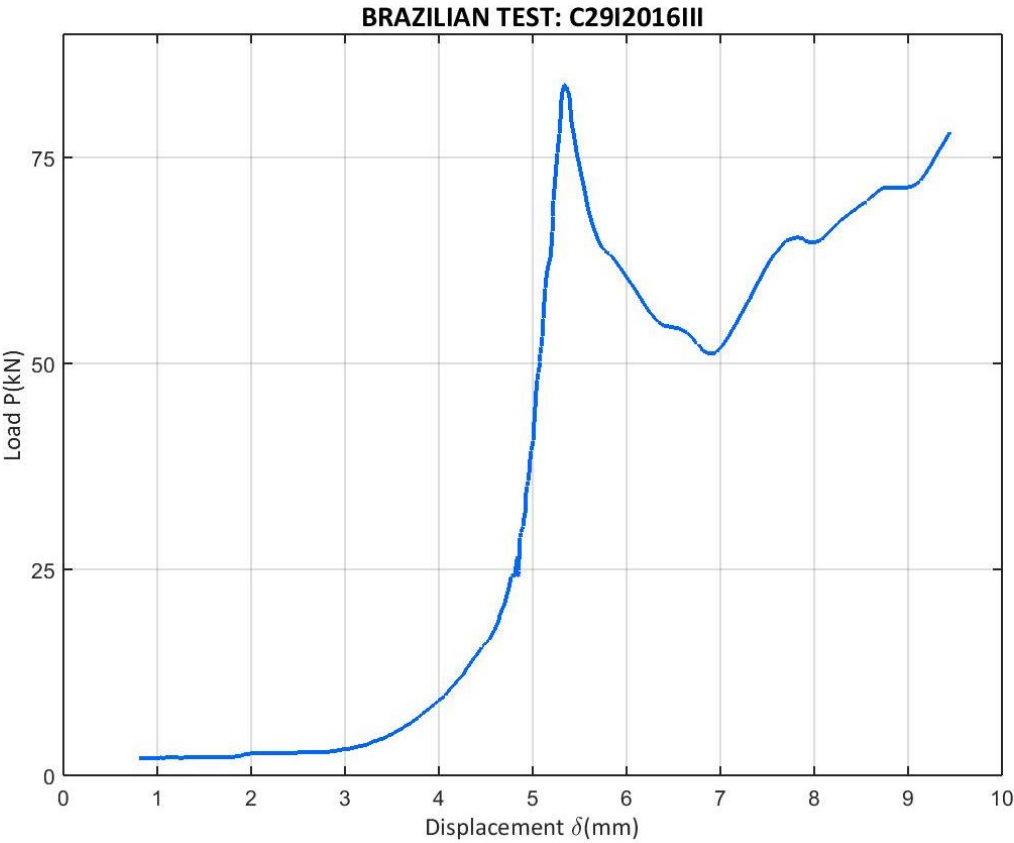


Figure 135: Load vs. vertical displacement for the Brazilian test of C29I2016III

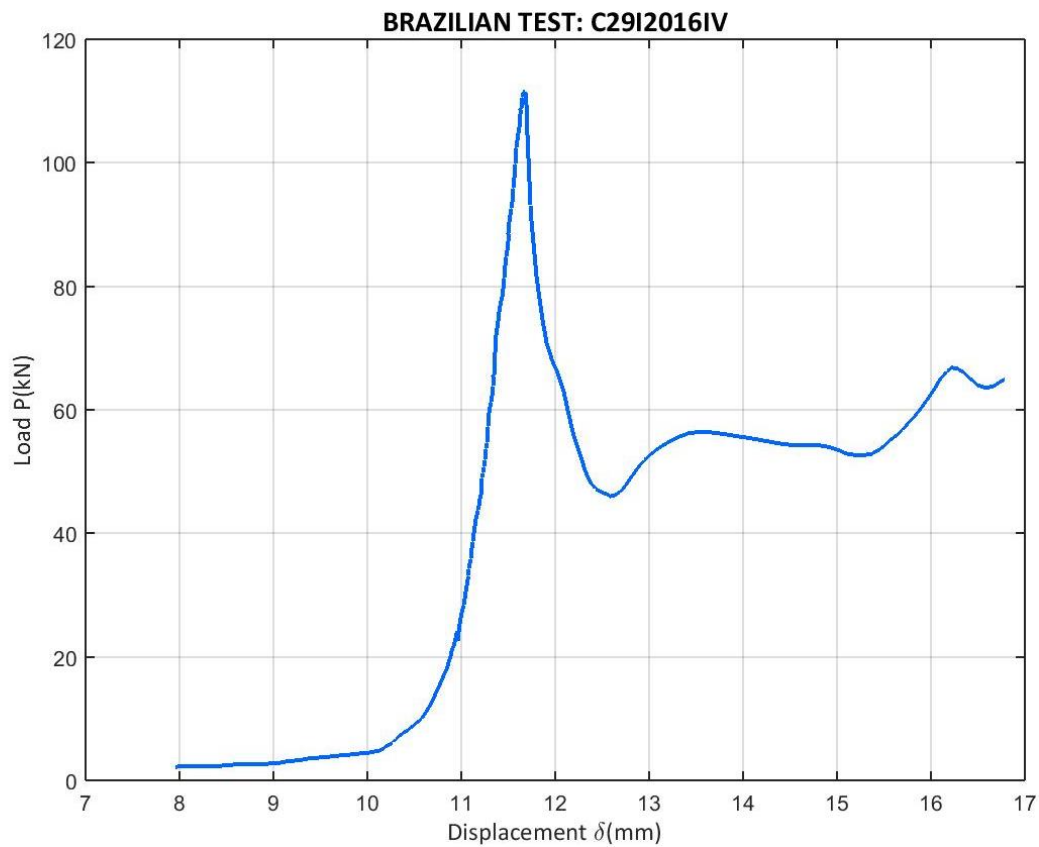


Figure 136: Load vs. vertical displacement for the Brazilian test of C29I2016IV

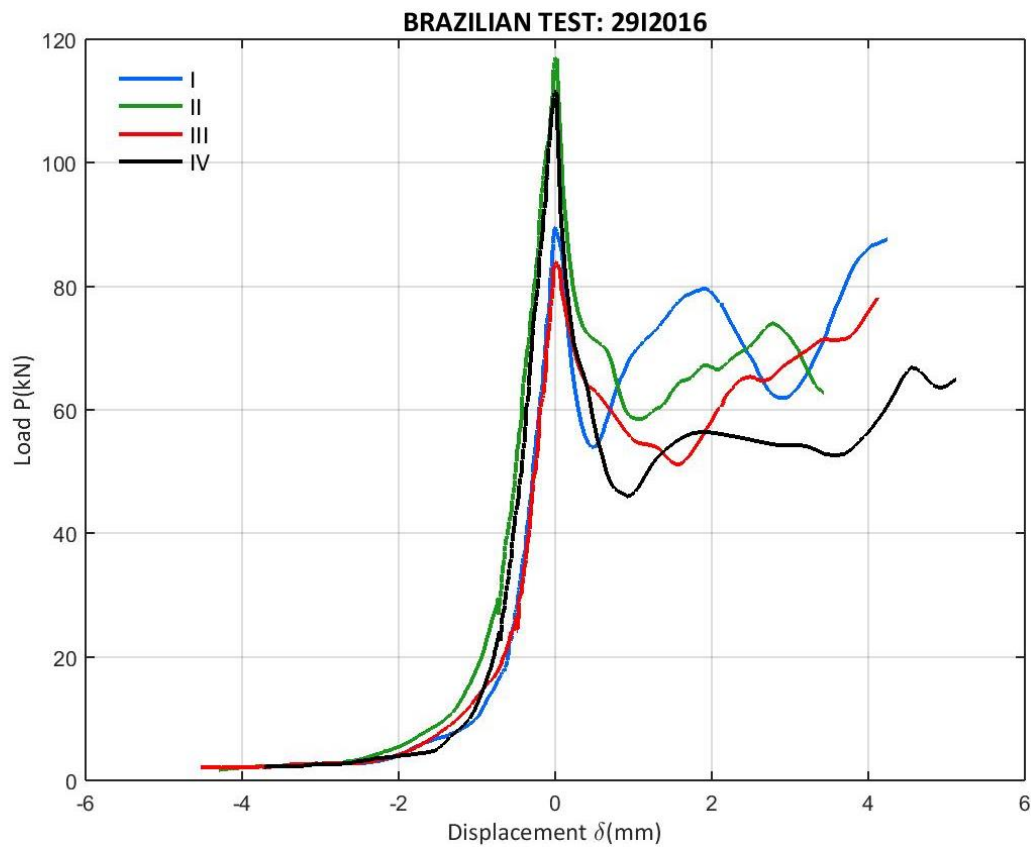


Figure 137: Load vs. vertical displacement for the Brazilian test of all C29I2016

A.4.4 10III2016 CAMPAIGN

The procedure detailed at Appendix A.3 is applied to two cylinder-type specimens for this campaign, giving the results written at Table 62.

Table 62: Data for the 10III2016 campaign tensile strength determination

f_t 10III2016	Plot	D (mm)	L (mm)	P_u (kN)	f_t (MPa)
C10III2016II	Figure 138	150	300	7.917	1.120
C10III2016III	Figure 139	150	300	7.446	1.053

The mean tensile strength for this campaign is 1.087MPa with a standard deviation of 0.047MPa.

A comparison graph is given at Figure 140.

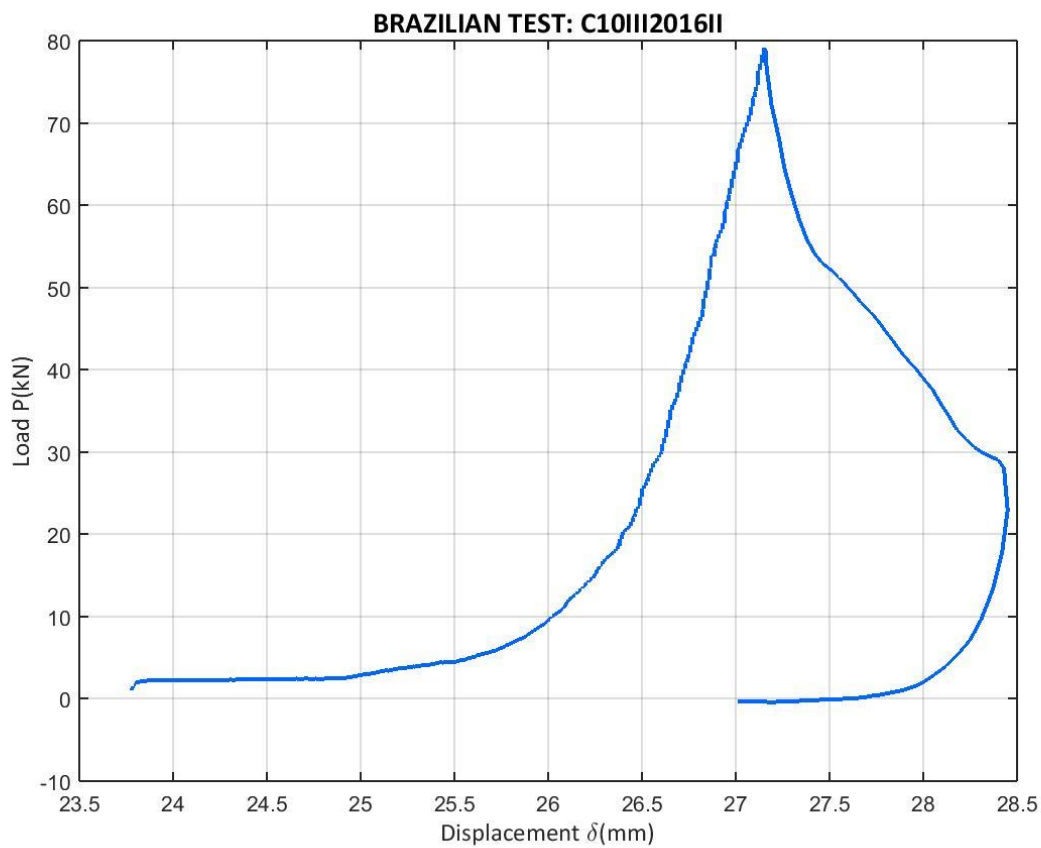


Figure 138: Load vs. vertical displacement for the Brazilian test of C10III2016II

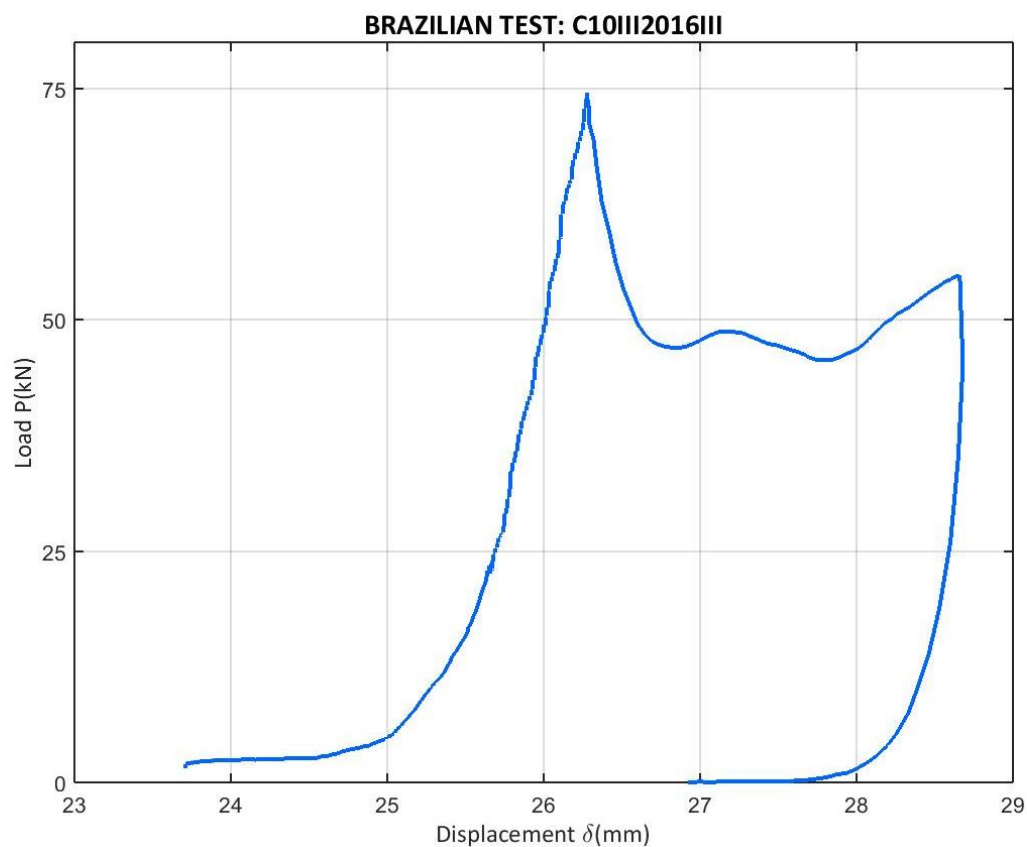


Figure 139: Load vs. vertical displacement for the Brazilian test of C10III2016III

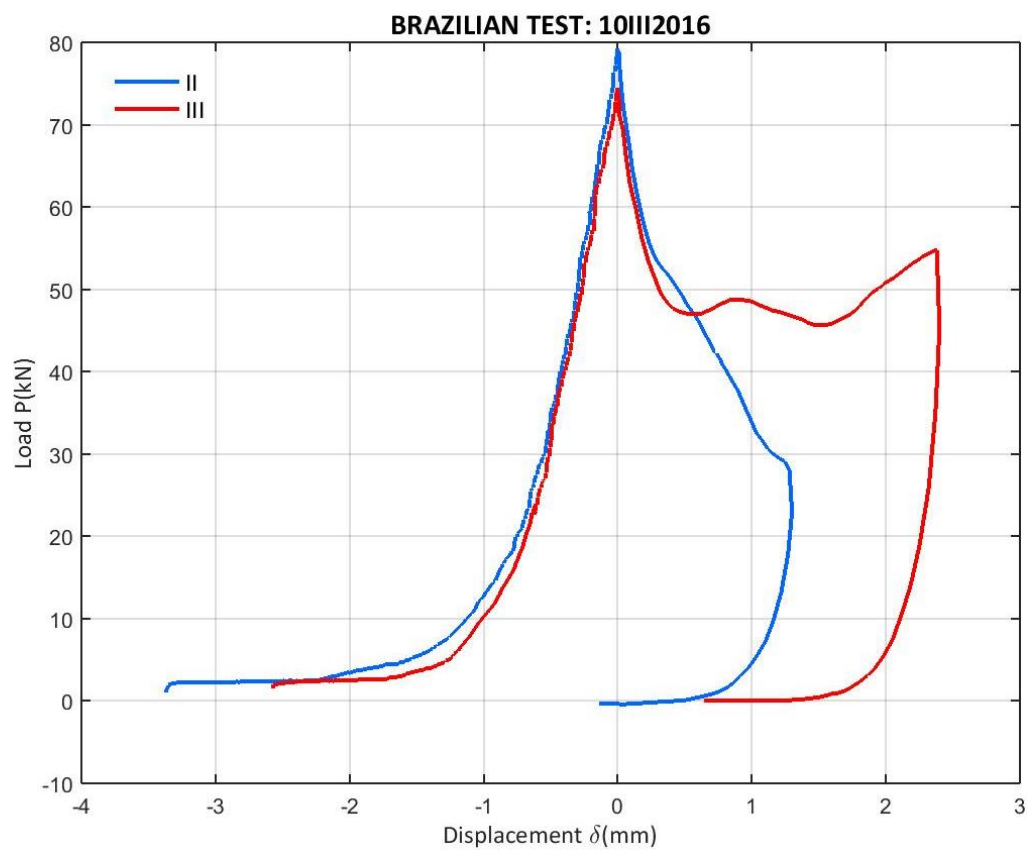


Figure 140: Load vs. vertical displacement for the Brazilian test of all C10III2016

A.4.5 17III2016 CAMPAIGN

The test and calculation detailed at Appendix A.3 is applied to two cylindrical specimens for the 17III2016 campaign. The individual results are given at Table 63, along with their graphs and a comparative one at Figure 143.

Table 63: Data for the 17III2016 campaign tensile strength determination

f_t 17III2016	Plot	D (mm)	L (mm)	P_u (kN)	f_t (MPa)
C17III2016II	Figure 141	150	300	123.017	1.740
C17III2016III	Figure 142	150	300	115.954	1.640

The conclusion from these results is a tensile strength of 1.690MPa with a standard deviation of 0.071MPa.

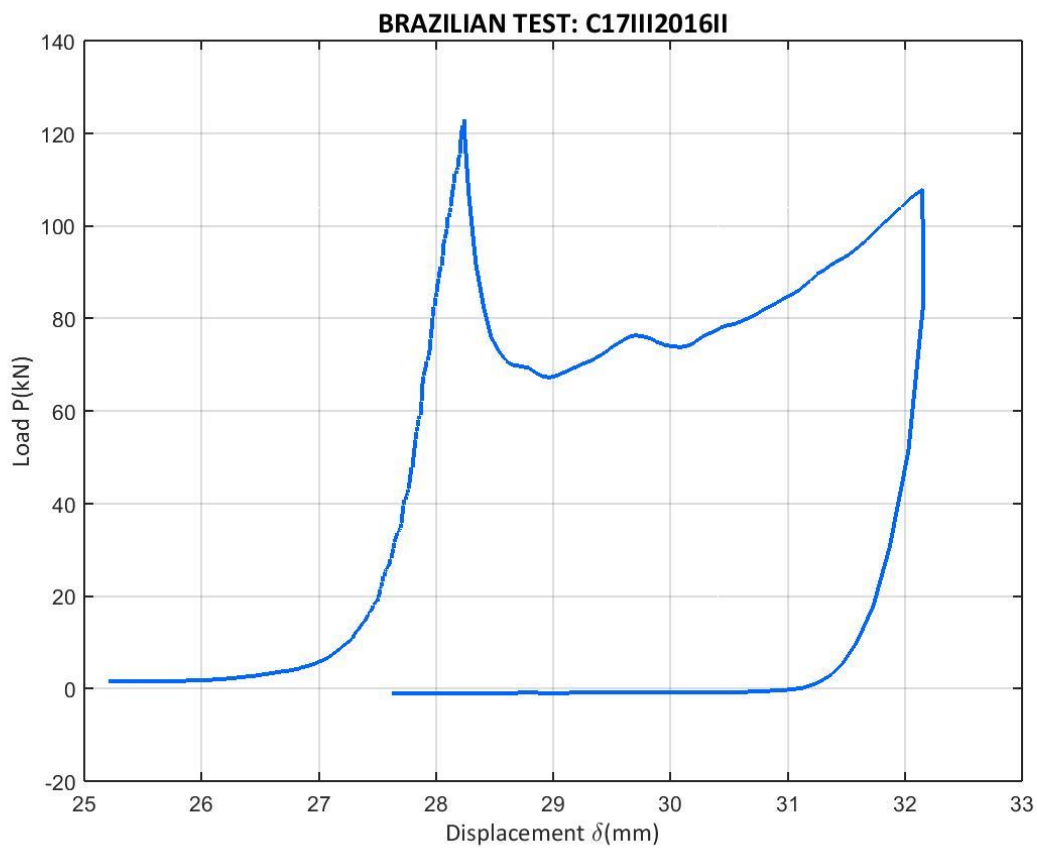


Figure 141: Load vs. vertical displacement for the Brazilian test of C17III2016II

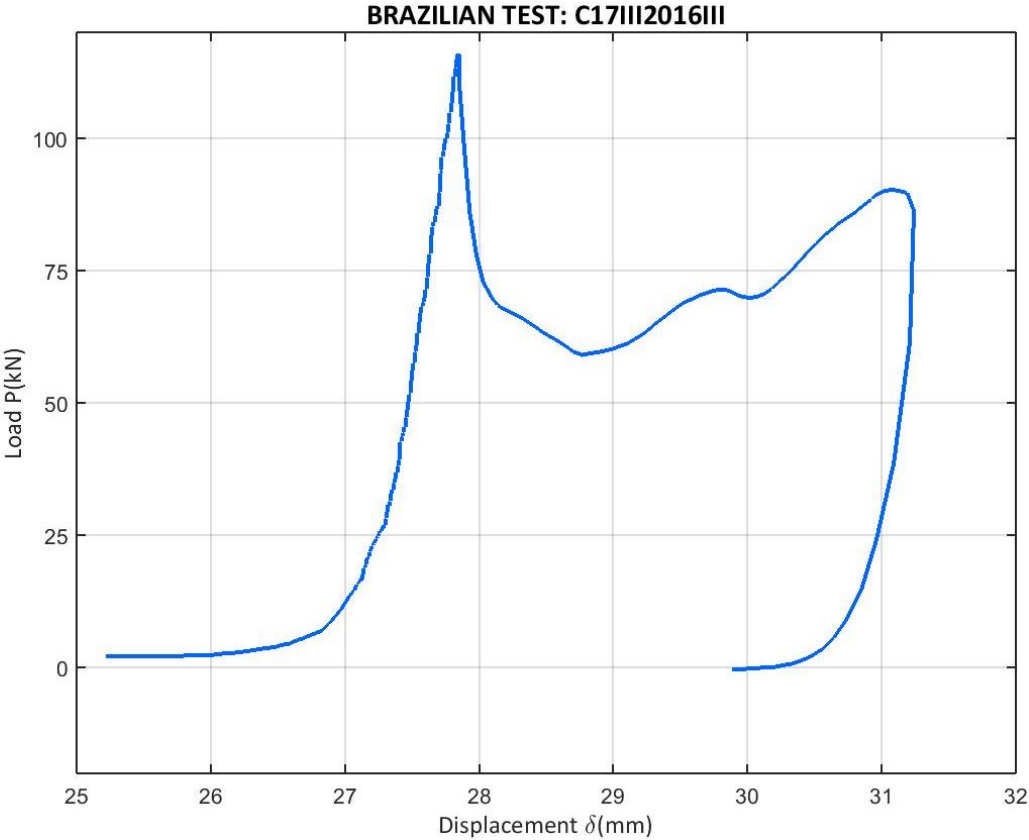


Figure 142: Load vs. vertical displacement for the Brazilian test of C17III2016III

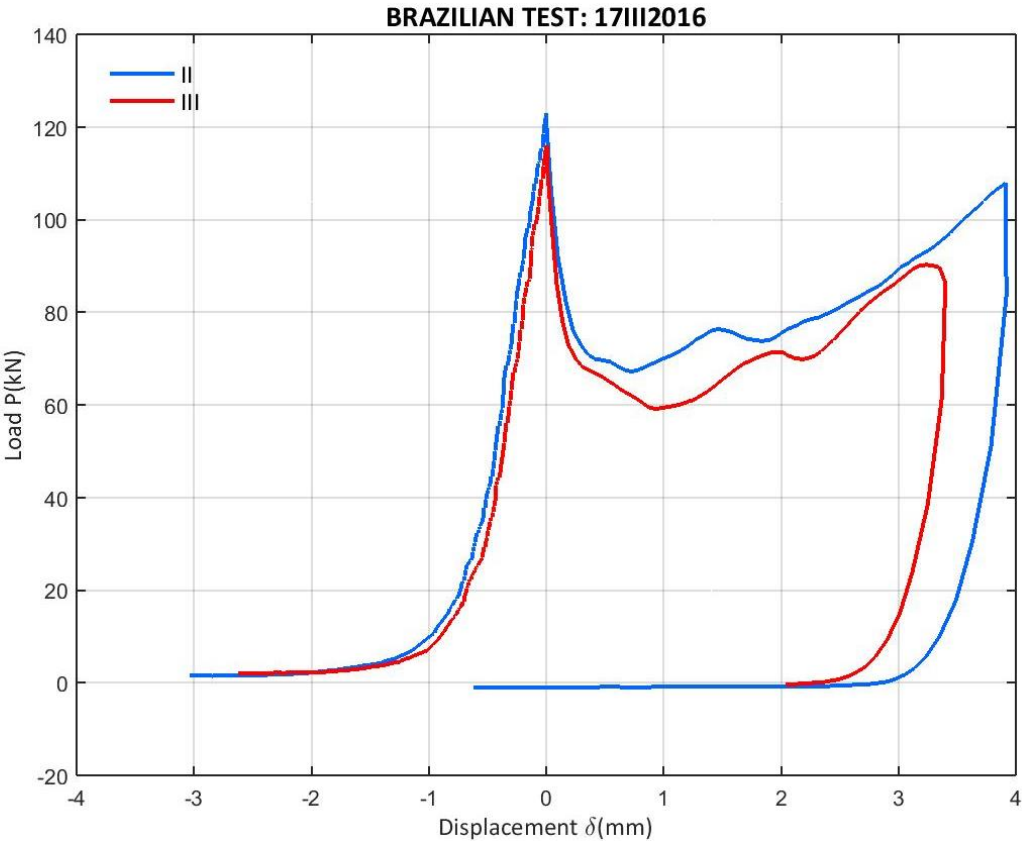


Figure 143: Load vs. vertical displacement for the Brazilian test of all C17III2016

A.4.6 01IV2016 CAMPAIGN

Applying the procedure exposed at Appendix A.3 for two cylinder-type specimens, the results for the tensile strength for this campaign are given at Table 64. A comparison graph is also given at Figure 146.

Table 64: Data for the 01IV2016 campaign tensile strength determination

f_t 01IV2016	Plot	D (mm)	L (mm)	P_u (kN)	f_t (MPa)
C01IV2016II	Figure 144	150	300	90.350	1.278
C01IV2016III	Figure 145	150	300	88.388	1.250

The mean tensile strength for the 01IV2016 campaign is about 1.264MPa with a standard deviation of 0.020MPa.

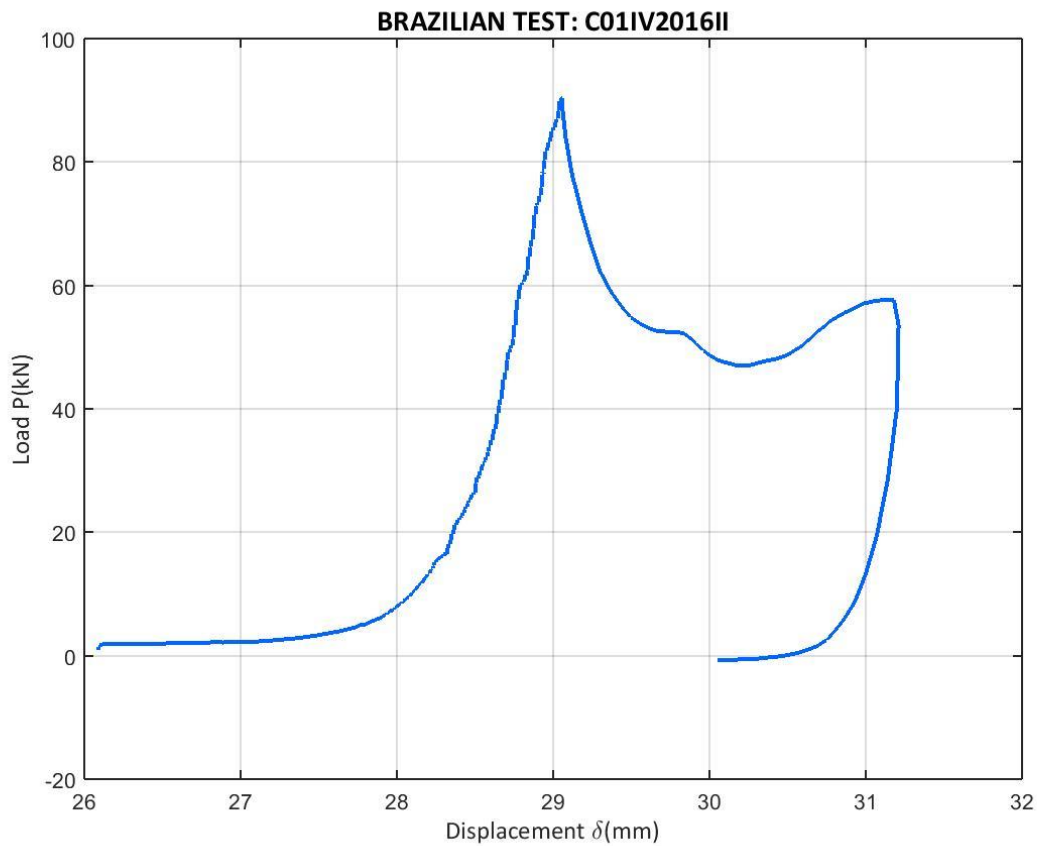


Figure 144: Load vs. vertical displacement for the Brazilian test of C01IV2016II

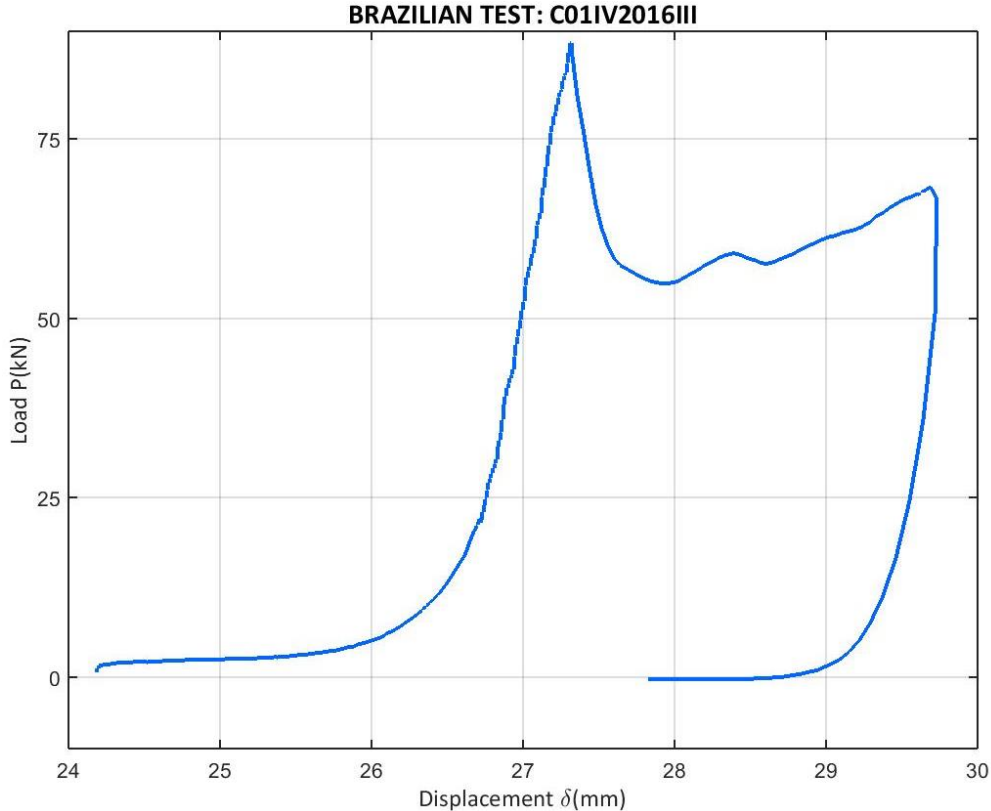


Figure 145: Load vs. vertical displacement for the Brazilian test of C01IV2016III

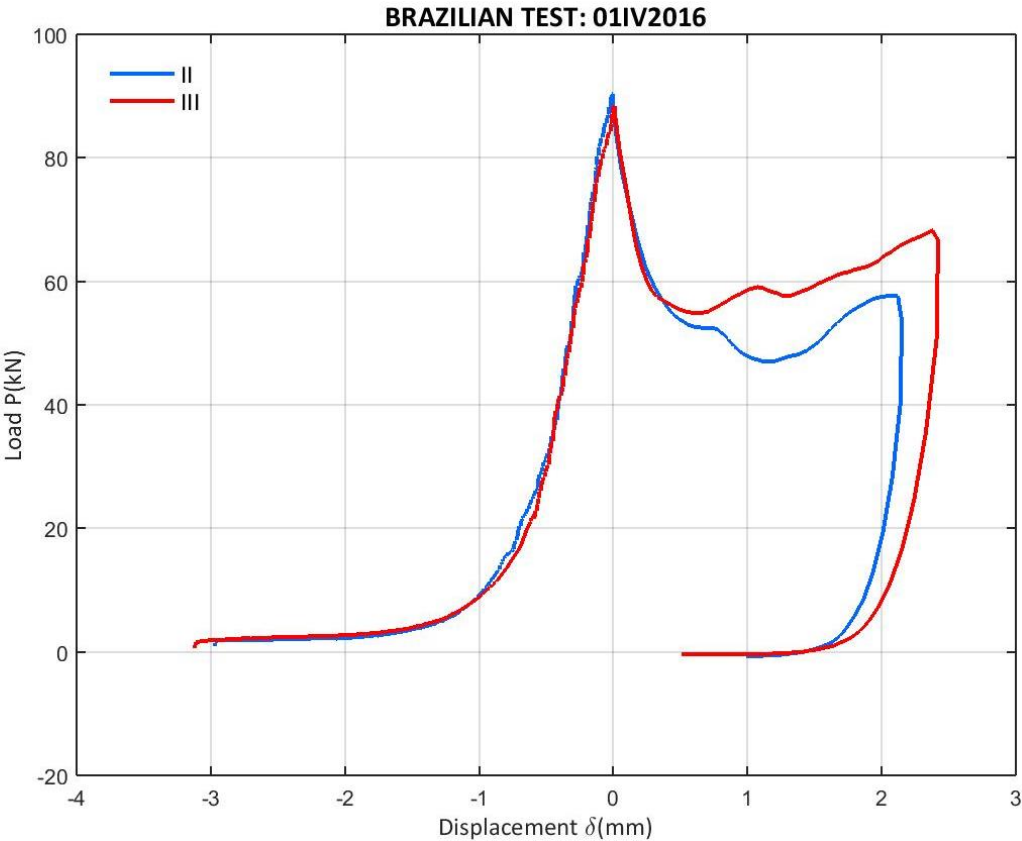


Figure 146: Load vs. vertical displacement for the Brazilian test of all C01IV2016

A.4.7 07IV2016 CAMPAIGN

For two cylinders from the 07IV2016 campaign, a Brazilian test is performed and the procedure detailed at Appendix A.3 is applied. The results of these tests are given at Table 65. A comparative graph is given at Figure 149.

Table 65: Data for the 07IV2016 campaign tensile strength determination

f_t 07IV2016	Plot	D (mm)	L (mm)	P_u (kN)	f_t (MPa)
C07IV2016II	Figure 147	150	300	98.100	1.388
C07IV2016III	Figure 148	150	300	105.065	1.486

The mean tensile strength for the 07IV2016 campaign is 1.437MPa with a standard deviation of 0.070MPa.

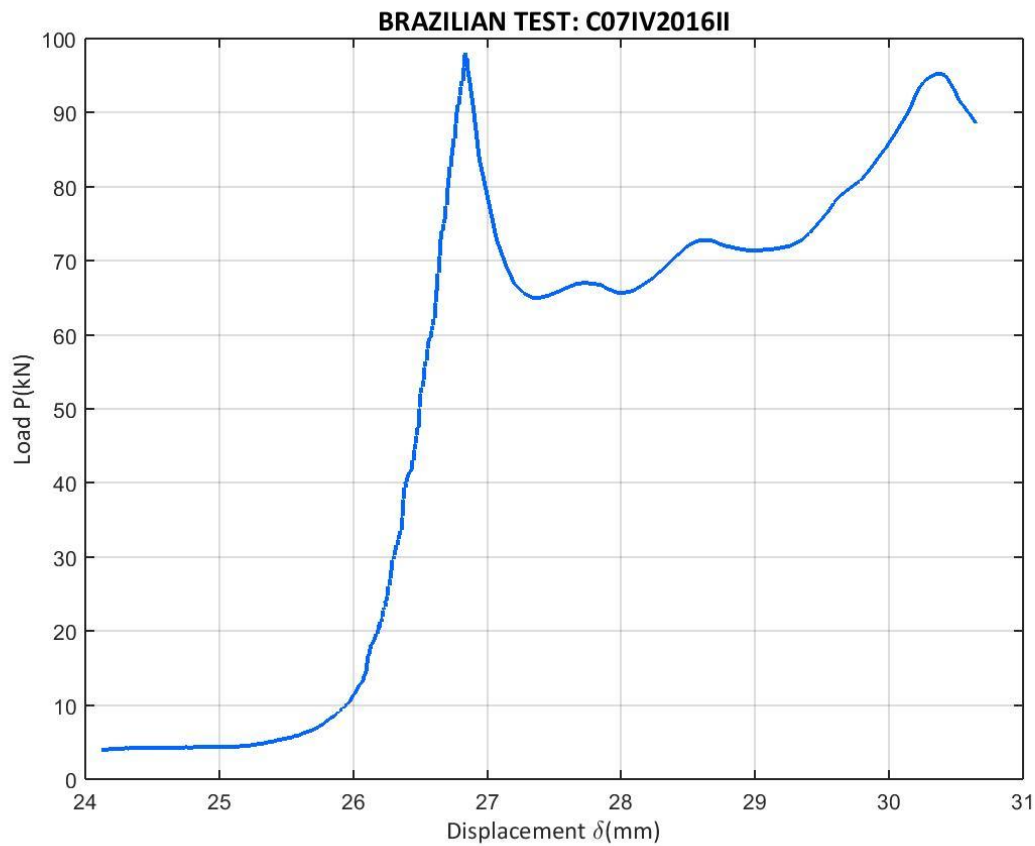


Figure 147: Load vs. vertical displacement for the Brazilian test of C07IV2016II

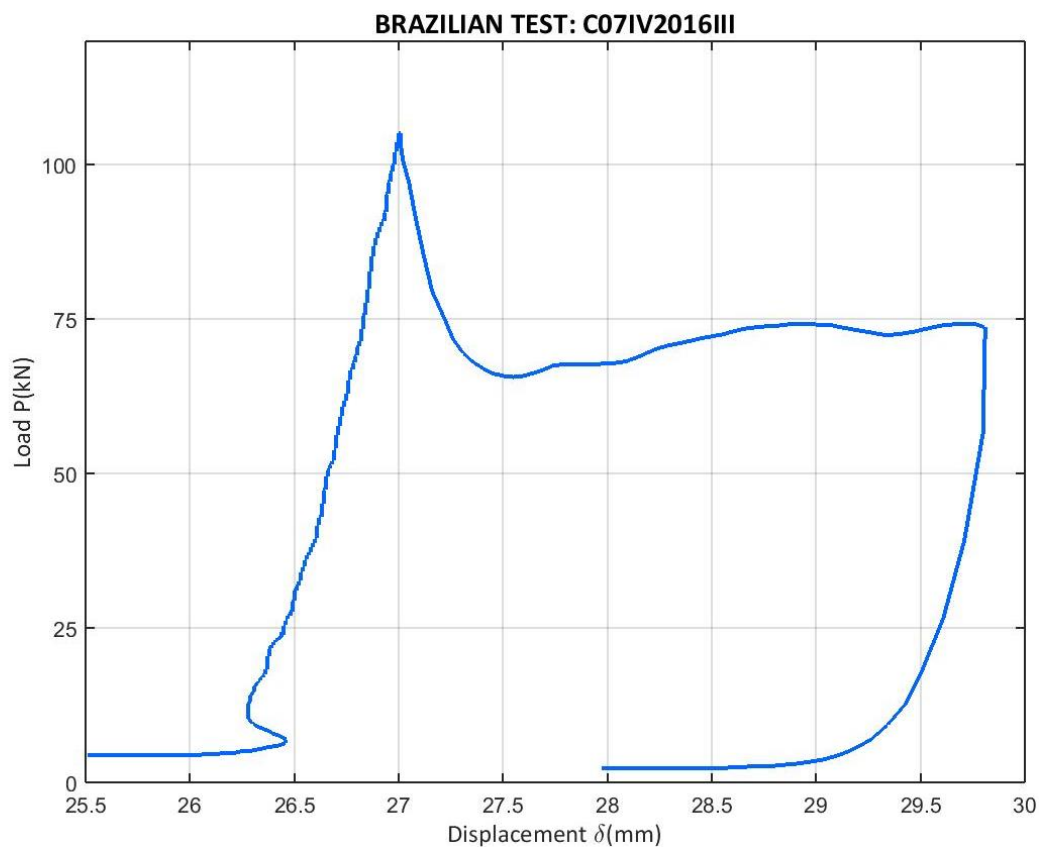


Figure 148: Load vs. vertical displacement for the Brazilian test of C07IV2016II

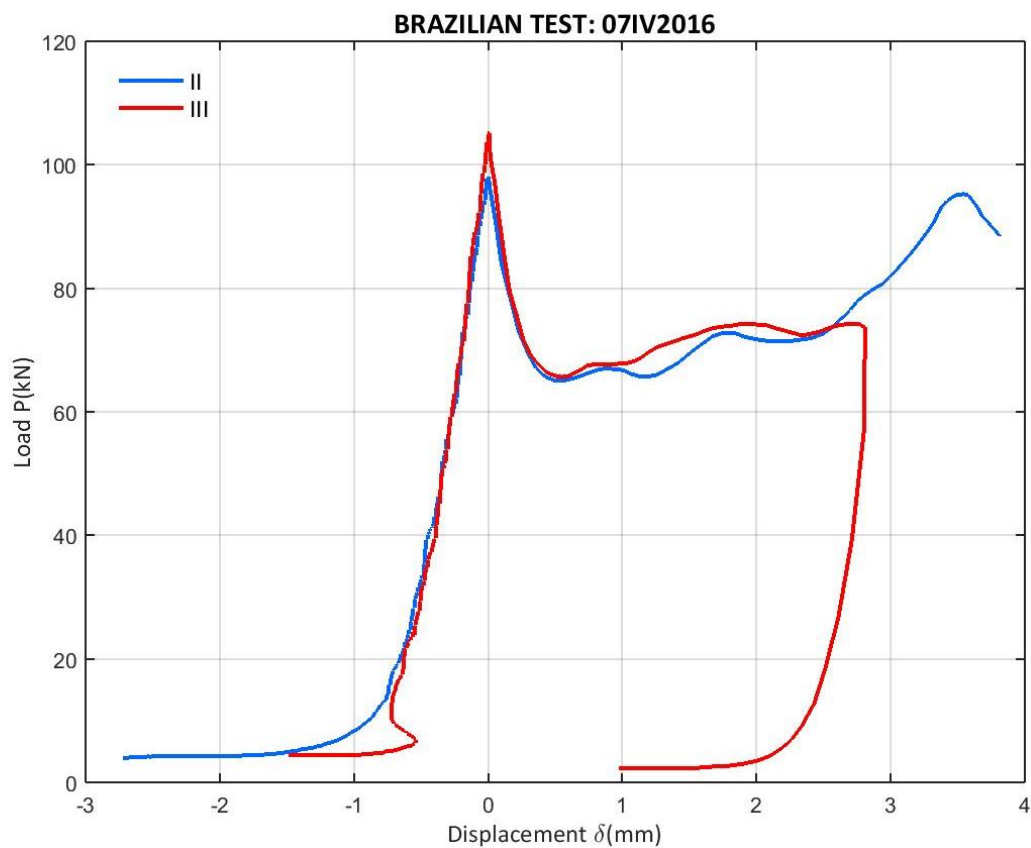


Figure 149: Load vs. vertical displacement for the Brazilian test of all C07IV2016

A.4.8 14IV2016 CAMPAIGN

For two cylindrical specimens, the test and procedure detailed at Appendix A.3 is applied, giving the results shown at Table 66. The graphs of the tests are given along with a comparative one at Figure 152.

Table 66: Data for the 14IV2016 campaign tensile strength determination

f_t 14IV2016	Plot	D (mm)	L (mm)	P_u (kN)	f_t (MPa)
C14IV2016II	Figure 150	150	300	159.118	2.251
C14IV2016III	Figure 151	150	300	142.932	2.010

The mean tensile strength for this campaign is 2.130MPa with a standard deviation of 0.171MPa.

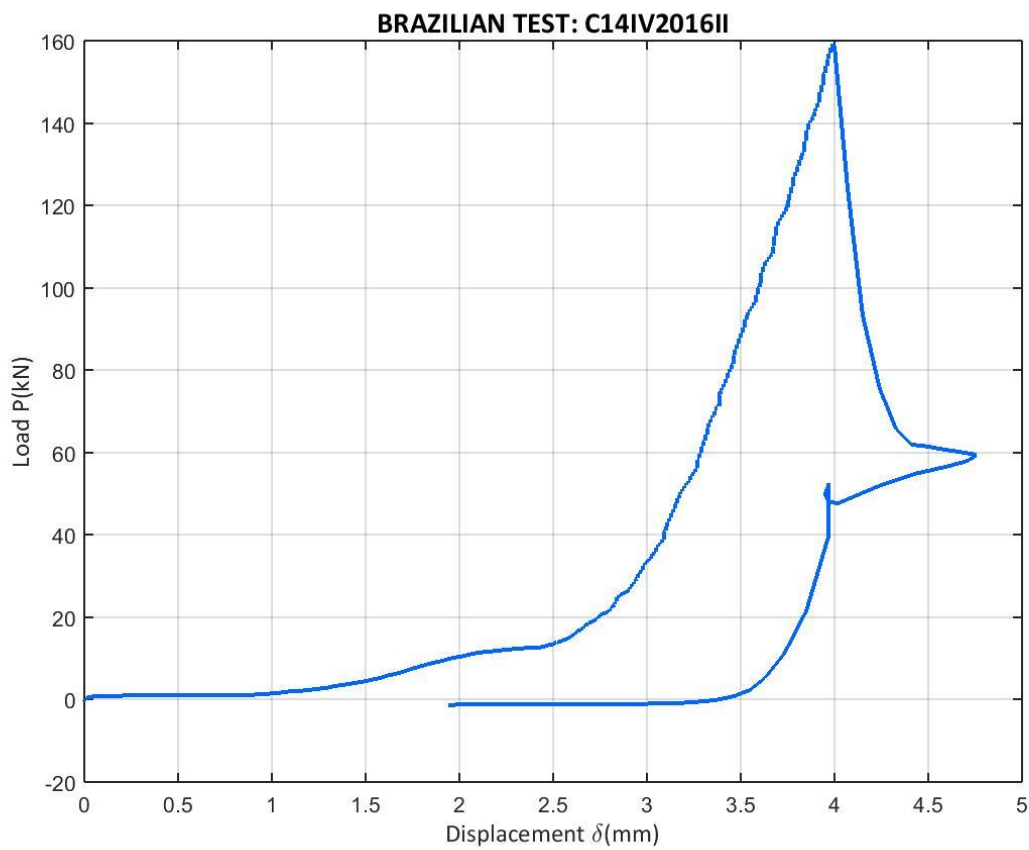


Figure 150: Load vs. vertical displacement for the Brazilian test of C14IV2016II

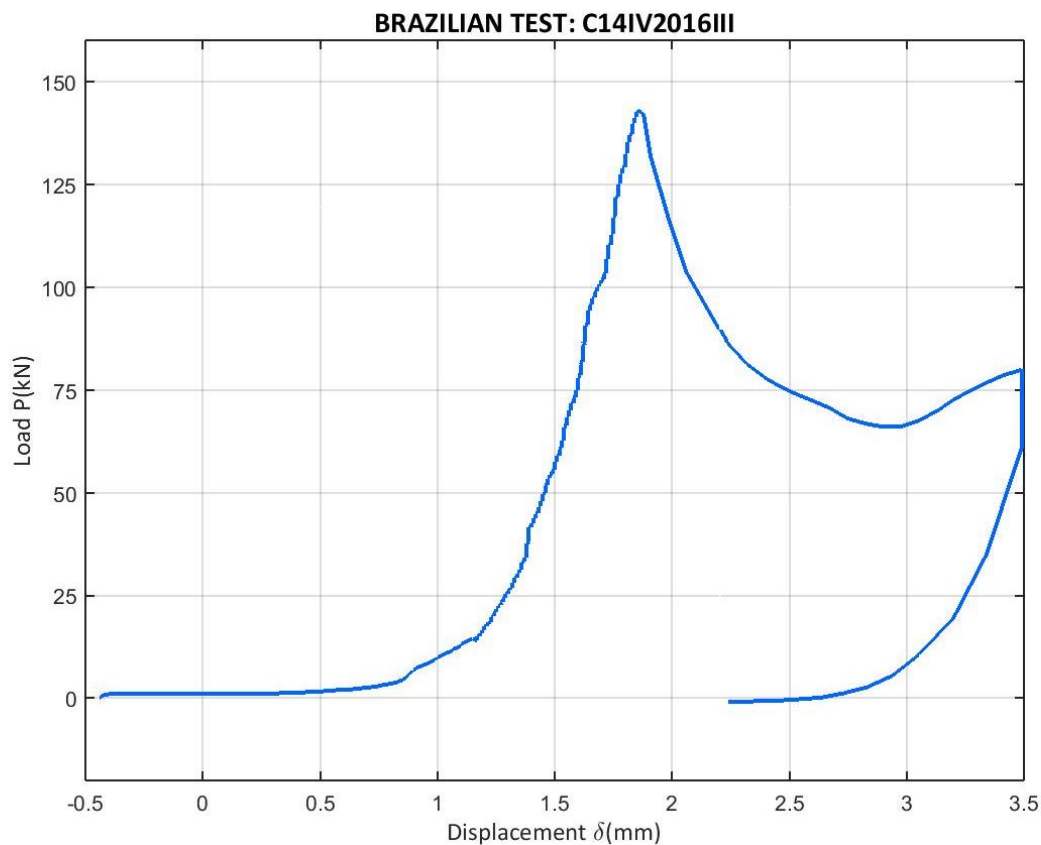


Figure 151: Load vs. vertical displacement for the Brazilian test of C14IV2016III

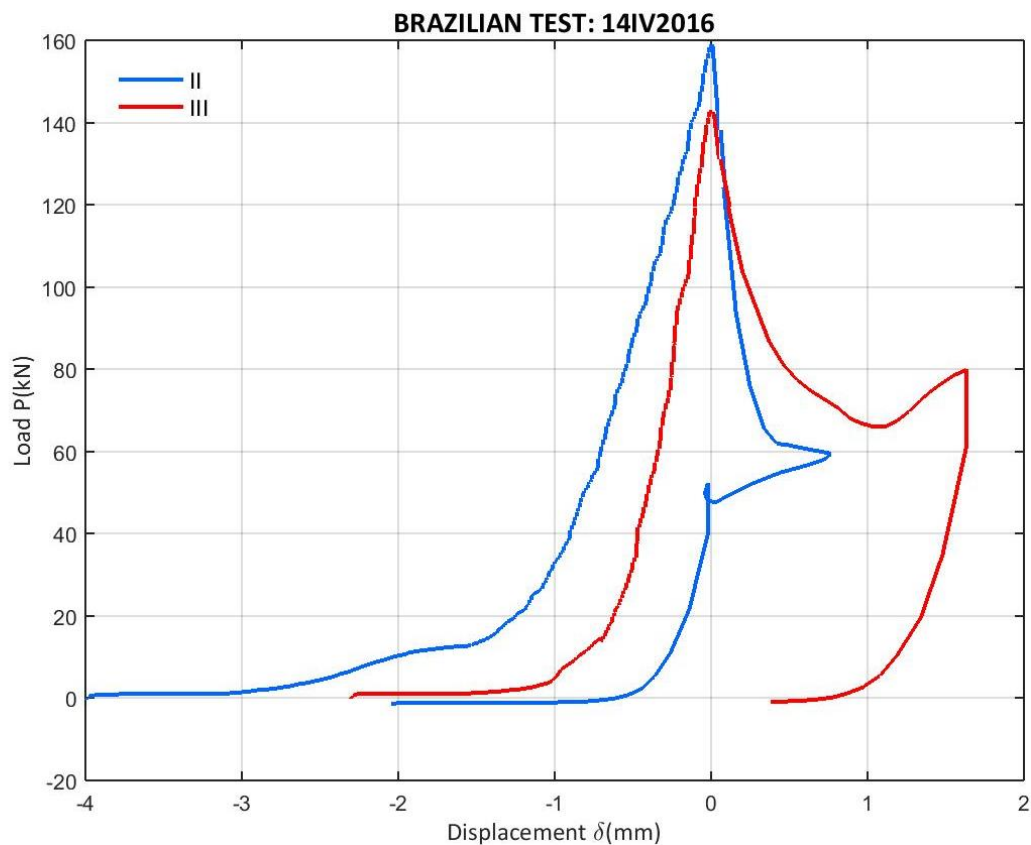


Figure 152: Load vs. vertical displacement for the Brazilian test of all C14IV2016

A.4.9 21IV2016 CAMPAIGN

The methodology detailed at Appendix A.3 is applied for two cylinders cast for the 21IV2016 campaign. The results for every Brazilian test are given at Table 67, along with their graphs and a comparative one at Figure 155.

Table 67: Data for the 21IV2016 campaign tensile strength determination

f_t 21IV2016	Plot	D (mm)	L (mm)	P_u (kN)	f_t (MPa)
C21IV2016II	Figure 153	150	300	80.442	1.138
C21IV2016III	Figure 154	150	300	92.410	1.307

The test C21IV2016II must be considered invalid, because the specimen splitting was incomplete, leaving one part of the specimen with a vertical crack and the other one without any kind of fracture.

This means that the tensile strength for this campaign is 1.307MPa with any available standard deviation.

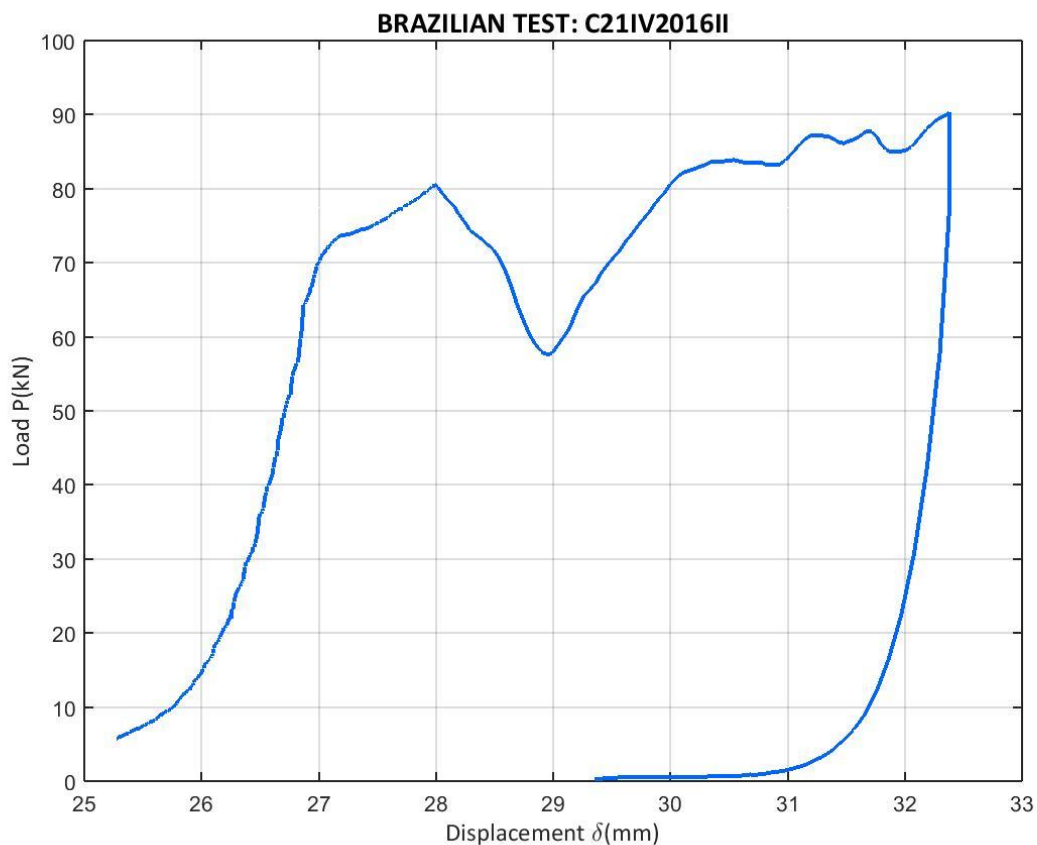


Figure 153: Load vs. vertical displacement for the Brazilian test of C21IV2016II

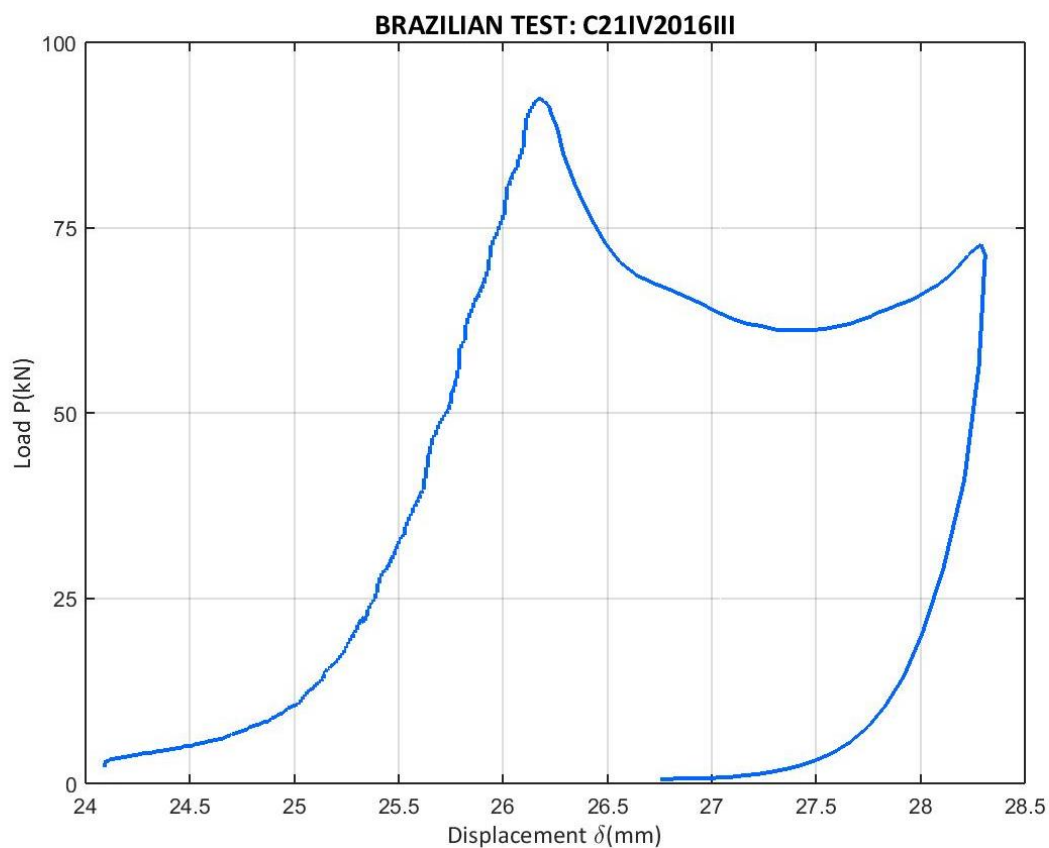


Figure 154: Load vs. vertical displacement for the Brazilian test of C21IV2016III

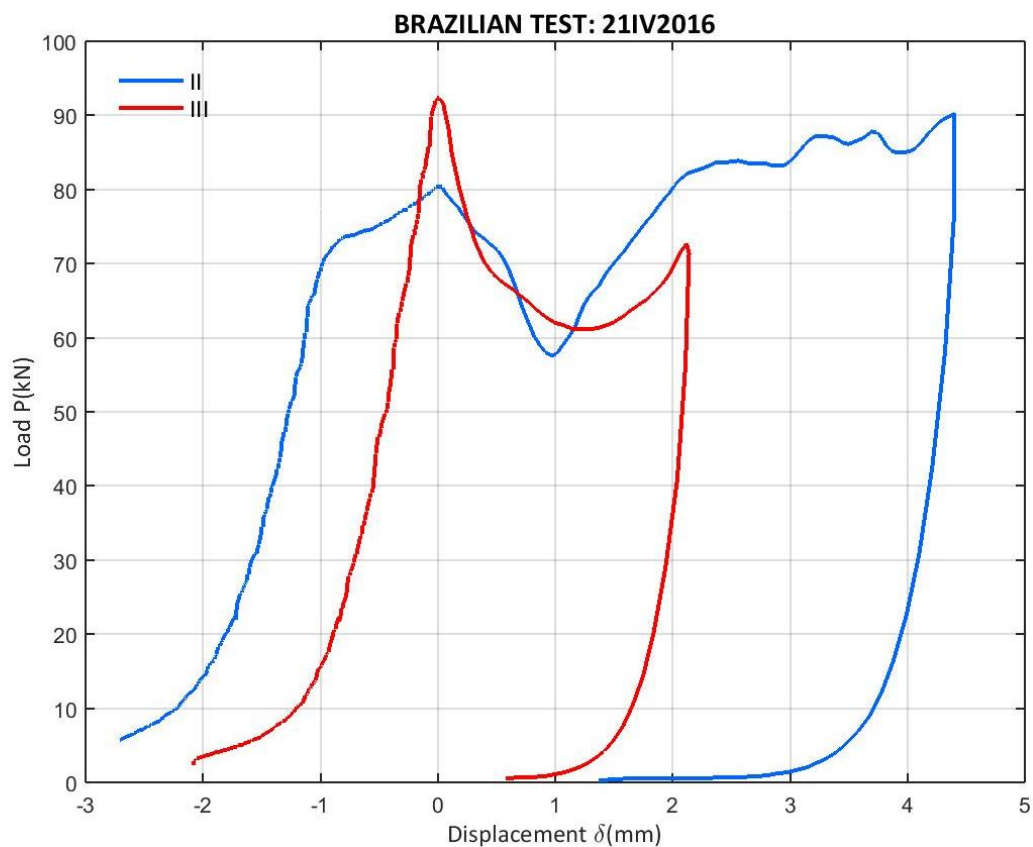


Figure 155: Load vs. vertical displacement for the Brazilian test of all C21IV2016

A.5 DETERMINATION OF THE COMPRESSIVE STRENGTH OF CONCRETE BY MEANS OF A COMPRESSION TEST

In order to find the compressive strength of the test campaigns the following procedure will be used, casting specimens within the dimensions considered in Appendix A.3 as recommended ³⁴:

- For cylindrical specimens ^{29,37}:

Cylindrical specimens will be tested in an axial compression state. The maximum load in compression is recorded. Then, the cylindrical compressive strength f_c is found in Equation A.5.1.

$$f_c = \frac{P_u}{A} = \frac{4P_u}{\pi D^2} \quad (A.5.1)$$

Where P_u is the maximum load and D is the diameter of the specimen.

- For cubic specimens ^{29,37}:

Cubic specimens will be tested in compression. In the same way, the maximum load is recorded. So, the compressive strength for cubic specimen $f_{c,cube}$ is found in Equation A.5.2.

$$f_{c,cube} = \frac{P_u}{A} = \frac{P_u}{D^2} \quad (A.5.2)$$

Where P_u is the maximum load and D is the edge length of the cube specimen.

However, this compressive strength is different for cube and cylindrical specimens ³¹, so a correction factor is applied. Table 68 summarizes the difference of compressive strength.

Table 68: Compressive strength for cylindrical and cubic specimens for different concrete classes

CLASS	C12/16	C16/20	C20/25	C25/30	C30/37	C35/45	C40/50	C45/55	C50/60
f_c	12MPa	16MPa	20MPa	25MPa	30MPa	35MPa	40MPa	45MPa	50MPa
$f_{c,cube}$	16MPa	20MPa	25MPa	30MPa	37MPa	45MPa	50MPa	55MPa	60MPa
$f_c/f_{c,cube}$	0.75	0.8	0.8	0.83	0.81	0.78	0.8	0.82	0.83

In order to compare the compressive strength $f_{c,cube}$ with f_c , Relation A.5.3 will be used.

$$f_c \approx 0.8 \cdot f_{c,cube} \quad (A.5.3)$$

Finally, the mix designation is commonly expressed in terms of the characteristic compressive strength for cylindrical and cube specimens as " $C\bar{f}/\bar{f}_{c,cube}$ ". The fracture must be satisfactory according to the figures at the codes ²⁹. The calculus is applied by a part of the Appendix C.1.2 code.

A.5.1 DIRECT COMPRESSION TEST APPARATUS

If we want to perform a direct compression test according the code of application ²⁹, we use the following elements:

- A *SERVOSIS* company compression testing machine, *MES* series, model 200, from the year 2007, working at 380V with a three-phase electric network (Figure 122). This is the same machine that has been detailed at Appendix A.3.1, which is built according the codes that the compression test codes require at its Chapter 4 ^{29,35}. Further details at Appendix A.3.1 or the following link with the catalogue: http://www.servosis.com/assets/2_21_serie_mes.pdf.
- If the specimen is not tall enough for obtaining the proper contact with the machine's maximum displacement, stiff slabs will be put on the support surface. The slabs are visible at the lower part of Figure 123.

The final configuration is something similar to Figure 156.



Figure 156: Cylinder-type specimen ready for a direct compression test

A.5.2 DIRECT COMPRESSION TEST CONFIGURATION

The control program is *PCD2K*. The software window, the calibration and the way to set up the program are detailed at Appendix A.3.2 and the windows are visible at Figure 125 and Figure 126.

For the direct compression tests, the ramp configuration is set up with a force control in the direction of compression with no acceleration and:

- For cubic specimens of 150x150x150mm, a constant speed of 600kg/s (near 0.26MPa/s)
- For cylinder specimens of 300mm long and 150mm of diameter, a speed of 900kg/s (near 0.5MPa/s)

The data is at the end exported to an ASCII text file, with 1024 register text file, which, after some adjustments, the data can be imported to the *MATLAB* platform. 1024 registers do not lose important information, because the tests are quite fast to perform.

A.6 COMPRESSIVE STRENGTH OF THE TESTED CAMPAIGNS

A.6.1 23X2015 CAMPAIGN

The results for the compressive strength for both cylindrical and cubic specimens are shown at the Table 69 for cylinders and Table 70 for cubes. The procedure detailed in Appendix A.5 is used.

Table 69: Data for the 23X2015 campaign compressive strength determination for cylindrical specimens

f_c 23X2015	Plot	$D(\text{mm})$	$L(\text{mm})$	$P_u(\text{kN})$	$f_c(\text{MPa})$
C23X2015I	Figure 157	150	300	117.818	6.67

Table 70: Data for the 23X2015 campaign compressive strength determination for cubic specimens

$f_{c,cube}$ 23X2015	Plot	$C(\text{mm})$	$P_u(\text{kN})$	$f_{c,cube}(\text{MPa})$
D23X2015I	Figure 158	150	174.128	7.74

Only one specimen of each shape was tested. So the characteristic compressive strength is 6.7MPa for cylindrical specimens and 7.7MPa for cubic specimens, with non-available standard deviation. The mix designation is C6.7/7.7, clearly lower than the first register from the Eurocode 2 (see Table 68).

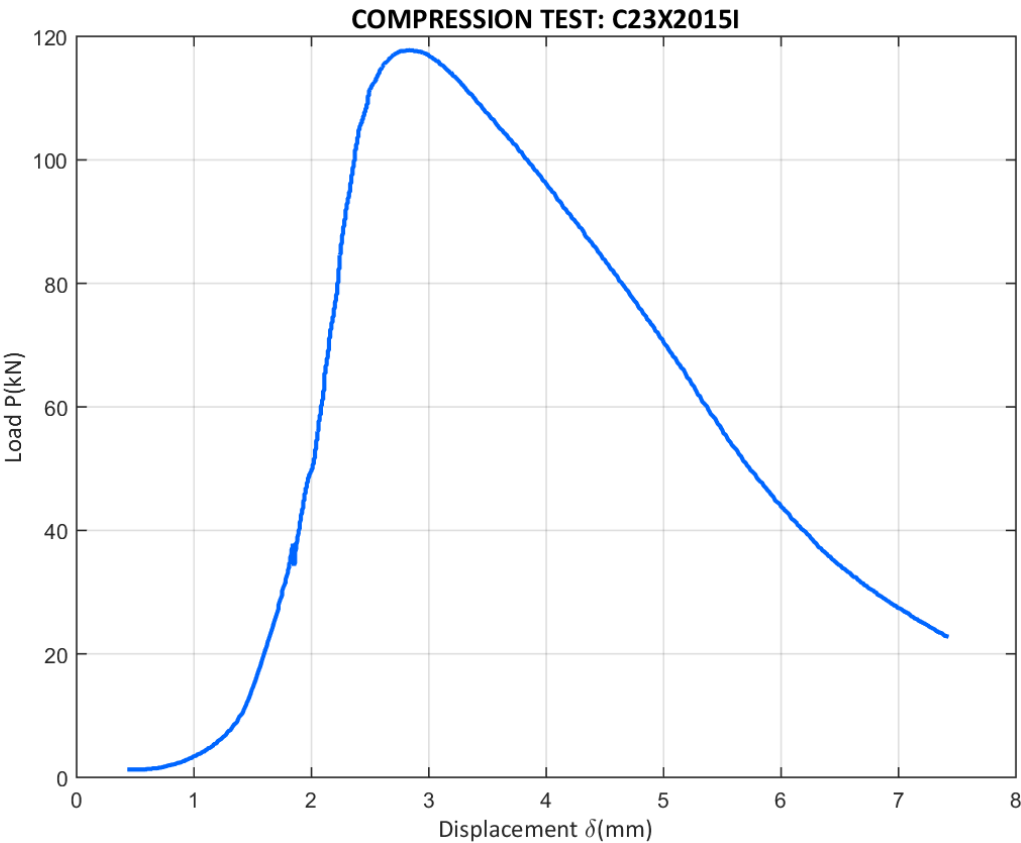


Figure 157: Load vs. vertical displacement for the direct compression test of C23X2015I

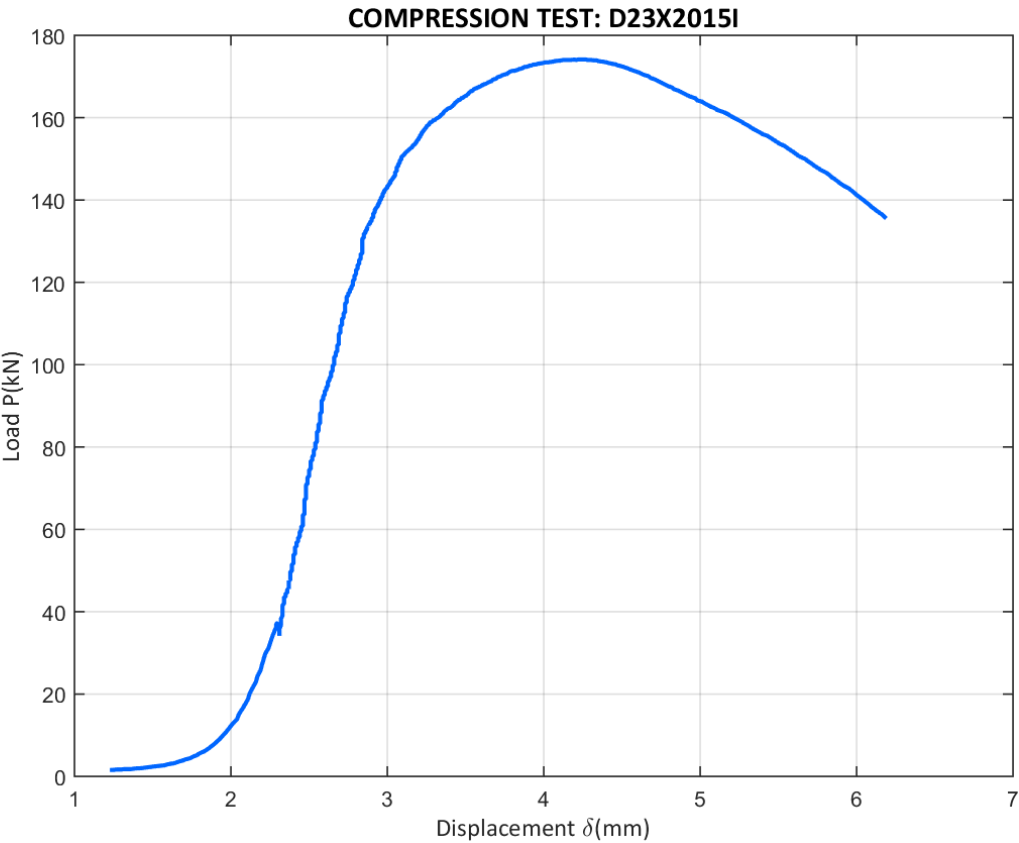


Figure 158: Load vs. vertical displacement for the direct compression test of D23X2015I

A.6.2 14XII2015 CAMPAIGN

Only one cylindrical-type specimen was tested for the compressive strength of the 14XII2015. Nevertheless, the result was not valid, because the specimen did not break as the codes affirm that a correct fracture for a valid test must be ²⁹. The fracture is similar to the F fracture pattern at Figure 4 of the code UNE-EN 12390-3:2009, reference ²⁹.

Table 71: Data for the 14XII2015 campaign compressive strength determination for cylindrical specimens

f_c 14XII2015	Plot	D (mm)	L (mm)	P_u (kN)	f_c (MPa)
C14XII2015I	Figure 159	150	300	300.971	17.031*

The compressive strength for the 14XII2015 is not known. The acquired results are not valid. However, as an informative data, the compressive strength for this series is 17.03MPa with a non-available standard deviation.

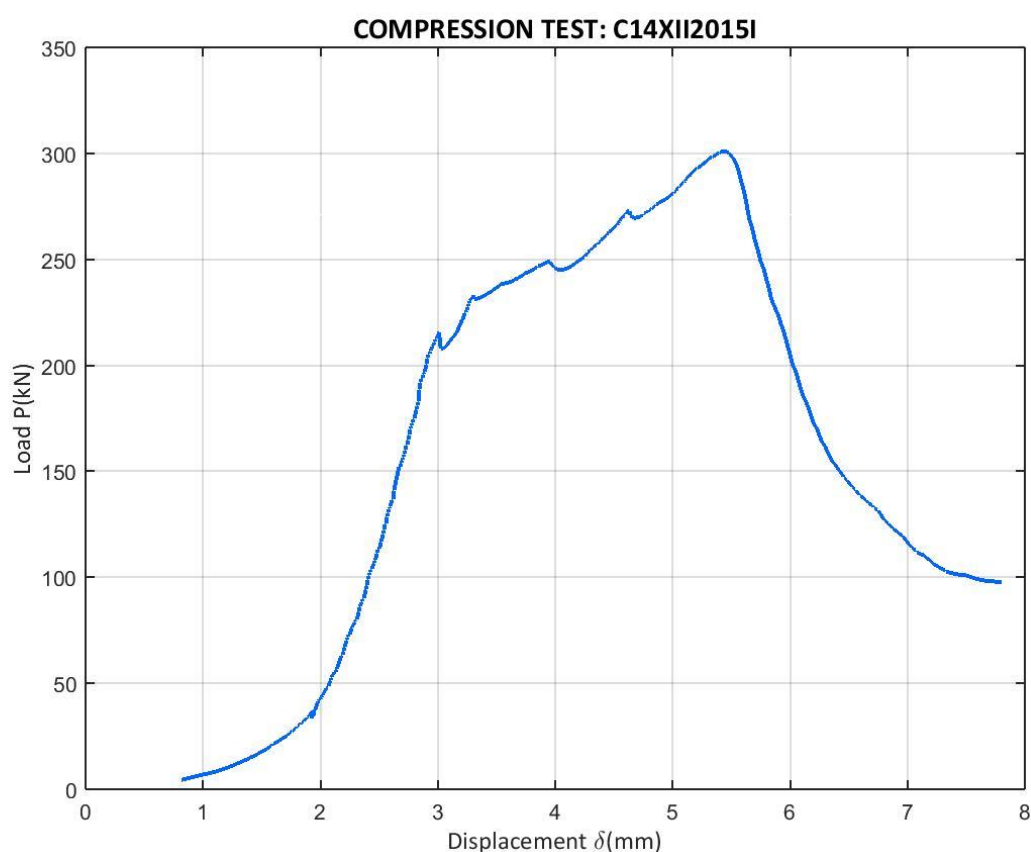


Figure 159: Load vs. vertical displacement for the direct compression test of C14XII2015I

A.6.3 29I2016 CAMPAIGN

The procedure detailed at Appendix A.5 was applied to two cubic specimens for the 29I2016 campaign. The results are given at Table 72, with its graphs and one comparative at Figure 162.

Table 72: Data for the 29I2016 campaign compressive strength determination for cubic specimens

$f_{c,cube}$ 29I2016	Plot	C(mm)	P_u (kN)	$f_{c,cube}$ (MPa)
D29I2016I	Figure 160	150	366.894	16.306*
D29I2016II	Figure 161	150	276.250	12.278*

Both tests have to be considered failed, because the fracture was not equal to all 4 faces and there were faces extremely damaged and others with a single horizontal crack. This is not accepted. Crack and fracture on D29I2016I and D29I2016II for all the surfaces were similar to Elements 1, 2 and 4 of the Figure 2 from the UNE-EN 12390-3:2009 and its *erratum* UNE-EN 12390-3:2009/AC:2011, references ^{29,30}, each Element for a different face. Just as information, the campaign mean compressive strength is 14.292MPa with a standard deviation of 2.849MPa. Both results are inside the first standard deviation, so it cannot be considered completely different types of concrete. Besides, the tests are not valid, so significant conclusions cannot be extracted.

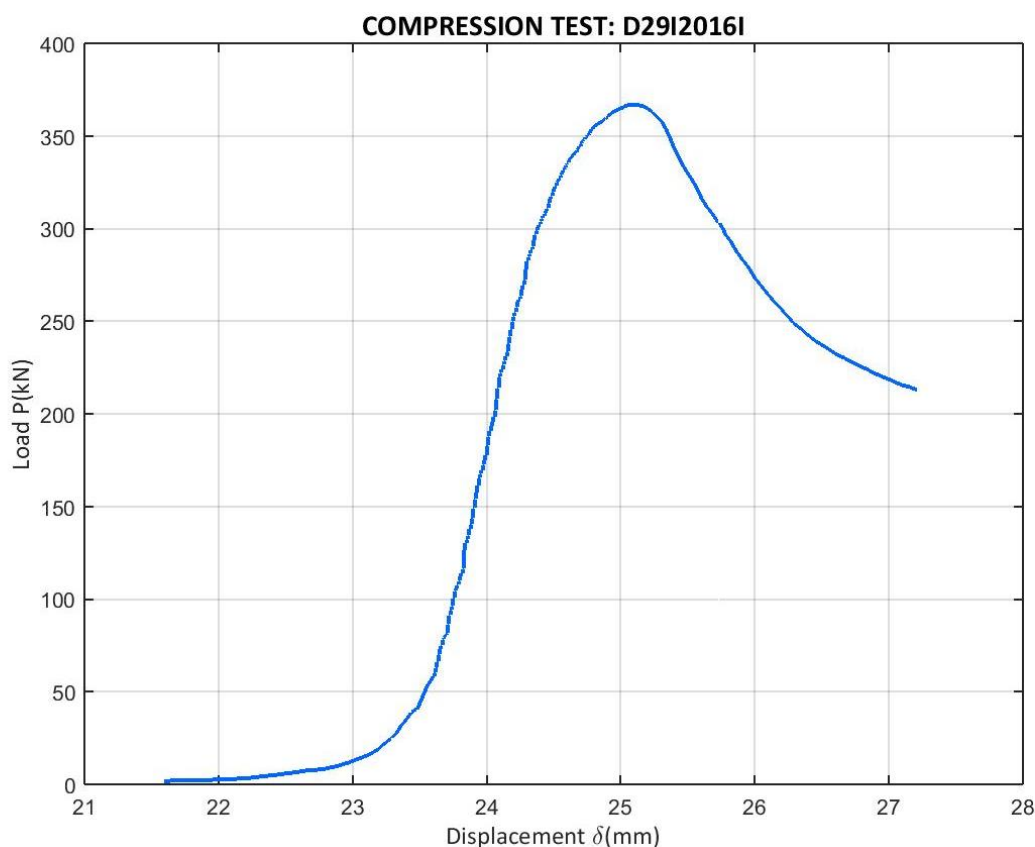


Figure 160: Load vs. vertical displacement for the direct compression test of D29I2016I

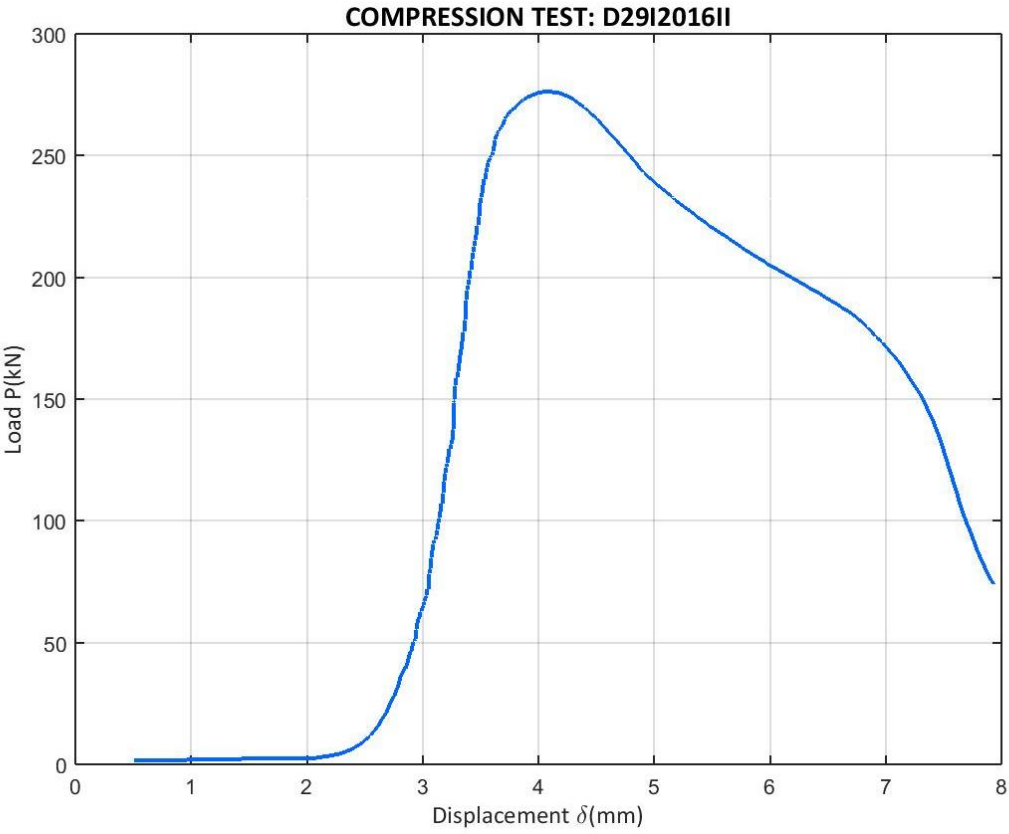


Figure 161: Load vs. vertical displacement for the direct compression test of D29I2016II

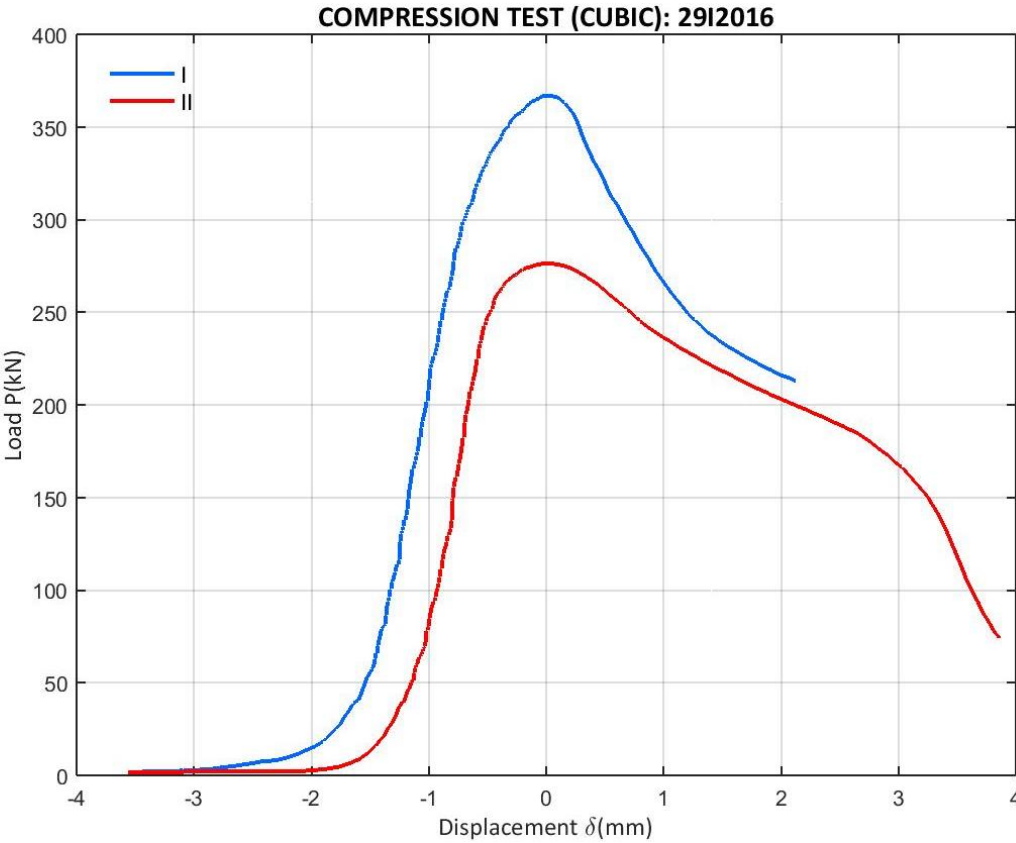


Figure 162: Load vs. vertical displacement for the direct compression test of all D29I2016

A.6.4 10III2016 CAMPAIGN

The procedure detailed at Appendix A.5 is applied to a single cylinder specimen for this campaign. Results are visible at Table 73.

Table 73: Data for the 10III2016 campaign compressive strength determination for cylindrical specimens

f_c 10III2016	Plot	$D(\text{mm})$	$L(\text{mm})$	$P_u(\text{kN})$	$f_c(\text{MPa})$
C10III2016I	Figure 163	150	300	163.729	9.265

The compressive strength for this campaign is 9.265MPa without an available standard deviation.

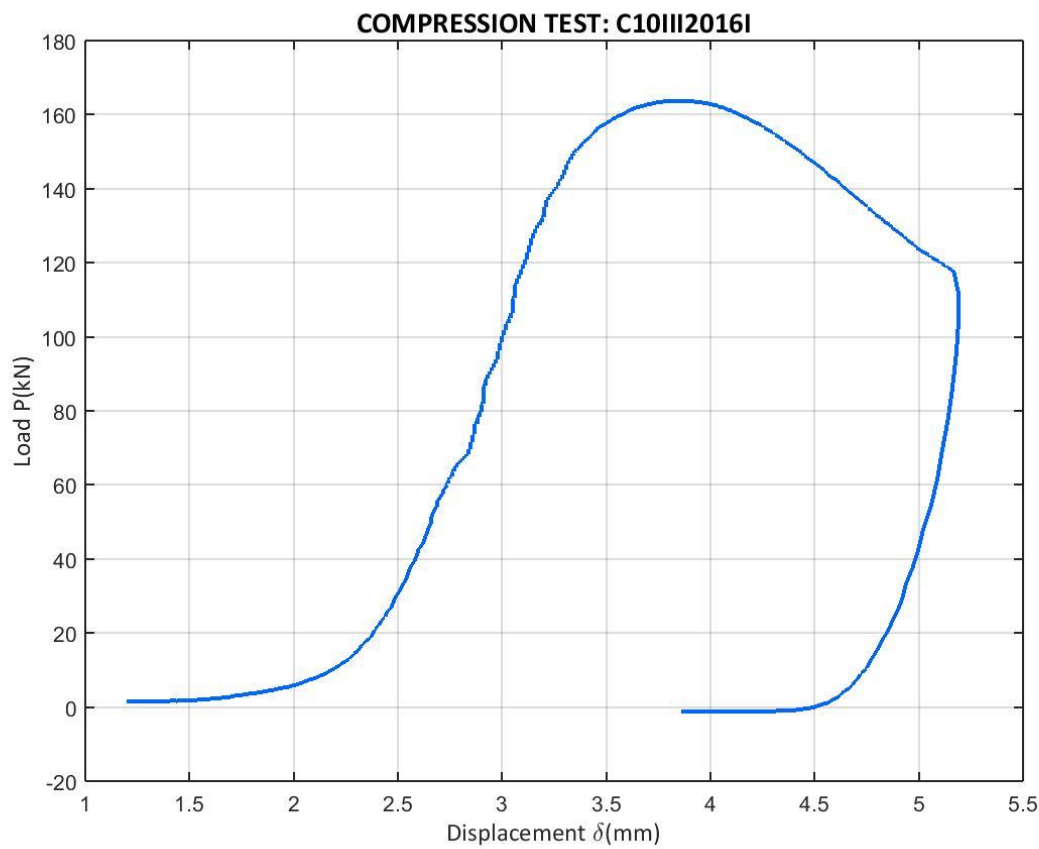


Figure 163: Load vs. vertical displacement for the direct compression test of C10III2016I

A.6.5 17III2016 CAMPAIGN

The methodology exposed at Appendix A.5 is applied to a single cylindrical specimen for the 17III2016 campaign, whose results are shown at Table 74.

Table 74: Data for the 17III2016 campaign compressive strength determination for cylindrical specimens

f_c 17III2016	Plot	D (mm)	L (mm)	P_u (kN)	f_c (MPa)
C17III2016I	Figure 164	150	300	245.152	13.873

The compressive strength for this campaign is 13.873MPa without any available standard deviation.

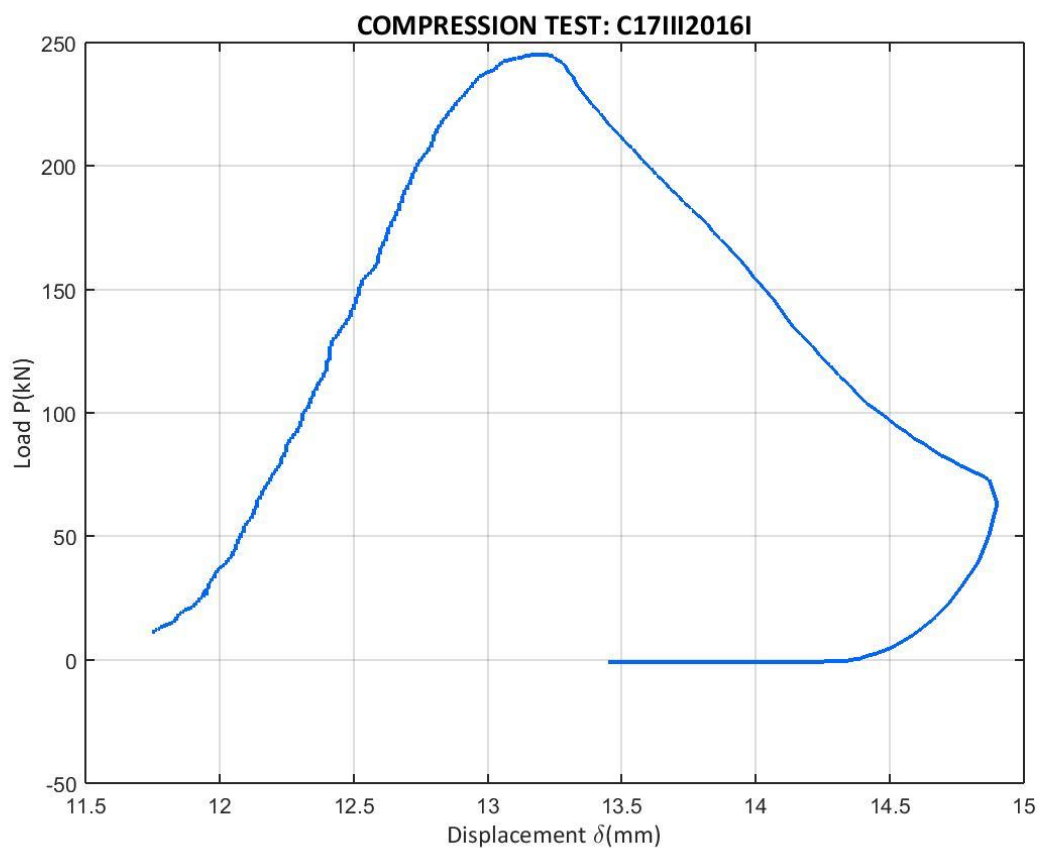


Figure 164: Load vs. vertical displacement for the direct compression test of C17III2016I

A.6.6 01IV2016 CAMPAIGN

The methodology detailed at Appendix A.5 is applied to a single cylinder-type specimen for the 01IV2016 campaign, giving the results for the compressive strength shown at Table 75.

Table 75: Data for the 01IV2016 campaign compressive strength determination for cylindrical specimens

f_c 01IV2016	Plot	D (mm)	L (mm)	P_u (kN)	f_c (MPa)
C01IV2016I	Figure 165	150	300	221.412	12.529

The final compressive strength for this campaign is 12.529MPa with non-available standard deviation.

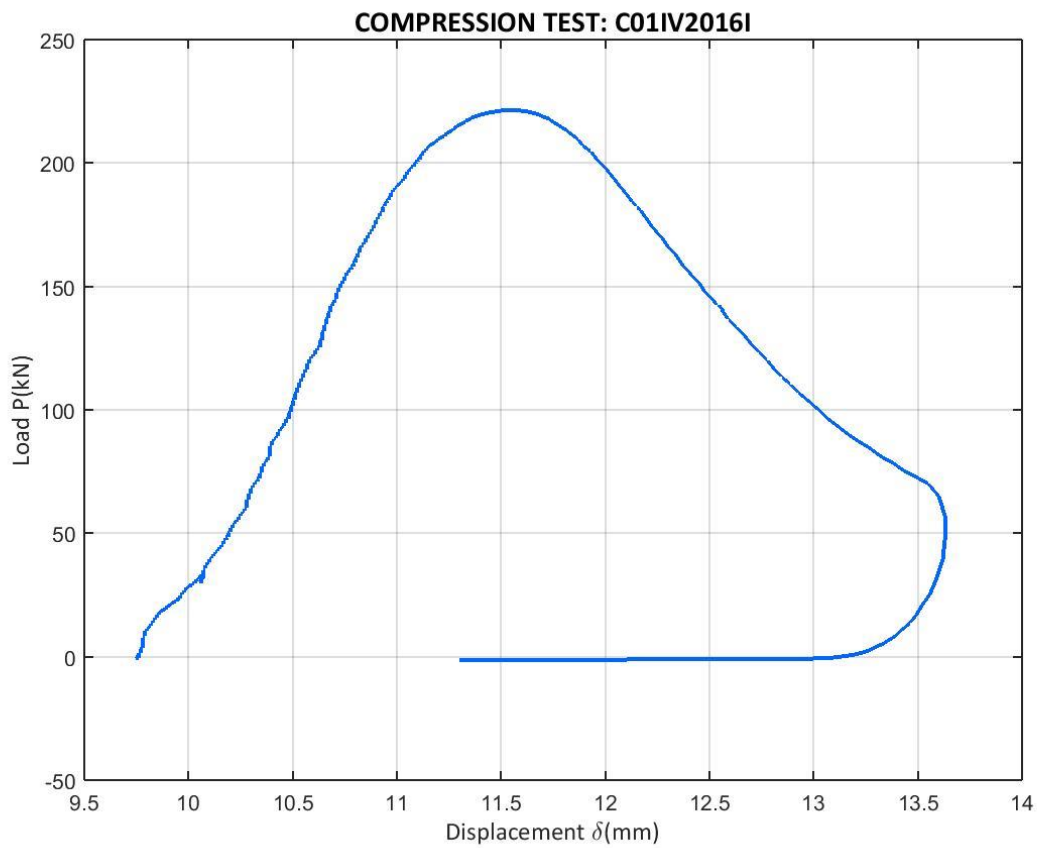


Figure 165: Load vs. vertical displacement for the direct compression test of C01IV2016I

A.6.7 07IV2016 CAMPAIGN

For a single cylinder from the 07IV2016 campaign, a direct compression test is performed and the procedure detailed at Appendix A.5 is applied. The result of this procedure is given at Table 76.

Table 76: Data for the 07IV2016 campaign compressive strength determination for cylindrical specimens

f_c 07IV2016	Plot	$D(\text{mm})$	$L(\text{mm})$	$P_u(\text{kN})$	$f_c(\text{MPa})$
C07IV2016I	Figure 166	150	300	271.639	15.372

The compressive strength for this campaign is 15.372MPa with no standard deviation available.

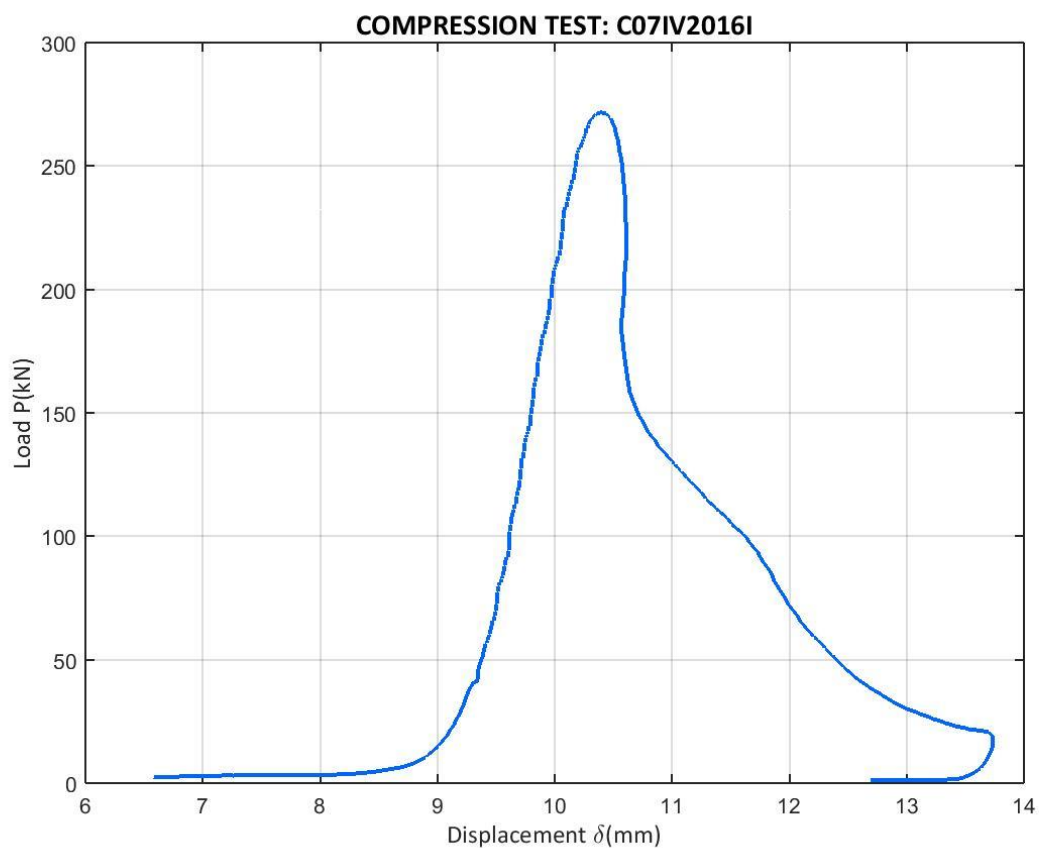


Figure 166: Load vs. vertical displacement for the direct compression test of C07IV2016I

A.6.8 14IV2016 CAMPAIGN

The test and procedure detailed at Appendix A.5 is applied once for a cylindrical specimen from the 14IV2016 campaign. The results of this process are visible at Table 77.

Table 77: Data for the 14IV2016 campaign compressive strength determination for cylindrical specimens

f_c 14IV2016	Plot	$D(\text{mm})$	$L(\text{mm})$	$P_u(\text{kN})$	$f_c(\text{MPa})$
C14IV2016I	Figure 167	150	300	359.831	20.362

The compressive strength for the 14IV2016 campaign is 20.362MPa. The standard deviation is not available.

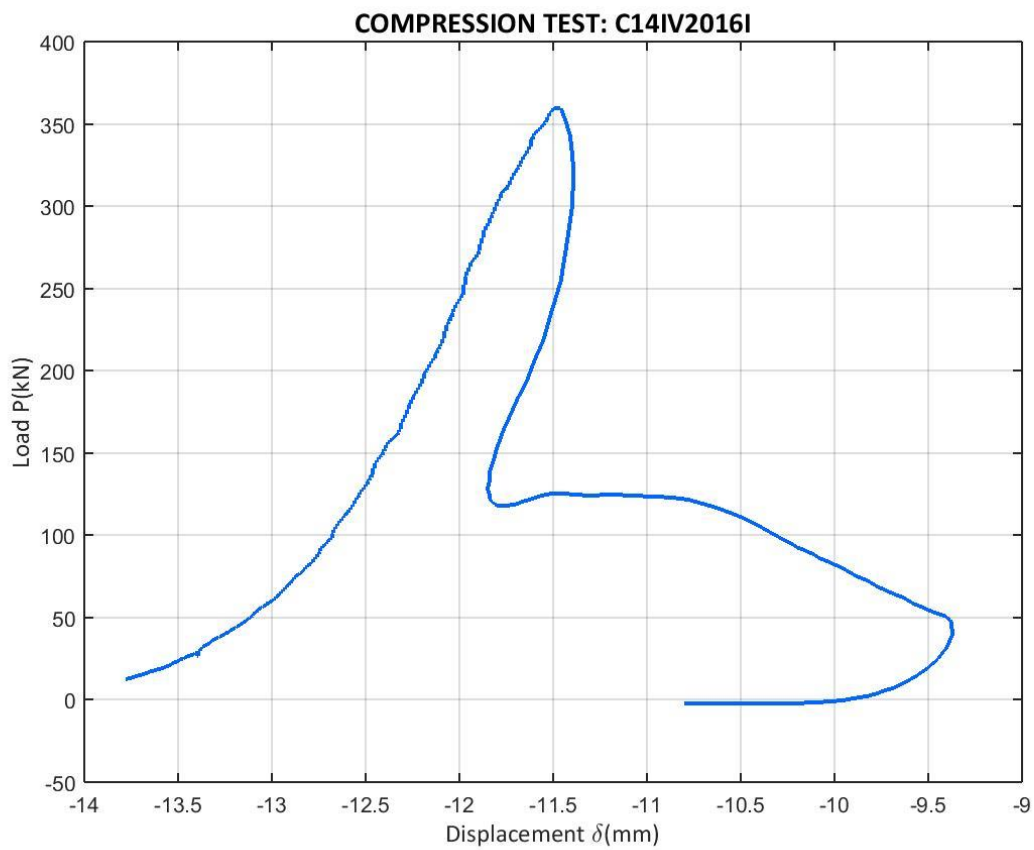


Figure 167: Load vs. vertical displacement for the direct compression test of C14IV2016I

A.6.9 21IV2016 CAMPAIGN

The methodology detailed at Appendix A.5 is applied for a single cylinder specimen cast for the 21IV2016 campaign. The result for the direct compression test is given at Table 78 with its graph.

Table 78: Data for the 21IV2016 campaign compressive strength determination for cylindrical specimens

f_c 21IV2016	Plot	$D(\text{mm})$	$L(\text{mm})$	$P_u(\text{kN})$	$f_c(\text{MPa})$
C21IV2016I	Figure 168	150	300	288.414	16.321

The compressive strength for this campaign is 16.321MPa with any available standard deviation.

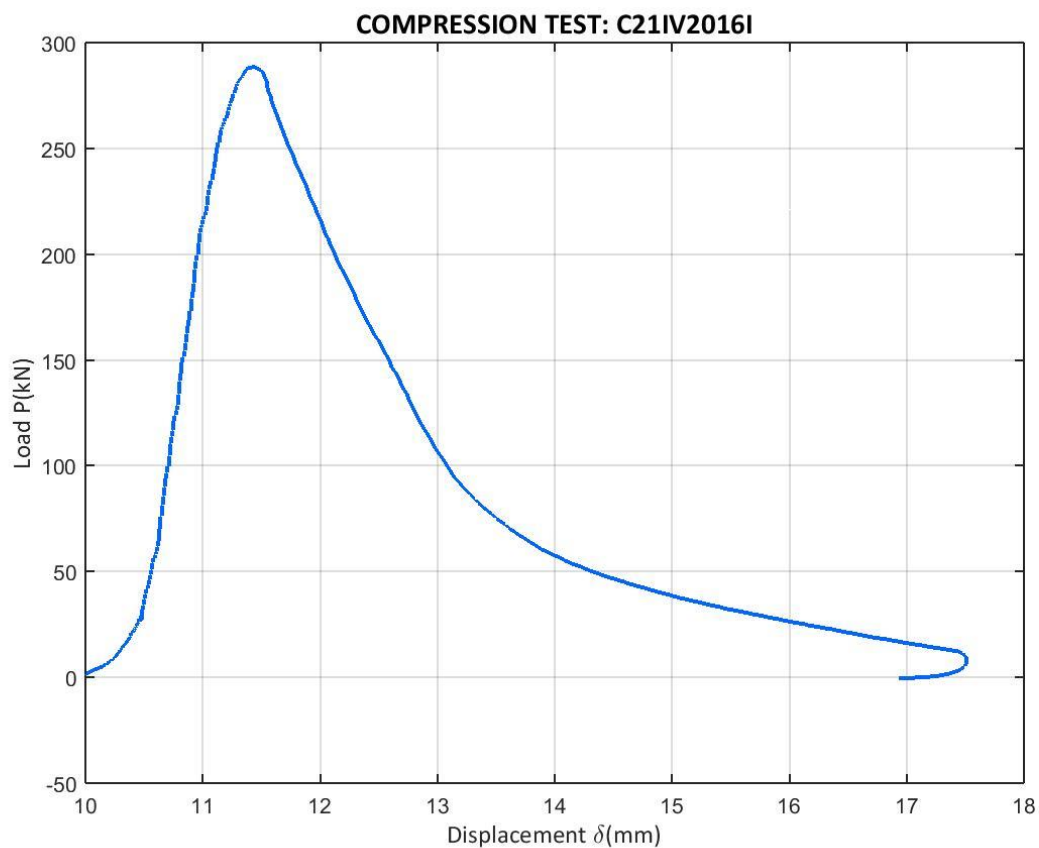


Figure 168: Load vs. vertical displacement for the direct compression test of C21IV2016I

B THREE POINT BENDING TESTS MISCELLANEA

B.1 FORMER TEST ATTEMPTS: 17VI2015 AND 13X2015 TESTS

This tests were performed with two C50 prismatic specimens, one was tested at 17th July 2015 and another one at 13th October 2015. The specimens were not cast for this project, but, somehow, we had them, so it was a chance to begin on realizing and arranging the three point bend tests. No information about the casting is given, but it does not matter, because these tests were only first attempts and this data is currently not used.

However, the result was unsatisfactory due sudden crack propagation in the 13X2015 attempt, which did not allow observing the full softening phenomenon and it lead to an invalid registered data. The 17VI2015 test attempt showed also quick crack propagation, but the softening phenomenon is still visible, even though a part of the $P - w$ curve is missing. See Figure 169, Figure 170, Figure 171 and Figure 172 to observe the missing data registers. The data was treated with the same procedure as the ones with the $P - \delta$ tail correction.

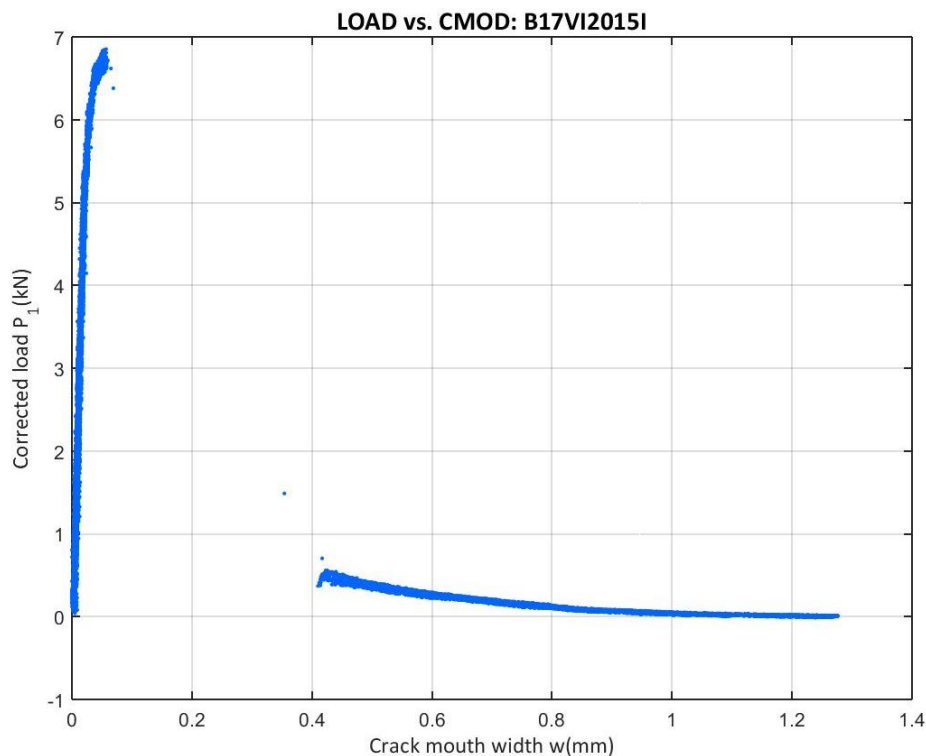


Figure 169: Corrected load vs. CMOD at the B17VI2015I test

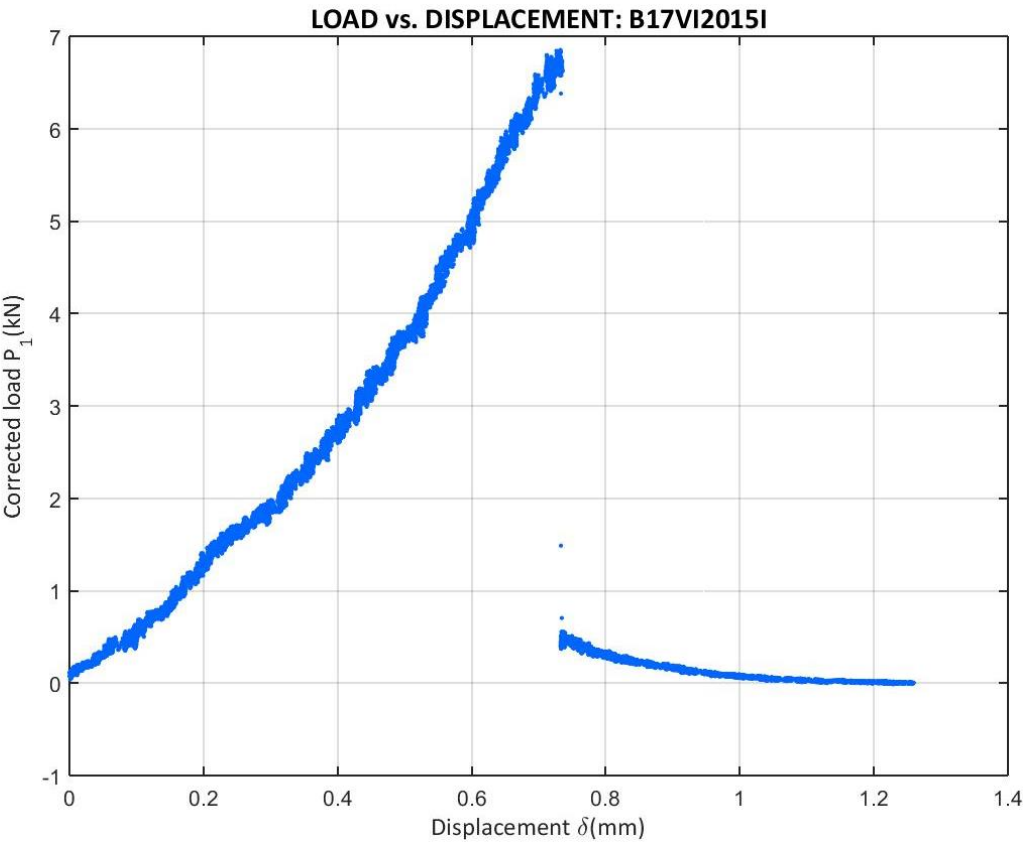


Figure 170: Corrected load vs. Displacement at the B17VI2015I test

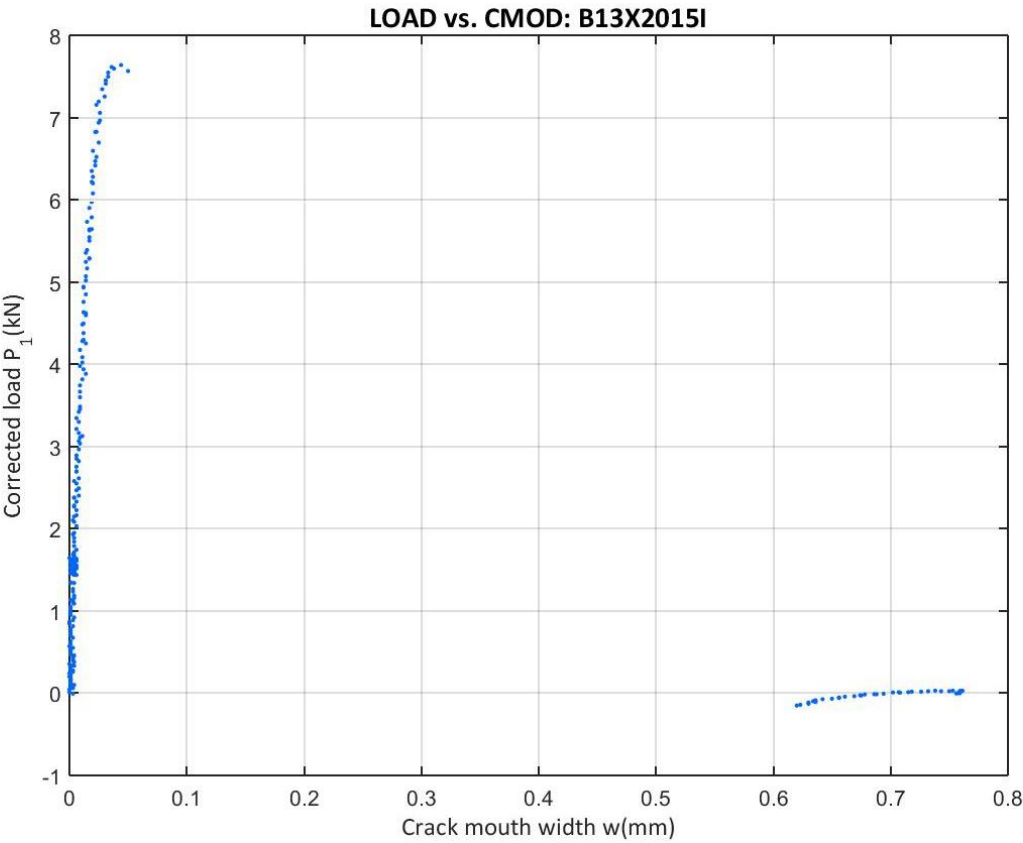


Figure 171: Corrected load vs. CMOD at the B13X2015I test

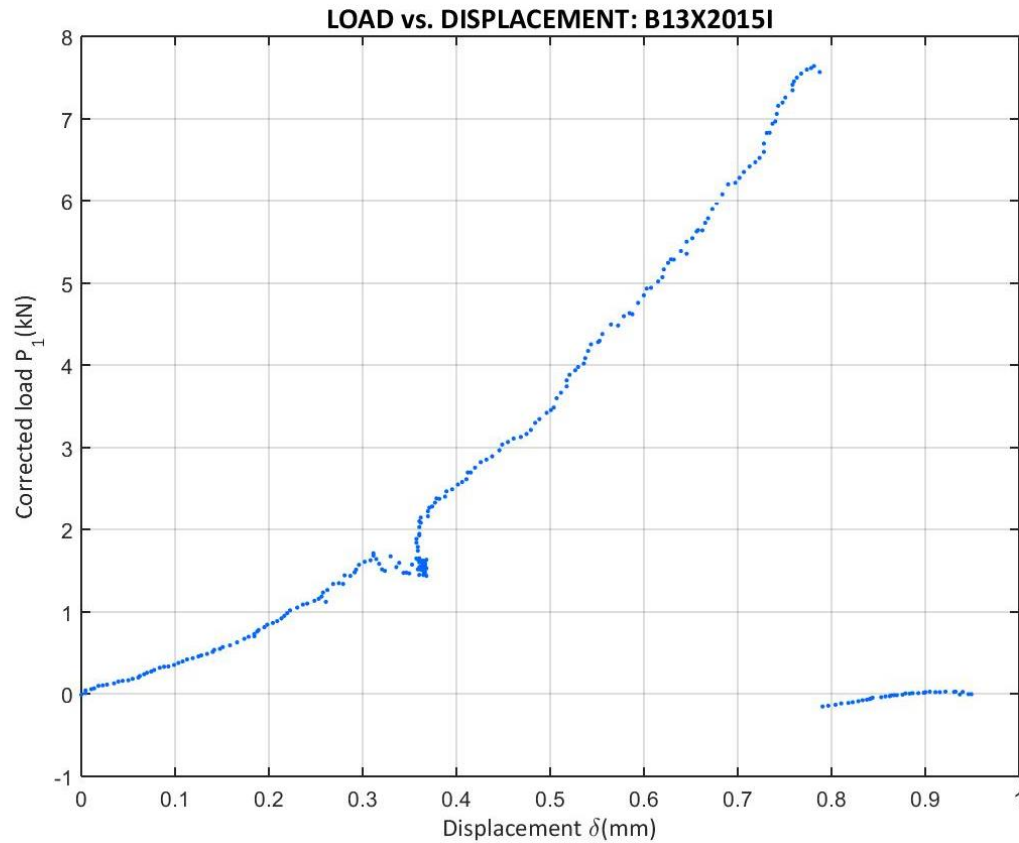


Figure 172: Corrected load vs. Displacement at the B13X2015I test

These facts lead to two conclusions:

- If more stable tests were wanted, the configuration of the test could be modified to change the speed of displacement control with a lower value. This is applied on the first campaigns. The current speed is between 6 – 9 $\mu\text{m/s}$ and it will be reduced on the future campaigns.
- If stable tests were wanted to check the feasibility of this project, it may be worth to consider beginning with a less brittle material, which means trying to begin not with high-strength concrete, but with low- or normal-strength concrete. This was searched on the first campaigns.

The difference between 17VI2015 and 13X2015 was the higher speed of the vertical displacement and the introduction of a new degree of freedom in the torsion rotation and the use of a stiffer machine, which will be conserved on the future campaigns. Nevertheless, for high-strength concrete it was not enough.

NOTE: The references for these two tests were not the date of unmolding, because it is unknown, but the date of testing.

B.2 MEASUREMENT STUDIES

B.2.1 STUDY OF THE DISPLACEMENT RECORDING

One of the fracture parameters is obtained thanks to a displacement record in order to process Equation 3.2.2. The machine does not work moving the head with the load applicator, but moving the whole base with a piston. Nevertheless, the process is still correct, because the forces at the three points create, at the end, the relative vertical downwards displacement of the central section. In order to check if the recorded displacement is the one we want, we create a first test with some extra outputs, because of the thought that in some cases the head could move.

- 17III2016 Campaign

A provisional setup is done. It can be seen at Figure 173 and Figure 174.



Figure 173: LDTs to record the absolute machine head displacement (right) and the relative piston-to-load applicator displacement (left) – Campaign 17III2016



Figure 174: Setup of LDTs to record other types of displacement, front view – Campaign 17III2016

This provisional setup extracts the displacements read from the machine piston transducer, the one we believe it is correct, and with 2 extra transducers we can record

- the displacement of the machine's head placing a *LDT* at the static base of the machine and the measuring point at the head bottom (Figure 173, right)
- the relative displacement from the piston to the load applicator, or the head (Figure 173 left and Figure 174)

This setup has a problem and it is that the relative displacement, as it is only recorded at one side of the load applicator, is not able to neglect the effect of torsion of the specimen or rotation of the bolts and the load applicator. Future versions of this study should correct this.

At the end, the valid displacement to compute the fracture energy is the one between the rollers and the load applicator. Due the difficulty of that, the one that should be nearest is the relative displacement of the piston, where the rollers are placed, respect the load applicator. If this relative record has little difference of speed with the direct machine record, the direct measurement is correct for the W_f calculation. This also means that the head displacement should be near zero.

The comparison is done from the first valid value of the test, where the correct load P_1 equals zero at the rising part considered for G_f calculation. The results of the first version from this substudy are given at Table 79.

Table 79: Results of the first speed study – 17III2016 campaign

TEST	Plot	ABS Piston	ABS Head	REL	$ e_{\text{ABSPiston-REL}} $	$ \text{Head/Piston} $
B17III2016II	Figure 175	0.839 $\mu\text{m/s}$	0.887nm/s	0.911 $\mu\text{m/s}$	8.60%	0.11%
B17III2016III	Figure 176	0.843 $\mu\text{m/s}$	5.110nm/s	0.848 $\mu\text{m/s}$	0.70%	0.61%
B17III2016IV	Figure 177	0.844 $\mu\text{m/s}$	22.495nm/s	0.854 $\mu\text{m/s}$	1.16%	2.66%

Without the correction for torsion and rotation of the load cell, the mean difference between the direct measured speed and the relative speed is about 3.48%, considering the results that show two values about 1% or lower. For this part, it cannot be considered a huge difference, so we keep the hypothesis that the valid displacement is the direct record one, until further studies can contradict it.

For the movement we thought the head of the machine would have, the mean contribution to this displacement is about 0.36%, with the two results of about 0.60% or under. Test IV cannot be taken into account due to external phenomena during the tests of sudden movement of the transducer base. So, the same conclusion can be extracted, we cannot affirm now that the direct record is not valid or incomplete because of the little movement the head showed.

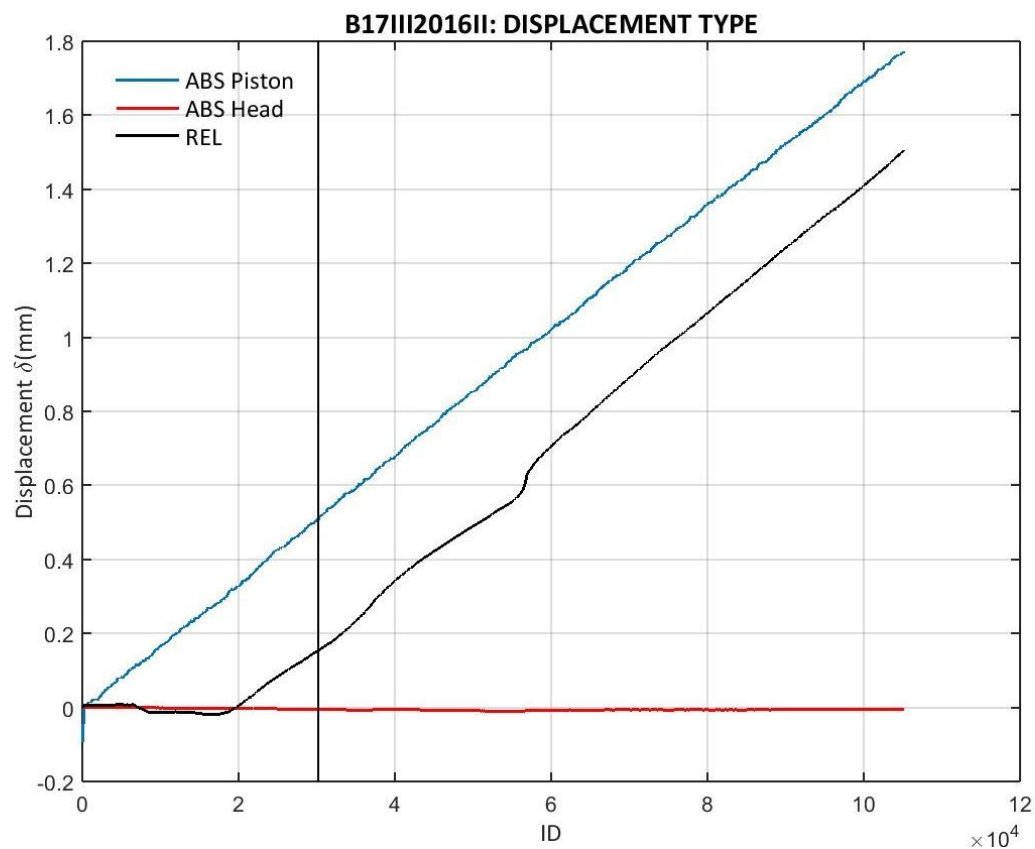


Figure 175: Types of displacement at the B17III2016II test. The line marks the real beginning of the test

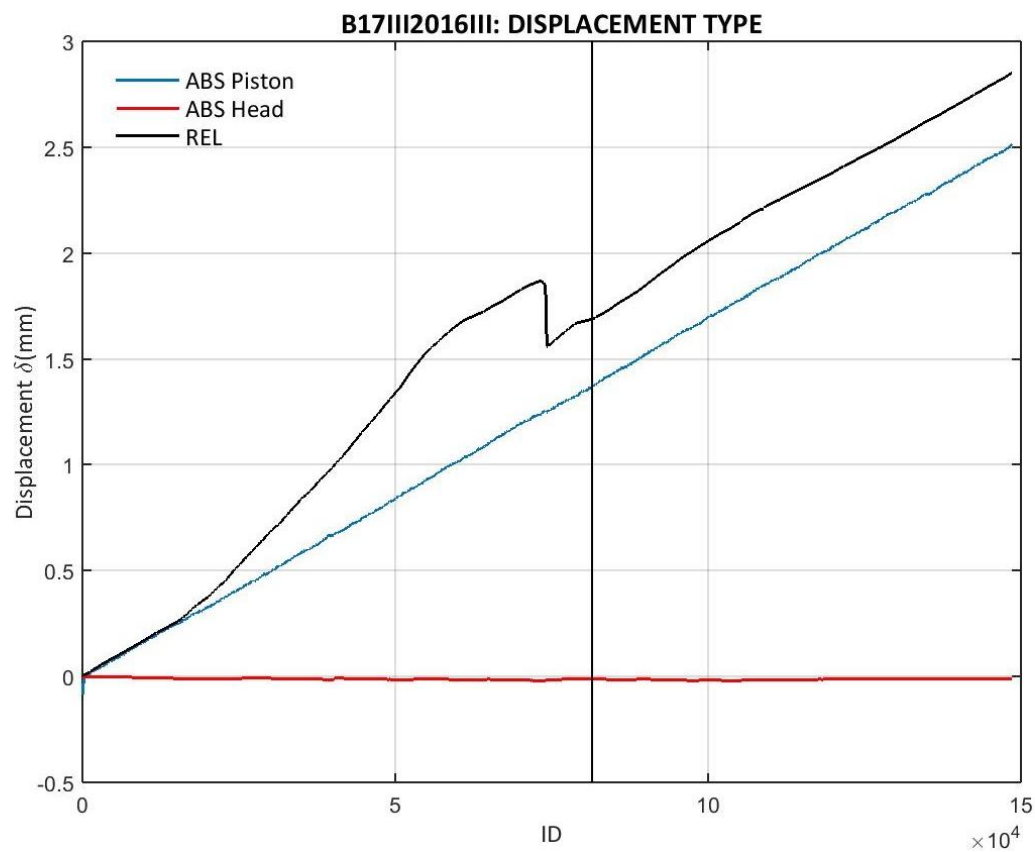


Figure 176: Types of displacement at the B17III2016III test. The line marks the real beginning of the test

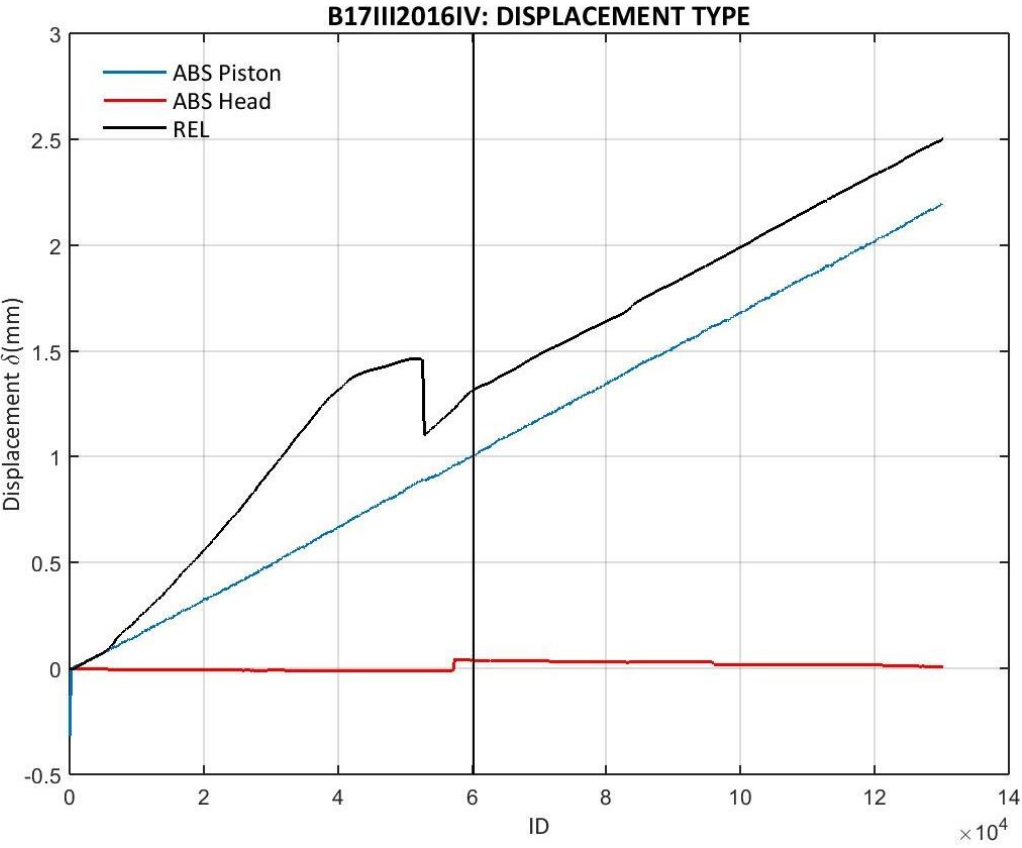


Figure 177: Types of displacement at the B17III2016IV test. The line marks the real beginning of the test

B.2.2 STUDY OF THE CRACK MOUTH OPENING DISPLACEMENT RECORDING

During the project, there was the possibility to perform a three point bending test with non-used beam specimens in the lab with the Digital Image Correlation (*DIC*) technique. The composition and casting date was unknown, so it is not any campaign, but an extra one, with reference 12I2016.

The basis of the *DIC* is, using a reference image in two dimensions or a calibration image set in three dimensions, to consider square regions on an gray-scaled image, what is call a *subset*, where a high-contrast random speckle pattern can be followed image-by-image with a correlation algorism, so the movement of the surface of interest can be computed in form of vertical and horizontal displacement fields and strain fields with postcalculation algorisms. For more details, see specialized papers on this field, because for what we want now, which are the fields of displacement, a reduced knowledge is enough.

We begin with the basis that the displacements fields are correct enough to believe them on a planar calculation (with the platform *Vic2D*, from Correlated Solutions) and the strain fields can show us the crack path, but not considering the strain values. Knowing the displacements, the crack width can be estimated with Equation B.2.1, taking the displacements for two points at both sides of the crack.

$$w = \sqrt{(u_r - u_l)^2 + (v_r - v_l)^2} \quad (B.2.1)$$

Where w is the crack width estimation, u and v are, respectively, the horizontal and vertical displacement of the points, both the right side of the crack r and left l .

So, we proceed on preparing the acquisition system for the *DIC*, preparing the surface with a speckle pattern and the lab with the proper lightning (see Figure 178 and Figure 179).

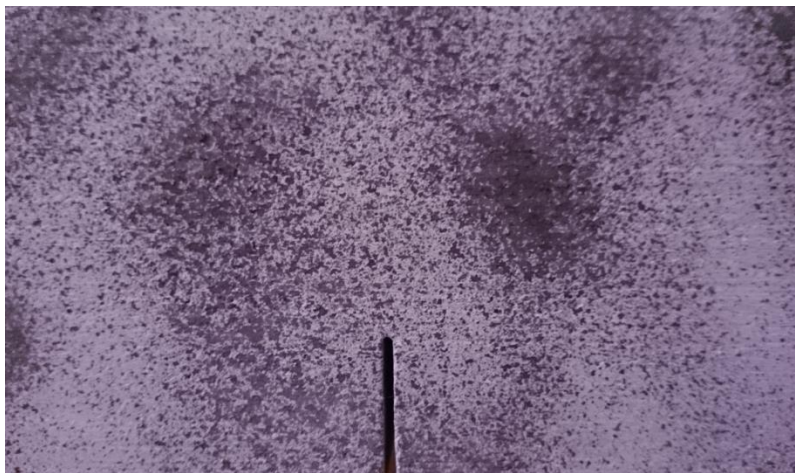


Figure 178: Example of a speckle pattern

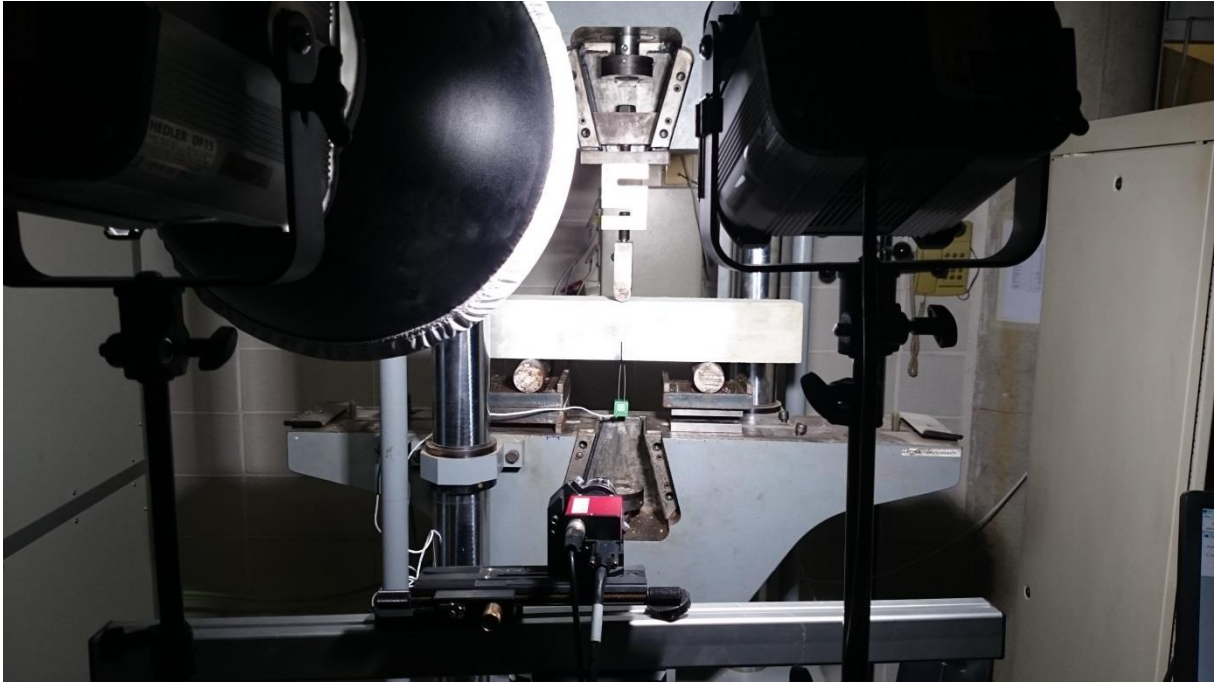


Figure 179: Three point bending test with the DIC setup

After acquiring the data and the images, these last ones are processed with the proper program and the fields of processed results can be showed on the images for the calculated variables (for example, the horizontal displacement on an initial stage Figure 180 and an advanced stage Figure 181). The original configuration shows lower values near purple and higher values near red.

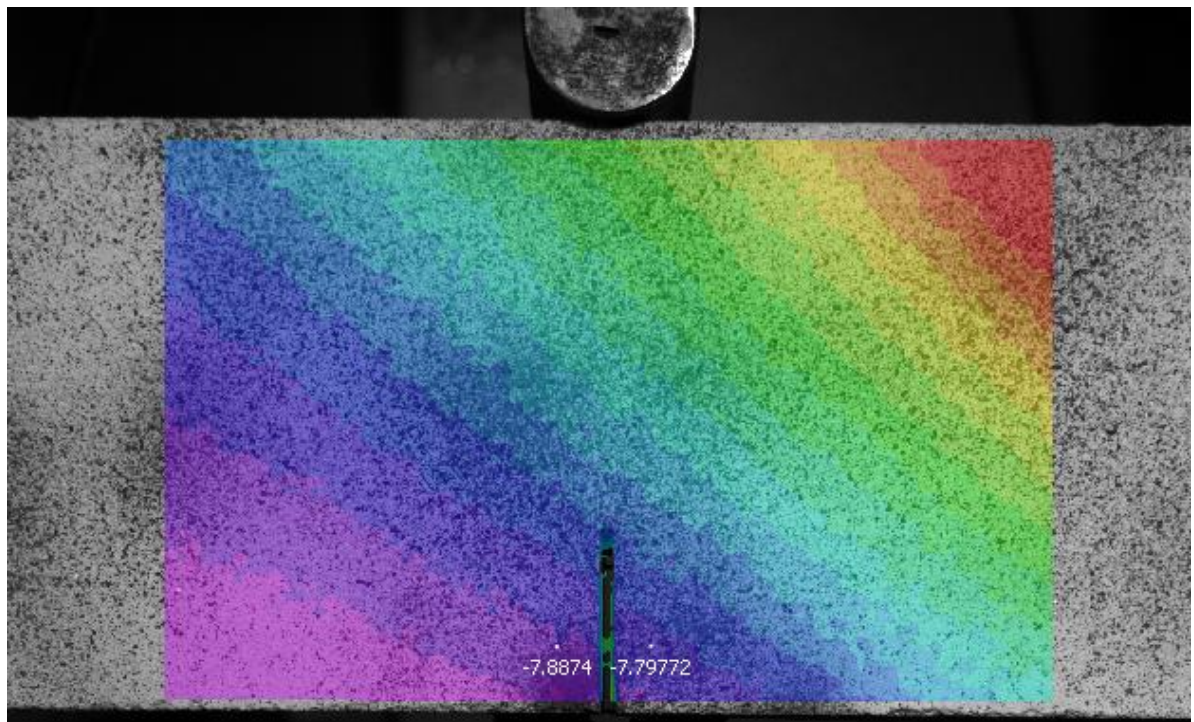


Figure 180: Horizontal displacement at an early stage of the test

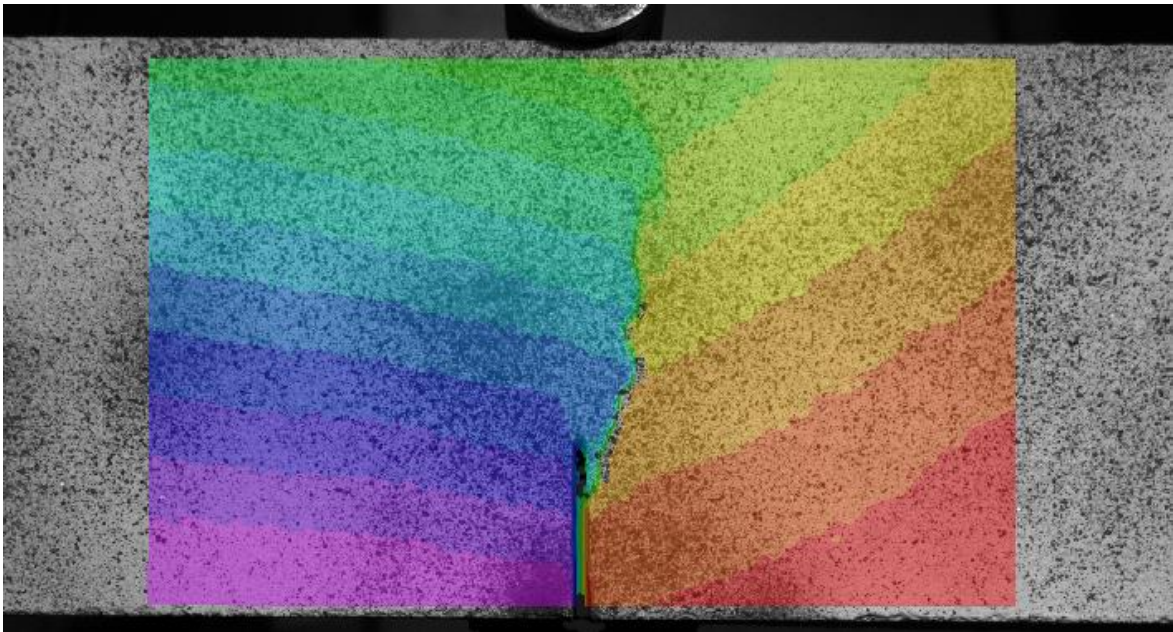


Figure 181: Horizontal displacement at an advanced stage of the test

When a crack appears, on the displacements fields exists a huge gradient of value at one side and another of the crack. On a strain field image, the higher values usually coincide with the crack path (see Figure 182).

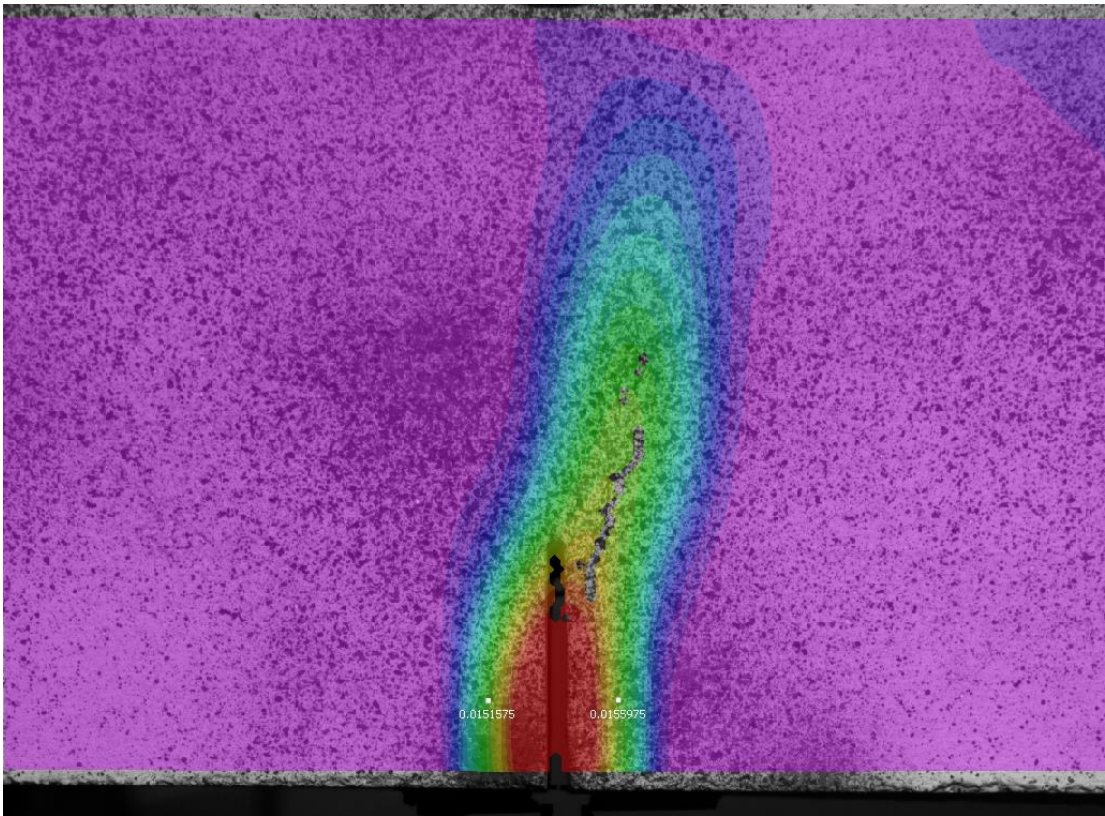


Figure 182: Horizontal axis strain field at an advanced stage of the test

On some figures, two points are visible; these are the ones where the data will be extracted. As a recommendation, it is better not to choose points near the edge of the area of interest or near the visible crack, because there can be easily calculation mistakes.

As the gage is placed 2mm under the bottom surface, the *DIC* crack width with the chosen points should be less than the record from the crack opening displacement gage. The chosen points are placed 10mm at each side of the crack and 10mm above the area of interest lower edge.

The result of this study is a graph, as Figure 183.

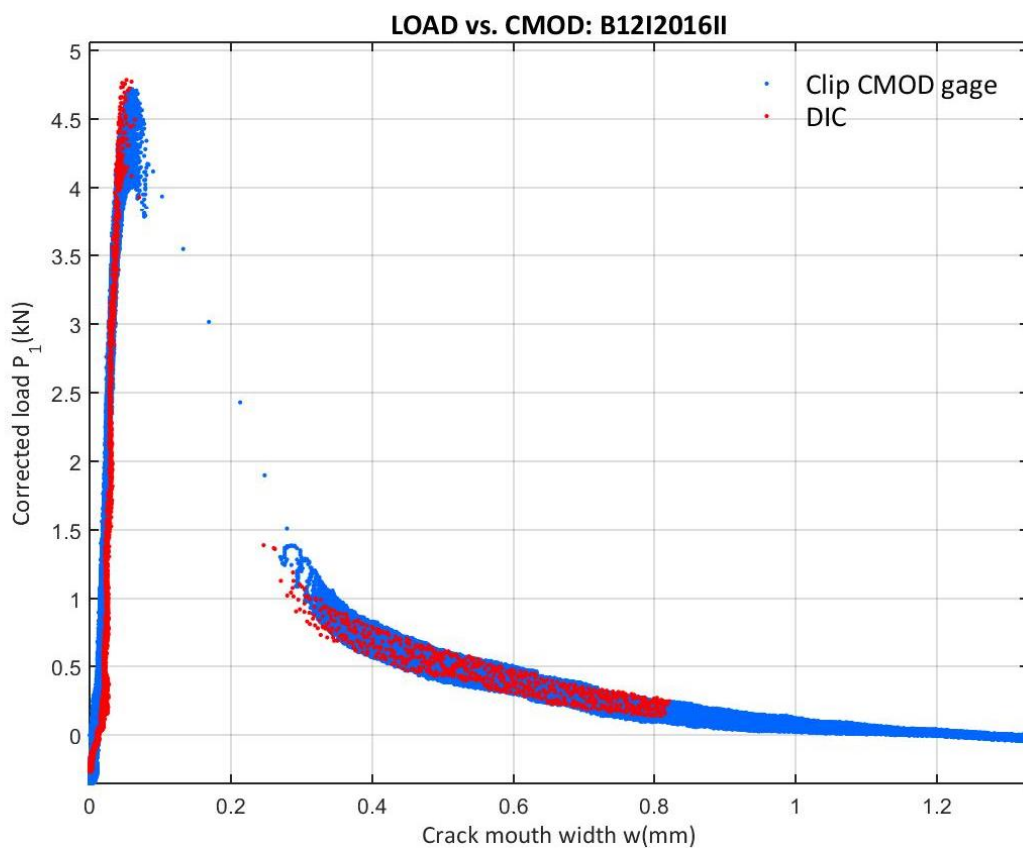


Figure 183: CMOD gage vs. DIC crack width

Values of crack width provided by the *DIC* and the gage are quite similar, but the ones from the gage are usually higher than the *DIC* values. This fact can be easily seen near the peak load and on the beginning of the unloading curve. The speed of the crack appearance makes impossible for a 2 seconds image acquisition rate to follow the phenomenon.

For this reason, we have not got any sign of bad configuration, calibration or placement of the gage and its recordings can be considered valid.

C USED CODES

C.1 MATLAB SCRIPTS

C.1.1 BASIS FOR THE TAIL CORRECTION IN THE LOAD VS. DISPLACEMENT GRAPH DATA PROCESSING CODE

```
%INDIVIDUAL SETTINGS FOR A SINGLE TEST WITH P-DELTA CORRECTION
%{
FUNCTIONS IN USE
GF_ajuste_cola
encuentra_valor
encuentra_valor_con_limite
encuentra_valor_intervalo
encuentra_zeros_limite
max_min_med_vec
E_flexion3P
%}
clc
close all
clear all
format long e

dataI=textread('B23X2015I.txt');
timeI=dataI(:,2);
IDI=dataI(:,1);
HPI=dataI(:,4);
HPI=HPI*9.81/1000; %kN
PI=dataI(:,6);
PI=-PI*9.81/1000; %kN
CMODI=dataI(:,5); %mm
DeltaI=dataI(:,3); %mm
clear data
%ALL mm
aI=31;
DI=100;
BI=100;
SI=300;
hI=2;

%Original variable plotting
plot(HPI,'Linewidth',2,'Color',[0 0.4 1])
xlabel ('ID','FontName','Calibri','FontSize', 12)
ylabel ('Load P(kN)','FontName','Calibri','FontSize', 12)
title('LOAD HEAD: B23X2015I','FontName','Calibri','FontSize',
14,'FontWeight','bold')
legend boxoff
grid on
print -djpeg SerieHP_B23X2015I
```

```

%Minimum equal to zero
CMODI=CMODI-min(CMODI);
DeltaI=DeltaI-min(DeltaI);
%FILTERING, WHEN NEEDED \\1=no
nCMOD=1;
nP=1;
nDelta=50;

for i=1:nP
    b(i)=1/(nP);
end
figure
plot(PI,'Linewidth',2,'Color',[0 0.4 1])
hold on
xlabel('ID','FontName','Calibri','FontSize',12)
ylabel('Load P(kN)','FontName','Calibri','FontSize',12)
title('LOAD: B23X2015I','FontName','Calibri','FontSize',
14,'FontWeight','bold')
PI=filter(b,1,PI);
if nP>1
    plot(PI,'Linewidth',2,'Color',[1 0 0])
    legend({'Original','Filtered'},'FontName','Calibri','FontSize',
14,'Location','Northeast')
    legend boxoff
end
grid on
print -djpeg SerieP_B23X2015I

for i=1:nCMOD
    b(i)=1/(nCMOD);
end
figure
plot(CMODI,'Linewidth',2,'Color',[0 0.4 1])
hold on
xlabel('ID','FontName','Calibri','FontSize',12)
ylabel('CMOD w(mm)','FontName','Calibri','FontSize',12)
title('CMOD: B23X2015I','FontName','Calibri','FontSize',
14,'FontWeight','bold')
CMODI=filter(b,1,CMODI);
if nCMOD>1
    figure
    plot(CMODI,'Linewidth',2,'Color',[1 0 0])
    legend({'Original','Filtered'},'FontName','Calibri','FontSize',
14,'Location','Northwest')
    legend boxoff
end
grid on
print -djpeg SerieCMOD_B23X2015I

for i=1:nDelta
    b(i)=1/(nDelta);
end
figure
plot(DeltaI,'Linewidth',2,'Color',[0 0.4 1])
hold on
xlabel('ID','FontName','Calibri','FontSize',12)
ylabel('Displacement \delta(mm)','FontName','Calibri','FontSize',12)
title('DISPLACEMENT: B23X2015I','FontName','Calibri','FontSize',
14,'FontWeight','bold')
DeltaI=filter(b,1,DeltaI);
if nDelta>1

```

```

    plot(DeltaI, 'Linewidth', 2, 'Color', [1 0 0])
    legend({'Original', 'Filtered'}, 'FontName', 'Calibri', 'FontSize',
14, 'Location', 'Northwest')
    legend boxoff
end
grid on
print -djpeg SerieDelta_B23X2015I
clear nCMOD nP nDelta b
clc

[GFI, GfI, WGI, inicioI, picoI, limiteI, finalI, XI, P1I, P1colaI, WMI, KI, AI] =
GF_ajuste_cola(aI, DI, BI, SI, CMODI, PI, DeltaI);
PRI=PI(finalI);
%New upper curve
[P1CMODI,~,WMI]=upper_lower(WMI(1:finalI),P1I(1:finalI),2e-3);
[P1DeltaI,~,DDI]=upper_lower(DeltaI(1:finalI),P1I(1:finalI),2e-3);
[inicioCMODI,~]=encuentra_zeros_limite(P1CMODI,length(WMI)/2);
[inicioDeltaI,~]=encuentra_zeros_limite(P1DeltaI,length(DDI)/2);
%To use if initial part is decreasing or non-zero
%[inicioDeltaIAUX,~]=encuentra_zeros_limite(P1DeltaI(inicioDeltaI+2:length(
DDI)),length(DDI)/2);
%inicioDeltaI=inicioDeltaIAUX+inicioDeltaI;
%[P1CMODI,~,WMI]=upper_lower(WMI(inicioCMODI:length(WMI)),P1CMODI(inicioCMO
DI:length(WMI)),2e-3);
%[P1DeltaI,~,DDI]=upper_lower(DDI(inicioDeltaI:length(DDI)),P1DeltaI(inicio
DeltaI:length(DDI)),2e-3);

%to zero
WMI=WMI-min(WMI);
DDI=DDI-min(DDI);
LASTCMODI=P1CMODI(length(WMI));
P1CMODI=P1CMODI-LASTCMODI;
LASTDELTAI=P1DeltaI(length(DDI));
P1DeltaI=P1DeltaI-LASTDELTAI;
WMAI=WMI(1);
WMRI=WMI(length(WMI));
DAI=DDI(1);
DRI=DDI(length(DDI));

%new fracture parameters
[PUI,~,~,~,picoCMODI,~]=max_min_med_vec(P1CMODI);
finalCMODI=length(WMI);
[limiteCMODI,~]=encuentra_valor_intervalo(P1CMODI,0.05*PUI,picoCMODI,finalC
MODI);
if limiteCMODI+1<=length(WMI)
    control=1;
    while (P1CMODI(limiteCMODI)>=0.05*PUI ||
P1CMODI(limiteCMODI+1)>=0.05*PUI) && control==1
        limiteCMODI=limiteCMODI+1;
        if limiteCMODI<length(P1CMODI)
            control=1;
        else
            control=0;
        end
    end
end
clear XI P1colaI
f=0;
for e=1:(finalCMODI-limiteCMODI+1)
    if P1CMODI(e-1+limiteCMODI)<=0.05*PUI
        f=f+1;

```

```

        PlcolaI(f)=PlCMODI(e-1+limiteCMODI);
        XI(f)=(4*DI/SI)^2*(1/(WMI(e-1+limiteCMODI)-WMI(1))^2-
1/(WMI(length(WMI))-WMI(1))^2);
    end
end

%g
modelFun = @(b,x) b(1).*x(1,:)+b(2).*(x(1,:)).^2;
startingVals = [1 1];
coefEsts = nlinfit(XI, PlcolaI, modelFun, startingVals);
AI=coefEsts(1);
KI=coefEsts(2);
WtailI=2*AI/(DDI(length(DDI))-DDI(1));
%Fracture work, under P1-Delta
WfI=0;
for i=2:length(DDI)
    WfI=WfI+0.5*(PlDeltaI(i)+PlDeltaI(i-1))*(DDI(i)-DDI(i-1));
end
GfI=WfI/(BI*1e-3*(DI-aI)*1e-3);
%real fracture energy
GFI=(WfI+WtailI)/(BI*1e-3*(DI-aI)*1e-3);
%clear Wf Wtail
%Gravity Center
WGI=4*AI/(BI*SI*GFI)*1e6; %kNm2/(mm2*N/m)=kNm/N->1kN/N*m*1000N/kN*1000mm/m

%Graph P1-X
figure
scatter(XI,PlcolaI,'MarkerEdgeColor',[0.5 0.5 0.5])
hold on
for i=1:length(XI)
    XX(i)=XI(i)*(AI+KI*XI(i));
end
clear i
plot(XI,XX,'Linewidth',2,'Color',[0 0.4 1])
xlabel('X(mm^-^2)','FontName','Calibri','FontSize',12)
ylabel('Corrected load P_1(kN)','FontName','Calibri','FontSize',12)
title('LOAD vs. X: B23X2015I','FontName','Calibri','FontSize',
14,'FontWeight','bold')
legend({'Data','Fitted'},'FontName','Calibri','FontSize',
14,'Location','SouthEast')
legend boxoff
grid on
print -djpeg P1-X_B23X2015I
%ELASTIC MODULUS
[EI,NEI,MEI,picI]=E_flexion3P(aI,DI,BI,SI,PI,CMODI,hI);
%Graph CMOD-P
figure
AA=CMODI(1:picI)*1000;
k=0;
for i=1:picI
    if PI(i)>=0.15*(PUI+PRI) && PI(i)<=0.55*(PUI+PRI)
        k=k+1;
        validPI(k)=PI(i);
        validAA(k)=AA(i);
        PrediccionCMOD(k)=(NEI+MEI*PI(i))*1000;
        PrediccionCMODLOAD(k)=PI(i);
    end
end
clear i
scatter(validPI,validAA,'MarkerEdgeColor',[0.5 0.5 0.5])
hold on

```

```

plot(PrediccionCMODLOAD,PrediccionCMOD,'Linewidth',2,'Color',[0 0.4 1])
xlabel ('Load P(kN)', 'FontName','Calibri','FontSize', 12)
ylabel ('CMOD w(\mum)', 'FontName','Calibri','FontSize', 12)
title('CMOD vs. LOAD (from 15% until 55%):
B23X2015I','FontName','Calibri','FontSize', 14,'FontWeight','bold')
legend({'Data','Fitted'}, 'FontName','Calibri','FontSize',
14,'Location','NorthWest')
legend boxoff
grid on
print -djpeg CMOD-P(15a100-55a100)_B23X2015I

%Comparison
%Graph P1-Delta COMP
%Coincident peaks
[~,picoDeltaORG]=max(P1I);
[~,picoDeltaMOD]=max(P1DeltaI);
figure
plot(DeltaI+(DDI(picoDeltaMOD)-DeltaI(picoDeltaORG)),PI-PRI-
LASTDELTAI, '.', 'Color',[0 0.4 1])
hold on
plot(DDI,P1DeltaI,'Linewidth',2,'Color',[1 0 0])
xlabel ('Displacement \delta(mm)', 'FontName','Calibri','FontSize', 12)
ylabel ('Corrected load P_1(kN)', 'FontName','Calibri','FontSize', 12)
axis ([0 DDI(length(DDI)) min(P1I) max(PI)])
title('LOAD vs. DISPLACEMENT: B23X2015I','FontName','Calibri','FontSize',
14,'FontWeight','bold')
legend({'Full spectrum','Upper curve'}, 'FontName','Calibri','FontSize',
14,'Location','Northeast')
legend boxoff
grid on
print -djpeg COMPARATIVEP1-DELTA_B23X2015I

%Graph P1-W COMP
[~,picoCMODORG]=max(P1I);
[~,picoCMODMOD]=max(P1CMODI);
figure
plot(CMODI+(WMI(picoCMODMOD)-CMODI(picoCMODORG)),PI-PRI-
LASTCMODI, '.', 'Color',[0 0.4 1])
hold on
plot(WMI,P1CMODI,'Linewidth',2,'Color',[1 0 0])
xlabel ('Crack mouth width w(mm)', 'FontName','Calibri','FontSize', 12)
ylabel ('Corrected load P_1(kN)', 'FontName','Calibri','FontSize', 12)
axis ([0 WMI(length(WMI)) min(P1I) max(PI)])
title('LOAD vs. CMOD: B23X2015I','FontName','Calibri','FontSize',
14,'FontWeight','bold')
legend({'Full spectrum','Upper curve'}, 'FontName','Calibri','FontSize',
14,'Location','Northeast')
legend boxoff
grid on
print -djpeg COMPARATIVEP1-W_B23X2015I
save 23X2015I

```

C.1.2 BASIS FOR THE STRENGTH TEST DATA PROCESSING CODE

```

%Obtaining the tensile, compressive and splitting strength
clear all
close all
clc
format long e
Diam=150; %mm - Diameter
L=300; %mm - Length
C=150; %mm - cube size
cilI=textread('Cil23X2015I.Txt'); %Compression test
cilII=textread('Cil23X2015II.Txt'); %Indirect tensile test
cubI=textread('Cub23X2015I.Txt'); %Compression test
PcilI=cilI(:,2); %T
PcilI=PcilI*9.81; %kN
PcilII=cilII(:,2); %T
PcilII=PcilII*9.81; %kN
PcubI=cubI(:,2); %T
PcubI=PcubI*9.81; %kN
dcilI=cilI(:,3); %mm
dcilII=cilII(:,3); %mm
dcubI=cubI(:,3); %mm
clear cilI cilII cubI

%COMPRESSION TEST FOR CILINDRICAL SPECIMENS
fc_cilI=max(PcilI*1000)/(pi/4*Diam^2); %MPa
figure
plot(dcilI,PcilI,'Linewidth',2,'Color',[0 0.4 1])
xlabel ('Displacement \delta(mm)', 'FontName','Calibri','FontSize', 12)
ylabel ('Load P(kN)', 'FontName','Calibri','FontSize', 12)
title('COMPRESSION TEST: C23X2015I', 'FontName','Calibri','FontSize',
14, 'FontWeight','bold')
grid on
print -djpeg fc_C23X2015I
fc_cil=mean([fc_cilI]);

%COMPRESSION TEST FOR CUBICAL SPECIMENS
fc_cubI=max(PcubI*1000)/C^2; %MPa
figure
plot(dcubI,PcubI,'Linewidth',2,'Color',[0 0.4 1])
xlabel ('Displacement \delta(mm)', 'FontName','Calibri','FontSize', 12)
ylabel ('Load P(kN)', 'FontName','Calibri','FontSize', 12)
title('COMPRESSION TEST: D23X2015I', 'FontName','Calibri','FontSize',
14, 'FontWeight','bold')
grid on
print -djpeg fc_D23X2015I
fc_cub=mean([fc_cubI]);

%INDIRECT TENSILE STRENGTH AND SPLITTING STRENGTH
ft_cilII=2*max(PcilII*1000)/(pi*Diam*L);
figure
plot(dcilII,PcilII,'Linewidth',2,'Color',[0 0.4 1])
xlabel ('Displacement \delta(mm)', 'FontName','Calibri','FontSize', 12)
ylabel ('Load P(kN)', 'FontName','Calibri','FontSize', 12)
title('BRAZILIAN TEST: C23X2015II', 'FontName','Calibri','FontSize',
14, 'FontWeight','bold')
grid on
print -djpeg ft_C23X2015II
ft=mean([ft_cilII]);
save 23X2015S

```

C.1.3 BASIS FOR THE BILINEAR APPROXIMATION BUILDING CODE

```

%BILINEAR APPROXIMATION x GF_cola
%FUNCTIONS REQUIRED
%ablandamiento_bilinear_mean
close all
clear all
clc
load 23X2015I
load 23X2015II
load 23X2015III
load 23X2015IV
load 23X2015S

aR=[aI aII aIII aIV];
DR=[DI DII DIII DIV];
BR=[BI BII BIII BIV];
SR=[SI SII SIII SIV];
Pu1R=[max(P1I) max(P1II) max(P1III) max(P1IV)];
PRR=[PRI PRII PRIII PRIV];
AR=[AI AII AIII AIV];
WMAR=[WMAI WMAII WMAIII WMAIV];
WMRR=[WMRI WMRII WMRIII WMRIV];
ER=[EI EII EIII EIV];
GFR=[GFI GFII GFIII GFIV];
WGR=[WGI WGII WGIII WGIV];
[sigmaK,WK,WC,Wl,WG,GF,E,l1R,fpR,PefR]
=ablandamiento_bilinear_mean(aR,DR,SR,BR,Pu1R,ft,AR,WMAR,WMRR,ER,GFR,WGR);
GF_bilinear=WK*1e-3*0.5*(ft+sigmaK)*1e6+0.5*sigmaK*1e6*(WC-WK)*1e-3;
WCHAR=GF/ft; %J/m2*mm2/N=N/m*mm^2/N=mm^2/m
WCHAR=WCHAR/1e3; %1mm2/m*1m/1000mm->mm
WW=[0:1e-6:WC]; %mm
for i=1:length(WW)
    if WW(i)<=WK
        SS(i)=ft-(ft-sigmaK)*WW(i)/WK;
    else
        SS(i)=sigmaK*WC/(WC-WK)-sigmaK*WW(i)/(WC-WK);
    end
end
figure
WW=WW*1000; %micrometers
plot(WW,SS,'Linewidth',2,'Color',[0 0.4 1])
xlabel('Crack width w(\mu m)','FontName','Calibri','FontSize',12)
ylabel('Normal stress \sigma(MPa)','FontName','Calibri','FontSize',12)
title('SOFTENING CURVE: 23X2015','FontName','Calibri','FontSize',14,'FontWeight','bold')
grid on
print -djpeg BilinearAPROX_23X2015
SS=SS/ft; %Reduced stress MPa/MPa=1[ADIM]
WW=WW*ft/GF; %Reduced crack width um*N/mm2*m/N->1e-6m2*1e6N/m2*m/N=1[ADIM]
figure
plot(WW,SS,'Linewidth',2,'Color',[0 0.4 1])
xlabel('Reduced crack width','FontName','Calibri','FontSize',12)
ylabel('Reduced normal stress','FontName','Calibri','FontSize',12)
title('REDUCED SOFTENING CURVE: 23X2015','FontName','Calibri','FontSize',14,'FontWeight','bold')
grid on
print -djpeg ReducedBilinearAPROX_23X2015
clear SS WW
save 23X2015

```


C.1.4 BASIS FOR THE COMPARISON OF ALL TESTS FROM ONE SINGLE CAMPAIGN

```

%BILINEAR APPROXIMATION
close all
clear all
clc
load 23X2015I
load 23X2015II
load 23X2015III
load 23X2015IV
load 23X2015S

aR=[aI aII aIII aIV];
DR=[DI DII DIII DIV];
BR=[BI BII BIII BIV];
SR=[SI SII SIII SIV];
Pu1R=[max(P1I) max(P1II) max(P1III) max(P1IV)];
PRR=[PRI PRII PRIII PRIV];
PuR=Pu1R+PRR;
AR=[AI AII AIII AIV];
WMAR=[WMAI WMAII WMAIII WMAIV];
WMRR=[WMRI WMRII WMRIII WMRIV];
ER=[EI EII EIII EIV];
GFR=[GFI GFII GFIII GFIV];
WGR=[WGI WGII WGIII WGIV];
[sigmaK,WK,WC,Wl,WG,GF,E]
=ablandamiento_bilineal_mean(aR,DR,SR,BR,Pu1R,ft,AR,WMAR,WMRR,ER,GFR,WGR);

%P1-Delta graph
figure
plot(DDI,P1DeltaI,'Linewidth',1.5,'Color',[0 0.4 1])
hold on
plot(DDII,P1DeltaII,'Linewidth',1.5,'Color',[0.1 0.6 0.1])
plot(DDIII,P1DeltaIII,'Linewidth',1.5,'Color',[1 0 0])
plot(DDIV,P1DeltaIV,'Linewidth',1.5,'Color',[0 0 0])
xlabel('Displacement \delta(mm)','FontName','Calibri','FontSize', 12)
ylabel('Corrected load P_1(kN)','FontName','Calibri','FontSize', 12)
title('LOAD vs. DISPLACEMENT: 23X2015','FontName','Calibri','FontSize',
14,'FontWeight','bold')
legend({'I','II','III','IV'},'FontName','Calibri','FontSize', 12)
legend boxoff
grid on
print -djpeg P1-DELTA_23X2015

%P1-W graph
figure
plot(WMI,P1CMODI,'Linewidth',1.5,'Color',[0 0.4 1])
hold on
plot(WMII,P1CMODII,'Linewidth',1.5,'Color',[0.1 0.6 0.1])
plot(WMIII,P1CMODIII,'Linewidth',1.5,'Color',[1 0 0])
plot(WMIV,P1CMODIV,'Linewidth',1.5,'Color',[0 0 0])
xlabel('Crack mouth width w(mm)','FontName','Calibri','FontSize', 12)
ylabel('Corrected load P_1(kN)','FontName','Calibri','FontSize', 12)
title('LOAD vs. CMOD: 23X2015','FontName','Calibri','FontSize',
14,'FontWeight','bold')
legend({'I','II','III','IV'},'FontName','Calibri','FontSize', 12)
legend boxoff
grid on
print -djpeg P1-W_23X2015

```

```

%Pl-X graph
figure
scatter(XI,PlcolaI, '.', 'MarkerEdgeColor',[0 0.4 1])
hold on
scatter(XII,PlcolaII, '.', 'MarkerEdgeColor',[0.1 0.6 0.1])
scatter(XIII,PlcolaIII, '.', 'MarkerEdgeColor',[1 0 0])
scatter(XIV,PlcolaIV, '.', 'MarkerEdgeColor',[0 0 0])
for i=1:length(XIV)
    XXIV(i)=XIV(i)*(AIV+KIV*XIV(i));
end
for i=1:length(XIII)
    XXIII(i)=XIII(i)*(AIII+KIII*XIII(i));
end
for i=1:length(XII)
    XXII(i)=XII(i)*(AII+KII*XII(i));
end
for i=1:length(XI)
    XXI(i)=XI(i)*(AI+KI*XI(i));
end
plot(XI,XXI,'Linewidth',2,'Color',[0 0.4 1])
plot(XII,XXII,'Linewidth',2,'Color',[0.1 0.6 0.1])
plot(XIII,XXIII,'Linewidth',2,'Color',[1 0 0])
plot(XIV,XXIV,'Linewidth',2,'Color',[0 0 0])
xlabel('X(mm^-^2)','FontName','Calibri','FontSize',12)
ylabel('Corrected load P_1(kN)','FontName','Calibri','FontSize',12)
title('LOAD vs. X: 23X2015','FontName','Calibri','FontSize',14,'FontWeight','bold')
legend({'I','II','III','IV','I','II','III','IV'},'FontName','Calibri','FontSize',12)
legend('Location','Southeast')
legend boxoff
grid on
print -djpeg Pl-X_23X2015

%Elastic moduli
figure
AAI=CMODI(1:picI)*1000;
k=0;
for i=1:picI
    if PI(i)>=0.15*(PUI+PRI) && PI(i)<=0.55*(PUI+PRI)
        k=k+1;
        validPI(k)=PI(i);
        validAAI(k)=AAI(i);
        PrediccionCMODI(k)=(NEI+MEI*PI(i))*1000;
        PrediccionCMODLOADI(k)=PI(i);
    end
end
AAII=CMODII(1:picII)*1000;
k=0;
for i=1:picII
    if PII(i)>=0.15*(PUII+PRII) && PII(i)<=0.55*(PUII+PRII)
        k=k+1;
        validPII(k)=PII(i);
        validAAII(k)=AAII(i);
        PrediccionCMODII(k)=(NEII+MEII*PII(i))*1000;
        PrediccionCMODLOADII(k)=PII(i);
    end
end
AAIII=CMODIII(1:picIII)*1000;
k=0;
for i=1:picIII

```

```

    if PIII(i) >= 0.15 * (PUIII + PRIII) && PIII(i) <= 0.55 * (PUIII + PRIII)
        k = k + 1;
        validPIII(k) = PIII(i);
        validAAIII(k) = AAIII(i);
        PrediccionCMODIII(k) = (NEIII + MEIII * PIII(i)) * 1000;
        PrediccionCMODLOADIII(k) = PIII(i);
    end
end
AAIV = CMODIV(1:picIV) * 1000;
k = 0;
for i = 1:picIV
    if PIV(i) >= 0.15 * (PUIV + PRIV) && PIV(i) <= 0.55 * (PUIV + PRIV)
        k = k + 1;
        validPIV(k) = PIV(i);
        validAAIV(k) = AAIV(i);
        PrediccionCMODIV(k) = (NEIV + MEIV * PIV(i)) * 1000;
        PrediccionCMODLOADIV(k) = PIV(i);
    end
end
clear i
scatter(validPI, validAAI, '.', 'MarkerEdgeColor', [0 0.4 1])
hold on
scatter(validPII, validAAII, '.', 'MarkerEdgeColor', [0.1 0.6 0.1])
scatter(validPIII, validAAIII, '.', 'MarkerEdgeColor', [1 0 0])
scatter(validPIV, validAAIV, '.', 'MarkerEdgeColor', [0 0 0])
plot(PrediccionCMODLOADI, PrediccionCMODI, 'Linewidth', 2, 'Color', [0 0.4 1])
plot(PrediccionCMODLOADII, PrediccionCMODII, 'Linewidth', 2, 'Color', [0.1 0.6 0.1])
plot(PrediccionCMODLOADIII, PrediccionCMODIII, 'Linewidth', 2, 'Color', [1 0 0])
plot(PrediccionCMODLOADIV, PrediccionCMODIV, 'Linewidth', 2, 'Color', [0 0 0])
xlabel('Load P(kN)', 'FontName', 'Calibri', 'FontSize', 12)
ylabel('CMOD w(\mu m)', 'FontName', 'Calibri', 'FontSize', 12)
title('CMOD vs. LOAD (from 15% until 55%): 23X2015', 'FontName', 'Calibri', 'FontSize', 14, 'FontWeight', 'bold')
legend({'I', 'II', 'III', 'IV', 'I', 'II', 'III', 'IV'}, 'FontName', 'Calibri', 'FontSize', 12)
legend('Location', 'Southeast', 'Orientation', 'Horizontal')
legend boxoff
grid on
print -djpeg CMOD-P(15a100-55a100)_23X2015

%Pl-Delta graph
[~, peakI] = max(P1DeltaI);
[~, peakII] = max(P1DeltaII);
[~, peakIII] = max(P1DeltaIII);
[~, peakIV] = max(P1DeltaIV);
figure
plot(DDI - DDI(peakI), P1DeltaI, 'Linewidth', 1.5, 'Color', [0 0.4 1])
hold on
plot(DDII - DDII(peakII), P1DeltaII, 'Linewidth', 1.5, 'Color', [0.1 0.6 0.1])
plot(DDIII - DDIII(peakIII), P1DeltaIII, 'Linewidth', 1.5, 'Color', [1 0 0])
plot(DDIV - DDIV(peakIV), P1DeltaIV, 'Linewidth', 1.5, 'Color', [0 0 0])
xlabel('Displacement \delta(mm)', 'FontName', 'Calibri', 'FontSize', 12)
ylabel('Corrected load P_1(kN)', 'FontName', 'Calibri', 'FontSize', 12)
title('LOAD vs. DISPLACEMENT: 23X2015', 'FontName', 'Calibri', 'FontSize', 14, 'FontWeight', 'bold')
legend({'I', 'II', 'III', 'IV'}, 'FontName', 'Calibri', 'FontSize', 12)
legend boxoff
grid on
print -djpeg P1-DELTA_23X2015equipeak

```

C.1.5 BASIS FOR THE LOCAL FRACTURE ENERGY METHOD DATA PROCESSING CODE

```

%INDIVIDUAL ADAPTATION CODE FOR Gf CORRECTIONS
%{
REQUIRED FUNCTIONS
energia_dependiente
encuentra_valor
encuentra_valor_con_limite
encuentra_valor_intervalo
encuentra_zeros_limite
max_min_med_vec
E_flexion3P
%}

clc
close all
clear all
format long e

PESOVIII=1; %1=Y 0=N
mVIII=15; %kg
dataVIII=textread('29I2016VIII.txt');
timeVIII=dataVIII(:,2);
IDVIII=dataVIII(:,1);
HPVIII=dataVIII(:,4);
HPVIII=HPVIII*9.81/1000; %kN
PVIII=dataVIII(:,6);
PVIII=-PVIII*9.81/1000; %kN
CMODVIII=dataVIII(:,5); %mm
DeltaVIII=dataVIII(:,3); %mm

clear data
% mm
aVIII=29;
DVIII=100;
BVIII=100;
SVIII=300;
hVIII=2;
%Data viewer
plot(HPVIII,'Linewidth',2,'Color',[0 0.4 1])
xlabel ('ID','FontName','Calibri','FontSize', 12)
ylabel ('Load P(kN)','FontName','Calibri','FontSize', 12)
title('LOAD HEAD: B29I2016VIII','FontName','Calibri','FontSize',
14,'FontWeight','bold')
legend boxoff
grid on
print -djpeg SerieHP_B29I2016VIII
%Begin at zero
CMODVIII=CMODVIII-min(CMODVIII);
DeltaVIII=DeltaVIII-min(DeltaVIII);
%FILTERS \\1=no filter
nCMOD=1;
nP=1;
nDelta=250;

for i=1:nP
    b(i)=1/(nP);
end
figure
plot(PVIII,'Linewidth',2,'Color',[0 0.4 1])

```

```

hold on
xlabel ('ID','FontName','Calibri','FontSize', 12)
ylabel ('Load P(kN)','FontName','Calibri','FontSize', 12)
title('LOAD: B29I2016VIII','FontName','Calibri','FontSize',
14,'FontWeight','bold')
PVIII=filter(b,1,PVIII);
if nP>1
    plot(PVIII,'Linewidth',2,'Color',[1 0 0])
    legend({'Original','Filtered'},'FontName','Calibri','FontSize',
14,'Location','Northeast')
    legend boxoff
end
grid on
print -djpeg SerieP_B29I2016VIII

for i=1:nCMOD
    b(i)=1/(nCMOD);
end
figure
plot(CMODVIII,'Linewidth',2,'Color',[0 0.4 1])
hold on
xlabel ('ID','FontName','Calibri','FontSize', 12)
ylabel ('CMOD w(mm)','FontName','Calibri','FontSize', 12)
title('CMOD: B29I2016VIII','FontName','Calibri','FontSize',
14,'FontWeight','bold')
CMODVIII=filter(b,1,CMODVIII);
if nCMOD>1
    plot(CMODVIII,'Linewidth',2,'Color',[1 0 0])
    legend({'Original','Filtered'},'FontName','Calibri','FontSize',
14,'Location','Northwest')
    legend boxoff
end
grid on
print -djpeg SerieCMOD_B29I2016VIII

for i=1:nDelta
    b(i)=1/(nDelta);
end
figure
plot(DeltaVIII,'Linewidth',2,'Color',[0 0.4 1])
hold on
xlabel ('ID','FontName','Calibri','FontSize', 12)
ylabel ('Displacement \delta(mm)','FontName','Calibri','FontSize', 12)
title('DISPLACEMENT: B29I2016VIII','FontName','Calibri','FontSize',
14,'FontWeight','bold')
DeltaVIII=filter(b,1,DeltaVIII);
if nDelta>1
    plot(DeltaVIII,'Linewidth',2,'Color',[1 0 0])
    legend({'Original','Filtered'},'FontName','Calibri','FontSize',
14,'Location','Northwest')
    legend boxoff
end
grid on
print -djpeg SerieDelta_B29I2016VIII
clear nCMOD nP nDelta b
clc

[GfVIII, inicioVIII, finalVIII, PlVIII, WMVIII]=energia_dependiente(PVIII, Delta
VIII, CMODVIII, PESOVIII, aVIII, DVIII, BVIII, mVIII);

PRVIII=PVIII(finalVIII);

```

```

%Upper curves
[P1CMODVIII,~,WMVIII]=upper_lower(WMVIII(1:finalVIII),P1VIII(1:finalVIII),2
e-3);
[P1DeltaVIII,~,DDVIII]=upper_lower(DeltaVIII(1:finalVIII),P1VIII(1:finalVII
I),2e-3);
[inicioCMODVIII,~]=encuentra_zeros_limite(P1CMODVIII,length(WMVIII)/2);
[inicioDeltaVIII,~]=encuentra_zeros_limite(P1DeltaVIII,length(DDVIII)/2);
%[inicioDeltaVIIIIAUX,~]=encuentra_zeros_limite(P1DeltaVIII(inicioDeltaVIII+
1:length(DDVIII)),length(DDVIII)*0.1);
%inicioDeltaVIII=inicioDeltaVIIIIAUX+inicioDeltaVIII;
%[P1CMODVIII,~,WMVIII]=upper_lower(WMVIII(inicioCMODVIII:length(WMVIII)),P1
CMODVIII(inicioCMODVIII:length(WMVIII)),2e-3);
%[P1DeltaVIII,~,DDVIII]=upper_lower(DDVIII(inicioDeltaVIII:length(DDVIII)),
P1DeltaVIII(inicioDeltaVIII:length(DDVIII)),2e-3);
%To zero
WMVIII=WMVIII-min(WMVIII);
DDVIII=DDVIII-min(DDVIII);
LASTCMODVIII=P1CMODVIII(length(WMVIII));
P1CMODVIII=P1CMODVIII-LASTCMODVIII;
LASTDELTAVIII=P1DeltaVIII(length(DDVIII));
P1DeltaVIII=P1DeltaVIII-LASTDELTAVIII;
WMAVIII=WMVIII(1);
WMRVIII=WMVIII(length(WMVIII));
DAVIII=DDVIII(1);
DRVIII=DDVIII(length(DDVIII));
%New fracture parameters
[PUVIII,~,~,~,picoCMODVIII,~]=max_min_med_vec(P1CMODVIII);
finalCMODVIII=length(WMVIII);
[limiteCMODVIII,~]=encuentra_valor_intervalo(P1CMODVIII,0.05*PUVIII,picoCMO
DVIII,finalCMODVIII);
if limiteCMODVIII+1<=length(WMVIII)
    control=1;
    while (P1CMODVIII(limiteCMODVIII)>=0.05*PUVIII ||
P1CMODVIII(limiteCMODVIII+1)>=0.05*PUVIII) && control==1
        limiteCMODVIII=limiteCMODVIII+1;
        if limiteCMODVIII<length(P1CMODVIII)
            control=1;
        else
            control=0;
        end
    end
end
end

WfVIII=0;
for i=2:length(DDVIII)
    WfVIII=WfVIII+0.5*(P1VIII(i)+P1VIII(i-1))*(DDVIII(i)-DDVIII(i-1));
end
if PESOVIII==0
    GfVIII=WfVIII/(BVIII*1e-3*(DVIII-aVIII)*1e-3);
elseif PESOVIII==1
    GfVIII=(WfVIII+mVIII*9.81*(DRVIII-DAVIII)*1e-3)/(BVIII*1e-3*(DVIII-
aVIII)*1e-3);
end

%ELASTIC MODULUS
[EVIII,NEVIII,MEVIII,picVIII]=E_flexion3P(aVIII,DVIII,BVIII,SVIII,PVIII,CMO
DVIII,hVIII);
figure
AA=CMODVIII(1:picVIII)*1000;
k=0;
for i=1:picVIII

```

```

    if PVIII(i) >= 0.15*(PUVIII+PRVIII) && PVIII(i) <= 0.55*(PUVIII+PRVIII)
        k=k+1;
        validPVIII(k)=PVIII(i);
        validAA(k)=AA(i);
        PrediccionCMOD(k)=(NEVIII+MEVIII*PVIII(i))*1000;
        PrediccionCMODLOAD(k)=PVIII(i);
    end
end
clear i
scatter(validPVIII,validAA,'MarkerEdgeColor',[0.5 0.5 0.5])
hold on
plot(PrediccionCMODLOAD,PrediccionCMOD,'Linewidth',2,'Color',[0 0.4 1])
xlabel('Load P(kN)','FontName','Calibri','FontSize',12)
ylabel('CMOD w(\mu m)','FontName','Calibri','FontSize',12)
title('CMOD vs. LOAD (from 15% until 55%):
B29I2016VIII','FontName','Calibri','FontSize',14,'FontWeight','bold')
legend({'Data','Fitted'],'FontName','Calibri','FontSize',
14,'Location','NorthWest')
legend boxoff
grid on
print -djpeg CMOD-P(15a100-55a100)_B29I2016VIII

%COMPARATIVE
%Graph P1-Delta COMP
%Coincident peaks
[~,picoDeltaORG]=max(P1VIII);
[~,picoDeltaMOD]=max(P1DeltaVIII);
figure
plot(DeltaVIII+(DDVIII(picoDeltaMOD)-DeltaVIII(picoDeltaORG)),PVIII-PRVIII-
LASTDELTAVIII,','Color',[0 0.4 1])
hold on
plot(DDVIII,P1DeltaVIII,'Linewidth',2,'Color',[1 0 0])
xlabel('Displacement \delta(mm)','FontName','Calibri','FontSize',12)
ylabel('Corrected load P_1(kN)','FontName','Calibri','FontSize',12)
axis([0 DDVIII(length(DDVIII)) min(P1VIII) max(PVIII)])
title('LOAD vs. DISPLACEMENT:
B29I2016VIII','FontName','Calibri','FontSize',14,'FontWeight','bold')
legend({'Full spectrum','Upper curve'],'FontName','Calibri','FontSize',
14,'Location','Northeast')
legend boxoff
grid on
print -djpeg COMPARATIVEP1-DELTA_B29I2016VIII

%Graph P1-W COMP
[~,picoCMODORG]=max(P1VIII);
[~,picoCMODMOD]=max(P1CMODVIII);
figure
plot(CMODVIII+(WMVIII(picoCMODMOD)-CMODVIII(picoCMODORG)),PVIII-PRVIII-
LASTCMODVIII,','Color',[0 0.4 1])
hold on
plot(WMVIII,P1CMODVIII,'Linewidth',2,'Color',[1 0 0])
xlabel('Crack mouth width w(mm)','FontName','Calibri','FontSize',12)
ylabel('Corrected load P_1(kN)','FontName','Calibri','FontSize',12)
axis([0 WMVIII(length(WMVIII)) min(P1VIII) max(PVIII)])
title('LOAD vs. CMOD: B29I2016VIII','FontName','Calibri','FontSize',
14,'FontWeight','bold')
legend({'Full spectrum','Upper curve'],'FontName','Calibri','FontSize',
14,'Location','Northeast')
legend boxoff
grid on
print -djpeg COMPARATIVEP1-W_B29I2016VIII
save 29I2016VIII

```

C.1.6 BASIS FOR THE FINAL CORRECTION OF THE FRACTURE ENERGY THROUGH THE LOCAL FRACTURE MODEL

```
%GF BY MEANS OF THE LOCAL FRACTURE ENERGY THEORY
%{
FUNCTIONS REQUIRED
GF_energia_local
%}

load 29I2016I
load 29I2016II
load 29I2016III
load 29I2016IV
load 29I2016V
load 29I2016VI
load 29I2016VII
load 29I2016VIII

%Define the other GF
GFR=[GFI GFII GFIII GFIV];
GFnloc=mean(GFR);
SDGFnloc=std(GFR);

%Define the longest notch depth series
DR1=[DV DVI];
aR1=[aV aVI];
GfR1=[GfV GfVI];
Gf1=mean(GfR1);
SDGf1=std(GfR1);
a1=mean(aR1);
SDa1=std(aR1);
D1=mean(DR1);
SDD1=std(DR1);

%Define the shortest notch depth series
DR2=[DVII DVIII];
aR2=[aVII aVIII];
GfR2=[GfVII GfVIII];
Gf2=mean(GfR2);
SDGf2=std(GfR2);
a2=mean(aR2);
SDa2=std(aR2);
D2=mean(DR2);
SDD2=std(DR2);

[GFloc,TZD,sit]=GF_energia_local(Gf1,Gf2,a1,a2,D1,D2)

save 29I2019LOCAL
```


C.1.7 FINAL PROCESSING CODE

```

%MULTICAMPAIGN COMPARISON
%{
FUNCTIONS REQUIRED
encuentra_valor
%}

clear all;close all;format long e;clc

%Campaign selection
DD=['23';'14';'29';'10';'17';'01';'07';'14';'21'];
MM=['00X';'XII';'00I';'III';'III';'0IV';'0IV';'0IV';'0IV'];
YYYY=['2015';'2015';'2016';'2016';'2016';'2016';'2016';'2016'];
Sand=[42.35,-100,40,44.34,38.95,43.14,38.15,43.14,38.15];
Agg=[47.05,-100,45,44.34,49.90,43.14,48.13,43.14,48.13];
MaxAgg=[10,15,10,10,10,10,10,10,10];
Cem32=[10.6,-100,15,11.32,11.15,13.72,13.72,13.72,13.72];
AC=[0.867,0.45,0.67,0.859,0.818,0.77,0.77,0.65,0.65];
SandProp=[850,-100,800,890,790,865,765,865,765];
AggProp=[950,-100,900,890,990,865,965,865,965];
Cem32Prop=[214,-100,300,225,225,275,275,275,275];
WaterProp=[185,124,200,195,184,211.75,211.75,179,179];

GFRR=[];
SDGFRR=[];
WGRR=[];
ERR=[];
sigmaKRR=[];
ftRR=[];
fcRR=[];
WKRR=[];
WCRR=[];
WlRR=[];
WCHARRR=[];

[a,~]=size(DD);
for ii=1:a
    if MM(ii,1)=='0'
        if MM(ii,1:2)=='00'
            M=MM(ii,3);
        else
            M=MM(ii,2:3);
        end
    else
        M=MM(ii,:);
    end
    clear DDI DDII DDIII DDIV DDV DDVI DDVII DDVIII PlDeltaI PlDeltaII
    PlDeltaIII PlDeltaIV PlDeltaV PlDeltaVI PlDeltaVII PlDeltaVIII
    clear WMI WMII WMIII WMIV WMV WMVI WMVII WMVIII PlCMODI PlCMODII
    PlCMODIII PlCMODIV PlCMODV PlCMODVI PlCMODVII PlCMODVIII
    load([DD(ii,:) M YYYY(ii,:) '.mat']);
    GFRR=[GFRR GF];
    SDGFRR=[SDGFRR SDGF];
    WGRR=[WGRR WG];
    ERR=[ERR E];
    sigmaKRR=[sigmaKRR sigmaK];
    ftRR=[ftRR ft];
    fcRR=[fcRR fc];
    WKRR=[WKRR WK];
    WCRR=[WCRR WC];
end

```

```

WlRR=[WlRR Wl];
WCHARRR=[WCHARRR WCHAR];
if strcmp([DD(ii,:) M YYYY(ii,:)], '14XII2015')==0 %4spec-series
    [~,peakI]=max(P1DeltaI);
    [~,peakII]=max(P1DeltaII);
    [~,peakIII]=max(P1DeltaIII);
    [~,peakIV]=max(P1DeltaIV);
    if strcmp([DD(ii,:) M YYYY(ii,:)], '23X2015')==1
        DD23X2015=[DDI-DDI(peakI); DDII-DDII(peakII); DDIII-
DDIII(peakIII); DDIV-DDIV(peakIV)];
        P1Delta23X2015=[P1DeltaI; P1DeltaII; P1DeltaIII; P1DeltaIV];
        WM23X2015=[WMI; WMII; WMIII; WMIV];
        P1CMOD23X2015=[P1CMODI; P1CMODII; P1CMODIII; P1CMODIV];
    elseif strcmp([DD(ii,:) M YYYY(ii,:)], '29I2016')==1
        DD29I2016=[DDI-DDI(peakI); DDII-DDII(peakII); DDIII-
DDIII(peakIII); DDIV-DDIV(peakIV)];
        P1Delta29I2016=[P1DeltaI; P1DeltaII; P1DeltaIII; P1DeltaIV];
        WM29I2016=[WMI; WMII; WMIII; WMIV];
        P1CMOD29I2016=[P1CMODI; P1CMODII; P1CMODIII; P1CMODIV];
    elseif strcmp([DD(ii,:) M YYYY(ii,:)], '10III2016')==1
        DD10III2016=[DDI-DDI(peakI); DDII-DDII(peakII); DDIII-
DDIII(peakIII); DDIV-DDIV(peakIV)];
        P1Delta10III2016=[P1DeltaI; P1DeltaII; P1DeltaIII; P1DeltaIV];
        WM10III2016=[WMI; WMII; WMIII; WMIV];
        P1CMOD10III2016=[P1CMODI; P1CMODII; P1CMODIII; P1CMODIV];
    elseif strcmp([DD(ii,:) M YYYY(ii,:)], '17III2016')==1
        DD17III2016=[DDI-DDI(peakI); DDII-DDII(peakII); DDIII-
DDIII(peakIII); DDIV-DDIV(peakIV)];
        P1Delta17III2016=[P1DeltaI; P1DeltaII; P1DeltaIII; P1DeltaIV];
        WM17III2016=[WMI; WMII; WMIII; WMIV];
        P1CMOD17III2016=[P1CMODI; P1CMODII; P1CMODIII; P1CMODIV];
    elseif strcmp([DD(ii,:) M YYYY(ii,:)], '01IV2016')==1
        DD01IV2016=[DDI-DDI(peakI); DDII-DDII(peakII); DDIII-
DDIII(peakIII); DDIV-DDIV(peakIV)];
        P1Delta01IV2016=[P1DeltaI; P1DeltaII; P1DeltaIII; P1DeltaIV];
        WM01IV2016=[WMI; WMII; WMIII; WMIV];
        P1CMOD01IV2016=[P1CMODI; P1CMODII; P1CMODIII; P1CMODIV];
    elseif strcmp([DD(ii,:) M YYYY(ii,:)], '07IV2016')==1
        DD07IV2016=[DDI-DDI(peakI); DDII-DDII(peakII); DDIII-
DDIII(peakIII); DDIV-DDIV(peakIV)];
        P1Delta07IV2016=[P1DeltaI; P1DeltaII; P1DeltaIII; P1DeltaIV];
        WM07IV2016=[WMI; WMII; WMIII; WMIV];
        P1CMOD07IV2016=[P1CMODI; P1CMODII; P1CMODIII; P1CMODIV];
    elseif strcmp([DD(ii,:) M YYYY(ii,:)], '14IV2016')==1
        DD14IV2016=[DDI-DDI(peakI); DDII-DDII(peakII); DDIII-
DDIII(peakIII); DDIV-DDIV(peakIV)];
        P1Delta14IV2016=[P1DeltaI; P1DeltaII; P1DeltaIII; P1DeltaIV];
        WM14IV2016=[WMI; WMII; WMIII; WMIV];
        P1CMOD14IV2016=[P1CMODI; P1CMODII; P1CMODIII; P1CMODIV];
    elseif strcmp([DD(ii,:) M YYYY(ii,:)], '21IV2016')==1
        DD21IV2016=[DDI-DDI(peakI); DDII-DDII(peakII); DDIII-
DDIII(peakIII); DDIV-DDIV(peakIV)];
        P1Delta21IV2016=[P1DeltaI; P1DeltaII; P1DeltaIII; P1DeltaIV];
        WM21IV2016=[WMI; WMII; WMIII; WMIV];
        P1CMOD21IV2016=[P1CMODI; P1CMODII; P1CMODIII; P1CMODIV];
    end
else %8spec-series
    [~,peakI]=max(P1DeltaI);
    [~,peakII]=max(P1DeltaII);
    [~,peakIII]=max(P1DeltaIII);
    [~,peakIV]=max(P1DeltaIV);

```

```

[~,peakV]=max(P1DeltaV);
[~,peakVI]=max(P1DeltaVI);
[~,peakVII]=max(P1DeltaVII);
[~,peakVIII]=max(P1DeltaVIII);
DD14XII2015=[DDI-DDI(peakI);DDII-DDII(peakII);DDIII-
DDIII(peakIII);DDIV-DDIV(peakIV);DDV-DDV(peakV);DDVI-DDVI(peakVI);DDVII-
DDVII(peakVII);DDVIII-DDVIII(peakVIII)];

P1Delta14XII2015=[P1DeltaI;P1DeltaII;P1DeltaIII;P1DeltaIV;P1DeltaV;P1DeltaV
I;P1DeltaVII;P1DeltaVIII];
WM14XII2015=[WMI;WMII;WMIII;WMIV;WMV;WMVI;WMVII;WMVIII];

P1CMOD14XII2015=[P1CMODI;P1CMODII;P1CMODIII;P1CMODIV;P1CMODV;P1CMODVI;P1CMO
DVII;P1CMODVIII];
end
end

%INDIVIDUAL RESULTS PLOTTING
figure
for ii=1:a %GF
    if MM(ii,1)=='0'
        if MM(ii,1:2)=='00';M=MM(ii,3);
        else;M=MM(ii,2:3);
        end
    else;M=MM(ii,:);
    end
    load([DD(ii,:) M YYYY(ii,:) '.mat']);clear FF ColorVec
    FF=ones(1,length(GFR))*ii;
    if strcmp([DD(ii,:) M YYYY(ii,:)],'23X2015')==1
        ColorVec=[0 0.4 1];
    elseif strcmp([DD(ii,:) M YYYY(ii,:)],'14XII2015')==1
        ColorVec=[0.1 0.6 0.1];
    elseif strcmp([DD(ii,:) M YYYY(ii,:)],'29I2016')==1
        ColorVec=[1 0 0];
    elseif strcmp([DD(ii,:) M YYYY(ii,:)],'10III2016')==1
        ColorVec=[0.6 0.2 0.8];
    elseif strcmp([DD(ii,:) M YYYY(ii,:)],'17III2016')==1
        ColorVec=[0.7 0.7 0];
    elseif strcmp([DD(ii,:) M YYYY(ii,:)],'01IV2016')==1
        ColorVec=[0.7 0.7 0.7];
    elseif strcmp([DD(ii,:) M YYYY(ii,:)],'07IV2016')==1
        ColorVec=[0 1 1];
    elseif strcmp([DD(ii,:) M YYYY(ii,:)],'14IV2016')==1
        ColorVec=[1 0.7 0.5];
    elseif strcmp([DD(ii,:) M YYYY(ii,:)],'21IV2016')==1
        ColorVec=[0 0 0];
    end
    scatter(FF,(GFR-
GFR)/SDGF,16,'MarkerEdgeColor',ColorVec,'MarkerFaceColor',ColorVec)
    hold on
end
ylabel('Normalized G_F deviation: (G_F_i-
G_F)/s_G_F','FontName','Calibri','FontSize',12)
axis([-5 ii+4 -6 6])
title('NORMAL DEVIATION FOR FRACTURE
ENERGY','FontName','Calibri','FontSize',14,'FontWeight','bold')
set(gca,'ytick',[-6 -5 -4 -3 -2 -1 0 1 2 3 4 5 6]);
set(gca,'xtick',[-10]);
legend({'23X2015','14XII2015','29I2016','10III2016','17III2016','01IV2016',
'07IV2016','14IV2016','21IV2016'},'Location','Northwest','FontName','Calibr
i','FontSize',12)

```

```

legend boxoff
text(ii+0.5,0,'MEAN','FontName','Calibri','FontSize',11,'FontWeight','bold'
);
text(ii+0.5,1,'USUAL','FontName','Calibri','FontSize',11,'FontWeight','bold'
);
text(ii+0.5,2,'CORRECT','FontName','Calibri','FontSize',
11,'FontWeight','bold');
text(ii+0.5,3,'SUSPICIOUS','FontName','Calibri','FontSize',11,'FontWeight',
'bold');
text(ii+0.5,4,'UNUSUAL','FontName','Calibri','FontSize',11,'FontWeight','bo
ld');
text(ii+0.5,5,'EXTREME','FontName','Calibri','FontSize',11,'FontWeight','bo
ld');
text(ii+0.5,-
1,'USUAL','FontName','Calibri','FontSize',11,'FontWeight','bold');
text(ii+0.5,-
2,'CORRECT','FontName','Calibri','FontSize',11,'FontWeight','bold');
text(ii+0.5,-
3,'SUSPICIOUS','FontName','Calibri','FontSize',11,'FontWeight','bold');
text(ii+0.5,-
4,'UNUSUAL','FontName','Calibri','FontSize',11,'FontWeight','bold');
text(ii+0.5,-
5,'EXTREME','FontName','Calibri','FontSize',11,'FontWeight','bold');
grid on
print -djpeg N-GF

```

```

MAXGF=-1e30;
MINGF=1e30;
figure
for ii=1:a %GF-REL
    if MM(ii,1)=='0'
        if MM(ii,1:2)=='00'
            M=MM(ii,3);
        else
            M=MM(ii,2:3);
        end
    else
        M=MM(ii,:);
    end
    load([DD(ii,:) M YYYY(ii,:) '.mat']);
    clear FF
    FF=ones(1,length(GFR))*ii;
    clear ColorVec
    if strcmp([DD(ii,:) M YYYY(ii,:)], '23X2015')==1
        ColorVec=[0 0.4 1];
    elseif strcmp([DD(ii,:) M YYYY(ii,:)], '14XII2015')==1
        ColorVec=[0.1 0.6 0.1];
    elseif strcmp([DD(ii,:) M YYYY(ii,:)], '29I2016')==1
        ColorVec=[1 0 0];
    elseif strcmp([DD(ii,:) M YYYY(ii,:)], '10III2016')==1
        ColorVec=[0.6 0.2 0.8];
    elseif strcmp([DD(ii,:) M YYYY(ii,:)], '17III2016')==1
        ColorVec=[0.7 0.7 0];
    elseif strcmp([DD(ii,:) M YYYY(ii,:)], '01IV2016')==1
        ColorVec=[0.7 0.7 0.7];
    elseif strcmp([DD(ii,:) M YYYY(ii,:)], '07IV2016')==1
        ColorVec=[0 1 1];
    elseif strcmp([DD(ii,:) M YYYY(ii,:)], '14IV2016')==1
        ColorVec=[1 0.7 0.5];
    elseif strcmp([DD(ii,:) M YYYY(ii,:)], '21IV2016')==1
        ColorVec=[0 0 0];

```

```

end
scatter(FF, (GFR-
GF)/GF*100,16, 'MarkerEdgeColor',ColorVec, 'MarkerFaceColor',ColorVec)
hold on
if max((GFR-GF)/GF)>MAXGF
    MAXGF=max((GFR-GF)/GF);
end
if min((GFR-GF)/GF)<MINGF
    MINGF=min((GFR-GF)/GF);
end
end
ylabel ('Relative G_F deviation: (G_F_i-G_F)/G_F
(%)', 'FontName', 'Calibri', 'FontSize', 12)
axis ([-4 ii+1 -100 100])
title('RELATIVE DEVIATION FOR FRACTURE
ENERGY', 'FontName', 'Calibri', 'FontSize', 14, 'FontWeight', 'bold')
set(gca, 'ytick', [-100 -80 -60 -40 -20 -10 -5 0 5 10 20 40 60 80 100]);
set(gca, 'xtick', [-10]);
legend({'23X2015', '14XII2015', '29I2016', '10III2016', '17III2016', '01IV2016',
'07IV2016', '14IV2016', '21IV2016'}, 'Location', 'Northwest', 'FontName', 'Calibr
i', 'FontSize', 12)
legend boxoff
grid on
print -djpeg R-GF
%DO THE SAME WITH OTHER PARAMETERS OF INTEREST

%FRACTURE ENERGY COMPARISON
figure
errorbar(ftRR(1), GFRR(1), SDGFRR(1), 'o', 'MarkerFaceColor', [0 0.4
1], 'Linewidth', 1.5, 'Color', [0 0.4 1])
hold on
errorbar(ftRR(2), GFRR(2), SDGFRR(2), 'o', 'MarkerFaceColor', [0.1 0.6
0.1], 'Linewidth', 1.5, 'Color', [0.1 0.6 0.1])
errorbar(ftRR(3), GFRR(3), SDGFRR(3), 'o', 'MarkerFaceColor', [1 0
0], 'Linewidth', 1.5, 'Color', [1 0 0])
errorbar(ftRR(4), GFRR(4), SDGFRR(4), 'o', 'MarkerFaceColor', [0.6 0.2
0.8], 'Linewidth', 1.5, 'Color', [0.6 0.2 0.8])
errorbar(ftRR(5), GFRR(5), SDGFRR(5), 'o', 'MarkerFaceColor', [0.7 0.7
0], 'Linewidth', 1.5, 'Color', [0.7 0.7 0])
errorbar(ftRR(6), GFRR(6), SDGFRR(6), 'o', 'MarkerFaceColor', [0.7 0.7
0.7], 'Linewidth', 1.5, 'Color', [0.7 0.7 0.7])
errorbar(ftRR(7), GFRR(7), SDGFRR(7), 'o', 'MarkerFaceColor', [0 1
1], 'Linewidth', 1.5, 'Color', [0 1 1])
errorbar(ftRR(8), GFRR(8), SDGFRR(8), 'o', 'MarkerFaceColor', [1 0.7
0.5], 'Linewidth', 1.5, 'Color', [1 0.7 0.5])
errorbar(ftRR(9), GFRR(9), SDGFRR(9), 'o', 'MarkerFaceColor', [0 0
0], 'Linewidth', 1.5, 'Color', [0 0 0])
xlabel ('Axial tensile strength f_t (MPa)', 'FontName', 'Calibri', 'FontSize',
12)
ylabel ('Real fracture energy G_F (J/m^2)', 'FontName', 'Calibri', 'FontSize',
12)
axis ([-0.4 3 0 max(GFRR)+1.6*max(SDGFRR)])
title('FRACTURE ENERGY vs. TENSILE
STRENGTH', 'FontName', 'Calibri', 'FontSize', 14, 'FontWeight', 'bold')
legend({'23X2015', '14XII2015', '29I2016', '10III2016', '17III2016', '01IV2016',
'07IV2016', '14IV2016', '21IV2016'}, 'Location', 'Northwest', 'FontName', 'Calibr
i', 'FontSize', 12)
legend boxoff
grid on
print -djpeg GF-ft_FINALE
%DO THE SAME WITH OTHER PROPERTIES OF INTEREST OR COMPOSITION

```

```

%SOFTENING CURVE APPROX. COMPARISON
WW=[0:1e-4:max(WCRR)]; %mm
for ii=1:length(WW)
    for j=1:length(WCRR)
        if WW(ii)<=WKRR(j)
            SS(ii,j)=ftRR(j)-(ftRR(j)-sigmaKRR(j))*WW(ii)/WKRR(j);
        elseif WW(ii)>=WCRR(j)
            SS(ii,j)=0;
        else
            SS(ii,j)=sigmaKRR(j)*WCRR(j)/(WCRR(j)-WKRR(j))-
sigmaKRR(j)*WW(ii)/(WCRR(j)-WKRR(j));
        end
    end
end
[final1,~]=encuentra_valor(WW,WCRR(1));
[final2,~]=encuentra_valor(WW,WCRR(2));
[final3,~]=encuentra_valor(WW,WCRR(3));
[final4,~]=encuentra_valor(WW,WCRR(4));
[final5,~]=encuentra_valor(WW,WCRR(5));
[final6,~]=encuentra_valor(WW,WCRR(6));
[final7,~]=encuentra_valor(WW,WCRR(7));
[final8,~]=encuentra_valor(WW,WCRR(8));
[final9,~]=encuentra_valor(WW,WCRR(9));
WW=WW*1000; %micrometer

PRIMERA=[WW(1:final1).' SS(1:final1,1)];
primera=[PRIMERA(:,1)*ftRR(1)/GFRR(1) PRIMERA(:,2)/ftRR(1)];
SEGUNDA=[WW(1:final2).' SS(1:final2,2)];
segunda=[SEGUNDA(:,1)*ftRR(2)/GFRR(2) SEGUNDA(:,2)/ftRR(2)];
TERCERA=[WW(1:final3).' SS(1:final3,3)];
tercera=[TERCERA(:,1)*ftRR(3)/GFRR(3) TERCERA(:,2)/ftRR(3)];
CUARTA=[WW(1:final4).' SS(1:final4,4)];
cuarta=[CUARTA(:,1)*ftRR(4)/GFRR(4) CUARTA(:,2)/ftRR(4)];
QUINTA=[WW(1:final5).' SS(1:final5,5)];
quinta=[QUINTA(:,1)*ftRR(5)/GFRR(5) QUINTA(:,2)/ftRR(5)];
SEXTA=[WW(1:final6).' SS(1:final6,6)];
sexta=[SEXTA(:,1)*ftRR(6)/GFRR(6) SEXTA(:,2)/ftRR(6)];
SEPTIMA=[WW(1:final7).' SS(1:final7,7)];
septima=[SEPTIMA(:,1)*ftRR(7)/GFRR(7) SEPTIMA(:,2)/ftRR(7)];
OCTAVA=[WW(1:final8).' SS(1:final8,8)];
octava=[OCTAVA(:,1)*ftRR(8)/GFRR(8) OCTAVA(:,2)/ftRR(8)];
NOVENA=[WW(1:final9).' SS(1:final9,9)];
novenas=[NOVENA(:,1)*ftRR(9)/GFRR(9) NOVENA(:,2)/ftRR(9)];

figure
plot(PRIMERA(:,1),PRIMERA(:,2),'Linewidth',1.5,'Color',[0 0.4 1])
hold on
plot(SEGUNDA(:,1),SEGUNDA(:,2),'Linewidth',1.5,'Color',[0.1 0.6 0.1])
plot(TERCERA(:,1),TERCERA(:,2),'Linewidth',1.5,'Color',[1 0 0])
plot(CUARTA(:,1),CUARTA(:,2),'Linewidth',1.5,'Color',[0.6 0.2 0.8])
plot(QUINTA(:,1),QUINTA(:,2),'Linewidth',1.5,'Color',[0.7 0.7 0])
plot(SEXTA(:,1),SEXTA(:,2),'Linewidth',1.5,'Color',[0.7 0.7 0.7])
plot(SEPTIMA(:,1),SEPTIMA(:,2),'Linewidth',1.5,'Color',[0 1 1])
plot(OCTAVA(:,1),OCTAVA(:,2),'Linewidth',1.5,'Color',[1 0.7 0.5])
plot(NOVENA(:,1),NOVENA(:,2),'Linewidth',1.5,'Color',[0 0 0])
xlabel('Crack width w (\mu m)','FontName','Calibri','FontSize',12)
ylabel('Stress \sigma (MPa)','FontName','Calibri','FontSize',12)
title('SOFTENING CURVE APPROXIMATION','FontName','Calibri','FontSize',
14,'FontWeight','bold')

```

```

legend({'23X2015','14XII2015','29I2016','10III2016','17III2016','01IV2016',
'07IV2016','14IV2016','21IV2016'}, 'Location', 'Northeast', 'FontName', 'Calibr
i', 'FontSize', 12)
legend boxoff
grid on
print -djpeg Bilinear_Approx_FINALE
%REDUCED FORM - CHANGE VARIABLE NAMES FROM CAPITAL TO NON-CAPITAL

%LAST COMPARISON
figure
scatter(DD23X2015,P1Delta23X2015,8.05, '.', 'MarkerEdgeColor',[0 0.4
1], 'LineWidth',0.5')
hold on
scatter(DD14XII2015,P1Delta14XII2015,8.05, '.', 'MarkerEdgeColor',[0.1 0.6
0.1], 'LineWidth',0.5')
scatter(DD29I2016,P1Delta29I2016,8.05, '.', 'MarkerEdgeColor',[1 0
0], 'LineWidth',0.5')
scatter(DD10III2016,P1Delta10III2016,8.05, '.', 'MarkerEdgeColor',[0.6 0.2
0.8], 'LineWidth',0.5')
scatter(DD17III2016,P1Delta17III2016,8.05, '.', 'MarkerEdgeColor',[0.7 0.7
0], 'LineWidth',0.5')
scatter(DD01IV2016,P1Delta01IV2016,8.05, '.', 'MarkerEdgeColor',[0.7 0.7
0.7], 'LineWidth',0.5')
scatter(DD07IV2016,P1Delta07IV2016,8.05, '.', 'MarkerEdgeColor',[0 1
1], 'LineWidth',0.5')
scatter(DD14IV2016,P1Delta14IV2016,8.05, '.', 'MarkerEdgeColor',[1 0.7
0.5], 'LineWidth',0.5')
scatter(DD21IV2016,P1Delta21IV2016,8.05, '.', 'MarkerEdgeColor',[0 0
0], 'LineWidth',0.5')
xlabel ('Displacement \delta (mm)', 'FontName', 'Calibri', 'FontSize', 12)
ylabel ('Corrected load P_1 (kN)', 'FontName', 'Calibri', 'FontSize', 12)
title('LOAD vs. DISPLACEMENT', 'FontName', 'Calibri', 'FontSize',
14, 'FontWeight', 'bold')
legend({'23X2015','14XII2015','29I2016','10III2016','17III2016','01IV2016',
'07IV2016','14IV2016','21IV2016'}, 'Location', 'Northeast', 'FontName', 'Calibr
i', 'FontSize', 12)
legend boxoff
grid on
print -djpeg P1-D_FINALE
%Do the same with P1-w

```

C.2 MATLAB FUNCTIONS

Here are included some of the functions used in the codes at Appendix C.1. Some of them give information about expressions exposed at Chapter 3, other are just support codes or data processing codes that have been attached to this project, because they have been used at some point of it.

C.2.1 MAIN PARAMETERS FOR THE BILINEAR APPROXIMATION OF THE SOFTENING CURVE

```
function [ sigmaK,WK,WC,W1,WG,GF,E,l1,fp,Pef ] =
ablandamiento_bilineal_mean( aR,DR,SR,BR,Pu1R,ft,AR,WMAR,WMRR,ER,GFR,WGR )
%Point a
for i=1:length(Pu1R)
    Pef(i)=Pu1R(i)+AR(i)/(WMRR(i)-WMAR(i))^2;
    fp(i)=Pef(i)*SR(i)/(2*BR(i)*(DR(i)-aR(i))^2); %kN*mm/mm3=kN/mm2=GPa
    fp(i)=fp(i)*1000; %1GPa=1E3MPa
    l1(i)=(1-(aR(i)/DR(i))^1.7)*DR(i)*(11.2/((ft/fp(i))^2-
1)^2+2.365/((ft/fp(i))^2));
end
%Point b
W1=2*ft*mean(l1)/mean(ER); %MPa*mm/GPa
W1=W1/1000; %MPa*mm/(GPa*1000MPa/1GPa)=mm
%Point c
GF=mean(GFR);
WCHAR=GF/ft; %J/m2*mm2/N=N/m*mm^2/N=mm^2/m
WCHAR=WCHAR/1e3; %1mm2/m*1m/1000mm->mm
%Point d
WG=mean(WGR);
WC=WCHAR*(3*WG-W1)/(2*WCHAR-W1)*(1+sqrt(1-2*W1*(3*WG-2*WCHAR)*(2*WCHAR-
W1)/(WCHAR*(3*WG-W1)^2)));
%Point e
sigmaK=ft*(2*WCHAR-W1)/(WC-W1);
WK=W1*(WC-2*WCHAR)/(WC-W1);
%Point f \\Main code

E=mean(ER);
if sigmaK<0 || WK<0 || W1<0 || WC<0
    sigmaK=0;
    WC=0;
    W1=-1;
    WK=-1;
    display('ERROR en s-w')
end

end
```


C.2.2 FRACTURE ENERGY AND MAIN PARAMETERS THROUGH THE TAIL OF THE LOAD VS. DISPLACEMENT CURVE CORRECTION

```

function [GF,Gf,WG,inicio,pico,limite,final,X,P1,P1cola,WM,K,A] =
GF_ajuste_cola(a,D,B,S,CMOD,P,Delta)
%Point a
condicion=4*D/300;
[limite,~]=encuentra_valor(CMOD,condicion);
if limite+1<=length(CMOD)
    control=1;
    while (CMOD(limite)<=condicion || CMOD(limite+1)<=condicion) &&
control==1
        limite=limite+1;
        if limite<length(CMOD)
            control=1;
        else
            control=0;
        end
    end
end
for e=1:(limite)
    P1(e)=P(e);
    WM(e)=CMOD(e);
end
clear e limite condicion control
%Point b
final=length(WM);
WMR=WM(final);
PR=P1(final);
%Point c
for i=1:final
    P1(i)=P1(i)-PR;
end
%Point d
limite=final/2;
[inicio,~]=encuentra_zeros_limite(P1,limite);
WMA=WM(inicio);
clear e limite
%Point e
[PU,~,~,~,pico,~]=max_min_med_vec(P1);
[limite,~]=encuentra_valor_intervalo(P1,0.05*PU,pico,final);
if limite+1<=length(CMOD)
    control=1;
    while (P1(limite)>=0.05*PU || P1(limite+1)>=0.05*PU) && control==1
        limite=limite+1;
        if limite<length(P1)
            control=1;
        else
            control=0;
        end
    end
end
end
for e=1:(final-limite+1) %Point f incluido
    P1cola(e)=P1(e-1+limite);
    X(e)=(4*D/S)^2*(1/(WM(e-1+limite)-WMA)^2-1/(WMR-WMA)^2);
end
clear e
%Point g
modelFun = @(b,x) b(1).*x(1,:)+b(2).*(x(1,:)).^2;

```

```

startingVals = [1 1];
coefEsts = nlinfit(X, Plcola, modelFun, startingVals);
A=coefEsts(1);
K=coefEsts(2);
clear startingVals coefEsts modelFun
%Point h
DR=Delta(final);
DA=Delta(inicio);
Wtail=2*A/(DR-DA);
%Fracture work
Wf=0;
for i=(inicio+1):final
    Wf=Wf+0.5*(P1(i)+P1(i-1))*(Delta(i)-Delta(i-1));
end
Gf=Wf/(B*1e-3*(D-a)*1e-3);
%Real fracture energy
GF=(Wf+Wtail)/(B*1e-3*(D-a)*1e-3);
%Gravity center
WG=4*A/(B*S*GF)*1e6; %kNmm2/(mm2*N/m)=kNm/N->1kN/N*m*1000N/kN*1000mm/m
end

```

C.2.3 DETERMINATION OF THE ELASTIC MODULI

```

function [ E,a0,a1,final ] = E_flexion3P( a,D,B,S,P,CMOD,h )
%Point a
Pu=max(P);
[final,~]=encuentra_valor(P,Pu);
%Point b & c
MTX_SYS=[0 0;0 0];
MTX_IND=[0;0];
for i=1:final
    if P(i)>=0.15*Pu && P(i)<=0.55*Pu
        MTX_SYS(1,1)=MTX_SYS(1,1)+1;
        MTX_SYS(1,2)=MTX_SYS(1,2)+P(i);
        MTX_SYS(2,1)=MTX_SYS(2,1)+P(i);
        MTX_SYS(2,2)=MTX_SYS(2,2)+(P(i))^2;
        MTX_IND(1,1)=MTX_IND(1,1)+CMOD(i);
        MTX_IND(2,1)=MTX_IND(2,1)+CMOD(i)*P(i);
    end
end
AA=MTX_SYS\MTX_IND;
Ci=AA(2);
%Point d
V=@(x)0.8-1.7*x+2.4*x^2+0.66/(1-x)^2+4*D/S*(-0.04-0.58*x+1.47*x^2-2.04*x^3);
alpha0=(a+h)/(D+h);
%Point e
E=6*S*a*V(alpha0)/(Ci*B*D^2);
a1=Ci;
a0=AA(1);
end

```

C.2.4 SIZE-DEPENDENT FRACTURE ENERGY

```

function [ Gf, inicio, final, P1, WM ] = energia_dependiente(
P, Delta, CMOD, PESO, a, D, B, m )
%Point a \\Limit the series
condicion=4*D/300;
[limite,~]=encuentra_valor(CMOD,condicion);
if limite+1<=length(CMOD)
    control=1;
    while (CMOD(limite)<=condicion || CMOD(limite+1)<=condicion) &&
control==1
        limite=limite+1;
        if limite<length(CMOD)
            control=1;
        else
            control=0;
        end
    end
end
for e=1:(limite)
    P1(e)=P(e);
    WM(e)=CMOD(e);
end
clear limite condicion control
%Point b
final=length(WM);
PR=P1(final);
%Point c
for i=1:final
    P1(i)=P1(i)-PR;
end
%Point d
limite=final/2;
[inicio,~]=encuentra_zeros_limite(P1,limite);
clear limite
%Work of fracture
Wf=0;
for i=(inicio+1):final
    Wf=Wf+0.5*(P1(i)+P1(i-1))*(Delta(i)-Delta(i-1));
end
if PESO==0
    Gf=Wf/(B*1e-3*(D-a)*1e-3);
elseif PESO==1
    Gf=(Wf+m*9.81*Delta(final)*1e-3)/(B*1e-3*(D-a)*1e-3);
end

end

```

C.2.5 FRACTURE ENERGY AND MAIN PARAMETERS THROUGH THE LOCAL FRACTURE ENERGY MODEL

```

function [ GF,A1,situacion ] = GF_energia_local( Gf1,Gf2,a1,a2,D1,D2 )
situacion=1;
final=0;
while final==0
    switch situacion
        case 1 %Case A
            A=Gf1*2*D1*(1-a1/D1);
            B=2*D1*(1-a1/D1);
            C=Gf2*2*D2*(1-a2/D2);
            D=2*D2*(1-a2/D2);
            A1=(B-A*D/C)/(1-A/C);
            GF=A/(B-A1);
            if 1-a1/D1>A1/D1 && 1-a2/D2>A1/D2 && GF>=0 && A1>=0
                final=1;
            else
                situacion=2;
            end
        case 2 %Case C+
            A=Gf1*2*D1*(1-a1/D1);
            B=2*D2*(1-a1/D2);
            C=Gf2*2/D2;
            D=1-a2/D2;
            A1=(B*C+sqrt((B*C)^2-4*C*A*D))/(2*C);
            GF=C*A1/D;
            if 1-a1/D1>A1/D1 && 1-a2/D2<=A1/D2 && GF>=0 && A1>=0
                final=1;
            else
                situacion=3;
            end
        case 3 %Case C-
            A=Gf1*2*D1*(1-a1/D1);
            B=2*D1*(1-a1/D1);
            C=Gf2*2/D2;
            D=1-a2/D2;
            A1=(B*C-sqrt((B*C)^2-4*C*A*D))/(2*C);
            GF=C*A1/D;
            if 1-a1/D1>A1/D1 && 1-a2/D2<=A1/D2 && GF>=0 && A1>=0
                final=1;
            else
                situacion=4;
            end
        case 4 %Case D+
            A=Gf2*2*D2*(1-a2/D2);
            B=2*D2*(1-a2/D2);
            C=Gf1*2/D1;
            D=1-a1/D1;
            A1=(B*C+sqrt((B*C)^2-4*C*A*D))/(2*C);
            GF=C*A1/D;
            if 1-a2/D2>A1/D2 && 1-a1/D1<=A1/D1 && GF>=0 && A1>=0
                final=1;
            else
                situacion=5;
            end
        case 5 %Case D-
            A=Gf2*2*D2*(1-a2/D2);
            B=2*D2*(1-a2/D2);

```

```

        C=Gf1*2/D1;
        D=1-a1/D1;
        A1=(B*C-sqrt((B*C)^2-4*C*A*D))/(2*C);
        GF=C*A1/D;
        if 1-a2/D2>A1/D2 && 1-a1/D2<=A1/D2 && GF>=0 && A1>=0
            final=1;
        else
            situacion=6;
        end
    case 6 %Case B
        final=1;
        GF=-1;
        A1=-1;
        display('El problema es indeterminado')
    end
end
end
end

```

C.2.6 FINDING NON-ZERO VALUES: WITHOUT LIMIT IN THE DATA RANGE

```

function [ i,e ] = encuentra_valor( X,n )
    i=0;
    %Direct search for the first value
    for j=1:length(X)
        if X(j)==n
            i=j;
            e=0;
        end
    end

    %If not found - the nearest
    if i==0
        min=1e30;
        for j=1:length(X)
            if X(j)==0
                De(j)=1;
            else
                De(j)=abs((X(j)-n)/X(j));
                if De(j)<min
                    min=De(j);
                    i=j;
                end
            end
        end
        e=min;
    end
end

```

C.2.7 FINDING NON-ZERO VALUES: WITH LIMIT IN THE DATA RANGE

```

function [ i,e ] = encuentra_valor_con_limite( X,n,ultimo )
    i=0;
    %Direct search for the first value
    j=1;
    while (j<=ultimo)&&(j<=length(X))
        if X(j)==n
            i=j;
            e=0;
        end
    end

```

```

        end
        j=j+1;
    end

    %If not found - the nearest
    if i==0
        j=1;
        min=1e30;
        while (j<=ultimo) && (j<=length(X))
            if X(j)==0
                De(j)=1;
            else
                De(j)=abs((X(j)-n)/X(j));
                if De(j)<min
                    min=De(j);
                    i=j;
                end
            end
            j=j+1;
        end
        e=min;
    end
end

```

C.2.8 FINDING NON-ZERO VALUES: WITHIN A DATA RANGE

```

function [ i,e ] = encuentra_valor_intervalo( X,n,io,iff )
    i=0;
    %Direct search for the first value
    j=io;
    while (j<=iff) && (j<=length(X))
        if X(j)==n
            i=j;
            e=0;
        end
        j=j+1;
    end

    %If not found - the nearest
    if i==0
        j=io;
        min=1e30;
        while (j<=iff) && (j<=length(X))
            if X(j)==0
                De(j)=1;
            else
                De(j)=abs((X(j)-n)/X(j));
                if De(j)<min
                    min=De(j);
                    i=j;
                end
            end
            j=j+1;
        end
        e=min;
    end
end

```

C.2.9 FINDING ZERO VALUES: WITH LIMIT IN THE DATA RANGE

```

function [ i,e ] = encuentra_zeros_limite( X,ultimo )
    i=0;
    j=1;
    while (j<=ultimo)&&(j<=length(X))
        if X(j)==0
            i=j;
            e=0;
        end
        j=j+1;
    end
    if i==0
        j=1;
        min=1e30;
        while (j<=ultimo)&&(j<=length(X))
            De(j)=abs((X(j)));
            if De(j)<min
                min=De(j);
                i=j;
            end
            j=j+1;
        end
        e=min;
    end
end

```

C.2.10 FINDING THE MAXIMUM AND MINIMUM, THEIR LOCATIONS, THE MEAN VALUE AND THE STANDARD DEVIATION OF A DATA SET OR VECTOR: WITHOUT LIMIT IN THE DATA RANGE

```

function [ max,min,med,sd,imax,imin ] = max_min_med_vec( X )
    max=-1e30;
    min=1e30;
    imax=0;
    imin=0;
    s=0;
    for i=1:length(X)
        if X(i)>max
            imax=i;
            max=X(i);
        end
        if X(i)<min
            imin=i;
            min=X(i);
        end
        s=X(i)+s;
    end
    med=s/length(X);
    s=0;
    for i=1:length(X)
        s=(X(i)-med)^2+s;
    end
    sd=sqrt(s/(length(X)-1));
end

```

C.2.11 FINDING THE MAXIMUM AND MINIMUM, THEIR LOCATIONS, THE MEAN VALUE AND THE STANDARD DEVIATION OF A DATA VECTOR: WITH LIMIT IN THE DATA RANGE

```
function [ max,min,med,sd,imax,imin ] = max_min_med_vec_limitado(X,limite)
    max=-1e30;
    min=1e30;
    imax=0;
    imin=0;
    s=0;
    for i=1:limite
        if X(i)>max
            imax=i;
            max=X(i);
        end
        if X(i)<min
            imin=i;
            min=X(i);
        end
        s=X(i)+s;
    end
    med=s/length(X);
    s=0;
    for i=1:length(X)
        s=(X(i)-med)^2+s;
    end
    sd=sqrt(s/(length(X)-1));
end
```

C.2.12 OBTAINING THE UPPER AND LOWER CURVE OF A COUPLED DATA SPECTRUM WITH AN ABSCISSA DATA RANGE AND DIVISION

```
function [ysup,yinf,xnew] = upper_lower(x,y,range)
xmin=min(x);      xmax=max(x);      steps=(xmax-xmin)/range;      w=0;
for i=1:(steps+1)
    xnewescalar=xmin+(i-1)*range;
    maximum=min(y);      minimum=max(y);
    k=0;
    for j=1:length(x)
        if x(j)>xnewescalar-0.5*range && x(j)<=xnewescalar+0.5*range
            if y(j)>=maximum
                maximum=y(j);
            end
            if y(j)<=minimum
                minimum=y(j);
            end
            k=k+1;
        end
    end
    if k~=0
        w=w+1;
        xnew(w,1)=xnewescalar;
        ysup(w,1)=maximum;
        yinf(w,1)=minimum;
    end
end
end
```


D MANUAL PROCESSING PROCEDURE FOR THE CAMPAIGNS ANALYSIS

This appendix is created because of the will of the author of detailing the data treatment in order to obtain the results that were wanted and, doing so, they can be reproduced by any other person. Every single consideration or worth information about the data will be written in this appendix.

Some of the parameters are referred to the codes at Appendix C.

D.1 17VI2015 TEST TRIAL

Method: based on the $P - \delta$ tail correction code for a single specimen. The data is recorded and save in the way that:

- The identifier ID is at column 1, as a number
- Time is at column 2 in seconds (s). These recordings are not used
- The machine load recording is at column 4 in kilogram (kg). These recordings are not used
- The load cell P recordings is at column 6 in kilogram (kg) with the negative sign
- The $CMOD$ values are stored at column 5 in millimeters (mm)
- The vertical displacement δ is saved at column 3 in millimeters (mm)

The P values will be set in kilonewton (kN) and the sign will be changed using Equation D.1.1.

$$P [kN] = -P [kg] \cdot 9.81 \frac{N}{kg} \cdot \frac{1kN}{1000N} \quad (D.1.1)$$

There are 15111 registers at the file. Load values and $CMOD$ values have an acceptable noise. Displacement records have a large noise. This means, that the filtering of the data will be set on:

- Load is not filtered. $nP = 1$ (at the code at Appendix C.1.1)
- $CMOD$ is not filtered. $nCMOD = 1$ (at the code at Appendix C.1.1)
- Displacement will be filtered. The filter value will be set at the mean of the 50 values before. $nDelta = 50$ (at the code at Appendix C.1.1)

The range of both upper curve construction code will be set in steps of $2\mu m$ ($range = 2e-3$, at the code at Appendix C.2.12). No further corrections are required. No further actions are performed.

D.2 13X2015 TEST TRIAL

Method: based on the $P - \delta$ tail correction code for a single specimen. The data is recorded and save in the way that:

- The identifier ID is at column 1, as a number
- The time values are at column 2 in seconds (s). These recordings are not used
- The machine load recording is at column 3 in kilogram (kg). These recordings are not used
- The load cell P recordings is at column 6 in kilogram (kg) with mainly negative values
- The $CMOD$ values are stored at column 5 in millimeters (mm)
- The vertical displacement δ is saved at column 4 in millimeters (mm)

The P values will be set in kilonewton (kN) and the sign will be changed using Equation D.1.1.

There are 406 registers at the file. Load and $CMOD$ values have an acceptable noise, but not the displacement records. The filtering of the data will be set on:

- Load is not filtered. $nP = 1$ (at the code at Appendix C.1.1)
- $CMOD$ is not filtered. $nCMOD = 1$ (at the code at Appendix C.1.1)
- Displacement will be filtered. The filter value will be set at the mean of the 20 values before. $nDelta = 20$ (at the code at Appendix C.1.1), then using the former 50 values filter with only 406 will be quite disproportionate.

The range of both upper curve construction code will be set in steps of $2\mu\text{m}$ ($range = 2e-3$, at the code at Appendix C.2.12). The displacement curve requires a new correction, because a large part of the initial $P_1 - \delta$ curve is under the horizontal axis. This test trial has failed, so no further actions are performed.

D.3 23X2015 CAMPAIGN

The method is based on the $P - \delta$ tail correction code for a single specimen. The data is recorded and save in the way that:

- The identifier ID is at column 1, as a number
- The time values are at column 2 in seconds (s). These recordings are not used
- The machine load recording is at column 4 in kilogram (kg). These recordings are not used
- The load cell P recordings is at column 6 in kilogram (kg) with negative sign
- The $CMOD$ values are stored at column 5 in millimeters (mm)
- The vertical displacement δ is saved at column 3 in millimeters (mm)

The P values will be set in kilonewton (kN) and the sign will be changed using Equation D.1.1.

About the register files:

- B23X2015I register file has a register of 21354 entries.
- B23X2015II has 26313 entries.
- B23X2015III has 37181 rows.
- B23X2015IV has 17310 registers.
- C23X2015I, C23X2015II and D23X2015I have 1024 registers each.

All the beam tests show that the load and $CMOD$ values have an acceptable noise, but displacement values have an important noise. The filtering of the data will be set on:

- Load is not filtered. $nP = 1$ (at the code at Appendix C.1.1)
- $CMOD$ is not filtered. $nCMOD = 1$ (at the code at Appendix C.1.1)
- Displacement will be filtered. The filter value will be set at the mean of the 50 values before. $nDelta = 50$ (at the code at Appendix C.1.1). The result must be a line of slope near $1\mu\text{m}/10ID$

The range of both upper curve construction code will be set in steps of $2\mu\text{m}$ ($range = 2e-3$, at the code at Appendix C.2.12). The displacement curve requires a new correction on all the beam specimens, because the initial $P_1 - \delta$ curve is under the horizontal axis or decreasing.

The elastic moduli are obtained with the full spectrum of the $P - w$ curve, no with just the upper curve.

No further actions are required.

D.4 14XII2015 CAMPAIGN

The three point bending test with the double length and the $P - \delta$ tail correction method was applied to the beam-type specimens. The data is recorded and stored using the channels configuration as:

- The identifier ID is at column 1, as a number
- The time values are at column 2 in seconds (s). These recordings are not used
- The machine load recording is at column 4 in kilogram (kg). These recordings are not used
- The load cell P recordings is at column 6 in kilogram (kg) with the sign changed
- The $CMOD$ values are stored at column 5 in millimeters (mm)
- The vertical displacement δ is saved at column 3 in millimeters (mm)

As usual, the P values are wanted positive and in kilonewton (kN), so it will be used Equation D.1.1.

About the register files and method:

- B14XII2015I register file has 20258 entries. Recorded at the maximum speed of the middle acquisition rate, that means, 10 points per second.
- B14XII2015II has 66189 rows. The file was recorded at the maximum speed of the high acquisition rate, which means 50 samples per second.
- B14XII2015III has 17429 points, acquired at 10 samples per second.
- B14XII2015IV has 21762 registers, acquired at 10 samples per second.
- B14XII2015V has 123880 registers in it, acquired at 50 points per second.
- B14XII2015VI has 11985 entries, recording 10 samples per second.
- B14XII2015VII has 16530 rows, recorded at 10 points per second.
- B14XII2015VIII has 95785 registers, acquired at 50 samples per second.
- All cylinder-type specimens have 1024 registers each one.

The same way of other cases, the load and $CMOD$ registers are of little noise, but displacement no:

- Load and $CMOD$ are not filtered. $nP = 1$ and $nCMOD = 1$ (at the code at Appendix C.1.1)
- Displacement is filtered. The filter value will be set at the mean of the 50 values before for a sample acquisition rate of 10 points per second. $nDelta = 50$ (at the code at Appendix C.1.1). The result must be a line of slope $1\mu\text{m}/10ID$ approx. When the acquisition is five times faster, the filter will be set, also, five times greater. $nDelta = 250$. These should be near $1\mu\text{m}/50ID$.

The upper curve code steps are of $2\mu\text{m}$ ($range = 2e-3$, Appendix C.2.12). The curves are corrected always except at B14XII2015II and B14XII2015VI. Elastic moduli computation uses all recorded points.

D.5 29I2016 CAMPAIGN

A three-point bending test was performed on all 8 beam-type specimens for this campaign, although with differences between them. The machine and the acquisition system is the same as former campaigns so the text files contain:

- The identifier *ID* is at column 1, as a number
- The time values are at column 2 in seconds (s). These recordings are not used
- The machine load recording is at column 4 in kilogram (kg). These recordings are not used
- The load cell *P* recordings is at column 6 in kilogram (kg) with the sign changed
- The *CMOD* values are stored at column 5 in millimeters (mm)
- The vertical displacement δ is saved at column 3 in millimeters (mm)

Channel 7 data, the one from the load cell, requires the use of Equation D.1.1.

With the experience of the last campaign, this time the acquisition rate is set to 50 points per second for all specimens, with the following results: 116945 registers for B29I2016I, 82975 for B29I2016II, 99362 for B29I2016III, 82009 for B29I2016IV, 124150 for B29I2016V, 102595 for B29I2016VI, 70745 for B29I2016VII and 146235 for B29I2016VIII.

The filtering procedure is the same as other cases: filter is *off* for load and *CMOD* and it is *on* with a value of 250 for displacement. The upper curve is built every 0.002mm.

A correction was done in order to delete the first part of the curve, which corresponds to the accommodation process with no strain energy storage, but mainly rigid-solid movement, with a significantly different slope on the loading part of the $P - \delta$ graph. The self-weight does not act in fracture at this part. The point was chosen where this slope changes for the upper curve as the following and it is considered the displacement zero: for B29I2016V, the cutting point is chosen at 0.592mm; for B29I2016VI, it is chosen at 0.194mm; for B29I2016VII, it is at 0.095mm and for B29I2016VIII, it is at 0.826mm

Another correction is done at B29I2016I, because a first fracture, but at the rolling supports of some imperfections of the specimen. The first peak will be made coincident to the same load at the second loading part and the first part will be advanced to make both load points coincident. This is: the peak at 0.49mm and 2.344kN is moved to 0.568mm to make it coincident with a 2.35kN point.

The last correction is the usual to prevent the negative values at the beginning, which is done at specimens B29I2016I, B29I2016II, B29I2016III and B29I2016IV.

D.6 10III2016 CAMPAIGN

A three point bending test was performed on the 4 beam specimens, recording:

- The identifier *ID* is at column 1, as a number
- The time values are at column 2 in seconds (s). These recordings are not used
- The machine load recording is at column 4 in kilogram (kg). These recordings are not used
- The load cell *P* recordings is at column 6 in kilogram (kg) with the sign changed
- The *CMOD* values are stored at column 5 in millimeters (mm)
- The vertical displacement δ is saved at column 3 in millimeters (mm)

Channel 7 data, the one from the load cell, requires the use of Equation D.1.1.

Files have an extension of 116290 rows for B10III2016I, 120016 for B10III2016II, 79047 for B10III2016III and 132567 for B10III2016IV.

Due to a mistake on the data collection, the displacement values are not collected and should not be used. Nevertheless, we can work with a safety file: the ASCII recording of the *PCD2K*, a text file with always 1024 registers (between 1.5 and 2 seconds from one register to another).

The *CMOD* values will be coupled with the load from the main register, the displacement values will be coupled with the load from the safety file and the union will be using the peak load. It will be considered that the peak exists at the same time for both registers. With this time, set to zero, the time registered at both files is equivalent, so one can know the first valid value and the last one by the time and not by the identifier of the element.

The filters will be off for the *CMOD* values and for the load values, both the main ASCII file and the safety file. The filter will be on for displacement with a value significantly lower than before, for instance, a value of 3.

A modification in order not to have an initial negative part at the $P - \delta$ curve is needed at all tests, except B10III2016I. The upper curve is built every 0.002mm.

No further actions are required.

At Appendix E.6.1 will be only visible the load recorded by the load cell, it is, the main file, not the safety file recording.

D.7 17III2016 CAMPAIGN

A three point bending test was performed on the 4 beam specimens, but with extra recordings for an additional study for the displacement measurement:

- The identifier ID is at column 1, as a number
- The time values are at column 2 in seconds (s). These recordings are not used
- The machine load recording is at column 4 in kilogram (kg). These recordings are not used
- The load cell P recordings is at column 6 in kilogram (kg) with the sign changed
- The $CMOD$ values are stored at column 5 in millimeters (mm)
- The piston absolute vertical displacement δ is saved at column 3 in millimeters (mm)
- Except at the B17III2016I test, the head absolute vertical displacement at column 7 in millimeters (mm)
- Except at the B17III2016I test, the relative piston-to-load applicator displacement at column 8 in millimeters (mm)

Channel 7 data, the one from the load cell at column 6, requires the use of Equation D.1.1.

The total registers recorded at each test are: 119515 for B17III2016I, 105159 for B17III2016II, 148639 for B17III2016III and 130170 for B17III2016IV. For cylinder tests, the size is 1024 registers each. The filter of the data is on with data at column 3 due its high noise and on for columns 7 and 8 in order to make the comparison correctly. The value is 250. For the other channels, the filter is off. The upper curve is built every 0.002mm.

The process follows the same structure than the former cases.

Further corrections are that, for specimens III and IV only, the second rising part marks the beginning of the test and on specimen II, the first rising part until the 90% of the first relative maximum of 1.5422kN is moved to the same value on the second rising part.

Other considerations for the new channels are done at Appendix B.2.

No further actions are required.

D.8 01IV2016 CAMPAIGN

A three point bending test was performed on the 4 beam specimens from this campaign, recording:

- The identifier ID is at column 1, as a number
- The time values are at column 2 in seconds (s). These recordings are not used
- The machine load recording is at column 4 in kilogram (kg). These recordings are not used
- The load cell P recordings is at column 6 in kilogram (kg) with the sign changed
- The $CMOD$ values are stored at column 5 in millimeters (mm)
- The vertical displacement δ is saved at column 3 in millimeters (mm)

Channel 7 data, the one from the load cell, requires the use of Equation D.1.1.

Files have an extension of 106124 rows for B01IV2016I, 88532 for B01IV2016II, 103667 for B01IV2016III, 106609 for B01IV2016IV and 1024 for C01IV2016I until C01IV2016III. The stable zero for B01IV2016III begins at the 9000th register approx. All data require a correction in order to prevent initial negative values at the $P - \delta$ curve.

The filters are the same as other campaigns:

- For load and $CMOD$ values, the filter is off
- For displacement values, the filter is on, with a value of 250 (see code at Appendix C.1.1).

The upper curves are built with a step of 0.002mm.

Registers from B01IV2016I and B01IV2016IV require another correction at the initial elastic loading stage of the test. For the B01IV2016I register, values from the first rising part until P_1 of 0.9822kN are moved forward, along with the values from the second rising part from 0.9822kN until 1.043kN, which are also moved forward. For B01IV2016IV test, the same is done with the first part until 0.7405kN and the second from 0.7405kN until 1.353kN. The load values are always corrected values.

No further actions are required.

D.9 07IV2016 CAMPAIGN

A three point bending test was performed on the 4 beam specimens for this campaign, recording:

- The identifier ID is at column 1, as a number
- The time values are at column 2 in seconds (s). These recordings are not used
- The machine load recording is at column 4 in kilogram (kg). These recordings are not used
- The load cell P recordings is at column 6 in kilogram (kg) with the sign changed
- The $CMOD$ values are stored at column 5 in millimeters (mm)
- The vertical displacement δ is saved at column 3 in millimeters (mm)

Channel 7 data, the one from the load cell, requires the use of Equation D.1.1.

Files have an extension of 123815 registers for B07IV2016I, 74473 for B07IV2016II, 123134 for B07IV2016III, 105762 for B07IV2016IV and 1024 for C07IV2016I, C07IV2016II and C07IV2016III.

The filters are set off for load and $CMOD$ values and it is set on with a value of 250 for displacement. The upper curves are built with a step of 0.002mm. The elastic modulus determination uses the entire register, not the upper curve only.

Register from B07IV2016III needs to be corrected on its elastic loading stage. The first value of corrected load equal to 0.355kN at the first rising part is moved to the last rising part with the same value.

All registers need to delete an initial negative part of the curves.

No further actions are required for this campaign.

D.10 14IV2016 CAMPAIGN

A three-point bending test was performed on 4 beam specimens for this campaign, recording:

- The identifier *ID* is at column 1, as a number
- The time values are at column 2 in seconds (s). These recordings are not used
- The machine load recording is at column 4 in kilogram (kg). These recordings are not used
- The load cell *P* recordings is at column 6 in kilogram (kg) with the sign changed
- The *CMOD* values are stored at column 5 in millimeters (mm)
- The vertical displacement δ is saved at column 3 in millimeters (mm)

Channel 7 data, the one from the load cell, requires the use of Equation D.1.1.

Files have an extension of 117341 registers for B14IV2016I, 78254 for B14IV2016II, 95537 for B14IV2016III, 124845 for B14IV2016IV and 1024 for C14IV2016I, C14IV2016II and C14IV2016III.

The upper curve is built with a step of 0.002mm, using the non-filtered values for load and *CMOD* and the filtered values for the piston displacement. The filter is set at 250 (*nDelta* at the codes at Appendix C.1).

The elastic modulus determination uses the entire register, not only the upper curve.

The data from B14IV2016IV shows a zone of relative maxima and minima at the initial elastic loading stage. The first maximum of 0.5117kN and the data before is moved to the last similar value of the elastic loading part, using the values after it.

All registers need to erase the initial negative part of the curves.

With this, no more actions are required.

D.11 21IV2016 CAMPAIGN

A three-point bending test was performed on 4 beam specimens for this campaign, recording:

- The identifier ID is at column 1, as a number
- The time values are at column 2 in seconds (s). These recordings are not used
- The machine load recording is at column 4 in kilogram (kg). These recordings are not used
- The load cell P recordings is at column 6 in kilogram (kg) with the sign changed
- The $CMOD$ values are stored at column 5 in millimeters (mm)
- The vertical displacement δ is saved at column 3 in millimeters (mm)

Channel 7 data, the one from the load cell, requires the use of Equation D.1.1.

Files have an extension of 96119 registers for B21IV2016I, 79892 for B21IV2016II, 65720 for B21IV2016III, 64320 for B21IV2016IV and 1024 for C21IV2016I, C21IV2016II and C21IV2016III.

The load data and the $CMOD$ data are not filtered, but the displacement data is filtered with a value of 250 ($nDelta$ at the codes at Appendix C.1).

All tests use the correction in order not to have negative initial curves.

A step of 0.002mm is chosen for the upper curves building.

For the B21IV2016I test, the first corrected value of 0.6864kN and the registers before are moved forward to the value of 0.6864kN at the second rising part.

The elastic modulus determination uses the entire recorded register.

No further actions are required after these corrections.

E TESTS' GRAPHS

This appendix will contain every single graph of every test, giving the chance to observe easily the individual representation of the data on one hand and the combined data graphs on the other hand. So, every test will have its representation alone with the recorded or generated data for it only.

The most important values are at the main memory or, when they have less importance, for the following appendix. The original recordings will not be given in this project, but in digital format, if this is possible. In any case, the original data will be also represented in this appendix.

E.1 17VI2015 TEST TRIAL

E.1.1 17VI2015 DATA

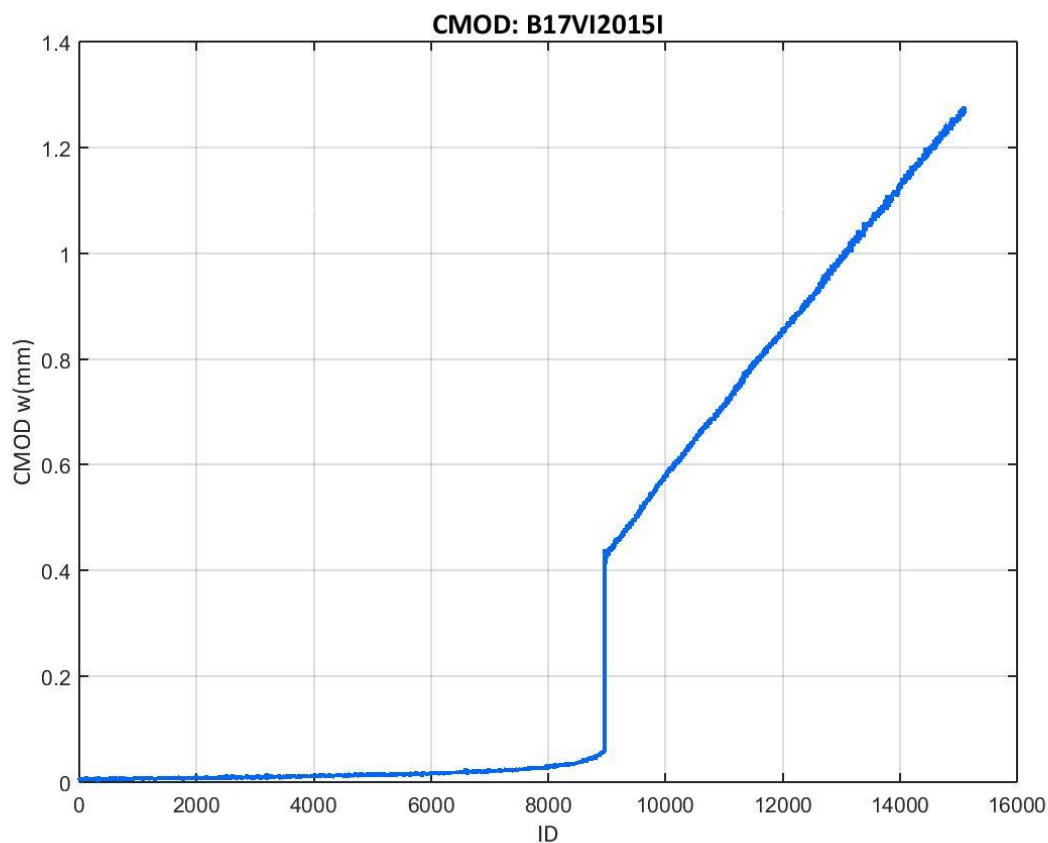


Figure 184: CMOD values recorded at the B17VI2015I test

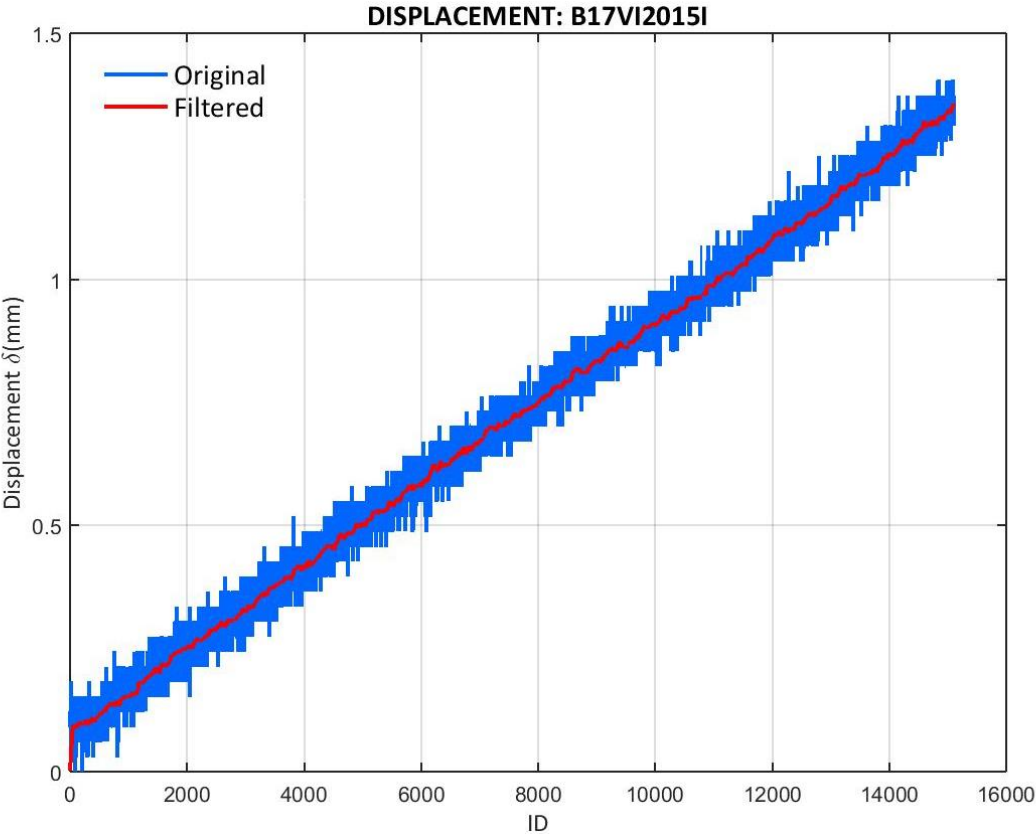


Figure 185: Displacement values recorded at the B17VI2015I test

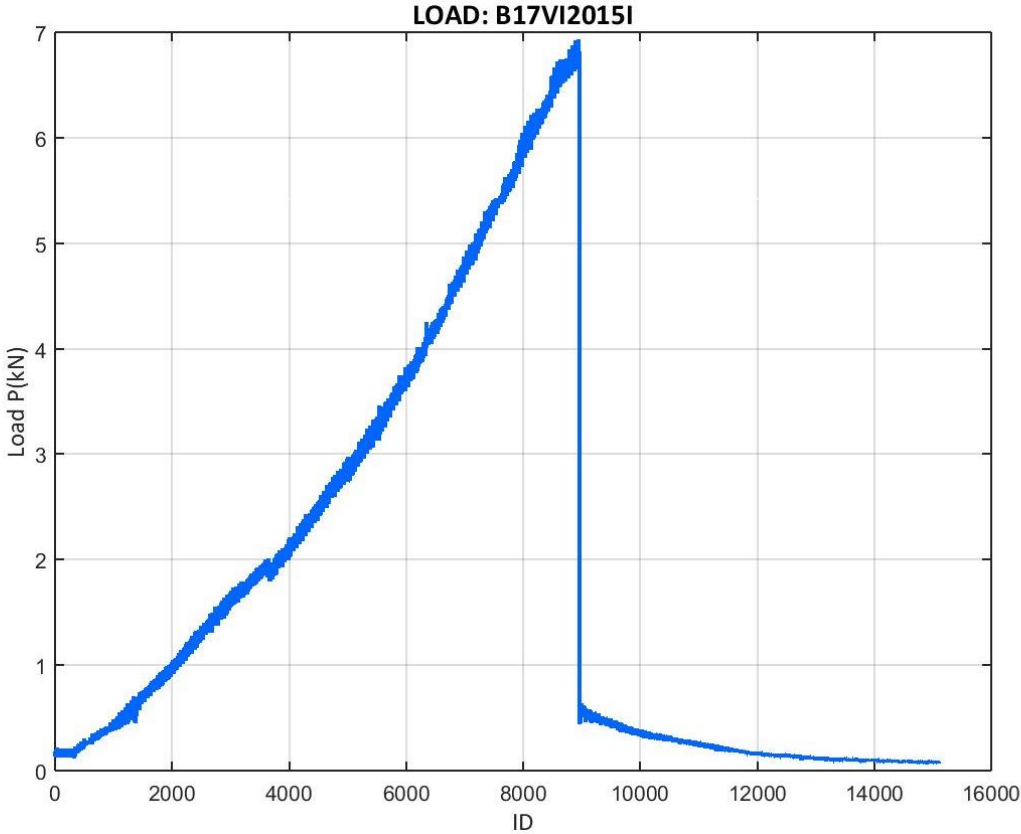


Figure 186: Load values recorded at the B17VI2015I test

E.2 13X2015 TEST TRIAL

E.2.1 13X2015 DATA

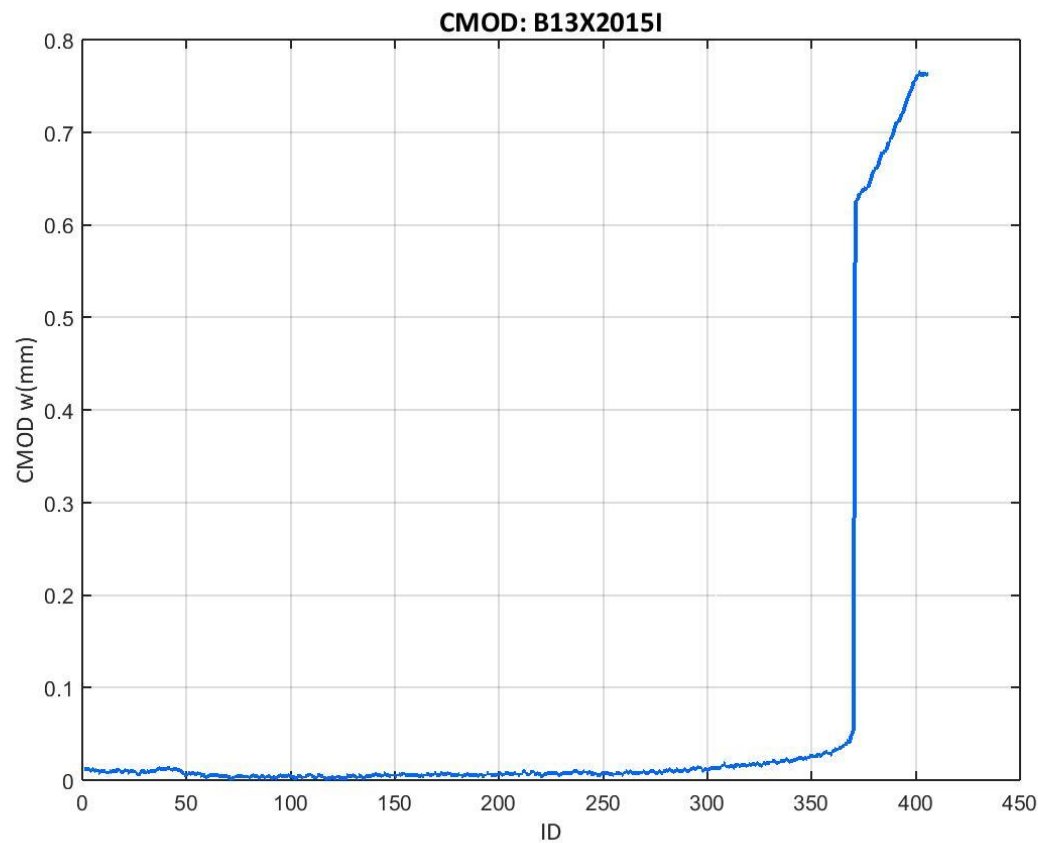


Figure 187: CMOD values recorded at the B13X2015I test

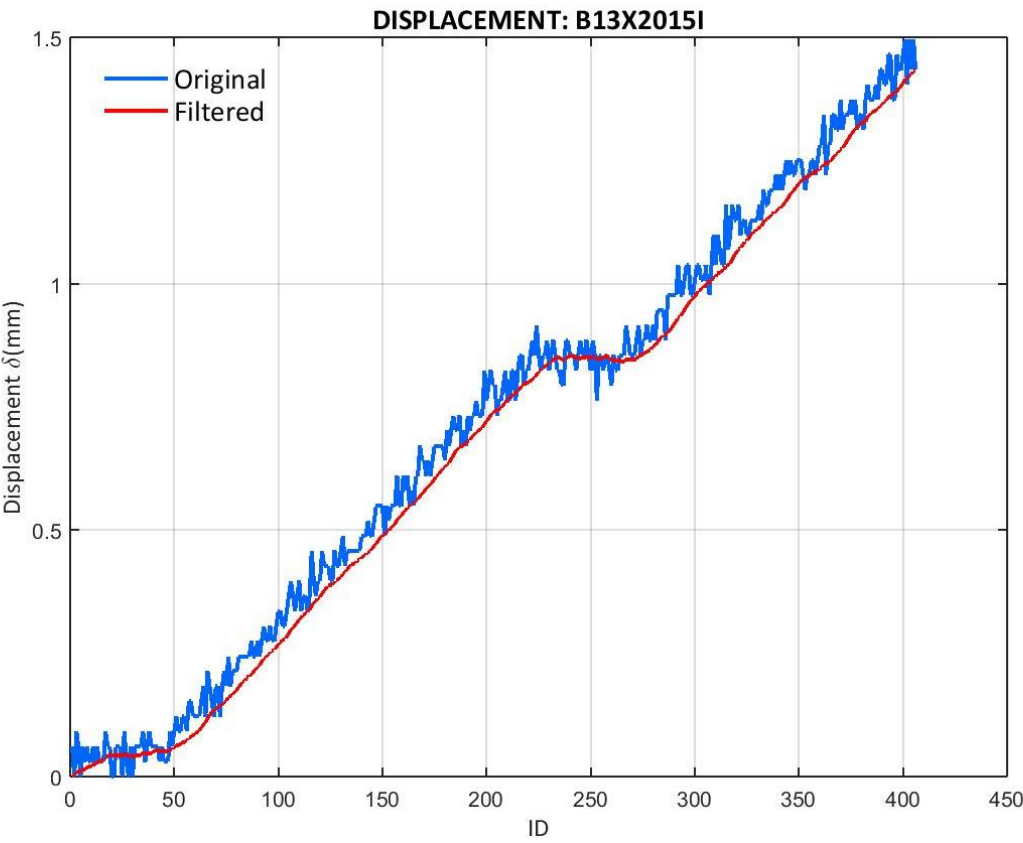


Figure 188: Displacement values recorded at the B13X2015I test

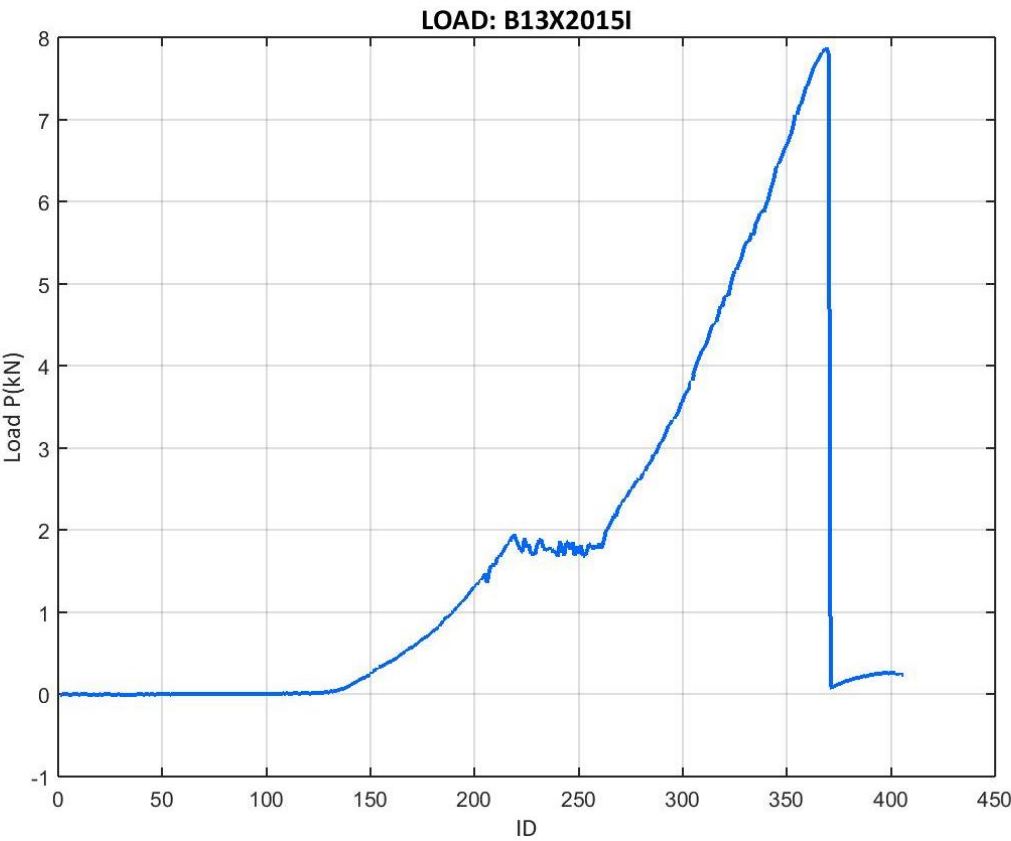


Figure 189: Load values recorded at the B13X2015I test

E.3 23X2015 CAMPAIGN

E.3.1 23X2015 DATA

- B23X2015I

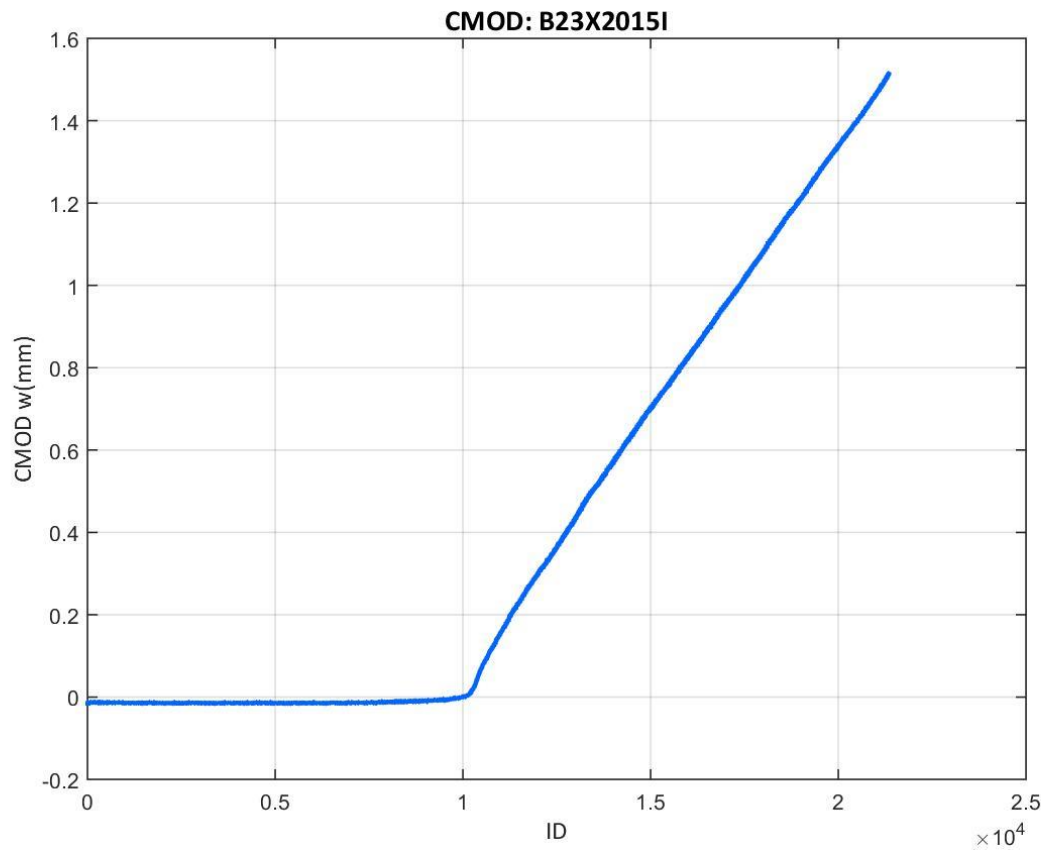


Figure 190: CMOD values recorded at the B23X2015I test

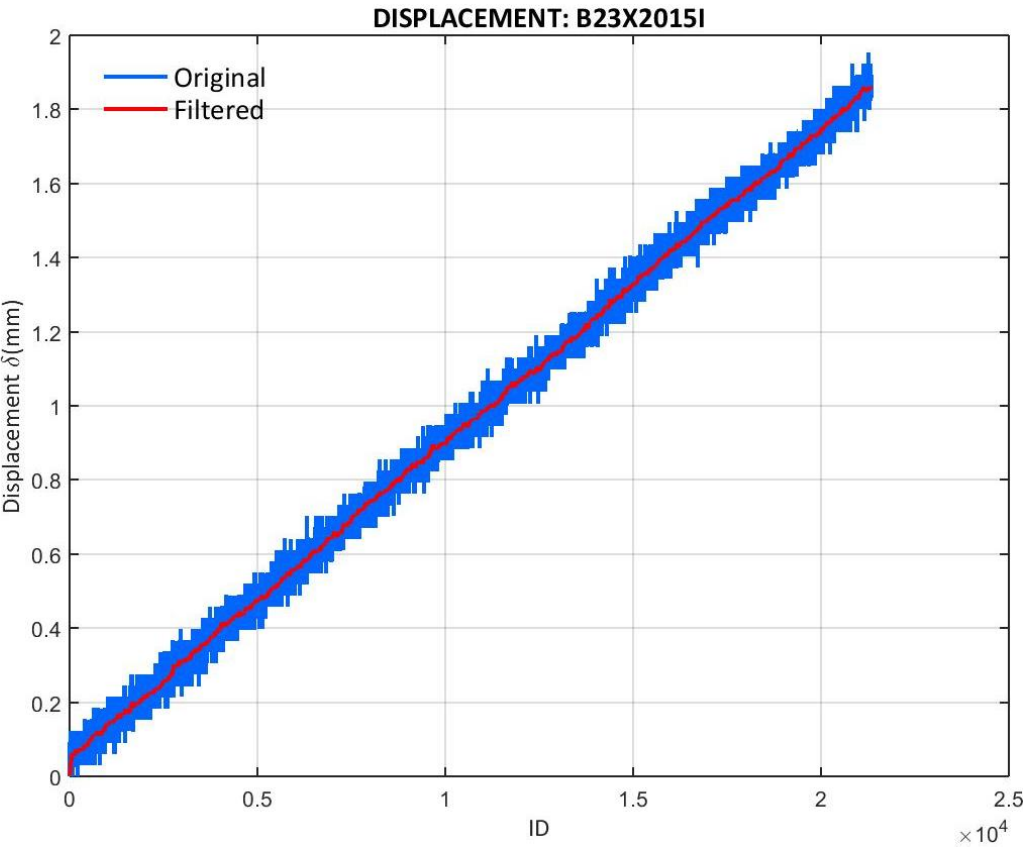


Figure 191: Displacement values recorded at the B23X2015I test

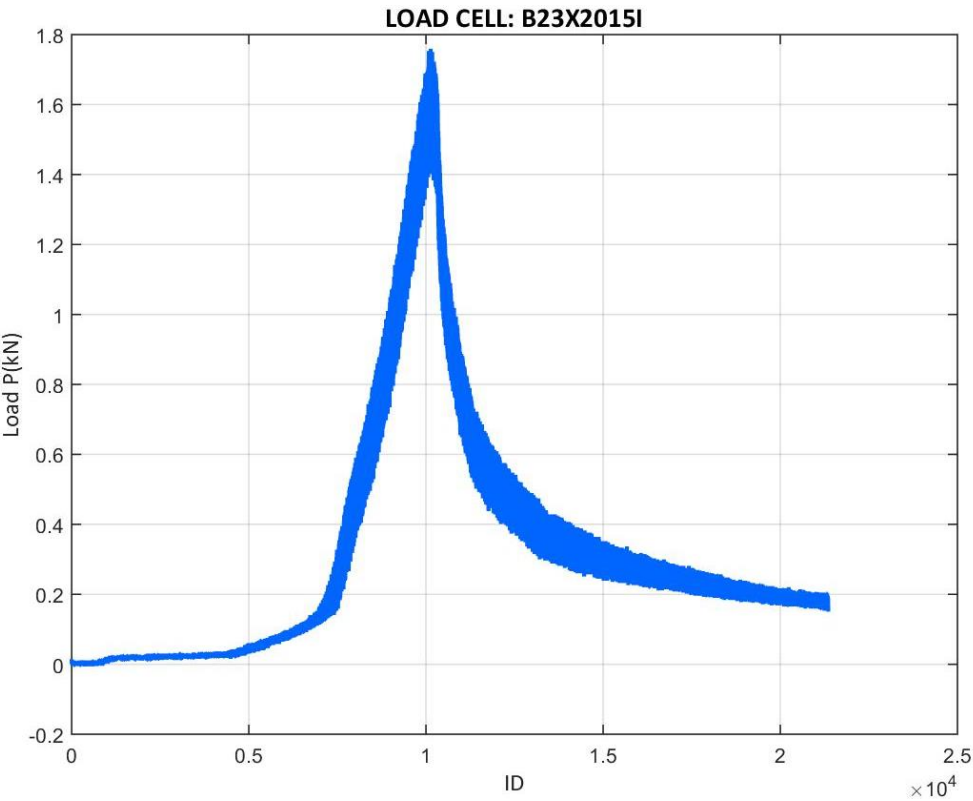


Figure 192: Load values recorded at the B23X2015I test

- B23X2015II

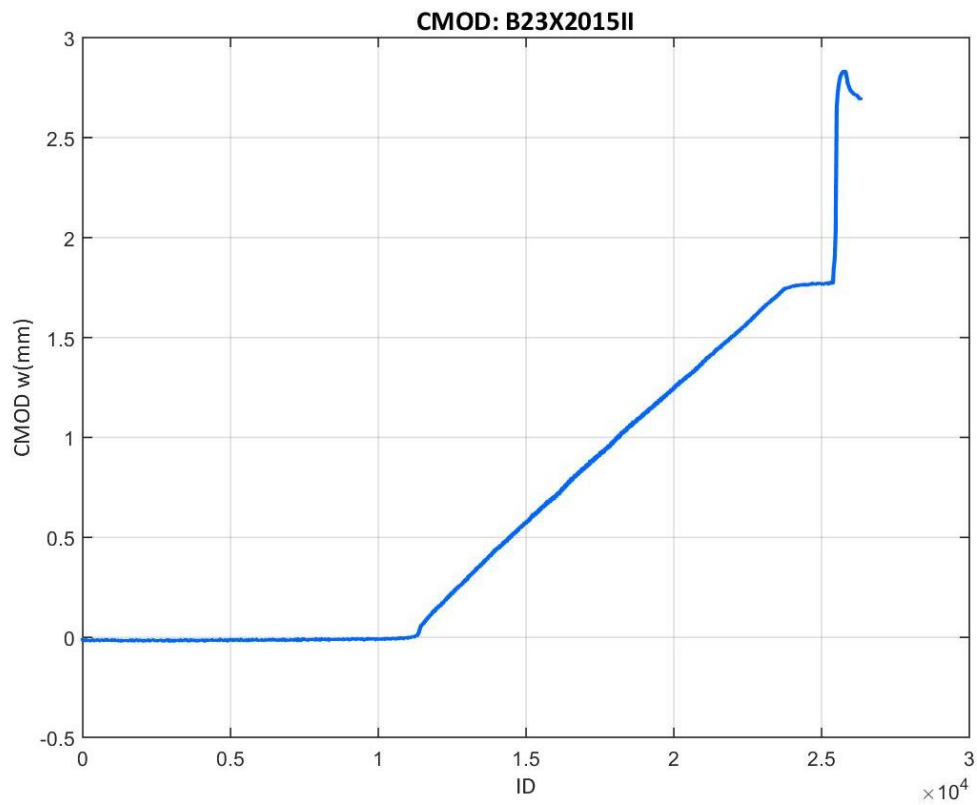


Figure 193: CMOD values recorded at the B23X2015II test

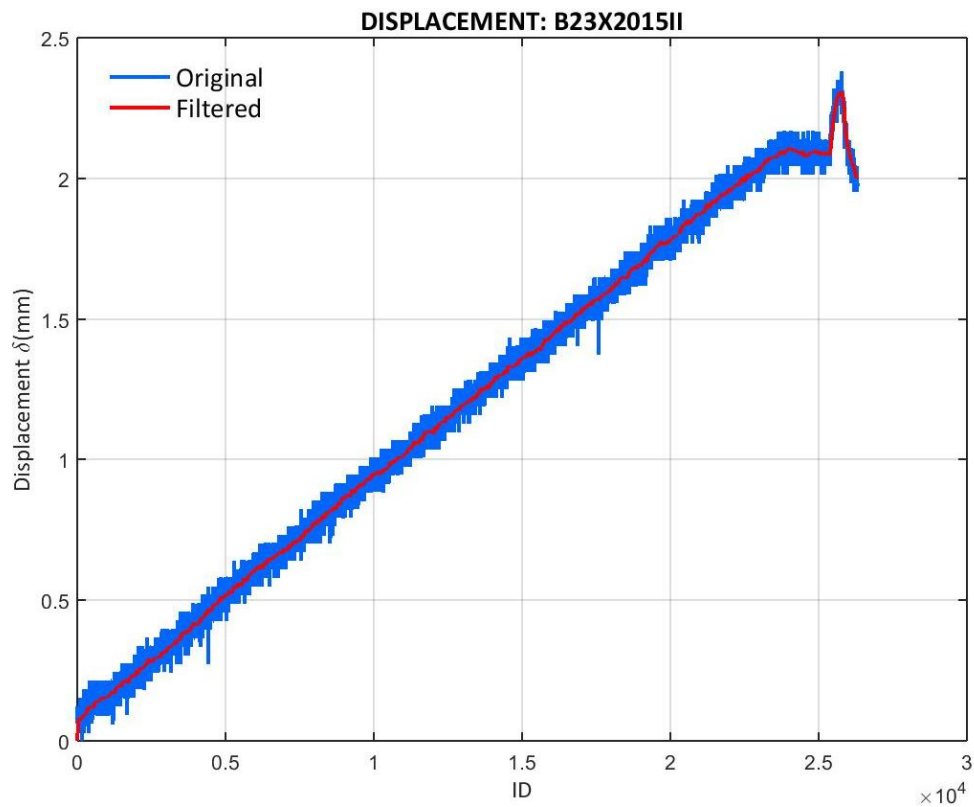


Figure 194: Displacement values recorded at the B23X2015II test

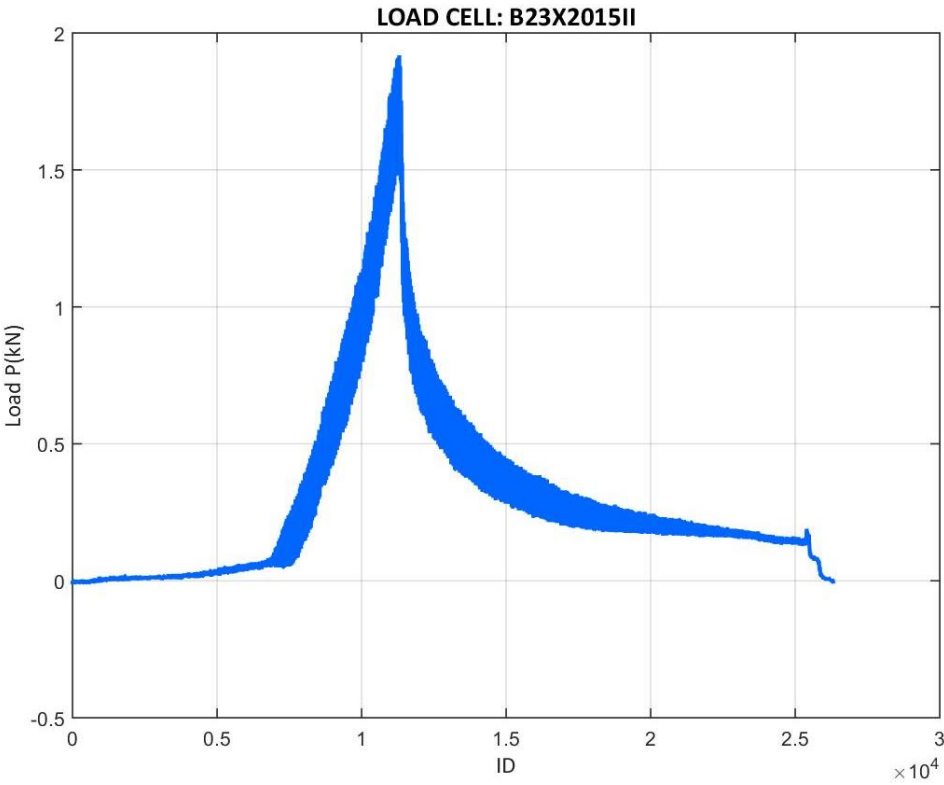


Figure 195: Load values recorded at the B23X2015II test

- B23X2015III

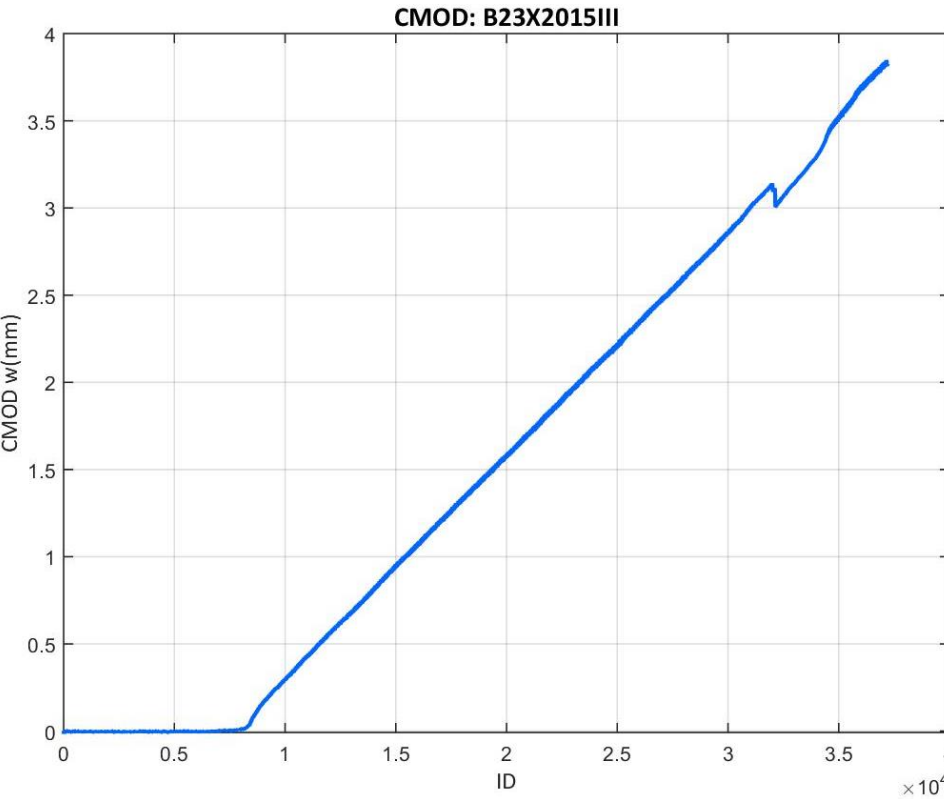


Figure 196: CMOD values recorded at the B23X2015III test

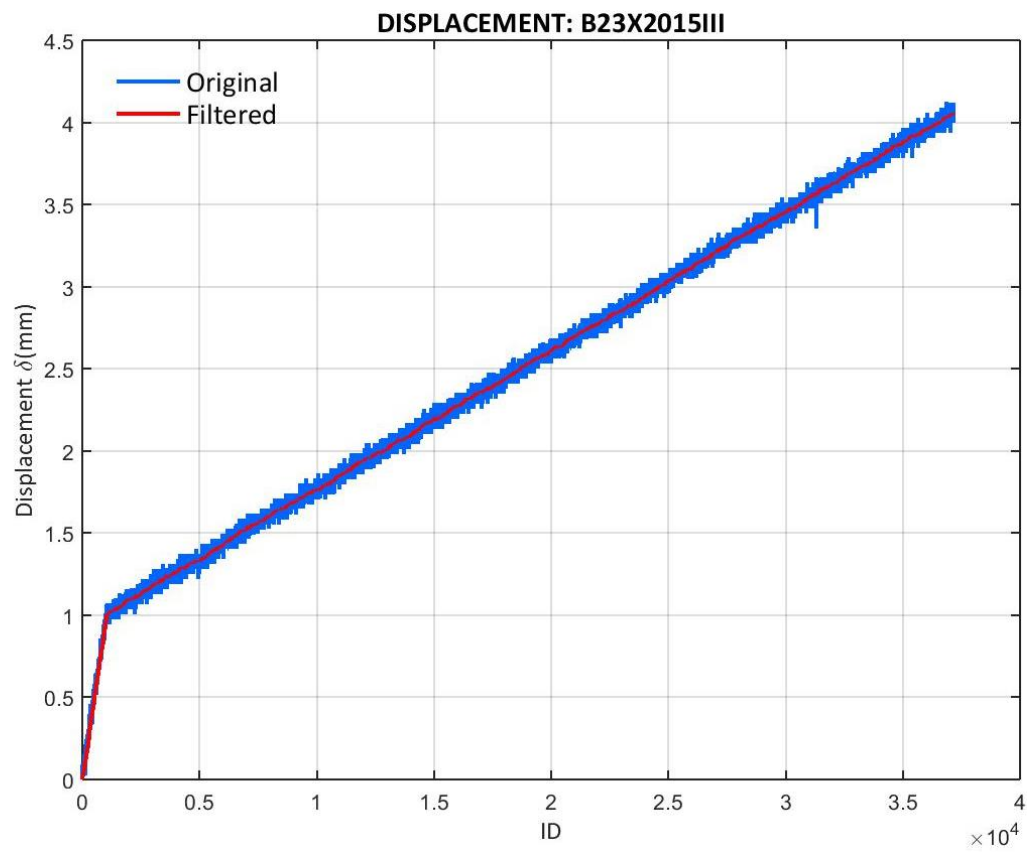


Figure 197: Displacement values recorded at the B23X2015III test

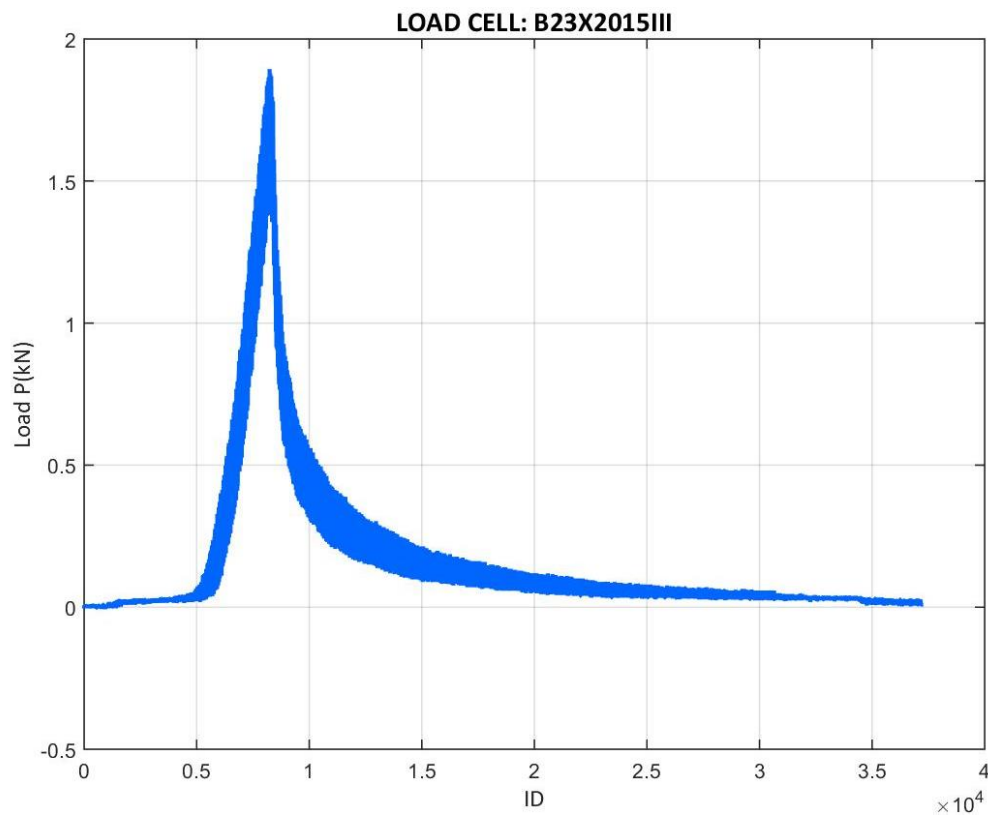


Figure 198: Load values recorded at the B23X2015III test

- B23X2015IV

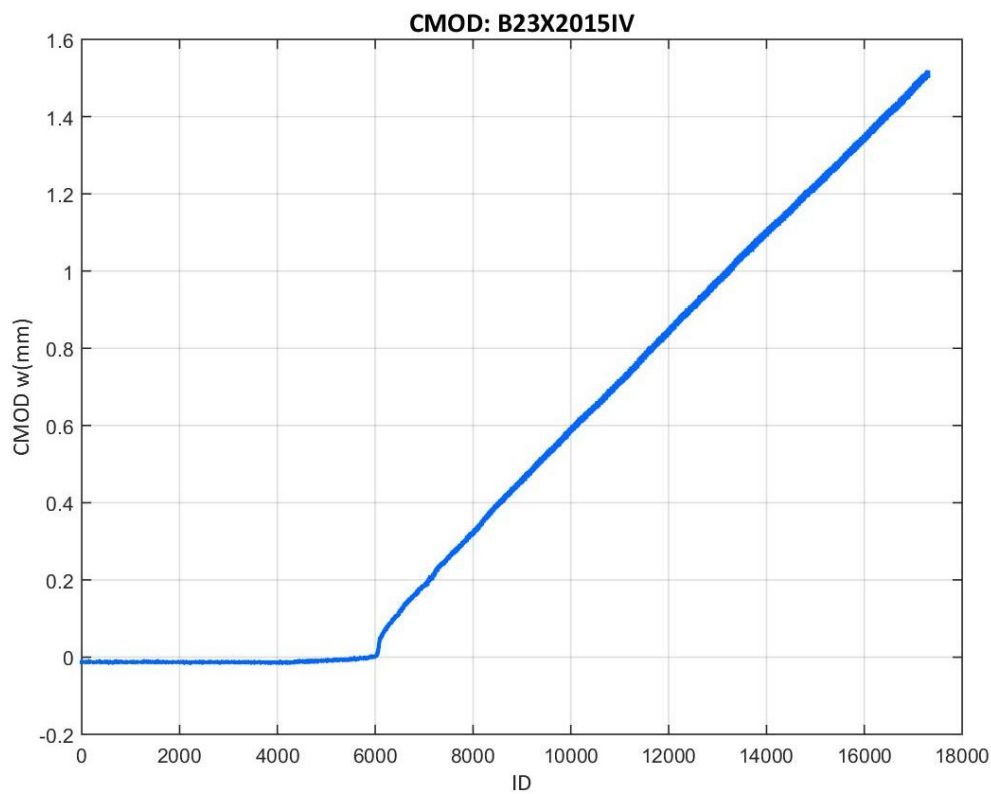


Figure 199: CMOD values recorded at the B23X2015IV test

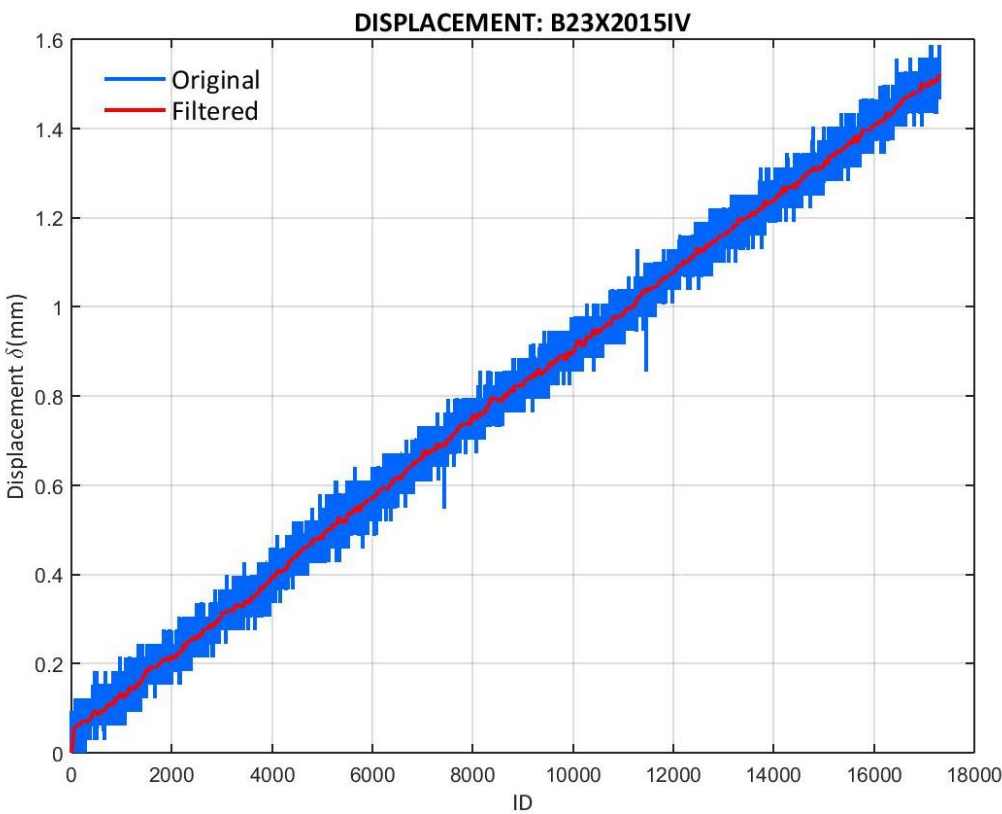


Figure 200: Displacement values recorded at the B23X2015IV test

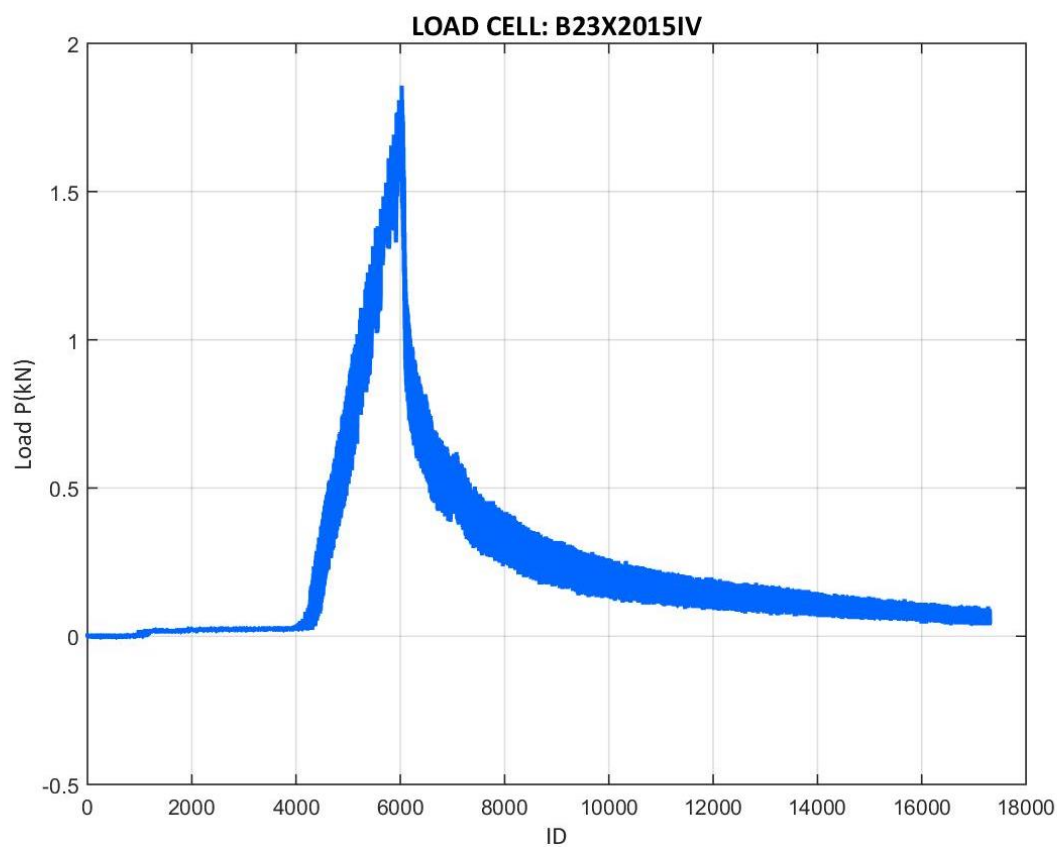


Figure 201: Load values recorded at the B23X2015IV test

E.3.2 23X2015 CORRECTED LOAD VS. CMOD

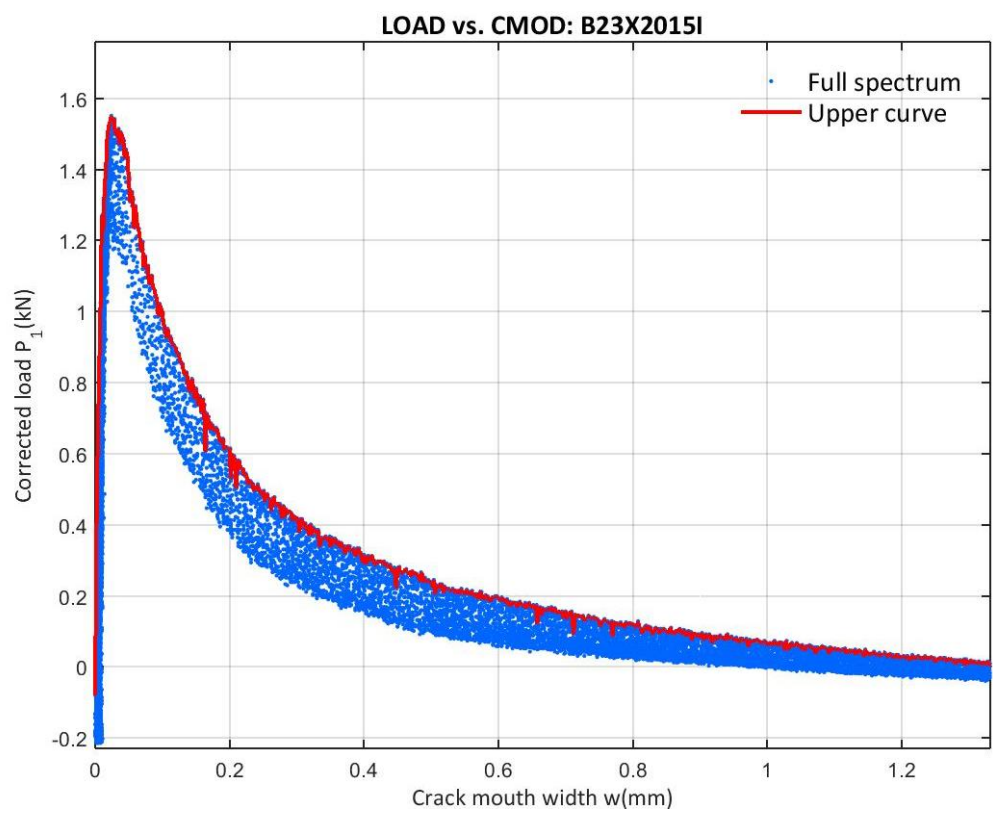


Figure 202: Corrected load vs. CMOD at the B23X2015I test

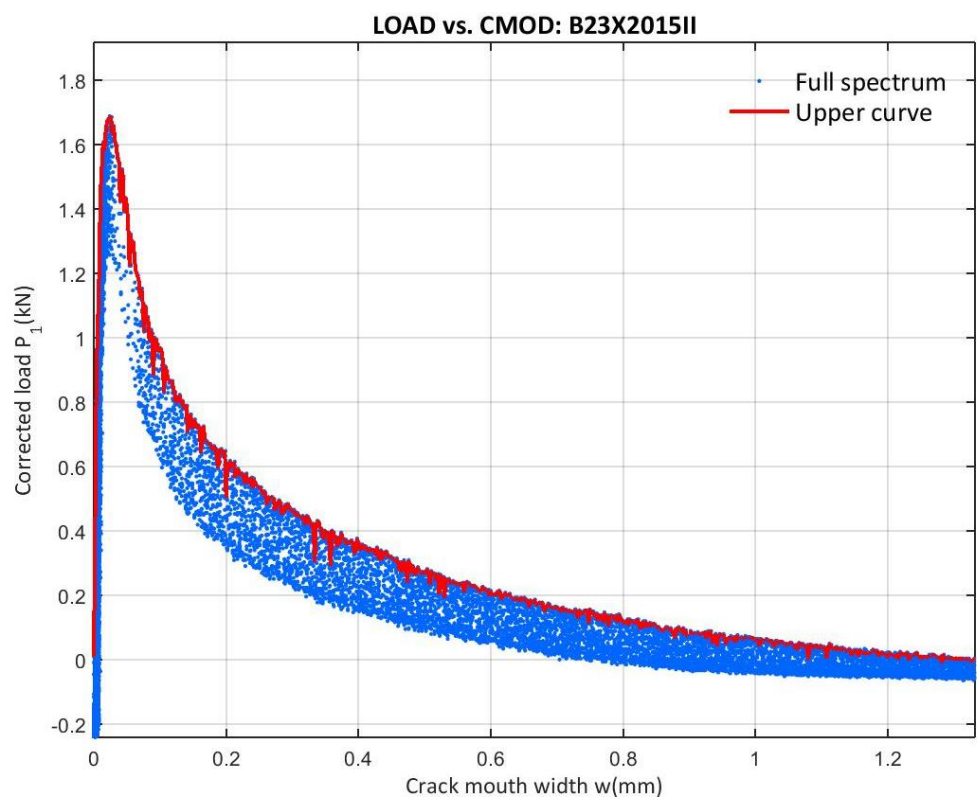


Figure 203: Corrected load vs. CMOD at the B23X2015II test

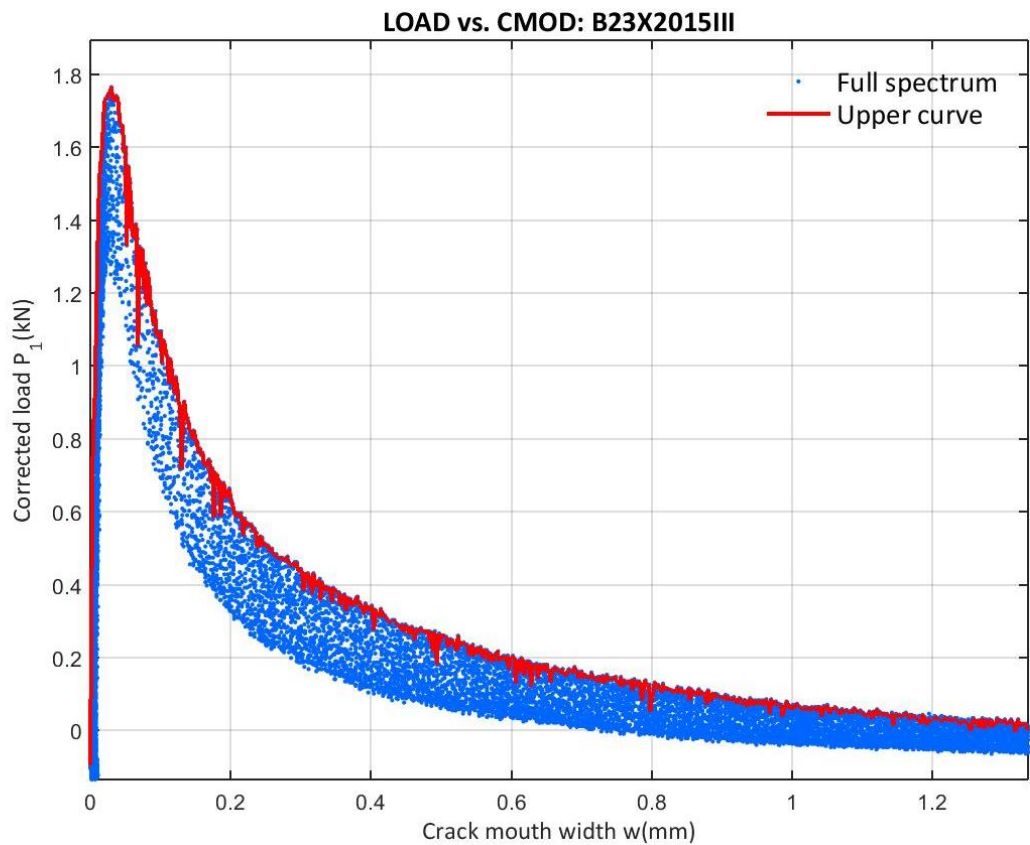


Figure 204: Corrected load vs. CMOD at the B23X2015III test

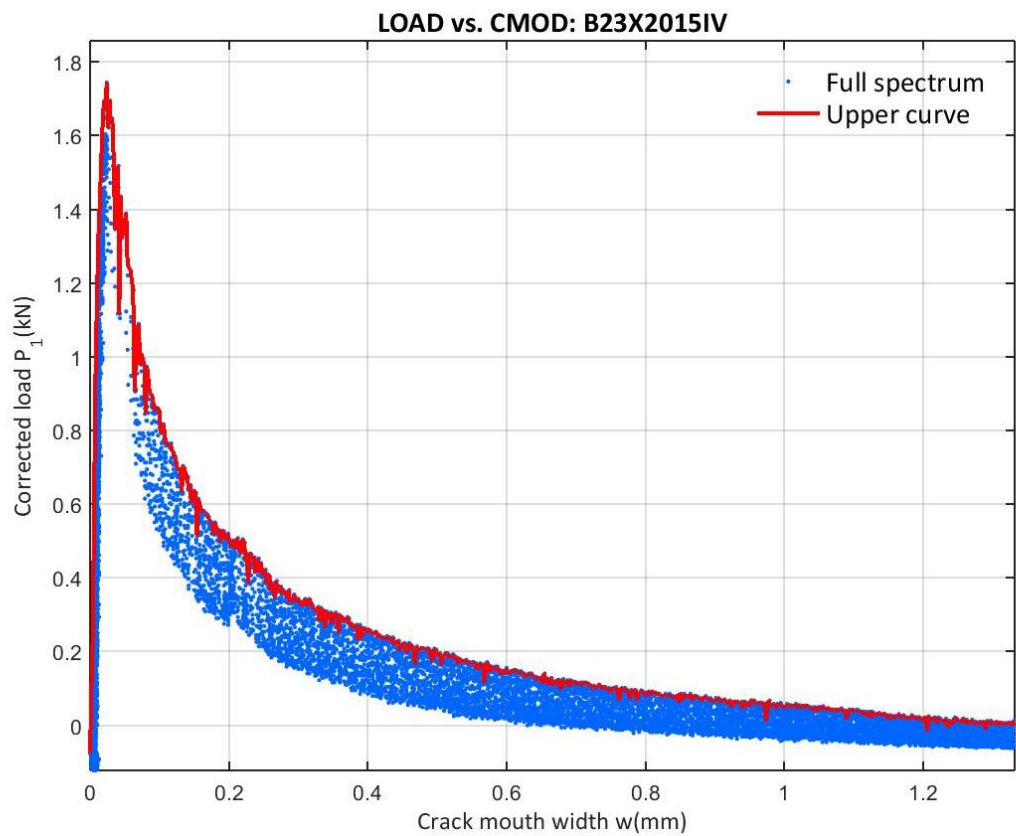


Figure 205: Corrected load vs. CMOD at the B23X2015IV test

E.3.3 23X2015 CORRECTED LOAD VS. VERTICAL DISPLACEMENT

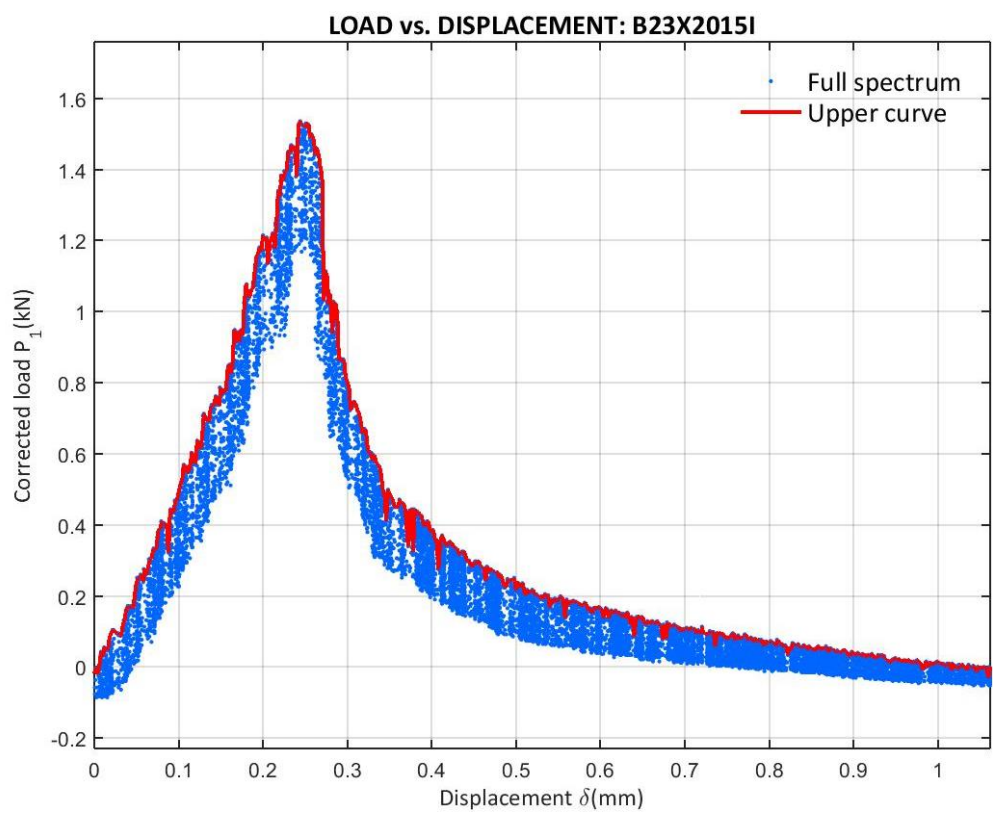


Figure 206: Corrected load vs. Displacement at the B23X2015I test

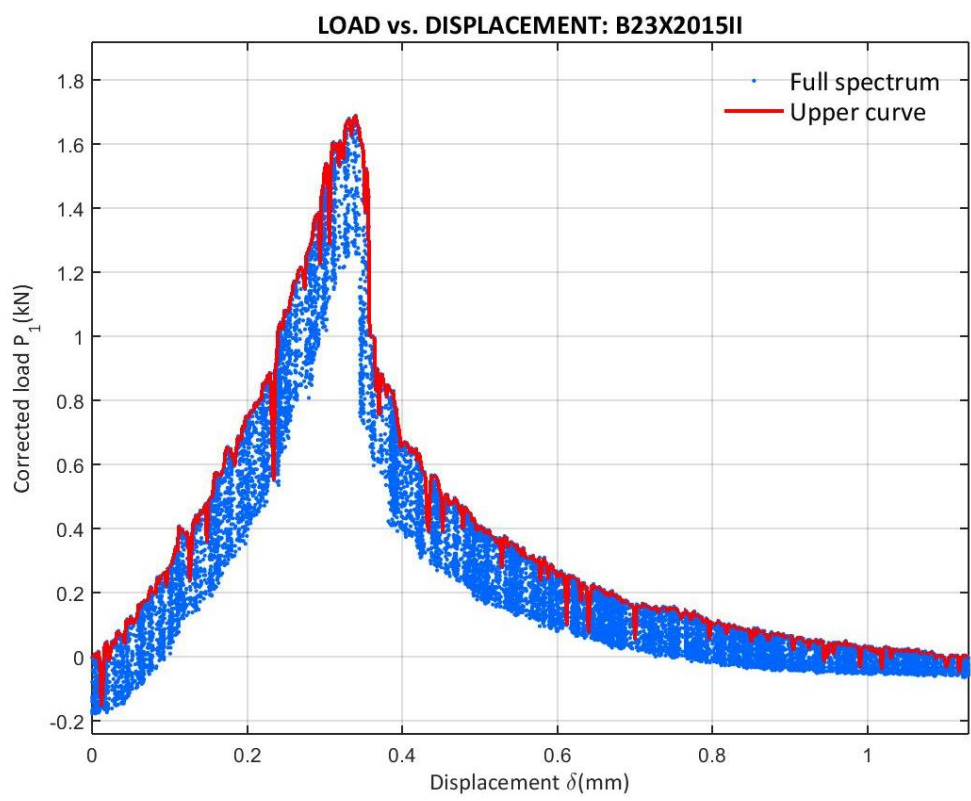


Figure 207: Corrected load vs. Displacement at the B23X2015II test

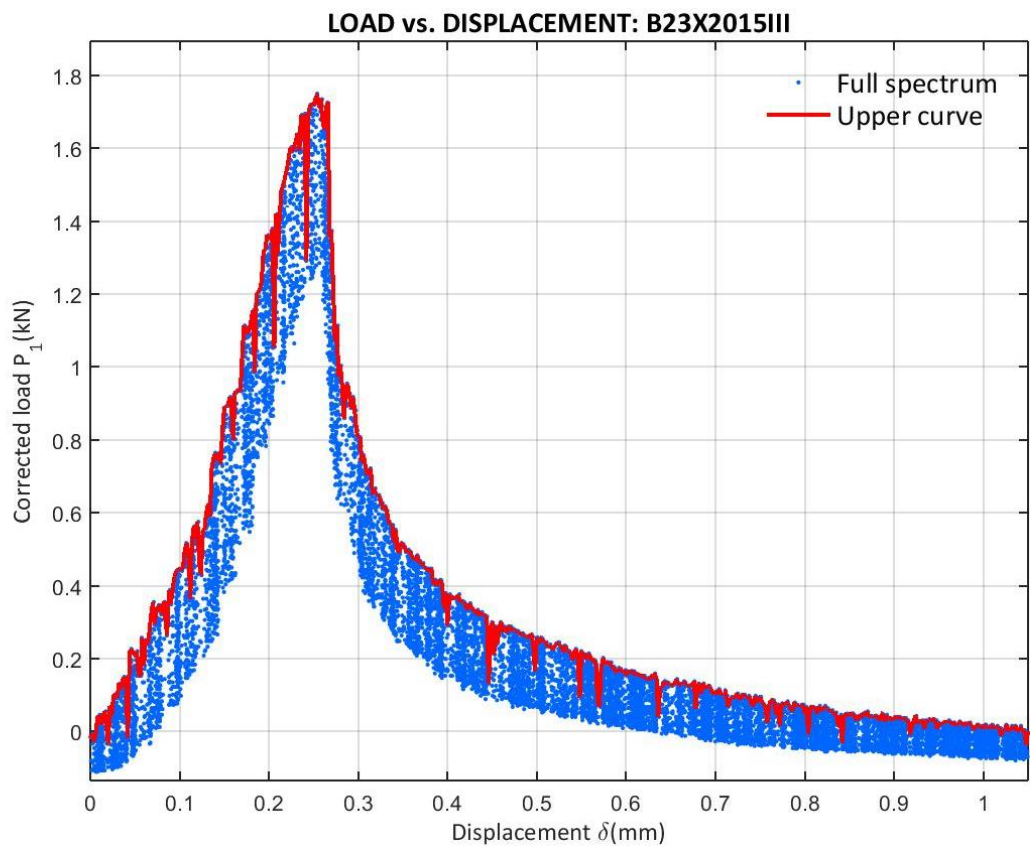


Figure 208: Corrected load vs. Displacement at the B23X2015III test

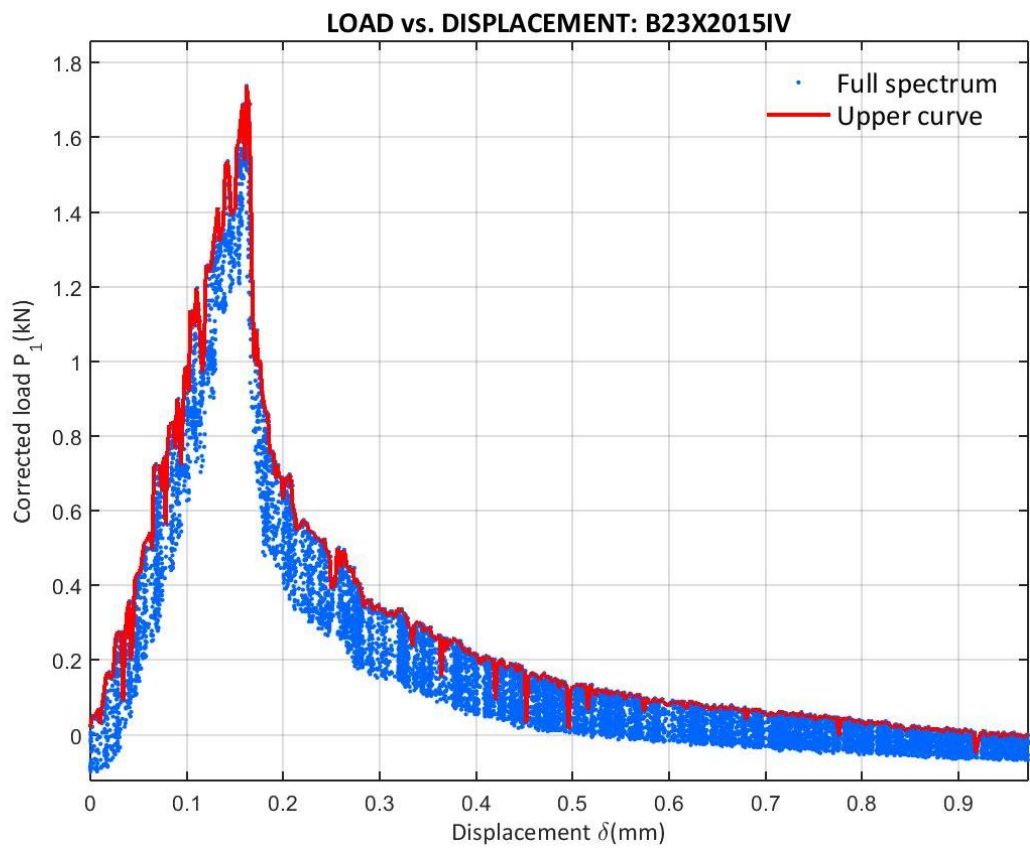


Figure 209: Corrected load vs. Displacement at the B23X2015IV test

E.3.4 23X2015 CORRECTED LOAD VS. X

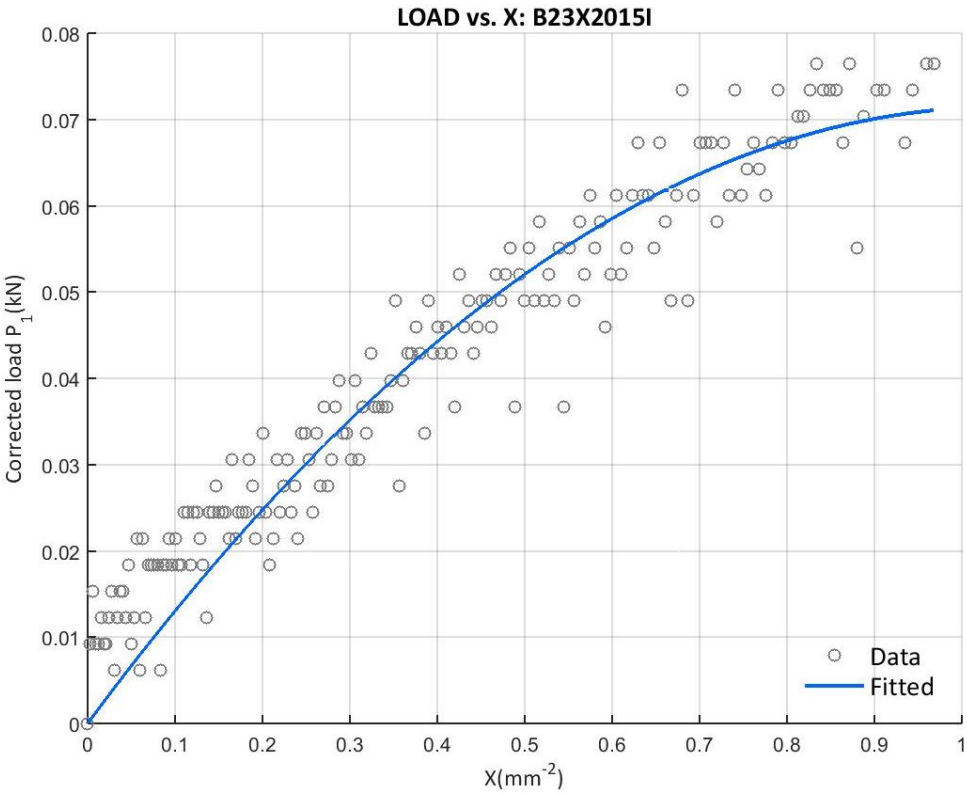


Figure 210: Corrected load vs. X at the B23X2015I test with the final upper curve data

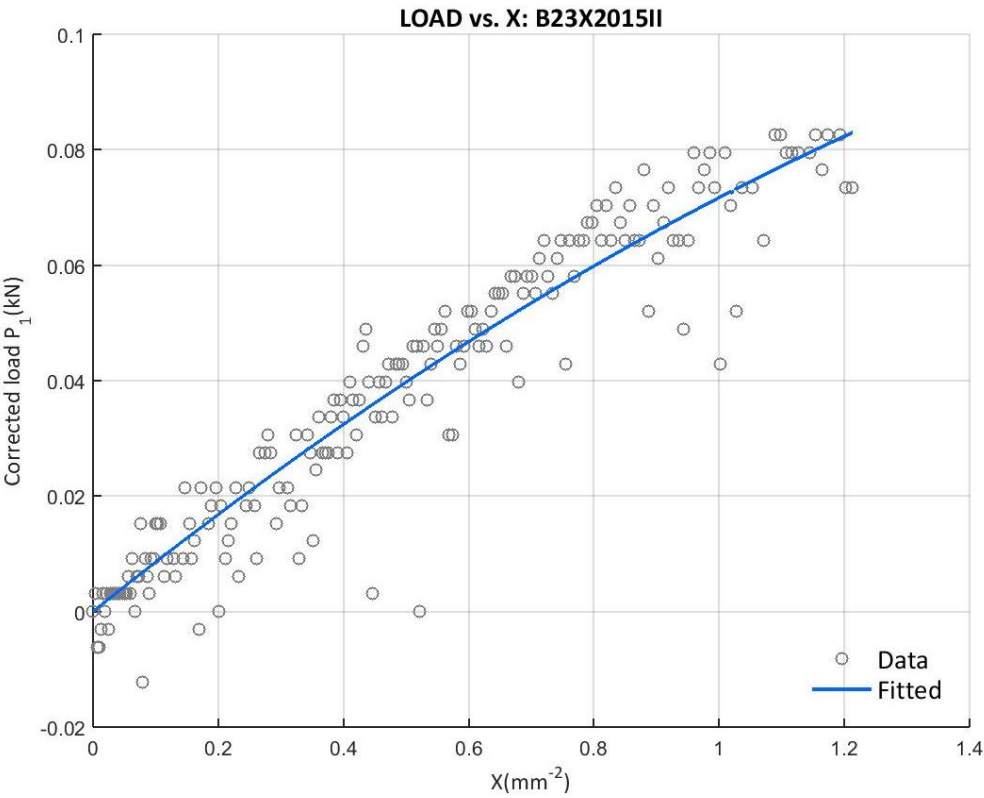


Figure 211: Corrected load vs. X at the B23X2015II test with the final upper curve data

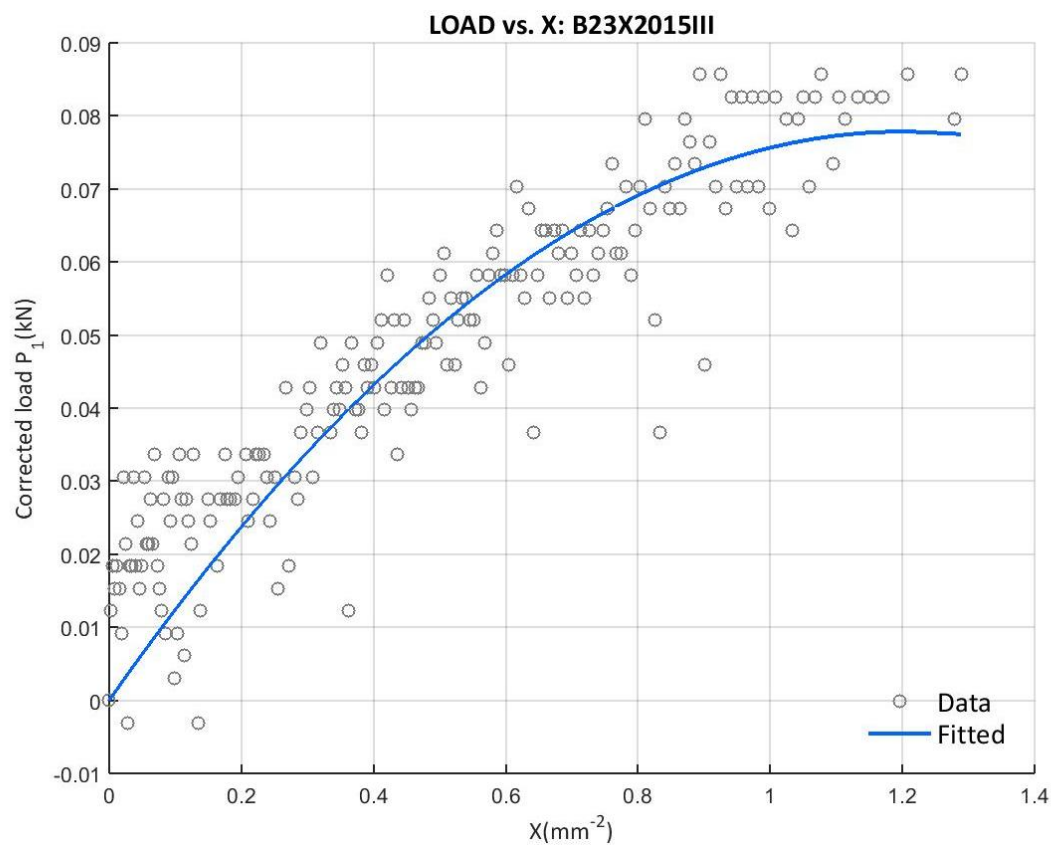


Figure 212: Corrected load vs. X at the B23X2015III test with the final upper curve data

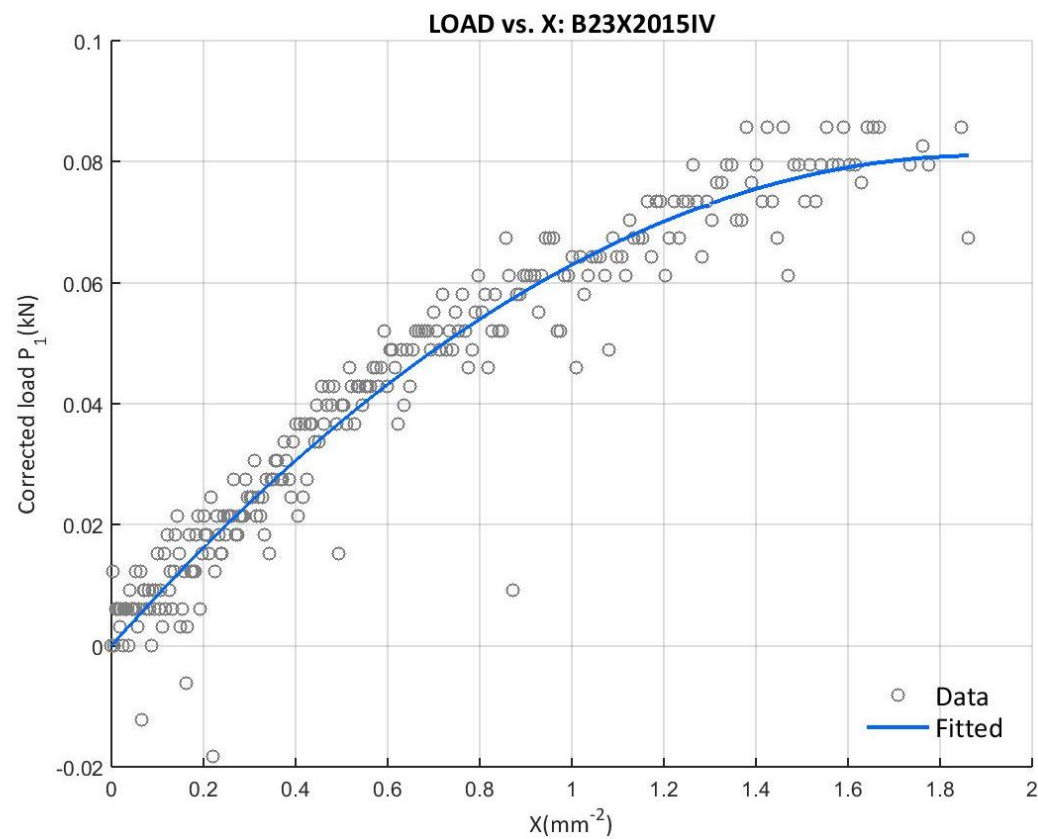


Figure 213: Corrected load vs. X at the B23X2015IV test with the final upper curve data

E.3.5 23X2015 SOFTENING CURVE BILINEAR APPROXIMATION

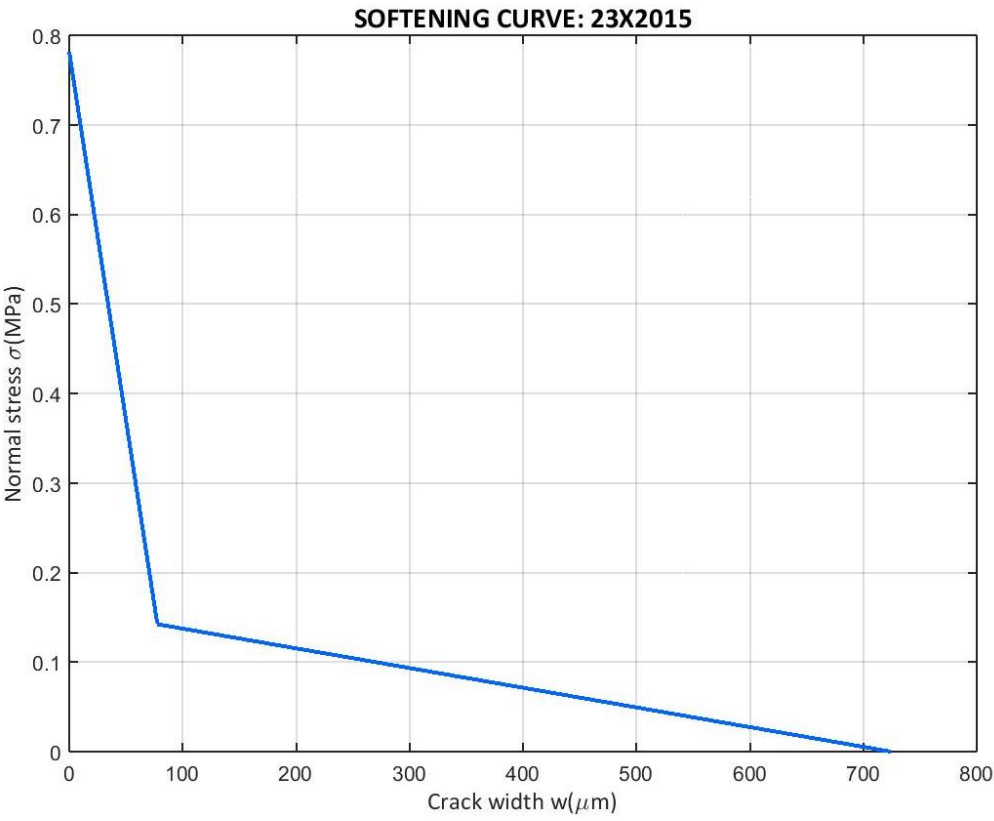


Figure 214: Softening curve bilinear approximation of the 23X2015 campaign

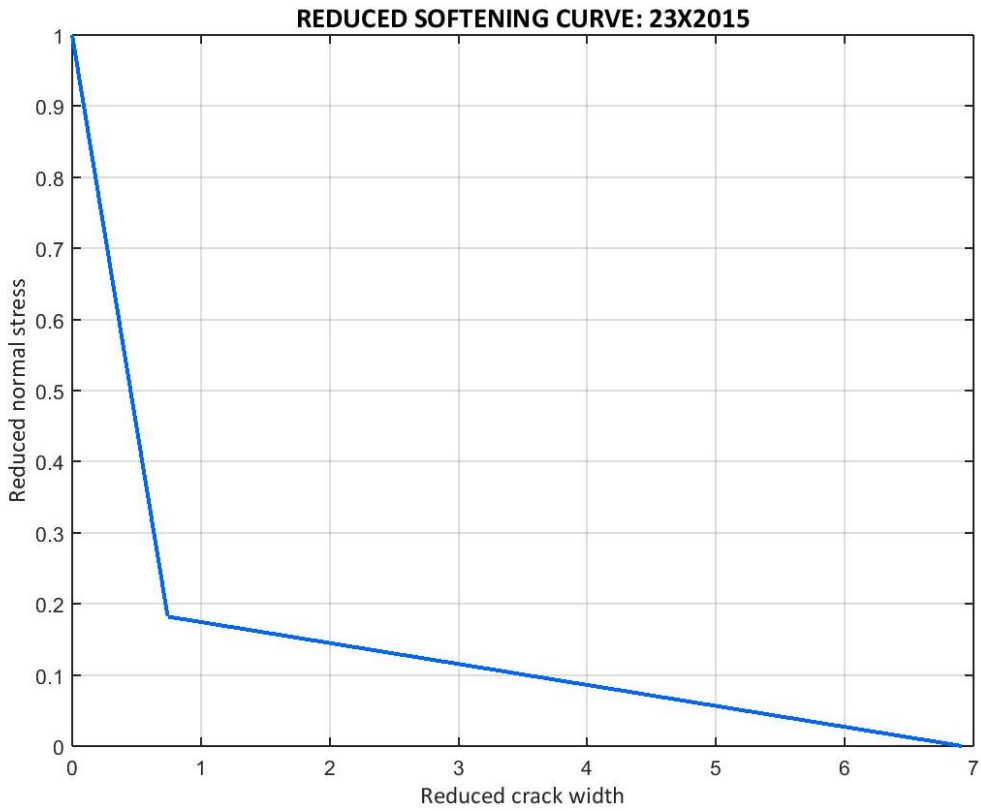


Figure 215: Softening curve bilinear approximation of the 23X2015 campaign in the reduced form

E.3.6 23X2015 SPECIMENS' COMPARISON

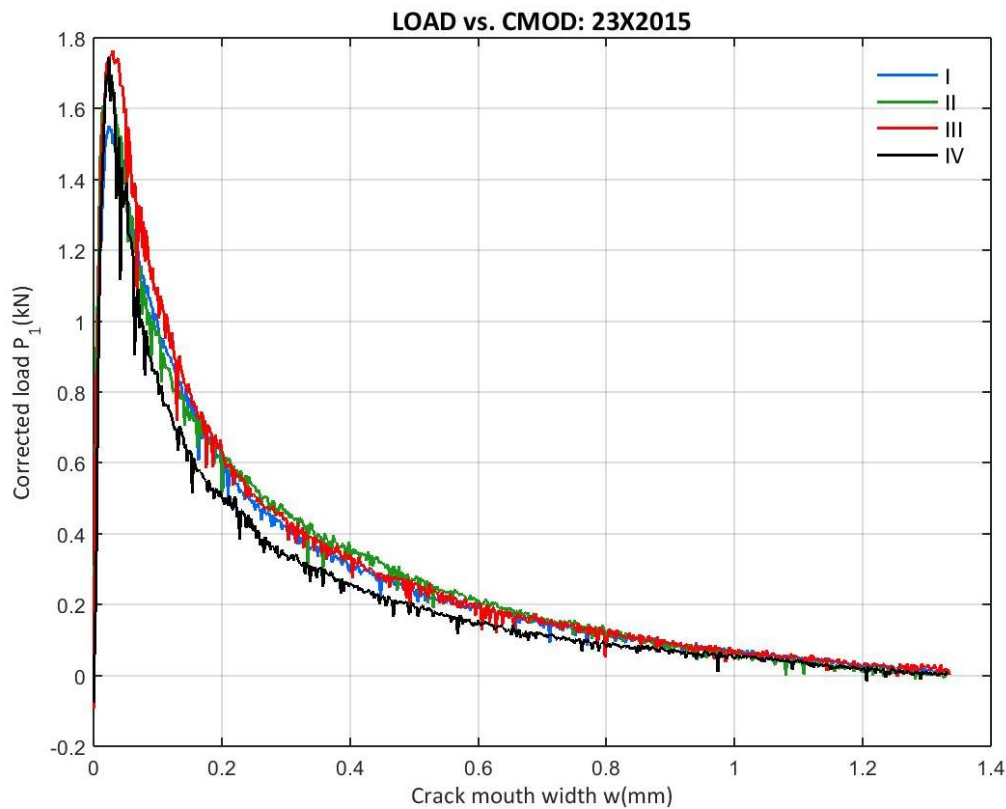


Figure 216: 23X2015 Corrected load vs. CMOD from the entire campaign

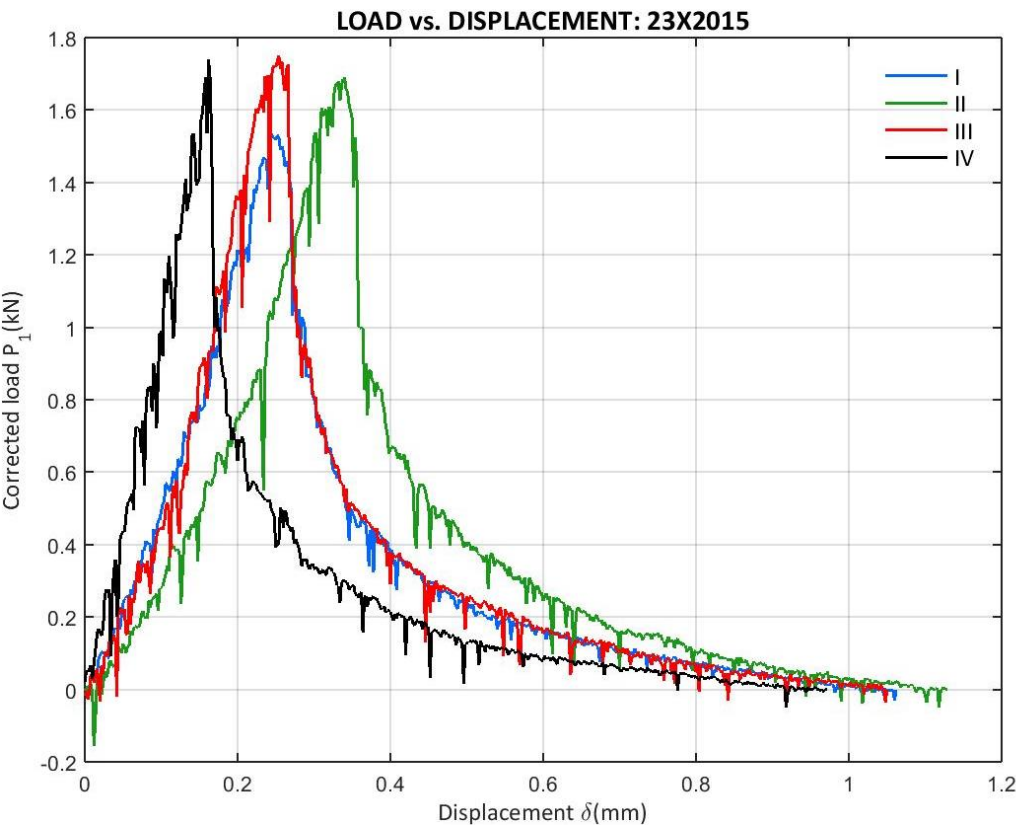


Figure 217: 23X2015 Corrected load vs. Displacement from the entire campaign

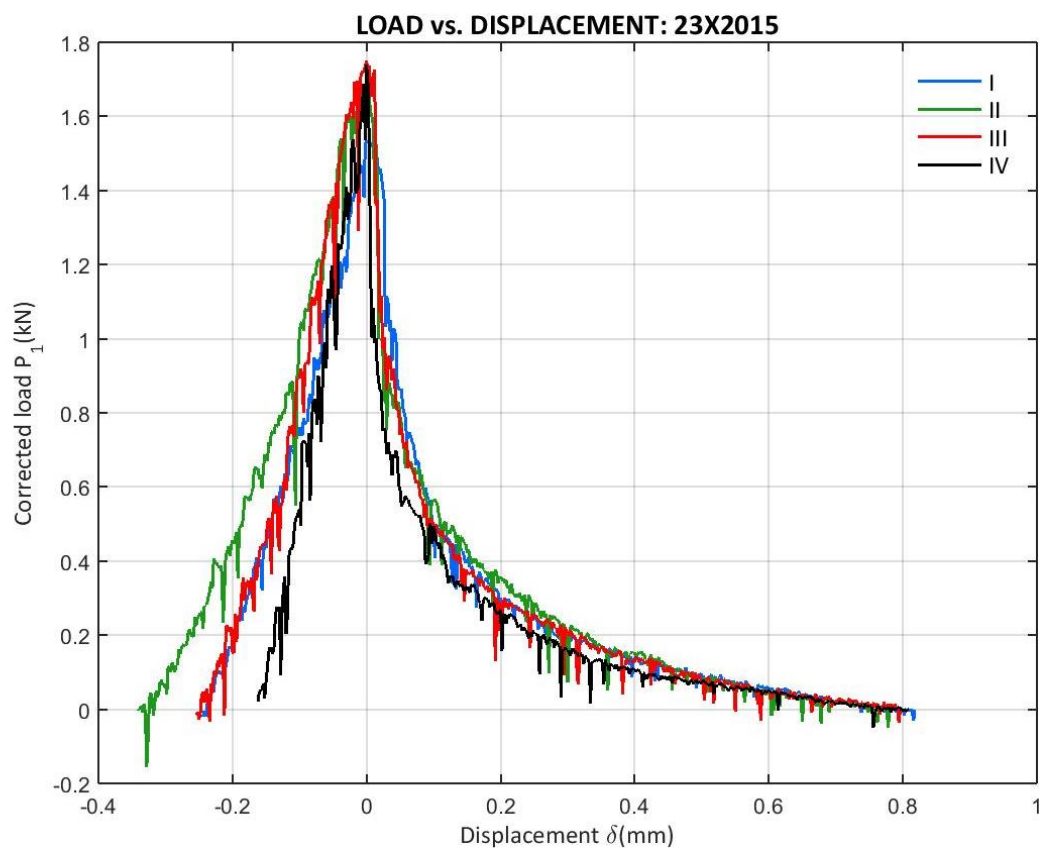


Figure 218: 23X2015 Corrected load vs. Displacement from the entire campaign (peak displacement zero)

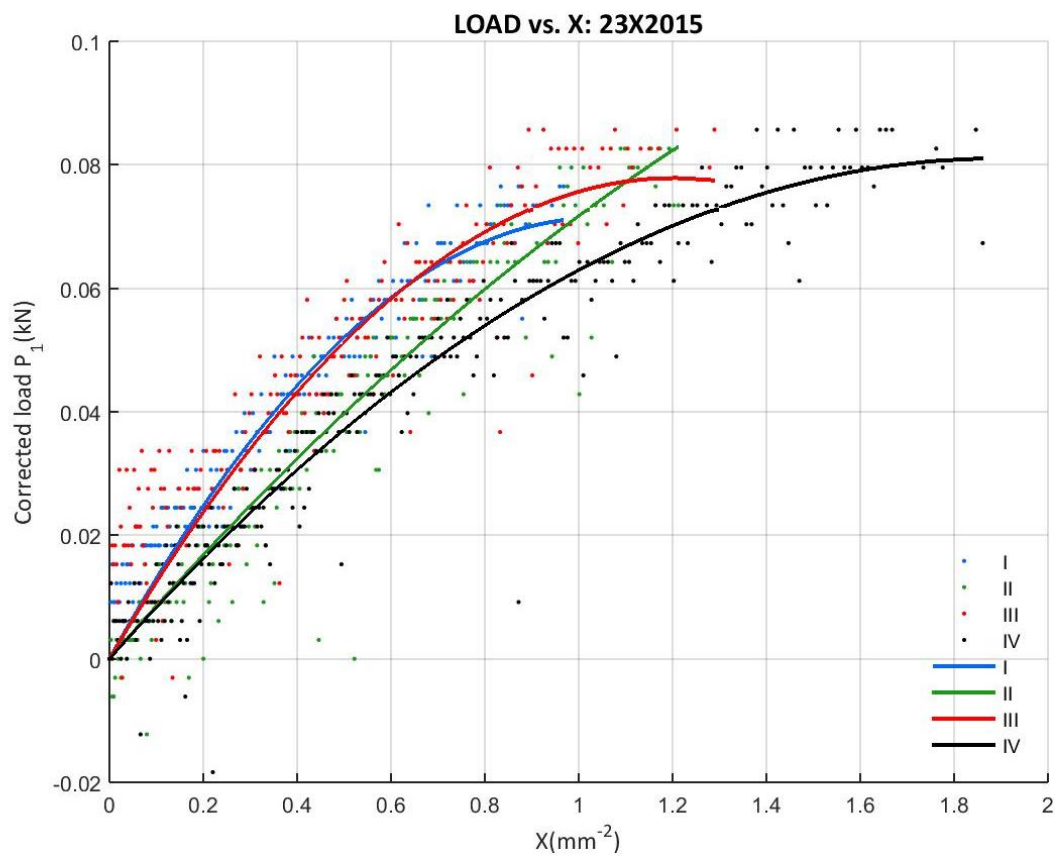


Figure 219: 23X2015 Corrected load vs. X from the entire campaign

E.4 14XII2015 CAMPAIGN

E.4.1 14XII2015 DATA

- B14XII2015I

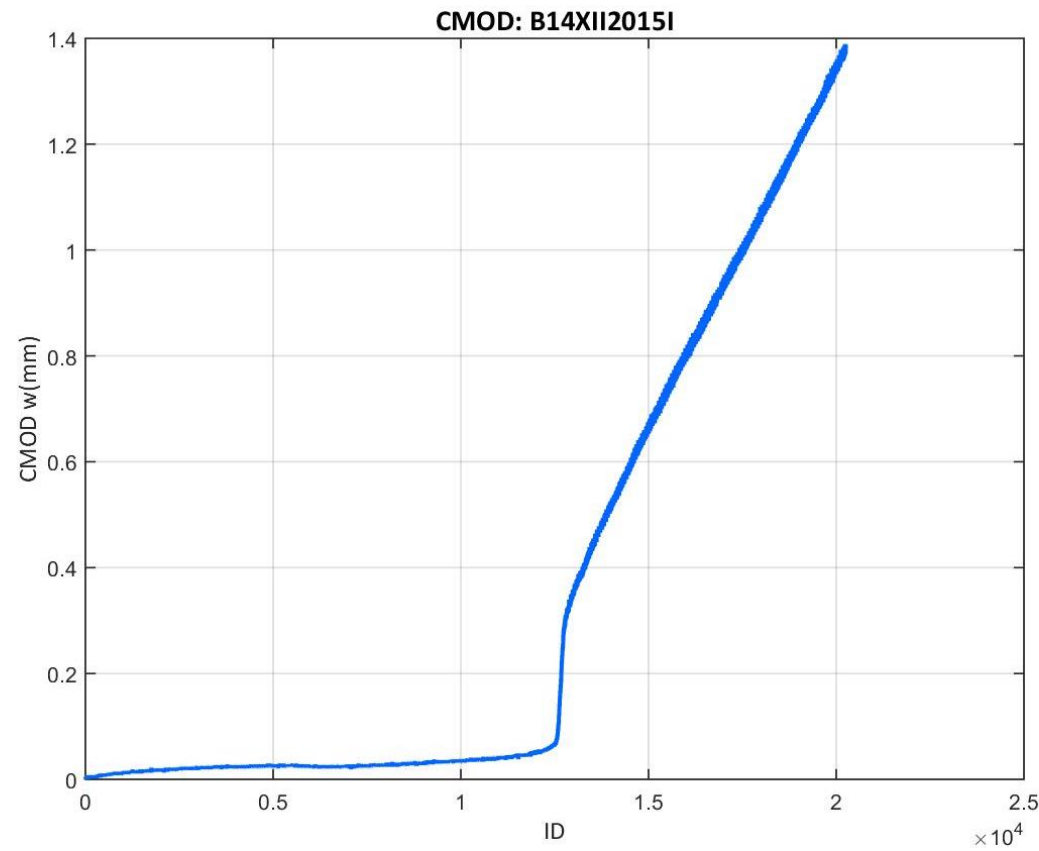


Figure 220: CMOD values recorded at the B14XII2015I test

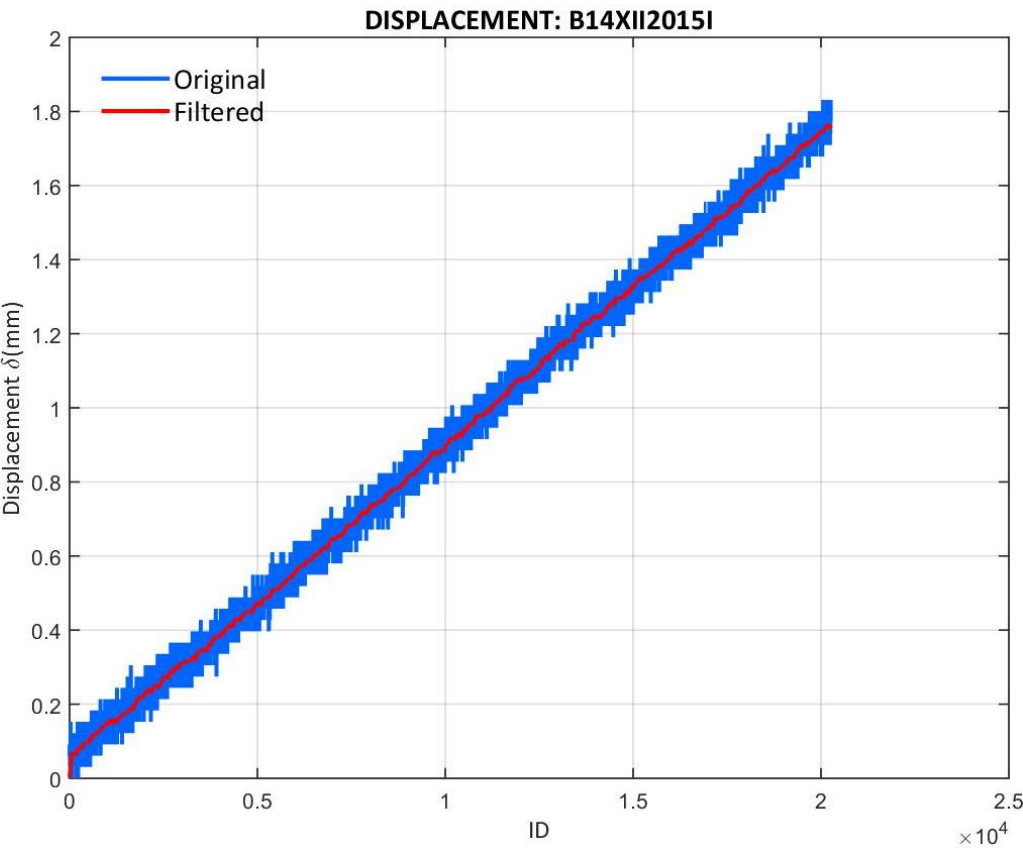


Figure 221: Displacement values recorded at the B14XII2015I test

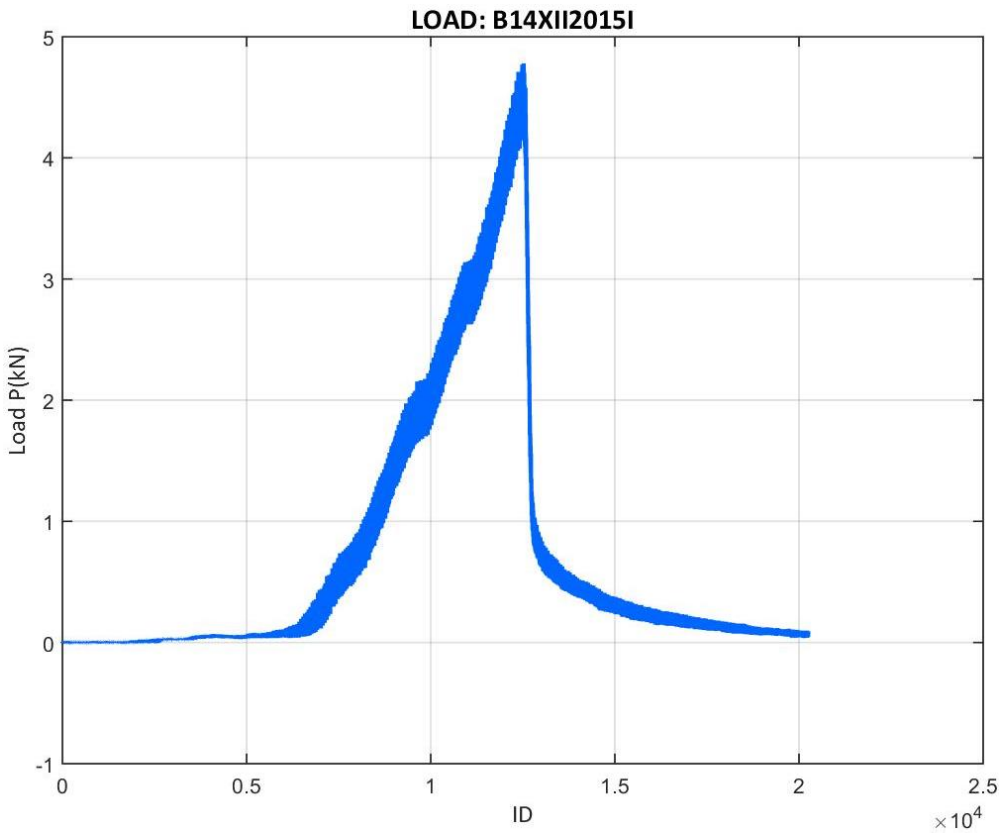


Figure 222: Load values recorded at the B14XII2015I test

- B14XII2015II

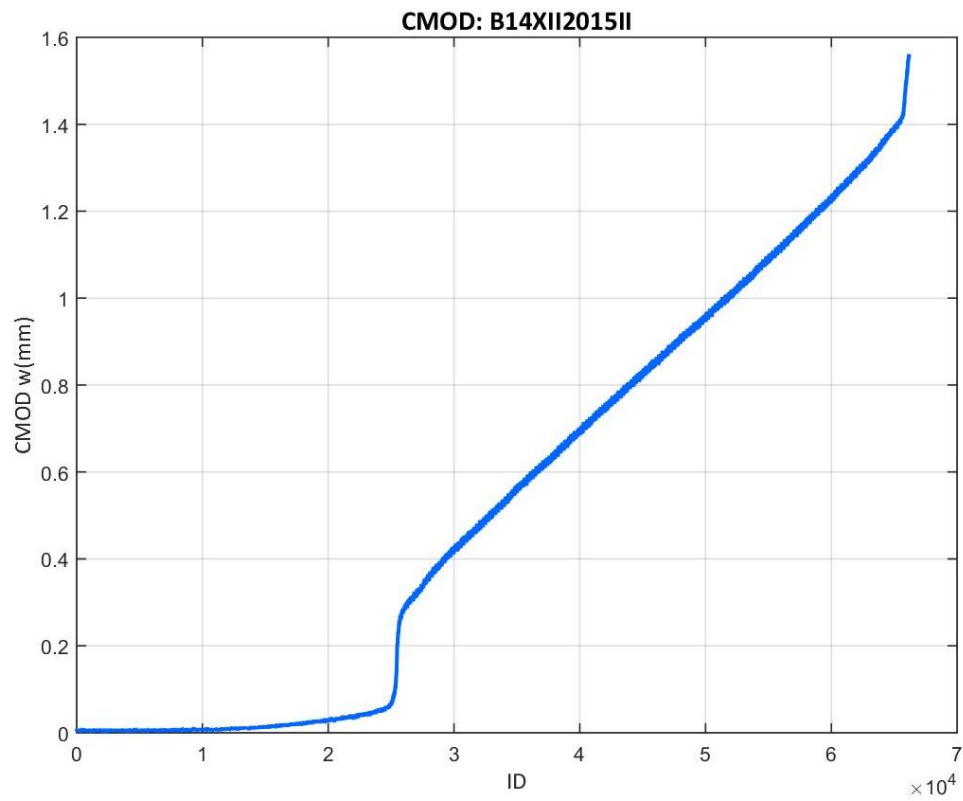


Figure 223: CMOD values recorded at the B14XII2015II test

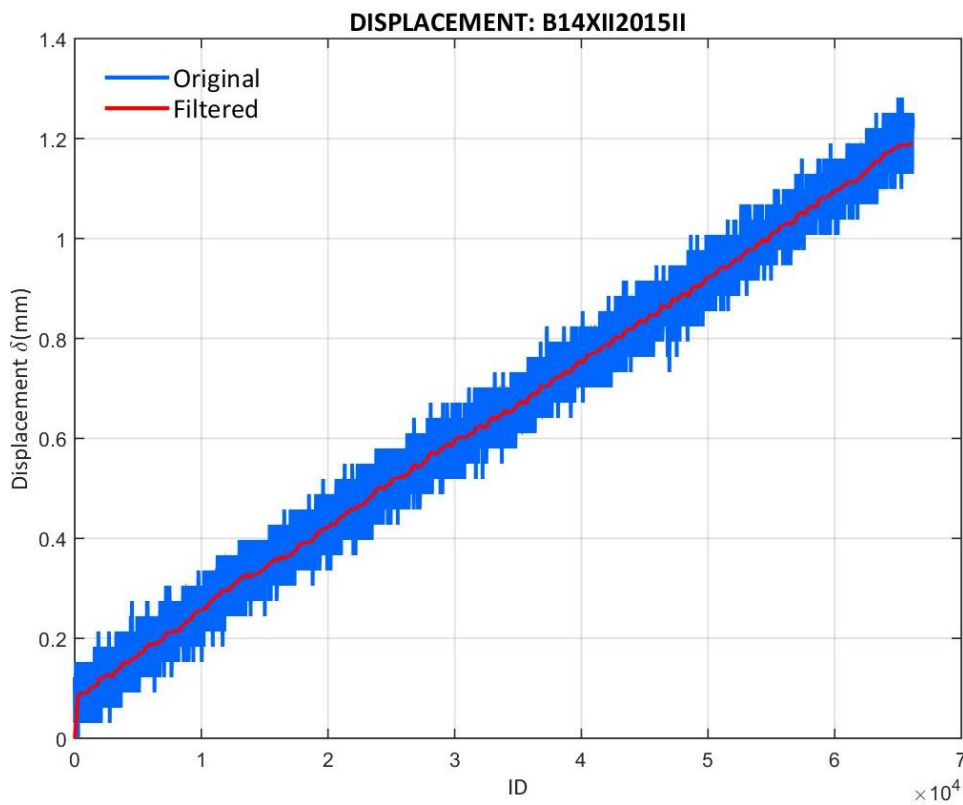


Figure 224: Displacement values recorded at the B14XII2015II test

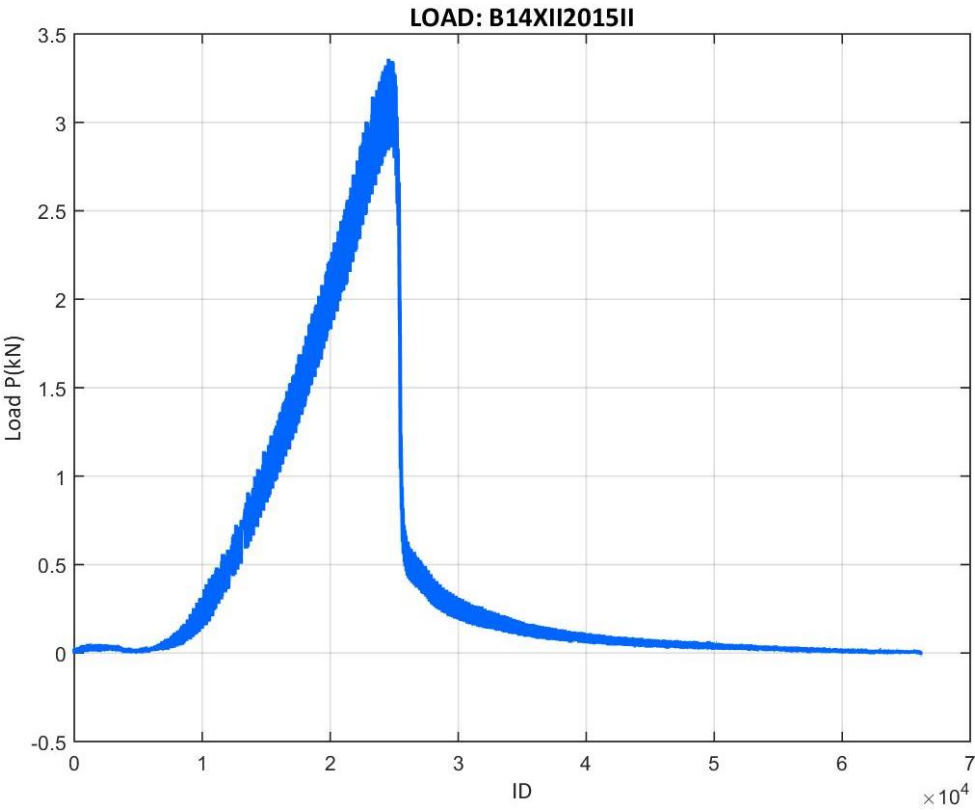


Figure 225: Load values recorded at the B14XII2015II test

- B14XII2015III

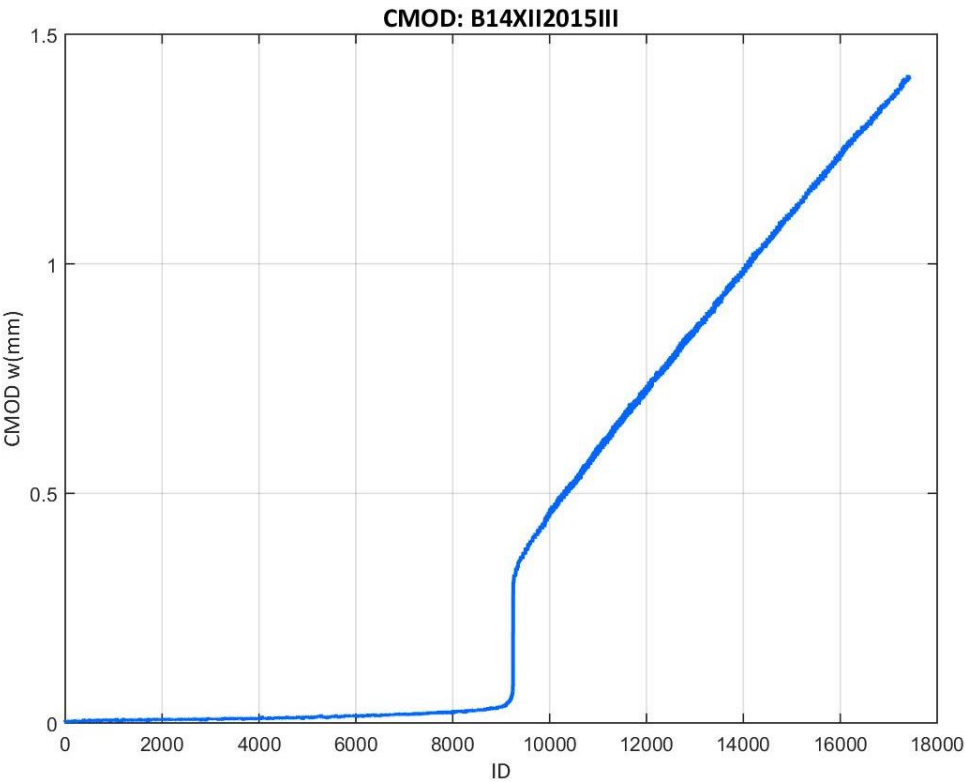


Figure 226: CMOD values recorded at the B14XII2015III test

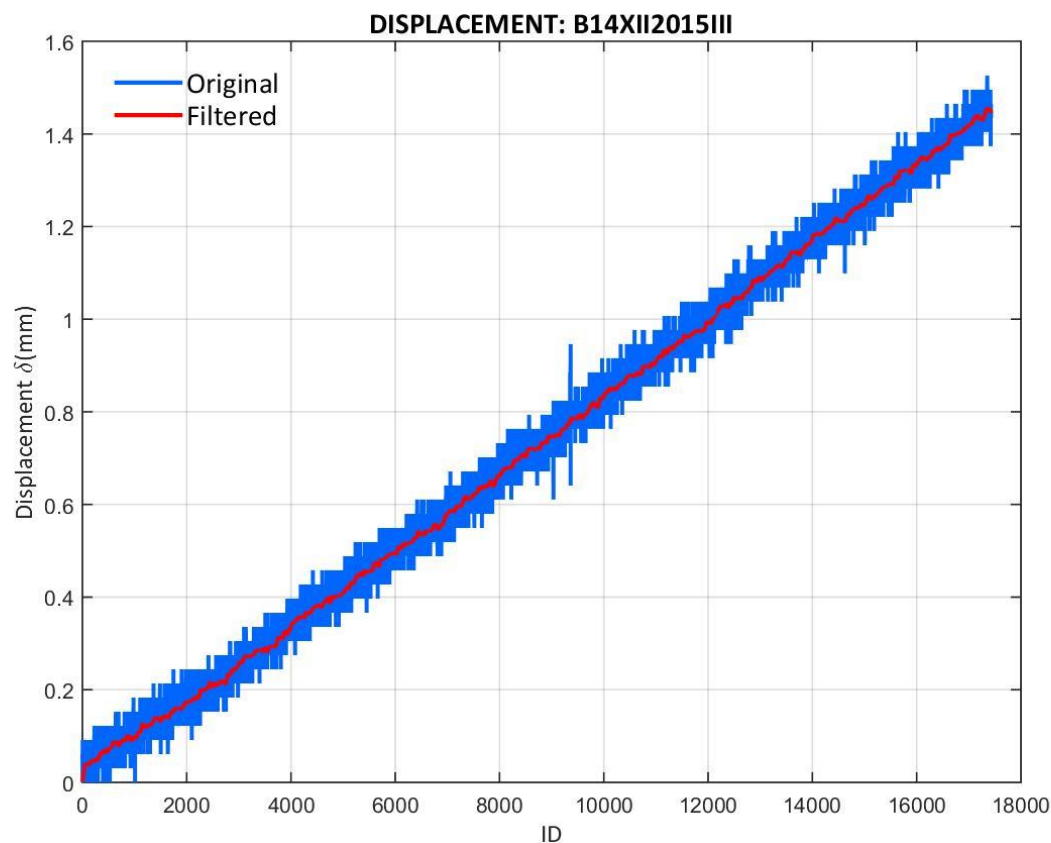


Figure 227: Displacement values recorded at the B14XII2015III test

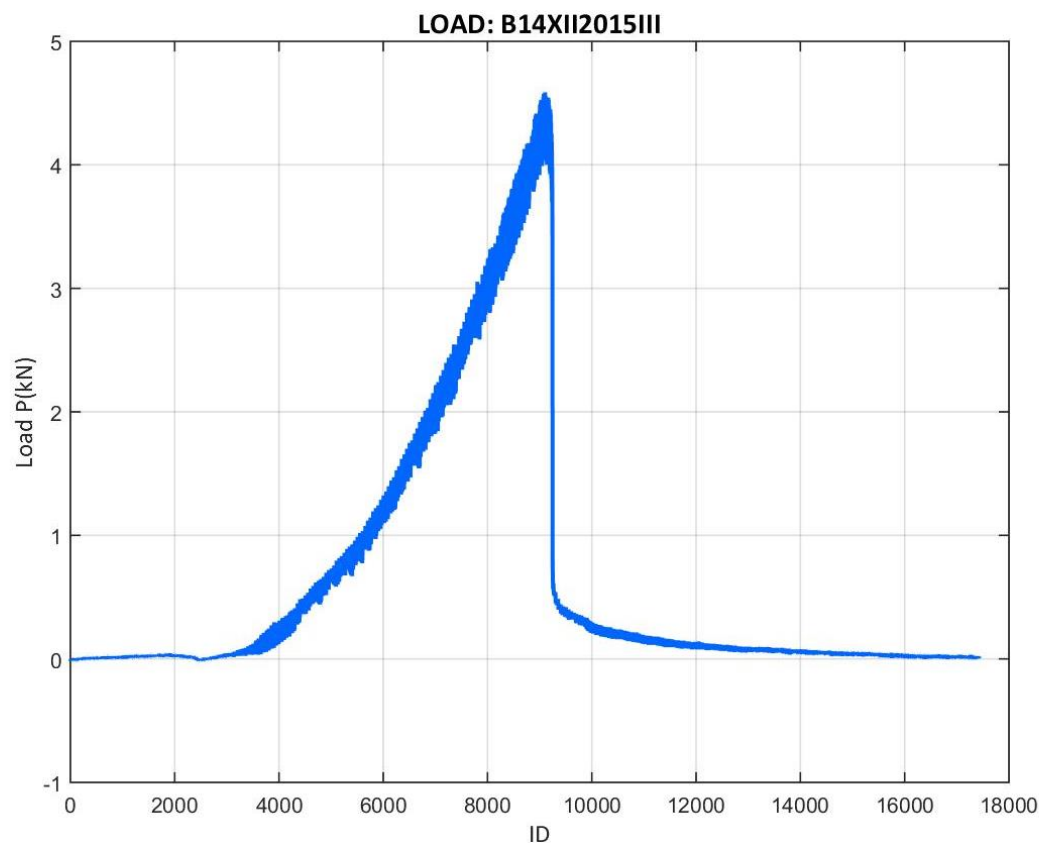


Figure 228: Load values recorded at the B14XII2015III test

- B14XII2015IV

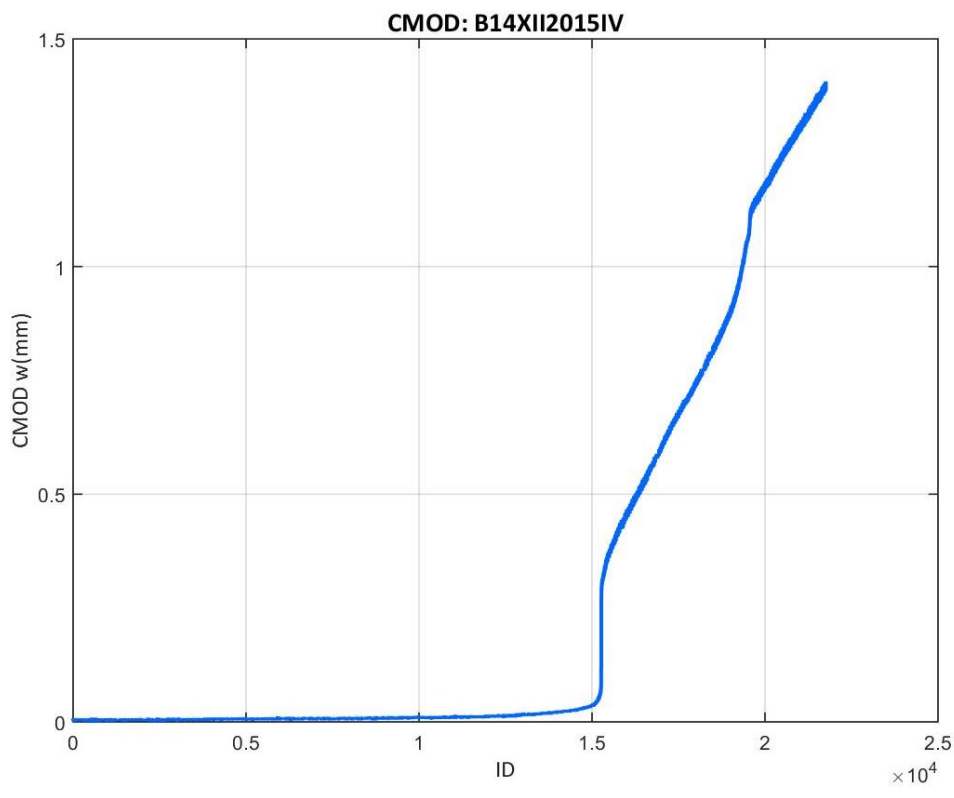


Figure 229: CMOD values recorded at the B14XII2015IV test

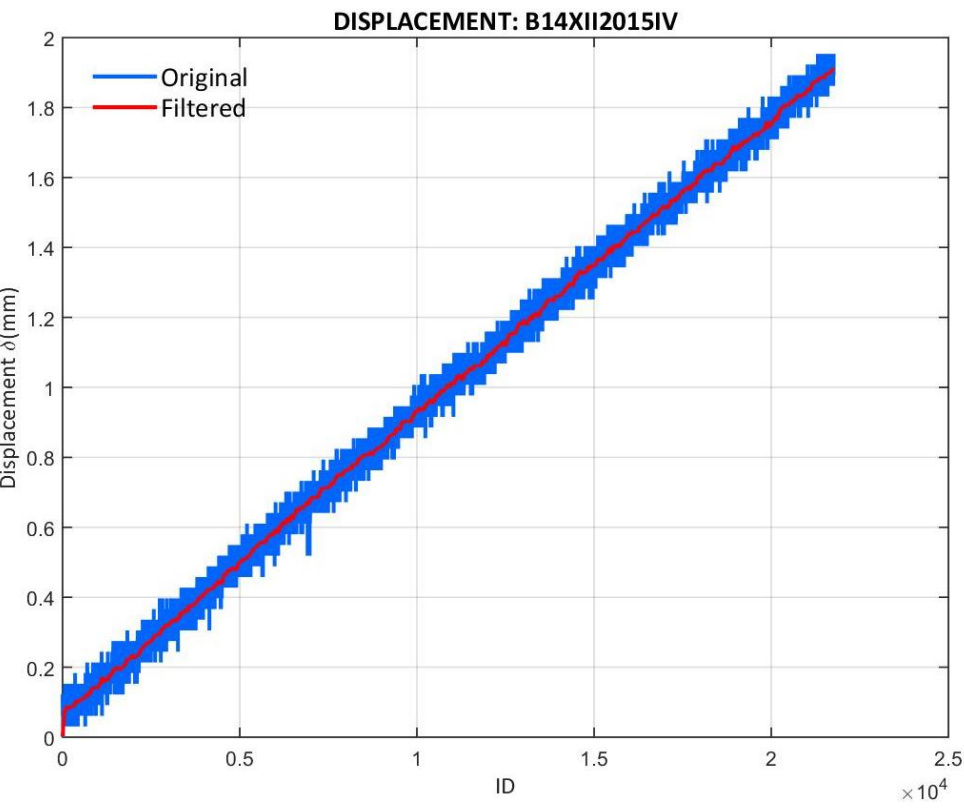


Figure 230: Displacement values recorded at the B14XII2015IV test

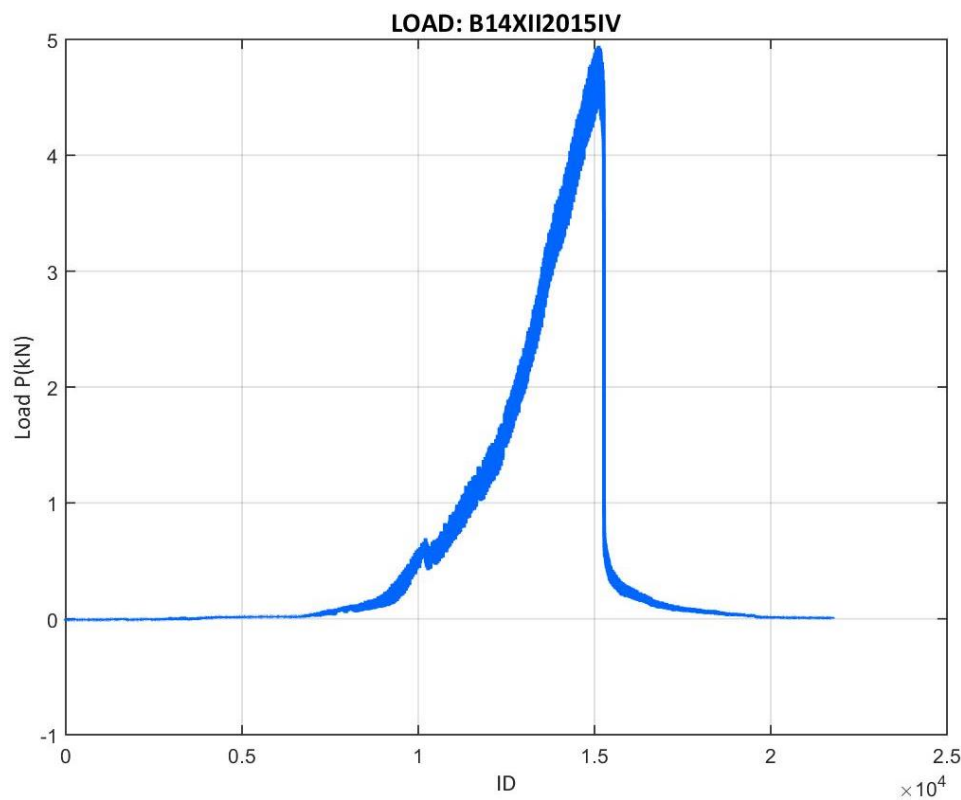


Figure 231: Load values recorded at the B14XII2015IV test

- B14XII2015V

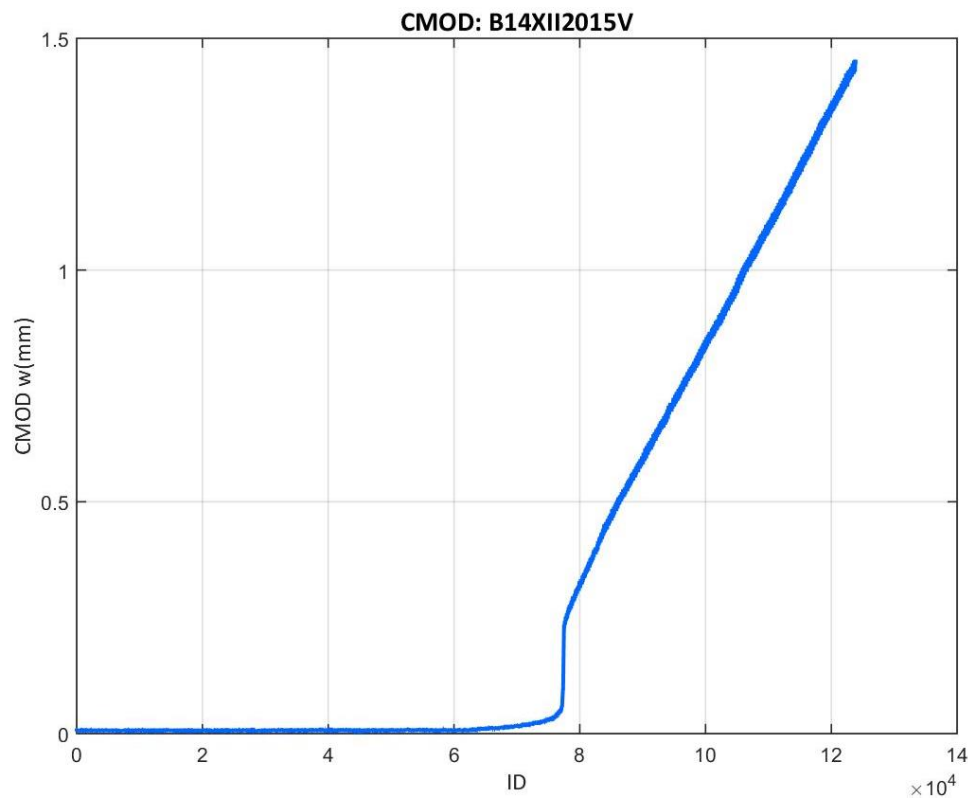


Figure 232: CMOD values recorded at the B14XII2015V test

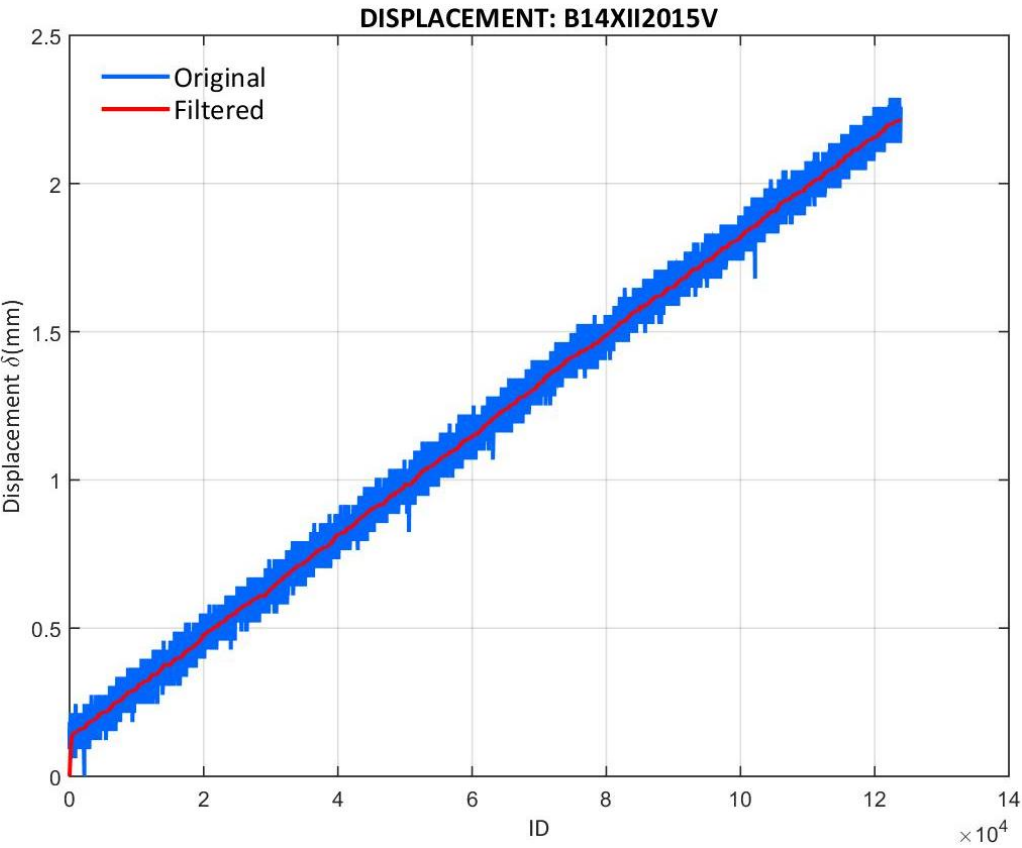


Figure 233: Displacement values recorded at the B14XII2015V test

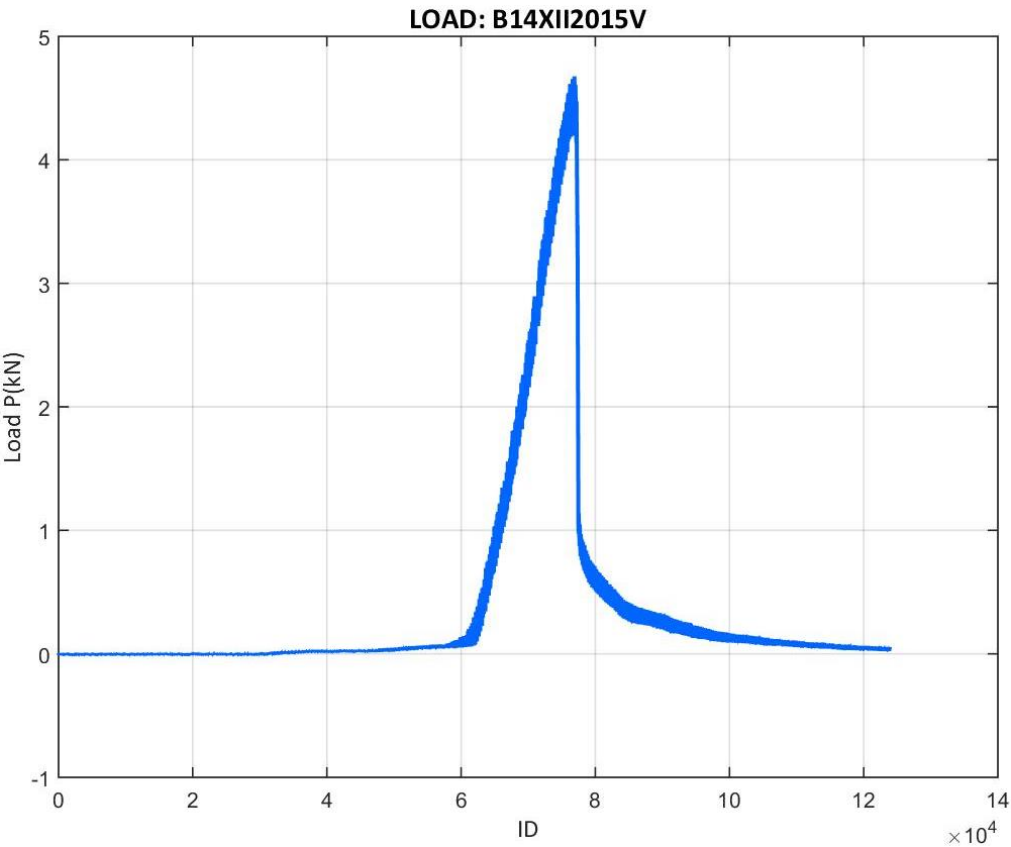


Figure 234: Load values recorded at the B14XII2015V test

- B14XII2015VI

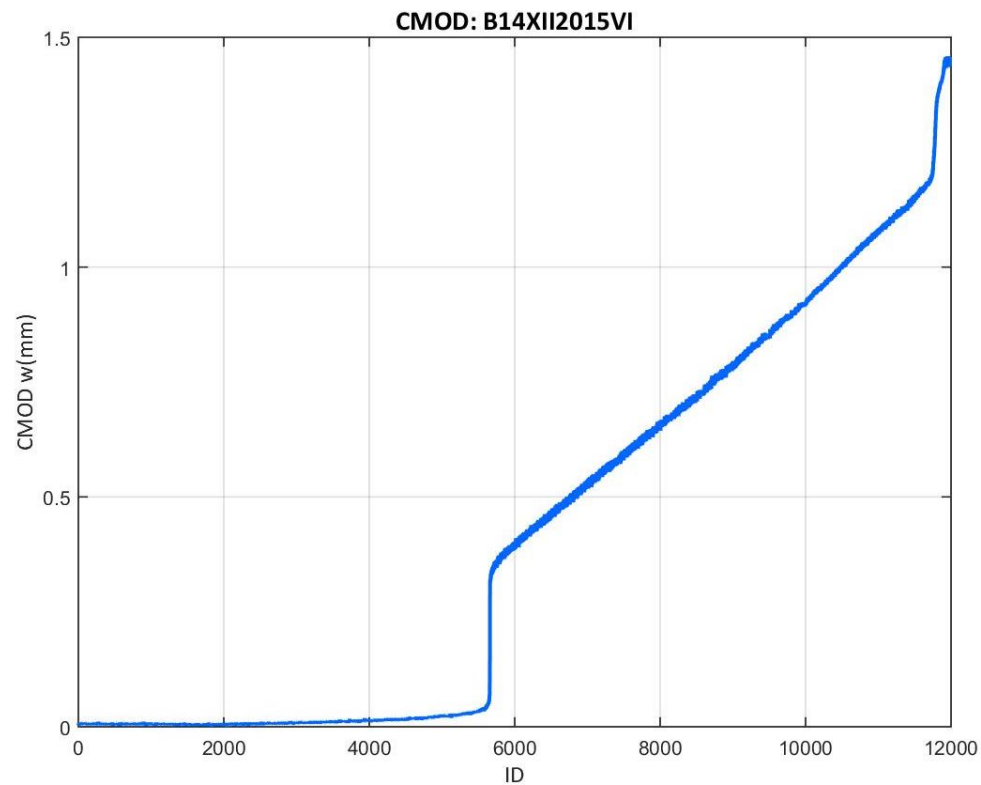


Figure 235: CMOD values recorded at the B14XII2015VI test

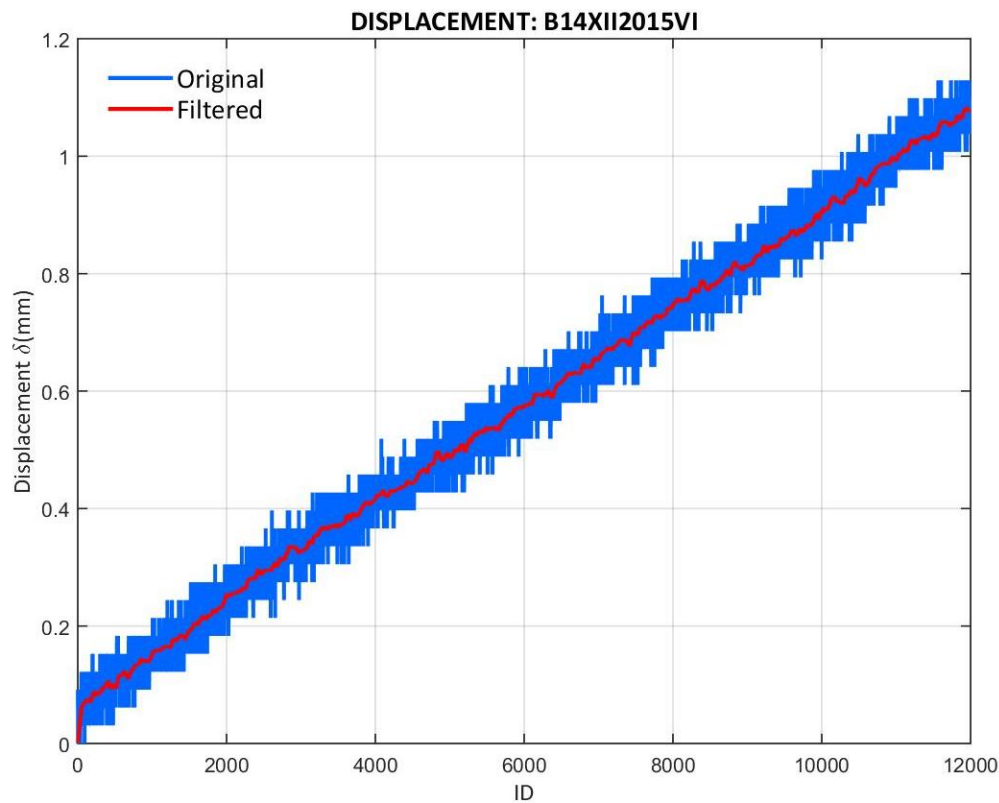


Figure 236: Displacement values recorded at the B14XII2015VI test

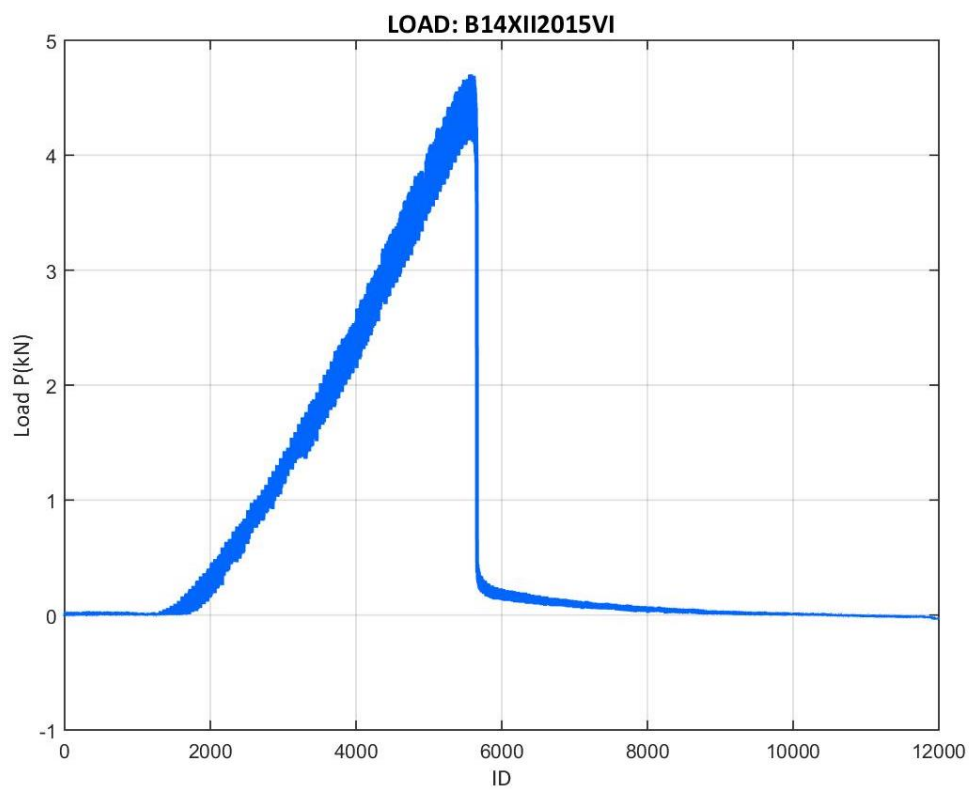


Figure 237: Load values recorded at the B14XII2015VI test

- B14XII2015VII

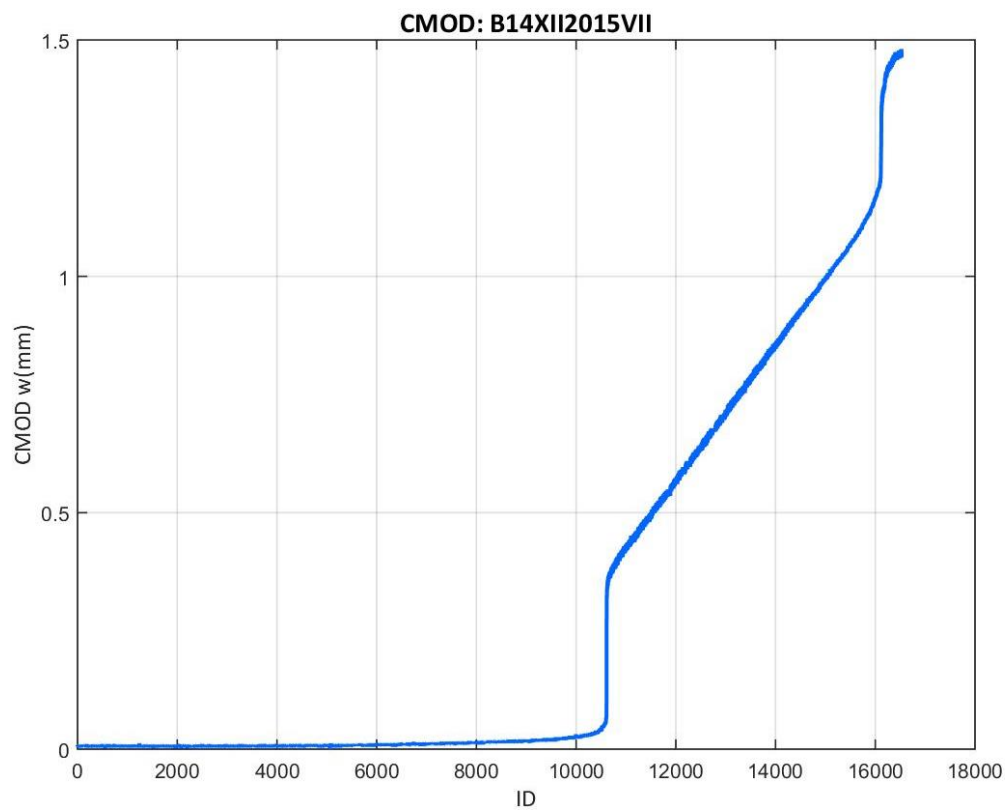


Figure 238: CMOD values recorded at the B14XII2015VII test

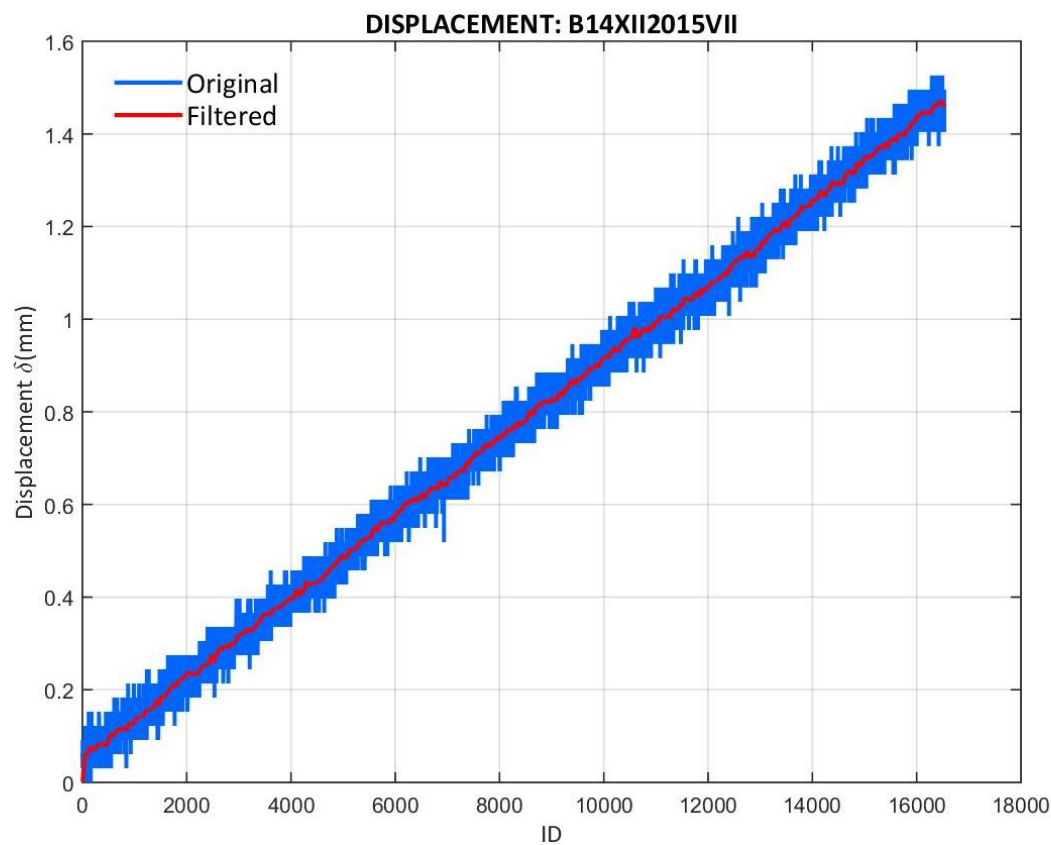


Figure 239: Displacement values recorded at the B14XII2015VII test

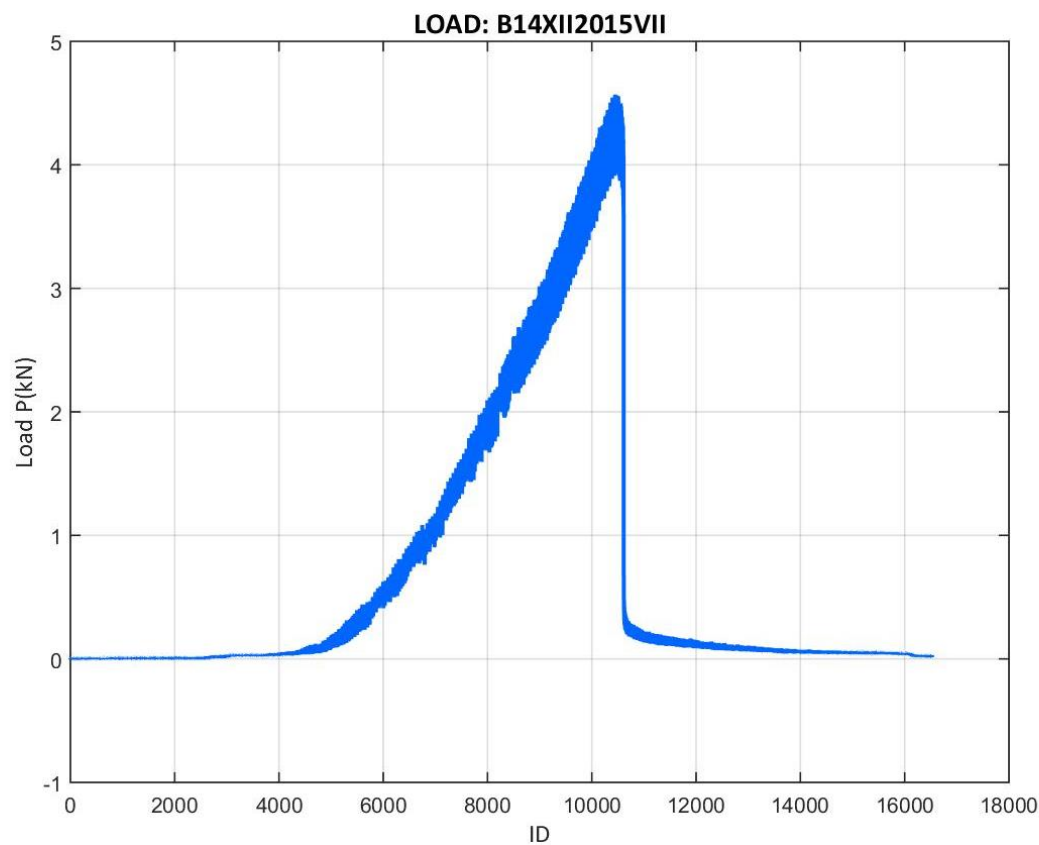


Figure 240: Load values recorded at the B14XII2015VII test

- B14XII2015VIII

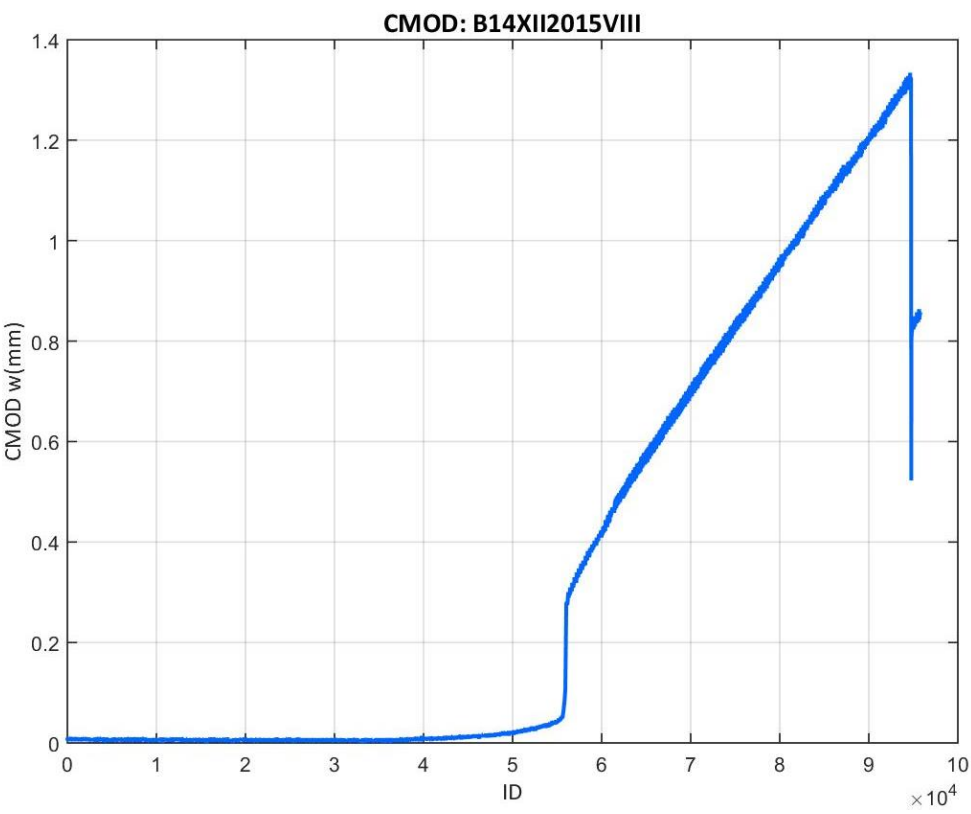


Figure 241: CMOD values recorded at the B14XII2015VIII test

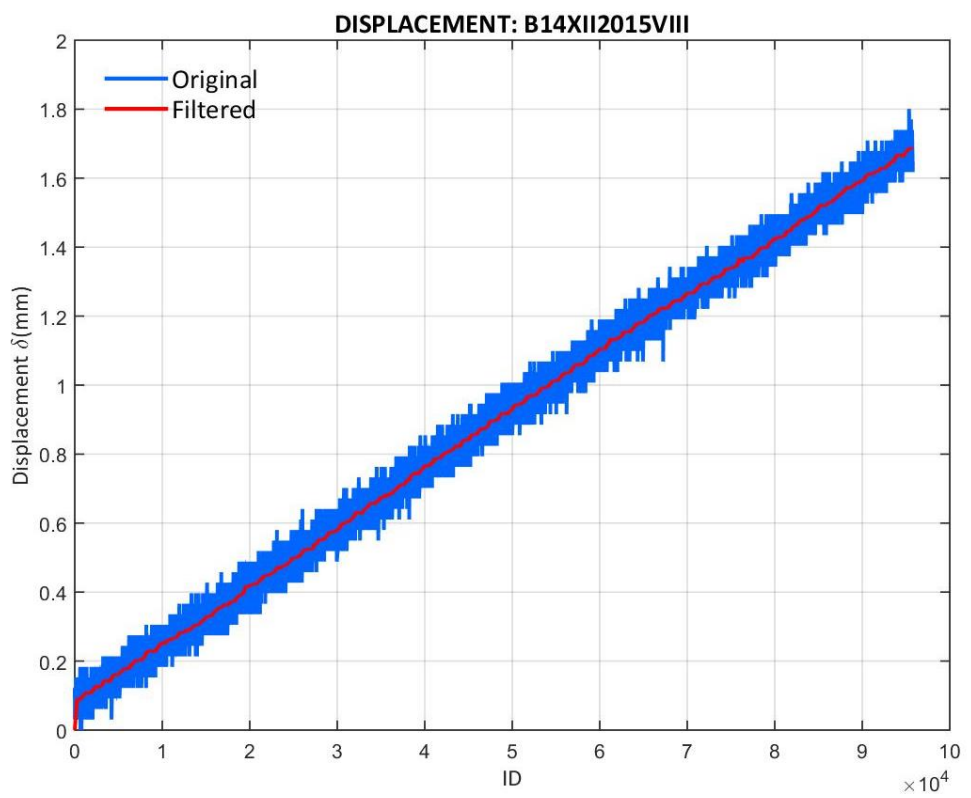


Figure 242: Displacement values recorded at the B14XII2015VIII test

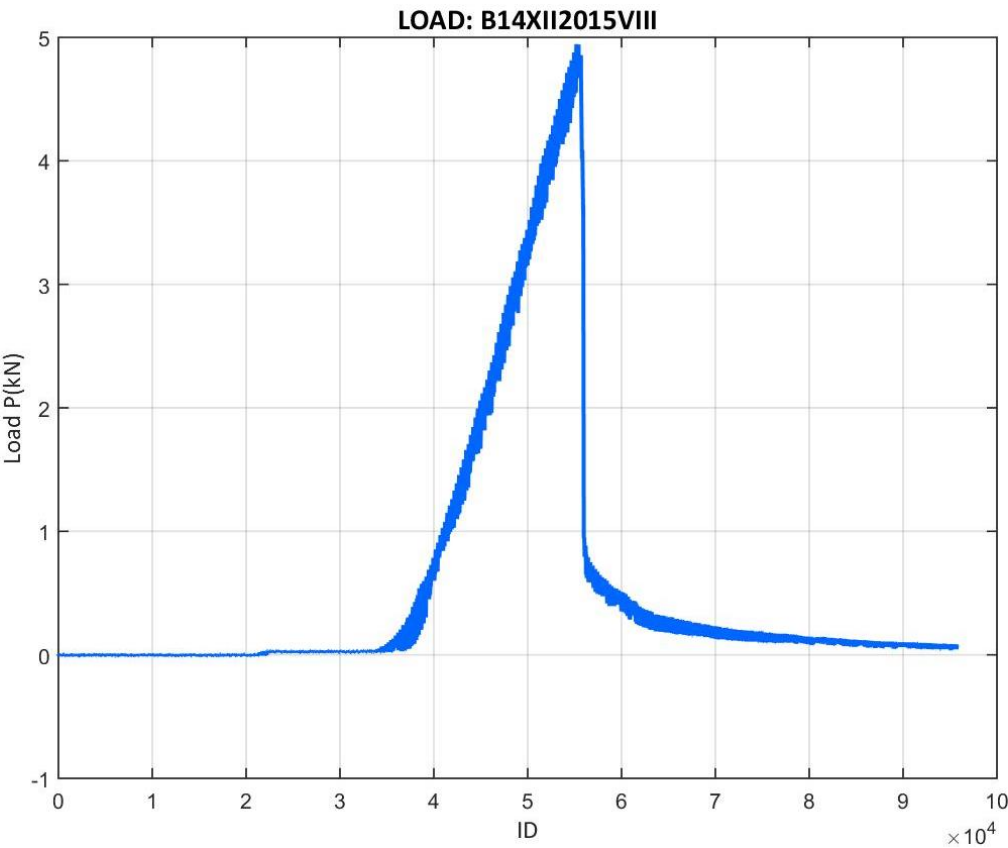


Figure 243: Load values recorded at the B14XII2015VIII test

E.4.2 14XII2015 CORRECTED LOAD VS. CMOD

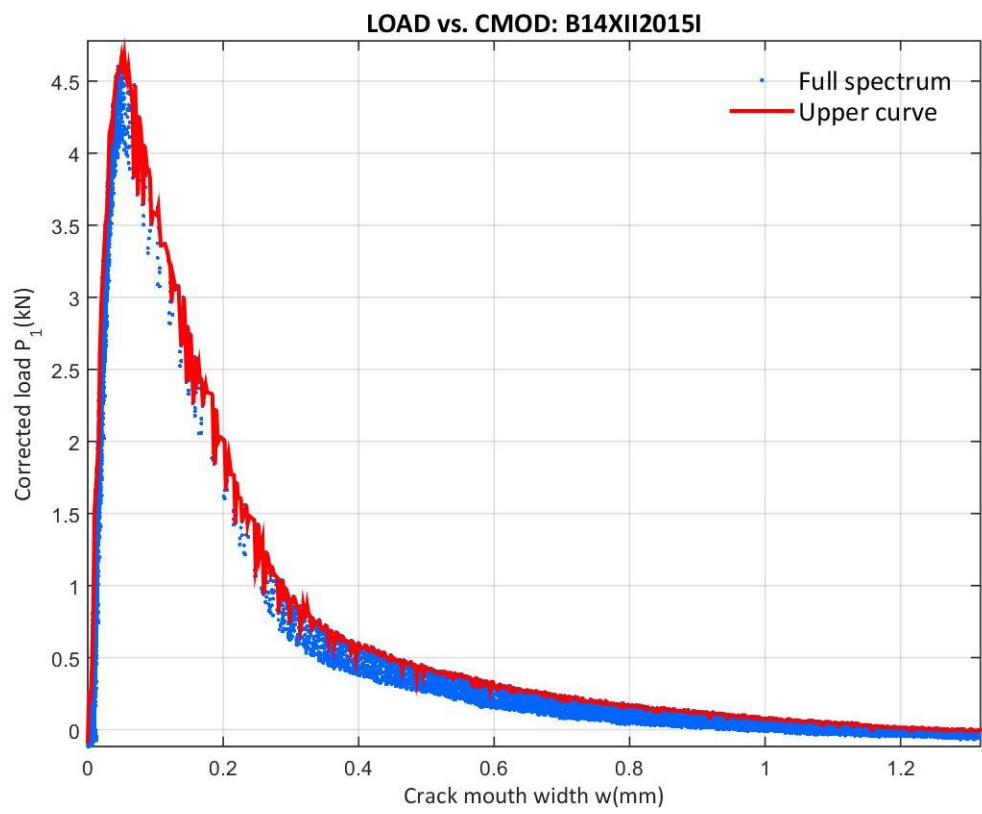


Figure 244: Corrected load vs. CMOD at the B14XII2015I test

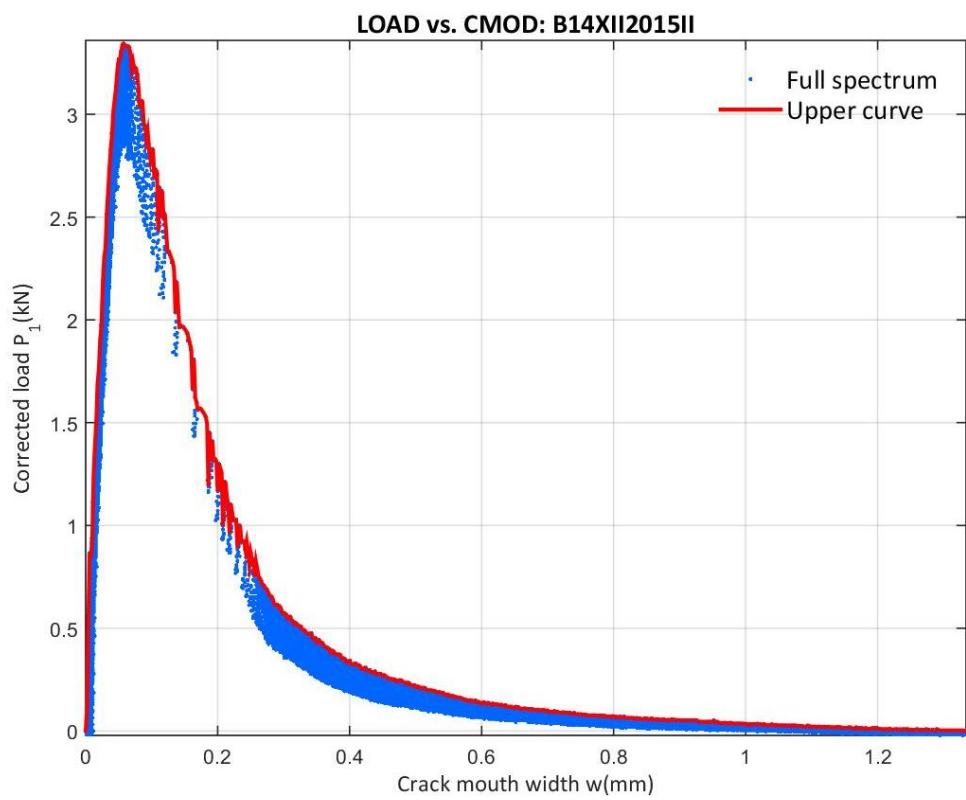


Figure 245: Corrected load vs. CMOD at the B14XII2015II test

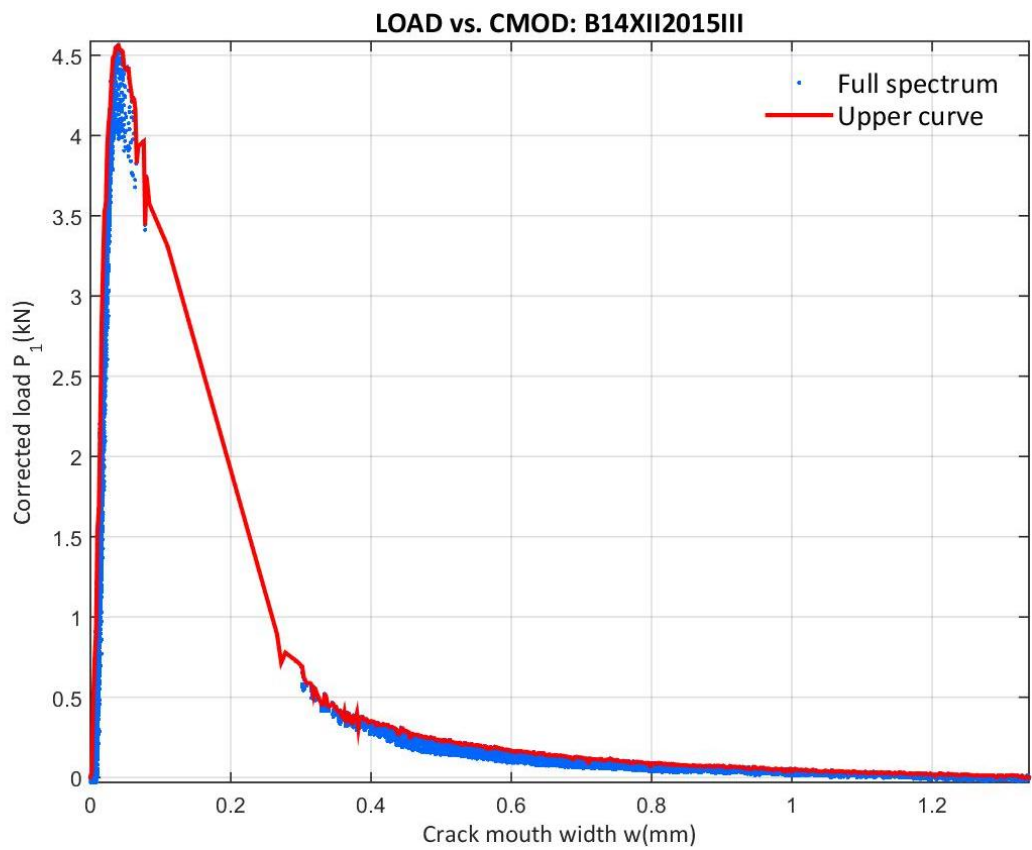


Figure 246: Corrected load vs. CMOD at the B14XII2015III test

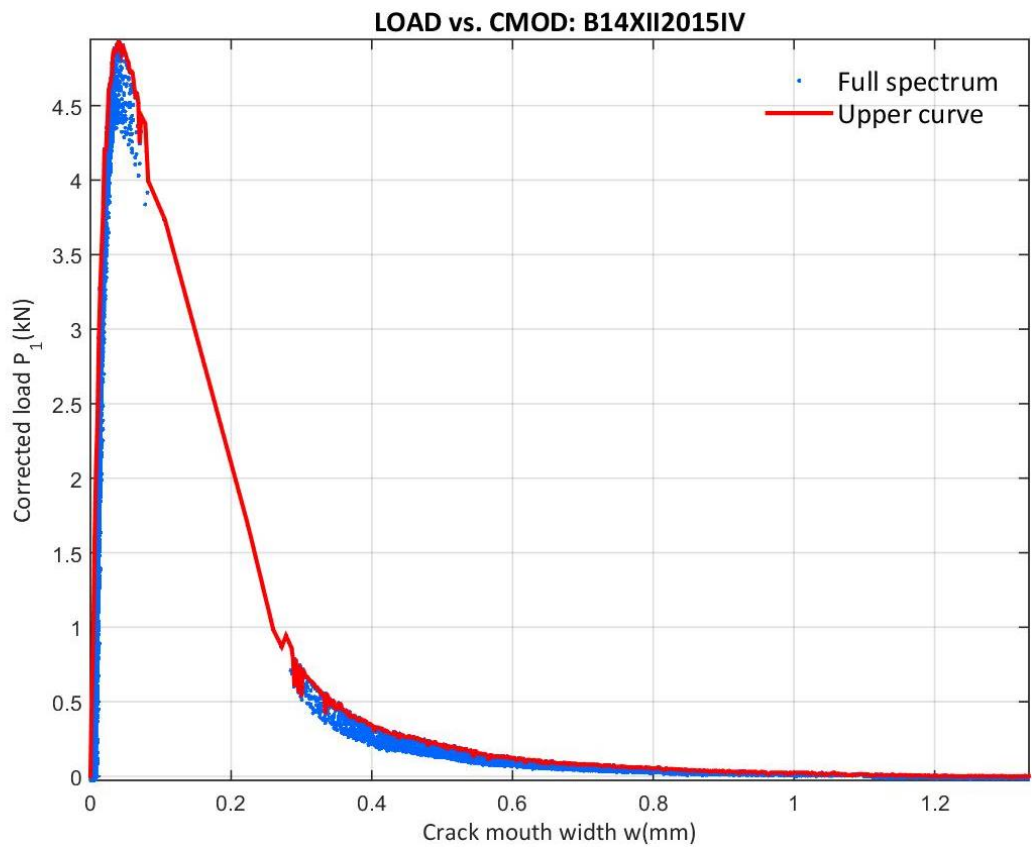


Figure 247: Corrected load vs. CMOD at the B14XII2015IV test

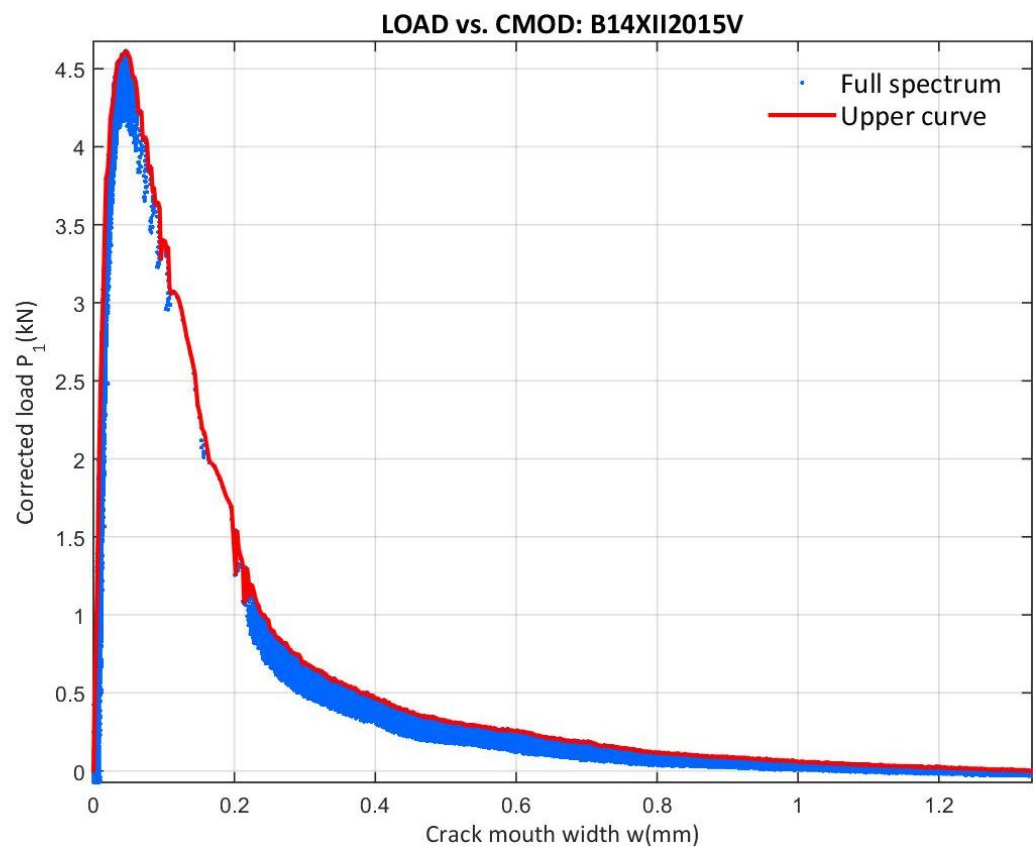


Figure 248: Corrected load vs. CMOD at the B14XII2015V test

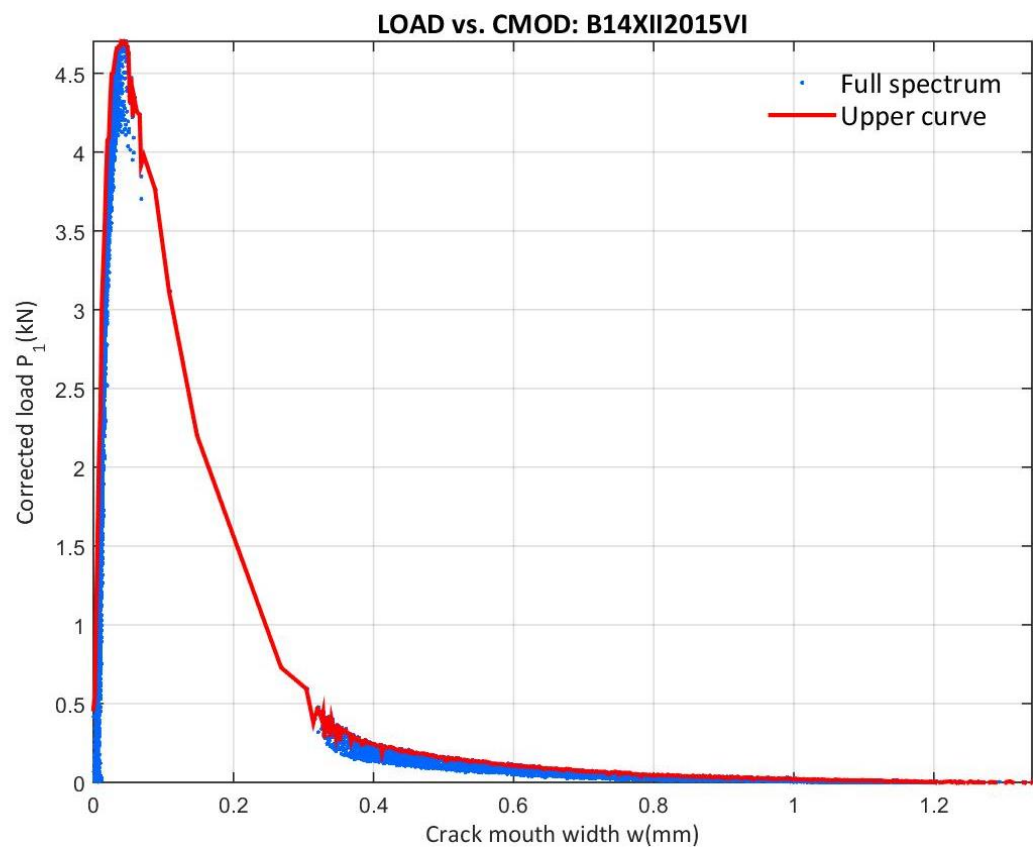


Figure 249: Corrected load vs. CMOD at the B14XII2015VI test

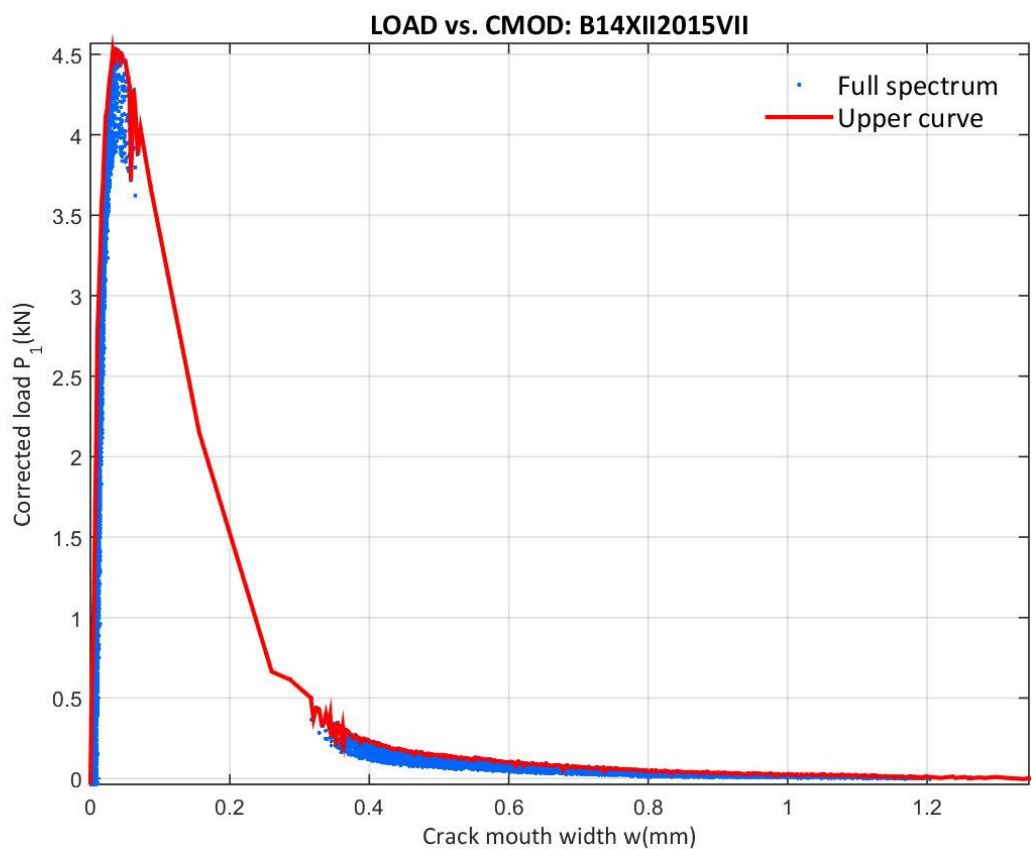


Figure 250: Corrected load vs. CMOD at the B14XII2015VII test

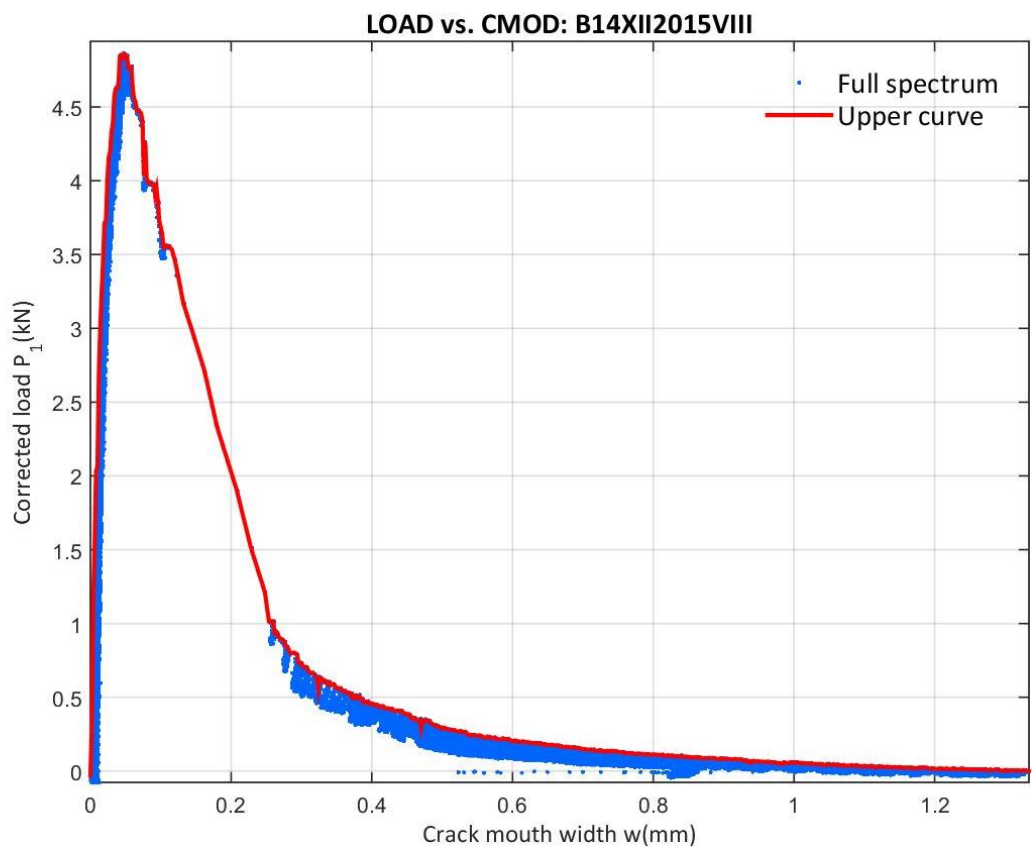


Figure 251: Corrected load vs. CMOD at the B14XII2015VIII test

E.4.3 14XII2015 CORRECTED LOAD VS. VERTICAL DISPLACEMENT

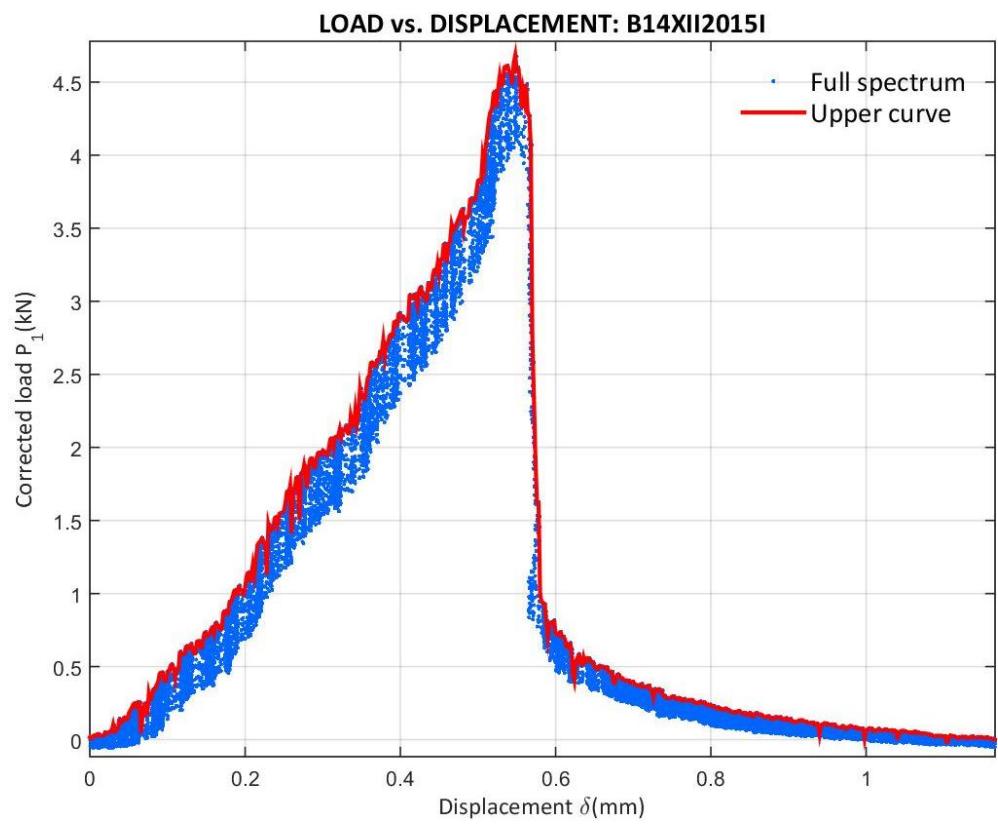


Figure 252: Corrected load vs. Displacement at the B14XII2015I test

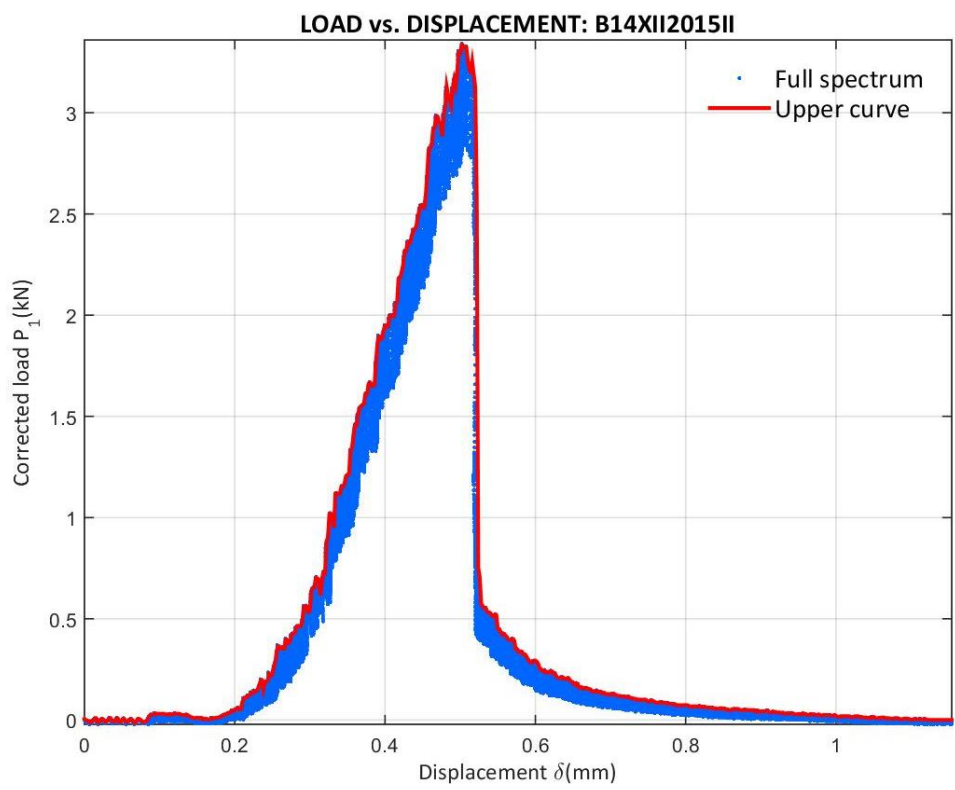


Figure 253: Corrected load vs. Displacement at the B14XII2015II test

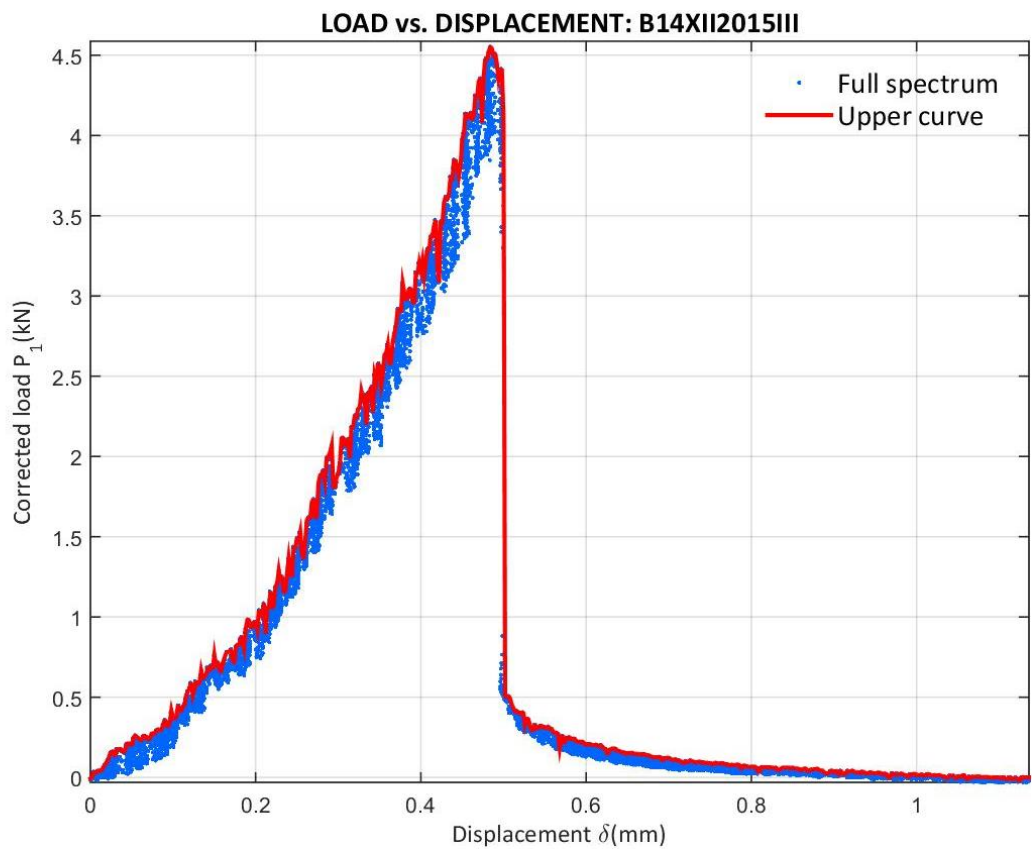


Figure 254: Corrected load vs. Displacement at the B14XII2015III test

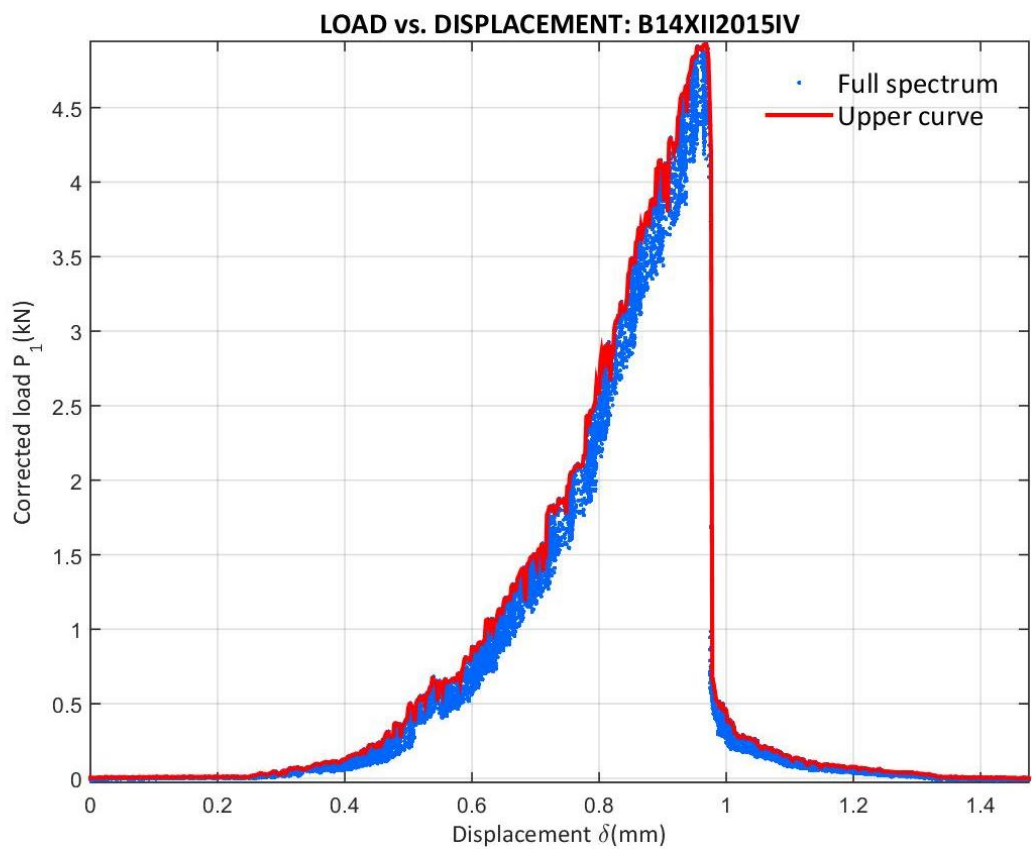


Figure 255: Corrected load vs. Displacement at the B14XII2015IV test

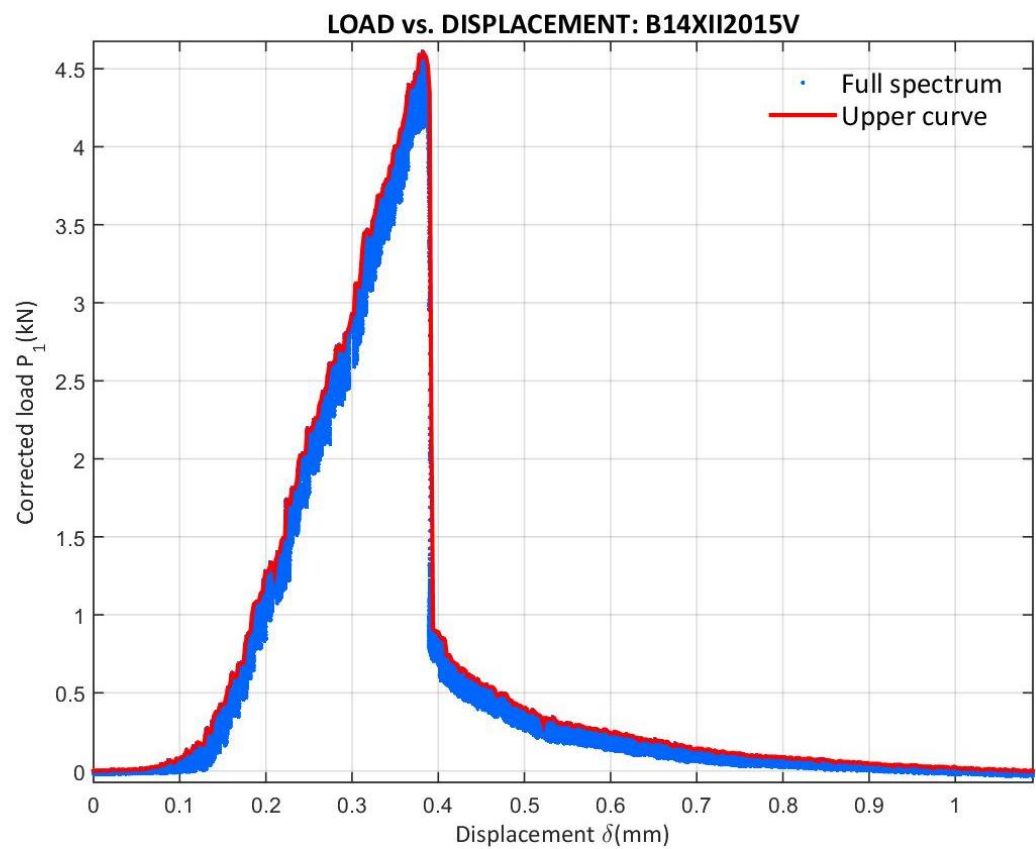


Figure 256: Corrected load vs. Displacement at the B14XII2015V test

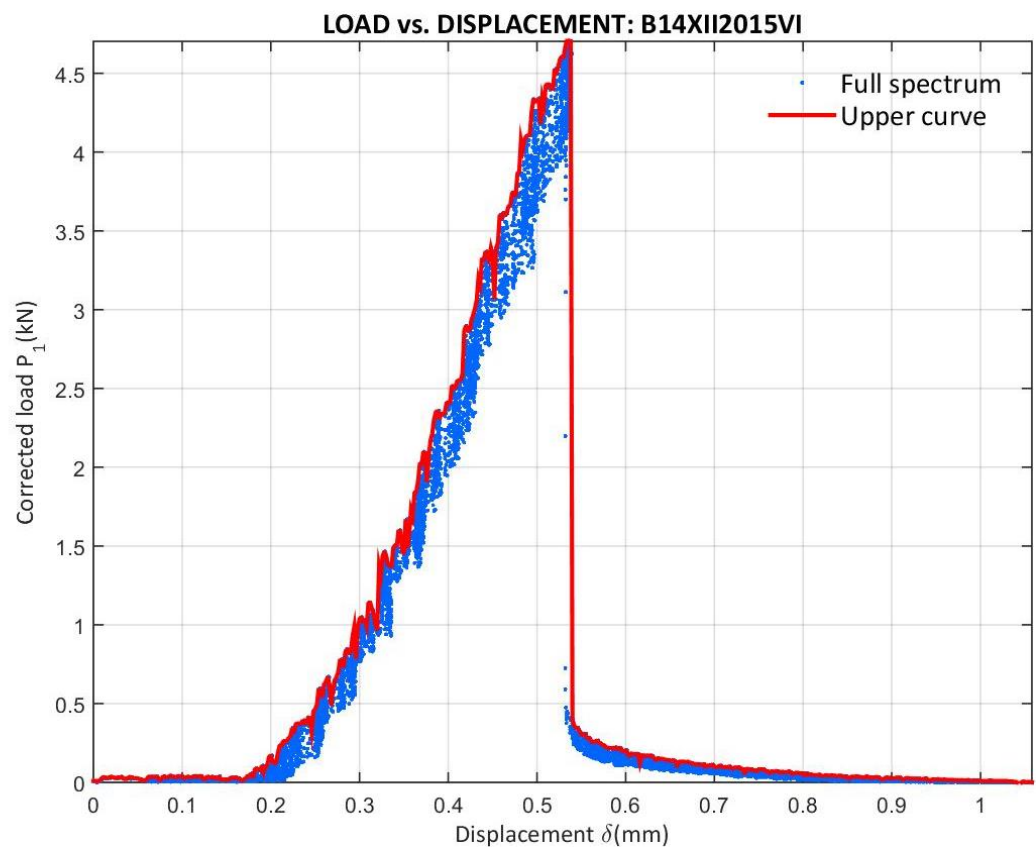


Figure 257: Corrected load vs. Displacement at the B14XII2015VI test

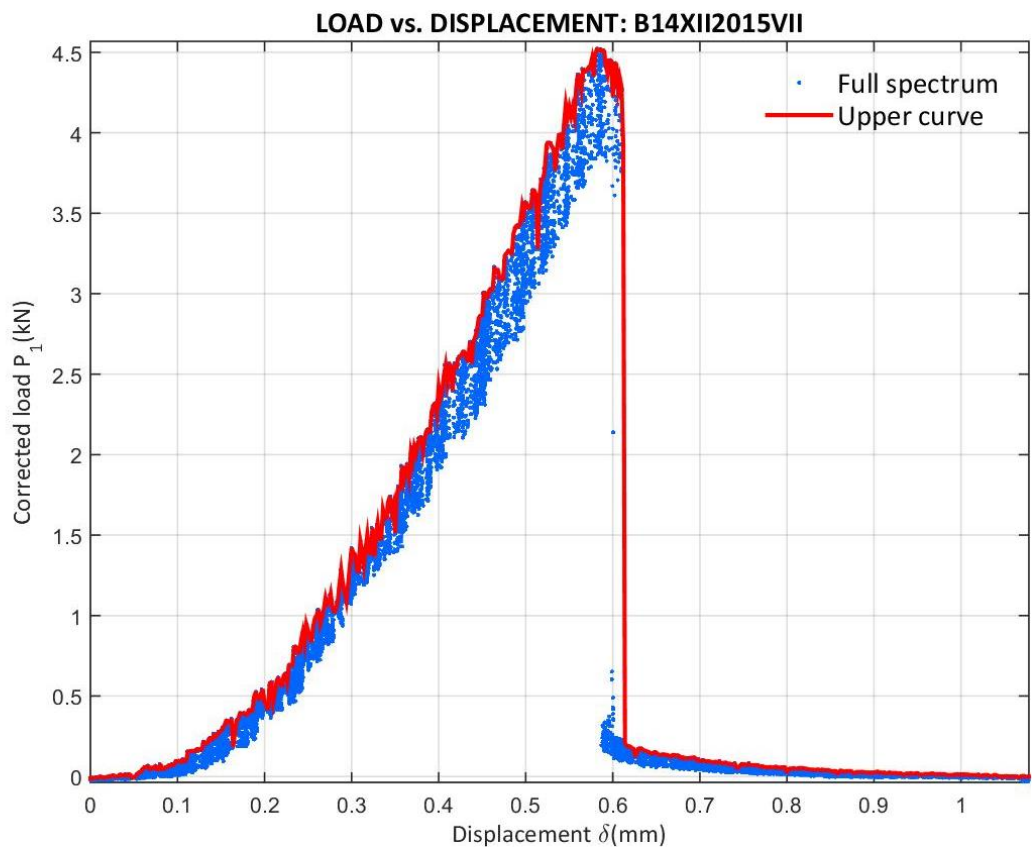


Figure 258: Corrected load vs. Displacement at the B14XII2015VII test

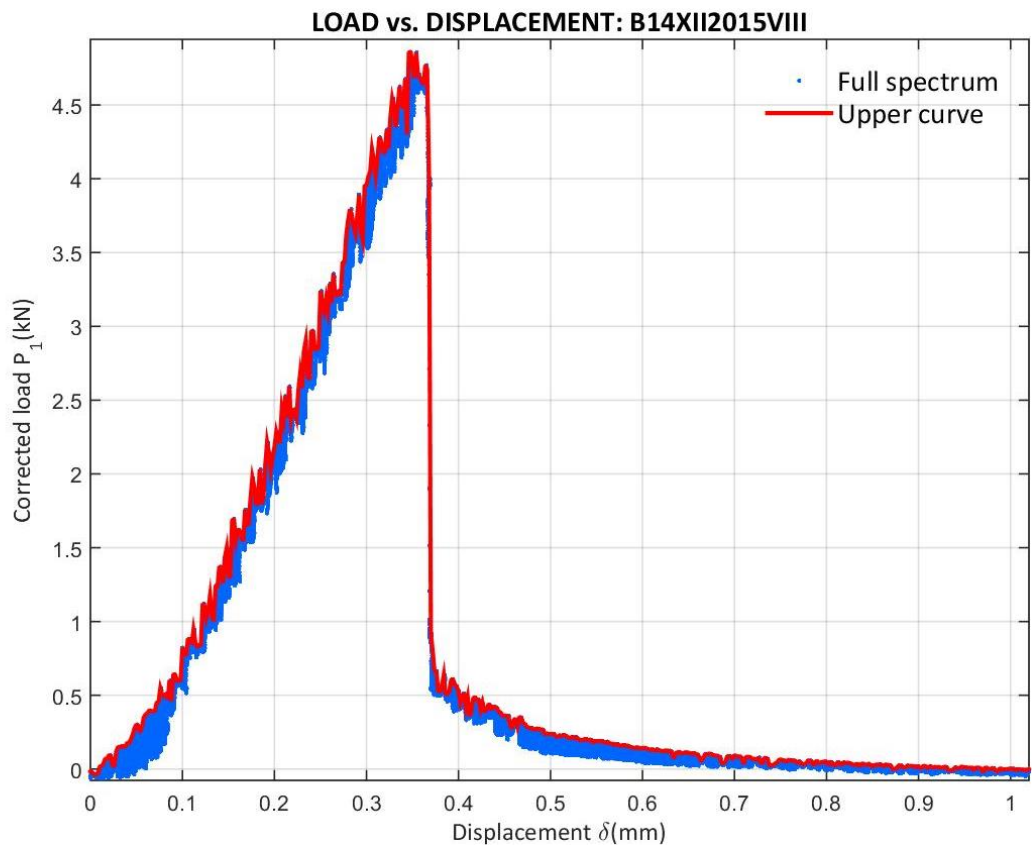


Figure 259: Corrected load vs. Displacement at the B14XII2015VIII test

E.4.4 14XII2015 CORRECTED LOAD VS. X

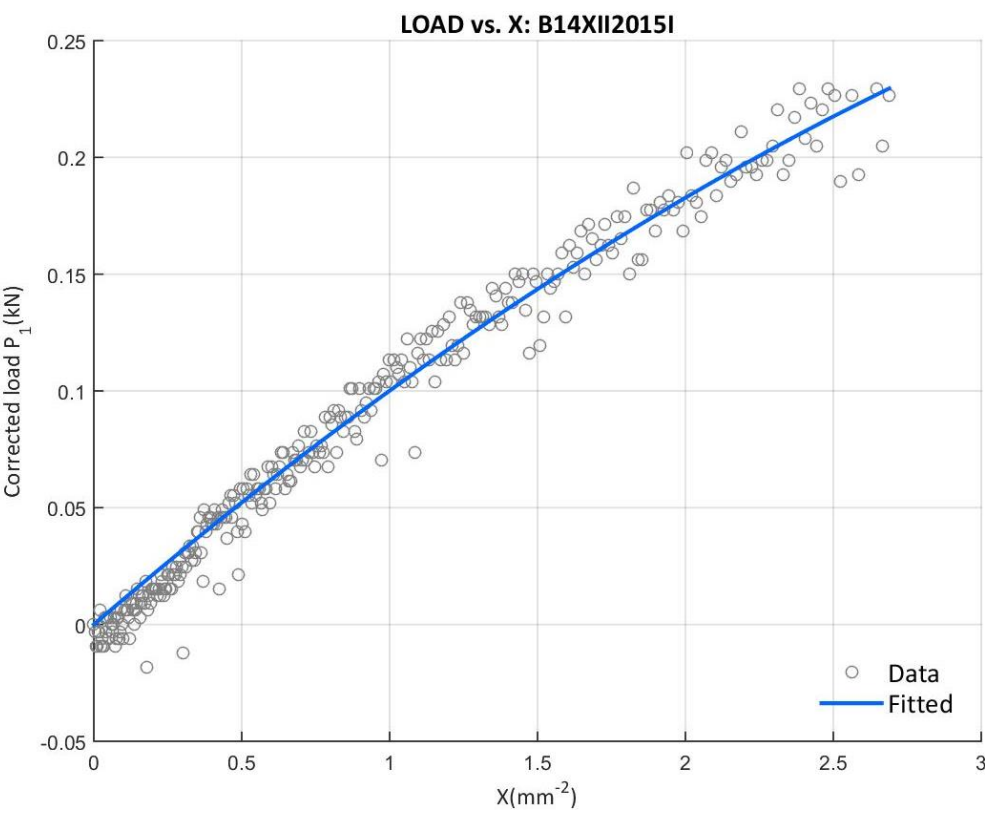


Figure 260: Corrected load vs. X at the B14XII2015I test with the final upper curve data

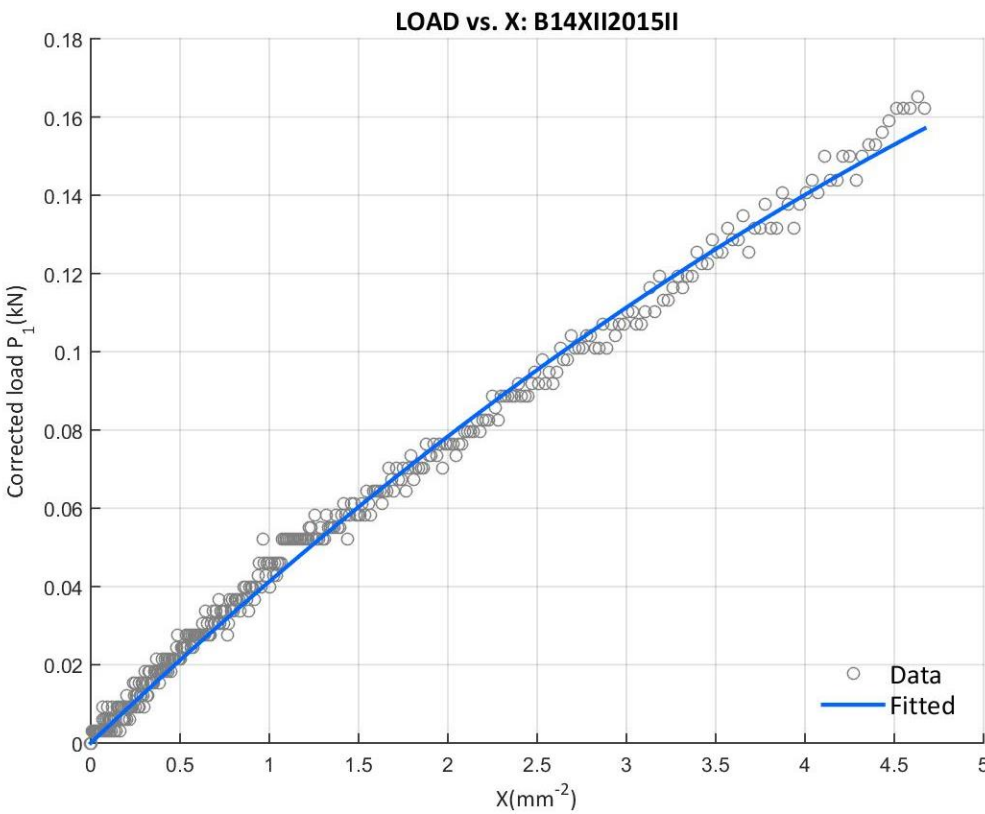


Figure 261: Corrected load vs. X at the B14XII2015II test with the final upper curve data

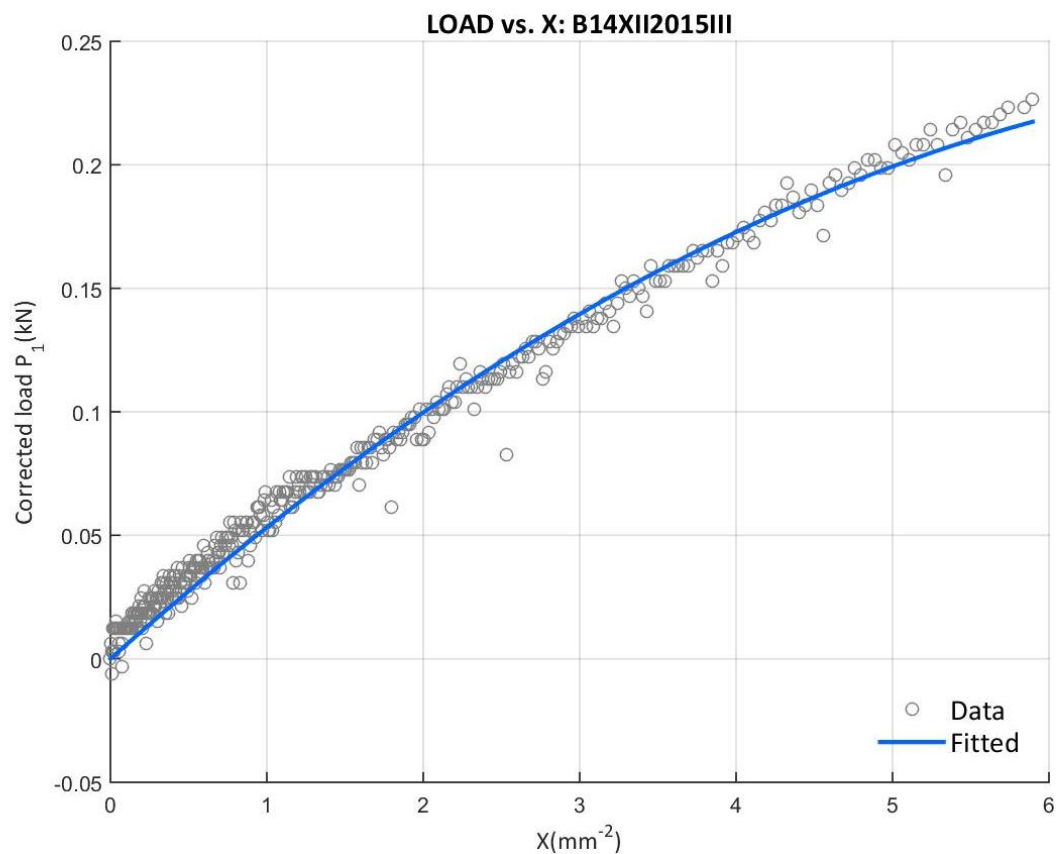


Figure 262: Corrected load vs. X at the B14XII2015III test with the final upper curve data

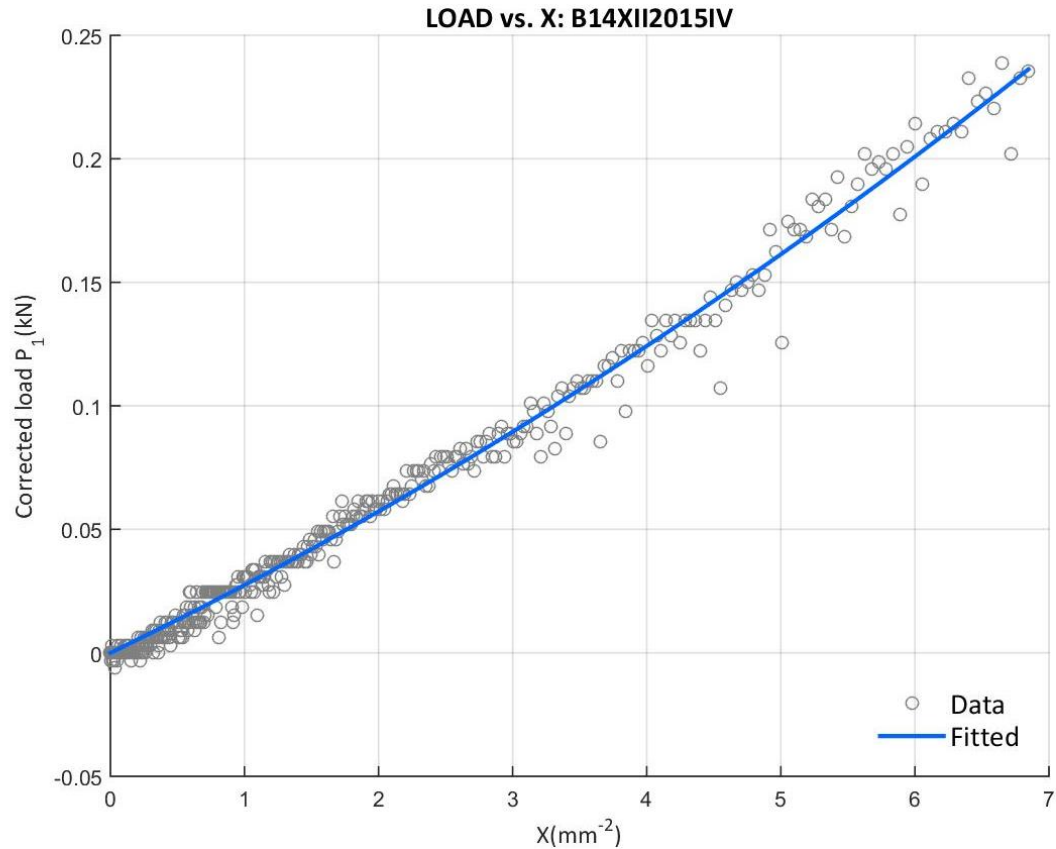


Figure 263: Corrected load vs. X at the B14XII2015IV test with the final upper curve data

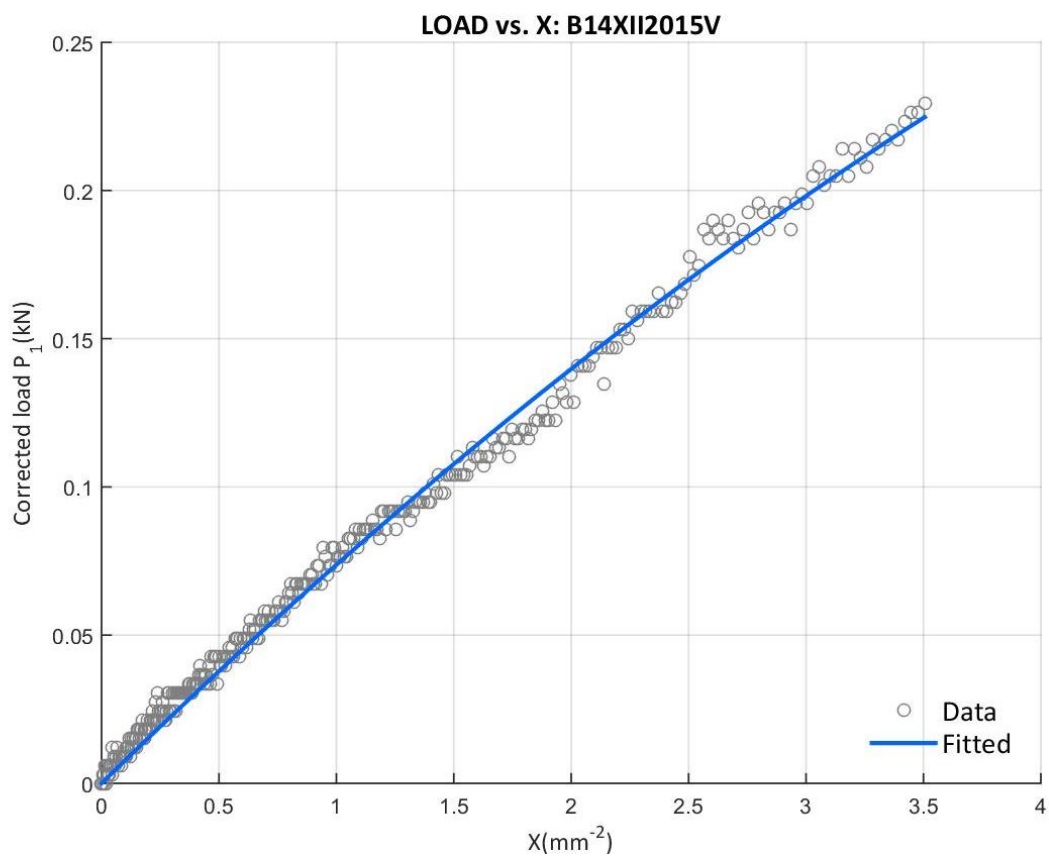


Figure 264: Corrected load vs. X at the B14XII2015V test with the final upper curve data

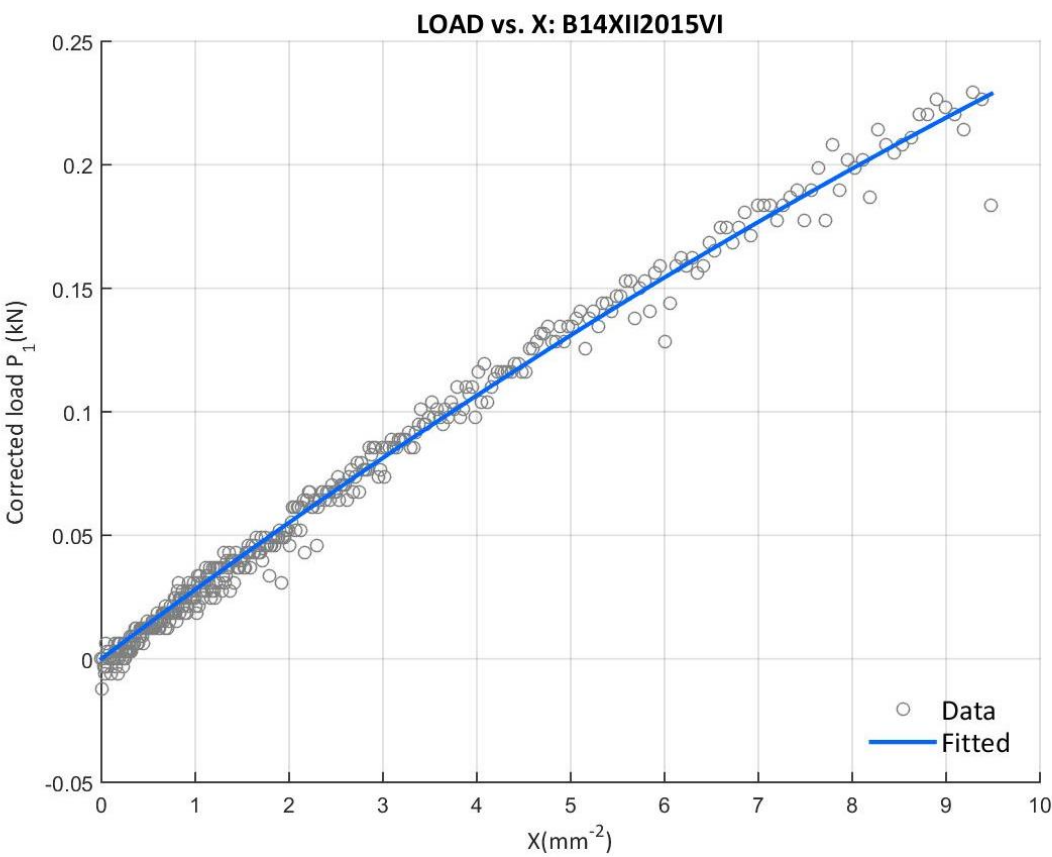


Figure 265: Corrected load vs. X at the B14XII2015VI test with the final upper curve data

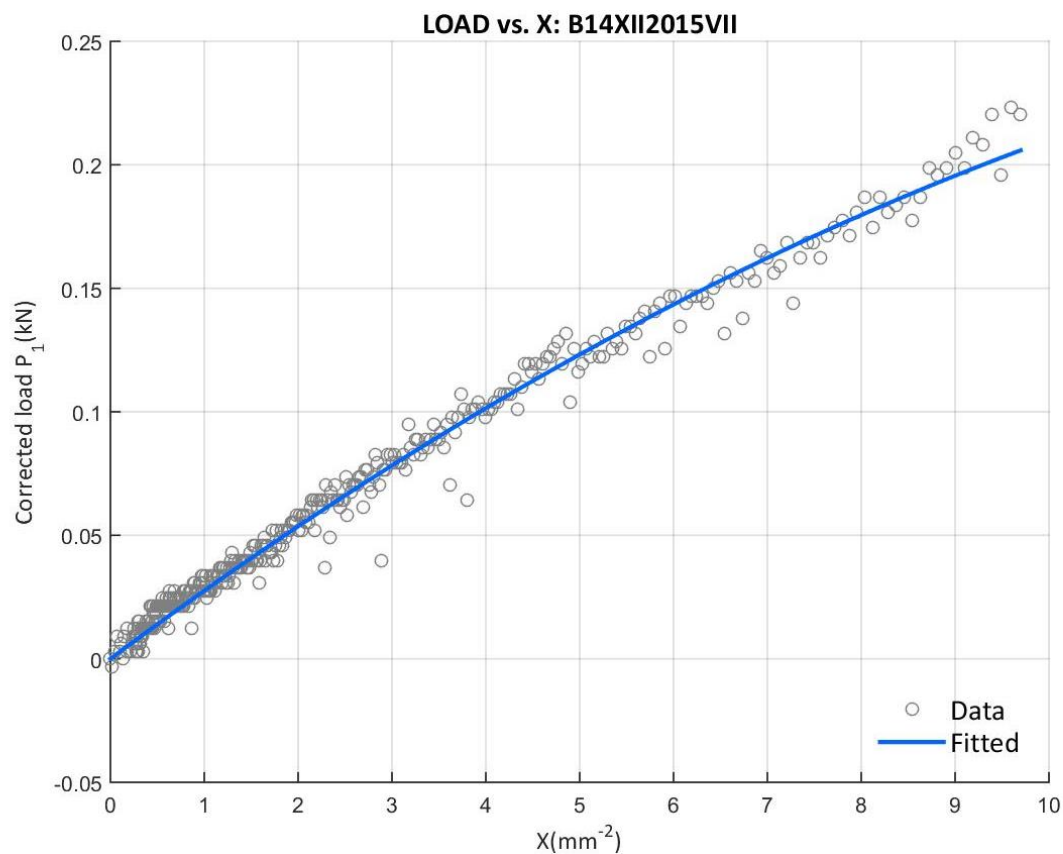


Figure 266: Corrected load vs. X at the B14XII2015VII test with the final upper curve data

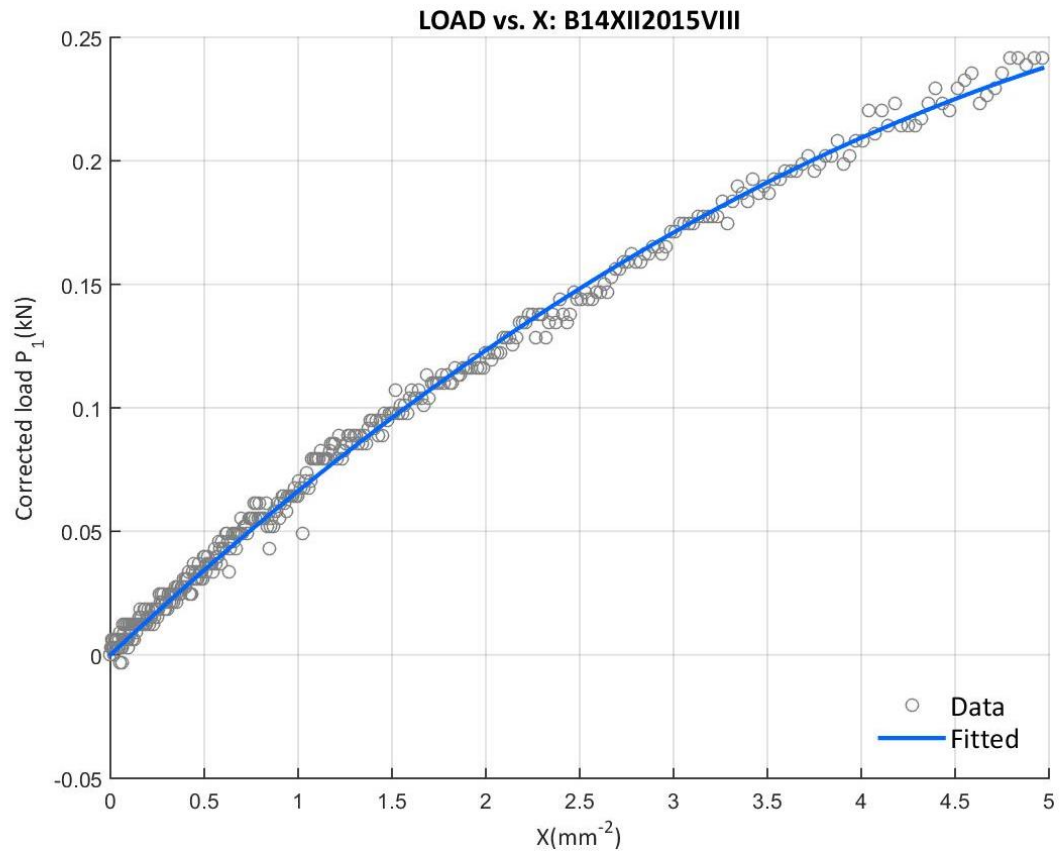


Figure 267: Corrected load vs. X at the B14XII2015VIII test with the final upper curve data

E.4.5 14XII2015 SOFTENING CURVE BILINEAR APPROXIMATION

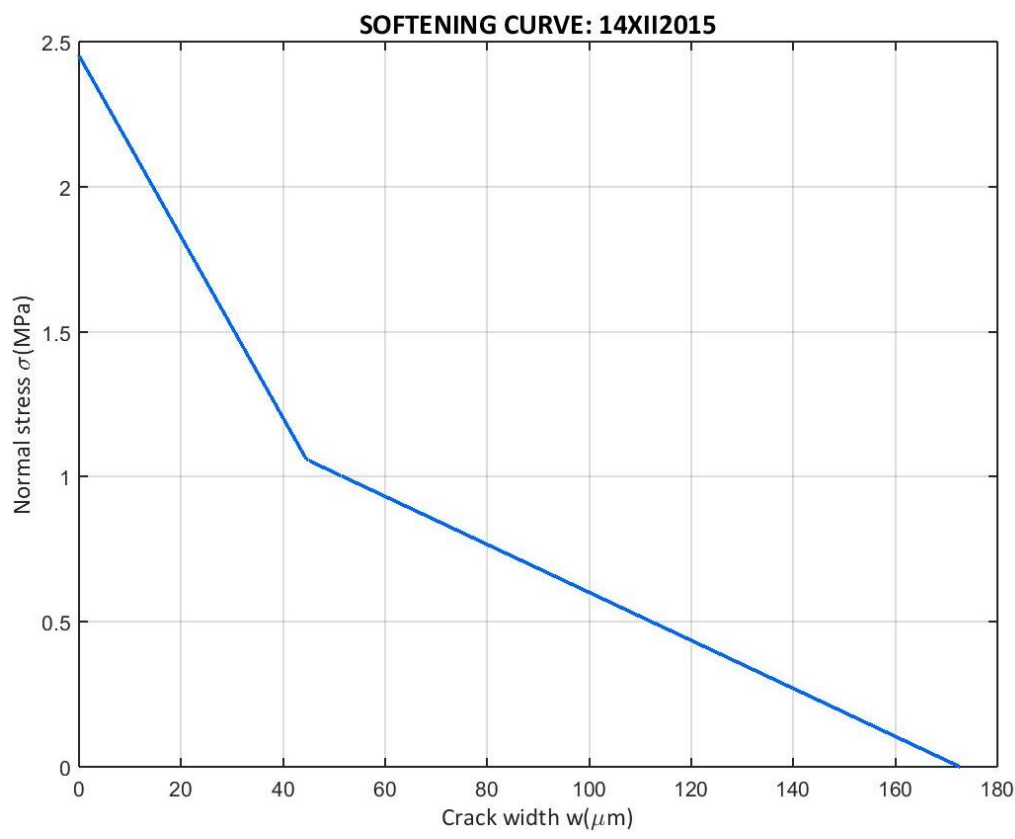


Figure 268: Softening curve bilinear approximation of the 14XII2015 campaign

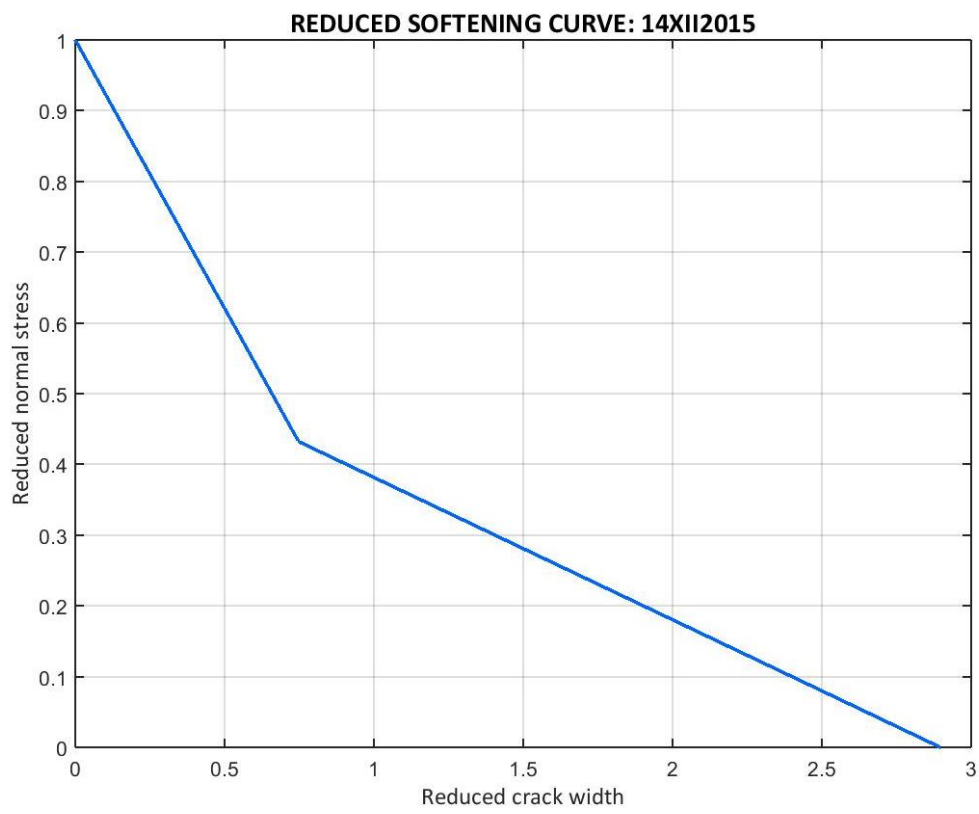


Figure 269: Softening curve bilinear approximation of the 14XII2015 campaign in the reduced form

E.4.6 14XII2015 SPECIMENS' COMPARISON

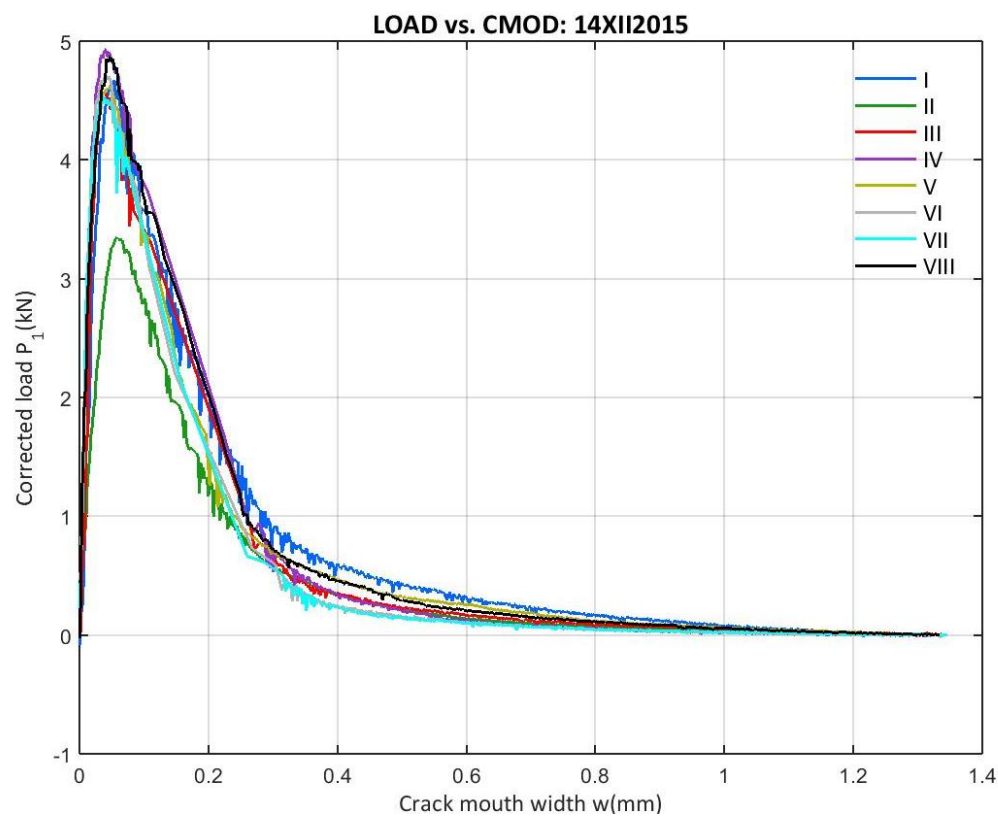


Figure 270: 14XII2015 Corrected load vs. CMOD from the entire campaign

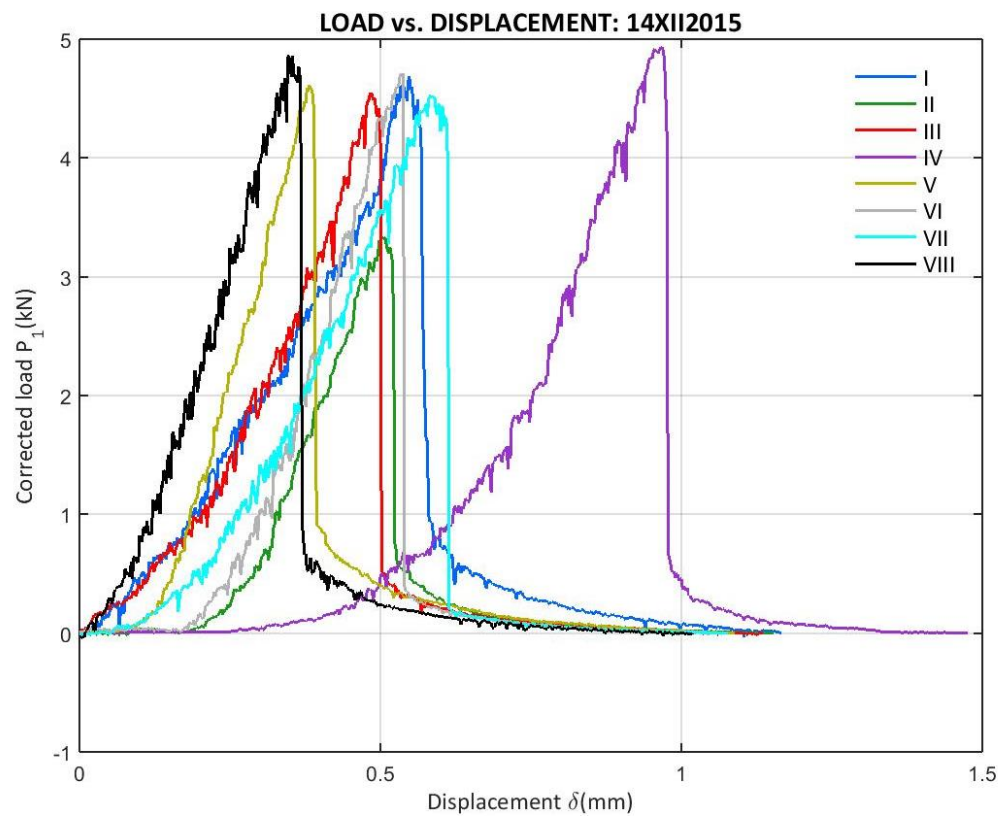


Figure 271: 14XII2015 Corrected load vs. Displacement from the entire campaign

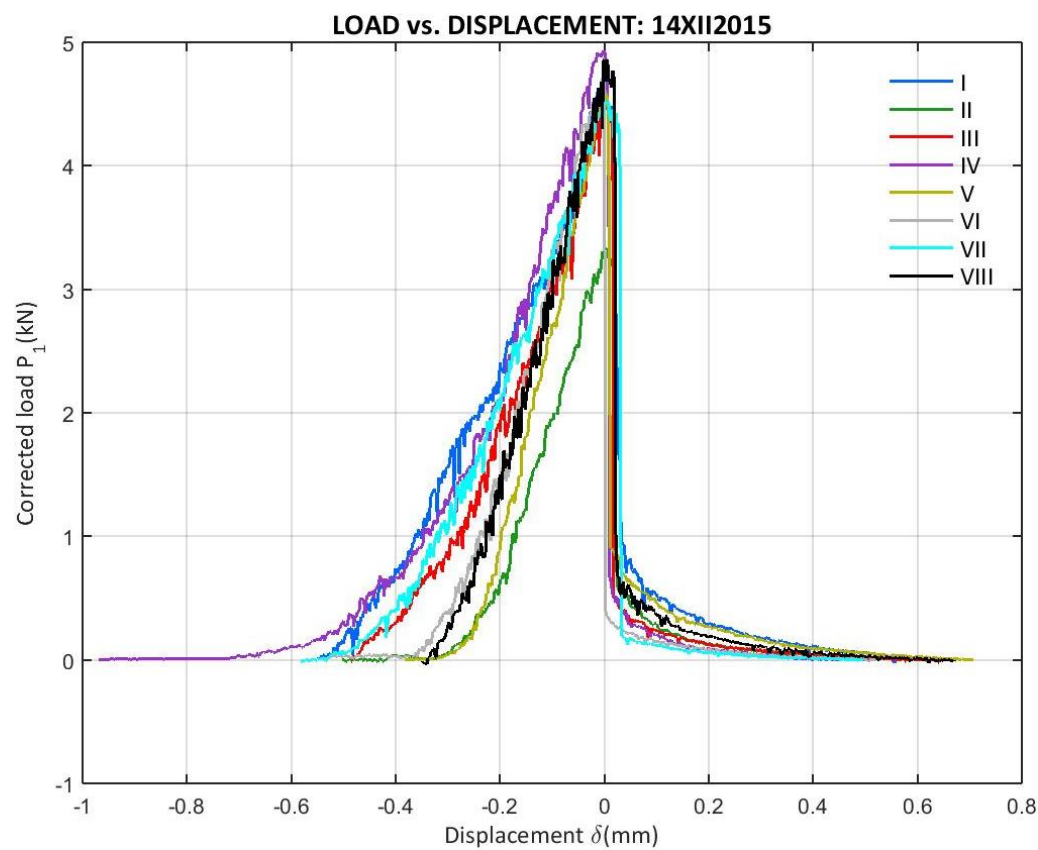


Figure 272: 14XII2015 Corrected load vs. Displacement from the entire campaign (peak displacement zero)

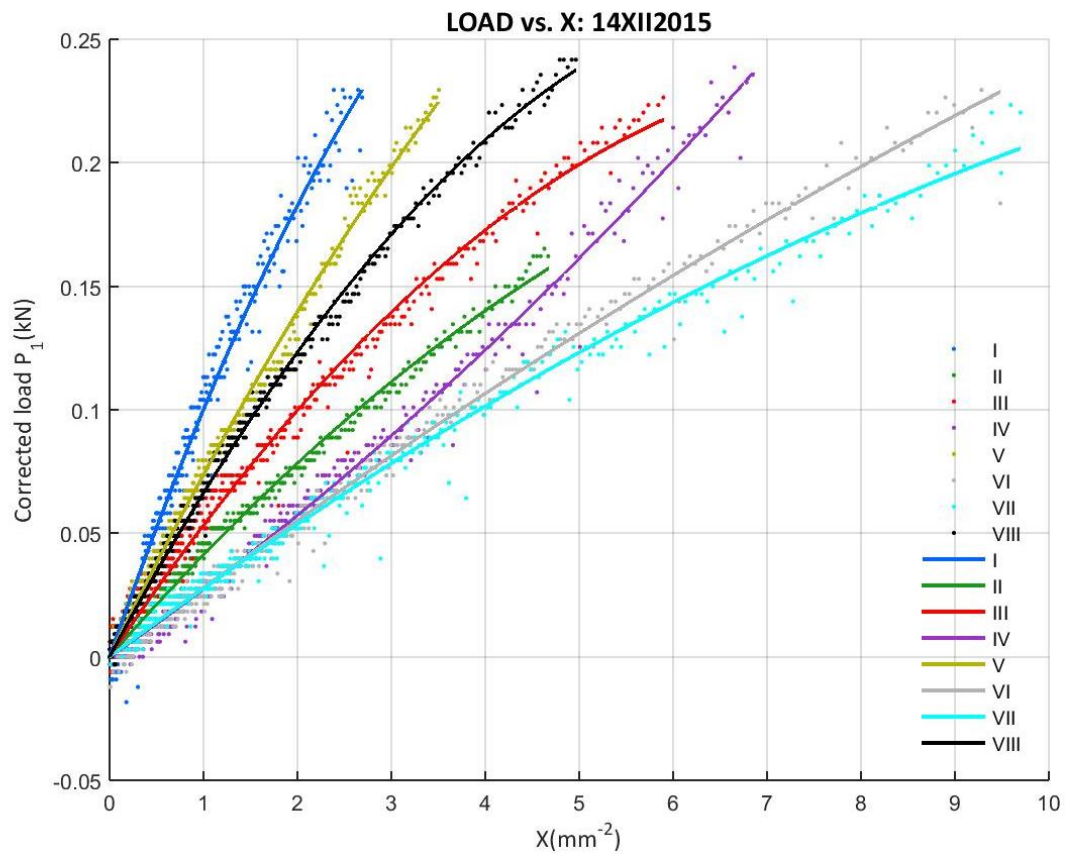


Figure 273: 14XII2015 Corrected load vs. X from the entire campaign

E.5 29I2016 CAMPAIGN

E.5.1 29I2016 DATA

- B29I2016I

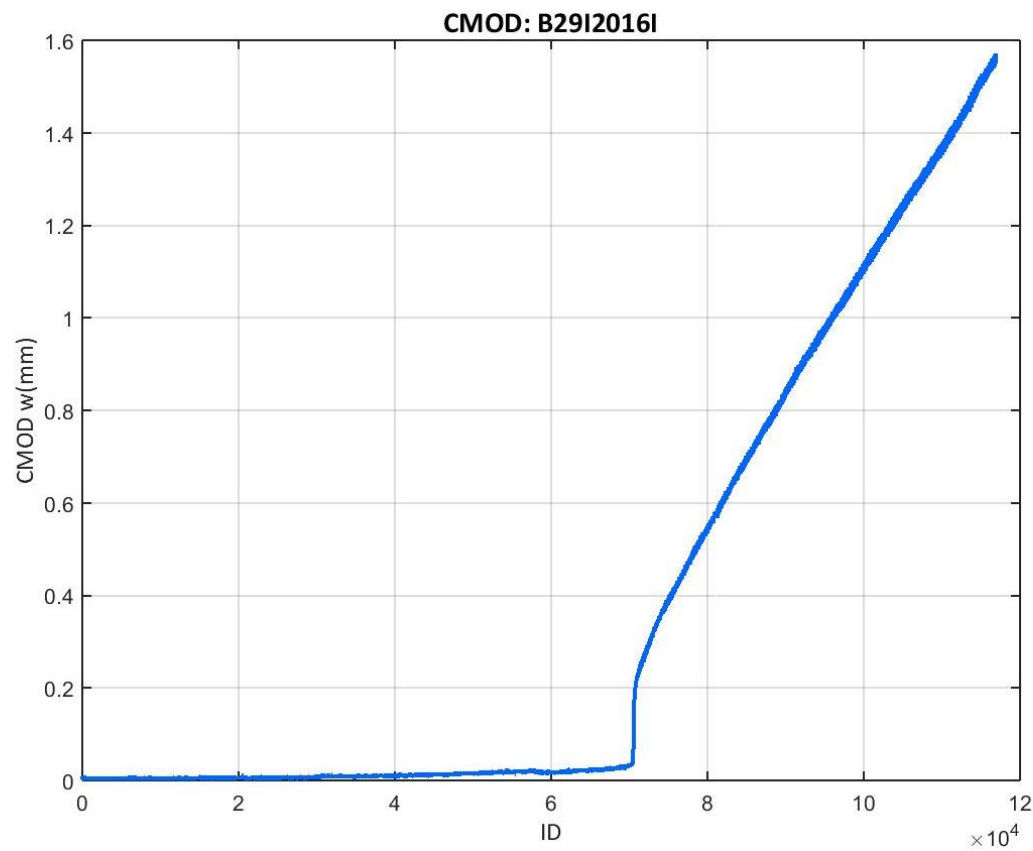


Figure 274: CMOD values recorded at the B29I2016I test

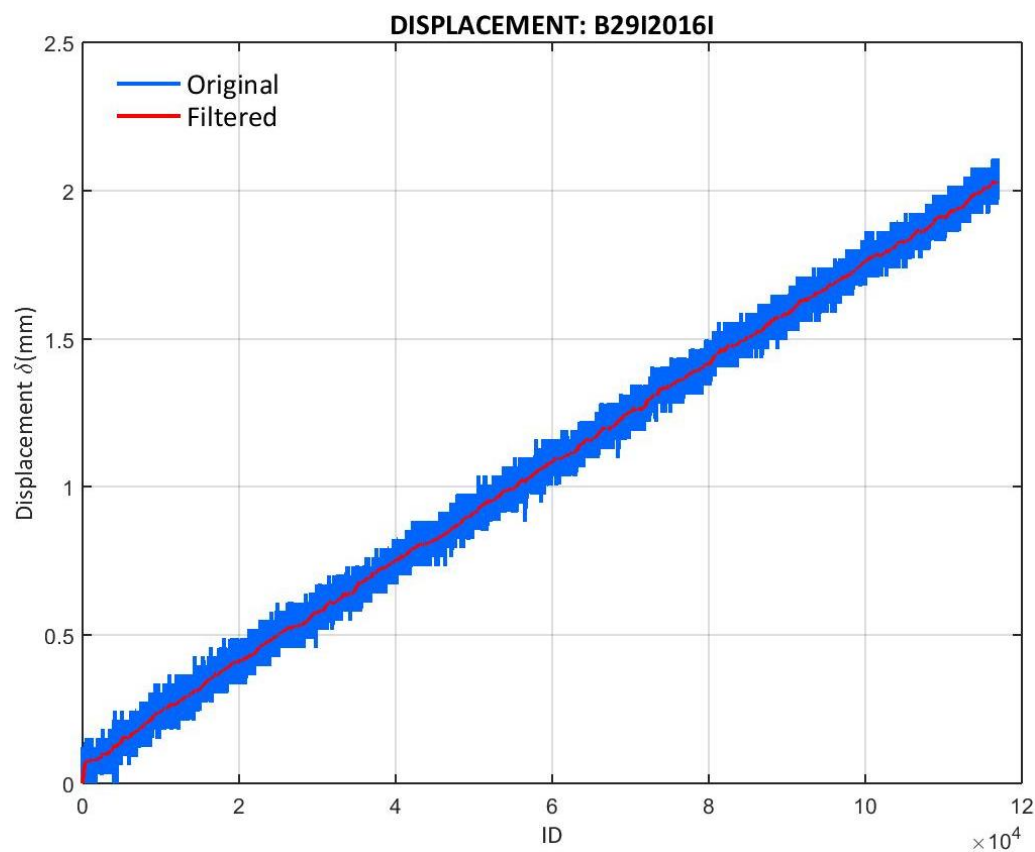


Figure 275: Displacement values recorded at the B29I2016I test

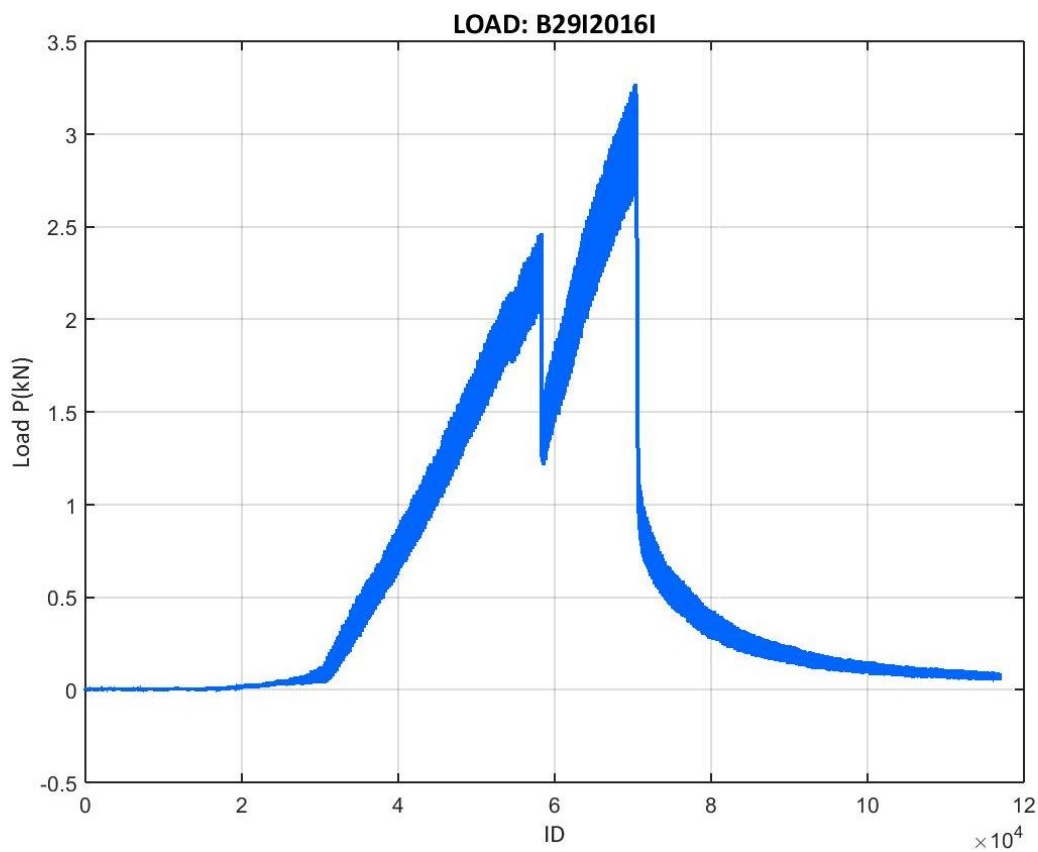


Figure 276: Load values recorded at the B29I2016I test

- B29I2016II

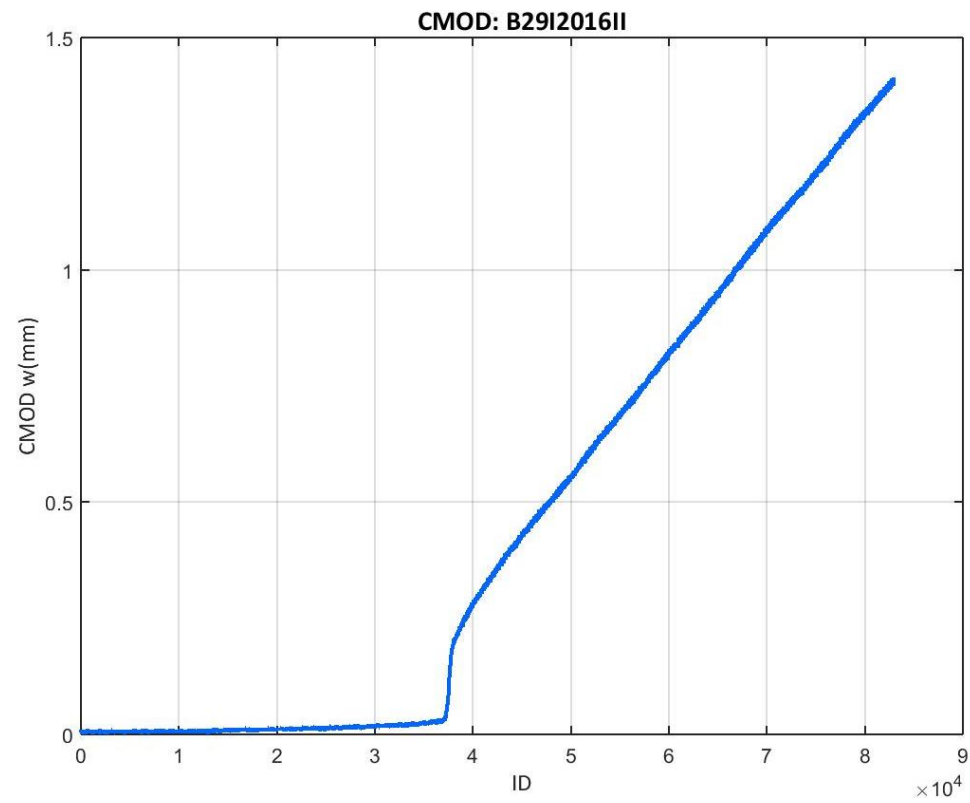


Figure 277: CMOD values recorded at the B29I2016II test

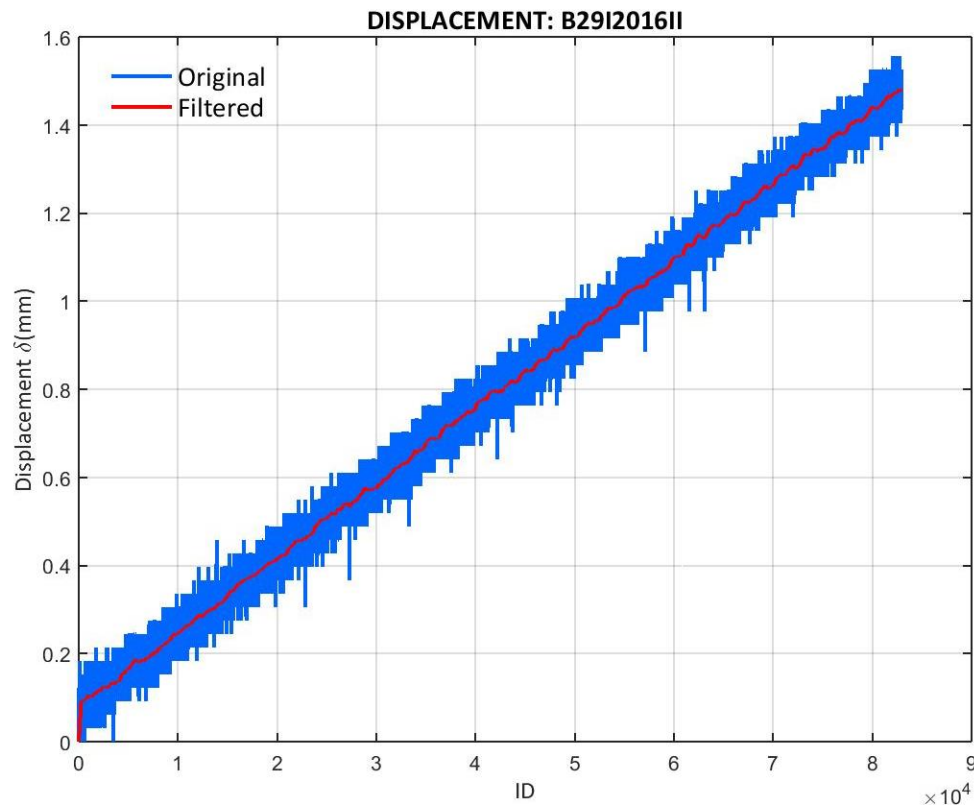


Figure 278: Displacement values recorded at the B29I2016II test

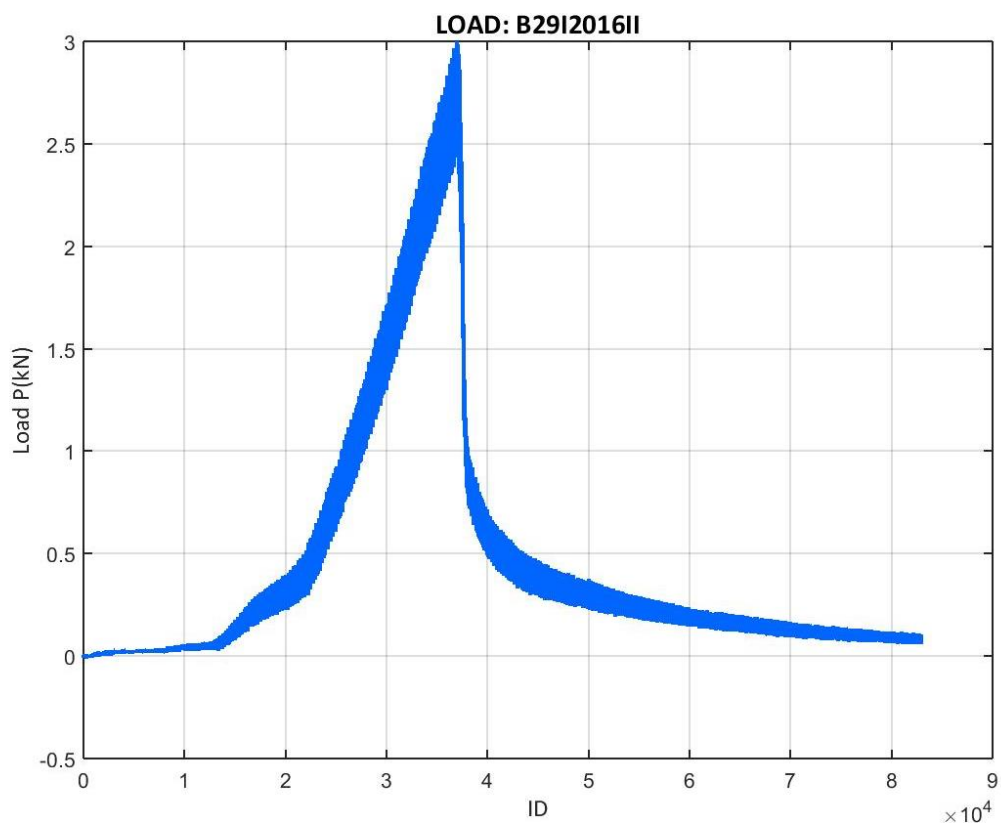


Figure 279: Load values recorded at the B29I2016II test

- B29I2016III

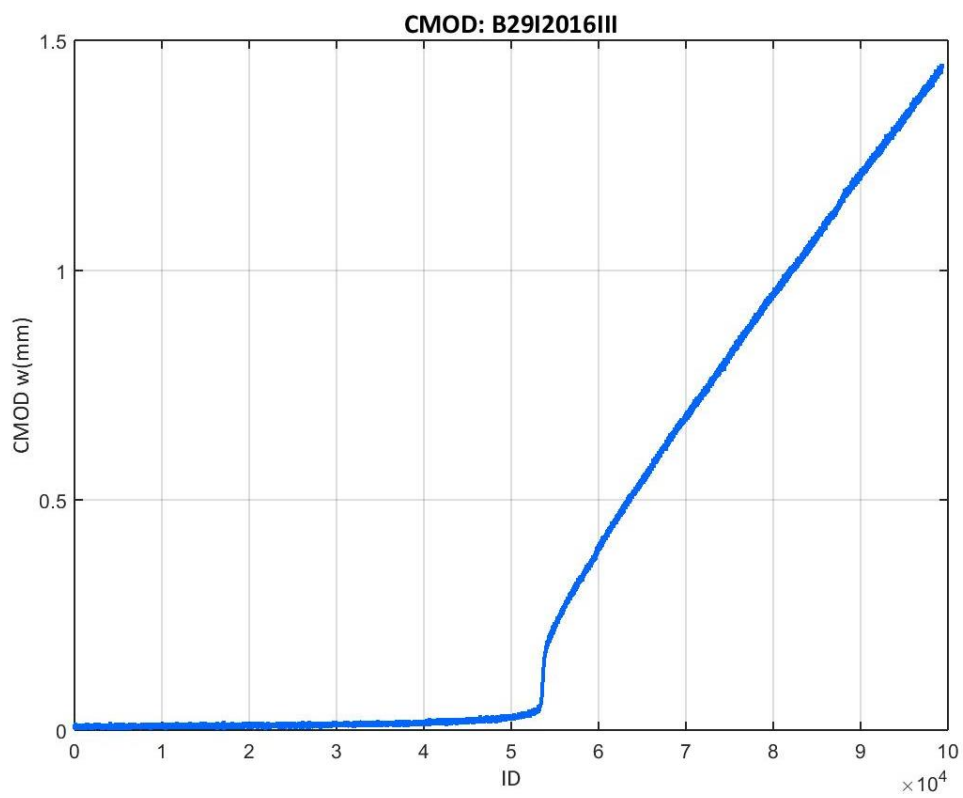


Figure 280: CMOD values recorded at the B29I2016III test

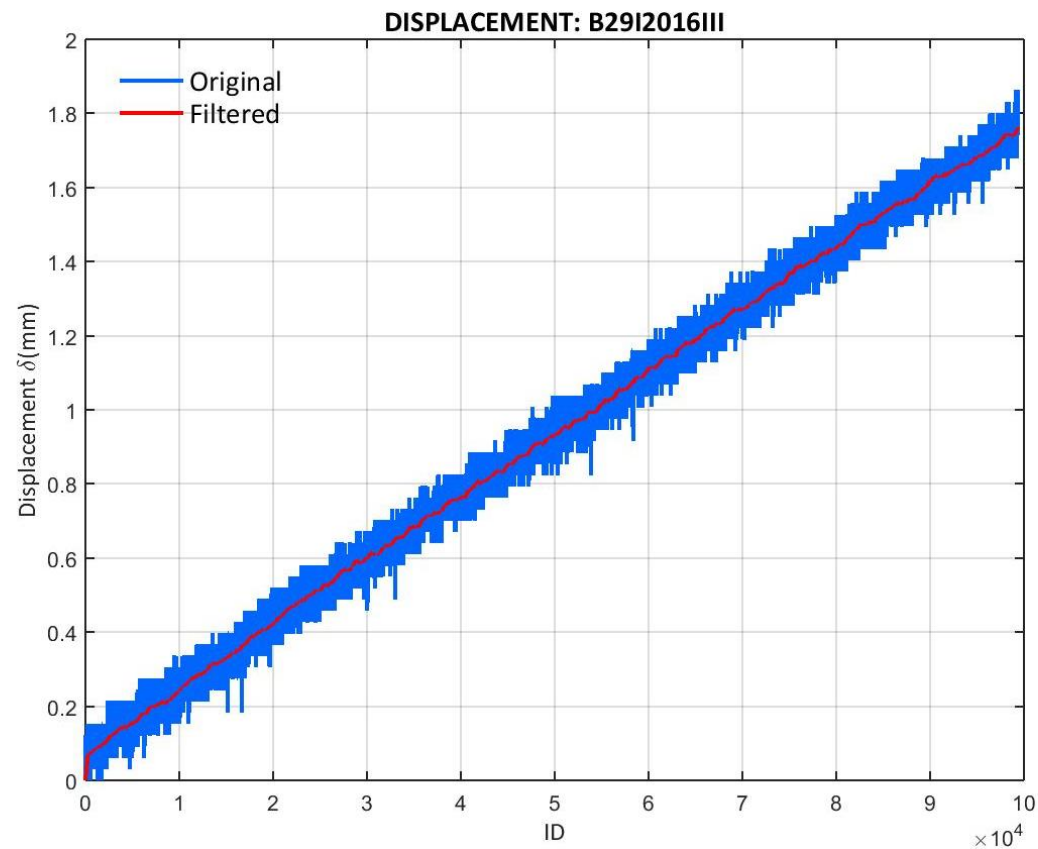


Figure 281: Displacement values recorded at the B29I2016III test

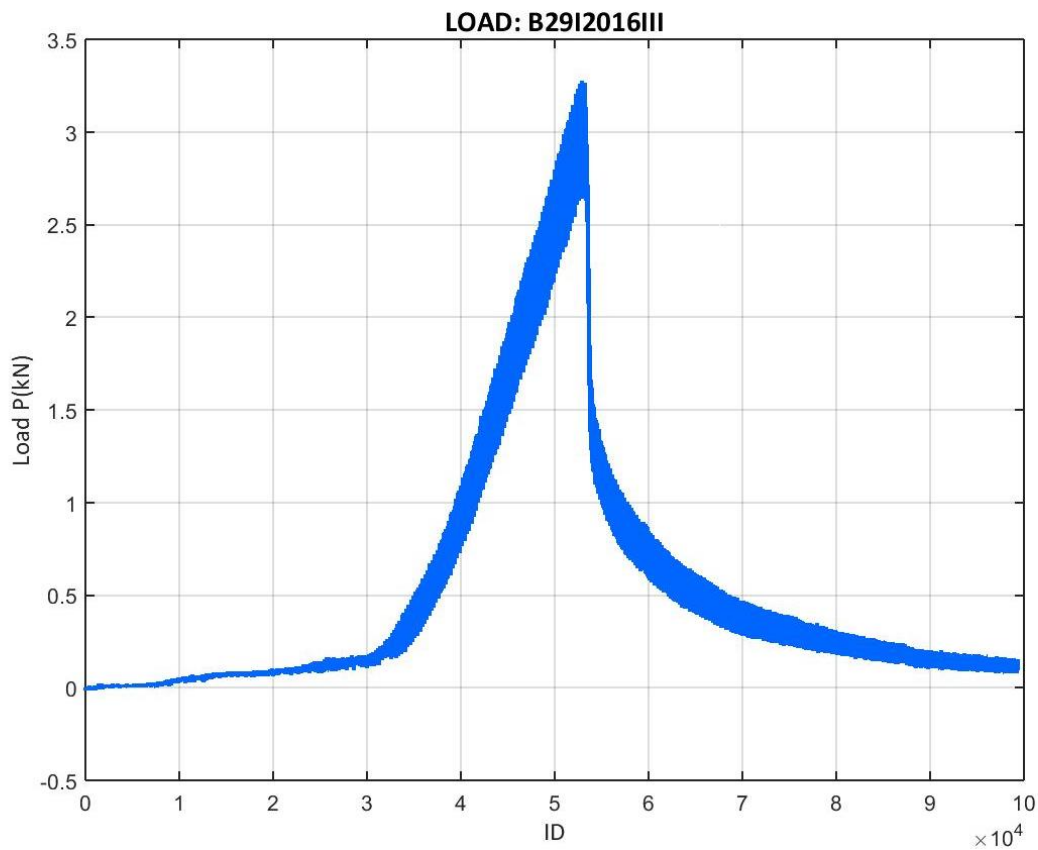


Figure 282: Load values recorded at the B29I2016III test

- B29I2016IV

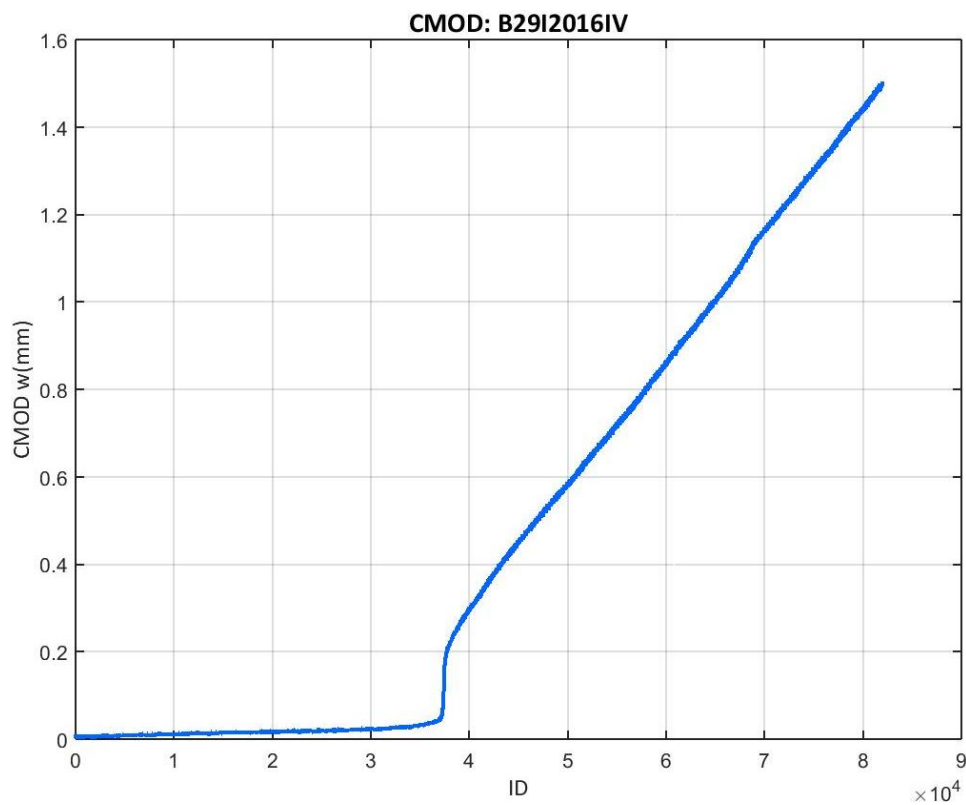


Figure 283: CMOD values recorded at the B29I2016IV test

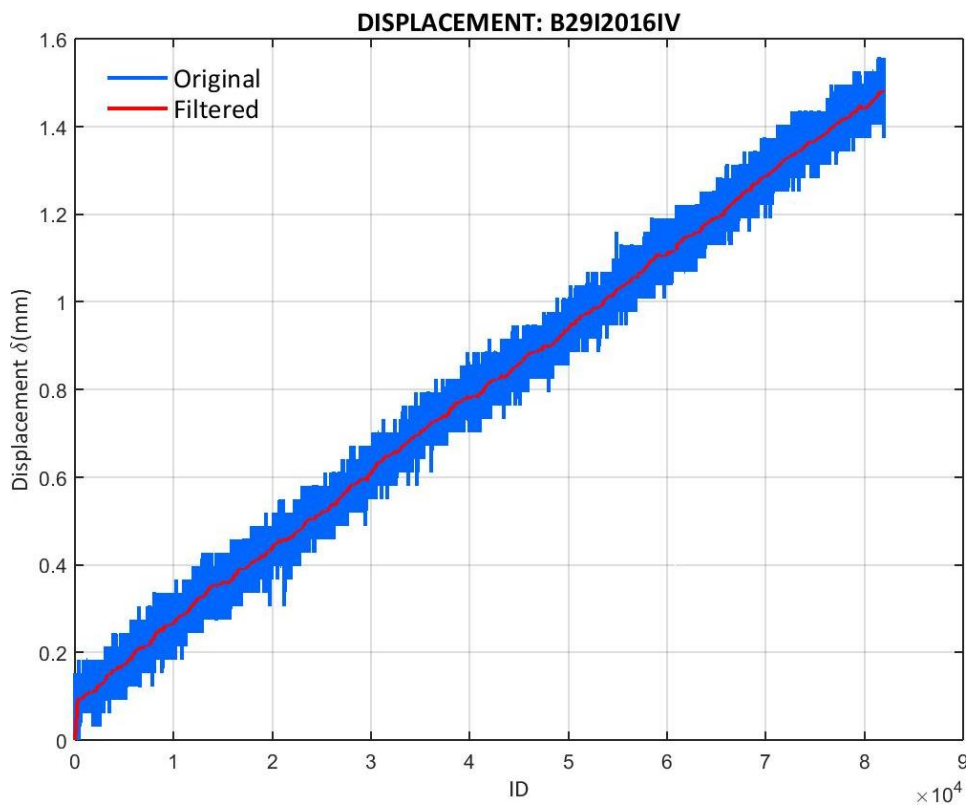


Figure 284: Displacement values recorded at the B29I2016IV test

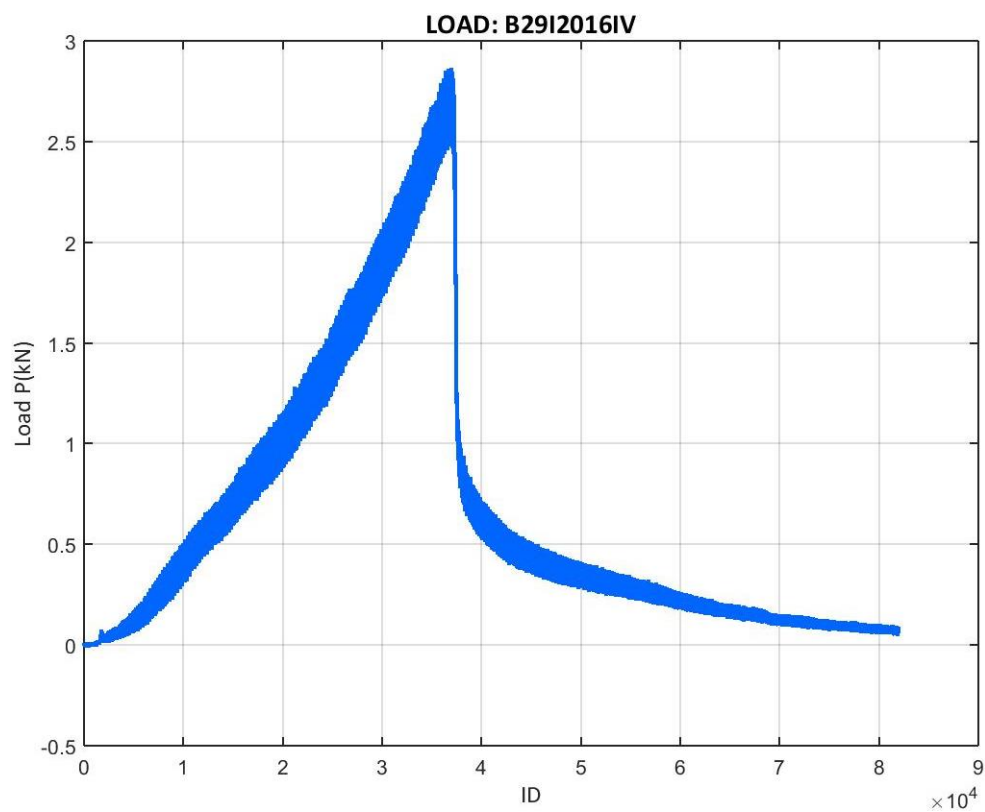


Figure 285: Load values recorded at the B29I2016IV test

- B29I2016V

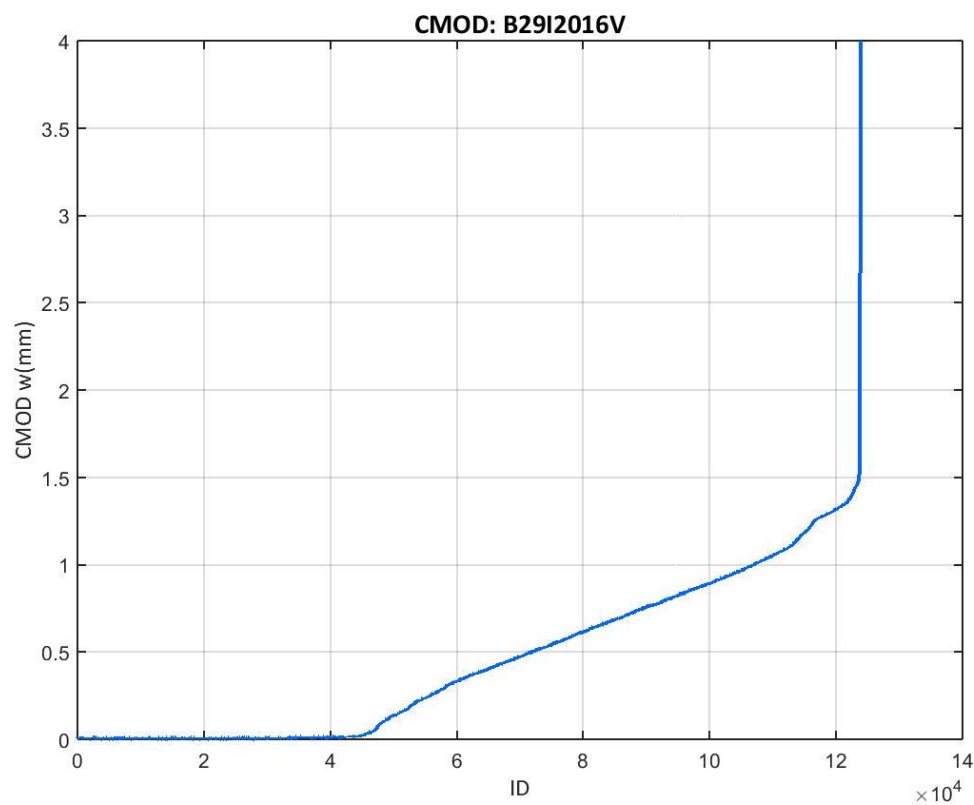


Figure 286: CMOD values recorded at the B29I2016V test

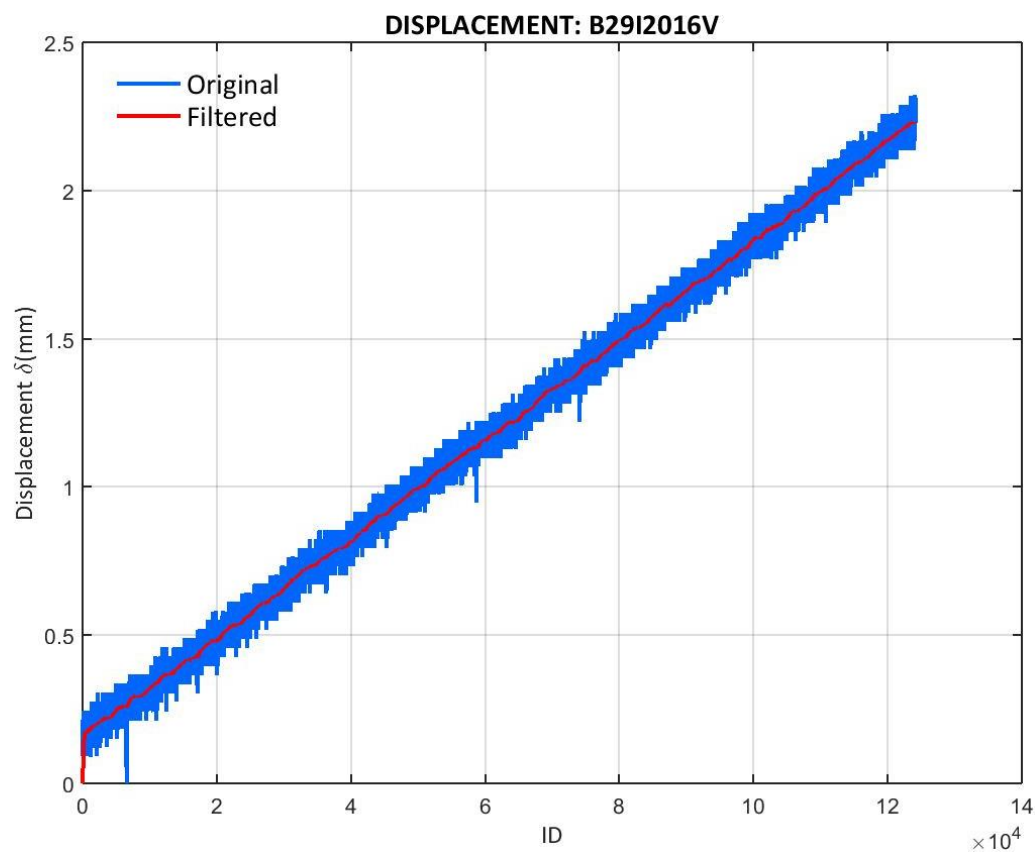


Figure 287: Displacement values recorded at the B29I2016V test

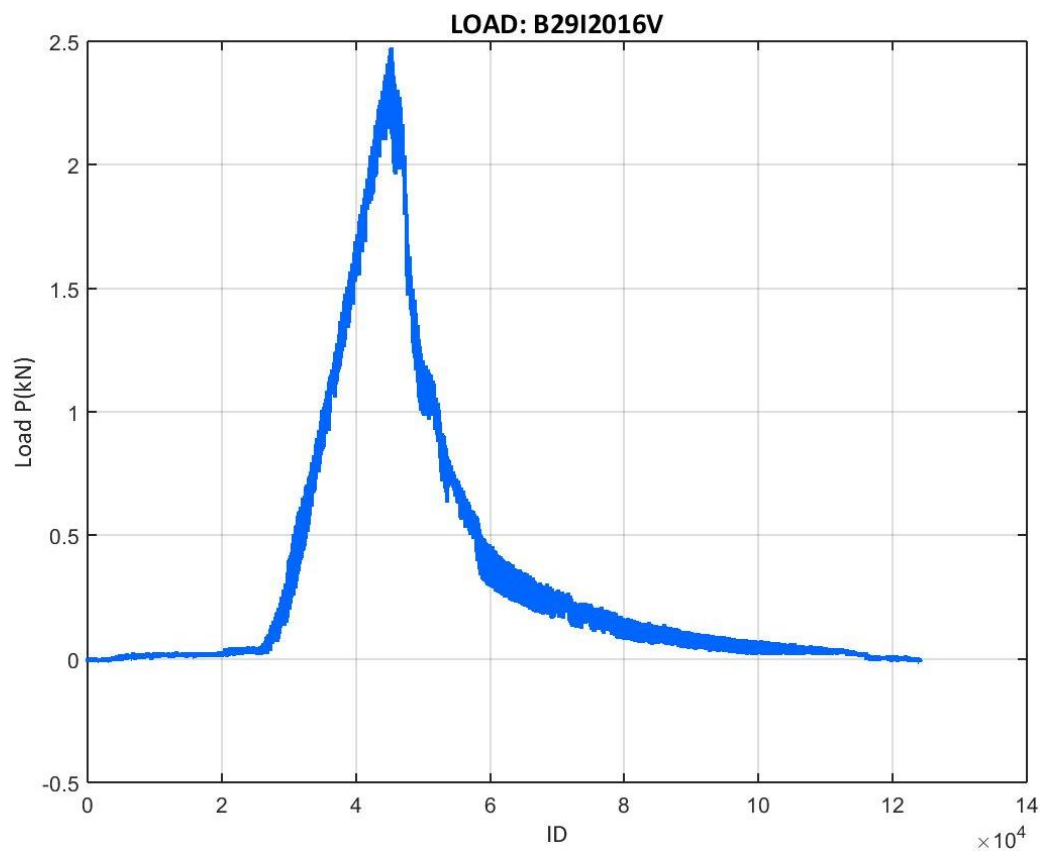


Figure 288: Load values recorded at the B29I2016V test

- B29I2016VI

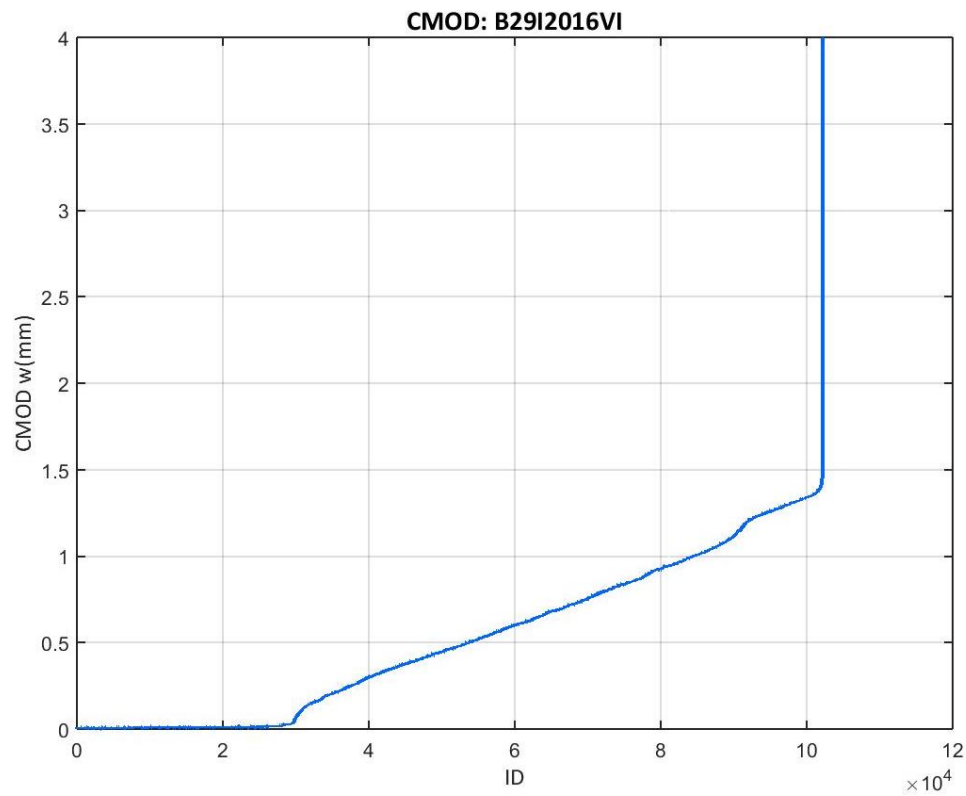


Figure 289: CMOD values recorded at the B29I2016VI test

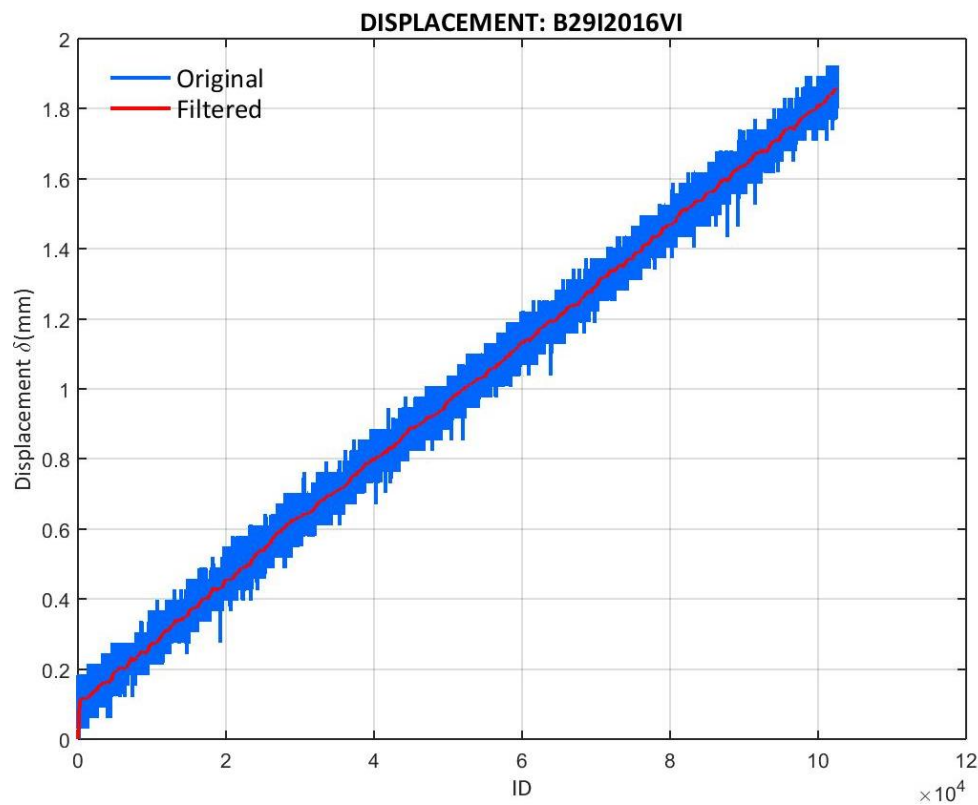


Figure 290: Displacement values recorded at the B29I2016VI test

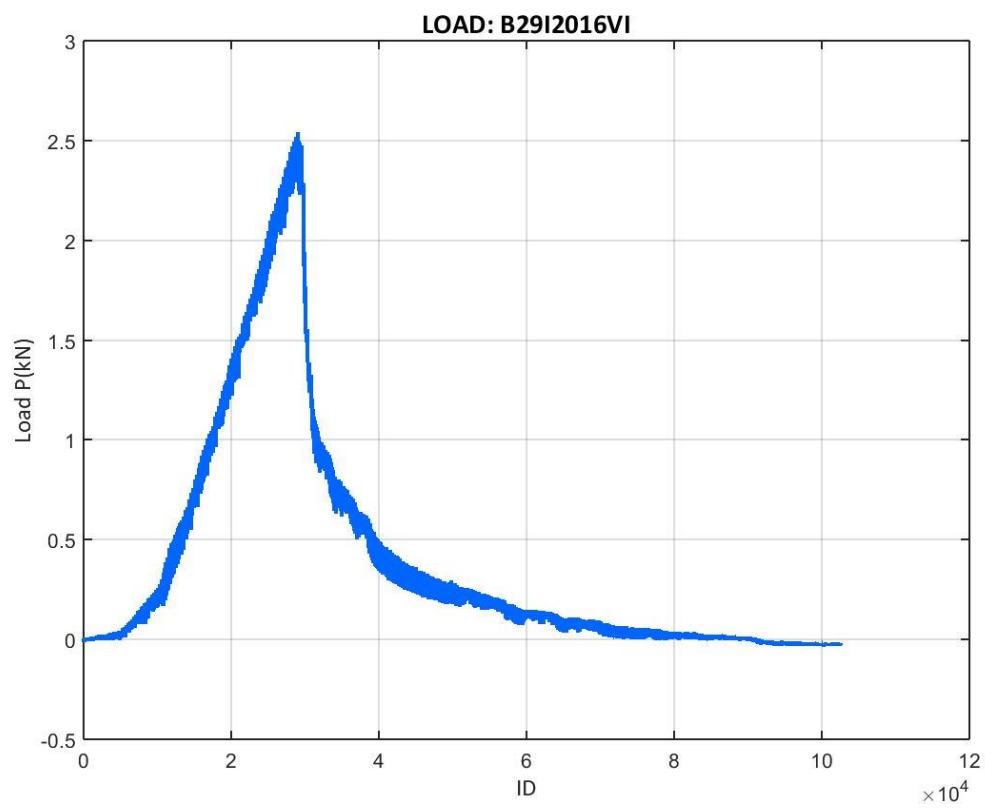


Figure 291: Load values recorded at the B29I2016VI test

- B29I2016VII

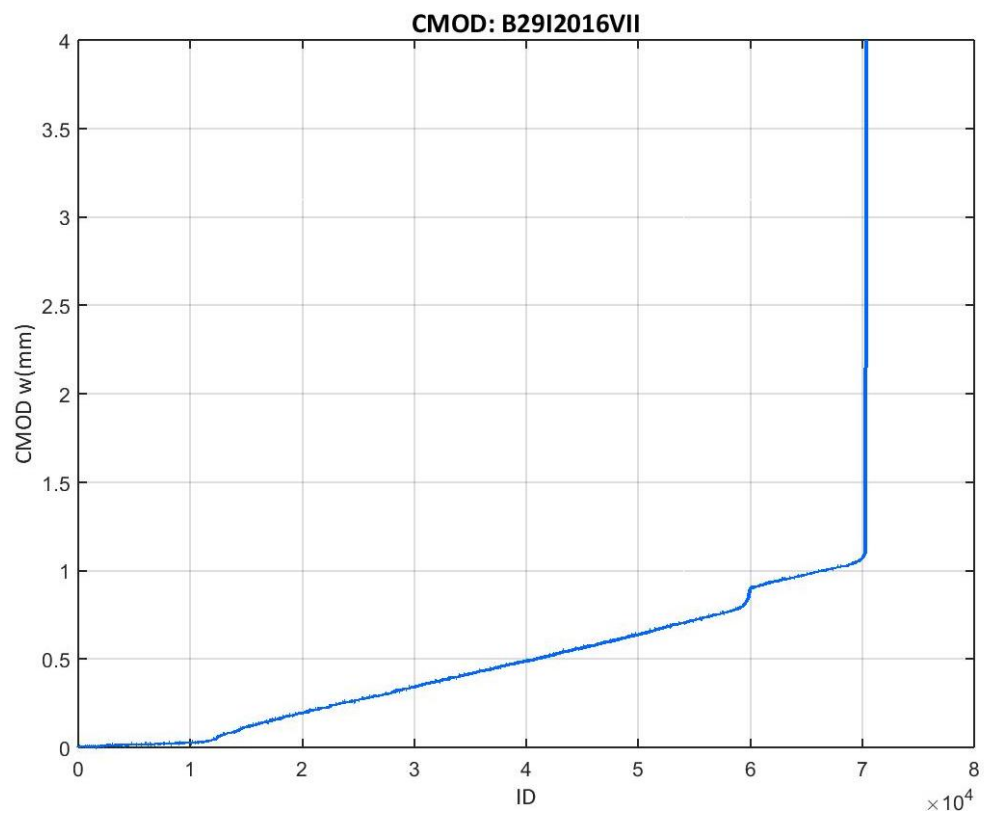


Figure 292: CMOD values recorded at the B29I2016VII test

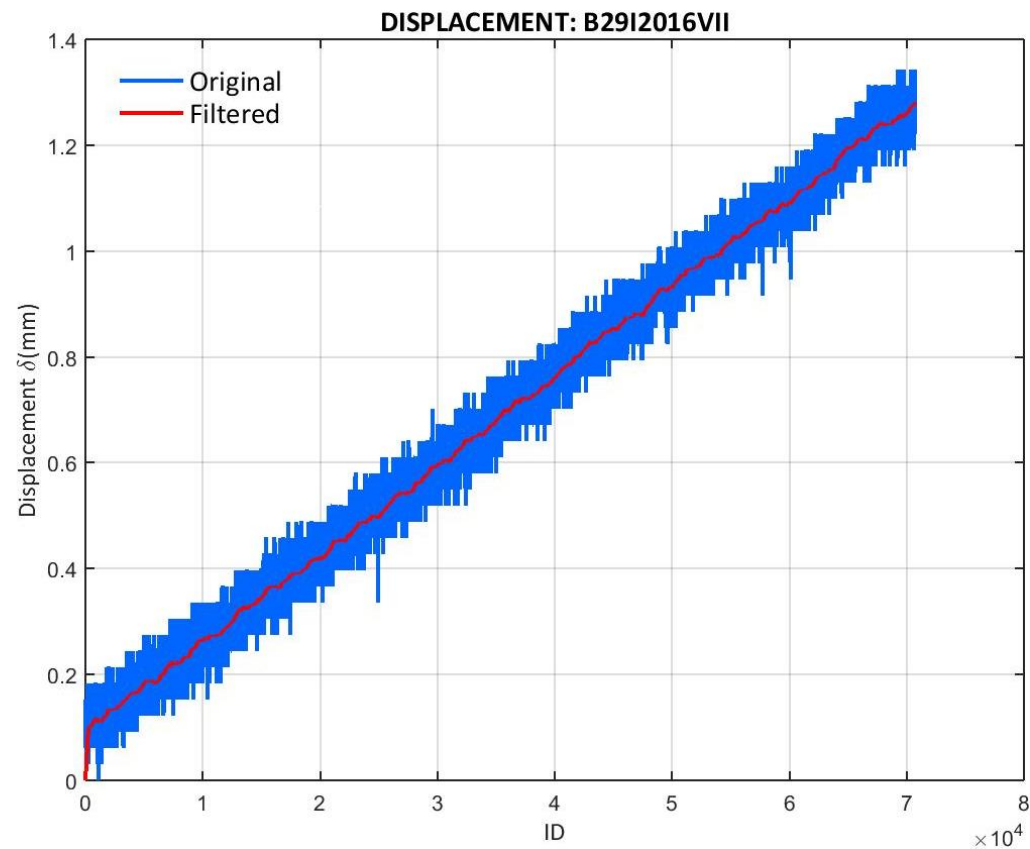


Figure 293: Displacement values recorded at the B29I2016VII test

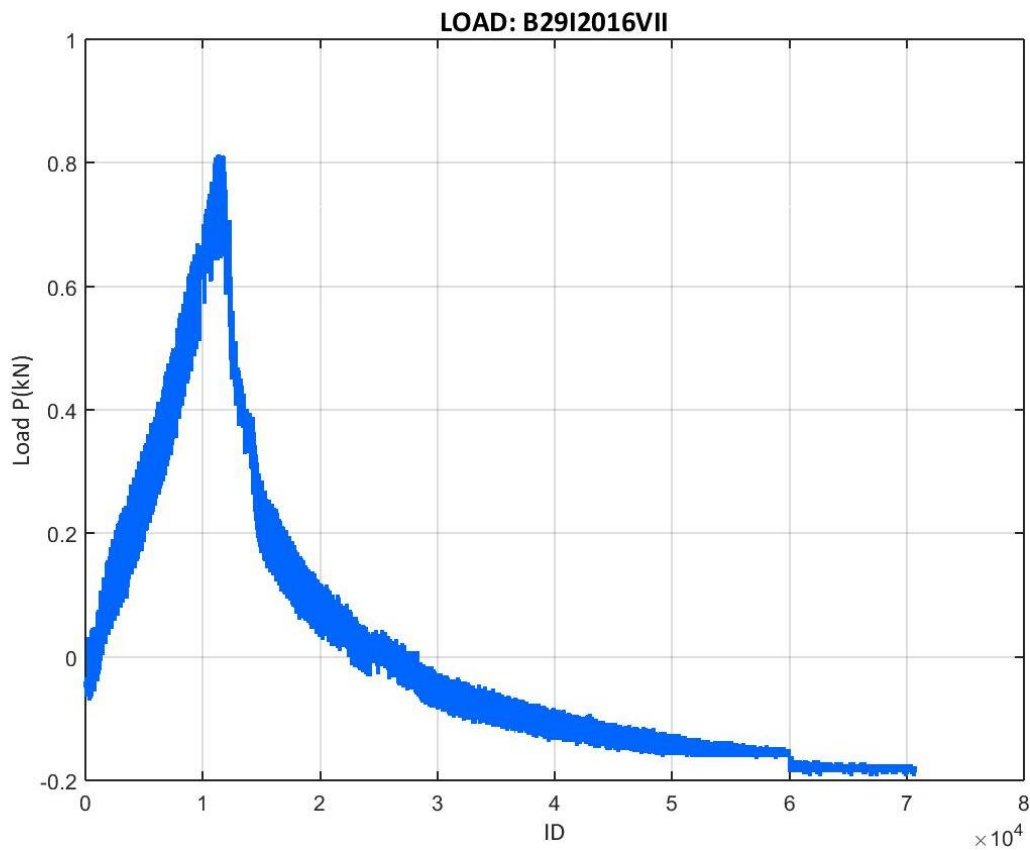


Figure 294: Load values recorded at the B29I2016VII test

- B29I2016VIII

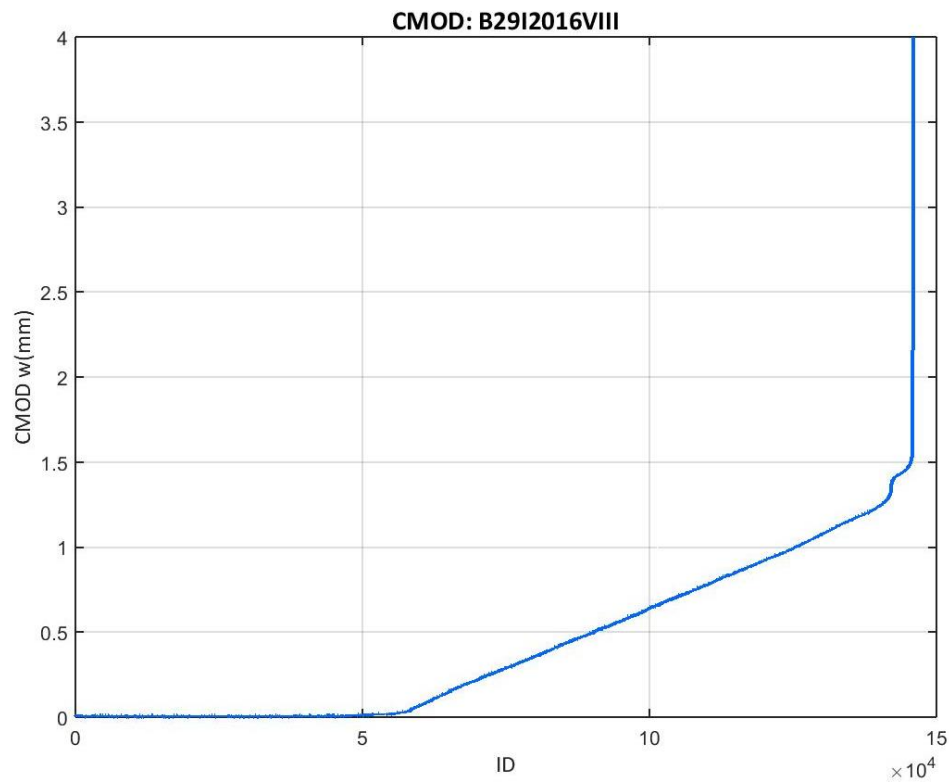


Figure 295: CMOD values recorded at the B29I2016VIII test

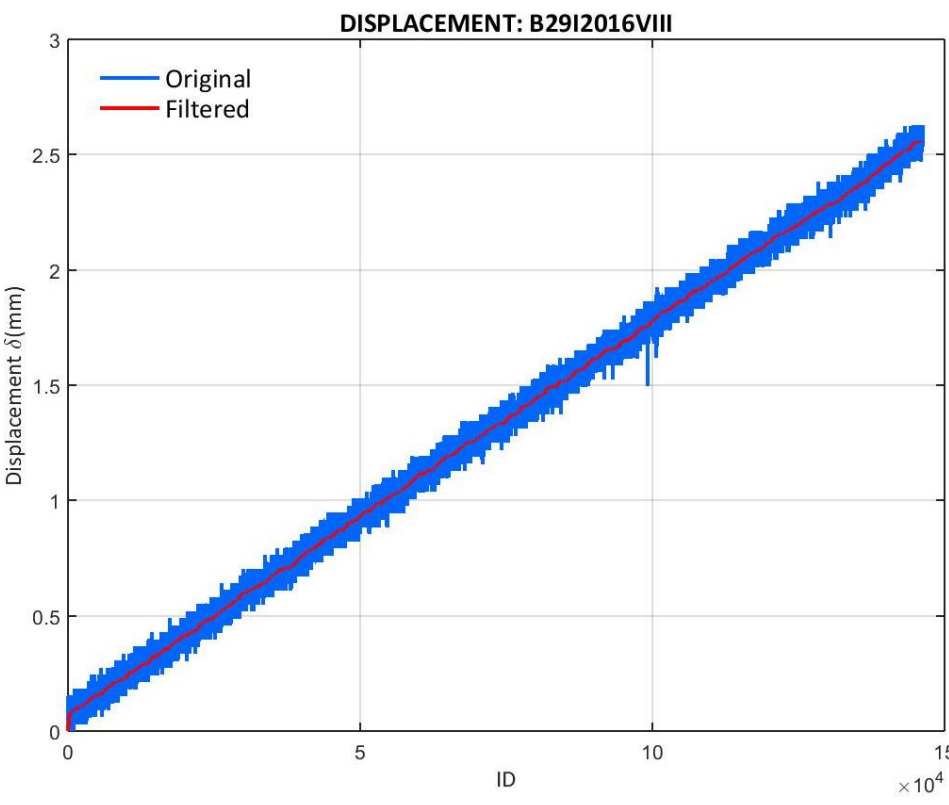


Figure 296: Displacement values recorded at the B29I2016VIII test

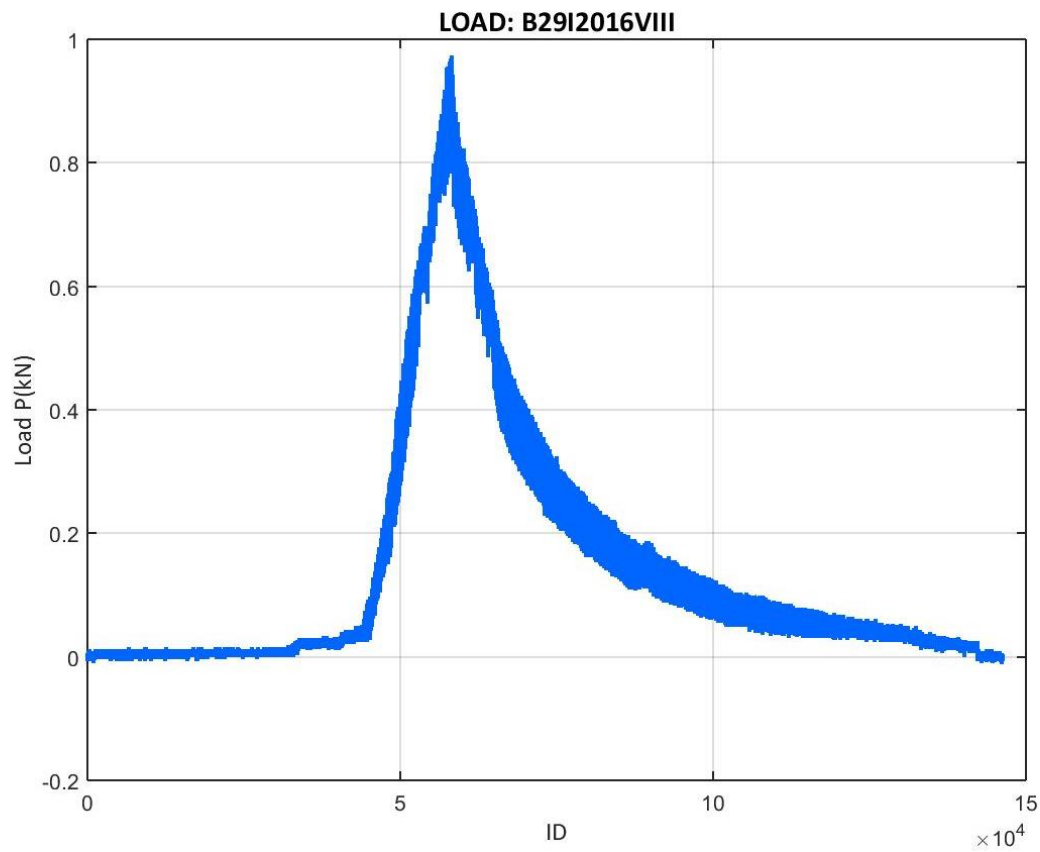


Figure 297: Load values recorded at the B29I2016VIII test

E.5.2 29I2016 CORRECTED LOAD VS. CMOD

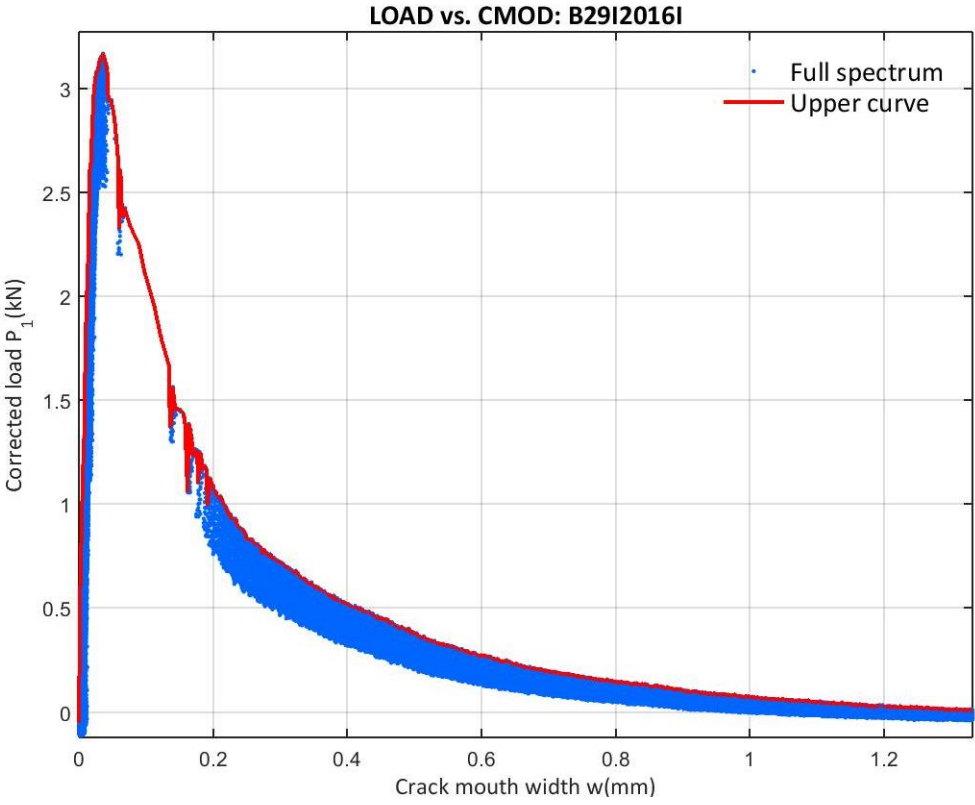


Figure 298: Corrected load vs. CMOD at the B29I2016I test

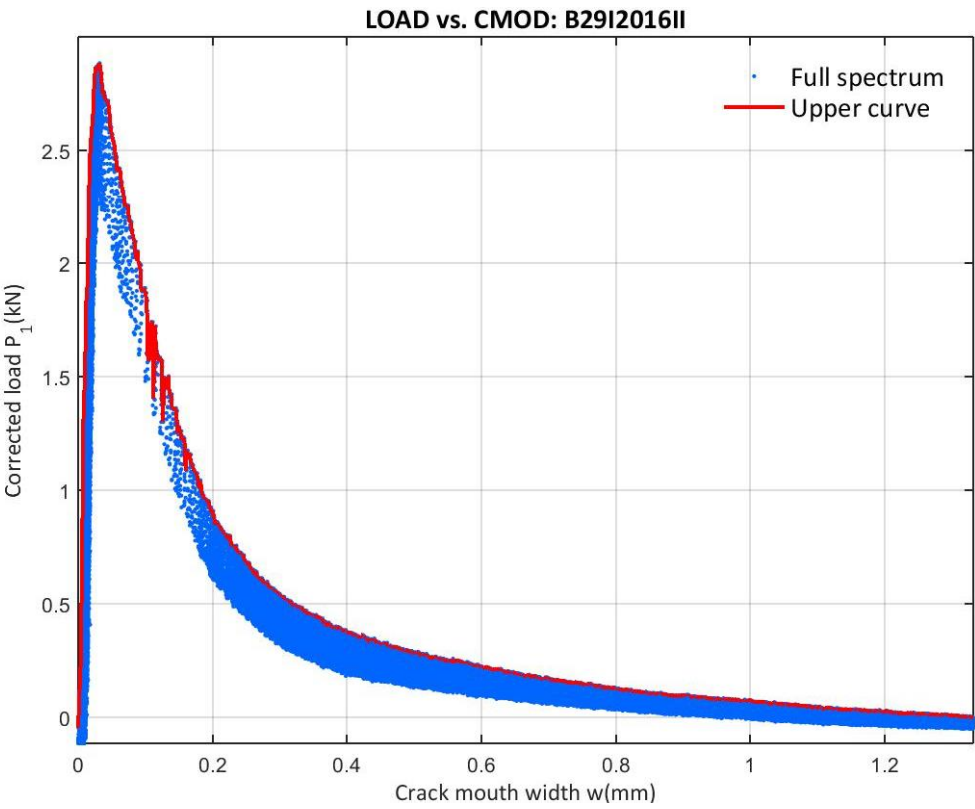


Figure 299: Corrected load vs. CMOD at the B29I2016II test

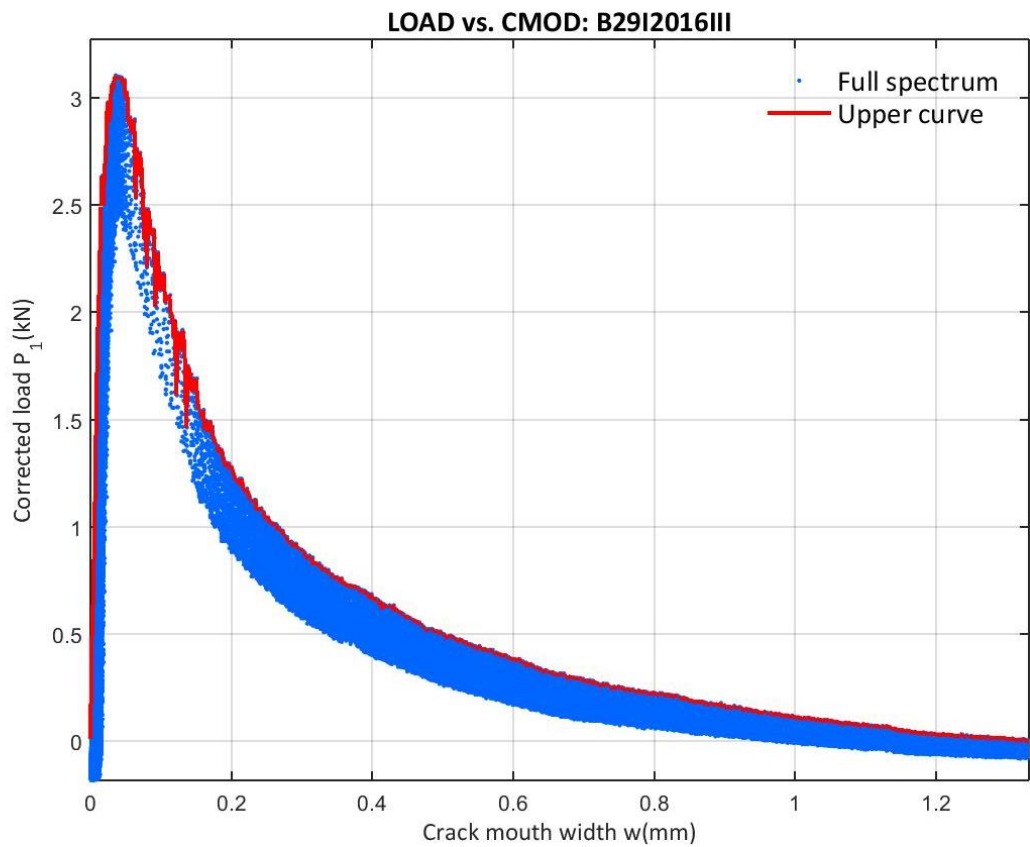


Figure 300: Corrected load vs. CMOD at the B29I2016III test

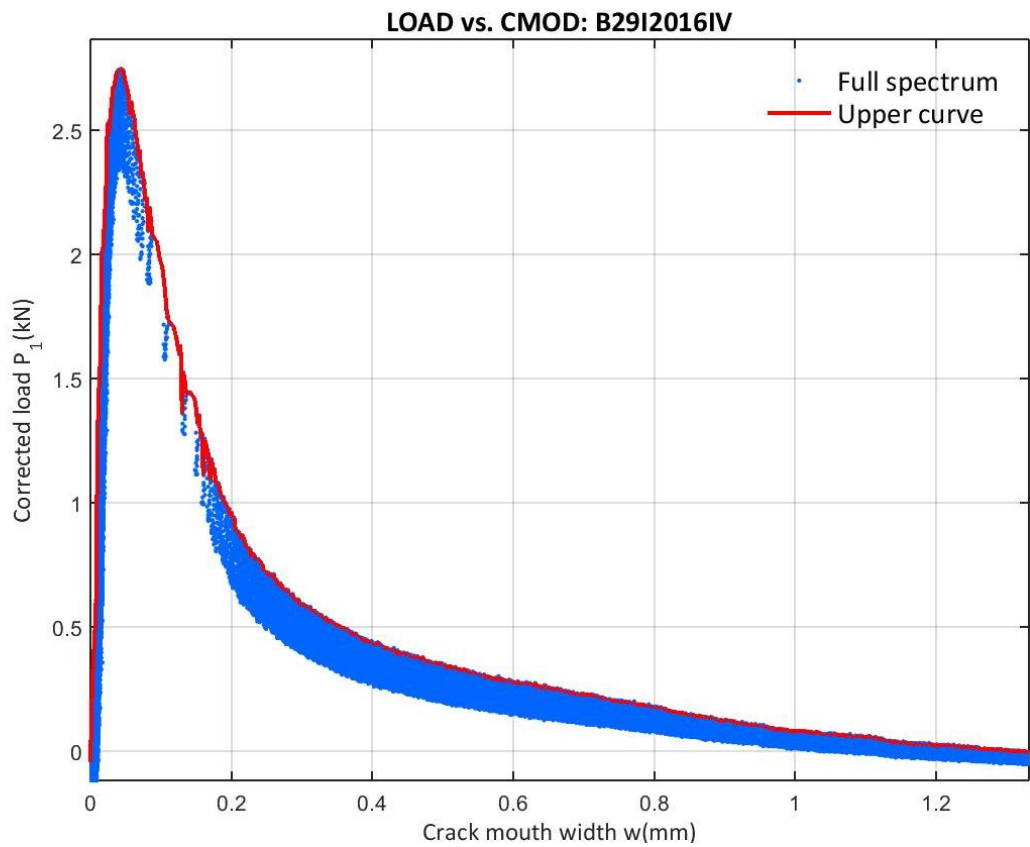


Figure 301: Corrected load vs. CMOD at the B29I2016IV test

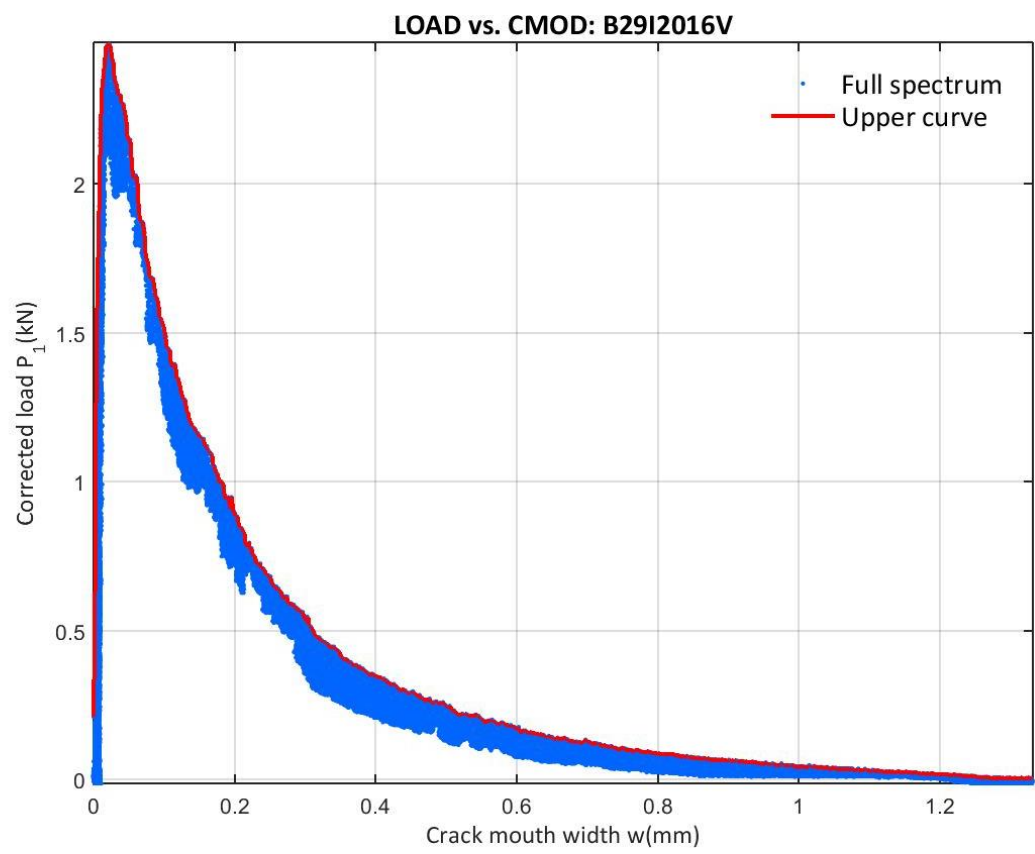


Figure 302: Corrected load vs. CMOD at the B29I2016V test

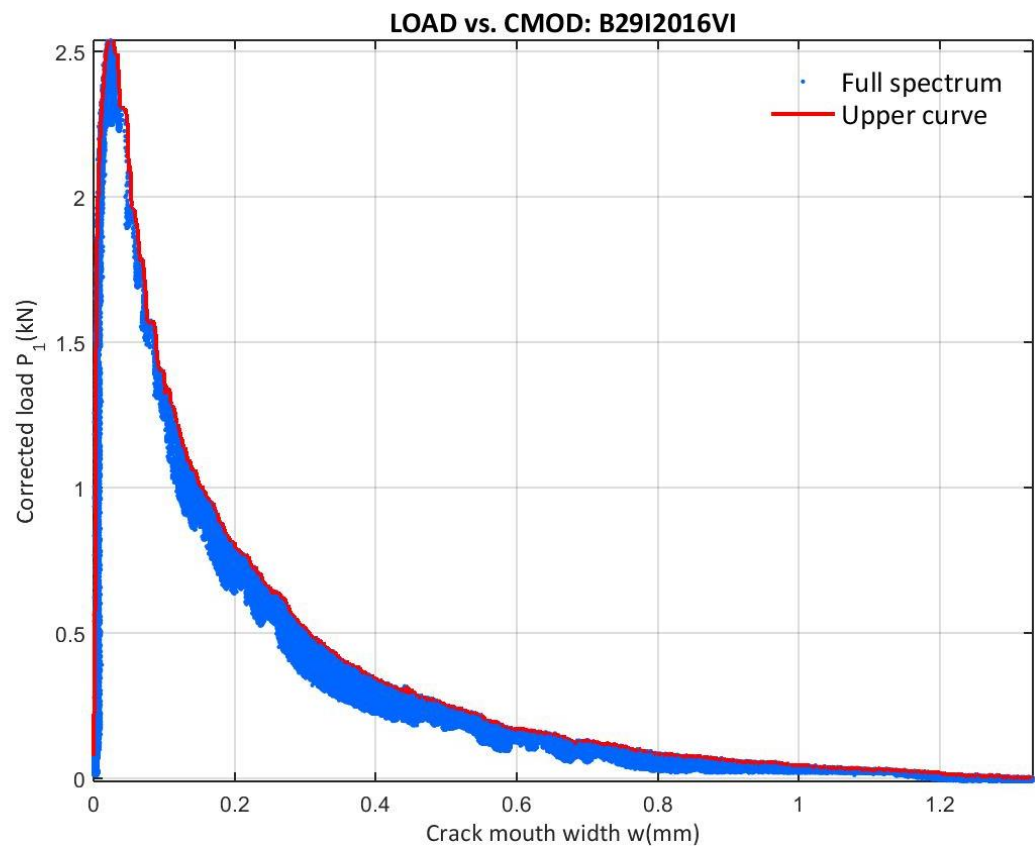


Figure 303: Corrected load vs. CMOD at the B29I2016VI test

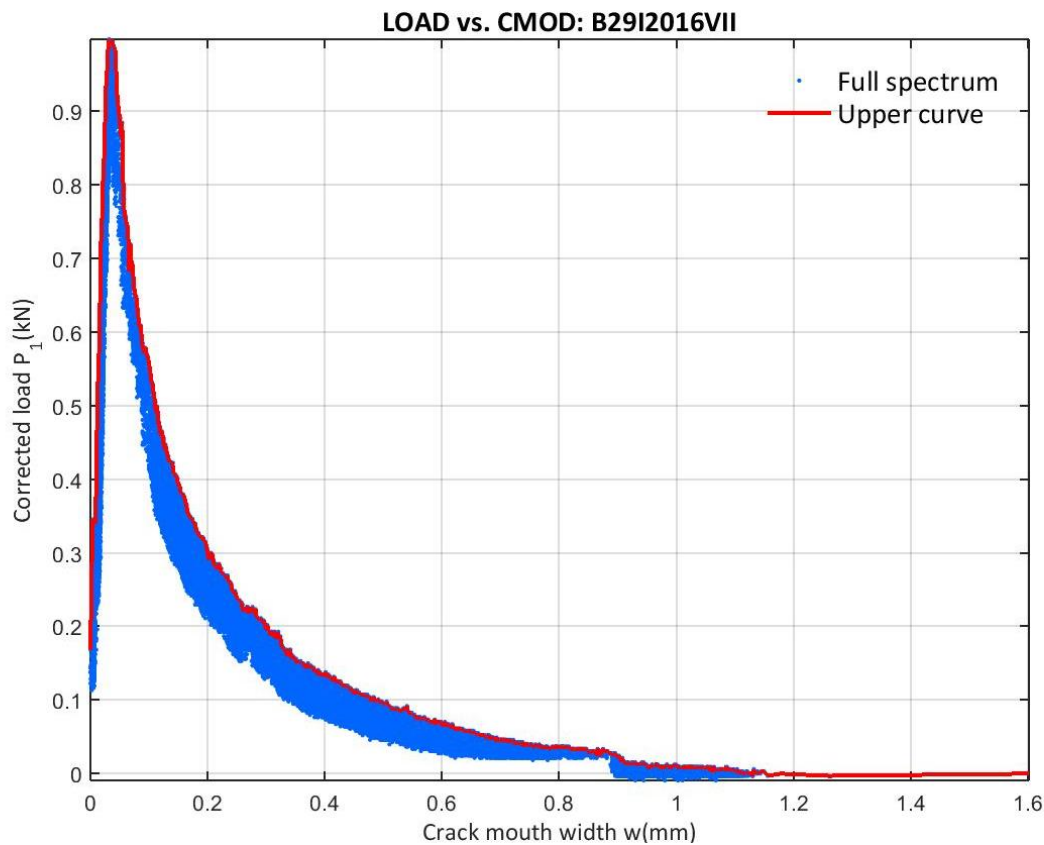


Figure 304: Corrected load vs. CMOD at the B29I2016VII test

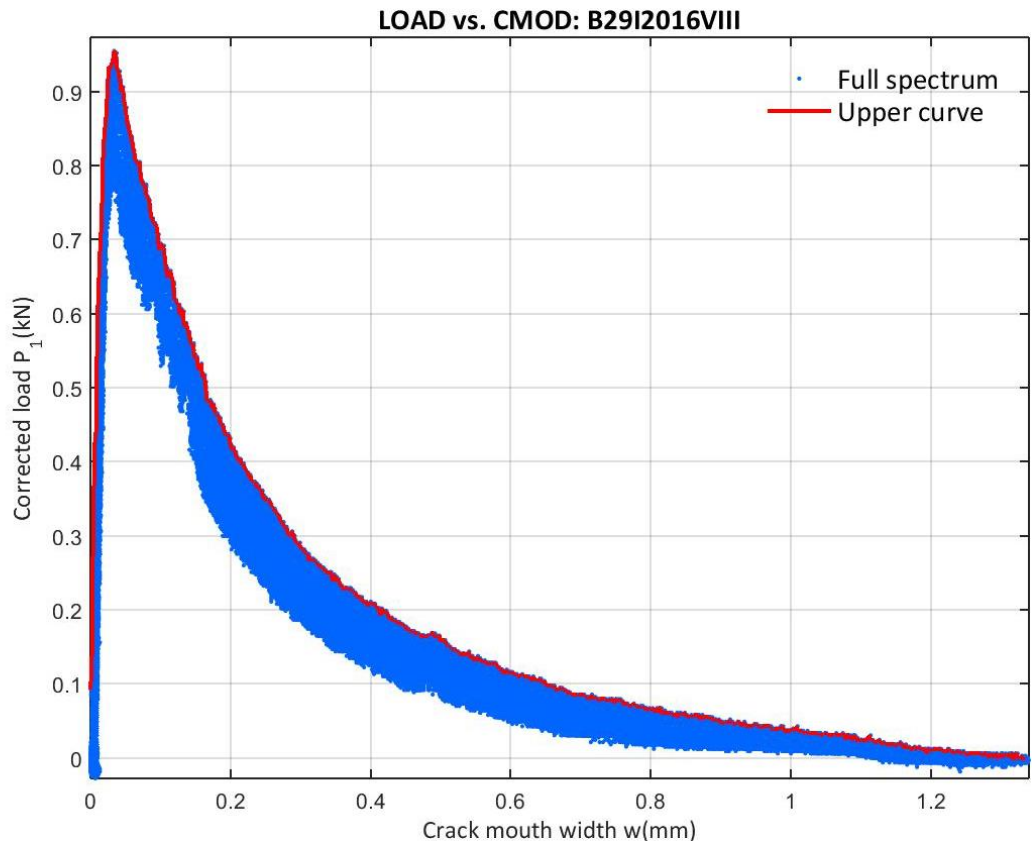


Figure 305: Corrected load vs. CMOD at the B29I2016VIII test

E.5.3 29I2016 CORRECTED LOAD VS. VERTICAL DISPLACEMENT

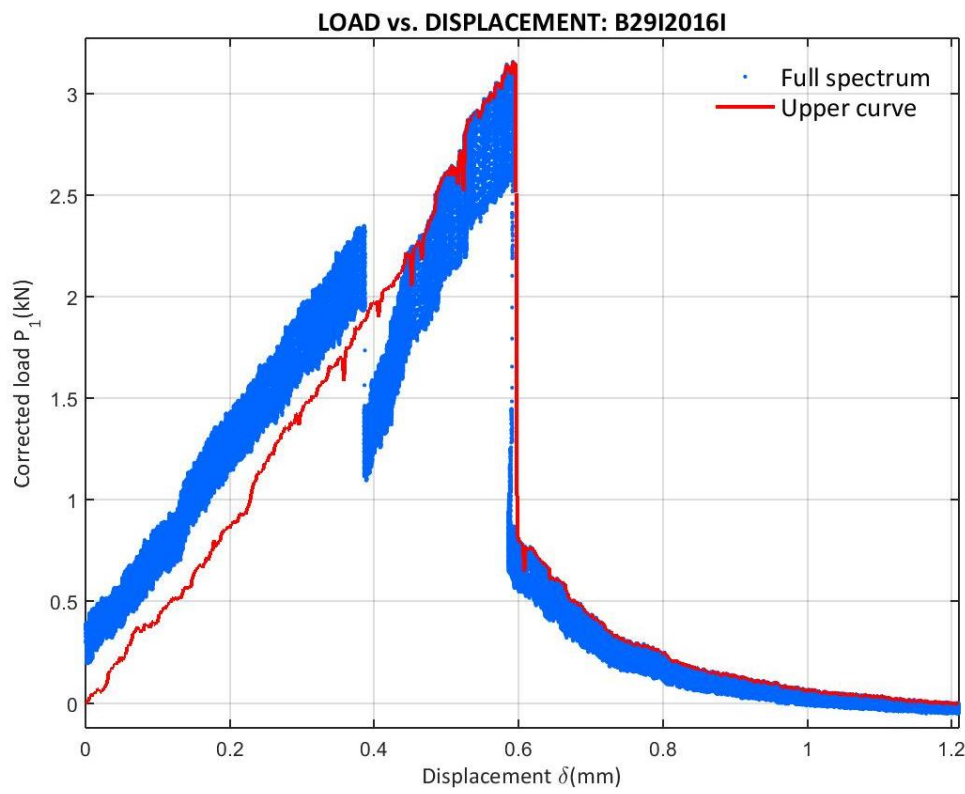


Figure 306: Corrected load vs. Displacement at the B29I2016I test

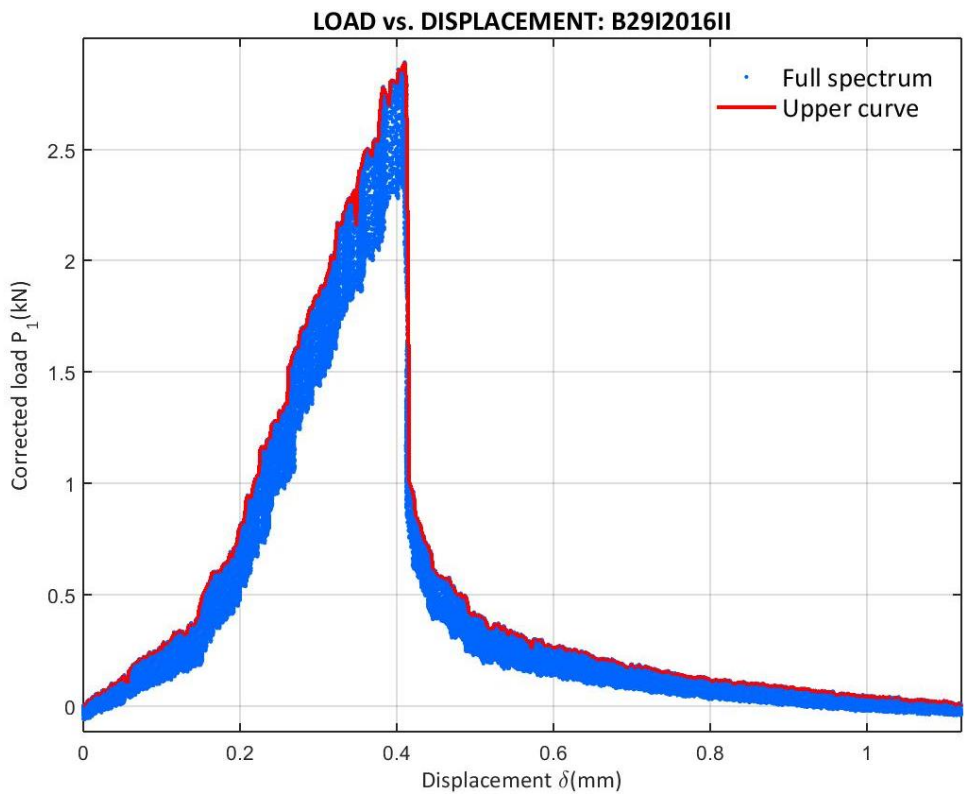


Figure 307: Corrected load vs. Displacement at the B29I2016II test

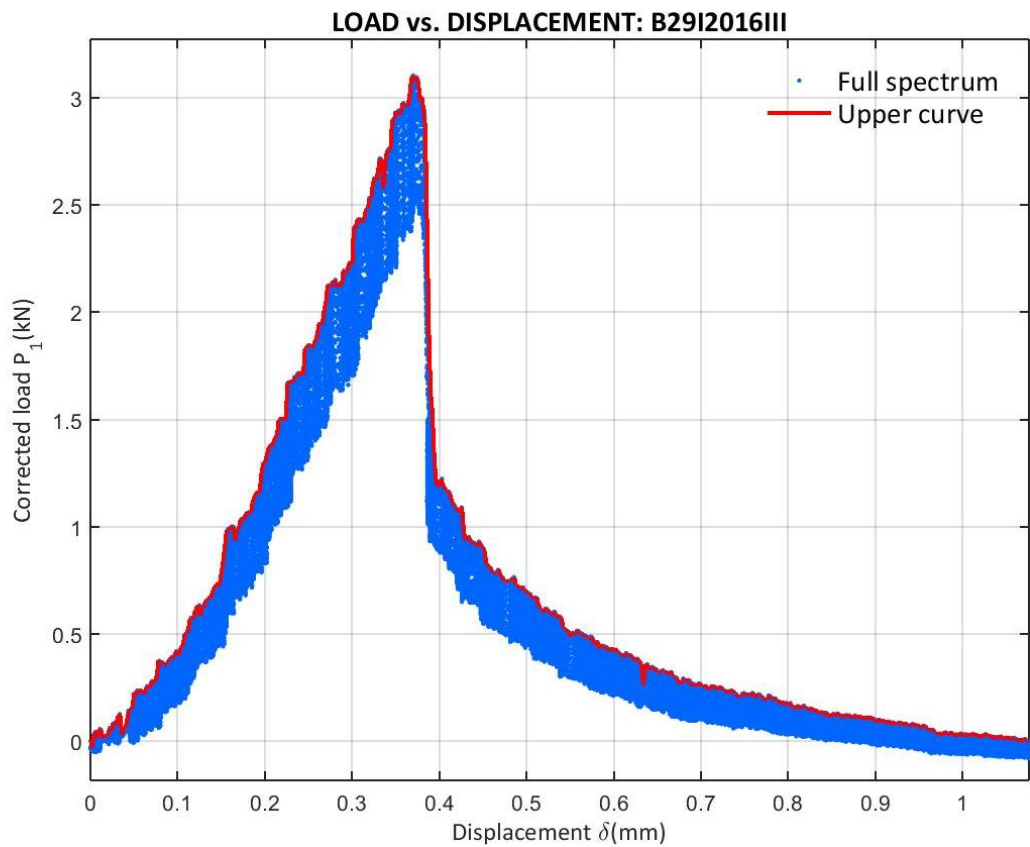


Figure 308: Corrected load vs. Displacement at the B29I2016III test

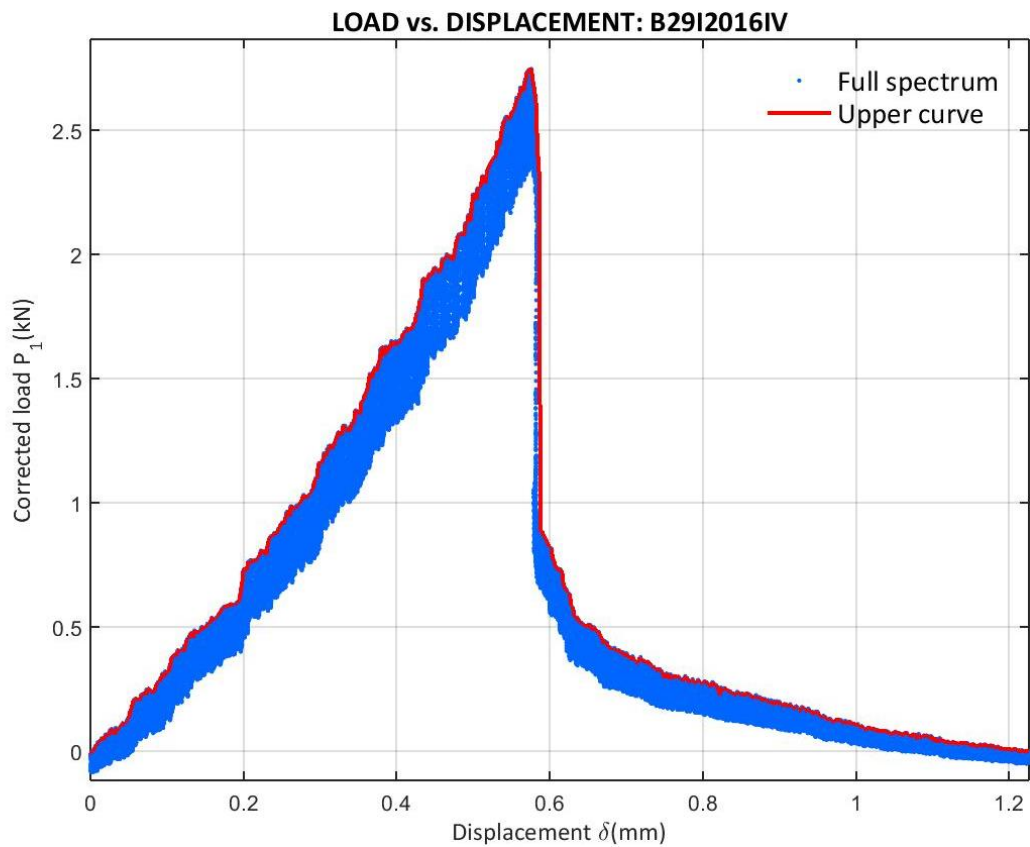


Figure 309: Corrected load vs. Displacement at the B29I2016IV test

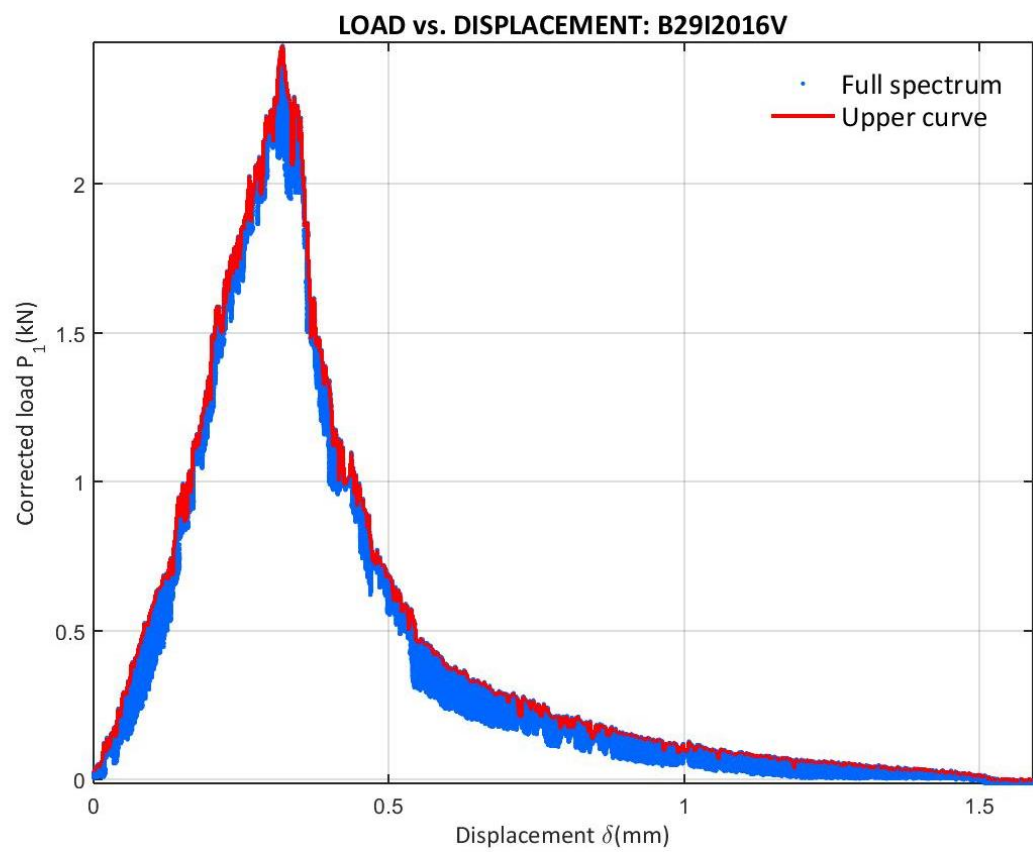


Figure 310: Corrected load vs. Displacement at the B29I2016V test

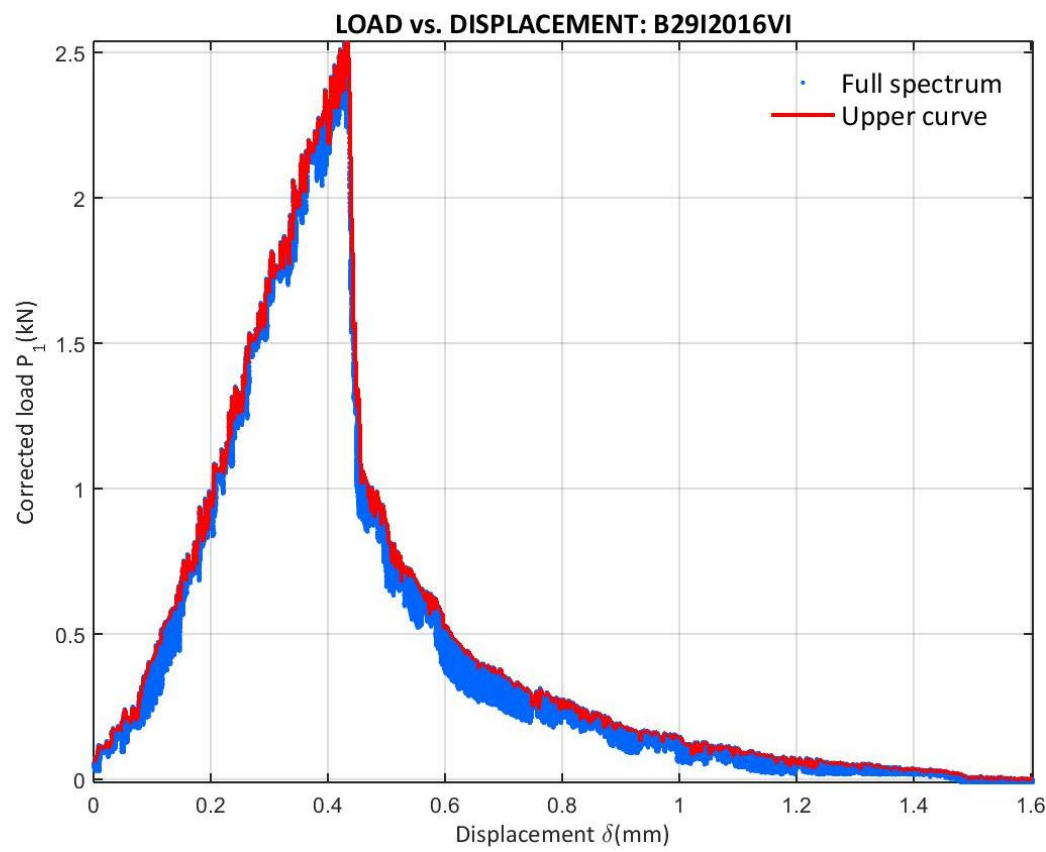


Figure 311: Corrected load vs. Displacement at the B29I2016VI test

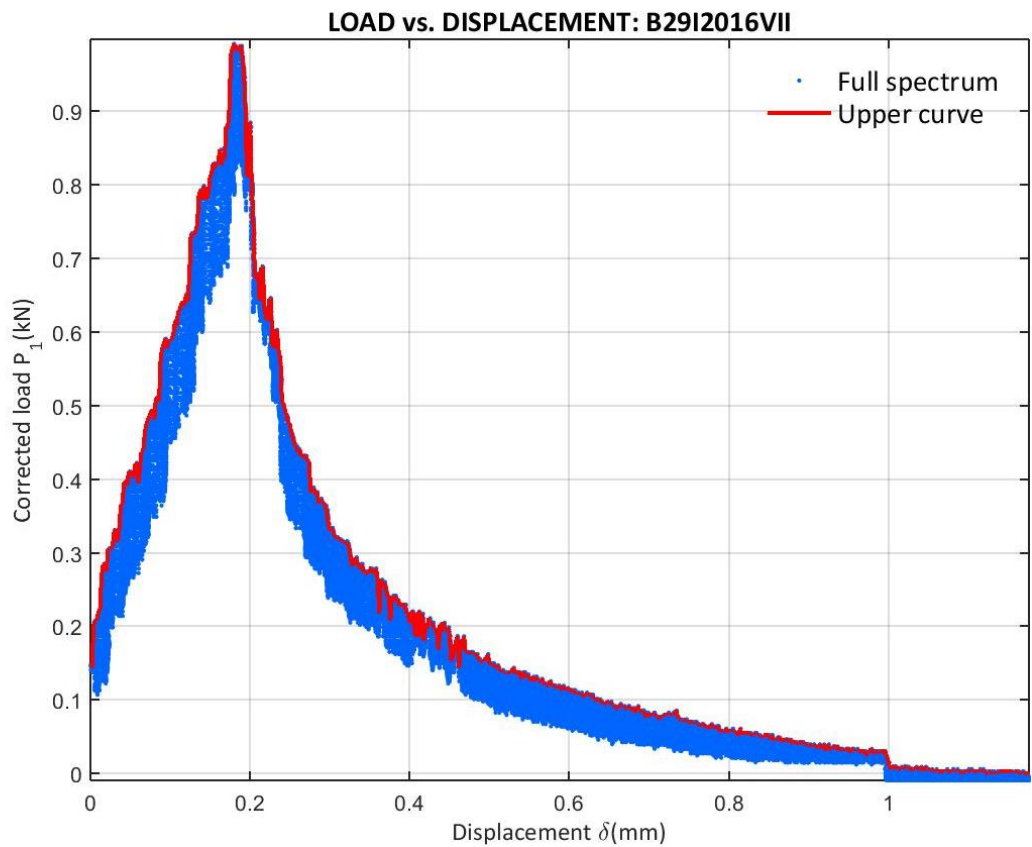


Figure 312: Corrected load vs. Displacement at the B29I2016VII test

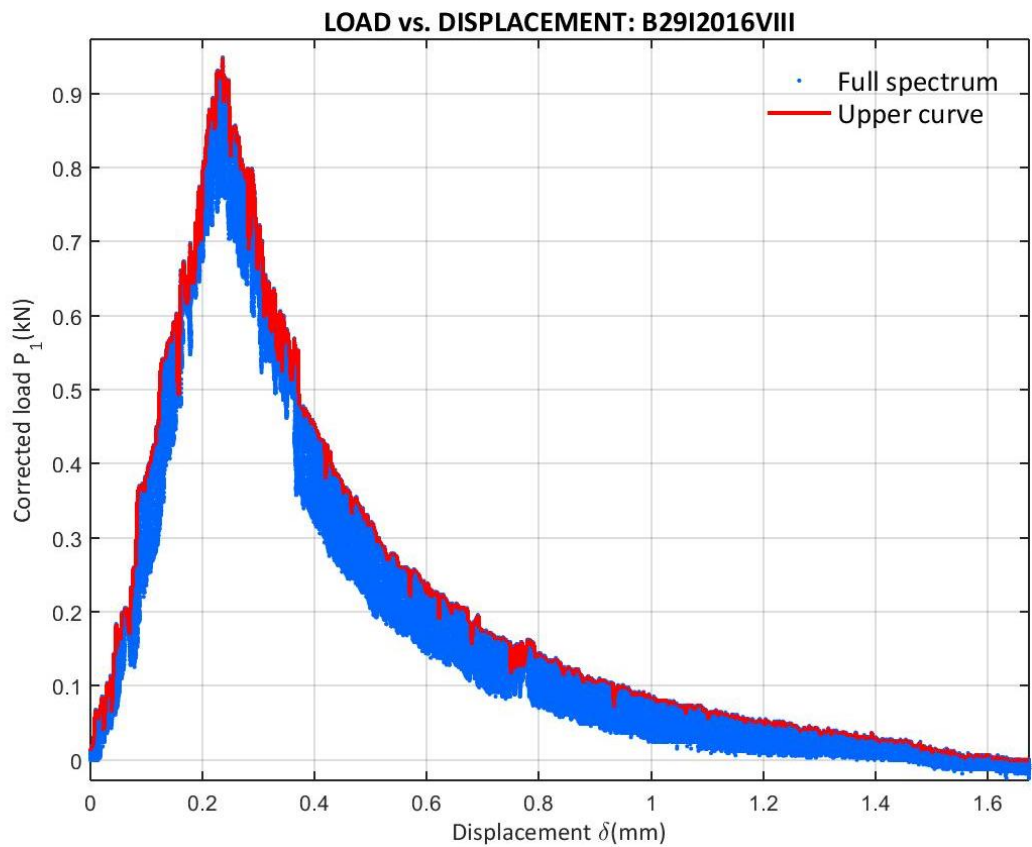


Figure 313: Corrected load vs. Displacement at the B29I2016VIII test

E.5.4 29I2016 CORRECTED LOAD VS. X

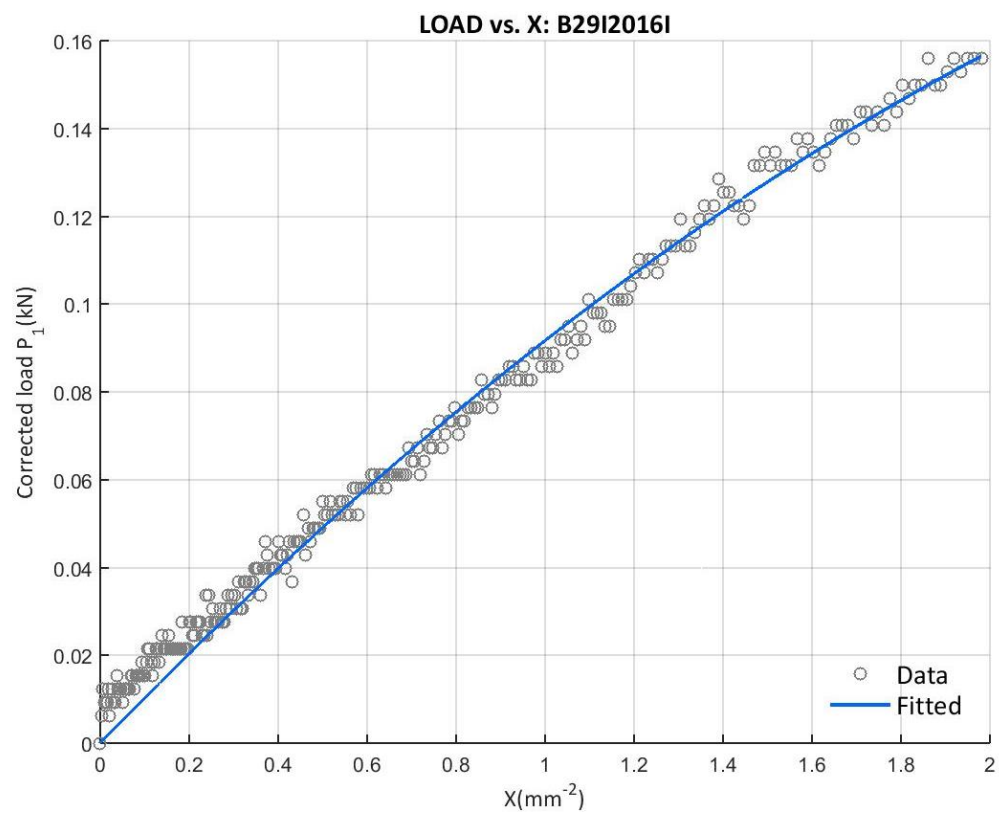


Figure 314: Corrected load vs. X at the B29I2016I test with the final upper curve data

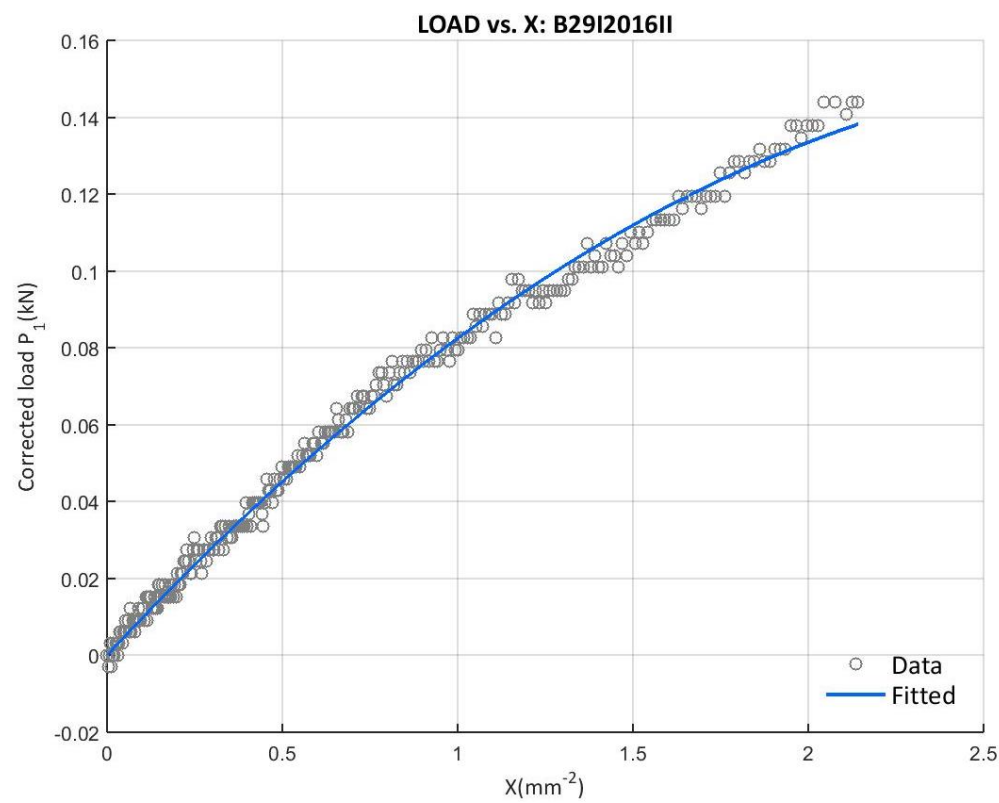


Figure 315: Corrected load vs. X at the B29I2016II test with the final upper curve data

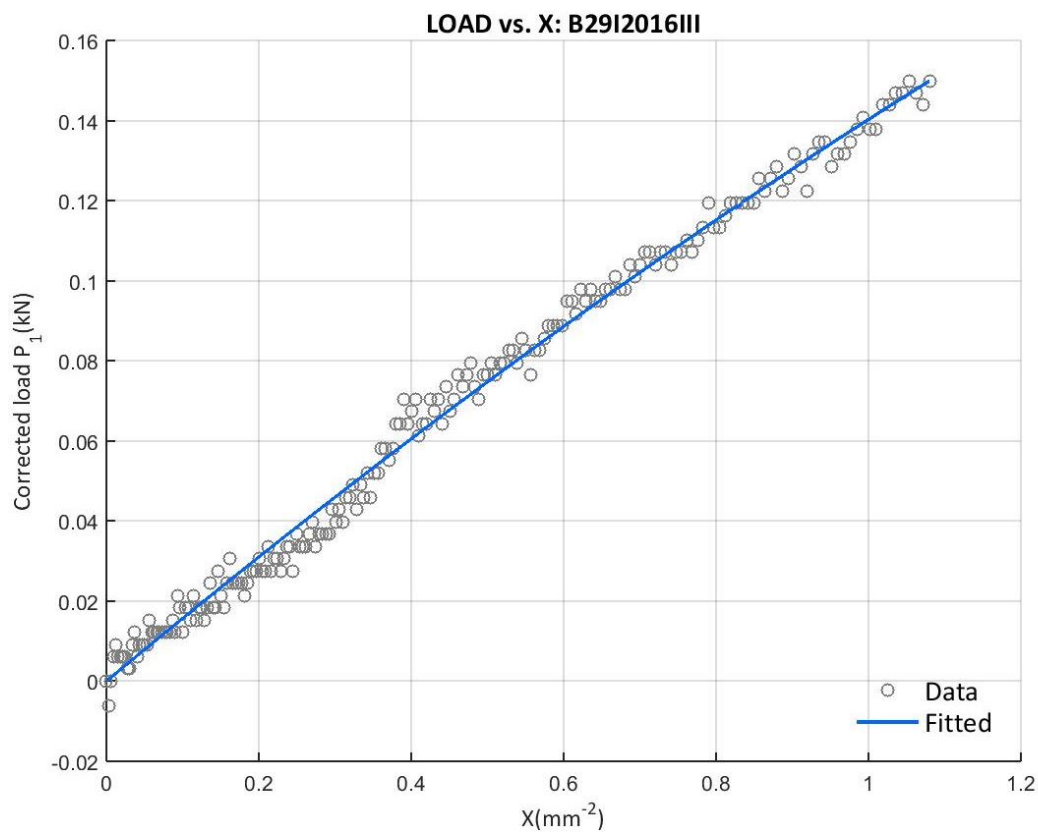


Figure 316: Corrected load vs. X at the B29I2016III test with the final upper curve data

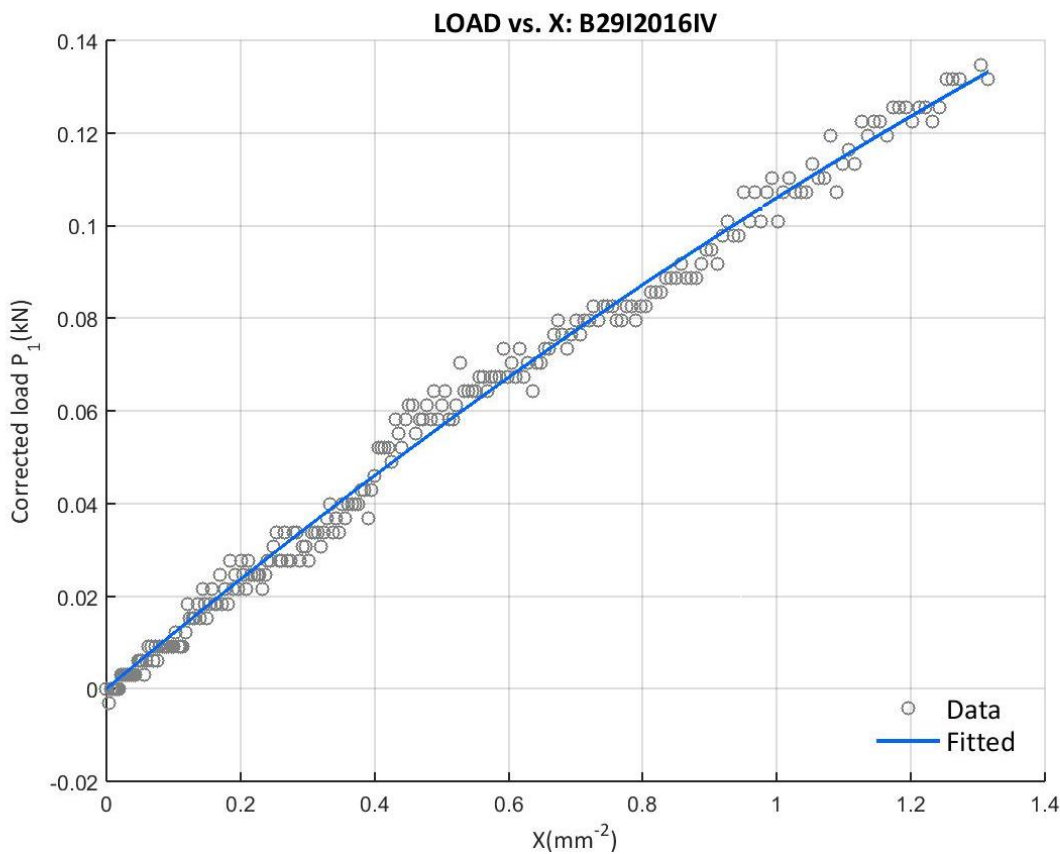


Figure 317: Corrected load vs. X at the B29I2016IV test with the final upper curve data

E.5.5 29I2016 SOFTENING CURVE BILINEAR APPROXIMATION

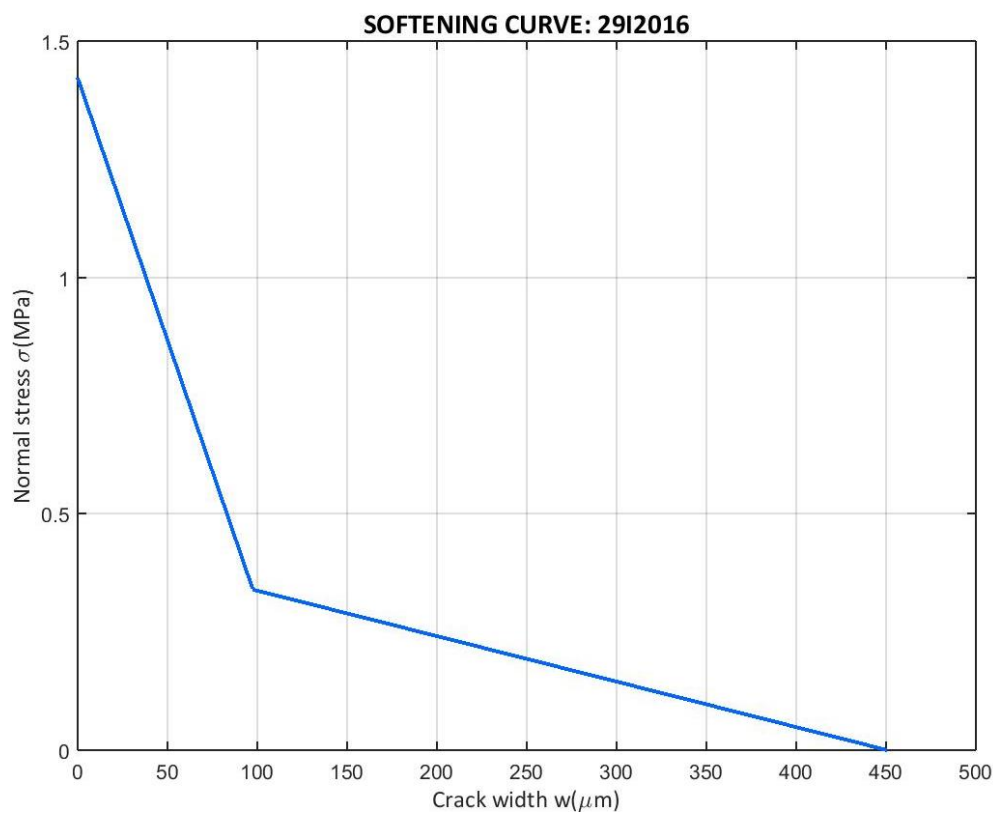


Figure 318: Softening curve bilinear approximation of the 29I2016 campaign

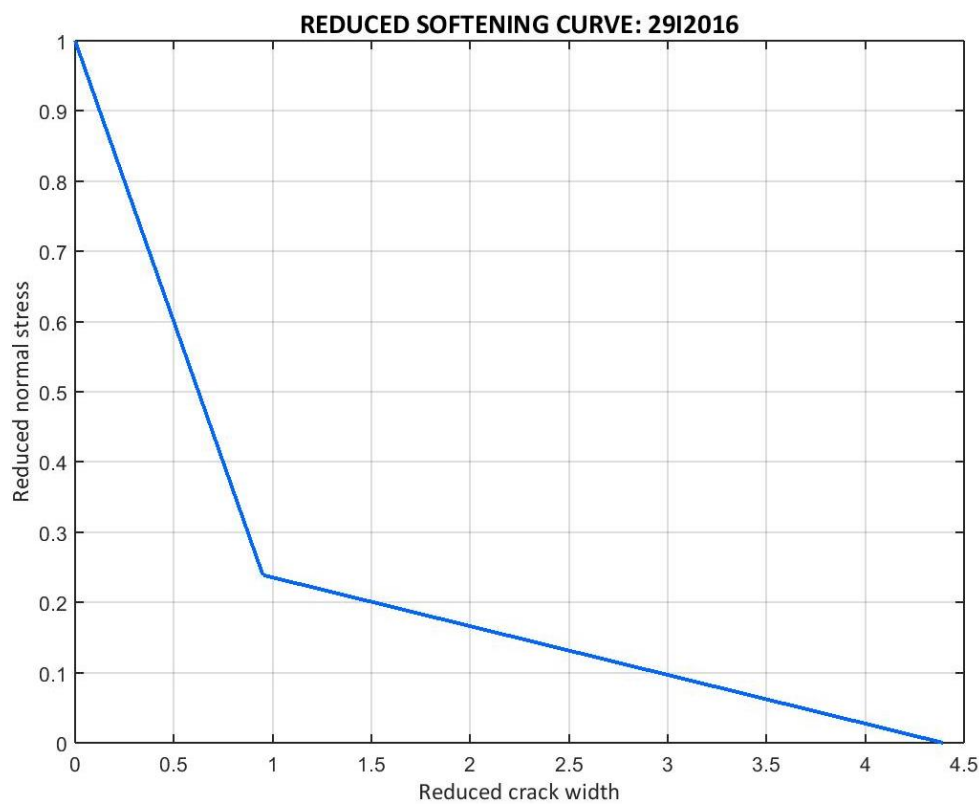


Figure 319: Softening curve bilinear approximation of the 29I2016 campaign in the reduced form

E.5.6 29I2016 SPECIMENS' COMPARISON

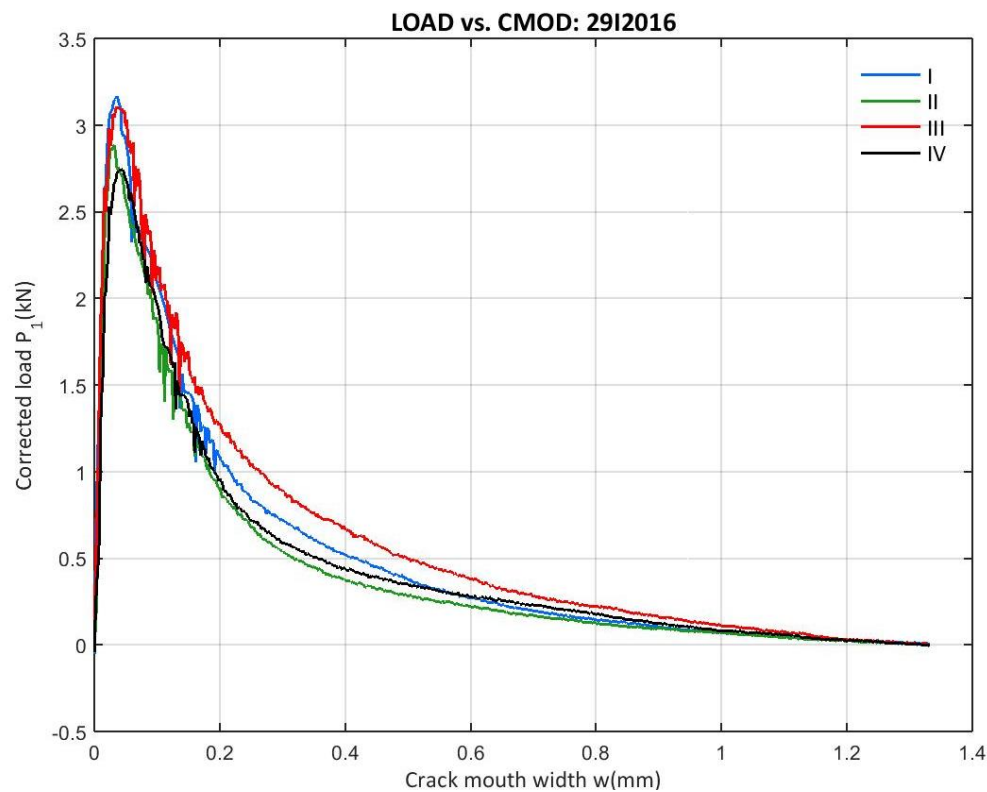


Figure 320: 29I2016 Corrected load vs. CMOD from the A-series

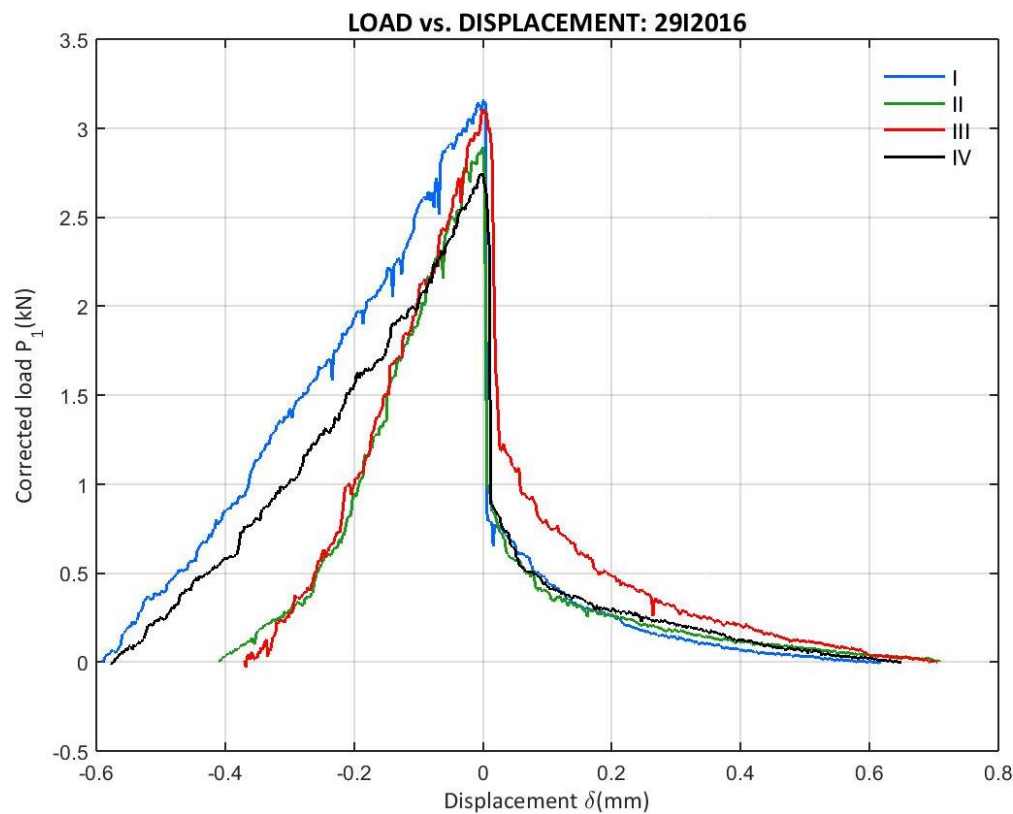


Figure 321: 29I2016 Corrected load vs. Displacement from the A-series (peak displacement zero)

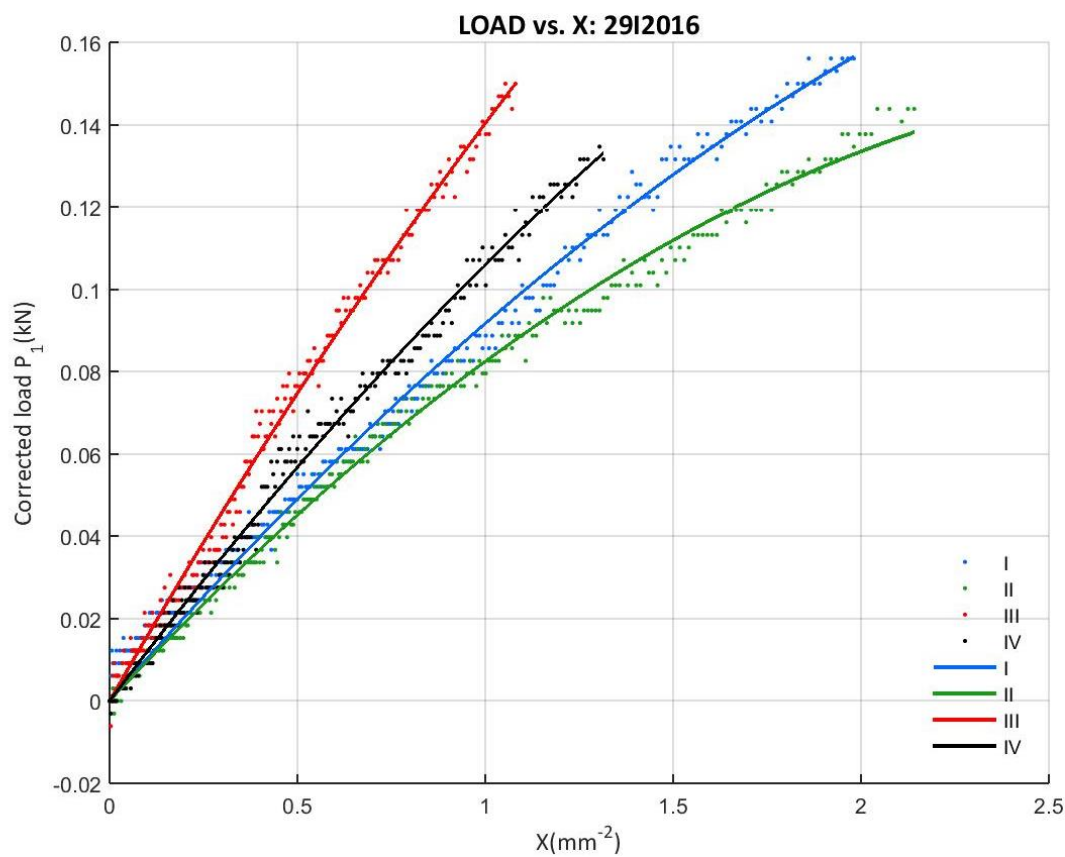


Figure 322: 29I2016 Corrected load vs. X from the A-series

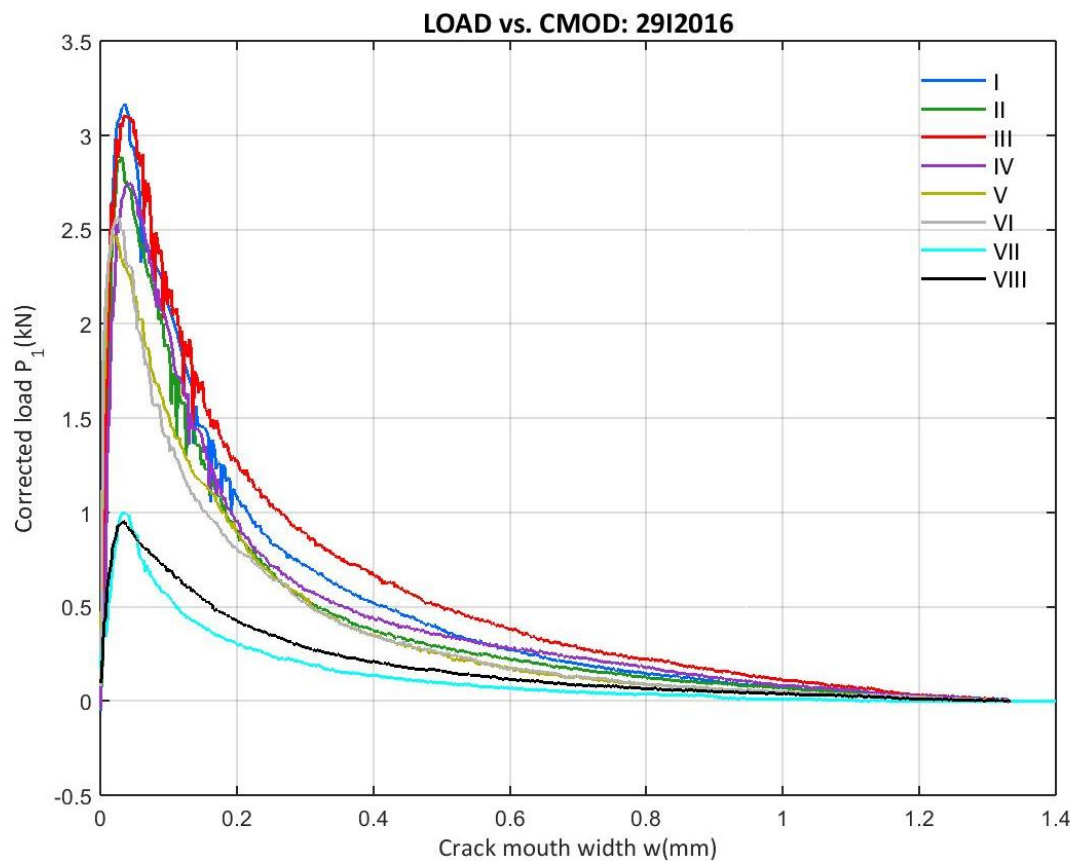


Figure 323: 29I2016 Corrected load vs. CMOD from the entire campaign

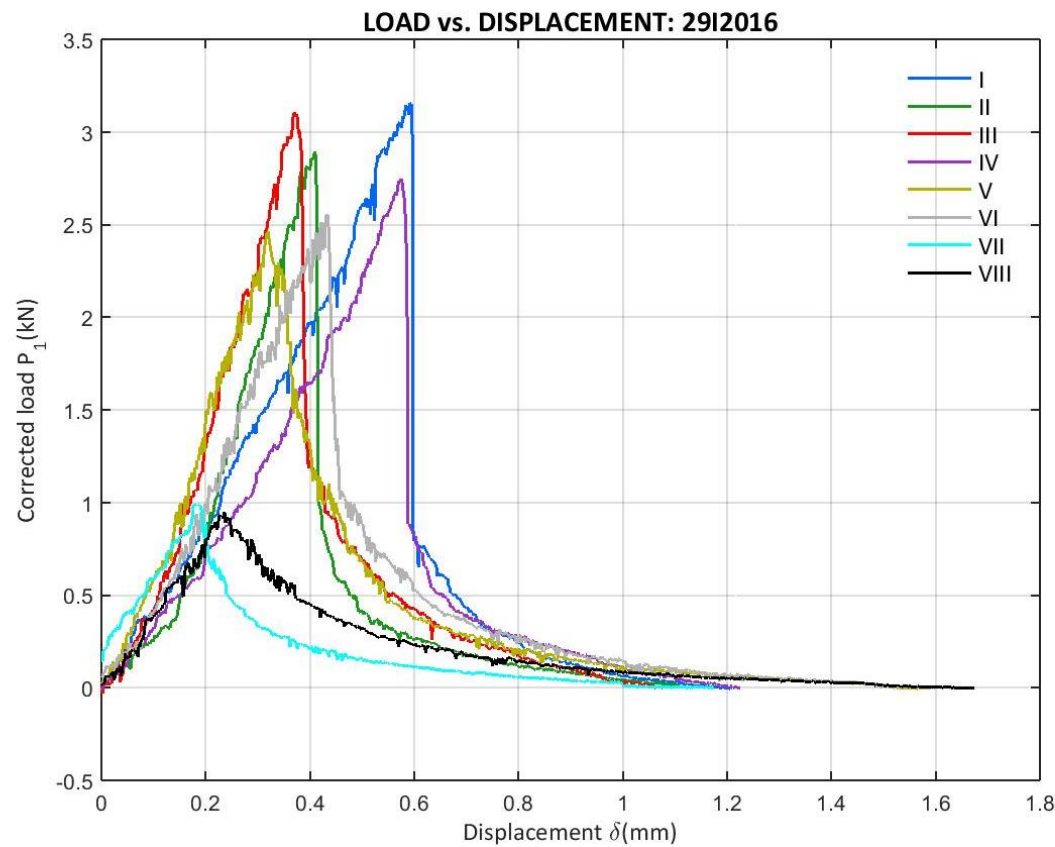


Figure 324: 29I2016 Corrected load vs. Displacement from the entire campaign

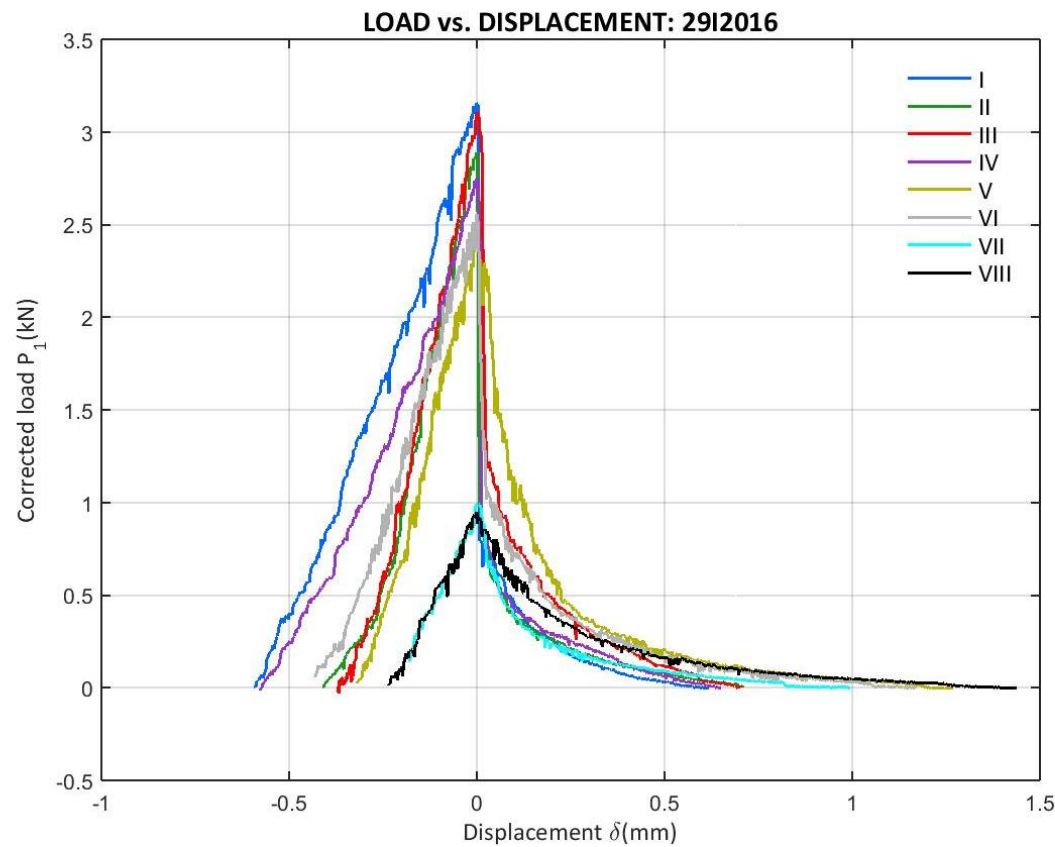


Figure 325: 29I2016 Corrected load vs. Displacement from the entire campaign (peak displacement zero)

E.6 10III2016 CAMPAIGN

E.6.1 10III2016 DATA

- B10III2016I

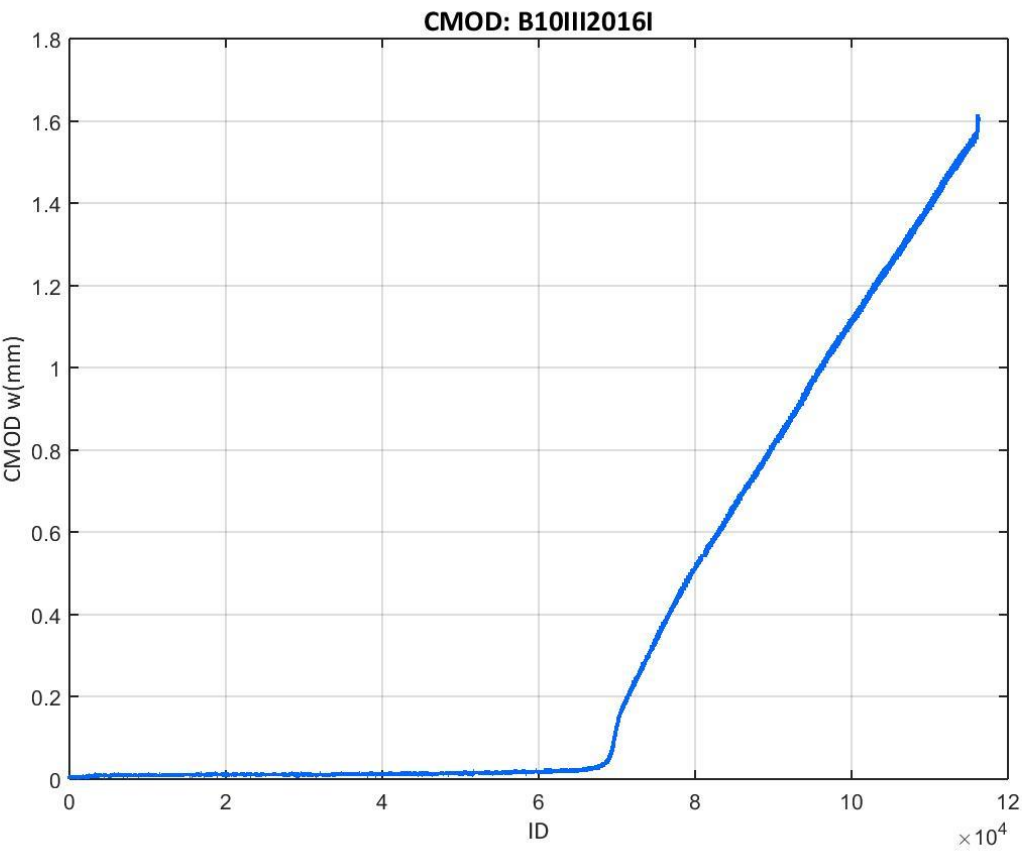


Figure 326: CMOD values recorded at the B10III2016I test

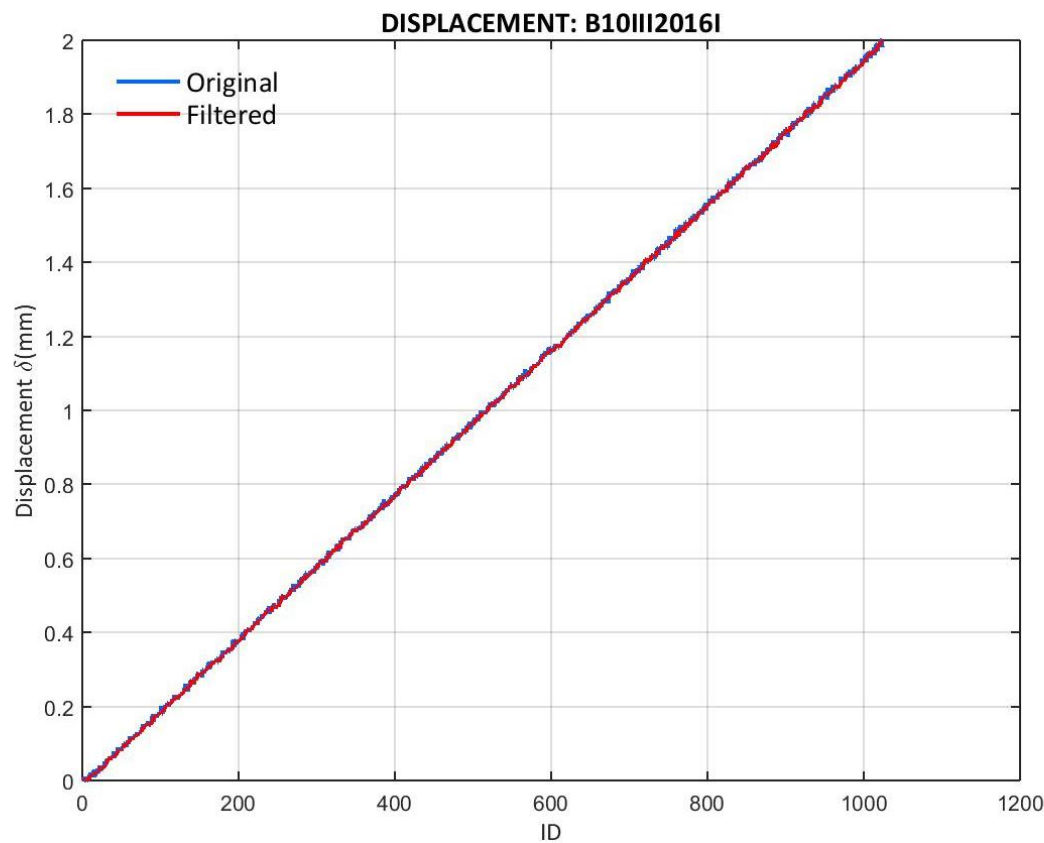


Figure 327: Displacement values recorded by the controller at the B10III2016I test

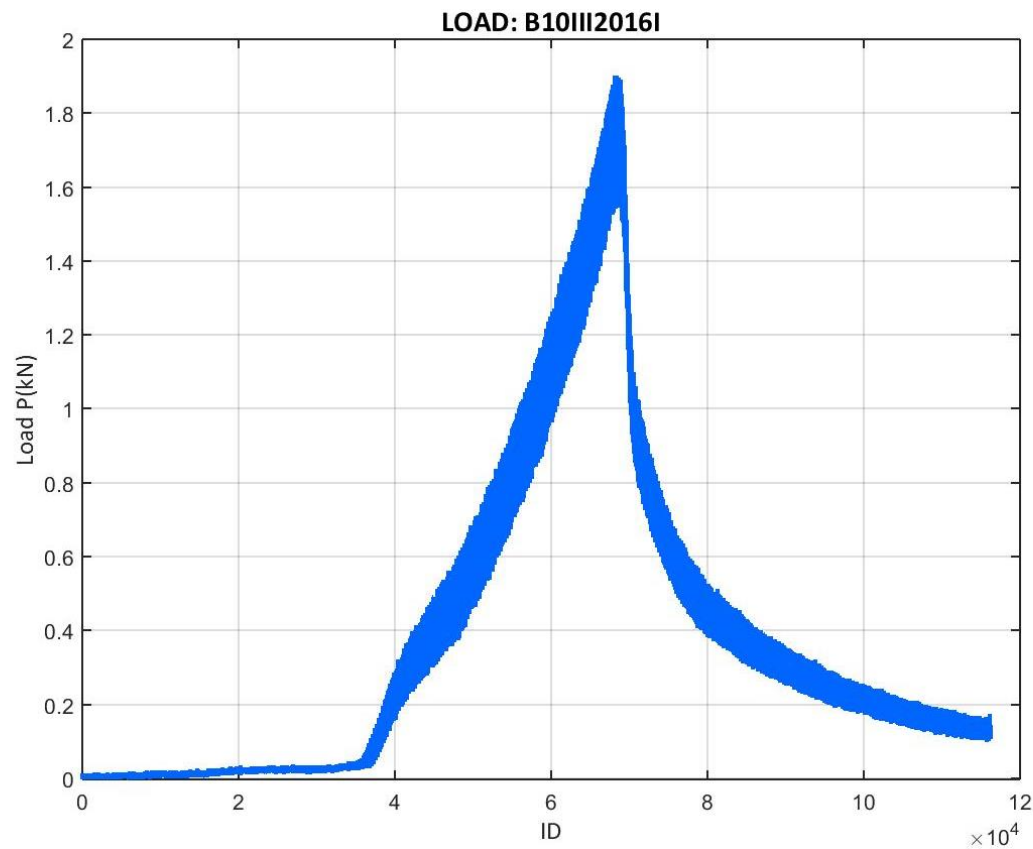


Figure 328: Load values recorded at the B10III2016I test

- B10III2016II

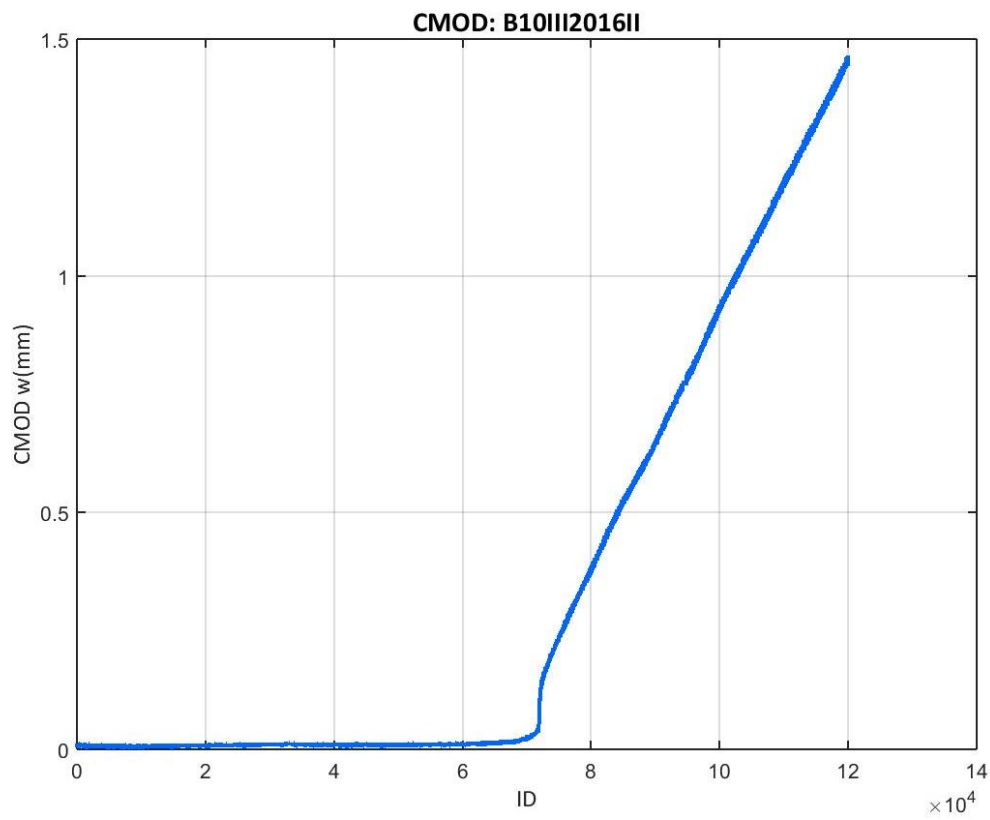


Figure 329: CMOD values recorded at the B10III2016II test

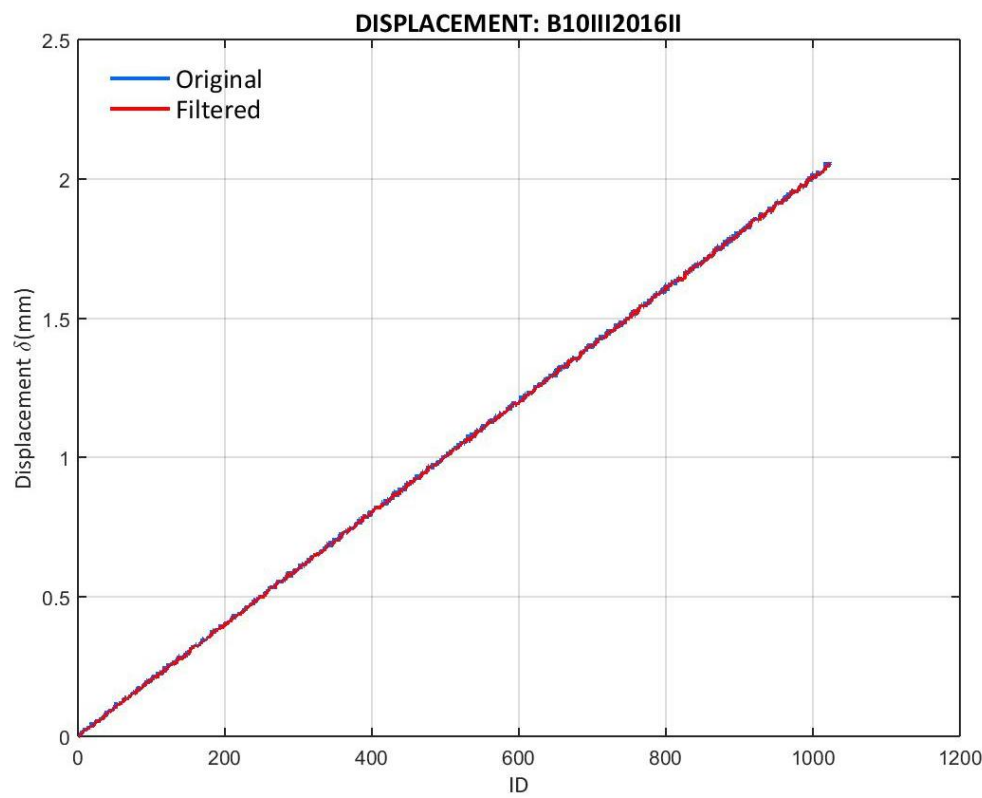


Figure 330: Displacement values recorded by the controller at the B10III2016II test

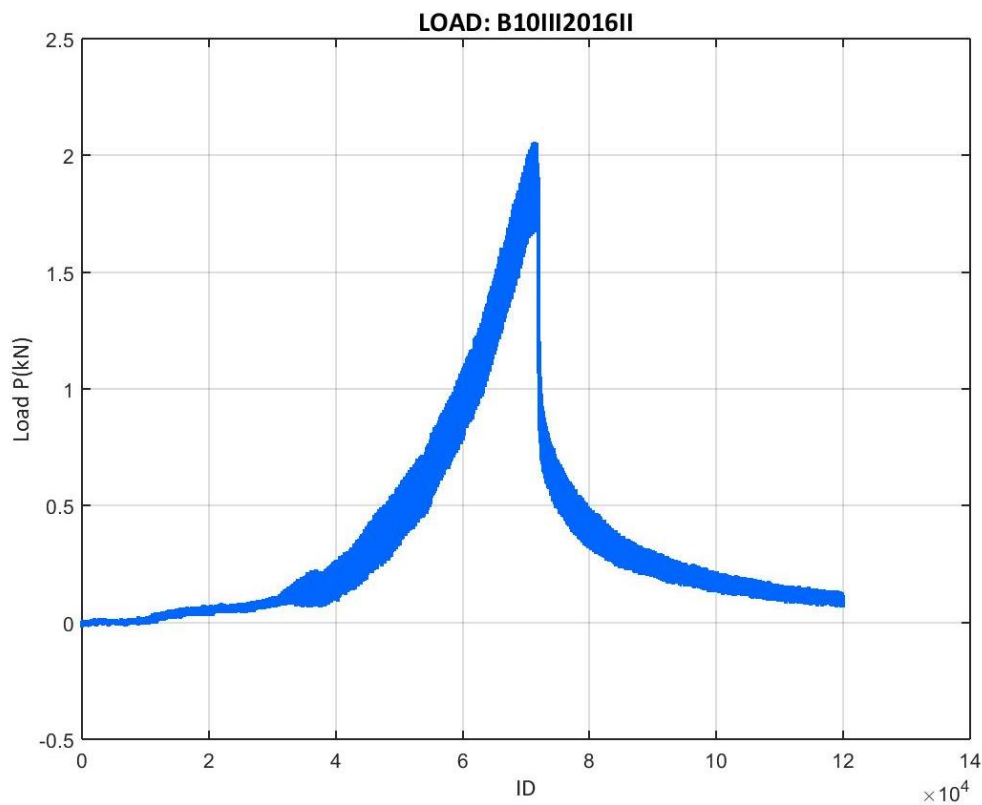


Figure 331: Load values recorded at the B10III2016II test

- B10III2016III

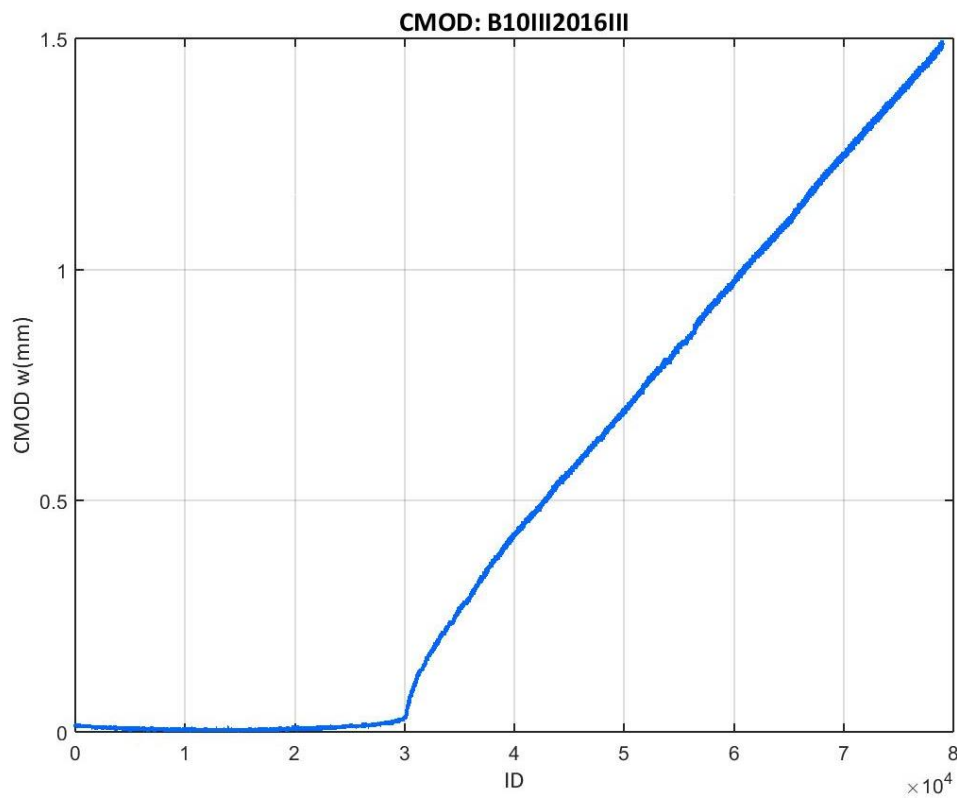


Figure 332: CMOD values recorded at the B10III2016III test

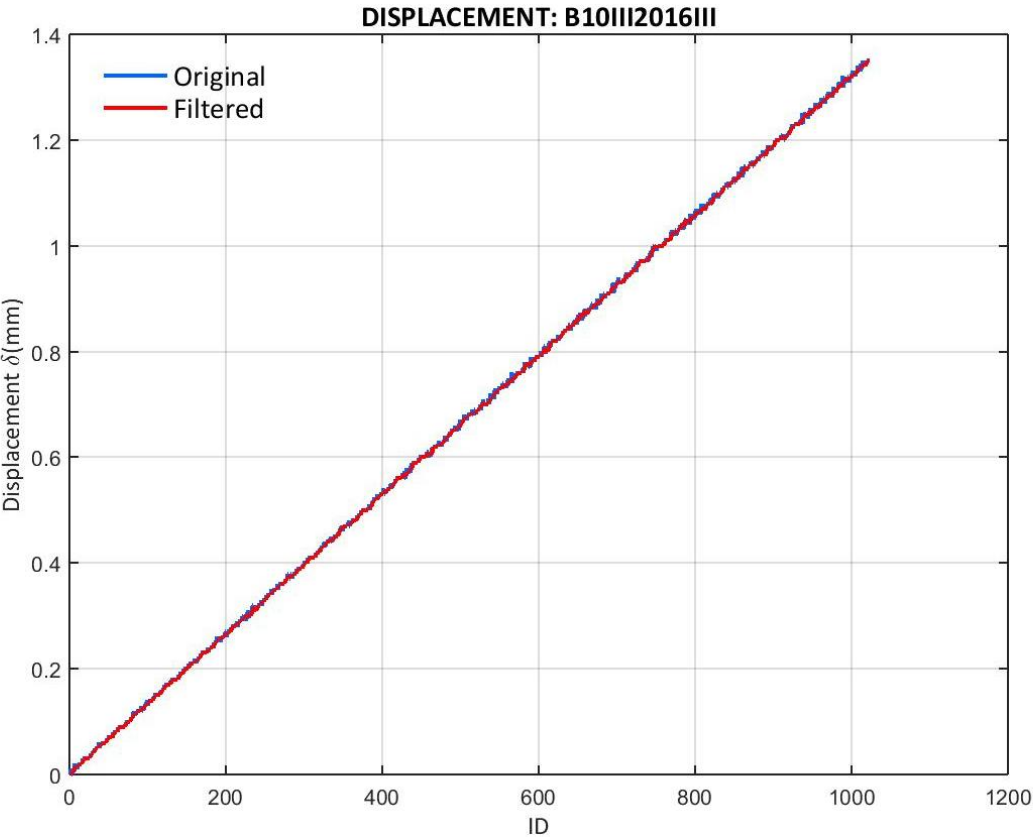


Figure 333: Displacement values recorded by the controller at the B10III2016III test

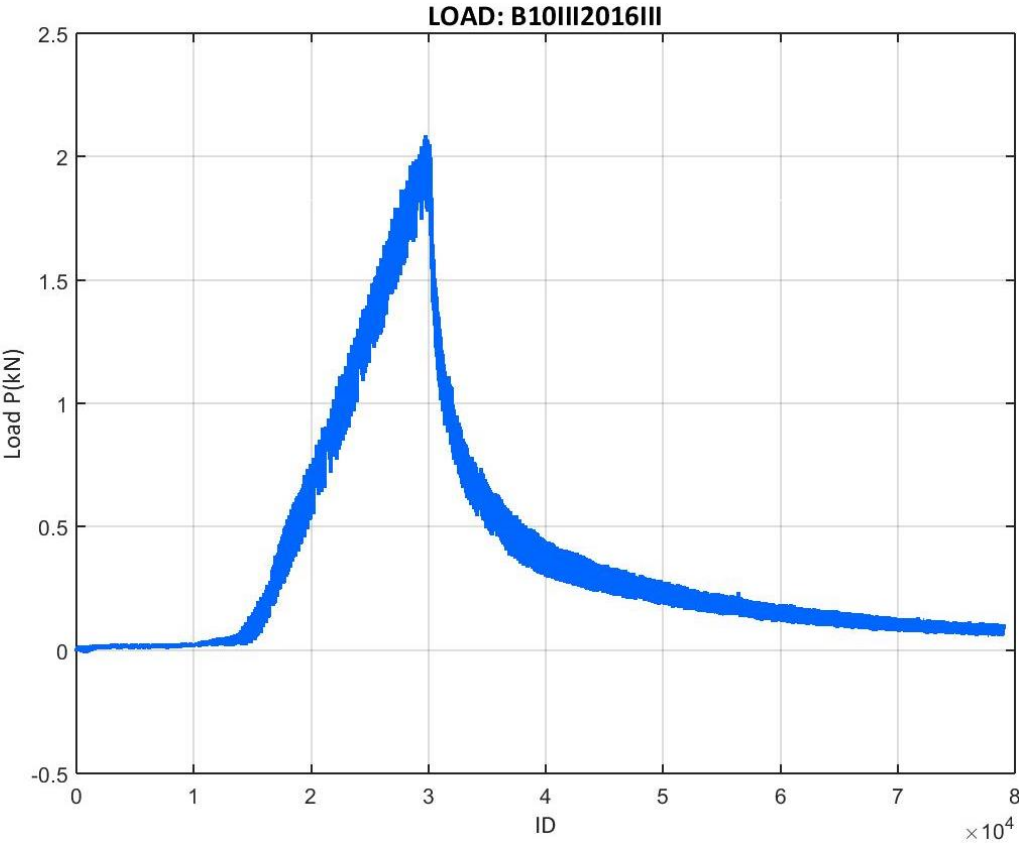


Figure 334: Load values recorded at the B10III2016III test

- B10III2016IV

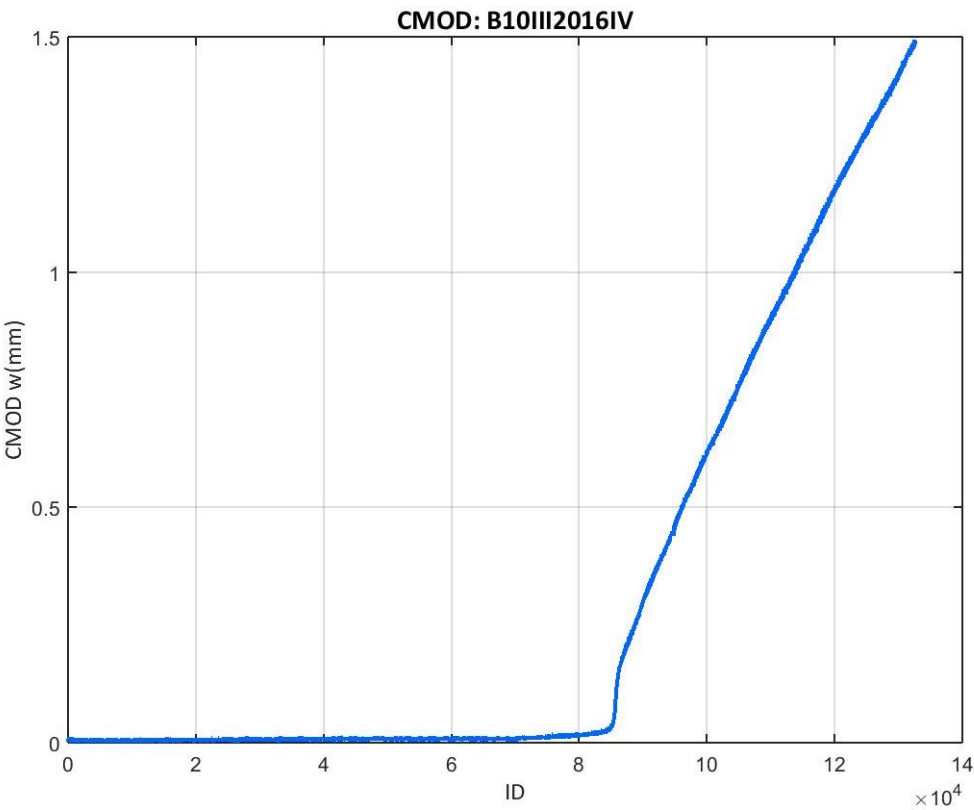


Figure 335: CMOD values recorded at the B10III2016IV test

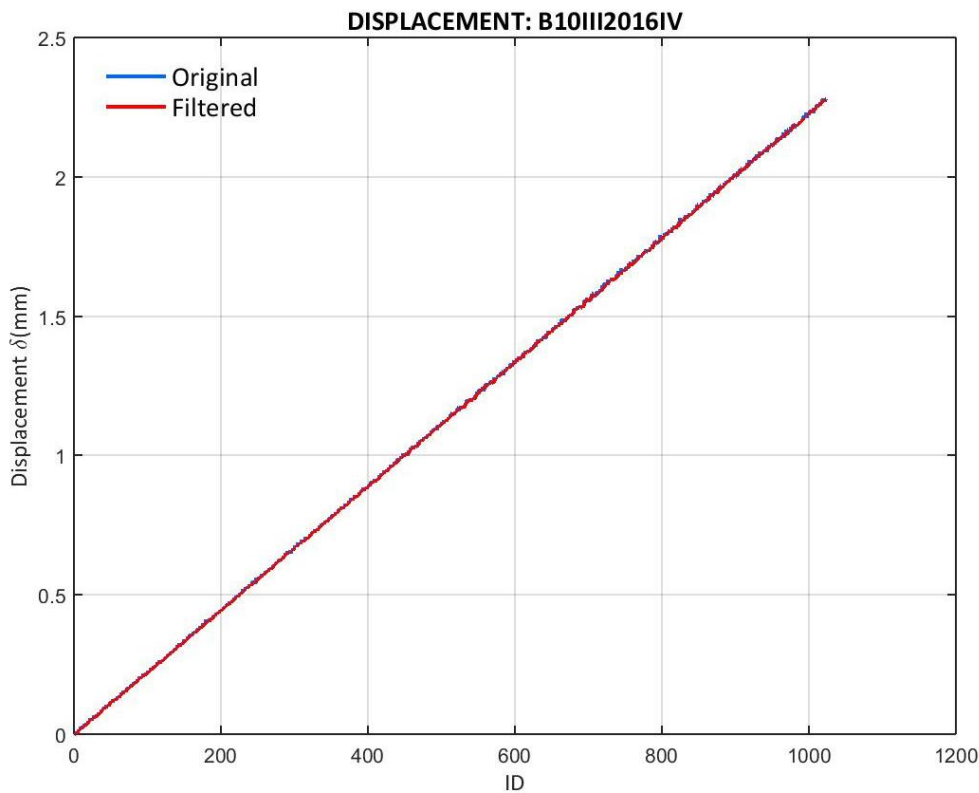


Figure 336: Displacement values recorded by the controller at the B10III2016IV test

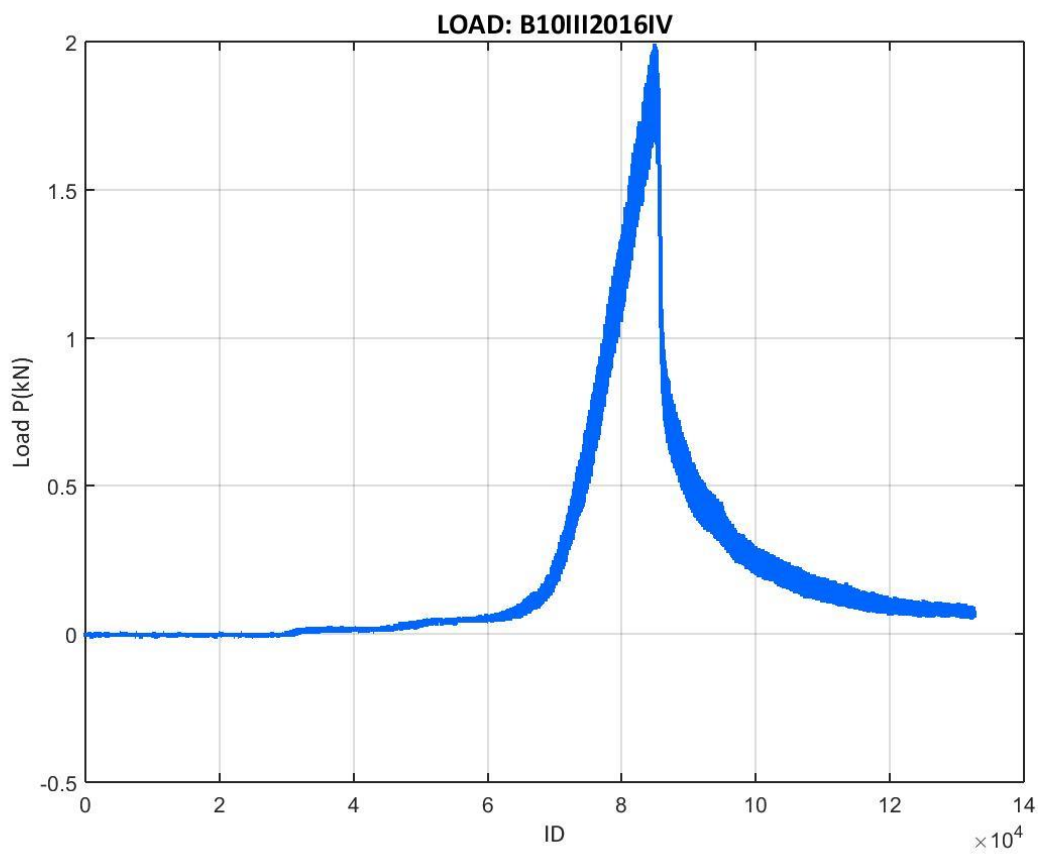


Figure 337: Load values recorded at the B10III2016IV test

E.6.2 10III2016 CORRECTED LOAD VS. CMOD

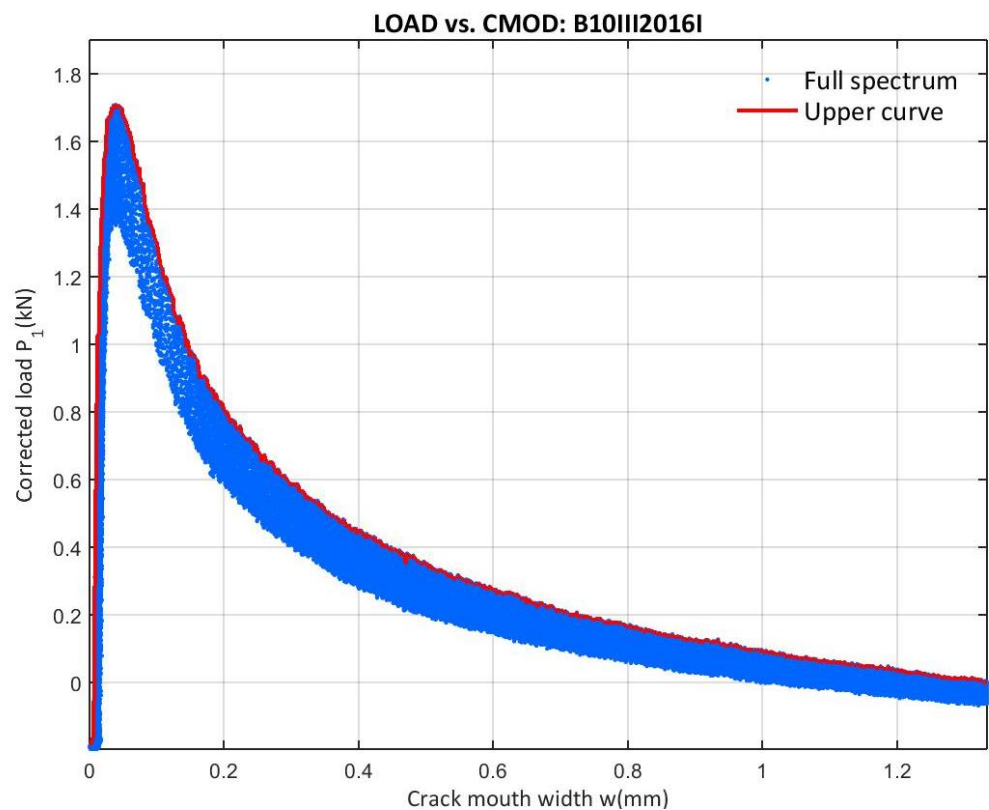


Figure 338: Corrected load vs. CMOD at the B10III2016I test

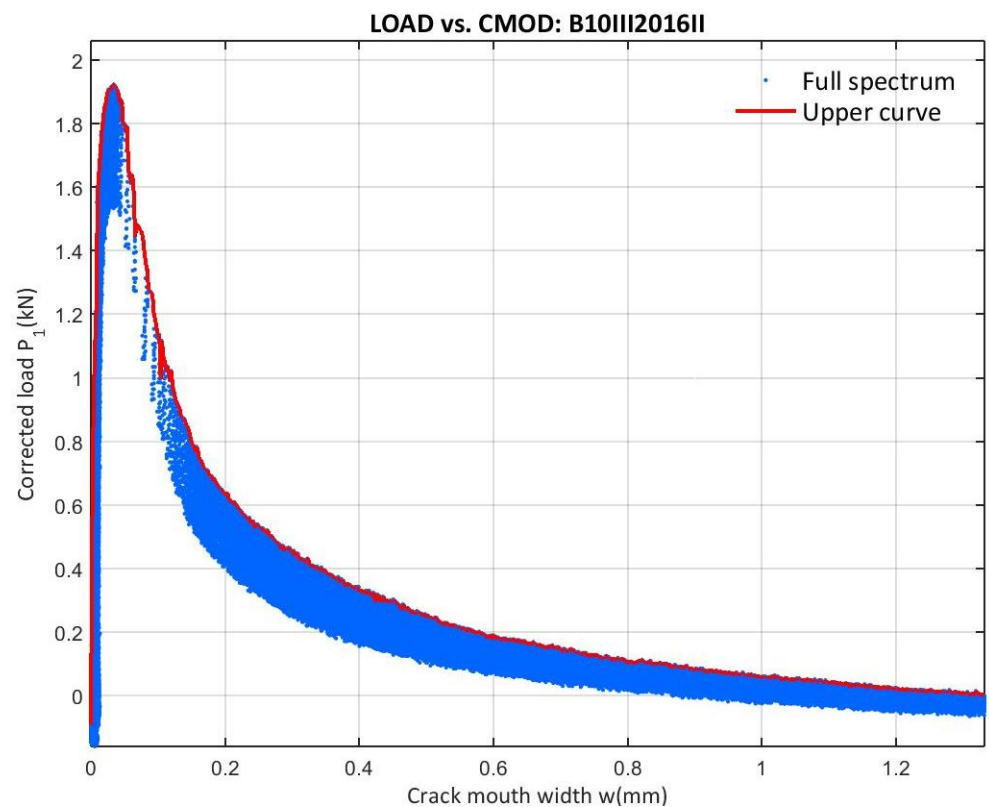


Figure 339: Corrected load vs. CMOD at the B10III2016II test

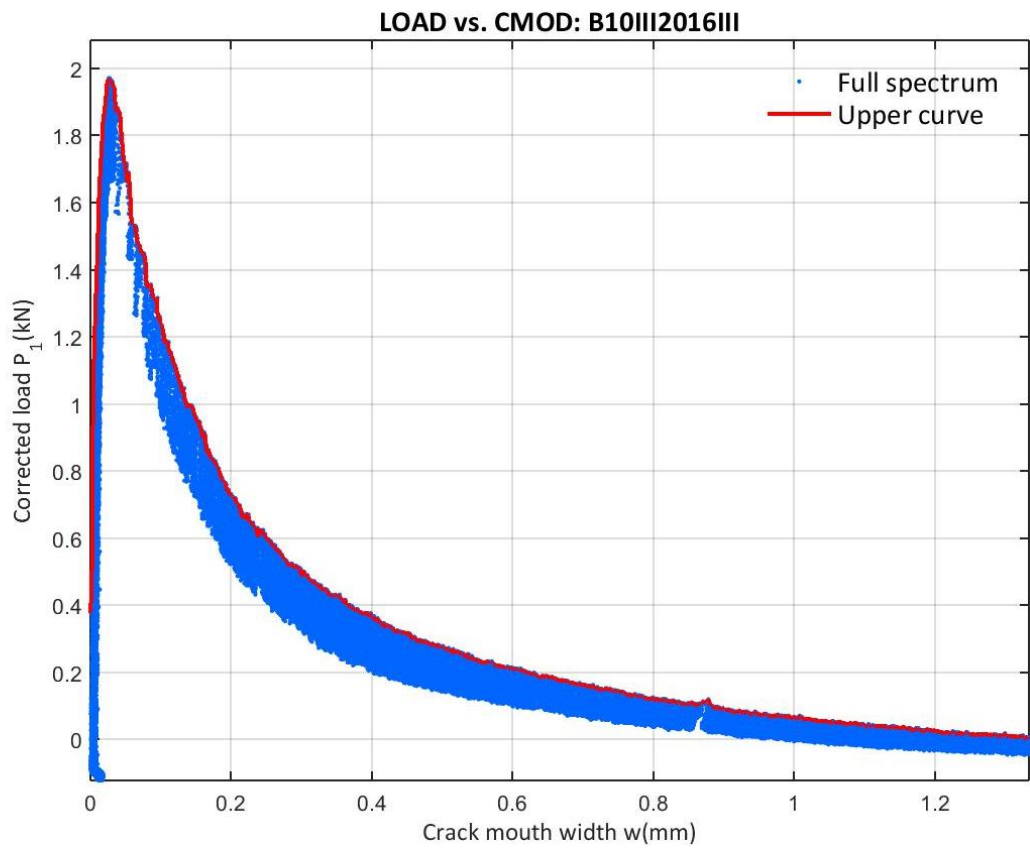


Figure 340: Corrected load vs. CMOD at the B10III2016III test

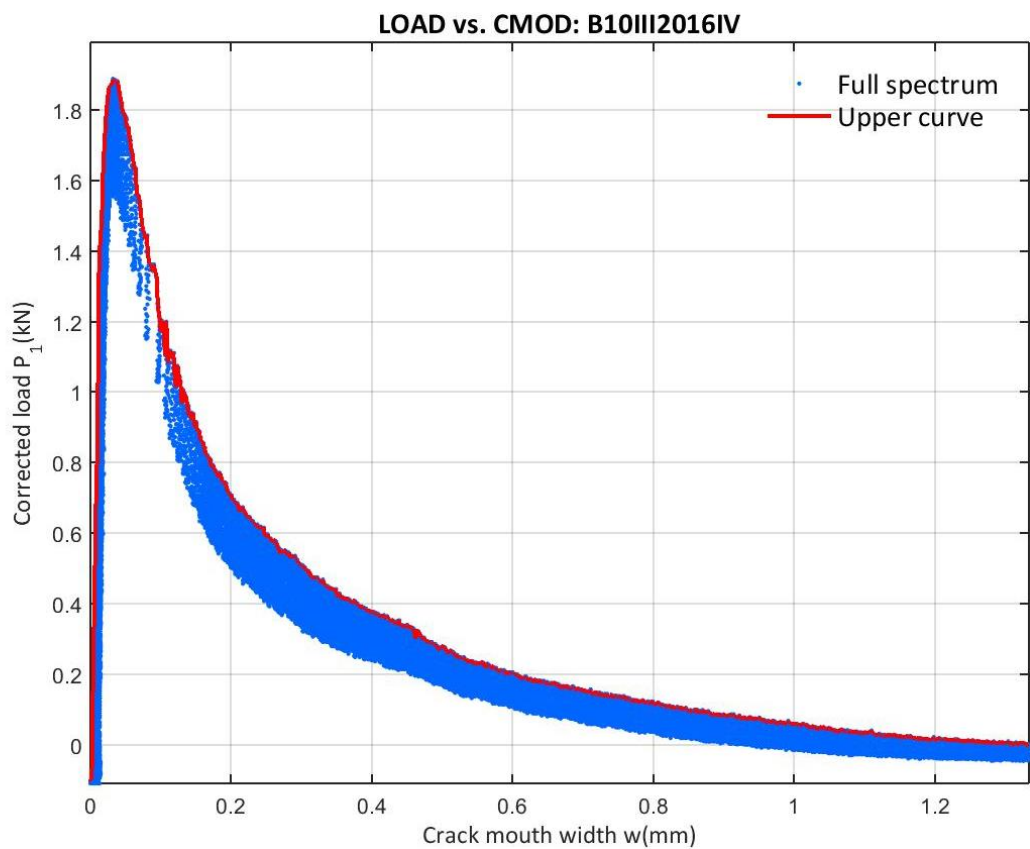


Figure 341: Corrected load vs. CMOD at the B10III2016IV test

E.6.3 10III2016 CORRECTED LOAD VS. VERTICAL DISPLACEMENT

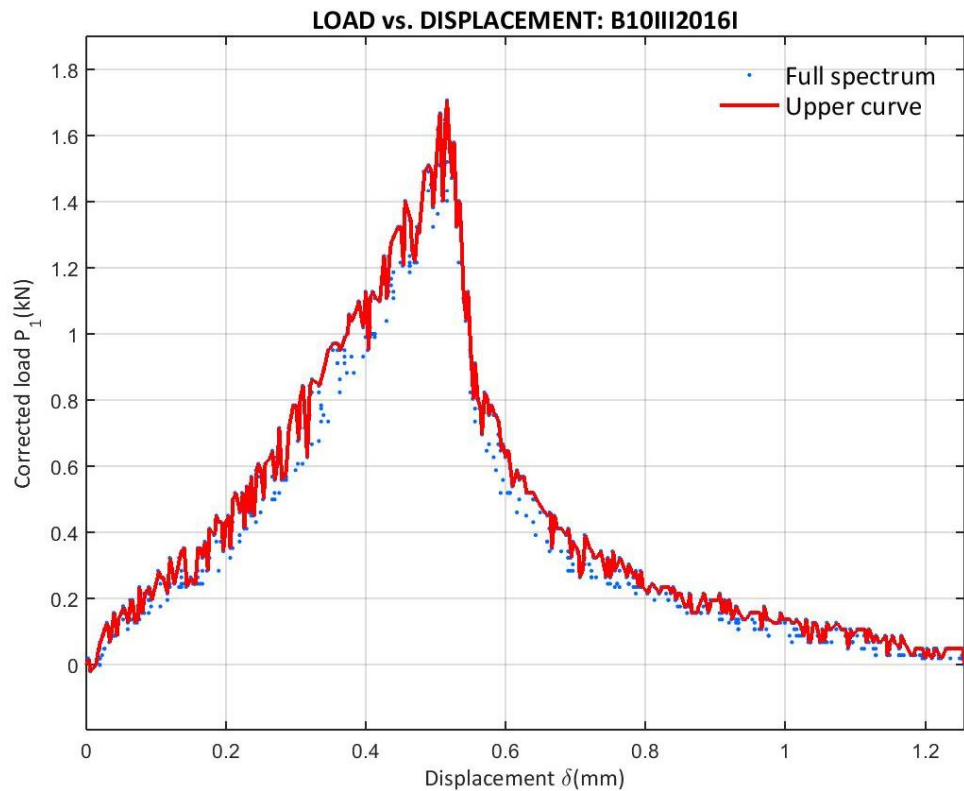


Figure 342: Corrected load vs. Displacement at the B10III2016I test recorded by the controller

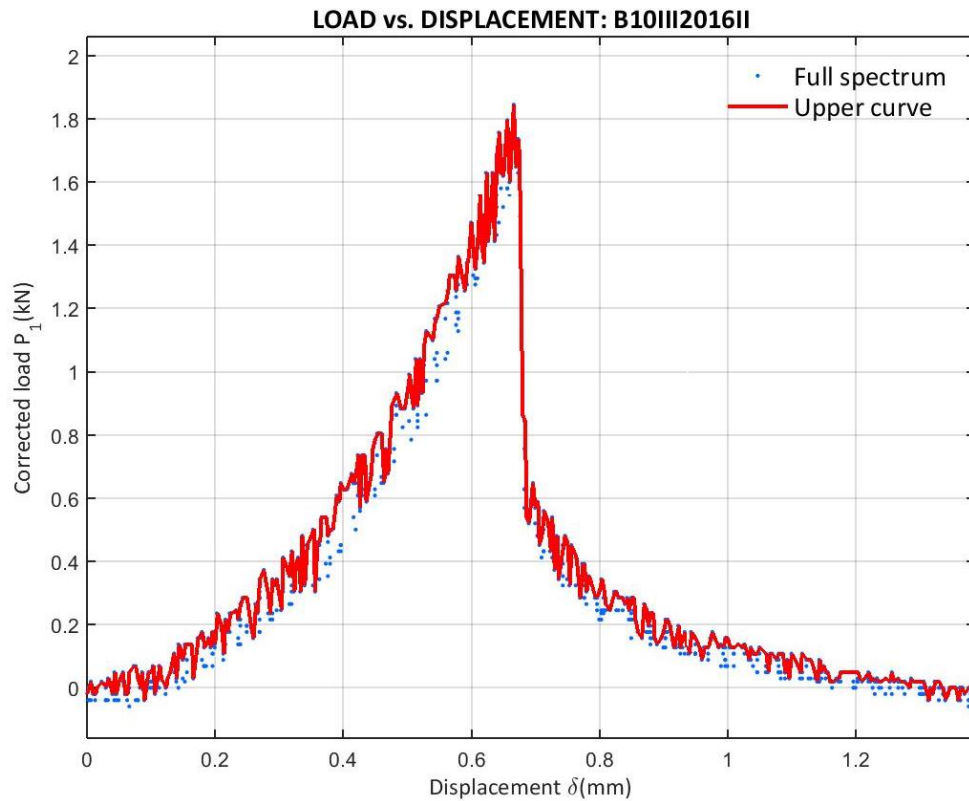


Figure 343: Corrected load vs. Displacement at the B10III2016II test recorded by the controller

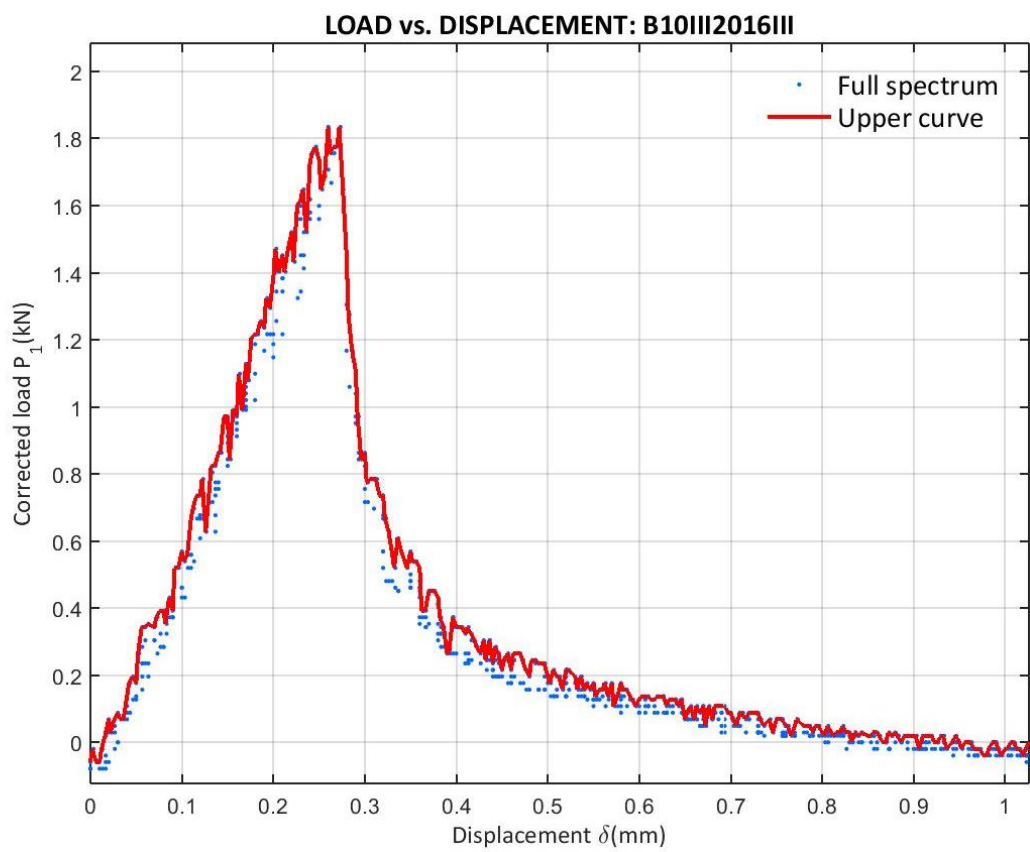


Figure 344: Corrected load vs. Displacement at the B10III2016III test recorded by the controller

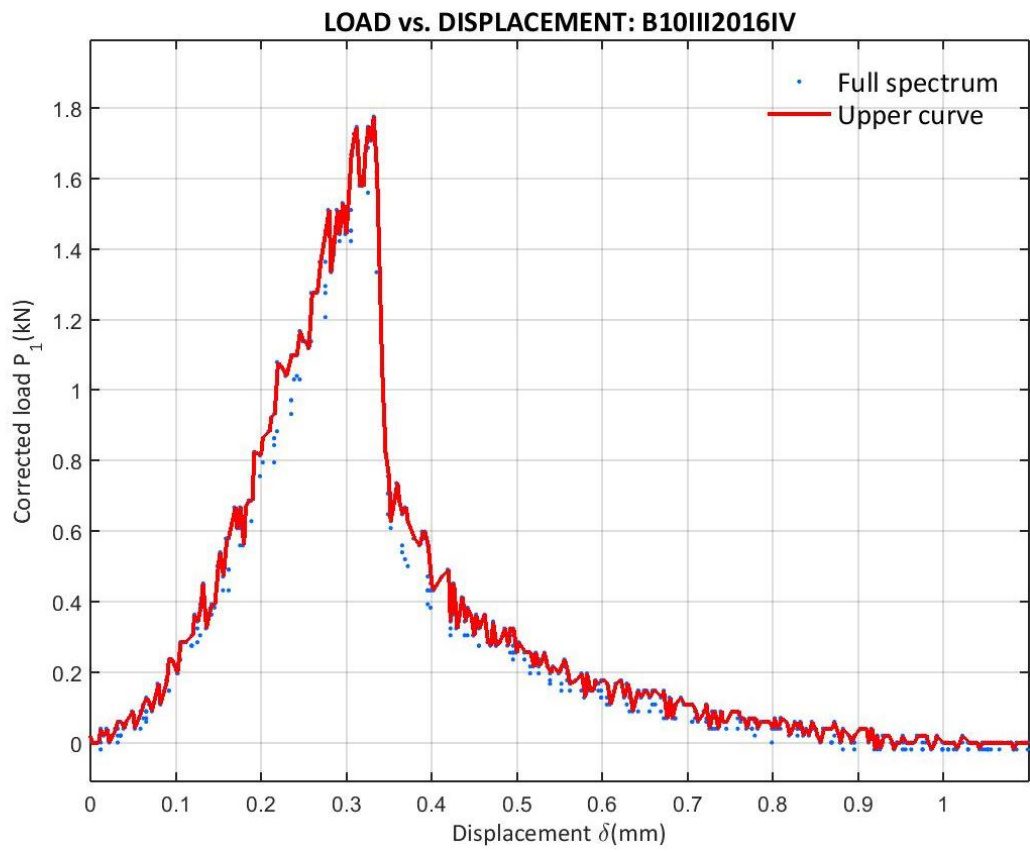


Figure 345: Corrected load vs. Displacement at the B10III2016IV test recorded by the controller

E.6.4 10III2016 CORRECTED LOAD VS. X

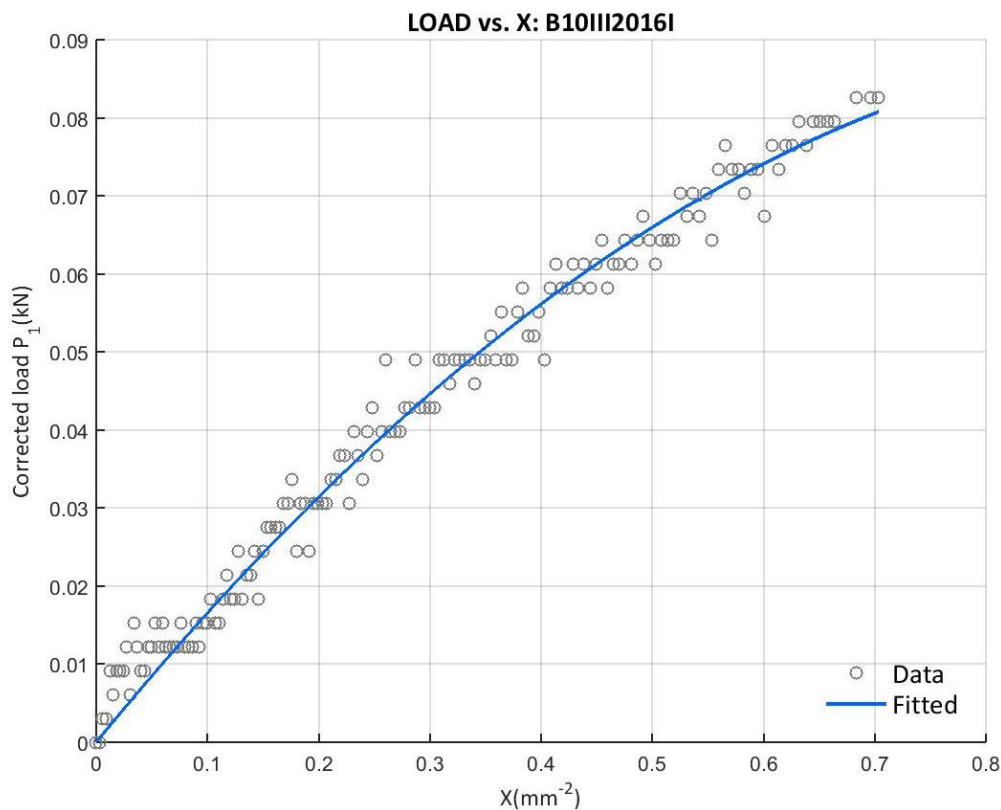


Figure 346: Corrected load vs. X at the B10III2016I test with the final upper curve data

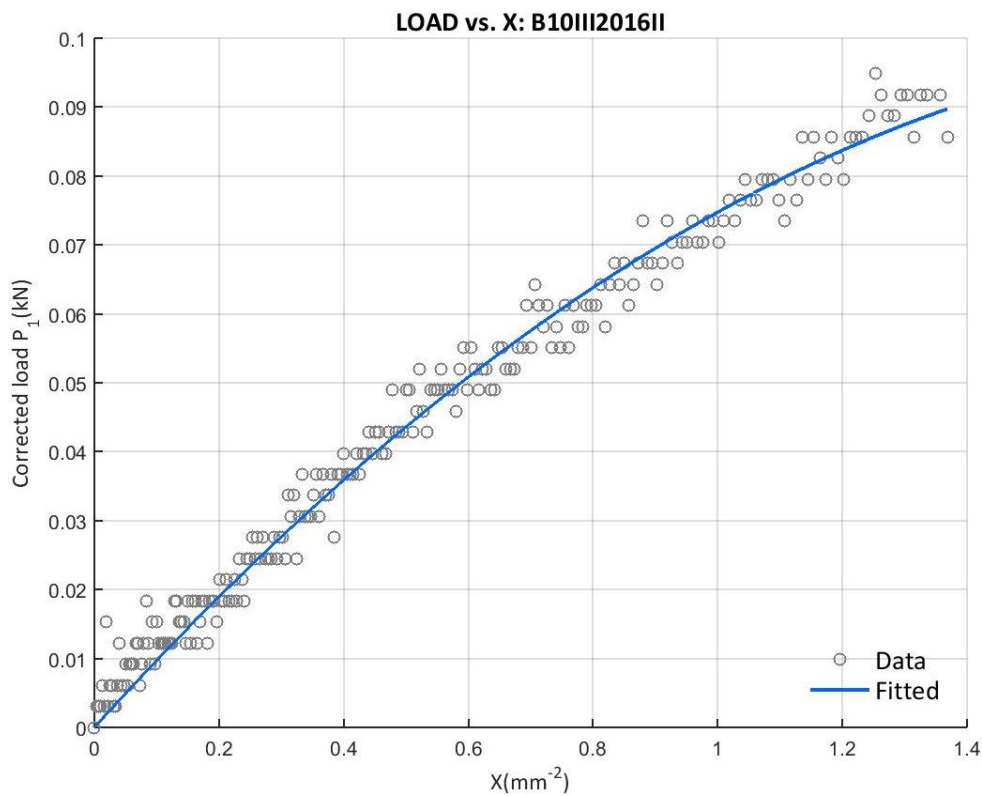


Figure 347: Corrected load vs. X at the B10III2016II test with the final upper curve data

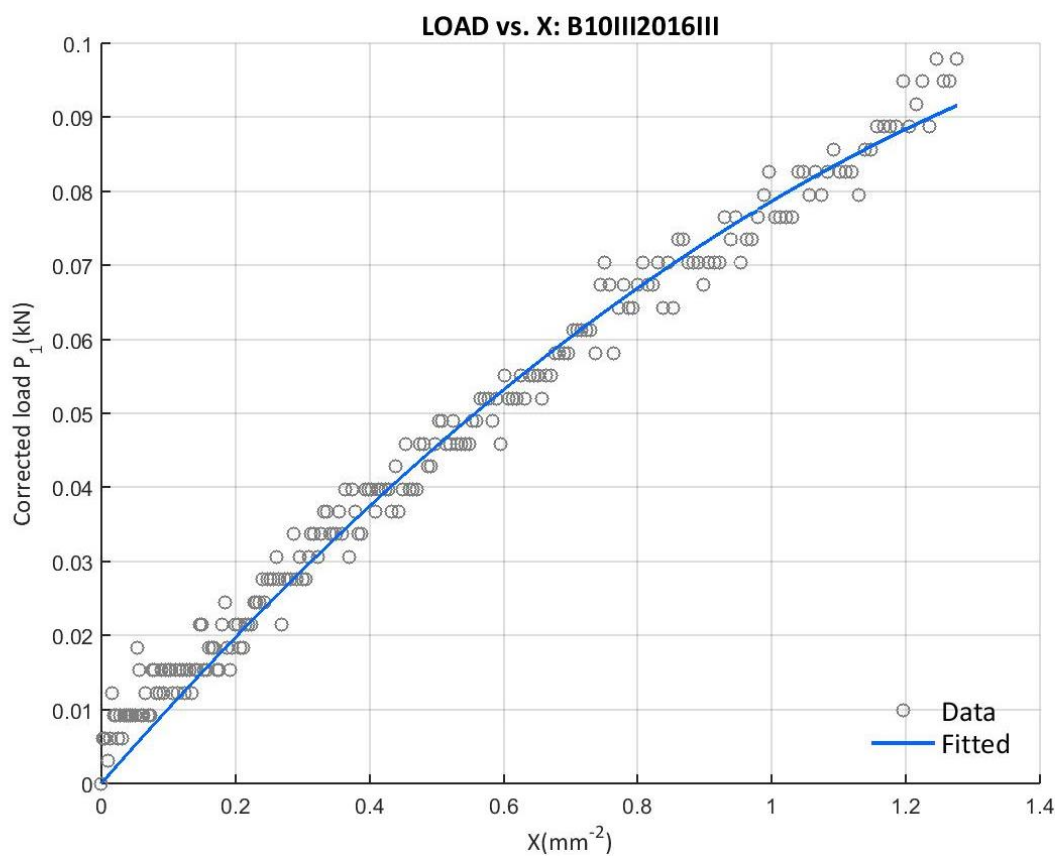


Figure 348: Corrected load vs. X at the B10III2016III test with the final upper curve data

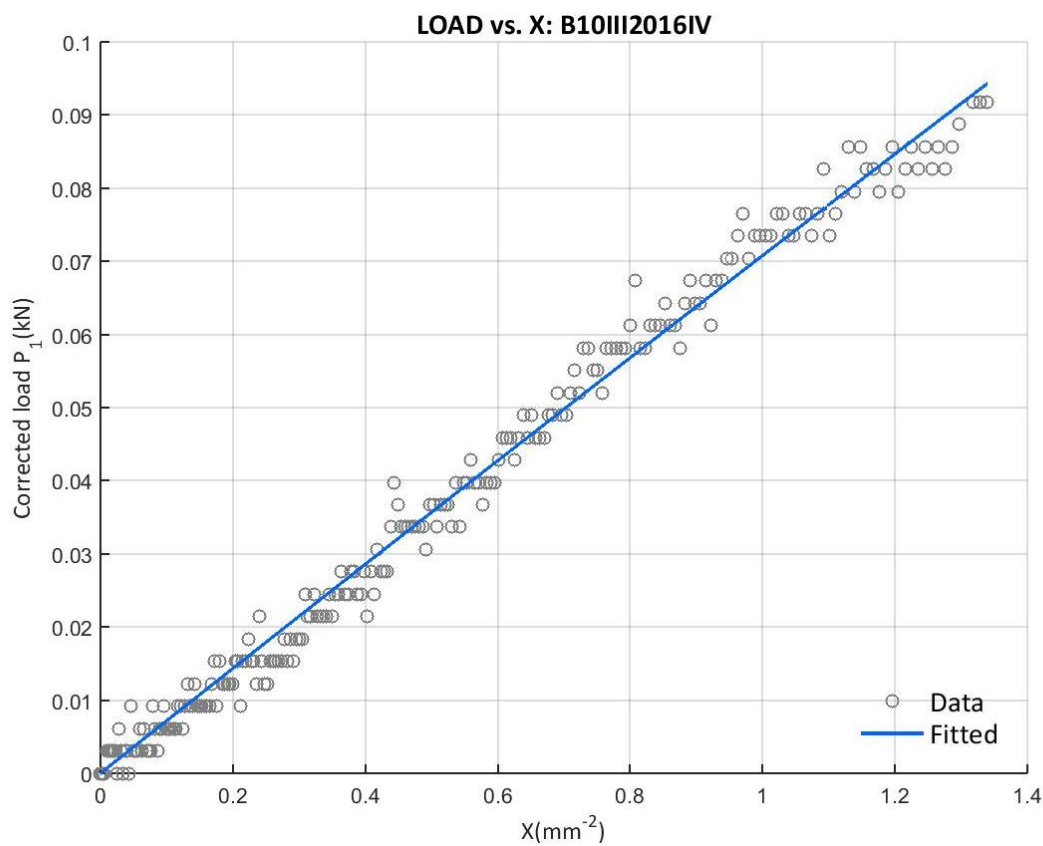


Figure 349: Corrected load vs. X at the B10III2016IV test with the final upper curve data

E.6.5 10III2016 SOFTENING CURVE BILINEAR APPROXIMATION

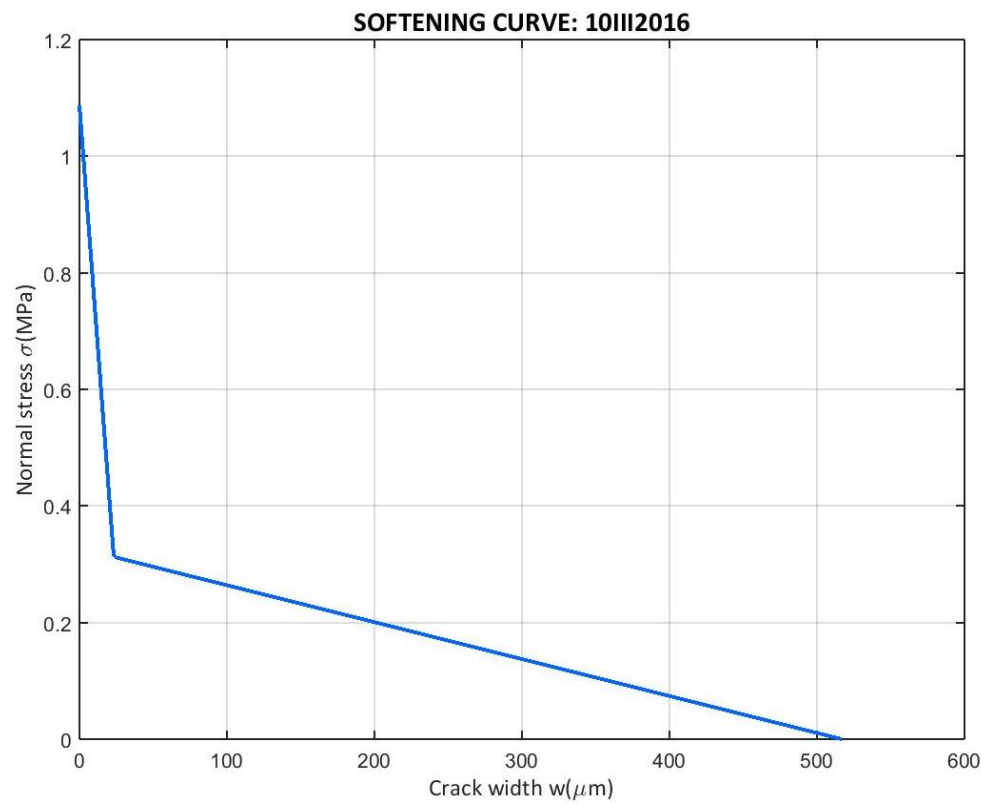


Figure 350: Softening curve bilinear approximation of the 10III2016 campaign

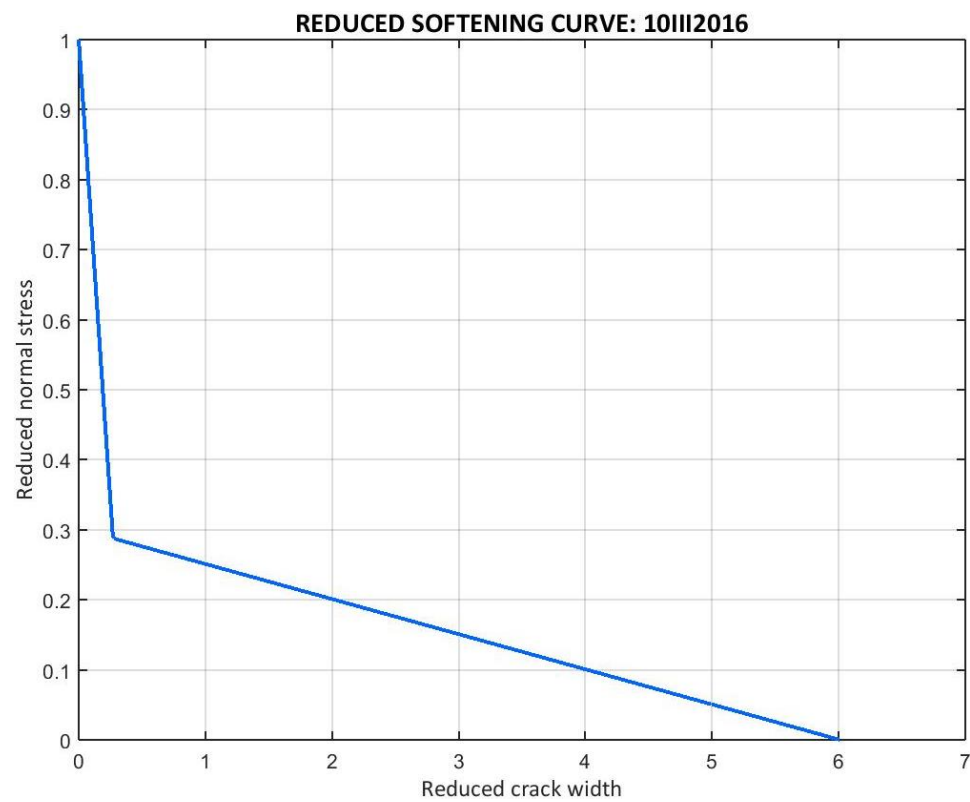


Figure 351: Softening curve bilinear approximation of the 10III2016 campaign in the reduced form

E.6.6 10III2016 SPECIMENS' COMPARISON

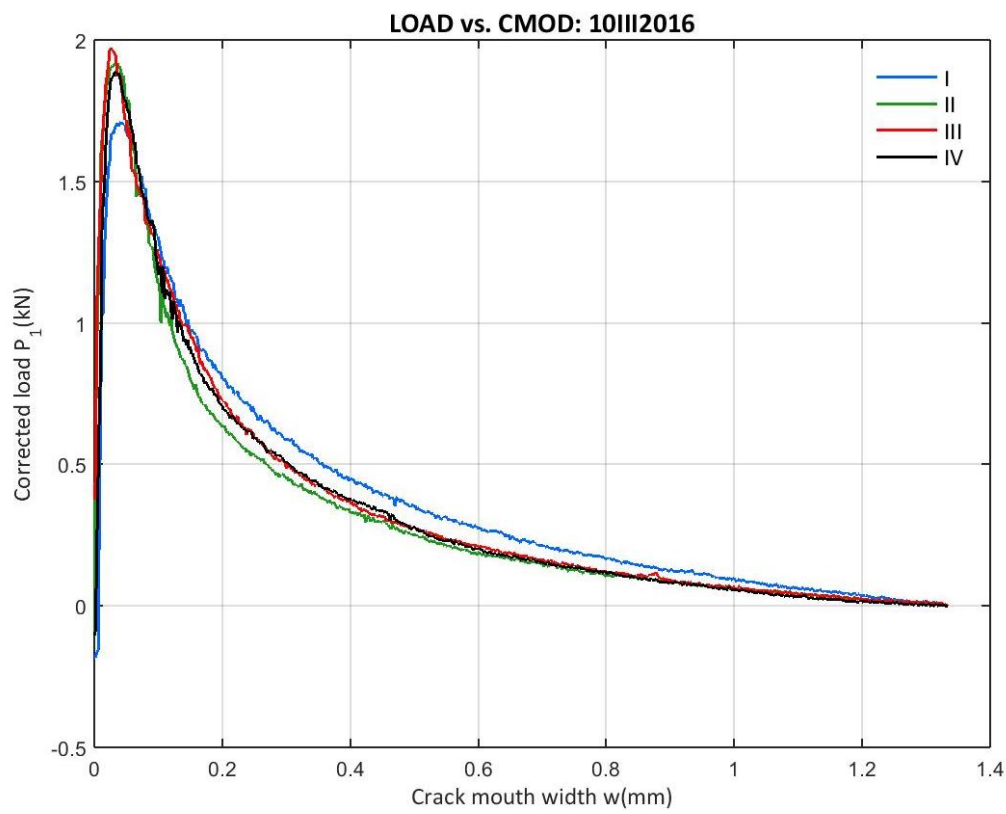


Figure 352: 10III2016 Corrected load vs. CMOD from the entire campaign

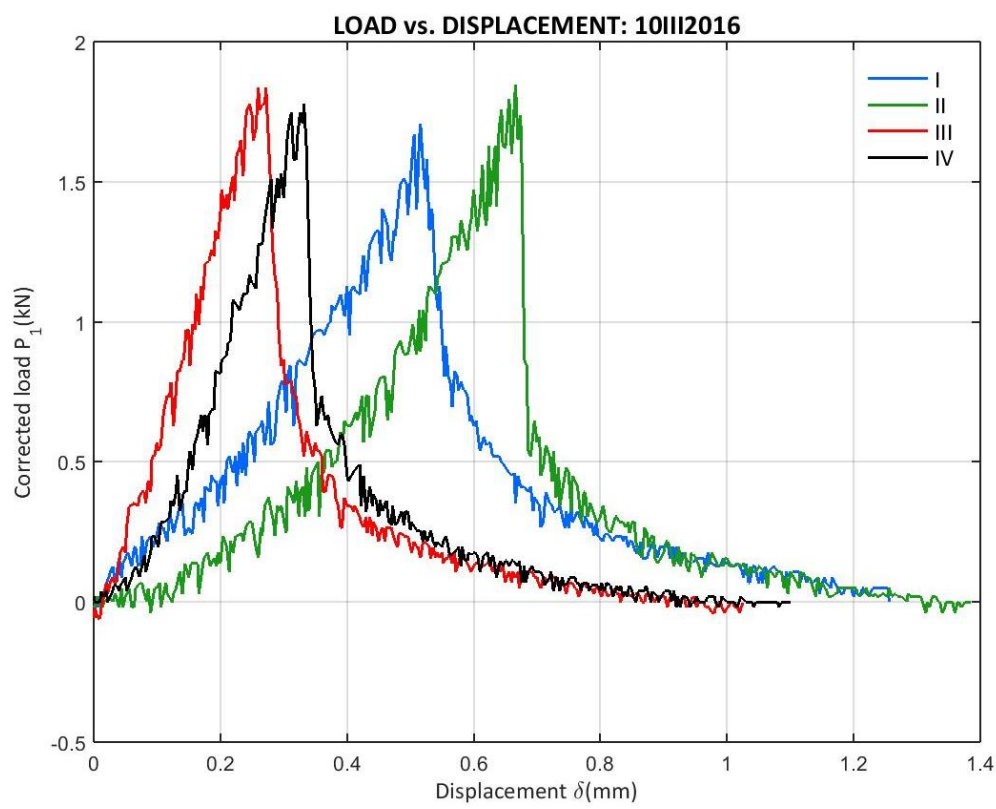


Figure 353: 10III2016 Corrected load vs. Displacement from the entire campaign

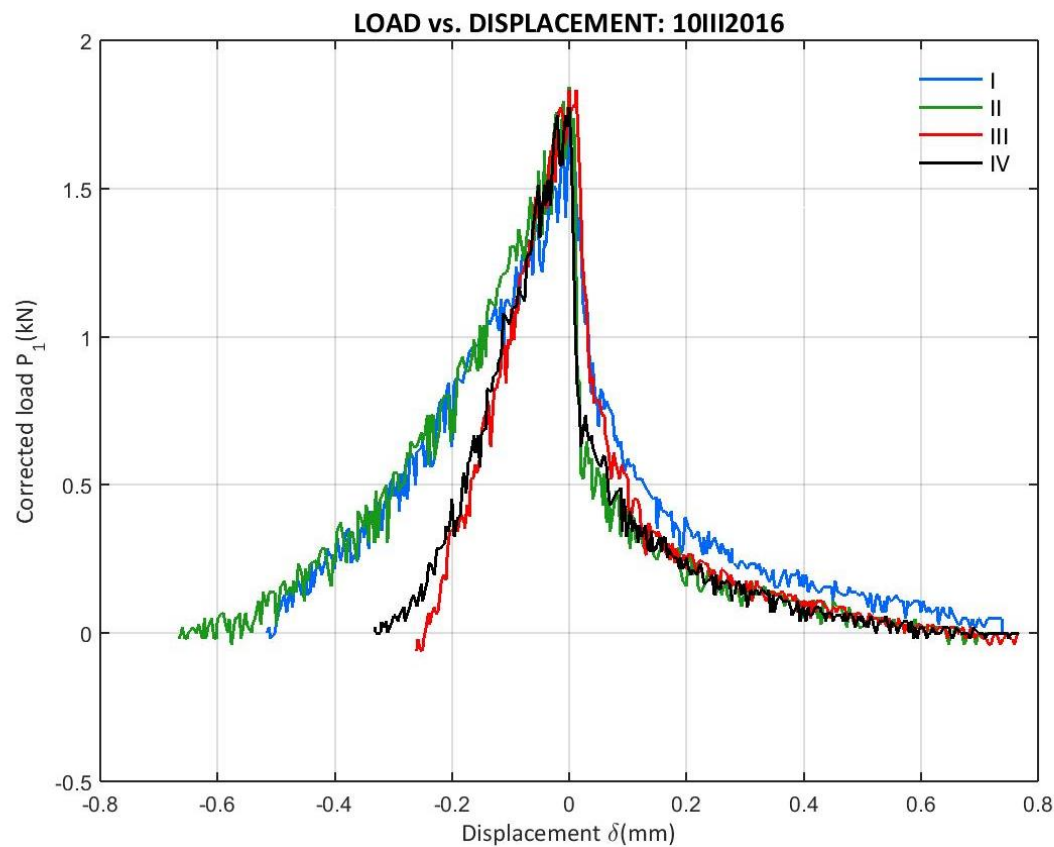


Figure 354: 10III2016 Corrected load vs. Displacement from the entire campaign (peak displacement zero)

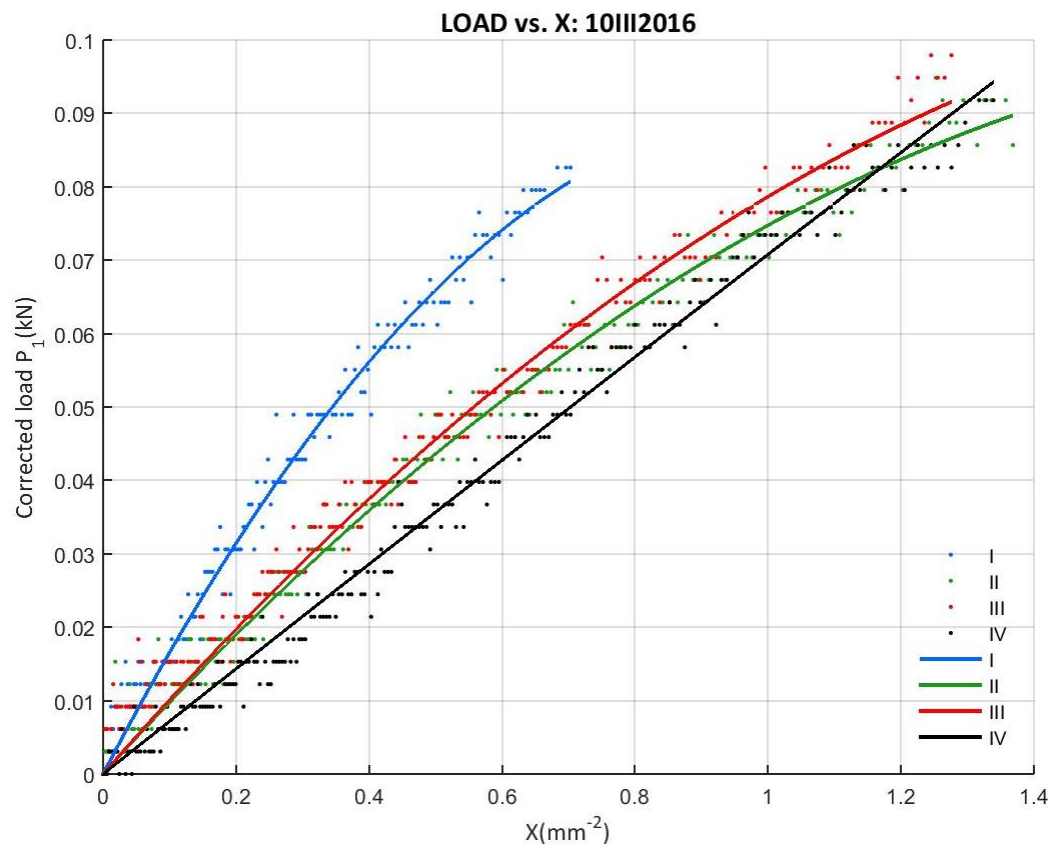


Figure 355: 10III2016 Corrected load vs. X from the entire campaign

E.7 17III2016 CAMPAIGN

E.7.1 17III2016 DATA

- B17III2016I

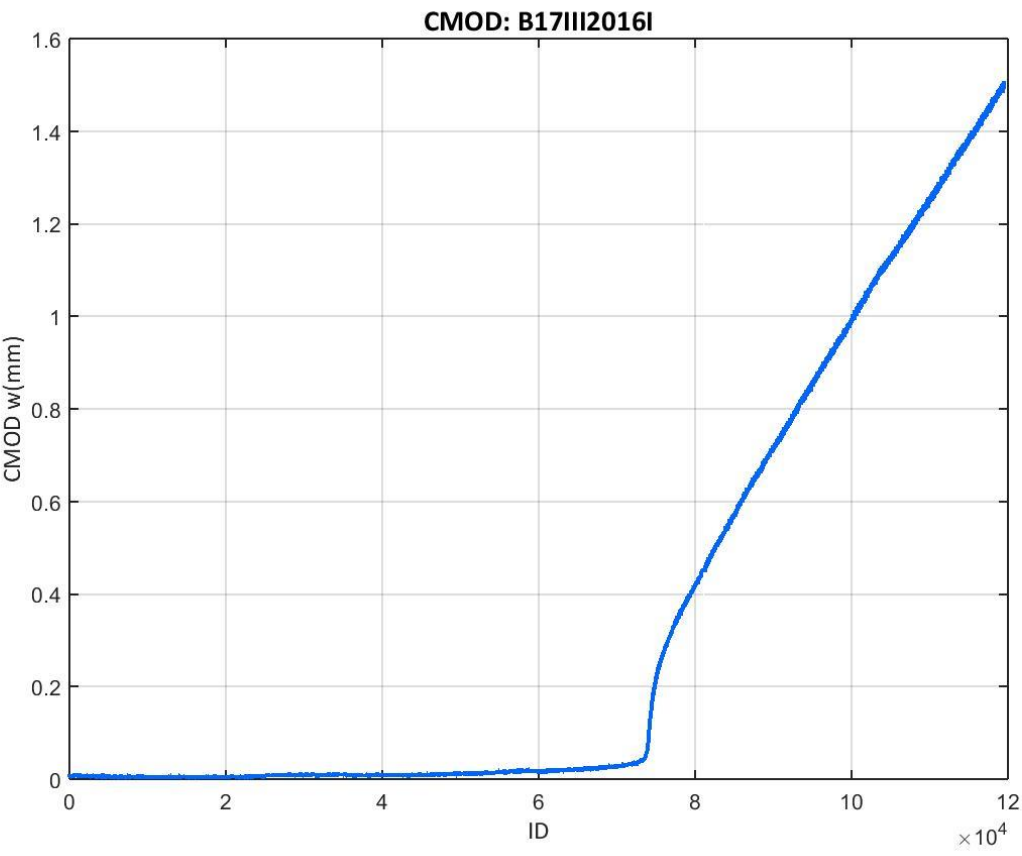


Figure 356: CMOD values recorded at the B17III2016I test

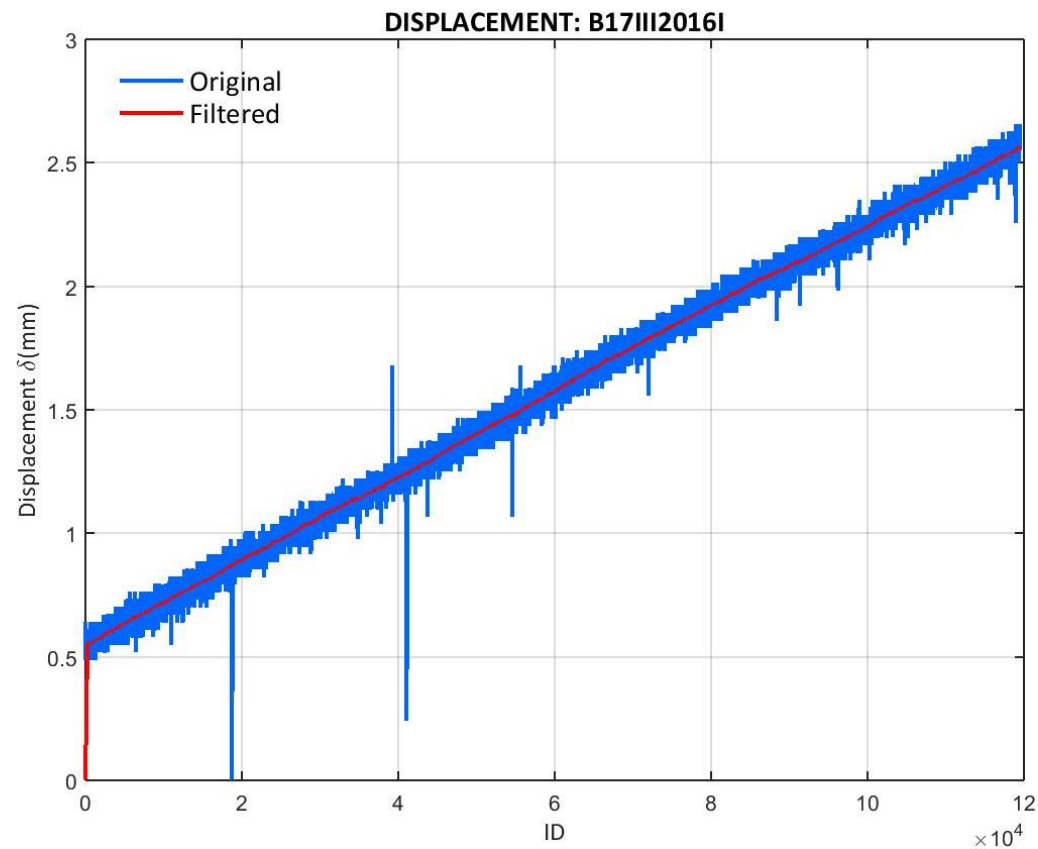


Figure 357: Displacement values recorded at the B17III2016I test

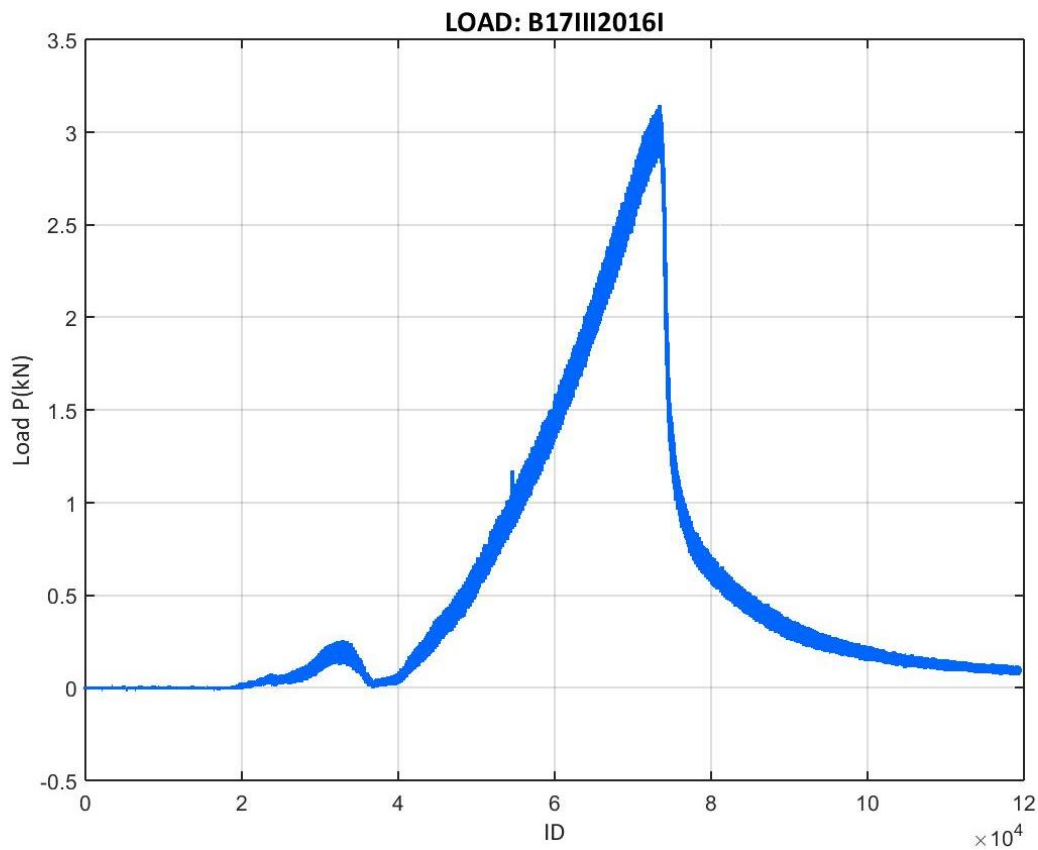


Figure 358: Load values recorded at the B17III2016I test

- B17III2016II

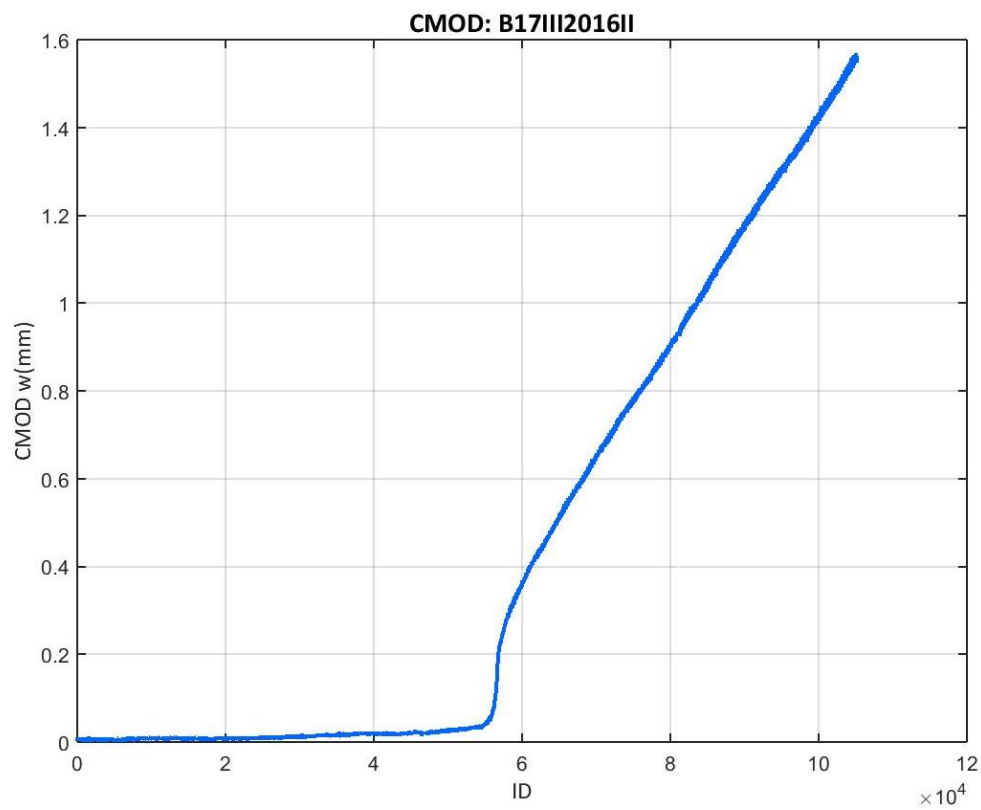


Figure 359: CMOD values recorded at the B17III2016II test

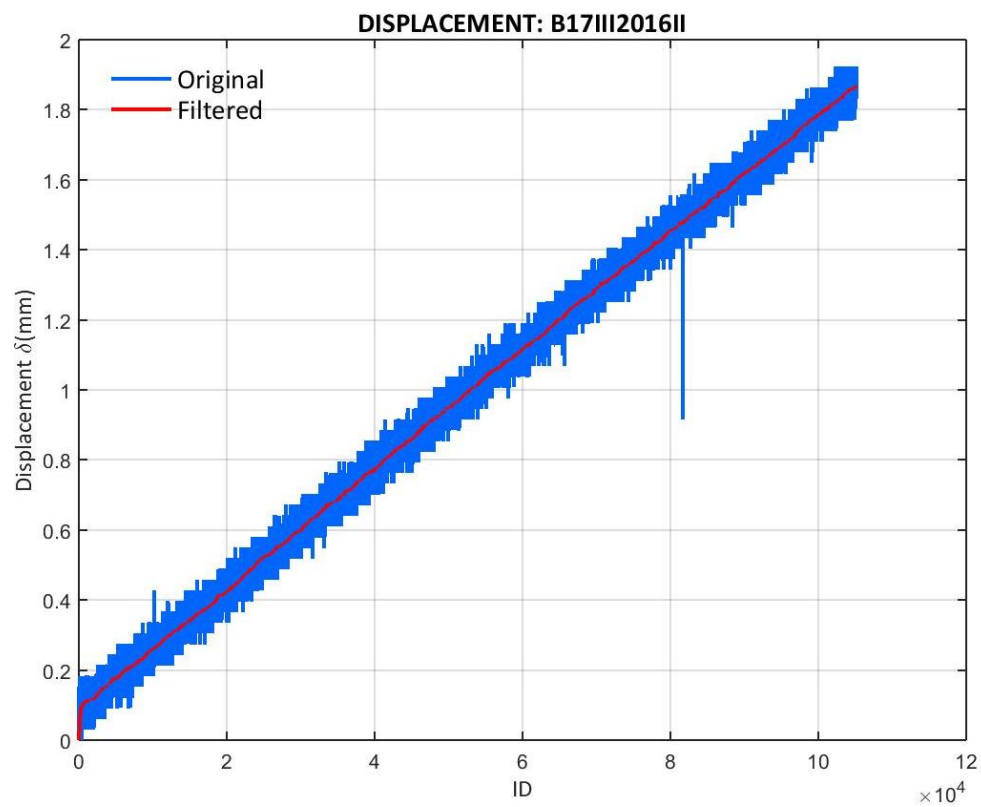


Figure 360: Displacement values recorded at the B17III2016II test

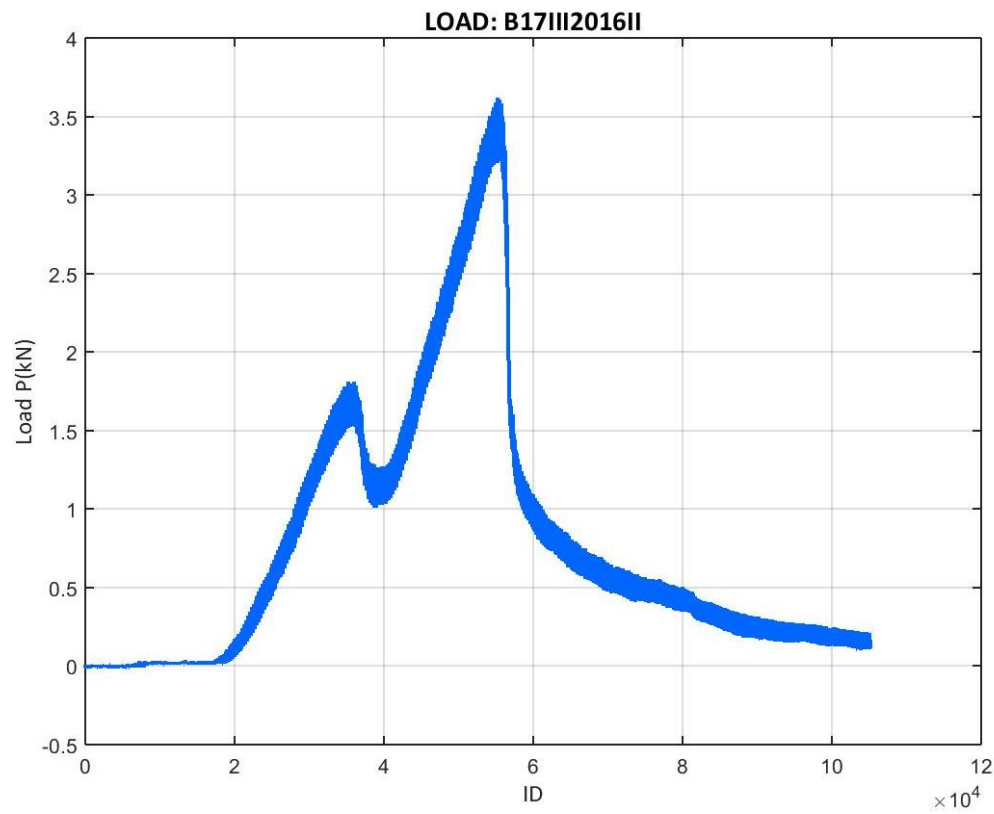


Figure 361: Load values recorded at the B17III2016II test

- B17III2016III

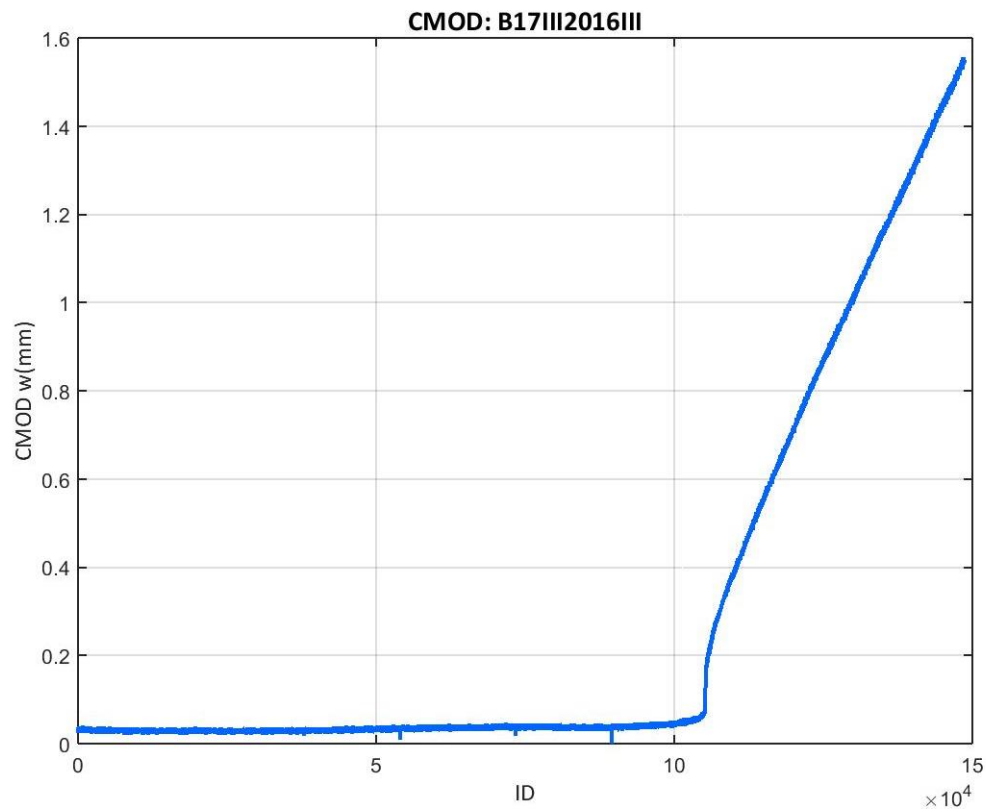


Figure 362: CMOD values recorded at the B17III2016III test

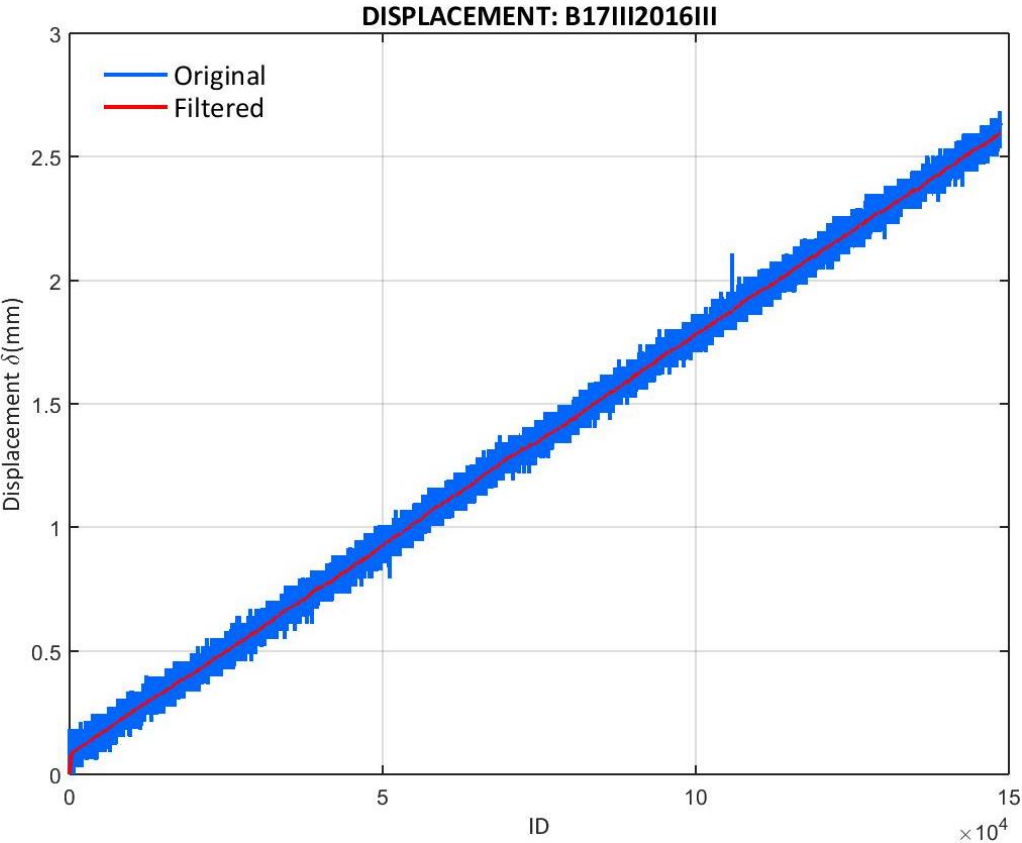


Figure 363: Displacement values recorded at the B17III2016III test

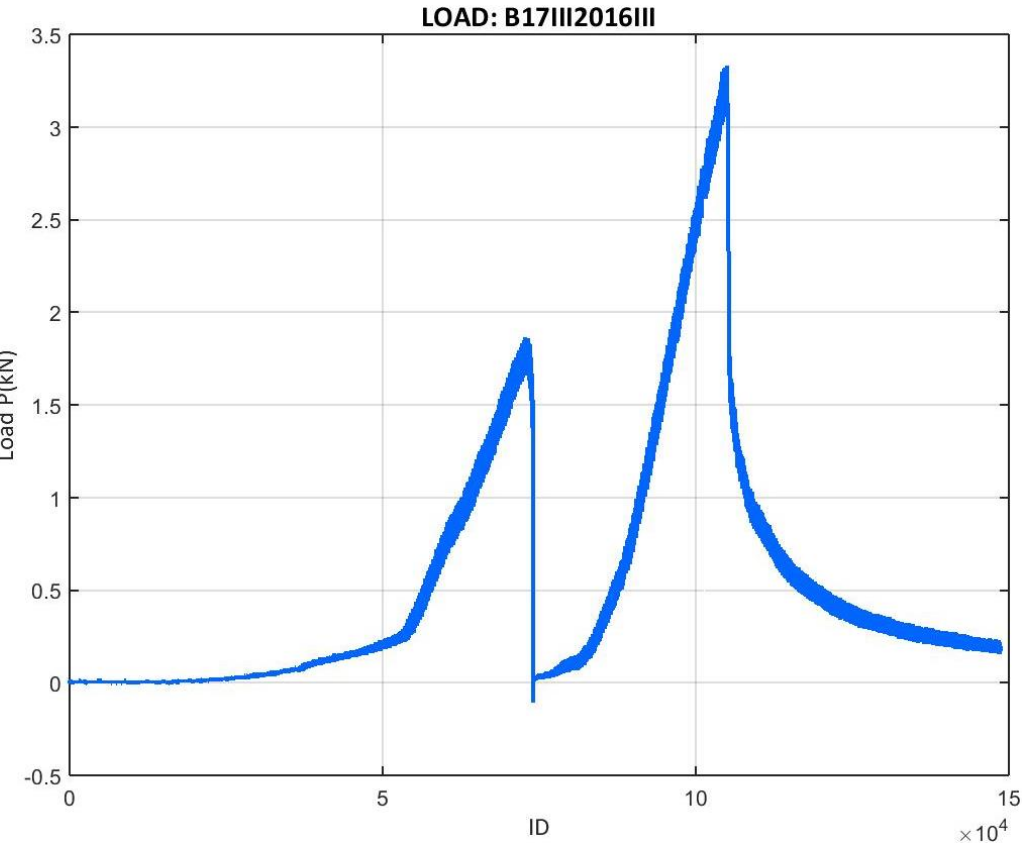


Figure 364: Load values recorded at the B17III2016III test

- B17III2016IV

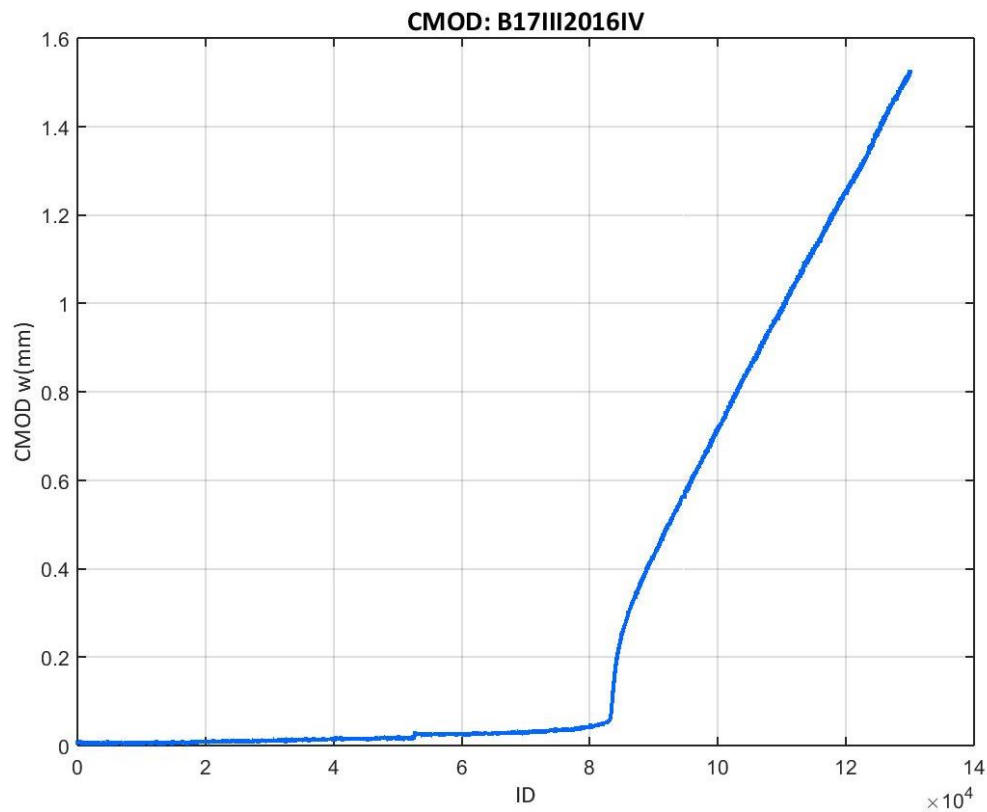


Figure 365: CMOD values recorded at the B17III2016IV test

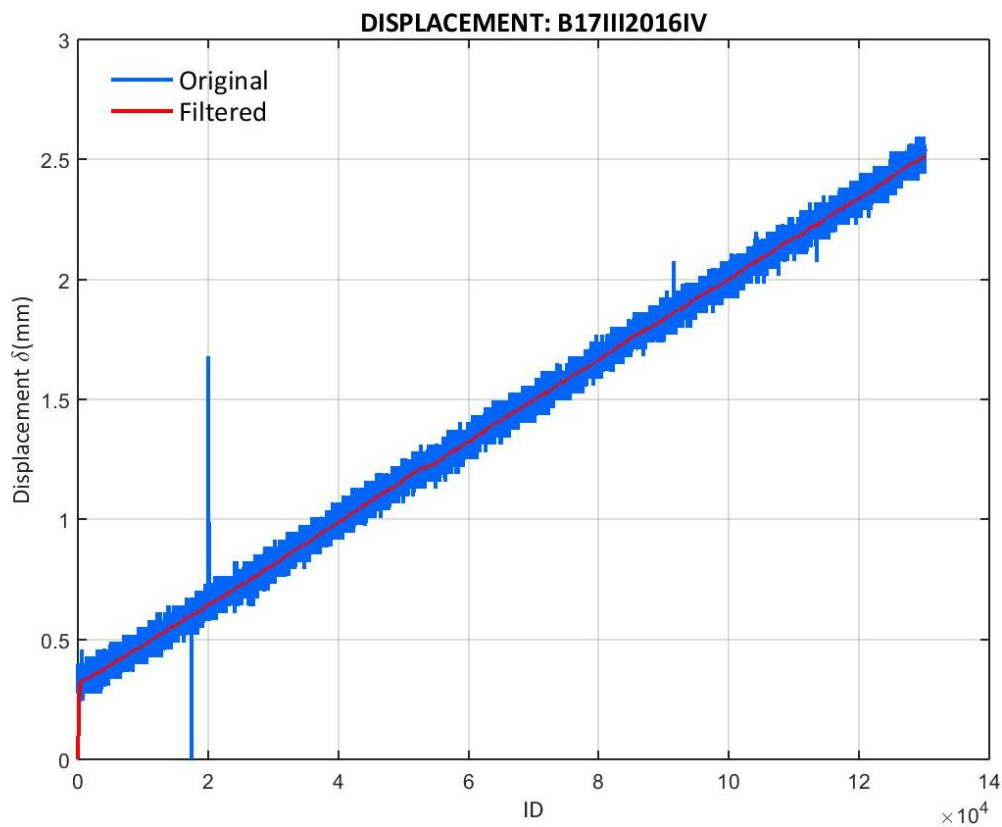


Figure 366: Displacement values recorded at the B17III2016IV test

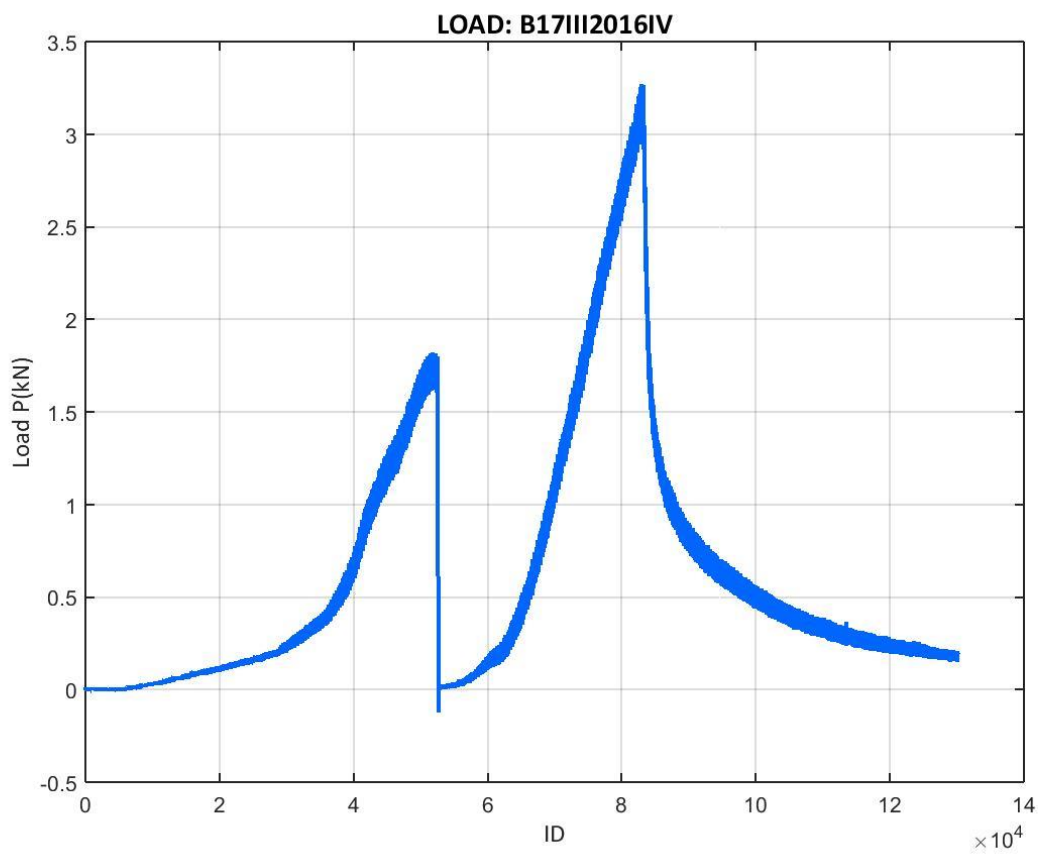


Figure 367: Load values recorded at the B17III2016IV test

E.7.2 17III2016 CORRECTED LOAD VS. CMOD

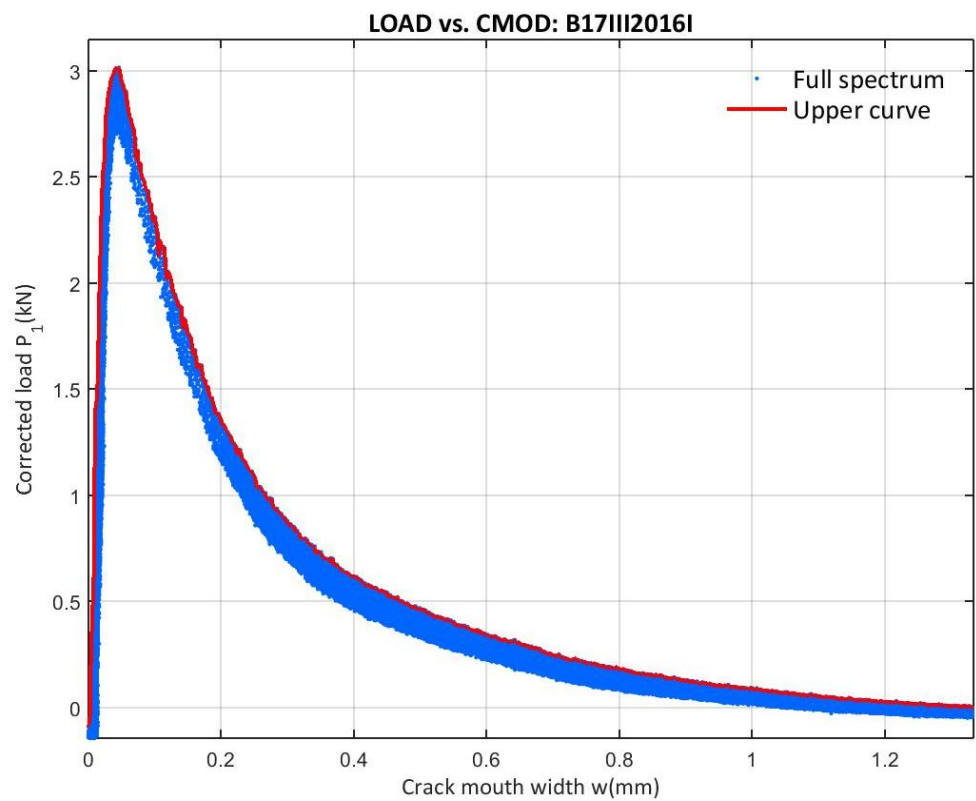


Figure 368: Corrected load vs. CMOD at the B17III2016I test

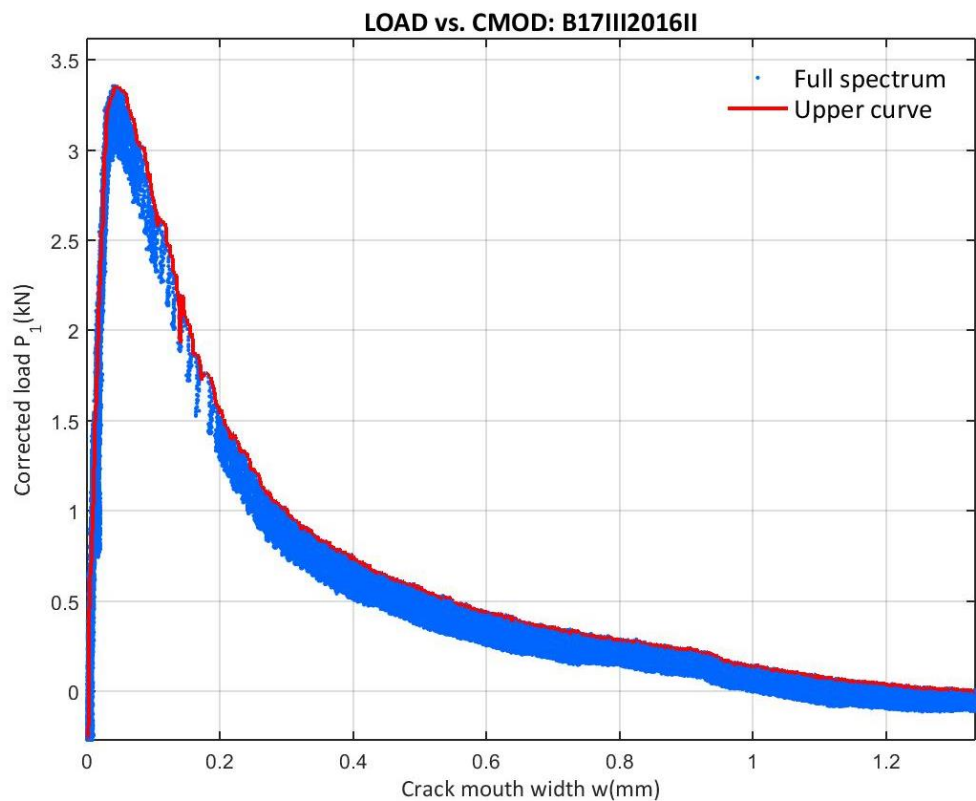


Figure 369: Corrected load vs. CMOD at the B17III2016II test

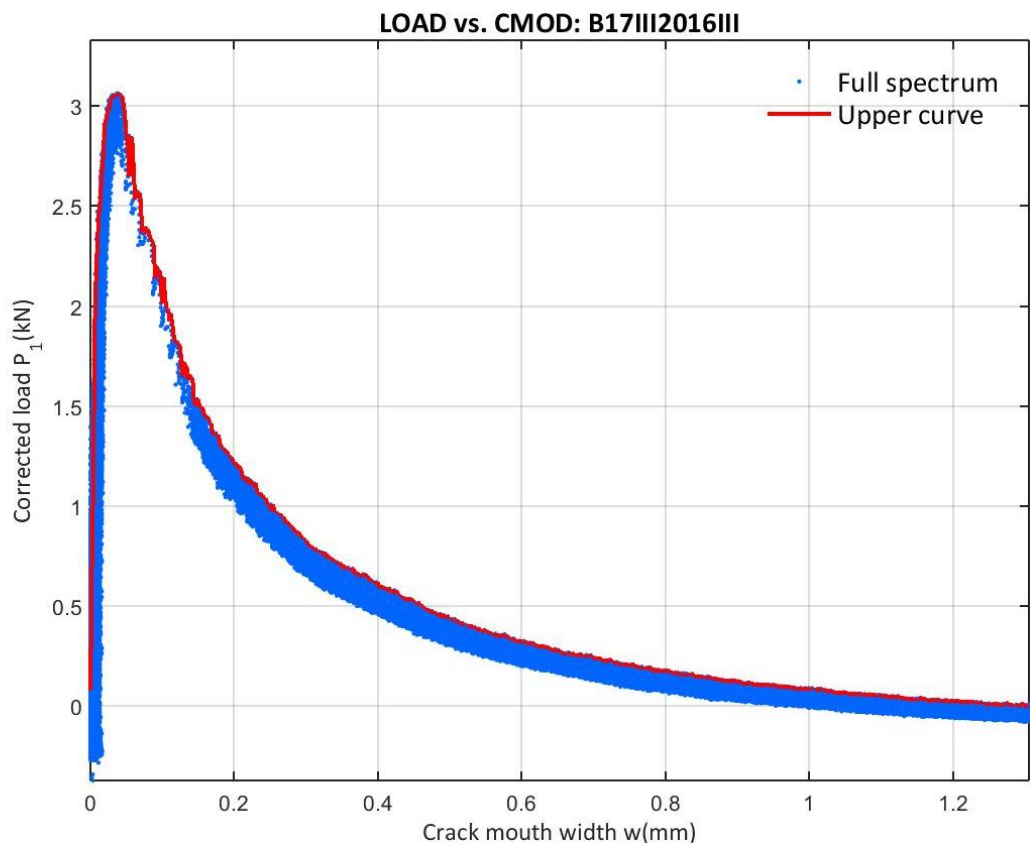


Figure 370: Corrected load vs. CMOD at the B17III2016III test

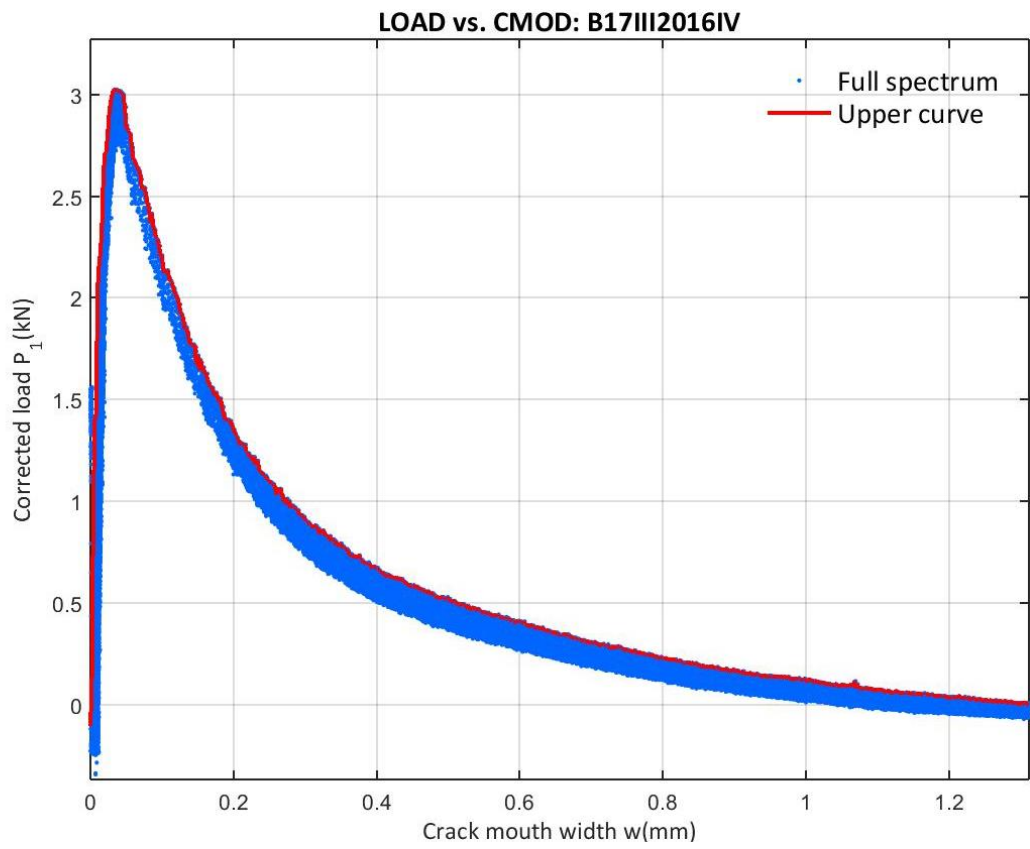


Figure 371: Corrected load vs. CMOD at the B17III2016IV test

E.7.3 17III2016 CORRECTED LOAD VS. VERTICAL DISPLACEMENT

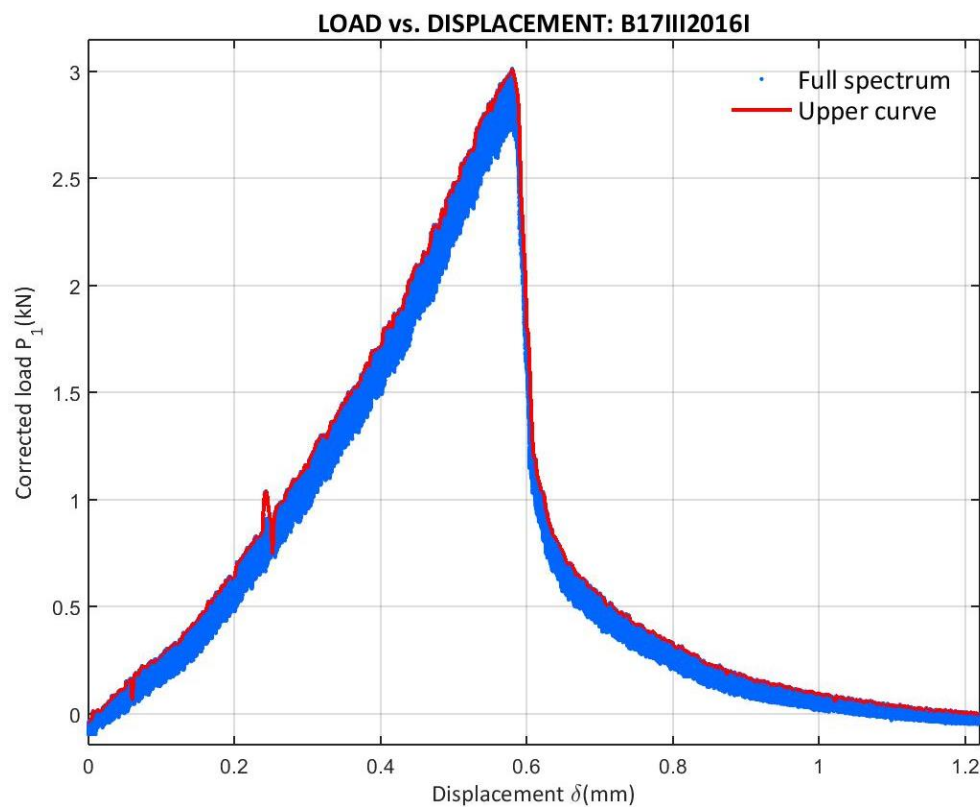


Figure 372: Corrected load vs. Displacement at the B17III2016I test

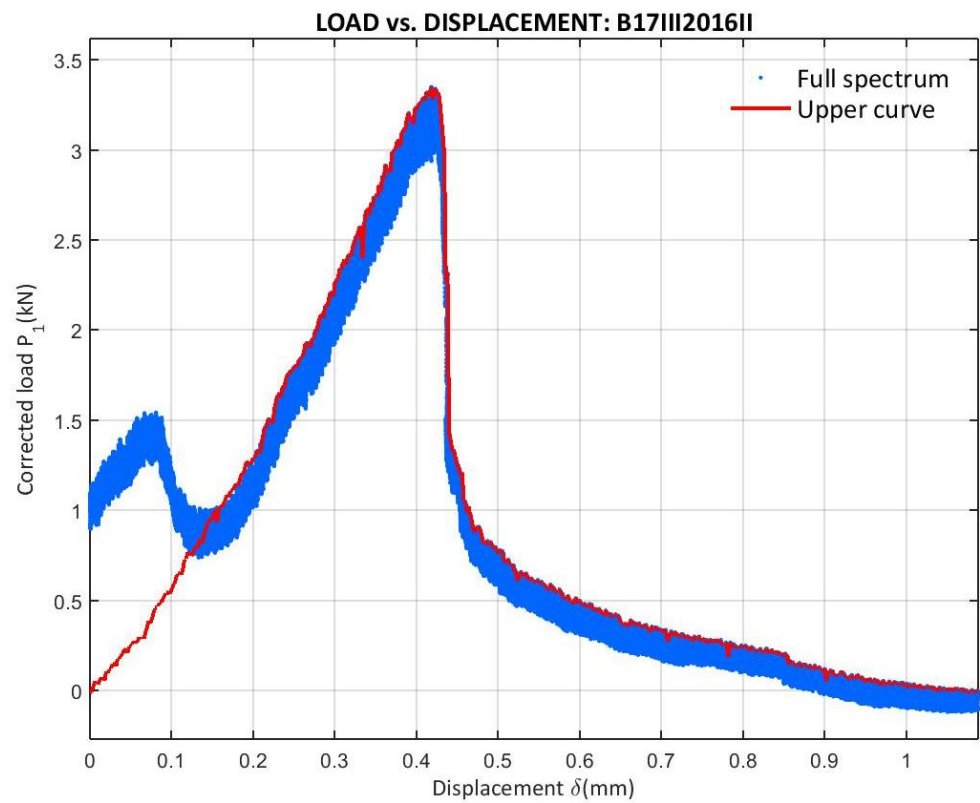


Figure 373: Corrected load vs. Displacement at the B17III2016II test

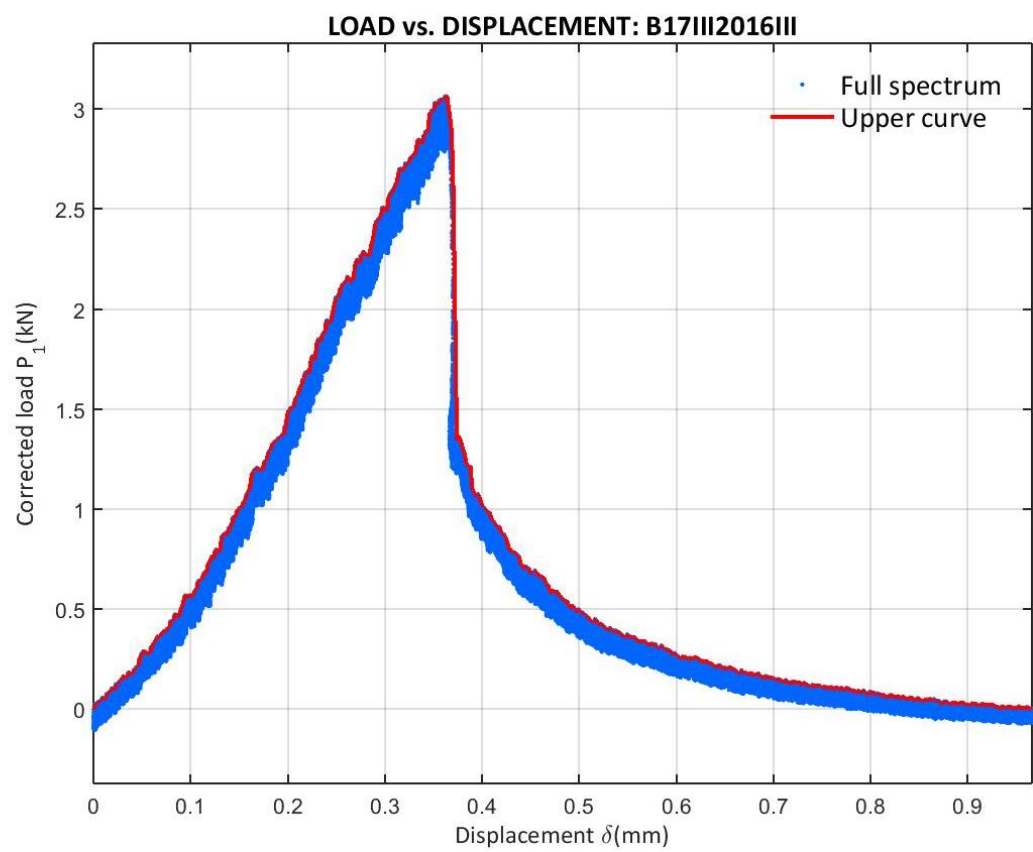


Figure 374: Corrected load vs. Displacement at the B17III2016III test

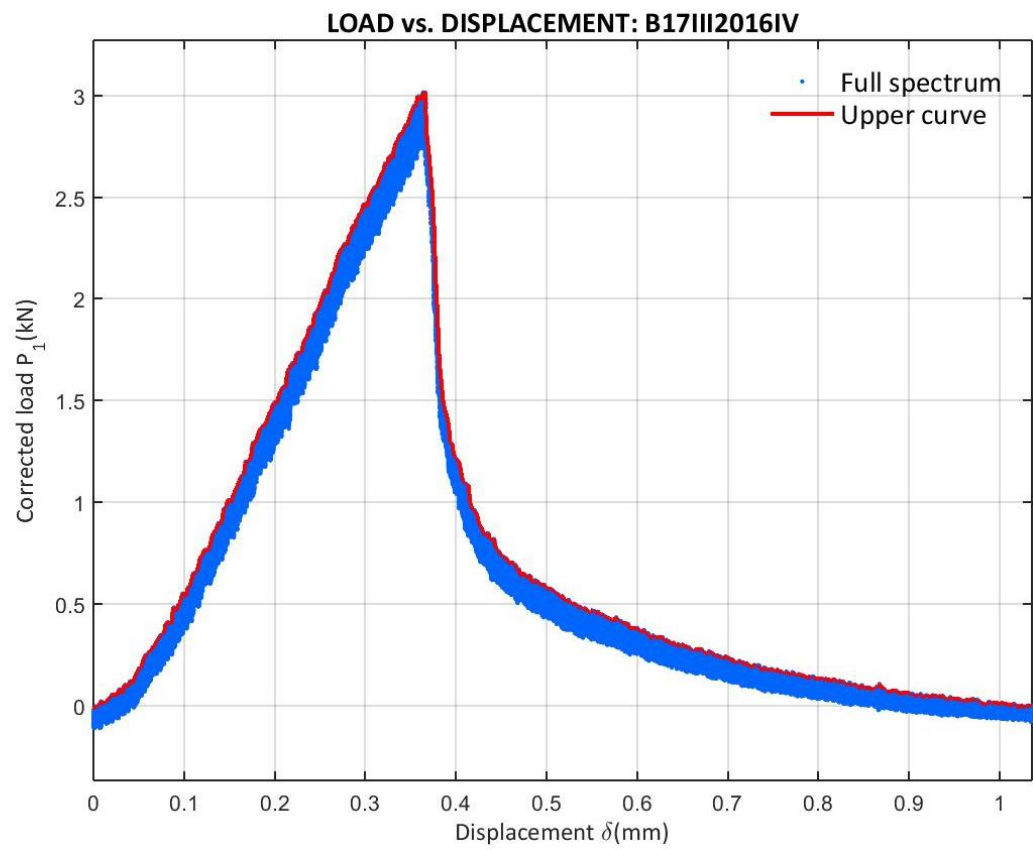


Figure 375: Corrected load vs. Displacement at the B17III2016IV test

E.7.4 17III2016 CORRECTED LOAD VS. X

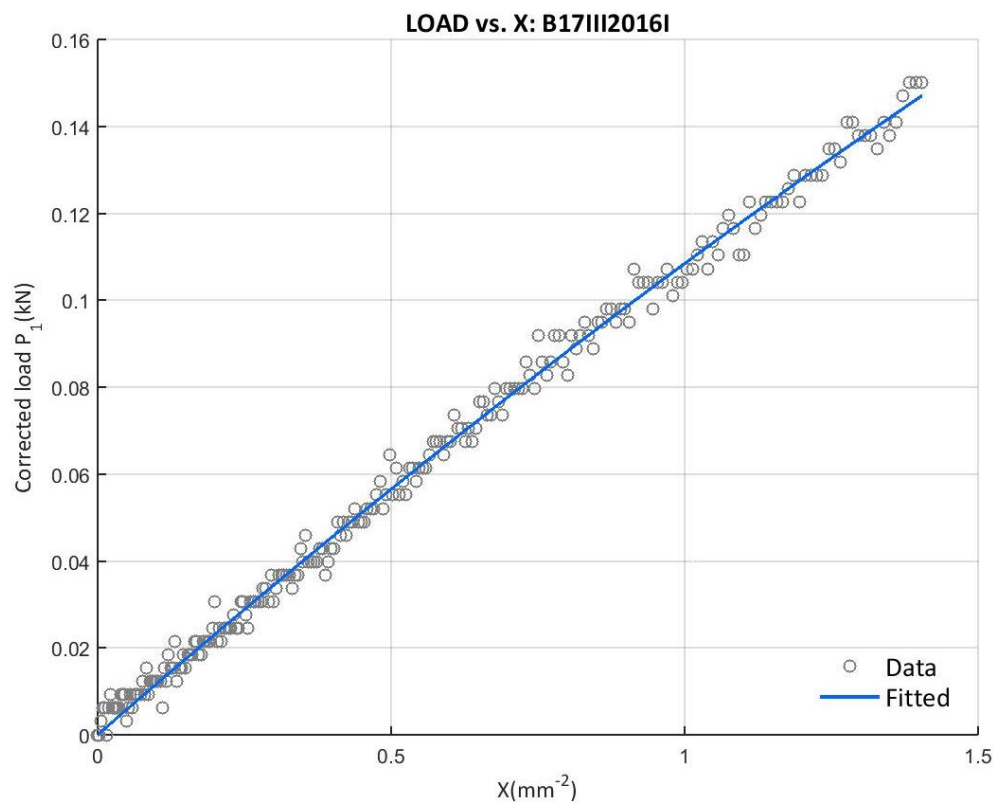


Figure 376: Corrected load vs. X at the B17III2016I test with the final upper curve data

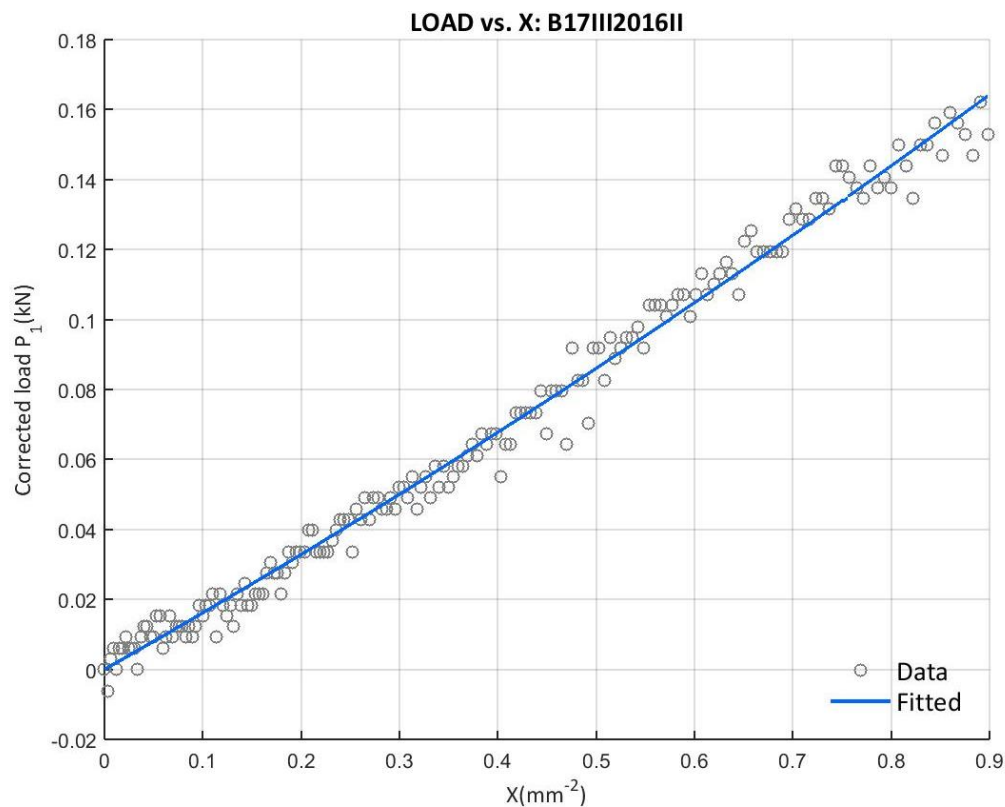


Figure 377: Corrected load vs. X at the B17III2016II test with the final upper curve data

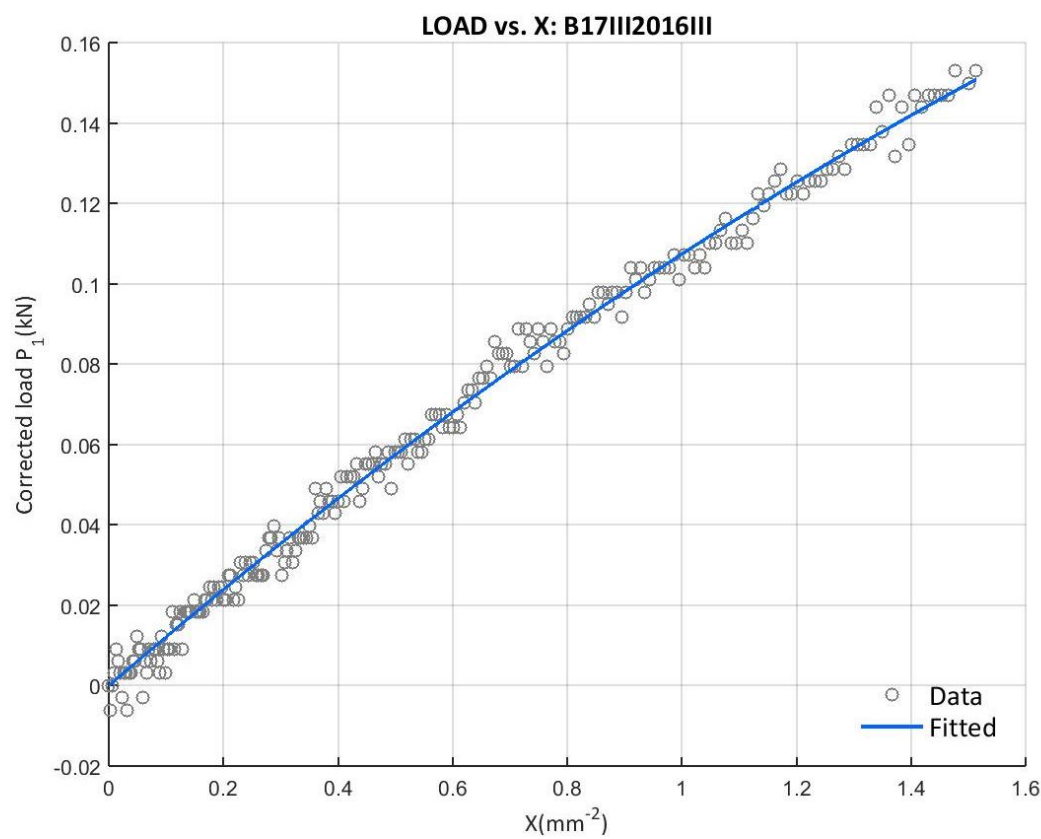


Figure 378: Corrected load vs. X at the B17III2016III test with the final upper curve data

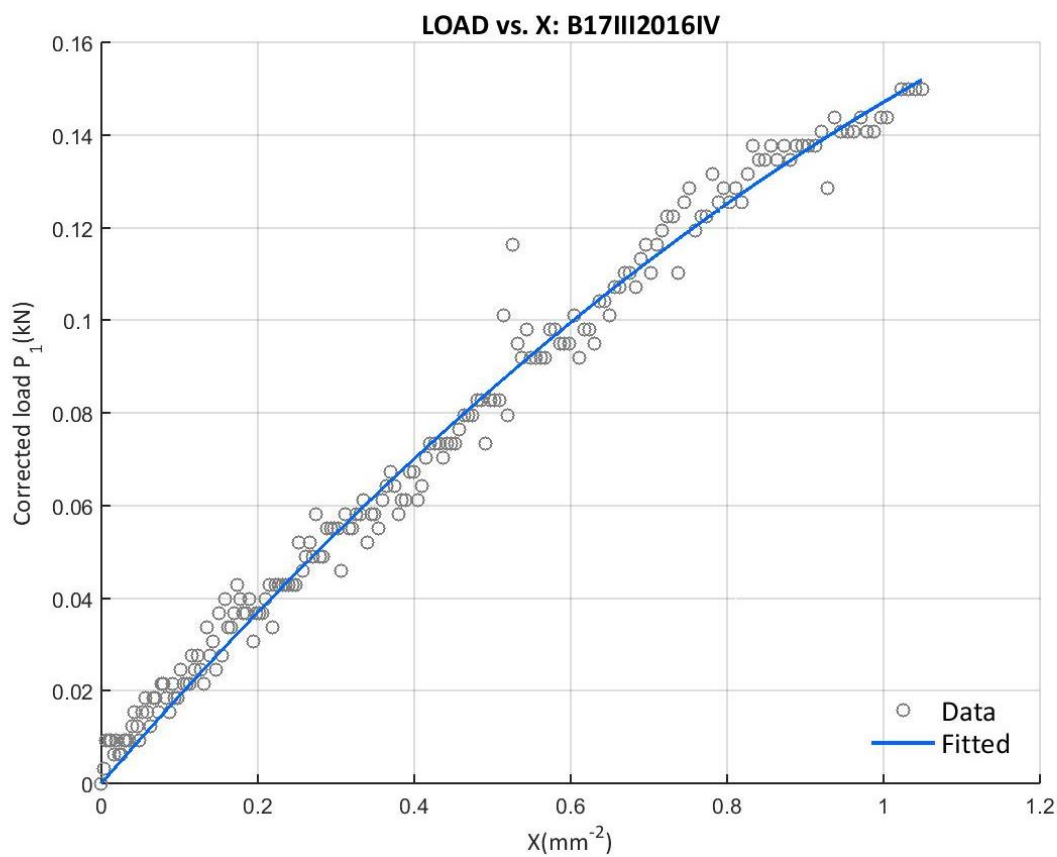


Figure 379: Corrected load vs. X at the B17III2016IV test with the final upper curve data

E.7.5 17III2016 SOFTENING CURVE BILINEAR APPROXIMATION

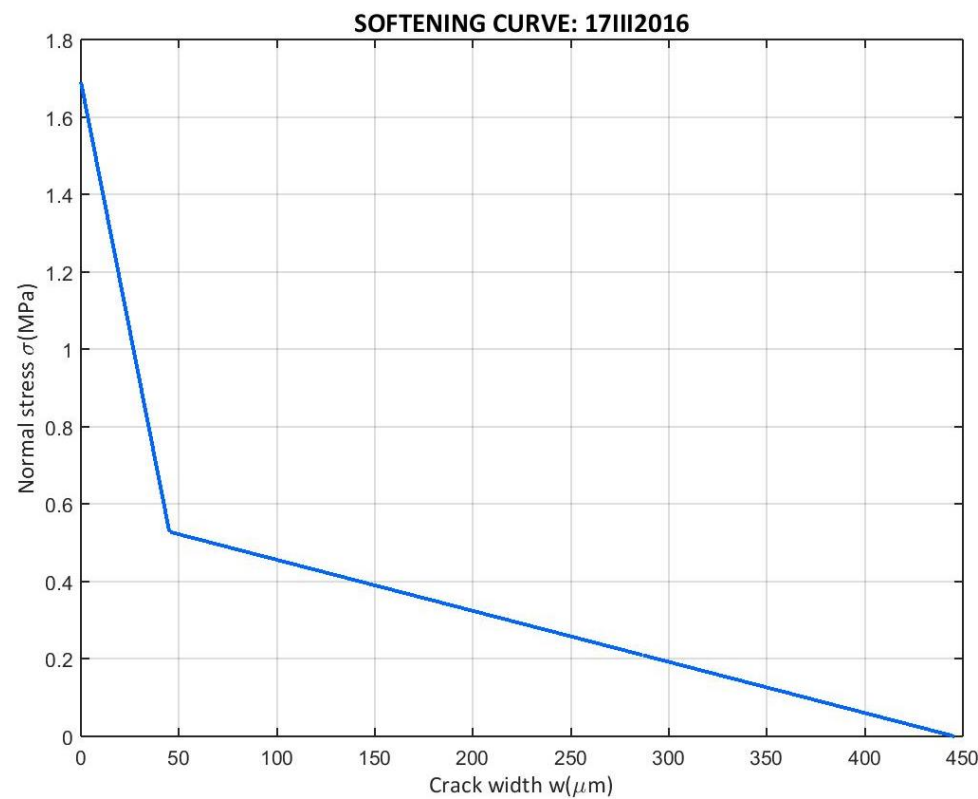


Figure 380: Softening curve bilinear approximation of the 17III2016 campaign

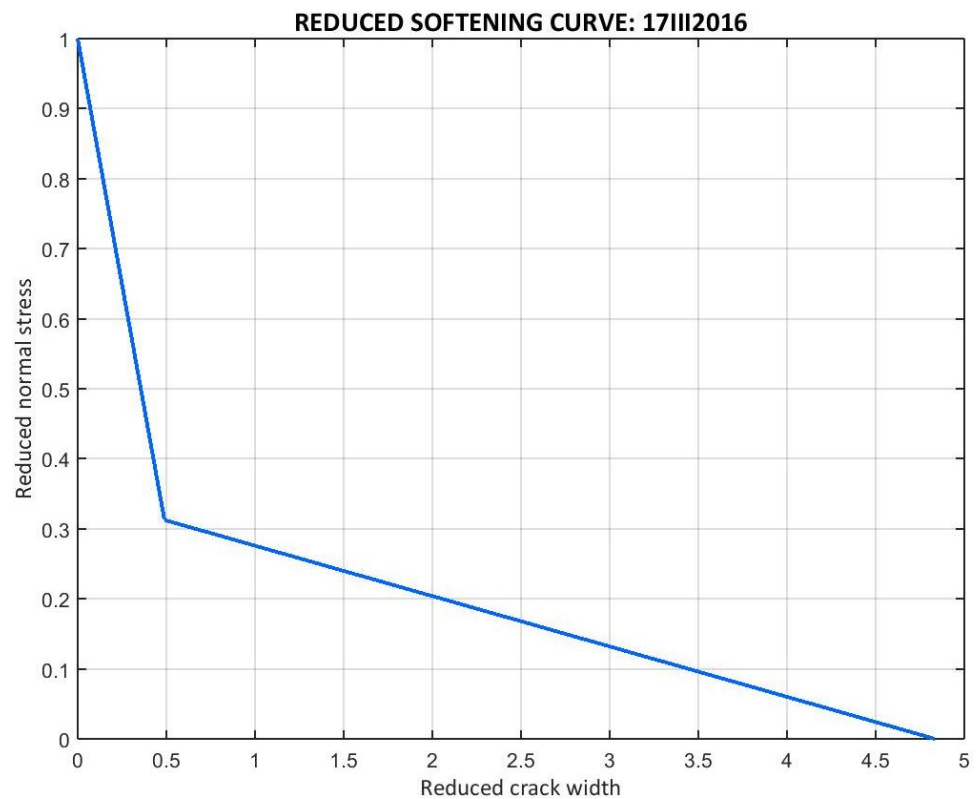


Figure 381: Softening curve bilinear approximation of the 17III2016 campaign in the reduced form

E.7.6 17III2016 SPECIMENS' COMPARISON

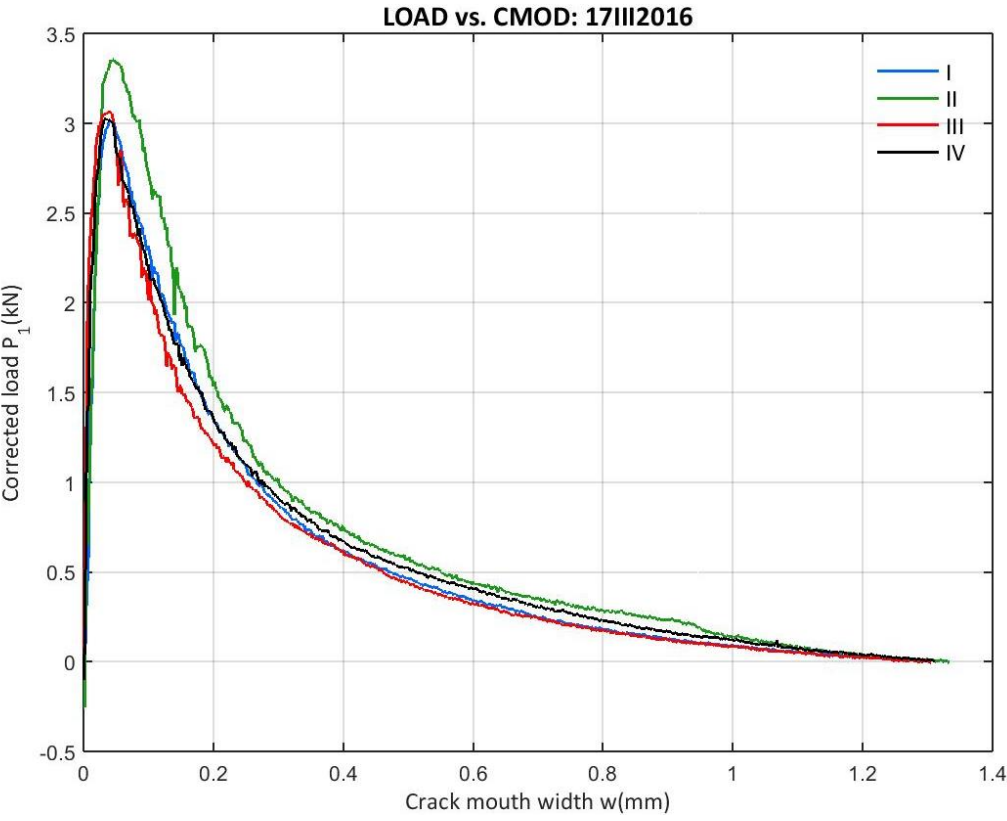


Figure 382: 17III2016 Corrected load vs. CMOD from the entire campaign

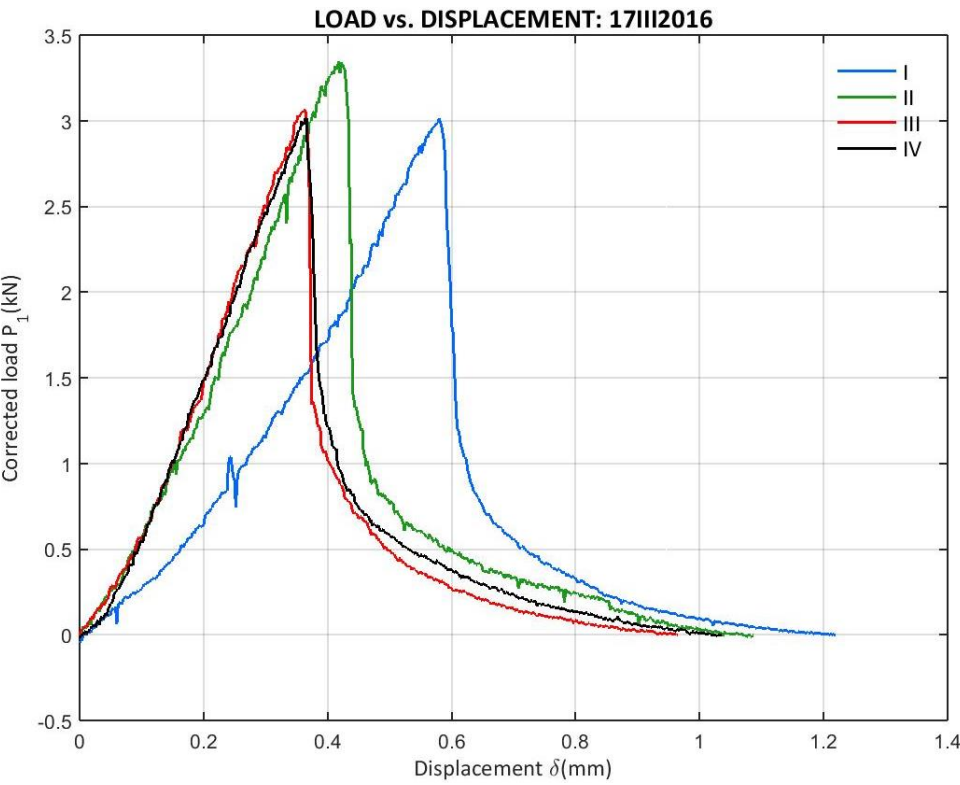


Figure 383: 17III2016 Corrected load vs. Displacement from the entire campaign

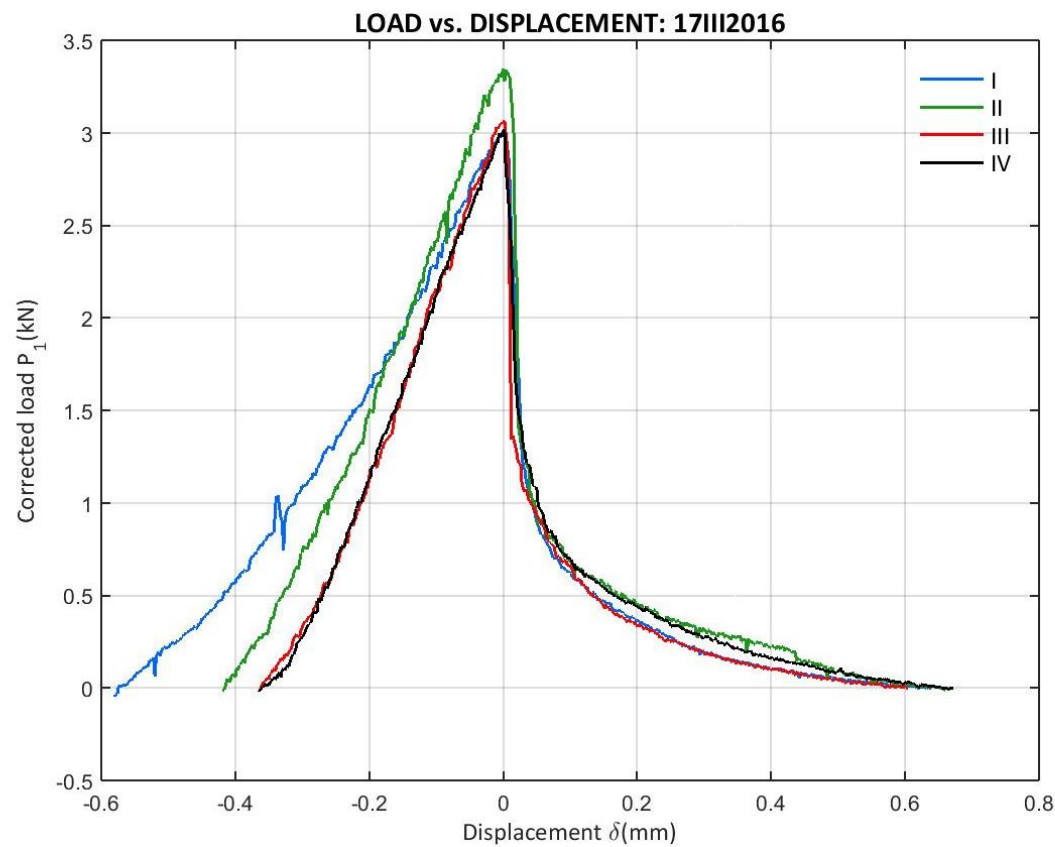


Figure 384: 17III2016 Corrected load vs. Displacement from the entire campaign (peak displacement zero)

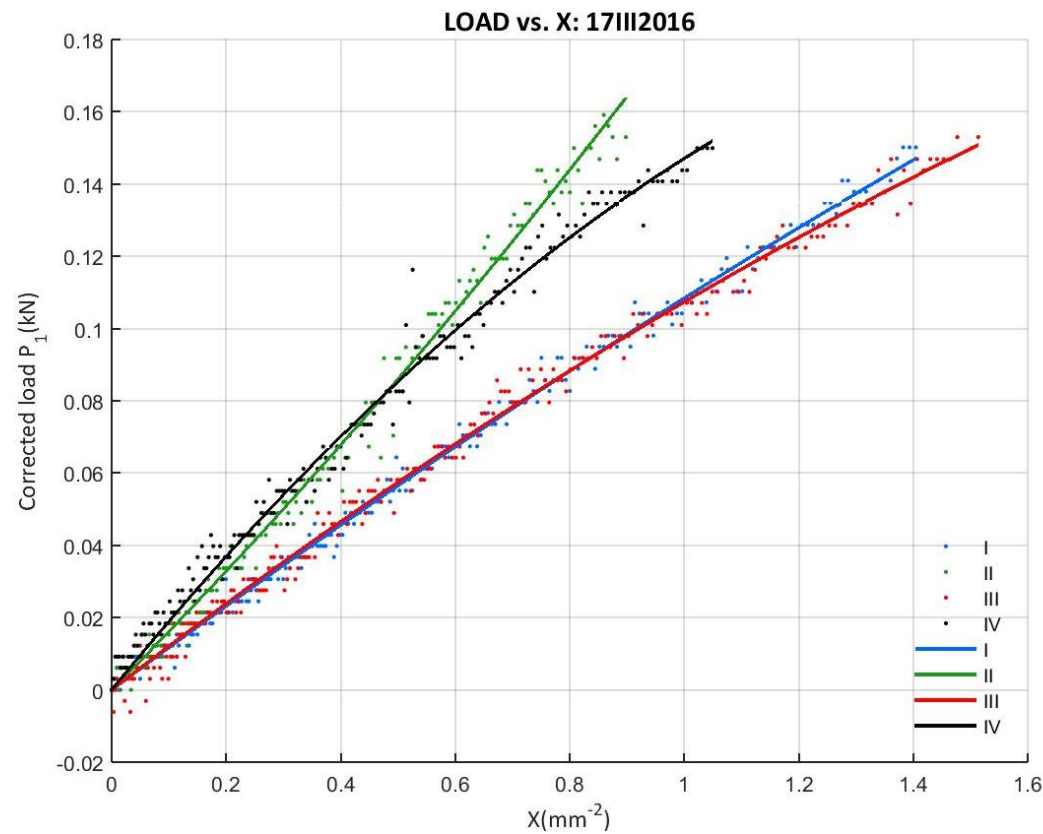


Figure 385: 17III2016 Corrected load vs. X from the entire campaign

E.8 01IV2016 CAMPAIGN

E.8.1 01IV2016 DATA

- B01IV2016I

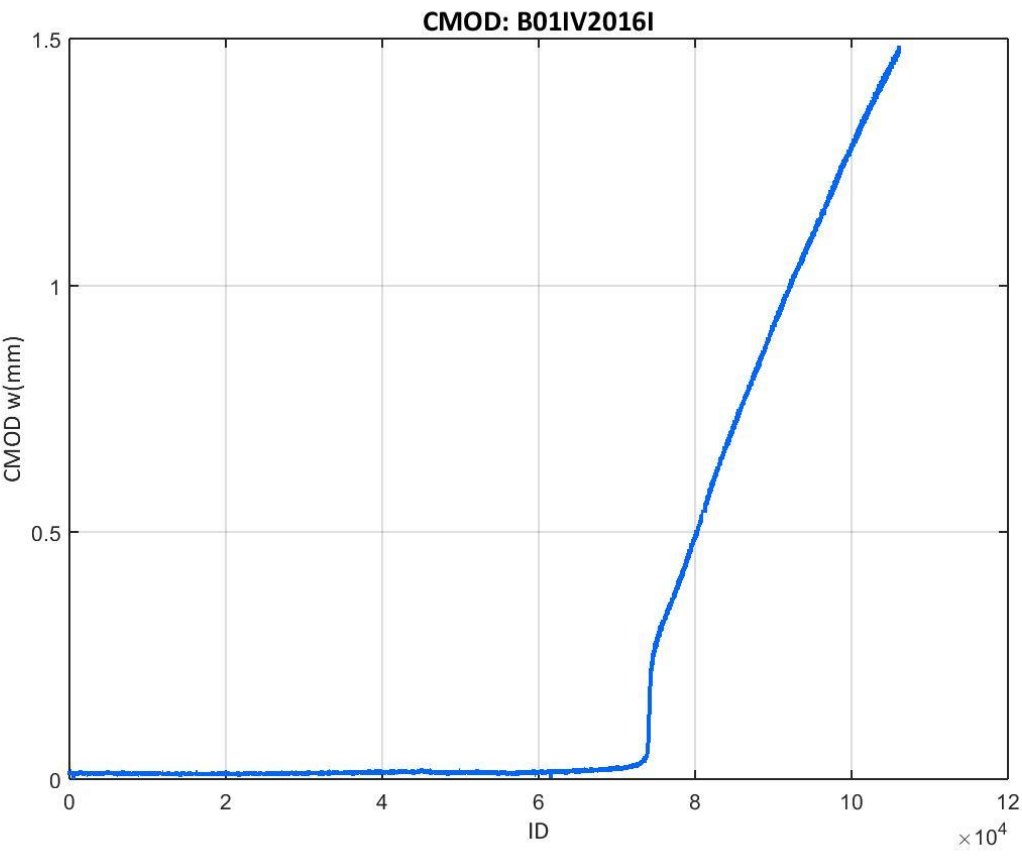


Figure 386: CMOD values recorded at the B01IV2016I test

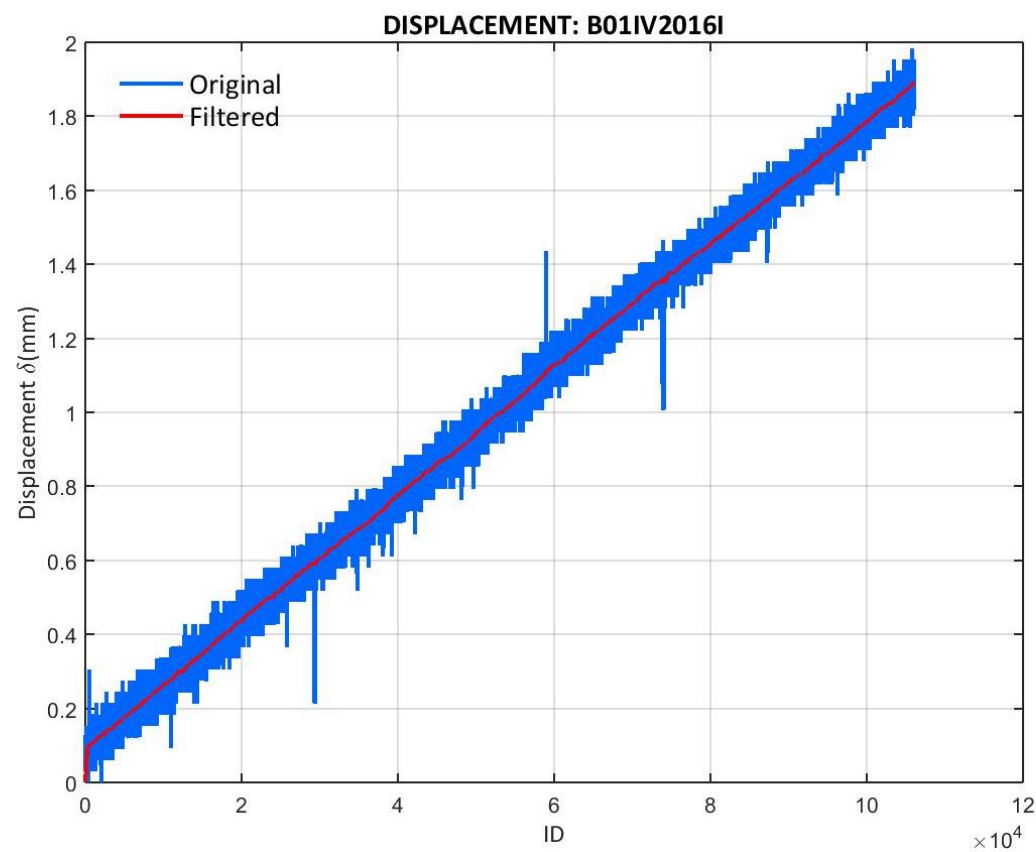


Figure 387: Displacement values recorded at the B01IV2016I test

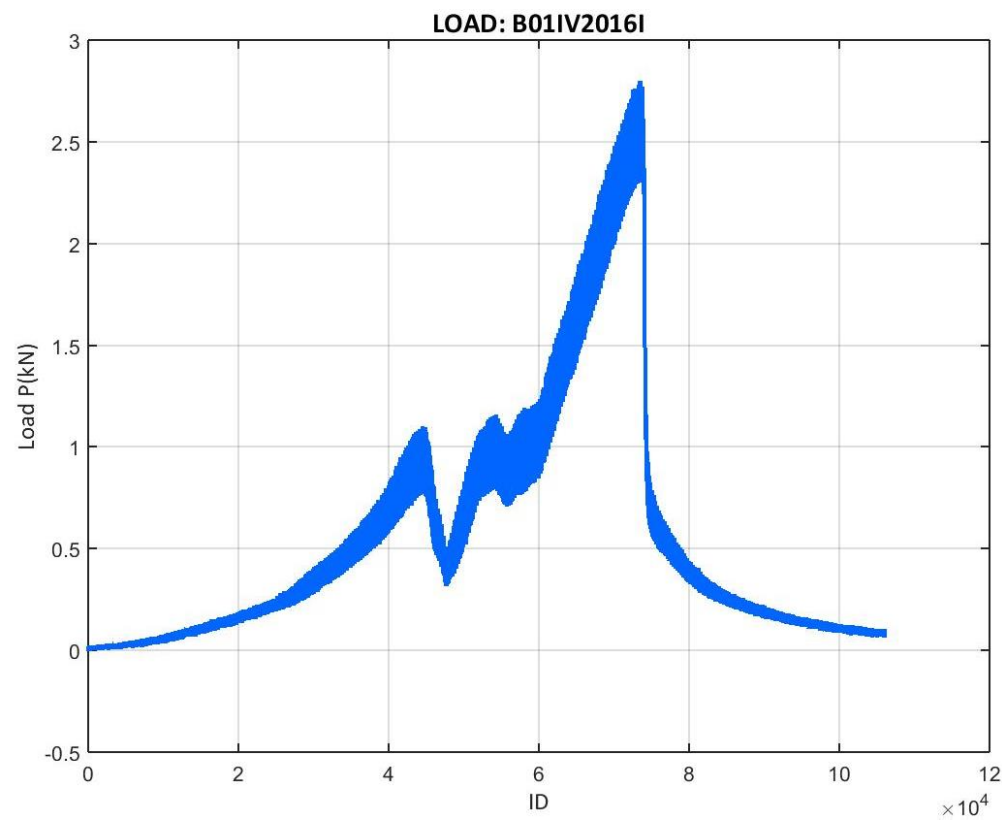


Figure 388: Load values recorded at the B01IV2016I test

- B01IV2016II

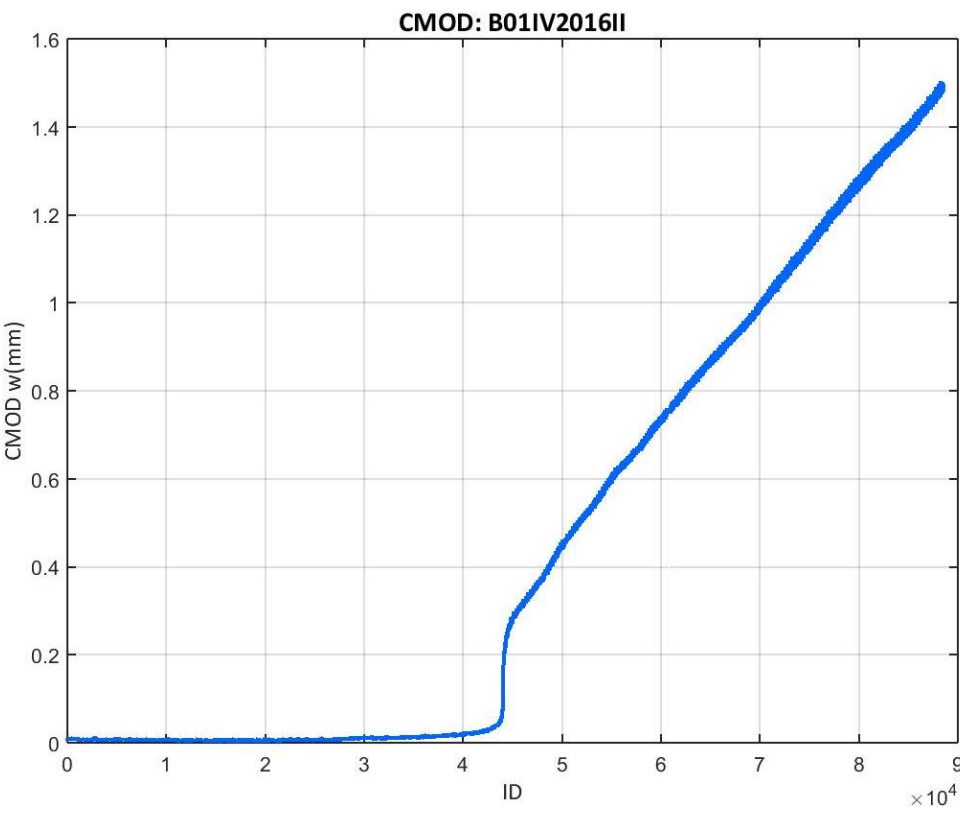


Figure 389: CMOD values recorded at the B01IV2016II test

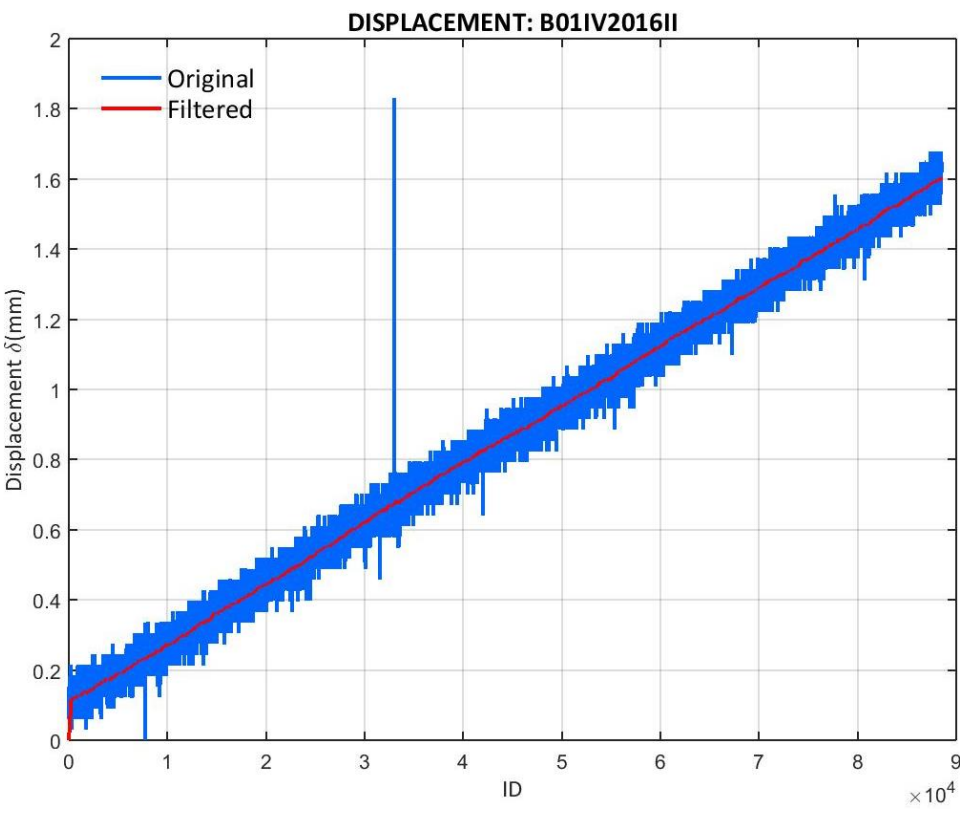


Figure 390: Displacement values recorded at the B01IV2016II test

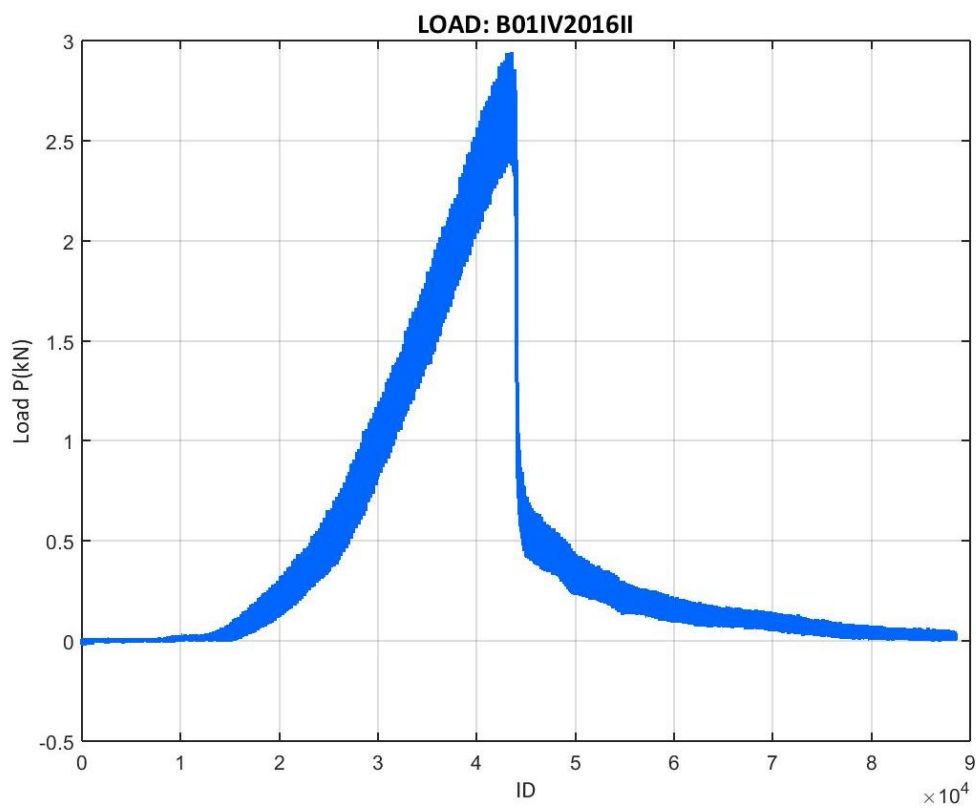


Figure 391: Load values recorded at the B01IV2016II test

- B01IV2016III

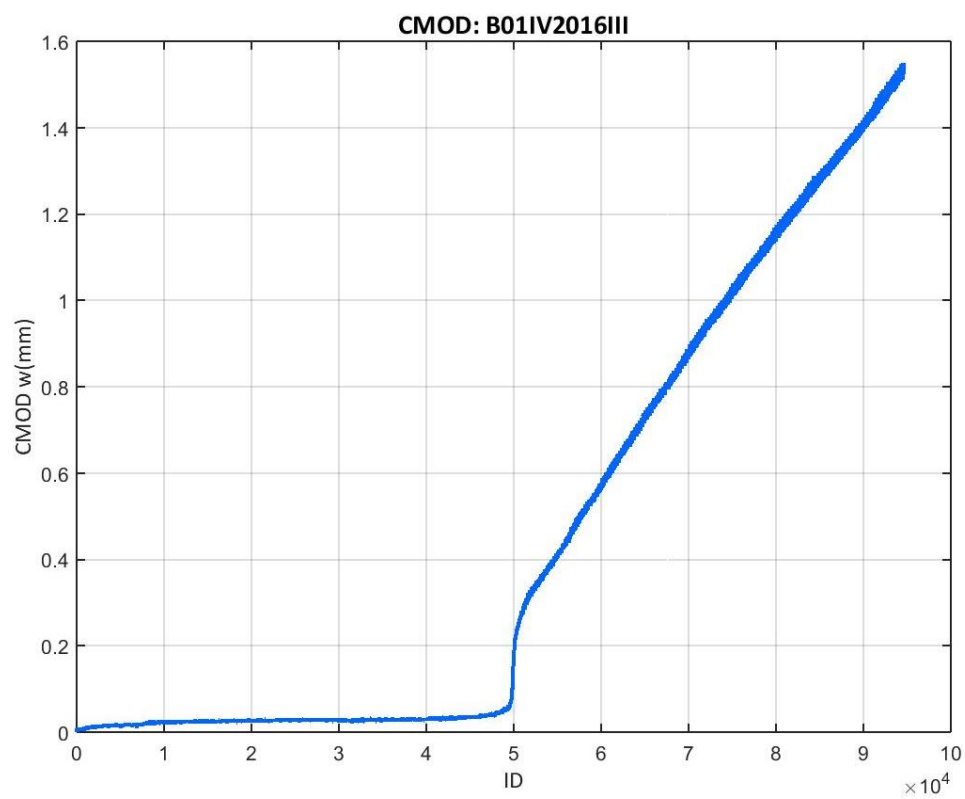


Figure 392: CMOD values recorded at the B01IV2016III test

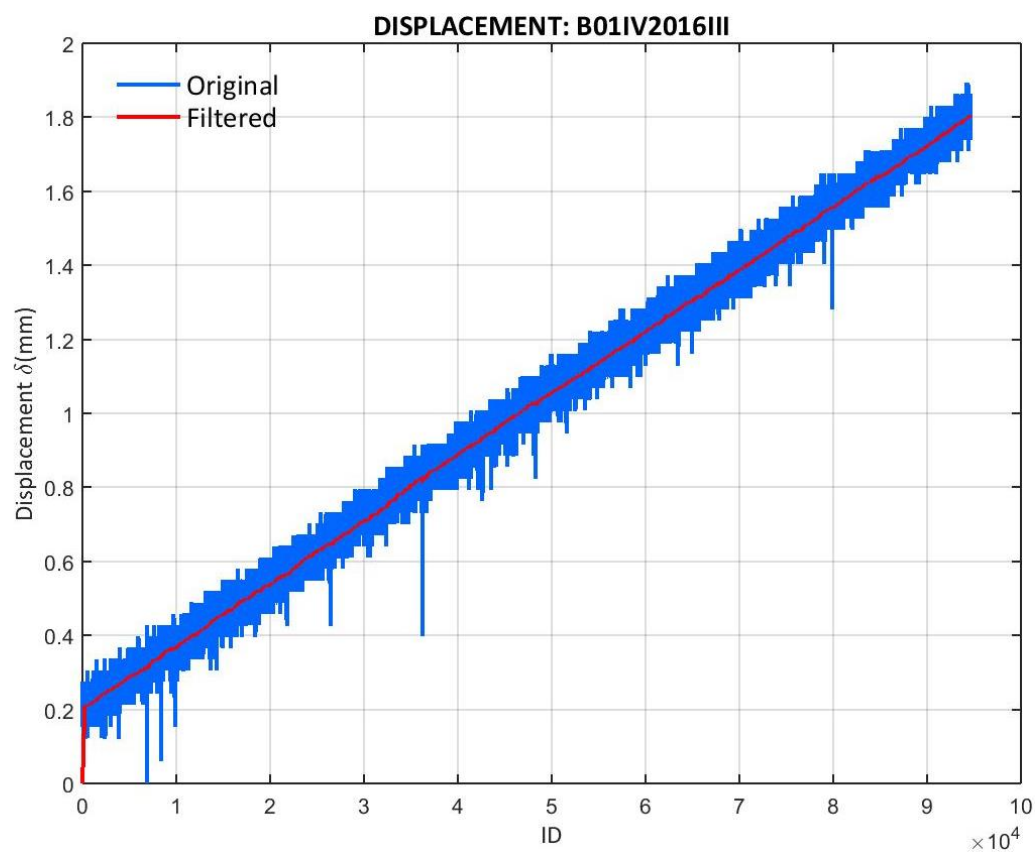


Figure 393: Displacement values recorded at the B01IV2016III test

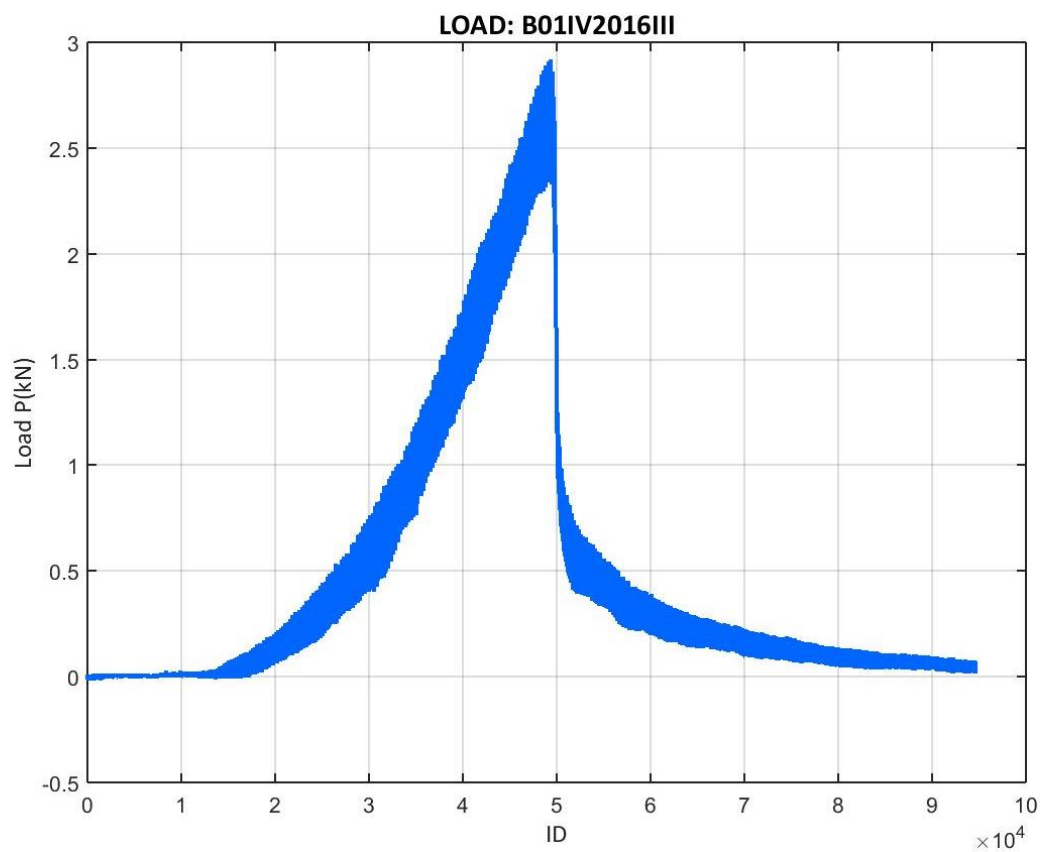


Figure 394: Load values recorded at the B01IV2016III test

- B01IV2016IV

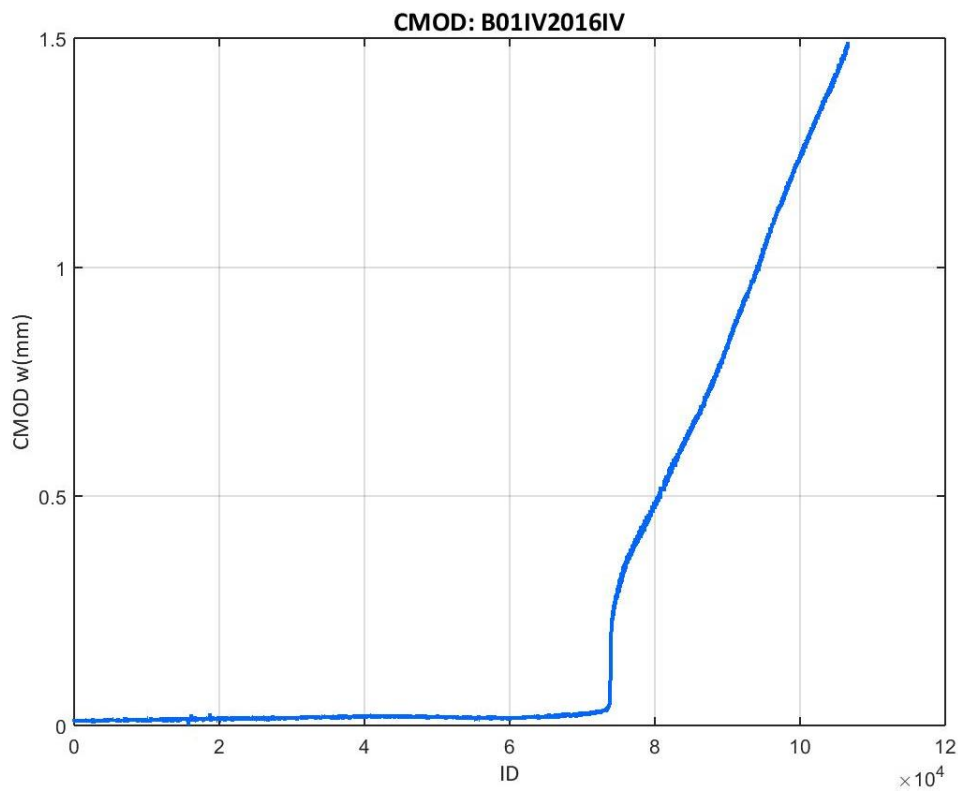


Figure 395: CMOD values recorded at the B01IV2016IV test

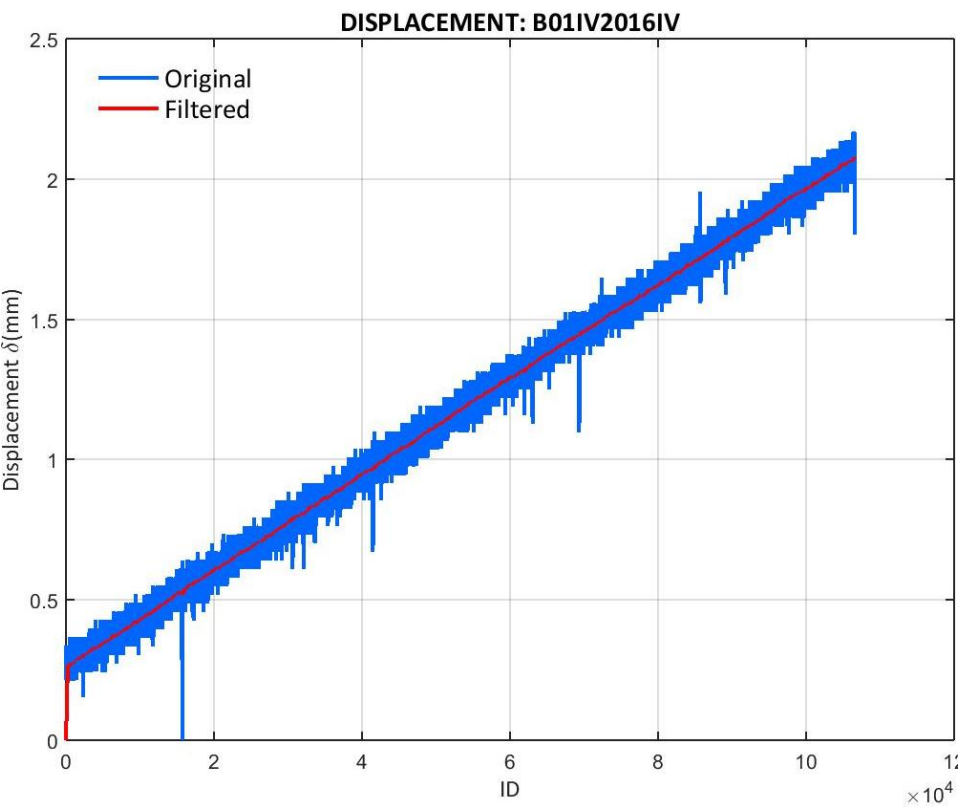


Figure 396: Displacement values recorded at the B01IV2016IV test

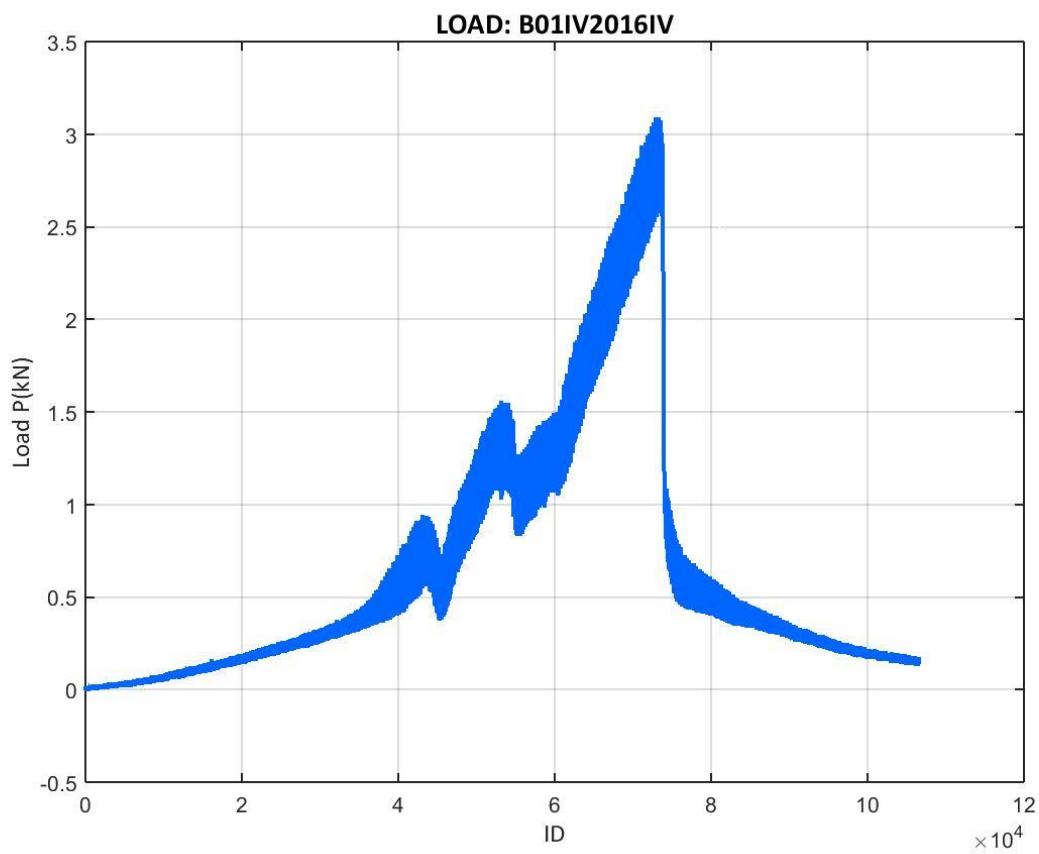


Figure 397: Load values recorded at the B01IV2016IV test

E.8.2 01IV2016 CORRECTED LOAD VS. CMOD

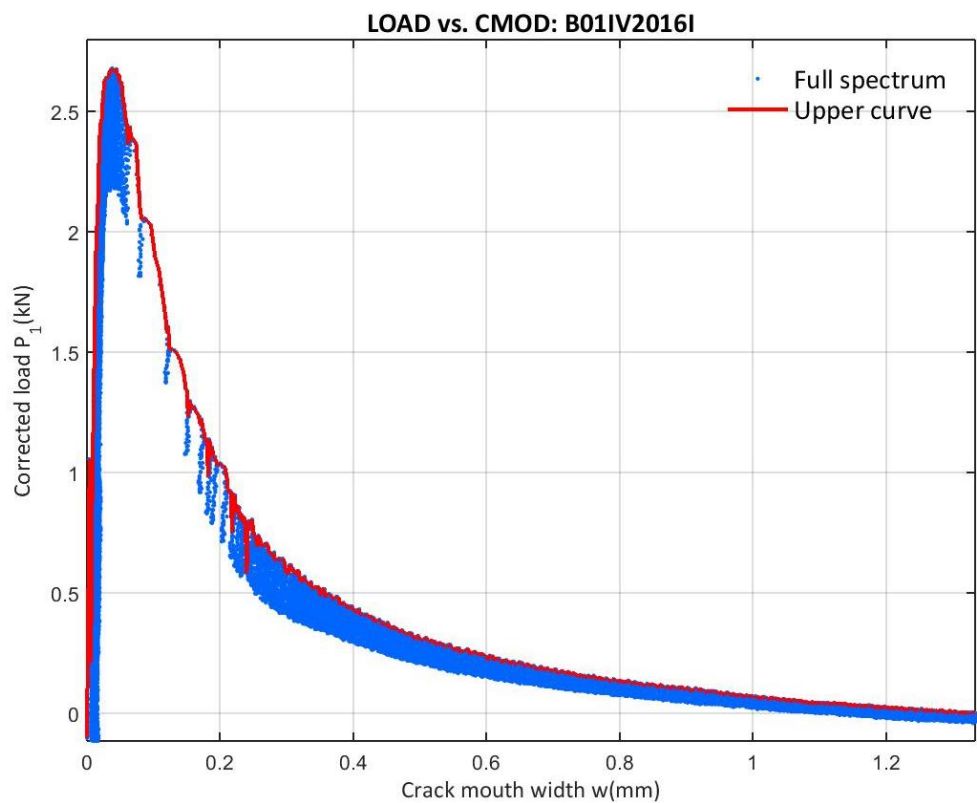


Figure 398: Corrected load vs. CMOD at the B01IV2016I test

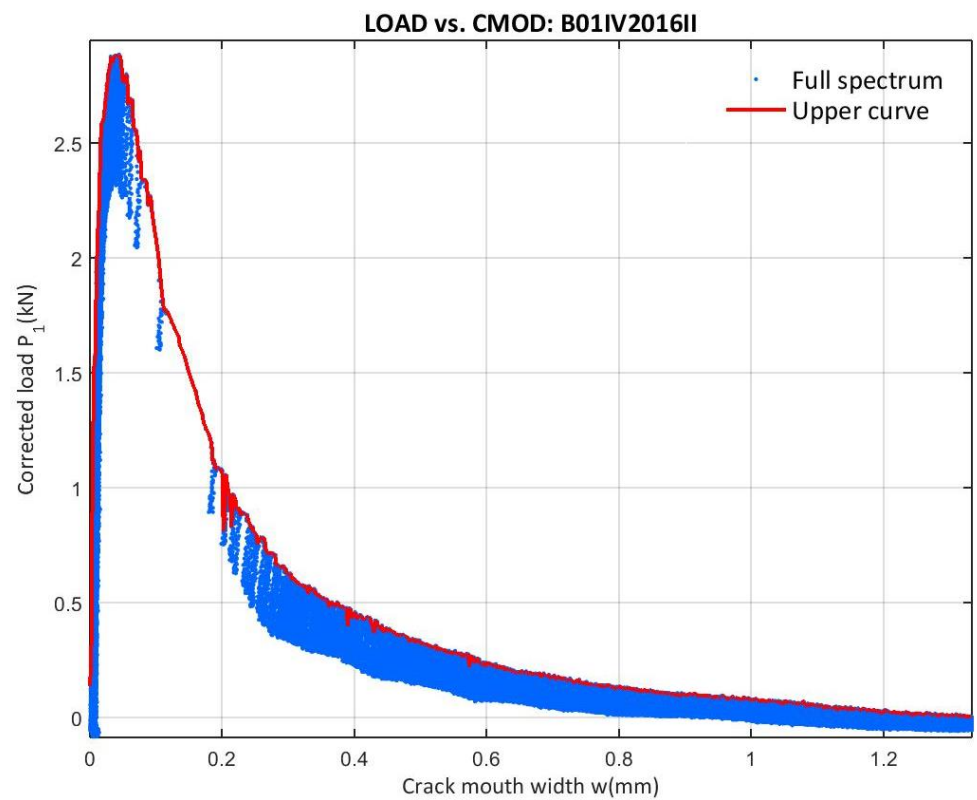


Figure 399: Corrected load vs. CMOD at the B01IV2016II test

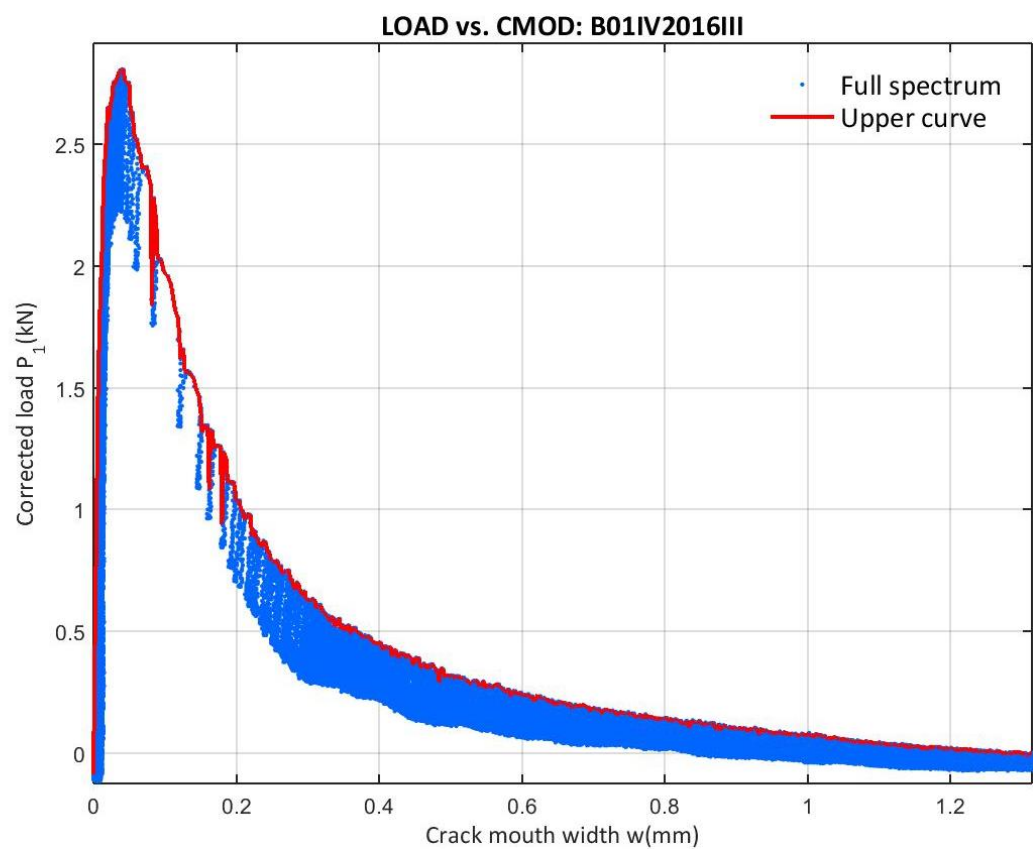


Figure 400: Corrected load vs. CMOD at the B01IV2016III test

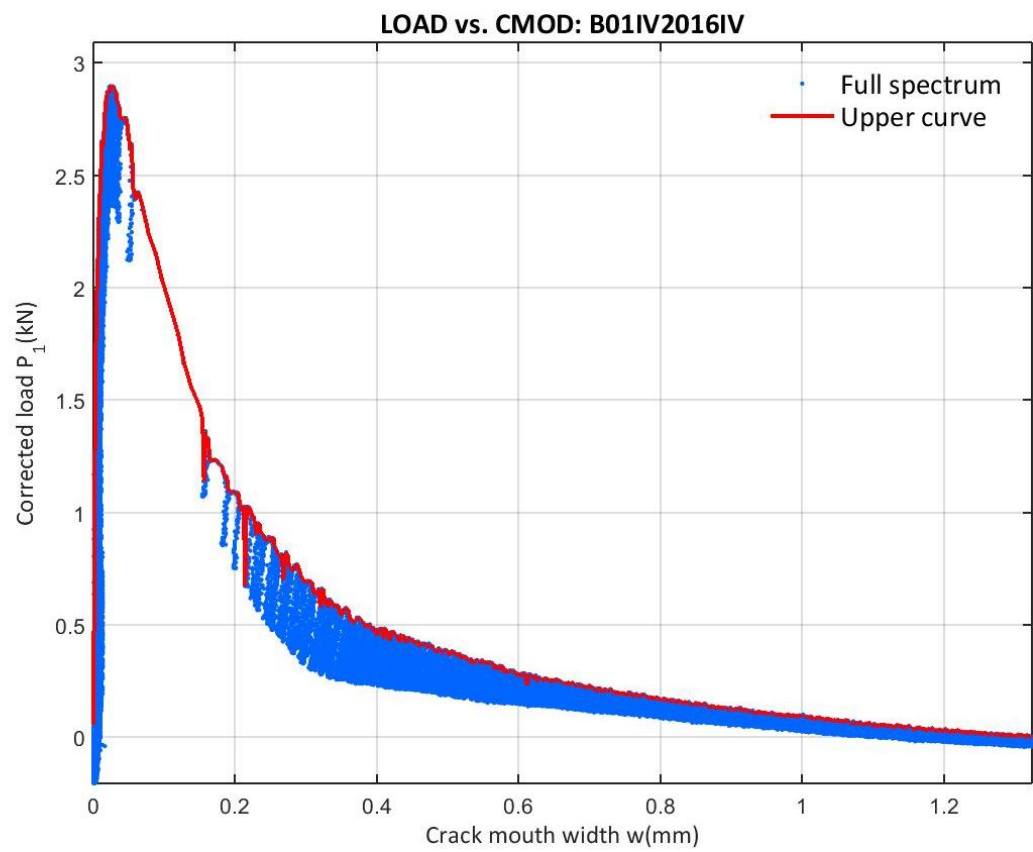


Figure 401: Corrected load vs. CMOD at the B01IV2016IV test

E.8.3 01IV2016 CORRECTED LOAD VS. VERTICAL DISPLACEMENT

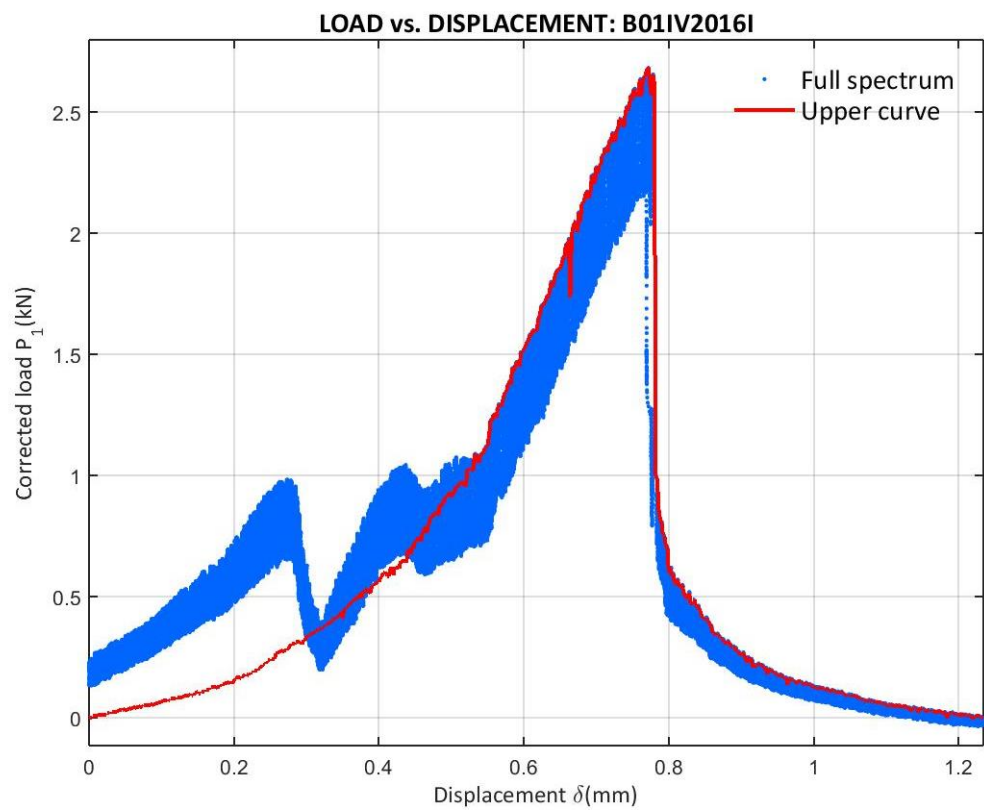


Figure 402: Corrected load vs. Displacement at the B01IV2016I test

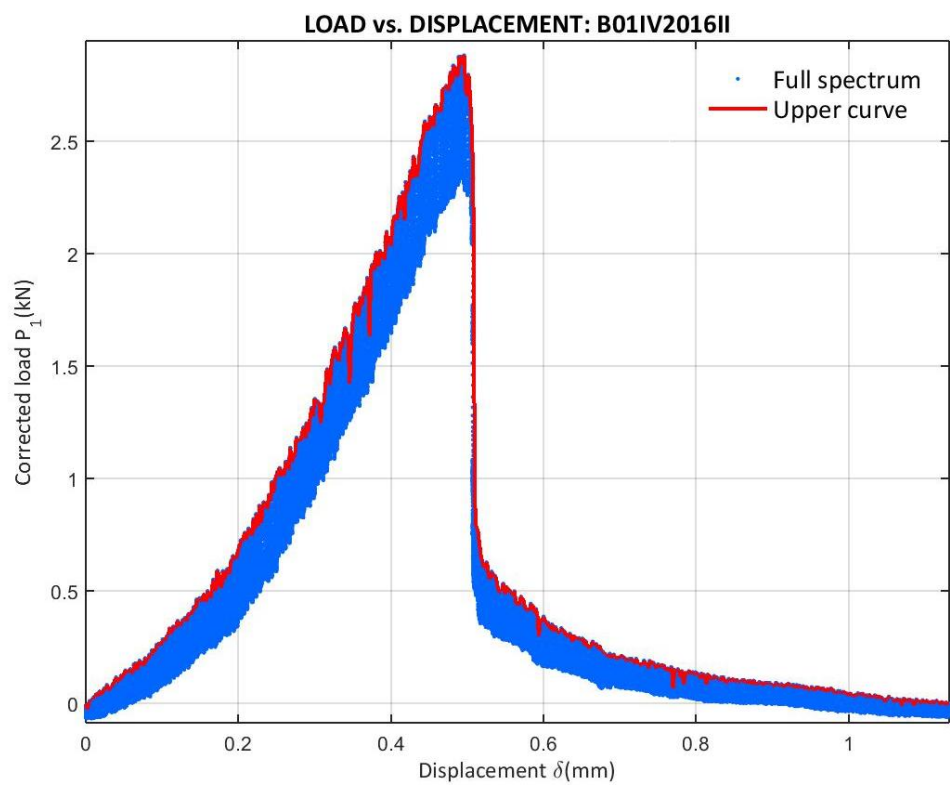


Figure 403: Corrected load vs. Displacement at the B01IV2016II test

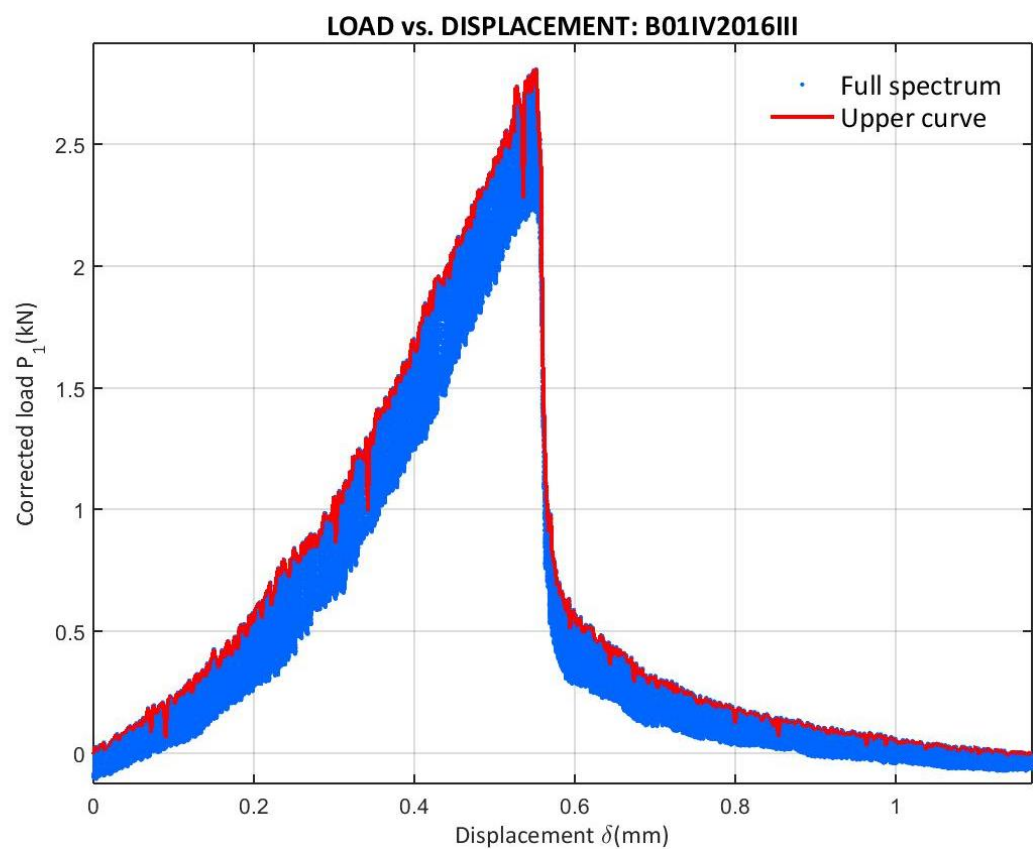


Figure 404: Corrected load vs. Displacement at the B01IV2016III test

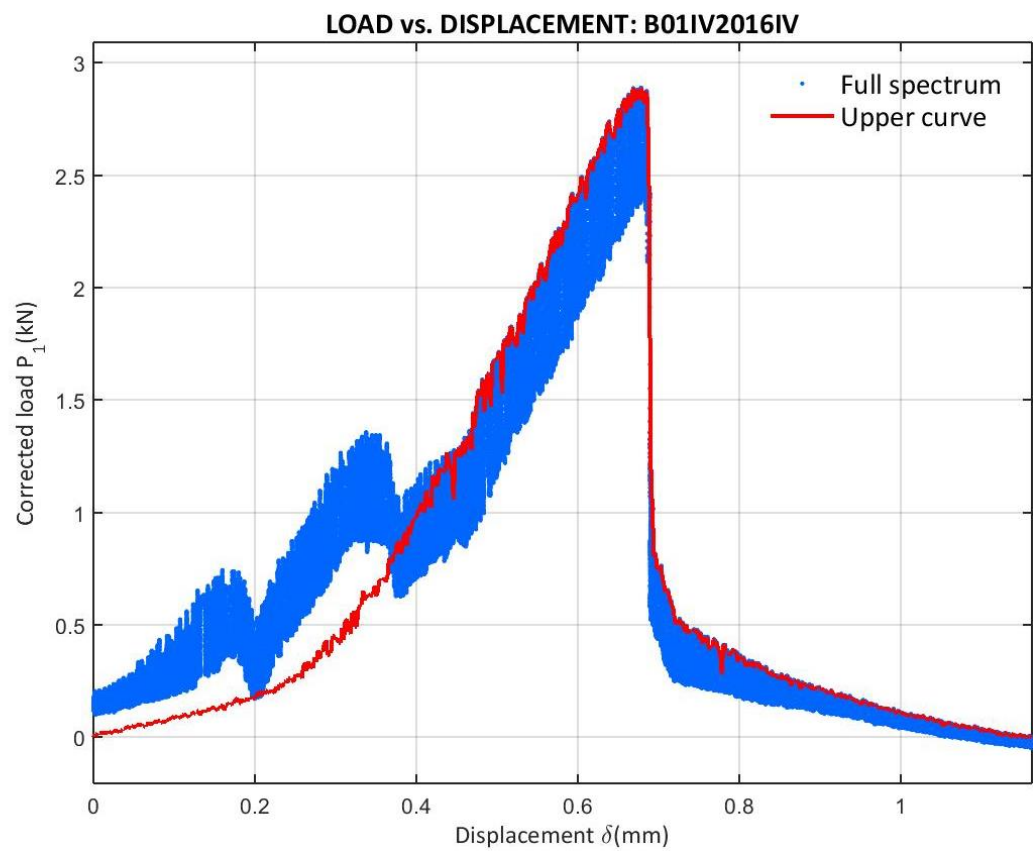


Figure 405: Corrected load vs. Displacement at the B01IV2016IV test

E.8.4 01IV2016 CORRECTED LOAD VS. X

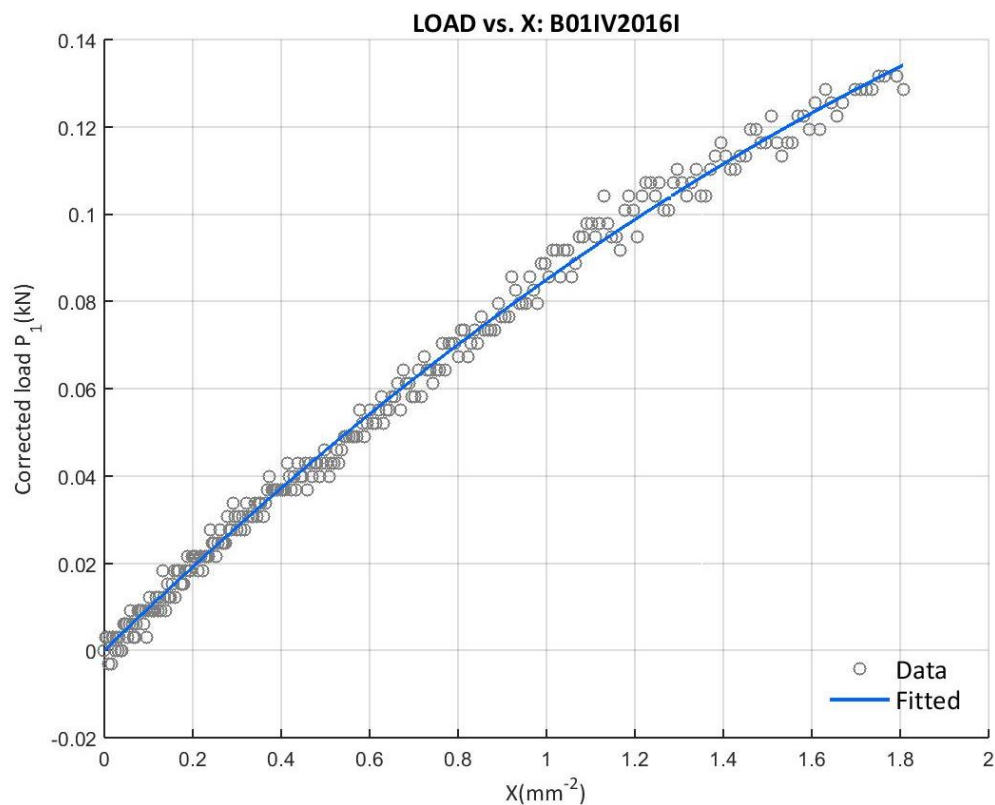


Figure 406: Corrected load vs. X at the B01IV2016I test with the final upper curve data

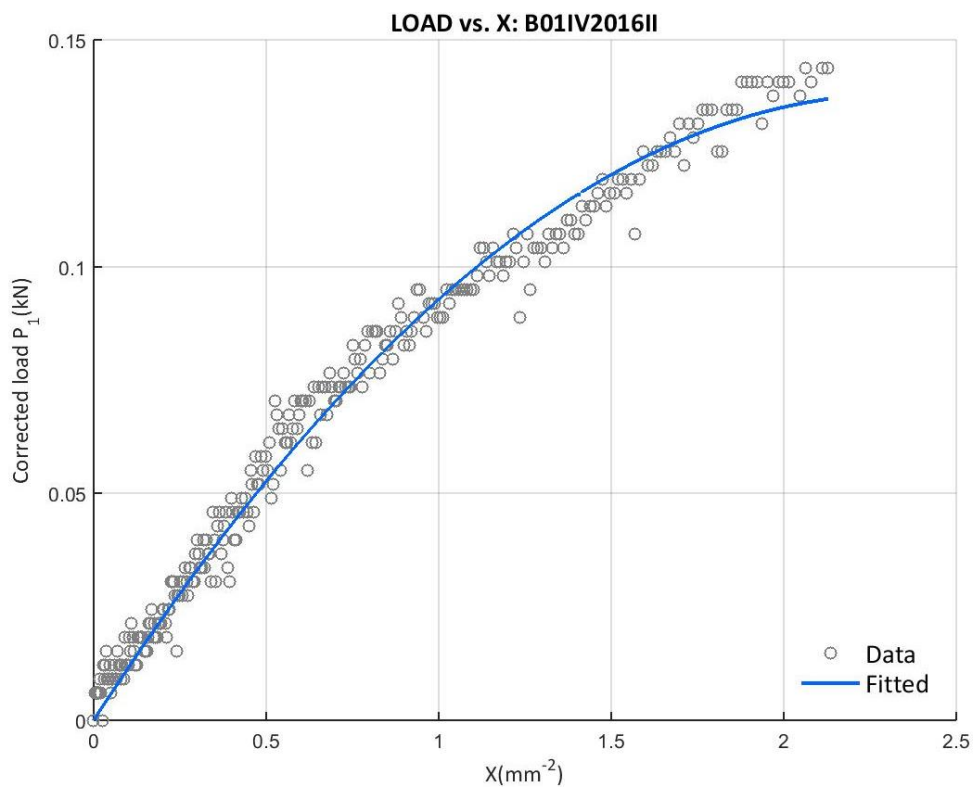


Figure 407: Corrected load vs. X at the B01IV2016II test with the final upper curve data

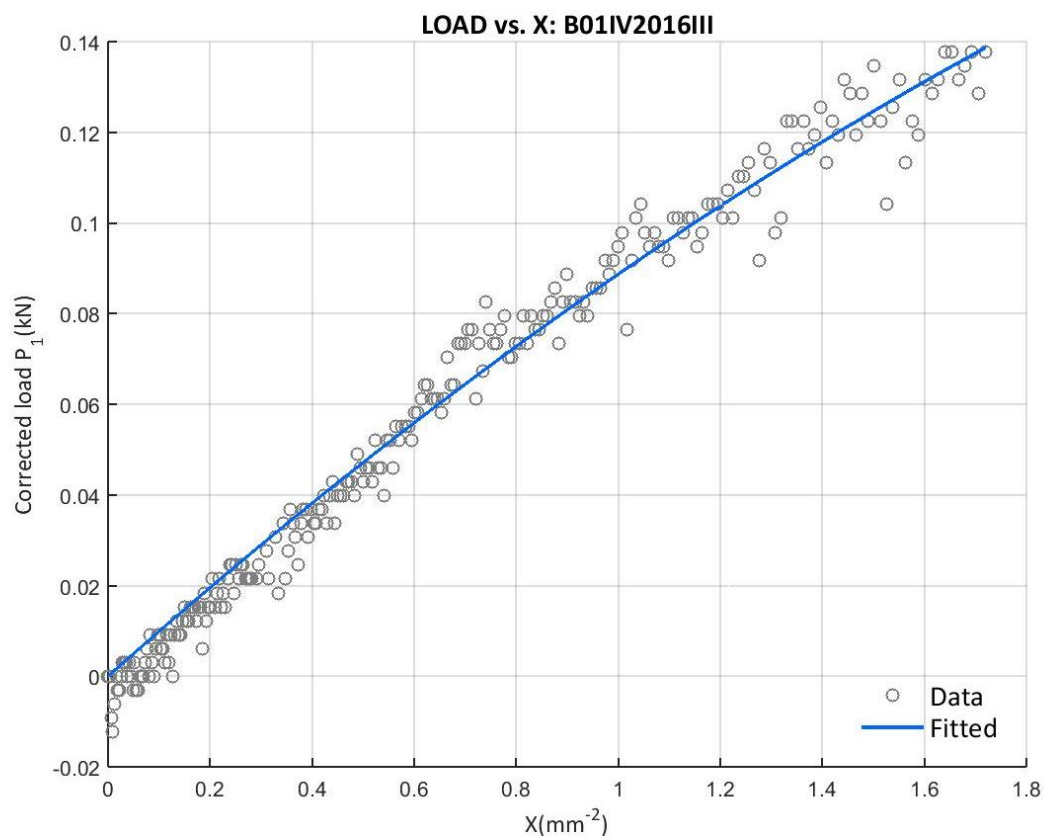


Figure 408: Corrected load vs. X at the B01IV2016III test with the final upper curve data

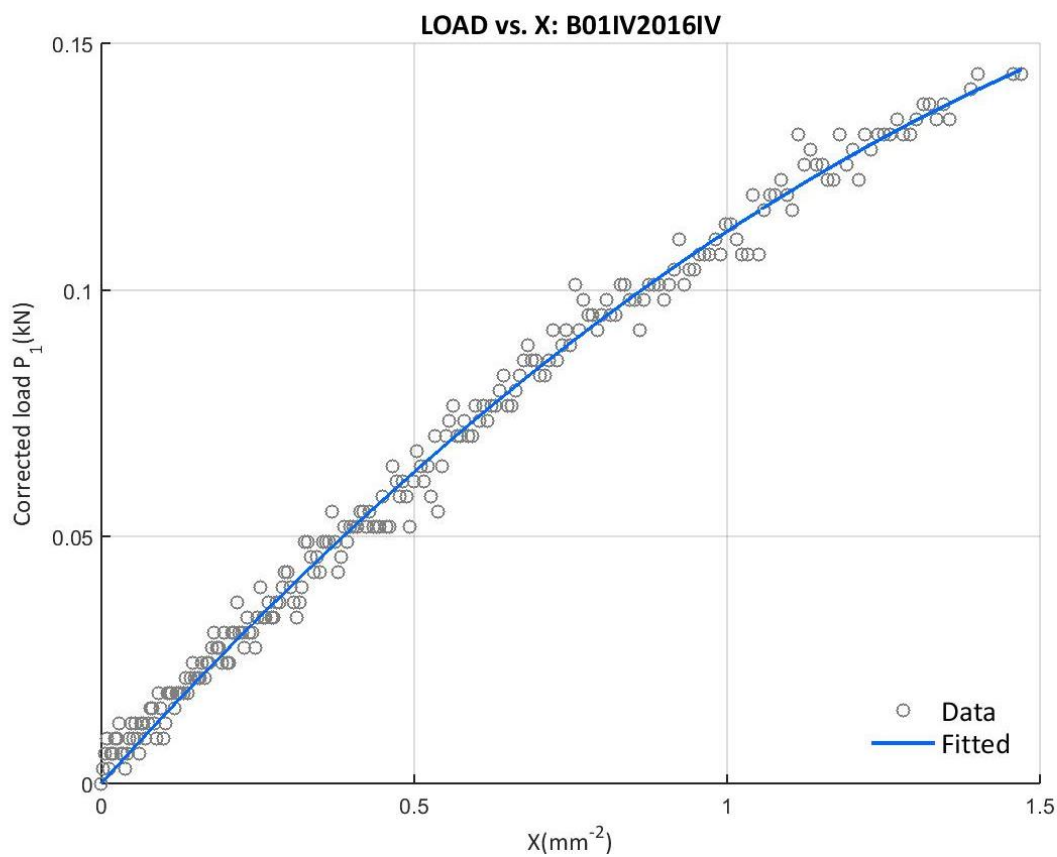


Figure 409: Corrected load vs. X at the B01IV2016IV test with the final upper curve data

E.8.5 01IV2016 SOFTENING CURVE BILINEAR APPROXIMATION

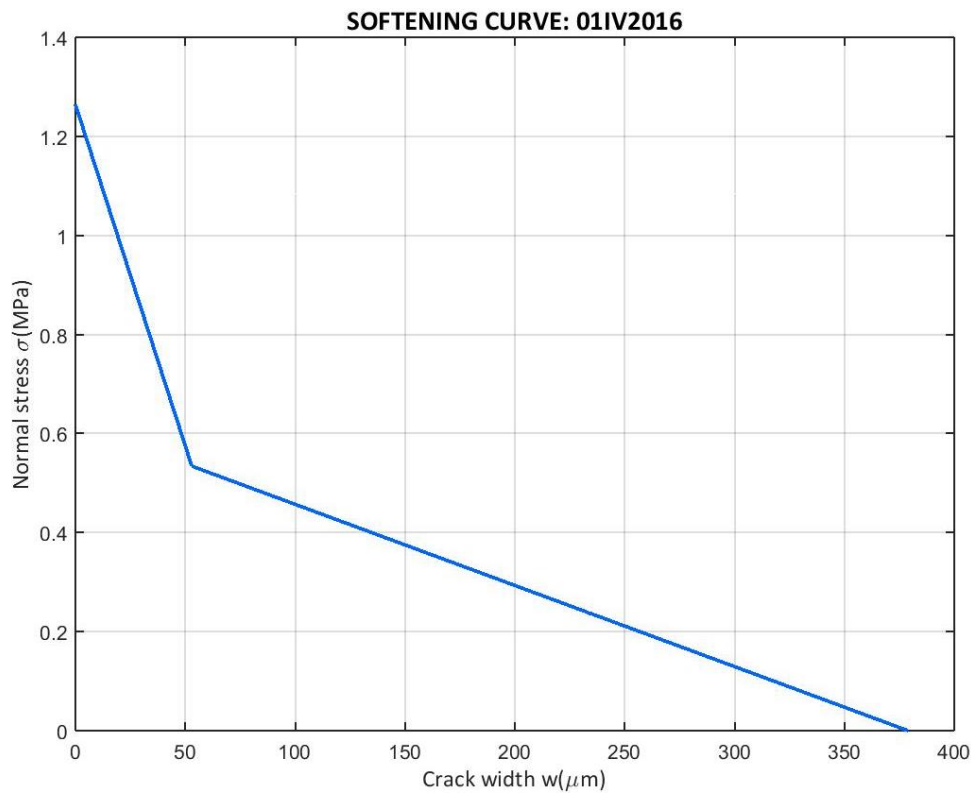


Figure 410: Softening curve bilinear approximation of the 01IV2016 campaign

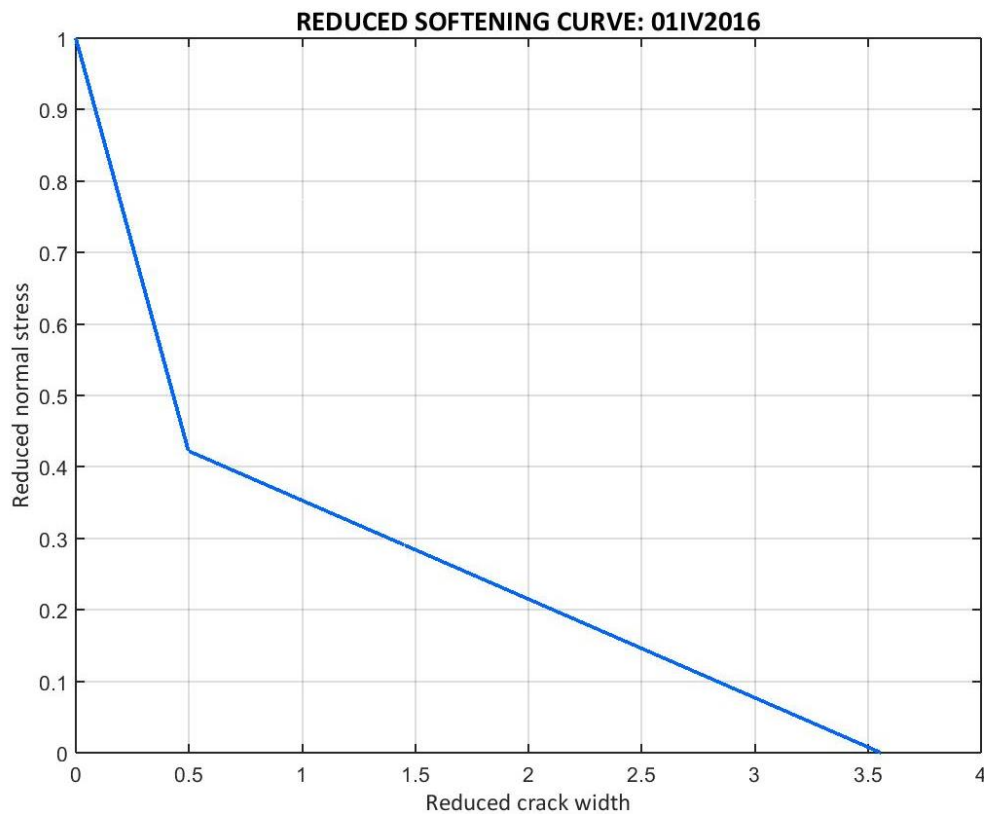


Figure 411: Softening curve bilinear approximation of the 01IV2016 campaign in the reduced form

E.8.6 01IV2016 SPECIMENS' COMPARISON

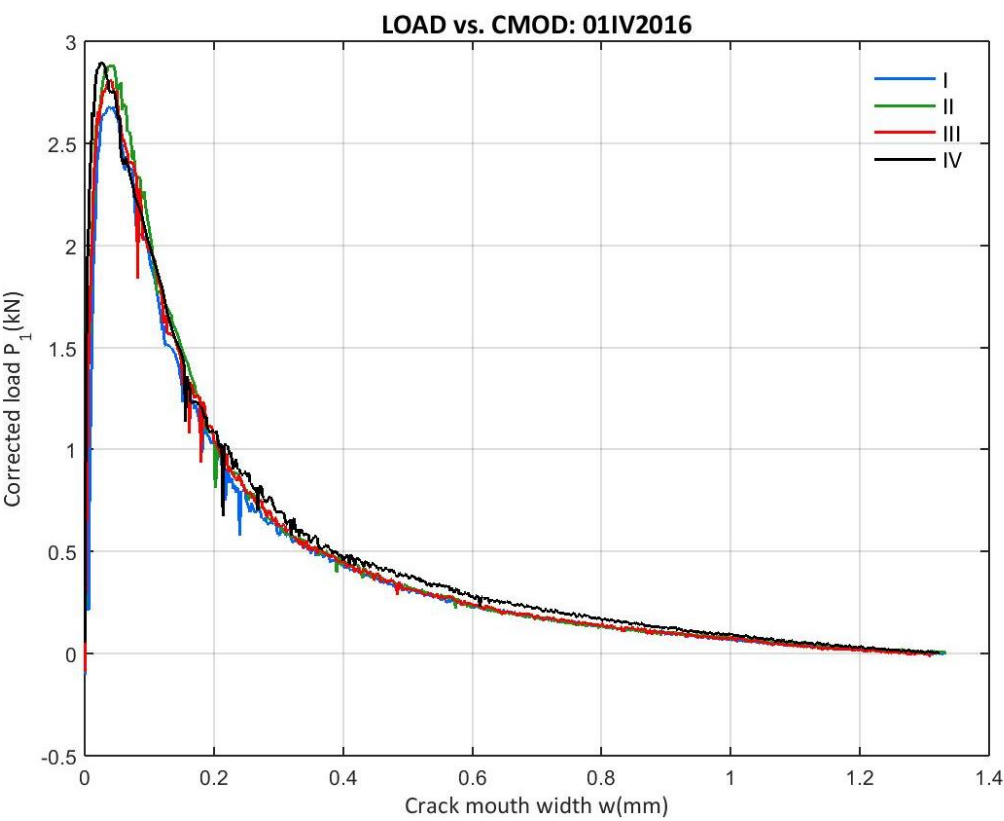


Figure 412: 01IV2016 Corrected load vs. CMOD from the entire campaign

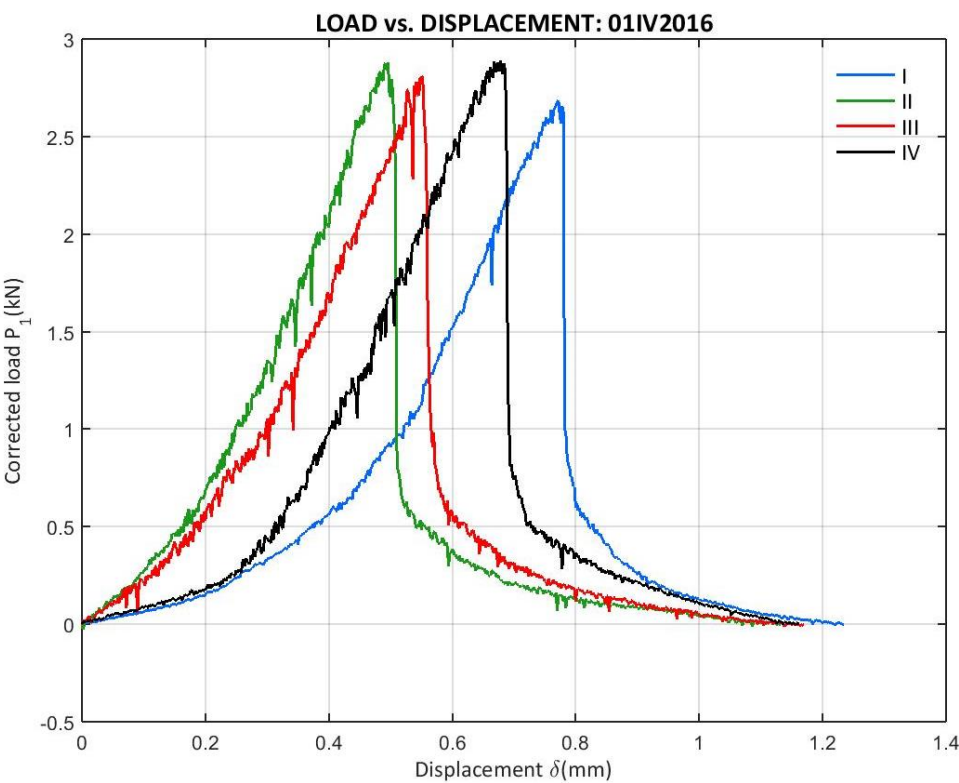


Figure 413: 01IV2016 Corrected load vs. Displacement from the entire campaign

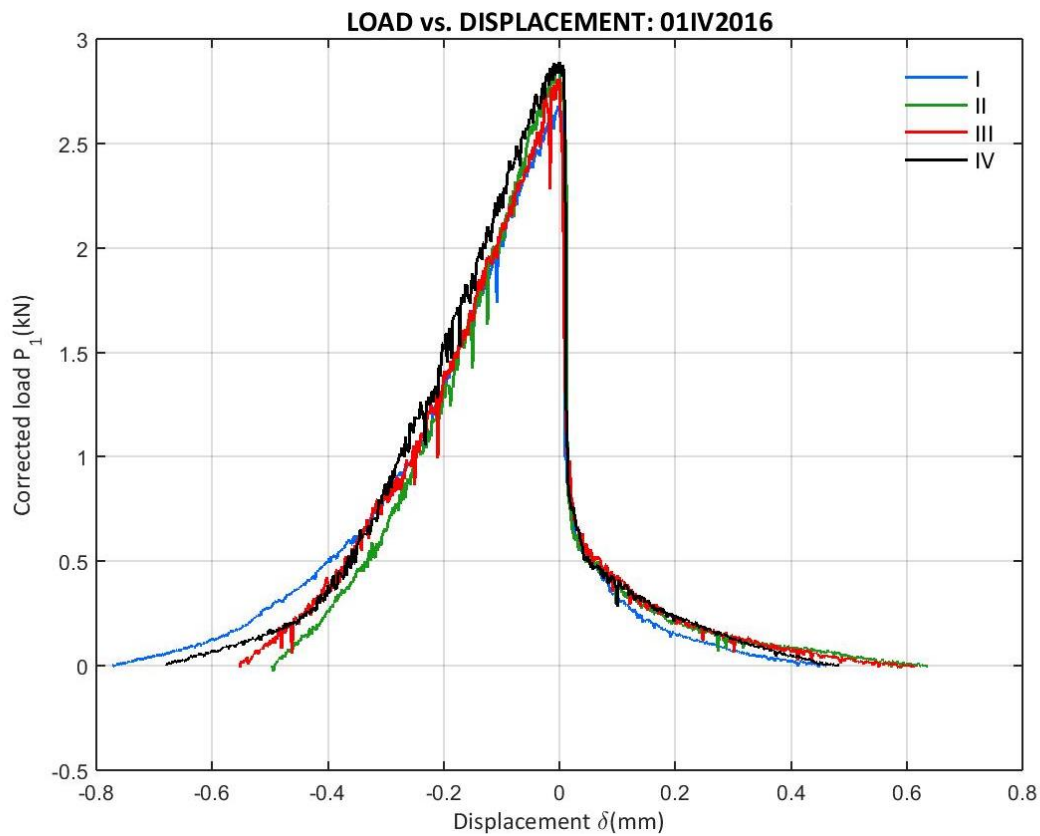


Figure 414: 01IV2016 Corrected load vs. Displacement from the entire campaign (peak displacement zero)

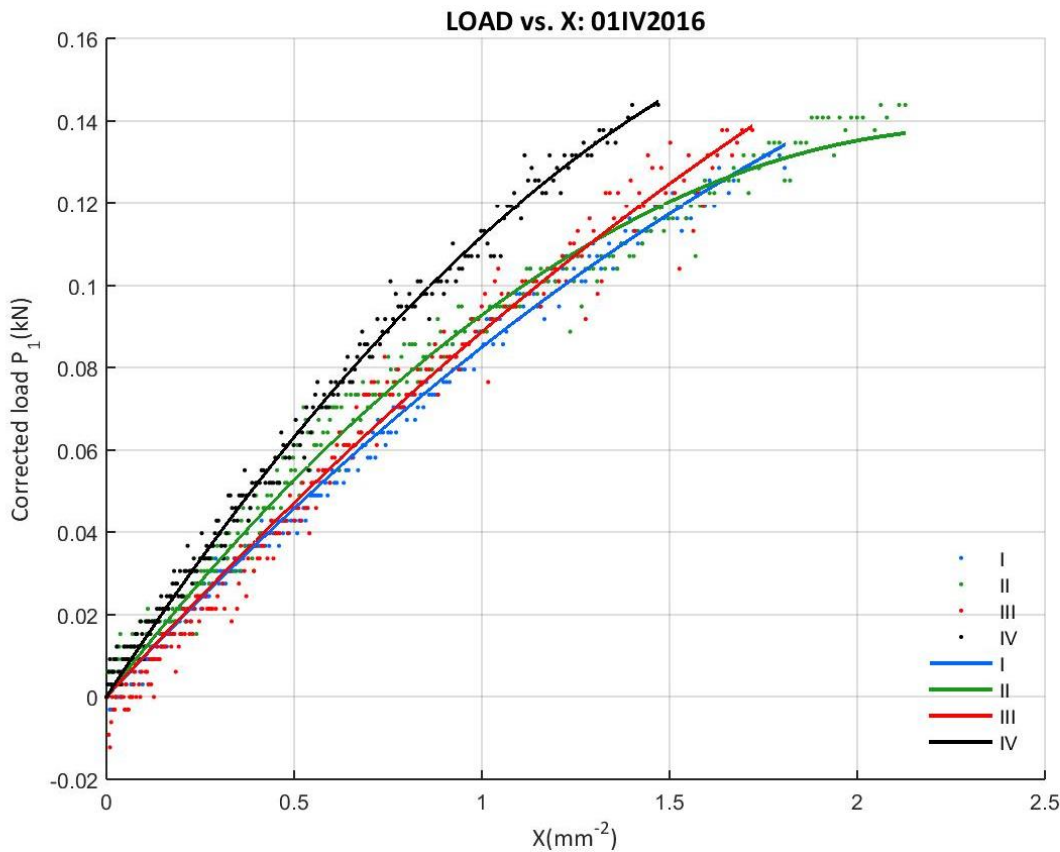


Figure 415: 01IV2016 Corrected load vs. X from the entire campaign

E.9 07IV2016 CAMPAIGN

E.9.1 07IV2016 DATA

- B07IV2016I

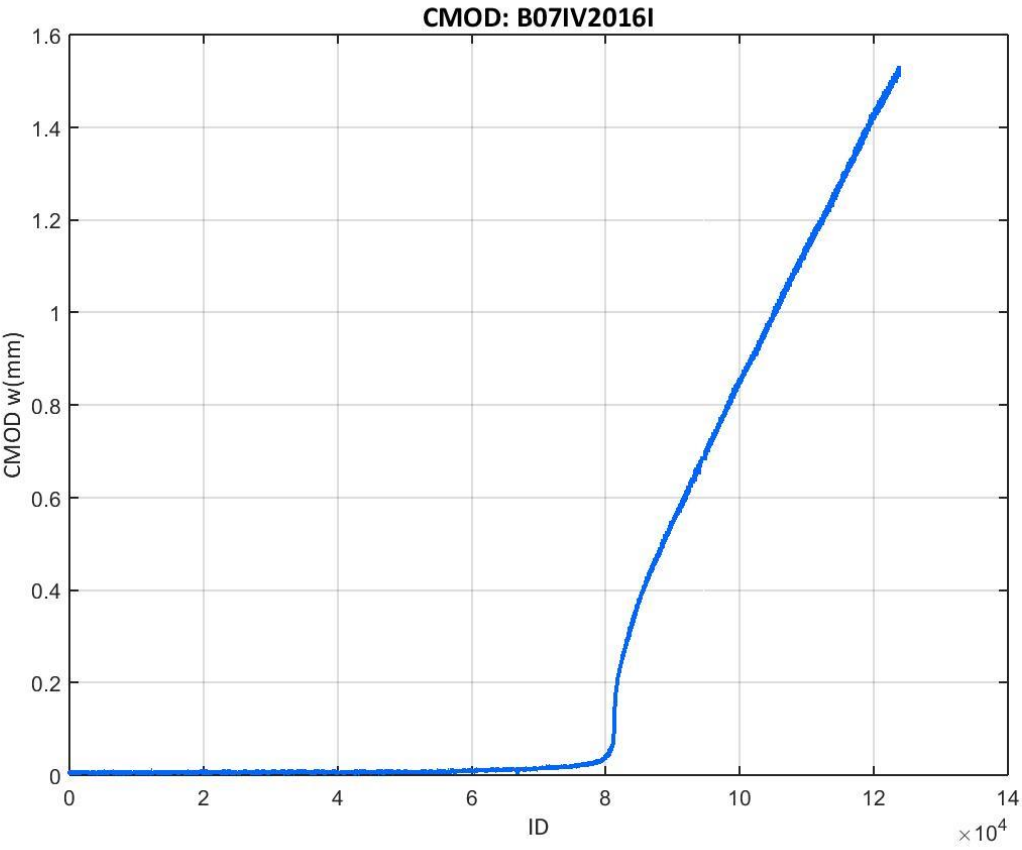


Figure 416: CMOD values recorded at the B07IV2016I test

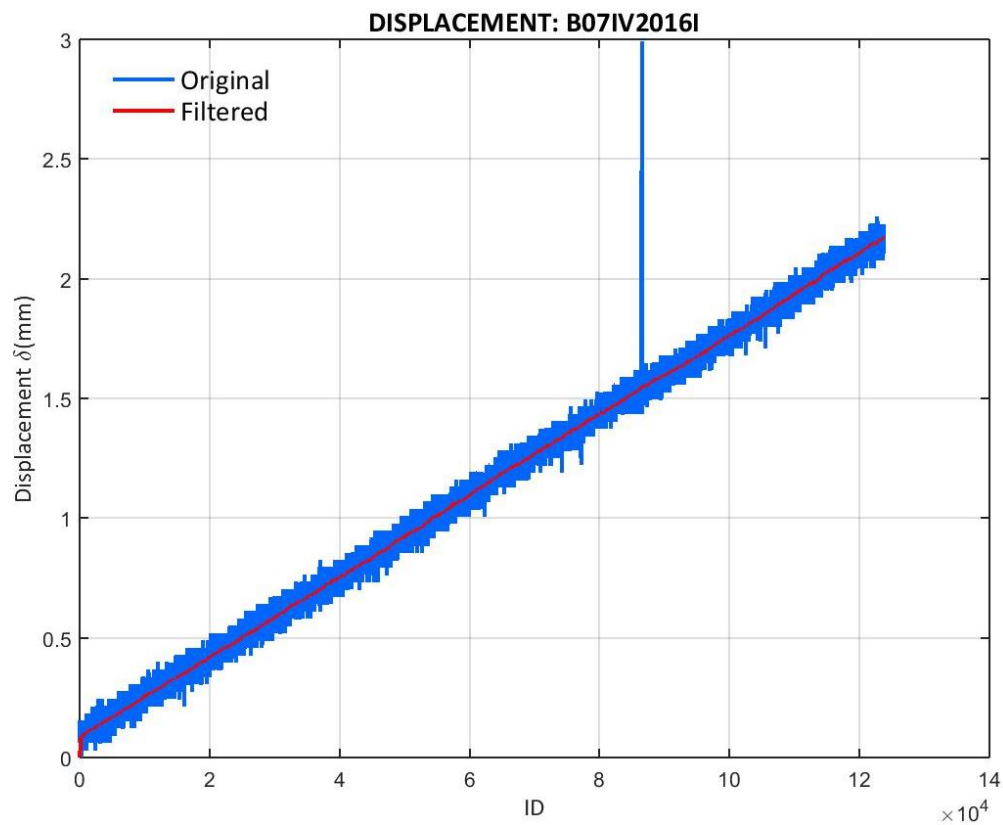


Figure 417: Displacement values recorded at the B07IV2016I test

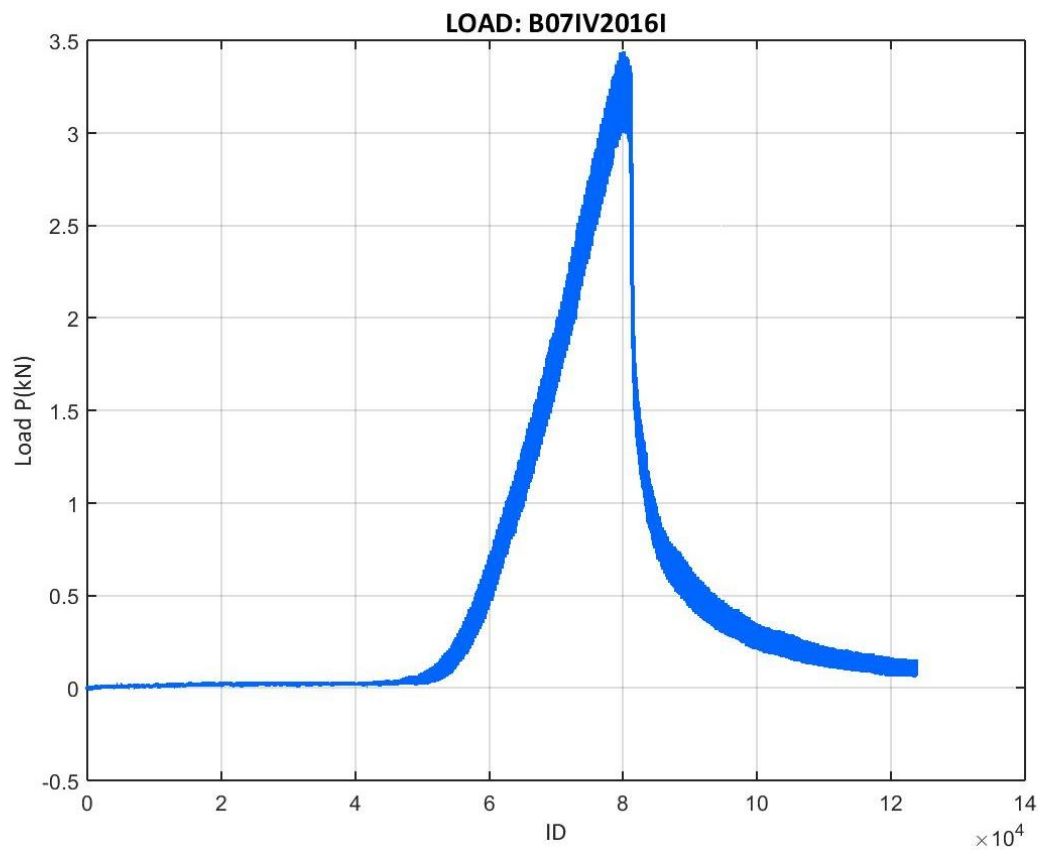


Figure 418: Load values recorded at the B07IV2016I test

- B07IV2016II

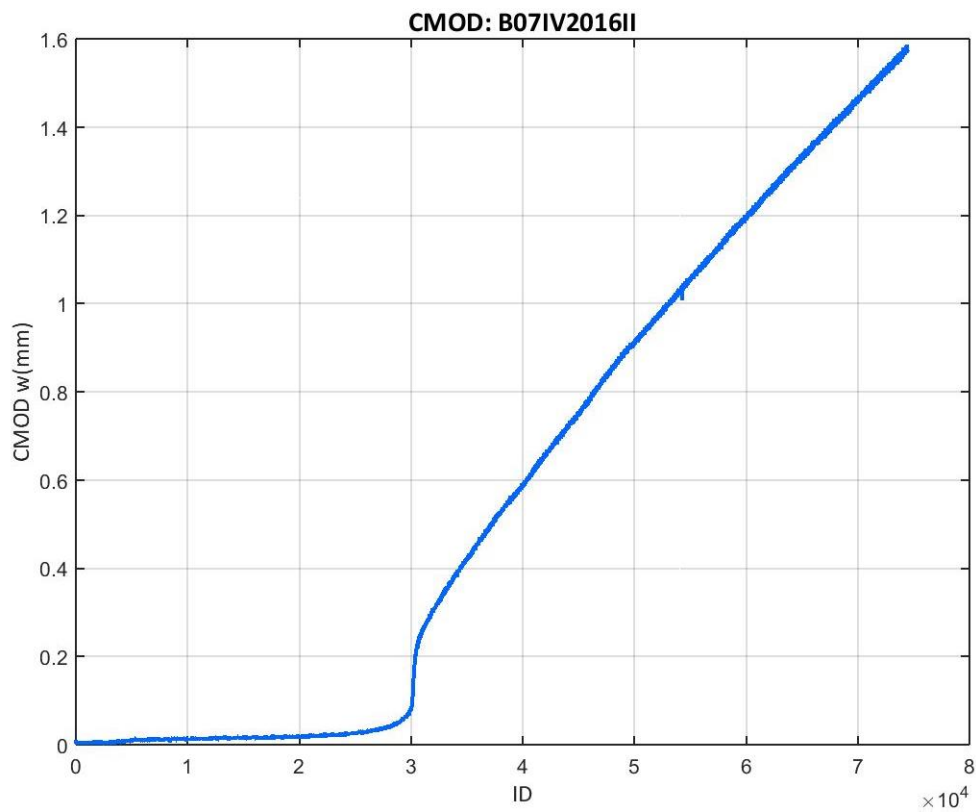


Figure 419: CMOD values recorded at the B07IV2016II test

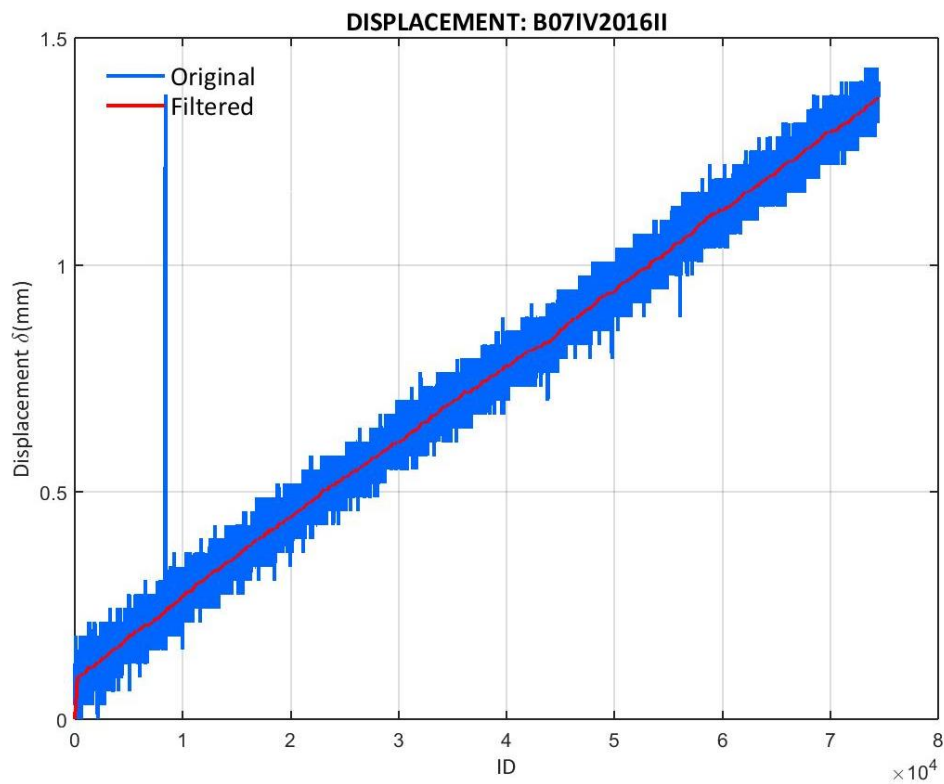


Figure 420: Displacement values recorded at the B07IV2016II test

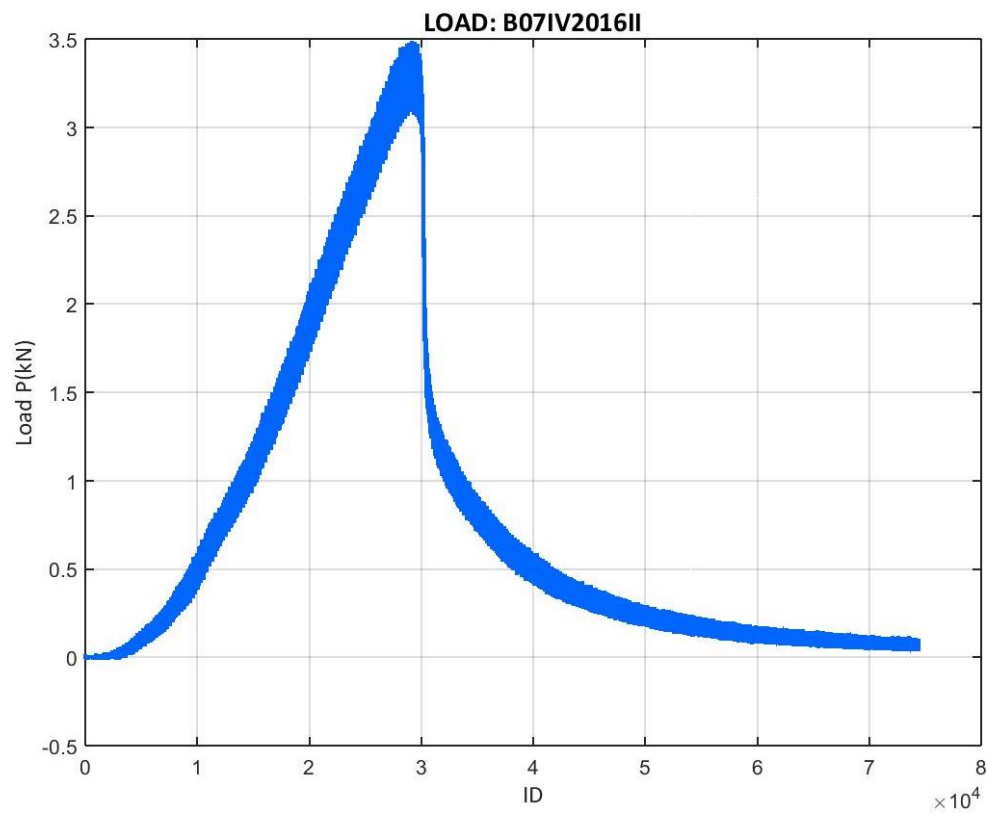


Figure 421: Load values recorded at the B07IV2016II test

- B07IV2016III

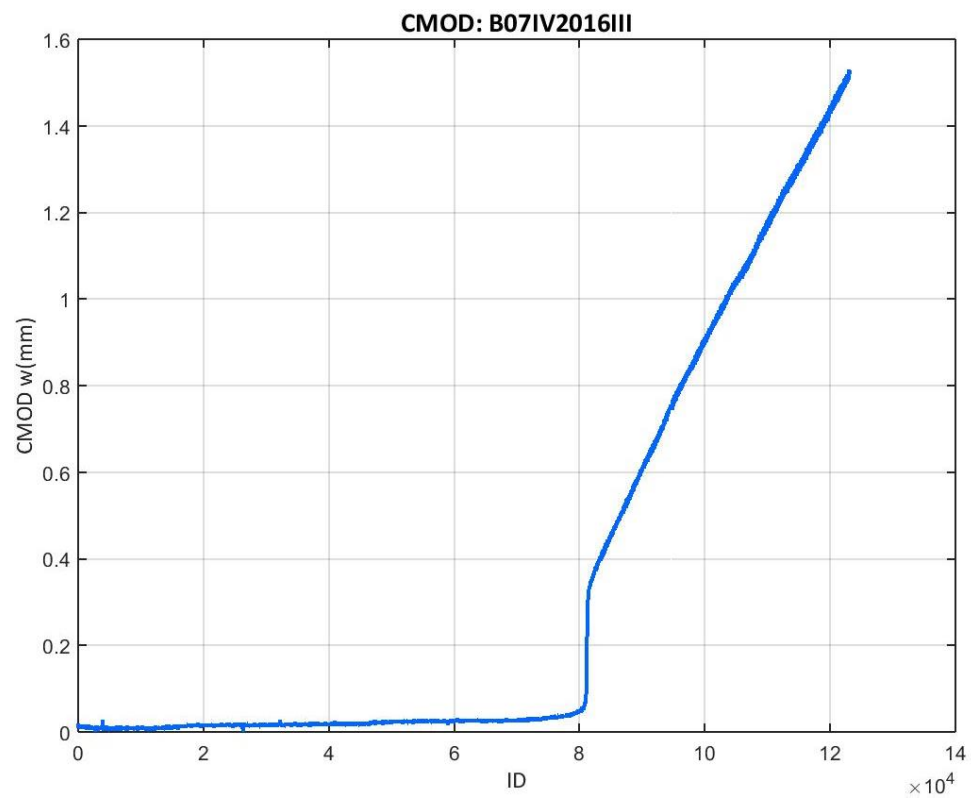


Figure 422: CMOD values recorded at the B07IV2016III test

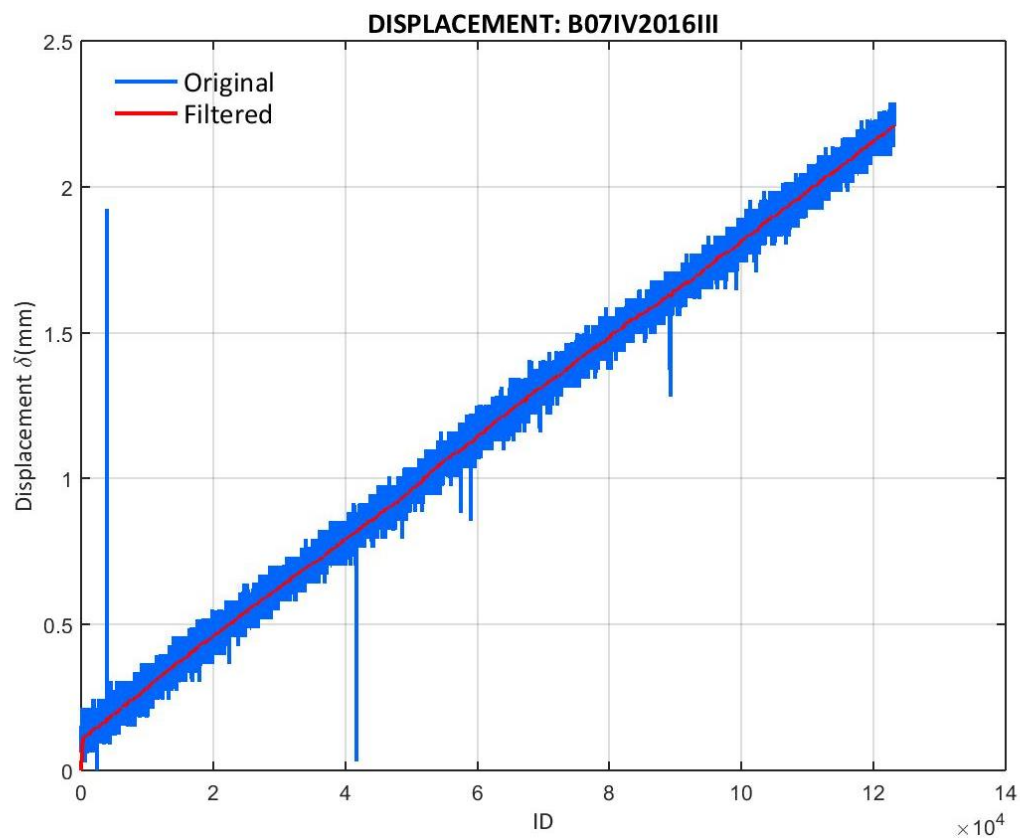


Figure 423: Displacement values recorded at the B07IV2016III test

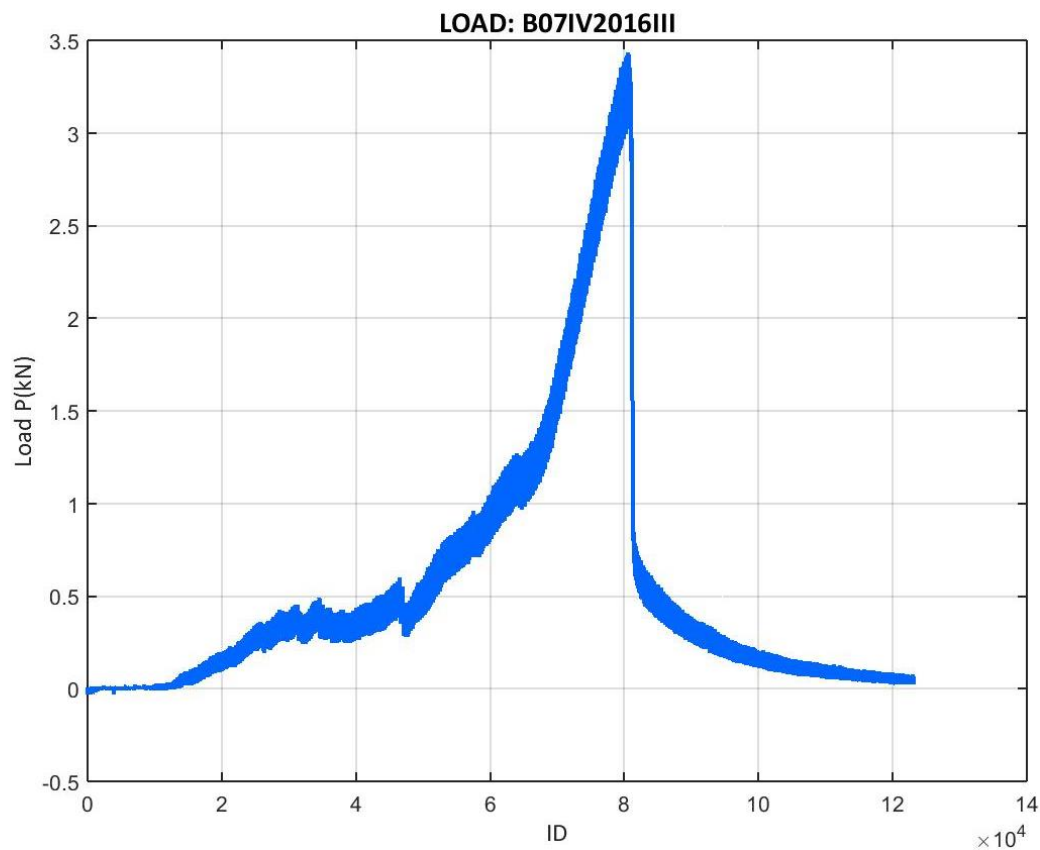


Figure 424: Load values recorded at the B07IV2016III test

- B07IV2016IV

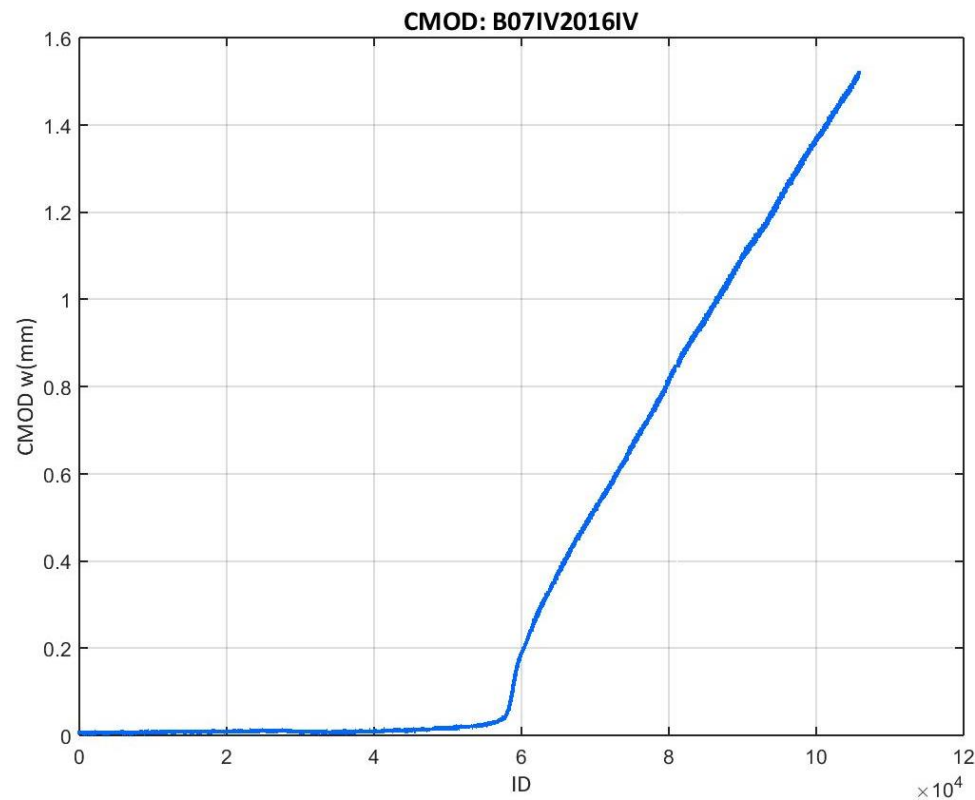


Figure 425: CMOD values recorded at the B07IV2016IV test

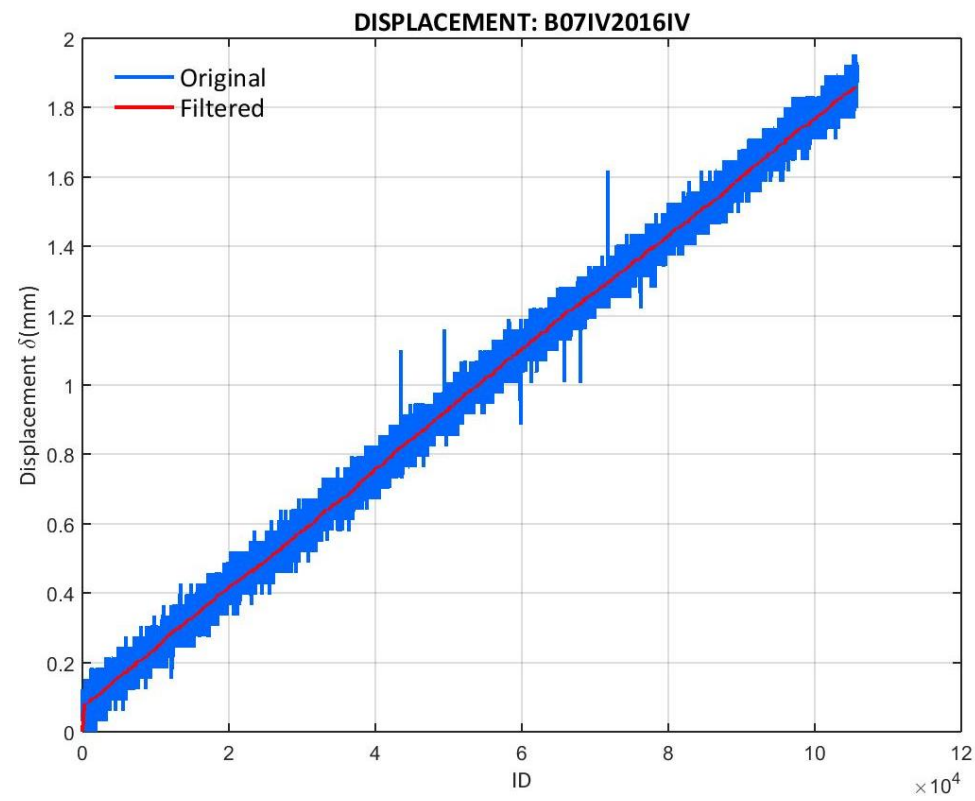


Figure 426: Displacement values recorded at the B07IV2016IV test

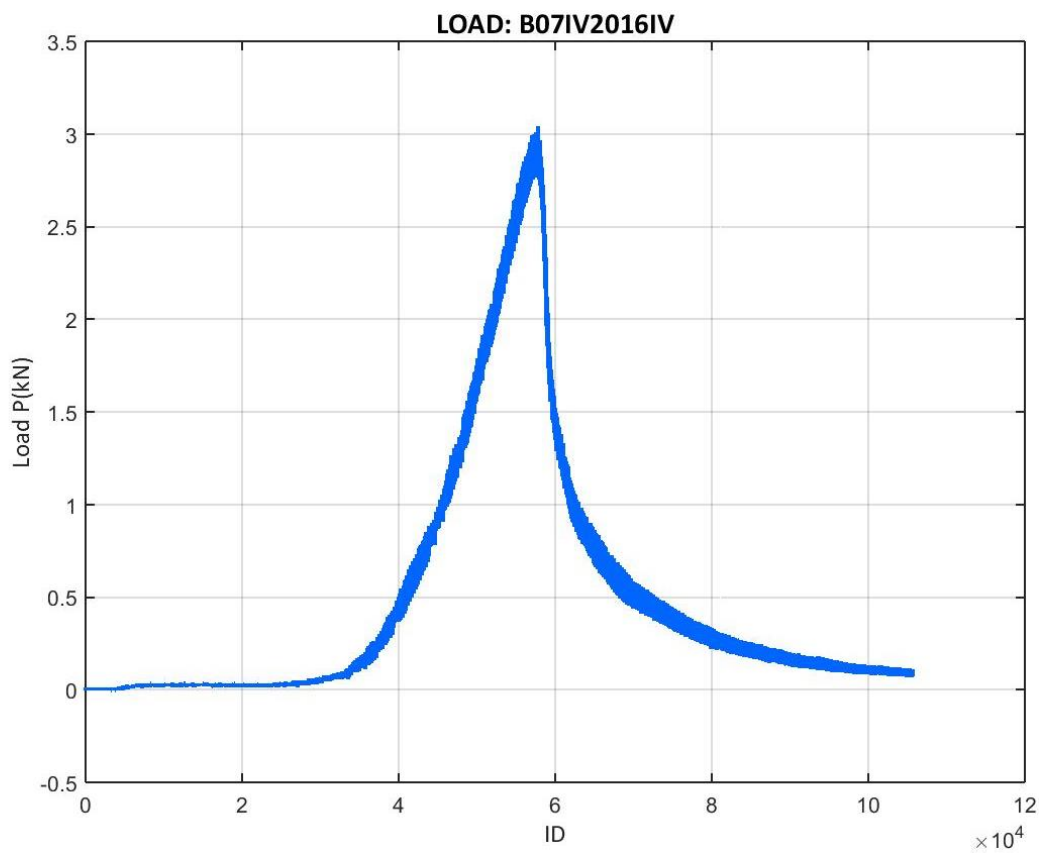


Figure 427: Load values recorded at the B07IV2016IV test

E.9.2 07IV2016 CORRECTED LOAD VS. CMOD

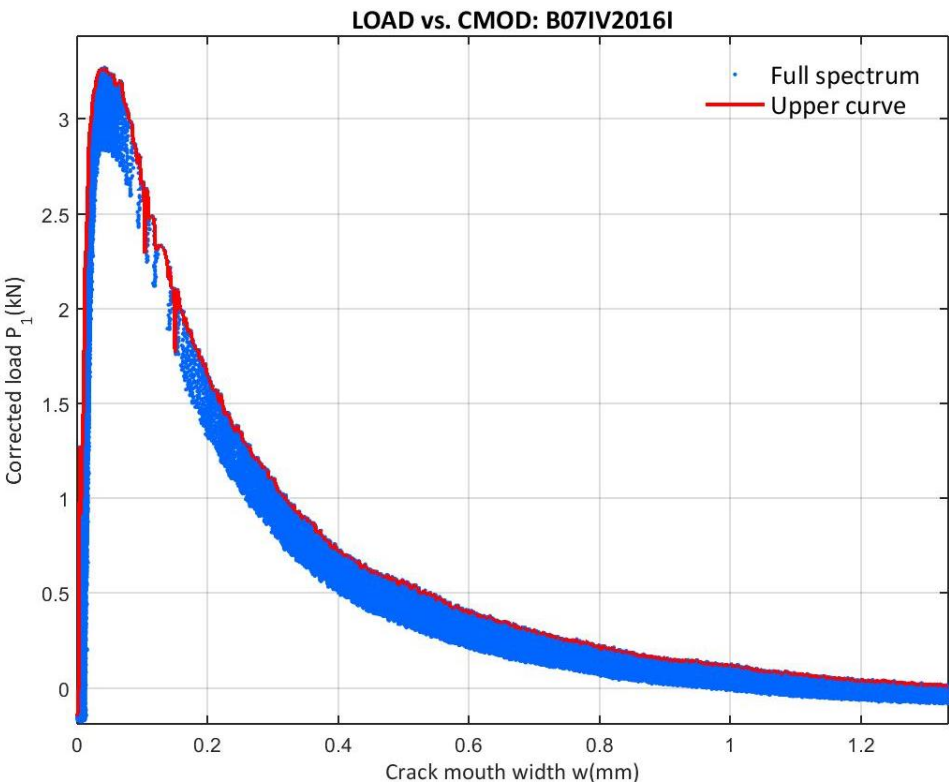


Figure 428: Corrected load vs. CMOD at the B07IV2016I test

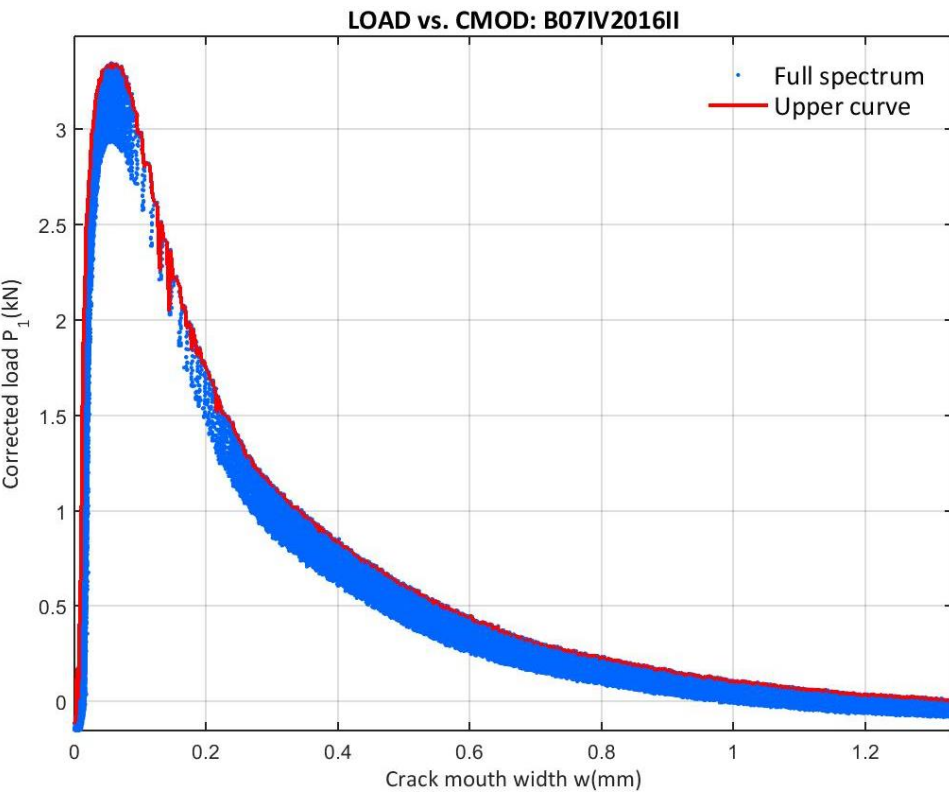


Figure 429: Corrected load vs. CMOD at the B07IV2016II test

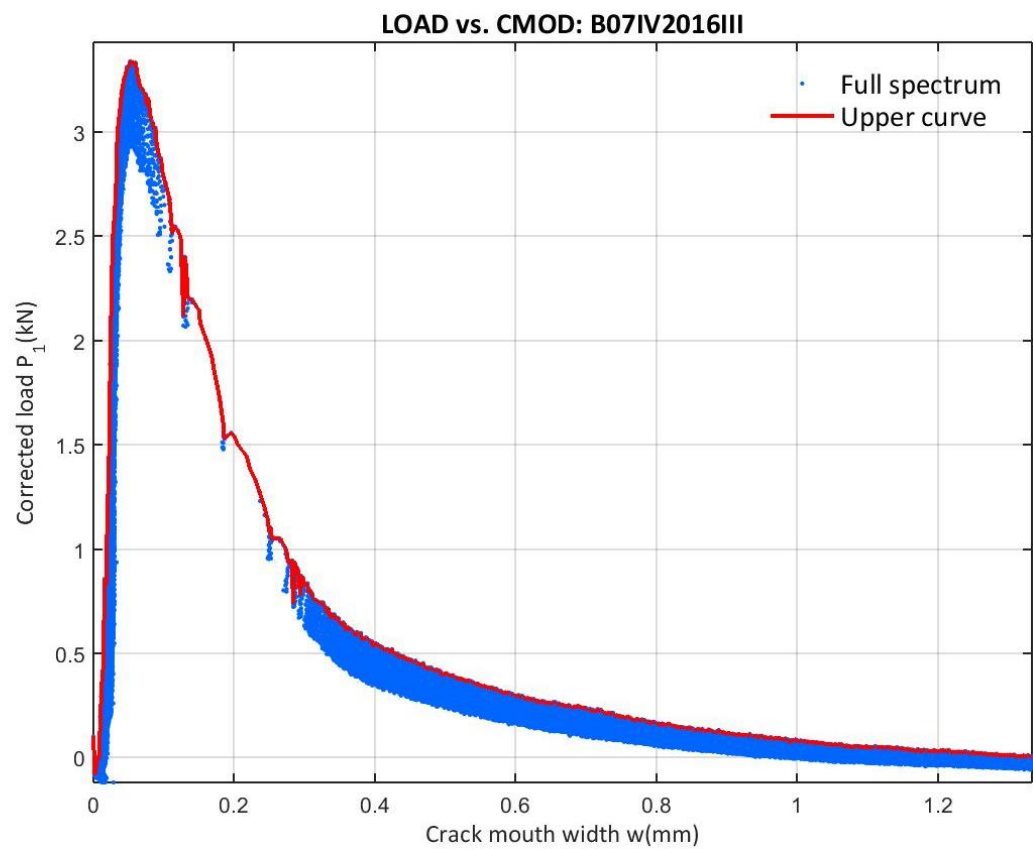


Figure 430: Corrected load vs. CMOD at the B07IV2016III test

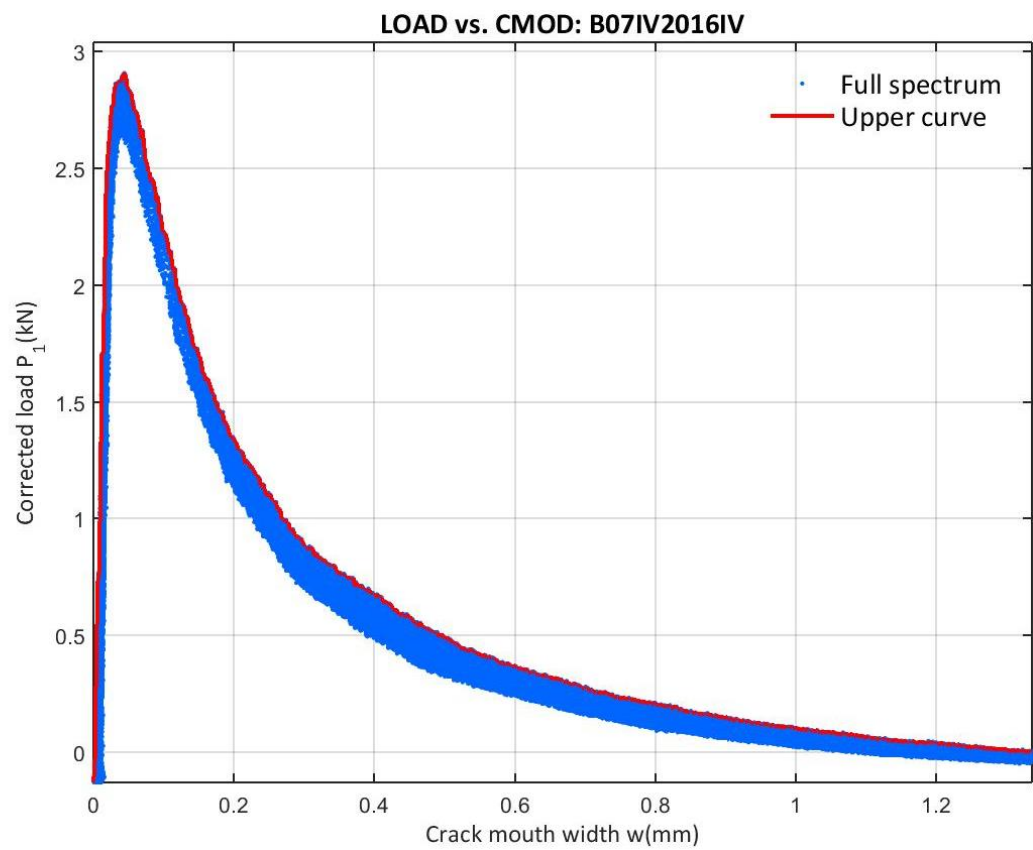


Figure 431: Corrected load vs. CMOD at the B07IV2016IV test

E.9.3 07IV2016 CORRECTED LOAD VS. VERTICAL DISPLACEMENT

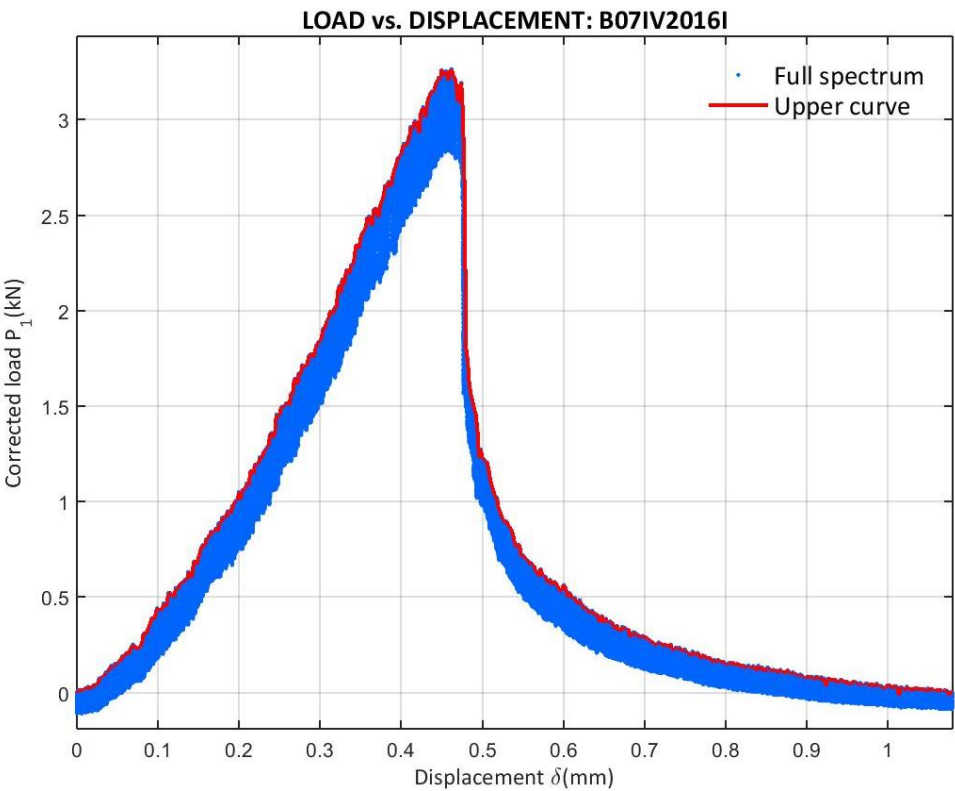


Figure 432: Corrected load vs. Displacement at the B07IV2016I test

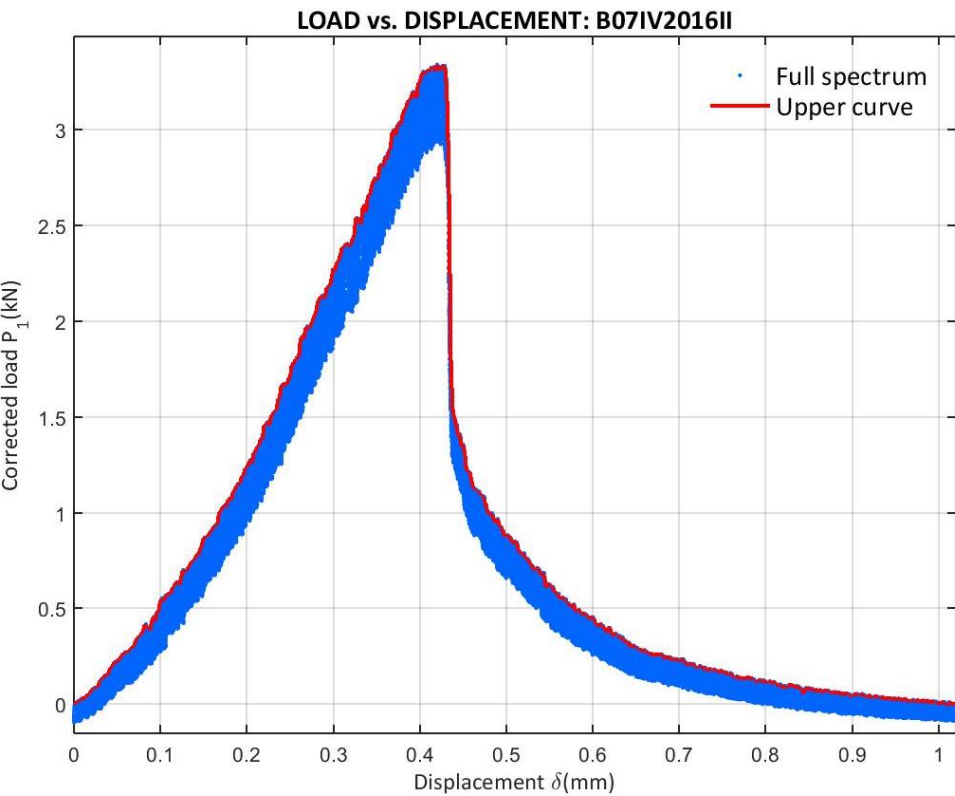


Figure 433: Corrected load vs. Displacement at the B07IV2016II test

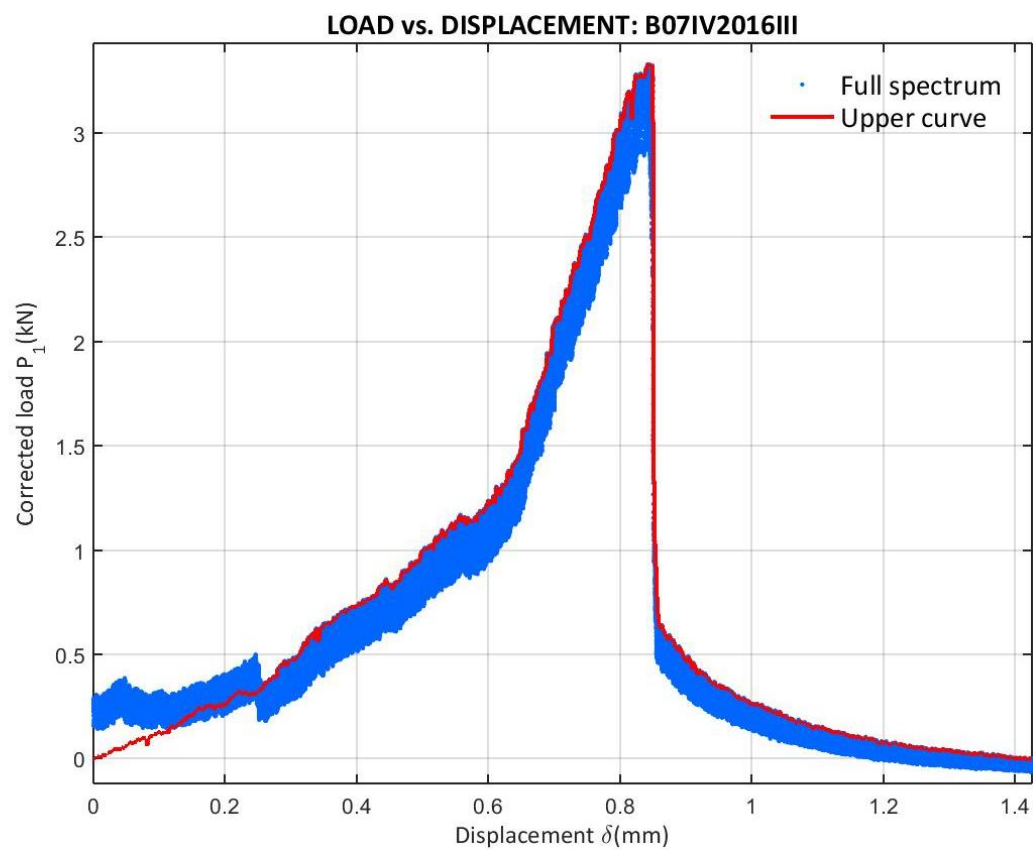


Figure 434: Corrected load vs. Displacement at the B07IV2016III test

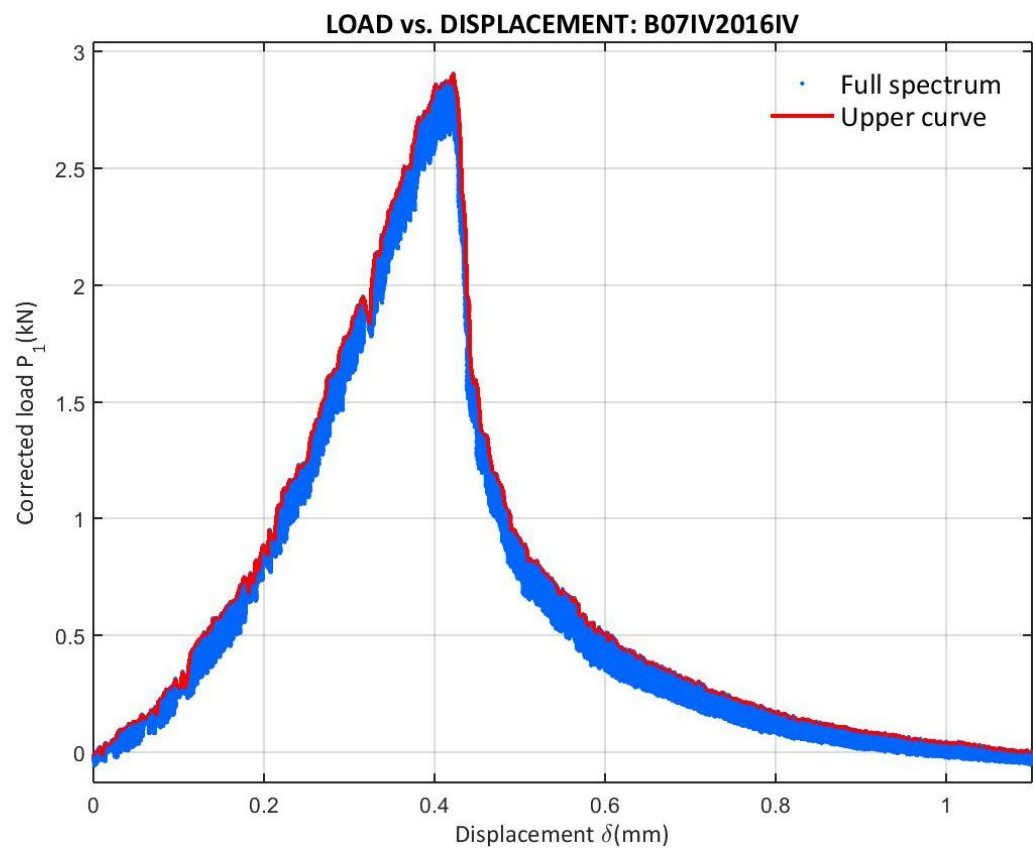


Figure 435: Corrected load vs. Displacement at the B07IV2016IV test

E.9.4 07IV2016 CORRECTED LOAD VS. X

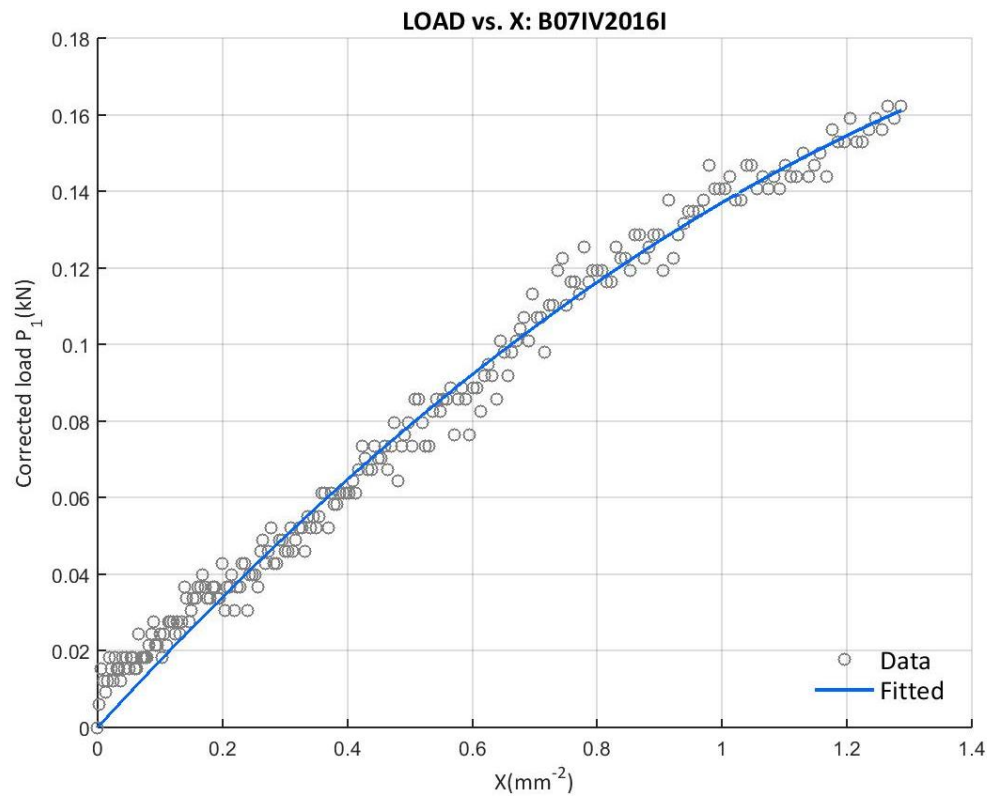


Figure 436: Corrected load vs. X at the B07IV2016I test with the final upper curve data

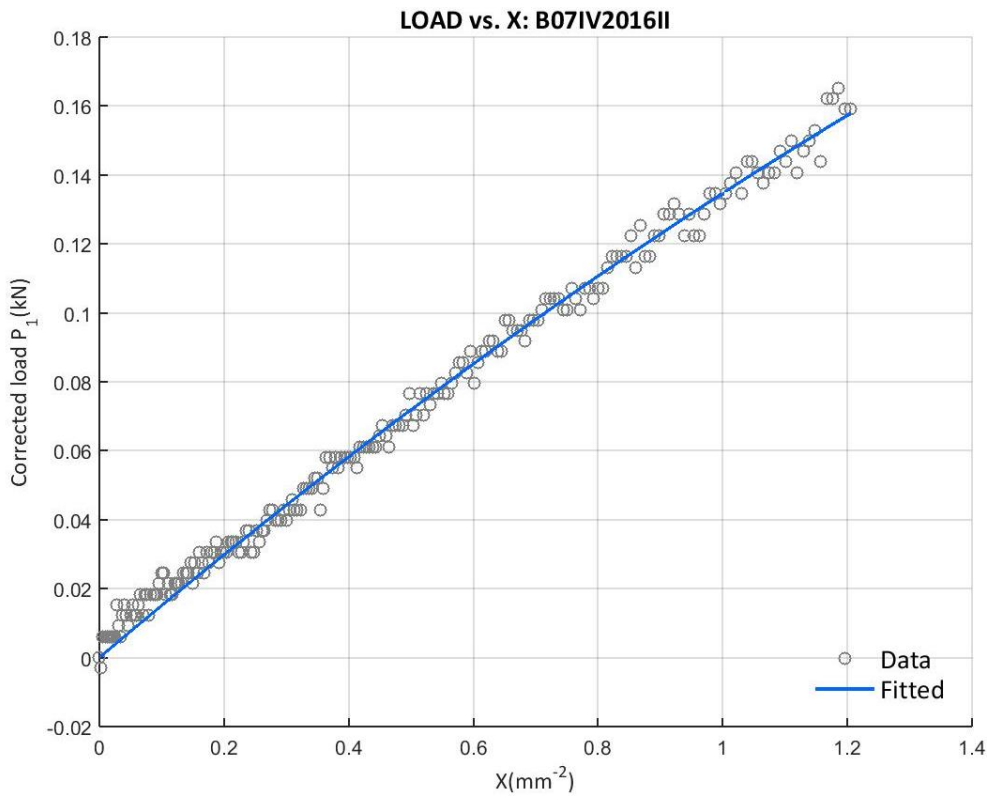


Figure 437: Corrected load vs. X at the B07IV2016II test with the final upper curve data

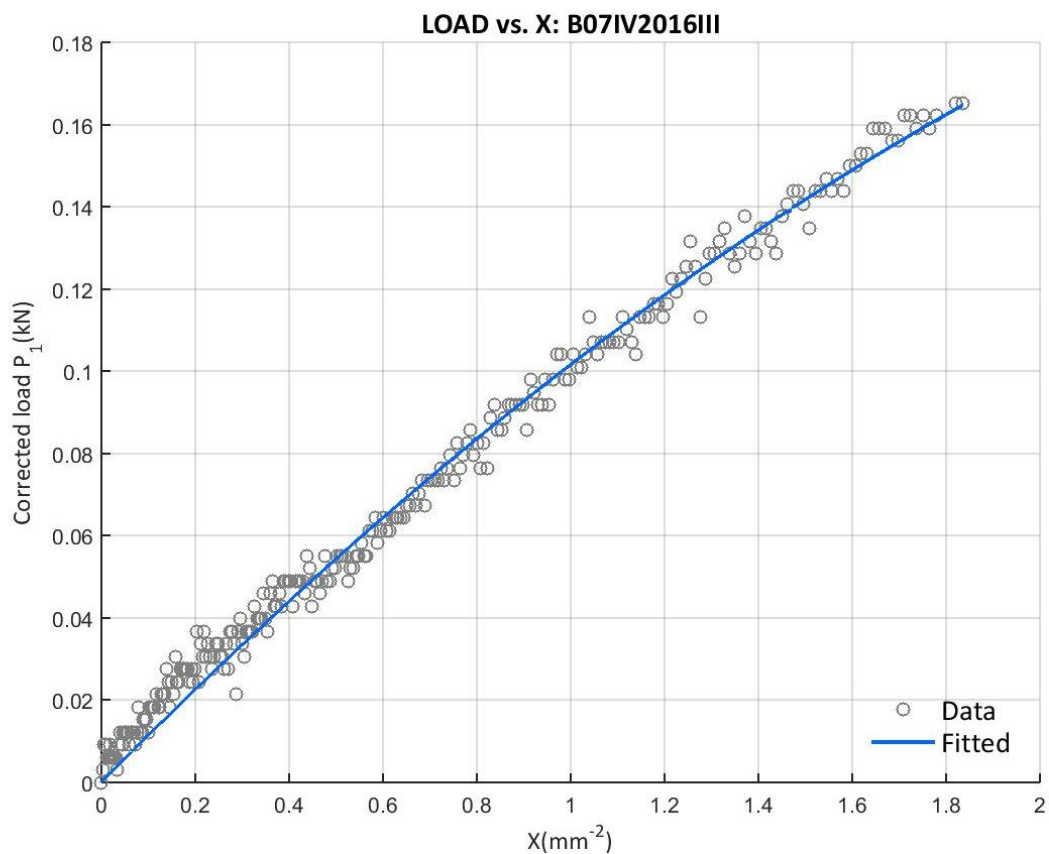


Figure 438: Corrected load vs. X at the B07IV2016III test with the final upper curve data

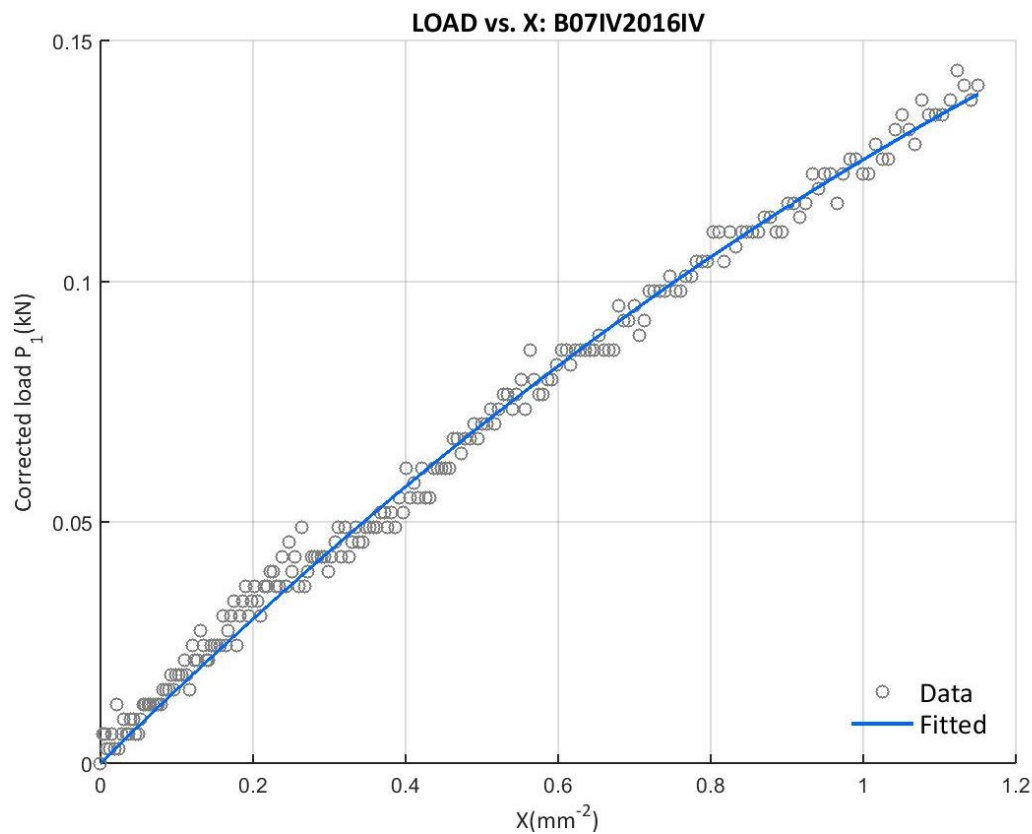


Figure 439: Corrected load vs. X at the B07IV2016IV test with the final upper curve data

E.9.5 07IV2016 SOFTENING CURVE BILINEAR APPROXIMATION

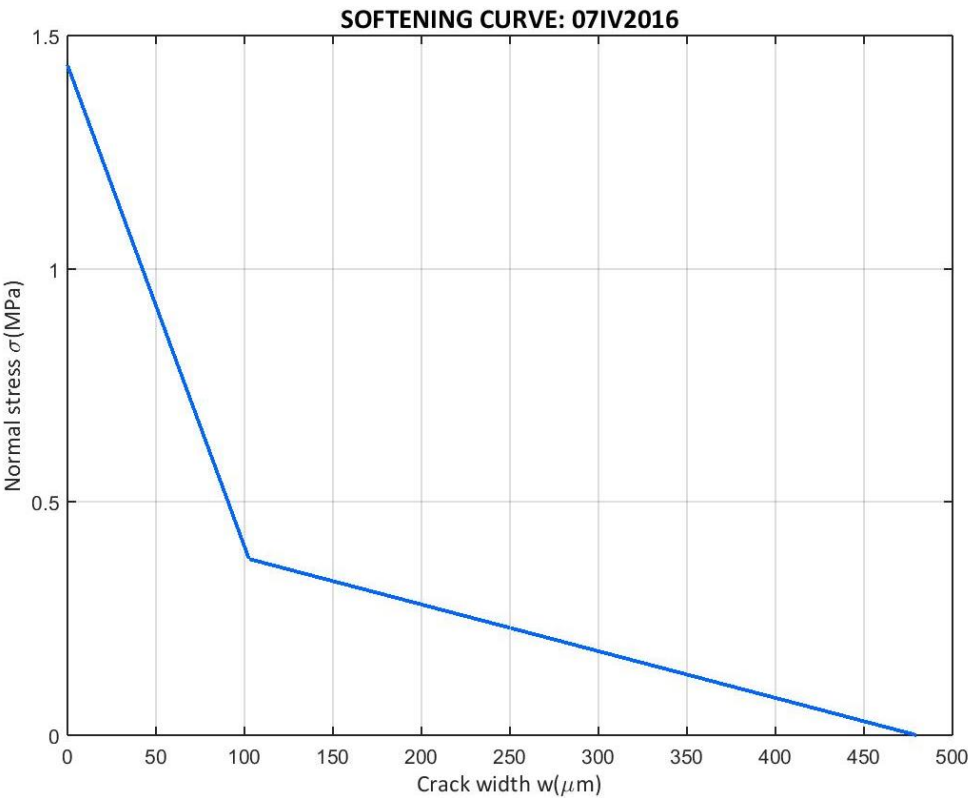


Figure 440: Softening curve bilinear approximation of the 07IV2016 campaign

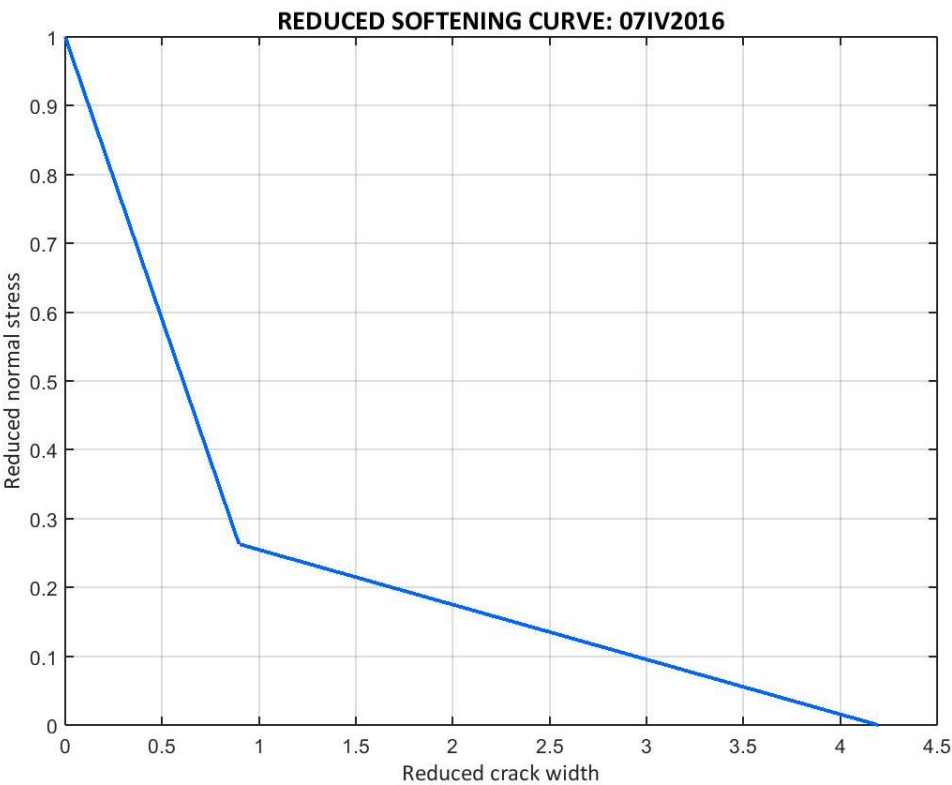


Figure 441: Softening curve bilinear approximation of the 07IV2016 campaign in the reduced form

E.9.6 07IV2016 SPECIMENS' COMPARISON

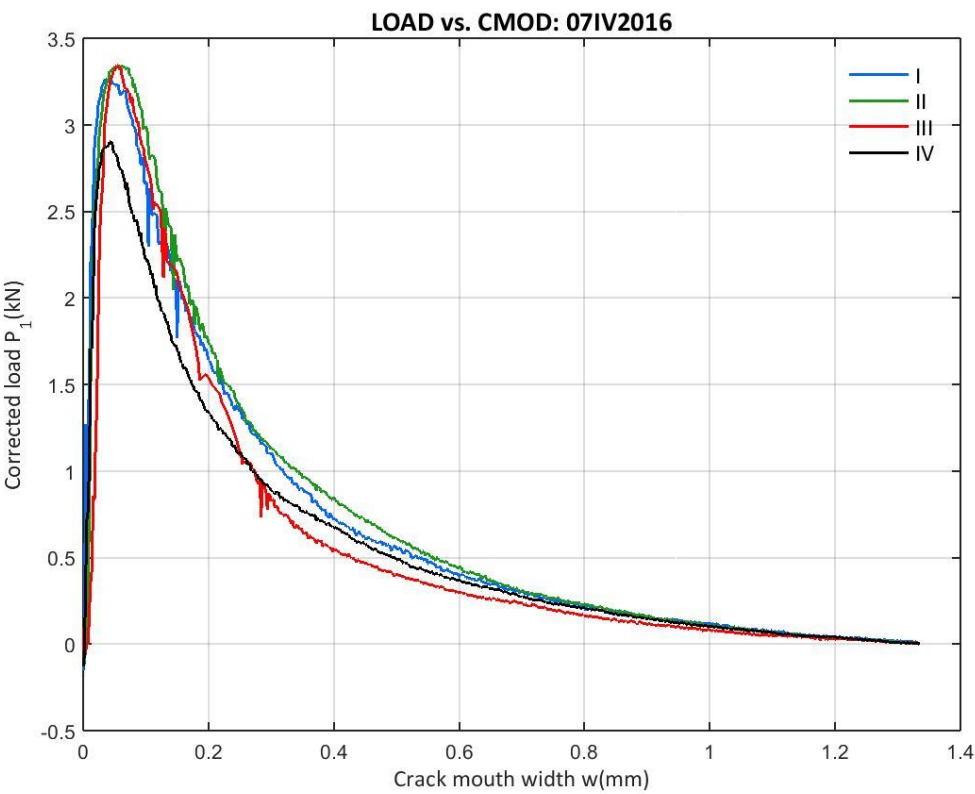


Figure 442: 07IV2016 Corrected load vs. CMOD from the entire campaign

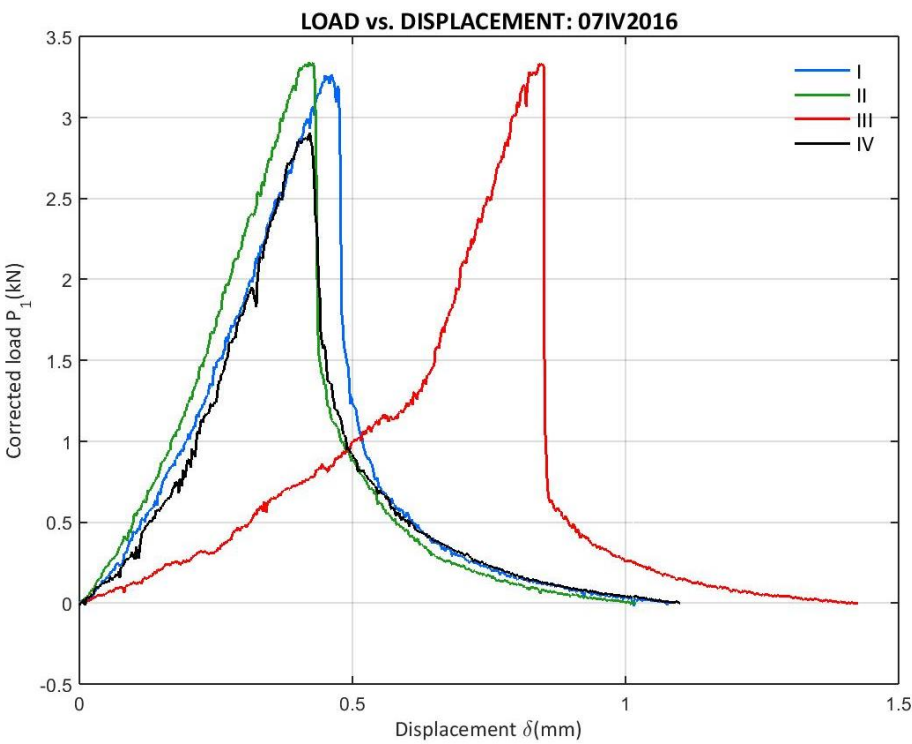


Figure 443: 17III2016 Corrected load vs. Displacement from the entire campaign

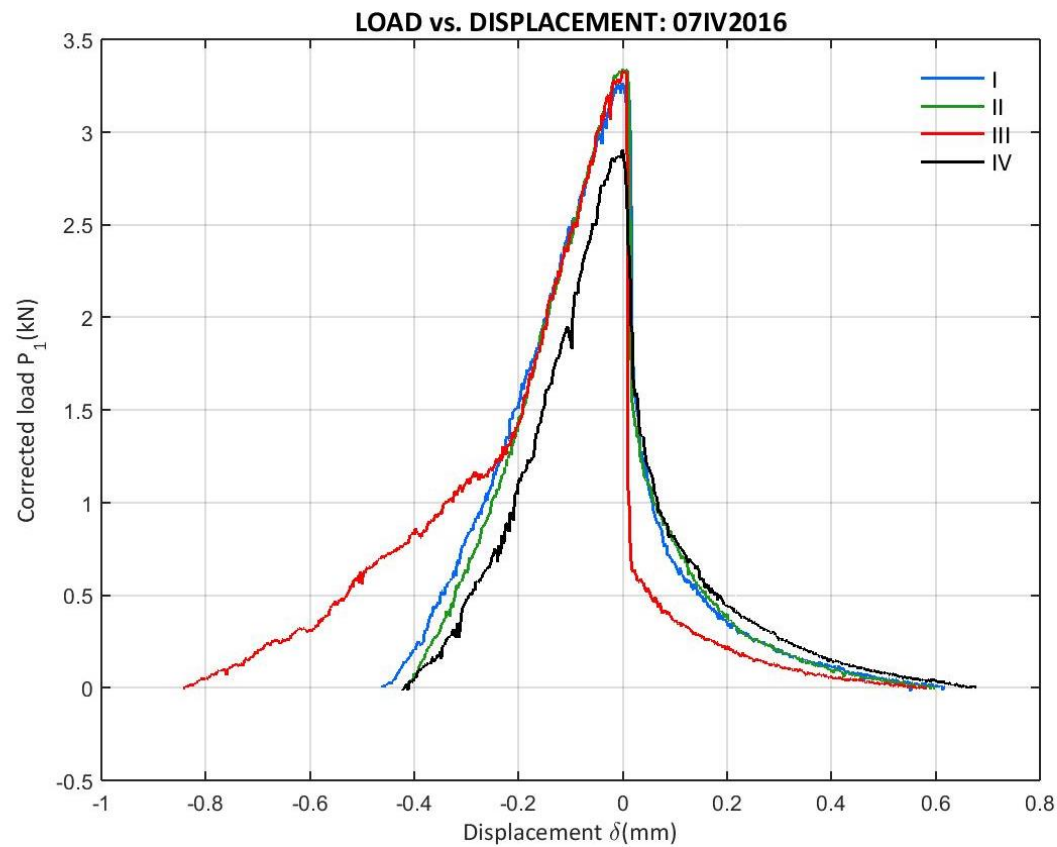


Figure 444: 07IV2016 Corrected load vs. Displacement from the entire campaign (peak displacement zero)

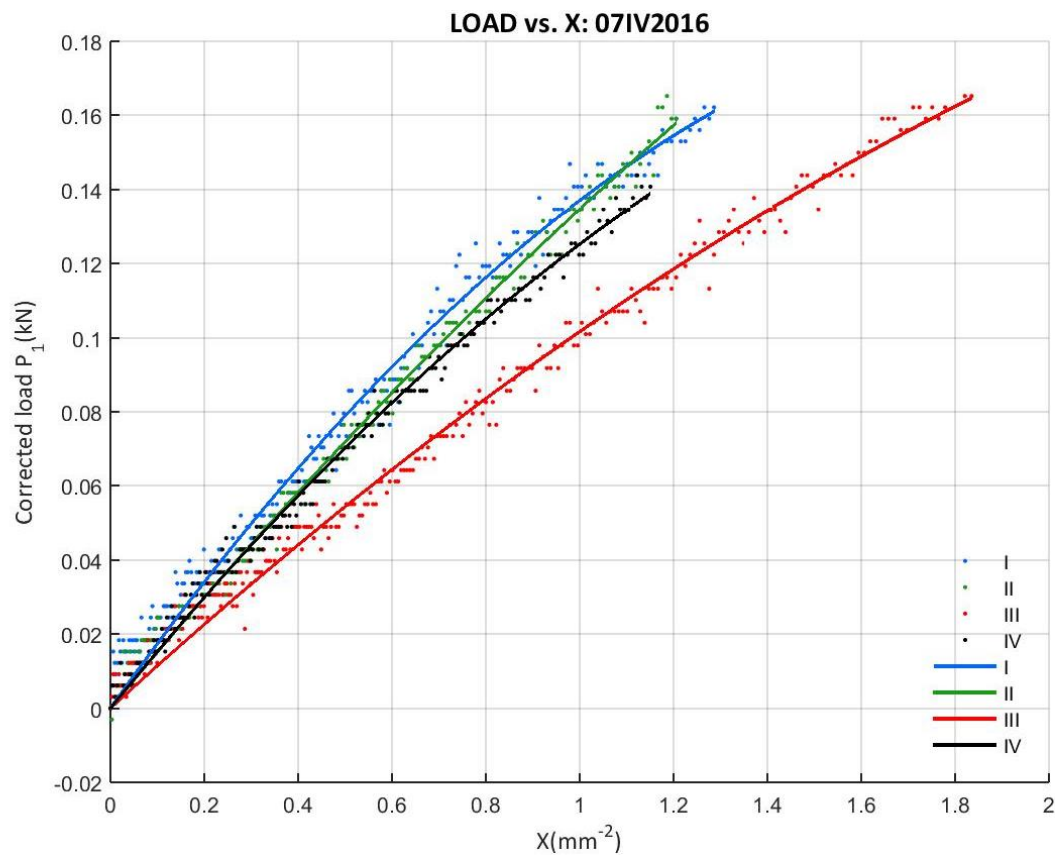


Figure 445: 07IV2016 Corrected load vs. X from the entire campaign

E.10 14IV2016 CAMPAIGN

E.10.1 14IV2016 DATA

- B14IV2016I

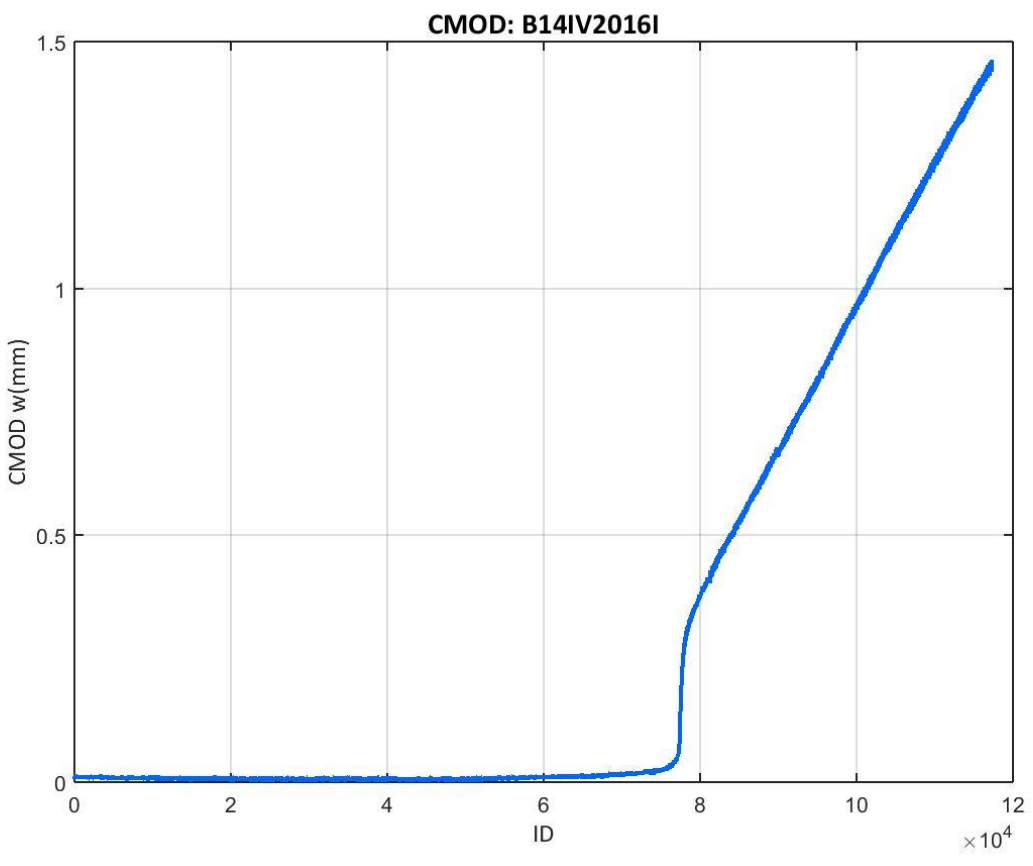


Figure 446: CMOD values recorded at the B14IV2016I test

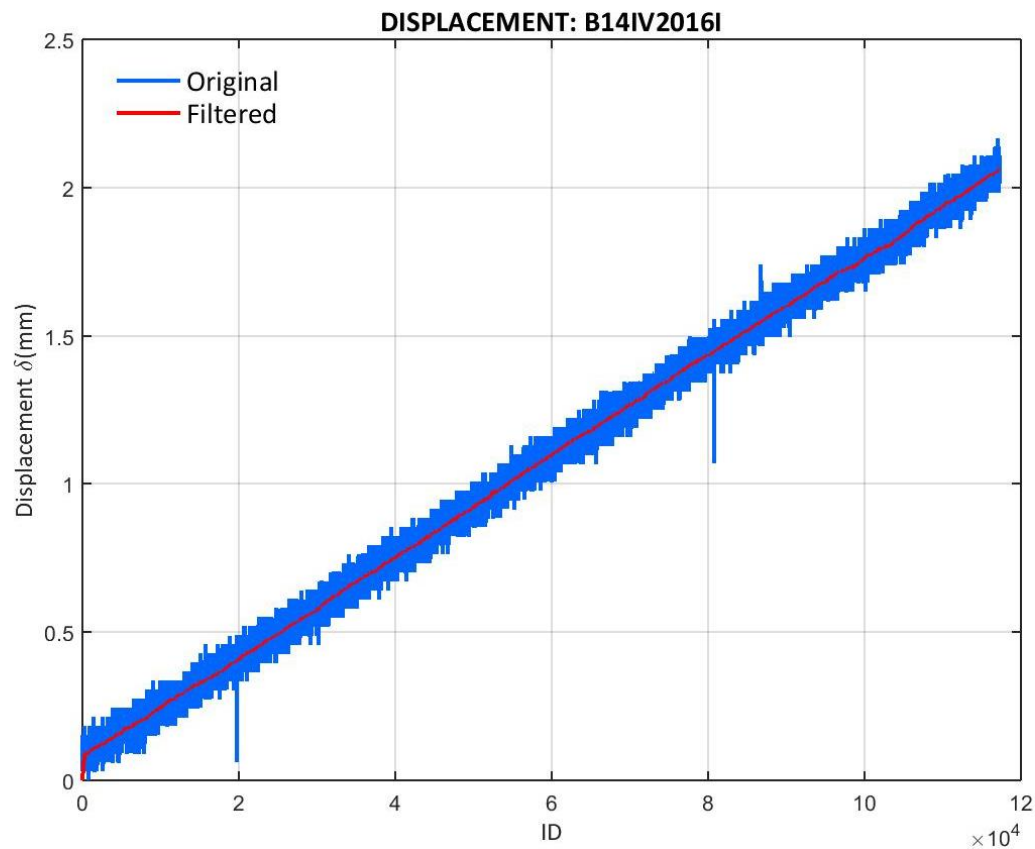


Figure 447: Displacement values recorded at the B14IV2016I test

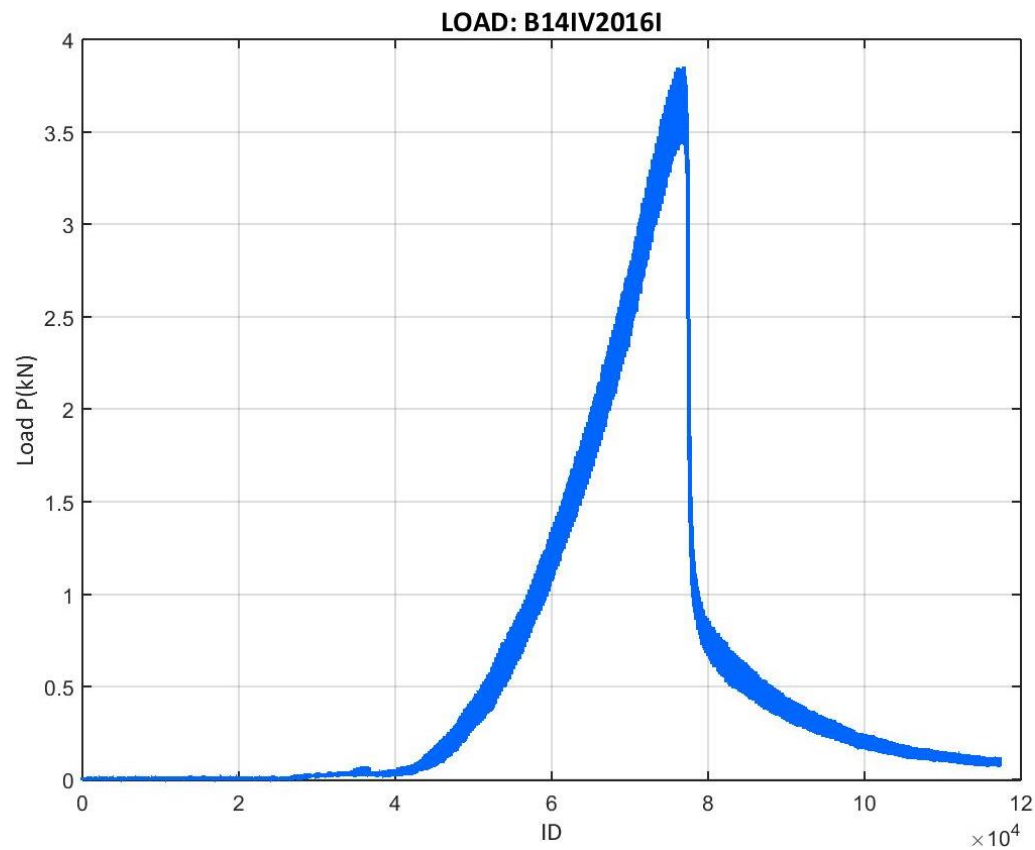


Figure 448: Load values recorded at the B14IV2016I test

- B14IV2016II

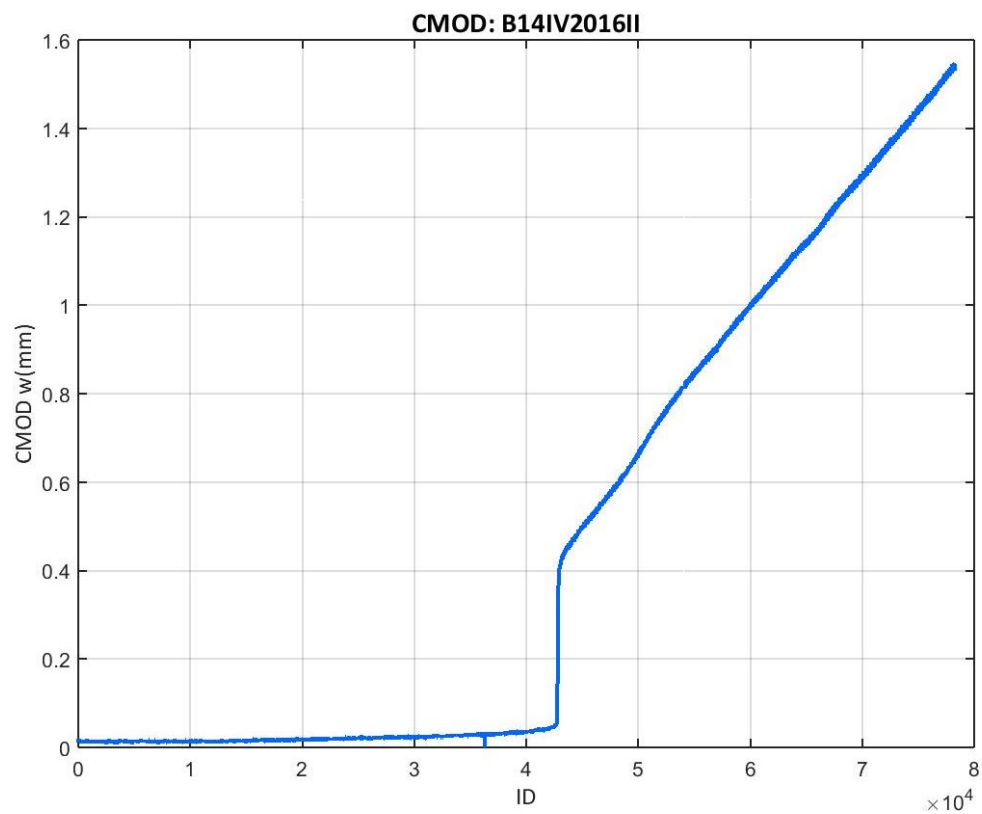


Figure 449: CMOD values recorded at the B14IV2016II test

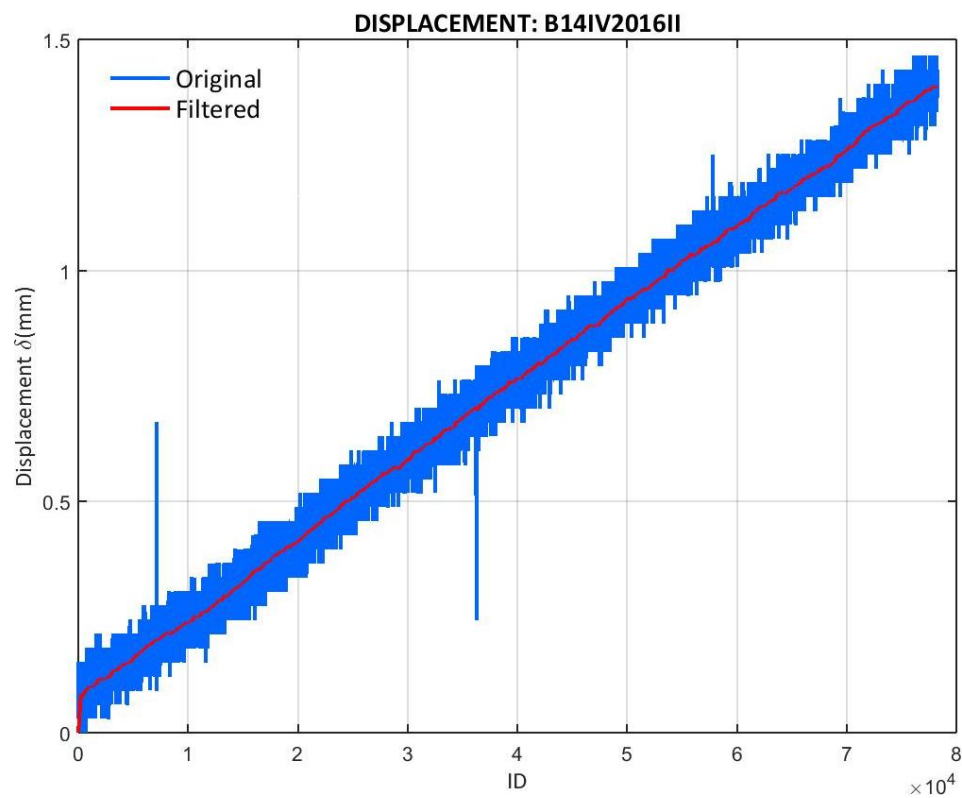


Figure 450: Displacement values recorded at the B14IV2016II test

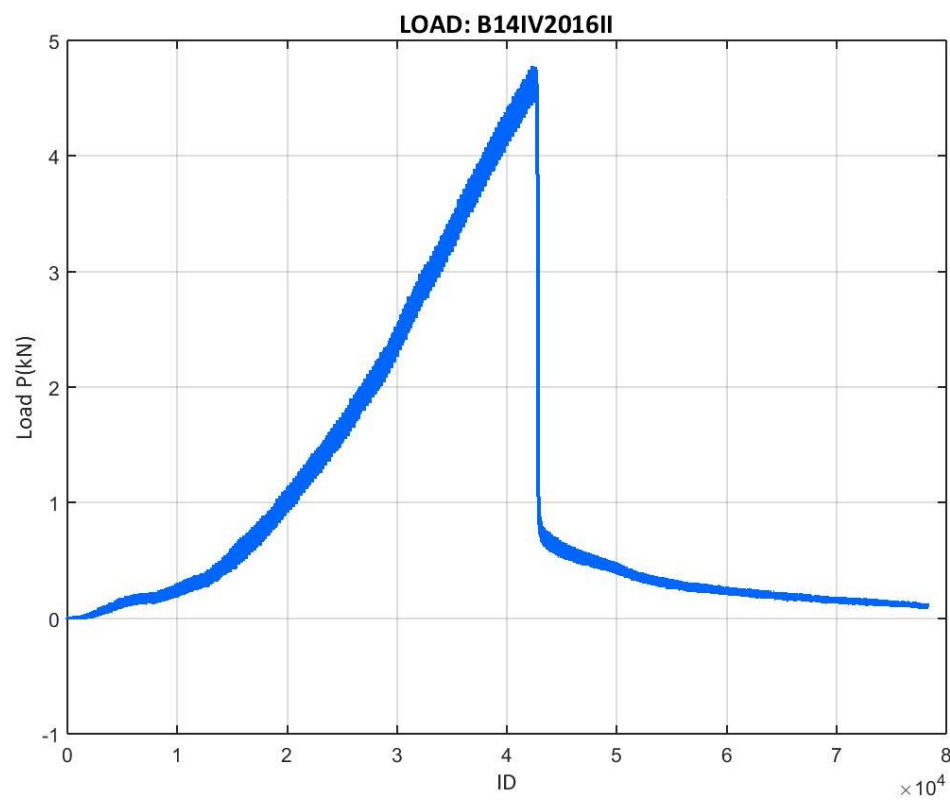


Figure 451: Load values recorded at the B14IV2016II test

- B14IV2016III

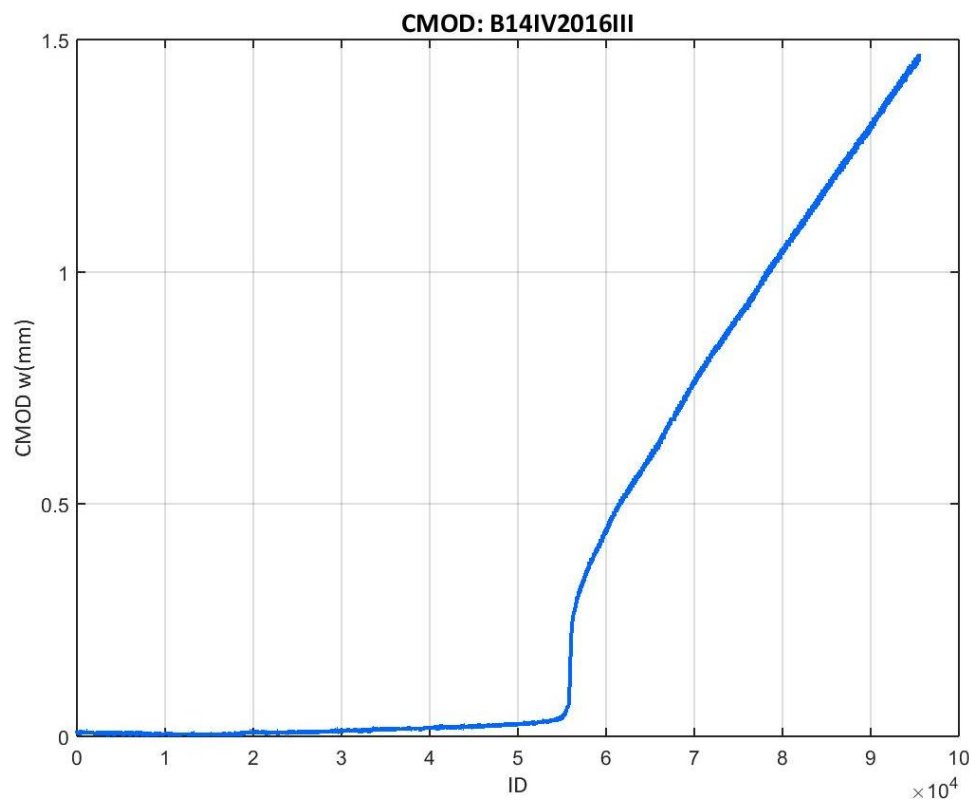


Figure 452: CMOD values recorded at the B14IV2016III test

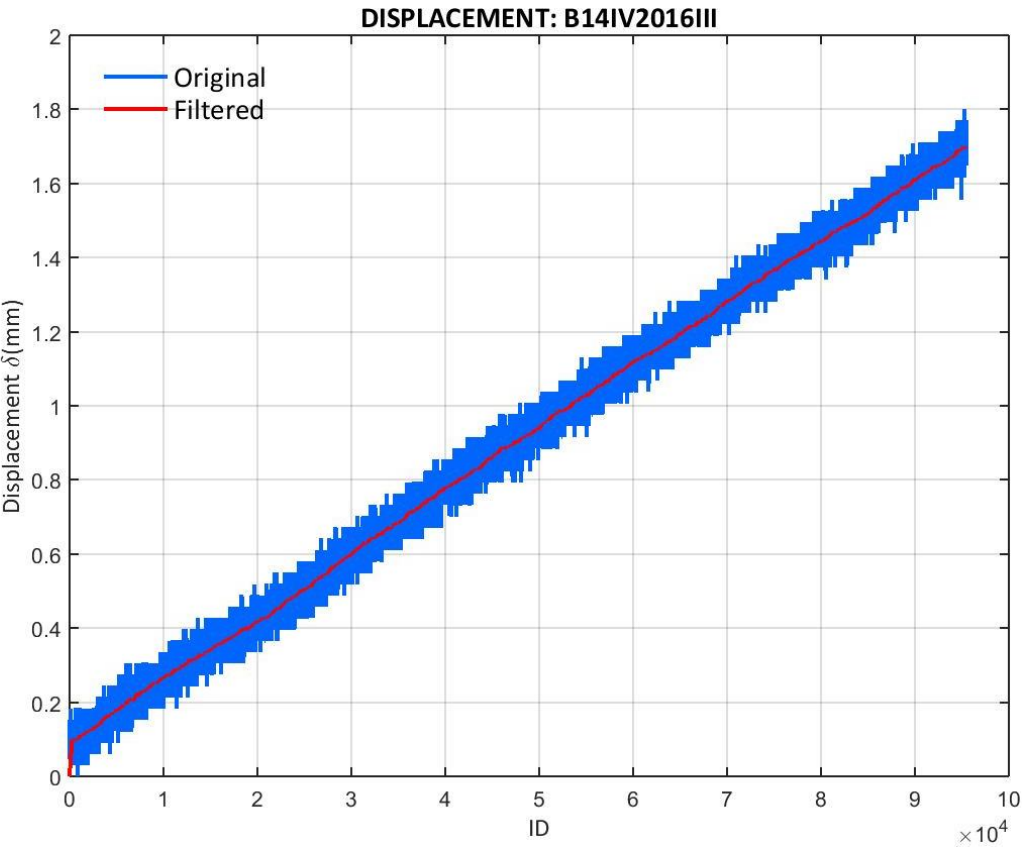


Figure 453: Displacement values recorded at the B14IV2016III test

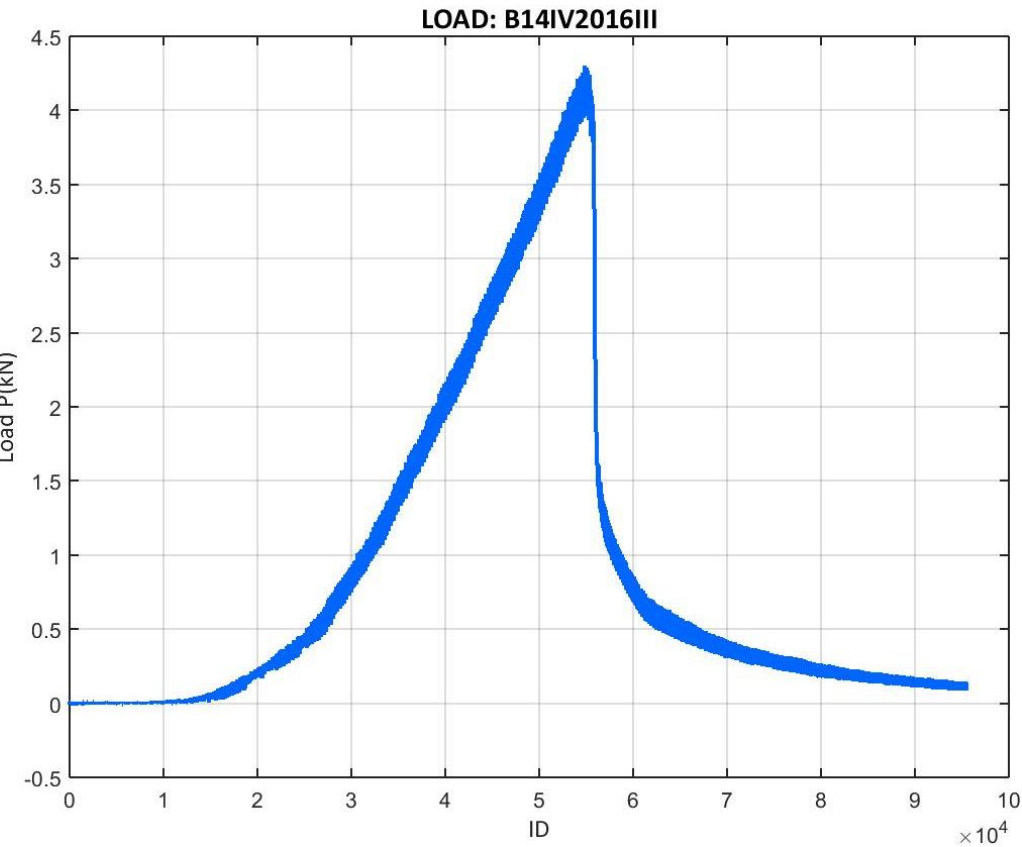


Figure 454: Load values recorded at the B14IV2016III test

- B14IV2016IV

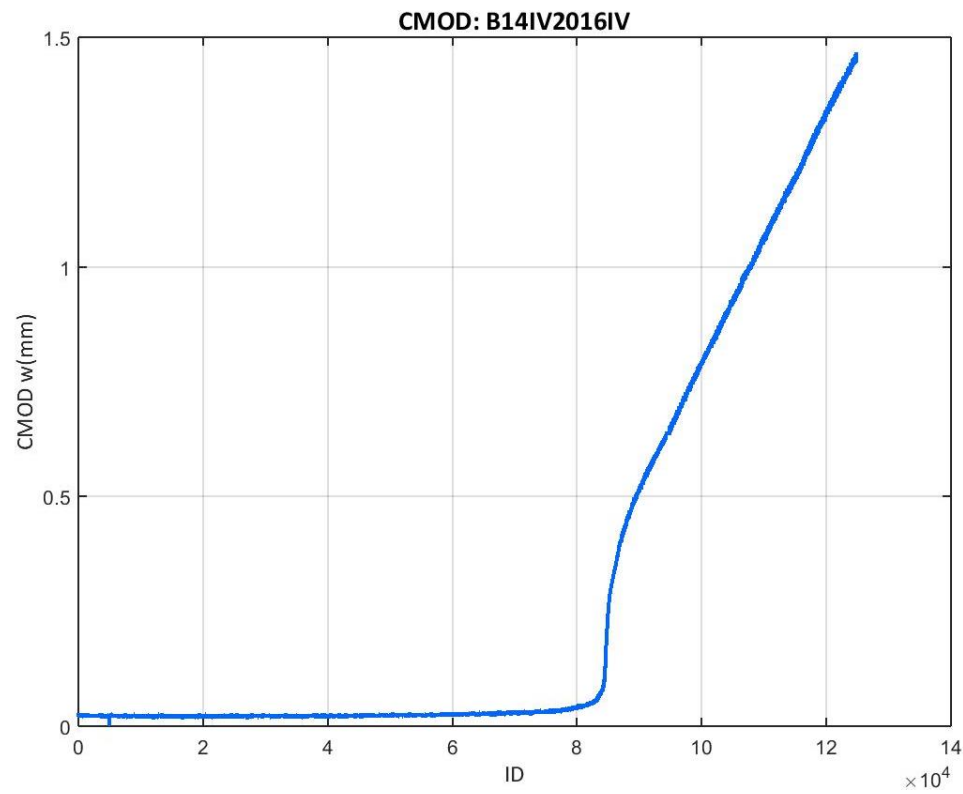


Figure 455: CMOD values recorded at the B14IV2016IV test

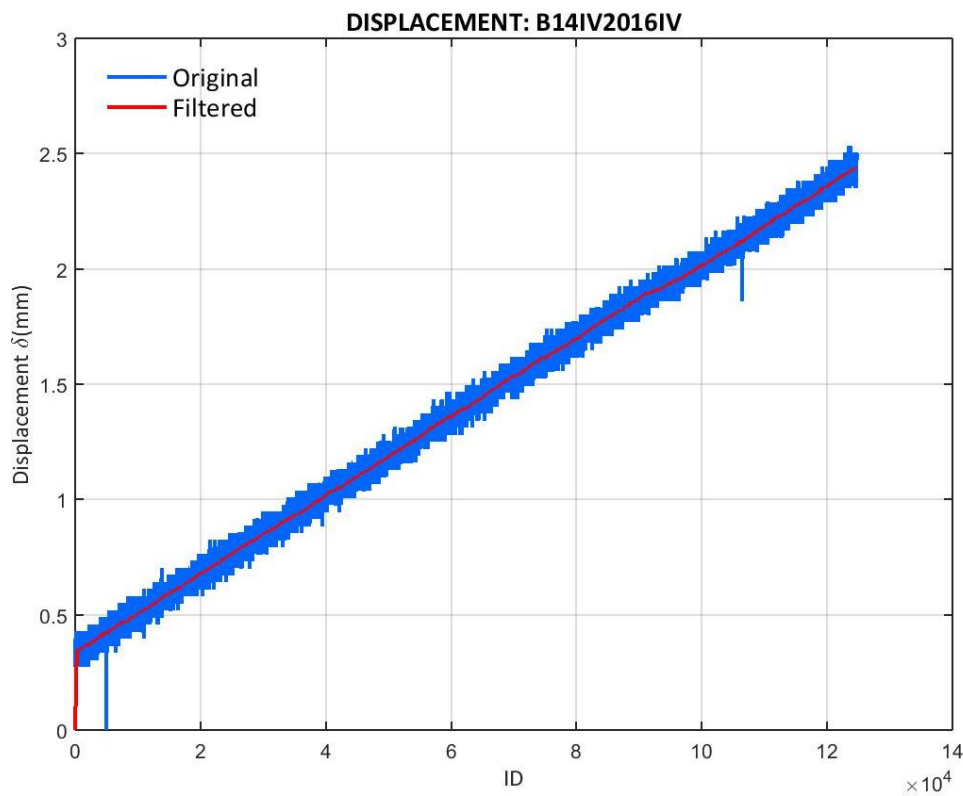


Figure 456: Displacement values recorded at the B14IV2016IV test

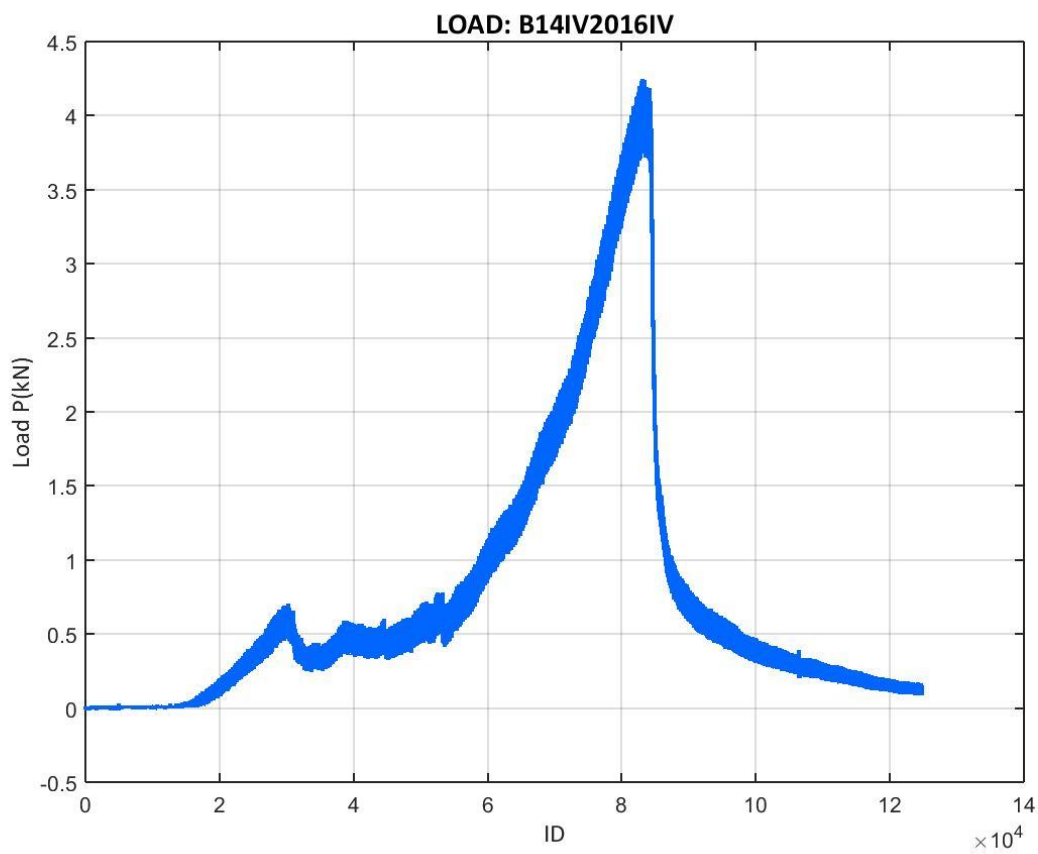


Figure 457: Load values recorded at the B14IV2016IV test

E.10.2 14IV2016 CORRECTED LOAD VS. CMOD

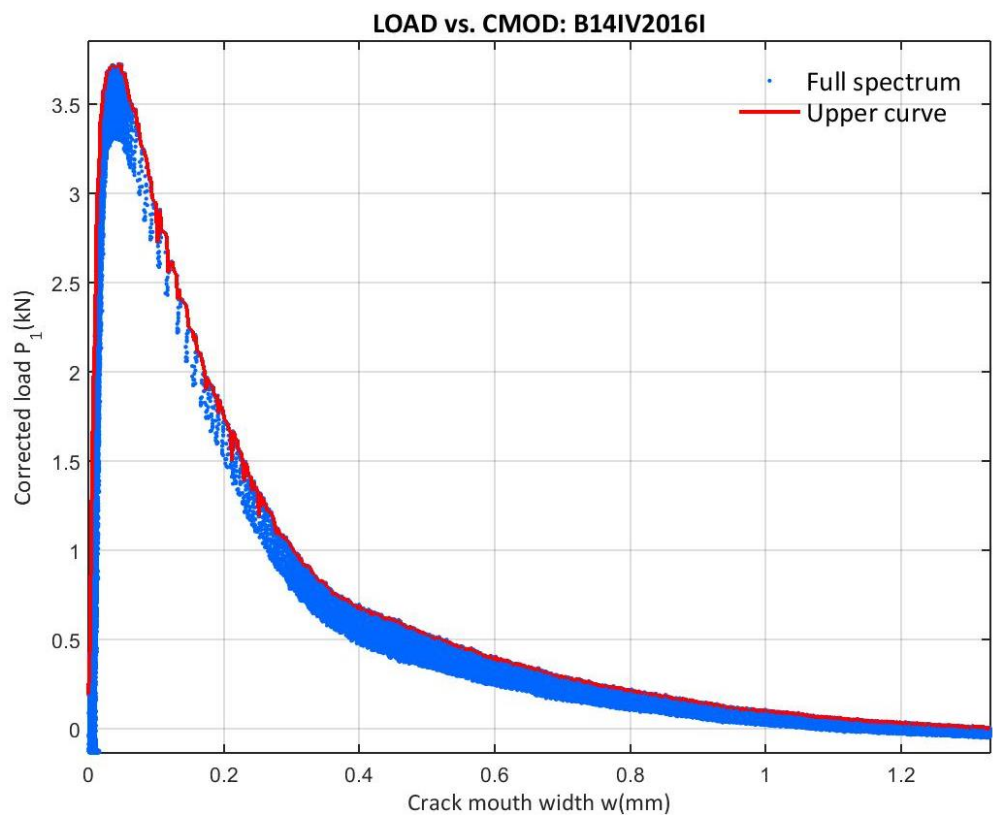


Figure 458: Corrected load vs. CMOD at the B14IV2016I test

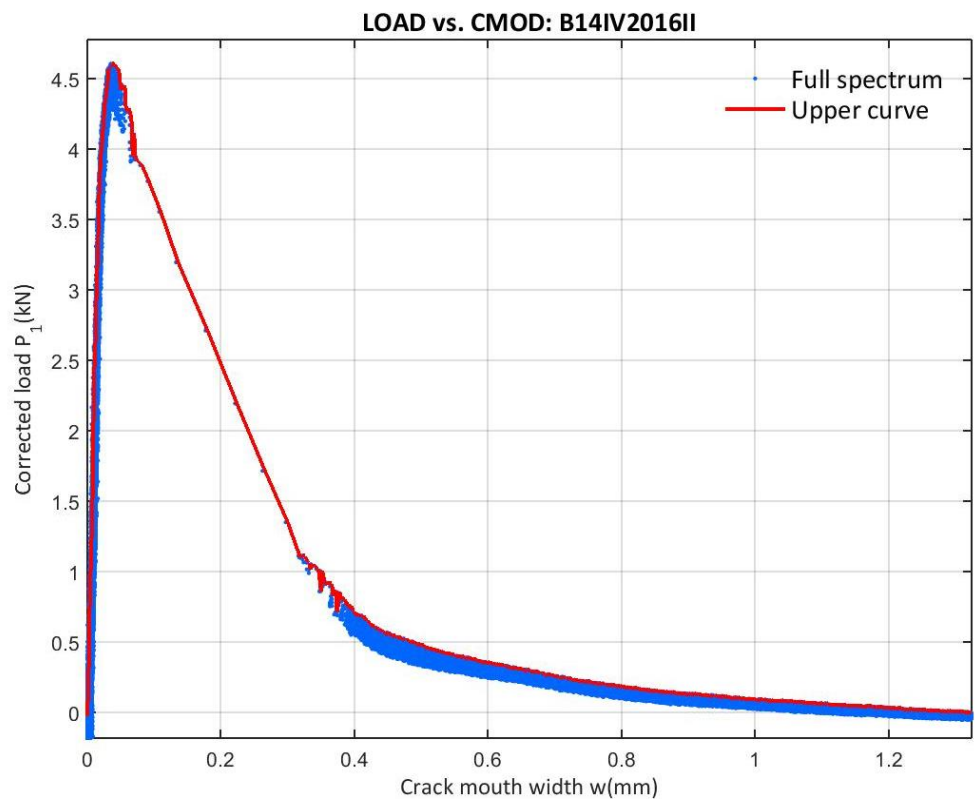


Figure 459: Corrected load vs. CMOD at the B14IV2016II test

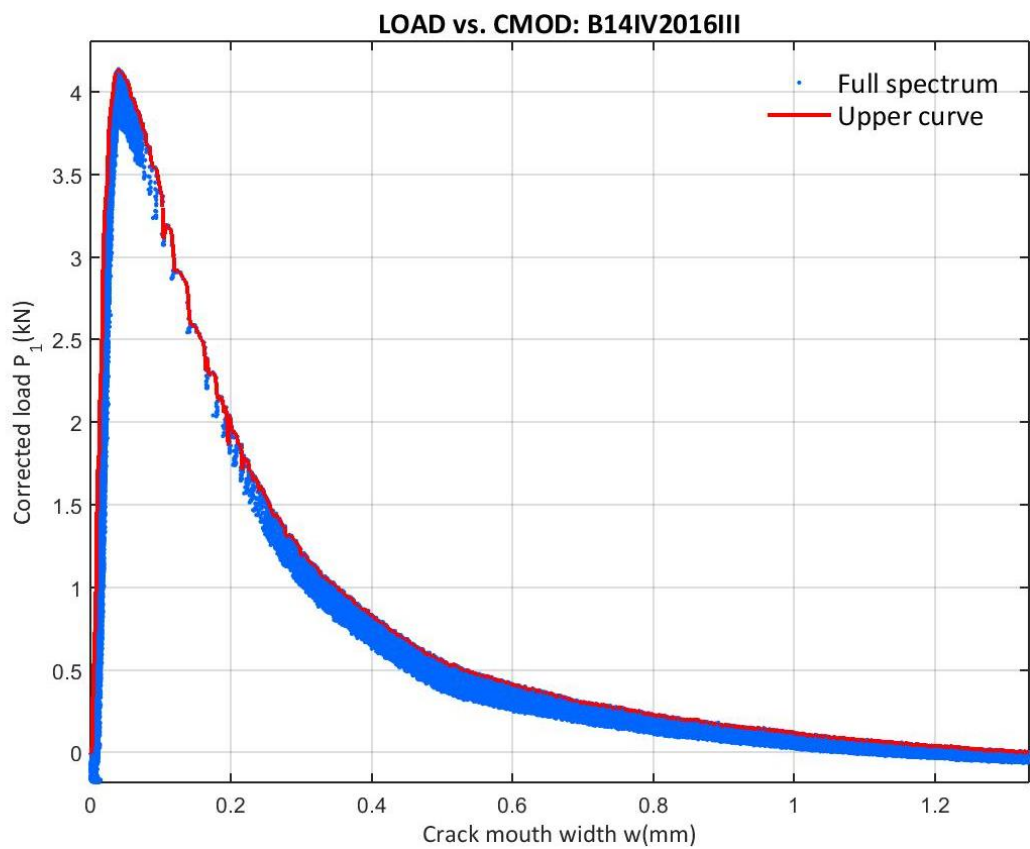


Figure 460: Corrected load vs. CMOD at the B14IV2016III test

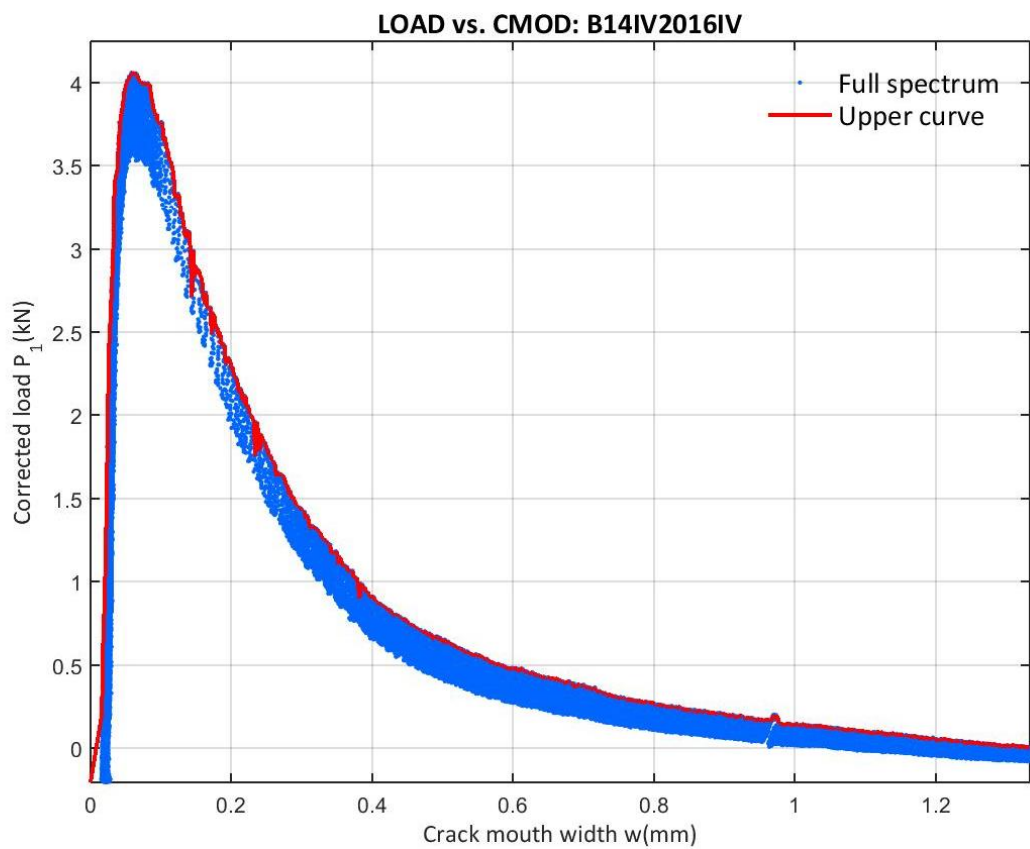


Figure 461: Corrected load vs. CMOD at the B14IV2016IV test

E.10.3 14IV2016 CORRECTED LOAD VS. VERTICAL DISPLACEMENT

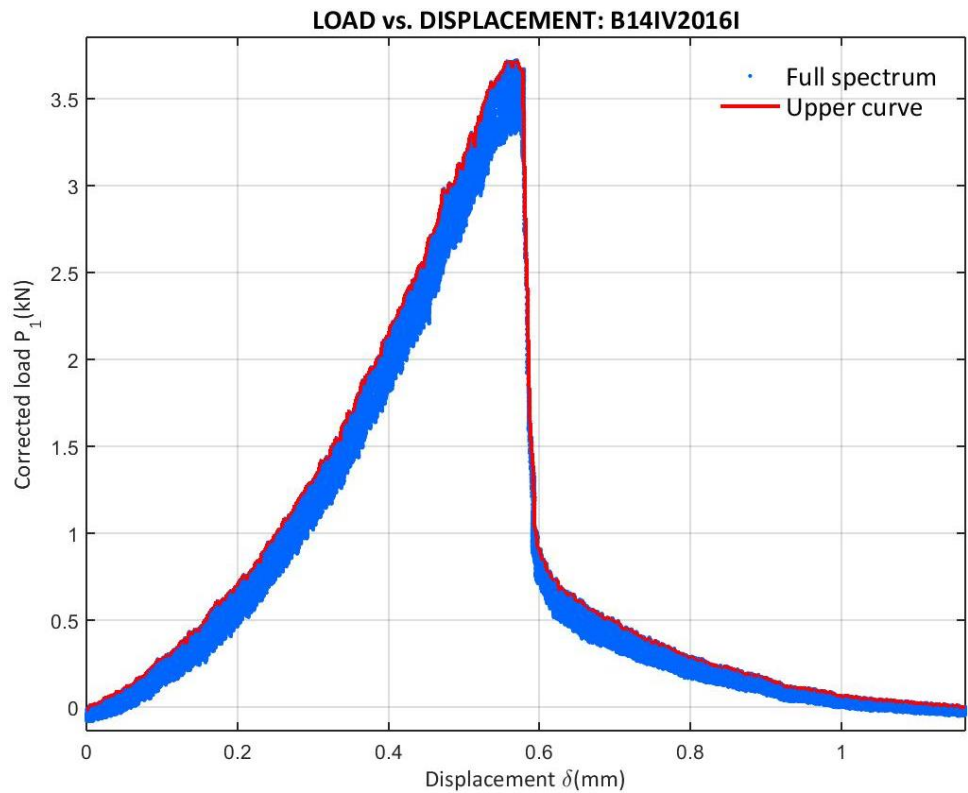


Figure 462: Corrected load vs. Displacement at the B14IV2016I test

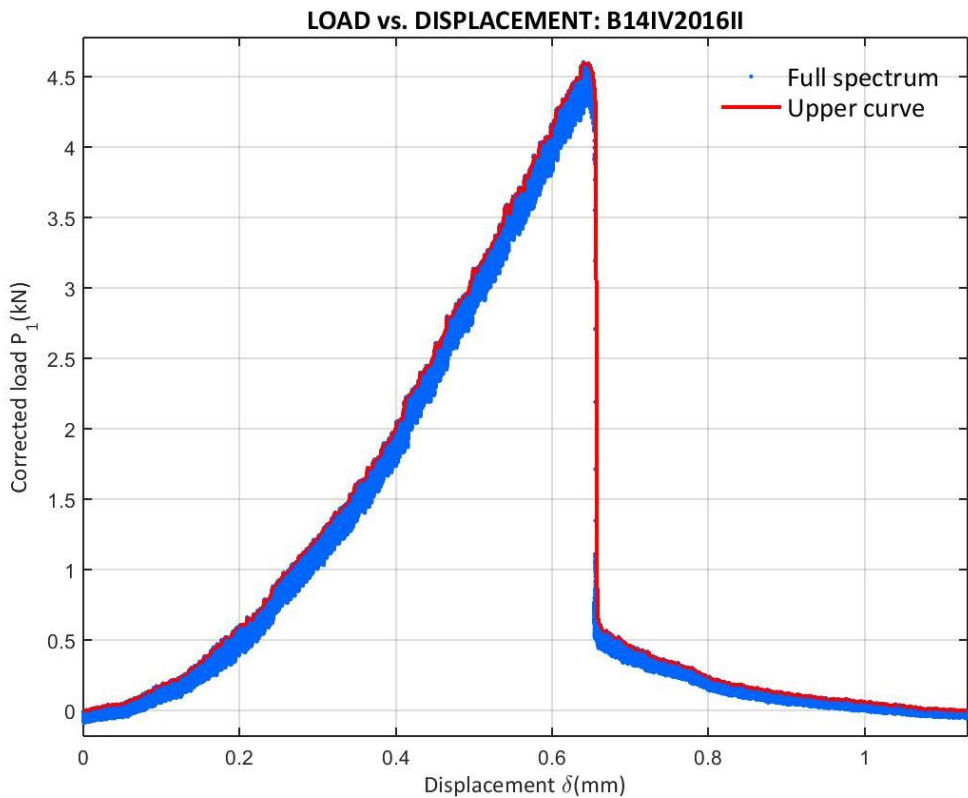


Figure 463: Corrected load vs. Displacement at the B14IV2016II test

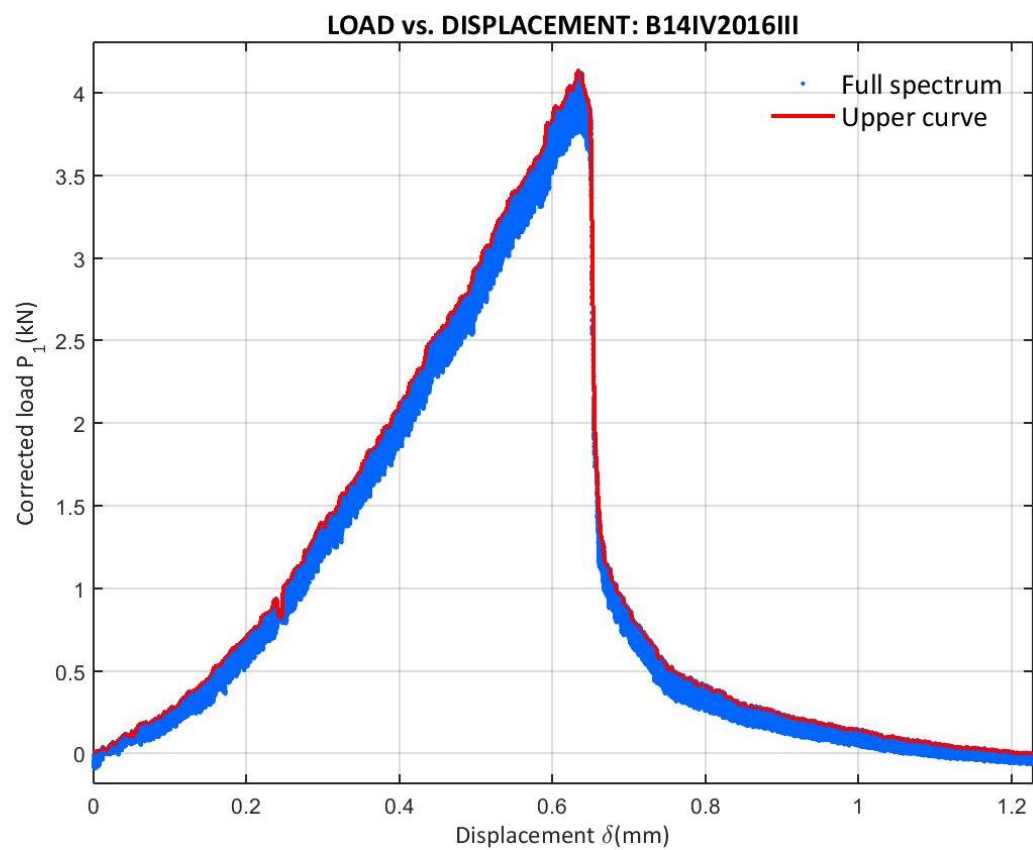


Figure 464: Corrected load vs. Displacement at the B14IV2016III test

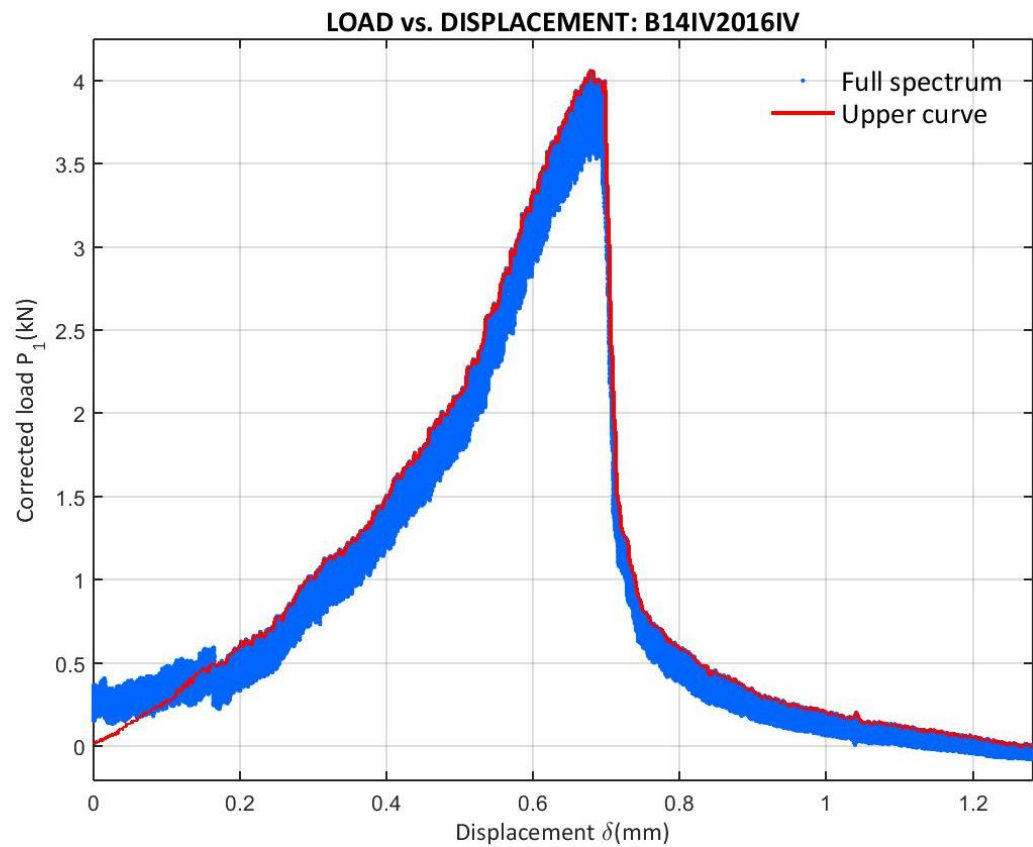


Figure 465: Corrected load vs. Displacement at the B14IV2016IV test

E.10.4 14IV2016 CORRECTED LOAD VS. X

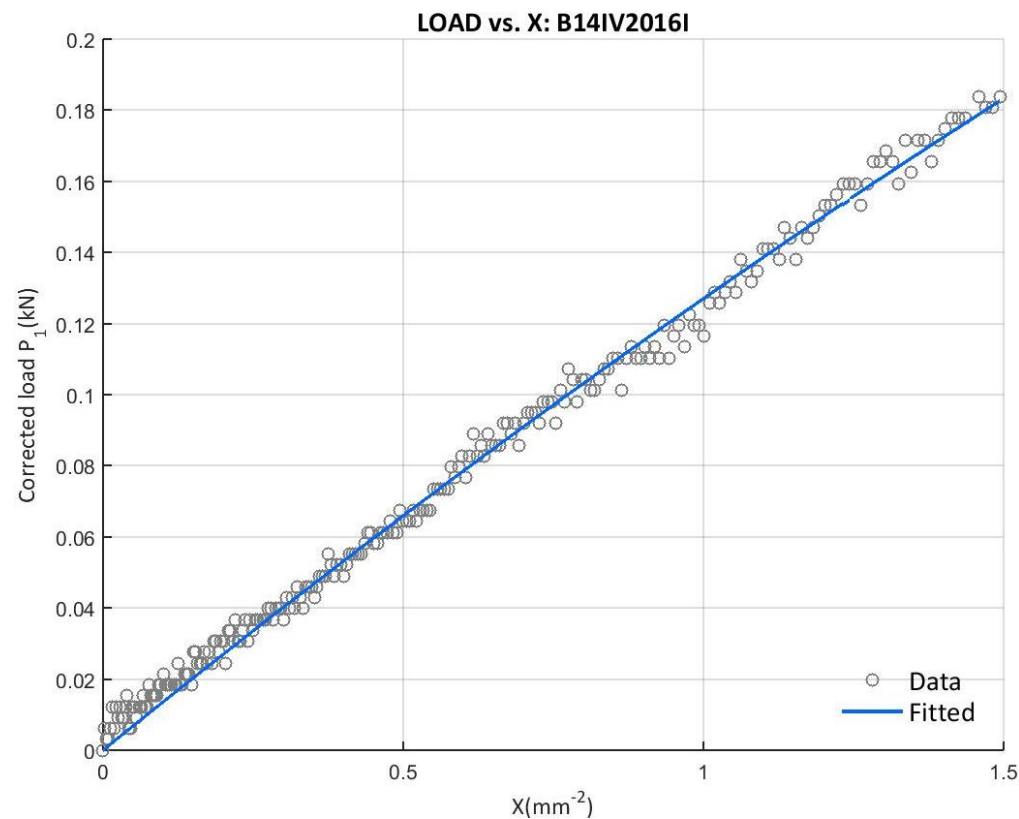


Figure 466: Corrected load vs. X at the B14IV2016I test with the final upper curve data

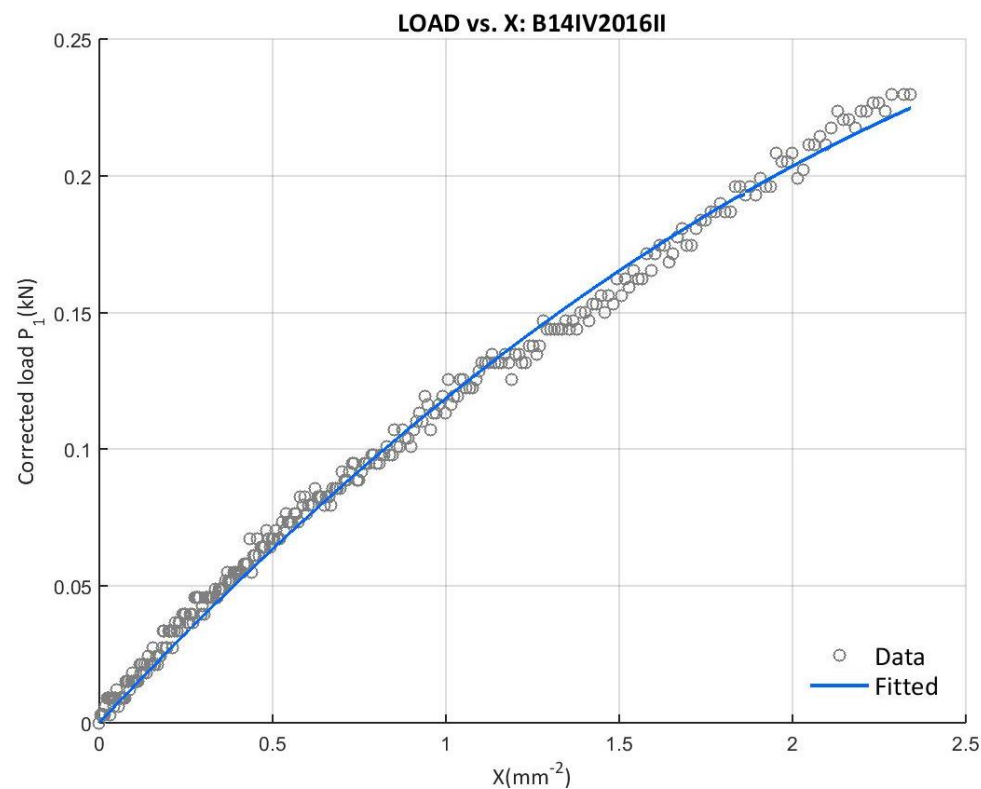


Figure 467: Corrected load vs. X at the B14IV2016II test with the final upper curve data

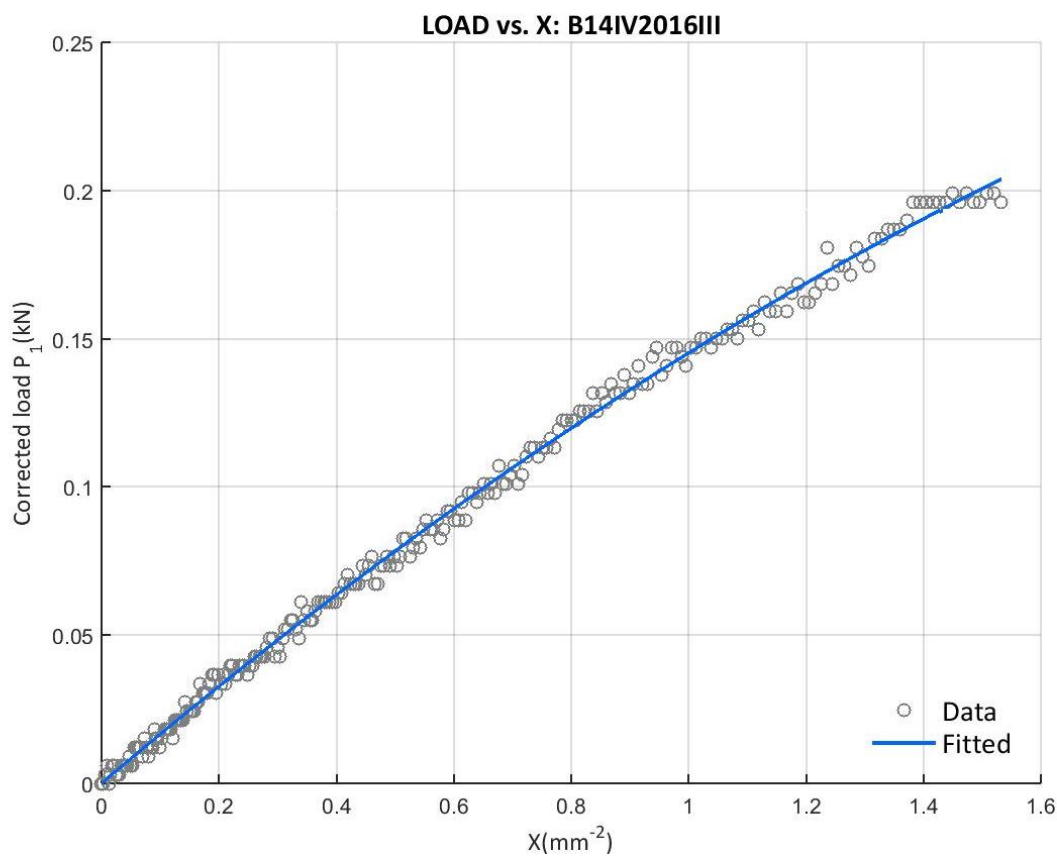


Figure 468: Corrected load vs. X at the B14IV2016III test with the final upper curve data

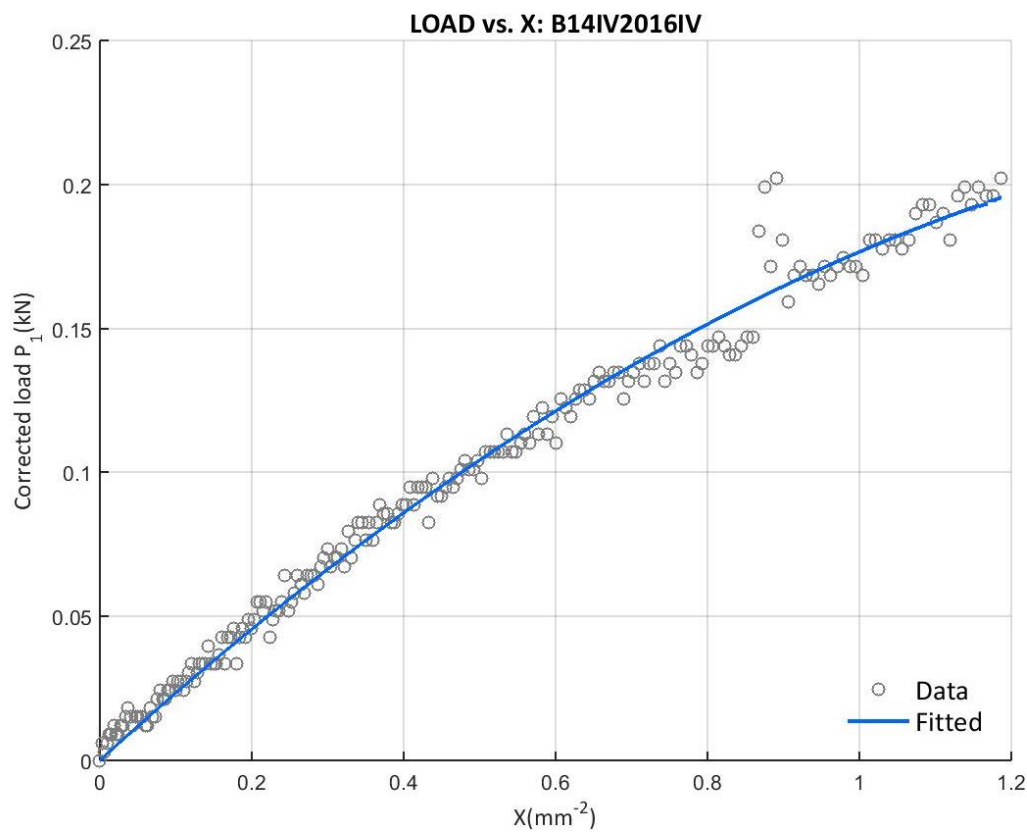


Figure 469: Corrected load vs. X at the B14IV2016IV test with the final upper curve data

E.10.5 14IV2016 SOFTENING CURVE BILINEAR APPROXIMATION

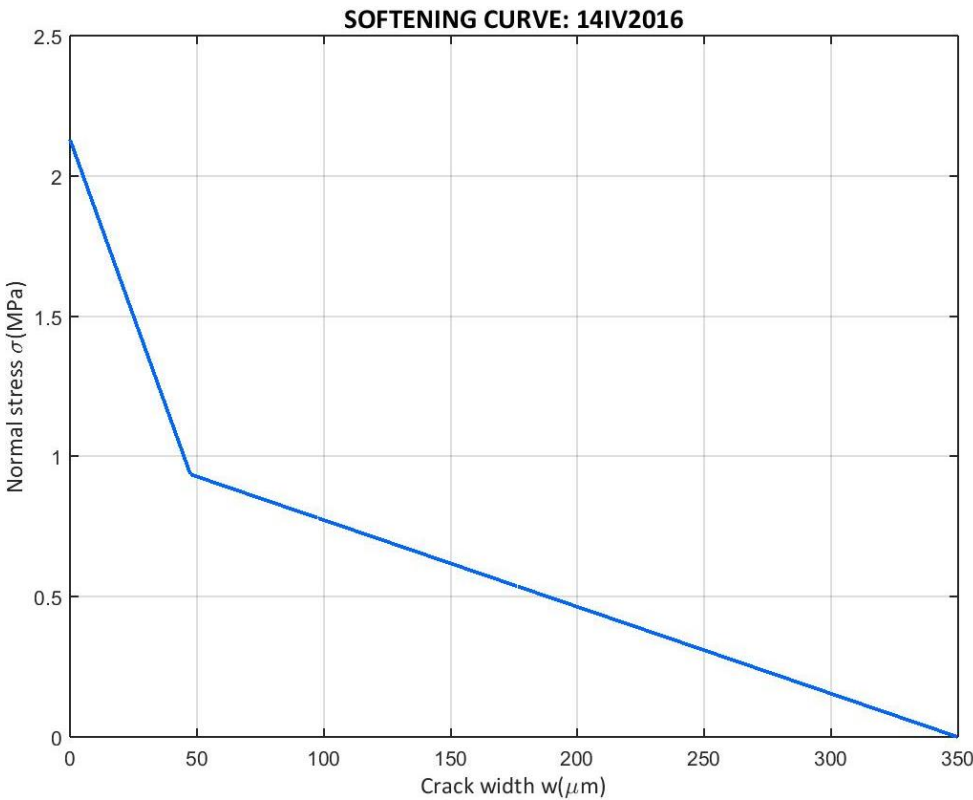


Figure 470: Softening curve bilinear approximation of the 14IV2016 campaign

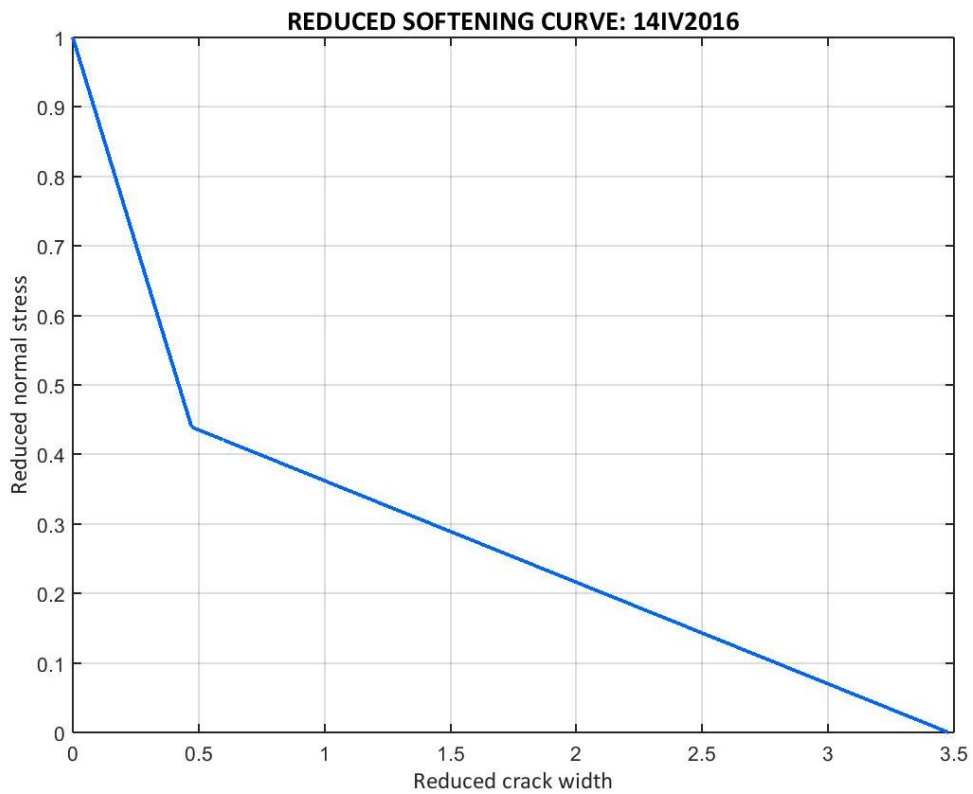


Figure 471: Softening curve bilinear approximation of the 14IV2016 campaign in the reduced form

E.10.6 14IV2016 SPECIMENS' COMPARISON

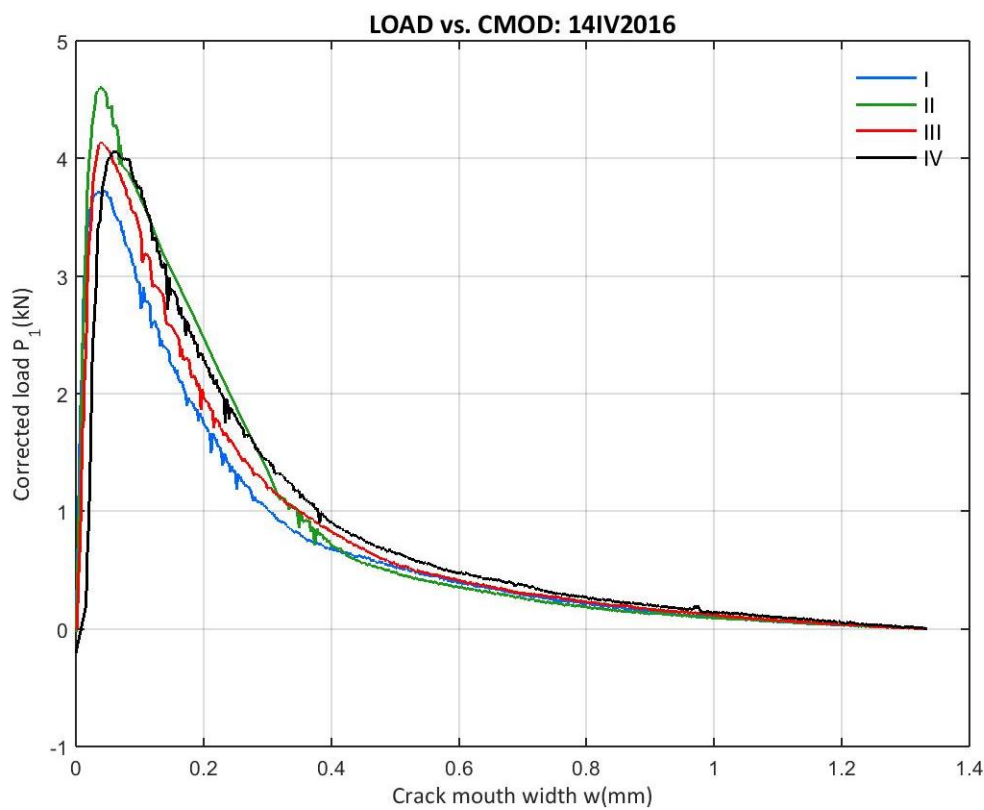


Figure 472: 14IV2016 Corrected load vs. CMOD from the entire campaign

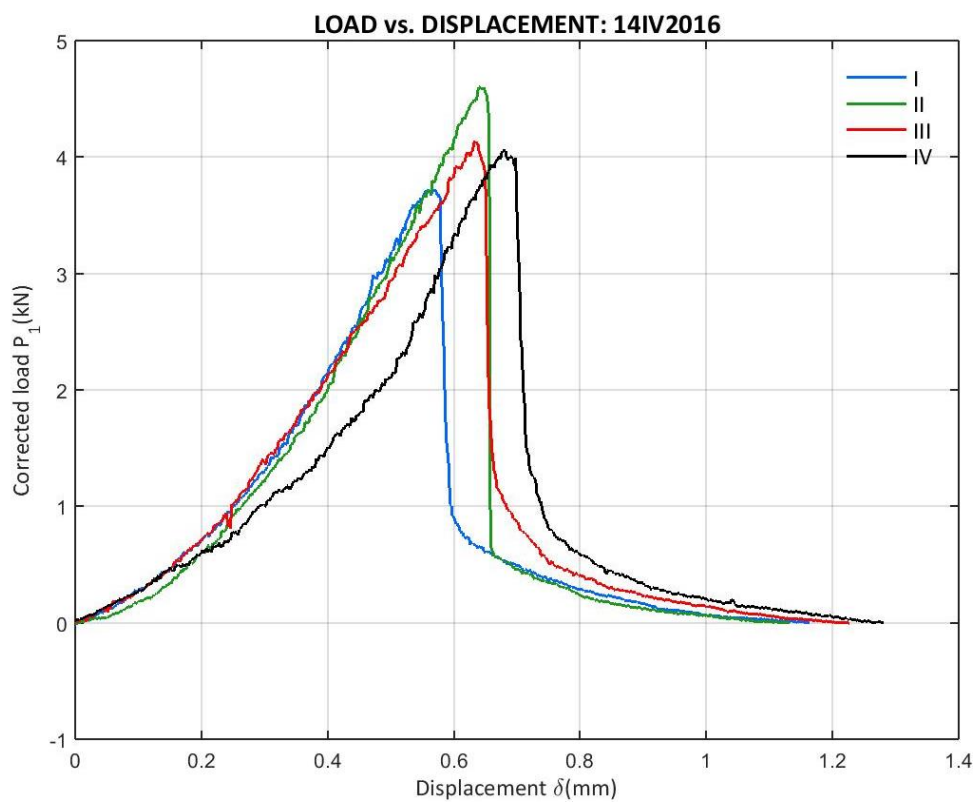


Figure 473: 14IV2016 Corrected load vs. Displacement from the entire campaign

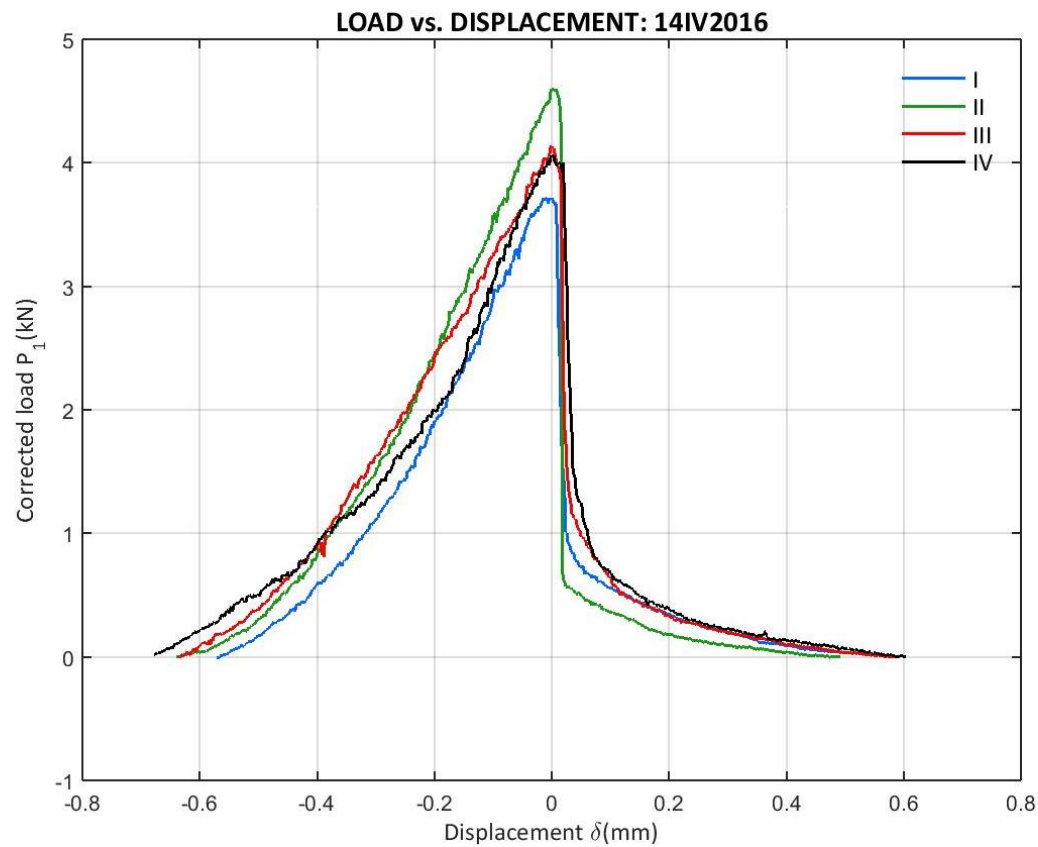


Figure 474: 14IV2016 Corrected load vs. Displacement from the entire campaign (peak displacement zero)

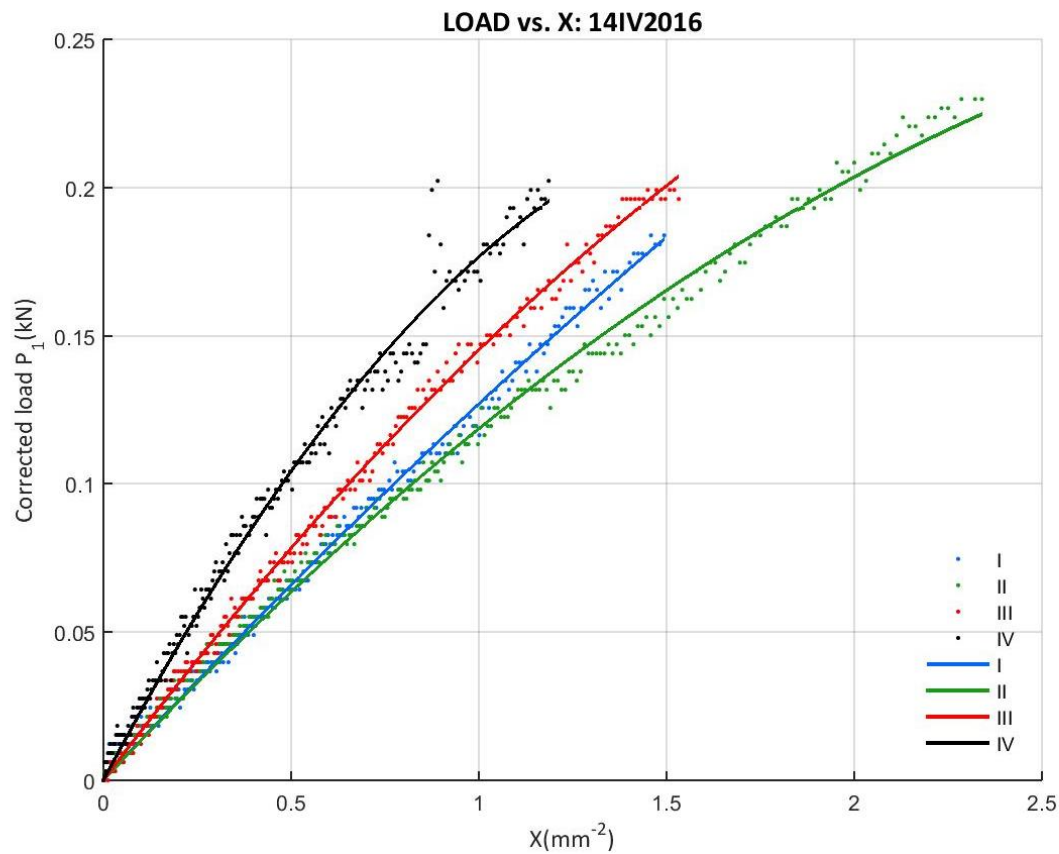


Figure 475: 14IV2016 Corrected load vs. X from the entire campaign

E.11 21IV2016 CAMPAIGN

E.11.1 21IV2016 DATA

- B21IV2016I

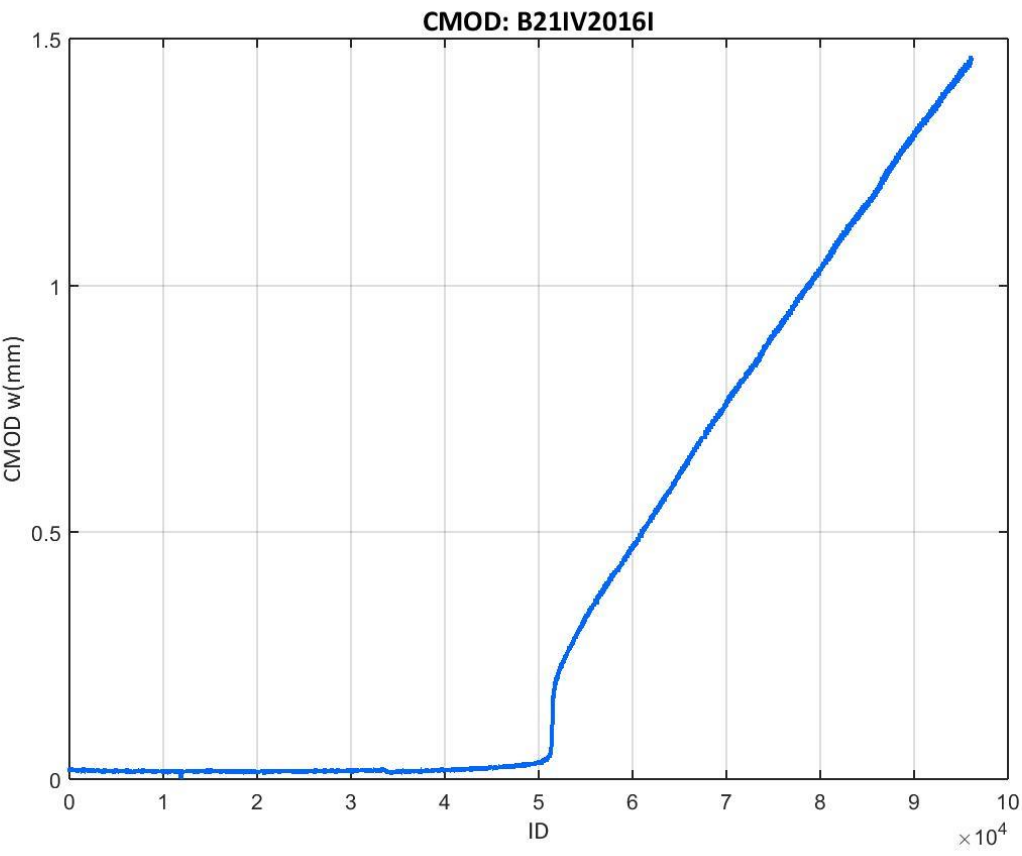


Figure 476: CMOD values recorded at the B21IV2016I test

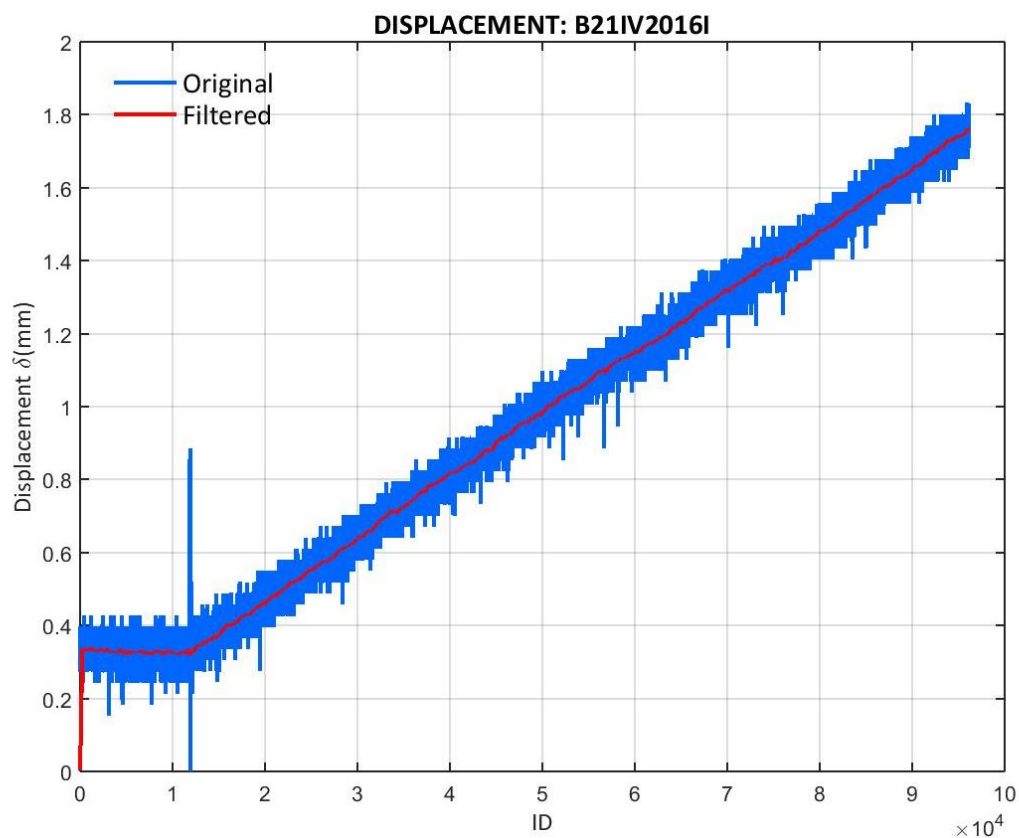


Figure 477: Displacement values recorded at the B21IV2016I test

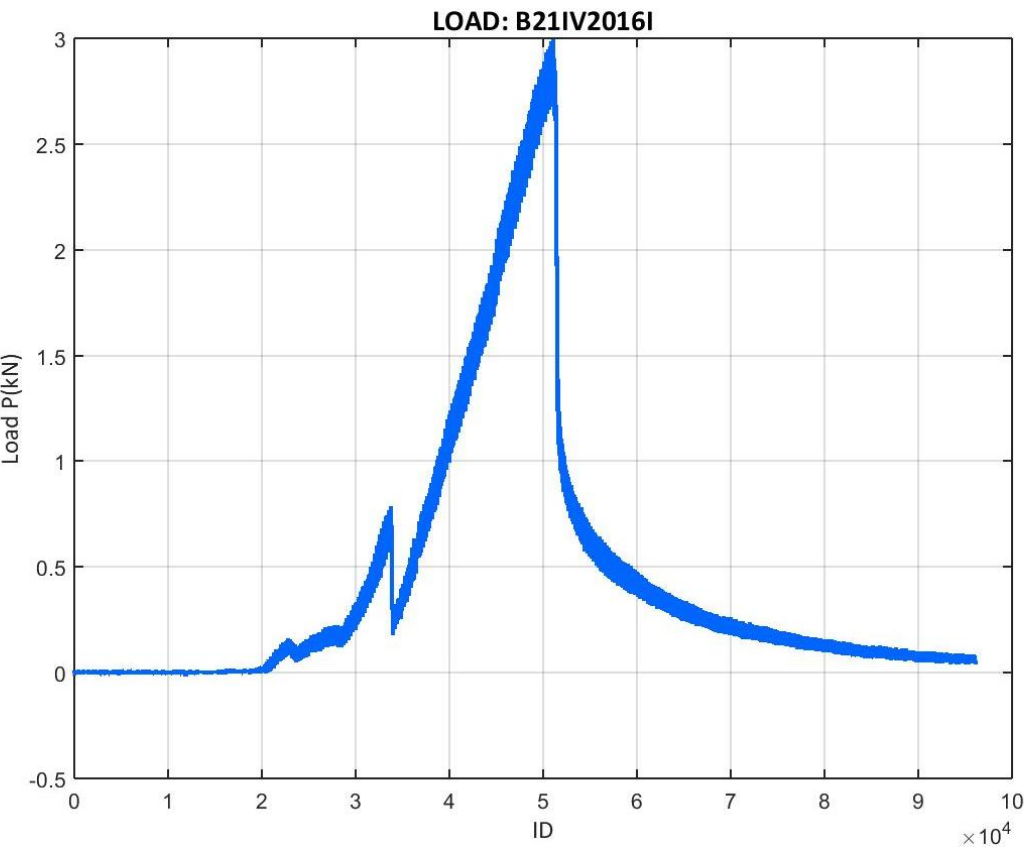


Figure 478: Load values recorded at the B21IV2016I test

- B21IV2016II

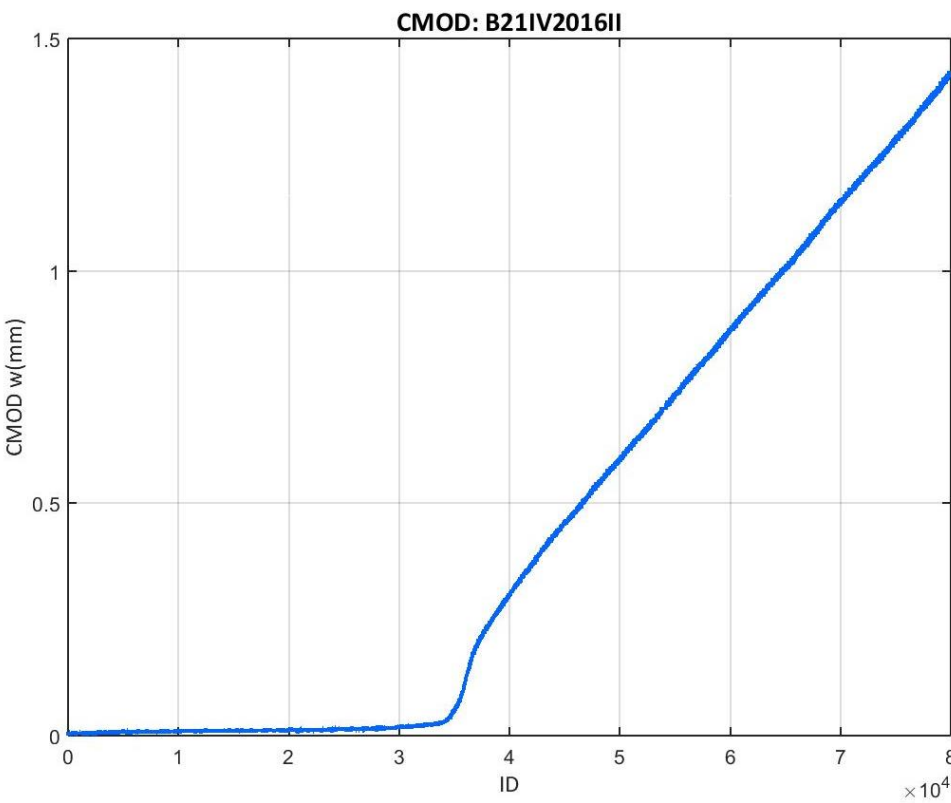


Figure 479: CMOD values recorded at the B21IV2016II test

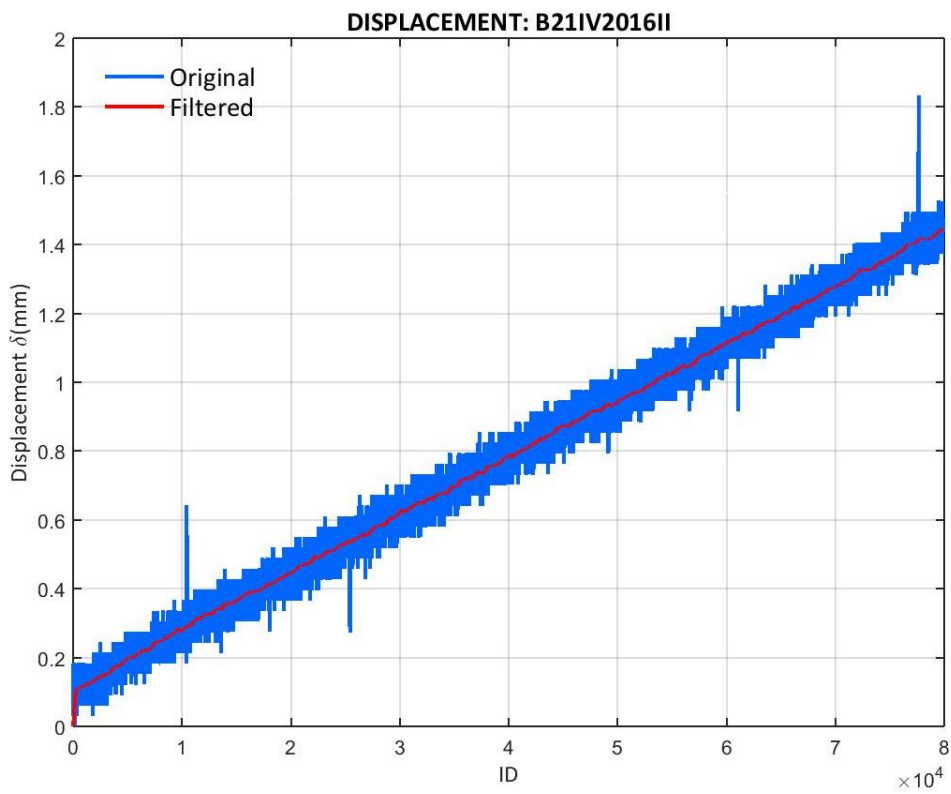


Figure 480: Displacement values recorded at the B21IV2016II test

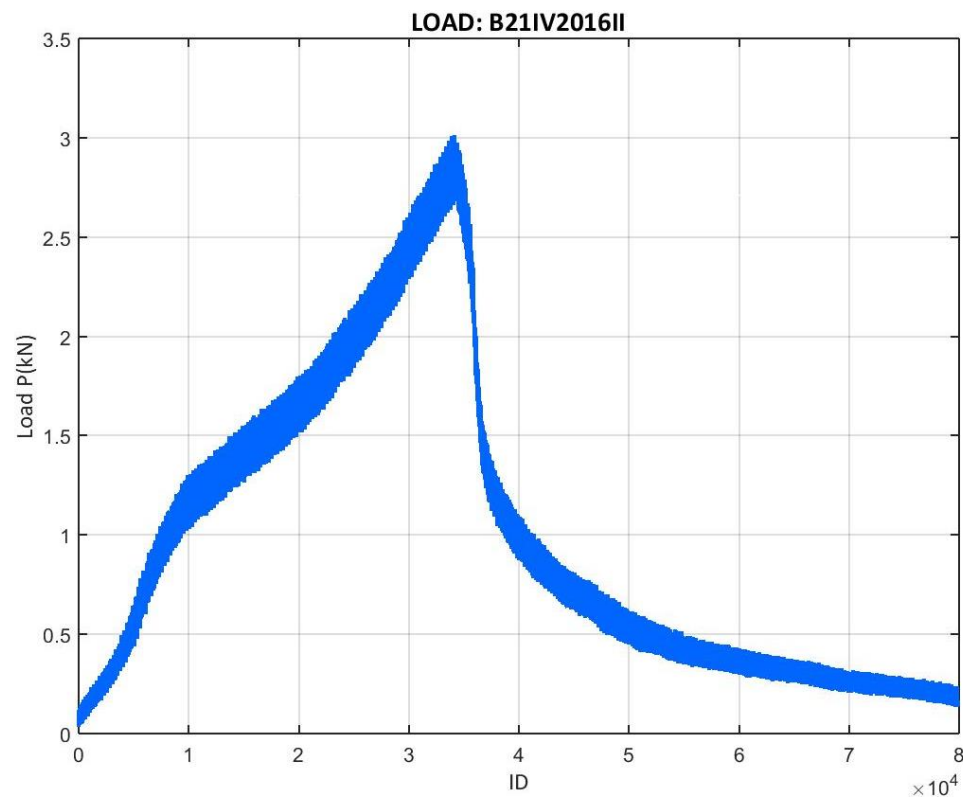


Figure 481: Load values recorded at the B21IV2016II test

- B21IV2016III

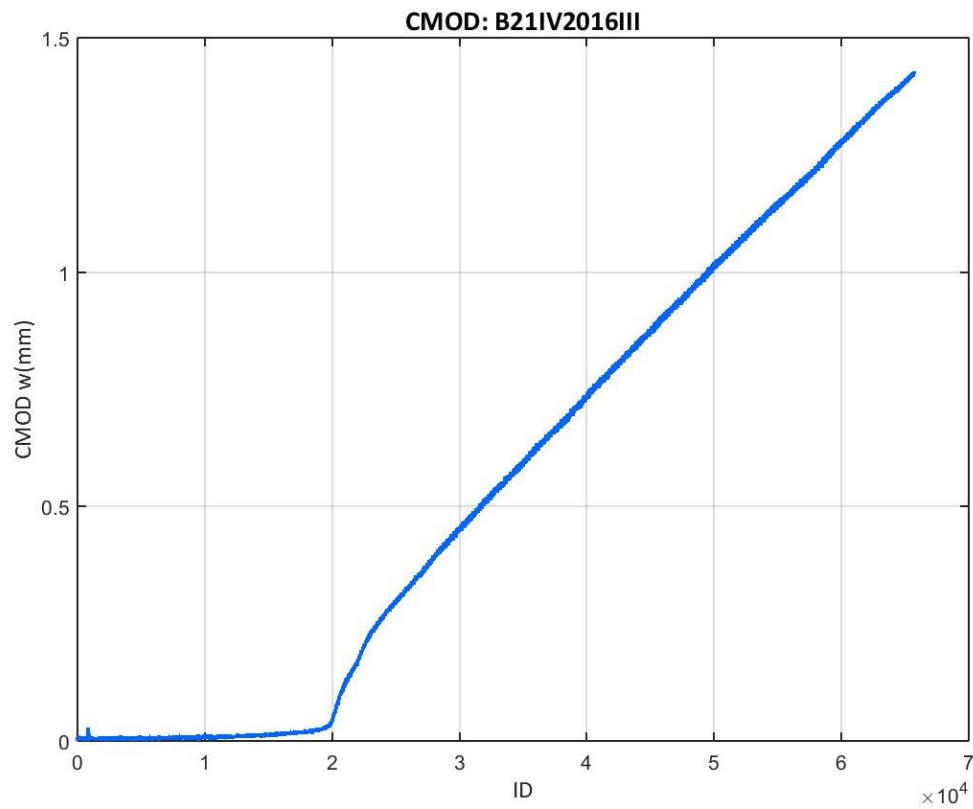


Figure 482: CMOD values recorded at the B21IV2016III test

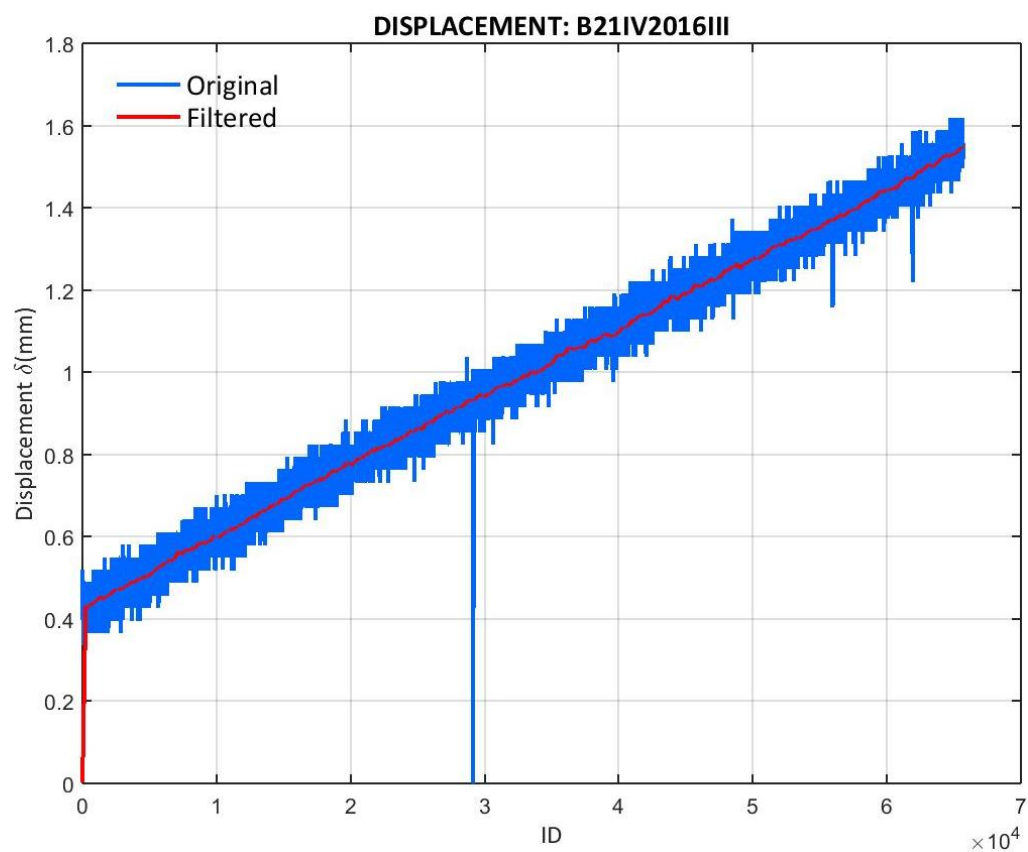


Figure 483: Displacement values recorded at the B21IV2016III test

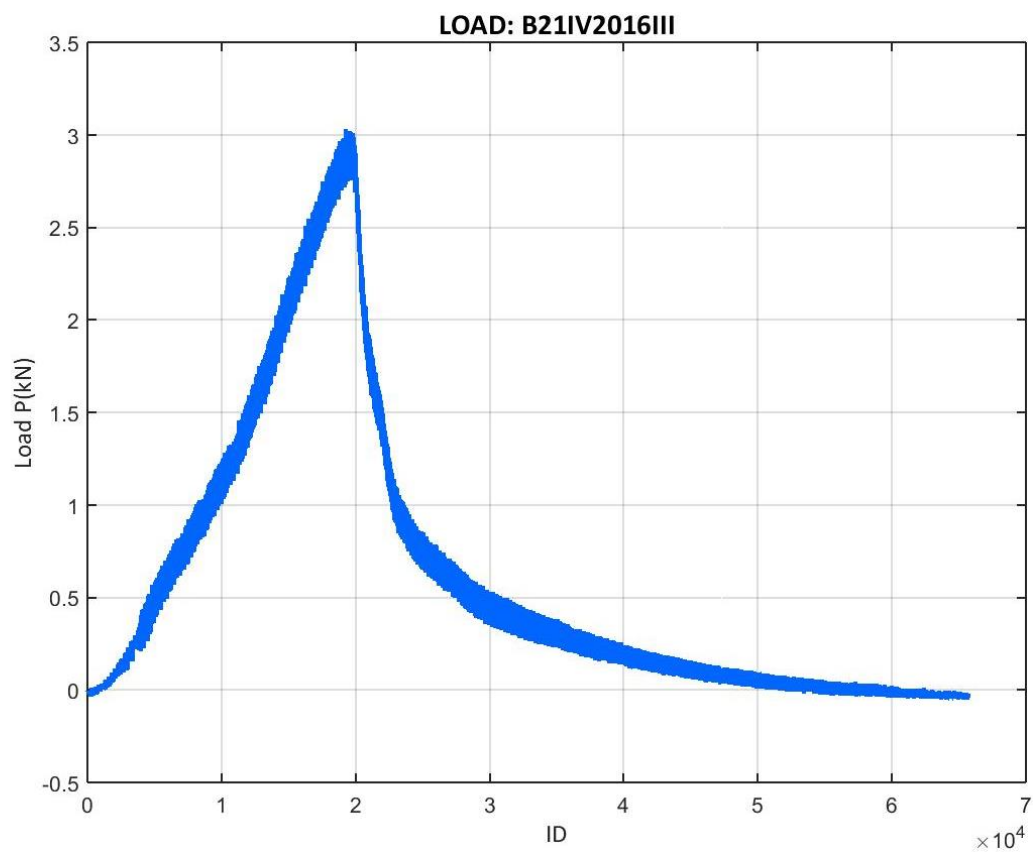


Figure 484: Load values recorded at the B21IV2016III test

- B21IV2016IV

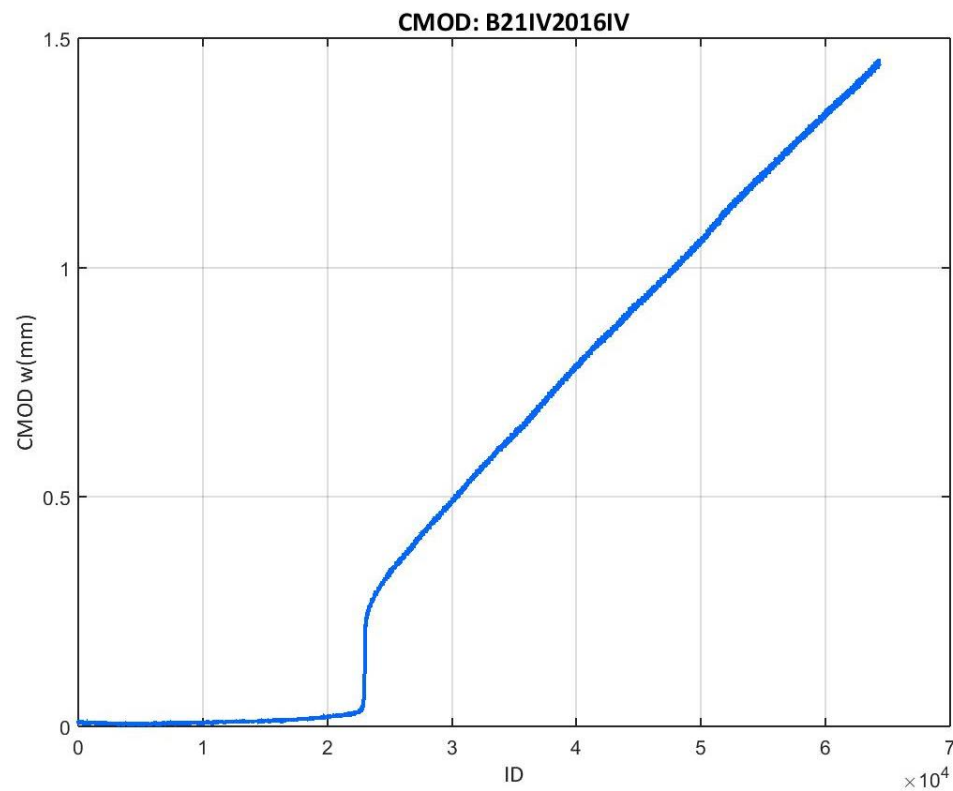


Figure 485: CMOD values recorded at the B21IV2016IV test

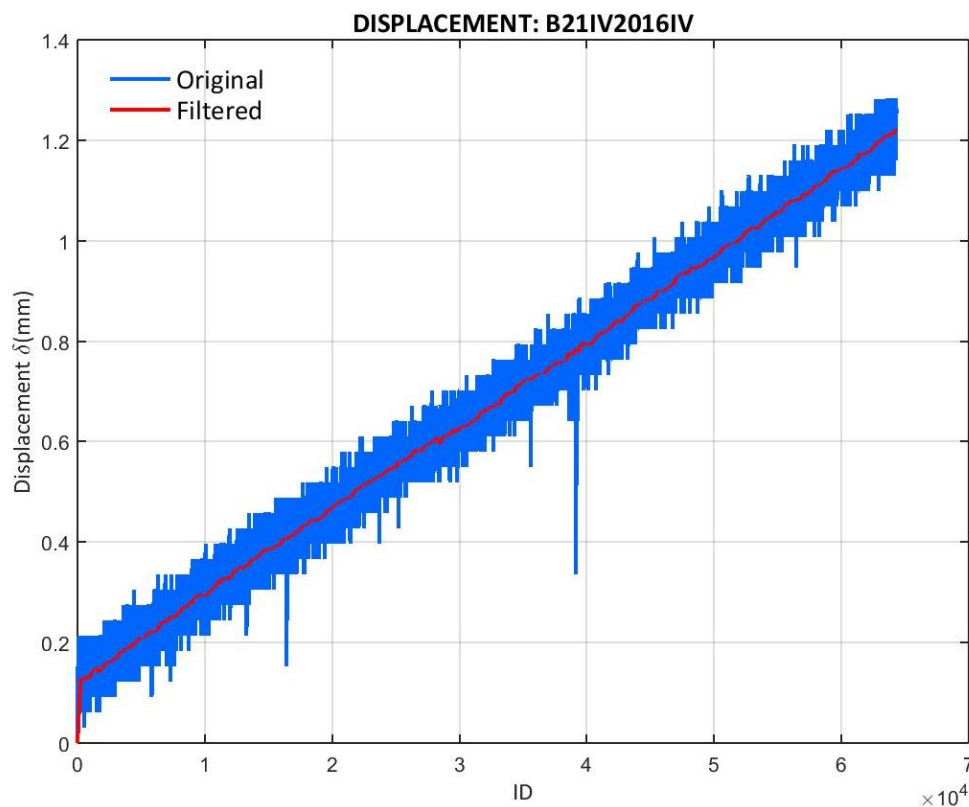


Figure 486: Displacement values recorded at the B21IV2016IV test

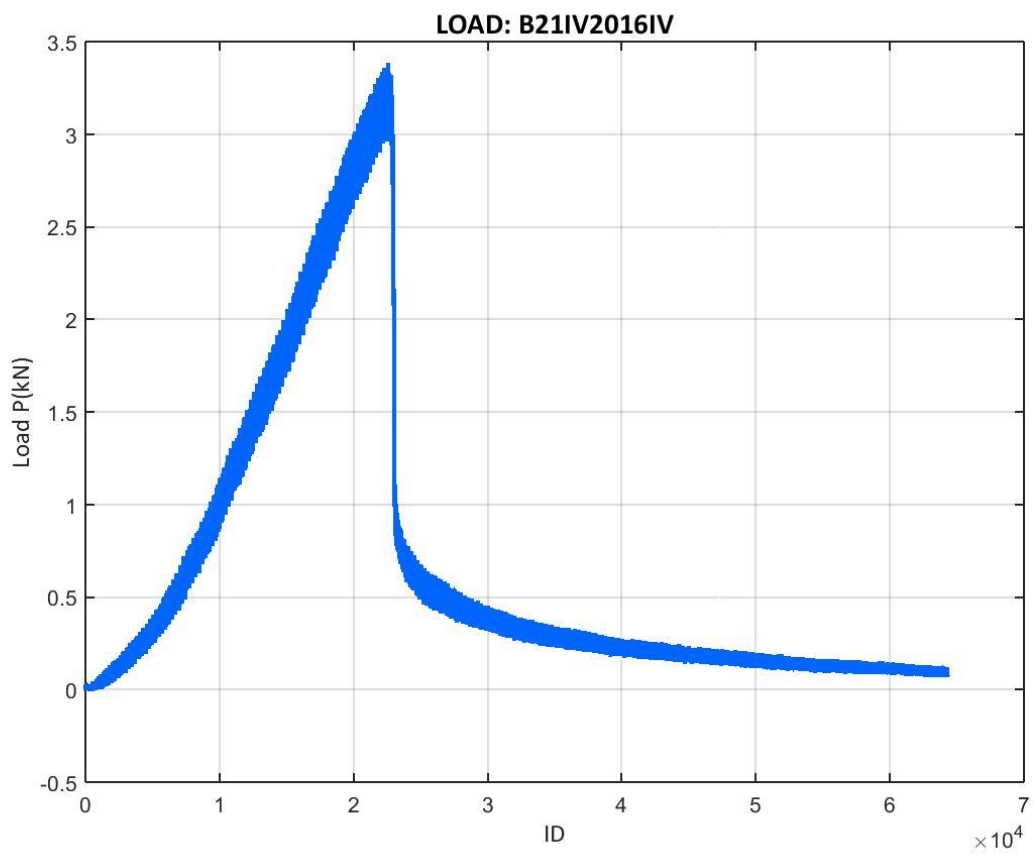


Figure 487: Load values recorded at the B21IV2016IV test

E.11.2 21IV2016 CORRECTED LOAD VS. CMOD

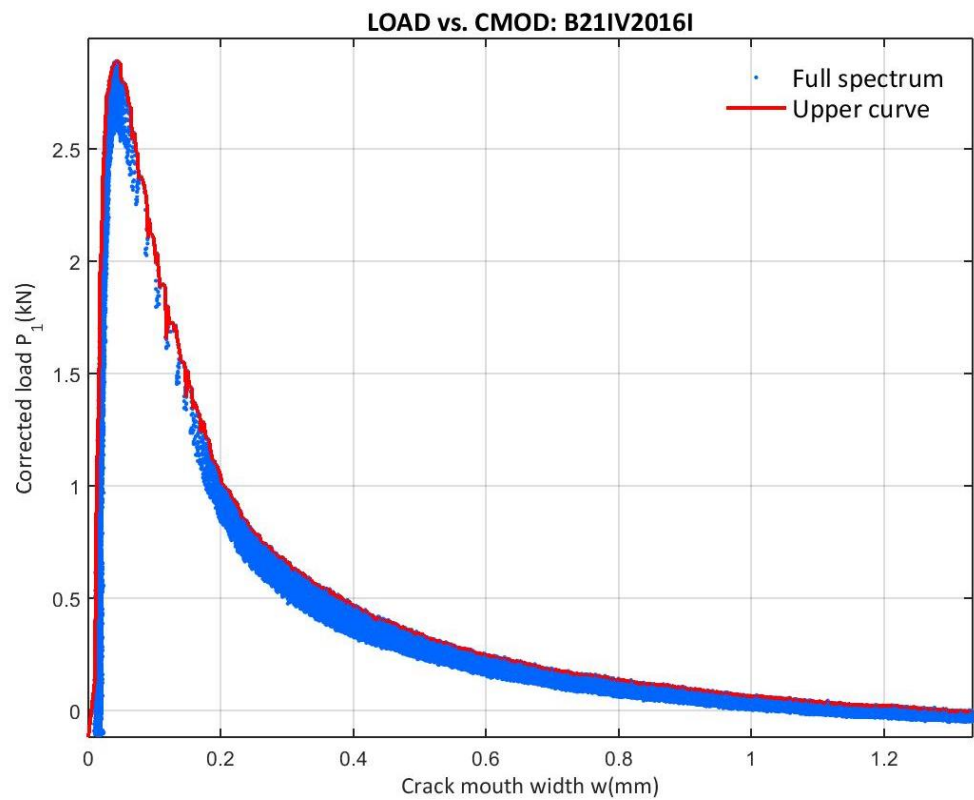


Figure 488: Corrected load vs. CMOD at the B21IV2016I test

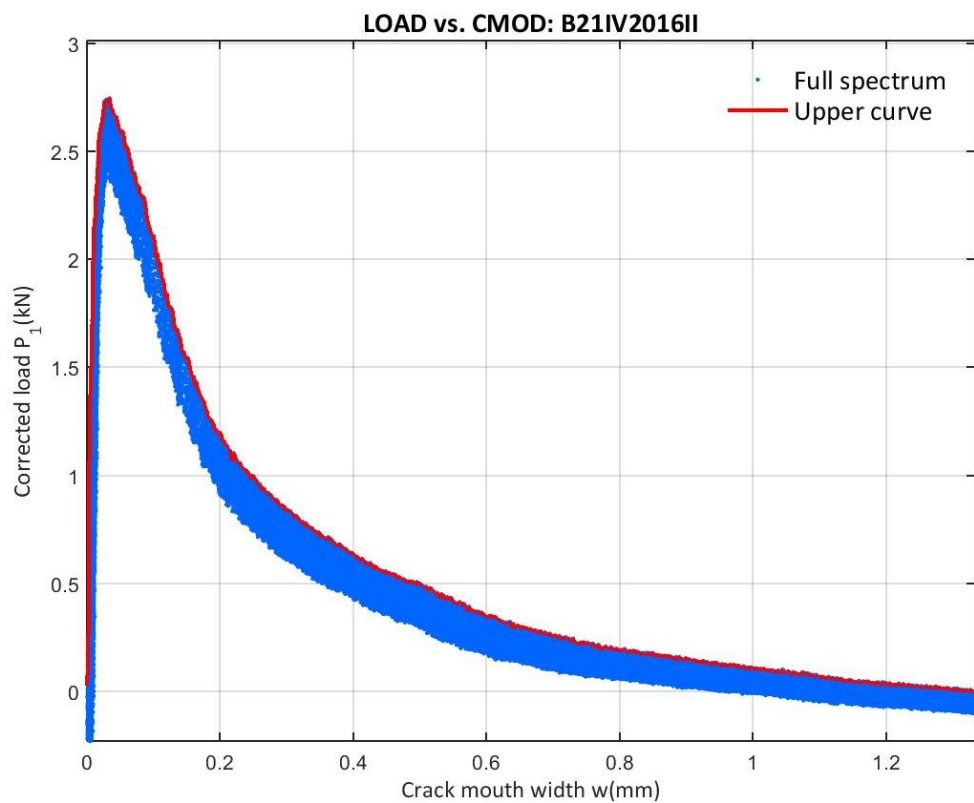


Figure 489: Corrected load vs. CMOD at the B21IV2016II test

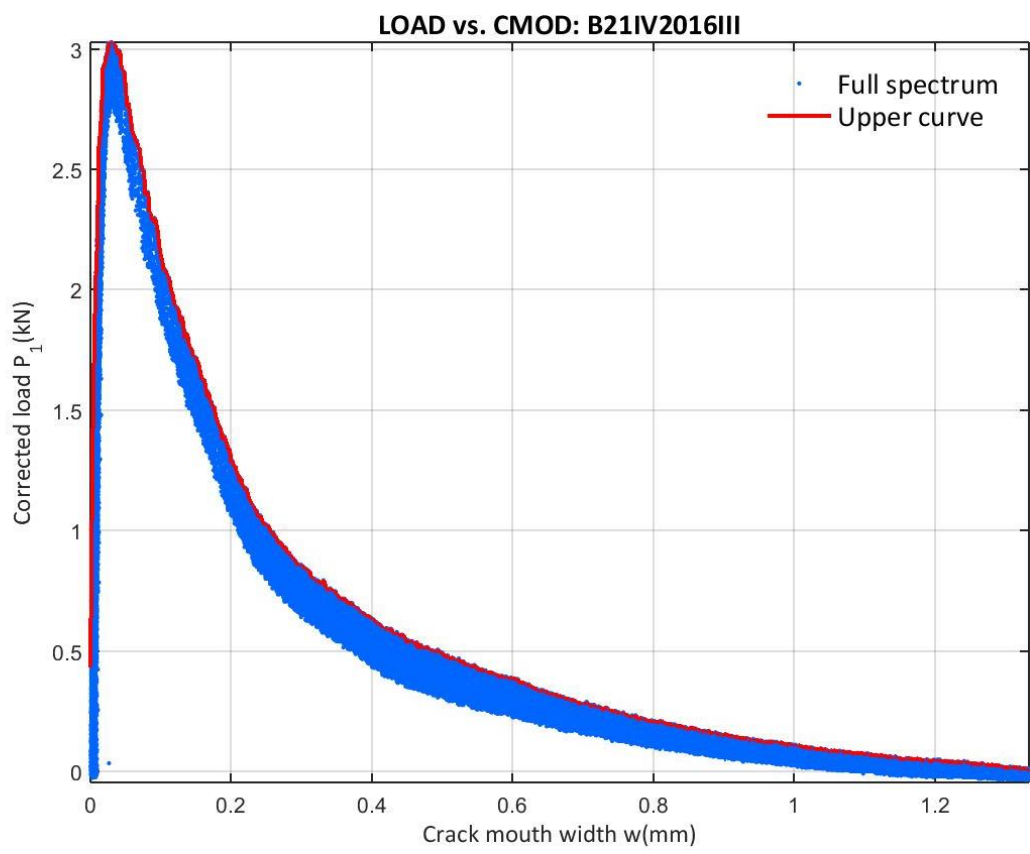


Figure 490: Corrected load vs. CMOD at the B21IV2016III test

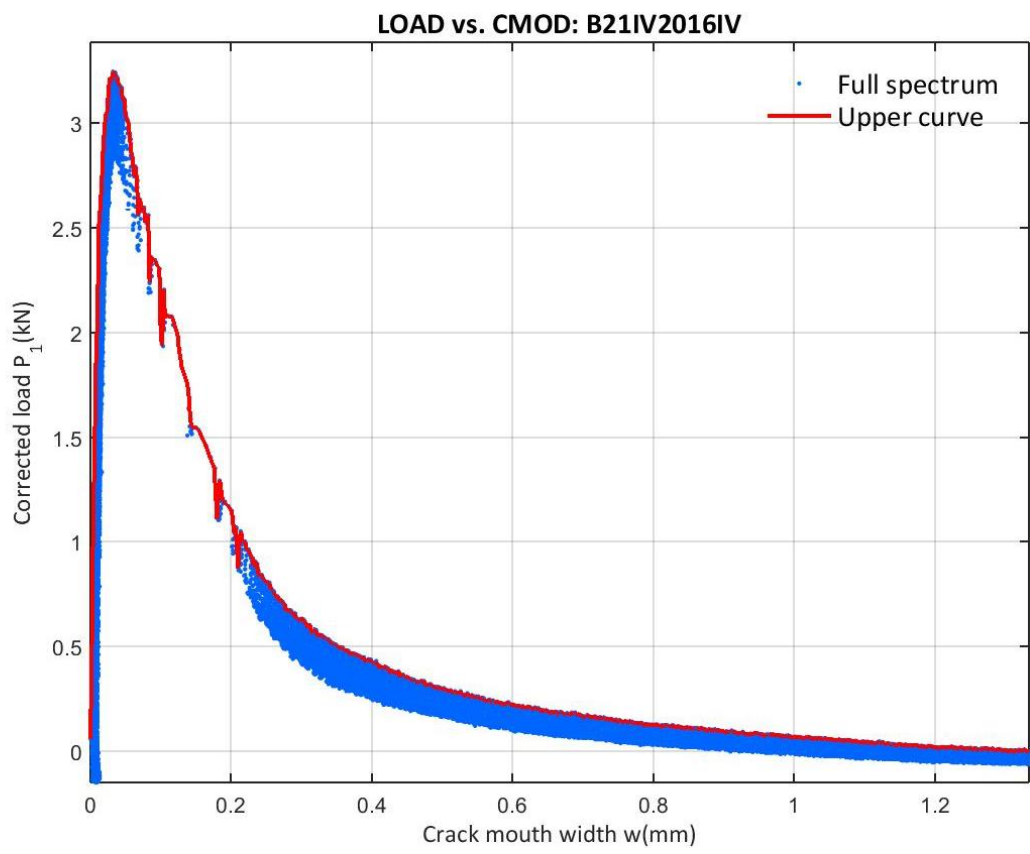


Figure 491: Corrected load vs. CMOD at the B21IV2016IV test

E.11.3 21IV2016 CORRECTED LOAD VS. VERTICAL DISPLACEMENT

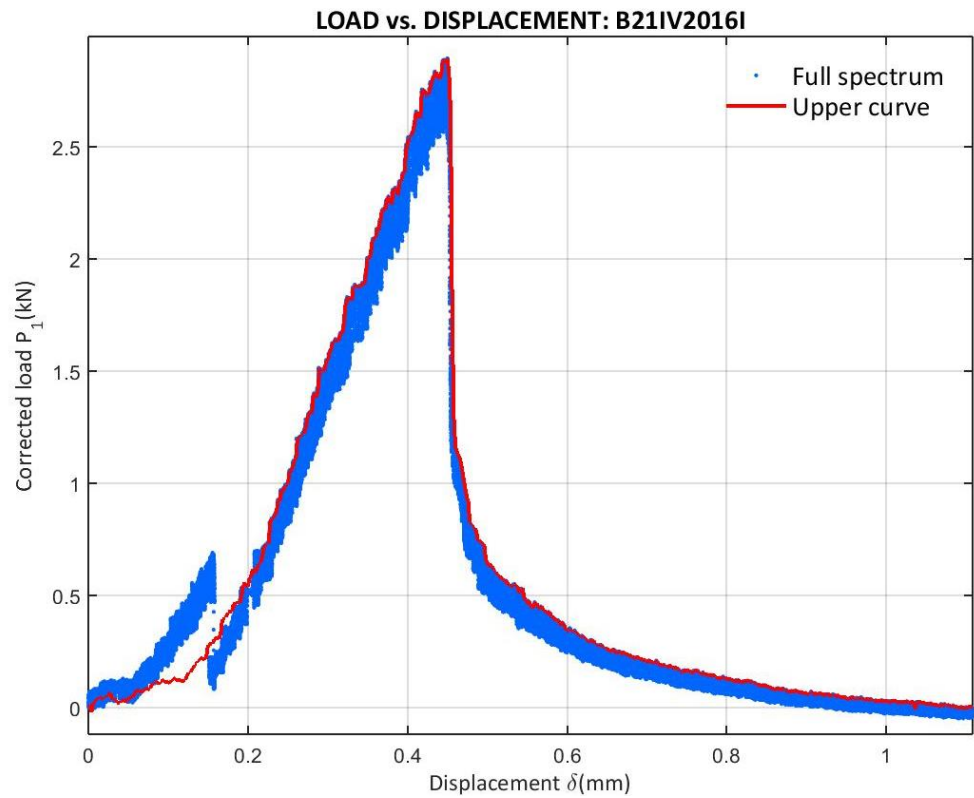


Figure 492: Corrected load vs. Displacement at the B21IV2016I test

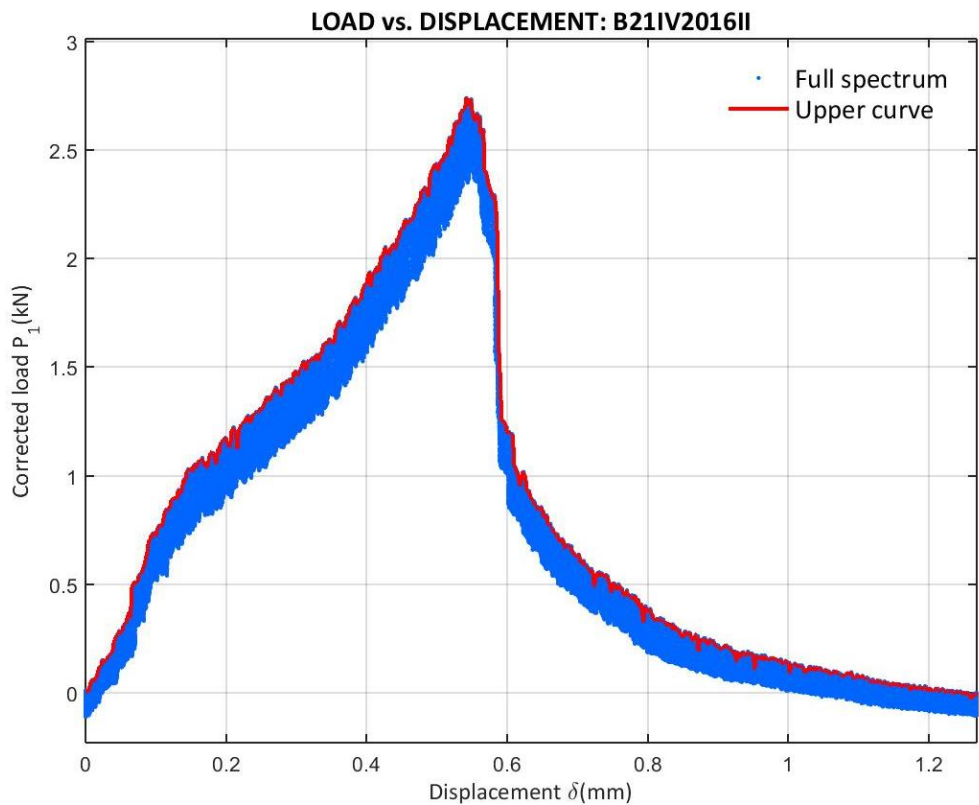


Figure 493: Corrected load vs. Displacement at the B21IV2016II test

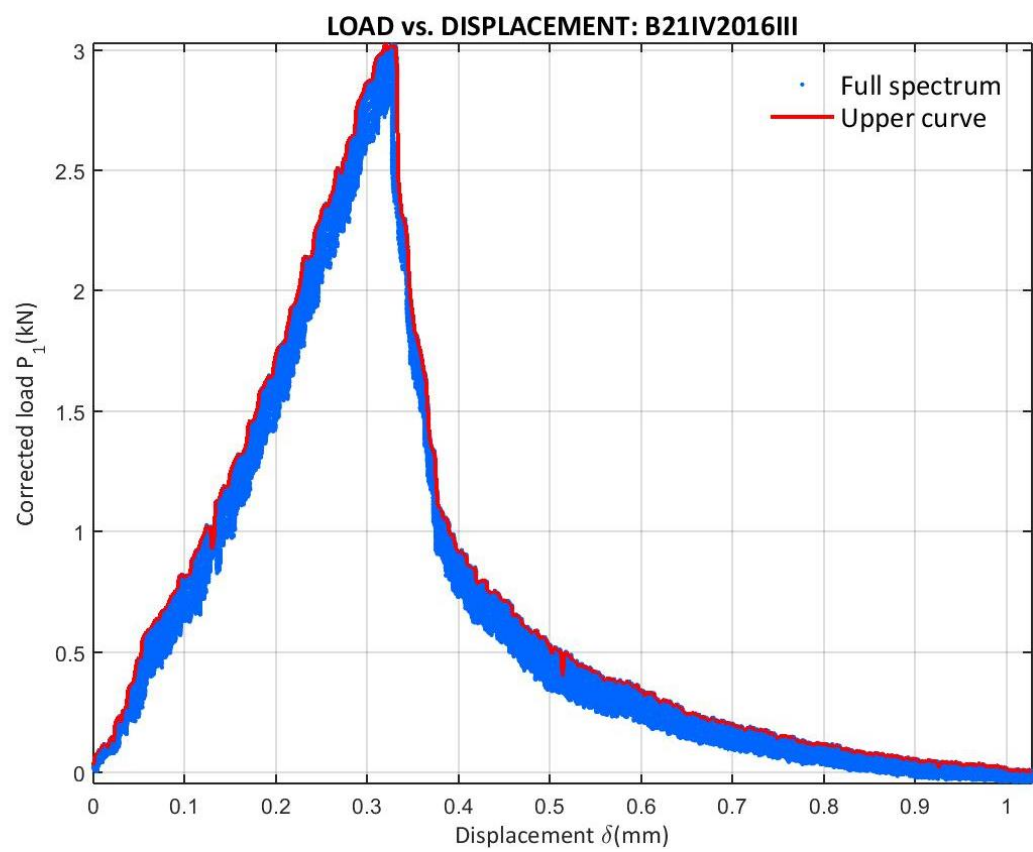


Figure 494: Corrected load vs. Displacement at the B21IV2016III test

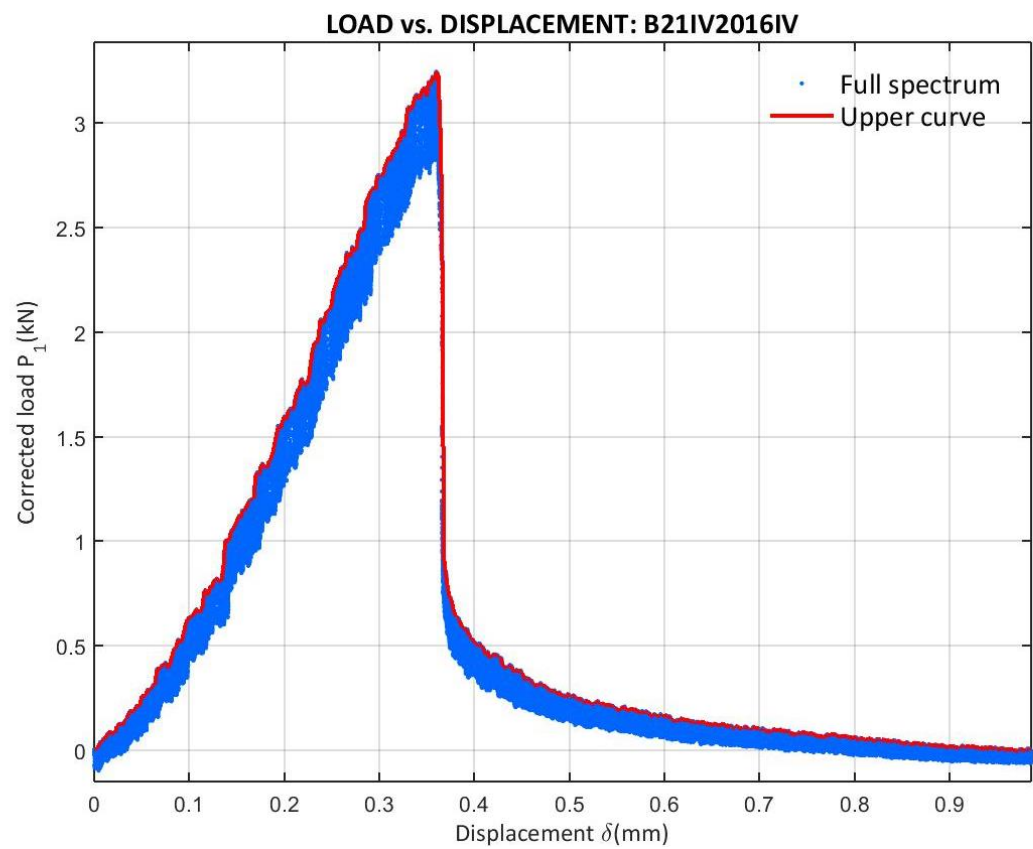


Figure 495. Corrected load vs. Displacement at the B21IV2016IV test

E.11.4 21IV2016 CORRECTED LOAD VS. X

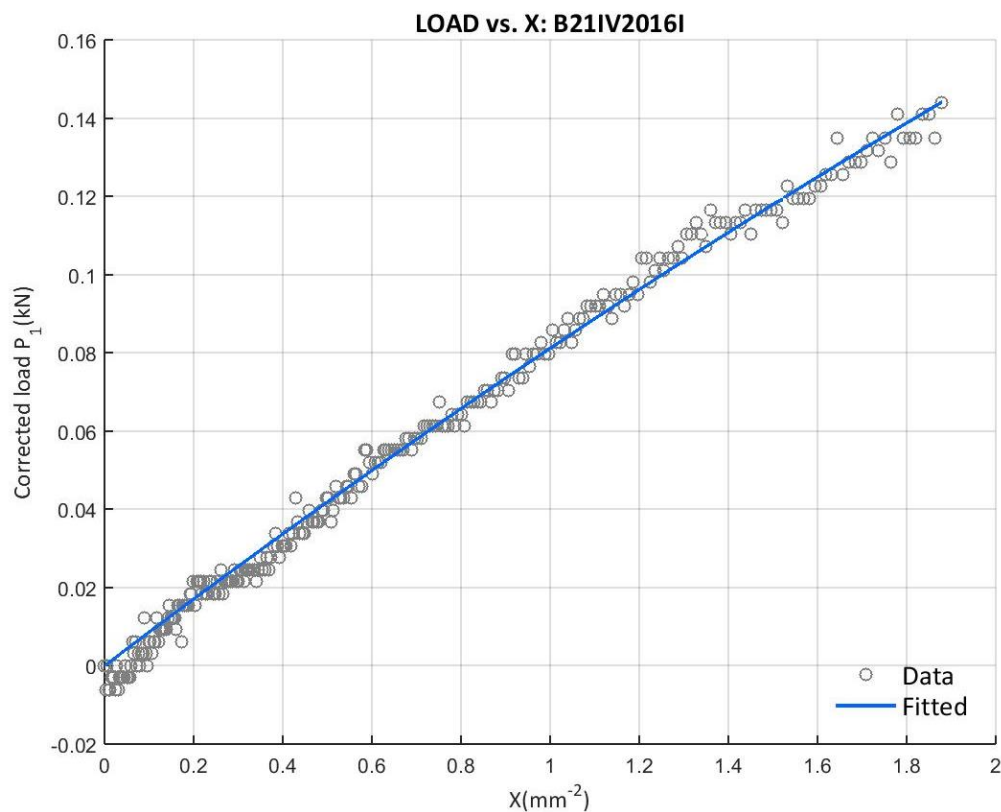


Figure 496: Corrected load vs. X at the B21IV2016I test with the final upper curve data

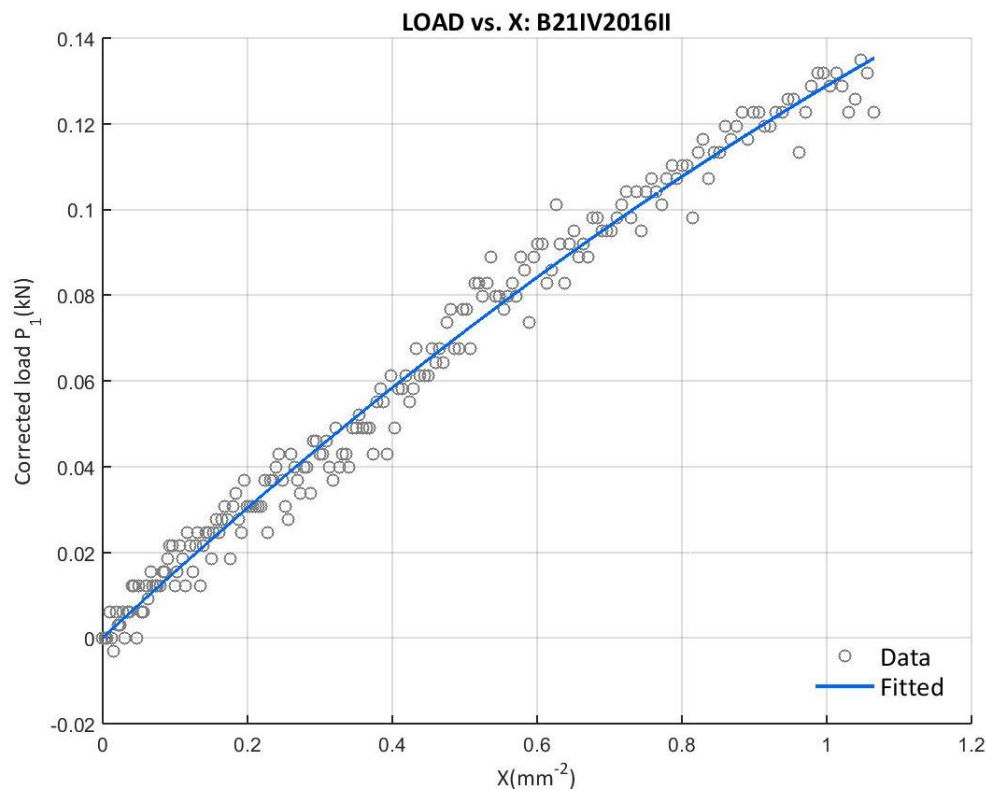


Figure 497: Corrected load vs. X at the B21IV2016II test with the final upper curve data

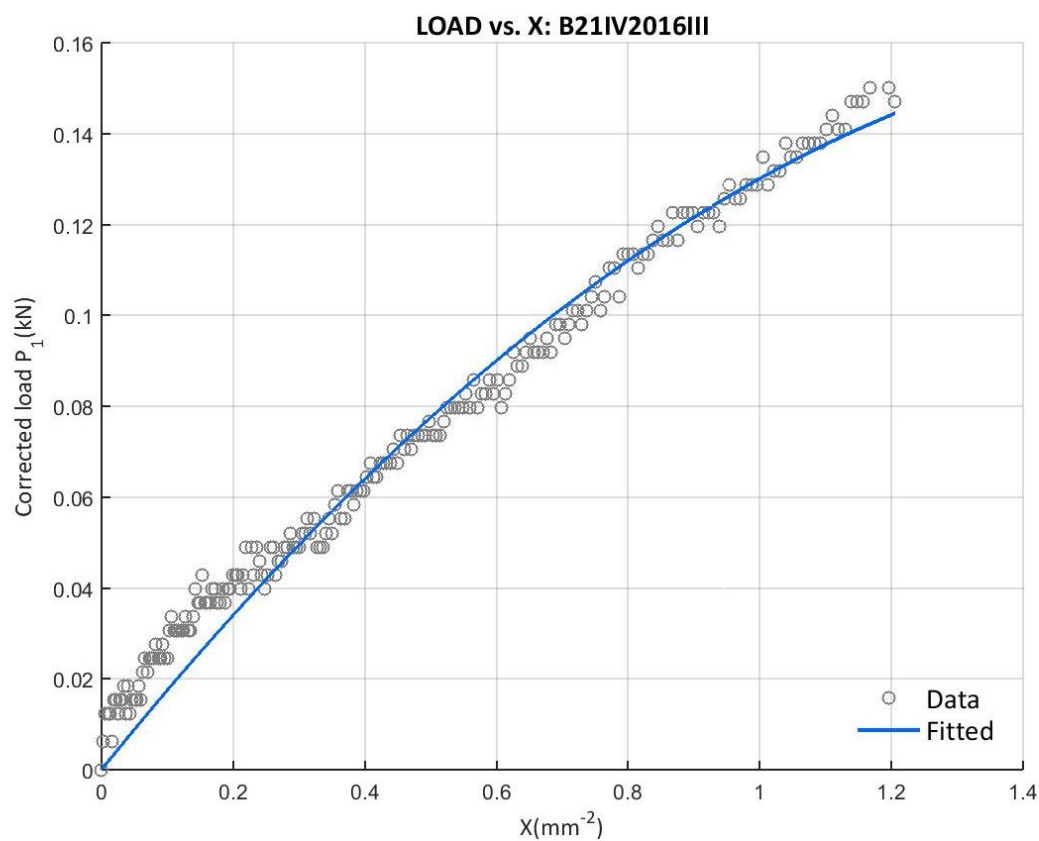


Figure 498: Corrected load vs. X at the B21IV2016III test with the final upper curve data

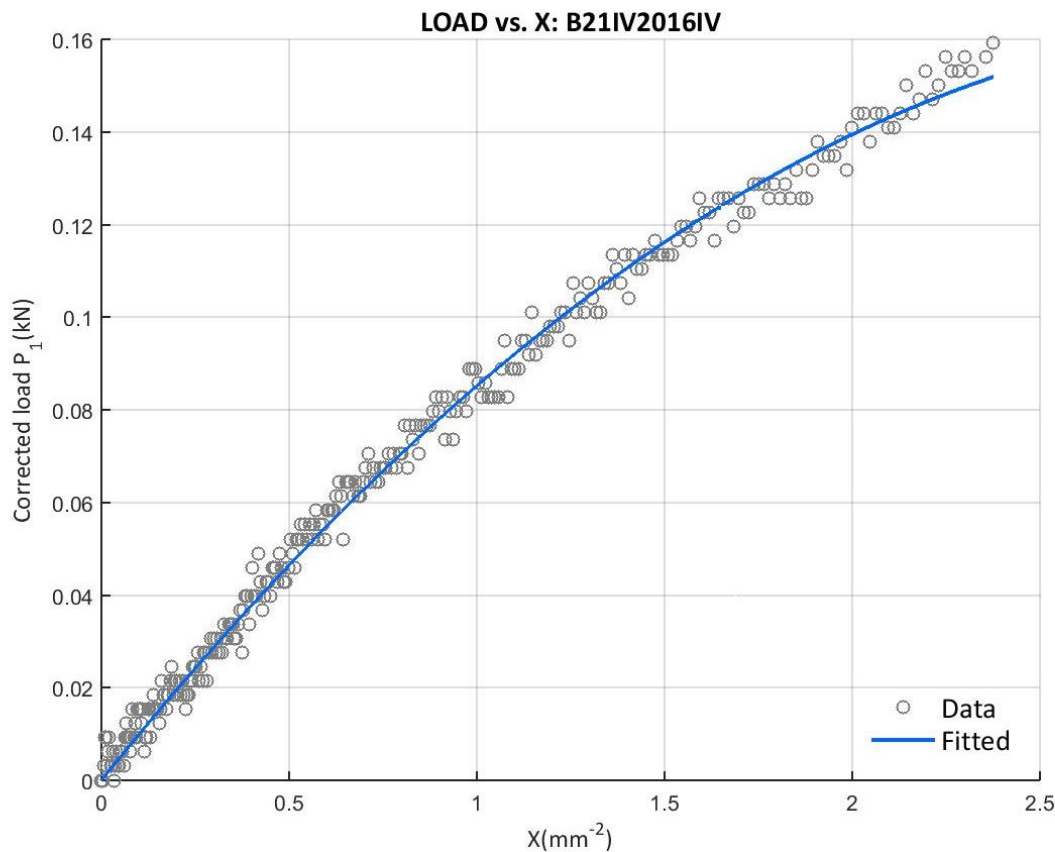


Figure 499: Corrected load vs. X at the B21IV2016IV test with the final upper curve data

E.11.5 21IV2016 SOFTENING CURVE BILINEAR APPROXIMATION

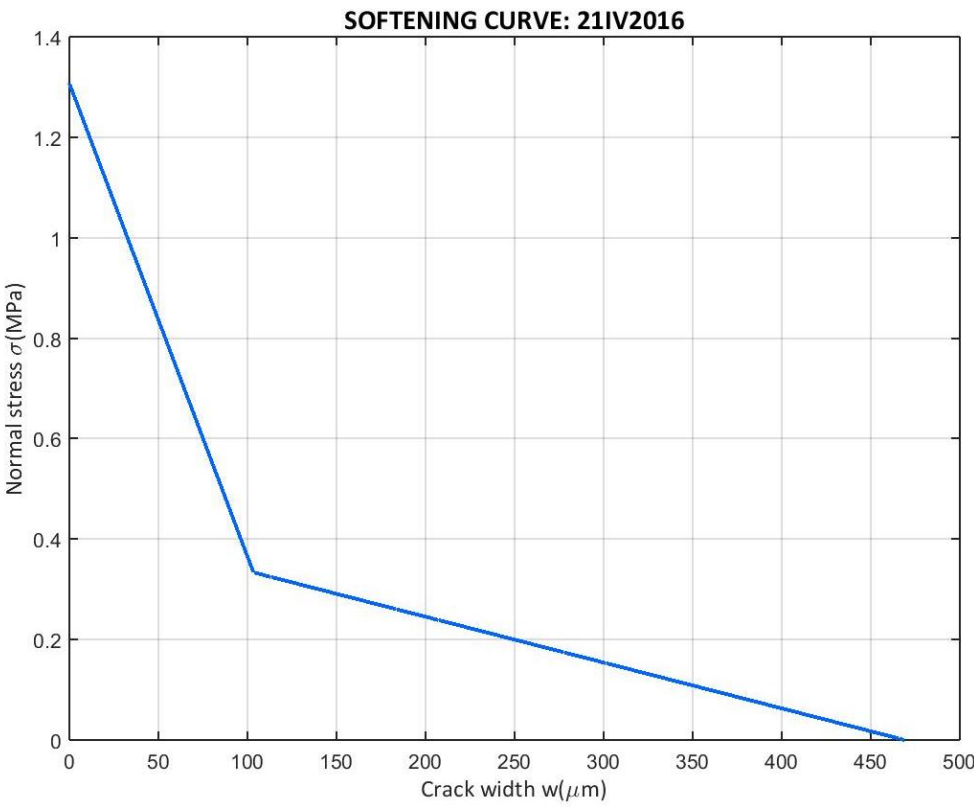


Figure 500: Softening curve bilinear approximation of the 21IV2016 campaign

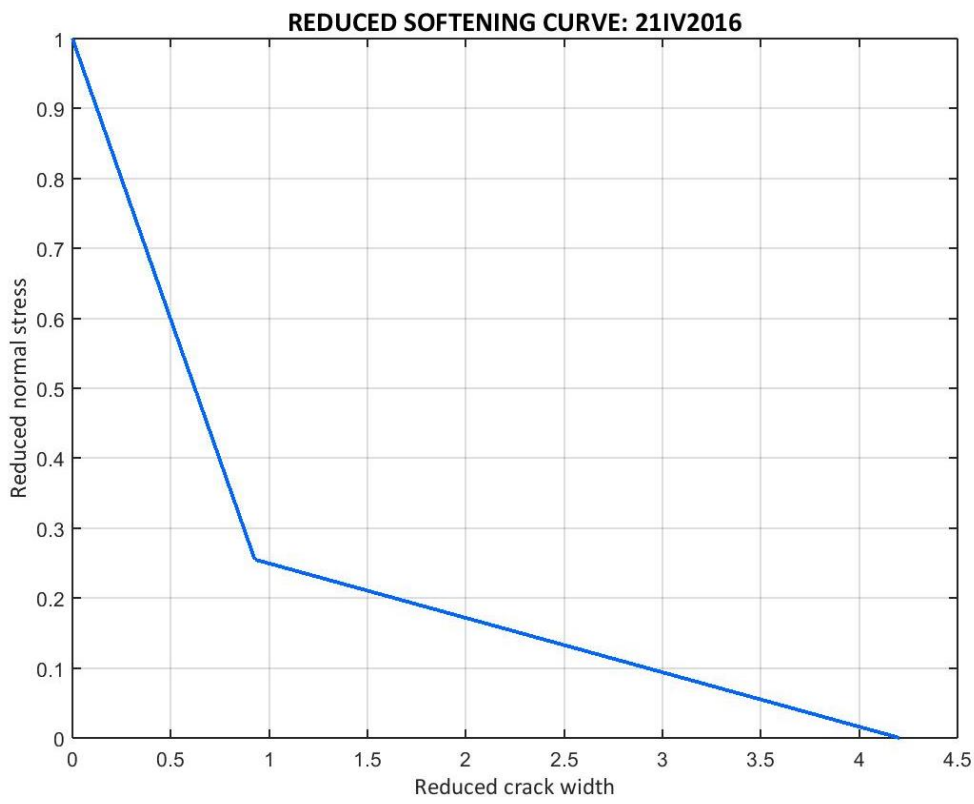


Figure 501: Softening curve bilinear approximation of the 21IV2016 campaign in the reduced form

E.11.6 21IV2016 SPECIMENS' COMPARISON

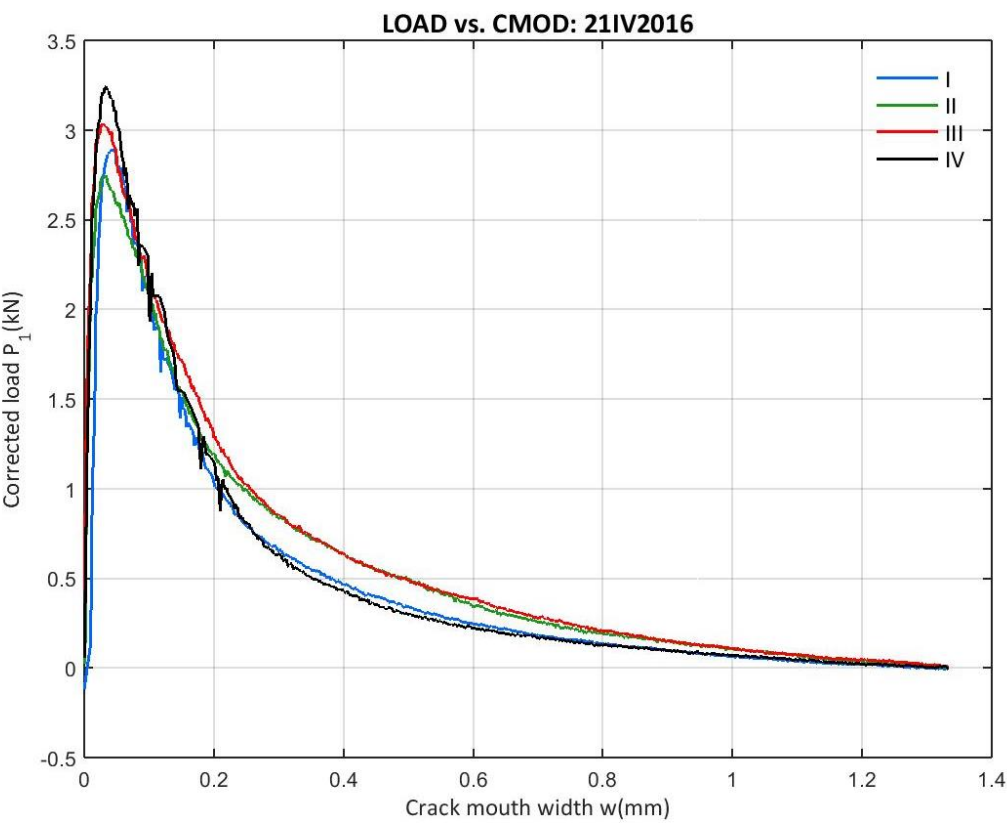


Figure 502: 21IV2016 Corrected load vs. CMOD from the entire campaign

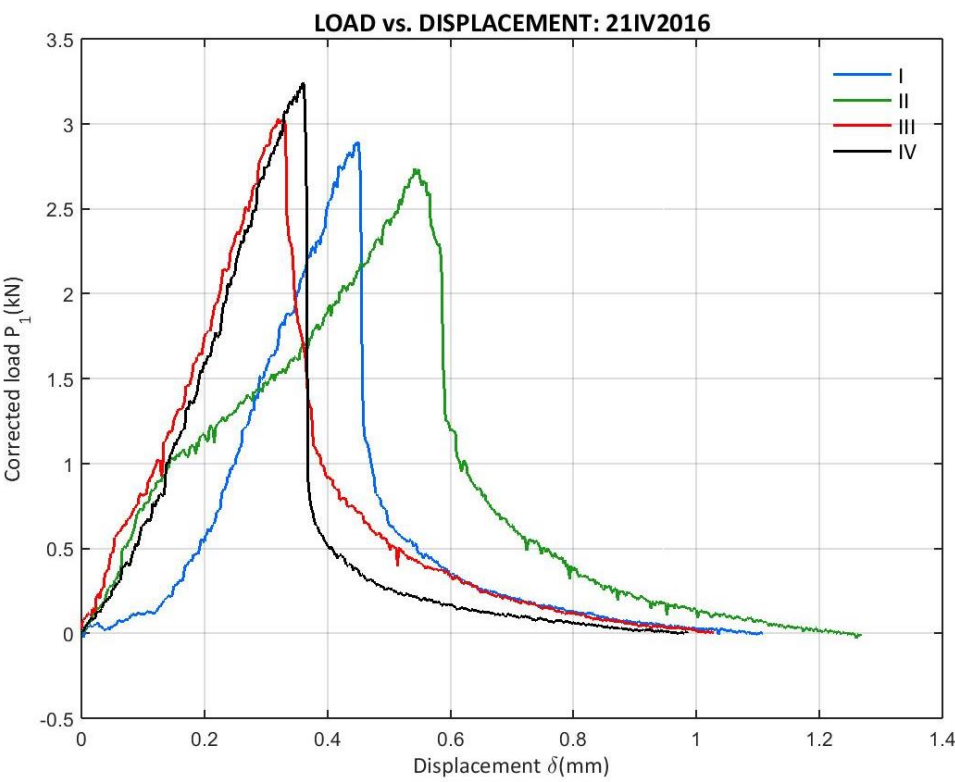


Figure 503: 21IV2016 Corrected load vs. Displacement from the entire campaign

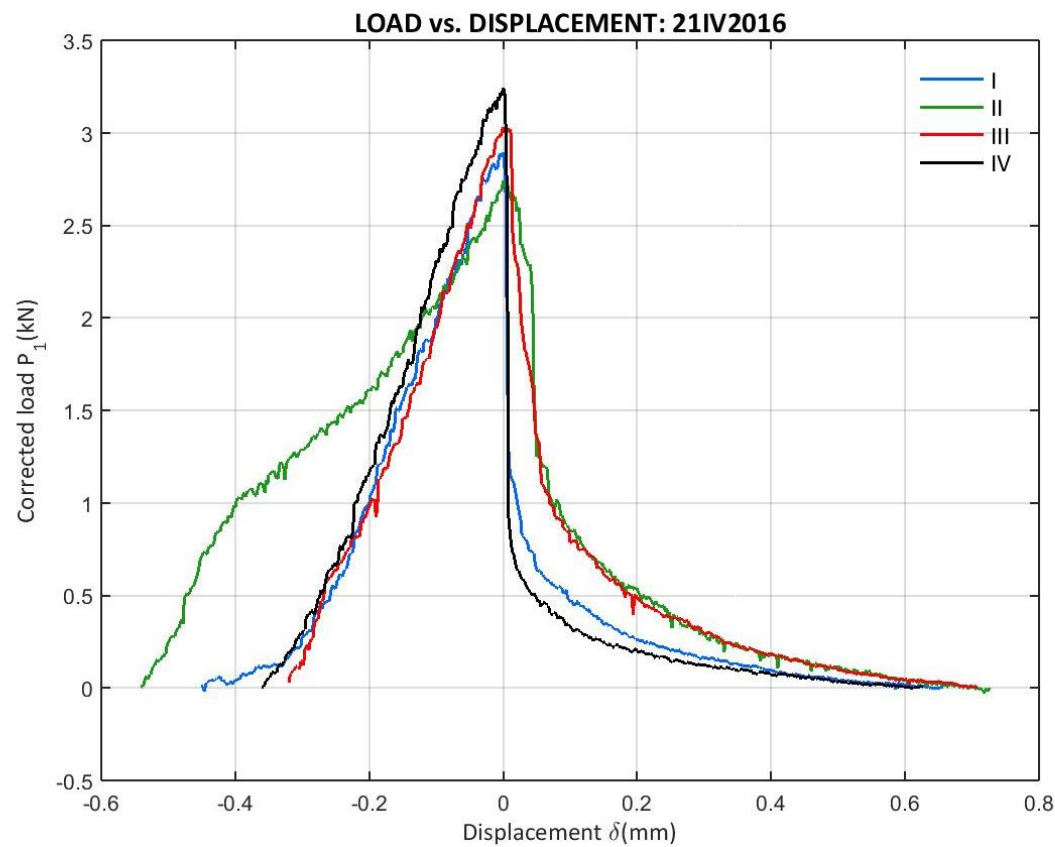


Figure 504: 21IV2016 Corrected load vs. Displacement from the entire campaign (peak displacement zero)

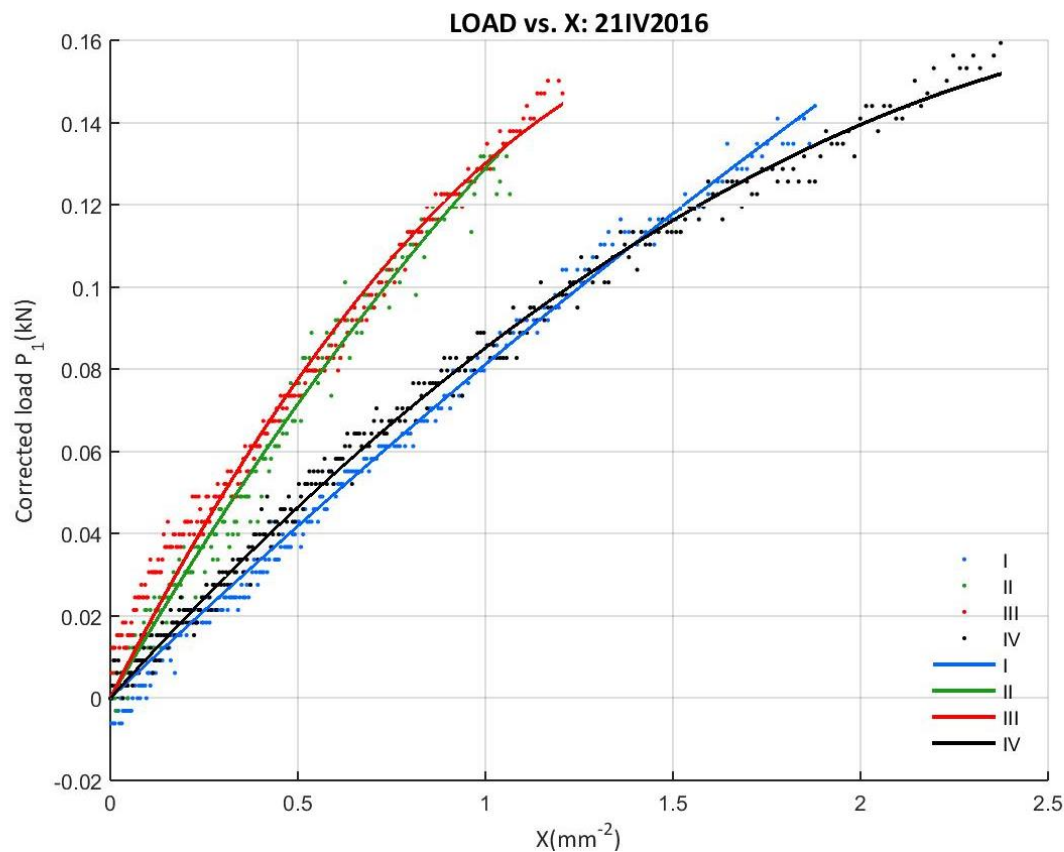


Figure 505: 21IV2016 Corrected load vs. X from the entire campaign

F TESTS' INDIVIDUAL RESULTS

After processing all the data acquired at the tests, visible at Appendix E and, whenever it is possible, in digital text format, this appendix contains the results of every single test closely related to the main purpose of this project. Results extracted from the data using the functions at Appendix C.2 and the basis of the codes at Appendix C.1, employing the expressions at Chapter 3 and Appendix G and other parameters for the codes and further actions detailed at Appendix D.

All beam-type post-processing results are registered at this appendix and the most important results will be sent to Chapter 5. This is done in order not to widen excessively the core of this project, the same way every campaign graph and the single specimen graphs are attached at Appendix E. The only part that is not included from a three point bending test is the elastic moduli determination, because it is at Appendix A.1 and A.2.

The test series 17VI2015 and 13X2015 will not be written, because their post-process results have minor importance.

F.1 23X2015 CAMPAIGN

A total of 4 beam-type specimens were tested at the 23X2015 campaign with the $P - \delta$ tail correction. The data recorded is visible at Appendix E.3.1 and the used $P - \delta$ and $P - w$ curves used for each specimen are given at Appendix E.3.2 and E.3.3 respectively; curves result of applying the appropriate codes from Appendix C.1.1, the dependent functions at Appendix C.2, and the considerations for them at Appendix D.3.

The correction method introduced at Chapter 3.3 is used, generating the new variable X with the Equation 3.3.15, coupled with the correct load data that Equation 3.3.14 restricts. The result of this new register and the second order fitting imposing an independent term zero is given in a graph form for each specimen at Appendix E.3.4. The comparison between all specimens is also given with graphs at Appendix E.3.6.

The numerical results for the parameters acquired at each test are written at Table 80. The table contains both data for G_F determination with the procedure at Chapter 3.3 and part of the data for

the bilinear approximation for the softening curve from Chapter 3.3.1, which is given in Appendix E.3.5 along with its reduced form (see Chapter 2.2).

Table 80: Campaign 23X2015 individual results

SPECIMEN	$G_f(\text{Jm}^{-2})$	$P_{1u}(\text{N})$	$P_R(\text{N})$	$W_f(\text{mJ})$	$W_{tail}(\text{mJ})$	$w_G(\mu\text{m})$	$A(\text{Nmm}^2)$	$P_{ef}(\text{N})$	$l_1(\text{mm})$
B23X2015I	89.569	1536.1	223.4	360.3	257.7	203.7	136.9	1613.2	606.8
B23X2015II	82.770	1689.1	229.5	425.0	154.4	140.5	87.2	1738.3	825.3
B23X2015III	89.892	1765.6	128.5	373.8	246.5	191.9	129.4	1838.1	1549.0
B23X2015IV	65.188	1744.2	113.2	280.4	175.9	174.9	85.5	1792.4	1024.7
23X2015	81.855	1683.7	173.7	359.9	208.6	177.8	109.7	1745.5	1001.4
	(11.587)	(103.6)	(61.3)	(59.9)	(51.2)	(27.5)	(27.2)	(97.2)	(403.0)

The last rows at Table 80 show the mean values and the standard deviation, in brackets, of every parameter for the entire campaign. The total displacements are (or the last values, because a zero was done at the beginning for these values):

- B23X2015I: 1.062mm of vertical displacement and 1.332mm of *CMOD*
- B23X2015II: total displacement of 1.13mm and total *CMOD* of 1.332mm
- B23X2015III: 1.05mm of displacement and 1.336mm of *CMOD*
- B23X2015IV: 0.972mm of displacement and 1.332mm of *CMOD*

The final values for this campaign are for the bilinear curve approximation:

- The kink point is located at $(w_k, \sigma_k) = (77.5\mu\text{m}, 0.1425\text{MPa})$
- The initial intercept w_1 is about 94.8 μm
- The characteristic crack opening w_{ch} is 104.8 μm
- The critical crack opening w_c is 723.5 μm

F.2 14XII2015 CAMPAIGN

This campaign was tested in order to apply the $P - \delta$ correction method with no self-weight action. The same procedure and process for campaign 23X2015 was made (see Appendix F.1), but now the parameters and considerations done at the post-process are at Appendix D.4 and all the graphic series are at Appendix E.4: E.4.1 for the data, E.4.2 for $P - \delta$ curves, E.4.3 for $P - w$ curves, E.4.4 for $P - X$ curves for the tail correction, E.4.5 for the softening curve approximation and E.4.6 for the campaign comparison graph series. Table 81 contains all numerical results. The total displacements and crack mouth displacements are:

- B14XII2015I: load total displacement of 1.166mm and 1.318mm of *CMOD*
- B14XII2015II: total vertical displacement of 1.154mm and 1.334mm of *CMOD*
- B14XII2015III: 1.136mm of vertical displacement and a 1.338mm *CMOD*
- B14XII2015IV: 1.476mm of displacement and a total *CMOD* of 1.334mm
- B14XII2015V: vertical displacement of 1.09mm and *CMOD* of 1.332mm
- B14XII2015VI: total displacement of 1.058mm and a 1.34mm *CMOD*
- B14XII2015VII: 1.078mm of displacement and 1.346mm of *CMOD*
- B14XII2015VIII: 1.02mm of displacement and 1.334mm of *CMOD*

Table 81: Campaign 14XII2015 individual results

SPECIMEN	$G_f(\text{Jm}^{-2})$	$P_{1u}(\text{N})$	$P_R(\text{N})$	$W_f(\text{mJ})$	$W_{tail}(\text{mJ})$	$w_G(\mu\text{m})$	$A(\text{Nmm}^2)$	$P_{ef}(\text{N})$	$l_1(\text{mm})$
B14XII2015I	207.854	4672.6	107.1	1268.3	186.6	69.8	108.8	4735	353.8
B14XII2015II	89.636	3344.5	15.3	561.3	75.1	64.5	43.3	3369	74.4
B14XII2015III	149.637	4571.6	15.3	948.0	99.5	50.3	56.5	4603	305.4
B14XII2015IV	170.373	4932.7	12.2	1157.1	35.5	20.5	26.2	4947	450.1
B14XII2015V	128.812	4614.4	61.2	759.4	142.3	80.3	77.6	4658	324.6
B14XII2015VI	119.077	4727.6	-24.5	779.7	53.9	31.9	28.5	4744	357.1
B14XII2015VII	160.902	4537.9	30.6	1073.9	52.4	23.4	28.3	4554	289.2
B14XII2015VIII	142.542	4880.6	64.3	873.0	139.1	66.4	70.9	4921	376.4
14XII2015	146.104 (35.586)	4535.2 (501.2)	35.2 (40.7)	927.6 (232.4)	98.0 (53.4)	50.9 (22.9)	55.0 (29.4)	4566 (504)	316.4 (109.6)

And the remaining data for the bilinear approximation for the softening curve using the procedure at Chapter 3.3.1 are:

- Kink point at 44.6 μm and 1.06MPa
- Initial intercept w_i at 78.5 μm
- Characteristic crack width w_{ch} of 59.6 μm
- Critical crack width w_c of 172.6 μm

F.3 29I2016 CAMPAIGN

The 29I2016 campaign was planned in order to give qualitative and quantitative information about the correctness of the $P - \delta$ tail correction method using an alternative theory, the local fracture energy theory. A-series was tested with the usual three-point bending test configuration for the $P - \delta$ tail correction method with no self-weight action. B-series was tested also with a three-point bending test, but with different configuration and the action of the specimen weight. The results for A-series are given at Table 82 and for B-series at Table 83. The only use of the B-series is checking the current methodology, which means that, at the end, the data used for the comparison will be from the A-series, not the B-series.

The data acquired can be seen at Appendix E.5.1. When the specimen broke, on the *CMOD* data an extremely sharp increase of the value can be seen. The $P - \delta$, $P - w$ and $P - X$ curves of use are given at Appendix E.5.3, E.5.2 and E.5.4 respectively. The correction applied at the $P - \delta$ curves of the loading part of the B29I2016I specimen and the initial point considered at B-series can be seen (see Appendix D.5 for further information about the corrections). Only A-series is at Appendix E.5.4, because the local fracture theory does not need the artificial variable X . The softening curve with the data from the A-series and the properties given at Chapter 4.1.3 are reproduced at Appendix E.5.5. Finally, the comparative graphs for the entire campaign are visible at Appendix E.5.6.

Table 82: Campaign 29I2016 individual results

SPECIMEN	$G_f(\text{Jm}^{-2})$	$P_{1u}(\text{N})$	$P_R(\text{N})$	$W_f(\text{mJ})$	$W_{tail}(\text{mJ})$	$w_G(\mu\text{m})$	$A(\text{Nmm}^2)$	$P_{ef}(\text{N})$	$l_1(\text{mm})$
B29I2016I	168.535	3157.9	113.2	1001.6	170.7	82.8	104.6	3216.8	984.7
B29I2016II	113.109	2891.7	107.1	615.0	175.3	115.7	98.2	2947.0	536.3
B29I2016III	151.690	3105.9	168.3	761.2	286.4	139.5	158.7	3195.3	950.9
B29I2016IV	150.314	2760.1	104.0	850.4	195.6	107.4	121.1	2828.3	433.2
29I2016A	145.912 (23.385)	2978.9 (185.9)	123.2 (30.3)	807.0 (162.0)	207.0 (54.0)	111.3 (23.4)	120.6 (27.1)	3046.9 (190.3)	726.3 (282.4)

Table 83: Campaign 29I2016 individual results for the local fracture energy theory

SPECIMEN	$G_f(\text{J/m}^2)$	$P_{1u}(\text{N})$	$P_R(\text{N})$	$W_f(\text{mJ})$	$m(\text{kg})$	$\delta_u(\text{mm})$	α	29I2016B
B29I2016V	108.330	2475.5	0	758.2	13.451	1.590	0.1064	$G_f(\text{J/m}^2)$
B29I2016VI	113.195	2561.2	-21.4	795.7	13.724	1.604	0.1063	
29I2016B-S1	110.762 (3.440)	2518.4 (60.6)	-10.7 (15.1)	776.9 (26.5)	13.588 (0.193)	1.597 (0.010)	0.1064 (0.0001)	154.359
B29I2016VII	73.035	997.5	-183.6	254.2	13.587	1.176	0.4201	$a_1(\text{mm})$
B29I2016VIII	100.943	954.7	18.4	360.7	13.487	1.674	0.4233	50.48
29I2016B-S2	86.989 (19.734)	976.1 (30.3)	-82.6 (142.8)	307.4 (75.3)	13.537 (0.071)	1.425 (0.352)	0.4217 (0.0023)	CASE A

The total valid displacements for all the specimens are:

- 1.21mm of vertical displacement for the B29I2016I and 1.332mm of *CMOD*
- For B29I2016II: 1.12mm of vertical displacement and 1.332mm of *CMOD*
- B29I2016III had a valid vertical movement of 1.076mm and a valid opening of 1.332mm
- B29I2016IV had a total vertical displacement of 1.226mm and an opening of 1.332mm
- The specimens for B-series had the total displacement shown at Table 83. The crack mouth opening has no interest for the local fracture energy correction, although it has been registered.

The data for the bilinear approximation of the softening curve for this campaign is:

- The kink point is located at 97.5 μ m and 0.34MPa
- The initial intercept is at 128.1 μ m
- The characteristic crack width is about 102.6 μ m
- The critical crack width is 450.7 μ m

F.4 10III2016 CAMPAIGN

The graphs of the acquired data are given at Appendix E.6.1; the ones of the used $P - w$ curves at Appendix E.6.2; the ones of the used $P - \delta$ curves at Appendix E.6.3; the fitting of $P - X$ at Appendix E.6.4; the bilinear approximation for the softening curve at Appendix E.6.5 and the comparisons at Appendix E.6.6.

The three point bending tests with the procedure considered at Chapter 3 and Chapter 4.1.4, with the codes derived from Appendix C and the parameters and considerations marked at Appendix D.6 gave the results visible at Table 84.

Table 84: Campaign 10III2016 individual results

SPECIMEN	$G_F(\text{Jm}^{-2})$	$P_{1u}(\text{N})$	$P_R(\text{N})$	$W_f(\text{mJ})$	$W_{tail}(\text{mJ})$	$w_G(\mu\text{m})$	$A(\text{Nmm}^2)$	$P_{ef}(\text{N})$	$l_1(\text{mm})$
B10III2016I	123.810	1707.5	192.8	565.3	277.0	187.3	187.3	1805.2	218.5
B10III2016II	93.989	1921.7	137.7	510.3	143.8	145.5	141.4	1977.8	275.8
B10III2016III	84.594	1973.7	110.2	383.3	202.0	163.3	163.3	2031.9	334.8
B10III2016IV	71.258	1897.2	94.9	363.9	130.7	138.4	134.6	1937.6	255.4
10III2016	93.413 (22.308)	1875.0 (116.2)	133.9 (43.1)	455.7 (97.7)	188.4 (66.7)	158.6 (21.8)	156.6 (23.9)	1938.1 (96.7)	271.1 (48.6)

The total valid displacements are:

- For B10III2016I, 1.256mm of total piston displacement and total $CMOD$ of 1.334mm
- For B10III2016II, 1.386mm of total piston displacement and total $CMOD$ of 1.332mm
- For B10III2016III, 1.026mm of total piston displacement and total $CMOD$ of 1.334mm
- For B10III2016IV, 1.100mm of total piston displacement and total $CMOD$ of 1.334mm

Finally, the softening curve approximation is built with the following parameters, obtained with the procedure detailed at Chapter 3.3.1:

- Kink point at $23.3\mu\text{m}$ and 0.313MPa
- Initial intercept w_I at $32.7\mu\text{m}$
- Characteristic crack width w_{ch} of $86.0\mu\text{m}$
- Critical crack width w_c of $516.6\mu\text{m}$

F.5 17III2016 CAMPAIGN

The graphs of the acquired and processed data for this campaign is given at Appendix E.7 with the directly acquired and filtered data at Appendix E.7.1, the $P - w$ curves at Appendix E.7.2, the $P - \delta$ curves at Appendix E.7.3, the $P - X$ curves at Appendix E.7.4 and the specimens' comparison at Appendix E.7.6. Finally, the obtained softening function graph is given at Appendix E.7.5.

The individual results obtained with the base of the codes at Appendix C, the considerations at Appendix D.7 and the methodology at Chapter 3 are given at Table 85 for this campaign.

Table 85: Campaign 17III2016 individual results

SPECIMEN	$G_F(\text{Jm}^{-2})$	$P_{1u}(\text{N})$	$P_R(\text{N})$	$W_f(\text{mJ})$	$W_{tail}(\text{mJ})$	$w_G(\mu\text{m})$	$A(\text{Nmm}^2)$	$P_{ef}(\text{N})$	$l_1(\text{mm})$
B17III2016I	161.773	3015.2	131.8	948.9	192.8	96.9	117.6	3081.3	245.2
B17III2016II	175.903	3362.9	254.0	910.6	292.3	120.5	159.0	3452.2	630.8
B17III2016III	133.231	3063.0	266.2	709.6	253.4	122.5	122.4	3134.8	215.0
B17III2016IV	152.747	3026.3	244.8	752.1	374.4	169.3	193.9	3139.0	182.6
17III2016	155.914 (17.874)	3116.9 (165.3)	224.2 (62.2)	830.2 (117.1)	278.2 (76.1)	127.3 (30.3)	148.2 (35.6)	3201.8 (169.0)	318.4 (209.8)

The total valid displacements are:

- For B17III2016I, 1.220mm of total piston displacement and total $CMOD$ of 1.334mm
- For B17III2016II, 1.088mm of total piston displacement and total $CMOD$ of 1.332mm
- For B17III2016III, 0.966mm of total piston displacement and total $CMOD$ of 1.306mm
- For B17III2016IV, 1.036mm of total piston displacement and total $CMOD$ of 1.312mm

Finally, the softening curve approximation is built with the following parameters, obtained with the procedure detailed at Chapter 3.3.1:

- Kink point at $45.1\mu\text{m}$ and 0.528MPa
- Initial intercept w_1 at $65.6\mu\text{m}$
- Characteristic crack width w_{ch} of $92.2\mu\text{m}$
- Critical crack width w_c of $445.8\mu\text{m}$

F.6 01IV2016 CAMPAIGN

The graphs of the acquired data are given at Appendix E.8.1; the $P - w$ curves at Appendix E.8.2; the $P - \delta$ curves at Appendix E.8.3; the fitting of $P - X$ at Appendix E.8.4; the bilinear approximation for the softening curve at Appendix E.8.5 and the comparisons at Appendix E.8.6.

The individual tests results are obtained with the base of the codes at Appendix C, applying the calculation and procedures detailed at Chapter 3, according the considerations done at Appendix D.8. Those results are given at Table 86 for the 01IV2016 campaign.

Table 86: Campaign 01IV2016 individual results

SPECIMEN	$G_F(\text{Jm}^{-2})$	$P_{1u}(\text{N})$	$P_R(\text{N})$	$W_f(\text{mJ})$	$W_{tail}(\text{mJ})$	$w_G(\mu\text{m})$	$A(\text{Nmm}^2)$	$P_{ef}(\text{N})$	$l_1(\text{mm})$
B01IV2016I	129.909	2686.6	113.2	748.8	159.2	100.8	98.2	2741.9	708.9
B01IV2016II	131.074	2879.4	64.3	712.7	208.4	120.0	118.0	2945.7	1087.1
B01IV2016III	130.264	2809.1	107.1	740.8	170.7	102.2	99.9	2866.9	947.3
B01IV2016IV	147.418	2894.7	195.9	792.8	241.9	127.1	140.6	2974.9	1192.6
01IV2016	134.666 (8.515)	2817.5 (94.9)	120.1 (55.0)	748.8 (33.2)	195.1 (37.6)	112.5 (13.1)	114.2 (19.7)	2882.3 (104.2)	984.0 (209.1)

The total valid displacements are:

- For B01IV2016I, 1.234mm of total piston displacement and total $CMOD$ of 1.334mm
- For B01IV2016II, 1.132mm of total piston displacement and total $CMOD$ of 1.334mm
- For B01IV2016III, 1.170mm of total piston displacement and total $CMOD$ of 1.314mm
- For B01IV2016IV, 1.162mm of total piston displacement and total $CMOD$ of 1.324mm

Finally, the softening curve approximation is built with the following parameters, obtained with the procedure detailed at Chapter 3.3.1:

- Kink point at $53.0\mu\text{m}$ and 0.534MPa
- Initial intercept w_i at $91.7\mu\text{m}$
- Characteristic crack width w_{ch} of $106.5\mu\text{m}$
- Critical crack width w_c of $378.9\mu\text{m}$

F.7 07IV2016 CAMPAIGN

The graphs of the acquired data are given at Appendix E.9.1; the $P - w$ curves at Appendix E.9.2; the $P - \delta$ curves at Appendix E.9.3; the fitting of $P - X$ at Appendix E.9.4; the bilinear approximation for the softening curve at Appendix E.9.5 and the specimens' comparison at Appendix E.9.6.

The procedure detailed at Chapter 3 is applied for four beams and the results for their three point bending tests with self-weight correction. The results obtained processing the data acquired with the codes at Appendix C and the considerations done at appendix D.9 are given for every specimen and the entire campaign at Table 87.

Table 87: Campaign 07IV2016 individual results

SPECIMEN	$G_F(\text{Jm}^{-2})$	$P_{1u}(\text{N})$	$P_R(\text{N})$	$W_f(\text{mJ})$	$W_{tail}(\text{mJ})$	$w_G(\mu\text{m})$	$A(\text{Nmm}^2)$	$P_{ef}(\text{N})$	$l_1(\text{mm})$
B07IV2016I	174.910	3258.9	177.5	899.1	330.3	136.0	178.4	3359.1	1110.2
B07IV2016II	166.711	3347.6	140.8	868.4	299.7	122.2	152.8	3433.5	1378.9
B07IV2016III	165.012	3338.4	91.8	995.7	162.5	93.6	115.9	3403.5	1253.3
B07IV2016IV	150.697	2916.1	122.4	771.6	282.9	137.6	155.6	3003.3	555.2
07IV2016	164.332 (10.065)	3215.3 (203.3)	133.1 (35.8)	883.7 (92.4)	268.8 (73.6)	122.4 (20.4)	150.7 (25.9)	3299.9 (200.0)	1074.4 (363.1)

The total valid displacements are:

- For B07IV2016I, 1.080mm of total piston displacement and total $CMOD$ of 1.334mm
- For B07IV2016II, 1.020mm of total piston displacement and total $CMOD$ of 1.334mm
- For B07IV2016III, 1.426mm of total piston displacement and total $CMOD$ of 1.334mm
- For B07IV2016IV, 1.100mm of total piston displacement and total $CMOD$ of 1.336mm

Finally, the softening curve approximation is built with the following parameters, obtained with the procedure at Chapter 3.3.1:

- Kink point at $102.6\mu\text{m}$ and 0.378MPa
- Initial intercept w_1 at $139.2\mu\text{m}$
- Characteristic crack width w_{ch} of $114.3\mu\text{m}$
- Critical crack width w_c of $479.7\mu\text{m}$

F.8 14IV2016 CAMPAIGN

The graphs of the acquired data are given at Appendix E.10.1; the $P - w$ curves at Appendix E.10.2; the $P - \delta$ curves at Appendix E.10.3; the fitting of $P - X$ at Appendix E.10.4; the bilinear approximation for the softening curve at Appendix E.10.5 and the specimens' comparison at Appendix E.10.6.

For four beam specimens, the procedures detailed at Chapter 3 are applied and the test described at Chapter 4.2 is performed on them. The registers from these tests are processed with the codes at Appendix C and the considerations done at Appendix D.10, according to the methodology of the $P - \delta$ tail correction exposed at Chapter 3.3. The final results for the 14IV2016 are shown at Table 88.

Table 88: Campaign 14IV2016 individual results

SPECIMEN	$G_F(\text{Jm}^{-2})$	$P_{1u}(\text{N})$	$P_R(\text{N})$	$W_f(\text{mJ})$	$W_{tail}(\text{mJ})$	$w_G(\mu\text{m})$	$A(\text{Nmm}^2)$	$P_{ef}(\text{N})$	$l_1(\text{mm})$
B14IV2016I	182.895	3723.1	128.7	1049.5	234.8	99.6	136.6	3800.1	231.0
B14IV2016II	212.223	4608.6	168.5	1247.3	239.3	85.1	135.4	4685.9	757.6
B14IV2016III	224.831	4136.7	168.5	1310.4	273.8	99.7	168.1	4231.2	384.6
B14IV2016IV	237.038	4057.1	190.0	1292.3	375.0	135.2	240.4	4192.1	372.2
14IV2016	214.247 (23.227)	4131.4 (365.2)	163.9 (25.6)	1224.9 (119.9)	280.7 (65.2)	104.9 (21.3)	170.1 (49.2)	4227.3 (362.4)	436.3 (225.2)

The total valid displacements are:

- For B14IV2016I, 1.164mm of total piston displacement and total $CMOD$ of 1.332mm
- For B14IV2016II, 1.132mm of total piston displacement and total $CMOD$ of 1.324mm
- For B14IV2016III, 1.228mm of total piston displacement and total $CMOD$ of 1.334mm
- For B14IV2016IV, 1.282mm of total piston displacement and total $CMOD$ of 1.336mm

Finally, the softening curve approximation is built with the following parameters, obtained with the procedure at Chapter 3.3.1:

- Kink point at 47.5 μm and 0.936MPa
- Initial intercept w_1 at 84.7 μm
- Characteristic crack width w_{ch} of 100.6 μm
- Critical crack width w_c of 349.8 μm

F.9 21IV2016 CAMPAIGN

The graphs of the registered data are given at Appendix E.11.1; the used $P - w$ curves at Appendix E.11.2; the used $P - \delta$ curves at Appendix E.11.3; the fitting of $P - X$ at Appendix E.11.4; the bilinear approximation for the softening curve at Appendix E.11.5 and the comparison of the beam specimens at Appendix E.11.6.

A total of four beams were tested according the procedure detailed at Chapter 4.2 and the methodology at Chapter 3.3. The registered data is processed according the considerations written at Appendix D.11 using the codes at Appendix C. The results for the four three-point bending test, other parameters for the tail correction and furthermore are given at Table 89.

Table 89: Campaign 21IV2016 individual results

SPECIMEN	$G_f(\text{Jm}^{-2})$	$P_{1u}(\text{N})$	$P_R(\text{N})$	$W_f(\text{mJ})$	$W_{tail}(\text{mJ})$	$w_G(\mu\text{m})$	$A(\text{Nmm}^2)$	$P_{ef}(\text{N})$	$I_1(\text{mm})$
B21IV2016I	113.229	2889.6	101.1	638.3	155.7	101.5	86.2	2938.0	865.1
B21IV2016II	188.624	2745.6	266.6	1072.5	248.2	111.2	157.4	2834.0	692.2
B21IV2016III	158.942	3024.4	3.1	766.0	350.1	151.0	180.0	3125.5	1341.3
B21IV2016IV	122.390	3242.0	141.0	654.7	204.1	109.6	100.6	3298.5	2157.9
21IV2016	145.796 (34.716)	2975.4 (211.1)	127.9 (109.1)	782.9 (201.3)	239.5 (82.9)	118.3 (22.2)	131.0 (44.8)	3049.0 (205.5)	1264.1 (656.0)

The total valid displacements are:

- For B21IV2016I, 1.108mm of total piston displacement and total $CMOD$ of 1.334mm
- For B21IV2016II, 1.268mm of total piston displacement and total $CMOD$ of 1.334mm
- For B21IV2016III, 1.028mm of total piston displacement and total $CMOD$ of 1.334mm
- For B21IV2016IV, 0.986mm of total piston displacement and total $CMOD$ of 1.334mm

Finally, the softening curve approximation is built with the following parameters, obtained with the procedure at Chapter 3.3.1:

- Kink point at $103.4\mu\text{m}$ and 0.334MPa
- Initial intercept w_I at $138.8\mu\text{m}$
- Characteristic crack width w_{ch} of $111.5\mu\text{m}$
- Critical crack width w_c of $469.0\mu\text{m}$

G MATHEMATICAL DEVELOPMENTS

This appendix contains all mathematical developments from the expressions found at the literature review whenever further expressions were needed, but they were not given at the references.

G.1 EXPRESSION FOR THE SOFTENING CURVE BILINEAR APPROXIMATION

Equation 3.3.27 is not given at any journal article, book or other paper mentioned at Chapter 8, or, at least, it was not found if it exists there. The information we have is:

- The initial point at a zero crack width is a stress equivalent to the mean axial tensile strength
- The final point at stress zero is located at w_c
- The function is lineal in the range from w equal to zero until w_k and from w_k until w_c
- There is a point where the slope changes, which is the kink point, given by Equation 3.3.25 and 3.3.26
- The area enclosed down the softening curve equals G_F
- The first part of the bilinear approximation cuts the horizontal axis at w_1

The data can be reproduced on a plane, which will be similar to Figure 506.

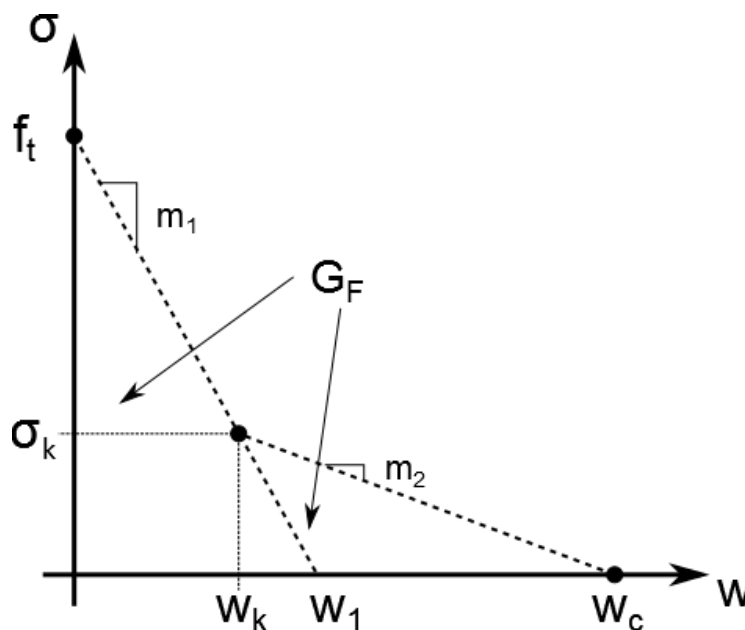


Figure 506: Basis for the construction of the bilinear approximation function

A general expression to build a first order function is Equation G.1.1, where the slope m if we have two points from this function is defined as Equation G.1.2, where y is the dependent variable, x the independent variable, and n is the image at the X-axis origin and the point 2 is after 1 taking into account the independent variable X-axis.

$$y = mx + n \quad (G.1.1)$$

$$m = \frac{y_2 - y_1}{x_2 - x_1} \quad (G.1.2)$$

Applying Equation G.1.2, one can find slopes m_1 and m_2 at Figure 506 (see Equation G.1.3 and G.1.4).

$$m_1 = -\frac{\bar{f}_t - \sigma_k}{w_k} = -\frac{\bar{f}_t}{w_1} \quad (G.1.3)$$

$$m_2 = -\frac{\sigma_k}{w_c - w_k} \quad (G.1.4)$$

About the origin n of both parts, n_1 is easily found as the mean axial tensile strength if we take as a reference point $(0, \bar{f}_t)$, as it is done at Equation G.1.5, but n_2 requires another step, taking as the reference the point $(w_c, 0)$, the development is visible at Equation G.1.6.

$$\bar{f}_t = m_1 \cdot 0 + n_1 \rightarrow n_1 = \bar{f}_t \quad (G.1.5)$$

$$0 = m_2 \cdot w_c + n_2 \rightarrow n_2 = -m_2 \cdot w_c = \frac{\sigma_k w_c}{w_c - w_k} \quad (G.1.6)$$

Using these two reference point and the two slopes considered (in Equation G.1.3 can be both), the part from the crack width zero until the kink point is defined by Equation G.1.7 and the rest until the critical crack width by Equation G.1.8, whose union forms Equation 3.3.27.

$$\sigma_1(w) = \bar{f}_t - \frac{\bar{f}_t - \sigma_k}{w_k} \cdot w \quad \text{if } w \in [0, w_k] \quad (G.1.7)$$

$$\sigma_2(w) = \frac{\sigma_k w_c}{w_c - w_k} - \frac{\sigma_k}{w_c - w_k} \cdot w \quad \text{if } w \in (w_k, w_c] \quad (G.1.8)$$

G.2 APPLICATION OF THE LOCAL FRACTURE ENERGY EQUATIONS

At any point of the reviewed papers in order to seek for information to prepare this project the development of Equation 3.4.1 in order to apply the equation system was found. For this reason, a general manual solution for G_F and a_1 instead of using any kind of numerical method, which would be the last resource, is searched. Doing so, one can extract far more information about the solution and if it exists or not.

First, the two equations from the system must be written to reproduce two different notches to depth ratios α with different G_f . Then, one has Equation G.2.1 and G.2.2 considering that G_F and a_1 are material independent properties, so they do not depend on the specimen series chosen.

$$G_{fi} = G_F \left(1 - \frac{a_1}{2D_i(1 - \alpha_i)} \right) \quad \text{if } D_i - a_i > a_1 \quad (G.2.1)$$

$$G_{fi} = G_F \frac{(1 - \alpha_i)D_i}{2a_1} \quad \text{if } D_i - a_i \leq a_1 \quad (G.2.2)$$

As we do not know the restrictions which are true for a single series, we must consider all the possibilities. These form four situations:

- A. Equation G.2.1 applies to both first and second series of notch to depth ratio
- B. Equation G.2.2 applies to both series
- C. Equation G.2.1 applies to the first series and Equation G.2.2 applies to the second
- D. Equation G.2.2 applies to the first series and Equation G.2.1 applies to the second

Situations differentiated at the code at Appendix C.2.5 and they will be studied at this appendix.

G.2.1 CASE A

The resulting equation system is given at Equation G.2.3 along with the restrictions of application.

$$\begin{cases} G_{fI} = G_F \left(1 - \frac{a_1}{2D_I(1 - \alpha_I)} \right) & \text{if } D_I - a_I > a_1 \\ G_{fII} = G_F \left(1 - \frac{a_1}{2D_{II}(1 - \alpha_{II})} \right) & \text{if } D_{II} - a_{II} > a_1 \end{cases} \quad (G.2.3)$$

While one unknown is G_F , whose position allows a division between both expressions at Equation G.2.3 in order to make it disappear leaving one equation with one unknown, this will be the applied method. After some changes, the new equation is found at Equation G.2.4.

$$\frac{2D_I(1 - \alpha_I)G_{fI}}{2D_{II}(1 - \alpha_{II})G_{fII}} = \frac{2D_I(1 - \alpha_I) - a_1}{2D_{II}(1 - \alpha_{II}) - a_1} \rightarrow \frac{A}{C} = \frac{B - a_1}{D - a_1} \quad (G.2.4)$$

Where A , B , C and D are constants at this equation. The solution for a_1 is Equation G.2.5.

$$\frac{AD}{C} - \frac{A}{C}a_1 = B - a_1 \rightarrow \left(1 - \frac{A}{C}\right)a_1 = B - \frac{AD}{C} \rightarrow a_1 = \frac{B - \frac{AD}{C}}{1 - \frac{A}{C}} \quad (G.2.5)$$

With this solution and the created constants, we enter to the first equation at Equation G.2.3 and we finally find G_F as Equation G.2.6. The only action that rests is to check if the restrictions at Equation G.2.3 are true or not. If not, the next case should be applied.

$$2D_I(1 - \alpha_I)G_{fI} = G_F(2D_I(1 - \alpha_I) - a_1) \rightarrow A = G_F(B - a_1) \rightarrow G_F = \frac{A}{B - a_1} \quad (G.2.6)$$

G.2.2 CASE B

In this case, the system of equations to be solved and its restrictions of application are shown at Equation G.2.7. The same procedure as in case A will be applied, obtaining Equation G.2.8.

$$\begin{cases} G_{fI} = G_F \frac{(1 - \alpha_I)D_I}{2a_1} & \text{if } D_I - a_I \leq a_1 \\ G_{fII} = G_F \frac{(1 - \alpha_{II})D_{II}}{2a_1} & \text{if } D_{II} - a_{II} \leq a_1 \end{cases} \quad (G.2.7)$$

$$\frac{2G_{fI}a_1}{2G_{fII}a_1} = \frac{(1 - \alpha_I)D_I}{(1 - \alpha_{II})D_{II}} = \frac{G_{fI}}{G_{fII}} \quad (G.2.8)$$

This equation does not allow solving any equation, because it is an expression formed only by constants. This case is undetermined and no solution exists. The next case should be applied directly.

G.2.3 CASE C

The system of equations that needs to be solved is Equation G.2.9, along with its restrictions. Its solution can be obtained dividing both expressions giving Equation G.2.10.

$$\begin{cases} G_{fI} = G_F \left(1 - \frac{a_1}{2D_I(1 - \alpha_I)}\right) & \text{if } D_I - a_I > a_1 \\ G_{fII} = G_F \frac{(1 - \alpha_{II})D_{II}}{2a_1} & \text{if } D_{II} - a_{II} \leq a_1 \end{cases} \quad (G.2.9)$$

$$\frac{2D_I(1-\alpha_I)G_{fI}}{2G_{fII}a_1} = \frac{2D_I(1-\alpha_I)-a_1}{(1-\alpha_{II})D_{II}} \rightarrow \frac{A}{Ca_1} = \frac{B-a_1}{D} \rightarrow AD - BCa_1 + Ca_1^2 = 0 \quad (G.2.10)$$

Solving this equation, one can find that a_1 is found with Equation G.2.11, which is the general root for a second order function.

$$a_1 = \frac{BC \pm \sqrt{B^2C^2 - 4CAD}}{2C} \quad (G.2.11)$$

With this parameter, one can use the second equation at Equation G.2.9 in order to find G_F (Equation G.2.12). While a_1 can be two different values, Equation G.2.12 must be used twice. The sign at Equation G.2.11 whose solution for G_F and a_1 makes true the restrictions at Equation G.2.9 is the correct answer. Whenever neither positive nor negative sign make these restrictions true, case D should be used.

$$2G_{fII}a_1 = G_F(1-\alpha_{II})D_{II} \rightarrow Ca_1 = G_FD \rightarrow G_F = \frac{Ca_1}{D} \quad (G.2.12)$$

G.2.4 CASE D

This last case is formed by Equation G.2.13, where the same procedure will be applied, giving Equation G.2.14.

$$\begin{cases} G_{fI} = G_F \frac{(1-\alpha_I)D_I}{2a_1} & \text{if } D_I - a_I \leq a_1 \\ G_{fII} = G_F \left(1 - \frac{a_1}{2D_{II}(1-\alpha_{II})}\right) & \text{if } D_{II} - a_{II} > a_1 \end{cases} \quad (G.2.13)$$

$$\frac{2G_{fI}a_1}{2D_{II}(1-\alpha_{II})G_{fII}} = \frac{(1-\alpha_I)D_I}{2D_{II}(1-\alpha_{II})-a_1} \rightarrow \frac{Ca_1}{A} = \frac{D}{B-a_1} \rightarrow AD - BCa_1 + Ca_1^2 = 0 \quad (G.2.14)$$

If we use the auxiliary constants A , B , C and D in the shown order, Equation G.2.14 is equal to Equation G.2.10 and Equation G.2.11 and G.2.12 applies the same way as they do at case C. Once both possibilities are solved and they restrictions are checked, if one of these possibilities fulfills the restrictions, it is the final answer. If not, while these were all the possible cases, the problem has not any solution and one must remark that this procedure led to an undetermined test result, which is the same to say the test failed.

H ECONOMIC VALUATION

H.1 SIMPLE ELEMENTS COSTS

H.1.1 UNIT COSTS FOR MATERIALS

Material 1: Sand 0/2, for use in building

- Measurement unit: *kilogram (kg)*
- Approximate cost: *0'80€ per 25kg*
- Unit cost: *0'032€/kg*

Material 2: Aggregate 5/10, for use in building

- Measurement unit: *kilogram (kg)*
- Approximate cost: *0'75€ per 25kg*
- Unit cost: *0'03€/kg*

Material 3: Cement CEM II/B-L 32.5N

- Measurement unit: *kilogram (kg)*
- Approximate cost: *2'77€ per 25kg*
- Unit cost: *0'1108€/kg*

Material 4: Water (common)

- Measurement unit: *liter (L) or cubic decimeter (dm³)*
- Approximate cost: *1'67€ per 1m³*
- Unit cost: *0'00167€/L*

Material 5: Concrete HA-25/F/15/IIa, according the EHE-08 instruction

- Measurement unit: *cubic meter (m³)*
- Unit cost: *68'10€/m³*

Material 6: Dust 0/2, for use in building

- Measurement unit: *kilogram (kg)*
- Approximate cost: *1€ per 25kg*
- Unit cost: *0'04€/kg*

Material 7: Admixture for concrete, type plasticizer

- Measurement unit: *kilogram (kg)*
- Unit cost: *1'49€/kg*

Material 8: Cement CEM I 52.5R

- Measurement unit: *kilogram (kg)*
- Unit cost: *0'129€/kg*

Material 9: Paper, printed in a grey scale for both sides

- Measurement unit: *unit (u)*
- Unit cost: *0'05€/u*

Material 10: Paper, printed in colors for both sides

- Measurement unit: *unit (u)*
- Unit cost: *0'38€/u*

Material 11: Wood, agglomerate and waterproof, 22mm thickness

- Measurement unit: *square meter (m²)*
- Unit cost: *13'01€/m²*

Material 12: Bicomponent adhesive for concrete, type X60, from HBM

- Measurement unit: *unit (u)*
- Unit cost: *52'00€/u*

Material 13: Iron (common)

- Measurement unit: *cubic decimeter (dm³)*
- Approximate cost and density: *0'68€/kg, with 7'85kg/dm³*
- Unit cost: *5'338€/dm³*

Material 14: Bolt for wood, 100mm long

- Measurement unit: *unit (u)*
- Approximate cost: *13'95€ for a 20u pack*
- Unit cost: *0'6975€/u*

H.1.2 UNIT COSTS FOR MANPOWER

Manpower 1: Trowel, for concrete building

- Measurement unit: *hour (h)*
- Unit cost: 22'31€/h

Manpower 2: Engineer

- Measurement unit: *hour (h)*
- Unit cost: 24'95€/h

**It is included in concepts directly related to the campaigns in form of "test" concepts (use: 0%)*

H.1.3 UNIT COSTS FOR MACHINERY AND TESTS

Machine 1: Cement mixer, 100L capacity

- Measurement unit: *hour (h)*
- Unit cost: 1'75€/h

Machine 2: Needle vibrator for concrete

- Measurement unit: *hour (h)*
- Unit cost: 1'38€/h

Machine 3: Saw

- Measurement unit: *hour (h)*
- Unit cost: 1'99€/h

Test 1: Bending test with a universal testing machine for fracture mechanics, according the UNE-EN 12390-1/-2/-4 and similar to UNE-EN 12390-5 codes for testing on hardened concrete

- Measurement unit: *unit (u); includes carrying out the test, the control and the data treatment*
- Unit cost: 34'75€/u

Test 2: Brazilian test with a compression testing machine, according the UNE-EN 12390-1/-2/-4 codes and especially UNE-EN 12390-6 for testing on hardened concrete

- Measurement unit: *unit (u); includes carrying out the test, the control and the data treatment*
- Unit cost: 36'39€/u

Test 3: Direct compression test with a compression testing machine, according the UNE 12390-1/-2/-4 codes and especially UNE-EN 12390-3 for testing on hardened concrete

- Measurement unit: *unit (u); includes carrying out the test, the control and the data treatment*
- Unit cost: 18'56€/u

H.2 SIMPLE ELEMENTS MEASUREMENT

The measurements are done according to the following structure:

- *DATE*: when it is used or done
- *CONCEPT*: what we want to measure
- *UNIT*: how we measure it
- *QUANTITY (QNT.)*: how many units are approximately used, result of applying Equation H.2.1
- *USE*: how many units are really used, which is the waste or correction factor
- *TOTAL*: total amount of units for the cost analysis

$$QNT = A \cdot B \cdot C \cdot D \cdot N; N \in \mathbb{N}^+ \quad (H.2.1)$$

H.2.1 MATERIALS MEASUREMENT

Table 90: Measurement for material 1 – Sand 0/2

DATE	CONCEPT	UNIT	A	B	C	D	N	QNT.	USE	TOTAL
MAT#1	Sand 0/2	kg								414'020
22/10/2015	23X2015 Campaign	kg	36'000	1'000	1'000	1'000	1	36'000	100%	36'000
27/01/2016	29I2016A Campaign	kg	36'000	1'000	1'000	1'000	1	36'000	100%	36'000
27/01/2016	29I2016B Campaign	kg	36'000	1'000	1'000	1'000	1	36'000	100%	36'000
07/03/2016	10III2016 Trial	kg	36'000	1'000	1'000	1'000	1	36'000	100%	36'000
07/03/2016	10III2016 Campaign	kg	44'100	1'000	1'000	1'000	1	44'100	100%	44'100
09/03/2016	Trial 1	kg	16'000	1'000	1'000	1'000	1	16'000	100%	16'000
09/03/2016	Trial 2	kg	16'000	1'000	1'000	1'000	1	16'000	100%	16'000
14/03/2016	17III2016 Campaign	kg	35'600	1'000	1'000	1'000	1	35'600	100%	35'600
30/03/2016	01IV2016 Campaign	kg	41'520	1'000	1'000	1'000	1	41'520	100%	41'520
04/04/2016	07IV2016 Campaign	kg	36'720	1'000	1'000	1'000	1	36'720	100%	36'720
11/04/2016	14IV2016 Campaign	kg	41'520	1'000	1'000	1'000	1	41'520	100%	41'520
18/04/2016	21IV2016 Campaign	kg	38'560	1'000	1'000	1'000	1	38'560	100%	38'560

Table 91: Measurement for material 2 – Aggregate 5/10

DATE	CONCEPT	UNIT	A	B	C	D	N	QNT.	USE	TOTAL
MAT#2	Aggregate 5/10	kg								472'000
22/10/2015	23X2015 Campaign	kg	40'000	1'000	1'000	1'000	1	40'000	100%	40'000
27/01/2016	29I2016A Campaign	kg	40'500	1'000	1'000	1'000	1	40'500	100%	40'500
27/01/2016	29I2016B Campaign	kg	40'500	1'000	1'000	1'000	1	40'500	100%	40'500
07/03/2016	10III2016 Trial	kg	44'100	1'000	1'000	1'000	1	44'100	100%	44'100
07/03/2016	10III2016 Campaign	kg	44'100	1'000	1'000	1'000	1	44'100	100%	44'100
09/03/2016	Trial 1	kg	19'600	1'000	1'000	1'000	1	19'600	100%	19'600
09/03/2016	Trial 2	kg	19'600	1'000	1'000	1'000	1	19'600	100%	19'600
14/03/2016	17III2016 Campaign	kg	45'600	1'000	1'000	1'000	1	45'600	100%	45'600
30/03/2016	01IV2016 Campaign	kg	41'520	1'000	1'000	1'000	1	41'520	100%	41'520
04/04/2016	07IV2016 Campaign	kg	46'320	1'000	1'000	1'000	1	46'320	100%	46'320
11/04/2016	14IV2016 Campaign	kg	41'520	1'000	1'000	1'000	1	41'520	100%	41'520
18/04/2016	21IV2016 Campaign	kg	48'640	1'000	1'000	1'000	1	48'640	100%	48'640

Table 92: Measurement for material 3 – CEM II/B-L 32.5N

DATE	CONCEPT	UNIT	A	B	C	D	N	QNT.	USE	TOTAL
MAT#3	CEM II/B-L 32.5N	kg								118'130
22/10/2015	23X2015 Campaign	kg	9'000	1'000	1'000	1'000	1	9'000	100%	9'000
27/01/2016	29I2016A Campaign	kg	13'500	1'000	1'000	1'000	1	13'500	100%	13'500
27/01/2016	29I2016B Campaign	kg	13'500	1'000	1'000	1'000	1	13'500	100%	13'500
07/03/2016	10III2016 Trial	kg	7'220	1'000	1'000	1'000	1	7'220	100%	7'220
07/03/2016	10III2016 Campaign	kg	11'250	1'000	1'000	1'000	1	11'250	100%	11'250
14/03/2016	17III2016 Campaign	kg	10'200	1'000	1'000	1'000	1	10'200	100%	10'200
30/03/2016	01IV2016 Campaign	kg	13'200	1'000	1'000	1'000	1	13'200	100%	13'200
04/04/2016	07IV2016 Campaign	kg	13'200	1'000	1'000	1'000	1	13'200	100%	13'200
11/04/2016	14IV2016 Campaign	kg	13'200	1'000	1'000	1'000	1	13'200	100%	13'200
18/04/2016	21IV2016 Campaign	kg	13'860	1'000	1'000	1'000	1	13'860	100%	13'860

Table 93: Measurement for material 4 – Water

DATE	CONCEPT	UNIT	A	B	C	D	N	QNT.	USE	TOTAL
MAT#4	Water	L								1217'891
22/10/2015	23X2015 Campaign	L	7'800	1'000	1'000	1'000	1	7'800	150%	11'700
23/10/2015	Preserve B23X2015	L	3'142	2'250	2'250	6'000	1	95'426	62%	59'164
23/10/2015	Preserve C-D23X2015	L	3'142	2'500	2'500	2'500	1	49'087	79%	38'779
14/12/2015	Preserve B14XII2015	L	3'142	2'250	2'250	6'000	2	190'852	62%	118'328
14/12/2015	Preserve C14XII2015	L	3'142	2'500	2'500	2'500	2	98'175	79%	77'558
27/01/2016	29I2016A Campaign	L	9'100	1'000	1'000	1'000	1	9'100	150%	13'650
27/01/2016	29I2016B Campaign	L	9'000	1'000	1'000	1'000	1	9'000	150%	13'500
29/01/2016	Preserve B29I2016	L	3'142	2'250	2'250	6'000	2	190'852	62%	118'328
29/01/2016	Preserve C-D29I2016	L	3'142	2'500	2'500	2'500	2	98'175	79%	77'558
07/03/2016	10III2016 Trial	L	6'540	1'000	1'000	1'000	1	6'540	150%	9'810
07/03/2016	10III2016 Campaign	L	9'660	1'000	1'000	1'000	1	9'660	150%	14'490
09/03/2016	Trial 1	L	2'460	1'000	1'000	1'000	1	2'460	150%	3'690
09/03/2016	Trial 2	L	2'860	1'000	1'000	1'000	1	2'860	150%	4'290
10/03/2016	Preserve B10III2016	L	3'142	2'250	2'250	6'000	1	95'426	62%	59'164
10/03/2016	Preserve C10III2016	L	3'142	2'500	2'500	2'500	1	49'087	79%	38'779
14/03/2016	17III2016 Campaign	L	8'340	1'000	1'000	1'000	1	8'340	150%	12'510
17/03/2016	Preserve B17III2016	L	3'142	2'250	2'250	6'000	1	95'426	62%	59'164
17/03/2016	Preserve C17III2016	L	3'142	2'500	2'500	2'500	1	49'087	79%	38'779
30/03/2016	01IV2016 Campaign	L	10'164	1'000	1'000	1'000	1	10'164	150%	15'246
01/04/2016	Preserve B01IV2016	L	3'142	2'250	2'250	6'000	1	95'426	62%	59'164
01/04/2016	Preserve C01IV2016	L	3'142	2'500	2'500	2'500	1	49'087	79%	38'779
04/04/2016	07IV2016 Campaign	L	10'164	1'000	1'000	1'000	1	10'164	150%	15'246
07/04/2016	Preserve B07IV2016	L	3'142	2'250	2'250	6'000	1	95'426	62%	59'164
07/04/2016	Preserve C07IV2016	L	3'142	2'500	2'500	2'500	1	49'087	79%	38'779
11/04/2016	14IV2016 Campaign	L	8'580	1'000	1'000	1'000	1	8'580	150%	12'870
14/04/2016	Preserve B14IV2016	L	3'142	2'250	2'250	6'000	1	95'426	62%	59'164
14/04/2016	Preserve C14IV2016	L	3'142	2'500	2'500	2'500	1	49'087	79%	38'779
18/04/2016	21IV2016 Campaign	L	9'010	1'000	1'000	1'000	1	9'010	150%	13'515
21/04/2016	Preserve B21IV2016	L	3'142	2'250	2'250	6'000	1	95'426	62%	59'164
21/04/2016	Preserve C21IV2016	L	3'142	2'500	2'500	2'500	1	49'087	79%	38'779

Table 94: Measurement for material 5 – Concrete HA-25/F/15/Ila

DATE	CONCEPT	UNIT	A	B	C	D	N	QNT.	USE	TOTAL
MAT#5	Concrete HA-25/F/15/Ila	m³								0'078
10/12/2015	B14XII2015 Campaign	m ³	0'100	0'100	0'600	1'000	8	0'048	105%	0'050
10/12/2015	C14XII2015 Campaign	m ³	3'142	0'075	0'075	0'300	5	0'027	105%	0'028

Table 95: Measurement for material 6 – Dust 0/2

DATE	CONCEPT	UNIT	A	B	C	D	N	QNT.	USE	TOTAL
MAT#6	Dust 0/2	kg								15'300
07/03/2016	10III2016 Trial	kg	8'100	1'000	1'000	1'000	1	8'100	100%	8'100
09/03/2016	Trial 1	kg	3'600	1'000	1'000	1'000	1	3'600	100%	3'600
09/03/2016	Trial 2	kg	3'600	1'000	1'000	1'000	1	3'600	100%	3'600

Table 96: Measurement for material 7 - Plasticizer

DATE	CONCEPT	UNIT	A	B	C	D	N	QNT.	USE	TOTAL
MAT#7	Admixture - Plasticizer	kg								1'478
07/03/2016	10III2016 Trial	kg	0'300	1'000	1'000	1'000	1	0'300	100%	0'300
07/03/2016	10III2016 Campaign	kg	0'200	1'000	1'000	1'000	1	0'200	100%	0'200
09/03/2016	Trial 1	kg	0'045	1'000	1'000	1'000	1	0'045	100%	0'045
09/03/2016	Trial 2	kg	0'045	1'000	1'000	1'000	1	0'045	100%	0'045
14/03/2016	17III2016 Campaign	kg	0'140	1'000	1'000	1'000	1	0'140	100%	0'140
30/03/2016	01IV2016 Campaign	kg	0'130	1'000	1'000	1'000	1	0'130	100%	0'130
04/04/2016	07IV2016 Campaign	kg	0'130	1'000	1'000	1'000	1	0'130	100%	0'130
11/04/2016	14IV2016 Campaign	kg	0'238	1'000	1'000	1'000	1	0'238	100%	0'238
18/04/2016	21IV2016 Campaign	kg	0'250	1'000	1'000	1'000	1	0'250	100%	0'250

Table 97: Measurement for material 8 – CEM I 52.5R

DATE	CONCEPT	UNIT	A	B	C	D	N	QNT.	USE	TOTAL
MAT#8	CEM I 52.5R	kg								6'420
09/03/2016	Trial 1	kg	3'210	1'000	1'000	1'000	1	3'210	100%	3'210
09/03/2016	Trial 2	kg	3'210	1'000	1'000	1'000	1	3'210	100%	3'210

Table 98: Measurement for material 9 – Paper, gray scaled, two faces

DATE	CONCEPT	UNIT	A	B	C	D	N	QNT.	USE	TOTAL
MAT#9	Paper B/N 2-sides	u								310'000
13/06/2016	Project copy	u	0'500	1'000	1'000	1'000	470	235'000	100%	235'000
13/05/2015	Codes/Articles printing	u	0'500	1'000	1'000	1'000	150	75'000	100%	75'000

Table 99: Measurement for material 10 – Paper, color, two faces

DATE	CONCEPT	UNIT	A	B	C	D	N	QNT.	USE	TOTAL
MAT#10	Paper Color 2-sides	u								239'000
13/06/2016	Project original	u	0'500	1'000	1'000	1'000	470	235'000	100%	235'000
13/06/2016	Project abstract	u	0'500	1'000	1'000	1'000	8	4'000	100%	4'000

Table 100: Measurement for material 11 – 22m thickness agglomerate waterproof wood

DATE	CONCEPT	UNIT	A	B	C	D	N	QNT.	USE	TOTAL
MAT#11	Wood	m²								2'717
10/05/2015	Wood for molds - Large	m ²	0'605	0'105	5'000	1'000	8	2'541	100%	2'541
10/05/2015	Wood for molds - Short	m ²	0'105	0'105	2'000	1'000	8	0'176	100%	0'176

Table 101: Measurement for material 12 – Concrete adhesive

DATE	CONCEPT	UNIT	A	B	C	D	N	QNT.	USE	TOTAL
MAT#12	Adhesive	u								2'000
10/10/2015	Bicomponent adhesive X60	u	1'000	1'000	1'000	1'000	1	1'000	100%	1'000
29/02/2016	Bicomponent adhesive X60	u	1'000	1'000	1'000	1'000	1	1'000	100%	1'000

Table 102: Measurement for material 13 – Iron

DATE	CONCEPT	UNIT	A	B	C	D	N	QNT.	USE	TOTAL
MAT#13	Iron	dm³								2'730
10/05/2015	Supports - Common	dm ³	0'250	1'500	1'500	1'000	3	1'688	100%	1'688
28/10/2015	Supports - Antitortion	dm ³	0'150	1'200	1'200	1'000	2	0'432	100%	0'432
10/05/2015	Roller - D50	dm ³	3'142	0'250	0'250	1'500	2	0'589	100%	0'589
28/10/2015	Roller - D15	dm ³	3'142	0'075	0'075	1'200	1	0'021	100%	0'021

Table 103: Measurement for material 14 – 100mm long wood bolt

DATE	CONCEPT	UNIT	A	B	C	D	N	QNT.	USE	TOTAL
MAT#14	Bolt	u								144'000
10/05/2015	Bolts - Large face	u	4'000	2'000	1'000	1'000	8	64'000	100%	64'000
10/05/2015	Bolts - Short face	u	5'000	2'000	1'000	1'000	8	80'000	100%	80'000

H.2.2 MANPOWER MEASUREMENT

Table 104: Measurement for manpower 1 – Concrete building trowel

DATE	CONCEPT	UNIT	A	B	C	D	N	QNT.	USE	TOTAL
MNPW#1	Trowel	h								26'500
22/10/2015	23X2015 Campaign	h	2'000	1'000	1'000	1'000	1	2'000	100%	2'000
10/12/2015	14XII2015 Campaign	h	2'000	1'000	1'000	1'000	2	4'000	100%	4'000
27/01/2016	29I2016A Campaign	h	1'000	1'000	1'000	1'000	2	2'000	100%	2'000
27/01/2016	29I2016B Campaign	h	1'000	1'000	1'000	1'000	2	2'000	100%	2'000
07/03/2016	10III2016 Trial	h	0'750	1'000	1'000	1'000	2	1'500	100%	1'500
07/03/2016	10III2016 Campaign	h	1'000	1'000	1'000	1'000	2	2'000	100%	2'000
09/03/2016	Trial 1	h	0'750	1'000	1'000	1'000	2	1'500	100%	1'500
09/03/2016	Trial 2	h	0'750	1'000	1'000	1'000	2	1'500	100%	1'500
14/03/2016	17III2016 Campaign	h	1'000	1'000	1'000	1'000	2	2'000	100%	2'000
30/03/2016	01IV2016 Campaign	h	1'000	1'000	1'000	1'000	2	2'000	100%	2'000
04/04/2016	07IV2016 Campaign	h	1'000	1'000	1'000	1'000	2	2'000	100%	2'000
11/04/2016	14IV2016 Campaign	h	1'000	1'000	1'000	1'000	2	2'000	100%	2'000
18/04/2016	21IV2016 Campaign	h	1'000	1'000	1'000	1'000	2	2'000	100%	2'000

Table 105: Measurement for manpower 2 – Engineer

DATE	CONCEPT	UNIT	A	B	C	D	N	QNT.	USE	TOTAL
MNPW#2	Engineer	h						308'000	48'1%	148'000
V/2015	Initiation	h	2'00	9'00	1'00	1'00	1	18'000	100%	18'000
VI/2015-V/2016	Knowledge acquisition*	h	3'00	3'00	40'00	1'00	1	360'00*	0%	0'000
VI/2015-V/2016	Management and treatment	h	2'00	2'00	25'00	1'00	1	100'000	100%	100'000
X/2015-XI/2015	23X2015 Control	h	2'00	4'00	1'00	1'00	1	8'000	0%	0'000
XI/2015	23X2015 Testing	h	8'00	1'50	1'00	1'00	1	12'000	0%	0'000
XII/2015-I/2016	14XII2015 Control	h	2'00	4'00	1'00	1'00	1	8'000	0%	0'000
I/2016	14XII2015 Testing	h	8'00	2'00	1'00	1'00	1	16'000	0%	0'000
I/2016-II/2016	29I2016 Control	h	2'00	4'00	1'00	1'00	1	8'000	0%	0'000
II/2016	29I2016 Testing	h	8'00	1'50	1'00	1'00	1	12'000	0%	0'000
III/2016-IV/2016	10III2016 Control	h	2'00	4'00	1'00	1'00	1	8'000	0%	0'000
III/2016-IV/2016	17III2016 Control	h	2'00	4'00	1'00	1'00	1	8'000	0%	0'000
III/2016-IV/2016	01IV2016 Control	h	2'00	4'00	1'00	1'00	1	8'000	0%	0'000
IV/2016	10III2016 Testing	h	8'00	1'00	1'00	1'00	1	8'000	0%	0'000
IV/2016	17III2016 Testing	h	8'00	1'00	1'00	1'00	1	8'000	0%	0'000
IV/2016	01IV2016 Testing	h	8'00	1'00	1'00	1'00	1	8'000	0%	0'000
IV/2016-V/2016	07IV2016 Control	h	2'00	4'00	1'00	1'00	1	8'000	0%	0'000
IV/2016-V/2016	14IV2016 Control	h	2'00	4'00	1'00	1'00	1	8'000	0%	0'000
IV/2016-V/2016	21IV2016 Control	h	2'00	4'00	1'00	1'00	1	8'000	0%	0'000
V/2016	07IV2016 Testing	h	8'00	1'00	1'00	1'00	1	8'000	0%	0'000
V/2016	14IV2016 Testing	h	8'00	1'00	1'00	1'00	1	8'000	0%	0'000
V/2016	21IV2016 Testing	h	8'00	1'00	1'00	1'00	1	8'000	0%	0'000
V/2016-VI/2016	Writing and revisions	h	3'00	5'00	2'00	1'00	1	30'000	100%	30'000

H.2.3 MACHINERY AND TESTS MEASUREMENT

Table 106: Measurement for machine 1 – 100L cement mixer

DATE	CONCEPT	UNIT	A	B	C	D	N	QNT.	USE	TOTAL
MACH#1	Cement mixer	h								14'250
22/10/2015	23X2015 Campaign	h	2'000	1'000	1'000	1'000	1	2'000	100%	2'000
10/12/2015	14XII2015 Campaign	h	2'000	1'000	1'000	1'000	1	2'000	100%	2'000
27/01/2016	29I2016A Campaign	h	1'000	1'000	1'000	1'000	1	1'000	100%	1'000
27/01/2016	29I2016B Campaign	h	1'000	1'000	1'000	1'000	1	1'000	100%	1'000
07/03/2016	10III2016 Trial	h	0'750	1'000	1'000	1'000	1	0'750	100%	0'750
07/03/2016	10III2016 Campaign	h	1'000	1'000	1'000	1'000	1	1'000	100%	1'000
09/03/2016	Trial 1 and 2	h	0'750	1'000	1'000	1'000	2	1'500	100%	1'500
14/03/2016	17III2016 Campaign	h	1'000	1'000	1'000	1'000	1	1'000	100%	1'000
30/03/2016	01IV2016 Campaign	h	1'000	1'000	1'000	1'000	1	1'000	100%	1'000
04/04/2016	07IV2016 Campaign	h	1'000	1'000	1'000	1'000	1	1'000	100%	1'000
11/04/2016	14IV2016 Campaign	h	1'000	1'000	1'000	1'000	1	1'000	100%	1'000
18/04/2016	21IV2016 Campaign	h	1'000	1'000	1'000	1'000	1	1'000	100%	1'000

Table 107: Measurement for machine 2 – Needle vibrator

DATE	CONCEPT	UNIT	A	B	C	D	N	QNT.	USE	TOTAL
MACH#2	Needle vibrator	h								14'250
22/10/2015	23X2015 Campaign	h	2'000	1'000	1'000	1'000	1	2'000	100%	2'000
10/12/2015	14XII2015 Campaign	h	2'000	1'000	1'000	1'000	1	2'000	100%	2'000
27/01/2016	29I2016A Campaign	h	1'000	1'000	1'000	1'000	1	1'000	100%	1'000
27/01/2016	29I2016B Campaign	h	1'000	1'000	1'000	1'000	1	1'000	100%	1'000
07/03/2016	10III2016 Trial	h	0'750	1'000	1'000	1'000	1	0'750	100%	0'750
07/03/2016	10III2016 Campaign	h	1'000	1'000	1'000	1'000	1	1'000	100%	1'000
09/03/2016	Trial 1 and 2	h	0'750	1'000	1'000	1'000	2	1'500	100%	1'500
14/03/2016	17III2016 Campaign	h	1'000	1'000	1'000	1'000	1	1'000	100%	1'000
30/03/2016	01IV2016 Campaign	h	1'000	1'000	1'000	1'000	1	1'000	100%	1'000
04/04/2016	07IV2016 Campaign	h	1'000	1'000	1'000	1'000	1	1'000	100%	1'000
11/04/2016	14IV2016 Campaign	h	1'000	1'000	1'000	1'000	1	1'000	100%	1'000
18/04/2016	21IV2016 Campaign	h	1'000	1'000	1'000	1'000	1	1'000	100%	1'000

Table 108: Measurement for machine 3 – Saw

DATE	CONCEPT	UNIT	A	B	C	D	N	QNT.	USE	TOTAL
MACH#3	Saw	h								11'000
17/11/2015	23X2015 Campaign	h	1'000	1'000	1'000	1'000	1	1'000	100%	1'000
08/01/2016	14XII2015 Campaign	h	2'000	1'000	1'000	1'000	1	2'000	100%	2'000
23/02/2016	29I2016A Campaign	h	1'000	1'000	1'000	1'000	1	1'000	100%	1'000
23/02/2016	29I2016B Campaign	h	1'000	1'000	1'000	1'000	1	1'000	100%	1'000
04/04/2016	10III2016 Campaign	h	1'000	1'000	1'000	1'000	1	1'000	100%	1'000
11/04/2016	17III2016 Campaign	h	1'000	1'000	1'000	1'000	1	1'000	100%	1'000
25/05/2016	01IV2016 Campaign	h	1'000	1'000	1'000	1'000	1	1'000	100%	1'000
02/05/2016	07IV2016 Campaign	h	1'000	1'000	1'000	1'000	1	1'000	100%	1'000
09/05/2016	14IV2016 Campaign	h	1'000	1'000	1'000	1'000	1	1'000	100%	1'000
16/05/2016	21IV2016 Campaign	h	1'000	1'000	1'000	1'000	1	1'000	100%	1'000

Table 109: Measurement for test 1 – Bending test

DATE	CONCEPT	UNIT	A	B	C	D	N	QNT.	USE	TOTAL
TST#1	Bending test	u								44'000
19/11/2015	23X2015 Campaign	u	1'000	1'000	1'000	1'000	4	4'000	100%	4'000
11/01/2016	14XII2015 Campaign	u	1'000	1'000	1'000	1'000	8	8'000	100%	8'000
24/01/2016	29I2016A Campaign	u	1'000	1'000	1'000	1'000	4	4'000	100%	4'000
24/01/2016	29I2016B Campaign	u	1'000	1'000	1'000	1'000	4	4'000	100%	4'000
05/04/2016	10III2016 Campaign	u	1'000	1'000	1'000	1'000	4	4'000	100%	4'000
12/04/2016	17III2016 Campaign	u	1'000	1'000	1'000	1'000	4	4'000	100%	4'000
27/04/2016	01IV2016 Campaign	u	1'000	1'000	1'000	1'000	4	4'000	100%	4'000
03/05/2016	07IV2016 Campaign	u	1'000	1'000	1'000	1'000	4	4'000	100%	4'000
10/05/2016	14IV2016 Campaign	u	1'000	1'000	1'000	1'000	4	4'000	100%	4'000
17/05/2016	21IV2016 Campaign	u	1'000	1'000	1'000	1'000	4	4'000	100%	4'000

Table 110: Measurement for test 2 – Brazilian test

DATE	CONCEPT	UNIT	A	B	C	D	N	QNT.	USE	TOTAL
TST#2	Brazilian test	u								21'000
23/11/2015	23X2015 Campaign	u	1'000	1'000	1'000	1'000	1	1'000	100%	1'000
12/01/2016	14XII2015 Campaign	u	1'000	1'000	1'000	1'000	4	4'000	100%	4'000
27/01/2016	29I2016A Campaign	u	1'000	1'000	1'000	1'000	2	2'000	100%	2'000
27/01/2016	29I2016B Campaign	u	1'000	1'000	1'000	1'000	2	2'000	100%	2'000
05/04/2016	10III2016 Campaign	u	1'000	1'000	1'000	1'000	2	2'000	100%	2'000
12/04/2016	17III2016 Campaign	u	1'000	1'000	1'000	1'000	2	2'000	100%	2'000
27/04/2016	01IV2016 Campaign	u	1'000	1'000	1'000	1'000	2	2'000	100%	2'000
03/05/2016	07IV2016 Campaign	u	1'000	1'000	1'000	1'000	2	2'000	100%	2'000
10/05/2016	14IV2016 Campaign	u	1'000	1'000	1'000	1'000	2	2'000	100%	2'000
17/05/2016	21IV2016 Campaign	u	1'000	1'000	1'000	1'000	2	2'000	100%	2'000

Table 111: Measurement for test 3 – Direct compression

DATE	CONCEPT	UNIT	A	B	C	D	N	QNT.	USE	TOTAL
TST#3	Compression test	u								11'000
19/11/2015	23X2015 Campaign	u	1'000	1'000	1'000	1'000	2	2'000	100%	2'000
12/01/2016	14XII2015 Campaign	u	1'000	1'000	1'000	1'000	1	1'000	100%	1'000
25/01/2016	29I2016A Campaign	u	1'000	1'000	1'000	1'000	1	1'000	100%	1'000
25/01/2016	29I2016B Campaign	u	1'000	1'000	1'000	1'000	1	1'000	100%	1'000
05/04/2016	10III2016 Campaign	u	1'000	1'000	1'000	1'000	1	1'000	100%	1'000
12/04/2016	17III2016 Campaign	u	1'000	1'000	1'000	1'000	1	1'000	100%	1'000
27/04/2016	01IV2016 Campaign	u	1'000	1'000	1'000	1'000	1	1'000	100%	1'000
03/05/2016	07IV2016 Campaign	u	1'000	1'000	1'000	1'000	1	1'000	100%	1'000
10/05/2016	14IV2016 Campaign	u	1'000	1'000	1'000	1'000	1	1'000	100%	1'000
17/05/2016	21IV2016 Campaign	u	1'000	1'000	1'000	1'000	1	1'000	100%	1'000

H.3 PROJECT COSTS**H.3.1 DIRECT COSTS CLASSIFIED BY NATURE****Table 112: Material direct costs by element**

CONCEPT	UNIT	QNT.	UNIT COST	TOTAL	
Sand 0/2	kg	414'020	0'03200 €	13'25 €	3'21%
Aggregate 5/10	kg	472'000	0'03000 €	14'16 €	3'44%
CEM II/B-L 32.5N	kg	118'130	0'11080 €	13'09 €	3'18%
Water	L	1217'891	0'00167 €	2'03 €	0'49%
Concrete HA-25/F/15/IIa	m ³	0'078	68'10000 €	5'33 €	1'29%
Dust 0/2	kg	15'300	0'04000 €	0'61 €	0'15%
Admixture - Plasticizer	kg	1'478	1'49000 €	2'20 €	0'53%
CEM I 52.5R	kg	6'420	0'12900 €	0'83 €	0'20%
Paper B/N 2-sides	u	310'000	0'05000 €	15'50 €	3'76%
Paper Color 2-sides	u	239'000	0'38000 €	90'82 €	22'03%
Wood	m ²	2'717	13'01000 €	35'35 €	8'58%
Adhesive	u	2'000	52'00000 €	104'00 €	25'23%
Iron	dm ³	2'730	5'33800 €	14'57 €	3'54%
Bolt	u	144'000	0'69750 €	100'44 €	24'37%
			MATERIALS	412'19 €	100%

Table 113: Manpower direct costs by element

CONCEPT	UNIT	QNT.	UNIT COST	TOTAL	
Trowel	h	26'500	22'31000 €	591'22 €	13'80%
Engineer	h	148'000	24'95000 €	3692'60 €	86'20%
			MANPOWER	4.283'82 €	100%
			AUXILIARY COSTS	85'68 €	2'00%

Table 114: Machinery and tests direct costs by element

CONCEPT	UNIT	QNT.	UNIT COST	TOTAL	
Cement mixer	h	14'250	1'75000 €	24'94 €	0'97%
Needle vibrator	h	14'250	1'38000 €	19'67 €	0'77%
Saw	h	11'000	1'99000 €	21'89 €	0'85%
Bending test	u	44'000	34'75000 €	1.529'00 €	59'64%
Brazilian test	u	21'000	36'39000 €	764'19 €	29'81%
Compression test	u	11'000	18'56000 €	204'16 €	7'96%
			MACHINERY AND TESTS	2.563'84 €	100%

H.3.2 TOTAL COSTS SUMMARY

Table 115: Total costs summary

Materials		412'19 €
Manpower		4.369'49 €
Machinery and tests		2.563'84 €
DIRECT COSTS		7.345'52 €
INDIRECT COSTS	6%	440'73 €
TOTAL COSTS		7.786'25 €
GENERAL COSTS	13%	1.012'21 €
PROFIT	8%	622'90 €
EXECUTION BUDGET		9.421'36 €
V.A.T.	21%	1.978'49 €
EXECUTION BUDGET (PLUS V.A.T.)		11.399'85 €

The project has a total cost of ELEVEN THOUSAND THREE HUNDRED NINETY-NINE EUROS AND EIGHTY-FIVE CENTS (11.399'85€), taxes included.

H.3.3 CAMPAIGN COST SUMMARY CLASSIFIED BY NATURE

Table 116: Campaign costs by nature

CAMPAIGN	MAT	MNPW+AUX	MACH+TST	INDIRECT	GENERAL	PROFIT	V.A.T.	FINAL COST
PROJECT	368'21 €	3.868'85 €	7'04 €	254'65 €	584'84 €	359'90 €	1.143'13 €	6.586'63 €
23X2015	3'53 €	45'51 €	220'76 €	16'19 €	37'18 €	22'88 €	72'67 €	418'72 €
14XII2015	5'65 €	91'02 €	452'36 €	32'94 €	75'66 €	46'56 €	147'88 €	852'08 €
29I2016A	4'05 €	45'51 €	235'46 €	17'10 €	39'28 €	24'17 €	76'77 €	442'34 €
29I2016B	4'05 €	45'51 €	235'46 €	17'10 €	39'28 €	24'17 €	76'77 €	442'34 €
10III2016	4'47 €	45'51 €	235'46 €	17'13 €	39'33 €	24'21 €	76'88 €	442'99 €
17III2016	4'03 €	45'51 €	235'46 €	17'10 €	39'27 €	24'17 €	76'76 €	442'31 €
01IV2016	4'42 €	45'51 €	235'46 €	17'12 €	39'33 €	24'20 €	76'87 €	442'91 €
07IV2016	4'41 €	45'51 €	235'46 €	17'12 €	39'33 €	24'20 €	76'87 €	442'90 €
14IV2016	4'58 €	45'51 €	235'46 €	17'13 €	39'35 €	24'21 €	76'91 €	443'16 €
21IV2016	4'79 €	45'51 €	235'46 €	17'15 €	39'38 €	24'23 €	76'97 €	443'48 €
TOTAL	412'19 €	4.369'49 €	2.563'84 €	440'73 €	1.012'21 €	622'90 €	1.978'49 €	11.399'85 €

Campaign, type 4 beam plus 3 cylinders/cubes with 4 bending tests, 1 compression test and 2 Brazilian tests; and monthly mean costs are given at Table 117. A campaign has a mean direct cost of TWO HUNDRED EIGHTY-ONE EUROS AND NINETY-FIVE CENTS (281'95€).

Table 117: Mean costs by nature

CONCEPT	MAT	MNPW+AUX	MACH+TST	INDIRECT	GENERAL	PROFIT	V.A.T.	FINAL COST
CAMPAIGN	4'00 €	45'51 €	232'44 €	16'92 €	38'85 €	23'91 €	75'94 €	437'57 €
MONTH	31'71 €	336'11 €	197'22 €	33'90 €	77'86 €	47'92 €	152'19 €	876'91 €

I SCHEDULE

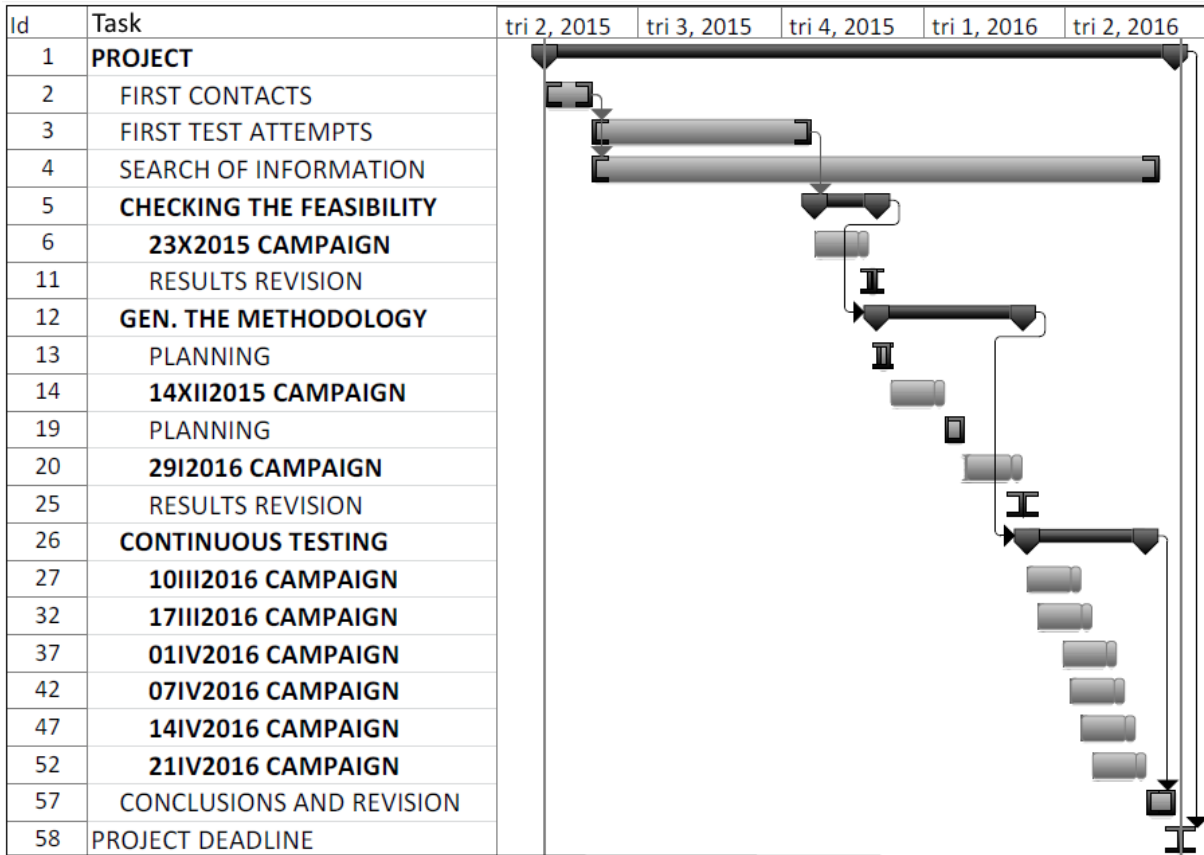


Figure 507: Summarized schedule on a Gantt diagram

Table 118: Detailed schedule

ID	TASK	BEGINNING	END	AFTER
1	1.PROJECT	01/05/2015	10/06/2016	
2	1.1.First contacts	01/05/2015	31/05/2015	
3	1.2.First test attempts	01/06/2015	19/10/2015	2
4	1.3.Search of information and data treatment	01/06/2015	31/05/2016	2
5	1.4.CHECKING THE FEASIBILITY	22/10/2015	01/12/2015	3
6	1.4.1.23X2015 CAMPAIGN	22/10/2015	25/11/2015	
7	1.4.1.1.Casting	22/10/2015	22/10/2015	
8	1.4.1.2.Unmolding	23/10/2015	26/10/2015	7
9	1.4.1.3.Hardening	22/10/2015	19/11/2015	7
10	1.4.1.4.Testing	19/11/2015	25/11/2015	9
11	1.4.2.Results revision	25/11/2015	01/12/2015	
12	1.5.CHECKING AND GENERALYZING THE METHODOLOGY	01/12/2015	04/03/2016	5
13	1.5.1.Planning	01/12/2015	09/12/2015	

14	1.5.2.14XII2015 CAMPAIGN	10/12/2015	13/01/2016	13
15	1.5.2.1.Casting	10/12/2015	10/12/2015	
16	1.5.2.2.Unmolding	11/12/2015	14/12/2015	15
17	1.5.2.3.Hardening	10/12/2015	07/01/2016	15
18	1.5.2.4.Testing	07/01/2016	13/01/2016	17
19	1.5.3.Planning	14/01/2016	26/01/2016	
20	1.5.4.29I2016 CAMPAIGN	27/01/2016	03/03/2016	
21	1.5.4.1.Casting	27/01/2016	27/01/2016	
22	1.5.4.2.Unmolding	28/01/2016	30/01/2016	21
23	1.5.4.3.Hardening	28/01/2016	25/02/2016	21
24	1.5.4.4.Testing	26/02/2016	03/03/2016	23
25	1.5.5.Results revision	04/03/2016	04/03/2016	24
26	1.6.CONTINUOUS TESTING	07/03/2016	22/05/2016	12
27	1.6.1.10III2016 CAMPAIGN	07/03/2016	10/04/2016	
28	1.6.1.1.Casting	07/03/2016	07/03/2016	
29	1.6.1.2.Unmolding	08/03/2016	10/03/2016	28
30	1.6.1.3.Hardening	07/03/2016	04/04/2016	28
31	1.6.1.4.Testing	04/04/2016	10/04/2016	30
32	1.6.2.17III2016 CAMPAIGN	14/03/2016	17/04/2016	
33	1.6.2.1.Casting	14/03/2016	14/03/2016	
34	1.6.2.2.Unmolding	15/03/2016	17/03/2016	33
35	1.6.2.3.Hardening	14/03/2016	11/04/2016	33
36	1.6.2.4.Testing	11/04/2016	17/04/2016	35
37	1.6.3.01IV2016 CAMPAIGN	30/03/2016	03/05/2016	
38	1.6.3.1.Casting	30/03/2016	30/03/2016	
39	1.6.3.2.Unmolding	31/03/2016	02/04/2016	38
40	1.6.3.3.Hardening	30/03/2016	27/04/2016	38
41	1.6.3.4.Testing	27/04/2016	03/05/2016	40
42	1.6.4.07IV2016 CAMPAIGN	04/04/2016	08/05/2016	
43	1.6.4.1.Casting	04/04/2016	04/04/2016	
44	1.6.4.2.Unmolding	05/04/2016	07/04/2016	43
45	1.6.4.3.Hardening	04/04/2016	02/05/2016	43
46	1.6.4.4.Testing	02/05/2016	08/05/2016	45
47	1.6.5.14IV2016 CAMPAIGN	11/04/2016	15/05/2016	
48	1.6.5.1.Casting	11/04/2016	11/04/2016	
49	1.6.5.2.Unmolding	12/04/2016	14/04/2016	48
50	1.6.5.3.Hardening	11/04/2016	09/05/2016	48
51	1.6.5.4.Testing	09/05/2016	15/05/2016	50
52	1.6.6.21IV2016 CAMPAIGN	18/04/2016	22/05/2016	
53	1.6.6.1.Casting	18/04/2016	18/04/2016	
54	1.6.6.2.Unmolding	19/04/2016	21/04/2016	53
55	1.6.6.3.Hardening	18/04/2016	16/05/2016	53
56	1.6.6.4.Testing	16/05/2016	22/05/2016	55
57	1.7.Conclusions and project revision	23/05/2016	10/06/2016	26
58	2.PROJECT DEADLINE	13/06/2016	14/06/2016	1

J GALLERY

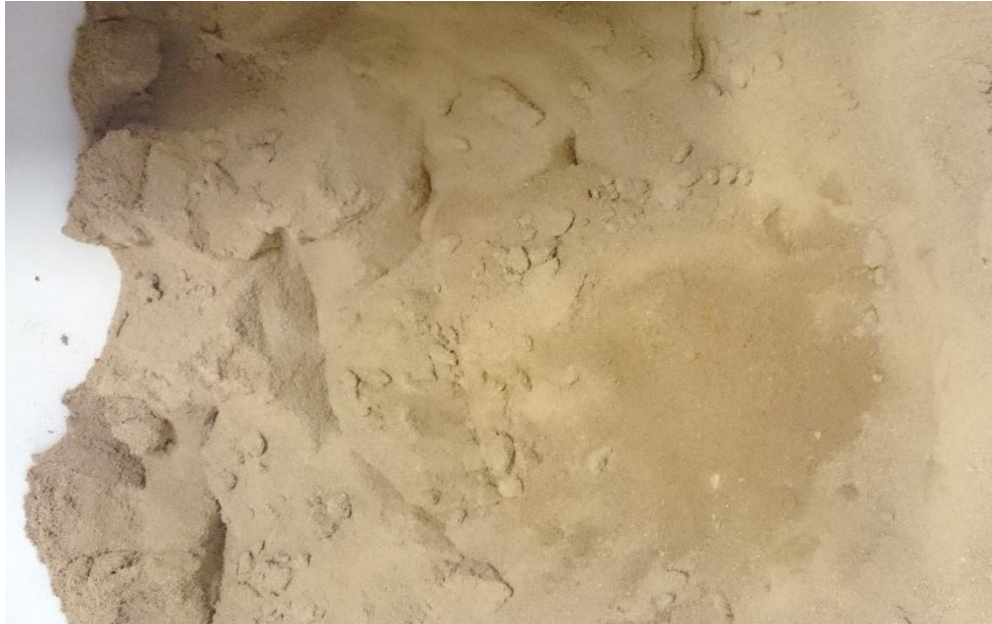


Figure 508: Material used – Sand 0/2



Figure 509: Material used – Aggregate 5/10



Figure 510: Material used – CEM II/B-L 32.5N



Figure 511: Machinery used – 100L cement mixer



Figure 512: Materials for a single campaign made with a cement mixer



Figure 513: Example of underwater preservation



Figure 514: Just after casting – Beams and cylinders with their molds and a machine used – Needle vibrator

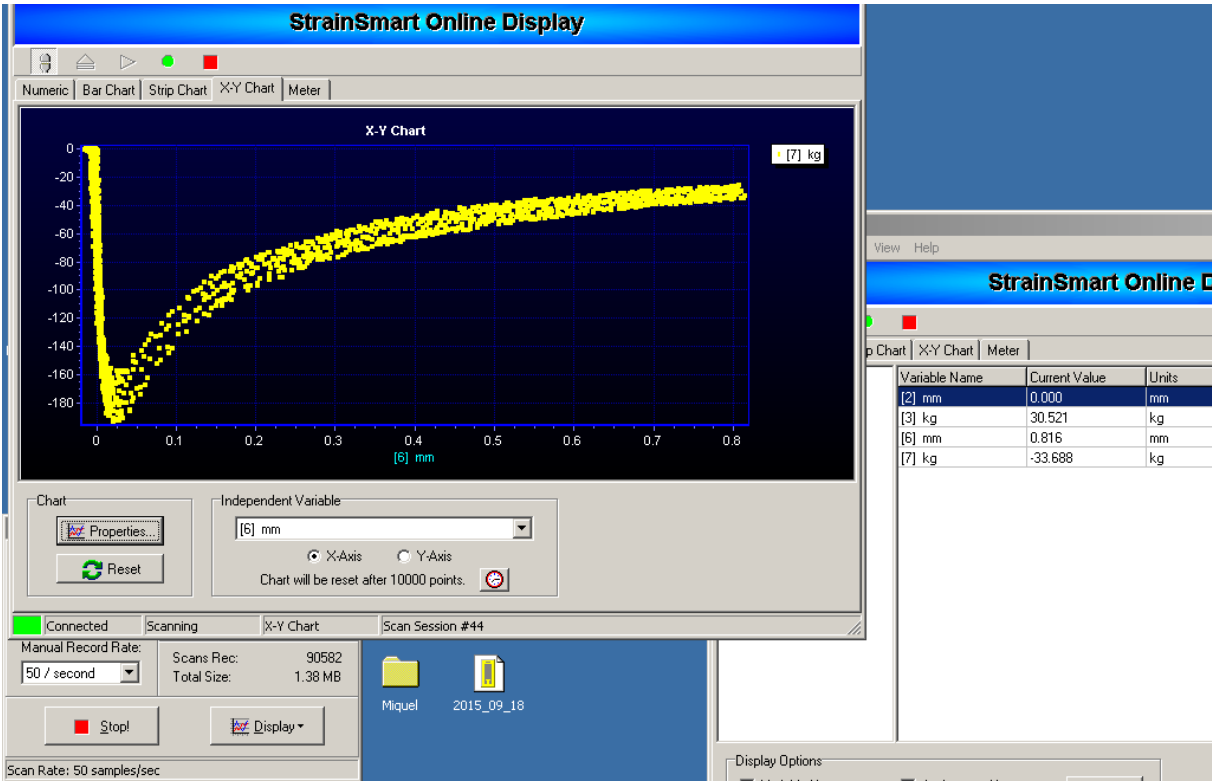


Figure 515: On-live recording program – StrainSmart 5000



Figure 516: Visible crack after the peak load

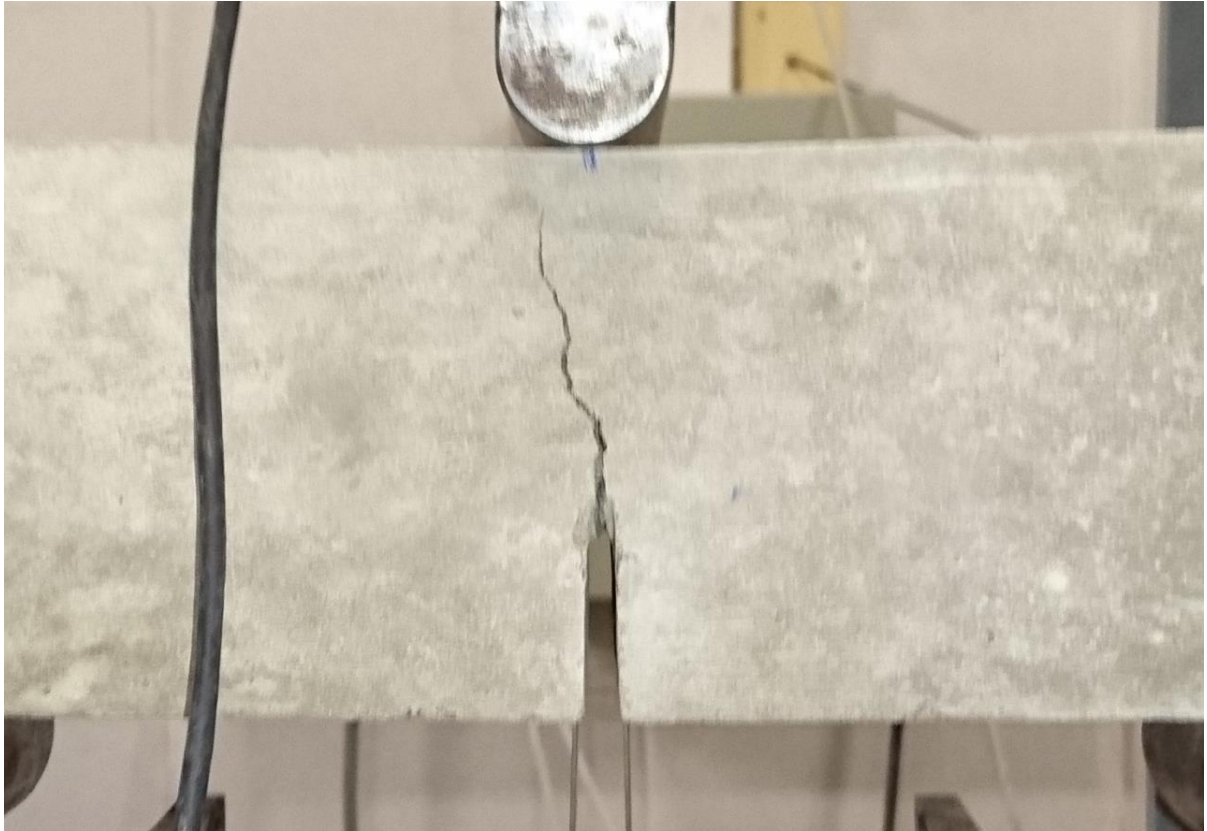


Figure 517: Crack at an advanced stage of the test, near the end of it



Figure 518: Result of a three-point bending test

The author:

Santiago Rodríguez Lorente

Girona, Monday 13th June 2016